12th international conference on flow-induced vibration

Charbel Habchi, Pierre Moussou, Laurent Zimmer

Proceedings of the 12th International Conference on Flow-Induced Vibration

cea
CentraleSupélec
université PARIS-SACLAY
cnrs
EDF
ÉCOLE POLYTECHNIQUE
IP PARIS
IMSIA

Editors :

C. Habchi - P. Moussou
IMSIA, CNRS-EDF-CEA-ENSTA
EDF Recherche et Développement 7 boulevard
Gaspard Monge, 91120 Palaiseau
France

Proceedings of the 12th International Conference on Flow-Induced Vibration
ISBN : 979-10-699-9682-3

Foreword

Flow-Induced Vibration remains a challenge for design engineers and operators across multiple industries, including vehicle manufacturing and power production, among many others. Despite decades of research and development, there is still much to be learned in this domain. Specific areas warrant special attentions, such as fluid-elastic instability of tube bundles, multiphase flows and their effects on flexible structures, vortex shedding in their many manifestations, and the intricacies of axial flow instabilities. Even seemingly simple scenarios, like a single cylinder in crossflow, continue to intrigue researchers, leading to the publication of new scientific articles.

The first European conference of the cycle took place in Keswick in 1973, and despite the wonderful advancement in measuring techniques and computer simulations, the today's reader venturing into the proceedings will sense a strong connection with the physical approaches and the presentation of the results. This is the mark of a genuine and thriving knowledge lineage passed down from teacher to scholar. Lessons from the past are valuable when derived from high-quality articles; an undergraduate student in 2022 can still grasp the fundamentals of vibrations by reading Theory of Sound.

After attending the conferences in Luzern (2000), Paris (2004), Prag (2008), Dublin (2012), and The Hague (2016), where I had the opportunity of meeting wonderful people and excellent scientists, I feel greatly honored and grateful to have had the privilege of organizing the 12th conference of the cycle. My sincere thanks go to the Scientific Committee, who supported the event despite the sanitary constraints of the Covid period and the subsequent postponements from 2020 to 2021, and from 2021 to 2022. Their constant assistance and their scientific rigor have greatly contributed to the high quality of the final papers.

To William, Jordan, Aurélien, Adela, Charbel, Laurent, Marie-Line, Sophie, Maud, Domenico, Romain, and all members of the Organizing Committee, I extend my heartfelt gratitude for taking on the challenge of organizing a conference during the Covid period, where the submission deadline had to be extended beyond the norm. The delayed delivery of the paper proceedings was a direct consequence of this courageous decision, with the last revised submission occurring after the event commenced. Your hard work made the event possible, in good spirits and in a relaxed atmosphere, facilitating fruitful exchanges, altogether with high-level scientific discussions. Encore merci à vous tous.

A further expression of gratitude is owed to Prof. Sébastien Candel, who honored us by inaugurating the conference and providing a comprehensive overview of the field of Flow-Induced Vibration. His confidence in the merits and the perspective of modern mechanics as a thriving science is inspiring.

As the 2022 conference was held in Paris, near the Ecole Polytechnique and the Commissariat à l'Energie Atomique[CH3] , it is essential to pay homage to the memory of René-Jean Gibert (1942-2020), who was a French pioneer in the domain and who

contributed to the education of many scientists and engineers. While he may not be famous outside France, his exceptional talent for explaining to explain complicated vibration patterns in industrial facilities through a mere single degree of freedom oscillator, coupled with the adequate physical analogies, makes him a distinguished member of the community.

Let us not to forget our sponsors: the Commissariat à l'Energie Atomique, whose generous contribution aided in organizing the event; Electricité de France, who provided their facilities in Palaiseau; and the Centre National de la Recherche Scientifique, who also contributed and hosted the conference website through the laboratory IMSIA, serving as the treasurer of the event. Special thanks are owed to Matthias Heil, the editor of the Journal of Fluids and Structures, who agreed to feature extended papers in a special issue of the Journal.

Allow me to share a few words about future conferences. First of all, I am convinced that there is no such a thing as an online international conference. The earth is just not flat enough to conveniently accommodate participants from Europe, the Americas and Far-East at the same time.[CH4] The question of keeping an alternance of European and American cycles or to merge merging them lies in the hands of the Scientific Committee. My personal opinion is that the major issue lies in having people from all around the world to meet together during the conferences.

Is the field of Flow-Induced Vibration at risk of stagnation in the coming decades? As long as poorly inspired decision-makers continue to increase the flow velocity and reduce the thickness of pressure vessels to boost the profitability of industrial facilities, there will be no shortage of Flow-Induced Vibration challenges, along with an array of new phenomena to study. Furthermore, the technical challenge of reducing greenhouse gas emissions will require the development of new facilities and processes, introducing a host of new vibrations to be studied in the future.

A final crucial requirement for future conferences is to maintain a harmonious blend of attendees from both academia and industry. This is a somehow unique feature of the Flow-Induced Vibration community which made it successful its success in the past and will continue to be so in the future.

For the organizers,
P. Moussou
Palaiseau
July 2023

Scientific committee

Gustavo Assi, Brazil

Yves Aurégan, France

László Baranyi, Hungary

Peter Bearman, Great Britain

Stefan Belfroid, The Netherlands

Sofiane Benhamadouche, France

Emmanuel de Langre, France

Christophe Eloy, France

Hugh Goyder, Great Britain

Ramiro Godoy-Diana, France

Charbel Habchi, France

Marwan Hassan, Canada

Mico Hirschberg, The Netherlands

Shigehiko Kaneko, Japan

Randolph C. R. Leung, P. R. of China

Craig Meskell, Ireland

Yahya Modarres-Sadeghi, USA

Atef Mohany, Canada

Sergio Möller, Brazil

Njuki Mureithi, Canada

Peter Oshkai, Canada

Michael Païdoussis, Canada

Petr Sidlof, Czech Republic

David Sumner, Canada

Dave Weaver, Canada

Sponsors

Organizing committee

Jose Antunes, Universidade de Lisboa, CEA
William Benguigui, EDF R&D, IMSIA
Marie-Line Bonnialy, EDF R&D, IMSIA
Jordan Curt, EDF R&D, IMSIA
Charbel Habchi, EDF R&D, IMSIA
Aurélien Joly, EDF R&D, IMSIA
Maud Kocher, EDF R&D, IMSIA
Romain Lagrange, CEA, IMSIA
Pierre Moussou, EDF R&D, IMSIA
Domenico Panunzio, CEA, IMSIA
Maria-Adela Puscas, CEA
Sophie Ramananarivo, École Polytechnique, LadHyX
Laurent Zimmer, CentraleSupélec, EM2C

Table of contents

Start time	Tuesday, 5th			
8h30	Authors breakfast - The authors delivering a speech on Tuesday are invited to meet their chairman in order to have their presentations ready.			
9h00	Registration and breakfast			
9h30	A word of welcome			
10h00	**S. Candel**, French Academy of Science			
10h30	Break			
11h00	**Chair: M. Hassan**		**Chair: L. Baranyi / Amphithéâtre 1**	
	BB1	Dimensioning of a solar tracker torque tube for torsional galloping, **Martínez García E., Parrondo Gayo J., Blanco Marigorta E., Navarro Manso A.**	AL1	Impact of the nozzle geometry on the aeroelastic instability of a plate subjected to an air jet, **Tatin A., Cluzel X., Mourlot Y., Hémon P., Ramananarivo S.**
	BB4	Study of the oscillation process and the wake resulting from the accelerated flow over two free-to-rotate tandem cylinders and the effect of a perturbation applied on the flow, **Habowski P., Fiorot G., Neumeister R., Möller S.**	FSI-AL2	The Effects of a Passive Tail on Escape Performance in a Robotic Fast-Start Fish Capable of Rapid Underwater Locomotion, **Currier T., Modarres-Sadeghi Y.**
	BB6	Vortex-induced vibration of a circular cylinder subjected to low-Keulegan-Carpenter-number oscillatory flow, **Dorogi D.**	FSI-AL1	Quantitative Flow Imaging Approach to Unsteady Loading on High-Inertia Oscillating Foils, **Oshkai P., Lee W., Iverson D., Rahimpour M.**
	BB7	Vortex-Induced Vibrations of a One-Degree-of-Freedom Cylinder Transitioning from the Inline to the Crossflow Direction, **Benner B., Modarres-Sadeghi Y.**	FV1	Simultaneous control rod 3D displacement and 3D flow measurements via time resolved 3D3C PTV with one camera only, **Fichet V., Daoudi M., Zimmer L.**
12h30	Lunch			
14h00	Vibration in steam generators - **Prof. M. Hassan**, Guelph University			
15h00	Break			
15h30	**Chair: P. Hémon**		**Chair: M. Hirschberg / Amphithéâtre 1**	
	TV3	Flow-induced vibrations of a flexibly mounted cylinder in the proximity of a stationary parallel cylinder, **Riazat M., Kheiri M., Vermeire B.C.**	FSI3	Developing numerical methods for predicting flow-induced underwater radiated noise from ships, **Mcintyre D., Oshkai P.**
	TV6	GO-VIKING: a HORIZON europe project on flow-induced vibrations, **Zwijsen K., Papukchiev A., Vivaldi D., Hadzic H., Benhamadouche S., Benguigui W., Planquart P.**	FSI2	Articulated beam behaviour under grazing flow, **Abily T., Humbert T., Aurégan Y.**
	TV8	Numerical prediction of Axial-Flow-Induced Vibrations in nuclear fuel rod, **Salachna J., Cioncolini A., Iacovides H.**	FSI1	A Perforated Plate Solution to Mitigate Relief Valve Piping Vibration due to Flow-Excited Acoustic Resonance, **Pontaza J., Menon R.**
	CF2	Passive control of the turbulent flow past a finite circular cylinder fitted with eight peripheral rods, **Carvalho I., Assi G.**	FSI4	Direct measurements of the dynamic lift force acting on rectangular rods in cross-flow during acoustic resonance excitation, **Shoukry A., Mohany A.**
	CF1	Experimental investigation on the optimal control of vortex shedding of a circular cylinder with rotating rods at moderate Reynolds numbers, **Silva P., Assi G.**	FSI9	Using flow to control the damping of a resonant duct, **Humbert T., Aurégan Y.**
17h30	End of the day			

Start time	Wednesday, 6th			
8h30	Authors breakfast - The authors delivering a speech on Wednesday are invited to meet their chairman in order to have their presentations ready.			
9h00	**Chair: S. Möller / Auditorium**		**Chair: C. Habchi / Amphithéâtre 1**	
	TA4	On the stability of the rotated square array in two-phase flow using the quasi-steady model, **Darwish S., Mureithi N., Cho M.**	CFD5	FSI simulations of fluid-elastic instabilities of a clamped-clamped cylinder in axial flow, **Delcour L., Dolfen H., Van Langenhove L., Degroote J.**
	TA2	Experimental investigation of cross-flow fluidelastic instability for rotated triangular tube bundles subjected to single-phase and two-phase transverse flows, **Panunzio D., Lagrange R., Piteau P., Delaune X., Antunes J.**	CFD2	A practical approach to using CFD as an early design tool for estimating aerodynamic force coefficients of bridge decks, **Duranovic M., Dempsey T., Meskell C.**
	TA5	Theoretical and experimental study on the fluidelastic instability of rod bundle subjected to jet cross-flow, **Gadelhak I., Mureithi N., Karazis K.**	CFD3	CFD analysis of two-phase flow induced forces on a test flow loop, **Emmerson P., Lewis M., Barton N.**
	BB3	Influence of a control wire on vortex shedding from side-by-side cylinders, **Hammad O., Mohany A.**	CFD1	A discrete forcing method to solve hyperelastic deformation induced by two-phase flow, **Merigoux N., Benguigui W., Baraglia F.**
	BB5	Unsteady wall pressure measurements on a full scale flexible chimney subject to natural wind, **Manal Y., Hémon P.**	CFD7	Multi-scale methodology for the large eddy simulation of steam control valves, **Galpin J., Amice B., Goreaud N., Leconte G., Joly A., Moussou P., Glau A.**
11h00	Break			
11h30	The way of the SDOF – A tribute to R. J. Gibert,			
12h30	Lunch			
14h00	Smart morphing and sensing for aeronautical configurations - **Prof. M. Braza**, Institut de Mécanique des Fluides de Toulouse			
15h00	Break			
15h30	**Chair: J. Antunes / Auditorium**		**Chair: P. Oshkai / Amphithéâtre 1**	
	SM2	Wind Energy Harvesting from Flow-Induced Vibration of Prisms Using Magnetostrictive Material, **Heragy M., Kiwata T., Shima T., Kono T., Hamano T., Ueno T., Ekmekci A.**	FSI5	Flow structure, dynamic lift force, and aeroacoustic response of finned cylinders in cross-flow, **Alziadeh M., Mohany A.**
	SM1	Pressure Driven Soft Vortex Generator, **Khanjian A., Habchi C., Russeil S., Bougeard D., Lemenand T.**	FSI6	Flow-induced tones in a deep periodic cavity, **Golliard J., Aurégan Y.**
	TV5	Fluid structure interaction in a pressure vessel: turbulent forcing, **Kocher M., Moussou P., Panunzio D., Lagrange R., Joly A.**	FSI7	On broad-band noise of thick square-edged orifices in water-pipe flow, **Kottapalli S., Hirschberg A., Waterson N., Smeulders D., Nakiboglu G.**
	TV4	Fluid structure interaction in a pressure vessel: a multipole approach for acoustic analysis, **Moussou P., Kocher M., Panunzio D., Lagrange R., Joly A.**	FS8	The aeroacoustics repsonse of cylindrical cavities in confined flow, **Hanna M., Mohany A.**
17h10	End of the day			
19h30	Conference dinner			

Start time	Thursday, 7th			
8h30	Authors breakfast - The authors delivering a speech on Thursday are invited to meet their chairman in order to have their presentations ready.			
9h00	**Chair: G. Assi / Auditorium**		**Chair: A. Mohany / Amphithéâtre 1**	
	TV1	Aspects of vortex-induced in-line vibration at low Reynolds numbers, **Konstantinidis E., Dorogi D., Baranyi L.**	AF1	Aeroelastic effects in a planar flat blade cascade at high Mach number flow, **Šidlof P., Šimurda D., Lepicovsky J., Štěpán M., Vomáčko V.**
	TV9	Numerical simulation of cantilever cylinders in cross-flow: participation to the OECD/NEA fluid-structure interaction benchmark, **Zwijsen K., Hussain M., Roelofs F., Van Zuijlen A.**	CFD6	Modelling vortex induced vibrations in a model of the northern spire bridge, **Duranovic M., Dempsey T., Meskell C.**
	TV10	Numerical simulations of experimental fluid-induced vibrations of cylinders in cross-flow, **Vivaldi D., Ricciardi G.**	MF6	Two-phase flow induced vibration in a tube bundle of steam generators, **Fichet V., Khaddaj Mallat B., Mourgues A., Moulin J., Andrzejewski Q.**
	TV7	In wind tunnel simulation of vortex shedding behind circular cylinders at high reynolds number regimes is incomplete, **Hémon P., Ellingsen O., Amandolese X.**	MF2	Experimental investigation of void fraction distribution behind a cylinder, **Benguigui W., Pinto C., Ries O.**
	TV2	Experimental investigation of vortex-induced vibrations of a circular cylinder under rotary oscillations, **Schmider A., Kerherve F., Cordier L., Spohn A.**	MF1	A new experimental facility for two phase flow characterization in a tube bundle and vibration study, **Spina G., Vivaldi D., Brillant G., Colin C., Benguigui W., Denèfle R., Lelong M.**
11h00	Break			
11h30	Damping in fluids and structures - **Dr. H. G. D. Goyder**, Cranfield University			
12h30	Lunch			
14h00	Free afternoon, with optional tourist tours - The local committee will be pleased to assist attendees in visiting famous and less known places around Paris.			

Start time	Friday, 8th			
8h30	Authors breakfast - The authors delivering a speech on Friday are invited to meet their chairman in order to have their presentations ready.			
9h00	Uses of potential flow solutions in fluid-structure interaction - **Prof. Ch. Eloy**, IRPHE Marseilles			
10h00	Break			
10h30	**Chair: C. Habchi / Auditorium**		**Chair: P. Šidlof / Amphithéâtre 1**	
	MF4	High pressure multiphase induced vibrations: influence of pipe orientation, **Belfroid S., Gonzalez-Diez N., Lunde K., Orre S.**	BIO1	Mitigating jet cross-flow induced vibrations using a bio-inspired nozzle, **Gadelhak I, Mureithi N., Karazis K.**
	MF3	Forces and displacements in a bend subjected to an air-water flow, **De Moerloose L., Dolfen H., De Paepe M., Degroote J.**	BIO2	Self-Oscillating Hydrogel-Based Vocal Fold Models for Voice Production Research, **Thomson S., Greenwood T.**
	MF5	Periodic Wake Shedding of Tube Bundles Subjected to Two-Phase Cross Flow, **Taylor C., Pettigrew M.**	TA3	Experimental investigation of in-flow fluidelastic instability for rotated triangular tube bundles subjected to single-phase and two-phase transverse flows, **Antunes J., Piteau P., Delaune X., Panunzio D., Lagrange R.**
	DSS1	Development of an efficient calculation technique for dynamics of mooring lines by using discrete forms of rotation, **Hara K., Shimojima K., Yamaguchi T.**	TA6	Transient vibration phenomenon due to passing of gap vortex street in FSI simulation of tube bundle with eccentricity, **Dolfen H., Degroote J.**
	DSS2	Performance of a Closed Cycle Power Take Off for Mutriku breakwater, **Bellec M., Gurhy C., Gibson L., Meskell C.**	TA1	A new criterion for the instability threshold of a square tube bundle subject to an air-water cross-flow, **Lagrange R., Panunzio D., Piteau P., Delaune X., Antunes J.**
12h30	Lunch			
14h00	**Chair: G. Assi / Auditorium**		**Chair: Y. Aurégan / Amphithéâtre 1**	
	BB8	Wake induced vibration in tandem cylinders: part 1- wake perturbation analysis, **Neumeister R., Ost A., Habowski P., De Paula A., Petry A., Möller S.**	AF2	Axial flow damping investigation by means of 2D CFD, **Berland J., Corre S., Joly A., Martin A.,Moussou P.**
	BB9	Wake induced vibration in tandem cylinders: part 2 - hilbert-huang spectral analysis, **Ost A., Neumeister R., Petry A., Möller S.**	AF3	Dynamics of cantilevered pipes conveying fluid and subjected to reverse annular external flow: experimental investigation of the influence of external flow confinement, **Chehreghani M., Shaaban A., Misra A., Paidoussis M.**
	BB2	Flow-induced vibration of a circular cylinder transverse to oscillatory flow at a high Keulegan-Carpenter number, **Dorogi D., Baranyi L., Konstantinidis E.**	CFD4	Dynamic response of a cantilevered pipe aspirating fluid and subjected to reverse confined external flow: a computational coupled two-way fluid-structure interaction analysis, **Daneshmand F., Liaghat T., Paidoussis M.**
16h00	End of the congress			

Plenary

DAMPING IN FLUIDS AND STRUCTURES

Hugh Goyder
Cranfield University, Shrivenham, United Kingdom

ABSTRACT

All flow-induced vibration problems involve damping. Damping removes energy from a vibrating system and controls the amplitude of vibration when a structure is vibrating in resonance. For instabilities it controls the threshold of stability. It is therefore important as the only mechanism preventing excessive vibration; however, it is a difficult parameter to determine if definite values are needed. In general damping cannot be predicted and it is necessary to take measurements if confidence in a value is required. Damping from various sources are discussed and it is shown that damping from a fluid is generally small. Several measurement strategies are reviewed including methods that are appropriate for linear and nonlinear systems. A new method which involves filtering the time history of vibration decay is presented.

1. INTRODUCTION

Damping is often a key parameter when considering flow-induced vibration and noise in engineering system. However, it remains an elusive parameter if definite values must be found for calculations or assessment purposes.

The objective of this paper is to identify why dealing with damping is important and why it is so difficult to find appropriate values.

The standard vibration mechanisms for flow-induced vibration are buffeting, vortex shedding and instabilities. Each of these mechanisms requires an understanding of damping and standard assessment formula all contain the damping of the structure being considered. For acoustic-structure interaction both the damping of the acoustic system and the structure need to be identified. Consequently, it would be expected that much is known about damping. However, damping continues to be one of the least well understood parameters in flow-induced vibration problems.

Damping is one of the structural parameters that cannot be predicted using simulation methods and if reliable structures are to be build experimental work is required to obtain damping values. This places a large burden upon development work.

This paper starts by describing how damping enters into structural dynamic models. Examples are then given of experiments which have sought to determine damping for flow-induced vibration mechanisms.

The paper concludes with a novel method for extracting damping which is applicable for linear and nonlinear systems.

2. DEFINITION OF DAMPING

A very clear definition of damping is needed particularly when dealing with nonlinear systems. To put the definition into context three items can be defined.

i) Vibration is due to the interchange of kinetic and potential energy within a structure.
ii) Damping is any mechanism that permanently removes energy from a vibrating system.
iii) In the case of flow-induced vibration and noise there may also be an input of energy from a fluid flow or acoustic source.

Damping is important because it permanently removes energy from a vibrating system. It is therefore the reason why amplitudes of vibration may be limited and not grow to excessive values.

3. WHY DAMPING IS DIFFICULT

The effect of damping is difficult to observe because the energy removed by damping is small compared to the energy being interchanged between kinetic and potential states. Consider the standard linear single degree of freedom structure which has the differential equation

$$\ddot{x} + 2\zeta\omega_0\dot{x} + \omega_0^2 x = f/m \qquad (1)$$

where x is the displacement, ω_0 the natural frequency, ζ the damping ratio, f the applied force and m the mass. Then the energy dissipated in one cycle divided by the total energy in the system is given by

$$4\pi\zeta = \frac{Energy\ dissipated\ in\ onecycle}{Energy\ stored\ in\ system} \qquad (2.)$$

Values of damping ratio are usually small with typical values for engineering structures in the range $\zeta = 0.001$ to 0.01. Values may be smaller than this for some structures. Consequently, any measurements being made are attempting to measure a small force within a background of larger forces.

The two cases where damping shows up are at resonance and in free decay. For harmonic excitation, the single degree of freedom system in Equation 1 has the solution

$$\frac{X}{F} = \frac{1}{m\left(\omega_0^2 - \omega^2 + 2\,i\,\zeta\,\omega\,\omega_0\right)} \qquad (3)$$

where X is the amplitude of the displacement and F the amplitude of the response. Also, m, ω_0, ω and ζ are the mass, natural frequency, excitation frequency and damping ratio of the of the oscillator. Finally, i is the imaginary unit. When the excitation frequency is equal to the natural frequency the vibration amplitude is given by

$$\frac{X}{F} = \frac{1}{m\,2\,i\,\zeta\,\omega_0^2} = \frac{1}{2\,i\,\zeta\,k} \qquad (4)$$

where k is the stiffness in the oscillator. This simple equation shows that at resonance the amplitude is proportional to the reciprocal of the damping ratio. It is this fact that makes damping such a key parameter in all vibration work.

It is revealing to plot the reciprocal of the real and imaginary parts of Equation 3. These are shown in Figure 1. The very different scales between the real and imaginary parts should be noted again emphasizing how the damping is generally small compared to the inertia and stiffness forces. The real part goes to zero at the resonance frequency as the inertia and stiffness forces cancel each other and in a small interval around the resonance the imaginary part is larger than the real part. This interval is given by

$$\omega_0(1-\zeta) < \omega < \omega_0(1+\zeta) \qquad (5)$$

which is known as the bandwidth of the resonance. The form of plotting data in Figure 1 provides a good method for measuring the natural frequency and damping ratio. The procedure is to fit the data with the simple function the reciprocal form provides. The method is described in Ewins (2000).

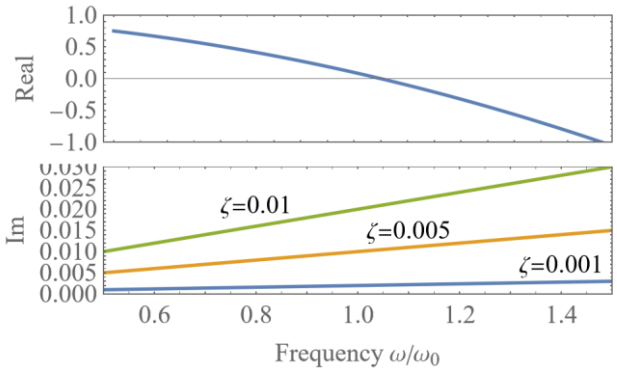

Figure 2. The real and imaginary parts of the reciprocal of a frequency response function. Note the very different scales of the real and imaginary parts.

The second method for exposing damping is to use a free decay. An example of a measured free decay is given in Figure 2. In this case the decay is nonlinear which may be seen from the envelope which is not an exponential decay.

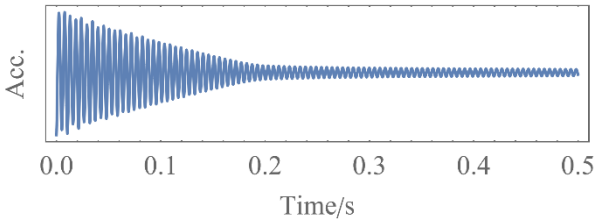

Figure 2. Time history of the free decay of vibration. The structure is nonlinear

The time history of a vibration decay is a good method for observing damping. The dominant mechanism continues to be the inertia and stiffness which controls the frequency giving rise to the sinusoidal motion. The effect of damping is small and may be seen in the decrease in amplitude in each cycle. Further discussion on how damping data can be extracted from time histories is given in Section 9.

In summary a damping force is difficult to observe because it is usually dominated by inertia and stiffness forces.

4. DAMPING IN SYSTEMS

When a structure has several degrees of freedom it is difficult to include damping. The starting point is to consider a linear system with no damping. This may be represented by a mass matrix, $\boldsymbol{M}$ and a stiffness matrix, $\boldsymbol{K}$. The equation for the system is then

$$\boldsymbol{M}\,\ddot{\boldsymbol{y}} + \boldsymbol{K}\,\boldsymbol{y} = \boldsymbol{f} \qquad (6)$$

Where $\boldsymbol{y}$ is the displacement vector and $\boldsymbol{f}$ a vector of forces. Both $\boldsymbol{M}$ and $\boldsymbol{K}$ are generally full symmetric matrices. Such a system can be simplified by performing an eigen decomposition. This decomposition provides a transformation matrix, $\boldsymbol{R}$, which can be applied to the physical coordinates to give new set of transformed coordinates. The transformation is also applied to the force so that work done can be expressed in terms of the new coordinates. The new coordinates and the new version of Equation 6 are then

$$\begin{aligned} &\text{with } \boldsymbol{y} = \boldsymbol{R}\,\boldsymbol{q} \quad \text{and } \boldsymbol{R}^T\boldsymbol{f} = \boldsymbol{p} \\ &\boldsymbol{R}^T\boldsymbol{M}\,\boldsymbol{R}\,\ddot{\boldsymbol{q}} + \boldsymbol{R}^T\boldsymbol{K}\,\boldsymbol{R}\,\boldsymbol{q} = \boldsymbol{p} \end{aligned} \tag{7}$$

When the products $\boldsymbol{R}^T\boldsymbol{M}\,\boldsymbol{R}$ and $\boldsymbol{R}^T\boldsymbol{K}\,\boldsymbol{R}$ have are calculated the matrices become diagonal so the equations take the form

$$\begin{pmatrix} m_1 & 0 & 0 & 0 \\ 0 & m_2 & 0 & 0 \\ 0 & 0 & m_3 & 0 \\ 0 & 0 & 0 & \dots \end{pmatrix}\begin{pmatrix} \ddot{q}_1 \\ \ddot{q}_2 \\ \ddot{q}_3 \\ \dots \end{pmatrix} + \begin{pmatrix} \omega_1^2 m_1 & 0 & 0 & 0 \\ 0 & \omega_2^2 m_2 & 0 & 0 \\ 0 & 0 & \omega_3^2 m_3 & 0 \\ 0 & 0 & 0 & \dots \end{pmatrix}\begin{pmatrix} q_1 \\ q_2 \\ q_3 \\ \dots \end{pmatrix} = \begin{pmatrix} p_1 \\ p_2 \\ p_3 \\ \dots \end{pmatrix} \tag{8}$$

where the diagonal elements are m_n and $\omega_n^2 k_n$. This is clearly very useful since the diagonal equations can be solved individually. They are uncoupled.

When damping is included the matrix equation for the system becomes

$$\boldsymbol{M}\,\ddot{\boldsymbol{y}} + \boldsymbol{C}\,\dot{\boldsymbol{y}} + \boldsymbol{K}\,\boldsymbol{y} = \boldsymbol{f} \tag{9}$$

Where $\boldsymbol{C}$ is a symmetric matrix of damping values. Unfortunately, it is not possible to find a transformation that diagonalizes all three of the matrices in Equation 9. One approach is to apply the transformation as in Equation 7 so that it reads

$$\boldsymbol{R}^T\boldsymbol{M}\,\boldsymbol{R}\,\ddot{\boldsymbol{q}} + \boldsymbol{R}^T\boldsymbol{C}\,\boldsymbol{R}\,\dot{\boldsymbol{q}} + \boldsymbol{R}^T\boldsymbol{K}\,\boldsymbol{R}\,\boldsymbol{q} = \boldsymbol{p} \tag{10}$$

Or with the elements written out

$$\begin{pmatrix} m_1 & 0 & 0 & 0 \\ 0 & m_2 & 0 & 0 \\ 0 & 0 & m_3 & 0 \\ 0 & 0 & 0 & \dots \end{pmatrix}\begin{pmatrix} \ddot{q}_1 \\ \ddot{q}_2 \\ \ddot{q}_3 \\ \dots \end{pmatrix} + \begin{pmatrix} c_{11} & c_{12} & c_{13} & \dots \\ c_{21} & c_{22} & c_{23} & \dots \\ c_{31} & c_{32} & c_{33} & \dots \\ \dots & \dots & \dots & \dots \end{pmatrix}\begin{pmatrix} \dot{q}_1 \\ \dot{q}_2 \\ \dot{q}_3 \\ \dots \end{pmatrix} + \begin{pmatrix} \omega_1^2 m_1 & 0 & 0 & 0 \\ 0 & \omega_2^2 m_2 & 0 & 0 \\ 0 & 0 & \omega_3^2 m_3 & 0 \\ 0 & 0 & 0 & \dots \end{pmatrix}\begin{pmatrix} q_1 \\ q_2 \\ q_3 \\ \dots \end{pmatrix} = \begin{pmatrix} p_1 \\ p_2 \\ p_3 \\ \dots \end{pmatrix} \tag{11}$$

The damping matrix continues to be full. One approach is to ignore the off-diagonal terms thus giving a diagonal matrix which is easy to manipulate. This is unsatisfactory and does not enable coupled problems to be modelled.

5. ADDING DAMPING CAN CHANGE-NUMBER OF DEGREES OF FREEDOM

The number of degrees of freedom for a system without damping is given by the number of coordinates that are required to define the position of each mass. Adding damping can change the number of degrees of freedom required to model the system. In Figure 3 (a) there is a standard single degree of freedom system. One coordinate is required to specify the position of the mass, spring and damper. In Figure 3 (b) a damper has been added that divides the spring into two parts. In order to model this system, it is necessary to have two coordinates; one to model the position of the mass and one to model the position of the lower spring and damper. This is a surprising result.

This simple example shows how complex damping can become and how difficult it is to model.

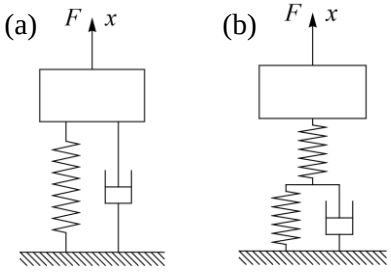

Figure 3. a) A single degree of freedom system with mass, spring and damper. b) The damper divides the spring. This is a two degree of freedom system.

6. DAMPING IN A COUPLED SYSTEM (ACOUSTIC-STRUCTURAL)

An example of a coupled system where damping is important is acoustic excitation of pipework. In these circumstances the fluctuating forces on the pipe bends due to an acoustic wave in a pipe can cause significant structural vibration that can lead to structural fatigue and pipe failure. This problem typically occurs in gas pipelines where pressures may be 100 bar or more. One cause of acoustic waves in pipelines is the presence of corrugated pipes which, because of their flexibility, are used as risers or jumpers Goyder (2010).

The typical pipework configuration where acoustic excitation is a problem is shown in Figure 4. An acoustic standing wave is shown in a side branch of a pipeline. The standing wave has positive and negative lobes which are harmonically varying. The pressure on the waves acts on the pipe bends. Configuration (a) shows the severe case where a positive and negative pressure wave act in unison to promote vi-

bration. In configuration (b) the positive and negative waves act in opposition and do not cause significant vibration.

The system to be investigated is a coupled system involving both the acoustic wave and the pipe vibration. Note that if the acoustic wave can cause vibration in the pipe, then the pipe vibration can also set up an acoustic wave which interacts with the primary wave.

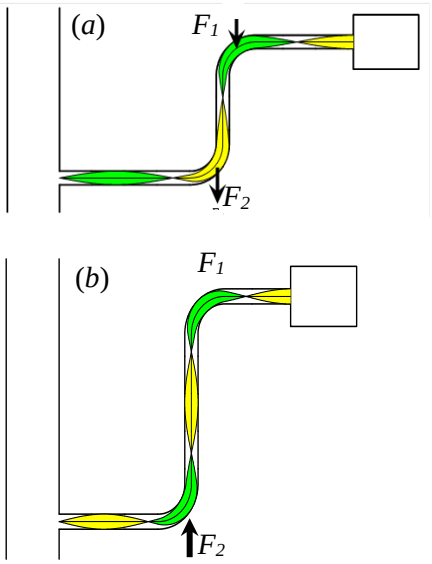

Figure 4. Acoustic standing waves acting on pipe bends; positive and negative pressures shown in differing colours. a) Positive and negative waves both contribute in-phase forces F_1 and F_2 to pipe vibration. b) Pressure at bends applies forces F_1 and F_2 which are out-of-phase and cancel excitation.

A simplified system, which captures the acoustic structure interaction, is shown in Figure 5. Here an acoustic source of strength Q maintains acoustic waves in a pipe of length L and cross section S. Damping in the acoustic system is provided by a small pipe of cross section S_1 which conducts waves to infinity. The pipe is modelled by a mass-spring-damper system. The stress in the pipe system, is equivalent to the force in the spring.

The equations describing this system are given in the appendix. When assessing such a system the concern is when a structural natural frequency matches the acoustic system. As the system is coupled the structural and acoustic natural frequencies can't be treated separately. This is shown in Figure 6.

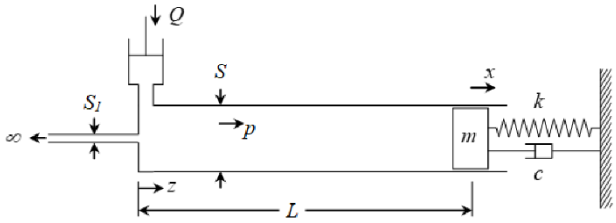

Figure 5. Simple model of acoustic structure interaction. Acoustic waves in the pipe of length L act on the mass-spring-dashpot system. The acoustic source Q maintains the vibration while the small pipe of cross section area S_1 removes some acoustic energy thus modelling acoustic damping.

The equations describing this system are given in the appendix. When assessing such a system the concern is when a structural natural frequency matches the acoustic system. As the system is coupled the structural and acoustic natural frequencies can't be treated separately. This is shown in Figure6

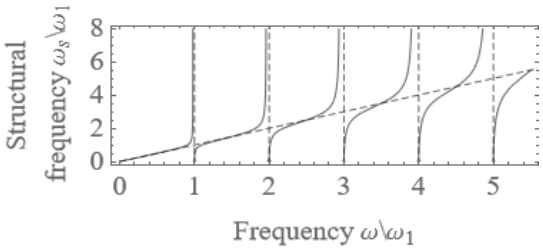

Figure 6. Coupled acoustic structural natural frequency of the system in Figure. The frequency, normalized by the first uncoupled acoustic natural frequency is given on the horizontal axis. The vertical axis covers a range of uncoupled structural frequencies. The dashed lines are the natural frequencies of the uncoupled system

Here the vertical dashed lines correspond to the uncoupled acoustic natural frequencies. The dashed diagonal line corresponds to the to the structural natural frequency which is varied as a parameter and plotted on the vertical axis. As can be seen when the acoustic and structural system are coupled the curve starts aligned with the structural system and veers to the acoustic system near the intersection of the uncoupled system.

If a simulation is performed by choosing one particular structural frequency and including damping, then a frequency response function may be calculated. Figure 7 shows such a response spectrum calculated for a case near the intersection of the uncoupled first acoustic natural frequency and structural frequency. There are two peaks. This should be expected since the combination of a structural and acoustic system generates a two-degree of freedom system.

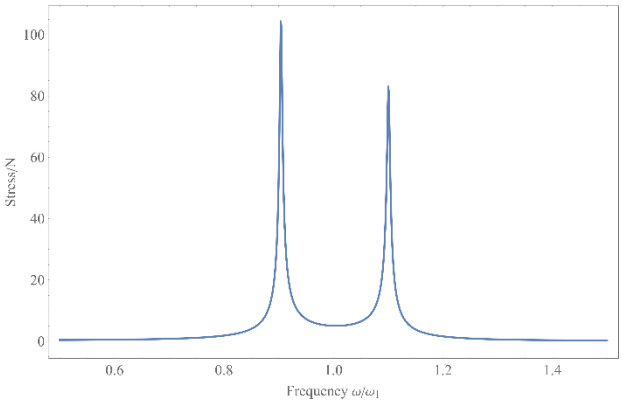

Figure 7. Frequency spectrum of coupled acoustic structural system near first acoustic resonance.

Although the peaks in Figure 7 indicate a large stress they do not capture the maximum stress. This is a danger of doing a simple simulation without doing a full exploration. In fact, the maximum stresses seen by this system are 63% and 48% larger than those given in the spectrum of Figure 7. A detailed analysis, that looks at a range of structural natural frequencies that are close to the acoustic natural frequencies, is shown in Figure 8.

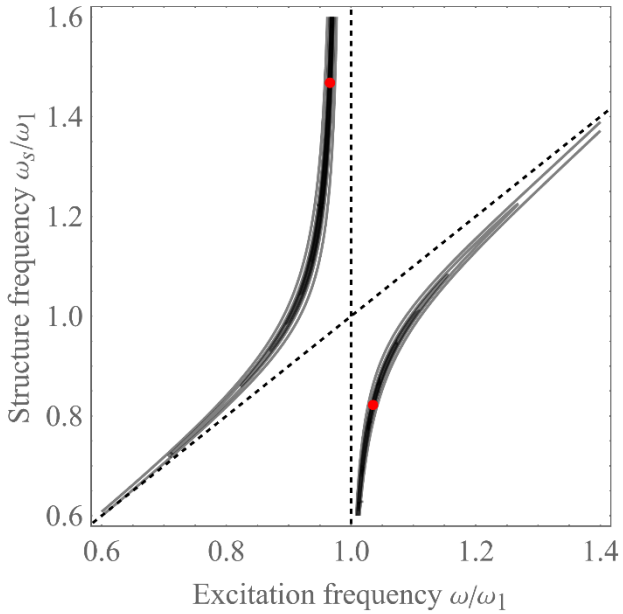

Figure 8. Contour plot of response of coupled acoustic structural system. The diagonal lines are the frequencies of the uncoupled system. The red dots indicate where the response is a maximum.

Although the system shown in Figure 5 is straight forward the system as a whole is very complicated. After expressing the key parameter as nondimensional groups there are five parameters. These are the excitation frequency, the coupling parameter, the structural frequency and the damping in the structural and acoustic system.

Clearly understanding this interaction is not simple and attempting to make a structural integrity assessment is not going to be straightforward. Further, the parameters that need to be determined before an assessment may be made are the damping of both the acoustic and structural system. Data for these parameters is not readily available.

7. DAMPING OF SUBMERGED PIPES

Systems that are underwater are very vulnerable to flow-induced vibration because they cannot be easily inspected, and consequently, they may be experiencing vibration without anyone realizing there is a problem. So called covert excitation. It is sometimes suggested that being immersed in water will add damping and that therefore there is a reduced risk of vibration. However, this is not true.

Figure 9 shows a full-scale pipework system that was tested in air and water. Figure 10 shows a diagrammatic version that gives pipe diameters and support structures.

Figure 9. A full-scale pipework system that was tested in air and also in water.

Frequency response measurements were made at several locations and damping values found by circle fitting the resonance data. In total 33613 values were

measured for the dry condition and 31037 values for the wet conditions.

The damping values are given as damping ratios in Figures 11 and 12. As can be seen there is a wide spread in values. The usual approach is to look at the smallest values since these are the most problematic.

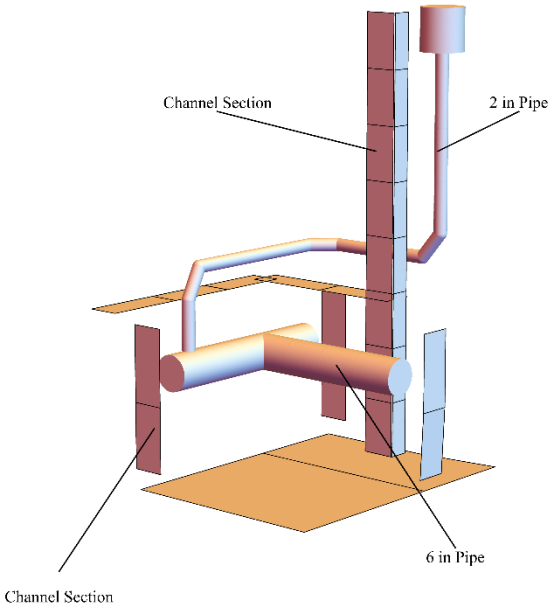

Figure 10. Diagrammatic picture of pipework in Figure 9 showing pipe dimensions.

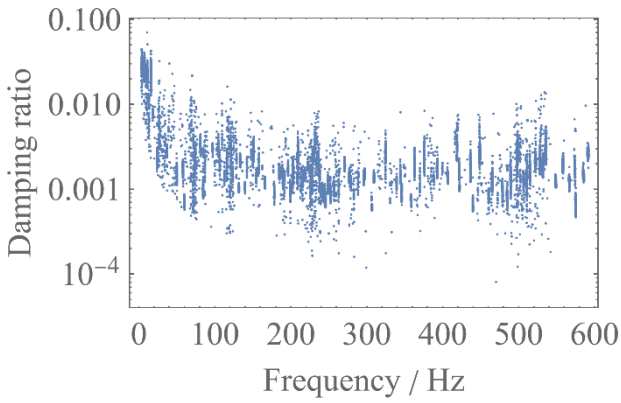

Figure 11. Damping and natural frequency values of pipework in air.

It should be noted that the effect of added mass in water is considerable. When vibrating in water the kinetic energy of the water must be added to the kinetic energy of the pipe. This causes a significant change in natural frequency. When examining the spectra from the experiments in air and water it was not possible to find frequencies and mode shapes that corresponded to an "in air" case being simply shifted to an "in water" case. There was clearly a change in mode shape and number of modes within the frequency range being examined. Consequently, the various friction sites that cause damping were probably being excited in a different manner in both air and water. In addition, the water will enter into pipe supports and other locations with small clearances causing changes in the damping.

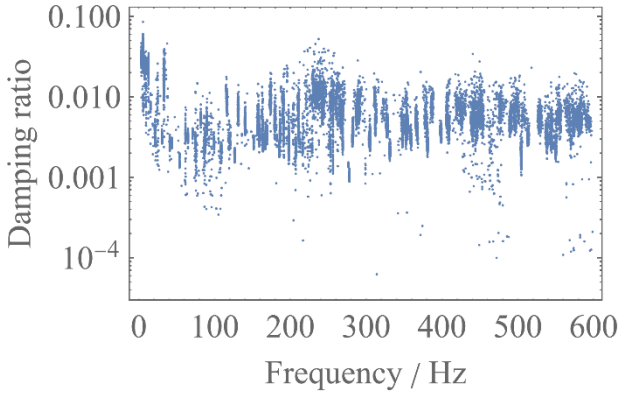

Figure 12. Damping and natural frequencies of pipework in water.

In summary, the damping of the pipework is not changed significantly by being immersed in water. In particular the very small values of damping ratio of about 0.0001 to 0.001 are found in both configurations. Such small damping values are problematic.

8. DAMPING IN A STILL FLUID

How much damping can you get from a fluid? Is it possible to place vanes on subsea systems and thus promote damping? The apparatus in Figure 13 was used to look at the effect of vanes on the vibration of an L-shaped pipe. Figure 14 shows a diagrammatic view of the vanes on the pipe. Three types of vanes were examined. One was solid and the other two had holes with two different pitches. The whole apparatus was in a tank which could be filled to different depths so that the damping could be progressively studied for different depths of water in the tank. The damping was measured by observing the free decay of vibration following an initial impulse on the pipe. Figure 15 shows the damping ratio for different depths of immersion. It can be seen that the damping values are still small despite the vane being of large size relative to the pipe.

An attempt was made to calculate the damping on the vane. This was achieved by first calculating the potential flow around the vane. This is straightforward calculation since an ideal fluid satisfies Laplace's equation. In an ideal fluid there is tangential motion of the fluid next to the surfaces. With a knowledge of the tangential velocity a boundary

layer was assumed and the damping due to the boundary layer calculated. The resulting damping is shown in Figure 15. The theory does not match the experiment well. However, the order of magnitude is correct and this is a very satisfactory result given the usual difficulty in determining damping.

Further details of the experiment can be found in Goyder(2016)

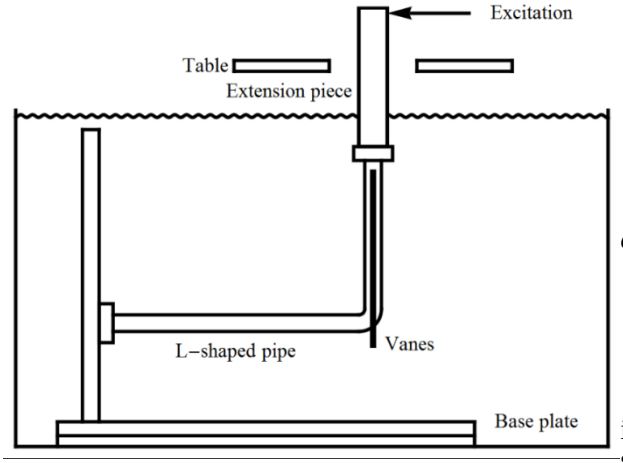

Figure 13. A tank in which an L-shaped pipe could vibrate. Vanes, seen edge on, were attached to the pipe to promote damping.

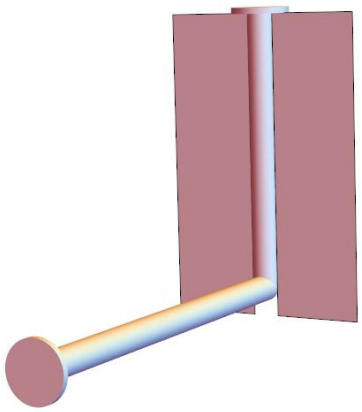

Figure 14. A diagrammatic 3D view of the vanes on the L-shaped pipe shown in figure 13.

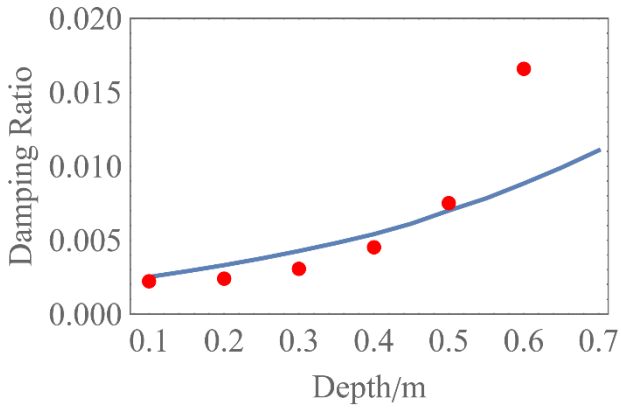

Figure 15. Damping results for the vane. Red dots experiment. Blue line theory.

9. MEASURING DAMPING

Measuring damping accurately is difficult because it only becomes significant, compared to inertial and stiffness forces when resonant conditions are achieved. Consequently, damping is generally only measured in two ways i) by exciting a structure at resonance and observing the maximum values or ii) releasing a structure from an initial condition and observing the vibration decay. These methods are well documented for linear systems. What happens if the system is nonlinear?

Exciting a nonlinear system at resonance using a shaker often reveals changes in the stiffness as the amplitude of vibration is changed. Typically, one can detect changes in stiffness by observing the natural frequency and seeing if this is increased or decreased as the amplitude is changed. However, it is difficult to extract information about the damping. Note that if there are changes in the natural frequency with amplitude then any consideration of bandwidth of the resonance are not valid.

Methods based on random excitation can be successful. Here the nonlinear effects are treated as noise and noise rejection methods are used Goyder (1988).

Methods based on the decay of vibration are very effective when nonlinearities are present. An example of this method, which is still under development, is shown in the following example.

An impact test using a hammer was performed on a bolted structure producing the decay time history shown in Figure 16. The Fourier transform of this time history is shown in Figure17 It is clear that there are peaks which are narrow, but the shape of the peaks is very different from that seen in a linear system. Each peak can be identified as existing mostly

within a narrow frequency band. These frequency bands were noted and used in the following subsequent analysis. The procedure is to return to the time history and to use narrow bandpass filters to breakdown the time history into a set of time histories each one associated with the frequency bands identified in the frequency domain. The result is shown in Figure 18.

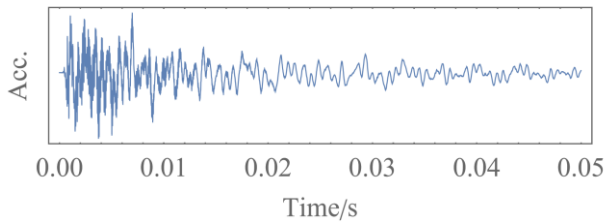

Figure 16. Time history of nonlinear system following impulse excitation.

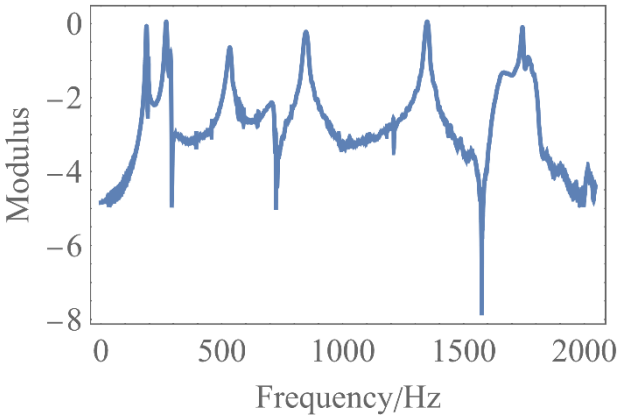

Figure 17. Spectrum of time history shown in Figure 16. Note nonlinear peaks.

Here the time domain responses are easily interpreted. For the first vibration peak there is large damping at large amplitudes but only small amounts of damping as small amplitudes.

The second resonance is revealed as two close natural frequencies. The behaviour at other resonances is easily identified.

An import aspect of the narrow band filtering is that the time histories are reversed before filtering. If they are not reversed then the sudden start of the time history causes oscillations in the filter.

If the structure is linear then the frequency and damping ratio are unaffected by the filtering process. However, if the damping is nonlinear then further signal processing is required to extract instantaneous natural frequencies and damping ratios.

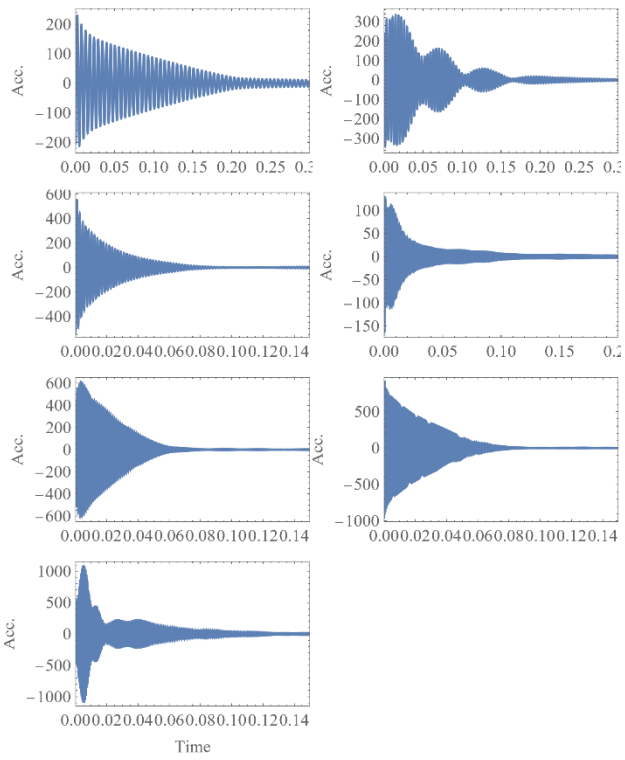

Figure 18. Time histories for the first seven modes extracted from the data in Figure 16.

10. CONCLUSIONS

The following conclusions may be drawn.

1. All flow-induced vibration mechanisms involve damping as a required parameter. This is true for buffeting, vortex shedding, instabilities and acoustic structure interactions.
2. Damping can only be measured if the vibration is in resonant conditions or in free vibration decay. In other conditions forces due to stiffness or inertia dominate over any damping force.
3. Acoustic-structure interaction is particularly difficult because both acoustic and structural damping are important parameters.
4. Immersing a structure composed of pipes and supports in a fluid such as water does not significantly increase the damping.
5. The addition of vanes to a pipe does not significantly add damping as only viscous forces will act.

11. ACKNOWLEDGMENTS

The author acknowledgements the support of Cranfield University in the preparation of this paper.

This paper is being presented as a keynote lecture in 2022. The author acknowledges that he has been rather indulgent in presenting his own work on this topic.

12. REFERENCES

Ewins, D. J. 2000, *Modal testing,* Research Studies Press Ltd. 16 Coach House Cloisters, England SG7 6AE. Section4.7.3

Goyder HGD, 2010. *On the modelling of noise generation in corrugated pipes.* J. Pressure Vessel Technol. Aug 2010, 132(4):

Goyder HGD 2016. *Vibration of vanes in a fluid.* 11th International Conference on Flow-Induced Vibration. 4th -6 th July, The Hague, Netherlands.

Goyder HGD 1988 *An experimental technique for investigating nonlinear structures. Recent advances in Structural Dynamics*. Southampton July 1988 Edited by Petyt, Wolfe and Mei

APPENDIX – EQUATIONS FOR ACOUSTIC STRUCTURE COUPLED SYSTEM

The equations for the coupled system are formulated in the frequency domain. The common frequency of the source, the acoustic waves and the piston system is ω. The position along the pipes is z with $z = 0$ at the left hand end with the main pipe in the region $0 < z < L$. The small pipe is taken to lie in $-\infty < z < 0$. The acoustic pressure, p, in the main pipe is given by

$$p = A_1 e^{-ikz} + A_2 e^{ikz} \tag{A1}$$

where A_1 and A_2 are wave amplitudes, for waves travelling in the positive and negative z directions respectably and k is the acoustic wave number ($k = \omega / c$). In the small pipe the acoustic pressure, p_0, is given by

$$p_0 = B e^{ikz} \tag{A2}$$

where B is the acoustic wave amplitude in the pipe.

The displacement of the piston, X, is given by

$$X = \frac{F}{m\left(\omega_0^2 - \omega^2 + 2i\zeta\omega\omega_0\right)} \tag{A3}$$

where F is the force on the piston, m is the mass of the piston, ω_0 the piston natural frequency and ζ the structural damping ratio. The force in the spring is related to the displacement of the piston by

$$f = \omega_0^2 m \tag{A4}$$

and the force on the piston is given by

$$F = S\, p\big|_{z=L}$$

The boundary conditions for the system are as follows. The pressure at $z = 0$ is equal in the main pipe and the small pipe thus

$$A_1 + A_2 = B \tag{A5}$$

The volume velocity due to source and the waves adds to zero at $z=0$. Thus

$$-\frac{S_1}{i\omega\rho}\frac{\partial p_0}{\partial z}\bigg|_{z=0} + Q = -\frac{S}{i\omega\rho}\frac{\partial p}{\partial z}\bigg|_{z=0} \tag{A6}$$

The velocity of the acoustic waves and the piston are the same at $z=L$. Hence

$$-\frac{1}{i\omega\rho}\frac{\partial p}{\partial z}\bigg|_{z=L} = \frac{i\omega F}{m\left(\omega_0^2 - \omega^2 + 2i\zeta\omega\omega_0\right)} \tag{A7}$$

The acoustic pressures may be substituted into the three boundary conditions to give the values for the wave amplitudes A_1, A_2 and B in terms of the acoustic source term Q. This enables the force on the piston to be determined and hence the force in the spring. These manipulations were undertaken using a computer algebra system (Mathematica [4]) which is essential to avoid slips.

$$\frac{f}{\rho c Q} = \frac{\pi\frac{\omega_0^2}{\omega_1^2}}{\beta\frac{\omega}{\omega_1}\left(i\cos\left(\frac{\pi\omega}{\omega_1}\right) - \alpha\sin\left(\frac{\pi\omega}{\omega_1}\right)\right) - \pi\left(\frac{\omega^2}{\omega_1^2} - 2i\zeta\frac{\omega\omega_0}{\omega_1^2} - \frac{\omega_0^2}{\omega_1^2}\right)\left(\alpha\cos\left(\frac{\pi\omega}{\omega_1}\right) + i\sin\left(\frac{\pi\omega}{\omega_1}\right)\right)} \tag{A8}$$

$$\frac{f}{\rho c Q} = \frac{2(-1)^{-n} i \pi \omega_0^2 \omega_1}{\beta \omega_1^2 (\omega_0 + n\omega_1) - 4\pi^2 \omega_0 (\omega_0 - \omega + i\zeta\omega_0)(n\omega_1 - \omega + i\zeta_a n\omega_1)} \tag{A9}$$

Axial Flow and thin shells

AEROELASTIC EFFECTS IN A PLANAR FLAT BLADE CASCADE AT HIGH MACH NUMBER FLOW

Petr Šidlof, Martin Štěpán, Václav Vomáčko
Technical University of Liberec, NTI FM, Liberec, Czech Republic
David Šimurda, Jan Lepicovsky
Institute of Thermomechanics, Czech Academy of Sciences, Prague, Czech Republic

ABSTRACT

The paper reports on measurements of unsteady pressure and aeroelastic response of a simplified turbine blade cascade under kinematic excitation. The flow velocities ranged from high subsonic to transonic regimes and reduced frequencies were between k = 0 – 0.41. Unsteady pressures measured by six miniature pressure transducers in the oscillating blade are shown for one representative measurement, and blade oscillation amplitudes compared for the whole measurement matrix. The results show strong pressure oscillations near the leading edge due to switching between subsonic and supersonic airflow. The oscillation amplitudes of the blade sharply increase with the frequency and are weakly influenced by the Mach number.

1. INTRODUCTION

Flow-induced vibration of the blades in front stages of compressors and aft stages or turbines represents a major and persistent concern for their designers and operators. This dangerous phenomenon may lead to catastrophic consequences, such as the CFM56-7B24 turbofan engine fan blade failure during the Boeing 737 flight from New York to Dallas in 2018. Fortunately, this incident did not result in loss of the whole aircraft; however, one passenger was fatally injured.

Unlike the classical coupled-mode flutter in external flows, where two structural eigenmodes are coupled due to fluid-structure interaction, flutter in turbomachines is usually related to a single structural mode (Srinivasan, 1997; Ferria, 2011; Chahine, 2019). The stiffness of the blades and the mass ratio is higher than in the case of isolated airfoils, and the flow is usually assumed not to modify the modeshape and frequency.

The aeroelastic instability of turbomachinery blades (flutter or non-synchronous vibration) may arise from a number of physical mechanisms. The internal damping in the bladed discs being very low, the critical issue is the aerodynamic damping from unsteady aerodynamic forces, which may be positive (stable) or negative (potentially unstable). The flow-induced vibration may also occur when blade vibration locks in with a specific unstable aerodynamic behavior, such as boundary layer separation, shock wave oscillation or shock wave – boundary layer interaction.

The tip sections of the long blades in modern large turbomachines often operate under transonic flow regimes. Despite the rapid progress in the CFD techniques and available computational power, transonic flow still represents a challenging regime for contemporary numerical schemes. Experimental data remains indispensable for flutter testing and CFD code validation.

In open literature, there is a number of reports about test facilities for blade flutter research. However, only few dedicated test facilities in the world can operate for transonic flow velocities and reduced frequencies above 0.2. Such facilities are mostly linear cascades, although some semi- or fully-circular cascade facilities have been built. Among the leading world research laboratories are EPFL Lausanne in Switzerland (Zanker, 2013), KTH Stockholm in Sweden (Vogt, 2007), TU Darmstadt (Holzinger, 2015) or the NASA Glenn Research Center (GRC) in Cleveland, Ohio, USA (Lepicovsky, 2008).

During last three years, a new flutter research test facility was designed and built at the Institute of Thermomechanics of the Czech Academy of Sciences, based on the experience of J. Lepicovsky with

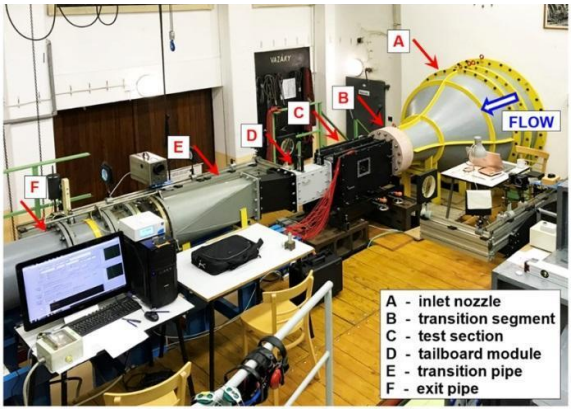

Figure 1. Overall view of the transonic wind tunnel with the flutter test section.

the NASA Transonic Cascade, and previous measurements of isolated airfoil flutter in the Institute of Thermomechanics (Šidlof, 2016). This paper reports on the aeroelastic response of a blade oscillating at high Mach number flow and moderate reduced frequency, measured using this new facility.

2. METHODS

2.1. Experimental setup

The experimental setup consists of a test section mounted in the open suction-type high-speed modular wind tunnel of the Institute of Thermomechanics (see Figure 1). The test section has an internal cross-section of 160 mm (along the blade span) x 195 mm. The blade cascade is composed of five blades with a simple shape – flat plates with circular leading and trailing edges. The chord length of the blades is $c = 120$ mm and thickness of the blades is $h = 5$ mm. The geometry of the blade cascade and location of the static pressure probes monitoring the inlet and outlet isentropic Mach number are shown in Figure 2.

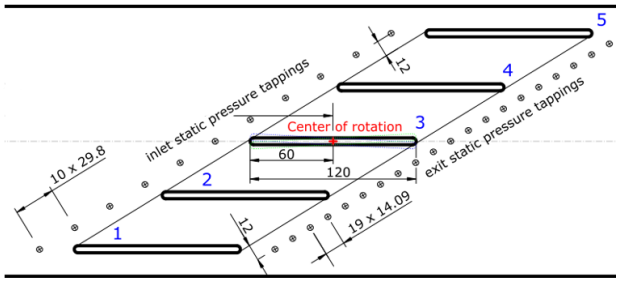

Figure 2. Geometry of the blade cascade.

The incidence angles of individual blades can be varied, while the stagger angle of the entire cascade (58.51°) and pitch (74.52 mm) stay unchanged. Therefore, the torsional deformation of real blades can be readily simulated. The middle blade (no. 3) is linked to a high-speed electric motor and blade drive mechanism transforming the steady rotational motion into torsional oscillation (see Figure 3).

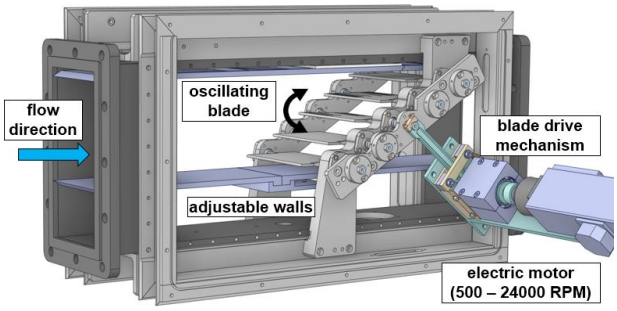

Figure 3. Arrangement of the blade cascade with the drive mechanism mounted to blade no. 3.

The blade can be either fixed with a specific incidence angle, or undergo forced torsional oscillation (pitching) with amplitudes $1 - 3$ deg (measured at the hexagonal shoulder) and frequencies up to 200 Hz. More details can be found in (Lepicovsky, 2021; Fürst, 2021).

The modal properties of the blades have been both computed numerically (using the COMSOL finite element software) and measured on a blade mounted in the test section. In both cases, the blade was clamped in the hexagonal shoulder, and supported by bearings on both pins. The experimental configuration also includes effects of friction damping, which are difficult to be captured by simulation. The eigenmodes are listed in Table 1 and Figure 4.

Eigenfrequency	Computed	Measured
f_1	272 Hz	267 Hz
f_2	522 Hz	600 Hz
f_3	827 Hz	825 Hz
f_4	1100 Hz	-
f_5	1597 Hz	-
f_6	1672 Hz	1714 Hz

Table 1. Computed and measured eigenfrequencies of the blade.

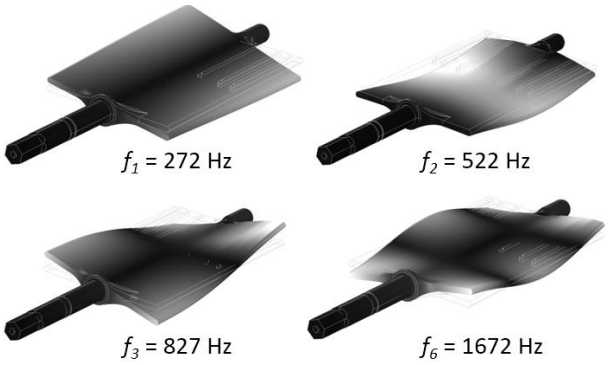

Figure 4. Computed blade modeshapes.

2.2. Pressure measurements

The sidewalls of the wind tunnel are equipped with two rows of static pressure probes, used for measurement of the reference Mach number (see Figure 2). In the case of the current simplified flat blades, which behave like a turbine cascade (with outlet pressure lower than inlet pressure), the reference velocity is the outlet (isentropic) Mach number M_{2is}, which is evaluated as

$$M_{2is} = \sqrt{\frac{2}{\gamma - 1}\left[\left(\frac{p_{2,avg}}{p_{1,t}}\right)^{\frac{1-\gamma}{\gamma}} - 1\right]}, \qquad (1)$$

where $p_{2,\mathrm{avg}} = \frac{1}{20}\sum_{k=1}^{20} p_{2,k}$ is the average pressure from the exit static pressure ports, $p_{1,t}$ is the total pressure at inlet measured by a Prandtl probe, and $\gamma = \frac{c_p}{c_v} = 1.4$ is the specific heat ratio for air. The inlet isentropic Mach number M_{1is} is calculated in the same way.

Further, the blades are instrumented either by static pressure probes, or with miniature dynamic pressure sensors Kulite XCQ-IC-062-25A (diameter 1.67 mm, length 100 mm, pressure range 0 - 1.7 bar abs., frequency range up to 200 kHz) installed in the grooves machined in the blades, see Figure 5 and Figure 6. The sensors are fixed immediately below the pressure ports (on the reverse side of the blade) so that the frequency range is not limited by acoustic resonances.

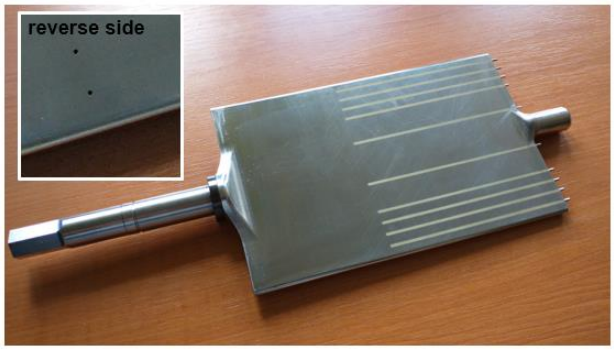

Figure 5. Flat blade with static pressure probes.

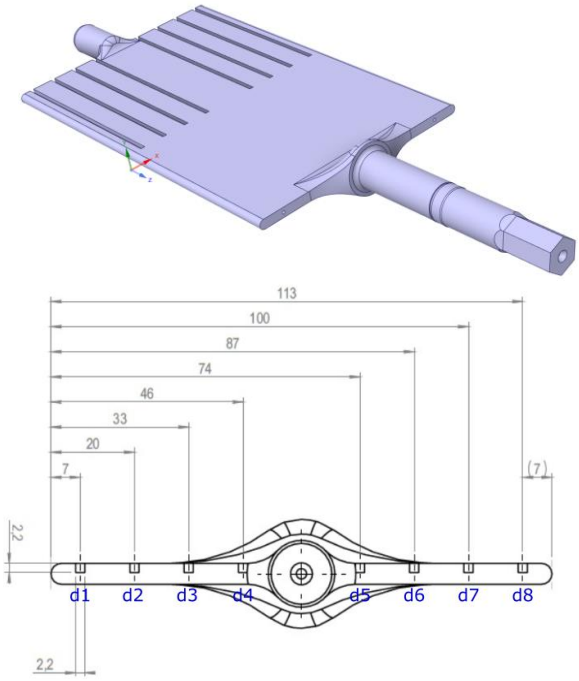

Figure 6. Flat blade with trenches for Kulite pressure transducers (labeled d1-d8).

The signal from the Kulite pressure transducers could be influenced by acceleration, which reaches (for frequency 200 Hz, amplitude 3 deg and the transducer most remote from the rotation axis) up to 450 g. However, in the configuration with sensor membrane perpendicular to the acceleration vector it has been confirmed that the parasitic signal arising from acceleration is negligible with respect to the measured pressure signal.

In the current measurements, six Kulite pressure probes were installed in trenches no. d1, d2, d4, d5, d6 and d8 (see Figure 6). The tubes for the pressure probes are cemented close to the upper blade surface, but the pressure measurement ports are drilled towards the lower surface of the blade.

2.3. Measurement of blade vibration

The blade drive mechanism can be regarded as kinematic excitation, which imposes torsional harmonic oscillation of the hexagonal shoulder of the blade

$$\Phi(t) = \Phi_0 \, sin(2\pi \, f \, t)\,, \qquad (2)$$

where Φ_0 is the angular amplitude and f is the frequency of oscillation. In the current setup, the amplitude at the hexagonal shoulder has been set to $\Phi_0 = 1$ deg. However, in the case of high-frequency oscillation, the blade undergoes elastic deformation, whose amplitudes can significantly exceed the rigid body deflections. A numerically simulated deformed shape of the blade is displayed in Figure 7, showing the real incidence angle $\alpha(z)$, which varies along the span of the blade. In the experiment, the incidence angle is measured at blade midspan ($z = 0$) by a laser triangulation sensor MicroEpsilon ILD 2310-40. The sensor monitors the vertical displacement at the leading edge of the blade, see Figure 8 and Figure 9.

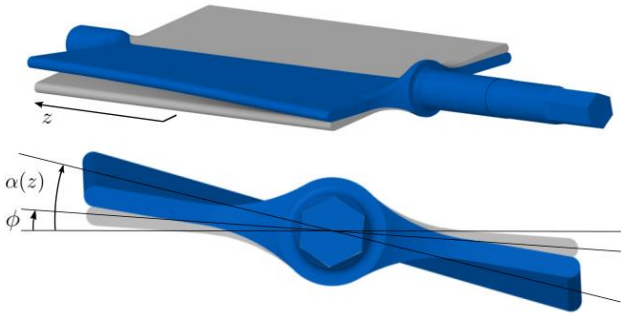

Figure 7. Deformation of the blade during high-frequency oscillation. Position of the idealized rigid blade in gray, real shape in blue.

Both the experimental and computational data suggest that during forced blade oscillation in the frequency range $f = 10 - 200$ Hz, the blade deforms

mostly according to the first torsional eigenmode f_1 (see Figure 4).

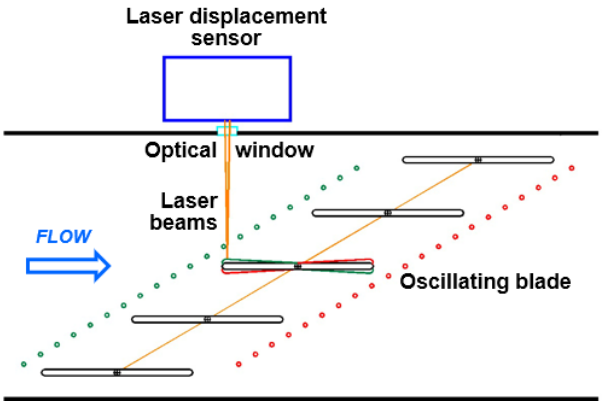

Figure 8. Measurement of the blade oscillation with the laser displacement sensor – side view.

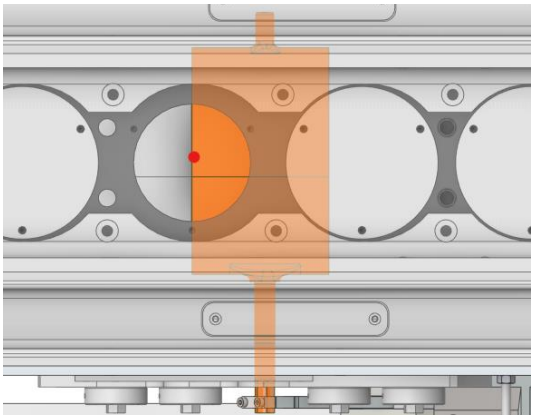

Figure 9. Measurement spot of the laser displacement sensor – top view.

2.4. Additional measurement techniques and data acquisition

In addition to pressure and blade motion measurements, the test section is equipped with further measurement and visualization techniques. First, strain-gauge bridges are installed on the shafts of blades no. 2, 3 and 4. In the case of static blades, the strain gauges measure the total aerodynamic moment. When the middle blade no. 3 undergoes forced torsional oscillation, the strain gauge signal contains both the aerodynamic and inertial torque, caused by the mass (moment of inertia) of the blade.

Next, the test section has optical windows through the sidewalls of the wind tunnel, providing optical access to the upstream sections of interblade channels no. 2-3 and 3-4. Through these optical-grade acrylic windows, qualitative Schlieren visualizations or newly developed digital holographic interferometric measurements of the flow field can be accomplished, see (Psota, 2021). Further, split-fiber probe and four-hole probe measurements in the wake of the blades are planned in near future. However, the results of these measurements will be reported elsewhere.

The signals from the Kulite pressure transducers and from the laser triangulation sensor are amplified, sampled and registered using a Dewetron 800 data acquisition system with DAQP-STG input modules. The system features a Dewe-Orion-1624-200 card with simultaneous 24bit A/D sampling. For the measurements reported here, the sampling frequency of 40 kHz was used.

3. RESULTS

In the current study, the first governing parameter is the Mach number

$$M = \frac{u}{a}, \tag{3}$$

where u is the flow velocity, $a = \sqrt{\gamma RT}$ the local speed of sound, $\gamma = c_p/c_v$ the specific heat ratio, R the specific gas constant and

$$T = T_0 \left(1 + \frac{\gamma - 1}{2} M^2\right)^{-1} \tag{4}$$

the local temperature. The second one is the frequency of blade oscillation f, which can be normalized by the first natural frequency f_1. The Mach number is a purely aerodynamic parameter, while the frequency ratio f/f_1 relates exclusively to the structure. A relevant dimensionless number is also the reduced frequency

$$k = \frac{\omega\, b}{u} \tag{5}$$

based on the semi-chord $b = c/2 = 60$ mm and angular frequency $\omega = 2\pi f$. The reduced frequency quantifies the degree of unsteadiness of the airflow and combines both aerodynamic and structural properties.

In the current study, results from a set of 50 measurements are reported. The values of the inlet and outlet Mach number, listed in Table 2 together with the reduced frequency ranges, fall into four regimes: 1) still-air conditions, 2) fully subsonic regime, 3) supercritical regime (subsonic inlet and outlet but supersonic velocities reached within the interblade channel), and 4) a transonic case with subsonic inlet and supersonic outlet. The exact value of the Mach number cannot be measured directly. Instead, the isentropic Mach number downstream of the blade cascade calculated from the static pressure measurements is used, see (1).

The dimensional frequency of blade oscillation ranged from $f = 0$ Hz (steady case) to $f = 200$ Hz, i.e. 75% of the first natural frequency (see Table 1 and Figure 4). In our case, the limiting factor was not the blade drive, which can operate up to 400 Hz, and not even the structural stresses in the blade, manufactured from high-strength steel. The oscillation frequency was limited by elastic deflection of the blade, which would collide with the sidewall slots if frequency increased beyond 200 Hz.

Flow regime	M_{1is}	M_{2is}	k
still-air	0	0	-
high subsonic	0.454	0.529	0 – 0.41
supercritical	0.604	0.777	0 – 0.28
transonic	0.648	1.018	0 – 0.22

Table 2. Flow regimes measured – inlet and outlet isentropic Mach numbers and reduced frequency.

Figure 10 shows the signal from the laser displacement sensor, monitoring the blade incidence angle at midspan, together with the waveforms of the static pressures at six locations along the chord of the lower surface of blade no.3, all displayed during two periods of blade oscillation. As a representative case, the supercritical regime ($M_{2is} = 0.777$) and the highest frequency of oscillation $f = 190$ Hz were chosen here. The blade oscillation is well harmonic with an amplitude of 3.23 deg. Signals close to the leading edge (K3-d1 and K3-d2, see also Figure 6) show periodic switching between subsonic (> 51 kPa) and supersonic (< 51 kPa) flow, related to the oblique shock wave shortly downstream of the leading edge, which arises for negative angles of attack of blade no. 3. Further from the leading edge, for relative chord positions $x/c > 0.38$ (sensors K3-d4 … K3-d8), the flow remains subsonic throughout the entire oscillation period. The peak pressure at the first pressure port ($x/c = 0.058$, K3-d1) is slightly phase-delayed behind the blade motion. The other pressure sensors are in phase with the blade incidence angle.

For the transonic regime $M_{2is} = 1.018$, the pressure waveforms are similar, yet the amplitudes and pressure level quite different due to different shock wave structure. These results will be reported in a separate paper.

From the perspective of aerodynamic loading of the blade, an important result is the pressure profile along the blade chord, and its development in time during one oscillation period. In Figure 11, the pressures profiles are presented in the form of dimensionless pressure coefficient

$$c_p = \frac{p - p_{2,avg}}{\frac{1}{2}\,\gamma\, p_{2,avg}\, M_{2is}^2}\,, \qquad (6)$$

where p is the local static pressure measured by the Kulite probes and $p_{2,avg}$ the average static pressure downstream of the blade, as in equation (1).

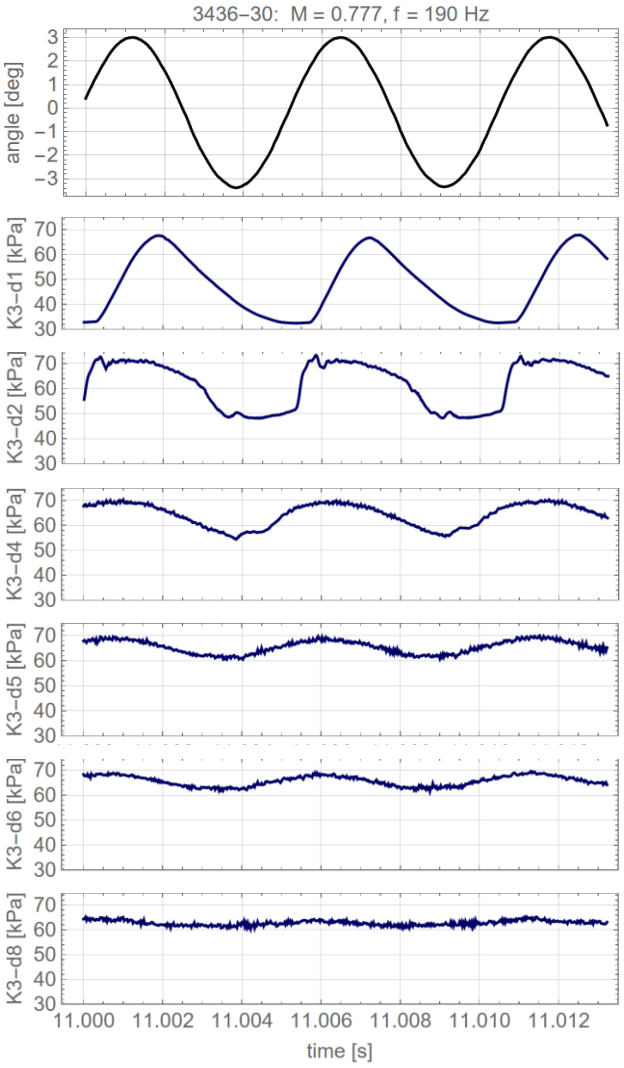

Figure 10. Blade oscillation and signals from Kulite pressure sensors mounted in the blade during two periods of oscillation.

The profiles are shown in eight phases of one oscillation period T, denoted by vertical lines in the subfigures. The plots reveal a zone of low pressure near the leading edge throughout most of the oscillation period except the phase around $0.375\,T$, when the blade has positive incidence and negative angular velocity. From Figure 10 it can be deduced that the highest pressure at sensor K3-d1 occurs at $0.377\,T$. Towards the trailing edge, the pressure coefficient approaches the zero value with significantly lower variations throughout the oscillation period.

Moreover, Figure 11 clearly demonstrates that for this flow velocity and frequency of oscillation, the degree of unsteadiness is high. Deliberately, similar

colors were chosen for the same angular position of the blade, e.g. green for phases 0.125 T and 0.375 T or blue for 0 T, 0.5 T and 1 T. Comparing the blue curves, one can see that the pressure profiles at the start and mid-period (zero incidence) are very different when the leading edge travels upwards (0 T) and downwards (0.5 T). This is not surprising, since the value of the reduced frequency in this case is $k = 0.28$, which falls into the highly unsteady aeroelastic range.

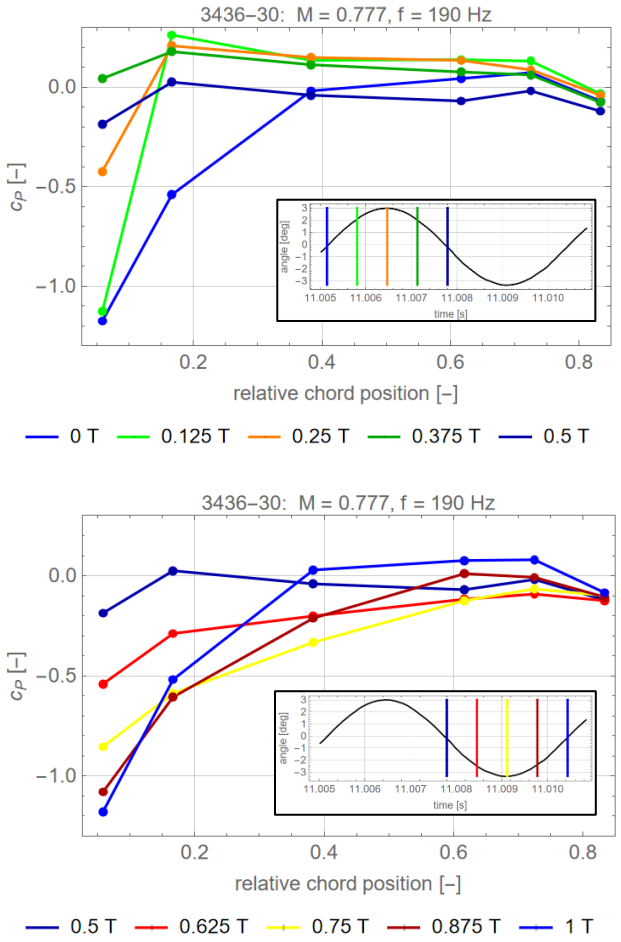

Figure 11. Pressure profiles along the lower side of blade no. 3 during eight phases of the oscillation period T. Time instants are shown in the subfigures.

In addition to detailed analysis of the pressure signals for one flow and oscillation regime ($M = 0.777$, $f = 190$ Hz), the blade angular amplitude has been evaluated for the entire set of measurements. The angular amplitude is caused both by inertial structural moments and aerodynamic forces. Theoretically, the inertial forces due to kinematic excitation scale with square of the oscillation frequency. However, near resonance the amplitudes increase even faster and are strongly influenced by structural (internal and frictional) damping, which is unknown. As the flow velocities range from subsonic to transonic, the effect of aerodynamic forces is nontrivial and is difficult to be approximated by linearized theory.

Figure 12 and Figure 13 show the measured relative amplitude as a function of frequency ratio and Mach number. The angular amplitude is normalized by the amplitude Φ_0 at the hexagonal shoulder, i.e. amplitude with which the blade would oscillate if it were perfectly rigid. The dependence of the amplitude on the frequency indeed displays quadratic behavior for frequency ratios up to about $f/f_1 = 0.3$. Further, the amplitude increases significantly faster. The effect of the Mach number in Figure 13 shows an interesting trend: the highest aeroelastic amplitudes were not reached for the highest flow velocity $M_{2is} = 1.018$, but for $M_{2is} = 0.777$. To explain this phenomenon, the aerodynamic loading on the whole blade surface (not only the lower side) will need to be analyzed from numerical simulation or optical measurements.

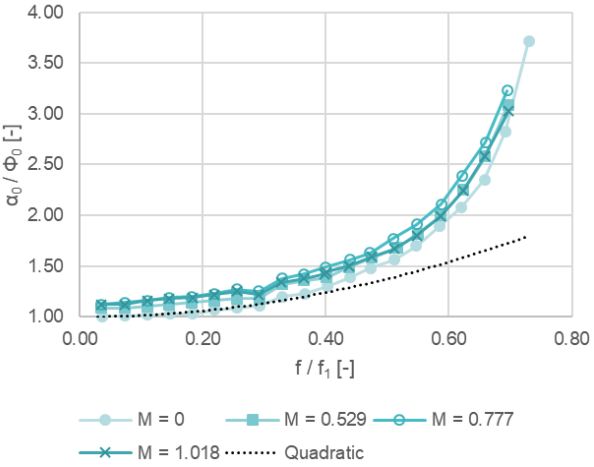

Figure 12. Relative amplitude of the blade as a function of the frequency ratio.

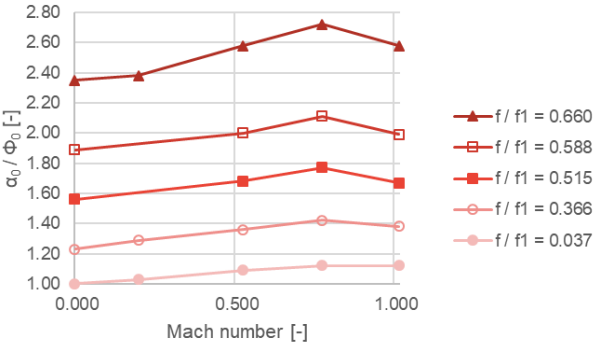

Figure 13. Relative amplitude of the blade as a function of the Mach number.

4. DISCUSSION AND CONCLUSIONS

Using a newly designed facility for experimental research of blade flutter in turbomachinery, the aeroelastic effects were measured on a simplified blade cascade under kinematic excitation for flow velocities ranging from high subsonic to transonic regimes and reduced frequencies between $k = 0 - 0.41$. Within this study, the unsteady pressure measured on the oscillating blade was reported for one representative measurement, and blade amplitudes compared for the whole measurement matrix.

The unsteady pressure signals at the supercritical case $M_{2is} = 0.777$ and highest frequency $f = 190$ Hz (corresponding to reduced frequency $k = 0.28$) reveal intensive pressure oscillations especially near the leading edge of the blade, where the airflow switches between subsonic and supersonic in each oscillation cycle. The pressure profiles evaluated throughout the oscillation period also confirm that the aeroelastic regime is highly unsteady, and that a quasisteady approximation, which is tempting both from the experimental and computational perspective, cannot be used for such high reduced frequencies.

The motion of the oscillating blade is composed of rigid-body pitching due to the kinematic excitation, and elastic torsional deformation due to inertial and aerodynamic moments. The angular amplitudes measured at blade midspan sharply increase with frequency. Up to about $f/f_1 = 0.3$, the trend is quadratic since the inertial moment scales with the square of frequency. Closer to the first blade natural frequency f_1 the amplitudes rise rapidly. The angular amplitudes are also dependent on the Mach number, with a maximum at $M_{2is} = 0.777$.

The spatial resolution of the measurement, with six Kulite pressure probes along blade chord (moreover only from one side in the current setup) does not allow to evaluate the overall aerodynamic moment and to calculate the energy transferred from the airflow to the structure and aerodynamic damping. However, in a follow-up study these crucial aeroelastic parameters will be estimated from the torque and motion signals. Moreover, the experimental data will serve to validate the numerical codes developed in parallel to experiments. From the 3D simulations using the in-house CFD codes optimized for transonic flow regimes, the energy per cycle can be evaluated precisely and aeroelastic stability of the system assessed.

5. ACKNOWLEDGEMENTS

The research has been supported by the Czech Science Foundation (GACR) under grant no. 20-11537S *Experimental research on flutter excitation function in turbomachinery.*

6. REFERENCES

Chahine C., Verstraete T., He L. (2019), A comparative study of coupled and decoupled fan flutter prediction methods under variation of mass ratio and blade stiffness, *Journal of Fluids and Structures* **85**, pp. 110–125.

Ferria H. (2011), Contribution to Numerical and Experimental Studies of Flutter in Space Turbines. Aerodynamic Analysis of Subsonic or Supersonic Flows in Response to a Prescribed Vibratory Mode of the Structure, Ph.D. thesis, Ecole Centrale de Lyon, KTH Stockholm.

Fürst J., Lasota M., Lepicovsky J., Musil J., Pech J. et al. (2021), Effects of a Single Blade Incidence Angle Offset on Adjacent Blades in a Linear Cascade, *Processes* **9**(11), pp. 1974.

Holzinger F., Wartzek F., Schiffer H.-P., Leichtfuss S., Nestle M. (2015), Self-Excited Blade Vibration Experimentally Investigated in Transonic Compressors: Acoustic Resonance, *Journal of Turbomachinery* **138**(4).

Lepicovsky J. (2008), Investigation of flow separation in a transonic-fan linear cascade using visualization methods, *Experiments in Fluids* **44**(6), pp. 939–949.

Lepicovsky J., Šidlof P., Šimurda D., Štěpán M., Luxa M. (2021), New test facility for forced blade flutter research, *AIP Conference Proceedings*, pp. 030001

Psota P., Çubreli G., Hála J., Šimurda D., Šidlof P. et al. (2021), Characterization of Supersonic Compressible Fluid Flow Using High-Speed Interferometry, *Sensors* **21**(23), pp. 8158.

Šidlof P., Vlček V., Štěpán M. (2016), Experimental investigation of flow-induced vibration of a pitch-plunge NACA 0015 airfoil under deep dynamic stall, *Journal of Fluids and Structures* **67**, pp. 48-59.

Srinivasan A. V. (1997), Flutter and Resonant Vibration Characteristics of Engine Blades, *ASME Turbo Expo: Power for Land, Sea and Air, Volume 4*.

Vogt D. M., Fransson T. H. (2007), Experimental Investigation of Mode Shape Sensitivity of an Oscillating Low-Pressure Turbine Cascade at Design and Off-Design Conditions, *Journal of Engineering for Gas Turbines and Power* **129**(2), pp. 530–541.

Zanker A., Ott P., Calza P. (2013) Experimental Aeroelastic Analysis of Clustered Turbine Blades Vibrating in Mixed Torsion/Bending Mode, *31st AIAA Applied Aerodynamics Conference, 3152*

AXIAL FLOW DAMPING INVESTIGATION BY MEANS OF 2D CFD

Aurélien Joly, Sébastien Corre, Julien Berland, Pierre Moussou
EDF R&D, IMSIA UMR CNRS-EDF-CEA-ENSTA 9219, Palaiseau, France

Alexandre Martin
Université Clermont Auvergne, Laboratoire de Mathématiques Blaise Pascal UMR 6620, Aubière, France

ABSTRACT

Cylinders in axial flow are known to be subject to strong damping when vibrating transversely to the flow. The aim of the paper is to assess the ability of a 2D CFD method in predicting accurately the damping coefficient. For this study, the specific geometry of a confined 3x3 cylinder array is chosen, since recent experimental and 3D numerical results are available for this configuration. The numerical method can be understood as a 2D–3C (two dimensinoal, three components) resolution of the fluid dynamics case. The fluid domain has only one layer of cells in the main flow direction and periodic boundary conditions are applied on both sides. This way, the three components of the outlet velocity are reinjected at the inlet. The flow is maintained by means of a momentum source term in each cell that compensates for the friction losses. A harmonic transverse motion is imposed on the central cylinder. The fluid force is recorded; the damping coefficient is obtained from the fluid force component in phase with the motion velocity. Its value is close to the one from experiments and 3D CFD, which validates the method. A parametric study on confinement shows a relatively low sensitivity to that parameter. Imposing a circular motion on the cylinder, i.e. a composition of two harmonic motions (one in each transverse direction), reveals that the damping coefficient is the same in both directions and very similar to that of a simple harmonic motion. The 2D-3C method used here has thus proven useful in characterizing axial flow damping, since its lower computational cost allowed parametric studies, although it requires some subtle tuning of the momentum source term.

1. INTRODUCTION

Axial flow damping is a major parameter in the computations for the seismic design of fuel assemblies of pressurized water reactors. A fuel assembly consists of a bundle of 17x17 fuel rods tied together with spacer grids. Comprehensive tests on a real-scale fuel assembly mockup have allowed to determine the value of the damping (Moussou et al., 2017). Additionally, a simpler geometry was previously introduced (Joly et al., 2021) in order to carry out more fundamental research on the fluid forces in a slightly perturbed cylinder array in axial flow. Experimental as well as 3D CFD investigations were carried out. By means of a quasi-steady approach, they gave access to the axial flow damping coefficient for a single cylinder in a confined configuration. Yet they were quite time-consuming and did not provide much flexibility on the geometry that was tested. Another study (Berland, 2016; Divaret et al., 2011) made use of 2D numerical simulations in order to assess the axial flow damping coefficient of an oscillating cylinder bundle (array of 11x11 cylinders); these run much faster than 3D simulations, thus giving the possibility of carrying out broader parametric studies. However, the configuration tested in Berland (2016) has not been validated by comparison with experiments or 3D simulations. The goal of the present paper is to use the 2D approach of Berland (2016) on the comprehensively investigated configuration of Joly et al. (2021).

In section 2, a basic understanding of axial flow damping is given. Section 3 describes the characteristics of the simulations. The results are presented in section 4.

2. AXIAL FLOW DAMPING

Here, only the simple case of a rigid cylinder submitted to an axial flow and oscillating transversely to it is presented. In that case, provided that the transverse motion is slow compared to the flow velocity (quasi-steady (QS) assumption), the classical model of fluid forces that can be found in Païdoussis (2016) reduces to an added mass term and an added damping term:

$$f_N = -\chi\rho S\ddot{y} - \frac{1}{2}\rho U D c_N \dot{y}, \qquad (1)$$

where f_N is the normal force per unit length on a cylinder section, y is the displacement in the direction transverse to the flow, ρ is the fluid density, D is the cylinder diameter, $S = \pi D^2/4$ is the cylinder

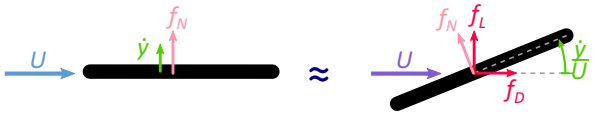

Figure 1. Apparent angle of incidence in the QS approach.

cross-sectional area, U is the flow velocity. The overdot stands for time derivation. χ is the added mass coefficient and c_N is the axial flow damping force coefficient.

In the framework of the QS assumption, the transverse velocity of the cylinder is equivalent to a slight change of angle of incidence α of a static cylinder, with $\alpha = \dot{y}/U$, see figure 1. The added damping stems from the fact that the lift force of a slightly inclined cylinder is proportional to the angle of incidence and that its drag is constant (experimental evidence by Divaret et al., 2014):

$$f_L = -\frac{1}{2}\rho U^2 D c_L \alpha, \tag{2}$$

$$f_D = \frac{1}{2}\rho U^2 D C_D, \tag{3}$$

$$f_N \simeq f_L - \alpha f_D = -\frac{1}{2}\rho U D \underbrace{(c_L + C_D)}_{c_N} \dot{y}, \tag{4}$$

where f_L and f_D are the local lift and drag forces on the inclined cylinder (figure 1).

Assessing the axial flow damping means determining the value of c_N. This can be done by two different approaches. In the static approach, which is the scope of Joly et al. (2021), the cylinder is slightly inclined at different angles of incidence, so that the coefficient c_L can be determined. With an additional measure of C_D, the value of c_N can be retrieved. In the dynamic approach, which is the scope of the present paper, an oscillating motion is prescribed on the cylinder. The fluid force transverse to the main flow direction is recorded and fitted to expression (1). This gives c_N, and additionally the value of the added mass coefficient χ.

3. 2D SIMULATIONS

The simulation method proposed in Divaret et al. (2011) and Berland (2016) is not exactly two-dimensional. All three components of the velocity field are computed, yet this is done on a mesh consisting of a single layer of cells. Therefore, it would be more appropriate to describe it as a 2D-3C method (as is usually done in the flow visualization community). Periodic boundary conditions are applied in the axial direction: the velocity vectors flowing out of the domain are reintroduced at the entrance of the domain. In order to maintain the average flow velocity, which would otherwise decrease over time because of friction, a momentum source term is introduced in each cell. This momentum source term is adjusted at every time step in order to reach the desired average flow velocity in the domain.

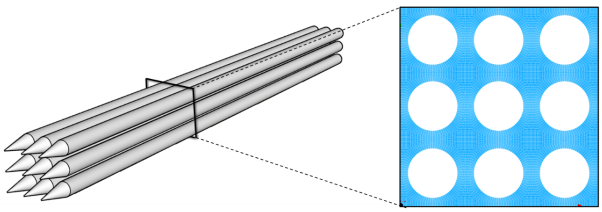

Figure 2. Experimental geometry (left) and 2D geometry for numerical simulations (right).

The other features of the numerical procedure are relatively standard. U-RANS (unsteady Reynolds-averaged Navier–Stokes) simulations are carried out in Code_Saturne 4.0, an EDF in-house open CFD tool (Archambeau et al., 2004), using a $k-\omega$ SST (shear stress transport) model with a two-scale wall law for turbulence modelling. The fluid is modelled as incompressible air at room temperature, with density $\rho = 1.2\,\mathrm{kg/m^3}$ and kinematic viscosity $\nu = 1.5\times10^{-5}\,\mathrm{m^2/s}$.

The same mesh pattern as in Joly et al. (2021) is used. Cell sizes in radial, orthoradial and streamwise directions are adjusted according to the best practices for these types of flow and turbulence model, see Joly et al. (2018).

The time step is chosen so that the Courant number remains below 1.

The geometry consists of a 3x3 cylinder array with pitch-to-diameter ratio $P/D = 4/3$ (figure 2). The diameter of the cylinders is $D = 4.5\,\mathrm{cm}$.

The walls of the cylinders are modeled as smooth walls and a sliding wall boundary condition is applied to the side borders of the domain. The hydraulic diameter, defined as four times the cross-sectional area of the flow divided by the wetted perimeter, is therefore $D_h = D\left(\frac{4}{\pi}\left(\frac{P}{D}\right)^2 - 1\right) = 5.7\,\mathrm{cm}$.

The momentum source term is tuned and controlled throughout the simulation so as to achieve a flow velocity of $U = 17.9\,\mathrm{m/s}$ (average of the cross-section), which is the same as in the 3D simulations (Joly et al., 2021). The Reynolds number based on the hydraulic diameter therefore reaches 68 000. Over the simulation, the control mechanism on the momentum source term produces small fluctuations of the flow rate through the domain, but it remains within $\pm 0.3\,\%$ of the target value.

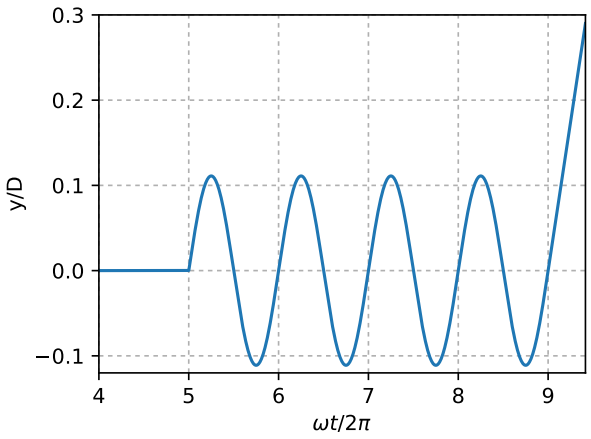

Figure 3. Prescribed transverse displacement of the cylinder.

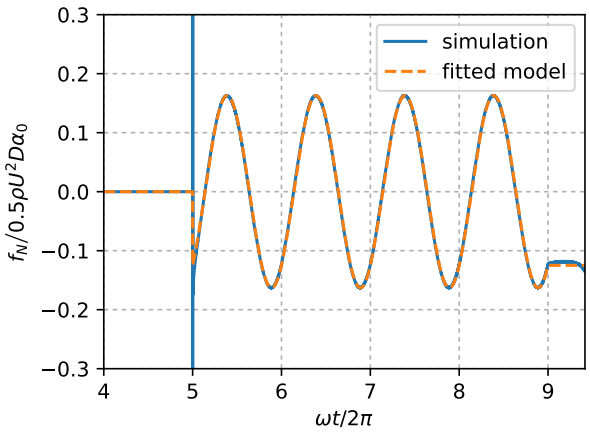

Figure 4. Non-dimensional transverse force during cylinder transverse motion.

The ALE (arbitrary Lagrangian-Eulerian) module of Code_Saturne is used in order to prescribe a sinusoidal motion of the central cylinder. The displacement amplitude is $A = 5\,\text{mm}$, which gives $A/D = 0.11$.

The oscillation frequency is $f = \omega/2\pi = 2.5\,\text{Hz}$, which gives the maximum apparent angle of incidence $\alpha_0 = A\omega/U = 0.25°$: the QS assumption is valid. Each period of oscillation is simulated by 4000 time steps.

Practically, the cylinder is first fixed for the first two seconds of the computation, while the flow velocity stabilizes to the target value. A sinusoidal motion is then started. It lasts for four periods. At the end of the computation, a short time is dedicated to a constant-velocity motion of the cylinder with $\dot{y} = A\omega = \alpha_0 U$. See figure 3.

4. RESULTS

4.1. Transverse oscillation

Figure 4 shows the transverse force upon the cylinder recorded from the numerical simulations. It is first uniformly zero, while the cylinder is at rest. When the motion starts, the velocity discontinuity (figure 3) causes the force to reach very high absolute values for a short time (at the first time step after the beginning of the motion, the non-dimensional value of the force reaches -59, while it later remains in the range between -0.2 and 0.2). This could have been avoided by smoothing the starting phase of the motion. Despite this irregularity, the force very quickly reaches a sinusoidal regime, with a non-zero phase shift relatively to the displacement (compare figures 3 and 4). At the end of the simulation, when the cylinder velocity is constant, the recorded force remains quite stable.

Looking back at the model of transverse fluid force in (1), during a sinusoidal motion of the cylinder, the force was indeed expected to be sinusoidal, with a component in phase with the velocity and another one in phase with the acceleration (i.e. also with the displacement). Practically, the amplitude and phase shift of the force signal are obtained from the maximum value of the force and the time delay between force maximum and displacement maximum. From the amplitude and phase shift, the coefficients c_N and χ of (1) are directly deduced. The axial flow damping force coefficient is here $c_N = 0.125$, which is very close to the value obtained from the static experiments of Joly et al. (2021), where $c_N = 0.12$. The added mass coefficient is estimated here to be $\chi = 1.69$. This agrees relatively well with the experimental value 1.38 obtained by Moretti & Lowery (1976) via experiments in quiescent water with a bundle of 3x3 cylinders with the same pitch-to-diameter ratio as in our geometry, but with outer walls further away from the bundle.

The modeled fluid force is also represented in figure 4. It fits very well with the recorded force from the numerical simulation. The expected behaviour when the cylinder velocity is constant is represented as well (from $\omega t/2\pi = 9$). The force model then reduces to the term proportional to $\dot{y}$; it is constant and $f_N/0.5\rho U^2 D\alpha_0 = -c_N$, hence the fitted value of c_N can be directly read from the vertical axis of figure 4.

From this section, it can be concluded that the 2D-3C numerical approach succeeds in yielding results that agree with previous works, both qualitatively (a prescribed sinusoidal motion leads to a sinusoidal force) and quantitatively (the values of the coefficients are close to the ones obtained experimentally with similar geometries). Now that it has been

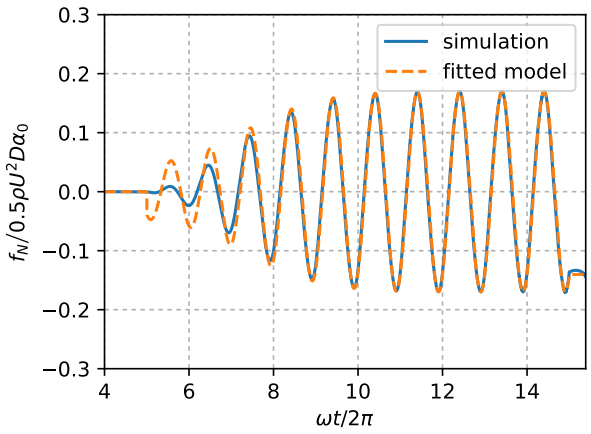

Figure 5. Circular motion: non-dimensional transverse force in y direction.

Table 1. Values of the force coefficients for a circular motion, compared to a 1-degree of freedom (DOF) sinusoidal motion.

Motion	direction	c_N	χ
1-DOF sinusoidal	y	0.125	1.69
circular	y	0.141	1.53
circular	z	0.140	1.55

validated, this approach can be used to assess the influence of different parameters on axial flow damping.

4.2. Circular motion

Here, instead of a simple transverse motion, a circular motion is prescribed to the central cylinder. It boils down to two superposed sinusoidal motions, one in each transverse direction (y and z, x being the main flow direction). The same method as in the previous section can be used in each direction independently to evaluate the force coefficients. Figure 5 shows the recorded transverse force in y direction. The motion was prescribed progressively in order to avoid discontinuities; in the stable regime ($\omega t/2\pi > 11$), the sinusoidal behaviour of the transverse force is to be observed again and the fitting with the model from (1) is accurate. The results for the model coefficients are presented in table 1. The values are very similar in both directions (differences of about 1 % between y and z direction), which was expected because of symmetry. The damping coefficient c_N is about 13 % higher than in the 1-DOF case, while the added mass coefficient χ is about 9 % lower. From an engineering point of view, these can be considered to be minor variations.

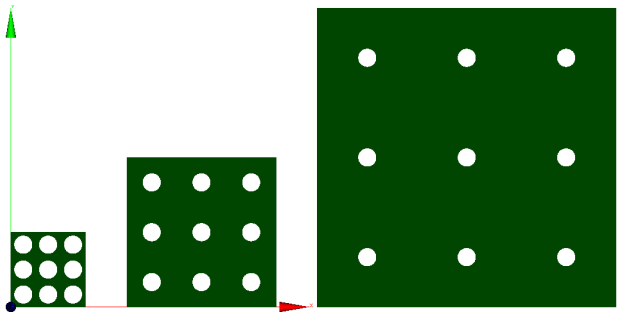

Figure 6. Fluid domain for pitch-to-diameter ratios $P/D = 1.3$, 2.7 and 5.3.

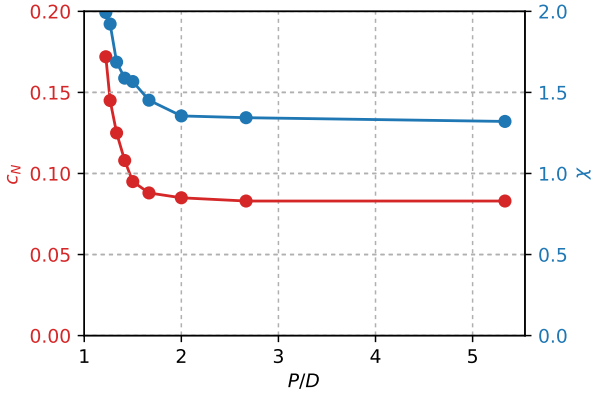

Figure 7. Influence of the pitch-to-diameter ratio on c_N and χ.

4.3. Confinement effect

Coming back to simulations with a simple transverse motion of the cylinder, the parameter tested in the present section is the pitch-to-diameter ratio, see figure 6. Figure 7 shows the results for c_N and χ. Both have stable values for $P/D > 2$ and rise when P/D gets close to 1 (cylinder contact). A comprehensive study on confinement effect would require more simulations, since the amplitude of oscillation may play a role at low values of P/D (here, at the lowest P/D tested, the non-dimensional distance left between two cylinders is $(P-D)/D = 22\,\%$, while the amplitude of motion is $A/D = 11\,\%$). Still, it can be observed from the present results that the value of c_N does not change by orders of magnitude when P/D is varied (for the confinement conditions tested here, c_N ranges from 0.08 to 0.17). Further investigations should also take a look at the value of χ at high P/D, which is expected to reach the theoretical value of 1, while here it seems to stabilize at about 1.3.

Table 2. Values of c_N from several studies with different approaches.

Reference	Geometry	Approach		c_N
Ersdal & Faltinsen (2006)	unconfined cylinder	experiments	static	0.07
De Ridder et al. (2015)	confined in circular channel	CFD	static	0.08–0.12
Divaret et al. (2014)	unconfined cylinder	experiments	static	0.11
		experiments	dynamic	0.17
		CFD, 3D	static	0.13
Berland (2016)	11x11 confined bundle	CFD, 2D-3C	dynamic	0.12
Joly et al. (2021)	confined in square array of cylinders	experiments	static	0.12
		CFD, 3D	static	0.16
Present	confined in square array of cylinders	CFD, 2D-3C	dynamic	0.13

5. CONCLUSION

The 2D-3C numerical approach presented here and already used previously has been validated on a simple geometry consisting of a 3x3 confined cylinder bundle for its ability to predict the axial flow damping coefficient c_N. The dynamic numerical results were compared with experimental steady force measurements, in the framework of the quasi-steady assumption. The 2D-3C method is an efficient way of estimating the value of c_N in various configurations, since the computations are much less time-consuming than full 3D simulations or experiments. The method does require some additional preprocessing effort, especially in the tuning mechanism for the momentum source term.

The values obtained for c_N in the present study and in previous ones are summarized in table 2. Note that in the case of Berland (2016), a complete bundle of 11x11 cylinders was moving as a whole (figure 8), and c_N is obtained by dividing the force by the number of cylinders in the bundle. It can be concluded from table 2 that the value of the axial flow damping coefficient is quite robust, since the various methods reported here lead to values of c_N between 0.1 and 0.2.

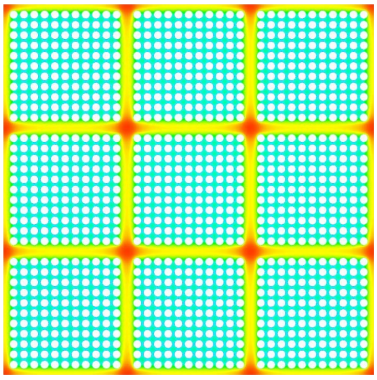

Figure 8. Geometry and flow velocity in the simulations by Berland (2016).

6. REFERENCES

Archambeau, F. et al., 2004, Code_Saturne: a Finite Volume Code for the Computation of Turbulent Incompressible Flows. *International Journal on Finite Volumes*.

Ersdal, S. and Faltinsen, O.M., 2006, Normal forces on cylinders in near-axial flow. *Journal of Fluids and Structures* **22(8)**: 1057–1077.

Berland, J., 2016, Modèle numérique simplifié local pour le calcul des forces fluides agissant sur un assemblage combustible sous séisme. *EDF Internal Report*.

Divaret, L. et al., 2011, U-RANS simulation of fluid forces exerted upon an oscillating tube array in axial flow at large Keulegan-Carpenter numbers. *ERCOFTAC Bulletin* **86**: 20–25.

Divaret, L. et al., 2014, Normal forces exerted upon a long cylinder oscillating in an axial flow. *Journal of Fluid Mechanics* **752**: 649–669.

De Ridder, J. et al., 2015, Simulating the fluid forces and fluid-elastic instabilities of a clamped–clamped cylinder in turbulent axial flow. *Journal of Fluids and Structures* **55**: 139–154.

Joly, A. et al., 2018, Experimental and numerical investigation of steady fluid forces in axial flow on a cylinder confined in a cylinder array. *IUTAM Symposium on Critical Flow Dynamics involving Moving/Deformable Structures with Design applications*, Santorini, Greece, Springer.

Joly, A. et al., 2021, Direct measurement of steady fluid forces upon a deformed cylinder in confined

axial flow. *Journal of Fluids and Structures* **104**: 103326.

Moretti, P. M. and Lowery, R. L., 1976, Hydrodynamic inertia coefficients for a tube surrounded by rigid tubes. *Journal of Pressure Vessel Technology* **98**: 190–193.

Moussou P. et al., 2017, Fluid damping in fuel assemblies. *ASME PVP Conference 2017*, Waikoloa, USA.

Païdoussis, Michael P., 2016, *Fluid-Structure Interactions : Slender Structures and Axial Flow, vol. 2*, Elsevier Academic Press.

DYNAMICS OF CANTILEVERED PIPES CONVEYING FLUID AND SUBJECTED TO REVERSE ANNULAR EXTERNAL FLOW: EXPERIMENTAL INVESTIGATION OF THE INFLUENCE OF EXTERNAL FLOW CONFINEMENT

Mahdi Chehreghani & Ahmed Shaaban & Arun K. Misra & Michael P. Païdoussis
Department of Mechanical Engineering, McGill University, Montreal, QC, Canada H3A 0C3

ABSTRACT

The present paper deals with the dynamics of a hanging cantilevered pipe discharging fluid downwards and subjected to a counter-current partially confined external axial flow over its upper portion. This study is both 'curiosity driven' and application oriented. A bench-top-size apparatus consisting of a pressure vessel filled with water, a hanging cantilevered pipe and a shorter concentric outer rigid tube was utilized. For various ratios of the external to internal flow velocity, U_o/U_i, the effect of the size of the annular gap between the pipe and the outer rigid tube was investigated. It was found that for the same U_o/U_i, not only does confinement affect the onset of instability, but also its type. For $U_o/U_i > 0.055$ and a wider outer tube, as the flow velocity increased, the pipe underwent first mode oscillations prior to second mode flutter, eventually impacting on the outer rigid tube. For a narrower outer rigid tube, static deformation took place prior to oscillatory instability and impacting.

1. INTRODUCTION

Pipelines, submarine systems, and renewable energy harvesters are among the many industrial applications where slender structures interact with fluid flow (Gao et al., 2003; Santillan et al., 2010; Michelin and Doaré, 2013). Blood vessels and urinary tracts are physiological examples of this (Tubaldi et al., 2018). Apart from these real-world applications, the dynamics of pipes conveying fluid has become a paradigm in dynamics, serving as a simple tool to illustrate known dynamical behaviour or a means to explore new dynamical characteristics (Païdoussis, 2014).

The literature on the dynamics of pipes conveying fluid or subjected to simultaneous internal and external flow is very extensive. However, the literature survey in this paper highlights the most relevant studies. The interested reader is referred to Païdoussis (2014) and Païdoussis et al. (2021) for a comprehensive review.

For the first time, Cesari and Curioni (1971) studied the stability of pipes with different boundary conditions, simultaneously subject to internal and external axial flows. Afterwards, the dynamics of a pipe subjected to independent and concurrent internal and external axial flow was studied by Hannoyer and Païdoussis (1978). It was found that for the case of cantilevered pipes, when either internal or external flow is just below the onset of instability, by further increasing the other flow, in some cases the instability could be avoided.

A theoretical model was derived by Païdoussis et al. (2008) for a hanging cantilevered pipe discharging fluid downwards, and subjected to a counter-current interdependent external axial flow through an annular region formed by the pipe and a concentric rigid outer tube. For relatively small confinement of the annular flow, the internal flow was found to be dominant; whereas, for high enough degrees of confinement, the annular flow governed the dynamics, giving rise to flutter at relatively low internal flow velocities.

Later on, Moditis et al. (2016) extended the work of Païdoussis et al. (2008) to examine the dynamics of a hanging flexible cantilevered pipe, coaxial with a shorter rigid outer tube. This study was motivated by applications in solution-mined caverns utilized to store hydrocarbons. Abdelbaki et al. (2020) derived a weakly nonlinear model to investigate the dynamics of the system studied by Moditis et al. (2016). It was concluded that at sufficiently high flow velocities, the system loses stability via flutter in the second mode. The amplitude and frequency of oscillations were predicted to increase with increasing flow velocity. Moreover, it was postulated that longer and tighter annuli destabilize the system. Chehreghani et al. (2021) conducted systematic experiments on the dynamics of a cantilevered pipe discharging fluid and subjected to a reverse external axial flow over its upper portion. Various confinement lengths and ratios of external to internal flow velocities were examined. In addition to the critical flow velocity for the onset of instabilities, the post-critical behaviour of the system with impacting was explored.

The foregoing review makes it clear that further experiments are required to investigate the influence of some parameters, such as external flow confinement. The main purpose of the present study is to character-

Material	Silicone-rubber
EI	7.37×10^{-3} [N m^2]
m	0.191 kg m^{-1}
L	441 mm
D_i	6.35 mm
D_o	16 mm

Table 1. Mechanical and geometrical properties of the flexible pipe utilized in the experiments.

ize the influence of external flow confinement on the dynamics of a hanging cantilevered pipe conveying fluid and counter-currently subjected to a partially confined external axial flow. Besides displaying a rich dynamical behaviour, this flow configuration also simulates one of the *modi operandi* of solution-mined caverns utilized for liquid or gas storage.

2. EXPERIMENTAL SETUP AND METHODOLOGY

The bench-top-size apparatus shown in figure 1 was used in this experiment. The test-section consists of a cylindrical pressure vessel with four plexiglas windows, a hanging flexible silicone rubber pipe (cast in house) and a shorter coaxial outer rigid plexiglas tube.

The material properties and dimensions of the pipe are listed in table 1; EI denotes its flexural rigidity, m its mass per unit length, L its length, and D_i and D_o its inner and outer diameter, respectively. The pipe and the surrounding rigid tube are both cantilevered from their top end. The outer tube length was $L' = 206.5$ mm, which corresponds to $r_{ann} = L'/L = 0.478$. To investigate the effect of external flow confinement, i.e. the size of the annular gap between the pipe and the outer rigid tube, an outer tube of diameter $D_{ch} = 54$ mm was used and the results are compared to those of Chehreghani et al. (2021) with the same r_{ann} and $D_{ch} = 31.5$ mm.[1]

The pipe discharges fluid downwards with flow velocity U_i. The fluid, upon exiting the pipe, is aspirated by the annular region formed by the gap between the upper portion of the pipe and the outer rigid tube with flow velocity U_o in the upward direction. Additional fluid may enter the pressure vessel at the bottom to achieve higher ratios of U_o/U_i— refer to figure 1(b). To do so, two centrifugal pumps move water from a storage tank to the pressure vessel; the first pump is responsible for the flow in the pipe, Q_i, while the other one provides additional flow to the pressure vessel from the bottom, Q_a. Therefore,

[1] D_{ch} =31.5 mm and 54 mm correspond to $\alpha_{ch} = D_{ch}/D_o = 1.97$ and 3.37, and $\chi = \frac{D_{ch}^2 + D_o^2}{D_{ch}^2 - D_o^2} = 1.69$ and 1.19, respectively.

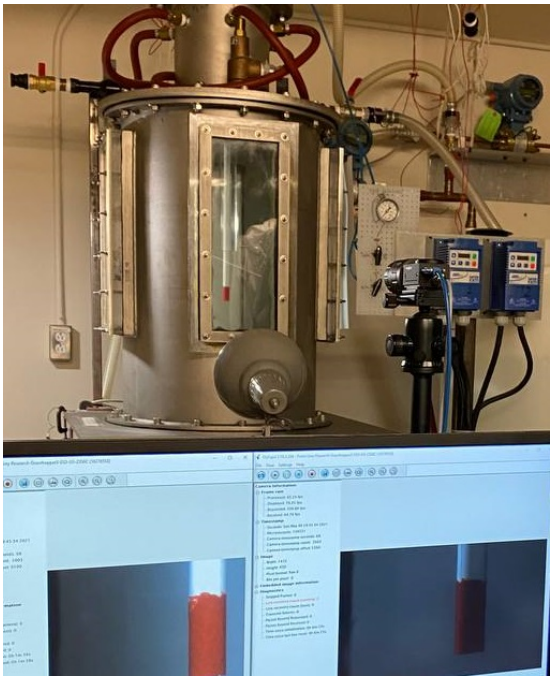

(a)

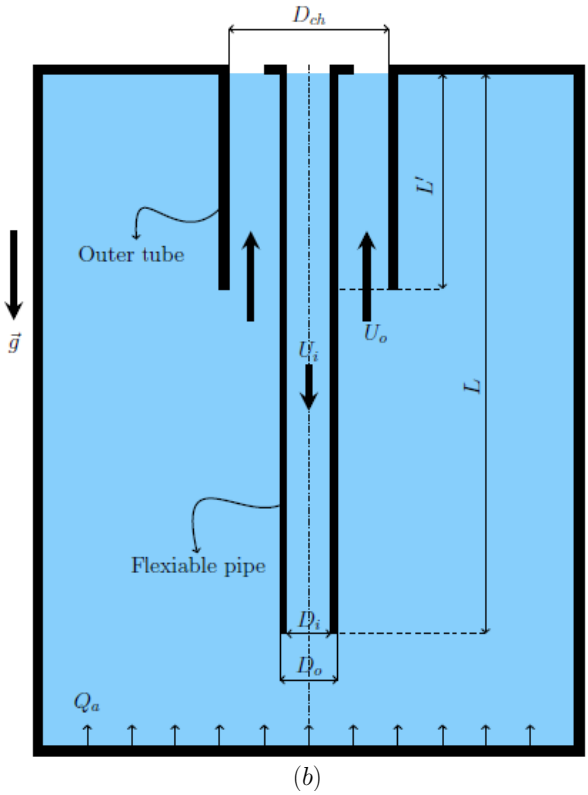

(b)

Figure 1. (a) Photograph of the experimental setup; (b) schematic view of the test-section with flow directions; Q_a is the additional volumetric flow rate into the pressure vessel in order to increase the U_o/U_i ratio.

$Q_o = Q_i + Q_a$ and thus $U_o A_{ch} = U_i A_i + Q_a$, where $A_{ch} = (\pi/4)(D_{ch}^2 - D_o^2)$ and $A_i = (\pi/4)D_i^2$. The flow rates related to each of the two pumps, i.e. Q_i, and Q_a, were measured using two magnetic flow-meters, thereby, determining the internal and external flow velocities, U_i and U_o, from the geometry of the system. Also, making use of a conventional Bourdon tube pressure gauge, the static pressure in the vessel was measured.

Two synchronized FLIR Grasshopper3 2.3 MP cameras perpendicular to each other were used to track the displacement of the pipe tip. These two cameras were triggered using a function generator with a frame rate of 64 fps. The centroid of the 'red-marked' region near the free-end of the pipe served as the displacement follower. This red colour was used to facilitate the processing of the videos. Then the recorded videos for each flow velocity step were fed into an image-processing Matlab (Mathworks, Inc.) script. In each processed frame, the red marker is detected first, and is then followed in the next frame. Since the width of the marker is known (the outer diameter of the pipe) the pixel location of the centroid of the marker can be related to the displacement. Thus, a displacement-time series can be obtained. For more details on the image processing, the interested reader is referred to Chehreghani et al. (2021).

Thereafter, the obtained time series signals at each flow velocity were processed and visualized by plotting bifurcation diagrams, PSDs, phase portraits, etc., to understand the dynamics of the system. It is noteworthy that the initial position of the pipe at zero flow velocity serves as a reference for each experiment.

The effects of confinement of the external flow, i.e. D_{ch}, on the fluid-elastic instability and amplitude of motions was investigated. To this end, for given values of U_o/U_i ranging from 0.015 to 0.8, the flow velocity was increased progressively. At each step, after approaching steady-state, the motion of the pipe was traced for a time interval of 300 seconds using the synchronized dual-camera system.

3. RESULTS AND DISCUSSION

In what follows, results are given in dimensional terms to provide a better "feel". Nevertheless, to allow comparison with theoretical or experimental results to be obtained in future, the dimensionless flow velocity, u_i, and frequency, ω, commonly used in the fluid-structure interaction community can be employed:

$$u_i = \left(M_i/EI\right)^{1/2} L U_i,$$
$$\omega = \left(m + M_i + \rho A_o/EI\right)^{1/2} L^2 \Omega, \qquad (1)$$

where U_i is the internal flow velocity, $M_i = \rho A_i$, ρ is the fluid density, $A_i = \frac{1}{4}\pi D_i^2$ and $A_o = \frac{1}{4}\pi D_o^2$ and $\Omega = 2\pi f$ is the radian frequency, with f in Hz.

For the pipe used in the experiments reported in this paper, $u_i = 0.914 \times [U_i \text{ (m/s)}]$ and $\omega = 9.265 \times f$.

3.1. Results for U_o/U_i=0.015 and 0.055

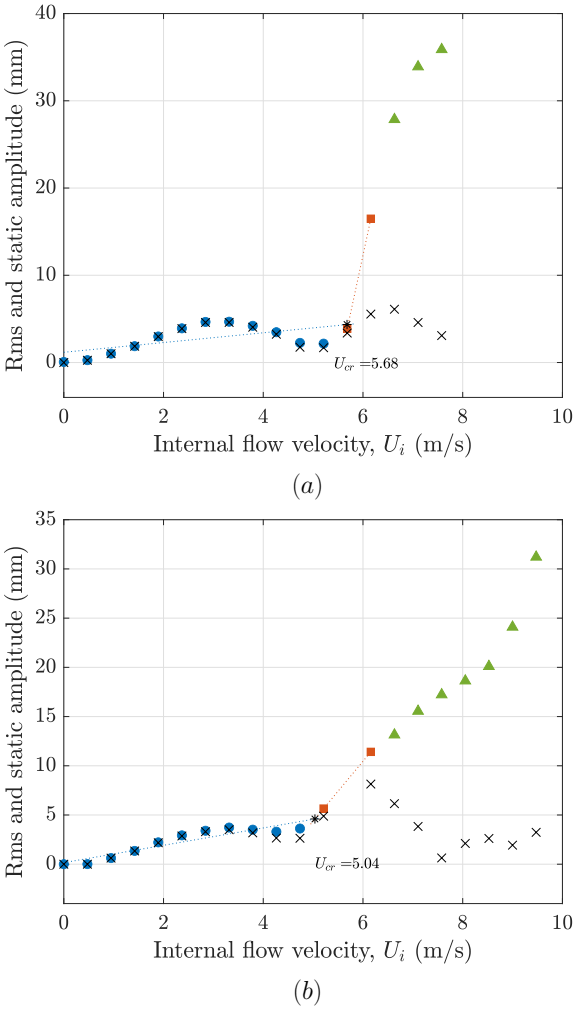

Figure 2. Bifurcation diagrams showing the rms amplitude of oscillations and the mean deflection as a function of U_i for Q_a =0 and (a) U_o/U_i=0.015 and D_{ch}=54 mm; (b) U_o/U_i=0.055 and D_{ch} =31.5 mm. Rms amplitude: (●) pre-instability, (■) instability, (▲) impact; (×) mean deflection.

With no additional flow from the bottom of the pressure vessel, i.e. $Q_a = 0$, by continuity $U_o A_{ch} = U_i A_i$. Therefore, for D_{ch} =54 mm and 31.5 mm, we have U_o/U_i = 0.015 and 0.055, respectively. Figure 2(a) shows the experimental bifurcation diagram for U_o/U_i =0.015 obtained in the present study, and figure 2(b) that for U_o/U_i =0.055 obtained by Chehreghani et al. (2021). Qualitatively, the dynamical behaviour is similar.

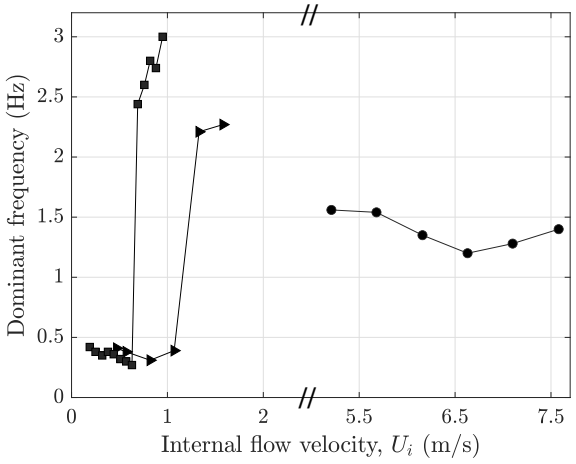

Figure 3. Dominant frequency of oscillation versus internal flow velocity for D_{ch}=54 mm: (●) U_o/U_i =0.015, (►) U_o/U_i =0.4 and (■) U_o/U_i=0.8.

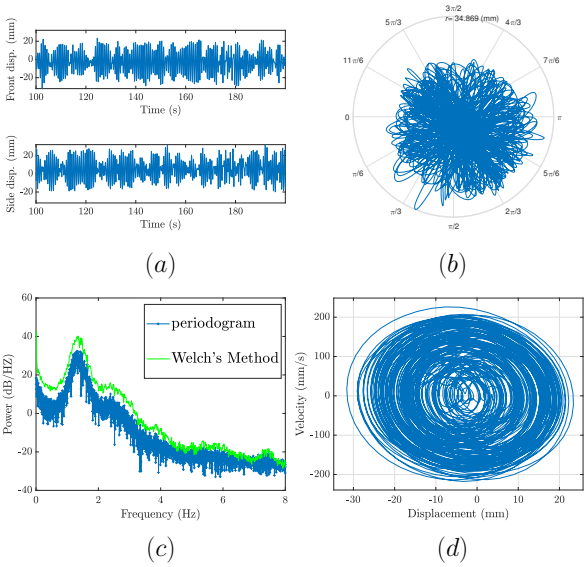

Figure 4. Dynamics of the system for U_o/U_i=0.015 and D_{ch} =54 mm at U_i = 6.16 m/s illustrated by means of: (a) time traces; (b) polar displacement; (c) PSD of motions; (d) phase portrait of the displacement (front camera).

As shown in figure 2(a), for relatively small internal flow velocities, the pipe remained more or less motionless at its undeformed shape. Weak motions commenced as the flow velocity increased; these small amplitude random-like motions were presumably excited by turbulence, or they arose from accentuation of initial imperfections, as no dominant frequency could be determined. At U_i = 5.21 m/s, very weak small amplitude second mode oscillations were observed, as indicated in figure 3. At U_i= 5.68 m/s, however, a dominant frequency of f = 1.54 Hz could be determined and oscillations became notably more powerful, specifying the threshold of flutter in the second mode. Considerably higher amplitude oscillations materialized as the flow rate was increased further. These high amplitude oscillations can be investigated further through the time series, polar displacement, PSD and phase plane plots shown in figure 4. These suggest an unsteady, nearly intermittent motion with a strong harmonic component, but also with some chaotic content as well.

Ultimately, the pipe began impacting on one side of the outer rigid tube at U_i= 6.63 m/s, and then two-sided impacting took place mixed with some rotation.

3.2. Results for $U_o/U_i > 0.055$

In this case, water was pumped into the pressure vessel from the bottom of the pressure vessel and therefore Q_a is not zero anymore, refer to figure 1. Hence, $U_o A_{ch} = U_i A_i + Q_a$. By adapting the value of Q_a, the desired values of U_o/U_i =0.4 and 0.8 were obtained, so that they could be compared to those of Chehreghani et al. (2021) for the same U_o/U_i, but with a narrower annular gap. In this way, the effect of the external flow confinement could be investigated, while other system parameters remained the same.

Experimental bifurcation diagrams showing the rms amplitude of oscillations and the mean deflection versus the internal flow velocity for D_{ch} =54 mm, and U_o/U_i=0.4 and 0.8 are presented in figures 5(a) and 6(a), respectively. These bifurcation diagrams can be compared to those of Chehreghani et al. (2021) for the same U_o/U_i, but with D_{ch} =31.5 mm, depicted in figures 5(b) and 6(b).

For U_o/U_i=0.4 and 0.8 and D_{ch} =54 mm, compared to U_o/U_i=0.015, two distinct dynamical features can be noticed. First of all, at relatively small flow velocities, remarkably strong first-mode oscillations materialized, followed by flutter in the second mode at higher flow rates, as shown in the figures 5(a), 6(a) and 3. Secondly, the one- or two-sided impacting in these cases did not take place; instead, the pipe partially or completely rubbed the rim of the outer rigid tube.

For U_o/U_i=0.4 and 0.8 the dynamics is also different for D_{ch} =54 mm in comparison to that for D_{ch} =31.5 mm. More specifically, for U_o/U_i=0.4 and D_{ch} =31.5 mm, a static instability at relatively low flow velocities which is followed by weak oscillations superimposed on the mean deflection at higher flows was reported. On the other hand, for D_{ch} =54 mm, first-mode oscillations at U_i = 0.47 m/s initiated; at U_i =1.33 m/s, the oscillations were in the second mode with a dominant frequency of f =2.21 Hz.

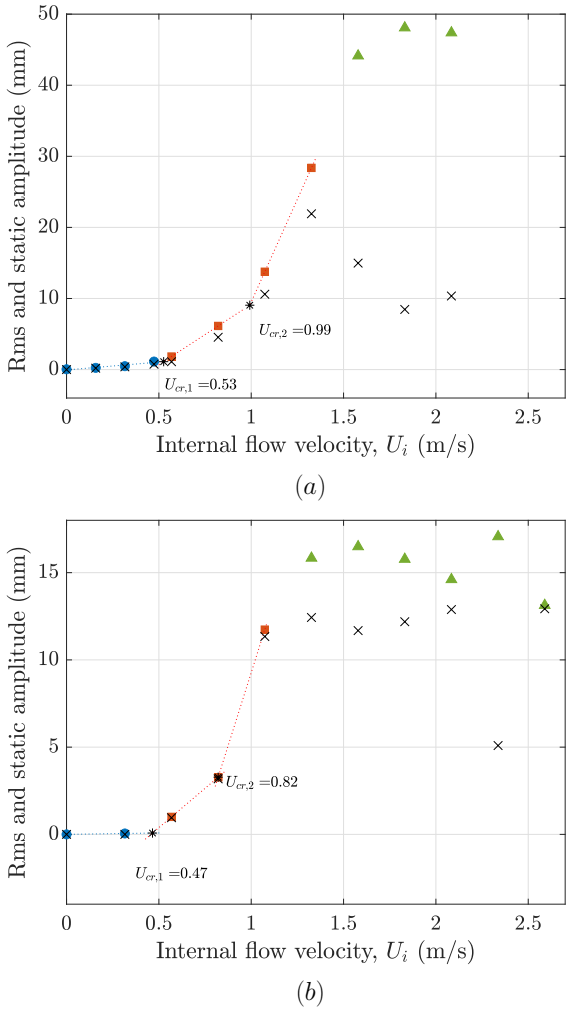

Figure 5. Bifurcation diagrams showing the rms amplitude of oscillations and the mean deflection versus U_i for U_o/U_i =0.4 and (a) D_{ch}=54 mm; (b) D_{ch}=31.5 mm. Rms amplitude: (●) pre-instability, (■) instability, (▲) impact; (×) mean deflection.

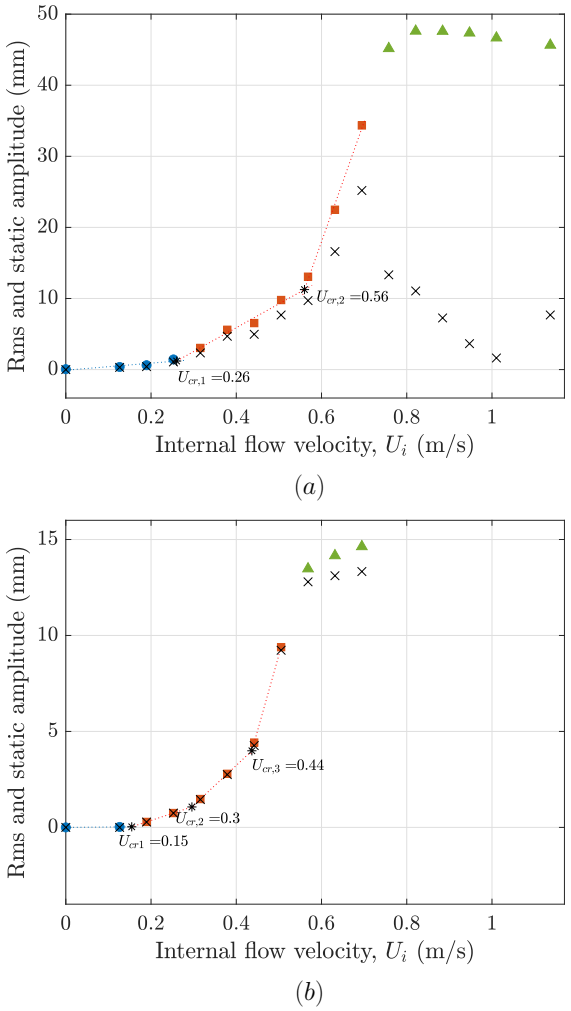

Figure 6. Bifurcation diagrams showing the rms amplitude of oscillations and the mean deflection as a function of the U_i for U_o/U_i =0.8 and (a) D_{ch}=54 mm; (b) D_{ch}=31.5 mm. Rms amplitude: (●) pre-instability, (■) instability, (▲) impact; (×) mean deflection.

For U_o/U_i=0.8 and D_{ch} =31.5 mm, a static instability at U_i=0.15 m/s, followed by weak first-mode and then second-mode oscillations at higher flows was reported. But, for D_{ch} =54 mm, the static instability did not occur; first mode oscillations began at U_i = 0.25 m/s, and at U_i =0.69 m/s the pipe became unstable via second-mode flutter with a dominant frequency of f =2.44 Hz.

4. SUMMARY OF THE RESULTS AND CONCLUSION

In the present study, the dynamics of a pipe subjected to internal and counter-current external flows has been explored experimentally. The pipe is hung vertically and discharges fluid downwards in a pressure vessel surrounding the pipe. Fluid, upon exiting the pipe, exits the reservoir through an annular region formed by the upper part of the pipe and a shorter outer rigid tube. Additional fluid might be added to the reservoir from the bottom to modify the ratio of external to internal flow velocities, U_o/U_i.

The experiments were conducted to examine the influence of varying the external flow confinement, i.e. the size of the annular gap between the pipe and the outer rigid tube, on the fluid-elastic instability of the system. In the first case, no additional flow was added from the bottom and hence, by continuity $U_o A_{ch} = U_i A_i$, and U_o/U_i=0.015. In the second case, when adding additional flow from the bottom, two ratios, U_o/U_i =0.4 and 0.8, were tested to be compared

	D_{ch} =54 mm		D_{ch}=31.5 mm	
U_o/U_i	$U_{cr,1}$	$U_{cr,2}$	$U_{cr,1}$	$U_{cr,2}$
0.015	5.68	-	-	-
0.055	-	-	5.04	-
0.4	0.53	0.99	0.47	0.82
0.8	0.26	0.56	0.15	0.30

Table 2. Summary of the results presenting the critical U_i [m/s] *for instability.*

to those of the same ratio, but for a narrower outer rigid tube of diameter D_{ch} =31.5 mm in Chehreghani et al. (2021).

For U_o/U_i=0.015, the pipe became unstable via flutter in the second mode at relatively high flow velocity. Increasing the flow velocity gave rise to oscillations of higher amplitude. Ultimately, the pipe hit the rigid tube surrounding the upper part of the pipe.

For U_o/U_i=0.4 and 0.8, a significant destabilizing effect on the system was observed as U_o/U_i was increased. For both wider and narrower outer tubes, the onset of instability decreased dramatically with increasing U_o/U_i, as shown in table 2. However, this effect is more pronounced for the narrower outer tube.

Decreasing the external flow confinement, i.e. increasing the outer rigid tube diameter, was found to have a strong stabilizing effect on the pipe; refer to table 2. For U_o/U_i =0.4, the first and second critical flow velocities increased by 13% and 21%, respectively, and for U_o/U_i =0.8 by 73% and 87%, respectively.

Confinement also affected the dynamics qualitatively. For the narrower outer rigid tube, average deflections of remarkably high amplitude were reported prior to weak first or second mode flutter. The pipe started rubbing against the outer rigid tube before any strong oscillatory motions developed. This can be due to the narrowness of the gap that prevents the development of an strong oscillatory instability. On the other hand, for the wider outer rigid tube, with increasing flow velocity, strong oscillations of first and then second mode were observed.

5. REFERENCES

Abdelbaki, A.R. et al., 2020, A nonlinear model for a hanging cantilevered pipe discharging fluid with a partially-confined external flow. *International Journal of Non-Linear Mechanics*, **118**: 103290.

Cesari, F. and Curioni, S., 1971, Buckling instability in tubes subject to internal and external axial fluid flow. *Proceedings of the 4th Conference on Dimensioning*, Hungarian Academy of Science, Budapest: 301-311.

Chehreghani, M. et al., 2021, Experiments on the dynamics of a cantilevered pipe conveying fluid and subjected to reverse annular flow. *Journal of Sound and Vibration*, **515**:116480.

Gao, F.P. et al., 2003, Physical modeling of untrenched submarine pipeline instability. *Ocean Engineering* volume:30, **10**:1283-1304.

Hannoyer, M.J. and Païdoussis, M.P., 1978, Instabilities of tubular beams simultaneously subjected to internal and external axial flows. *ASME Journal of Mechanical Design*, **100**:328-336.

Michelin, S. and Doaré, O., 2013, Energy harvesting efficiency of piezoelectric flags in axial flows. *Journal of Fluid Mechanics*, **714**:489–504.

Moditis, K. et al., 2016, Dynamics of a partially confined, discharging, cantilever pipe with reverse external flow. *Journal of Fluids and Structures*, **63**:120-139.

Païdoussis, M.P. et al., 2008, Dynamics of a long tubular cantilever conveying fluid downwards, which then flows upwards around the cantilever as a confined annular flow. *Journal of Fluids and Structures*, **24**:111-128.

Païdoussis, M.P., 2014, *Fluid-Structure Interactions: Slender Structures and Axial Flow*, volume 1, 2nd edition, Academic Press.

Païdoussis, M.P. et al., 2021, Dynamics of a cantilevered pipe subjected to internal and reverse external axial flow: A review. *Journal of Fluids and Structures*, **106**:103349.

Santillan, S. et al., 2010, Static and dynamic behavior of highly deformed risers and pipelines. *ASME Journal of Offshore Mechanics and Arctic Engineering*, **132**:1283-1304.

Tubaldi, E. et al., 2018, Nonlinear dynamics of Dacron aortic prostheses conveying pulsatile flow. *ASME Journal of Biomechanical Engineering*, **140(6)**:061004.

Annular and leakage flow

IMPACT OF THE NOZZLE GEOMETRY ON THE AEROELASTIC INSTABILITY OF A PLATE SUBJECTED TO AN AIR JET

Antoine Tatin
LadHyX (CNRS-Ecole polytechnique) & Fives Stein, France
Xavier Cluzel, Yannick Mourlot
Fives Stein, Maisons-Alfort, France
Pascal Hémon, Sophie Ramananarivo
LadHyX, CNRS-Ecole Polytechnique, Institut Polytechnique de Paris, Palaiseau, France

ABSTRACT

We study experimentally the flutter instability of a rigid plate supported elastically and impacted by an air jet. The behavior of the plate, modelled as a damped oscillator, is altered by the jet which can generate a negative added damping. As the total damping becomes negative, the plate undergoes growing amplitudes oscillations. We discuss the influence of the geometry of the nozzle, appearing as one of the crucial parameter in the aeroelastic mechanism. The results are compared with the theoretical model of Antoine et al (2008), showing some discrepancies.

1. INTRODUCTION

Gas jets are widely used in industrial processes for cooling or drying due to their thermal properties. This is notably the case of steel strip production lines, where batteries of air jets are used after galvanization, for example, to control the zinc coating thickness and lower the strip temperature. Such steel strips are thin and elongated, which make them particularly flexible and deformable. The interaction with impinging jets can then lead to instabilities, such as self-sustained oscillations or sudden buckling of the strip. The latter are detrimental for the quality of the strips, forcing the industrial line to slow down production.

Jets impinging stationary walls have been extensively characterized (Glauert (1956); Beltaos and Rajaratnam (1973); Fairweather and Hargrave (2002); Maurel et al (2003)), but less is known about their interaction with a moving surface and subsequent instabilities. The few existing studies on the subject investigated fluid-structure interaction mechanisms on simplified model systems, consisting of a rigid plate supported elastically and impacted by normal jets. The motion of the plate is restrained to either pure torsion (Nyirumulinga et al (2008, 2009)) or pure translation (Antoine et al (2007, 2008)), reproducing the fundamental modes of deformation of industrial strips. Instabilities are reported in both cases, which are attributed to the coupling between the plate motion and the flow at the outlet of the jets. Fluid forces can then be expressed as an aeroelastic added stiffness and added damping, which can lead respectively to divergence and flutter when overcoming the structural stiffness and damping of the system.

While only divergence instabilities have been observed for the rotating plate of Nyirumulinga et al (2008, 2009), flutter does occur for the translational set up of Antoine et al (2008) on which we are focusing here. In the latter, a key aspect is the confinement of the flow in the narrow passage between the plate and the jet nozzle, and oscillations develop below a critical plate-nozzle distance. In that respect, the system belongs to the broader framework of flexible plate-like structures subject to leakage flows, which have proved notoriously prone to fluid-elastic instabilities (Mulcahy (1988); Inada & Hayama (1990); Porcher & de Langre (1996); Paidoussis (2004)). The geometry and extent of the confined region is then an important parameter, as confirmed by the results of Antoine et al (2008) on two different planar and circular nozzles. However the impact of geometrical factors such as the jet width and the thickness of the nozzle walls has not been explored yet.

Here, we extend the study of Antoine et al (2008) on the aeroelastic instability of a plate oscillating in translation. We investigate the impact of the nozzle size and wall thickness, and compare the results to the theoretical model of Antoine et al (2008). We further propose potential refinements for the latter to account for discrepancies with experimental results.

2. AN AEROELASTIC INSTABILITY

2.1. Experimental set-up and results

The set-up consists of a 150×90 mm aluminium rigid plate mounted with four identical springs, as il-

lustrated in Fig. 1a. Taut nylons wires are attached to the corners of the plate and to the supporting structure to restrict the movement to vertical translation. Furthermore, we have verified, by video analysis, that the plate moves indeed in translation and rotation is negligible. The plate is subjected to an impinging air jet generated by a nozzle orthogonal to the plate. The latter is connected upstream to a plenum chamber to stabilize the pressure ahead of the nozzle, and a manometer to change the flow velocity. The present set-up does not allow for direct measurement of the velocity at the outlet of the jet U_j. It is instead estimated from the pressure reading of the manometer, using Bernoulli equation. We thus have limited control over its value here, which is dependent upon the pneumatic circuit. As U_j is a key physical parameter, it restricts to a certain extent the interpretation of the experimental results, and on-going work is being done to better control it.

A micrometer screws enable to precisely control the distance H between the nozzle and the plate. Note that the equilibrium plate-nozzle distance slightly increases upon triggering of the jet, and H refers to this shifted position. Finally, the vertical position of the plate is tracked using a laser displacement sensor with an acquisition frequency of 1000 Hz. We extract the angular frequency of the oscillations ω through a fast Fourier transform of the data. Furthermore, the system reduced damping η (explicitly defined later in the text) is measured from the growth rate of the plate oscillations in the unstable case, or its decay rate following a perturbation in the stable case. Namely, local oscillation maximas are detected and the evolution of the logarithmic values with time is fitted with a linear regression. In the paper, each data point for η is averaged over five different acquisitions and error bars corresponds to the standard deviation.

In the present work, we use two different nozzle geometries: a planar and axisymmetric one shown in Fig. 1b. The planar nozzle has an elongated rectangular shape with an inner length $L = 70$ mm that is large compared to the inner width d. The nozzles are 3D-printed, thus allowing to easily change the width within $d = 1-5$ mm, as well as the wall thickness $e = 1-3$ mm that dictates the size of the jet confined region. The axisymmetric nozzle has a circular cross-section with inner diameter $d = 4-6$ mm and wall thickness $e = 1-4$ mm. To change e, we mount 3D-printed collars at the end of the metal tube that forms the nozzle.

Consistently with Antoine et al (2008), we observe self-sustained oscillations below a critical nozzle-plate distance for both geometries. This transition is interpreted in light of the damping in the system η. As reported in Fig.1c-d, we observe that η decreases when reducing distance H, and the critical distance of the instability coincides with η becoming negative. We further compare our results to the theoretical model from Antoine et al (2008), which is succinctly presented in the following.

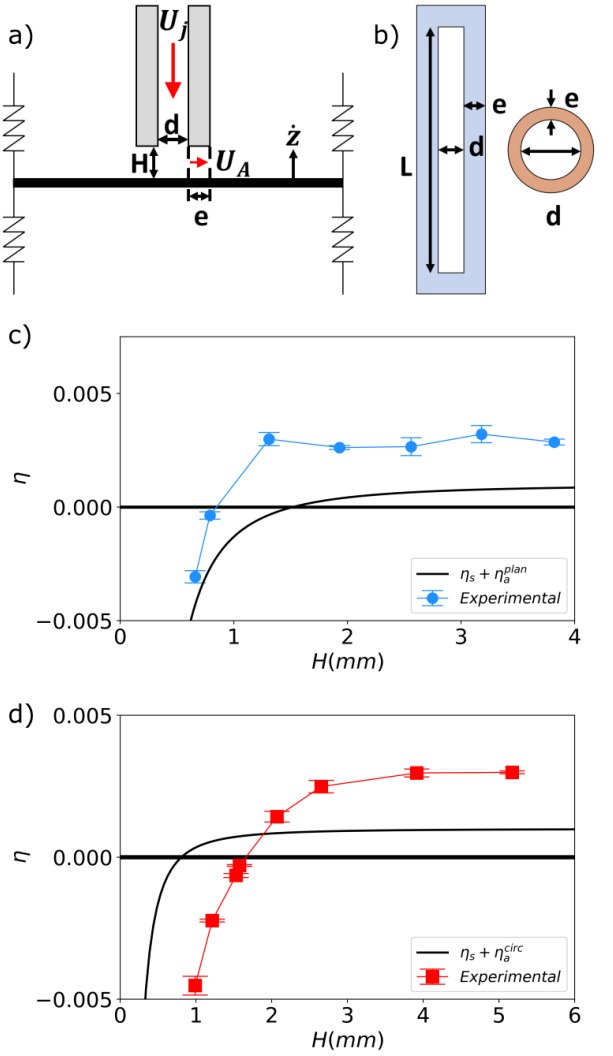

Figure 1. (a) Schematics of the experimental set-up. (b) Nozzles with a planar and axisymmetric cross section. Evolution of the total damping η with the plate-nozzle distance H for, (c) a planar nozzle with $d = 2$ mm and $e = 1.5$ mm, and (d) an axisymmetric one with $d = 4.5$ mm and $e = 0.75$ mm. Experimental results are compared with the prediction of the theoretical model of Antoine et al (2008) (solid lines).

2.2. Theoretical model from Antoine et al (2008)

The plate behaves as an harmonic damped oscillator, and its vertical position z verifies the equation:

$$m\ddot{z} + c\dot{z} + kz = F(z, \dot{z}, \ddot{z}) \qquad (1)$$

with m the mass of the oscillator, k its spring stiffness, and c the structural damping. F denotes the force exerted by the jet as it impacts the plate and seeps through the confined region between the nozzle and the plate. Time derivative is noted with dots. For such leakage flow, pressure is sensitive to the plate motion so that the resulting force F, obtained by integrating the pressure in the confined region, may depend on the plate's position z, velocity $\dot{z}$ and acceleration $\ddot{z}$. It is computed in Antoine et al (2008) based on the model of Porcher & de Langre (1996), in the approximation of small oscillations. The jet force then primarily writes as a negative added damping term η_a, which can negate structural damping and thus trigger the instability:

$$\ddot{z} + 2\omega_0 \eta \dot{z} + \omega_0^2 z = 0 \text{ with } \eta = \eta_s + \eta_a \quad (2)$$

Here, $\omega_0 = \sqrt{k/m} = 77$ s^{-1} is the natural angular frequency. It is chosen in the range of the frequencies observed on production lines. $\eta_s = c/(2m\omega_0) = 8.10^{-4}$ is the structural damping coefficient, both measured experimentally. The expressions of η_a obtained by Antoine et al (2008) for the planar and circular geometry are:

$$\eta_a^{circ} = -\pi\rho U_A \frac{(d/2+e)^3 - (d/2)^3}{3\sqrt{km}} \frac{1}{H} \quad (3a)$$

$$\eta_a^{plan} = -\frac{\rho U_A L e^2}{2\sqrt{km}} \frac{1}{H} \quad (3b)$$

with ρ the air density and U_A the mean flow velocity in the confined region between the plate and nozzle (see Fig.1a). It can be related to the velocity at the jet outlet U_j through arguments of conservation of the flow rate, and we obtain:

$$U_A^{circ} = \frac{d}{4H} U_j \quad (4a)$$

$$U_A^{plan} = \frac{d}{2H} U_j \quad (4b)$$

Note that those expressions for U_A differ from the ones reported in Antoine et al (2008). It modifies the dependency of η_a on the plate-nozzle distance H, which varies as $1/H^2$. The latter is made explicit by expressing Eq.3 as :

$$\eta_a^{circ} = -\pi\rho U_j \frac{(d/2+e)^3 - (d/2)^3}{12\sqrt{km}} \frac{d}{H^2} \quad (5a)$$

$$\eta_a^{plan} = -\frac{\rho U_j L e^2}{4\sqrt{km}} \frac{d}{H^2} \quad (5b)$$

Theoretical prediction for η_a are computed for both nozzle geometries, and the total damping η is compared to experimental results in Fig.1c-d. The model qualitatively captures the observed trends with a sharp decay of η as the plate-nozzle distance is reduced, which eventually becomes negative leading to growing amplitude oscillations. Discrepancies are however observed for the value of the critical distance, which is overestimated for the planar geometry (Fig.1c) and underestimated for the circular one (Fig.1d). In both cases, damping at large H also have lower values than in experiments. However, as will be discussed later, bodies oscillating in a flow are generally subjected to an additional positive damping that is not accounted for in the present model. Adding this contribution would tend to shift the theoretical curve upwards, also affecting the value of the critical distance.

The model captures the decrease of the damping with distance H, but it also indicates a strong influence of the geometry of the nozzle (namely the nozzle width d and wall thickness e) on the onset of the instability. In the following, we study the influence of both geometrical parameters, which were not explored in Antoine et al (2008).

3. INFLUENCE OF THE NOZZLE GEOMETRY

3.1. Influence of the nozzle wall thickness

The wall thickness of the nozzle e is an important parameter as it determines the size of the confined region between the plate and the nozzle. The theoretical model notably predicts a strong dependency of the added damping on e in Eq.5.

We tested planar nozzles with varying thicknesses within $e = 1-3$ mm, and the same jet width $d = 2$ mm. Experiments are performed with the same pressure, which is expected to produce similar jet velocities U_j since the nozzles have the same inner cross section. The evolution of the damping η with the nozzle-plate distance H is shown in Fig.2a. Contrary to what was expected, e seems to have little influence on the behavior of the plate and the curves $\eta(H)$ overlap for all the nozzles tested. We also report in Fig.2b the evolution of the angular frequency of the oscillations ω with H, which shows similar results across variations in e. Moreover, we observe that ω increases as the jet is brought closer to the plate, reflecting a rise in the system stiffness. It supports the nature of the underlying mechanism as a dynamic instability, and not a static one (with an added stiffness cancelling the structural one and causing a divergence) as was the case for the rotating plate of Nyirumulinga et al (2009).

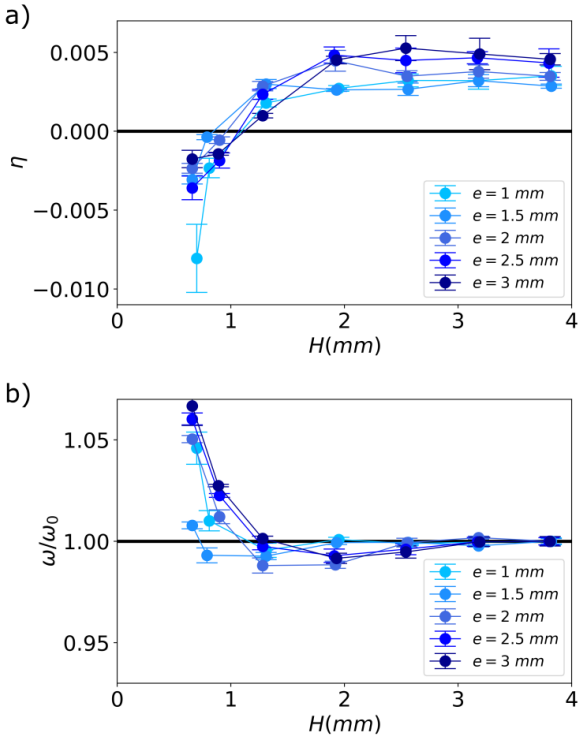

Figure 2. Evolution with H of (a) the total damping coefficient and, (b) the angular frequency of the oscillation ω (compared to that in the absence of jet ω_0), for planar nozzles with different wall thicknesses e and same width $d = 2$ mm.

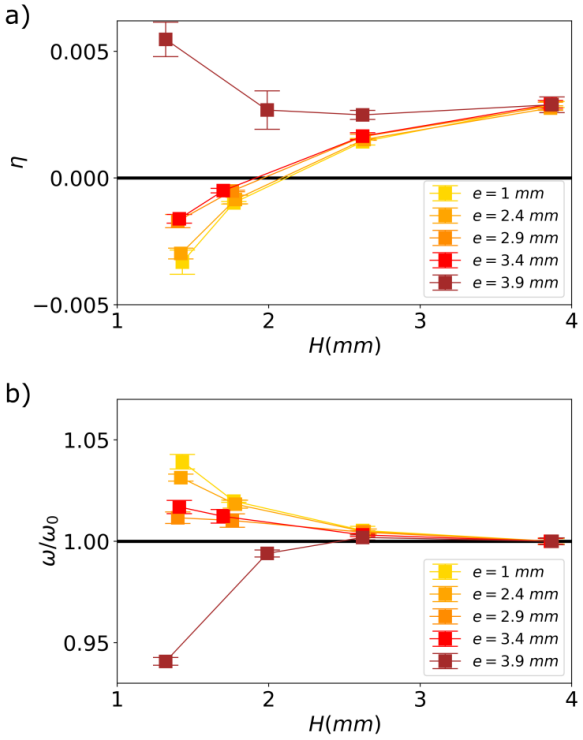

Figure 3. Evolution with H of (a) the total damping coefficient and, (b) the dimensionless angular frequency of the oscillation ω/ω_0, for circular nozzles with different wall thicknesses e and same width $d = 6$ mm.

We further tested axisymmetric nozzles with different wall thicknesses within $e = 1 - 3.9$ mm and the same inner diameter $d = 6$ mm. As with the planar geometry, we observe little influence of e on the behavior of the plate in Fig.3 for $e \leq 3.4$ mm. However, different results are obtained when the thickness of the nozzle exceeds a particular value close to the nozzle radius $d/2$. Namely, no instability is reported for $e = 3.9$ mm, and contrary to previous results, the damping of the plate tends to increase with smaller H in Fig.3a. The evolution of the frequency with H also exhibits a different trend, with a drop of ω reflecting a softening of the system. This phenomenon was also reported by Nyirumulinga (2011). The constriction between the plate and the nozzle's walls results in high-velocity flows, with low pressure according to Bernoulli's principle. For thick nozzles, this low-pressure region is large enough to generate a significant suction force on the plate, which overcomes the pushing force due to the jet impact. It acts in the direction of the displacement and increases as the plate draws nearer to the nozzle, resulting in a negative added stiffness for the system. Further increasing the thickness of the nozzle's walls (with e =5, 10, and 20 mm) amplifies this aerodynamic force, which can then overcome the structural stiffness of the oscillator. In the latter cases, we observe that the plate is jammed close to the nozzle.

3.2. Influence of the jet width

We then study the influence of the jet width d. The latter impacts the ratio between the flow velocity in the confined region U_A and at the jet outlet U_j, as shown in Eq.4. For circular nozzles, varying the jet width also changes the area of the confined region, leading to the dependence on d of the damping coefficient η_a^{circ} in Eq.5a. Results for circular nozzle are however not presented in this paper, due to a large uncertainty on the velocity of the jet. In order to change d, tubes with varying section were adapted at the outlet of the plenum chamber through diverging/converging connectors, and those changes of the pneumatic circuit are suspected to impact U_j. Planar nozzles were directly connected to the plenum chamber, thus reducing those effects.

We tested planar nozzles with different jet width $d = 1 - 3$ mm and the same wall thickness $e = 1.5$ mm. As shown in Fig.4, the total damping of the system is amplified as d decreases, also shifting the onset

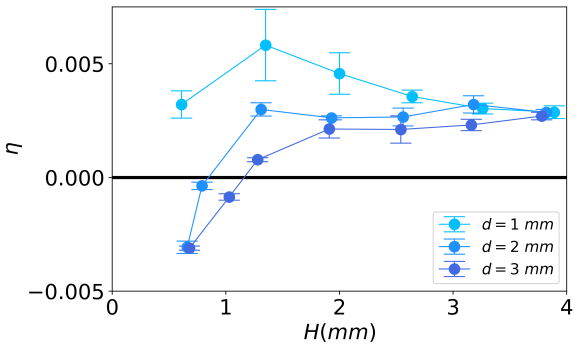

Figure 4. Total damping coefficient as a function of the plate-nozzle distance, for planar nozzles with various jet widths d and same wall thickness e = 1.5 mm.

of the instability towards smaller H. For the smallest width $d = 1$ mm, the plate remains stable (with positive damping) across the range of H explored. While our results show an effect of the jet width, a characterization over a larger range of d is required to identify the dependency of η_a on d, which is the subject of on-going work.

4. POSITIVE ADDED DAMPING

As noted previously, there is a discrepancy between experiments and theory in Fig.1c-d for large distances between the plate and the nozzle. While theoretical predictions for η converge towards the structural damping coefficient η_s for large H, experimental results reach a higher value for both planar and axisymmetric nozzles. The influence of the jet is expected to vanish as we move the nozzle away from the plate (with η decaying down to η_s), but it is still non-negligible for the largest distances tested here of $H/d \sim 4$. In this intermediate regime, the jet may cause an additional positive damping, as is generally the case for objects oscillating in the direction of the flow (Hémon, 2006). The plate motion along the direction of the jet modifies the relative velocity of the incoming flow as $U_J - \dot{z}$. This normal flow exert a force F^* on the plate similar to a drag force, and of the form:

$$F^* = \frac{1}{2}\rho CS(U_J - \dot{z})^2 \tag{6}$$

with C a numerical coefficient to be determined and S the impact surface of the jet. Given the small nozzle-plate distances here, the jet does not have enough space to develop radially and S correspond roughly to the area of cross-sectional area of the nozzle. In the approximation of small oscillations, F^* rewrites to the first order:

$$F^* = \frac{1}{2}\rho CSU_J^2 - \rho CSU_J\dot{z} \tag{7}$$

The zeroth order term, the repulsive force, $\frac{1}{2}CS\rho U_J^2$ is responsible for the initial displacement of the equilibrium position when triggering the jet. The second term depends on $\dot{z}$ and leads to an additional damping term η_j in Eq.2:

$$\eta_J = \frac{\rho CSU_J}{2\sqrt{km}} \tag{8}$$

We estimate the unknown product CS by measuring the static force $\frac{1}{2}CS\rho U_J^2$ for different jet velocities U_J. In practice, we infer it from the displacement of the plate, resulting from the balance between this aerodynamic contribution and the elastic restoring force. We obtains values of $CS^{plan} = 5.10^{-6}m^2$ for the planar nozzle, which corresponds to 3.5% of the jet surface area Ld, and $CS^{circ} = 1.2.10^{-5}m^2$ for the axisymmetric one corresponding to 75% of the jet surface area $\pi d^2/4$. Its yields $\eta_J^{plan} = 4.10^{-5}$ and $\eta_J^{circ} = 2.10^{-4}$. Those values significantly underestimates the gap between experimental and theoretical η in Fig.1, and CS^{plan} is low compared to the surface area of the jet. The measurement of those parameters however depends on the degree of accuracy on U_j, which is limited with the present set-up. Additionally, the estimate can be improved by taking into account the velocity gradient in the direction of the jet (Hémon (2006)).

5. CONCLUSION

In line with Antoine et al (2008), we show that a plate subjected to an air jet undergoes a flutter instability, which is attributed to a negative aeroelastic damping generated by the flow going through the narrow passage between the plate and the nozzle. We further studied the influence of the nozzle geometry, and notably the thickness of the nozzle's walls which dictates the extent of the confined region. Contrary to what was expected and predicted by the model of Antoine et al (2008), it seems to have little influence on the behavior of the plate. In contrast, changing the nozzle inner width significantly modifies the critical distance below which oscillations start to grow. While the model captures the effect of the width, it is not consistent with the results for different wall thicknesses. Ongoing work is pursued on refining the model to account for it, but also to extend experiments. In particular, a limiting factor of the present set-up is the lack of direct velocity measurement at the jet outlet. A sensor will be mounted on the nozzle to control it more precisely. It will notably allow

to evaluate the additional positive damping of the jet observed at larger nozzle-plate distances.

6. ACKNOWLEDGEMENTS

This work is part of a research collaboration between LadHyX (CNRS-Ecole Polytechnique) and Fives Stein. A. Tatin acknowledges funding from Fives Stein.

7. REFERENCES

Antoine, M. et al, 2008, Aeroelastic instability of plate subject to normal jet, In *Proc. of 9th Int. Conference on Flow-Induced Vibrations, Prague, Czech Republic, 2008.*

Antoine, M. et al, 2007, Aeroelastic instability in a jet-plate interaction, *Comptes Rendus Mécaniques*, 335(11): 691-695.

Nyirumulinga, Y. et al, 2008, Impinging jets on a plate with a degree of freedom in torsion - Theoretical and experimental preliminary results, *International Congress of Theoretical and Applied Mechanics, ICTAM 2008*, Aug 2008, Adelaide, Australia.

Nyirumulinga, Y. et al, 2009, Experimental approach to the aeroelastic behaviour of an oscillating plate by interacting high velocity gas jets, In *ASME 2009 Fluids Engineering Summer Meeting, FEDSM 2009*, Aug 2009, Vail, Colorado, USA.

Nyirumulinga, Y., 2011, Etude expérimentale de l'aéroélasticité d'une plaque oscillante impactée par une batterie de jets turbulents, *Conservatoire national des arts et metiers - CNAM, 2011*.

Hémon, P., 2006, *Vibrations des structures couplées avec le vent*, Éditions École Polytechnique, 2006.

Paidoussis, M. P., 2004, *Fluid-structure interactions: slender structures and axial flow, Volume 2*, Academic press.

Glauert, M. B., 1956, The wall jet, *Journal of Fluid Mechanics*,1(6), 625-643.

Beltaos, S. and Rajaratnam, N., 1973, Plane turbulent impinging jets, *Journal of Hydraulic Research*, 11(1), 29-59.

Fairweather, M. and Hargrave, G.K., 2002, Experimental investigation of an axisymmetric, impinging turbulent jet. 1. Velocity field, *Experiments in Fluids* 33(3), 464-471.

Renard, M. et al, 2003, Rapid cooling in continuous annealing and galvanizing lines, *Metallurgical Research Technology*, 100(7-8), 751-756.

Maurel, S. et al, 2003, Caractéristiques cinématiques et structurelles d'un jet d'air plan turbulent frappant une plaque plane placée à distance variables, *Mechanics & Industry*, 5(3), 317-329.

Mulcahy, T.M., 1988, One-dimensional leakage-flow vibration instabilities, *Journal of Fluids and Structures*, 2(4), 383-403.

Inada, F. & Hayama, S., 1990, A study on leakage-flow-induced vibrations. Part 1: Fluid-dynamic forces and moments acting on the walls of a narrow tapered passage, *Journal of Fluids and Structures*, 4(4), 395-412.

Inada, F. & Hayama, S., 1990, A study on leakage-flow-induced vibrations. Part 2: Stability analysis and experiments for two-degree-of-freedom systems combining translational and rotational motions, *Journal of Fluids and Structures*, 4(4), 413-428.

Porcher, G. & de Langre, E., 1996, *Fluidelastic instability in a confined annular flow : an experimental and analytical approach* (No. CEA-CONF–12422). CEA Centre d'Études de Saclay.

Bluff bodies Bluff body/near-wake interactions

DIMENSIONING OF A SOLAR TRACKER TORQUE TUBE FOR TORSIONAL GALLOPING

Eva Martínez García
Energy Department. University of Oviedo, Asturias, Spain
Eduardo Blanco Marigorta
Energy Department. University of Oviedo, Asturias, Spain
Jorge Parrondo Gayo
Energy Department. University of Oviedo, Asturias, Spain
Antonio Navarro Manso
Energy Department. University of Oviedo, Asturias, Spain

ABSTRACT

Solar trackers with a single axis (longitudinally arranged panels on a torque tube, driven by a motor in the central section) have evolved to extremely slender structures, due to the competitiveness and optimization that the market is carrying out. In the present work, an analytical and experimental approach has been developed about the aeroelastic phenomena found in these solar trackers with one degree of freedom. On the one hand, the analytical study has identified the dimensionless parameters governing the differential equation of movement. On the other hand, systematic wind tunnel experiments have been carried out with a 3D full aeroelastic scale model. It has been found that the tests reproduce correctly the aeroelastic phenomena found on a real situation. The main result has been the critical galloping velocity for every tilt angle, and a calculation methodology for the solar tracker shaft.

1. INTRODUCTION

Nowadays the trend for increasing profits on solar photovoltaic energy is the use of single axis solar trackers with one degree of freedom. The design of these trackers places the solar panels longitudinally on a tube ("torque tube"), driven by a motor in the central section. This system makes possible the orientation of the azimuth but not the altitude. Although the energy obtained is smaller than with a two degree of freedom solar tracker, is still a 30% higher than the obtained with fixed solar panels (Bruno et.al, 2015).

The structural typology of these solar trackers consists on several solar panels distributed longitudinally over a torsional axis. The shaft is supported by several pillars that allow only the rotational movement. One end of the shaft is free, and the other is fixed to a gearmotor (driver) in charge of angular positioning. Usually, these structures are in a symmetrical arrangement with a row of panels on each side of the driver. Figure 1 shows an example of the structural scheme and dimensions of this kind of solar tracker.

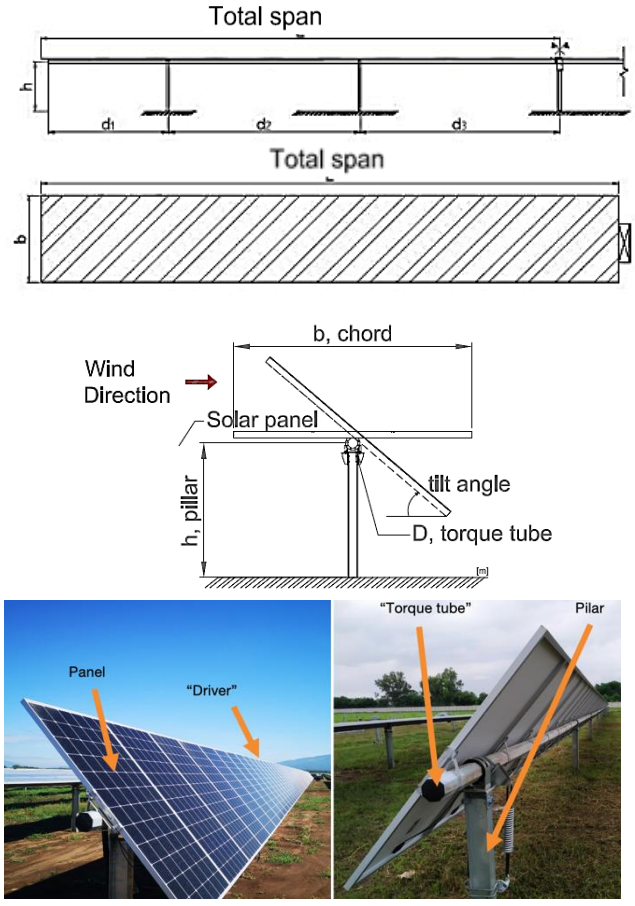

Figure 1. Scheme of single axis solar tracker.

Due to the evolution and mechanical optimization that the market is carrying out, these structures are extremely slender; although the design against static loads and non-extreme accidental situations is correctly solved, aeroelastic instability may occur for some particular situations (Zachary et al, 2020).

Figure 2. Single axis solar tracker facilities collapse (Source: www.pv-magazine-australia.com).

The failures occurring all over the world during the last years are attributed to torsional galloping, flutter or torsional divergence. The components most commonly subjected to fatigue and collapse are the positioning motor, the driver supports and the main axis. Although usually, this also means the panels destruction (Figure 2).

Basic aeroelastic effects (Païdoussis et.al, 2011) (Blevins, 1990) are normally covered by current construction standards (Dyrbye et al, 1997), however, it is increasingly clear that they do not consider the specific effects of wind on single-axis solar trackers. For the correct calculation of these structures, a deeper understanding of the aeroelastic phenomenon is necessary, usually based or complemented with wind tunnel tests (Zachary et al, 2020). Along this line, this work develops a method of analysis and calculation that allows to determine the necessary resistance of the structure to avoid the failures due to these phenomena.

During the experimental test, it could be expected to find aeroelastic phenomena such as induced vibrations by vortex shedding, torsional galloping and flutter. The torsional galloping is a kind of flow-induced oscillation instability with one degree of freedom. Many studies on flat plate aerodynamics have been done, for instance analytical studies on single degree of freedom models (Yang, 2010). There is also experimental aerodynamic tunnel (Strobel et.al, 2014) and Computational Fluid Dynamics, CFD (Jubayer et.al, 2014) researches, including tests of single and complete solar photovoltaic fields of solar trackers. The latter have been usually made with static models and study the effect of wind directionality and the interferences between different rows of trackers.

Only a few of these investigations have also developed full aeroelastic tests (Roedel et.al, 2018).

As the state of the technique is still in a young phase (Rohr et al, 2015), regarding this structural typology, in this research an inspectional analysis of the differential equation of the axis torsional motion has been done, obtaining the descriptive dimensionless parameters for the aerodynamic and structural phenomena. Based on these analyses full scaled aeroelastic models have been developed and tested in an aerodynamic wind tunnel.

The experimental campaign was focused on the following objectives:

- Phenomenological explanation of the aeroelastic phenomena causing instability in the solar tracker structure.
- Finding out the critical velocities for different tilt angles.
- Developing of a safe design criterion in terms of project wind velocities and rigidity of the structure, for the analyzed case.

2. NON-DIMENSIONAL ANALYSIS

In this specific case, for the dimensionless analysis it is necessary to take in account nine variables.

Three of them, correspond to the fluid: velocity, density and viscosity (U, ρ, μ). Four are related to the structure: characteristic length (L), typically span or chord), torsional stiffness (K); moment of inertia with respect to the axis (I); and structural damping (c). The last variables arise from the aerodynamic forces, which in this case can be reduced to the torque magnitude (T), and frequency (ω).

From the relationship between the variables corresponding to the fluid and aerodynamic forces, come up the typical dimensionless numbers of Euler (C_m), in this case as the moment coefficient), Strouhal (St) and Reynolds (Re).

$$C_m = \frac{T}{\frac{1}{2}\rho U^2 L^3} \quad \#(1)$$

$$S_t = \frac{\omega L}{U} \quad \#(2)$$

$$R_e = \frac{\rho UL}{\mu} \quad \#(3)$$

On the other hand, these numbers related to the properties of the structure derive from the equation of torsional motion of the structure:

$$I\frac{d^2\theta}{dt^2} + c\frac{d\theta}{dt} + K\theta = T \quad \#(4)$$

These numbers are, first the torsional stiffness coefficient (C_k):

$$C_K = \frac{K}{1/2\,\rho U^2 L^3} \quad \#(5)$$

Second, the reduced frequency (ω_r), which has the same structure than St but relating to the natural frequency of the structure instead of the aerodynamic phenomenon frequency.

$$\omega_r = \frac{\pi}{2}\frac{L}{U}\sqrt{K/I} \quad \#(6)$$

And finally, the damping ratio (ξ), corresponding to the relationship between structural and critical damping:

$$\xi = \frac{c}{\sqrt{2(KI)}} \quad \#(7)$$

Typically, using these groups, the aerodynamic forces can be expressed as St and C_m as a function of the other four:

$$C_m = (Re, C_K, \omega_r, \xi) \quad \#(8)$$

$$St = (Re, C_K, \omega_r, \xi) \quad \#(9)$$

Thus, if a scale model maintains these four dimensionless numbers, is possible to achieve the similarity of the aerodynamical phenomenon.

Regarding the scaled model for wind tunnel tests, as usual in many of these cases, the Reynolds number is not compatible with the other dimensionless groups.

However, in this specific case, the most important aerodynamic effects are generated by vortex shedding of bluff body separation instead of boundary layer detachment. Because of this, the Reynolds number influence is expected to be smaller for fully developed turbulent flows.

In order to preserve the dimensionless numbers C_k, ω_n and ξ when making the scale model, it is necessary to maintain the damping ratio between model and prototype, usually through the mechanical properties of the materials.

$$\xi_m = \xi_p \quad \#(10)$$

And there is also a fixed relationship between the model and prototype inertia, determined by the scale.

$$I_m = I_p \left(\frac{L_m}{L_p}\right)^5 \quad \#(11)$$

However, for the torsional stiffness coefficient, (C_k), the relation obtained from the prototype is:

$$K_m = K_p \left(\frac{U_m}{U_p}\right)^2 \left(\frac{L_m}{L_p}\right)^3 \quad \#(12)$$

The scale and the torsional stiffness ratio of the model and prototype are not uniquely related. Which also, allows to use different stiffness in the materials to adjust the velocities at which the aerodynamic phenomena occur in the wind tunnel.

3. EXPERIMENTAL METHODOLOGY

The experimental tests were developed in the aerodynamic wind tunnel, named EB40-Owt, at the Energy Department of the University of Oviedo (based on Rodríguez Lastra et. al, 2013). It has a maximum velocity of 35 m/s, nominal power of 30 kW; 14.25 m length and a test section of 0.7 x 0.7 m; the turbulence is below 3% at the test chamber. The single axis solar tracker prototype studied has the basic morphology of this kind of structures, with the features indicated in the table 1.

Description	Value
Tracker shaft length [m]	30
Shaft diameter [m]	0.210
Shaft thickness [mm]	6
Shaft stiffness [Nm]	113450
Inertia [kg·m²]	1668
Panel chord [m]	3
Panel thickness [m]	0.0135

Table 1. Prototype solar tracker dimensions.

In this kind of solar trackers, damping ratios are low and correspond to the natural value of the materials, mostly of the shaft. The torsion values of the structure are determined only by the shaft because the panel's stiffness has little influence on this property of the structure.

However, the inertia of the system comes determined by the panels surface because the shaft mass is small and concentrated on the axis. The solar tracker is supported by four pillars and the height from the torsional axis respect to the floor is 20% bigger than half of the panel chord.

Taking advantage of the symmetry of the solar tracker, the experimental model represents only half of the structure from the driver (fixed end) to the free end. To take full advantage of the test section, the scale is 1/45, meaning a blockage below 7 or 8% in any azimuthal position

Figure 3 show the experimental model installed on the open test section.

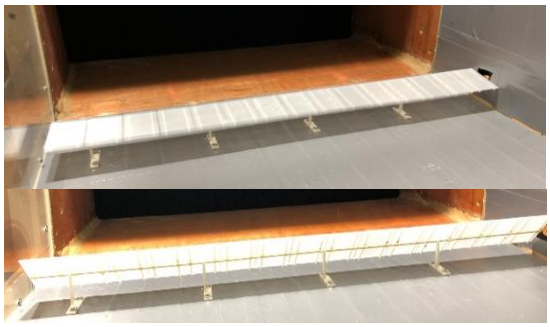

Figure 3. Full aeroelastic scale model.

The model has been built mostly with PLA material, using additive manufacturing technologies.

In the case of model's shaft, two materials were chosen: steel and brass, with the aim to study the influence of the torsional stiffness in the critical velocity. Table 2 contains detailed information of the complete model.

Description	Value
Tracker shaft length [m]	0.67
Panel chord [m]	0.067
Support height [m]	0.04
Purlin thickness [m]	0.003

Table 2. Solar tracker model: panels and supports main features.

Two different models have been built for evaluation on the wind tunnel. Both have the same features except for the torsional stiffness of their shaft since one is made of steel, with K=0.092 Nm, and the other of brass with a K= 0.2 Nm. Table 3 collects the properties of the models based on the type of shaft.

Concept	Brass	Steel
K[Nm]	0.092	0.200
I [kg·m²]	9.02e-6	9.02e-6
ξ[%]	1.6	2.4
ω_n[Hz]	25.3	37.2

Table 3. Principal features of the models.

Several impact tests have been performed to obtain the natural frequency of the structure and its damping ratio.

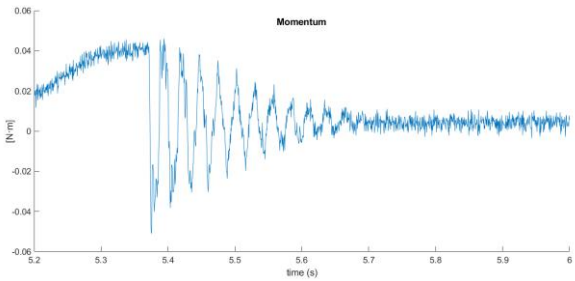

Figure 4. Time signal of the impact test. Moment at the driver.

One of the temporal signals obtained during the tests is represented on figure 4, in which the logarithmic decrement of the moment on the driver can be appreciated.

A frequency analysis of an impact test signal can be seen in the figure 5. The first peak at 37 Hz corresponds the main natural frequency of the structure with the steel shaft. The second peak about 110 Hz, corresponds to the third harmonic and there are also smaller excitations at higher frequencies, representing higher order harmonics and other less important vibration modes.

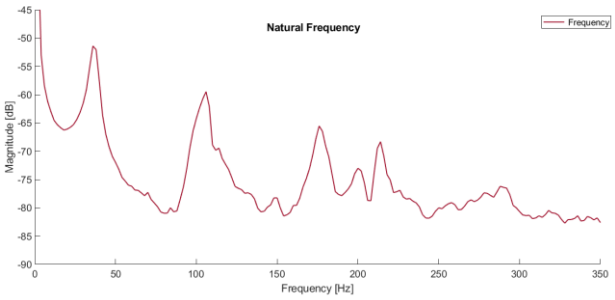

Figure 5. Frequency analysis of the impact test.

Because inertia of the structure is distributed along the axis, the natural frequencies of the vibration correspond to the expression (Rao, S.S., 2007):

$$\omega_n = \frac{(2n+1)\pi}{2}\sqrt{\frac{K}{I}} \quad \#(13)$$

The experimental procedure consists on setting the solar tracker on a determined tilt angle (solar azimuthal orientation) and test increasing speeds until the instabilities are found. The tested azimuthal angles range from +75° degrees to -75°.

4. EXPERIMENTAL RESULTS

In the different models tested, as the velocity increases, small vibrations can be observed, due to the inflow turbulence (Fig. 6).

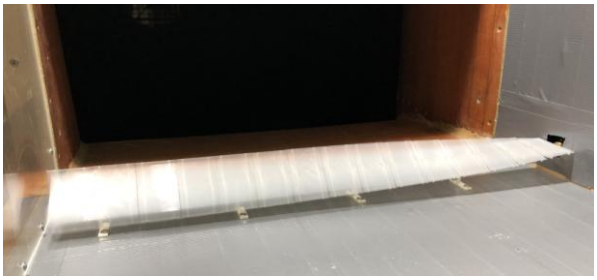

Figure 6. Non-linear deformation of structure, torsional galloping

These oscillations are somewhat random, but in any case, they involve only small amplitudes. Nevertheless, a much more intense vibration develops from a certain velocity upwards.

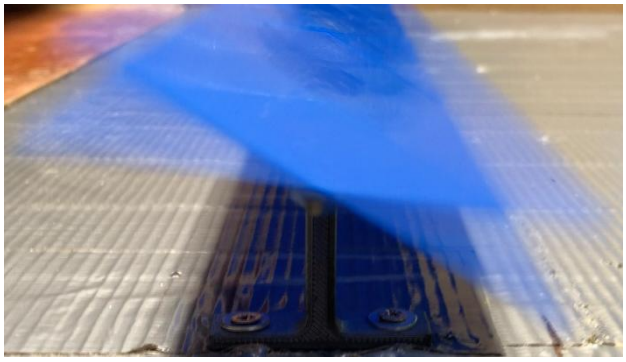

Figure 7. Twisted angle of the structure on the free end.

Figure 7 shows the magnitude of the oscillations once galloping is triggered; amplitude seen increases as the wind velocity rises.

Essentially, the oscillation occurs centered in the original azimuthal angle, and it is caused by the torsional moment because of the vortex shedding on the leading and trailing edges. Figure 8 represents the numerical simulation of this phenomenon where vortex shedding on the leading edge is stronger and seems to be the main factor in the phenomenon (Rohr et al, 2015).

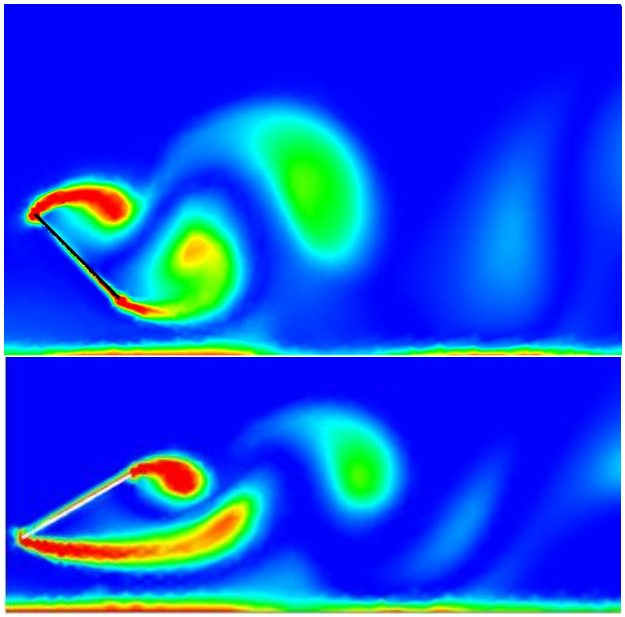

Figure 8. Numerical simulation of the torsional galloping (contours of vorticity).

Once the phenomenon begins, the oscillation frequency corresponds to the structural natural frequency not changing with the velocity increase. With a higher velocity, the oscillation doesn't disappear and its amplitude and strength seems to be amplified up to the collapse of the structure. This fact allows to discard that the phenomenon is a vortex induced vibration (VIV).

From a structural perspective, torsional divergence (TD) is also discarded because this divergence is mainly a steady state phenomenon. Another reason is that regarding the specific bibliography of flat plates twisting on their axis, it is noted that torsional moment decreases inversely to the tilt angle, reaching zero on the vertical position (Meseguer et.al, 2013). Hence, these structures topology does not seem to be susceptible to suffer this kind of instability.

Actually, based on the tests findings, the present instability has been identified as torsional galloping, or one degree of freedom flutter (Scannlan, H.R, 1986).

The amplitude of the oscillation varies along the axis of the solar tracker from zero at the driver side to its maximum value at the free end, producing a longitudinal sinusoidal twist of the panel (in contrast with a linear distribution when the momentum is concentrated on the free end), see figure 9.

As commented before, in the beginning of the oscillation the amplitude is small, and when the velocity increases the amplitude intensifies exponentially. If the solar tracker is maintained in the range of oscillations of small amplitude, fatigue effects may appear in the structure. However, with a small increase in the wind velocity, larger amplitudes will appear, generating loads on the structure (much higher than the static loads usually considered), and the solar tracker can reach structural collapse.

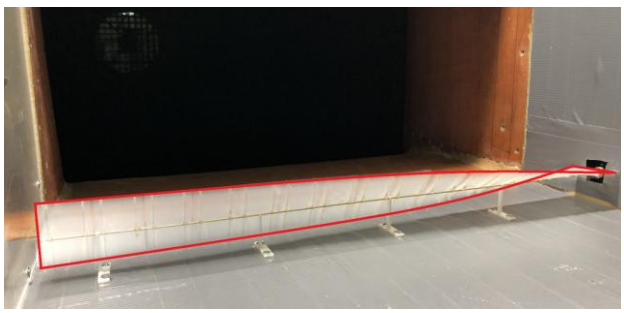

Figure 9. Full aeroelastic model tested for torsional galloping.

For this investigation, the most important part of the wind tunnel tests is the definition of the critical velocity at which the torsional galloping phenome-

non appears. This velocity depends on the azimuthal position angle of the solar tracker. Figure 10 illustrates these values expressed as non-dimensional reduced velocity.

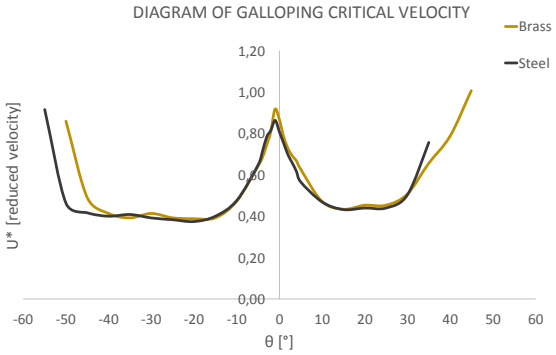

Figure 10. Evolution of reduced critical velocity as a function of the azimuthal angles.

The reduced velocity corresponds to the wind speed adimensionalized by the chord and natural frequency.

$$U^* = \frac{U}{b}\frac{2}{\pi}\sqrt{\frac{I}{K}} \quad \#(14)$$

The oscillation phenomenon does not appear on every azimuthal angle, it is restricted between approximately +50° and -55° degrees. The minimum critical velocities show up in the range of -45° to -15° and from 20° to 40°, this velocity is more or less uniform in these ranges; and it has a value of 0.37 on the negative side and 0.43 for the positive one. For azimuthal angles closed to zero, the critical velocities are higher, up to 0.86 for an angle of -1°. The maximum value is not zero centered due to the asymmetry induced by the ground. The critical velocities also increase at the extremal angles (± 50°), where the phenomenon disappears.

The plot behavior shows several aspects of the phenomenon:

1) Considering the stable velocity on the angles ranging from -45° to -15° and from 20° to 40°, it seems to indicate that it is necessary a certain kinetic energy for the oscillatory phenomenon to develop.

2) At small tilt angles, between -10° and +5° approximately, the critical velocity is considerably higher. It is known that a flat plate with small angles of inclination does not shows the vortex shedding phenomenon (Robert Blevins, 2003). However, due to the structure flexibility, when the velocity grows, the angle of the free end deviates with respect to the driver end; the higher the velocity, the higher the difference. For example, if the azimuthal position of the model solar tracker is 5°, when the wind velocity is 15 m/s, the free end angle is around 8°or 9°. What it means is that vortex shedding can be triggered on the free end with a velocity high enough. If this velocity is sufficient for the necessary kinetic energy, the tracker will then go into the torsional galloping phenomenon.

3) When the absolute value of the azimuthal angles is high enough, the torsional galloping phenomenon does not activate. It is possible that the flow detachment at the leading or trailing edge close to the ground is much less energetic and is not sufficient to develop the instability. Or perhaps, the lack of symmetry makes more difficult the beginning of the instability.

Another aspect of the experimental results is that the values for the critical reduced velocity are basically the same on the two tested models in spite of the difference of the shaft's torsional stiffness (K). In fact, this is a consequence of the fact that the expression used for reduced velocity maintains the dimensionless torsional stiffness coefficient (C_k). In other words, two test with the same reduced velocity keep the similarity (with respect to the stiffness).

Only models with the same value of moment of inertia (I) have been tested, so it is still unknown its possible effect on the galloping critical velocity.

The damping ratio (ξ) values in both models are rather different but both are also quite small. Although not included in this work, other tests with different materials have been inchoated, and the preliminary results corroborate the idea that, when the damping ratio is small, it has little influence on the onset of torsional galloping.

5. SHAFT DIMENSIONING

This previous analysis and experimental results allows to calculate the maximum wind velocity that a determined prototype of solar tracker will stand before the onset of the torsional galloping.

For instance, for the prototype of solar tracker in this study, if the threshold value of the reduced critical velocity is set at 0.37, the galloping critical velocity is:

$$U_{cr} = U_{cr}^* \cdot \frac{b \cdot \pi}{2} \cdot \sqrt{\frac{K}{I}} \approx 14.4 \ m/s \#(15)$$

Alternatively, it is also possible to calculate the shaft stiffness for a specified critical galloping velocity or maximum project wind speed, for example, for 100 km/h:

$$K_{cr} = \frac{U_{cr}^2}{U_{cr}^{*2}}\frac{4I}{L^2\pi^2} = \approx \ 420998 \ Nm \ \#(16)$$

Which corresponds to a shaft thickness of 33 mm, instead of 6 mm of the original prototype.

Normally, operation procedure in a photovoltaic facility calls for the solar tracker to assume a stow position when the wind is above a certain value; usually zero or a slightly negative tilt angle. In this case, the reduced critical velocity can reach a value around 0.8. This corresponds to a galloping critical velocity of 31.13 m/s, for the original prototype, or for a shaft thickness of 5 mm to withstand up to 100 km/h.

6. CONCLUSIONS

An analytical and experimental analysis of the aeroelastic instabilities of single axis solar trackers has been carried out. The analytical procedure has identified an evaluated the dimensionless variables related to the phenomenon. Based on this study, a scaled experimental model has been developed and tested in a wind tunnel. The model has been able to reproduce the phenomenon of torsional galloping that shows up when wind velocities reach relatively high values. The results show that in order for torsional galloping to appear, it is necessary, on the one hand, that the azimuthal angle of the solar tracker be adequate for the vortex shedding condition and, on the other hand, that the flow contains the necessary kinetic energy.

The measurements have identified the galloping critical velocities for the whole range of azimuthal positions. It has been found that the stable value of the reduced critical velocities, have a minimum on the entire range which can be used as a threshold. These velocities are higher when close to horizontal angles. In addition, there is a certain positive and negative angle, from which the instability no longer develops. The threshold value of the reduced critical velocity has been used to determine the wind speed at which the aeroelastic instabilities begin to develop and the necessary shaft thickness for a given project wind speed.

7. ACKNOWLEDGEMENTS

This research has been developed in the framework of the FC-GRUPIN- IDI/2018/000205 project, supported by the Principado de Asturias – Plan de Ciencia, Tecnología e Innovación-, co-financed by FEDER funds.

8. REFERENCES

Blevins, R. D., 1990, Flow-Induced Vibration, Van Nostrand Reinhold, 2nd edition, New York.

Bruno, R., Bevilacqua, P., Longo, L., Arcuri, N, 2015, Small Size Single-axis PV Trackers: Control and System Layout for Energy Optimization, Energy Procedia 82: 737 – 743.

Dyrbye, C. and Hansen, S. O., 1997, Wind Loads on Structures, John Wiley and Sons, Chichester (UK). ISBN: 978-0-471-95651-8.

Jubayer, C. M., Hangan, H., 2014, Numerical Simulation of Wind Effects on a Stand-Alone Ground Mounted Photovoltaic (PV) System, J. Wind Eng. Ind. Aerodyn., 134: 56–64.

Païdoussis, M. P., Price, S. J., De Langre, E., 2011, Fluid-Structure Interactions - Cross-Flow-Induced Instabilities, Cambridge University Press, New York.

Rao, S.S. Vibration of Continuous Systems, 2007, John Wiley & Sons, Inc. New Jersey.

Rodríguez Lastra, M., Fernández Oro, J. M., Galdo Vega, M., Blanco Marigorta, E., Santolaria Morros, C., 2013, Novel Design and Experimental Validation of a Contraction Nozzle for Aerodynamic Measurements in a Subsonic Wind Tunnel, Journal of Wind Engineering and Industrial Aerodynamics, 118: 35–43.

Roedel, A., Upfill-Brown, S., 2018, Designing for The Wind, Using Dynamic Wind Analysis and Protective Stow Strategies to Lower Solar Tracker Lifetime Costs, Nextracker Whitepaper, MKT-000073.

Rohr, C., Bourke, P. A., Banks, D., 2015, Torsional Instability of Single-Axis Solar Tracking Systems, ICWE14, Porto Alegre, Brazil.

Scannlan R.H.; Simiu E.; 1986, Wind Effects on Structures, John Wiley&Sons,Inc.

Strobel, K., Banks, D., 2014, Effects of Vortex Shedding in Arrays of Long Inclined Flat Plates and Ramifications for Ground-Mounted Photovoltaic Arrays, J. Wind Eng. Ind. Aerodyn., 133: 146–149.

Yang, Y., 2010, Experimental Investigations of Vortex Induced Vibration of a Flat Plate in Pitch Oscillation, MSc. Thesis, Texas A&M University.

Zachary, J.Taylor; Mathew, T.L. Browne., 2020. Hybrid pressure integration and buffeting analysis for multi-row wind loading in an array of single axis trackers. Journal of Wind engineering and Industrial Aerodynamics, 197:104056.

FLOW-INDUCED VIBRATION OF A CIRCULAR CYLINDER TRANSVERSE TO OSCILLATORY FLOW AT A HIGH KEULEGAN-CARPENTER NUMBER

Dániel Dorogi & László Baranyi
University of Miskolc, Miskolc-Egyetemváros, Hungary

Efstathios Konstantinidis
University of Western Macedonia, Kozani, Greece

ABSTRACT

This work investigates the excitation of flow-induced vibrations of a circular cylinder in a uniform oscillatory flow at the Keulegan-Carpenter number of 500, i.e. in the drag-dominated regime. The cylinder was allowed to vibrate only in the direction transverse to the incident flow. The governing equations for fluid flow and cylinder motion were solved in a non-inertial frame of reference using an in-house finite-difference code. Simulations were conducted for a system with a mass ratio of 2 and zero structural damping. The maximum Reynolds number and the corresponding maximum reduced velocity were set to 150 and 5, respectively. The results show that the cylinder response comprises low-frequency wave-induced oscillations and superimposed high-frequency vortex-induced vibrations (VIV). The most important finding is that the VIV response displays strong hysteresis, as illustrated by plots of the phase-averaged vibration amplitude and magnitude of fluid forces as functions of the time-dependent reduced velocity, despite the fact that the frequency of the oscillatory flow is extremely small compared to the natural frequency of the cylinder. It is further shown that the phase-averaged vibration amplitude over the deceleration stage follows quite closely data points from steady-flow tests, but not so during the acceleration stage. However, the magnitude of the phase-averaged fluid forces that drive the motions as functions of the time-dependent reduced velocity in oscillatory flow are markedly different during most part of both acceleration and deceleration stages than those at the corresponding steady flows.

1. INTRODUCTION

Vortex-induced vibration (VIV) of bluff structural elements is a practical problem playing a significant role e.g. in offshore platforms, risers, wind turbines, and high buildings. Due to its importance, VIV has been thoroughly investigated in the past decades using both laboratory tests and numerical simulations. Several significant review papers can be found in this field; see e.g. Bearman (1984, 2011), Sarpkaya (2004) and Williamson and Govardhan (2004).

The majority of the VIV studies have considered the case of an elastically supported circular cylinder placed into a uniform free stream (see e.g. Khalak and Williamson, 1999; Konstantinidis et al., 2020; Dorogi and Baranyi, 2020). However, engineering structures are often exposed to waves; VIV studies on waves include Williamson (1985); Sumer and Fredsøe (1988); Lipsett and Williamson (1994). Waves are usually modelled using a uniform oscillatory flow, where the velocity of the stream can be written as $\widetilde{U}(t) = U_m \sin(2\pi f_o t)$, where t is the time, U_m and f_o are the magnitude and frequency of the stream velocity, respectively. The Keulegan-Carpenter number $K_C = U_m/(f_o D)$ and the Reynolds number $Re = U_m D/\nu$ are the dimensionless groups used to characterise the incoming stream, where D is the cylinder diameter and ν is the kinematic viscosity of the fluid.

In practice, the cylinder generally can move in two directions, i.e. both streamwise with and transverse to the free stream (Lipsett and Williamson, 1994; Domenichini, 2002). However, researchers often consider one-degree-of-freedom cylinder motion. Williamson (1985) constructed an analytical approach to predict streamwise-only VIV of a circular cylinder. The author solved the equation of cylinder motion together with Morison et al's. equation for the streamwise fluid force (Morison et al., 1950). Williamson (1985) found that the predicted response compares well with experimental results. Anagnostopoulos and Iliadis (1998) and Taheri et al. (2020) investigated similar problems using two-dimensional (2D) computational fluid dynamics (CFD) simulations.

Transverse-only vortex-induced vibrations have been found to be more important, because the oscillation amplitudes are higher in this direction than those in the streamwise direction. Sumer and Fredsøe (1988) experimentally investigated the VIV of a circular cylinder in the Keulegan-Carpenter number range of $K_C = 5 - 100$. They showed that when K_C increases above 5 the cylinder undergoes high-amplitude vibrations with the amplitude depending on the value of the reduced velocity $U_r = U_m/(f_n D)$, where f_n is the natural frequency of the cylinder in vacuum. In contrast to the VIV response in a uniform free stream, synchronisation occurs over different U_r ranges. McConnell and Jiao (1986) observed similar characteristics in their experimental results. Zhao et al. (2012) carried out extensive 2D simulations for $K_C = 10$ and 20. They found that in the reduced velocity domain of $U_r < 8$ the frequency spectra of cylinder displacement contains one dominant peak at twice the flow oscillation frequency. However, above $U_r = 8$ Zhao et al. (2012) identified multiple peaks, which were whole number multiples of the frequency of the free stream. More recently, Zhao et al. (2017) found similar features, i.e. multiple frequency peaks in the cylinder response, using three-dimensional simulations.

The studies mentioned above have been limited to low Keulegan-Carpenter numbers, i.e. $K_C < 100$. The authors are not aware of any results at large K_C numbers. In this study transverse-only VIV of a circular cylinder placed into an oscillatory flow is investigated at $K_C = 500$ by means of 2D numerical simulations. The parameters of this study are fixed at $U_r = 5, Re = 150$, $\mu = 2$ and $\zeta = 0$, where μ and ζ are the mass and structural damping ratio values, respectively. Since the difference between K_C and U_r is large, the cylinder response might be expected to be quasi-steady.

2. METHODOLOGY

The two-dimensional flow of the Newtonian incompressible constant property fluid is governed by the two components of the Navier-Stokes equations written in a non-inertial reference frame attached to the vibrating cylinder, the continuity equation and the pressure Poisson equation. The non-dimensional forms of these equations are written as follows:

$$\frac{\partial u}{\partial t} + u\frac{\partial u}{\partial x} + v\frac{\partial u}{\partial y} = -\frac{\partial p}{\partial x} + \frac{1}{Re}\nabla^2 u + \dot{U}, \qquad (1)$$

$$\frac{\partial v}{\partial t} + u\frac{\partial v}{\partial x} + v\frac{\partial v}{\partial y} = -\frac{\partial p}{\partial y} + \frac{1}{Re}\nabla^2 v - \ddot{y}_c, \qquad (2)$$

$$\mathscr{D} = \frac{\partial u}{\partial x} + \frac{\partial v}{\partial y} = 0, \qquad (3)$$

$$\nabla^2 p = 2\left(\frac{\partial u}{\partial x}\frac{\partial v}{\partial y} - \frac{\partial u}{\partial y}\frac{\partial v}{\partial x}\right) - \frac{\partial \mathscr{D}}{\partial t}, \qquad (4)$$

where t is the dimensionless time, x and y are the non-dimensional Cartesian coordinates in the streamwise and transverse directions, respectively, u and v are the non-dimensional streamwise and transverse velocity components of the fluid, p is the non-dimensional pressure, $\mathscr{D}$ is the dilation and $\ddot{y}_c$ is the non-dimensional acceleration of the cylinder in the transverse direction. In this study the cylinder diameter D and the magnitude of the stream velocity U_m are used as length and velocity scales, respectively. In Eq. (1) $\dot{U}$ is the dimensionless flow acceleration, i.e., the time derivative of the non-dimensional velocity of the fluid stream $U(t) = \sin(2\pi t/K_C)$, where $K_C = U_m/(f_o D)$ is the Keulegan-Carpenter number based on the flow oscillation frequency f_o. In Eqs. (1) and (2) $Re = U_m D/\nu$ is the maximum Reynolds number, where ν is the kinematic viscosity of the fluid. The acceleration of the cylinder in Eq. (2) is obtained by solving Newton's second law of cylinder motion, which can be written in non-dimensional form as

$$\ddot{y}_c + \frac{4\pi\zeta}{U_r}\dot{y}_c + \left(\frac{2\pi}{U_r}\right)^2 y_c = \frac{2}{\pi\mu}F_y^*(t), \qquad (5)$$

where y_c, $\dot{y}_c$ and $\ddot{y}_c$ are the non-dimensional cylinder displacement, velocity and acceleration, respectively, (the overdots represent differentiation with respect to dimensionless time) $U_r = U_m/(f_n D)$ is the maximum reduced velocity, where f_n is the natural frequency of the cylinder in vacuum, ζ and μ are the structural damping ratio and the mass ratio, respectively, and $F_y^*(t)$ is the non-dimensional sectional fluid force acting on the cylinder.

The physical domain of the computations is the area confined between two concentric circles: R_1 is the non-dimensional radius of the cylinder surface, while R_2 is that of the outer surface. On $R = R_1$ no-slip boundary conditions are applied for u and v, while for the fluid pressure a Neumann-type condition is used. On $R = R_2$, the

pressure gradient is set to zero, while the two velocity components are chosen to be $u = U(t)$ and $v = -\dot{y}_c(t)$.

In order to achieve high degree of accuracy the physical domain is transformed to a computational domain on which an equidistant grid is generated; the mesh is boundary-fitted on the physical plane. The transformed governing equations with boundary conditions are solved using an in-house CFD code based on the finite difference method.The spatial derivatives are approximated using fourth-order accurate central difference schemes except for the convective terms, which are discretised by applying a modified third-order upwind difference scheme. Eqs. (1) and (2) are integrated with respect to time using the explicit Euler approach, while the fourth-order explicit Runge-Kutta method is implemented for the temporal discretisation of Eq. (5). The successive over-relaxation method is used to solve the linear system resulting from the discretization of the pressure Poisson equation while satisfying the continuity equation in each time step.

Based on the previous independence studies published in Baranyi (2008), Dorogi and Baranyi (2020) and Konstantinidis et al. (2021) the number of grid points in the peripheral and radial directions are set to 361 and 314, respectively, the radius ratio R_2/R_1 is chosen to be 240 and the dimensionless time step is fixed at $\Delta t = 0.0005$. The CFD code employed in this study has been extensively validated against data from the literature for stationary, forced oscillations, and vortex-induced vibrations of isolated cylinders in uniform free stream in previous works (Baranyi, 2008; Dorogi and Baranyi, 2020; Konstantinidis et al., 2021).

3. RESULTS AND DISCUSSION

This paper reports two-dimensional CFD computations carried out to investigate flow-induced vibrations of a circular cylinder placed into an oscillatory flow at $K_C = 500$. The maximum Reynolds number, maximum reduced velocity and mass and structural damping ratio values are fixed at $Re = 150$, $U_r = 5$, $\mu = 2$, and $\zeta = 0$, respectively.

Figure 1 shows the time histories of the non-dimensional cylinder displacement y_c, instantaneous amplitude A^* and frequency f_y^*. Note that the time histories in this and subsequent figures correspond to the time interval $t/K_C = 50 - 54$, i.e. over four periods of the oscillatory flow. The displacement displays intervals of high-amplitude oscillation interspersed between intervals of low-amplitude oscillation in each flow cycle (see Fig. 1a). By applying the Hilbert transform to the y_c signal it is possible to obtain the instantaneous amplitude and frequency of cylinder oscillation, which are shown in Fig. 1b and 1c, respectively. As can be seen in Fig. 1b the time-dependent amplitude varies approximately between 0 and 0.6. The maximum value is close to the peak amplitude of transverse response in uniform free stream at low Reynolds numbers in the laminar regime (Singh and Mittal, 2005; Govardhan and Williamson, 2006). As seen in Fig. 1c, the time-dependent vibration frequency varies from a minimum value of approximately 0.05 up to 0.20. The maximum value corresponds to the inverse of the maximum reduced velocity U_r^{-1}. It is interesting to note that neither $A^*(t)$ nor $f_y^*(t)$ display smooth harmonic-like variations (see further below for a discussion of their phase-averaged variations).

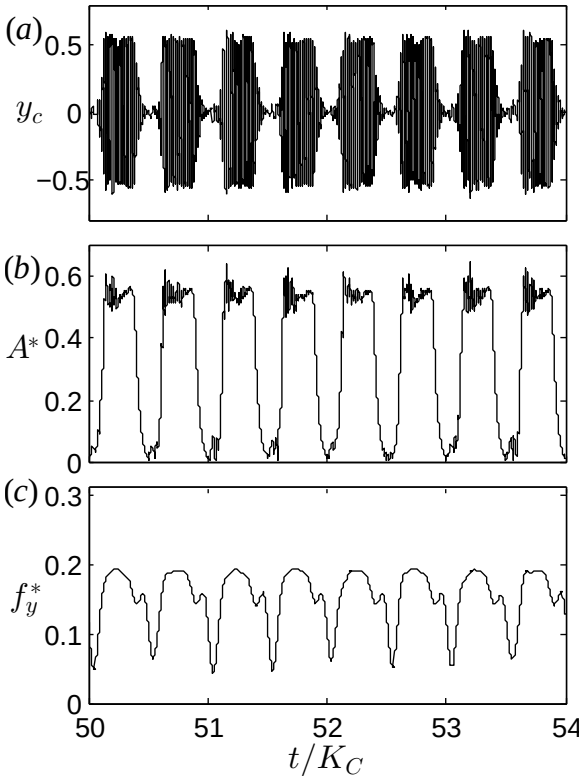

Figure 1. Time histories of (a) cylinder displacement y_c, (b) instantaneous amplitude A^* and (c) instantaneous frequency f_y^* of cylinder oscillation.

Figure 2 shows time histories of the transverse fluid force F_y^*, i.e. the motion-driving force, and its instantaneous magnitude C_y and instan-

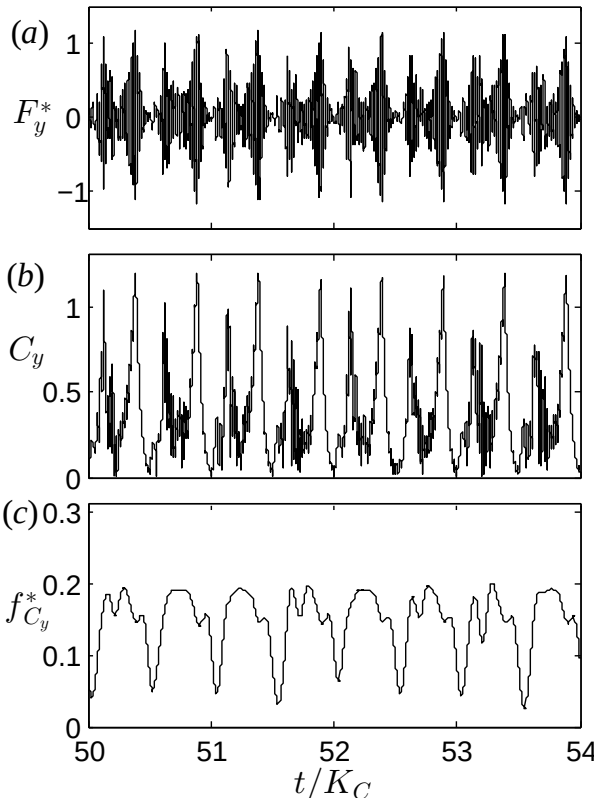

Figure 2. Time histories of (a) transverse fluid force F_y^*, (b) and magnitude C_y and (c) frequency $f_{C_y}^*$ of F_y^*.

taneous frequency $f_{C_y}^*$ obtained again using the Hilbert transform. As can be seen in Fig. 2b, C_y fluctuates between a minimum value of approximately zero and a maximum value slightly above 1.0. It might be noted that fluctuations in the time-dependent force magnitude occur at four times the frequency of flow oscillation due to peaking twice each time the flow speed increases either in the positive or the negative direction. Despite $C_y(t)$ being essentially periodic, $F_y^*(t)$ fluctuations display stochastic cycle-to-cycle variations, which is also evident in the time history of its instantaneous frequency $f_{C_y}^*(t)$ (see Fig. 2c).

Figure 3 shows the instantaneous frequency of the driving force against the instantaneous frequency of cylinder vibration in the time interval $50K_C \leq t \leq 54K_C$, i.e. the period analysed in Figs. 1 and 2. It can be seen in Fig. 3 that the driving force and the cylinder oscillationhave the same frequency over part of the flow oscillation. However, $f_{C_y}^*(t)$ and $f_y^*(t)$ are different over another part of the flow oscillation; the elliptical-like trajectory suggests that there is a definite relationship between them. In addition, there also

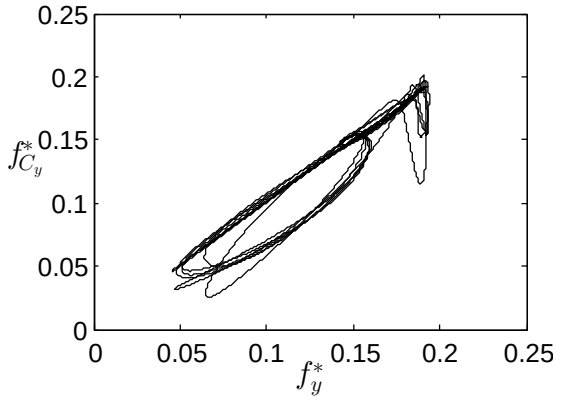

Figure 3. Variation of the instantaneous frequency of cylinder vibration against the instantaneous frequency of the transverse fluid force within the interval $50K_C \leq t \leq 54K_C$.

exist deviations from the elliptical-like trajectory, which might be attributed to the stochastic cycle-to-cycle variations in the behaviour of the system.

Figure 4a shows the time history of the fluid force acting in the direction of the incident flow. The streamwise fluid force F_x^* displays high-amplitude fluctuations at the period of flow oscillation and overriding high-frequency fluctuations that appear at intervals near its peak magnitude. The low- and high-frequency fluctuations were segregated using a low-pass filter in order to analyse the streamwise force more thoroughly. The low-frequency force component F_{xf}^* displays very repeatable oscillations (see Fig. 4b). This component can be modelled very accurately using Morison et al.'s equation (Morison et al., 1950) but this is not explored further here for economy of space.

The high-frequency component obtained by subtracting the low-frequency component from the total force $F_x^* - F_{xf}^*$ is shown in Fig. 4c (black line). Then, the time-dependent magnitude $C_x(t)$ and frequency $f_{C_x}^*(t)$ were obtained by applying the Hilbert transform to the high-frequency streamwise force. The resulting time histories are plotted in Fig. 4c (red line) and 4d, respectively. It can be seen in Fig. 4c that $C_x(t)$ displays a variation similar to that of $A^*(t)$, i.e. intervals of high amplitudes interspersed intervals of low-amplitude. As can be seen in Fig. 4d, the maximum of $f_{C_x}^*$ is approximately 0.4, which is roughly twice the peak values of f_y^* or $f_{C_y}^*$ (see Figs. 1c and 2c). This finding is consistent with the results from VIV in a steady free stream where the

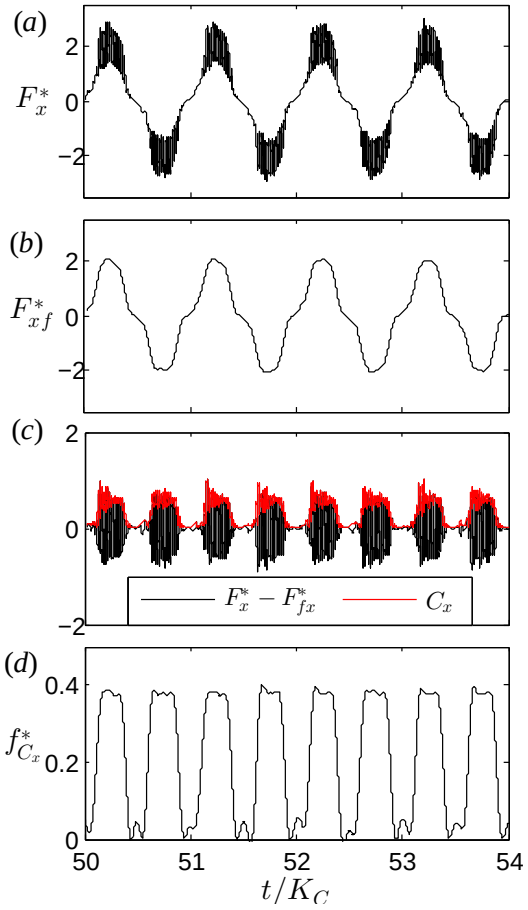

Figure 4. Time histories of (a) streamwise fluid force F_x^*, (b) low-frequency component of force F_{xf}^*, (c) high-frequency component of F_x^* and its magnitude C_x and (d) frequency of the high-frequency force component $f_{C_x}^*$.

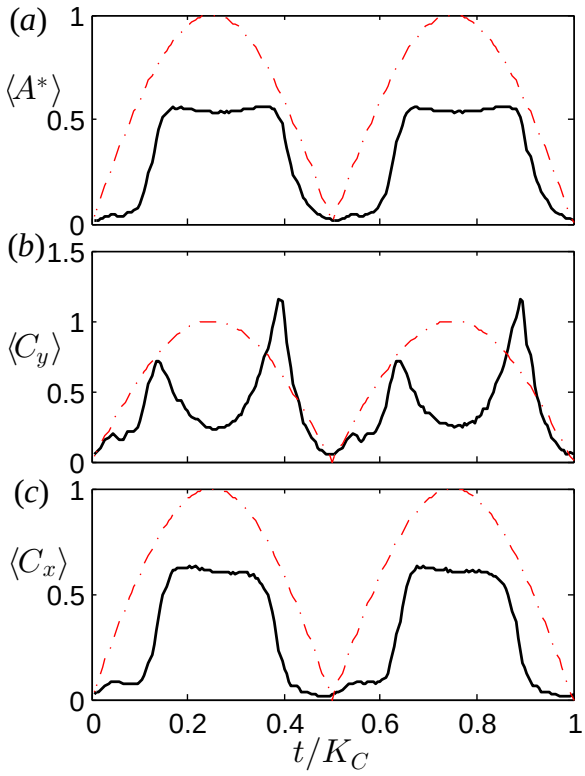

Figure 5. Phase-averaged (a) amplitude of cylinder displacement, (b) transverse fluid force and (c) streamwise fluid force. The red dashed line represents $|U(t)|$.

frequency of F_x^* is always twice the frequency of F_y^* (Singh and Mittal, 2005). In addition, it is interesting to note that the minimum value of $f_{C_x}^*$ is approximately zero; this contrasts with the variation of $f_{C_y}^*$ (see Fig. 2c).

The displacement and force signals over 100 flow cycles were phase averaged using 200 non-overlapping bins, each containing 5000 data points. Phase-averaged results for the response amplitude $\langle A^* \rangle$ are shown in Fig. 5a. It can be seen that the amplitude response is high during the part of high-speed flow as might be expected in quasi-steady response. Remarkably, $\langle A^* \rangle$ increases and decreases much more abruptly than the flow speed does and attains two local maxima; one during the flow deceleration stage ($t/K_C = 0 - 0.25$) and another during the flow acceleration stage ($t/K_C = 0.25 - 0.5$). These local maxima are accompanied by marked increases in the phase-averaged magnitude of the transverse force $\langle C_y \rangle$, as can be seen in Fig. 5b. During the deceleration stage the driving force leads the motion, whereas force and motion are almost in phase during the acceleration stage. Furthermore, the local peak in $\langle C_y \rangle$ is much higher (nearly double) during the acceleration stage than during the deceleration stage. These observations signify fundamental differences in the mechanisms related to flow-induced vibration during different parts of the flow-oscillation cycle. On the other hand, the variation of the phase-averaged magnitude of the streamwise force $\langle C_x \rangle$ is very similar to that of $\langle A^* \rangle$, as can be seen in Fig. 5c.

Additional simulations were conducted for the case when the cylinder is placed into a uniform free stream. For simplicity we will refer to this case as 'steady-VIV'. The parameters of these computations (i.e. the Reynolds number and reduced velocity) are chosen so as to correspond to the conditions at selected points of the oscillatory flow. Figure 6 provides comparisons of the phase-averaged results in oscillatory flow against

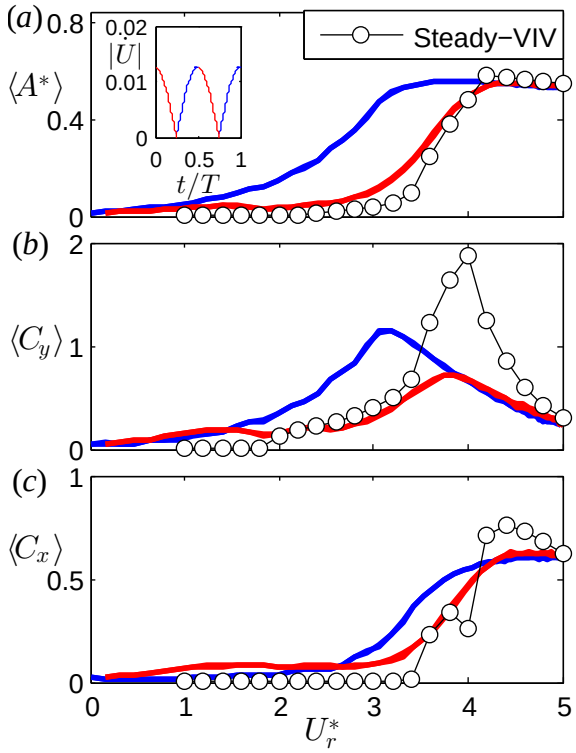

Figure 6. Comparison of VIV results for oscillatory flow (coloured lines) against corresponding steady flow (black circles+lines). The insert shows the stages of flow acceleration (blue) and deceleration (red) in terms of the absolute accelelration in oscillatory flow.

steady-VIV data. It can be seen that the time-dependent amplitude response over the deceleration stage in oscillatory flow (see red curves in Fig. 6) follows quite closely the path traced by the steady-VIV amplitude as a function of the time-dependent reduced velocity $U_r^*(t) = \widetilde{U}/(f_n D)$. At the peak reduced velocity (i.e. $U_r^*(t) = U_r$), results for both oscillatory-VIV and steady-VIV almost coincide, including the magnitude of the fluid forces. However, during the acceleration stage (blue), the response amplitude is markedly higher in oscillatory-VIV than in steady-VIV and a hysteresis loop is formed in the plot of $\langle A^* \rangle$ as a function of $U_r^*(t)$. Similar trends can be observed in the variation of the magnitude of the unsteady fluid forces (high-frequency components). Furthermore, it is interesting to observe the marked differences in the magnitude of the transverse force near $U_r^*(t) = 4$, where $\langle C_y \rangle$ for steady-VIV is more than twice its value for oscillatory-VIV, despite the fact that the amplitude is almost the same for both cases.

4. CONCLUSIONS

In this paper we reported a study of vortex-induced vibrations of a circular cylinder placed into a high-Keulegan-Carpenter-number (i.e. $K_C = 500$) oscillatory flow by means of two-dimensional simulations. The maximum Reynolds number, the maximum reduced velocity and the mass and structural damping ratios are fixed at the values of $Re = 150$, $U_r = 5$, $\mu = 2$, and $\zeta = 0$, respectively.

The time-dependent magnitudes and frequencies of the cylinder displacement and fluid forces were obtained from the Hilbert transform of the high-frequency (filtered) signals. The oscillation amplitude and the magnitude of the streamwise fluid force follow similar trends: in each cycle of flow oscillation there is an interval of high amplitudes between intervals of low amplitude. In contrast, the magnitude of the transverse fluid force fluctuates at twice the frequency of oscillation of the instantaneous amplitude. The maximum frequency of cylinder displacement and transverse fluid force are approximately 0.2, which is identical to the reciprocal value of the maximum reduced velocity U_r^{-1}. However, the peak frequency of the streamwise fluid force is approximately 0.4, i.e. close to the value of $2U_r^{-1}$.

Plots of the phase-averaged vibration amplitude and fluid forces (calculated based on 100 flow oscillation cycles) display strong hysteresis, which is unexpected given the very slow variation of the flow speed. The simulation results for oscillatory flow were compared with the corresponding steady-flow VIV (i.e. cases where the cylinder is placed into a steady free stream at a fixed reduced velocity). Although the amplitude of cylinder vibration and the magnitude of the streamwise fluid force compare relatively well, substantial differences were found for the magnitude of the transverse fluid force. The above findings highlight the strongly nonlinear dynamics of vortex-induced vibration in unsteady flow, which is markedly different from a quasi-steady approximation.

Acknowledgements DD and LB was supported by the European Union and the Hungarian State, co-financed by the European Regional Development Fund in the framework of the GINOP-2.3.4-15-2016-00004 project, aimed to promote the cooperation between the higher education and the industry.

5. REFERENCES

Anagnostopoulos, P. & Iliadis, G., 1998, Numerical Study of the Flow Pattern and the In-Line Response of a Flexible Cylinder in an Oscillating Stream. Journal of Fluids and Structures 12: 225–258.

Baranyi, L., 2008, Numerical Simulation of Flow Around an Orbiting Cylinder at Different Ellipticity Values. Journal of Fluids and Structures 24: 883–906.

Bearman, P.W., 1984, Vortex Shedding from Oscillating Bluff Bodies. Annual Review of Fluid Mechanics 16: 195–222.

Bearman, P.W., 2011, Circular Cylinder Wakes and Vortex-Induced Vibrations. Journal of Fluids and Structures 27: 648–658.

Domenichini, F., 2002, Quasiperiodicity and Chaos in the Dynamics of an Elastically Mounted Circular Cylinder. European Journal of Mechanics-B/Fluids 21: 341–354.

Dorogi, D. & Baranyi, L., 2020, Identification of Upper Branch for Vortex-Induced Vibration of a Circular Cylinder at $Re = 300$. Journal of Fluids and Structures 98: Art. No. 103135.

Govardhan, R. & Williamson, C.H.K., 2006, Defining the 'Modified Griffin Plot' in Vortex-Induced Vibration: Revealing the Effect of Reynolds Number Using Controlled Damping. Journal of Fluid Mechanics 561: 147–180.

Khalak, A. & Williamson, C.H.K., 1999, Motions, Forces and Mode Transitions in Vortex-Induced Vibrations at Low Mass-Damping. Journal of Fluids and Structures 13: 813–851.

Konstantinidis, E., Dorogi, D. & Baranyi, L., 2021, Resonance in Vortex-Induced In-Line Vibration at Low Reynolds Numbers. Journal of Fluid Mechanics 907: Art. No. A34.

Konstantinidis, E., Zhao, J., Leontini, J., Lo Jacono, D. & Sheridan, J., 2020, Phase Dynamics of Effective Drag and Lift Components in Vortex-Induced Vibration at Low Mass–Damping. Journal of Fluids and Structures 96: Art. No. 103028.

Lipsett, A. W. & Williamson, I.D., 1994, Response of a Cylinder in Oscillatory Flow. Journal of Fluids and Structures 8: 681–709.

McConnell, K. G. & Jiao, Q., 1986, The In-Line Forces Acting on an Elastically Mounted Cylinder Oscillating in Still Water. Experimental Mechanics 26: 66–70.

Morison, J.R., O'Brien, M.P., Johnson, J.W. & Schaaf, S.A., 1950, The Force Exerted by Surface Waves on Piles. AIME Petroleum Transactions 189: 149–154.

Sarpkaya, T., 2004, A Critical Review of the Intrinsic Nature of the Vortex-Induced Vibrations. Journal of Fluids and Structures 197: 389–447.

Singh, S.P. & Mittal, S., 2005, Vortex-Induced Oscillations at Low Reynolds Numbers: Hysteresis and Vortex-Shedding Modes. Journal of Fluids and Structures 20: 1085–1104.

Sumer, B. M. & Fredsøe, J., 1988, Transverse Vibrations of an Elastically Mounted Cylinder Exposed to an Oscillating Flow. Journal of Offshore Mechanics and Arctic Engineering 110: 387–394.

Taheri, E., Zhao, M., Wu, H. & Tong, F., 2020, Numerical Investigation of Streamwise Vibration of an Elastically Mounted Circular Cylinder in Oscillatory Flow. Ocean Engineering 209: Art. No. 107300.

Williamson, C.H.K., 1985, In-Line Response of a Cylinder in Oscillatory Flow. Applied Ocean Research 7: 97–106.

Williamson, C.H.K. & Govardhan, R., 2004, Vortex-Induced Vibration. Annual Review of Fluid Mechanics 36: 413–455.

Zhao, M., Cheng, L. & An, H., 2012, Numerical Investigation of Vortex-Induced Vibration of a Circular Cylinder in Transverse Direction in Oscillatory Flow. Ocean Engineering 41: 39–52.

Zhao, M., Pearcey, T., Cheng, L. & Xiang, Y., 2017, Three-Dimensional Numerical Simulations of Vortex-Induced Vibrations of a Circular Cylinder in Oscillatory Flow. Journal of Waterway, Port, Coastal, and Ocean Engineering 143: Art. No. 04017007.

INFLUENCE OF A CONTROL WIRE ON VORTEX SHEDDING FROM SIDE-BY-SIDE CYLINDERS

Omar S. Hammad & Atef Mohany
Fluid-Structure Interaction and Noise Control Laboratory, Ontario Tech University, Oshawa, Canada

ABSTRACT

Vortex-shedding behind bluff bodies can induce noise and vibration problems when it engages in a feedback cycle of oscillations with an acoustic or structural mode. Therefore, several passive and active flow control techniques have been developed to suppress vortex shedding behind a single bluff body. However, less attention was given to the case of multiple bluff bodies in cross-flow. Therefore, in this paper, a numerical investigation is performed to investigate the effect of adding a small wire in the vicinity of two side-by-side cylinders on the vortex shedding characteristics and the hydrodynamic fluid forces. The simulations are conducted at a Reynolds number of $Re = 200$ *and the side-by-side cylinders have a spacing ratio of* $T^* = 2.5$*. The control wire is placed at a center-to-center ratio of* $R^* = R/D = 1$*, where R is the center to center distance between the wire and the cylinder and D is the cylinder diameter, with different angular positions relative to the flow stagnation point. The base case of side-by-side cylinders without the control wire is characterized by a synchronized, out-of-phase flow regime. However, when the wire is placed around the cylinders, three flow regimes are observed over the range of wire angles; bistable flow, stable biased flow, and merged wake flow regimes. The stable biased flow regime has resulted in the maximum reduction of the fluctuating lift coefficient, especially at* $\theta = 135^\circ$*. Adding a second wire to the other cylinder has further reduced the fluctuating lift coefficient. A summary of the results is presented in the paper.*

1. INTRODUCTION

Engineers regularly use cylindrical structures in numerous applications. Offshore constructions, marine risers, chimney stacks, heat exchanger tubes, bridge piers, stays, masts, and wind turbines are all examples. The main design considerations for such structures are the fluid forces and the predominant vortex shedding frequency. The fluid forces and their behaviour are affected by the flow structure. Alternating vortex shedding is accompanied by pressure fluctuations on the body of interest which may produce vibrations and noise. This may lead to a resonant condition where complete failure of the structure is imminent (Weaver et al., 2000). Thus, it is crucial to study the suppression techniques of vortex shedding of circular cylinders to enhance the designs and prevent threatening failures.

The flow behaviour around multiple bodies in close proximity is more complicated than that of a single bluff body. Zdravkovich (1988) classified the flow structure according to the flow interaction, the gap ratio, and the upstream flow direction. Four regimes are classified as; proximity interference, wake interference, proximity and wake interference, and no interference. The flow regime around side-by-side cylinders is dependent on the gap ratio T^*, where $T^* = T/D$. For small gap ratios $1.0 < T^* < 1.2$, the gap flow is so weak that the two cylinders shed as one body and the vortices are shed from the outer sides of the two cylinders. While in the intermediate gap ratios $1.2 < T^* < 2.0 - 2.2$, the gap flow now has enough momentum to form a roll up motion that will form a biased flow towards one cylinder and this results in a narrow wake and a wide wake downstream the cylinders (i.e. bistable flow). As the gap ratio increases ($2.2 < T^* < 4.0 - 5.0$), the gap flow separates the two streets while the streets are still coupled in an out-of-phase mode (Mohany et al., 2014).

Several techniques are studied in the literature to suppress the vortex shedding as it is considered to be the main reason for Vortex-Induced Vibrations (VIV) and flow-excited acoustic resonance (**?**). The suppression techniques are active closed-loop, active open-loop, and passive as illustrated by Rashidi et al. (2016). The active methods are energy-consuming which adds operational cost to the system. So, the passive methods received most of the attention in the literature since they can be installed on existing structures like finned cylinders (Alziadeh et al., 2019) or being secondary bodies like control wires (Strykowski et al., 1990).

Suppression of vortex shedding from circular cylinders using a control wire has gained the attention of several researchers since Strykowski et al. (1990) pioneered this method. It has been shown that the flow behaviour depends on the radial position of the

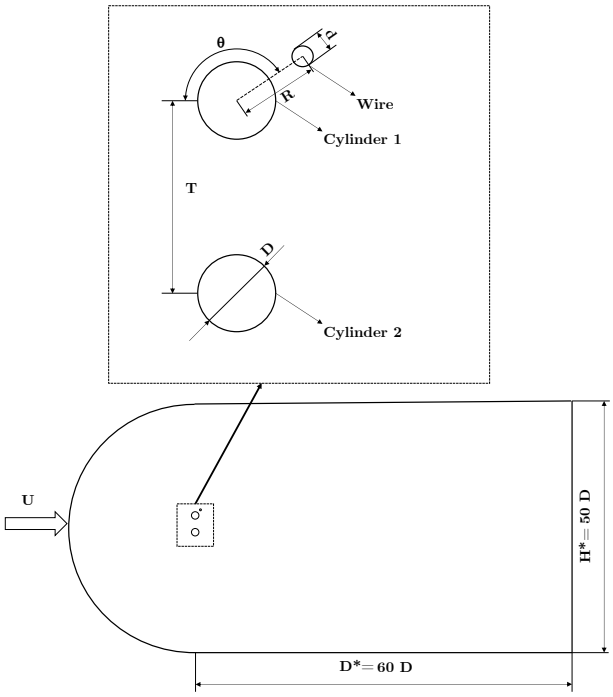

Figure 1. The computational domain of the two side-by-side cylinders with a control wire

wire, the angular position of the wire, and the ratio between the diameters of the primary cylinder and the control wire (Cicolin et al., 2021). Moreover, there is a significant dependency of the optimal location of the wire on Reynolds number. This dependency was shown by Dalton et al. (2001) when they observed full suppression of the vortex shedding at Re=100. Nevertheless, at Re=3000, the drag coefficient was reduced by 25% and the root-mean square lift coefficient was reduced by 85% for the same position of the wire at both cases. Cicolin et al. (2021) investigated experimentally the effect of the angular position of the wire on the hydrodynamic forces of a single cylinder in cross-flow. Also, they devised a method to correlate the mean gap flow velocity, between the cylinder and the control wire, and the observed four flow regimes. However, no attempts were made to investigate the influence of adding a control wire on the flow structure and the hydrodynamic forces for side-by-side cylinders within the proximity interference region.

Min Lou et al. (2017) investigated experimentally the suppression of VIV by using multiple control wires on side-by-side cylinders at large spacing ratios ($T^* = 4-8$); where no synchronization between the vortex street is present as illustrated by Sumner et al. (1999). The results have shown suppression of 90% of the amplitude of the vibration at $Re = 4500$. However, the effect of the number of wires on the flow regime or the angular position of the wires was not investigated.

Investigating the effect of the number of control wires, Reynolds number, the angular position of the wires, and the spacing ratio between the wires and the cylinder on the flow behaviour from side-by-side cylinders are of great interest. This will provide better understanding of the interaction mechanism between the wire and wakes of the cylinders, which can help in suppressing the vortex-induced vibrations and noise if the wires are strategically placed around the cylinders.

Abdelmwgoud et al. (2021) showed that strategic placement of a control wire at a cavity leading edge can alter the formation of the shear layer leading to a suppression of the flow-induced noise, regardless to the wire's diameter. Moreover, Cicolin et al. (2021) showed that the diameter ratio between the wire and the main cylinder is irrelevant to the system physics when compared to the position of the wire. Therefore, the main goal of this study is to investigate the influence of the angular position of a control wire on the vortex shedding from two side-by-side cylinders with synchronized out-of-phase vortex shedding.

2. METHODOLOGY AND MATHEMATICAL FORMULATION

2.1. The Physical Model

The adopted physical model in this study consists of two identical side-by-side cylinders of diameter D, and center-to-center gap T, as shown in Figure 1. Where the spacing ratio $T^* = 2.5$. At this spacing ratio, the flow regime is observed by Williamson (1985) to be out-of-phase, synchronized vortex street. The numerical study is carried out at $Re = 200$ and the control wire is located around the upper cylinder with diameter ratio $d/D = 0.25$ and center-to-center ratio R^*, where $R^* = R/D = 1$. Yildirim et al. (2010) reported the same R^* to be very effective in suppressing the vortex shedding at $Re = 100$ from a single cylinder. The angular position of the wire lies between $90^\circ \leq \theta \leq 180^\circ$ relative to the flow stagnation point with a step of 11.25° since this range is common to several previous studies on single cylinders.

2.2. The Computational Domain And Governing Equations

The computational domain is adopted from Shaaban et al. (2018) to optimize the grid and save the needed computational power. The domain size and the number of elements used in this study are shown in Table 1 and compared with the reported values in the literature for numerical simulations of two side-by-side cylinders. Each cylinder is discretized into 100 equal

Researcher	D*	H*	No. of Elelments
Kang (2003)	100	30	95,823
Lee et al. (2009)	80	50	613,800
Bao et al. (2013)	55	55	42,058
Current Study	60	50	105,865

Table 1. The computational domain for side-by-side cylinders.

segments and the element size in the proximity of the cylinders was kept below $\Delta x = 0.015D$ to capture the boundary layer and the interactions in the near-wake. On the other hand, the global element size is kept below $\Delta x = 0.05D$ at the zero-shear walls of the domain.

The flow is governed by the incompressible Navier-Stokes equations, which are written in the vector form in Eq. 1 and 2.

$$\nabla \cdot \mathbf{U} = 0, \tag{1}$$

$$\frac{\partial \mathbf{U}}{\partial t} + \mathbf{U} \cdot \nabla \mathbf{U} = -\frac{1}{\rho_f} \nabla p + \frac{\mu}{\rho_f} \nabla^2 \mathbf{U}. \tag{2}$$

In these equations, $\mathbf{U} = (u, v)$ is the velocity vector based on the Cartesian plane (x,y). While p, t, ρ_f, μ are the pressure, time, fluid density, and the dynamic viscosity, respectively. These equations are solved directly without averaging.

These Equations are discretized in space using second order upwind discretization to ensure higher accuracy of the higher-order term.

The face value of the calculated property is calculated using Equation 3.

$$\phi_{f,SOU} = \phi + \nabla\phi \cdot \vec{r}. \tag{3}$$

Here ϕ, $\nabla\phi$, and $\vec{r}$ are the face-centered value of the calculated property, the face gradient from the upstream face, and the displacement vector between the centroid of the current face and the upstream face. The discretized equations are solved using pressure-based solver, and the velocity and the pressure are directly coupled. The coupling is done by implicit discretization of the pressure gradient term in the momentum equation and the mass flux term.

The summation of the pressure force and the viscous force on each element of the cylinders are integrated as the aerodynamic force per unit length on the cylinders, which will be resolved into the stream-wise direction F_x and the transverse direction F_y. Then, the lift and drag coefficients are calculated based on the cylinders and wire diameters, as shown in Eq. 4 and 5. Moreover, the overall force coefficient is calculated as the resultant of the drag and lift coefficients, as shown in Eq. 6. In the base case, without the control wire, fluid forces coefficients are reported and noted as *C no wire*.

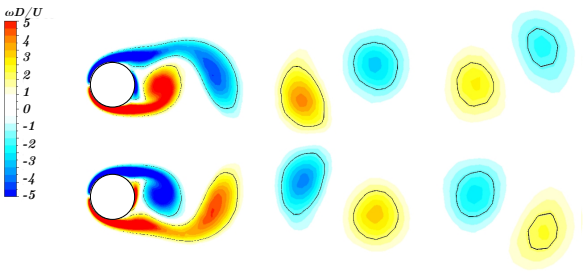

Figure 2. Instantaneous normalized vorticity contours for the base case of Side-By-Side cylinders with spacing ratio $T^* = 2.5$

$$C_{L_{1,2}} = \frac{F_{y_{1,2}}}{\frac{1}{2}\rho U^2 D}, \quad C_{L_{wire}} = \frac{F_{y_{wire}}}{\frac{1}{2}\rho U^2 d}, \tag{4}$$

$$C_{D_{1,2}} = \frac{F_{x_{1,2}}}{\frac{1}{2}\rho U^2 D}, \quad C_{D_{wire}} = \frac{F_{x_{wire}}}{\frac{1}{2}\rho U^2 d}, \tag{5}$$

$$C_{*1,2} = \sqrt{{C_D}^2 + {C_L}^2}. \tag{6}$$

3. RESULTS AND DISCUSSION

The presence of one wire around the cylinder changed the flow regime of both cylinders and decreased the fluctuating lift forces on both cylinders when compared with the base case of side-by-side cylinders. The base case is characterized by synchronized, out-of-phase vortex shedding regime, as shown in Figure 2. However,when adding the wire to the side-by-side cylinders, three flow regimes are identified based on the angular postilion of the wire. These flow regimes show the effect of the wire on the outer shear layer of the upper cylinder (Cylinder 1) and ultimately on the flow structure from both cylinders. The limits of the regimes are identified from visual inspection of the wake structure using the vorticity field. One angle is chosen to show the cumulative effect of having two wires around both cylinders on the vorticity field and the hydrodynamic forces, which is discussed in Section 3.5.

The base case of two side-by-side cylinders at $T^* = 2.5$ is simulated and validated across the reported data in literature. Williamson (1985) reported Strouhal number of $St \simeq 0.208$ which is in good agreement with the simulation results with 4% deviation.

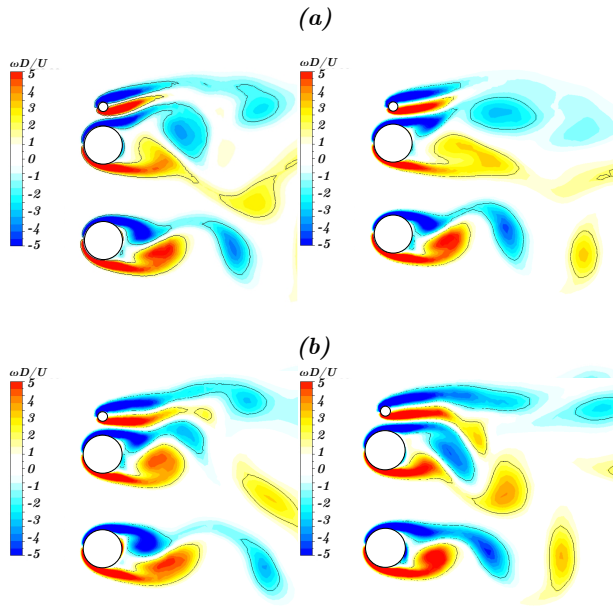

Figure 3. Instantaneous normalized vorticity contours for Flow Regime I indicating the bistable flow at $\theta = 90^\circ$ (a) the narrow wake of the wire (b) the wide wake of the wire

3.1. Flow Regime I

The presence of the wire around the upper cylinder (Cylinder 1) in the range between $90^o \leq \theta \leq 108^o$ has eliminated the synchronization of the vorticies between the upper and the lower cylinders. Moreover, the gap flow between the wire and the upper cylinder is strong enough to create two separate shear layers from both sides of the gap flow and form a roll up motion that will form a biased flow towards one cylinder. Thus, bistable gap flow is created, as shown in Figure 3, which has the same characteristics of the bistable flow in the case of two side-by-side cylinders with intermediate gap between $1.2 < T^* < 2.0 - 2.2$.

For this case with $\theta = 90^o$, the gap between the wire and the cylinder can be normalized with the diameter of the cylinder to show that this gap will result in a bistable behaviour similar to the case of the base case of side-by-side cylinders. The bistable behaviour has a period of a multiple vortex shedding cycles, similar to the bistable flow period of the base case of side-by-side cylinders at the same Reynold's number (Kang, 2003). Finally, the near wake of the lower cylinder is uninterrupted, but its vortex street is drifted away from the center of the cylinder due to the wide vortex street of the upper cylinder and the wire.

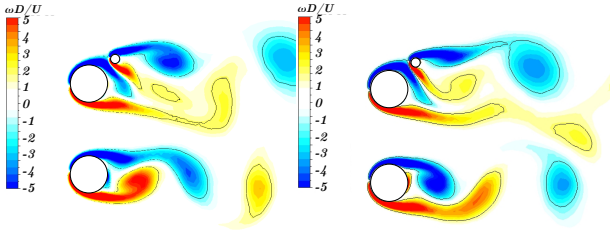

Figure 4. Instantaneous normalized vorticity contours for Flow Regime II indicating the biased stable flow at $\theta = 135^\circ$

3.2. Flow Regime II

As the angle of the wire increases, the gap flow becomes weaker. For $108^\circ \leq \theta \leq 140^\circ$, stable biased flow is observed, as shown in Figure 4. The top shear layer of the upper cylinder (Cylinder 1) is drifted into its wake, the interaction between the positive and negative vorticity of the three shear layers (the two shear layers of the cylinder and the bottom shear layer of the wire) results in biased and irregular vortex street. This behaviour affects the lower cylinder (Cylinder 2) as well.

Maximum reduction in the fluctuating lift force, and mean drag force is observed in this range. However, the mean lift force is maximized due to the asymmetry in the flow structure downstream of the two cylinders. The flow regime of the upper cylinder and the wire is similar to the flow regime of two staggered cylinders as reported by Sumner et al. (2000), which is called Induced Separation (IS). However, this behaviour is maintained until $\theta = 140^\circ$ instead of $\theta = 120^\circ$ in the case of two identical cylinders. This discrepancy is due to the difference in the separation angle which is affected by Reynolds number, the smaller diameter of the wire, and the gap between the cylinder and the wire compared to the staggered identical cylinders.

3.3. Flow Regime III

This flow regime is observed at wire angles between $140^\circ \leq \theta \leq 180^\circ$. The shear layer of the upper cylinder takes over the gap flow and the wake of the wire disappeared due to its presence in the wake of the cylinder. The key features of this flow regime are cyclic vortex shedding from both cylinders and interacting vortex streets, as shown in Figure 5. Moreover, the vortex formation length of the upper cylinder increased because the wire extends the shear layer to shed the vorticies at a further downstream position.

To illustrate, the vortex formation length of the upper cylinder at wire angle $\theta = 168.75^\circ$ has increased by 29.6% (2.19 D) compared to the base case (1.69

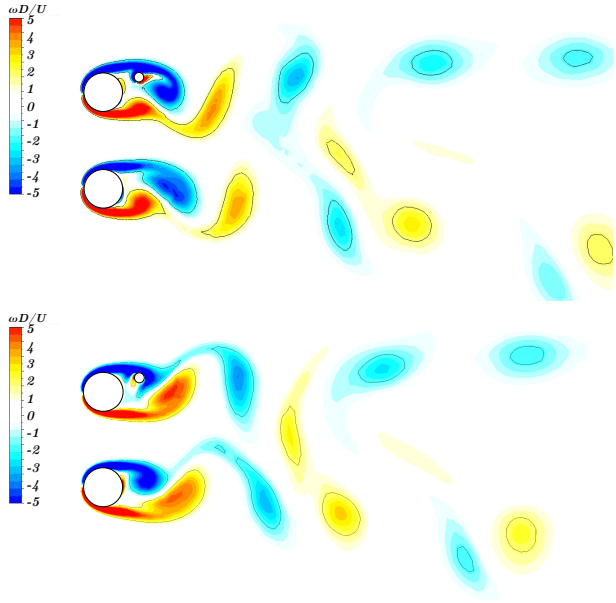

Figure 5. Instantaneous normalized vorticity contours for Flow Regime III indicating the merged wake pattern at $\theta = 157.5°$

D). Furthermore, the vortex formation length of the lower cylinder is slightly increased as well by 3% (1.74 D) compared to the base case.

The difference in the vortex formation length between the upper and the lower cylinders (Cylinder 1 and Cylinder2, respectively) resulted into stronger vortex street for the lower cylinder that the positive vorticies from the upper cylinder die out after three shedding cycles while the negative vorticies is sustained in the far wake. The variation in the vortex street strength is observed in the fluctuating transverse velocity of each wake ($\overline{v'}/U$) where the upper cylinder had less fluctuating transverse velocity in its wake by 12.8% ($\overline{v'}/U$=0.604) compared to the lower cylinder ($\overline{v'}/U$=0.693).

3.4. Fluid Force Statistics

The different regimes of the flow structure at different wire angles affect the fluid forces on the cylinders. The mean drag coefficient, root-mean-square lift coefficient, mean lift coefficient, and the total force coefficient of the two cylinders and the wire at different wire angles are shown in Figures 6, 7, 8, and 9, respectively, compared with the base case force coefficients. The limits of the flow regimes are superimposed on the figures.

The presence of the wire in the vicinity of the upper cylinder (Cylinder 1) enhanced its drag coefficient, especially when the wire is present in its wake. However, when the wire is masked by the top shear

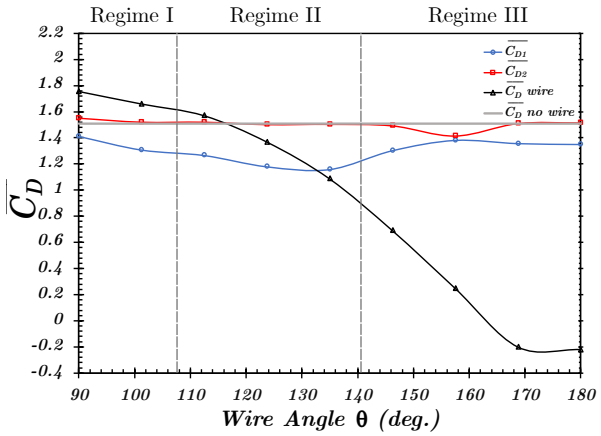

Figure 6. Variations of the time-averaged drag coefficient with the wire angle

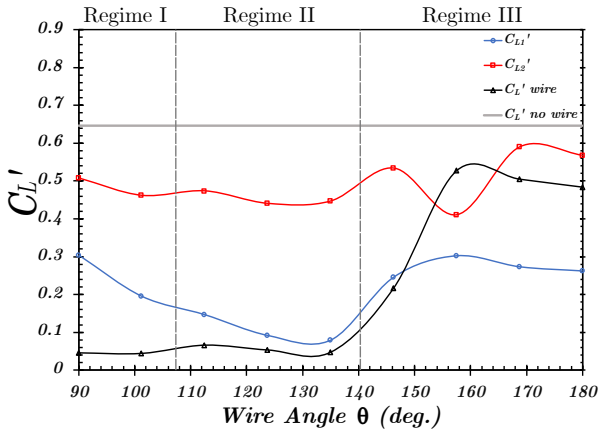

Figure 7. Variations of the rms values of the lift coefficient fluctuations with the wire angle

layer of the cylinder, the mean drag of the wire decreased dramatically until it reached negative values at $\theta > 160°$. Since the wire is placed around the upper cylinder, the mean drag force on the lower cylinder (Cylinder 2) is almost the same compared to the base case of side-by-side cylinders.

The introduction of the wire on the upper cylinder has decreased the fluctuating lift coefficient on both cylinders for all wire angles when compared with the base case. Comparing all studied angles, Flow Regime II shows the most reduction for the fluctuating lift coefficient, where the stable biased flow suppresses vortex shedding from the upper cylinder and induces wake interaction between the upper and lower cylinders. For example, the fluctuating lift coefficient is reduced by 87% and 30% for the upper and lower cylinders, respectively, at a wire angle of $\theta = 135°$. Flow Regime I enhances the fluctuating lift coefficient due to the irregular nature of the bistable flow. However, Flow Regime III was the least effective flow regime in suppressing the fluctuating lift

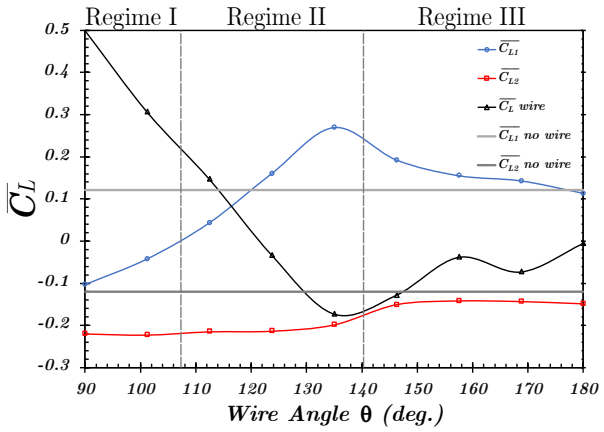

Figure 8. Variations of the time-averaged lift coefficient with the wire angle

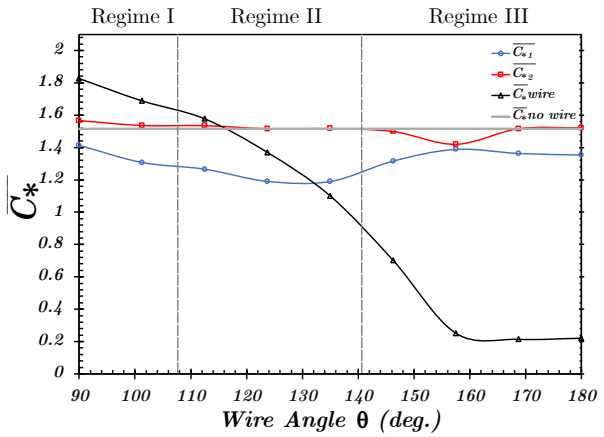

Figure 9. Variations of the time-averaged total force coefficient with the wire angle

coefficient due to the regular, cyclic vortex shedding from both cylinders. It should also be mentioned that placing the wire at the angular positions that correspond to Flow Regime III has decreased the strength of the shed vorticies from both cylinders which decreased the fluctuating lift coefficient.

The presence of the wire induced a mean lift force on the whole system, opposing the symmetric base case. However, the trend of the overall force coefficient is similar to the drag coefficient, as shown in Figure 6, and 9. The mean lift on the upper cylinder is negative in Flow Regime I due to the bistable flow and the strong repulsion force between the wire and the upper cylinder which overcomes the typical repulsive force between the upper and lower cylinders. However, the stable biased flow (Flow Regime II) has the opposite effect on the lift force due to the asymmetry of the wake. The mean lift coefficient on the lower cylinder is almost unchanged in Flow Regime I and II at (-0.215) which is higher than the base case (-0.12) due to the presence of the wider wake of the

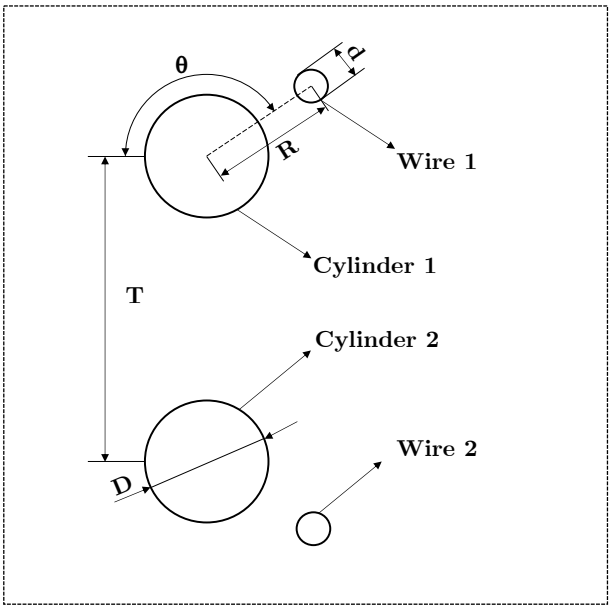

Figure 10. Configuration of the two-wire case.

upper cylinder and the wire.

For Flow Regime III, the mean lift of the upper cylinder gradually decreases until the wire reaches an angle of 180° where the mean lift of the upper cylinder is almost the same as that of the base case and the mean lift on the wire is zero due to symmetry. Also, the mean lift on the lower cylinder is almost constant at a value of (-0.145) compared to (-0.12) in the base case of side-by-side cylinders.

3.5. Effect Of Adding Two Wires Around Both Cylinders

Since it has been observed that Flow Regime II has the largest influence on the flow structure and the fluid forces, an extra wire is added to the lower cylinder in a symmetric configuration to investigate its effect on the flow regime and the fluid forces. The two wires had the same angle of $\theta = 123.75°$, as shown in Figure 10.

The flow field is characterized by the stable biased flow on both cylinders, while the outer sides of the wires are shedding vorticies regularly, as shown in Figure 11. The vortex street is weaker than the single wire cases due to strong interactions between the shear layers of the cylinders and the inner shear layer of the wires. However, the symmetry of the geometry and the stronger gap flow, compared to the 1-wire case at $\theta = 123.75°$, separates the wakes of the two cylinders for four shedding cycles before its momentum diffuses and the wakes interact.

The fluctuating lift coefficient decreased considerably when compared with the base case of two side-

Case	$\overline{C_{D1}}$	$\overline{C_{D2}}$	C'_{L1}	C'_{L2}
Base	1.51	1.51	0.646	0.646
1-wire	1.18	1.5	0.092	0.44
	(21.85%)	(0.66%)	(85.76%)	(31.89%)
2-wire	1.25	1.25	0.037	0.037
	(17.21%)	(17.21%)	(94.27%)	(94.27%)

Table 2. Comparison between the fluid forces on the cylinders for the base side-by-side case, a single wire case, and the two-wire case. Reduction percentage of the force coefficient compared to the base case is reported between parenthesis.

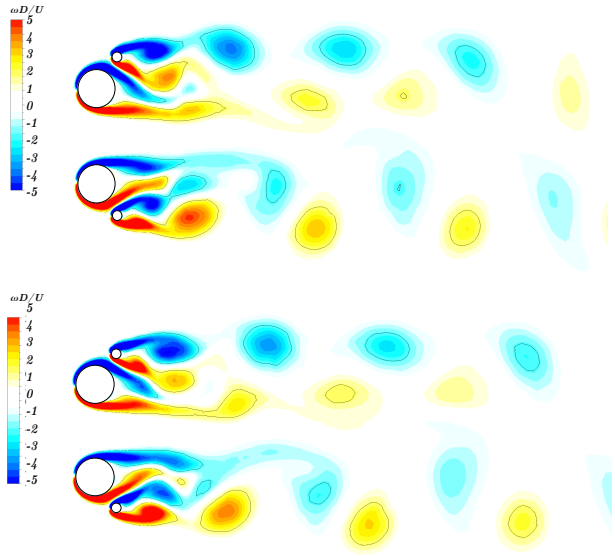

Figure 11. Instantaneous normalized vorticity contours for the two-wire case at Flow Regime II indicating the biased stable flow on both cylinders at $\theta = 123.75°$

by-side cylinders and the single wire case. Moreover, the drag has decreased on the lower cylinder (Cylinder 2) when compared with the single wire case due to the wake change from the typical vortex shedding to the biased flow regime. However, the drag on the upper cylinder (Cylinder 1) has increased when compared with the single wire case. Fluid force coefficients for the two cylinders are reported in Table 2 along with the reduction percentage of the force coefficients compared with the base case of side-by-side cylinders.

4. CONCLUSIONS

In the present study, the effect of adding a control wire around a side-by-side arrangement of cylinders at a spacing ratio of 2.5 is investigated. The parameter of interest is the wire angular position around the cylinders, while the diameter of the wire and other wire parameters are kept constant. Three flow structures were identified and compared to the base case with no wire. The bistable flow regime is observed in a range of wire angles between $90° \leq \theta \leq 108°$. While the stable biased flow is observed in the range between $108° \leq \theta \leq 140°$, and the merged wake regime is observed in the range between $140° \leq \theta \leq 180°$.

Results show that the presence of the wire decreased the drag force on the upper cylinder compared with the base case, while it barely altered the drag force on the lower cylinder. Furthermore, the fluctuating lift coefficient on the upper cylinder experienced a large decrement (87% at $\theta = 135°$) compared with the base case, especially in Flow Regime II. Also, the lower cylinder experienced an average of 25% reduction in the fluctuating lift coefficient. The mean lift on the upper cylinder is highly dependent on the position of the wire, and the mean lift coefficient on the lower cylinder is dependent on the presence of the wire wake.

Adding a second wire to the other cylinder in the range of angles that corresponds to Flow Regime II ($108° \leq \theta \leq 140°$) has affected both cylinders. The flow field becomes symmetric with strong gap flow. Moreover, further decrement in the fluctuating lift coefficient is observed on both cylinder (94.27% at $\theta = 123.75°$). The results of this study show that using a control wire located at strategic positions around an arrangement of two side-by-side cylinders has great influence on the wake structure and the dynamic loading and can be effectively used to suppress vortex shedding.

5. REFERENCES

Abdelmwgoud, M. et al., 2021, Control of the self-sustained shear layer oscillations over rectangular cavities using high-frequency vortex generators. *Physics of Fluids* **33** : 045115.

Alziadeh, M. et al., 2019, Passive noise control technique for suppressing acoustic resonance excitation of spirally finned cylinders in cross-flow." *Experimental Thermal and Fluid Science* **102** : 38-51.

Bao, Y. et al., 2013, Flow characteristics of two in-phase oscillating cylinders in side-by-side arrangement, *Computers & Fluids* **71** : 124-145.

Cicolin, M. et al., 2021, The role of separation on the forces acting on a circular cylinder with a control rod, *Journal of Fluid Mechanics*, **915**, A33.

Dalton, C. et al., 2001, The suppression of lift on a circular cylinder due to vortex shedding at moderate

reynolds numbers. *Journal of Fluids and Structures*, **15**: 617–628.

Hanson, R. et al., 2009, Flow-excited acoustic resonance of two side-by-side cylinders in cross-flow. *Journal of Fluids and Structures*, **25**: 80-94.

Kang, S., 2003, Characteristics of flow over two circular cylinders in a side-by-side arrangement at low Reynolds numbers. *Physics of Fluids*, **9**: 2486–2498.

Lee, D.S. et al., 2009, A numerical study on the flow patterns of two oscillating cylinders, *Journal of Fluids and Structures*, **25:2**, 263-283.

Min Lou et al., 2017, Experimental investigation on the suppression of vortex-induced vibration of two interfering risers by control rods, *Ships and Offshore Structures*, **12:8**, 1117-1126.

Mohany, A., et al., 2014, Numerical and experimental investigation of flow-acoustic resonance of side-by-side cylinders in a duct. *Journal of Fluids and Structures,* **48**: 316-331.

Rashidi, S. et al., 2016, Vortex shedding suppression and wake control: A review. *Ocean Engineering,* **126**: 57-80.

Shaaban, M. et al., 2018, Flow-induced vibration of three unevenly spaced in-line cylinders in cross-flow. *Journal of Fluids and Structures*, **76**: 367–383.

Strykowski, P.J. et al., 1990, On the formation and suppression of vortex shedding at low Reynolds numbers. *Journal of Fluid Mechanics* **218**: 71-107.

Sumner, D. et al., 2000, Flow-pattern identification for two staggered circular cylinders in cross-flow. *Journal of Fluid Mechanics*, **411**: 263–303.

Sumner, S. et al., 1999, Fluid behaviour of side-by-side circular cylinders in steady cross-flow, *Journal of Fluids and Structures*, **13(3)**: 309–338.

Weaver, D. et al., 2000, Flow-Induced Vibrations in Power and Process Plant Components - Progress and Prospects, *Journal of Pressure Vessel Technology*, **122(3)**: 339–348.

Williamson, C.H.K., 1985, Evolution of a single wake behind a pair of bluff bodies. *Journal of Fluid Mechanics*, **159**: 1.

Yildirim, I. et al., 2010, Vortex dynamics in a wire-disturbed cylinder wake. *Physics of Fluids*, **22(9)**: 094101.

Zdravkovich, M.M., 1988. Review of interference-induced oscillations in flow past two circular cylinders in various arrangements. *Journal of WindEngineering and Industrial Aerodynamics*,**38**: 197–211.

STUDY OF THE OSCILLATION PROCESS AND THE WAKE RESULTING FROM THE ACCELERATED FLOW OVER TWO FREE-TO-ROTATE TANDEM CYLINDERS AND THE EFFECT OF A PERTURBATION APPLIED ON THE FLOW

Patrick Batista Habowski, Guilherme Henrique Fiorot, Roberta Fátima Neumeister, Sérgio Viçosa Möller
UFRGS, Federal University of Rio Grande do Sul, Porto Alegre, RS, Brazil

ABSTRACT

This paper presents the experimental study of the oscillation process of two circular cylinders (D = 25 mm) with a fixed pitch-to-diameter ratio P/D=1.26 attached to a free-to-rotate circular table placed in a wind tunnel submitted to a turbulent crossflow. One of the cylinders is aligned with the circular table axis, while the second one is placed eccentrically. The experimental analysis employed a hot-wire anemometer placed in the cylinders' wake synchronized to a high-speed digital camera. Results of velocity time series and angular displacement of the cylinders were analyzed through Fourier and wavelet transforms. The time series of the cylinders' angular displacements were obtained from the digital movies. When submitted to the uniform flow, the cylinder set aligns with the flow in a tandem arrangement. After that, it starts oscillating with a low steady amplitude. The flow is then disturbed by inserting and removing a cylinder with 32 mm of diameter, parallel to the cylinders and tangent to the channel wall. The main mechanism for initiating the low amplitude oscillation is the shedding of vortices. Applying the disturbance permanently increases the amplitude of the angular oscillation, even after it is removed. This high amplitude oscillation was found to be caused by the flow pattern through the cylinders' gap. Considering the observations made in the present work, the oscillator configuration analyzed may work as a vortex shedding suppressor.

1. INTRODUCTION

Cylinders in crossflow are one of the most common configurations in engineering, from bridge pillars to risers of offshore oil wells, transmission lines, wind power towers, etc. Since the works of Strouhal (1878), who related the Aeolian tones (frequency) to the air velocity, and Bènard (1908a, b), vortex shedding has been the subject of many studies in the literature. When the wakes of two or more cylinders interact, some interesting phenomena may occur, like those found in the Aeolian harps from the ancient Greeks (Païdoussis et al., 2011). In Aeolian harps, the sound comes from strings strummed by the wind; the interaction of the wakes and resonances produces the sound.

According to Zdravkovich (2002) the interaction of wakes from two or more bluff bodies placed in crossflow to a stream lead to forces and vortex shedding patterns that can be completely different from the wake of a single body at the same Reynolds number (Re). This appears in the case of bistability of cylinders side-by-side (Alam et al., 2003) and for tandem cylinders (Igarashi, 1981).

In the tandem configuration, the interaction between the first cylinder wake and the second cylinder can involve different mechanisms. The RMS distribution of the wall pressure fluctuation on one cylinder affects the other cylinder, up or downstream. For the downstream cylinder, considering the same Re, the maxima of the RMS-values occur at angles different than those from a single cylinder. More recently, Habowski et al. (2020a) showed the dynamical properties of the wake flow behind fixed cylinders with a small spacing ratio and demonstrated that a well-behaved wake appears for the tandem configuration. However, that is not the case when cylinders have a degree of freedom. Kim et al. (2009) have studied the flow-induced vibrations (FIV) in tandem cylinders, considering that either both cylinders or only one (up or downstream) were free-to-vibrate, and they were able to establish different vibration regimes according to the spacing ratio (pitch-diameter parameter – P/D).

The spacing ratio and the flow regime can generate a low-pressure region or an incoming excitation with a defined frequency. The main mechanisms of flow-induced vibration are vortex shedding, wake galloping (buffeting), wake induced vibration, among others.

The vortex shedding patterns in a pair of fixed circular cylinders depends on factors such as the P/D-ratio, Re, and the cylinders' alignment to the flow (Zhou and Alam, 2016). The wake galloping is observed in configurations with non-circular structures (Blevins, 2001), but is also reported in arrangements with parallel cylinders where the downstream cylinder has a degree of freedom (Bokaian and Geoola, 1984). Finally, the wake-induced vibration (WIV) of the downstream cylinder is caused by the unsteady vortex-structure interactions between the cylinder

body and the upstream cylinder wake (Assi et al., 2010).

To investigate the wake-induced vibration modes, Yao and Jaiman (2019) presented a stability analysis (WIV-modes) of two cylinders with equal diameters in a tandem arrangement at a low Re number. The upstream cylinder was fixed, while the downstream cylinder was free-to-vibrate in the transverse direction, considering P/D-ratios: 2 and 4. Their results showed the critical Re number reduces as the P/D-ratio increases, leading to lower velocities for the onset of WIV. Such observation is important for structure design since their efficiency would be directly related to flow configurations established in the wake.

In our Laboratory, Neumeister et al. (2021) made a comprehensive experimental FIV study of a single cylinder and two cylinders in tandem and side-by-side configurations in a subcritical regime with changes in the blockage ratio employing a P/D-ratio of 1.26: upstream cylinder free-to-vibrate (FV); downstream cylinder free-to-vibrate (SV); and both cylinders (BV) free-to-vibrate. The experimental analysis considered 25 different cases by changing the mass and damping ratios, the natural frequency of the cylinders, and the blockage ratio. The results showed that the interaction between the cylinders' wake was perceived differently up and downstream. When comparing the FV and SV cases, the authors verified that the amplitude of the oscillations was greater for the first one. However, when both cylinders were free-to-vibrate (BV-case), the second cylinder presented a higher amplitude and a sudden increase of the amplitude (jump). This suggested that the dynamical interaction between the wakes is constructive and leads to an amplification of the system oscillation.

The observation of the experiments by Neumeister et al. (2021) motivated the development of a test section where two cylinders were attached to a free-to-rotate table inside the wind tunnel (Habowski et al., 2020b). One of the cylinders was aligned with the circular table axis, while the second one was eccentrically placed. The airflow, accelerated by throat-like obstacles, forced the cylinders set to oscillate, resembling the BV case by Neumeister et al. (2021). Results showed that a proportionality relation could be found regarding the flow Re number and the amplitude of the oscillations.

The experimental works reported here presented several aspects that show the system composed of a binary cylinder set with at least one of them with a degree of freedom is a natural oscillator when in presence of a turbulent flow. Based on the observations of Neumeister et al. (2021) and Habowski et al. (2020a, b), this study aims to investigate the dynamic properties of a natural oscillator. The wake characteristics and their interrelation with the oscillating process are investigated. A set of cylinders of equal diameter $D = 25$ mm are placed in proximity, separated by a fixed distance P (Fig. 1). The cylinder set is attached to a free-to-rotate circular table where the upstream cylinder is aligned with the circular table axis, being able to rotate with the circular table, while the downstream one is placed eccentrically and can assume an angular displacement θ. The set is then subdued to an air crossflow with mean flow velocity, U_∞.

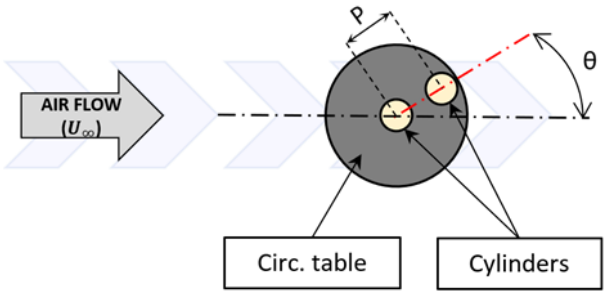

Figure 1. Representation of the observed phenomenon for the setup with two circular cylinders tandem placed on a free-to-rotate circular table.

2. MATHEMATICAL TOOLS

The signal analysis tools considered in the present study were time-domain, frequency-domain, and time-frequency domain.

The time-domain analysis consists of computing the first four statistical moments: mean value, variance, skewness, and kurtosis (Tennekes and Lumley, 1972).

In turn, the frequency-domain analysis can be performed using the Fourier analysis, but it does not allow the identification of non-stationary phenomena in the physical space (Indrusiak et al., 2016).

The non-stationary phenomena observed in the oscillation process demanded a tool that allows the time-frequency window analysis. For the time-frequency domain, wavelets analysis has been employed (Percival and Walden, 2000; Indrusiak and Möller, 2011). The wavelet functions are used for the determination of the Discrete Wavelet Transform (DWT), which decomposes the signal in dyadic frequency ranges, and the Continuous Wavelet Transform (CWT), which allows to observe the energy levels in frequency and time domains. From the CWT of two different signals, a coherence wavelet can be obtained. It shows the correlation between the signal frequencies along time and indicates the phase angle between them.

The wavelet analysis employed a Db20 function with reconstruction level 8, generating a reconstructed signal with spectral components ranging from 0 to 3.9063 Hz.

3. EXPERIMENTAL PROCEDURE

The study was executed in one of the wind tunnels of the Fluid Mechanics Laboratory of UFRGS (Fig. 2a), which is a 2.29 m long channel with a rectangular cross-section of 0.193 m in width and 0.146 m in height, made of acrylic glass. At the entrance, the airflow, provided by a centrifugal blower of 0.75 kW, passes through a diffuser, two honeycombs, and two screens, to reduce the flow turbulence intensity to about 1% when reaching the test section. In the test section, two rigid smooth cylinders made of commercial PVC tubes (Polyvinyl chloride) with a diameter $D = 25$ mm each were placed on a free-to-rotate circular table, as shown schematically in Fig. 2b. One of the cylinders is aligned with the circular table axis, while the second one is eccentrically placed. The distance between the cylinders is 6.5 mm, so the P/D-ratio of the cylinder set was 1.26, being P the pitch, the distance between the cylinders' centers. The circular table is coupled to the upper and lower channel walls using low-wear bearings. The blockage ratio of the cylinders is 13% when the set is perfectly aligned with the flow. To disturb the flow, a disturbance device (DD) was used to momentarily reduce the channel cross-section and disturb the flow velocity close to the cylinders' set (Fig. 2b). It consisted of a cylinder (diameter of 32 mm) parallel to the free-to-oscillate cylinders' set, which was inserted from the outlet, sliding tangent to the side wall up to the upstream cylinder, and then removed. Upstream of the test section, a Pitot tube is placed on one of the sidewalls (Fig. 2a) and measures the free stream velocity. This is considered as the mean velocity in the channel used for the calculation of the Re number. The Re number of the experiment was 16.6×10^4 based on the cylinder diameter and the steady-state free stream velocity (U_∞).

The axial velocity component (U) of the flow velocity and its fluctuations are measured with a DANTEC StreamLine constant hot-wire anemometry system, equipped with one single wire probe. The hot-wire was aligned with the cylinders' centerline and used to investigate the wake characteristics behind the oscillating cylinders. The sampling frequency was 1 kHz with a low pass filter at 300 Hz and the time acquisition was 32.768 s. Two wavelet analyses were employed using CWT with Db20 function and DWT with reconstruction level 8, generating a reconstructed signal with spectral components ranging from 0 to 3.9063 Hz. The uncertainty in the measurement of velocity series through the anemometry system is in the range of 2 to 7%. To process data from anemometry, Fourier and wavelet analyses were performed using the MATLAB® Software.

The oscillation of the cylinder set was studied using a high-speed Phantom V411 – Ametek camera. It was equipped with a 50 mm AF-S VR Micro-Nikkor lens. The camera resolution was 640 × 480 pixels and the speed was 1000 frames per second, corresponding to the 1 kHz sampling frequency of the hot-wire signal. The camera was triggered and synchronized with the CTA by its output via an Ethernet cable. A mirror inclined at 45° was mounted at the top of the wind tunnels to track the position of a pointer, which indicated the angle between the cylinders and the main flow during the experiments (Fig. 2b). The open-source software Tracker© was used to analyze the resulting digital movies to generate time series of the angular displacement (θ) of the cylinders. The mean error for this analysis is 1.37°.

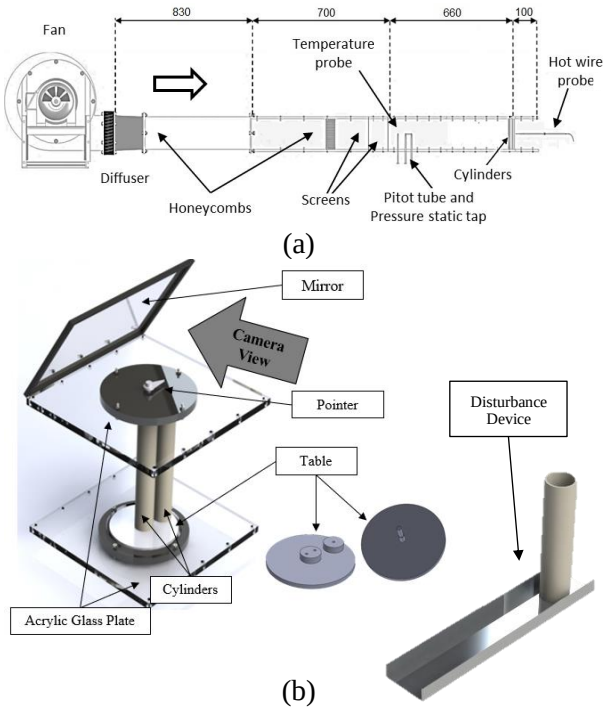

Figure 2. Main dimensions and details of the wind tunnel (a). Details about the assembly of the free-to-rotate cylinders and the disturbance device (b). Dimensions are in [mm].

The natural frequency and the damping ratio of the assembly were obtained by measuring the natural oscillation of the cylinders' set in still air in the horizontal position. The procedure was to move the eccentric cylinder to a 90° position, then release the cylinder, and let it oscillate without external influence. The angular displacement was recorded with a frequency of 60 fps, and with the logarithmic decrement technique, the damping ratio ζ of the system was obtained. The value of the natural frequency f_n was obtained from the power spectrum. The system's natural frequency is 1.4 Hz, and the damping ratio is 0.019.

The experimental procedure to obtain the data is the same employed in Habowski et al. (2022a): hot-

wire anemometry acquisition and video recording started while the air blower was turned on. After the setup achieved an apparent stabilization, oscillating in a steady regime, the disturbance device was inserted from downstream the cylinders and tangent to the walls up to be aligned with the cylinder's setup. Thus, the device was immediately removed, performing the same movement in the opposite direction. The overall perturbation movement lasts about 2.4 seconds. Experimental data, including digital movies, are available in Habowski et al. (2022b).

4. RESULTS

The oscillation process observed with the assembly apparatus is analyzed with the angular displacement of the second cylinder. The angular displacement was monitored using the pointer presented in Fig. 2b. The angular displacement along time is presented in Fig. 3. To avoid jittering in the results of angular displacement, the DWT was applied to the signals, reconstructing the signal from 0 to 3.9063 Hz with a Db20 wavelet function. DWT did not alter the shape of the results, and, through such analysis, only the frequencies of interest, defined by the predominant frequency observed in the experiments, are presented and used to compute the results.

In Fig. 3 is observed a steady-state at rest (0 – 11.99 s) followed by an oscillatory motion between ± 2.29° (11.99 – 19.32 s), started by the flow from the impeller. At 19.32 s, the disturbance in the flow was applied and extinguished at a time of 21.62 s. After the disturbance, the system presented a secondary steady oscillatory motion (21.62 – 31.95 s), ten times higher, between ± 22.92°.

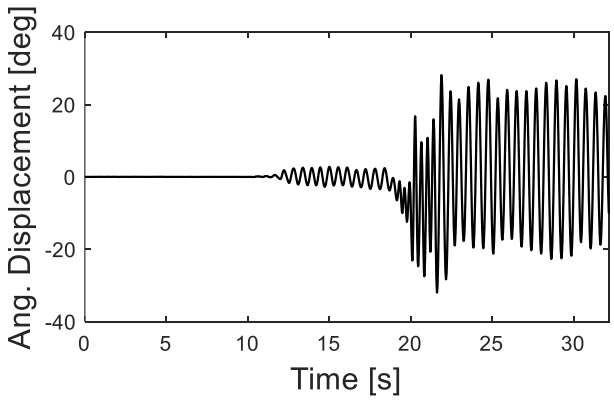

Figure 3. Reconstructed signal of angular displacement employing DWT.

Statistical analysis for the angular displacement is presented in Table 1, where the main observed phenomena in Fig. 3 are detailed. In this analysis, the observed phenomenon was identified as well as its time interval, its frequency (f), and the mean value of angular amplitudes (M). Four main phenomena were observed: Rest, representing the initial observations and the required time for the flow to achieve the steady free flow velocity; Low Amplitude Oscillation (LAO), where the setup started to oscillate without external interferences; Disturbance, representing the effects in the angular amplitude due to insertion of the disturbance device; High Amplitude Oscillation (HAO), which occurred after removing the disturbance device.

Time int. [s]	Obs. Phen.	f [Hz]	M [°]
0 – 11.99	Rest	–	–
11.99 – 19.32	LAO[1]	1.842	02.46
19.32 – 21.62	Disturb.	2.826	14.95
21.62 – 31.95	HAO[2]	1.694	22.80

Table 1. Details about the observed phenomena in the angular amplitude analysis. [1]Low Amplitude Oscillation, [2]High Amplitude Oscillation.

The initial oscillation observed in Fig. 3 indicates that the flow has sufficient kinetic energy to take the system out of the rest without external interferences. After the flow hits the steady regime, an oscillation process of low amplitude is observed with an angular mean crest of 2.46°. The insertion of the disturbance device affected the amplitudes, leading to an angular trough of −31.98°. Lastly, after removing the disturbance, the oscillation of the experiment presented an angular mean crest of 22.80°.

Some selected photographs of the top and side views of the cylinder set obtained from the high-speed movies are presented in Fig. 4. In the top view, a pointer is shown, which gives the angular position of the cylinder's set.

Figure 4a shows the moment in which the data acquisition was turned on by the anemometry system's signal. The pointer is aligned with the angular position zero, representing the time 0 – 11.99 s in Fig. 3, the rest regime. Figure 4b is when the perturbation starts to be inserted; (c-e) describes the movement to insert the disturbance device (DD), and (f) is the moment in which the configuration achieved a crest in the angular displacement.

The oscillation process in the assembly of tandem cylinders with $P/D = 1.26$ presented two main regions: one up to the disturbance was applied, where the angular displacement remained under 2.5°, and other after the disturbance, where the angular displacement increased up to 22.8°. The response to the excitation is distinct in both cases and the flow mechanisms involved change. The flow pattern and the mechanisms for the initial oscillation process are described in Fig. 5a.

The spacing ratio between the first and the second cylinders aligned or with small angles in the staggered arrangement presents the replacement of the

shear layer from the first cylinder and this can be a mechanism dominant in the initial oscillation.

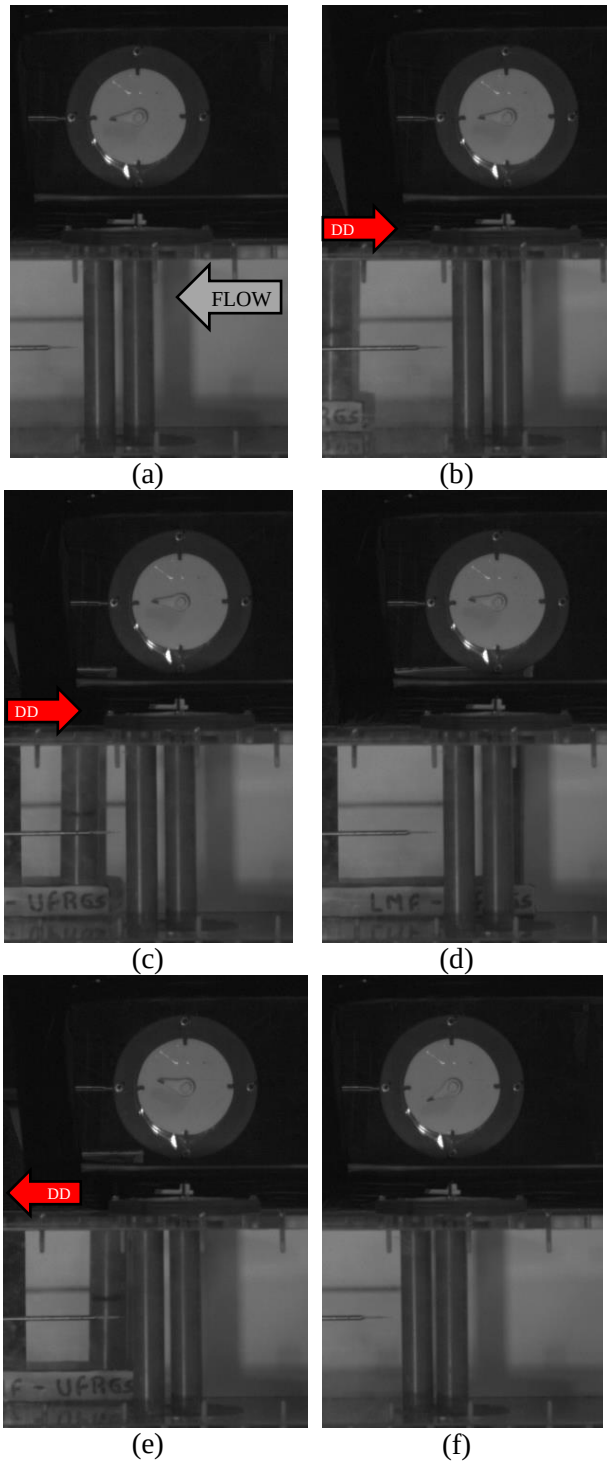

Figure 4. Details about the disturbance insertion since the beginning of data acquisition (a), disturbance insertion (b-e), and maximum angular displacement achieved (f).

The studies carried out by Igarashi (1981) presented six distinct patterns in the flow on aligned cylinders related to the spacing and the Re number. Space ratio < 2 and low Re show that the shear layer of the first cylinder does not reattach in the second cylinder. With the increase of the Re number to around 2×10^4, the reattachment of the shear layer of the first cylinder in the second cylinder is observed, and it is synchronized, occurring for an $P/D < 1.5$.

Zdravkovich (2002) reports that this pattern occurs up to $P/D = 1.3$ for low Re The wake was reported to be formed by the shear layer of the first cylinder and its reattachment to the second cylinder, showing to be permanent in the space ratio from $1.3 > P/D < 1.8$.

Fixed staggered cylinders analysis with angles up to 5° and $P/D = 1.7$ showed that the shear layer connects the cylinders (Gu and Sun, 1999). A similar result was observed for 10° and $P/D = 1.1$ including a separation bubble between the cylinders (Alam et al., 2005). In the study by Alam et al. (2005), the author observed a bistable flow over the two fixed cylinders, and two modes (mode 1 and mode 2) of the flow structure occurred intermittently and switched from one to the other at 10º. The main reason is that the inner shear layer of the downstream cylinder sweeps on its surface of for a longer peripheral length, creating a higher suction pressure before separation. The occurrence of the inner shear layer reattachment was confirmed by the surface oil-flow visualization pattern on the downstream cylinder. It was found that, as the staggered angle of the cylinders was slightly increased or decreased, say at 8º, mode 1 only was observed, and at 12º, mode 2 only was observed.

At angles from 5° to 25°, a gap flow is formed between the cylinders. Due to the staggered arrangement, the shear layer from the first cylinder impinges on the front region of the second cylinder (Fig. 5b), as observed by Gu and Sun (1999) at angles 15°–25° for $P/D = 1.7$. For 25°, $P/D = 1.1$ and $P/D = 1.3$, a similar response was found by Alam et al. (2005), where the lift coefficient of the upstream cylinder changes briskly from a value of 0.08, for $P/D = 1.1$, to the minimum, 1.03, at $P/D = 1.3$, whereas the corresponding drag coefficient follows a change pattern at $P/D = 1.10 – 1.30$. The outer and inner shear layers around the upstream cylinder separate and the inner shear layer reattaches steadily onto the downstream cylinder, as shown in Fig. 5c. The outer part of the reattached shear layer separates and part of the reverse flow reattaches again onto the rear surface of the upstream cylinder. The reverse flow in the gap between the inner side surface upstream cylinder and the front surface of the downstream cylinder is steady, resulting in a clear reattachment line on the rear surface of the upstream cylinder.

The oscillation process observed can be described using the flow characteristics presented in Figure 5a and b.

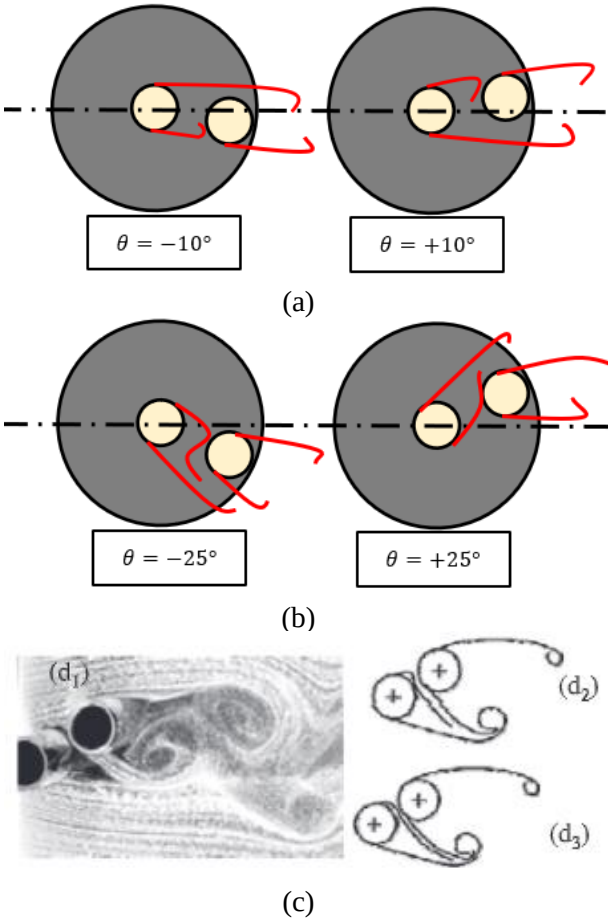

Figure 5. Schematic representation of the flow over cylinders with $P/D = 1.26$ in an angle at ± 10º (a) and ± 25º (b). Flow pattern observation by Alam et al. (2005) and Gu and Sun (1999) in a similar configuration (c) (Adapted from Zhou and Alam, 2016).

The initial oscillation (11.99 – 19.32 s) can be associated with the modes of flow observed by Alam et al. (2005), in the study of the flow modes change due to the fixed condition of the cylinders. In the present case, the cylinders are free-to-rotate along time while the second cylinder moves as a response to the pressure distribution on the cylinder mainly linked to the reattachment of the shear layer in the second cylinder.

The oscillation after the perturbation (21.62 – 31.95 s) presents a flow between the cylinder (Alam et al., 2005). The space between the cylinder is small and the velocity increases forming a gap flow and this region presents a decrease in the pressure. The cylinders with the freedom-to-rotate respond to the pressure unbalance in the surface and are pushed towards by the flow to the region of low pressure. This force is high enough to make the second cylinder cross the region and a new gap flow is formed. This behavior occurs periodically during the rest of the experiment.

During the oscillation process, the wake velocity was monitored and in Fig. 6 the wavelet analysis results for U from the hot-wire signals are presented. Reconstructed velocity signals using DWT are presented in Fig. 6, where velocity peaks (highlighted) in the results were observed. These peaks were caused right after disturbing the system, since the insertion of the disturbance device increases the blockage ratio, accelerating the flow. After removing the device, the velocity level returns to the initial level. The energy content analysis, performed through CWT, is presented in Fig. 6. The energy level is related to the frequency, where the black color represents high energy content, and the white color, the low energy content (Fig. 6). Through this analysis, the higher levels of energy occur when the velocity peaks were found. This behavior was expected since the increase in velocity induces an increase in kinetic energy. According to Habowski et al. (2020a), the energy values are more likely to increase with velocity fluctuations than with the velocity levels. In this study, the insertion of the disturbance increased both velocity and velocity fluctuations, leading to the formation of velocity peaks.

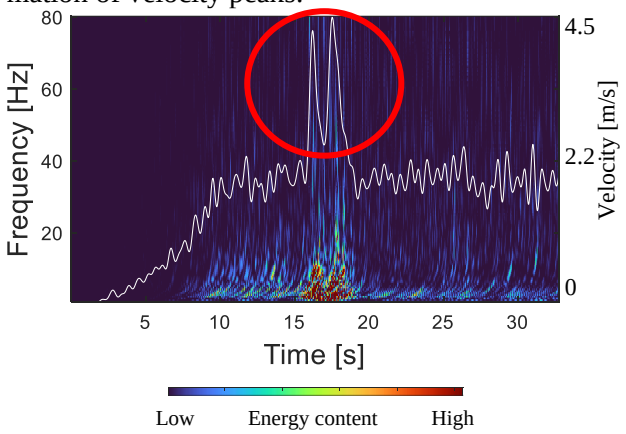

Figure 6. Reconstructed signal of velocity employing DWT plotted over the energy content analysis (CWT). Highlight the observed velocity peaks. Velocity scale at the right.

A Fourier analysis was performed to identify frequencies in the spectrum related to the disturbance applied to the flow on the wake velocity. Fig 7 presents the energy spectrum before and after the disturbance. To generate this chart, the mean value of the velocity signal was computed and extracted from each point of the original signal. Thus, the results were computed only with the velocity fluctuations. Considering the similarity of the signals before and after the disturbance, the main conclusion of these

results is the fact that the disturbance did not generate other maximum points of energy in the spectrogram.

Figure 7 also presents the results obtained by Habowski et al. (2020a), which explored results for a configuration with two circular cylinders rigidly tandem assembled in a wind tunnel. The authors found a visible peak at 70 Hz, which generates a Strouhal number of 0.154 computed for local velocity (11.4 m/s) and the cylinder diameter. This Strouhal number corresponds to the vortex shedding, following the results obtained by Neumeister et al. (2021). In the present study, different from the study proposed by Habowski et al. (2020a), the cylinders have the freedom-to-rotate and do not allow a perceptive vortex shedding. This result can be interpreted as follows: the vortex shedding that would be perceived with the cylinders rigidly assembled in the wind tunnel is the main mechanism to take the system out of the rest and induce the oscillatory movement. Small peaks close to 70 Hz are observed in the proposed experiment, indicating attempts to shed the vortex.

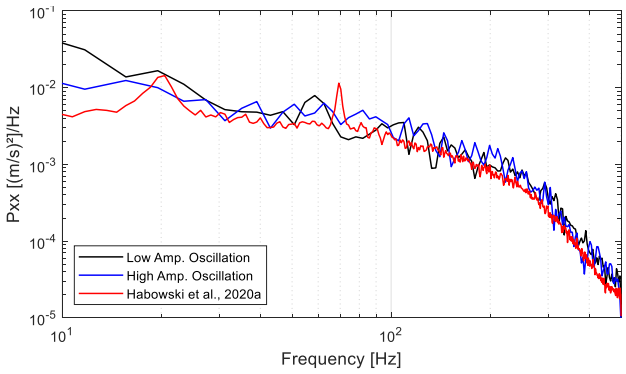

Figure 7. Fourier analysis for the fluctuation's velocities before and after the disturbance insertion.

A Fourier analysis was performed also using the signal from Fig. 3 to identify frequencies in the spectrum related to the disturbance applied to the flow. The frequency identified on the initial oscillation from 11.99 – 19.32 s is 1.95Hz. The frequencies identified in the oscillation from 21.62 – 31.95 s are 1.71 Hz and 2.4 Hz.

To understand the relationship between the wake velocity and angular displacement, Fig. 8 presents the wavelet coherence of these two signals (Fig. 3 and Fig. 7). Through this analysis, it is possible to identify that the coherence of the signals increases at frequencies under 2 Hz, after 23 s.

Comparing the results of Fig. 7, the Fourier analysis of Fig. 3, and the crosswavelet coherence (Fig. 8), there is no evidence of coherence between the vortex shedding from the first cylinder and the oscillation process. The high coherence observed occurs under 2 Hz and can be related to the oscillation movement imposed by the cylinders' set on the flow. The coherence increases after 23 s while the HAO starts at 21.62 s, showing the before mentioned relation with the observed result.

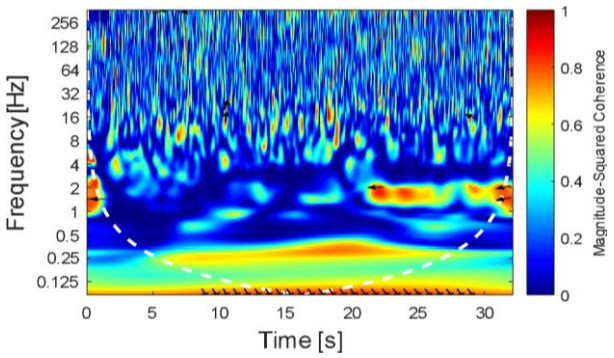

Figure 8. Crosswavelet analysis of wake velocity and angular displacement of the setup.

5. CONCLUSION

This paper presents the study of an oscillator composed of a binary set of cylinders subdue to a cross-flow. The experiment consisted of a free-to-rotate circular table with two smooth circular cylinders ($D = 25$ mm) with a pitch-to-diameter ratio $P/D = 1.26$ submitted to an accelerating flow in a wind tunnel. The setup was initially placed in a tandem position to the flow, with a Re number of 16.6×10^4, computed with the stable free flow velocity and the tube diameter. After the stabilization of the flow, a disturbance device ($D = 32$ mm) was inserted and removed. The purpose was to modify the flow close to the cylinder's setup during a short period.

The angular behavior analysis of the setup was presented. The objective was to observe and describe the effects caused by the insertion of the disturbance device using photograms from high-speed movies and the oscillation response. In the results of this study, it was observed two distinct regimes of oscillation with different amplitudes and similar frequencies. The oscillation regime with lower amplitude was identified to start by the vortex shedding, and the higher amplitude regime appeared after the flow disturbance and was maintained at the oscillation level by the gap flow between the cylinders.

Results for wake velocity and energy content were performed through wavelet transform, Fourier analysis, and wavelet coherence. The main conclusions of these results were the velocities and energy peaks caused by the insertion of the disturbance device and its consequent fluctuations in the velocity values. A comparison of the results presented in this article with the literature shows that the disturbance did not generate other significant levels of energy. In the wavelet coherence analysis, no correlation was identified between the signals of wake velocity and angu-

lar displacement, suggesting that the oscillation process is not a direct response to the wake from the first cylinder. The patterns of oscillation show that the interaction between the cylinder's shear layers and the gap flow are the main mechanisms related to the response observed.

6. REFERENCES

Alam, M.M., Moriya, M., Sakamoto, H., 2003, Aerodynamic characteristics of two side-by side circular cylinders and application of wavelet analysis on the switching phenomenon, *Journal of Fluids and Structures* **18**, p. 325–346.

Alam, M.M. and Sakamoto, H., 2005, Investigation of Strouhal frequencies of two staggered bluff bodies and detection of multistable flow by wavelets, *Journal of Fluids and Structures* **20**, p. 425-449.

Assi, G.R.S., Bearman, P.W. and Meneghini, J.R., 2010, On the wake-induced vibration of tandem circular cylinders: the vortex interaction excitation mechanism, *Journal of Fluid Mechanics* **661**, p. 365–401.

Bénard, H, 1908a, Formation périodique de centres de giration á l'arriére d'un obstacle en mouvement, *C. R. Acad. Sci.* **147**, p. 839–842.

Bénard, H., 1908b, Etude cinématographique des ramous et des rides produits par la translation d'un obstacle, *C. R. Acad. Sci.* **147**, p. 970–972.

Blevins, R.D., *Flow-Induced Vibration*, 2nd ed., Van Nostrand Reinhold, New York.

Bokaian, A. and Geoola, F., 1984, Wake-induced galloping of two interfering circular cylinders, *Journal of Fluid Mechanics* **146**, p. 383–415.

Gu, Z. and Sun, T., 1999, On interference between two circular cylinders in staggered arrangement at high subcritical Reynolds numbers, *Journal of Wind Engineering and Industrial Aerodynamics* **80**, p. 287-309.

Habowski, P. B., de Paula, A. V., Möller, S.V., 2020a, Wake behavior analysis for two circular cylinders placed at several angles to the flow, *Journal of the Brazilian Society of Mechanical Sciences and Engineering* **42**, 441.

Habowski, P. B., Fiorot, G. H., de Paula, A. V., Möller, S.V., 2020b, Unbalanced free to oscillate tandem cylinders in a turbulent crossflow. Proceedings of ENCIT 2020, *18th Brazilian Congress of Thermal Sciences and Engineering (2020)*, Porto Alegre – Brazil.

Habowski, P. B., Neumeister, R.F., de Paula, Petry, A.P., A. V., Möller, S.V., 2022a, On the interaction of the wake flow with the rotation process of two parallel free-to-rotate cylinders submitted to an accelerating flow, *Acta Mechanica* **233**, p. 813–815.

Habowski, P.B., Möller, S.V., Fiorot, G.H., 2022b. Wake flow and angular oscillation behavior of two cylinders in tandem arrangement forming a van der Pol oscillator, *Mendeley Data*.

Igarashi, T., 1981, Characteristics of the flow around two circular cylinders arranged in tandem, *Bulletin of the JSME* **24**, n. 188.

Indrusiak M. L. S., Kozakevicius A. J. and Möller S. V., 2016, Wavelet analysis considerations for experimental nonstationary flow phenomena, *Thermal Engineering* **15**, p. 67–76.

Indrusiak M. L. S. and Möller, S.V., 2011, Wavelet analysis of unsteady flows: application on the determination of the Strouhal number of the transient wake behind a single cylinder, *Experimental Thermal and Fluid Science* **35**, p. 319–327.

Kim, S., Alam, M.M., Sakamoto, H. and Zhou, Y., 2009, Flow-induced vibrations of two circular cylinders in tandem arrangement part 1: Characteristics of vibration, *Journal of Wind Engineering and Industrial Aerodynamics* **97**, issues 5–6, p. 304–311.

Neumeister, R. F., Petry, A. P. and Möller, S. V., 2021, Experimental flow-induced vibration analysis of the crossflow past a single cylinder and pairs of cylinders in tandem and side-by-side, *Journal of Pressure Vessel Technology - Transactions of the ASME* **143**, p. 031402.

Païdoussis, M. P., Price, S. J., and de Langre, E., 2011, *Fluid-structure interactions: cross-flow induced instabilities*, Cambridge University Press, New York.

Percival, D. B. and Walden, A. T., 2000, *Wavelet Methods for Time Series Analysis*, Cambridge University Press, Cambridge, UK.

Strouhal, V., 1878, Über eine besondere Art der Tonerregung, *Ann. Phys. und Chemie* **5**, New Series, p. 216–251.

Tennekes, H. and Lumley, J. L., 1972, *A First Course in Turbulence*, The MIT Press, Cambridge, MA.

Yao, W., Jaiman, R.K., 2019, Stability analysis of the wake-induced vibration of tandem circular and square cylinders, *Nonlinear Dynamics* **95**, p. 13–28.

Zdravkovich, M. M., 2002, *Flow Around Circular Cylinders: Applications*, v.2. Oxford Science Publications, Oxford, UK.

Zhou, Y, and Alam, M., 2016, Wake of two interacting circular cylinders: A review, *International Journal of Heat and Fluid Flow* **62**, p. 510–537.

UNSTEADY WALL PRESSURE MEASUREMENTS ON A FULL SCALE FLEXIBLE CHIMNEY SUBJECT TO NATURAL WIND

Yacine Manal
LadHyX, CNRS-Ecole polytechnique, Palaiseau, France & ENS Paris-Saclay, France
Pascal Hémon
LadHyX, CNRS-Ecole polytechnique, Palaiseau, France

ABSTRACT

A full scale flexible prototype chimney is erected on a natural site in order to study its excitation by wind, especially by the alternate vortex shedding. For the first time, unsteady wall pressure measurements are performed on the chimney. This experiment combines the two features that cannot be reproduced simultaneously in wind tunnel: a high Reynolds number and a turbulent boundary layer.

Preliminary results are presented, showing notably that the pressure distribution looks like the one measured in wind tunnel in supercritical conditions, with an additional turbulent noisy component.

1. INTRODUCTION

Vertical slender flexible structures are subject to wind-induced vibrations involving complex inflow conditions due to the atmospheric boundary layer. Especially structures with circular, or mostly circular, shapes, such as chimneys, stacks and launch vehicles, are responsive to alternate vortex shedding. However, there are a number of difficulties for studying such a phenomenon while respecting the natural wind characteristics such as the velocity gradient and the turbulence parameters. Moreover, wind tunnel tests in such cases are performed on scaled models, which do not respect the Reynolds similarity and introduce an additional difficulty then. For instance, numbers of authors add roughness elements on the surface model in order to simulate the high Reynolds number flow (Barré & Barnaud 1995) while the technique is not reliable (Ellingsen et al. 2022b).

Despite their interest, there are very few field studies of vortex-induced vibrations of chimneys that can serve as validation test cases for the prediction model, such as (Basu & Vickery 1983, Vickery & Basu 1983). In (Sageau 1978) and (Christensen et al. 1978) some wall pressure measurements were performed on some existing chimneys. An interesting experiment was presented in (Galemann & Ruscheweh 1992 ; Ruscheweh & Galemann 1996) where an experimental steel chimney of 28 m was equipped with a number of sensors, including wall pressure.

In all these experiments, only the time-averaged wall pressures were measured while unsteady data would be useful in the context of vortex shedding understanding in real wind conditions.

In 2018 a project was started under a partnership including the company Beirens, the CNES, the CSTB and LadHyX. One of its components was the erection of an experimental chimney on an observation site for which first results were presented in (Ellingsen et al. 2022a). The goal of the current paper is to present the preliminary results of the wall pressure measurements performed during a short term campaign in July 2021.

2. FIELD TEST PLATFORM

The observation site is located in Bouin (85, Département of Vendée) in the western part of France at about 2 km from the Atlantic seashore. The environment is a marsh which makes the relief very flat over a distance greater than 2 km around, as it can be seen in the Figures 1 and 2.

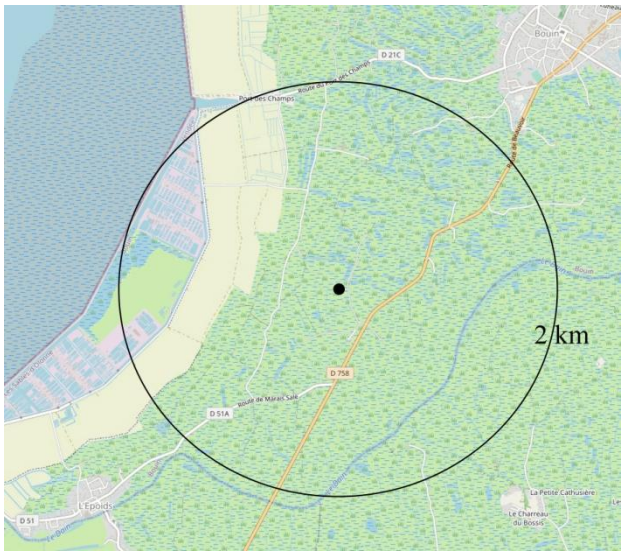

Figure 1. Map of the chimney site

2.1. The experimental chimney

The chimney is a steel tube with 35.5 m high and an external diameter of 1 m in the lower part from 0 to 12 m and 2 m in the upper part above 15 m. From 12 to 15 m the diameter linearly increases from 1 to 2 m (see Figure 3). It is clamped at the bottom in a concrete mass.

The purpose of this particular shape is to obtain a chimney with a low Scruton number and a first bending mode at a low frequency in order to get a lock-in with alternate vortex shedding at moderate winds.

Figure 2. Photos of the chimney and the wind mast

The total mass of the chimney is 11276 kg including all additional masses necessary for mounting, maintenance and human access. The equivalent mass m_e per unit of height is computed using the first mode shape $\psi(z)$ which is obtained via a structural analysis (Simiu & Scanlan 1978; Eurocode 2005):

$$m_e = \frac{\int_0^h \psi(z)^2 m(z) dz}{\int_0^h \psi(z)^2 dz} \qquad \#(1)$$

A value of $m_e = 322.6$ kg/m was obtained.

The Scruton number reads:

$$Sc = \frac{4\pi\eta\, m_e}{\rho d^2} \qquad \#(2)$$

The reduced structural damping referred to critical damping η was measured in situ in two normal directions via the records of the chimney motion after a manual release. It was found that $\eta = 0.185 \pm 0.005$ %. Using the air density $\rho = 1.225$ kg/m^3 and the upper diameter $d = 2$ m of the chimney, the Scruton number is $Sc = 1.53$.

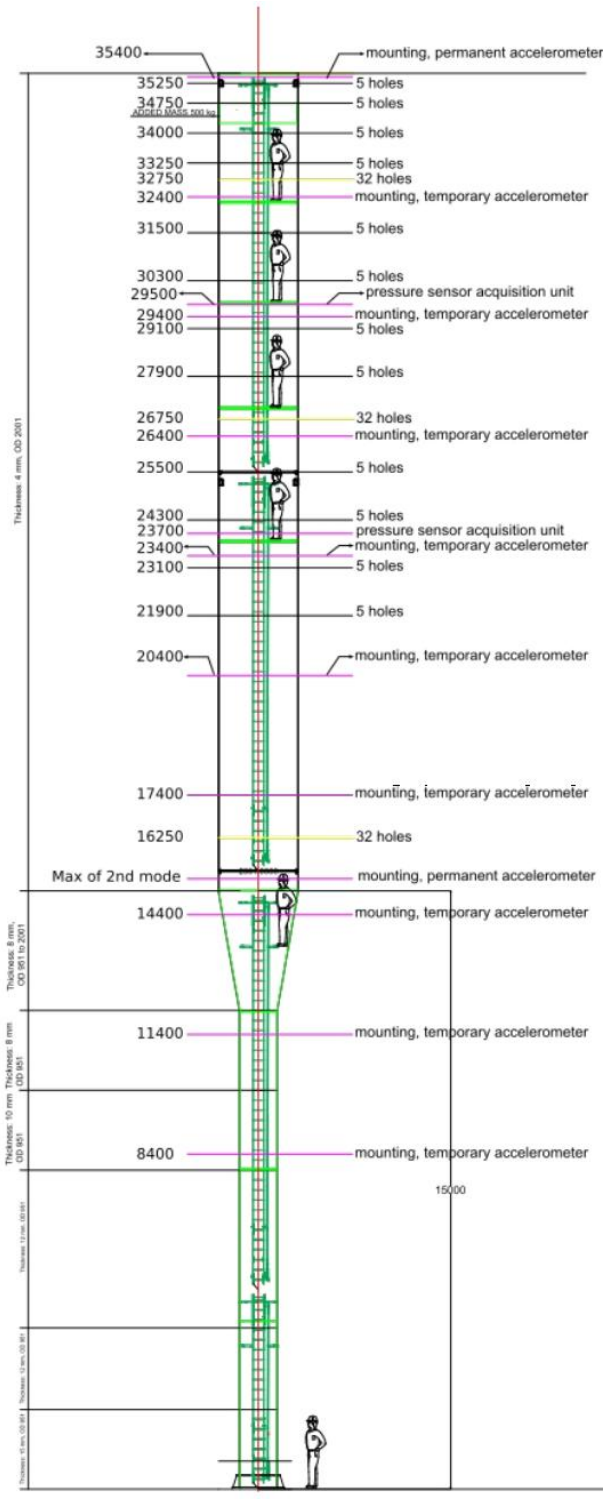

Figure 3. Detailed design of the chimney

The first bending frequency was measured in the same way as the reduced damping. It was found that $f = 0.868 \pm 0.001$ Hz.

The Strouhal number reads:

$$St = \frac{f\ d}{\overline{U}} \qquad \#(3)$$

It is supposed to be 0.18 in (Eurocode 2005) but potentially 0.21 (Ellingsen et al. 2022). Therefore the lock-in mean velocity is expected to be in the range $\overline{U}_c = 8.3 - 9.6$ m/s, a relatively moderate wind frequently observed on the site.

Associated to the low Scruton number mentioned above, high oscillation amplitudes at lock-in are expected.

2.2. Wind mast

A mast of 40 meters high is erected at the distance 55 meters from the chimney in the west direction. It is equipped with 4 anemometers at 10 (cup) , 18 (propeller), 25 (3D sonic) and 35 (propeller) meters of height. Three wind vanes complement the cup and the propeller anemometers. All these sensors are shifted from the mast axis by 1.5 m in order to limit the interactions.

Figure 4. Photo of the wind mast

The cup anemometer at 10 m has an accuracy of ±0.1 m/s, while the propellers at 18 and 35 m have and accuracy of ±0.3 m/s. The vanes provide the wind direction with an accuracy of ±3°.

The 3D sonic anemometer has better characteristics, with an accuracy of ±0.05 m/s and ±2°. It continuously records the wind velocity components at the sampling frequency of 5 Hz.

The 3 others anemometers record only statistical values (mean, RMS, maxima) of the velocity modulus and its direction in degree, referred to magnetic North, over sequences of 10 minutes.

2.3. Chimney measurement systems

Four single component accelerometers are mounted for the chimney motion measurement (type PCB 3741). They can measure in the frequency range [0-70 Hz] up to ±2 g with an accuracy better than ±0.04 g. Accelerometers #1 and #2 are fixed at 20.4 meters of height and #3 and #4 at the top, ie 35.5 meters. The directions of measurements are 45° (North-East) for accelerometers #1 and #3, and 315° (North-West) for #2 and #4. The record is continuous with a sampling frequency of 16 Hz.

Synchronized wall pressure measurements are performed by using 32-channel pressure scanners (32HD ESP pressure scanners from Pressure Systems Inc.) with multiplex frequency of 70 kHz. The global accuracy is about ±1 Pa, but difficulties in setting the zero value (the no wind response of the sensor) lead to much higher errors on the mean component. The records have a sampling frequency of 20 Hz and stored in sequences of 10 minutes long. A number of taps have been mounted (see Figure 3) but the most interesting ones are the 32 taps around the chimney at 26.75 meters of height. They are uniformly distributed around the circumference and spaced by 11.25° of the azimuth angle.

3. WIND CHARACTERISTICS

Due to the instrumentation complexity and the necessity of having a proper weather, notably without rain, observation and measurements of the wall pressures occurred during two days, July 19-20 2021. Some interesting events have occurred during these two days with a mean speed around 8-10 m/s and a wind coming from North-East, typically 50-70° referred to magnetic North.

Finally, four sequences have been selected for detailed processing and investigation. The two first from July the 19th are without motion of the chimney, while the two others from July the 20th are recorded during chimney oscillations. These four atmospheric boundary layers (ABL) are shown in Figure 5 where the mean velocity and the turbu-

lence intensity are presented versus altitude. They are compared with the Eurocode profiles for the roughness type II which is supposed to apply to the present site.

In such case, the mean velocity is given by

$$\bar{U}(z) = 0.19\,\bar{U}(10)\,ln\left(\frac{z}{z_0}\right) \qquad \#(4)$$

and the turbulence intensity by

$$I(z) = 1/\,ln\left(\frac{z}{z_0}\right) \qquad \#(5)$$

where the roughness height z_0 is 0.05 m (Eurocode 2005). One should note here that the mean speed at 10 m high is the reference speed for the type II roughness, so that every velocity profile should go through that point.

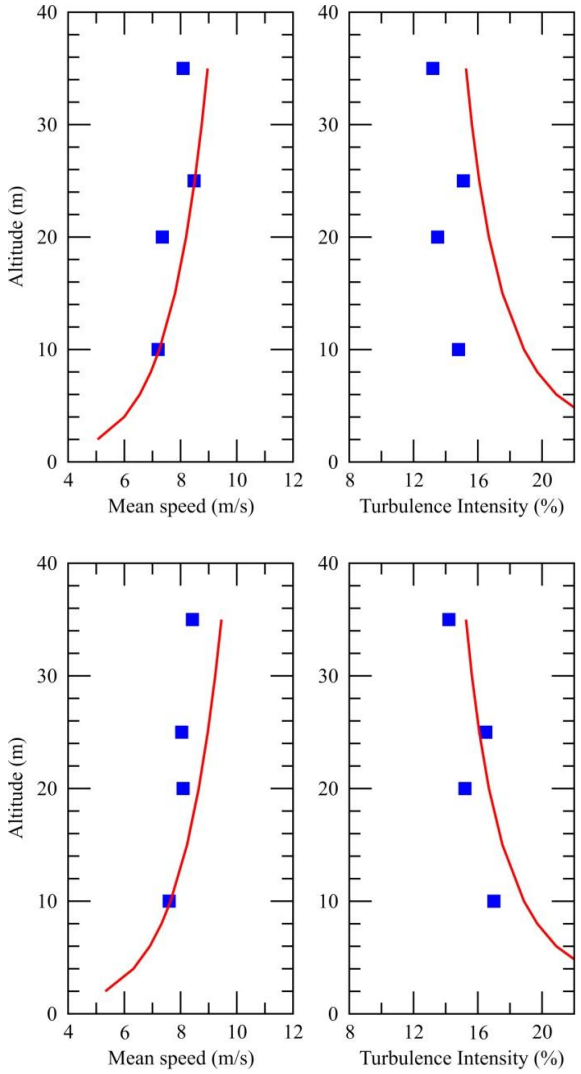

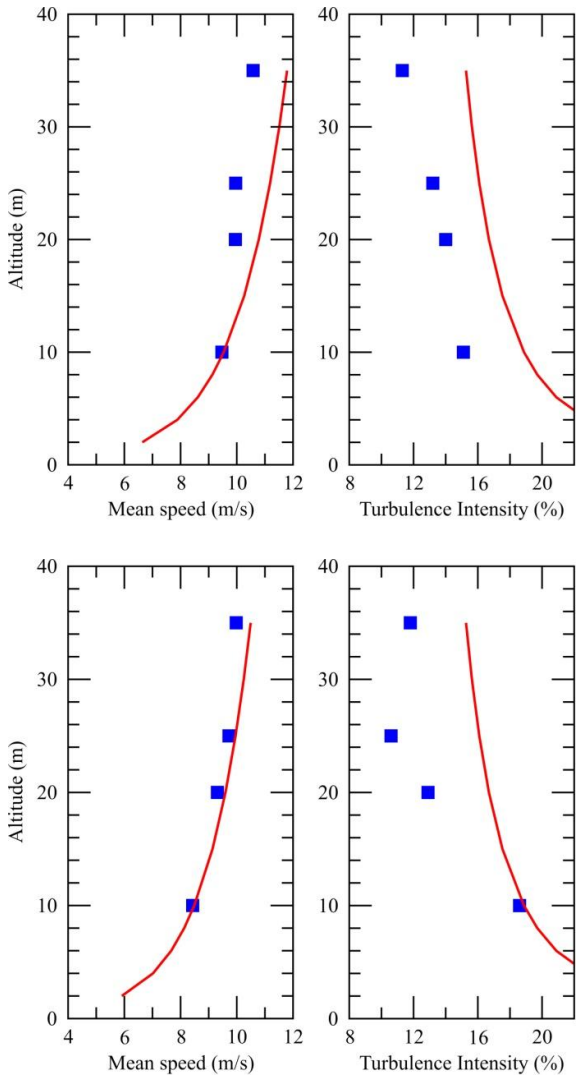

Figure 5. Measured ABL (blue square) compared with Eurocode type II ABL (red line, following Eq. 5 & 6) for four sequences; top to bottom: July 19th, 4:00 PM & 4:10 PM, and July 20th, 12:40 PM & 12:50 PM

By looking at Figure 5, it appears that, while the mean velocity gradient follows more or less well the Eurocode profile, the measured turbulence intensity is lower than the one furnished by Eurocode, excepted in one case, July 19th at 4:10 PM. Especially the last sequence presents a very low measured turbulence (10.5 % at 25 m), far from the value which is expected by the standards (16 %). Up to now, no explanation has been found to explain that behavior.

Note that the sonic anemometer located at the altitude of 25 m is supposed to be more accurate for the turbulence measurement, by comparison with the other cup or propeller anemometers that have an inertial effect.

The power spectral density (PSD) of the longitudinal velocity is computed thanks to the time records furnished by the sonic anemometer. It can be compared to the Von Karman spectrum $S_u(f)$ which reads (Simiu & Scanlan, 1978):

$$\frac{S_u(f)}{\sigma_u^2} = \frac{4\,L_u}{\overline{U}\left(1+70.7\left(\frac{f\,L_u}{\overline{U}}\right)^2\right)^{5/6}} \qquad \#(6)$$

where σ_u is the standard deviation of the velocity, f the frequency and L_u the integral scale of turbulence of the longitudinal component. The latter is determined by finding the best fit of the Von Karman model $\#(6)$ with the measured PSD, as shown in Figures 6 & 7 where $S_u(f)$ is normalized with σ_u^2 as in Eq. (6).

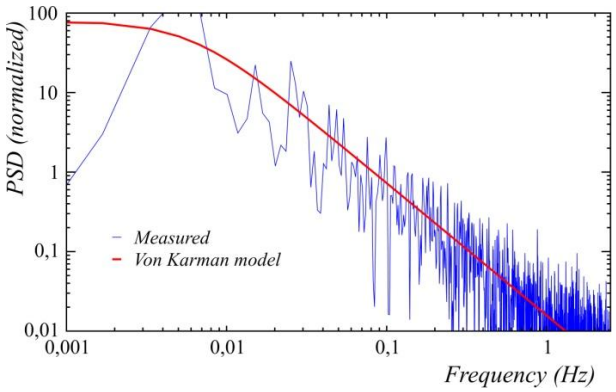

Figure 6. PSD of longitudinal velocity at 25 m, $\overline{U} = 8.49\ m/s$, $\sigma_u = 1.28\ m/s$, $L_u = 168\ m$ Direction 67°MN, July 19th, 4:00 PM.

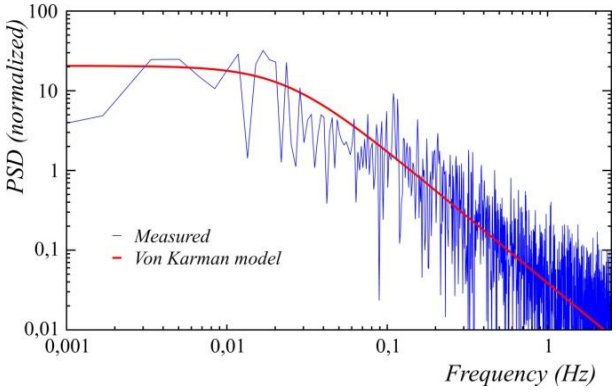

Figure 7. PSD of longitudinal velocity at 25 m $\overline{U} = 9.72\ m/s$, $\sigma_u = 1.03\ m/s$, $L_u = 50\ m$ Direction 73°MN, July 20th, 12:50 PM.

It turns out that although the two sequences correspond to the same wind direction with some comparable mean speed, their turbulence characteristics are found quite different. Especially the turbulence intensity is 15.1% versus 10.6% while the longitudinal turbulence scale is 168 m versus 50 m, leading to different PSD shapes.

4. PRESSURE DISTRIBUTION

4.1. Results with the motionless chimney

The wall pressures measured on the chimney at 26.75 m are presented. This altitude is at a distance 8.75 m (4.3 D) below the top and 11.75 m (5.9 D) upper the beginning of the diameter restriction. Therefore, one expects pressure distributions that should be close to those obtained with a 2D cylinder in a wind tunnel for high Reynolds flow regimes (Ellingsen et al. 2022c).

The time averaged pressure coefficients and the corresponding standard deviation are shown in Figure 8 for the first sequence.

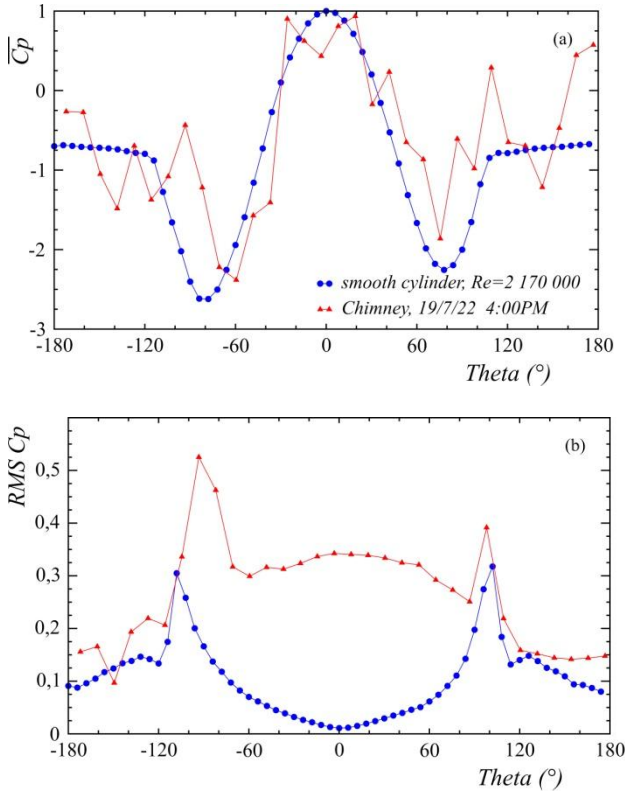

Figure 8. Time averaged (a) & standard deviation (b) of wall pressure coefficients distribution around the chimney at 26.75 m, July 19th 4:00 PM.

The pressure coefficient is defined as

$$Cp(\theta,t) = \frac{P(\theta,t)-P_{ref}}{\frac{1}{2}\rho\overline{U}^2} \qquad \#(7)$$

where $P(\theta,t)$ is the instantaneous measured pressure at the azimuth angle θ. The reference pressure

P_{ref} is the mean static pressure inside the chimney and ρ is the air density corrected by atmospheric pressure and air temperature.

The azimuth angle θ=0° is referred to the wind direction as in a wind tunnel test section, so the present data in natural wind have been rotated in order to reach a "symmetrical" result which is of course imperfect due to the natural scatter of these observations. Note also that the spacing between taps is larger in the field experiments (11.25 °) than in the wind tunnel tests (6°).

Despite all, the results are satisfactory because the main characteristics of the pressure distribution can be detected, particularly the location and the value of the Cp_{min}. By comparison with wind tunnel data in smooth flow (Ellingsen et al. 2022c), it shows that the flow regime is clearly supercritical despite the disturbance generated by the atmospheric turbulence and shear.

Concerning the standard deviations, the two peaks around 100-110° observed in wind tunnel are also present in the field experiments. The high level of fluctuations in front of the chimney is due to the upstream turbulence which was, in contrast, very low in the wind tunnel.

4.2. Results with the oscillating chimney

In the sequence of July 20th at 12:45PM the chimney encountered oscillations which were visible to the naked eye. The motion was measured with the top accelerometers, leading to a standard deviation $\sigma_a = 2.09$ m/s^2 and a peak to peak value of ±3.62 m/s^2. The PSD shown in Figure 9 present clearly a peak of the oscillation frequency at 0.848 Hz, slightly lower than the first natural frequency measured during the manual excitation (0.868 Hz, see section 2.1).

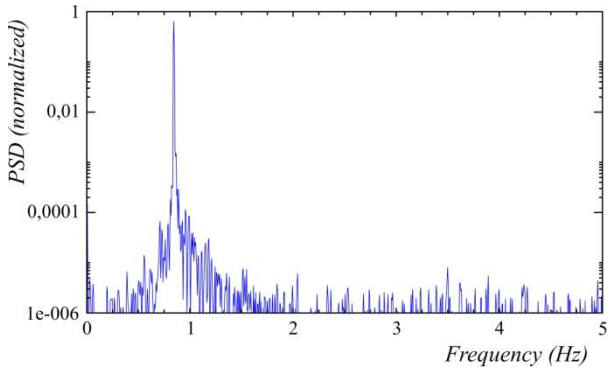

Figure 9. PSD of acceleration at the top, motion direction 43°MN $\sigma_a = 2.09\ m/s^2$ July 20th 12:45 PM

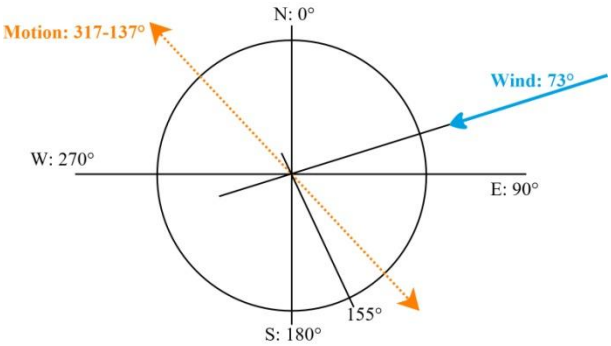

Figure 10. View in Magnetic North coordinate of the data from July 20th 12:45 PM.

From these data, the motion amplitude is estimated to be ± 0.128 m, which makes a peak to peak non dimensional amplitude of 0.128 D at the top. The direction of the motion, almost on a single axis, was measured and shown in the Figure 10. It appears that, in contrast to what could have been expected, the oscillations are not exactly normal to the mean wind direction, with an angle of 64° instead of the expected 90°. It might be the consequence of a memory effect of the flow or/and an inertial effect of the oscillating chimney from the past minutes prior the current observation.

The wall pressure distribution is presented in Figure 11. While it looks noisier, both mean values and fluctuating values are similar to the distribution observed the day before on the motionless chimney. It seems that the motion, which is after all not so large here, has no visible effect.

But more analysis and signal processing, such as bi-orthogonal decomposition (Hémon & Santi 2003), will be carried out in the near future.

Pressure taps along a vertical axis of the chimney are also available. Their angular position is 155° referred to magnetic North (see Figure 10) which is almost on the lateral right side relative to the wind direction. The correlation coefficient along this axis is shown Figure 12 for the two sequences of July the 19th on a motionless chimney and the 20th during oscillations. The reference location is taken at the top of the chimney. When the chimney is motionless, the correlation is surprisingly quite high, being still 0.24 at the distance 8.50 m (4.25 D). On the contrary, when the chimney oscillates, the correlation decreases more rapidly, down to 0.065 for the same distance.

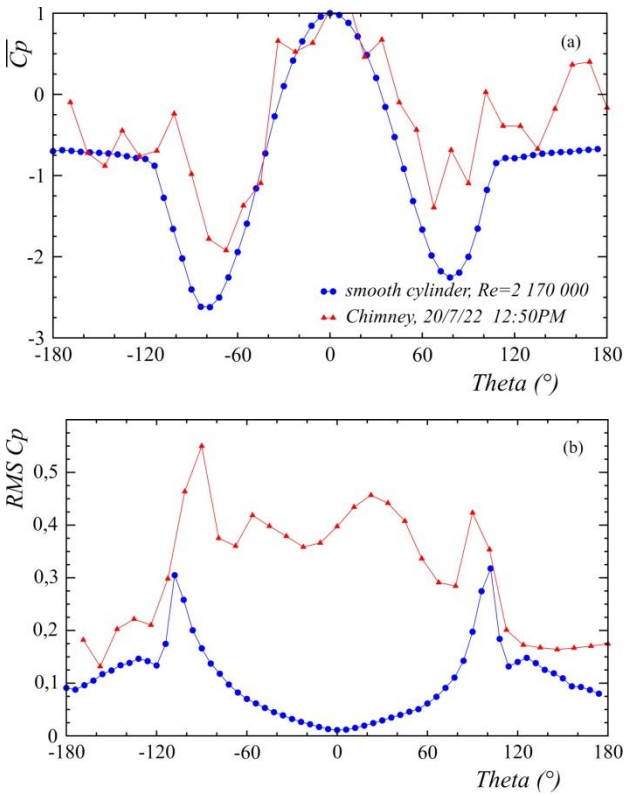

Figure 11. Time averaged (a) & standard deviation (b) of wall pressure coefficients distribution around the chimney at 26.75 m, July 20th 12:50 PM.

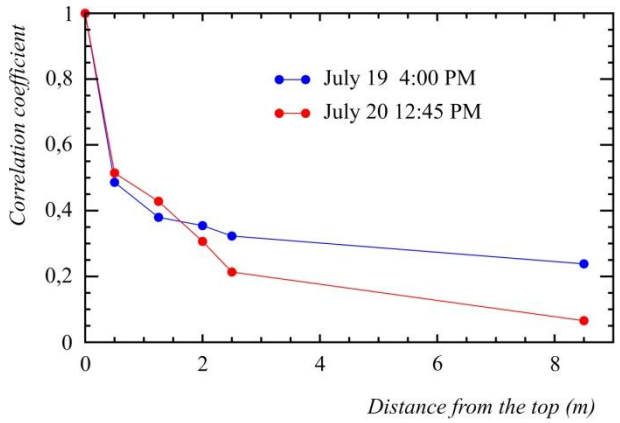

Figure 12. Correlation coefficient from the top (35.25 m) for pressure taps along the vertical axis at 155°MN, static chimney (July 19th) and oscillating (July 20th).

5. CONCLUSION

Unsteady wall pressure measurements have been performed on a full scale prototype chimney in natural wind. This experiment combines the two features that cannot be reproduced simultaneously in wind tunnel: a high Reynolds number and a turbulent boundary layer. Preliminary results have been presented, showing notably that the pressure distribution looks like the one measured in wind tunnel in supercritical conditions, with an additional turbulent noisy component.

More investigation are planned in the near future, especially signal processing using bi-orthogonal decomposition and Fourier analysis in order to better highlight the alternate vortex shedding in natural conditions.

6. ACKNOWLEDGEMENTS

This work is part of a partnership co-funded by Beirens (Poujoulat Group), Centre Scientifique et Technique du Bâtiment (CSTB), Centre National d'Etudes Spatiales (CNES) and LadHyX, CNRS-Ecole polytechnique.

Special acknowledgement is extended to Aurélien Jeanneton from Beirens for designing and constructing the chimney and to Olivier Flamand from CSTB for the measurement system operation.

7. REFERENCES

Barré, C. and Barnaud, G. 1995. High Reynolds number simulation techniques and their application to shaped structures model test. *J. Wind Eng. & Indus. Aerod.*, **57**, 145-157.

Basu RI, Vickery BJ. 1983 Across-wind vibrations of structure of circular cross-section. Part II. Development of a mathematical model for full-scale application. *J Wind Eng Ind Aerod.*;**12**(1), 75–97.

Christensen O, Askegaard V. 1978. Wind forces on and excitation of a 130-m concrete chimney. *J Wind Eng Ind Aerod.*, **3**(1), 61–77.

Ellingsen, Ø. M., Amandolese, X., Hémon, P., 2022a. In wind tunnel the reproduction of vortex shedding behind circular cylinder at high Reynolds number is incomplete. *Flow Induced Vibration*, FIV2022, Paris-Saclay, 5-8 July.

Ellingsen, Ø. M., Flamand, O., Amandolese, X., Coiffet, F., Hémon, P., 2022b. Field tests on a full-scale steel chimney subjected to vortex-induced vibrations. *Struct. Eng. Inter.*, **32**(1), 55-61.

Ellingsen, Ø. M., Amandolese, X., Flamand, O., Hémon, P., 2022c. Twin Strouhal numbers in pressure loading of circular cylinder at high Reynolds numbers. Submitted to *J. Fluids & Struct*.

European Committee for Standardization, 2005. Eurocode 1: Actions on structures - Part 1-4: General actions - Wind actions. Ref. n° EN 1991-1-4:2005 F.

Galemann T, Ruscheweyh H. 1992. Measurements of wind induced vibrations of a full-scale steel chimney. *J Wind Eng Ind Aerod.* ,**41**(1–3), 241–52.

Hémon, P., Santi, F., 2003. Applications of biorthogonal decompositions in fluid-structure interactions. *J. Fluids & Struct.*, **17.8**, 1123–1143.

Ruscheweyh H, Galemann T. 1996. Full-scale measurements of wind-induced oscillations of chimneys. *J Wind Eng Ind Aerod.*, **65**(1–3), 55–62.

Sageau, J.-F., 1978. Etude in situ du champ de pression stationnaire et instationnaire autour d'une cheminée de 240 m. *J. Wind Eng. & Indus. Aerod.*, **2**, 361–383.

Simiu, E., Scanlan, R., H., 1978. Wind effects on structures. An introduction to wind engineering. Wiley & Sons, New York.

Vickery BJ, Basu RI. 1983 Across-wind vibrations of structures of circular cross-section. Part I. Development of a mathematical model for two-dimensional conditions. J *Wind Eng Ind Aerod.* **12**(1), 49–73.

VORTEX-INDUCED VIBRATION OF A CIRCULAR CYLINDER SUBJECTED TO LOW-KEULEGAN-CARPENTER-NUMBER OSCILLATORY FLOW

Dániel Dorogi
University of Miskolc, Miskolc, Hungary

ABSTRACT

In this study vortex-induced vibration of a circular cylinder subjected to a uniform oscillatory stream is investigated. The cylinder is allowed to vibrate only transverse to the main flow. The non-dimensional governing equations of the fluid and cylinder motion are solved in a non-inertial reference frame using an in-house CFD code based on the finite difference method. The Keulegan-Carpenter number and the Reynolds number are fixed at the values of 5 and 100, respectively. Systematic simulations are carried out in the reduced velocity range of 1–12 at fixed mass and structural damping ratio values of 2 and 0, respectively. Two separate lock-in (LI) domains are identified. In the primary LI range the peak oscillation amplitude exceeds one cylinder diameter, and the vibration frequency locks to the flow oscillation frequency. However, in the secondary LI domain the peak amplitude is less than the half of the cylinder diameter and the vibration frequency synchronises with twice the flow oscillation frequency. Using the extended form of the Morison's equation available in the literature it was found that the linear drag component dominates the quadratic drag. This effect is more pronounced close to peak amplitude points.

1. INTRODUCTION

A circular cylinder exposed to waves is among others relevant to offshore oil and gas engineering applications. Fundamentally, waves are modelled using a uniform oscillatory stream which velocity can be written as $\widetilde{U} = U_m \sin(2\pi f_o t)$, where U_m and f_o are the magnitude and frequency of the flow, respectively and t is the time. Two non-dimensional parameters are used to govern this problem: the Keulegan-Carpenter number $K_C = U_m/(f_o D)$ and the Reynolds number $Re = U_m D/\nu$, where D is the cylinder diameter and ν is the kinematic viscosity of the fluid. Fluid flow around a stationary circular cylinder placed into an oscillatory flow has been extensively investigated (Honji, 1981; Bearman *et al.*, 1985; Sarpkaya, 2002). Tatsuno and Bearman (1990) and Dütsch *et al.* (1998) showed that the Keulegan-Carpenter number strongly influences the flow structure. At very low K_C values no vortex shedding occurs. However, increasing K_C leads to vortex formation in the cylinder wake, which can cause the vibration of the structure, i.e. vortex-induced vibrations (VIV). Although in general, VIV can occur both streamwise with and transverse to the main oscillatory stream, one-degree-of-freedom VIV (mostly transverse-only VIV) is often considered.

Sumer and Fredsøe (1988) carried out systematic laboratory measurements in the Keulegan-Carpenter number range of $5 \leq K_C \leq 100$ at high Reynolds numbers, i.e. between $Re = 2 \cdot 10^4$ and 10^5 to investigate the transverse-only VIV characteristics. For $K_C = 10$ Sumer and Fredsøe (1988) found that the vibration frequency of the cylinder f locks to twice the flow oscillation frequency ($f = 2f_o$) in all the investigated cases. As well as, the oscillation amplitude shows a single peak close to the point corresponding to $f \approx f_{n,a}$, where $f_{n,a}$ is the cylinder's natural frequency in a still fluid. Zhao *et al.* (2012) carried out two-dimensional CFD computations for $K_C = 10$ and 20 considering also transverse-only VIV. Similarly to the experimental findings of Sumer and Fredsøe (1988), Zhao *et al.* (2012) observed a single-peak response, and the vibration frequency locked mostly to $2f_o$. By increasing K_C between 20 and 40, Sumer and Fredsøe (1988) identified multiple lock-in domains within which the frequency of cylinder vibration synchronises with Nf_o, where N is a whole number typically between 2 and 7 (depending on K_C). The amplitude response which Sumer and Fredsøe (1988) identified was a *multi-peak response*; thus, within each lock-in domain the oscillation amplitude increases approximately up to the point where $f = f_{n,a}$, then it shows to decrease. McConnell and Jiao (1986) identified a similar feature (i.e. multi-peak response) for $K_C = 25$. Finally, Sumer and Fredsøe (1988) showed that the cylinder response follows completely different trends at high Keulegan-Carpenter numbers. In such cases (for $K_C = 100$) the response is very similar to that obtained earlier for uniform free stream (Khalak and Williamson, 1999), i.e. f does not lock to the whole number multiples of f_o and the multi-peak amplitude response is replaced by a single-peak response. The aforementioned studies focus mainly on

carrying out analyses in the high-Reynolds-number domain, i.e. for $Re = \mathcal{O}(10^4 - 10^5)$. To the best knowledge of the author VIV of a circular cylinder placed into a low-*Re* oscillatory flow (i.e. $Re = \mathcal{O}(10^2)$) has not yet been investigated.

Modelling the streamwise fluid force is another challenging area of research. For this purpose the Morison's equation is used most often, which divides the total streamwise fluid force into drag and inertia components (Morison *et al.*, 1950). Stokes (1851) and Wang (1968) assuming that the cylinder is at rest, the flow is laminar and no separation occurs developed an analytical solution for the streamwise fluid force. This solution is always referred to as the Stokes-Wang (SW) solution. Recently, Ren *et al.* (2021) showed that the results from their direct numerical simulations agree very well with the SW solution in a much wider parameter space than the constraints specified by Stokes (1851) and Wang (1968). In addition, Ren *et al.* (2021) found that the original Morison's equation is fundamentally incorrect at low K_C values, because the drag linearly varies with the time-dependent stream velocity. Originating from this finding Ren *et al.* (2021) extended the Morison's equation by introducing a linear drag term in addition to the quadratic drag and the inertia force. Ren *et al.* (2021) extensively tested the new approach for a stationary cylinder. However, the model has not yet been applied for a cylinder undergoing VIV.

The primary objective of this paper is to investigate transverse-only vortex-induced vibration characteristics of a circular cylinder placed into a low-*Re* and low-K_C oscillatory flow. For this aim systematic two-dimensional CFD simulations are carried out at the fixed Reynolds number and Keulegan-Carpenter number values of $Re = 100$ and $K_C = 5$, respectively. The reduced velocity is varied between $U_r = 1$ and 12, while the mass and structural damping ratio are kept constant at the values of $\mu = 2$ and $\zeta = 0$, respectively. In addition to the analysis of the cylinder response, the streamwise fluid force is modelled using the extended form of the Morison's equation proposed by Ren *et al.* (2021).

2. COMPUTATIONAL METHODOLOGY

In this study transverse-only vortex-induced vibration of a circular cylinder placed into an oscillatory flow is investigated by means of two-dimensional (2D) CFD simulations. Newton's second law of cylinder motion is solved to determine the non-dimensional cylinder displacement y_c, velocity $\dot{y}_c$ and acceleration $\ddot{y}_c$. Note that in this study the cylinder diameter D and the magnitude of the stream velocity U_m is used as length and velocity scales, respectively. The equation of cylinder motion in non-dimensional form can be written as follows:

$$\ddot{y}_c + \frac{4\pi\zeta}{U_r}\dot{y}_c + \left(\frac{2\pi}{U_r}\right)^2 y_c = \frac{2}{\pi\mu}F_y^*(t). \qquad (1)$$

In this equation overdot refers to differentiation with respect to the non-dimensional time t, ζ is the structural damping ratio, $U_r = U_m/(f_n D)$ is the reduced velocity, where f_n is the natural frequency of the cylinder in vacuum, μ is the mass ratio and $F_y^*(t)$ is the unsteady sectional fluid force acting on the cylinder in the transverse direction.

In parallel, the equations of fluid motion are solved which results are used to determine $F_y^*(t)$ that arises in Eq. (1). The governing equations of the 2D flow of an incompressible Newtonian constant property fluid are the two components of the Navier-Stokes equations written in a non-inertial frame of reference attached to the vibrating cylinder, the continuity equation and the pressure Poisson equation. These equations in non-dimensional forms can be written as follows:

$$\frac{\partial u}{\partial t} + u\frac{\partial u}{\partial x} + v\frac{\partial u}{\partial y} = -\frac{\partial p}{\partial x} + \frac{1}{Re}\nabla^2 u + \dot{U}, \qquad (2)$$

$$\frac{\partial v}{\partial t} + u\frac{\partial v}{\partial x} + v\frac{\partial v}{\partial y} = -\frac{\partial p}{\partial y} + \frac{1}{Re}\nabla^2 v - \ddot{y}_c, \qquad (3)$$

$$\mathscr{D} = \frac{\partial u}{\partial x} + \frac{\partial v}{\partial y} = 0, \qquad (4)$$

$$\nabla^2 p = 2\left(\frac{\partial u}{\partial x}\frac{\partial v}{\partial y} - \frac{\partial u}{\partial y}\frac{\partial v}{\partial x}\right) - \frac{\partial \mathscr{D}}{\partial t}, \qquad (5)$$

where u and v are the non-dimensional velocity components in the streamwise x and transverse y Cartesian directions, respectively, p is the non-dimensional pressure, $\mathscr{D}$ is the dilation and $Re = U_m D/\nu$ is the Reynolds number, where ν is the kinematic viscosity of the fluid. In Eq. (2) $U = \sin(2\pi t/K_C)$ is the non-dimensional velocity of the oscillatory stream, where $K_C = U_m/(f_o D)$ is the Keulegan-Carpenter number defined using the flow oscillation frequency f_o.

The physical domain of the computations is considered to be an area confined between two concentric circles: the inner circle represents the cylinder surface, while the outer circle is the outer surface, where the flow is assumed to be undisturbed. On both surfaces Dirichlet-type boundary conditions are satisfied for u and v, and Neumann-type boundary conditions are used for p.

Using linear mapping functions the physical domain as well as the governing equations and the boundary conditions are transformed to the computational domain on which an equidistant grid is created

(Baranyi, 2008). The mapped governing equations together with the transformed boundary conditions are solved using an in-housed CFD approach based on the finite difference method (Baranyi, 2008). For spatial discretisation fourth-order accurate central difference schemes are used except for the convective terms which are approximated using a third-order modified upwind difference scheme. The two components of the Navier-Stokes equations are integrated in time using the explicit Euler method, while the fourth-order explicit Runge-Kutta scheme is used for the temporal discretisation of the equation of cylinder motion. The linear system obtained by discretising the pressure Poisson equation is solved using the successive over-relaxation method, while the continuity equation is satisfied in each time step.

The computational grid is characterised by the number of grid points in the peripheral and radial directions ξ_{max} and η_{max}, respectively and the ratio of the non-dimensional cylinder radius and the dimensionless radius of the outer surface R_2/R_1. In addition, the dimensionless time step Δt also has to be considered. Based on the independence studies presented in our recent journal articles (Dorogi and Baranyi, 2020; Konstantinidis *et al.*, 2021) these values are fixed at $\xi_{max} = 360$, $\eta_{max} = 314$, $R_2/R_1 = 240$ and $\Delta t = 0.0005$. The currently applied CFD code has been extensively validated against data in the literature for stationary cylinder, forced cylinder oscillation and vortex-induced vibration cases (Baranyi, 2008; Dorogi and Baranyi, 2020; Konstantinidis *et al.*, 2021).

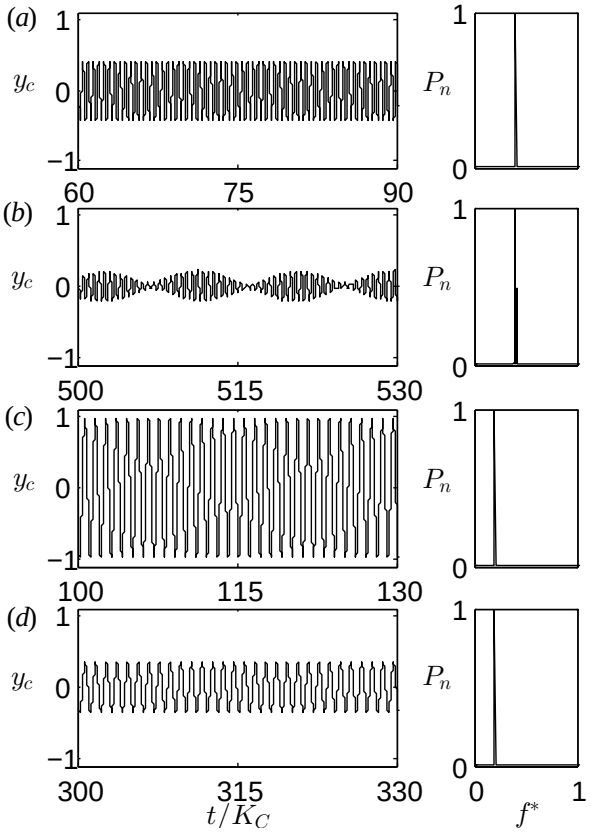

Figure 1. Time histories of the non-dimensional cylinder displacement y_c (plots on the left) and the FFT spectra of y_c normalised by the highest power-spectral density (right) for $U_r = 2$ (a), 2.1 (b), 5 (c) and 9 (d)

3. RESULTS AND DISCUSSION

In this study systematic 2D CFD simulations are carried out in order to analyse transverse-only vortex-induced vibration of a circular cylinder placed into a uniform low-*Re* and low-K_C oscillatory stream. The Reynolds number, the Keulegan-Carpenter number and the mass and structural damping ratios are fixed at the values of $Re = 100$, $K_C = 5$, $\mu = 2$ and $\zeta = 0$, respectively, while the reduced velocity is changed between $U_r = 1$ and 12.

Figure 1 shows the time histories of the non-dimensional cylinder displacement y_c within 30 flow oscillation cycles (plots on the left), and the normalised frequency spectra of the displacement signals P_n at different reduced velocity values. Note that P_n is obtained by dividing the power-spectral density P received using Fast Fourier Transform by the maximum value of P. It can be seen in Fig. 1*a*, 1*c* and 1*d* that the cylinder vibration is mostly sinusoidal; i.e. the amplitude of the signal is constant in time, and the FFT spectra of y_c contain one monoharmonic frequency component. In such cases 100 flow oscillation cycles are used to calculate the statistical quantities of the signals (i.e. the root-mean-square values and frequencies). However, as shown in Fig. 1*b*, in the thin reduced velocity domain of $2.08 \leq U_r \leq 2.2$ the oscillation amplitude displays strong fluctuations. Therefore, the statistics in this range are calculated by processing 500 flow cycles. Due to the sinusoidal nature of signals (except for the range of $2.08 \leq U_r \leq 2.2$), the non-dimensional oscillation amplitude A^* is obtained by multiplying the rms of y_c by $\sqrt{2}$.

Figure 2*a* and 2*b* shows the non-dimensional oscillation amplitude A^* and frequency f^* against the reduced velocity, respectively. Note that the non-dimensional vibration frequency at an arbitrary U_r value corresponds to the highest-intensity frequency peak in the FFT spectrum of y_c. It can be seen in Fig. 2*a* that there are two distinct U_r ranges (i.e. lock-in/synchronisation domains) within the interval of $1 \leq U_r \leq 12$, where the oscillation amplitude rapidly increases, and after peaking A^* shows to decrease.

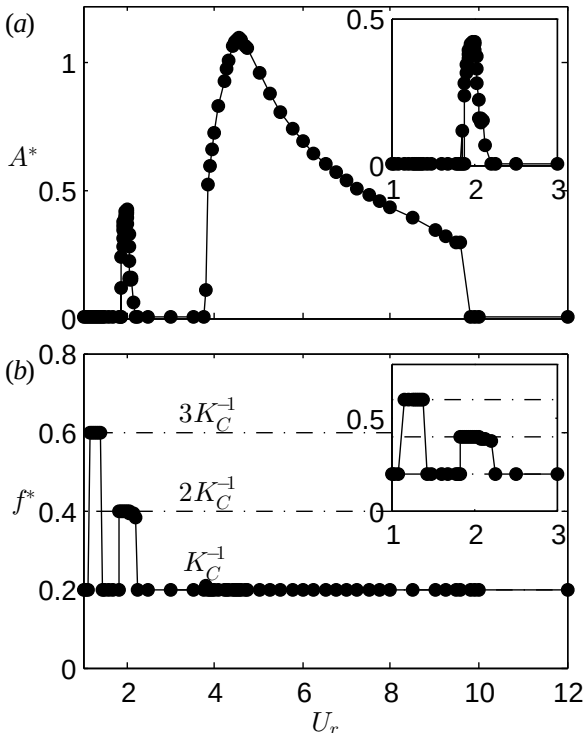

Figure 2. Non-dimensional amplitude (a) and frequency (b) of cylinder oscillation against the reduced velocity. The inset plots show the domain of $1 \leq U_r \leq 3$ *with higher resolution*

This amplitude response is very similar to that identified by Sumer and Fredsøe (1988) for $20 \leq K_C \leq 40$, which they denoted as *multi-peak response*. As can be seen in Fig. 2*a*, the range of $3.75 \leq U_r \leq 9.6$ is the most significant, because the peak oscillation amplitude occurs in this domain (i.e. $A^*_{max} = 1.092$ identified at $U_r = 4.55$) which value is more than 2.5 times the secondary amplitude peak identified in the range of $1.85 \leq U_r \leq 2.2$ (i.e. $A^*_{max} = 0.421$ at $U_r = 1.99$). The primary and secondary amplitude peaks, the corresponding frequency values and their locations are summarised in Table 1.

Branch	U_r	A^*_{max}	f^*
Primary	4.55	1.0920	0.2
Secondary	1.99	0.4212	0.4

Table 1. Summary of peak oscillation amplitudes and the corresponding reduced velocity and vibration frequency in the primary and secondary lock-in domains

Figure 2*b* suggests that different frequency characteristics belong to the U_r intervals prescribed earlier. In the range of $3.75 \leq U_r \leq 9.6$ the vibration frequency synchronises with the flow oscillation frequency, i.e. $f^* = K_C^{-1}$, while within $1.85 \leq U_r \leq 2.2$

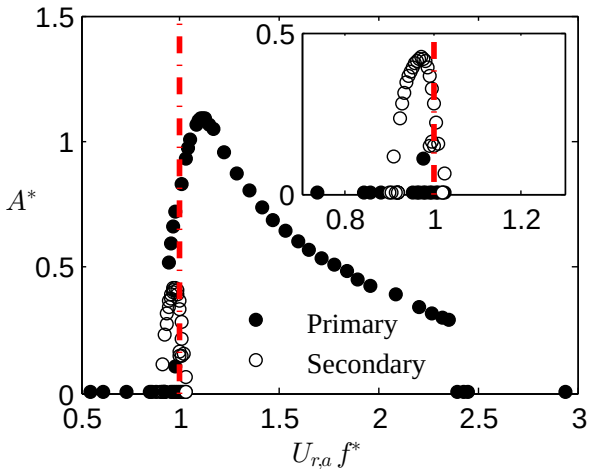

Figure 3. Non-dimensional amplitude of cylinder vibration against $U_{r,a}f^*$*. The red dotted vertical line represents the point corresponding to* $f = f_{n,a}$

the frequency of cylinder vibration locks to double the flow oscillation frequency, i.e. $f^* = 2K_C^{-1}$. In other words, two lock-in (LI) domains can be distinguished: (*i*) the primary LI domain, where $f^* = K_C^{-1}$ and (*ii*) the secondary LI range, where $f^* = 2K_C^{-1}$. Note that Fig. 2*b* displays another U_r interval ($1.15 \leq U_r \leq 1.4$), where $f^* = 3K_C^{-1}$. Although this could be referred to as the tertiary LI domain, the author thinks that introducing this terminology is not reasonable, because the oscillation amplitude is almost zero in $1.15 \leq U_r \leq 1.4$ (i.e. $A^* = \mathcal{O}(10^{-8})$). Sumer and Fredsøe (1988) also identified multiple lock-in domains, where the frequency of cylinder vibration locks to the whole number multiples of the flow oscillation frequency. Thus, the current simulation data for $Re = 100$ shows similar characteristics to those obtained using laboratory measurements at high Reynolds numbers (i.e. $Re = 2 \cdot 10^4 - 10^5$) (Sumer and Fredsøe, 1988).

Sumer and Fredsøe (1988) found also that the peak oscillation amplitudes in the distinct lock-in domains occur approximately at the point corresponding to $f = f_{n,a}$, where $f_{n,a}$ is the natural frequency of the cylinder in a still fluid. In order to explore this feature, we plotted the amplitude of cylinder oscillation against $U_{r,a}f^*$, where $U_{r,a}$ is the reduced velocity based on $f_{n,a}$ (see Fig. 3). It can be seen in Fig. 3 that similarly to the experimental findings of Sumer and Fredsøe (1988), the peak amplitudes in the primary and secondary LI domains occur close to the point corresponding to $U_{r,a}f^* = f/f_{n,a} = 1$.

Figure 4 shows the root-mean-square (rms) values of the transverse fluid force F^*_y against the reduced velocity. It can be seen in Fig. 4 that F^*_y displays dif-

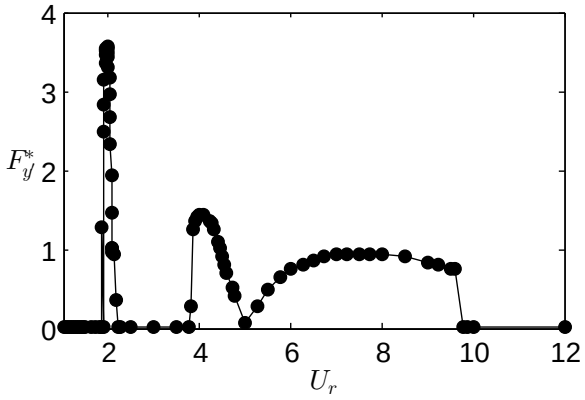

Figure 4. Root-mean-square values of the transverse fluid force against the reduced velocity

ferent tendencies in the two lock-in domains. By increasing U_r in the primary lock-in range (i.e. within $3.75 \leq U_r \leq 9.6$) $F^*_{y'}$ increases until $U_r = 4$. After peaking, $F^*_{y'}$ shows to decrease up to the reduced velocity value where the vibration frequency coincides with the natural frequency of the cylinder in vacuum, i.e. $f^* = U_r^{-1}$. Since $f^* = K_C^{-1}$ in the primary LI domain, the coincidence point can be characterised by $U_r = K_C\,(= 5)$. As shown in Fig. 4, $F^*_{y'}$ approaches zero at $U_r = 5$. Konstantinidis *et al.* (2021) investigated the streamwise-only VIV of a circular cylinder placed into a uniform free stream. They observed a similar phenomenon, i.e. the magnitude of the motion-driving force approaches zero at the point corresponding to $f^* = U_r^{-1}$. They explained this finding by the occurrence of a super-harmonic frequency component in the FFT spectra of the driving force. It can also be observed in Fig. 4 that between $U_r = 5$ and 7.5 $F^*_{y'}$ increases with the slope decreasing with U_r. Beyond $U_r = 7.5$ but still in the primary LI domain the rms of the transverse force slightly decreases.

In the secondary LI domain (within $1.85 \leq U_r \leq 2.2$) $F^*_{y'}$ shows the same tendency that observed in the oscillation amplitude (see Fig. 2). Thus, $F^*_{y'}$ monotonically increases between $U_r = 1.85$ and 1.99, and after peaking $F^*_{y'}$ decreases up to $U_r = 2.2$ (Fig. 4). As also seen in Fig. 4, the peak value observed in the rms of transverse fluid force in the secondary LI domain is roughly 2.5 times the corresponding value in the primary LI range. This finding is the opposite of that observed in A^*; the peak vibration amplitude in the primary LI domain is higher then the A^*_{max} in the secondary LI range (see Table 1).

Figure 5*a* shows the rms values of the streamwise fluid force $F^*_{x'}$ against U_r, as well as the Stokes-Wang solution (SW) $\left(F^*_{x'}\right)^{SW}$ corresponding to $K_C = 5$ for a

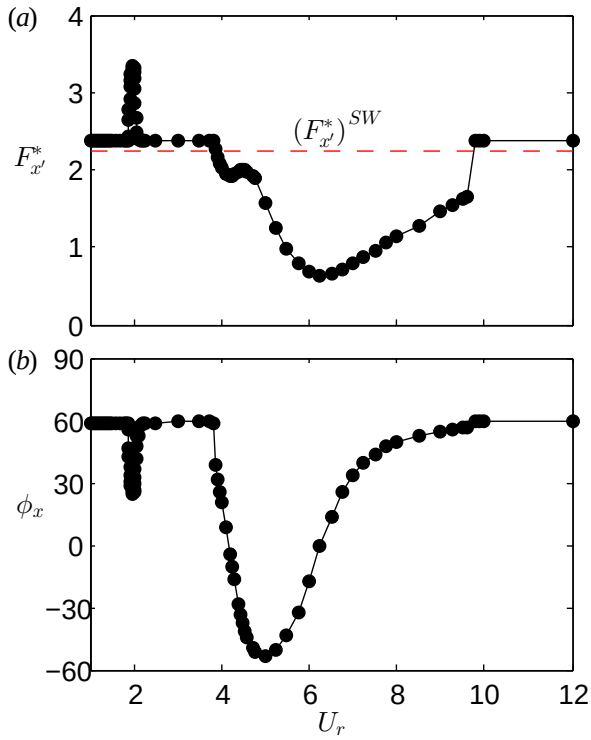

Figure 5. Root-mean-square values of the streamwise fluid force (a) and the phase angle (in degrees) between the streamwise force and the time-dependent stream velocity (b) against the reduced velocity. The red dashed horizontal line represents the Stokes-Wang solution for $K_C = 5$

stationary cylinder (see the red dashed horizontal line in the figure) (Stokes, 1851; Wang, 1968). It can be seen in Fig. 5*a* that for approximately zero oscillation amplitudes, i.e. in $U_r < 1.85$, $2.2 \leq U_r \leq 3.75$ and $U_r > 9.6$ the rms of the streamwise fluid force is close to the SW solution. The agreement is not exceptional, because separation occurs in all the investigated cases, which the SW solution does not consider. For non-zero oscillation amplitudes, i.e. in the primary and secondary LI domains $F^*_{x'}$ follows different tendencies (see Fig. 5*a*). In the secondary LI range $F^*_{x'}$ is always higher than the SW solution. As well as, the trends in $F^*_{x'}$ are the same as those observed in the oscillation amplitude (see Fig. 2*a*) and in the rms of transverse fluid force (Fig. 4): $F^*_{x'}$ increases between $U_r = 1.85$ and 1.99, and then it shows to decrease in the range of $1.99 \leq U_r \leq 2.2$.

However, the primary LI domain ($3.75 \leq U_r \leq 9.6$) is found to be more complex regarding the variation of $F^*_{x'}$ (see Fig. 5*a*). Initially, increasing the reduced velocity between $U_r = 3.75$ and 4.2 $F^*_{x'}$ decreases monotonically. After the local minimum point $F^*_{x'}$ increases up to $U_r = 4.55$ which coincides with the peak

oscillation amplitude point (see Table 1). Then, in the interval of $4.2 \leq U_r \leq 6.25$, $F_{x'}^*$ gradually decreases, and at $U_r = 6.25$ it reaches its minimum value. Beyond the minimum point but still in the primary LI domain $F_{x'}^*$ shows to increase.

In Fig. 5*b* the phase angle of the time-varying streamwise fluid force relative to the time-dependent stream velocity ϕ_x is plotted against the reduced velocity. It can be seen in Fig. 5*b* that for approximately zero oscillation amplitudes (outside the lock-in domains) $\phi_x \approx 60°$. However, when the amplitude of cylinder oscillation increases, the phase angle seems to decrease; thus, ϕ_x seems to behave reversely to A^* (see Figs. 2*a* and 5*b*). This finding is valid for the secondary LI domain. As shown in Fig. 5*b*, between $U_r = 1.85$ and 1.99 ϕ_x decreases, and in $1.99 \leq U_r \leq 2.2$ (beyond the local minimum and maximum points in ϕ_x and A^*, respectively) ϕ_x shows to increase. Although in the primary LI range the phase angle displays a similar variation trend as that observed in the oscillation amplitude (decreases then increases, see Fig. 2*a*), there is a 'shift' between A^* and ϕ_x. This means that the minimum point in ϕ_x ($U_r = 5$, see Fig. 5*b*) and the maximum point in A^* ($U_r = 4.55$, see Table 1) do not collapse. This finding suggests that there is a relationship between the streamwise fluid force and the vortex-induced cylinder motion, but to explore this, further analyses are required.

For modelling the streamwise fluid force the Morison's equation is used most often (Morison *et al.*, 1950). Ren *et al.* (2021) proposed the extended form of the Morison's equation, which in non-dimensional form (i.e. force per unit length normalised by $\frac{1}{2}\rho D U_m^2$, where ρ is the fluid density) can be written as follows:

$$F_x^*(t) = C_{d1} \sin\left(2\pi \frac{t}{K_C} + \frac{\pi}{4}\right) + C_{d2} U(t) |U(t)| + \frac{\pi}{2} C_m \dot{U}(t). \quad (6)$$

The first and second terms in the right-hand side (RHS) of Eq. (6) represent the viscous drag and form drag components, respectively; thus, C_{d1} and C_{d2} are the viscous drag and form drag coefficients, and C_m is the inertia coefficient. Note that by cancelling the linear drag term in Eq. (6) the original Morison's equation is obtained. The values of C_{d1}, C_{d2} and C_m are calculated by fitting Eq. (6) on the streamwise fluid force obtained from the CFD simulations. The accuracy of fitting is characterised by the root-mean-square value of the difference between the calculated and fitted signals $\Delta F_{x,rms}^*$. The lower the $\Delta F_{x,rms}^*$ the better the fit.

Figure 6 shows the time histories of the streamwise fluid force obtained from the CFD simulations (black solid lines), and the modelled $F_x^*(t)$ curves resulting from fitting the original Morison's equation (i.e. Eq. (6) without the linear drag term; blue dotted lines) and the extended Morison's equation (Eq. (6); red dotted lines) on the CFD data at different reduced velocity values. As well as, Table 2 contains the $\Delta F_{x,rms}^*$ values together with the belonging oscillation amplitudes. It can be seen in Fig. 6*a* that for approximately zero vibration amplitudes both the original and the extended Morison's equation model the streamwise fluid force very accurately. However, when A^* increases the extended Morison's equation still accurately models the streamwise fluid force, while the application of the original Morison's equation leads to a relatively poor fit (see Fig. 6*b* and 6*c*). Table 2 shows exactly the same feature: while for $U_r = 1.5$ $\Delta F_{x,rms}^*$ is very low for both formulations, for high oscillation amplitudes ($U_r = 2.0$ and 4.55) $\Delta F_{x,rms}^*$ resulting from fitting the original Morison's equation is much higher compared to the value obtained by fitting the extended Morison's equation. This finding indicates that the linear drag component in Eq. (6) in

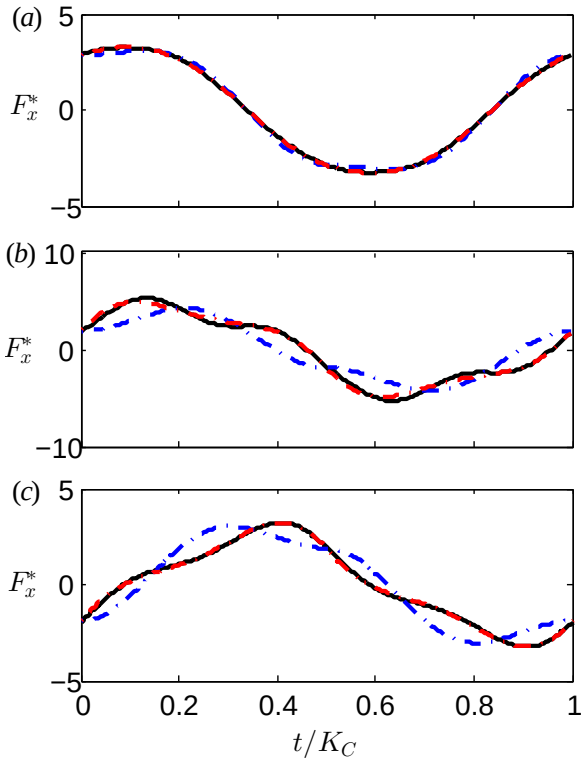

Figure 6. Comparison between the time histories of the computed and modelled phase-averaged streamwise fluid force for U_r= 1.50 (a), 2.00 (b) and 4.55 (c). Black solid line: computed; blue and red dotted lines: modelled using the original and the extended Morison's equation, respectively

U_r	A^*	$\Delta F^*_{x,rms}$	
		Extended	Original
1.50	≈ 0	0.0085	0.0555
2.00	0.4190	0.0580	0.2518
4.55	1.0920	0.0196	0.2307

Table 2. Curve-fitting errors obtained by using the original and extended forms of the Morison's equation to model the streamwise fluid force

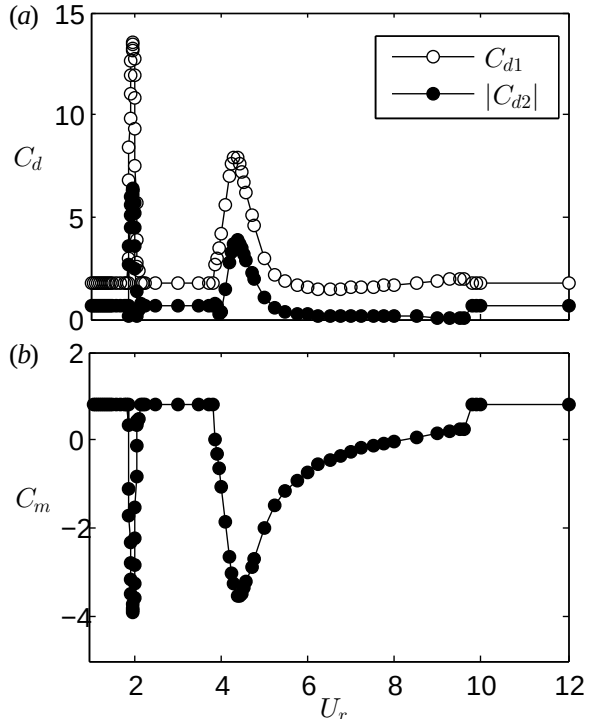

Figure 7. Viscous and form drag coefficients (a) and inertia coefficient (b) fitted on the streamwise fluid force against the reduced velocity

addition to the quadratic drag plays dominant role at low Keulegan-Carpenter number values; i.e. a similar finding obtained by Ren *et al.* (2021) for a stationary cylinder.

Figure 7*a* shows the viscous drag coefficient and the absolute values of form drag coefficient C_{d1} and $|C_{d2}|$, respectively, calculated by fitting Eq. (6) on $F^*_x(t)$ obtained from the CFD simulations against the reduced velocity. It can be seen in Fig. 7*a* that as expected, the viscous drag component plays a very important role. As shown in Fig. 7*a*, in the secondary LI domain ($1.85 \leq U_r \leq 2.2$) and at the beginning of the primary LI range ($3.75 \leq U_r \lesssim 5.5$); i.e. when the oscillation amplitude is close to peaking (see Fig. 2*a*), both C_{d1} and $|C_{d2}|$ show a dramatic increase, and then a gradual decreases. The peaks in C_{d1} and C_{d2} are identified at approximately the peak oscillation amplitude points (see Table 1). However, for intermediate A^* values (i.e. in $5.5 \lesssim U_r \leq 9.6$) the form drag is approximately zero; thus, the drag in such cases is almost linear. Again, for roughly zero-amplitude oscillations the combined effects of C_{d1} and C_{d2} prevail.

In Fig. 7*b* the inertia coefficient C_m is plotted against the reduced velocity. It can be seen that, similarly to the trends in ϕ_x (see Fig. 5), C_m varies reversely to A^*. However, in contrast to ϕ_x, C_m varies 'in-phase with' A^* which means that the minimum values in C_m and the maximum values in A^* in both lock-in domains are found to occur at the same reduced velocity values (see Fig. 7*b* and Table 1). This finding further confirms that there should be a relationship between the vortex-induced cylinder motion and the streamwise fluid force.

4. CONCLUSIONS

In this study transverse-only vortex-induced vibration of a circular cylinder placed into a uniform oscillatory flow is investigated by means of systematic 2D CFD simulation. The Keulegan-Carpenter number and the Reynolds number are fixed at the values as low as 5 and 100, respectively, while the reduced velocity is varied between 1 and 12. The mass ratio and the structural damping ratio were also constant in the simulations (i.e. 2 and 0, respectively).

The amplitude of cylinder oscillation plotted against the reduced velocity displays a multi-peak response, i.e. there are two reduced velocity ranges, where the amplitude first, rapidly increases, and after peaking it shows to decrease. The two reduced velocity ranges are two separate lock-in (LI) domains. In the primary LI domain the vibration frequency synchronises with the flow oscillation frequency, while in the secondary LI range it locks to twice the frequency of the main stream. The peak amplitude in the primary LI domain is found to be more than 2.5 times that in the secondary LI range. The maximum amplitude values are identified close to the point, where the vibration frequency coincides with the cylinder's natural frequency in a still fluid.

Within the secondary LI domain the root-mean-square (rms) values of the transverse and streamwise fluid forces plotted against the reduced velocity display similar trends to that observed in the oscillation amplitude: they increase up to peaking, then decrease. In the primary LI domain the rms of the transverse fluid force approaches zero at the point, where the vibration frequency is close to the cylinder's natural frequency in vacuum (i.e. the coincidence point). In addition, the rms of the streamwise fluid force mostly decreases in the primary LI range up to a reduced velocity value far from any notable

points (e.g. the peak oscillation amplitude point or the coincidence point), then it increases.

In the secondary LI domain the phase of the streamwise fluid force relative to the time-dependent stream velocity displays a reverse trend to that observed in the oscillation amplitude. However, in the primary synchronization range there is a 'shift' between the phase angle and the oscillation amplitude: the maximum in the amplitude and the minimum in the phase angle are identified at different reduced velocity values.

The time-dependent streamwise fluid force is modelled using the extended form of the Morison's equation proposed by Ren *et al.* (2021). Almost independently from the oscillation amplitude value, good agreement was found between the computed and modelled streamwise fluid forces. It was also found that close to the peak amplitude points, both viscous and form drag components play significant roles, but for intermediate oscillation amplitudes the form drag coefficient is close to zero. The inertia coefficient behaves reversely to the oscillation amplitude: its minimum and the amplitude's maximum are identified at the same reduced velocity values.

Acknowledgements. The author was supported by the European Union and the Hungarian State, co-financed by the European Regional Development Fund in the framework of the GINOP-2.3.4-15-2016-00004 project, aimed to promote the cooperation between the higher education and the industry.

5. REFERENCES

Baranyi, L., 2008, Numerical Simulation of Flow Around an Orbiting Cylinder at Different Ellipticity Values. *Journal of Fluids and Structures* **24**(6): 883–906.

Bearman, P.W., Downie, M.J., Graham, J.M.R. & Obasaju, E.D., 1985, Forces on Cylinders in Viscous Oscillatory Flow at Low Keulegan-Carpenter Numbers. *Journal of Fluid Mechanics* **154**: 337–356.

Dorogi, D. & Baranyi, L., 2020, Identification of Upper Branch for Vortex-Induced Vibration of a Circular Cylinder at $Re = 300$. *Journal of Fluids and Structures* **98**: Art. No. 103135.

Dütsch, H., Durst, F., Becker, S. & Lienhart, H., 1998, Low-Reynolds-Number Flow Around an Oscillating Circular Cylinder at Low Keulegan-Carpenter Numbers. *Journal of Fluid Mechanics* **360**: 249–271.

Honji, H., 1981, Streaked Flow Around an Oscillating Circular Cylinder. *Journal of Fluid Mechanics* **107**: 509–520.

Khalak, A. & Williamson, C.H.K., 1999, Motions, Forces and Mode Transitions in Vortex-Induced Vibrations at Low Mass-Damping. *Journal of Fluids and Structures* **13**: 813–851.

Konstantinidis, E., Dorogi, D. & Baranyi, L., 2021, Resonance in Vortex-Induced In-Line Vibration at Low Reynolds Numbers. *Journal of Fluid Mechanics* **907**: A34.

McConnell, K. G. & Jiao, Q., 1986, The In-Line Forces Acting on an Elastically Mounted Cylinder Oscillating in Still Water. *Experimental Mechanics* **26**: 66–70.

Morison, J.R., O'Brien, M.P., Johnson, J.W. & Schaaf, S.A., 1950, The Force Exerted by Surface Waves on Piles. *AIME Petroleum Transactions* **189**: 149–154.

Ren, C., Lu, L., Cheng, L. & Chen, T., 2021, Hydrodynamic Damping of an Oscillating Cylinder at Small Keulegan–Carpenter Numbers. *Journal of Fluid Mechanics* **913**: A36.

Sarpkaya, T., 2002, Experiments on the Stability of Sinusoidal Flow Over a Circular Cylinder. *Journal of Fluid Mechanics* **457**: 157–180.

Stokes, G.G., 1851, On the Effect of the Internal Friction of Fluids on the Motion of Pendulums. *Transactions of the Cambridge Philosophical Society* **9**: 8–106.

Sumer, B. M. & Fredsøe, J., 1988, Transverse Vibrations of an Elastically Mounted Cylinder Exposed to an Oscillating Flow. *Journal of Offshore Mechanics and Arctic Engineering* **110**: 387–394.

Tatsuno, M. & Bearman, P.W., 1990, A Visual Study of the Flow Around an Oscillating Circular Cylinder at Low Keulegan-Carpenter Numbers and Low Stokes Numbers. *Journal of Fluid Mechanics* **211**: 157–182.

Wang, C.-Y., 1968, On High-Frequency Oscillatory Viscous Flows. *Journal of Fluid Mechanics* **32**: 55–68.

Zhao, M., Cheng, L. & An, H., 2012, Numerical Investigation of Vortex-Induced Vibration of a Circular Cylinder in Transverse Direction in Oscillatory Flow. *Ocean Engineering* **41**: 39–52.

VORTEX-INDUCED VIBRATIONS OF A ONE-DEGREE-OF-FREEDOM CYLINDER TRANSITIONING FROM THE INLINE TO THE CROSSFLOW DIRECTION

Bridget Benner
University of Massachusetts, Amherst MA 01003 USA
Yahya Modarres-Sadeghi
University of Massachusetts, Amherst MA 01003 USA

ABSTRACT

Vortex-Induced Vibrations (VIV) of a cylinder in crossflow (i.e. the direction perpendicular to the incoming flow) is a fundamental problem in fluid-structure interactions (FSI) and several studies exist on different aspects of crossflow VIV. Some studies also exist on the case where the cylinder is allowed to oscillate in the direction of incoming flow (inline). Here, we study VIV of a cylinder with one degree of freedom, which is allowed to oscillate in directions ranging from purely inline to purely crossflow. Experiments are conducted in a recirculating water tunnel using a low mass-damping coefficient system. Force and displacement measurements together with flow visualization of the wake are used to characterize the response of the cylinder over a range of reduced velocities as the single degree of freedom incrementally deviates from the inline direction. It is shown that the first of two non-zero-amplitude regions, that are observed at low reduced velocities in a purely inline VIV response of the cylinder, slowly disappears as the angle is increased to approximately $\alpha = 45^\circ$ and the lock-in region, usually observed in a pure crossflow VIV, first appears at angles of approximately $\alpha = 25^\circ$. It is also shown that the observed vortex shedding modes change as the degree of freedom deviates from a pure inline direction. [1]

1. INTRODUCTION

When a bluff body with a circular cross-section is placed in flow, beyond a critical Reynolds number, vortices are shed in its wake (Mathis et al., 1984; Blevins 1990). The shedding frequency of these vortices increases linearly with the incoming flow velocity following the Strouhal law (Blevins 1990). If the cylinder is free to oscillate, then oscillations are observed when the shedding frequency and the natural frequency of the structure become equal. These oscillations are called Vortex-Induced Vibrations (VIV).

The majority of previous studies on VIV have been on a cylinder free to oscillate in the direction perpendicular to the direction of the incoming flow (transverse/crossflow – CF direction) (Bearman, 1984; Sarpkaya, 2004; Williamson and Govardhan, 2004). In these cases, a range of relatively large amplitude oscillations, with amplitudes of up to around one cylinder diameter, are observed for a range of reduced velocities (a dimensionless flow velocity defined as $U^* = U/f_{nw}D$, where U is the flow velocity, f_{nw} is the structure's natural frequency in otherwise still fluid, and D is the cylinder's diameter). These oscillations start at a $U^* \approx 5$, and extend to reduced velocities of $U^* \approx 8$–12, or even larger, depending on the system's mass ratio (Williamson and Govardhan, 2004).

If the cylinder is free to oscillate only in the direction of the incoming flow (inline – IL direction), then IL VIV is observed (Okajima et al., 2002; Jauvtis and Williamson, 2004; Cagney and Balabani, 2013a,b,c,2014; Konstantinidis, 2014; Gurian et al., 2019). In these cases, the response consists of two regions of nonzero amplitude oscillations as the reduced velocity is increased, both of which occur at lower reduced velocities compared with the range of oscillations in the CF direction. The first range of oscillations are observed at a range of $U^* \approx 1.7 - 2.5$, and the second range of oscillations are observed at a range of $U^* \approx 2.75 - 4$. The amplitudes of these oscillations are much smaller than those in the CF VIV, reaching values of less than $0.1D$. The first range of oscillations are observed only if the system is disturbed externally by giving nonzero initial conditions to the cylinder. These oscillations result in a symmetric shedding of the vortices in the wake, where two vortices of the same size are shed simultaneously from the two sides of the cylinder during each cycle of oscillations. Recently, an alternating-symmetric wake has been observed toward the end of

[1] A complete version of this work is published as Benner, B.M, Modarres-Sadeghi, Y. (2021). Vortex-Induced Vibrations of a One-Degree-of-Freedom Cylinder Transitioning from the Inline to the Crossflow Degree of Freedom. Physical Review Fluids. 6, 114702

this first region of oscillations in which while a pair of symmetric vortices is shed in the wake in each cycle of oscillations, the relative size of these vortices alternates, resulting in the shedding of a larger vortex from one side in one cycle followed by a larger vortex from the other side in the next cycle (Gurian et al., 2019). The oscillations of the second region in a pure IL direction are due to the synchronization between the fluctuating forces in the IL direction and the system's natural frequency. Since the fluctuating forces are at two times the shedding frequency in the IL direction, this synchronization occurs at a reduced velocity of approximately half of that for the onset of oscillations in the CF direction. The wake in the second region is an asymmetric wake, where one vortex is shed from each side of the cylinder in each cycle of oscillations.

Clearly there are differences both in the ranges of observed oscillations in the CF and IL directions and the observed vortices in their wakes. Oscillations in the IL direction occur at lower reduced velocities compared with the CF direction. Symmetric and alternating-symmetric wakes are observed only in the IL direction, and not in the CF direction. The questions then arise such as how far one can deviate from the inline direction while still observing symmetric and alternating-symmetric shedding.

2. EXPERIMENTAL SETUP

The experiments were conducted in a re-circulating water tunnel, with a test section of 1.27 m $\times$ 0.5 m $\times$ 0.38 m and a turbulence intensity of less than 1% for up to a flow velocity of $U = 0.3$ m/s. Two circular cylinders were used: one hollow aluminum cylinder that was used for $\alpha \leq 55^\circ$ to cover the entire IL-induced VIV response range, and one acrylic cylinder that was used for $\alpha \geq 40^\circ$ to cover higher angles at larger reduced velocities. The first cylinder had a diameter of $D = 25.4$ mm and was submerged in flow by a length of $L = 355$ mm which corresponded to an aspect ratio of $AR = 14$. The cylinder was comprised of a hollow aluminum tube with a wall thickness of 1.59 mm and ABS plastic printed parts consisting of an endcap and cylindrical extension that interfaced with the force sensor. Waterproof epoxy was used to join the hollow aluminum tube and ABS plastic printed parts to ensure the cylinder was sealed. The second cylinder was made of acrylic and had the same diameter as the hollow aluminum cylinder, $D_{acrylic} = 25.4$ mm, and its submerged length was $L_{acrylic} = 280$ mm, corresponding to an aspect ratio of $AR_{acrylic} = 11$. The acrylic cylinder was used for $\alpha \geq 40^\circ$ because the ABS plastic cylindrical extension affixed to the hollow aluminum cylinder could not withstand the flow forces at higher reduced velocities for which oscillations were observed for larger values of α. ABS plastic was chosen for the cylindrical extension for the aluminum cylinder setup to reduce the moving mass of the system for lower angles, for which mainly IL oscillations were expected. The experiments at $\alpha = 40^\circ$ were conducted using both cylinders to ensure that no significant change is observed due to the use of two different cylinders. Each cylinder was mounted on low-damping air bearings that allowed for one degree of freedom. Springs extended from the metal plate (atop the air bearings) to a fixed mounting point (Figure 1). This air bearing setup and hollow cylinder were used before for other IL VIV studies [13]. The mass ratio was $m^* = m/\rho V d = 1.5$ for the hollow aluminum cylinder and $m^* = 2.6$ for the acrylic cylinder, where m is the total moving mass of the system (including the cylinder, air bearings, mounting plate, force sensor and various cabling), ρ is the density of water and V_d is the volume of the submerged cylinder.

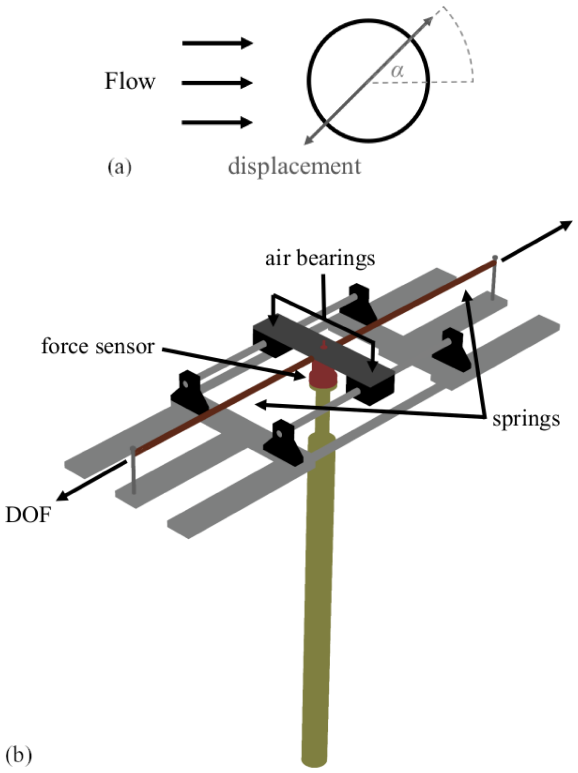

Figure 1. A schematic of the experimental setup.

Flow forces acting on the cylinder were measured using an ATI-Nano17/IP68 six-axis force sensor that was mounted to the cylindrical attachment affixed to the cylinder. Displacement of the cylinder was measured using a Micro-Epsilon ILD 1402-600 non-contacting displacement sensor for a duration of 60 seconds, once the system reached steady state, for each data point. Force and displacement measure-

ments were taken at a sampling frequency of 500 Hz for varying angles in the range of $0^\circ < \alpha < 90^\circ$ over a reduced velocity range of $1.0 < U^* < 14$, which correspond to a Reynolds number range of $700 < Re < 10,300$. Tests were conducted by covering the full reduced velocity range for each value of α. To change the angle at which the circular cylinder could freely move with respect to the flow (Figure 1 (a)), the entire setup (Figure 1(b)) was incrementally rotated to the desired angle. Decay tests were conducted in air and water by giving the cylinder an initial displacement and recording the response. The natural frequencies of the cylinders in water and in air were found using decay tests to be $f_{nw} \approx 1.19$ Hz and $f_{na} \approx 1.56$ Hz for the hollow aluminum cylinder, and $f_{nw} \approx 1.14$ Hz and $f_{na} \approx 1.35$ Hz for the acrylic cylinder. The corresponding structural damping ratio was found to $\zeta = 0.003$ for both cylinders, resulting in a mass-damping coefficient of $m^*\zeta = 0.005$ for the hollow aluminum cylinder and $m^*\zeta = 0.008$ for the acrylic cylinder. For all experiments, the water level was held constant and the flow velocity was increased in increments of ~ 2.5 mm/s to cover the reduced velocity range tested.

Flow visualization tests were conducted using hydrogen bubbles to study the vortex shedding patterns in the wake of the cylinder. The system used for hydrogen bubble generation has been used before by the authors [19,20]. Hydrogen bubbles were generated through electrolysis of water by which a negatively charged platinum-iridium wire with a diameter of 0.0508 mm acted as the anode and a positively charged graphite plate acted as the cathode. The wire was strung upstream from the structure across the test section perpendicular to the flow and the graphite plate was placed upstream from the platinum wire parallel to the flow. The potential difference between the charged wire and graphite plate caused a build-up of hydrogen bubbles along the platinum wire which, once separated from the wire, created a bubble plane used to view the wake structure. The wake images were captured using a Phantom Miro M110 high speed camera placed underneath the test section.

3. THE AMPLITUDE RESPONSE AT DIFFERENT ANGLES

Figure 2 shows the dimensionless amplitude of oscillations versus the reduced velocity for all angles where the third VIV range is observed. The blue markers represent results based on the hollow aluminum cylinder and the red markers represent results based on the acrylic cylinder . Since the hollow aluminum cylinder was replaced with the acrylic cylinder at $\alpha = 40^\circ$, amplitude values for both the aluminum (blue square markers) and acrylic (red triangle markers) cylinders are shown at this angle. The amplitude values for the acrylic cylinder are slightly smaller than the amplitude values for the aluminum cylinder because the mass-damping coefficient is greater for the acrylic cylinder setup compared with the aluminum cylinder setup. The difference in the mass-damping coefficient also impacts the lock-in range for both series of experiments at $\alpha = 40^\circ$, whereby the lock-in range is slightly wider for the aluminum cylinder setup (which has a lower mass-damping coefficient) as compared with the acrylic cylinder setup.

It is seen in Figure 2 that as α is increased, the width of the third lock-in region and the maximum amplitude of oscillations in that region increase as well. The lock-in region reaches a range of $U^* = 4 - 13$ at $\alpha = 90^\circ$ with a maximum amplitude of $A^* \approx 0.8$. For the pure CF case, both the upper branch and lower branch have been observed with their corresponding maximum amplitudes of $A^* = 0.8$ and 0.6, respectively, which are very close to values shown by Williamson and Govardhan (2004) for a system with $(m^* + C_A)\zeta = 0.011$. The upper branch has been observed also for lower angles of $\alpha = 70^\circ$ and 80°, with almost the same maximum amplitude as $\alpha = 90^\circ$, but it disappears at $\alpha = 60^\circ$. As α is decreased, the width of the lock-in region and the maximum amplitude of oscillations within the lock-in region decrease. The decrease in the width of the lock-in region is observed mainly as a sooner end of the synchronization. The peak amplitude moves to higher reduced velocities as α is decreased, except for the smallest angle for which this lock-in region has been observed: $\alpha = 25^\circ$. A major drop in the maximum amplitude is observed between $\alpha = 70^\circ$ and $\alpha = 60^\circ$, where maximum amplitude drops from $A^* \approx 0.7$ to $A^* \approx 0.4$, due to the disappearance of the upper branch at $\alpha = 60^\circ$

The corresponding dimensionless oscillation frequency plots of Figure 2 clearly show two different regions of synchronizations: one corresponding to the lock-in regions due to IL synchronization, and one corresponding to the lock-in due to the CF synchronization. Two lines, corresponding to the shedding frequency and two times the shedding frequency, estimated based on the Strouhal law are also plotted in the figure. The first region's synchronization is with two times the shedding frequency, since oscillations that are observed in this region are due to the IL synchronization that occurs when the natural frequency of the system equals two times the shedding frequency, since the fluctuating force frequency in the inline direction is two times the shedding frequency. This first region corresponds to both nonzero amplitude oscillation regions observed in the lower

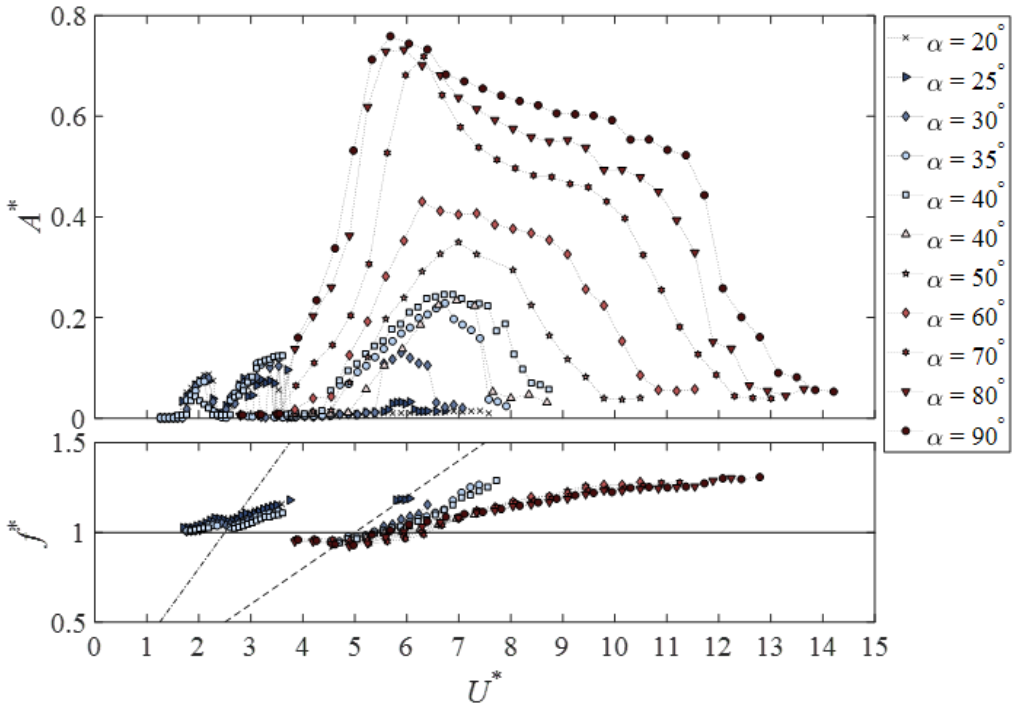

Figure 2. The amplitude response of the cylinder at different angles.

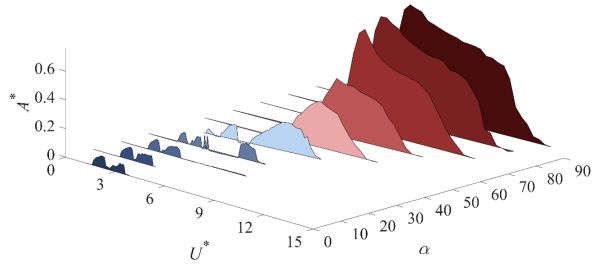

Figure 3. The 3D representation of the amplitude response of the cylinder at different angles.

reduced velocity cases, as well as the range of almost (but not completely) zero amplitude oscillations in between those two regions. As the reduced velocity is increased, oscillations are observed at higher reduced velocities, which correspond to a synchronization between the shedding frequency and the natural frequency, and those are the oscillations that resemble the typical CF VIV response. For both ranges, the oscillation frequency increases with increasing reduced velocity.

The plot of Figure 3 gives an overall view of the cylinder's response at different angles. Besides giving a clear comparison among the relative amplitudes of oscillations at different angles and at different reduced velocities, this plot shows that at lower angles, only the lock-in ranges due to the IL synchronization exist. Then as the angle is increased, for $\alpha = 30^\circ$ to $\alpha = 40^\circ$, all three lock-in ranges exist in the cylinder's response, and for higher angles, $\alpha > 40^\circ$, the lock-in range due to the CF synchronization is the only observed VIV response. Note that at $\alpha = 50^\circ$, Figure 3 shows only the response of the cylinder at higher reduced velocities (based on the data from the acrylic cylinder), and does not include the second IL lock-in region that is observed at lower reduced velocities with the hollow cylinder.

The results of Figures 2 and 3 can also shed light on what is observed in the VIV of a 2DOF system, in which a cylinder is free to oscillate in both the IL and CF directions. When in a 2DOF system, the natural frequencies in the CF and IL directions are identical as the reduced velocity is increased from zero, lock-in in the IL direction occurs first, and IL oscillations are observed, and CF oscillations start at higher reduced velocities where lock-in occurs in the CF direction. This corresponds to what is observed in Figure 2: the purely IL lock-in starts earlier than the CF lock-in. If, however, in a 2DOF system, the ratios of the IL and CF natural frequencies are set to be equal to 2 (Dahl et al., 2007,2010; Carlson et al., 2021), dual resonance can occur, in which the CF and the IL lock-in occur at the same time, since due to the 2:1 ratio between the IL and CF natural frequencies, the forcing frequency equals to both natural frequencies at the same reduced velocity. With a 2:1 ratio be-

tween the natural frequencies, the amplitude plot for the purely IL angle would have shifted to values of reduced velocity twice as large as their present values, and the onset of lock-in in both purely IL and purely CF directions would have been at the same value of reduced velocity.

4. FLOW VISUALIZATIONS

Four different shedding patterns have been observed in the literature for a circular cylinder undergoing inline VIV [13]. We have also observed these four patterns in the wake of our purely inline case as shown in the first row of Figure 4. At the beginning of the first lock-in range, a symmetric shedding is observed in which two vortices of the same size are shed simultaneously from the two sides of the cylinder in each cycle of oscillations (e.g., at $U^* = 1.9$, Figure 4(a)). Toward the end of the first lock-in range, Alternating-Symmetric (AS) shedding is observed in which while again two vortices are shed from the two sides of the cylinder simultaneously during each cycle of oscillations, the relative sizes of these vortices alternate in each cycle (e.g., at $U^* = 2.2$, Figure 4(b)). For the range of almost-zero-amplitude response between the two lock-in ranges, a competitive shedding is observed in which symmetric and asymmetric shedding patterns coexist (e.g., at $U^* = 2.8$, Figure 4(c)). In the second IL lock-in range, an asymmetric shedding is observed in which two single vortices are shed from the two sides of the cylinder, one after the other, in each cycle of oscillations (e.g., at $U^* = 3.3$, Figure 4(d)). Here, we consider four reduced velocities within these four regions with distinct shedding patterns, and we will discuss how these patterns change as α is increased. We discuss in detail how these wake structures and flow forces relate to one another in what follows.

The observed wake during the major part of the first lock-in range in a purely IL VIV case, $\alpha = 0^\circ$, is a symmetric shedding in which one pair of symmetric vortices of opposite signs are shed per oscillation cycle. This pattern is observed here for the pure IL case as well, as an example, at $U^* = 1.9$ (Figure 4a). As α is increased, this symmetric shedding wake pattern is observed for all angles up to $= 40^\circ$ (Figure 4e,i,m,q), and they only disappear when the first VIV region collapses at $\alpha = 45^\circ$ (Figure 4u). There are slight changes in the symmetric shedding as the angle is increased. Starting at $\alpha = 35^\circ$, a skewed symmetric shedding pattern is observed in which the vortex that is shed from the lower side of the cylinder is always slightly larger than the vortex that is shed from its upper side. At $\alpha = 40^\circ$ the oscillations of the cylinder are very small, and the shedding of vortices occurs further downstream relative to the smaller angles as shown in Figure 4(q). When the first VIV region collapses at $\alpha = 45^\circ$, the shear layers do not interact with each other until much farther downstream (Figure 4(u)) and do not impart forces that cause the cylinder to oscillate.

Toward the end of the first lock-in region, e.g., at $U^* = 2.2$, the cylinder exhibits AS shedding in the purely inline direction where two unequal-sized vortices are shed simultaneously per oscillation cycle and alternate in size for each cycle (Figure 4b). This shedding pattern was first identified and classified by Gurian et al. (2019). In the present study, this shedding pattern is observed beyond the purely inline case. In our visualizations, we observed the AS shedding for up to $\alpha = 20^\circ$. The shedding pattern transitions at $\alpha = 25^\circ$ at which point again skewed symmetric shedding is observed with the vortex that is shed from the side that is in the direction of the cylinder's oscillations is always slightly larger than the other vortex.

At an even higher reduced velocity, e.g., $U^* = 2.8$, weak and competitive shedding is observed in the purely inline direction, where the wake structure resembles both symmetric and asymmetric shedding patterns and is essentially indistinguishable. This shedding pattern remains consistent as the angle at which the cylinder is free to oscillate is increased (Figure 4), but the response of the cylinder changes. At lower angles ($\alpha = 0^\circ$ and 5°), the cylinder is between the two VIV regions and exhibits very small oscillation magnitudes. The corresponding fluctuating flow forces in both the x and y directions are also very small.

Within the second VIV region, e.g., at $U^* = 3.3$, asymmetric shedding is observed for the purely inline case where two vortices are shed from each side of the cylinder, one after the other, per oscillation cycle. The shedding pattern remains consistent at this reduced velocity for angles that deviate from the purely inline case (Figure 4) until the second VIV branch collapses at $\alpha = 55^\circ$.

5. CONCLUSION

The response of the cylinder in the purely streamwise direction, $\alpha = 0^\circ$, was consistent with what has been observed in previous studies [12,13] in that two regions of VIV responses are observed at relatively low reduced velocities. The wake structure transitions as the reduced velocity is increased and ultimately four wake structures are observed: symmetric shedding, alternating-symmetric shedding, weak and competitive shedding, and asymmetric shedding. At lower reduced velocities, when symmetric shedding occurs

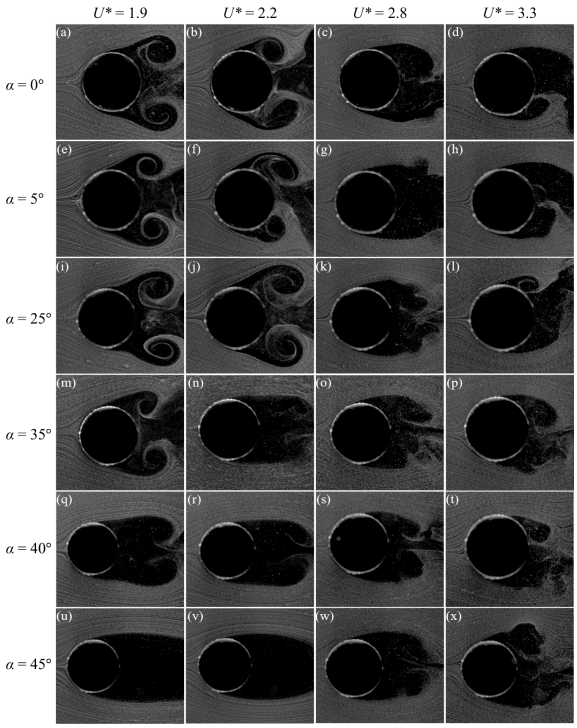

Figure 4. The cylinder's wake at different angles.

in the wake of the cylinder, the peak flow force frequency in the direction of motion (the streamwise direction) is equal to the natural frequency and the flow force frequencies in the direction perpendicular to the direction of motion (the crossflow direction) are negligible. As the reduced velocity is increased, and the wake structure transitions to alternating-symmetric shedding in the wake of the cylinder, a small frequency peak at half the natural frequency of the system, $f_{nw}/2$, emerges in the direction perpendicular to the direction of motion which indicates a slight asymmetry in the system. As the reduced velocity is increased further, and the wake structure transitions to asymmetric shedding, the peak at half the natural frequency of the system, $f_{nw}/2$, in the direction perpendicular to the direction of oscillations becomes the dominant frequency since two vortices are shed from opposite sides of the cylinder per shedding cycle.

At slightly higher angles, $1^\circ \leq \alpha \leq 15^\circ$, the amplitudes of oscillations and oscillation frequencies remain largely the same as the purely inline case, indicating that a deviation of up to $\alpha = 15^\circ$ has minimal effect on the IL VIV response of a circular cylinder. At $\alpha = 20^\circ$, the width of the first lock-in region decreases slightly. This trend continues as the angle of the degree of freedom is increased until the first lock-in region collapses at $\alpha = 45^\circ$. This again indicates that up to $\alpha = 40^\circ$, the main features of the pure IL VIV response are observed in the response of a cylinder that oscillates with a very large angle with respect to the purely inline degree of freedom. Oscillations in the second lock-in region are observed up to $\alpha = 50^\circ$, and at $\alpha = 55^\circ$ the second lock-in region collapses. The first signs of the third lock-in region, consistent with the response of a circular cylinder placed in crossflow, emerges at higher reduced velocities for $\alpha = 25^\circ$. As α is increased further, the peak amplitude of oscillations and the width of the lock-in range increases and the largest peak amplitude and the widest lock-in range occur at $\alpha = 90^\circ$, the purely crossflow case.

The symmetric shedding that is observed in the wake of the cylinder within the first lock-in range of a purely IL case persists for up to $\alpha = 30^\circ$, and the alternating-symmetric shedding, which is observed toward the end of the first lock-in range, persists up to $\alpha = 20^\circ$, both of which were confirmed through flow visualization. For higher angles, a skewed symmetric shedding is observed within the first lock-in range, in which one of the two shed vortices is consistently larger than the other one.

6. REFERENCES

Bearman, P., Vortex shedding from oscillating bluff bodies, Annu. Rev. Fluid Mech. 16, 195 (1984).

Benner, B., Carlson, D.W., Seyed-Aghazadeh, B., Modarres-Sadeghi, Y. (2019). Vortex-Induced Vibration of Symmetric Airfoils used in Vertical-Axis Wind Turbines. Journal of Fluids and Structures. 91, 102577.

Benner, B.M, Modarres-Sadeghi, Y. (2021). Vortex-Induced Vibrations of a One-Degree-of-Freedom Cylinder Transitioning from the Inline to the Crossflow Degree of Freedom. Physical Review Fluids. 6, 114702.

Blevins, R. D., Vortex Induced Vibrations. Van Nostrand Reinhold, New York, (1990).

Bourguet, R. (2019). Flow-induced vibrations of a rotating cylinder in an arbitrary direction. Journal of Fluid Mechanics, 860, 739-766.

Cagney N., Balabani, S., Mode competition in streamwise-only vortex induced vibrations, J. Fluid Struct. 41, 156 (2013).

Cagney N., Balabani, S., On multiple manifestations of the second response branch in streamwise vortex-induced vibrations, Phys. Fluids 25, 075110 (2013).

Cagney N., Balabani, S., Streamwise vortex-induced vibrations of cylinders with one and two degrees of freedom, J. Fluid Mech. 758, 702 (2014).

Cagney N., Balabani, S., Wake modes of a cylinder undergoing free streamwise vortex-induced vibrations, J. Fluid Struct. 38, 127 (2013).

Carlson, D.W., Currier, T., Modarres-Sadeghi, Y., Flow-Induced Vibrations of a Square Prism Free to Oscillate in the Crossflow and Inline Directions. Journal of Fluid Mechanics. 919, A2 (2021).

Dahl, J.M., Hover, F.S., Triantafyllou, M.S. Resonant vibrations of bluff bodies cause multi-vortex shedding and high frequency forces. Phys. Rev. Lett. 99, 144503 (2007).

Dahl, J.M., Hover, F.S., Triantafyllou, M.S., Oakley, O.H., Dual resonance in vortex-induced vibrations at subcritical and supercritical Reynolds numbers. J. Fluid Mech. 643, 395–424 (2010).

Gurian, T.D. , Currier, T., Modarres-Sadeghi, Y. (2019). Flow Force Measurements and the Wake Transition in Purely Inline Vortex-Induced Vibration of a Circular Cylinder. Physical Review Fluids. 4, 034701.

Jauvtis N., Williamson, C. H. K. , The effect of two degrees of freedom on vortex-induced vibration at low mass and damping, J. Fluid Mech. 509, 23 (2004).

Jauvtis, N., Williamson, C.H.K. The effect of two degrees of freedom on vortex-induced vibration at low mass and damping. J. Fluid Mech. 509, 23–62 (2004).

Konstantinidis, E., On the response and wake modes of a cylinder undergoing streamwise vortex-induced vibration, J. Fluid Struct. 45, 256 (2014).

Mathis, C. Provansal, M., Boyer, L., The benard-von karman instability: an experimental study near the threshold. Journal de Physique Lettres 45, 10, 483–491 (1984).

Modarres-Sadeghi, Y. Mukundan, H., Dahl, J.M., Hover, F.S., Triantafyllou, M.S. (2010). The Effect of Higher Harmonic Forces on Fatigue Life of Marine Risers. Journal of Sound and Vibration, 329, 43-55.

Mukundan, H., Modarres-Sadeghi, Y., Dahl, J.M., Hover, F.S., Triantafyllou, M.S. (2009). Monitoring Fatigue Damage on Marine Risers. Journal of Fluids and Structures, 25, 617-628.

Okajima, A., Kosugi, T., Nakamura, A., Flow-induced in-line oscillation of a circular cylinder in a water tunnel, J. Pressure Vessel Technol. 124, 89 (2002).

Ongoren A., Rockwell, D. (1988). Flow structure from an oscillating cylinder. Part 2. Mode competition in the near wake. Journal of Fluid Mechanics, 191, 225–245.

Sarpkaya, T., A critical review of the intrinsic nature of vortex induced vibrations, J. Fluid Struct. 19, 389 (2004).

Seyed-Aghazadeh, S., Carlson, D.W., Modarres-Sadeghi, Y. (2017). Vortex-Induced Vibration and Galloping of Prisms with Triangular Cross-Sections Placed in Water Flow. Journal of Fluid Mechanics. 817, 590-618.

Williamson, C. H. K., Govardhan, R., Vortex-induced vibrations, Annu. Rev. Fluid Mech. 36, 413 (2004).

Zheng, H., Price, R.E., Modarres-Sadeghi, Y., Triantafyllou, M.S. (2014). On Fatigue Damage of Long Flexible Cylinders due to the Higher Harmonic Force Components and Chaotic Vortex-Induced Vibrations. Ocean Engineering, 88, 318-329.

WAKE INDUCED VIBRATION IN TANDEM CYLINDERS: PART 1- WAKE PERTURBATION ANALYSIS

Roberta Fátima Neumeister, Ana Paula Ost, Patrick Batista Habowski, Alexandre Vagtinski de Paula, Adriane Prisco Petry, Sergio Viçosa Möller

UFRGS, Federal University of Rio Grande do Sul, Porto Alegre, RS, Brazil

ABSTRACT

Flow-induced vibration of a cylinder in the wake of another cylinder in a tandem arrangement is experimentally investigated in the present study. The first cylinder is rigidly mounted inside the aerodynamic channel, while the second one is free to vibrate transversally to the main flow. Normalized distance L/D between the cylinders ranged from 2.5 to 10. The cylinder free to vibrate presented a mass ratio of 539 and a damping ratio of 0.0169. Hotwires, microphones, and accelerometers were the experimental tools applied in this study. The Reynolds number obtained with the tube diameter and the main flow velocity ranged around 1.15x10^4. Fourier and Wavelet Transform supported by flow visualizations in a hydraulic channel was applied to analyze the acceleration results as well as velocity and pressure fluctuations. Results show the influence of the wake from the first cylinder on the lift force and vibration regime of the second cylinder. The wake from the first cylinder perturbs the second cylinder even for large pitch ratios and changes the response of force and vibration on the second cylinder. The acceleration in the transversal direction of the cylinder free to vibrate increases under the influence of the wake of the first cylinder for all spacing ratios, mainly values of L/D higher than 5. The perturbation generated by the first cylinder is observed in the acceleration results from the second cylinder.

Keywords: Cylinders, tandem, wake induced vibration.

1. INTRODUCTION

The crossflow over cylinders in tandem is found in many engineering applications such as tube banks, transmission lines, buildings, risers, and wind turbine towers, among others (Blevins, 1990). The main parameters associated with the tandem arrangement are presented in Fig. 1 a), where L represents the distance between the cylinders and D the cylinder diameter. Most of the studies relate to low space ratio, due to the direct interaction of the wake of the first cylinder with the second cylinder. Igarashi (1981) executed experimental investigations on the characteristics of the flow around two circular cylinders in tandem with Reynolds numbers between 8.7 x 10^3 and 5.2 x 10^4 and the space ratios ranged from 1.03 to 5. Results showed the dependency of the Strouhal number and Reynolds number for the space ratio 1.1 to 2.

Flow-induced streamwise oscillation of two tandem circular cylinders in a wind tunnel was studied by Okajima et al. (2007). One cylinder was elastically supported and allowed to move in the streamwise direction; the other was fixed to the tunnel sidewalls. Small values of the reduced mass-damping parameter were considered. When the upstream cylinder is free to oscillate, there are two excitation regions: one due to movement-induced excitation accompanied by symmetrical vortex shedding. The second excitation range is due to vortex excitation by alternate Kárman vortex shedding. The response when the downstream cylinder is free to oscillate has an excitation region due to Karman vortex shedding from the two cylinders, connected by the region between them and the second excitation region is due to symmetrical vortex shedding.

Bernitsas et al. (2008) presented a device that harvests energy using the vortex-induced vibration. It converts ocean/river current hydrokinetic energy to a usable form of energy such as electricity using VIV maximizing rather than spoiling vortex shedding and exploiting rather than suppressing VIV.

An investigation of the mechanism of wake-induced vibrations (WIV) of a pair of cylinders in the tandem arrangement was presented by Assi et al. (2010). A typical WIV response was characterized by a build-up of amplitude persisting to high reduced velocities; this is different from a typical vortex-induced vibration (VIV) response, which occurs in a limited resonance range. The authors suggested that the WIV of the downstream cylinder is excited by the unsteady vortex–structure interactions between the cylinder and the upstream wake. Coherent vortices interfering with the downstream cylinder induce fluctuations in the fluid force that are not synchronized with the motion. A favorable phase lag between the displacement and the fluid force guarantees that a positive energy transfer from the flow to the structure sustains the oscillations. If the unsteady

vortices are removed from the wake of the upstream cylinder, there will be no WIV excitation.

Soares and Srinil (2021) presented a new nonlinear wake-deficit oscillator model for predicting the combined WIV-VIV responses in the cross-flow direction of the downstream cylinder. The total cross-flow hydrodynamic force on the downstream cylinder was modeled as a combination of the wake-induced transverse force and the combined vortex-induced lift and drag forces. The model presented a good agreement with results from the experimental study of Assi et al. (2010).

Vortex-Induced Vibration (VIV) for the flow around two circular cylinders in tandem is presented by Derakhshandeh et al (2014). They showed that the amount of kinetic energy that can be captured by VIV is a function of the arrangement of the two cylinders. The upstream cylinder is fixed while the downstream is mounted elastically with one degree of freedom normal to the mean flow direction. The efficiency of the VIV power obtained from the downstream cylinder is compared for a different arrangement of the cylinders. For this purpose, the longitudinal and lateral distances between the cylinders were varied while the Reynolds number was kept constant. The results reveal that the arrangement of the cylinders can significantly change the efficiency. It is also observed that staggered cylinders have higher efficiency compared to cylinders with their centers aligned.

Experimental results for WIV and VIV acting on two circular cylinders were presented by Park et al. (2018). The tested cases considered the upstream cylinder fixed or allowed to have one degree of freedom motion and the downstream cylinder is allowed to have two degrees of freedom motion. The space ratio varied between 3 and 10. The responses of the WIV and VIV occurred together in the tandem cylinders, as the reduced velocity increased, the displacement of motion increased continuously. The effect of the WIV was the most significant at L/D of 3.0 and 4.0. The effect of the wake interference decreased as L/D increased and the L/D of 10.0 became similar to that of a single cylinder.

Xu et al. (2019) presented experimental results on flow-induced vibration (FIV) of two identical elastically mounted circular cylinders in tandem arrangement with both allowed to oscillate in the transverse direction. The Reynolds number was between 2.86×10^4 and 1.14×10^5. Four spacing ratios between 1.57 and 4.57 were tested. The experimental results indicated that the FIV characteristics of the upstream cylinder are similar to those of a single cylinder when the reduced velocity does not exceed 12.0. The vibration and the fluid force on the downstream cylinder are influenced by the upstream cylinder for the spacing range tested.

The present analysis is an experimental study of the flow over two cylinders in tandem with L/D from 2.5 to 10, with the second cylinder free to vibrate normally to the flow direction. The influence of the wake from the first cylinder on the vibration regime of the second cylinder is investigated using velocity, pressure fluctuations, and acceleration measurements of the second cylinder complemented with flow visualizations of the flow on fixed cylinders.

2. METHODOLOGY

The experimental study was executed in the aerodynamic channel of the Fluid Mechanics Laboratory – LMF of UFRGS. The aerodynamic channel is made of acrylic glass, with a rectangular test section of 0.146 m in height, a width of 0.193 m, and 1.62 m in length, as shown in Fig. 1 b). The test section is assembled with smooth PVC cylinders of 25mm diameter. The first cylinder is fixed on the channel walls while the second cylinder is fixed on two blades that allow it to vibrate transversally to the flow, being assembled to vibrate in the longitudinal direction. The system presents a mass ratio of 539, a damping ratio of 0.0169, and a natural frequency of 5.86 Hz, all parameters were obtained from the free vibration signal of the experimental setup. The blockage ratio is 13%. For the case tandem L/D = 10 the setup was changed, due to the increase in length of the longitudinal gap. For this case, the natural frequency is 3.906 Hz and the damping ratio is 0.011.

A centrifugal blower of 0.75 kW impels the air through a diffuser, two honeycombs, and two screens, to reduce the turbulence intensity to about 1% of the free stream velocity. Placed in one of the sidewalls, a Pitot tube measures the reference velocity of the non-perturbed flow, used to determine the Reynolds number, Re, of the experiments, defined with the cylinder diameter and the kinematic viscosity at the environmental conditions of the laboratory, with the value of $Re = 1.15 \times 10^4$.

The reduced velocity, Vr, is a parameter applied in vibration analysis. The free stream velocity is divided to the natural frequency and the cylinder diameter. The reduced velocity remains around Vr = 48 for the single cylinder, L/D =2.5. L/D = 5 and L/D = 8 cases. The case L/D = 10 presents a reduced velocity around Vr = 70, due to the change in the setup natural frequency.

Flow velocity and velocity fluctuations were measured using a DANTEC StreamLine constant hot-wire anemometry system. The acceleration was obtained with an analogic accelerometer, ADXL335, with the sensibility of 332 mV/g, a total scale of ± 3 g, and a natural frequency of 5.5 kHz. Pressure fluctuations are obtained with the condenser microphone Brüel & Kjaer Cartridge type 4138, with a diameter of 1/8”. The microphone is connected to an amplifier

Brüel & Kjaer type 2633. The position of the microphone and the hot wire anemometer are presented in Fig. 1 c).

Data acquisition of acceleration, velocity, and pressure were executed with an acquisition frequency of 1 kHz with an anti-aliasing low pass filter at 0.3 kHz employing a 16bits NI USB-9162 A/D board.

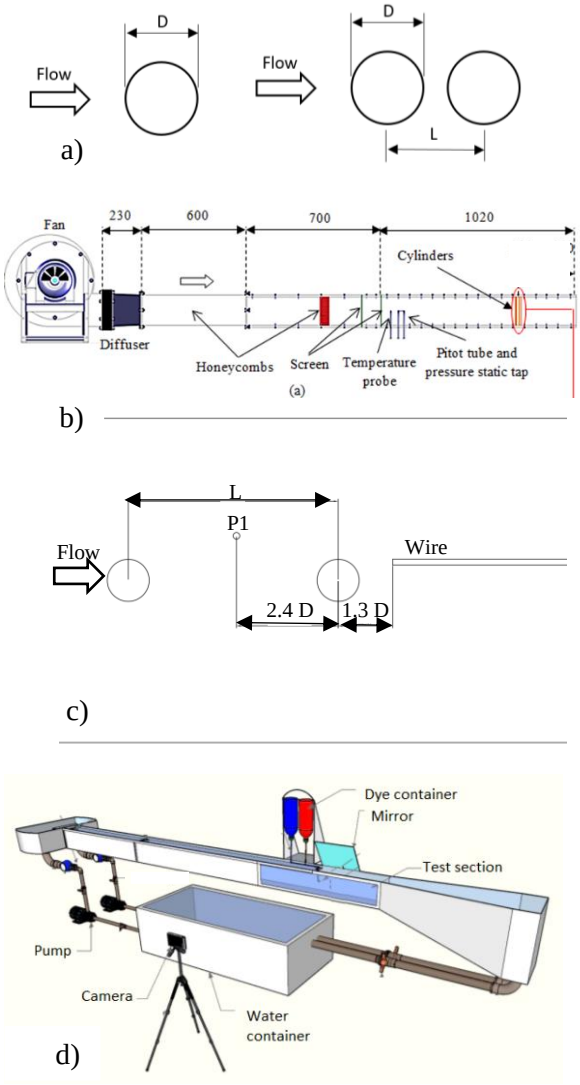

Figure 1. a) Geometric parameters for tandem arrangement, b) aerodynamic channel, c) wire and microphone positions and d) water channel, adapted from Woyciekoski et al. (2020).

Flow visualizations were executed with dye in the water channel of the Energy and Transport Phenomena Laboratory - LAEFT of UFRGS, as described in more detail in Woyciekoski et al. (2020). The water channel presents a rectangular test section of 0.146 m in height, the width of 0.193 m presented in Fig. 1 d). The Reynolds number for the visualization is Re = 2 x 10^3.

The signal analysis was executed using Fast Fourier Transform and Continuous wavelet transform. The wavelet function adopted was Db20, due to previous studies executed by Indrusiak and Möller (2011).

3. RESULTS

Preliminary FIV analysis was executed with a single cylinder, free to vibrate in crossflow. This analysis was followed by the measurements within a tandem arrangement for several L/D values.

3.1. Single Cylinder

The cylinder is instrumented with an accelerometer, the hot wire anemometer is positioned in the cylinder wake and the microphone is positioned upstream of the cylinder free to vibrate, as shown in Fig. 1 c). The Reynolds number is Re = 1.15 x 10^4. Figure 2 a) presents the power spectrum for the signals of acceleration, velocity, and pressure.

The main difference between the results of acceleration, velocity, and pressure, Figure 2 a), is the energy-related to each variable. The lower energy values correspond to pressure fluctuations due to the location of the pressure transducer. In the velocity frequency spectrum, a 50Hz peak is observed, corresponding to a Strouhal number 0.179. The power spectrum from acceleration and pressure presents a series of peaks, most of which are not with equivalent values. In the power spectrum of acceleration, there is one peak of about 8 Hz close to the natural frequency of 5.89Hz. In pressure fluctuation results, a peak at 40Hz is observed with low energy, which can be related to plane waves in the aerodynamic channel, since it is not present in velocity and acceleration results. In the velocity frequency spectrum, a 50Hz peak is observed, corresponding to a Strouhal number 0.179. Peaks over 200 Hz are related to aerodynamic noise from the protection grid of the pressure transducers and can be fully disregarded for this analysis.

Figure 2 b) presents the wavelet spectrum for the acceleration of the single cylinder without no significant energy associated. Figure 2 c) presents the wavelet spectrum from pressure fluctuations with the highest energy in the range of 40Hz. The wavelet spectrogram of the velocity presents energy peaks around 50Hz without a defined range but with points of high energy around 16 s, 18s, and 31 s.

Figure 3 presents the flow visualization with dye in water for a single cylinder, it can be observed the vortex street and the detachment happening at 80° ~ 90°.

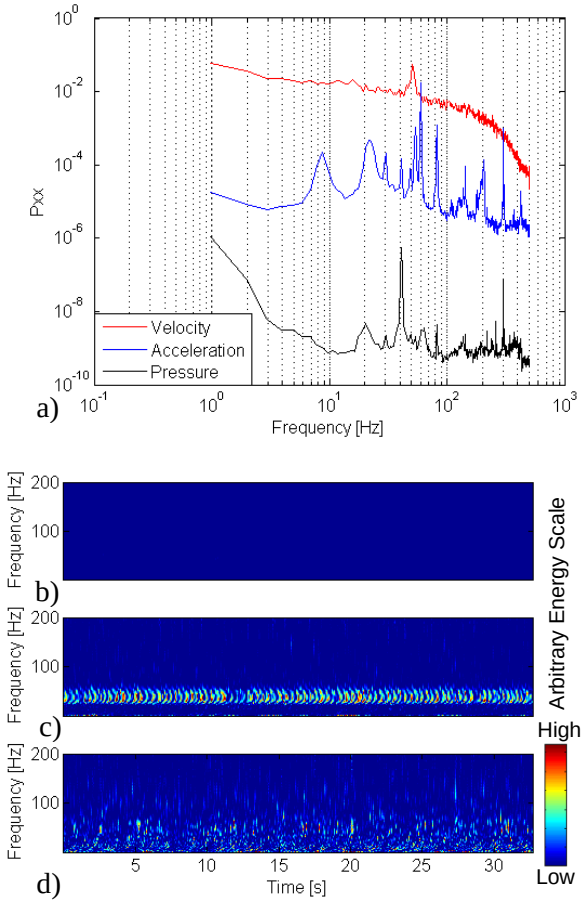

Figure 2. Single cylinder free to vibrate a) power spectrum from acceleration, velocity, and pressure. b) acceleration wavelet spectrogram, c) pressure wavelet spectrogram, and d) velocity wavelet spectrogram.

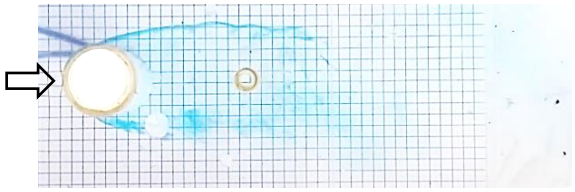

Figure 3. Flow visualization for single cylinder.

3.2. Tandem Cylinders L/D = 2.5

To observe the influence of the first cylinder on the vibration of the second cylinder, the arrangement tandem with L/D = 2.5 is studied. The signals of acceleration, pressure fluctuation, and wake velocity were acquired at the positions presented in Figure 1 c) with the Reynolds number of 1.15 x 10^4. The power spectra of acceleration, pressure, and velocity are presented in Fig. 4 a). The energy levels are lower for the pressure fluctuations. No peak is clear in the velocity results, just presents a region with higher energy between 40 Hz and 60 Hz. The acceleration presents a peak at about 8 Hz, which can be linked to the natural frequency. The spectrum of pressure fluctuations does not present relevant peaks.

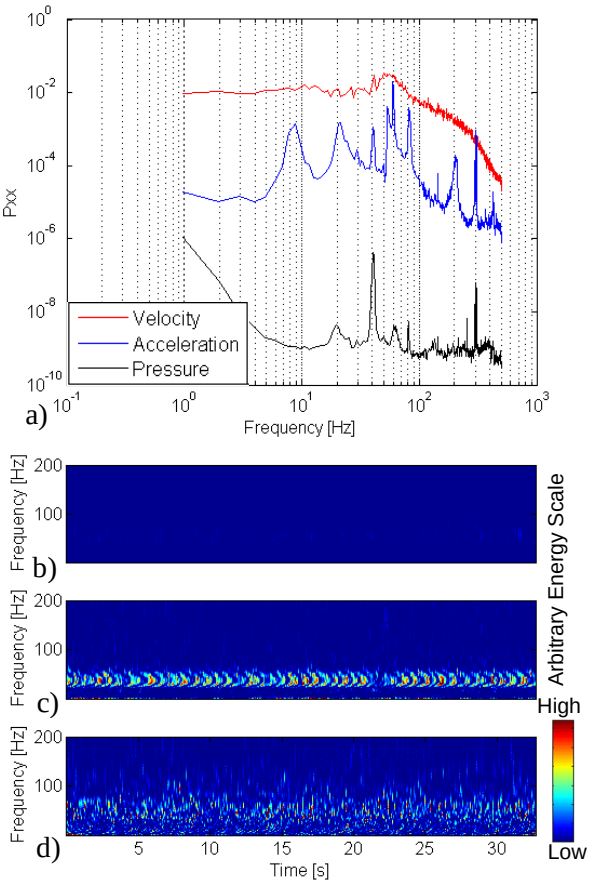

Figure 4. Cylinders in tandem with L/D = 2.5. Results for the second cylinder free to vibrate: a) power spectrum from each signal, b) acceleration wavelet spectrogram, c) pressure wavelet spectrogram, and d) velocity wavelet spectrogram.

In Figure 4 b), c) and d) wavelet spectrograms for acceleration, pressure, and velocity are presented. The acceleration does not present a region with visible energy, while the pressure fluctuations spectrogram, Fig. 4 c), presents a range of high energy around 40Hz, which is also visible in Fig. 2 c). The velocity spectrogram presents a region with high energy at about 50Hz, corresponding to the vortex shedding frequency. Compared with the results for a single cylinder, Fig. 2, it is observed an increase in pressure and velocity energy, which do not reflect in the acceleration energy.

The visualization of the flow on the cylinders in tandem with L/D = 2.5 is presented in Fig. 5. The blue dye is from the first cylinder and the red dye from the second cylinder, the Reynolds number for

the visualization is Re = 2 x 10^3. In Figure 5, it can be observed that the second cylinder is inside the wake of the first cylinder, which engulfs the second cylinder and generates a recirculation region, observed in the concentration of red dye upstream of the second cylinder. The interaction of the wakes is observed after the second cylinder, where both dye colors are simultaneously visible.

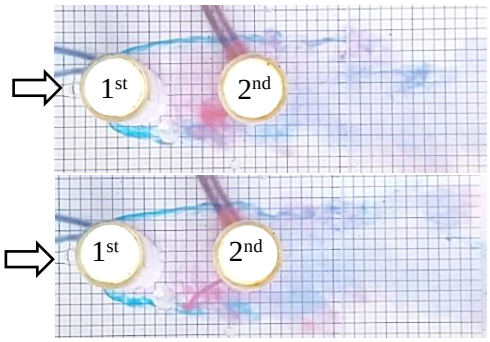

Figure 5. Flow visualization for cylinders in tandem with L/D = 2.5.

3.3. Tandem Cylinders L/D = 5

The vibration response of the second cylinder in a tandem arrangement is evaluated for a spacing ratio of 5 and the power spectrum for the acceleration, pressure, and velocity is presented in Figure 6 a). The pressure energy levels, in this case, are in the same range as the velocity results, showing the influence on the pressure field caused by the presence of the first cylinder. All the signals, acceleration, velocity, and pressure, present a peak at 50 Hz, which results in a Strouhal number of 0.179. The acceleration presents a peak around 8 Hz, associated with the natural frequency.

The acceleration spectrogram, Fig. 6 b), shows high energy in the range of 50 Hz, present also in the pressure and velocity spectrogram results, Fig. 6 c) and d).

Compared with the results for L/D = 2.5, Fig. 4, it is observed that the first cylinder wake increases its influence on the vibration response of the second cylinder.

The influence of the first cylinder wake on the wake behavior of the second cylinder can be observed in Fig. 7: there, the wake from the first cylinder impacts directly on the front side of the second cylinder, changing the side and the frequency of the vortex shedding from the second cylinder. Therefore, it is expected that this behavior influences the oscillation pattern of the second cylinder.

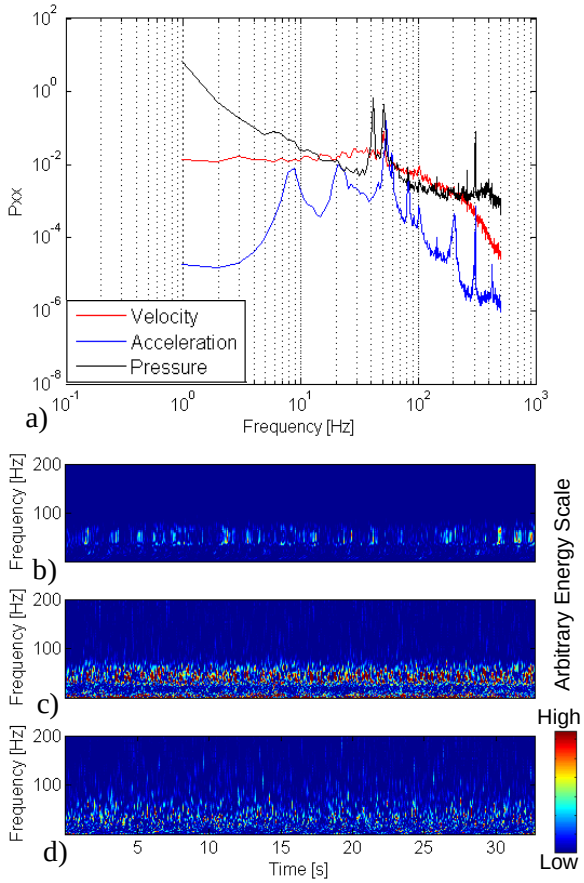

Figure 6. Cylinders in tandem with L/D = 5. Results for the second cylinder free to vibrate: a) power spectrum from each signal, b) acceleration wavelet spectrogram, c) pressure wavelet spectrogram, and d) velocity wavelet spectrogram.

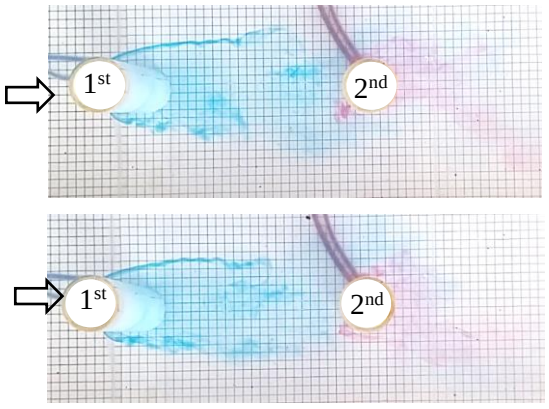

Figure 7. Flow visualization for cylinders in tandem with L/D = 5.

The results from Park et al. (2018) indicated that the effect of the WIV was the most significant at L/D of 3.0 and 4.0. In the results from Assi et al. (2010)

the amplitude of vibration increases for high reduced velocities for L/D up to 6.

3.4. Tandem Cylinders L/D = 8

For the case of L/D = 8, the power spectra of velocity, acceleration, and pressure fluctuation are presented in Fig. 8 a). In all cases, there is a peak at 50Hz that results in a Strouhal Number of 0.179.

The wavelet spectrogram presented in Fig. 8 b) shows the higher energy in the acceleration and the ranges with high energy are the same in the pressure and velocity signals, Fig. 8 c) and d). In Figure 8 b), it is visible that the levels of energy increase and decrease over time, as can be observed between 10 s and 15 s, where the level of energy is high at 10 s, decreases around 12 s, increases at about 14 s then decreases again.

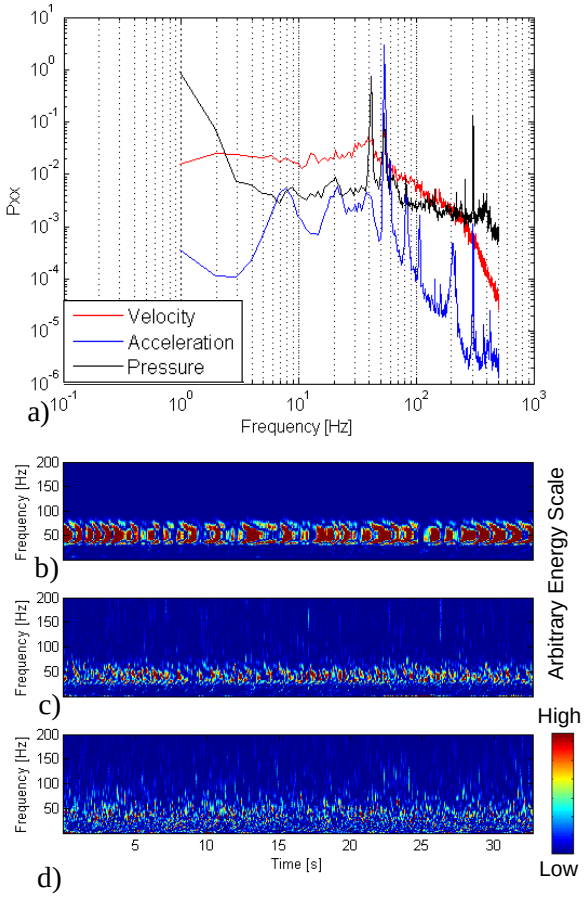

Figure 8. Cylinders in tandem with L/D = 8. Results for the second cylinder free to vibrate: a) power spectrum from each signal, b) acceleration wavelet spectrogram, c) pressure wavelet spectrogram, and d) velocity wavelet spectrogram.

The flow visualization for the tandem cylinders with L/D = 8 is presented in Figure 9 and shows the change in the second cylinder wake along time, with the wake one moment towards the upper side and sometimes towards the downside. This is a result of the first cylinder wake in the front of the second cylinder. Figure 9 shows that the side of the impact of the first cylinder wake, blue dye, is on the opposite side of the second cylinder wake, with red dye. This change in the second cylinder wake can be the mechanism associated with the energy changes observed in Fig. 8 b), since both cylinders are fixed in the flow visualization experiments.

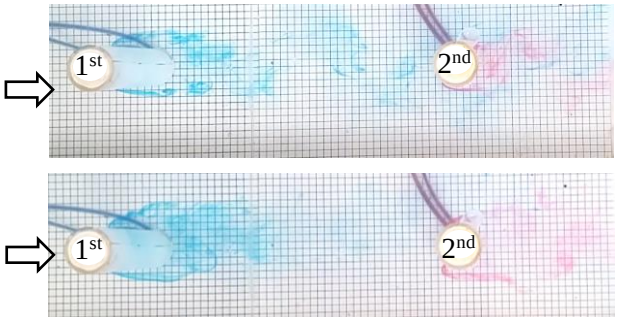

Figure 9. Flow visualization for cylinders in tandem with L/D = 8.

3.5. Tandem Cylinders L/D = 10

For the case with cylinders in tandem with L/D = 10, the natural frequency obtained in still air is 3.906 Hz with additional modes of vibration appearing at 12.7 Hz, 36.13Hz, and 55.6 Hz. The power spectrum from the acceleration, pressure, and velocity signals obtained with Re = 1.12 x 10^4 are presented in Fig. 10 a). The acceleration results show peaks at 6.8 Hz, 18Hz, 36 Hz, and 56 Hz, related to the vibration modes observed at the natural frequency.

The results for pressure and velocity present a peak at 56 Hz that is related to the vortex shedding and also the mode vibration of the cylinder.

In Figures 10 b), c), and d) the continuous wavelet transform is presented for acceleration, pressure, and velocity, respectively, and a region of high energy is observed around 50Hz in the acceleration, under 50 Hz in the pressure results, and without a clear region in the velocity.

The visualization results for L/D = 10 are presented in Figure 11 and the influence of the first wake is lower than for smaller space ratios but remains with influence by the way that the wake is formed behind the second cylinder. The visualizations show a higher impact from the first cylinder than the case with L/D = 2.5, as presented in Figures 4 and 5.

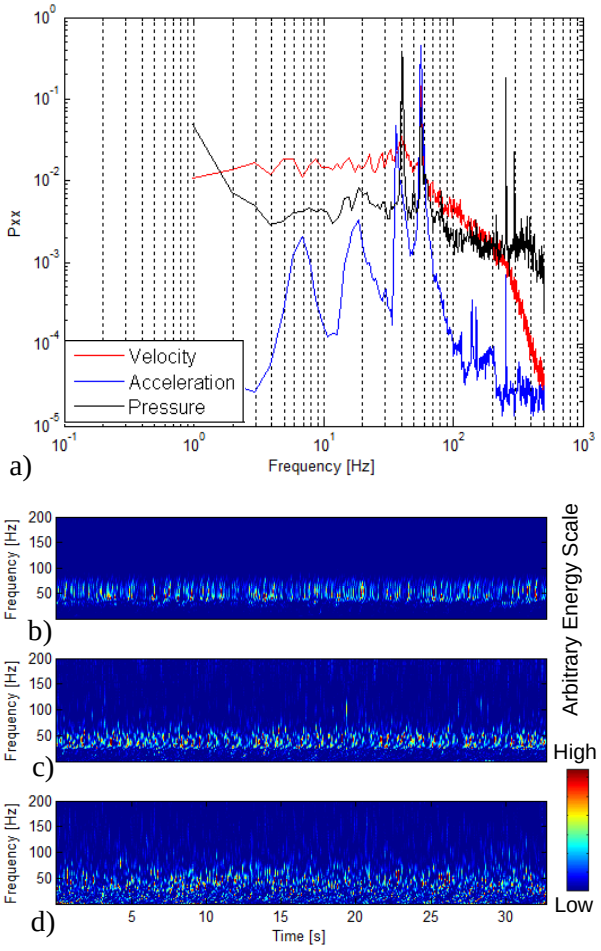

Figure 10. Cylinders in tandem with L/D = 10. Results for the second cylinder free to vibrate: a) power spectrum from each signal, b) acceleration wavelet spectrogram, c) pressure wavelet spectrogram, and d) velocity wavelet spectrogram.

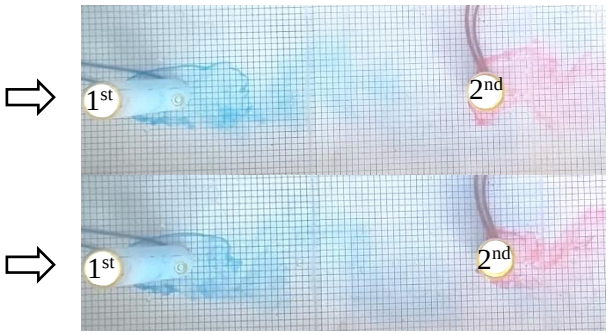

Figure 11. Flow visualization for cylinders in tandem with L/D = 10.

The results from Park et al. (2018) indicated that the effect of the wake interference decreased as L/D increased. For L/D of 10.0 it became similar to that of a single cylinder. This was not observed in the present analysis, where the acceleration magnitude s higher than for one single cylinder. The freedom of the first cylinder to vibrate can be the reason, why the pressure field would change the flow pattern on the first cylinder.

In the results from Assi et al. (2010) the vibration amplitudes remain higher than one single cylinder for all tested cases.

4. CONCLUDING REMARKS

The present study evaluated the influence of the wake of the first cylinder (upstream) on the second cylinder (downstream) for a tandem arrangement. The analysis was executed in an aerodynamic channel using measurements of the wake velocity and wall pressure fluctuations, as well as of the acceleration of the second cylinder, which was elastically mounted. Flow visualization in a water channel by injection of dye in the flow was used to complement the analysis from hot wires and microphones by observing the mechanisms of wake interaction at the tandem configurations analyzed.

Preliminary results showed that the increase in the distance between the cylinders, L/D, increases the influence of the first cylinder wake on the vibration mode of the second cylinder. This influence was observed in the acceleration magnitude of the second cylinder, in the levels of energy, and in the frequency response from the tested conditions. Further investigations for different Reynolds numbers will be conducted to confirm and extend the results.

The results from flow visualizations presented the influence of the wake of the first cylinder on the wake structure of the second cylinder, more pronounced for L/D = 5 and L/D = 8. This behavior observed in the wakes during the flow visualizations with two fixed cylinders can explain the vibration behavior of the second cylinder observed in the measurement results from the aerodynamic channel.

5. ACKNOWLEDGEMENTS

Brüel & Kjaer equipment was donated by KIT – *Karlsruhe Institut für Technologie*, Karlsruhe, Germany. Authors are gratefully indebted to Dr. L. Meyer.

This study was financed in part by the Coordenação de Aperfeiçoamento de Ensino Superior – Brasil (CAPES) – Finance Code 0001. Ana Paula Ost and Patrick Batista Habowski thank CAPES for their fellowships.

6. REFERENCES

Assi, G.R.S, Bearman, P.W. and Meneghini, J.R., 2010, On the wake-induced vibration of tandem circular cylinders: the vortex interaction excitation mechanism. *Journal of Fluid Mechanics* **661**: 365–401.

Bernitsas, M. M., Raghavan, K., Ben-Simon, Y., and Garcia, E. M. H., 2008, VIVACE (Vortex Induced Vibration Aquatic Clean Energy): A new concept in generation of clean and renewable energy from fluid flow. Journal of offshore mechanics and Arctic engineering, 130(4).

Blevins, R.D., 1990, *Flow-Induced Vibration*. 2nd Ed. New York: Van Nostrand Reinhold.

Derakhshandeh, J.F., Arjomandi, M., Dally, B., and Cazzolato, B., 2014, The effect of arrangement of two circular cylinders on the maximum efficiency of Vortex-Induced Vibration power using a Scale-Adaptive Simulation model. *Journal of Fluids and Structures* **49**: 654–666.

Igarashi, T., 1981, Characteristics of the flow around two circular cylinders arranged in Tandem. *Bulletin of the Japan Society of Mechanical Engineers* **24**: 323-331

Indrusiak, M.L.S., and Möller, S.V., 2011, Wavelet analysis of unsteady flows: Application on the determination of the Strouhal number of the transient wake behind a single cylinder. *Experimental Thermal and Fluid Science* **35**: 319–27.

Okajima, A., Yasui, S., Kiwata, T. and Kimura, S., 2007, Flow-induced streamwise oscillation of two circular cylinders in tandem arrangement. *International Journal of Heat and Fluid Flow* **28**: 552–560.

Park, C. Y., Lee, S. J., and Park, S. H., 2018, Experimental investigation of vortex-and wake-induced vibrations of tandem cylinders. *Ships and Offshore Structures*, **13(8)**: 877-884.

Soares, B., and Srinil, N., 2021, Modelling of wake-induced vibrations of tandem cylinders with a nonlinear wake-deficit oscillator. *Journal of Fluids and Structures*, **105**: 103340.

Woyciekoski, M.L., Endres, L.A.M, de Paula, A.V. and Möller, S.V., 2020, Influence of the free end flow on the bistability phenomenon after two side by side finite height cylinders with aspect ratios of 3 and 4 and high blockage. *Ocean Engineering* **195**: 1 -14.

Xu, W., Ji, C., Sun, H., Ding, W., and Bernitsas, M. M., 2019, Flow-induced vibration of two elastically mounted tandem cylinders in cross-flow at subcritical Reynolds numbers. *Ocean Engineer, **173**: 375-387*

WAKE-INDUCED VIBRATION IN TANDEM CYLINDERS: PART 2 – HILBERT-HUANG SPECTRAL ANALYSIS

Ana Paula Ost, Roberta Fátima Neumeister, Adriane Prisco Petry, Sergio Viçosa Möller

PROMEC/UFRGS, Federal University of Rio Grande do Sul, Porto Alegre, RS, Brazil

ABSTRACT

Flow-induced vibration of a cylinder in the wake of another cylinder in the tandem arrangement in an aerodynamic channel is experimentally investigated in the present study. The first cylinder is rigidly mounted inside the channel, while the second one is free to vibrate transversally to the main flow. The cylinder free to vibrate had a mass ratio of 539 and a damping ratio of 0.0169. Hot wires, microphones, and accelerometers are the experimental tools applied in this study. The Reynolds number obtained with the tube diameter and the main flow velocity ranged between $1.13x10^4$ and $2.29x10^4$. Hilbert-Huang Transform (HHT) is applied to analyze the acceleration results as well as velocity and pressure fluctuations. According to the literature, the wake-induced vibration (WIV) mechanism for tandem is sustained by unsteady vortex–structure interactions that input energy into the system as the second cylinder oscillates across the wake. As the second cylinder is moved farther downstream, vortices coming from the upstream wake have more time to diffuse and the resulting vortex–structure interaction is weakened. This paper presents the experimental study of the flow over two cylinders in tandem with L/D = 2.5 - 10, with the second cylinder free to vibrate. HHT is a tool of analysis for data emerged from non-linear and non-stationary systems and it is a combination of the Empirical Mode Decomposition (EMD) and the Hilbert Spectral Analysis (HSA). To successfully deal with the scale separation and the mode mixing, the Ensemble EMD (EEMD), a noise-assisted method, which is based on the statistical properties of white noise was used. The Hilbert Spectral analysis provides an accurate representation of the amplitude-frequency-time distribution of the flow. HHT is used to evaluate the velocity, pressure fluctuations, and acceleration results for two tandem cylinders, in an attempt to identify the relationship between the first cylinder perturbation and the second cylinder response.

1. INTRODUCTION

The importance of the study of the crossflow over cylinders in tandem is that they are simplifications of many engineering cases such as tube banks, transmission lines, buildings, and wind turbine towers, among others (Blevins, 1990). The main parameters associated with the tandem arrangement are L, which represents the distance between the cylinders, and D the cylinder diameter, as presented in the previous Part of this paper (Neumeister et al., 2022).

Most of the studies in the literature are focused on low space ratio, due to the direct interaction of the wake of the first cylinder with the second cylinder.

Data analysis in engineering is a necessary part of the determination of parameters, and the construction and validation of models that represent the studied phenomenon. Fourier analysis has dominated the data analysis and provided a general method for global energy-frequencies distributions, due to its simplicity being applied to all kinds of data, however, its application is limited since it cannot deal with series where the mean values vary with time (Abbate et al., 2002). Wavelet is another method that has been applied more recently in data analysis. The method consists of stretching and compressing the window of the windowed Fourier transform, according to the frequency to be localized, thus allowing the definition of all scales of interest in the time and frequency domain (Farge, (1992); Indrusiak et al., (2016)). It is a suitable method for linear and non-stationary data being very useful in analyzing data with gradual frequency changes. However, it also has limitations like border distortions, and energy leakage, which turns the interpretation of the results difficult.

Due to VIV non-linear and non-stationary characteristics, standard signal analysis techniques based on Fourier transform may not be sufficient. To overcome the limitations of the standard method a time-frequency analysis known as the Hilbert-Huang transform (HHT) was proposed for the analysis of non-linear and non-stationary data. HHT is a combination of the Empirical Mode Decomposition (EMD) and the Hilbert Spectral Analysis (HSA) (Huang et al., 1998).

The EMD is a direct and adaptive method, with a posteriori-defined basis derived from the data (Huang and Shen, 2005). The method identifies the intrinsic oscillatory modes by their characteristic time scales in the data; each of these oscillatory

modes is represented by an intrinsic mode function (IMF). The IMF can be considered a complete, adaptative, and almost orthogonal representation of the analyzed signal. Since it is almost a monocomponent, it can determine all the instantaneous frequencies from the non-linear, non-stationary data. Appling the Hilbert transform on the resulting IMF components, results in the HHT spectrum, which consists of an energy-time-frequency distribution and can localize any event in its corresponding time and instantaneous frequency (Peng et al., 2005). The Hilbert Spectrum can be defined through the following equation, where a_j is the instantaneous amplitude, and ω_j is the instantaneous frequency of the j^{th} IMF:

$$X_H(t) = \Re\left\{\sum_{j=1}^{n} a_j(t)\exp[i\int \omega_j(t)dt]\right\}. \quad (1)$$

The HHT has been employed in VIV investigations concerning a rigid cylinder assembled to elastic supports, cantilevered cylinders, and elastically mounted flexible cylinders, as can be found in Franzini et al. (2008), Franzini et al. (2014), Gonçalves et al.(2011), and Pesce et al. (2006)

Gonçalves et al., (2011) presented a study of Vortex-Induced Motion (VIM) using HHT as an analysis tool. The authors compared the results of motion obtained with the traditional methods and with HHT and concluded that for the motion in the transverse direction the differences were nonsignificant, but for the motion in-line direction, the differences in characteristic amplitude were about 25%. The authors point out that the results of HHT were more reliable than the traditional ones and that the method could be applied to other cases of fluid-structure interaction, like VIV of flexible cylinders.

Franzini et al., (2015) applied HHT analysis to a study of VIV in a long semi-immersed flexible cylinder. The results showed that the complimentary use of the Power Spectral Density (PSD) plots and the Hilbert spectrum analysis (HSA) is a fruitful analysis tool for the data obtained from a non-linear system under parametric excitation. The PSD plots indicate the existence of sum and difference frequencies, besides the fundamental one.

Ost et al. (2021-a) present the application of the Hilbert-Huang transform using the Ensemble Empirical Mode Decomposition (EEMD) to the analysis of hot wire signals obtained in the turbulent wake from circular cylinders.

In Ost et al. (2021-b), EEMD is applied to the analysis of signals of pressure and velocity fluctuations in the wake of a bistable flow behind two cylinders side-by-side. HHT results show all the instantaneous frequency modulations of the signals while the EEMD allows the identification of the most important oscillations of the flow that characterize bistability. However, the Hilbert spectra failed to identify the bistable flow.

The present analysis is an application of the Hilbert-Huang Transform (HHT) on the experimental study of the flow over two cylinders in tandem with L/D = 2.5 - 10, with the second cylinder free to vibrate normal to the flow direction. The use of HHT analysis of the influence of the wake from the first cylinder on the vibration regime of the second cylinder was chosen since HHT is suitable for non-linear and non-stationary data analysis.

2. METHODOLOGY

The test apparatus and main parameters associated with tandem arrangements are the same as those presented in the first part of this study, Neumeister et al., (2022). The test apparatus is an aerodynamic channel where a cylinder or a set of two cylinders in tandem arrangement and L/D values from 2.5 to 10 were placed, being the first cylinder (upstream) rigidly mounted on the channel walls and the second cylinder, downstream of the first is free to vibrate transversally to the flow. Velocity measurements were performed by DANTEC *StreamLine* constant hot-wire anemometry system. The acceleration was obtained with an analogic accelerometer, ADXL335, with the sensibility of 332 mV/g, a total scale of ± 3 g, and a natural frequency of 5.5 kHz. The pressure fluctuations are obtained with a Brüel and Kjaer condenser microphone.

The natural frequency and damping ratio were obtained from the free vibration signal, Fig. 1. The blockage ratio of the assembly is 13%.

The signal analysis is executed by means of the Hilbert-Huang Transform, assisted by the Fourier Transform.

3. RESULTS

3.1. Single cylinder

Figure 2 shows the power spectrum of acceleration, pressure, and velocity signals, respectively, together with the corresponding power spectral densities of the 8 first resulting IMF components, for the single-cylinder free to vibrate.

It is possible to see in the acceleration power spectra, Fig. 2a), some frequency peaks that are close to the natural frequency of the cylinder at 8.7 Hz and the second natural frequency at 21.5 Hz. Other frequencies are identified at 30.3Hz, 41Hz, 60 Hz, and 82Hz. The IMFs resulting from the EEMD are associated with specific frequency ranges. IMF 1(C1) corresponds to the highest frequencies in the signal, presenting peaks at 205 Hz and 303Hz

which are probably a result of noise. IMF 2 (C2) englobes the range of the spectrum where higher harmonics and the sum of frequencies are found. IMF C3 contains the vortex shedding frequency. IMF 4 and 5 (C4 e C5) contain the frequencies associated with the natural frequency and its harmonics.

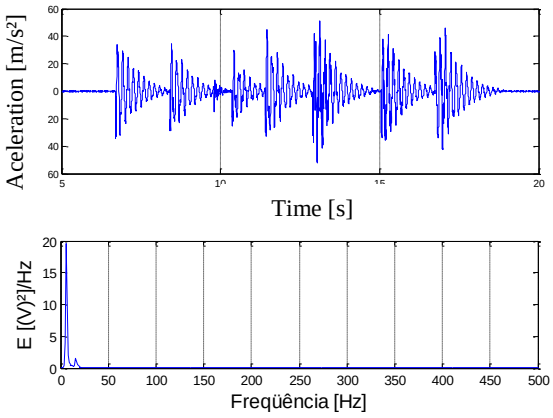

Figure 1. a) Free oscillation test for single cylinder and b) Power spectrum of the oscillation test signal.

In the power spectrum of pressure fluctuation, Fig. 2b), the frequency peaks identified are 41 Hz, 60 Hz, 82 Hz, related to the natural frequency and harmonics, and sums of main frequencies and harmonics, and 303.7 Hz which has no physical meaning, being an artifact caused likely by noise. The IMF 1 (C1) corresponds to the highest frequency, and in this case englobes the noise content of the signal. IMF 2 (C2) does not present any specific frequency but is located in the range of 100 – 175 Hz. The frequency peaks of 82 Hz and 60 Hz can be identified in IMF 3(C3). IMF 4 (C4) presents the small scales of the fluctuating signal, and the 41 Hz frequency, which is possibly a frequency generated by the aerodynamic channel.

In the velocity power spectrum, Fig. 2c), the only frequency identified is the vortex shedding frequency at 51,7Hz, which corresponds to a Strouhal number of 0.18. The IMFs in this context represent the flow scales. The smallest scales in the flow and the highest frequencies are englobed by C1 and C2. Component C3 corresponds to the vortex shedding frequency and the coherent part of the flow. IMFs C4 to C8 correspond to the largest scales in the flow. IMFs higher than C8 do not have physical meaning, being generated by the decomposition method, and are, therefore, discarded.

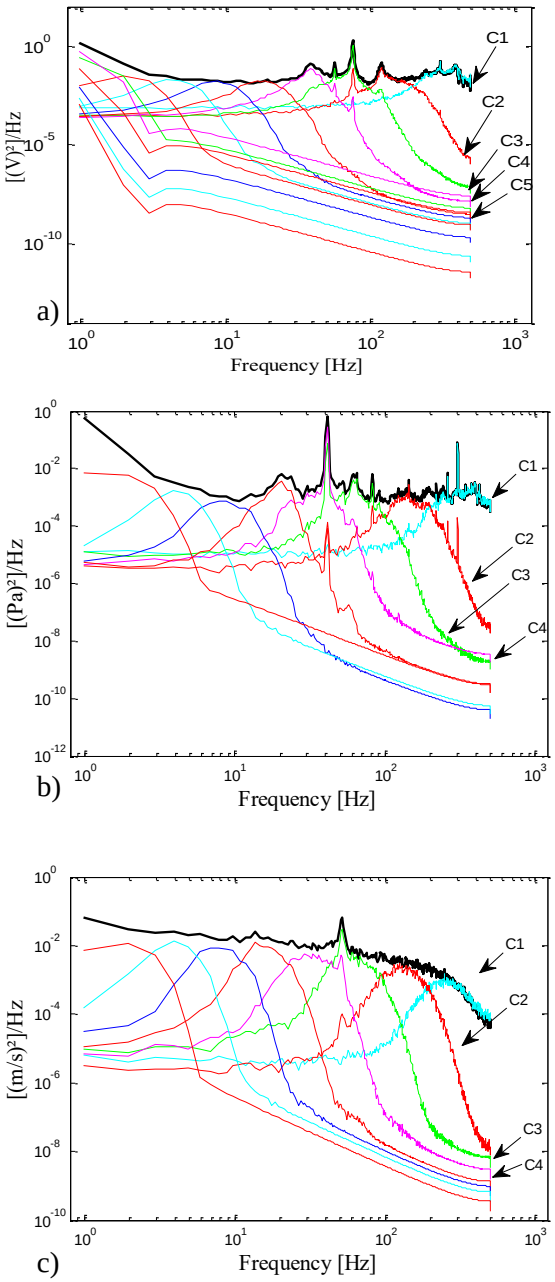

Figure 2. Power spectral density of 8 first IMF for a) acceleration, b) pressure fluctuation, and c) velocity for a single-cylinder free to vibrate.

Figure 3 shows the Hilbert spectrum of acceleration, pressure, and velocity for the 8 first IMF components. One can see that for all three cases the highest concentration of energy is in the range of 51 Hz. In the Hilbert spectrum for acceleration signal, Fig. 3a), there are also energy concentrations in the low frequencies close to the natural frequency and harmonics and at the high frequencies, in the range of 250 to 350 Hz. Those high frequencies are probably generated by external noise and have no physical meaning.

In the Hilbert spectrum of pressure, Fig. 3b), the energy mainly concentrates close to 50 Hz. Due to the highest fluctuations, there is a dispersion in the higher frequencies not being possible to identify any specific frequency value.

Figure 3c) presents the Hilbert spectrum of the velocity signal. Since the velocity IMFs are very smooth and with a filter bank characteristic, the Hilbert spectrum presents a dispersion of energy in a very wide range of frequencies. No main concentrations of energy can be identified in the Hilbert spectrum of the velocity signal.

3.2. Tandem Cylinders L/D = 2.5

Figure 4a) shows the displacement for the tandem configuration with L/D = 2.5 and Re = 1.15×10^4. The power spectrum of the displacement is shown in Fig. 4b). The spectrum shows frequency peaks at 8.7 Hz and 21 Hz that can be related to the first and second natural frequencies.

The Hilbert spectrum of the displacement is represented in Fig. 5. Only the 4 first IMFs, which are the ones with considerable frequency content, are shown. In this case, IMFs with higher-order present frequencies close to zero and are not physically significant. One can see that the energy concentrated mainly around 8Hz, and in the range of 50 and 70 Hz, which could be associated with the vortex shedding, also some frequency modulation is seen in the range of 20 Hz and could be associated with the natural frequency harmonic.

Figure 6 shows the Hilbert spectra of the 8 first IMFs, for acceleration, pressure, and velocity signals. In the acceleration Hilbert spectrum, Fig. 6a), is possible to notice that the mains amplitudes concentrate around 50 Hz, which is the vortex shedding frequency. Some dispersion is seen around 300 Hz, probably a consequence of noise.

In the Hilbert spectrum of the pressure fluctuation shown in Fig. 6b) the main concentration of energy is in the range of 40 Hz. The energy also disperses around 140 Hz and 300 Hz, probably as a result of the high fluctuations in the pressure signal. In the velocity Hilbert spectrum, Fig. 6c) the energy concentrates mainly around 50 Hz, which is the vortex shedding frequency.

3.3. Tandem Cylinders L/D = 5

The displacement for the two cylinders in a tandem arrangement, with L/D = 5, and Reynolds number Re = 1.15×10^4 is shown in Fig. 8a). The power spectrum of the displacement is in Fig. 8b).

The increase in the L/D ratio resulted in an increase in the mean amplitude and the maximum displacement for the L/D = 5. This behavior is probably caused by the influence of the wake of the first cylinder in the second one, and by the increase in the acceleration values for this spacing ratio.

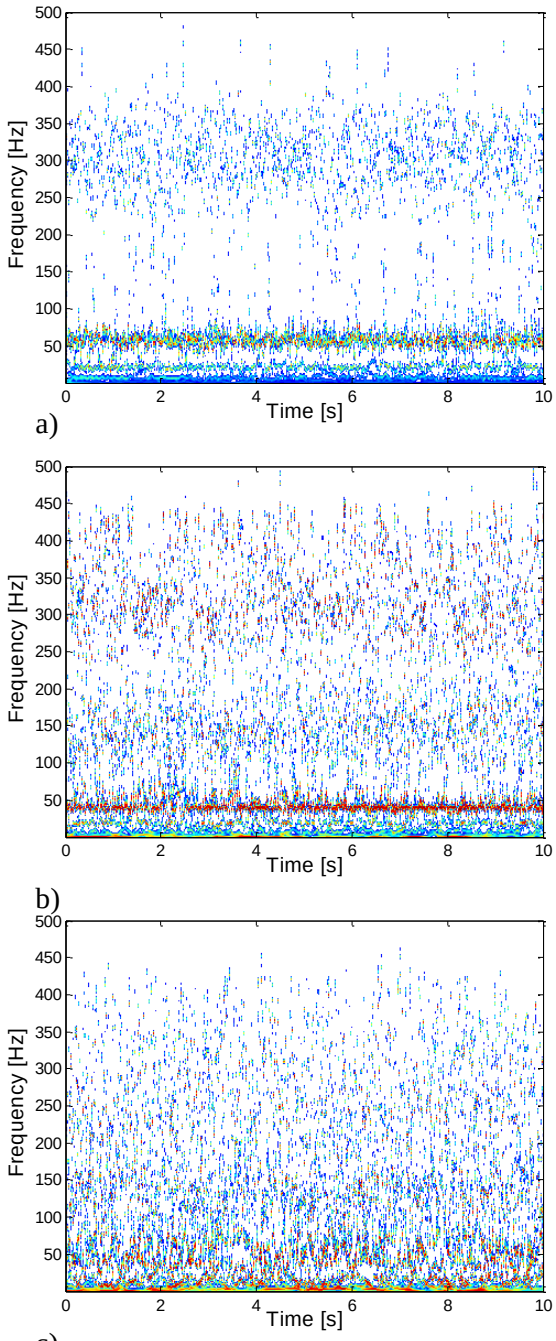

Figure 3. Hilbert Spectrum of 8 first IMF a) acceleration, b) pressure fluctuations, and c) velocity, for single cylinder free to vibrate.

In the power spectrum, Fig. 8b) the frequency peaks are 8.1 Hz and 20 Hz, associated with the natural frequencies of the cylinder.

The Hilbert spectrum of the 4 first IMFs from the displacement time series is presented in Fig. 9. The main amplitudes are concentrated around 8 Hz, associated with the natural frequency. Some frequency modulation is visible around 20 Hz and the nonlinear behavior can be observed in the discontinuous way the modulations appear. Some ampli-

tude concentrates around 50 Hz, associated with the vortex shedding frequency.

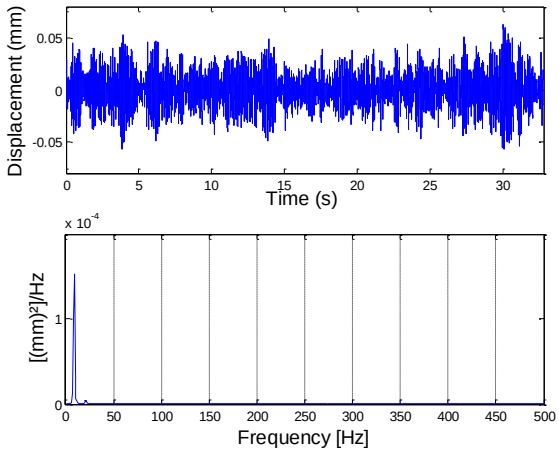

Figure 4. a) Displacement time series b) Power spectrum of displacement data, for L/D = 2.5.

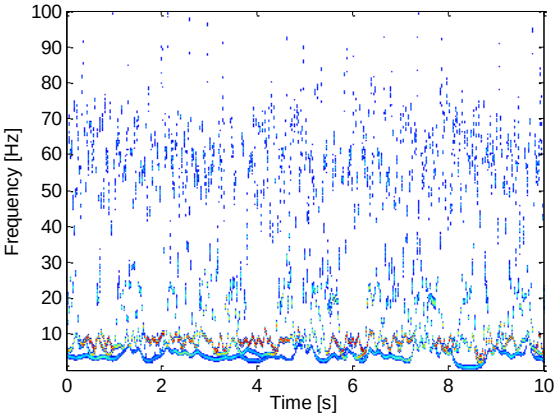

Figure 5. Hilbert Spectrum of 4 first IMF for displacement data. L/D = 2.5.

The Hilbert spectra of the 8 first IMF components for acceleration, pressure fluctuations, and velocity signals are presented in Fig. 10. As can be seen in the Hilbert spectrum of the acceleration, Fig. 10.a), the increase in the acceleration amplitudes caused the IMFs to disperse in a wider range of frequencies rather than highly concentrate on one specific frequency. Some amplitude concentrations can still be identified around 50 Hz.

The Hilbert spectrum of the pressure fluctuation, in Fig. 10.b) also presents the main energy around 50 Hz. Energy dispersion can be identified in the high frequencies.

However, in the Hilbert spectra of the velocity, presented in Fig. 10.c) the energy has a broad scattering around the shedding frequency of 5o Hz. This behavior is probably a consequence of the influence of the first cylinder wake on the second cylinder wake together with the displacement of the latter.

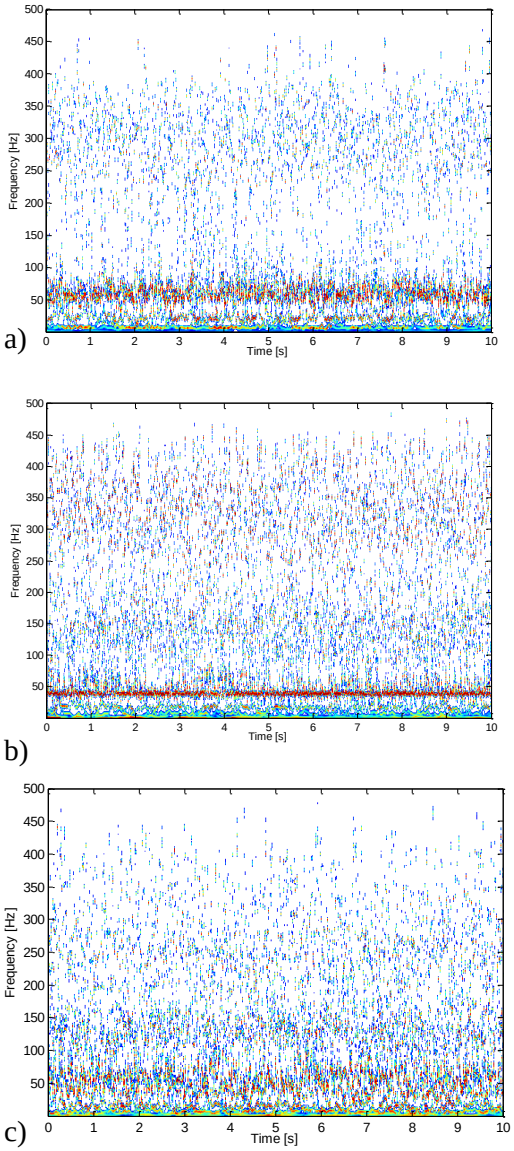

Figure 7. Hilbert spectrum of the 8 first IMFs for a) acceleration, b) pressure, and c) velocity for L/D = 2.5.

3.4. Tandem Cylinders L/D = 8

Figure 11a) shows the displacement time series for two tandem cylinders with L/D = 8, Re = 1.15×10^4. In this case, the mean amplitude remained close to the L/D = 5 cases, but the maximum value of the displacement increased. Table 1 summarizes the values of mean amplitude, maximum displacement, and standard deviation for the various L/D ratios at the same Reynolds number.

In the power spectrum, Fig. 11b) the frequency peak is at 7.8 Hz, associated with the natural frequency, 53.7 Hz, which is related to the vortex shedding frequency, and a small peak can be seen at 20.5 Hz and can be associated with the second natural frequency.

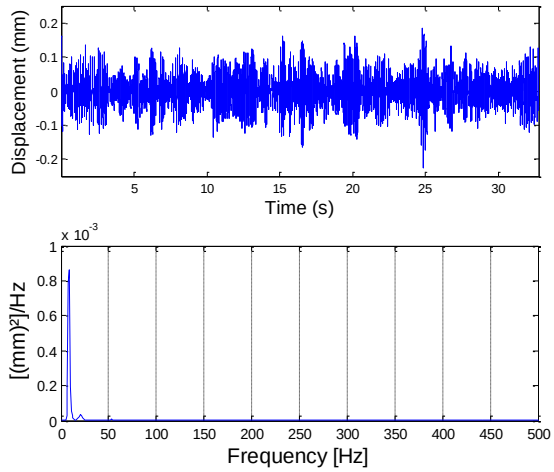

Figure 8. a) Displacement time series b) Power spectrum of displacement data, for L/D = 5.

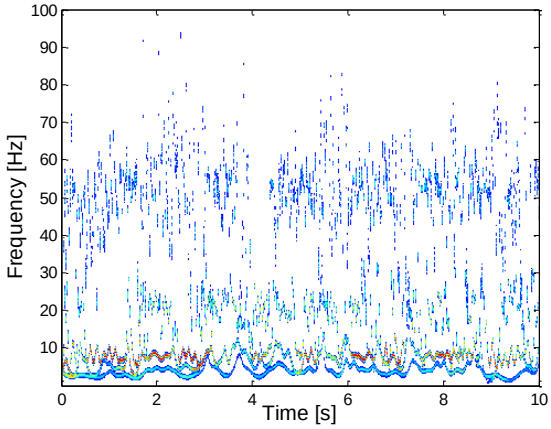

Figure 9. Hilbert Spectrum of 4 first IMF for displacement data. L/D = 5.

The Hilbert spectrum of the 4 first IMFs for the displacement is shown in Fig. 12. The amplitudes concentrate in a frequency lower than 10 Hz, which is related to the natural frequency visible in the power spectra. Also, the energy concentrates in the range between 50 Hz and 60 Hz, which is in the vortex shedding range. In this frequency band, it is possible to see a beat-like behavior, which is due to the changes in the wake influence on the second cylinder for L/D = 8, as shown in the flow visualizations in the first part of this study, Neumeister et al., (2020). Frequency modulation can also be identified in the range of 20 – 40 Hz.

The Hilbert spectra of the first 8 IMF components for acceleration, pressure fluctuations, and velocity, for L/D = 8, are presented in Fig. 13.

As can be seen in the acceleration Hilbert spectrum, Fig. 13a) the amplitude concentrates mainly in the range of 50 Hz, and the same beating-like behavior visible in the displacement Hilbert spectrum (Fig. 12) can also be seen here.

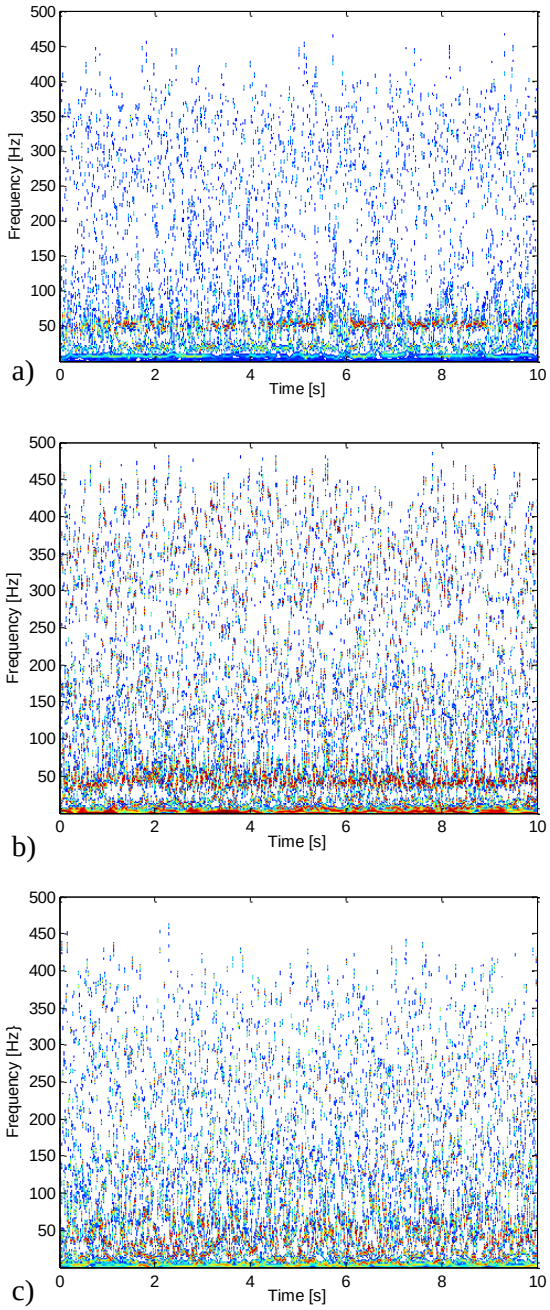

Figure 10. Hilbert spectrum of the8 first IMFs for a) acceleration, b) pressure, and c) velocity, for L/D = 5.

In the Hilbert spectrum of pressure fluctuation, shown in Fig. 13b) it is possible to see that the energy tends to concentrate mainly at 50 Hz, but some dispersion around 300 Hz can also be identified.

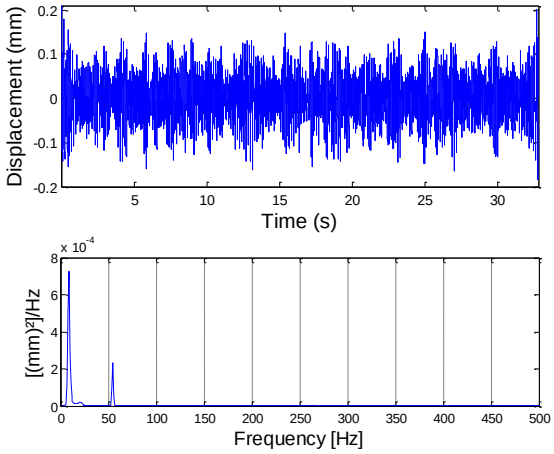

Figure 11. a) Displacement time series b) Power spectrum of displacement data, for L/D = 8.

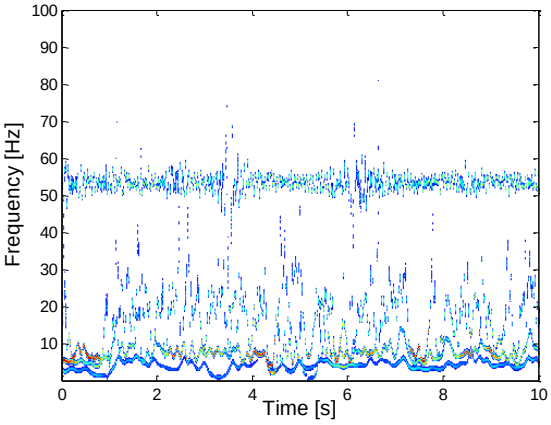

Figure 12. Hilbert Spectrum of 4 first IMF for displacement data. L/D = 8.

In the Hilbert spectrum of the velocity, in Fig. 13c) no energy concentration on specific frequencies can be identified, the energy tends to accumulate in frequencies lower than 50 Hz, but it also disperses in the higher frequencies. This behavior is probably caused by the influence of the first cylinder wake.

4. CONCLUDING REMARKS

This paper presented a study on the application of the Hilbert-Huang Transform (HHT) on the analysis of wake-induced vibration (WIV) for two cylinders in tandem configuration, for L/D ratios from 2.5 to 8. Hilbert-Huang Transform (HHT) was used as the analysis tool, due to the non-linear, non-stationary characteristics of WIV.

Results show that HHT is a suitable tool for the analysis of fluid-structure interactions. The vibration modes can be identified by the IMF components. The influence of the first cylinder wake causes significant changes in the Hilbert spectrum energy levels

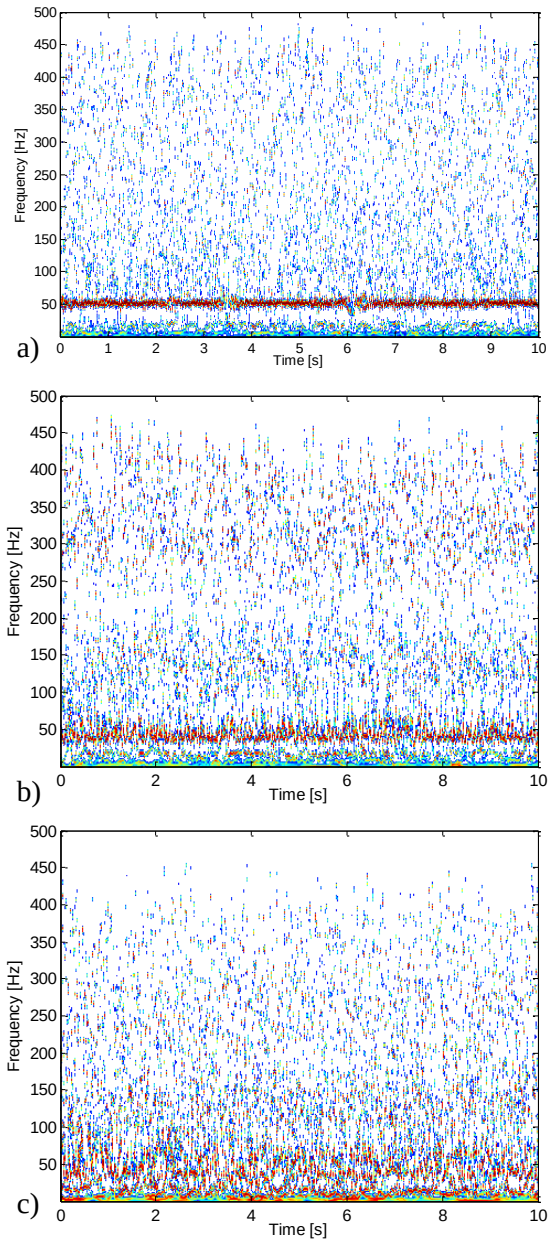

Figure 13. HS of a) acceleration, b) pressure, and c) velocity 8 first IMF for L/D = 8.

L/D	Mean Amplitude [mm]	Maximum disp. [mm]	Standard Deviation [mm]
2.5	0.0147	0.0628	0.0112
5	0.0409	0.1844	0.0364
8	0.0396	0.2284	0.0266

Table 1. Mean amplitude and maximum displacement for various L/D, Re = 1.15x10^4.

5. ACKNOWLEDGEMENTS

Brüel & Kjaer equipment was donated by KIT – *Karlsruhe Institut für Technologie*, Karlsruhe, Germany. Authors are gratefully indebted to Dr. L. Meyer.

This study was financed in part by the Coordenação de Aperfeiçoamento de Ensino Superior – Brasil (CAPES) – Finance Code 0001. Ana Paula Ost thanks CAPES for her fellowship.

6. REFERENCES

Abbate, A., DeCusatis, C.M., Das, P.K., 2002. *Time-Frequency Analysis of Signals*, in Wavelets and Subbands, Applied and Numerical Harmonic Analysis. Birkhäuser, Boston, MA, pp. 103–187.

Blevins, R.D., 1990, *Flow-Induced Vibration*. 2nd Ed. New York: Van Nostrand Reinhold.

Farge, M., 1992. Wavelet transforms and their applications to turbulence. *Annual Review of Fluid Mechanics*, v. 24, n. 1, p. 395–458.

Franzini, G.R., Pereira, A.A.P., Fujarra, A.L.C., Pesce, C.P., 2008, Experiments on VIV under frequency modulation and at constant Reynolds number. In: Proceedings of OMAE 08, 27th international conference on offshore mechanics and arctic engineering.

Franzini, G.R., Pesce, C.P., Gonçalves, R.T., Fujarra, A.L.C., Pereira, A.P.P., 2011, Concomitant vortex-induced vibration experiments: a cantilevered flexible cylinder and a rigid cylinder mounted on a leaf-spring apparatus. In: Proceeding of the XIV international symposium on dynamic problems of mechanics DINAME 2011.

Franzini, G.R., Pesce, C.P., Gonçalves, R.T., Fujarra, A.L.C., Pereira, A.P.P., 2015, Vortex-induced vibration experiments with a long semi-immersed flexible cylinder under tension modulation: Fourier transform and Hilbert–Huang spectral analyses. *Journal of the Brazilian Society of Mechanical Sciences and Engineering*, [s. l.], v. 37, n. 2, p. 589–599.

Gonçalves, R.T., Franzini, G.R., Rosetti, G.F., Fujarra, A.L.C., Nishimoto, K., 2011, Analysis Methodology for Vortex-Induced Motion (VIM) of a Monocolumn Platform Applying the Hilbert–Huang Transform Method. *Journal of Offshore Mechanics and Arctic Engineering*, [s. l.], v. 134, n. 1, p. 011103-011103–7.

Gonçalves, R.T., Franzini, G.R., Rosetti, G.F., Fujarra, A.L.C., Nishimoto, K., 2012, Analysis methodology for vortex-induced motion (VIM) of a monocolumn platform applying the HilbertHuang transform method. *J Offshore Mech Arct Eng* 134:0111031–011103-7.

Huang, N.E., Shen, S.S., 2005. *Hilbert-Huang Transform and Its Applications.* World Scientific, Singapore.

Huang, N.E., Shen, Z., Long, S.R., Wu, M.C., Shih, H.H., Zheng, Q., Yen, N.-C., Tung, C.C., Liu, H.H., 1998. The empirical mode decomposition and the Hilbert spectrum for nonlinear and non-stationary time series analysis. *Proc. R. Soc. Lond. A: Math. Phys. Eng. Sci*. 454, 903–995.

Indrusiak, M.L.S., Kozakevicius, A.J., Möller, S.V., 2016. Wavelet analysis considerations for experimental nonstationary flow phenomena. *Engenharia Térmica (Thermal Engineering)*, 15, 67-76. Available at:

Neumeister, R. F., Ost, A.P., Habowski, P., de Paula, A.V., Petry, A.P., Möller, S.V., 2020, Wake Induced Vibration in tandem cylinders: Part 1 – Wake perturbation analysis. In this Conference: Flow-Induced Vibration, Paris-Saclay, 2022.

Neumeister, R. F., Petry, A. P., & Möller, S. V., 2021. Experimental Flow-Induced Vibration Analysis of the Crossflow Past a Single Cylinder and Pairs of Cylinders in Tandem and Side-by-Side. Journal of Pressure Vessel Technology, 143(3).

Ost, A.P., Neumeister, R. F.; Möller, S. V. 2021-a, Analysis of wake velocities and pressure fluctuations in a bistable flow using Hilbert-Huang transform and wavelets. Journal of the Brazilian Society of Mechanical Sciences and Engineering, v. 43, p. 65.

Ost, A.P., de Paula, A. V.; Möller, S. V., 2021-b, Signal Analysis Through the Ensemble Empirical Mode Decomposition and Hilbert-Huang Transform-Application to Vortex Shedding. In: J. M. Balthazar. (Org.). Mechanisms and Machine Science. 1ed.Berlin: Springer International Publishing, p. 95-120.

Peng, Z. K.; Tse, P. W.; Chu, F. L., 2005 An improved Hilbert–Huang transform and its application in vibration signal analysis. *Journal of Sound and Vibration*, [s. l.], v. 286, n. 1–2, p. 187–205.

Pesce, C.P., Fujarra, A.L.C., Kubota, L., 2006, The Hilbert–Huang spectral analysis method applied to VIV. In: Proceedings of the 25th international conference on offshore mechanics and artic engineering OMAE2006, Hamburg, Germany.

Bio-mechanical FSI

MITIGATING JET CROSS-FLOW INDUCED VIBRATIONS USING A BIO-INSPIRED NOZZLE

Ibrahim Gad-el-Hak, Njuki Mureithi
Department of Mechanical Engineering, Polytechnique Montréal, Montreal, QC H3C 3A7, Canada
Kostas Karazis
Framatome Inc., 3315 Old Forest Road, Lynchburg, VA 24506, U.S.A

ABSTRACT

Sharks discharge a large amount of water flow after the oxygen has been extracted during ram ventilation. The efficient mixing of jet flow exiting the gill openings allows sharks to still have smooth mobility. In many industrial devices, a rapid mixing of jet flows is the important feature to ensure efficient operation. Furthermore, jet flow is critical in the design and operation of specific nuclear pressurized water reactors (PWRs). Jet flows are introduced into these reactors through multiple holes drilled in the baffle plate that surrounds fuel assemblies. The objective of these holes is to release the pressure build-up during a potential loss-of-coolant accident (LOCA). However, during normal operation, the jet flow could induce unwanted fuel rod vibration.

Preventing fuel rods vibration can be achieved by improving the mixing process between jet flow and the surrounding fluid. A biomimetic "shark nozzle" is proposed here to improve mixing between a jet flow and surrounding fluid. Thus, the jet momentum reaching the rods is reduced. The experimental results show that the new shark-inspired biomimetic nozzle has a greater stabilizing effect on rod bundle. Utilizing the biomimetic nozzle delays the critical velocity by 28%. In addition to postponing instability, utilizing the proposed shark-inspired nozzle instead of the circular nozzle resulted in an 88% reduction in post-instability vibration amplitudes.

1. INTRODUCTION

Jet flows have been investigated by extensive experimental and analytical work as reviewed by Ball et al. (2012). A jet is defined as a flow exiting from a nozzle (plane or round) into a surrounding fluid. Two main regions develop in jet flow: (i) the potential core region, and (ii) the shear layer region, as define in (Lee et al. , 2003). The flow velocity in the potential core region has the same velocity as the average exit velocity from the nozzle. The mixing and entrainment processes that take place between the potential core and the surrounding fluid create the shear layer region. The jet boundary is spread in the radial direction with downstream distance until viscous action dissipates energy and causes the jet to dissipate.

Circular and plane jets are used in many mechanical applications to transfer heat and mass between two fluids. Examples include gas burners, gas mixers, heat exchangers, and atomizers. Rapid mixing and potential core decay are key parameters to determine the efficiency of these devices. In nuclear engineering applications, jet flow is a safety feature designed to relieve pressure build-up in the event of a loss-of-coolant accident (LOCA). However, jet-induced fuel rod fretting near LOCA holes has been observed during normal operations of these reactors (IAEA , 2019). Enhancing the mixing between the injected flow from the LOCA holes with the surrounding flow around fuel rods could be an effective solution to mitigate fretting and wear of fuel rod due to jet cross-flow. Many studies have looked into passive flow control techniques for enhancing the rate of jet mixing in circular nozzle flows (Behrouzi et al. , 2008; Thangaraj et al. , 2022; Reeder and Samimy , 2008). Vortex generator tabs at the exit plane of the nozzle have been used to enhance the mixing rate. However, the mixing efficiency of tab-controlled jets depends on the tab geometry, tab number, tab orientation, tab size, and tab position relative to nozzle outlet. These parameters are still under investigation and need to be optimized.

Nature-inspired innovations can lead to problem solving opportunities that have previously been ignored. An example of applied biomimicry from birds is feather structure. Gad-el-Hak (2019) was inspired by bird feather structures, which ensure stable flying by resisting aerodynamic pressures in addition to their lower weight. The author designed a biomimetic composite turbine blade to be used for a low-temperature organic Rankine cycle (ORC) turbine. The same barb angle inspired by the bird feather was used to reduce deflection of the rotor blades, resulting in an 80 percent weight reduction of biomimetic blades over stainless steel rotor blades.

Sharks obtain oxygen from the surrounding water using their gill slits to absorb oxygen from the water and expel carbon dioxide from their bodies. The gill slits are located behind shark's head as shown in Figure 1. From an engineering point of view, the water that passes through the slits and into the ocean corresponds to a jet in cross-flow (JICF). Interestingly, these jet flows from slits are ejected with little influence on the sharks, allowing them to maneuver more smoothly and swim faster.

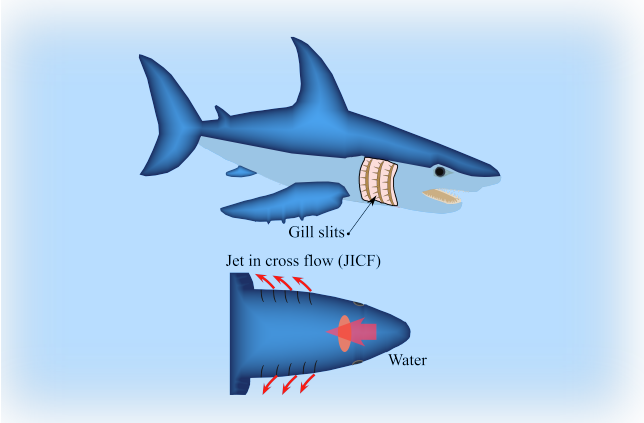

Figure 1. Biomimicry approach for proposing bio–inspired nozzle.

Inspired by sharks, a new biomimetic nozzle design is proposed in this work to improve the mixing rate of the jet flow with the surrounding flow. The biomimicry solution to mitigate jet cross-flow induced vibrations we propose is to circumferentially attach equal spaced thin fins to the circular nozzle to improve the mixing process as happens with gill slits. The effectiveness of the suggested biomimetic solution to delay the critical velocity at which unstable vibrations initiate is examined in this work by comparing the rod array vibration obtained from two nozzles, a plain circular nozzle and the shark-inspired nozzle.

2. BIO-INSPIRED NOZZLE DESIGN

The performance of the biomimetic inspired-shark nozzle design is experimentally evaluated by testing rod bundle vibration. The rod array response is measured and compared for two nozzles, a circular nozzle, and the shark-inspired nozzle. Figure 2 shows the two tested nozzles. The base diameter is the same for both nozzles. However, very thin fins (1 mm thick) are printed circumferentially and integrated at the circular nozzle base as shown in Figure 3, mimicking a shark's secondary lamella.

Gad-el-Hak et al. (2021) experimentally studied the effect of different jet flow parameters on a 6x6 rod array vibration. Jet eccentricity (ξ) was shown

Figure 2. (a) circular nozzle, and (b) shark-inspired nozzle.

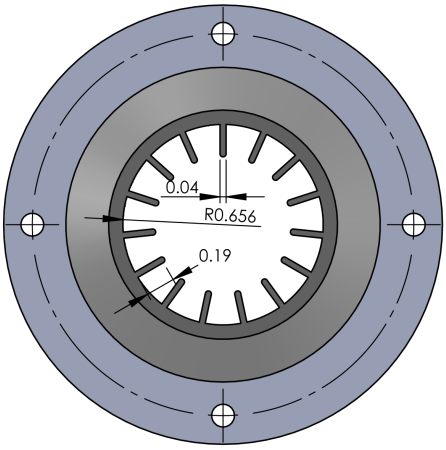

Figure 3. Detailed dimensions of the shark nozzle, all dimensions are in inches.

to be one of the most important parameters that affect the rod array stability. This parameter is defined as the transverse offset between the jet centreline and the array centerline as shown in Figure 4a. The authors found an offset of 25% of pitch makes the array more unstable compared to other two tested cases, ξ = 0 and 0.5P due to antisymmetric flow conditions around rods as shown in Figure 4b. In this study, this eccentricity (ξ = 0.25P) is selected to perform the fluidelastic instability (FEI) tests.

3. EXPERIMENTAL SETUP

FEI experiments were performed to determine the effect of the biomimetic nozzle on jet cross-flow induced vibrations. A 6x6 axisymmetric rod bundle

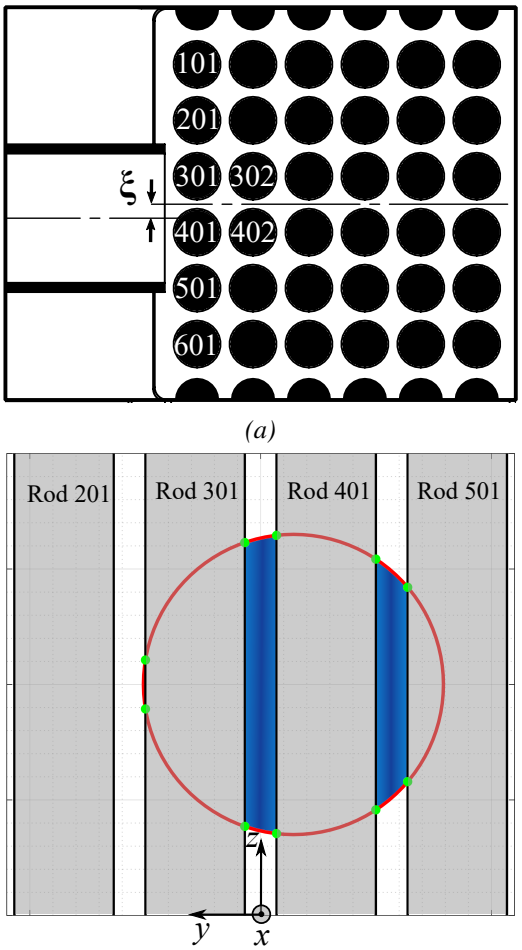

Figure 4. (a) Top view showing jet eccentricity with rod array for $\xi = 0.25P$, and (b) schematic drawing for the nozzle boundary with the rods in the array for $\xi = 0.25P$.

was subjected to localized jet cross-flow from the two nozzles. All flexible rods have frequency of 29 Hz in water. Simulating a fuel assembly, the rods are arranged in a square lattice with a pitch-to-diameter ratio (P/D) of 1.32 with a reduced length of 8 inches. The nozzles are positioned to provide jet flow at rod mid-span elevation. Figure 5 shows the test section with the rod bundle installed. The test section is designed to investigate rod bundle vibration under different jet flow conditions that induce fluid-elastic instability. A full-field vibration measurement is required to have an understanding of how the vibration changes in the direction of the decaying potential core. To achieve this, the rod array vibration is captured using a high-speed camera (Motion BLITZ Cube 4, MIKROTRON). A series of raw images of the rod bundle vibration is recorded and exported for image processing. Time traces of each rod's vibration are obtained by tracking the rod center in time.

As shown in Figure 5, the camera is perpendicularly installed above the top acrylic cover panel to view the 36 rods in the array.

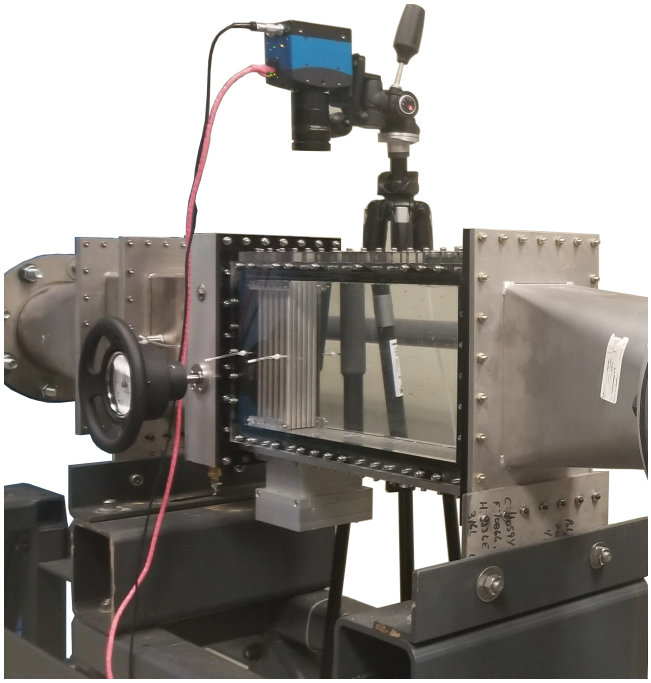

Figure 5. Test section showing installed rod bundle.

4. TEST RESULTS

4.1. Circular nozzle results

The vibrational behavior of the rod array is obtained for a range of jet velocities. The resultant rod RMS displacement is used in this study to quantify vibration response. Figure 6 shows the RMS response of the rod bundle subjected to the circular jet cross-flow. The rod array response is measured for a jet velocity range from 0.75 to 1.75 m/s. The resultant RMS vibration response normalized by the gap (gap=P-D). For brevity, we present the rod responses for the first two rows. The vibration of 12 rods is shown in Figure 6. The rods are excited by turbulence in the jet flow in the range of jet velocity from V_{Jet}= 0.75 m/s to 1.45 m/s as confirmed by the wide bandwidth PSD in Figure 7a. The critical jet velocity of 1.45 m/s is the stability boundary for the rod array for the circular nozzle case. Above this limit, the response increased sharply. Due to the tight spacing of this array, all rods vibrate above this velocity with different vibration amplitudes. As shown in Figure 7b, this corresponds to the phenomena of fluidelastic instability (FEI), in which rods vibrate sinusoidally at the single natural frequency of the rod bundle. The experimental results with the circular nozzle are considered as

a reference case to compare and evaluate the performance of the proposed bio-inspired nozzle.

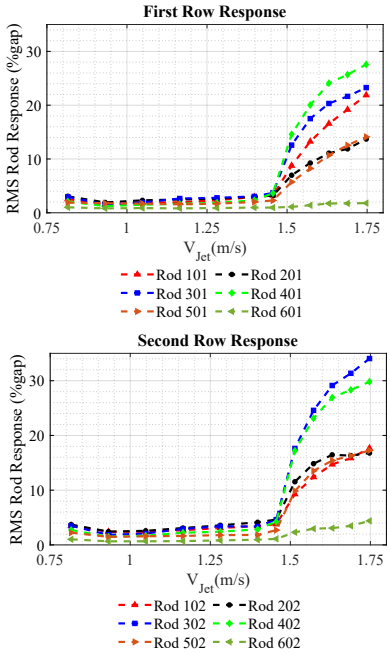

Figure 6. Two rows response with the circular nozzle.

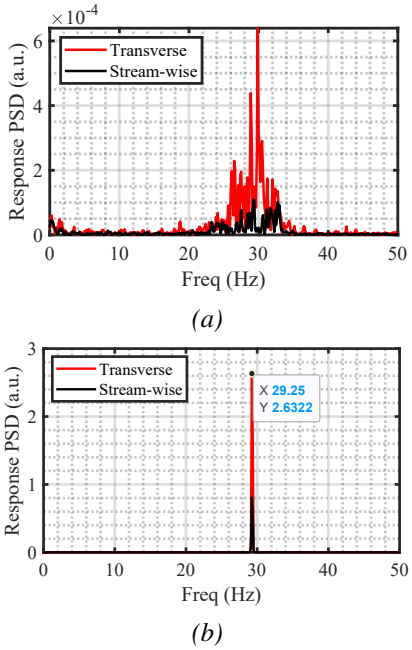

Figure 7. PSD for rod 401 with jet velocity: (a) V_{Jet} = 1 m/s, and (b) V_{Jet} = 1.6 m/s.

4.2. Shark-inspired nozzle performance

The circular nozzle is replaced by the shark-inspired nozzle with 15 fins in the test section to investigate the modified nozzle's effect on the rod array vibration. Figure 8 shows the response of the same 12 rods presented for the circular nozzle. As seen in the figure, the shark-inspired nozzle has a significant stabilizing effect on the rod bundle vibration.

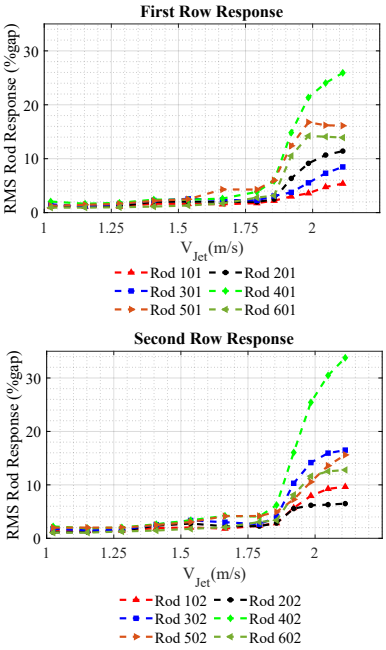

Figure 8. Two rows response with the shark-inspired nozzle.

The critical jet velocity is significantly delayed, from 1.45 m/s to 1.85 m/s. In comparison to the circular jet test, the rod 301 response is mitigated by 88% as shown in Figure 9.

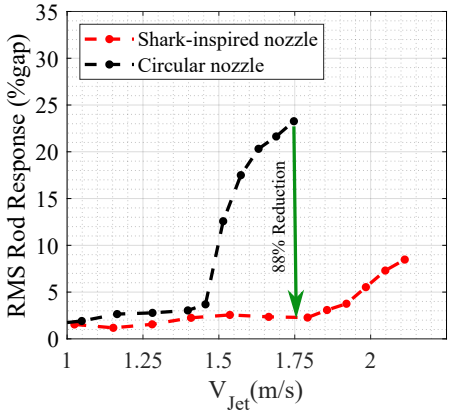

Figure 9. Comparison of rod 301 response with two tested nozzles, shark-inspired nozzle and circular nozzle.

5. DISCUSSION

A new biomimetic nozzle based on shark gill slits is designed in this work to suppress jet cross-flow induces vibrations by providing efficient and quick mixing between the jet flow and surrounding fluid. CFD simulations are performed to elucidate the mixing mechanism of the shark-inspired nozzle. Due to 3D flow feature of circular nozzle, 3D CFD models of the two nozzles are generated in ANSYS-DesignModeler as shown in Figure 10. The computational domains of the nozzles consist of two subdomains, (i) nozzle domain, and (ii) test section domain.

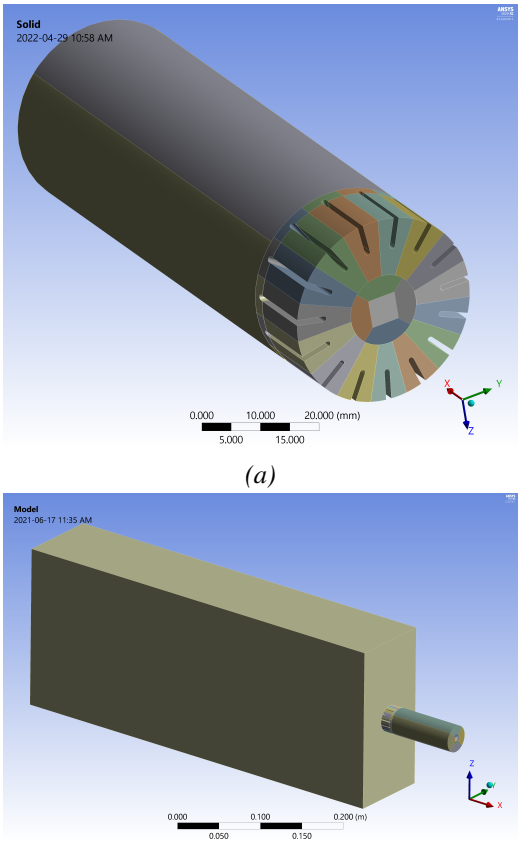

(a)

(b)

Figure 10. Computational domains: (a) the shark nozzle, and (b) the test section domain.

The nozzle injects produces high shear flow. Therefore selecting a proper turbulence model to simulate this flow is an important step. Laribi et al. (2012) compared results using three turbulence models, $k-\varepsilon$, $k-\omega$, and Reynolds Stress Model (RSM) with experiments conducted on a free round jet. The results showed that the simulation with the $k-\varepsilon$ and RSM turbulence model gave better prediction than the $k-\omega$ turbulence model. The $k-\varepsilon$ turbulence model with scalable wall function was selected in the current study.

A hybrid structured/unstructured mesh of the computational domain is generated using ANSYS-CFX. The structured meshing is done using a 3D blocking technique. The nozzle computational domain is divided into nine blocks, one at the core of the nozzle and the remaining blocks located circumferentially around the core as shown as shown in Figure 11.

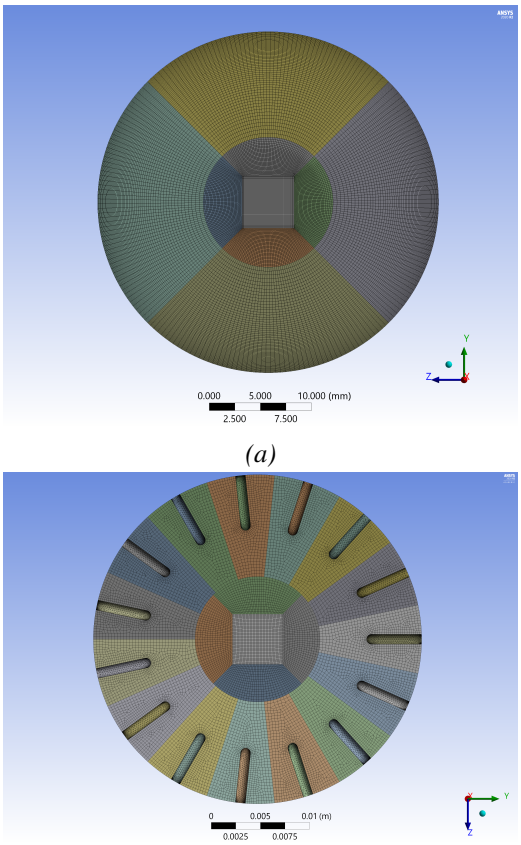

(a)

(b)

Figure 11. Computational grids: (a) circular nozzle, and (b) shark-inspired nozzle.

Grid independence tests were performed to investigate the influence of number of elements on the solution of the two nozzles for three of the computational grids. Table 1 and 2 provide some details of the grids for the circular nozzle and the shark-inspired nozzle, respectively, including the total number of elements, and the y^+ values.

The fundamental principle of the scalable wall function approach used in CFX, is to limit the y^+ value used in the logarithmic formulation by a value of $\tilde{y}^+ = max(y^+, 11.06)$, where 11.06 is the intersection of the logarithmic and linear near wall profiles (Menter and Esch , 2001; Paul et al. , 2008). The scalable wall function was generated to avoid the near-wall grid resolution constraints imposed by standard wall functions (Menter and Esch , 2001).

Steady simulations of the two nozzles are per-

Table 1. Grid details and y^+ values used in mesh independence tests for the circular nozzle.

Grid	Elements	$y^+_{avg,solver}$
A	1,503,860	13.4
B	1,762,380	13.4
C	2,120,268	13.3
D	11,757,245	11.1
E	12,205,165	11.1

Table 2. Grid details and y^+ values used in mesh independence tests for the shark-inspired nozzle.

Grid	Elements	$y^+_{avg,solver}$
A	3,083,331	11.4
B	3,679,678	11.4
C	5,200,439	11.3

formed with the same boundary conditions. The inlet velocity of the circular nozzle is 2.2 m/s. However, the inlet velocity of the shark-inspired nozzle is defined as slight lower (2 m/s) than the circular nozzle to accommodate the blockage effect of the fins. The two nozzles therefore have the same water flow rate. A pressure of 0 Pa (gauge) is defined at the outlet of the test section domain. The CFX-solver runs the steady state simulations for two nozzles until the RMS residuals reached to $5x10^{-5}$. The jet velocity profile obtained from the circular nozzle simulations is compared with Albertson formula (Albertson et al. , 1950) to validate the simulations. It is defined as follows in the potential core region:

$$\begin{aligned} V &= V_0; \quad y \leq R \\ V &= V_0 e^{[-\frac{(r-R)^2}{b^2}]}; \quad y \geq R \\ b &= \beta x \end{aligned} \tag{1}$$

where V_0 is the source velocity, y the direction vertical to jet flow, x the direction of jet flow, R the half-width of the potential core, b the width of the mixing layer, and β is the jet spread rate. $\beta = 0.114$ as found experimentally by (Albertson et al. , 1950).

Figure 12 shows the obtained jet velocity profiles from the three grids with that obtained from the Albertson formula. The CFD results show good agreement, however the maximum velocity from the CFD simulations is slightly higher than that obtained from the formula due to the boundary layer effect. The grid independence results for the shark simulations also showed that slight changes in velocity contour with the three tested grids.

Results of the CFD analysis with the circular nozzle and 15 fin shark-inspired nozzle are presented in terms of turbulence eddy frequency (TEF) and turbulence kinetic energy (TKE) to evaluate the mixing

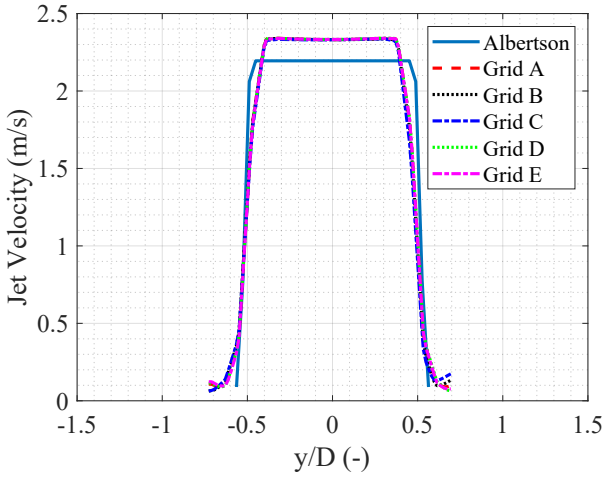

Figure 12. Comparison of jet velocity profile obtained from the three grids with Albertson formula (Albertson et al. , 1950) at x/D_{Jet} = 5%.

rates in the two nozzles. Figure 13 shows a comparison of the TEF for the two nozzles. The CFD results demonstrate that the presence of fins in the jet flow produces secondary high frequency vortices perpendicular to the jet centerline. These vortices entrain and draw fluid from the surrounding environment into the jet flow. This results in a decrease in net jet velocity due to the momentum transfer.

In addition, a large increase in turbulent kinetic energy immediately downstream of the nozzle exit improves the mixing rate as shown in Figure 14. As a result, the shear layer thickens, reducing the potential core of the resulting jet flow emanating from the shark-inspired nozzle.

6. CONCLUSION

This research is being carried out to find a solution to the grid-to-rod fretting of fuel assemblies located around loss-of-coolant accident (LOCA) holes. The proposed solution is to increase the mixing rate between the potential core of the jet flow with the surrounding fluid, thereby increasing the jet velocity decay rate. This mitigates the impact of the jet flow on the rods.

A biomimetic design concept employing the high mixing capacity of shark gill slits is introduced to design a new nozzle. The shark-inspired nozzle is fabricated by attaching fins on the base circular nozzle diameter mimicking the shark's secondary lamellae. Experiments show the shark-inspired nozzle has a significant mitigating effect on the rod bundle vibration. The critical velocity is increased for 1.45 m/s to 1.85 m/s in comparison to the case of the circular nozzle. This 28% delay in the stability limit reflects

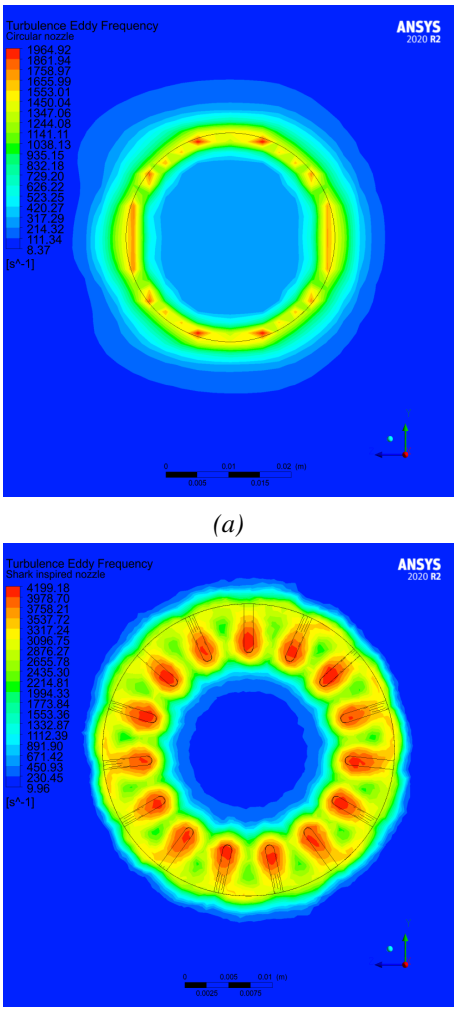

(a)

(b)

Figure 13. Turbulence eddy frequency contours at down-stream distance of x/D_{Jet} = 0.1 for two nozzles: (a) circular nozzle, and (b) shark-inspired nozzle.

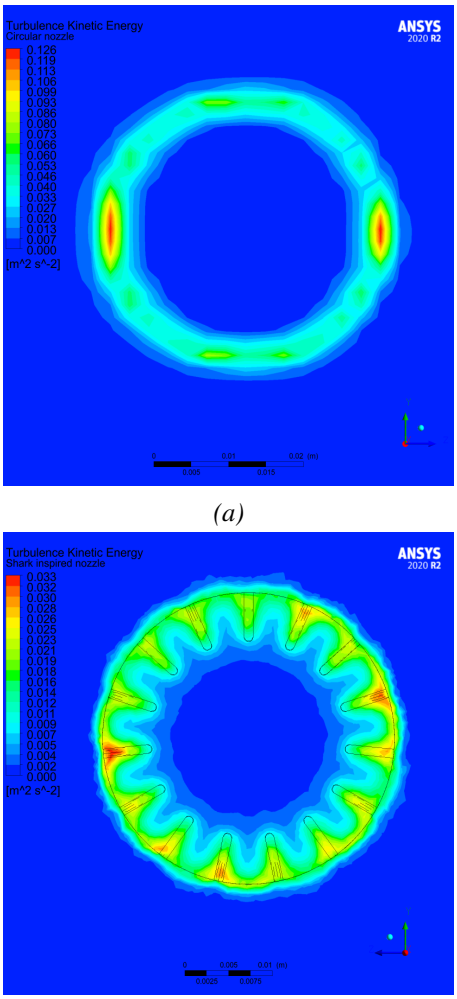

(a)

(b)

Figure 14. Turbulence kinetic energy contours at down-stream distance of x/D_{Jet} = 0.1 for two nozzles: (a) circular nozzle, and (b) shark-inspired nozzle.

also on the rod bundle vibration amplitude. The proposed nozzle reduces the vibration response by 88% relative to the results obtained with the basic circular nozzle.

Shark-inspired nozzles can be used in a variety of mechanical applications where the mixing rate is the key constraint, including in fuel injection systems, atomizers and gas mixers. The number of fins will directly affect the mixing efficiency. However, the fin number and thickness should be selected carefully and optimized to avoid unacceptable pressure losses.

7. REFERENCES

Albertson, M Li and Dai, YeB and Jensen, Ro A and Rouse, Hunter, 1950, Diffusion of submerged jets. *Transactions of the American Society of Civil Engineers*, **115**: 639-664.

Ball, C. G., Fellouah, H. and Pollard, A., 2012, The flow field in turbulent round free jets. *Progress in Aerospace Sciences*, **50**: 1-26.

Behrouzi, Parviz and Feng, T and McGuirk, James J, 2008, Active flow control of jet mixing using steady and pulsed fluid tabs. *Proceedings of the Institution of Mechanical Engineers, Part I: Journal of Systems and Control Engineering*, **222**: 381-392.

Gad-el-Hak, I., 2019, Fluid–Structure Interaction for Biomimetic Design of an Innovative Lightweight Turboexpander. *Biomimetics*, **27**.

Gad-el-Hak, I., Mureithi, N., Karazis, K., and Williams, G., 2021, Experimental Investigation of Jet

Cross-Flow Induced Vibration of a Rod Bundle, *In Pressure Vessels and Piping Conference (Vol. 85338, p. V003T04A014). American Society of Mechanical Engineers*.

International Atomic Energy Agency, 2019, Review of Fuel Failures in Water Cooled Reactors (2006–2015). IAEA Nuclear Energy Series No. NF-T-2.5, IAEA, Vienna.

Lee, J. H. W., Chu, V., and Chu, V. H., 2003, Turbulent jets and plumes: a Lagrangian approach. *Springer Science Business Media*.

Laribi, Boualem and Belkacemi, Djelloul and Abdellah, Hadj, 2012, Numerical investigation of turbulence models for free jet flow. *Applied Mechanics and Materials*, **27**: 2082-2085.

Menter, Florian and Esch, Thomas, 2001, Elements of industrial heat transfer predictions. *16th Brazilian Congress of Mechanical Engineering (COBEM)*, **109**.

Paul, SS and Ormiston, SJ and Tachie, MF, 2008, Experimental and numerical investigation of turbulent cross-flow in a staggered tube bundle. *International Journal of Heat and Fluid Flow*, **29**: 387-414.

Reeder and Samimy, 2008, The evolution of a jet with vortex-generating tabs: real-time visualization and quantitative measurements. *Journal of Fluid mechanics*, **311**: 73-118.

Thangaraj, Thillaikumar and Kaushik, Mrinal and Deb, Dipankar and Unguresan, Mihaela and Muresan, Vlad, 2022, Survey on Vortex Shedding Tabs as Supersonic Jet Control. *Frontiers in Physics*.

SELF-OSCILLATING HYDROGEL-BASED VOCAL FOLD MODELS FOR VOICE PRODUCTION RESEARCH

Scott L. Thomson
Brigham Young University, Provo, United States

Taylor E. Greenwood
Brigham Young University, Provo, United States

ABSTRACT

The fabrication and flow-induced vibratory response of a hydrogel-based, multi-layer, self-oscillating vocal fold model is reported. Two hydrogels of differing stiffness, prepared using readily-available materials, were sequentially cast to create two-layer vocal fold models. A thin layer of silicone was applied to the surfaces to represent the epithelium. The models self-oscillated in a manner similar to that of previously-reported silicone models. Evidence of mucosal wave-like motion, including the alternating converging-diverging profile characteristic of human phonation, was seen. The results show the potential for hydrogel and hydrogel-silicone models to be used for voice production research, thereby enabling respective characteristics of hydrogels and silicones to be leveraged for different desired purposes.

1. INTRODUCTION

Silicone, self-oscillating models of the vocal folds (VFs) with geometries based on human VFs have been used extensively for voice research (Kniesburges et al., 2011). Example applications include studies of the glottal jet (Neubauer et al., 2007), vocal fold contact pressure (Spencer et al., 2008; Motie-Shirazi et al., 2019), the effect of surface hydration on vibration (Van Hirtum et al., 2019; Bouvet et al., 2020a), and asymmetry (Zhang et al., 2013; Tokuda and Shimamura, 2017; Bouvet et al., 2020b). Early silicone models were homogeneous (one layer) (Thomson et al., 2005). Models with multiple layers were subsequently developed, including a two-layer body-cover model (Drechsel and Thomson, 2008) and the so-called "EPI" model (Murray and Thomson, 2012) with layers representing the epithelium, superficial lamina propria (SLP), ligament, and muscle. Other advancements have included models with geometries based on medical imaging data (Pickup and Thomson, 2010) and embedded fibers to create material nonlinearity (Shaw et al., 2012; Xuan and Zhang, 2014). Models are typically cast, but 3D-printed models have recently been reported (Greenwood and Thomson, 2021; Romero et al., 2021).

Models in these and other related studies have frequently been fabricated using the two-part silicone Ecoflex with varying amounts of Silicone Thinner to control stiffness (both products from Smooth-On, Inc.) Advantages of this approach include commercial availability, low cost, capability of sustaining uninterrupted vibration over long periods of time, ability to cast desired shapes, and ability to tune material stiffness to mimic VF tissue layers. Disadvantages include low fabrication yield due to challenges of working with ultra-soft Ecoflex formulations, difficulty of precisely controlling stiffness, and inherent material linearity.

In this paper a hydrogel-based, multi-layer VF model is introduced. Hydrogel preparation and model fabrication and testing processes are described. Results showing that hydrogel stiffness can be tuned to be within the range needed for VF modeling are then presented. It is demonstrated that the VF models are able to vibrate in a manner similar to that of previously-reported silicone VF models with responses that exhibit life-like characteristics. Potential advantages and limitations of the hydrogel-based VF model concept are discussed.

2. METHODS

2.1. Material preparation

Hydrogels for two VF layers (body and superficial lamina propria [SLP], described in Sec. 2.2) were prepared using readily-available, low-cost raw materials following the recent work of Baumgartner et al. (2020). Formulations were prepared as follows. Deionized water (12 g), citric acid (1.5 g; Ball), glycerol (7.5 g; CAS 56-81-5, Fischer Bioreagents), and sugar syrup (10.6 g; Light Corn Syrup, Karo) were combined and mixed using a magnetic stirrer hot plate (SH-2, Thermo Fisher Scientific) for 5 min (this and other times denoted in Sections 2.1 and 2.2 are approximate unless otherwise noted). Gelatin powder (Original Unflavored Gelatine, Knox) was added (3 g for the body layer, 1.125 g for the SLP layer), stirred, and allowed to rest for 5 min. This mixture was then stirred and heated to 70°C using the hot plate and then mixed under vacuum (2350 RPM, 450 mbar) for precisely 4 min in a planetary centrifugal mixer (DAC 150.1 FVZ-K, SpeedMixer). At this point, the mixture was a castable liquid.

2.2. Vocal fold model fabrication

The VF models (see Fig. 1) were based on the EPI VF model geometry of Murray and Thomson (2012) with a few minor modifications. Most notably, the original model included muscle, ligament, SLP, and epithelial layers, with a fiber inserted into the ligament layer and a stiff backing layer along the lateral surface for structural support. This same concept was used in the present study, but with muscle and ligament layers combined into what is here denoted as a single body layer. The backing was also of the same material as the body.

The models were fabricated using the general multi-step casting process described in Murray and Thomson (2012). Positive molds were printed on a Prusa i3 MK3 printer using PLA filament, negative molds were prepared from the positive molds using addition-cure silicones (two silicones were used, Smooth-Sil 936 and Mold Max 10; Smooth-On, Inc.), and negative molds were lightly coated with release agent (Pol-Ease 2300). In future studies, it is anticipated that negative molds could alternatively be directly 3D printed from PLA.

The body hydrogel material was first prepared as described in Sec. 2.1, with blue food coloring added for visibility. A fiber (thread) was pre-coated with body hydrogel and inserted into the negative mold through slits. Body hydrogel was poured into the corresponding mold and placed in a small freezer (Whynter CUF-112SS) for 10 min while the SLP hydrogel was prepared. The solidified body model was removed from the freezer, demolded, and warmed at room temperature for 20 min.

While still warm after mixing, the SLP hydrogel was poured into the SLP mold, and the body model was inserted into the SLP mold with the fiber inserted through slits in the SLP mold. The filled SLP mold was placed in the freezer for 30 min. The model was then demolded (while still cold), trimmed to remove backing flanges so as to fit in a mounting plate, and warmed at room temperature for 30 min. A silicone epithelial layer was created by mixing Dragon Skin 10 FAST and Silicone Thinner (Smooth-On, Inc.; mixing ratio 1:1:1 by weight of A:B:Thinner) at 2000 rpm for precisely 2 min using the planetary mixer, degassing for 2 min, pouring over the models, and curing for one hour. After curing, excess silicone around the model base was trimmed.

2.3. Vocal fold model vibration testing

Each VF model was adhered using Sil-Poxy (Smooth-On, Inc.) to 3D-printed (PLA) mounting plates. Two models in a full-larynx configuration (i.e., as shown in Fig. 1) were used. Prior to testing, the models were coated with talc powder to reduce surface tackiness. The plates were mounted to a flow supply as has been previously described (Murray and Thomson, 2012), which consisted of compressed air supply connected to a plenum via a long tube and inline flow meter, and an approximately 34 cm long tube connecting the plenum to the mounting plates. A pressure sensor (26PC 6CF6G, Honeywell) was located in the tube wall approximately 2 cm upstream of the mounting plates.

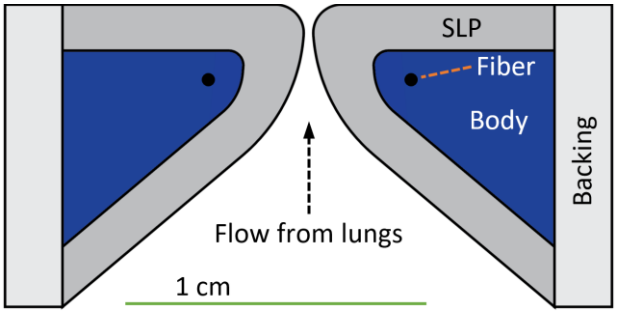

Figure 1. Schematic of multi-layer VF models with body (blue) and SLP (dark gray) layers. Backing facilitates ease of handling and mounting for flow-induced vibration testing. The anatomical medial-lateral sense is left-right and inferior-superior is bottom-to-top. Green scale bar is approximately 1 cm. Fiber location is approximate.

Onset pressure was estimated by observing pressure while manually increasing pressure until vibration commenced. The pressure was then slightly increased and high-speed video was acquired (Edgertronic SC2+, 7700 fps). Tests were performed at ambient temperature, although it was observed that the lights for high-speed video illumination (Model 900420H, Visual Instrumentation Corp.) generated a non-trivial amount of heat, and at one point the surface temperature of one model was measured to be approximately 27°C. Consequently, the hydrogel rheological properties were tested at two temperatures as described below.

2.4. Material property tests

Specimens for preliminary characterization of hydrogel material properties were created concurrently with VF models by pouring liquid material into negative molds coated with release agent. After pouring, overhead transparency material was placed on each mold to ensure a flat specimen surface. Specimens were tested within approximately three hours of initial fabrication and at the same general time as the VF model vibration testing described above.

Material characterization was performed using a uniaxial tensile tester (Instron 3342) with a 50 N force transducer (Instron 2519-102) and a rotational rheometer (AR 2000ex, TA Instruments) with parallel plate geometries. Dog bone-shaped specimens for tensile testing had a reduced section geometry of 5.75×3.66×30 mm, were mounted vertically, and were displaced at a rate of 150 mm/min after a pre-

cycling stage (five cycles at a rate of 500 %/min). (The reduced section geometry was 30 mm long, but the initial length used in strain calculations reported below was 31.5 mm due to slight change in specimen geometry when mounting to tensile test apparatus.) Elastic modulus values were calculated from the stress-strain data as explained in Sec. 3.1. Disk specimens for rheometer testing (40 mm diameter, 2 mm thick) were tested at a gap of 1700 µm (15% compression) between a roughened upper plate geometry (stainless steel, sandblasted, 40 mm plate, 519400.901, TA Instruments) and a lower Peltier plate covered with 220 grit adhesive-backed sandpaper. Storage modulus values (G') were measured at oscillation frequencies from 1 to 10 Hz under a controlled oscillation stress of 0.8 Pa. Disk specimens were tested at 22°C and 27°C.

3. RESULTS AND DISCUSSION

3.1. Hydrogel material properties

The results of the preliminary material property characterization tests are first here described. Engineering stress vs. strain measurement data are shown in Fig. 2 for the two hydrogel layers and the silicone epithelial layer from 0 to 10% strain. The data shown are those which were obtained after the five pre-cycles. All curves can be seen to be fairly linear over this range. Hydrogel elastic modulus values (the slopes of the stress-strain curves from 0 to 10% strain) ranged from 0.851 kPa (SLP) to 17.5 kPa (body, average of two specimens).

Rheological data are shown in Fig. 3. Storage modulus values (G') at 22°C ranged from approximately 4.2 kPa (1 Hz) to 5.2 kPa (10 Hz) for the body specimens. For the SLP specimens, G' ranged from approximately 0.26 kPa (1 Hz) to 0.37 kPa (10 Hz). On average, specimens exhibited G' increases of 18% (body) and 33% (SLP) from 1 to 10 Hz.

The hydrogel material properties were also sensitive to temperature. On average, the two body specimen storage modulus values decreased by 18% and 20% from 22°C to 27°C. The modulus of one of the SLP specimens (SLP 1 in Fig. 3) decreased by 26% over the same temperature range. The other, SLP 2, only decreased by 13%. However, it is important to note that all specimens were first tested at 22°C, followed by tests at 27°C. After loading each specimen and before each test, the lower Peltier plate was set to the desired temperature for 4 min. SLP 2 was the first specimen tested at the higher temperature, and it is possible that the apparatus and specimen temperature may not have yet reached steady state.

These tensile and rheological data demonstrate promise for the current hydrogels to be formulated with material properties that compare favorably with silicone properties reported in other synthetic VF modeling studies (Murray and Thomson, 2012). Further testing is required to verify these data and, in general, to explore effects on material properties of variables such as temperature, time after fabrication, material composition, and processing protocols.

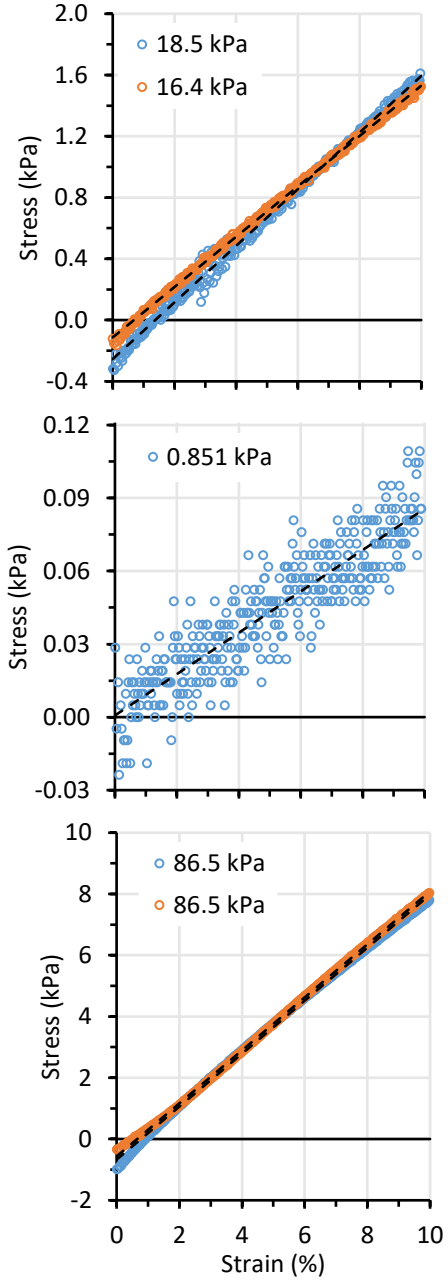

Figure 2. Hydrogel engineering stress vs. strain data for body (top; two specimens) and SLP (middle; one specimen) layers. Silicone epithelial layer data are also shown for reference (bottom; two specimens). Modulus values from the linear fits (black dashed lines) are given in the legends. Noise in the SLP data is primarily due to limited load cell resolution and sensitivity. Note different scales of y-axes.

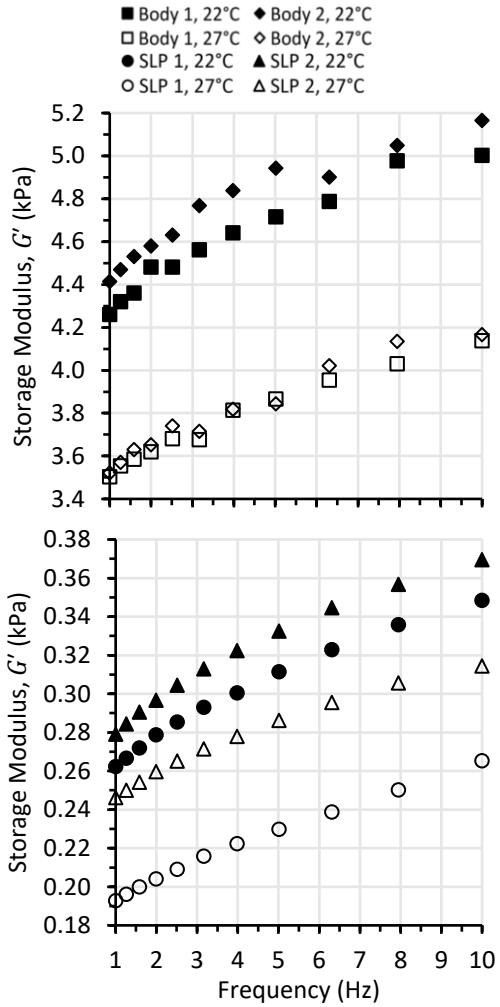

Figure 3. Preliminary hydrogel storage modulus data for body (top) and SLP (bottom) layers (two specimens each) at two temperatures. Note different scales of y-axes.

3.2. Hydrogel-based vocal fold models

Images of the hydrogel-based VF models are shown in Fig. 4. The fabricated geometries followed the desired geometries, and the SLP and body layers are evident. Even though the epithelium and SLP layers were of silicone and hydrogel, respectively, they remained sufficiently attached to each other during vibration. They could, however, be intentionally manually detached (e.g., with tweezers) as shown.

3.3. Flow-induced vibratory response

The models exhibited flow-induced vibration with an onset pressure between approximately 1.2 and 1.5 kPa, with variability due to factors such as model temperature, initial glottal gap, and length of time models had been vibrating. By comparison, Murray and Thomson (2012) reported onset pressures of 0.27 kPa for their EPI model, 0.84 kPa and 0.87 kPa for two two-layer models based on the M5 geometry of Scherer et al. (2001), and 1.68 kPa for a two-layer MRI-based model. The range of onset pressures of the current model is higher than these EPI and M5-based models, but lower than the MRI-based model. The pressure is still within the range of capability of the human lungs. The higher onset pressure is likely a function of the SLP layer being less flexible than in the EPI model and the subglottal tube being longer than in Murray and Thomson (2012).

Images from high-speed video during model vibration from two views are shown in Fig. 5. Prior to acquisition of these images, the onset pressure was approximately 1.2 kPa, and subglottal pressure during imaging was approximately 1.3 kPa. The frequency was 115 Hz, which is close to the typical frequency of an adult human male and in the range of the Murray and Thomson (2012) models.

Videokymography (VKG) and glottal width data were derived from the high-speed video and are shown in Figs. 6 and 7. These results are comparable to those previously reported using silicone VF models. Further, evidence of mucosal wave-like motion, including an alternating convergent-divergent intraglottal profile that is typical of human phonation, can be seen in Figs. 5 and 6. Asymmetric vibration suggests that the models were not perfectly symmetric, and glottal closure was never reached.

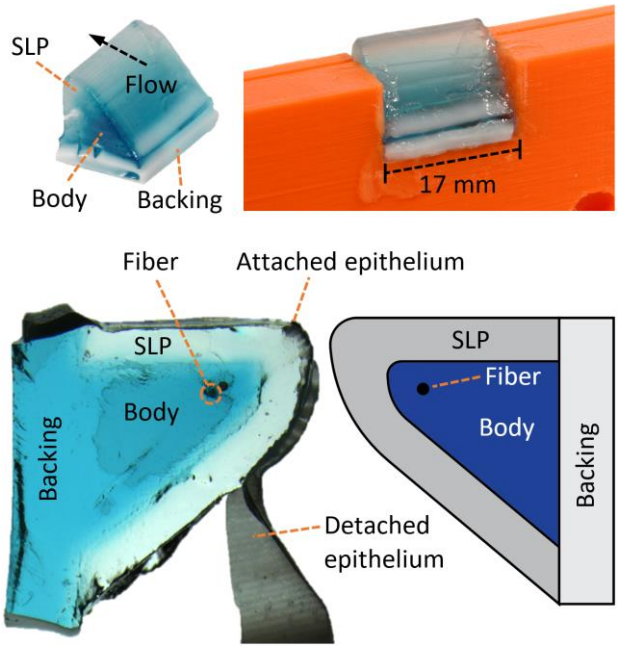

Figure 4. Images of VF models and geometry. (Top): Model after pouring epithelial layer (left) and adhering to mounting plate (right). (Bottom left): Image of model cross section with epithelial layer intentionally partially detached for visualization. Backing and body were cast as one piece. Some image backgrounds have been removed for improved visual clarity. (Bottom right): Illustration of model design.

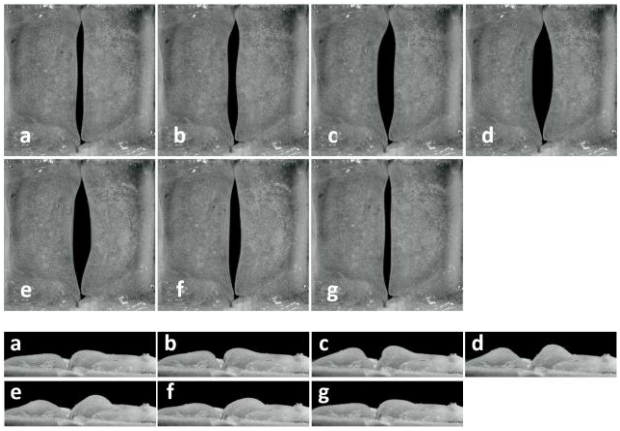

Figure 5. Images from high-speed video of model vibrating over one cycle, superior view (top set) and anterior view (bottom set). Every 11th frame shown.

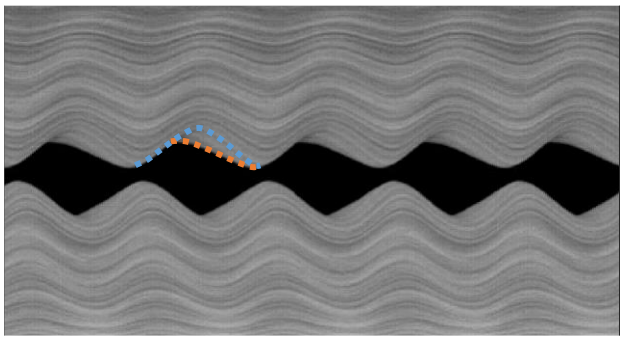

Figure 6. VKG from high-speed video of VF model vibrating over several cycles. Estimated locations of superior (blue) and inferior (orange) margins are denoted by dotted lines for one side of the model over one cycle. The glottal profile appears to have been divergent when both lines are visible and straight or convergent when the orange line is occluded.

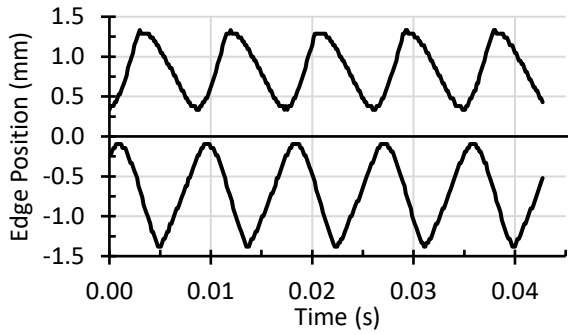

Figure 7. Distance vs. time between the approximate medial-lateral centerline and each side of the glottis near the anterior-posterior midplane. Minimum and maximum glottal widths at this location were 0.5 and 2.5 mm, respectively. The two sides' amplitudes were asymmetric and slightly out of phase.

Using these data the Reynolds ($\mathrm{Re} = \rho VD/\mu$) and Strouhal ($\mathrm{St} = fD/V$) numbers were estimated. Density and viscosity values of 1.01 kg/m^3 and 1.83×10^{-5} Pa·s were used. A mean velocity of $V = 50.7$ m/s was estimated using Bernoulli's equation with a subglottal pressure of 1.3 kPa. The frequency, f, was 115 Hz, and a mean glottal width of 1.52 mm was used as the characteristic length scale, D. These yielded $\mathrm{Re} = 4260$ and $\mathrm{St} = 0.0034$.

During the preliminary vibration tests reported here, it was observed that the models would initially vibrate at a given onset pressure, but would then require increasing flow to sustain the pressure required for vibration. This may have been due to the material stiffness decreasing. Two possible reasons include material relaxation caused by vibration-induced stresses and material softening due to heat from the high-intensity LEDs. Dehydration of the hydrogel layer is a consideration that will need further study. Preliminary tests indicate that models fabricated using the processes described herein are able to continuously vibrate for over one hour, although dehydration and other effects should be explored to characterize longevity and long-term vibratory responses of hydrogel VF models.

4. CONCLUSION

The fabrication and flow-induced responses of hydrogel-based synthetic, self-oscillating VF models is here reported. The hydrogel material properties and model vibration characteristics were generally similar to those observed in previously-reported silicone VF models. The use of hydrogels to fabricate VF models may facilitate new avenues of exploration in voice research, although further investigation and development is required. Some observations from this study regarding advantages, limitations, and potential capabilities of hydrogel-based VF models, particularly compared to silicone VF models, are here discussed.

While models with multiple hydrogel layers were successfully fabricated, the layers did not seem to bond as readily as the layers within silicone VF models. Success in this regard was found by casting the SLP layer while the SLP hydrogel liquid was still warm and after the body model had thawed at room temperature. This approach may result in some diffusion between hydrogel layers (presumably prior to complete curing), which would increase layer bonding but possibly make layer interfaces less distinct. Further exploration of bonding and diffusion between hydrogel layers is warranted.

The hydrogel properties were highly temperature-dependent, seemingly more so than silicone. This was advantageous in that cold-stiffened hydrogels were easier to demold and cut for cross sectioning, but disadvantageous in that warming altered material

properties, thus potentially necessitating model temperature to be monitored, and possibly controlled, in future studies.

The hydrophilic nature of hydrogel (vs. hydrophobic silicone) is an important distinction that may be useful. One such possibility is the use of hydrogel VF models to study the influence of airway surface liquid on VF vibration. To this end, in the present study, the epithelium was silicone, but it is expected that a stiffer hydrogel could instead be used. An additional possibility is to pursue whether material nonlinearity could be achieved using imbedded fibers that may adhere better to hydrogel than silicone.

The ability of the silicone to remain attached to the hydrogel suggests that models with different layers of different material types may be able to be fabricated (e.g., silicone body and hydrogel SLP) for specific research purposes. Further investigations into the types of silicone that may remain attached to the hydrogel, the processing parameters that favor such attachment, and measures of the resulting interfacial bond strength, are needed. Additional measures may be needed to strengthen hydrogel-silicone interfacial bonding, such as that which was reported by Yuk et al. (2016). Similarly, it is noted that the Sil-Poxy used for adhering the hydrogel models to the mounting plates is also used to mount silicone VF models.

The concept of 3D printing silicone VF models has recently been demonstrated (Greenwood and Thomson, 2021; Romero et al., 2021). However, hydrogels have also been 3D printed in other applications (Zhang et al., 2018), and it is possible that hydrogels may possess advantages over silicones in terms of suitability for 3D printing VF models.

The availability, affordability, and customizability of the hydrogels described here are strengths. These characteristics also allow for material customization. The preparation process is straightforward. Addition-cure silicones for VF models are commercially available, but the uncured materials have limited shelf life and are subject to material sedimentation which can affect cured material properties. On the other hand, silicone has advantages over hydrogels, such as reduced temperature sensitivity and potentially better long-term material stability once cured.

Hydrogel models will eventually dehydrate, but preliminary studies suggest that the time scale of dehydration may be acceptable for many studies. This should be explored and quantified. If dehydration were to become a concern for a given study, it is possible that performing experiments using humidified air and/or storing in a humidified chamber could slow dehydration. It is important to note, however, that the silicones used for VF modeling are not immune to aging effects, such as migration of uncured silicone thinner between layers and surrounding mounting structures due to silicone permeability. The time scale of such effects in silicone models is expected to be longer than in hydrogel models.

5. ACKNOWLEDGMENTS

This work was supported by grant R01 DC009616 from the U.S. National Institute on Deafness and Other Communication Disorders. Its content is solely the responsibility of the authors and does not necessarily represent the official views of the NIDCD or the National Institutes of Health (NIH).

6. REFERENCES

Baumgartner, M, Hartmann, F, Drack, M, Preninger, D, Wirthl, D, Gerstmayr, R, Lehner, L, Mao, G, Pruckner, R, Demchyshyn, S, Reiter, L, 2020, Resilient yet entirely degradable gelatin-based biogels for soft robots and electronics, *Nature Materials* **19**:1102-1109.

Bouvet, A, Pelorson, X, Van Hirtum, A, 2020a, Influence of water spraying on an oscillating channel, *Journal of Fluids and Structures* **93**:102840.

Bouvet, A, Tokuda, I, Pelorson, X, Van Hirtum, A, 2020b, Influence of level difference due to vocal folds angular asymmetry on auto-oscillating replicas, *Journal of the Acoustical Society of America* **147**:1136-1145.

Drechsel, JS, Thomson, SL, 2008, Influence of supraglottal structures on the glottal jet exiting a two-layer synthetic, self-oscillating vocal fold model, *Journal of the Acoustical Society of America* **123**:4434-4445.

Greenwood, TE, Thomson, SL, 2021, Embedded 3D printing of multi-layer, self-oscillating vocal fold models, *Journal of Biomechanics* **121**:110388.

Kniesburges, S, Hesselmann, C, Becker, S, Schlücker, E, Döllinger, M, 2013, Influence of vortical flow structures on the glottal jet location in the supraglottal region, *Journal of Voice* **27**:531-544.

Motie-Shirazi, M, Zañartu, M, Peterson, SD, Mehta, DD, Kobler, JB, Hillman, RE, Erath, BD, 2019, Toward development of a vocal fold contact pressure probe: sensor characterization and validation using synthetic vocal fold models, *Applied Sciences* **9**:3002.

Murray, PR, Thomson, SL, 2012, Vibratory responses of synthetic, self-oscillating vocal fold models, *Journal of the Acoustical Society of America* **132**:3428-3438.

Neubauer, J, Zhang, Z, Miraghaie, R, Berry, DA, 2007, Coherent structures of the near field flow in a self-oscillating physical model of the vocal folds,

Journal of the Acoustical Society of America **121**:1102-1118.

Pickup, BA, Thomson, SL, 2010, Flow-induced vibratory response of idealized versus magnetic resonance imaging-based synthetic vocal fold models, *Journal of the Acoustical Society of America* **128**:EL124-EL129.

Romero, RG, Colton, MB, Thomson, SL, 2021, 3D-printed synthetic vocal fold models, *Journal of Voice* **35**:685-694.

Scherer, RC, Shinwari, D, De Witt, KJ, Zhang, C, Kucinschi, BR, Afjeh, AA, 2001, Intraglottal pressure profiles for a symmetric and oblique glottis with a divergence angle of 10 degrees, *Journal of the Acoustical Society of America* **109**:1616-1630.

Shaw, SM, Thomson, SL, Dromey, C, Smith, S, 2012, Frequency response of synthetic vocal fold models with linear and nonlinear material properties, *Journal of Speech, Language, and Hearing Research* **55**:1395-1406.

Spencer, M, Siegmund, T, Mongeau, L, 2008, Determination of superior surface strains and stresses, and vocal fold contact pressure in a synthetic larynx model using digital image correlation, *Journal of the Acoustical Society of America* **123**:1089-1103.

Thomson, SL, Mongeau, L, Frankel, SH, 2005, Aerodynamic transfer of energy to the vocal folds, *Journal of the Acoustical Society of America* **118**:1689-1700.

Tokuda, IT, Shimamura, R, 2017, Effect of level difference between left and right vocal folds on phonation: Physical experiment and theoretical study, *Journal of the Acoustical Society of America* **142**:482-492.

Van Hirtum, A, Bouvet, A, Pelorson, X, 2019, Quantifying the auto-oscillation complexity following water spraying with interest for phonation, *Physical Review E* **100**:043111.

Xuan, Y, Zhang, Z, 2014, Influence of embedded fibers and an epithelium layer on the glottal closure pattern in a physical vocal fold model, *Journal of Speech, Language, and Hearing Research* **57**:416-425.

Yuk, H, Zhang, T, Parada, GA, Liu, X, Zhao, X, 2016, Skin-inspired hydrogel-elastomer hybrids with robust interfaces and functional microstructures, *Nature Communications* **7**:1-11.

Zhang, B, Li, S, Hingorani, H, Serjouei, A, Larush, L, Pawar, AA, Goh, WH, Sakhaei, H, Hashimoto, M, Kowsari, K, Magdassi, S, Ge, Q, 2018, Highly stretchable hydrogels for UV curing based high-resolution multimaterial 3D printing, *Journal of Materials Chemistry B* **20**:3246-3253.

Zhang, Z, Kreiman, J, Gerratt, BR, Garellek, M, 2013, Acoustic and perceptual effects of changes in body layer stiffness in symmetric and asymmetric vocal fold models, *Journal of the Acoustical Society of America* **133**:453-462.

Control of FIV and noise

PASSIVE CONTROL OF THE TURBULENT FLOW PAST A FINITE CIRCULAR CYLINDER FITTED WITH EIGHT PERIPHERAL RODS

Icaro A. Carvalho
Department of Mechanical Engineering, EPUSP, University of São Paulo, Brazil
Gustavo R. S. Assi
Department of Naval Architecture & Ocean Engineering, EPUSP, University of São Paulo, Brazil

ABSTRACT

Passive technologies devoted to the control of the flow past bluff bodies have been studied widely. However, most of these studies have focused on large aspect ratio, or infinitely-long cylinders. We have carried out detached eddy simulations at Reynolds number 10^3 *for both infinitely-long and low aspect ratio* ($L = 2D$) *configurations. These computations were conducted for the bare cylinder (of diameter D and length L, as a reference case) and for the system comprised by the same main body, but now fitted with eight wake-control rods (of diameter* $d = D/20$) *uniformly distributed around the main, but distant from it by a gap* $G = D/100$. *Our results showed that the low aspect ratio case relative to that of infinitely-long structures i) lowered mean drag and root mean square lift; ii) presented a more organised topology, although did not attain vortex shedding suppression; iii) the two frontal and the two rear rods concentrated most of the hydrodynamic loads, whereas intermediate rods faced less than 1/10 of these force coefficients – both cases generally following the same tendency; and iv) although both cases developed larger hydrodynamic loads when the main body was fitted with rods, the finite case produced a lower increase.*

1. INTRODUCTION

Vortex shedding is known to be responsible for hydrodynamic loads that affect bluff structures. The interplay between opposing vortices shed downstream is the root of vortex-induced vibrations (VIV) that cause the bluff structure to oscillate longitudinally, and principally, transversely to the flow, leading to fatigue, and possibly failure. In practice, VIV (sometimes also called VIM for vortex-induced motion) is observed in large offshore platforms, such as spar and monocolumn floating platforms.

Various are the methods dedicated to eliminate and attenuate vortex shedding, as reviewed by Zdravkovich (1981) and more recently by Choi et al. (2008). Passive solutions aim at suppressing VIV without power input. Common examples are shrouds (such as slender cylinders round a main body), near-wake stabilisers (such as end and splitter plates) and geometrical modifications (like helical strakes as reviewed by Zdravkovich, 1981).

From the seminal paper on the suppression of vortex shedding by a single control rod of Strykowski and Sreenivasan (1990), it is known that the presence of a passive secondary body can attenuate the growth of temporal instabilities and is able to not only reduce vortex shedding, but also to banish its inception entirely in a limited range of Reynolds numbers ($Re = U_\infty D/\nu$, where U_∞ is the freestream flow velocity, D is the diameter and ν is the kinematic viscosity of the fluid). In a more general sense, numerical and experimental results of Strykowski and Sreenivasan (1990) showed that local modifications led to global changes in the flow, and that in order to control the wake, interaction with the near field is of utmost importance.

Experiments with more complex systems, subjected to VIV, were conducted by Silva-Ortega and Assi (2017), with 2, 4 and 8 rods in turbulent regime. Drag and response amplitude were assessed regarding changes in gap between the main body and the fitted rods and their diameters. The authors showed that care must be taken with such a passive device, that may not only increase hydrodynamic loads, but also introduce galloping due to directional effects. With adequate parameters in a setup involving eight rods, merely residual VIV remained.

From a physical point of view, this passive category of solutions acts through different mechanisms. One of such is through elimination or delay of vortex shedding away in the wake downstream, thus diffusing vorticity concentration. Another is to avoid shear-layer interaction. It is known from the work of Gerrard (1966) that shear layers replenish the wake with vorticity and their interaction is of utmost relevance to the shedding frequency.

It was remarked by Mittal and Raghuvanshi (2001) that suppression of vortex shedding by proper placement of a fixed rod near the main cylinder was pos-

sible only at low Re. Nevertheless, wake control by a passive mechanism is a stepping stone toward effective solutions, such as active control through the injection of momentum into the boundary layer by spinning the rods (Korkischko and Meneghini, 2012).

Although both active and passive solutions have been employed to 2D laminar cases and 3D fully turbulent cases, there is a lack of research concerning both mechanisms for finite cylinders, subjected to end effects.

In fact, most previous works concern with bare cylinders. Farivar (1981) experimentally studied the turbulent flow at $Re = 7 \times 10^4$ about a cylinder with finite length. Supported by the work of Goldstein (1938) on the turbulent flow about a cylinder with different aspect ratios, Farivar (1981) attempted to describe the effect of the free end in regard to pressure and drag coefficients. Franzini et al. (2013) studied the problem of a bare cylinder subjected to VIV, for aspect ratios in the range of 0.3 to 2.0 and different mass ratios, and also reported the lack of studies of cylinders with small aspect ratios. Other studies concerned with free end shape and effect of aspect ratio are found in the literature. A good review is made by Luo et al. (1996). It is also found in such paper one of the few studies regarding the interaction between low aspect ratio cylinders, however that work did not concern with a passive mechanism as described above – but only with the interference of two bodies of the same length scale.

The present work intends to fulfill part of the gap found in the literature and to complement previous research in terms of hydrodynamic loads and wake topology of finite cylinders with a passive mechanism of wake control.

2. OBJECTIVE

The role of this paper is to compare the setups of spanwise infinitely-long and low aspect ratio cylinders, involving plain cylinder and this central body fitted with peripheral rods, envisioned to mitigate vortex shedding (as shown in figure 1). Considerations pertaining to wake dynamics and hydrodynamic loads are pursued.

3. METHODOLOGY

3.1. Problem description

Incoming uniform flow U_∞ past a plain cylinder of diameter D and past a system — comprised by a central cylinder (P_0) surrounded by eight peripheral rods (P_1, P'_1, …, P_4, P'_4 as in figure 1) — were considered in two respects concerning the cylinders' ends:

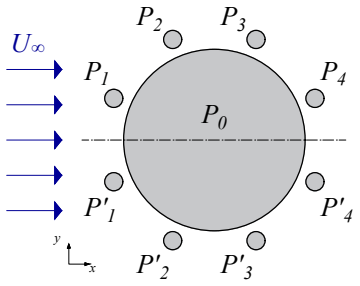

Figure 1. System comprised of a main cylinder (P_0) and eight rods (P_1, P_2, P_3, P_4 and their primed counterparts, symmetrically displayed with respect to the x-axis crossing the centre of the system).

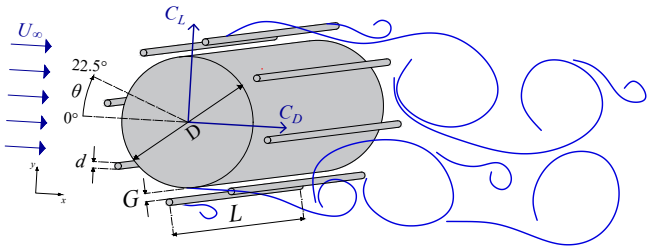

Figure 2. Parameters of the flow and of the system formed by the main cylinder and the eight fitted peripheral rods.

- **Case i**: the cylinders were considered nominally infinitely-long (i.e., end effects were disregarded), in opposition to *case ii*;
- **Case ii**: the cylinders were considered finite, i.e., with low aspect ratio.

Figure 2 represents the aforementioned system, showing the central body surrounded by eight fixed rods of diameter $d = D/20$. A gap $G = D/100$ is inserted between the main cylinder and the rods, following previous works (Assi et al., 2019; Carvalho et al., 2021; Carvalho and Assi, 2022, with spinning rods). It is to be noted that designated frontal (P_1, P'_1) and rear rods (P_4, P'_4) were deliberately displaced away from stagnation regions by an angle of 22.5°. Besides, rods' centres are evenly distributed along a circumference of radius $D/2+G+d/2$ centred at the origin of the entire system (coincident with the centre of the main body), angularly distant from one another by a 45° angle.

3.2. Finite volume scheme and meshing

Incompressible flow in turbulent regime was considered at Reynolds number $Re = Re_D = U_\infty D/\nu = 10^3$, based on the main cylinder's diameter D, on the incoming flow U_∞ and on the fluid viscosity, ν. In order to compute the flow about the system, finite volume

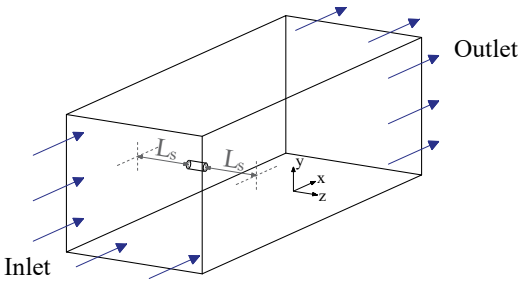

Figure 3. Inlet and outlet correspond to the respective surfaces where the flow enters and leaves the domain. The other boundaries correspond to the sides (of the parallelogram) and to the surface of the cylinders. Only the main cylinder is represented, for simplicity. L_s indicates the distance from the system ends to the sides.

simulations were carried in the open-source C++ library OpenFOAM to obtain second-order discretisation of the governing equations of mass conservation and momentum transport for incompressible flow and Newtonian fluid, as given by the Navier-Stokes equations:

$$\rho\left(\frac{\partial U_i}{\partial t}+U_j\frac{\partial U_i}{\partial x_j}\right)=-\frac{\partial p}{\partial x_i}+\mu\frac{\partial^2 U_i}{\partial x_j\partial x_j} \quad (1)$$

$$\frac{\partial U_j}{\partial x_j}=0 \quad (2)$$

The left hand side was discretised by means of an implicit backward scheme for the Eulerian term and with a second-order blend of the linear upwind and central scheme (with proportion 1:3) for the convective term. Gradients followed a cell-based least-squares procedure. Linear interpolation allowed for the computation of values on the surface of the cells from cell centre values. Together with the Gauss theorem and with a surface normal gradient corrected for non-orthogonality, the discretisation of the Laplacian term was attained. All turbulent quantities were subjected to a linear upwind discresation.

Symmetry (no cross-flow) boundary conditions were applied to the sides of the domain and the no-slip condition on the surfaces of the cylinders. The inflow input was specified by the flow velocity U_∞ and zero pressure gradient. Conversely, the outflow was given a fixed pressure value and null velocity gradient. Inlet and outlet are respectively shown in figure 3.

In case i, the nominally infinitely-long cylinder was reproduced by means of a spanwise length $L=\pi D$ (in agreement with Assi et al., 2018), accompanied by periodic boundary conditions on the sides of the domain. In this case, $L_s=0$ (as in figure 3) and the width of the domain matched the cylinders' spanwise length. On the other hand, case ii represented

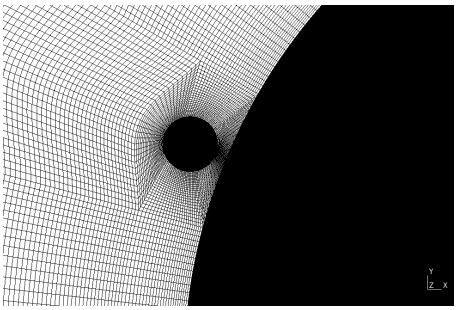

(a) Mesh round rod P_1 in the infinitely-long cylinders case i.

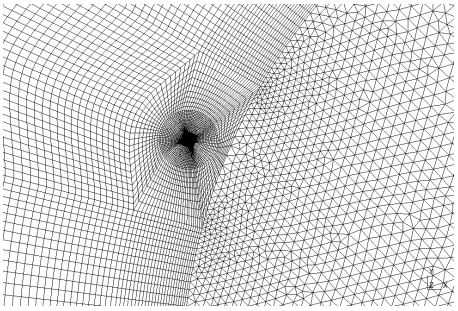

(b) Mesh round rod P_1 in case ii, of cylinders with low aspect ratio.

Figure 4. Mesh for the infinitely-long cylinder (above) and the low aspect ratio case (below). The latter requries meshing of the sides of every cylinder to capture end effects.

cylinders of low aspect ratio with $L=2D$, and the entire system laid distant $L_s=8D$ from any side of the domain. In this case, the sides of the cylinders were set to a no-slip condition, whereas the sides of the flow domain were maintained by a symmetric condition. In both cases, the main cylinder was distant $8D$ from top and bottom surfaces, and from the inlet; a greater distance of $20D$ was applied between the main cylinder's centre and the outlet downstream. This mesh geometry is in agreement with previous analyses to avoid blockage effects (Behr et al., 1995, 1991).

Structured, hexahedral, elements were exclusively used in case i; and predominantly used in case ii, especially to capture the boundary layer of the cylinders. Figure 4a shows the mesh round rod P_1 of case i. Unstructured, tetrahedral, cells were applied on the cells located on the sides of the cylinders of case ii, and in the region extruded away to the sides from these surfaces. A plane view of rod P_1 is shown in figure 4b, where triangular elements (of the yet non-extruded mesh) can be seen on the free end of the main cylinder.

The smallest element measured $10^{-3}D$ for the bare cylinder on its wall; and for the cases of the entire system, it spanned $1.54\times10^{-3}D$ for the main body,

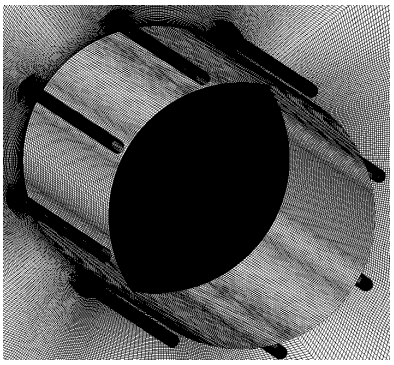

(a)

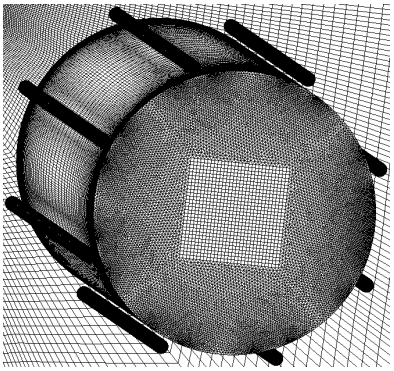

(b)

Figure 5. Extruded meshes for both cases of infinitely-long cylinder and that of low aspect ratio. In the former it is seen that spanwise mesh refinement is uniform; whereas for the latter refinement is enhanced near the ends of the cylinders.

and $3.77 \times 10^{-3} d$ for the rods to ensure good quality results near the boundary layer. It must be taken into account that the rods were on the verge of vortex shedding, because the Reynolds number based on their diameter $Re_d = Ud/\nu$ was merely 50.

Extrusion of cases i and ii are shown in figure 5. For the case of infinitely-long cylinders, figure 5a shows that uniform refinement was applied along the span of the bodies and their free ends were left open. In contrast, the second case (figure 5b) was more refined near the tips of the cylinders, which were closed by a side surface. In particular, this second figure shows the triangular elements that comprised part of the lateral surface of the main cylinder.

In terms of the entire domain of both cases, mesh refinement was increased toward the entire system. Away from it, the cells were made larger. Still, in order to capture typical gradients (related to vortices and eddies), the wake region was throughly refined, as portrayed by figure 6.

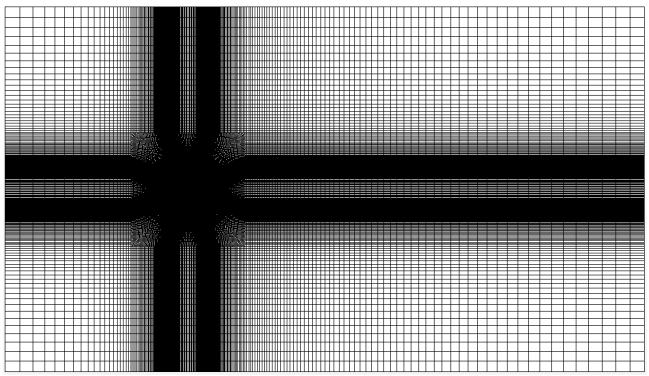

Figure 6. Meshed flow domain of any of the cases herein considered for a cross section through the system.

Table 1. Grid independence test with respect to mean drag ($\overline{C_D}$) and RMS lift ($\hat{C}_L$). Quantities between parentheses represent the percentual change from a mesh relative to the previous, coarser, one. The highlighted row shows variance below 10% relative to the most refined mesh hereby tested, thus providing a good compromise between computational resources and accuracy.

Number of cells	$\overline{C_D}$	$\hat{C}_L$
4,466,680	0.71 (-)	0.0414 (-)
6,679,440	0.69 (2.8%)	0.0708 (71.0%)
8,433,710	0.69 (0.0%)	0.0338 (52.3%)
10,198,560	0.68 (1.4%)	0.0380 (12.4%)
12,322,680	0.68 (0.0%)	0.0330 (13.2%)
15,293,080	0.69 (1.5%)	0.0330 (0.00%)

4. RESULTS

4.1. Reference simulations

Reference simulations were carried out first for verification, validation and grid independence test with respect to drag (C_D) and lift (C_L) coefficients, respectively given by the corresponding loads nondimensionalised by $\rho U^2 L/2$.

For case i, these results are found in Carvalho and Assi (2022) (under peer review). For case ii, validation was made with the results substantiated by Goldstein (1938) apud Farivar (1981) for cylinders of finite length, where the authors found that the mean drag $\overline{C_D} = 0.67$ at $Re = 8.8 \times 10^4$ for an aspect ratio of 1.98. Our simulation at $Re = 10^4$ produced $\overline{C_D} = 0.64$, in agreement with over 95.5%. Table 1 presents the grid independence test, performed in the same *Re*-regime, in relation to mean drag and root mean square (RMS) lift. The highlighted line corresponds to the mesh that will serve as a reference for the bare cylinder of low aspect ratio at $Re = 10^3$ that this work concerns with.

Due to the lack of results for the setup we have selected for the finite system and due to the more demanding computer resources required thereof, the same analysis is in order for future work. For now, we consider that the same numerical scheme applied to the case of a plain cylinder, a comparable cell growth ratio (for mesh refinement), corroborated by successful mesh convergence study made for the infinitely-long system (Carvalho and Assi, 2022), are features reliable enough for the following discussions regarding the entire system to be valid.

4.2. Time histories of hydrodynamic loads

All simulations were left to run for 15 vortex shedding cycles that we considered to be part of the numerical transient preceding convergence to realistic physical results. After this, in order to compute mean and RMS quantities, the simulations spanned at least another 20 additional cycles. In agreement with experiments (Norberg, 2001), the Strouhal number can typically be well approximated by $S_t = f_S/(U/D) \approx 0.2$ for an infinitely-long fixed cylinder in sub-critical regime, where $f_S = 1/T_S$ is the frequency of vortex shedding.

Thick and thin lines correspond, respectively, to lift and drag converged time histories in figure 7. It can be clearly noted that infinitely-long cylinders lead to the increase in hydrodynamic loads and to higher frequency of vortex shedding. Dampening of the frequencies of shedding is the most strikingly evident result for both setups of a plain cylinder and for the entire system in case ii compared with case i. Also notable is the fact that in any case, the entire system produced greater loads than the bare cylinder.

In terms of drag, this might be explained by the greater low-pressure region downstream of the system against that of the bare cylinder, produced by the wider wake shown in figure 8 for cases i and ii.

Lift increase is justified differently in regard to cases i and ii. For the former, the wider wake related to stronger opposing vortices whose response on the structure was translated into a greater transversal load to the flow (first row of figure 8). For the latter, higher lift is explained by the fact that a more organised wake resulted from the presence of the rods (second row of figure 8). Indeed, in case ii, the wake of the plain cylinder demonstrated a more chaotic aspect, containing a greater diversity of turbulence scales represented by small to middle eddies; whereas the wake of entire system was built upon larger scales that gave rise to a greater pressure imbalance crosswise. Furthermore, apparently greater vortex-formation length resulted for the entire system, responsible for a more distant shedding of vortices (although the wake topology did not recollect the Kármán vortex street).

This organisational effect draws attention to the extension to which an active mechanism of wake control, for example, spinning the rods, could have on vortex shedding. This effect has been widely corroborated for infinitely-long cylinders in the literature (Assi et al., 2018, 2019; Carvalho et al., 2021) and it has drawn attention to its optimisation as well (Fan et al., 2020; Bingham et al., 2018; Dehkordi et al., 2018). Considering the dampening of the fluctuation of the hydrodynamic loads, it is a open question whether an active mechanism could be more efficient in low aspect ratio cylinders than in infinitely-long cylinders.

It is an interesting feature common to both structures of case ii that coherent vortex structures did not seem to form, which may be due to the lack of correlation spanwise. As such, vortex shedding broke away from the usual 2S shedding mode (Williamson and Roshko, 1988).

Of course, it is relevant to observe that detached eddy simulations may introduce greater correlation in the flow structures spanwise than is found experimentally. Yet, we believe that qualitatively the present results are worthwhile and could be detected in a real setup.

4.3. Hydrodynamic loads on the individual cylinders

One important measure is that of hydrodynamic loads on the main body P_0 to which the passive mechanism was installed. Measurements of mean drag and RMS lift point that in case i, changing from the bare cylinder to entire system increased mean drag in 46.3% and RMS lift in 46.8% for the main body. In case 2, the respective changes were of 31.7% for both loads, thus, some relative gain of approximately 15% was observable for the passive mechanism in finite cylinders against the infinitely-long setup, although under any circumstance the passive rods enhanced hydrodynamic loads on the main body.

Figures 9a and 9b show mean drag and mean lift acting on each individual rod, according to their angular positions (see figure 2 for the θ-convention adopted in this paper). Rods P_2, P_2' were subjected to the greater absolute reduction in $\overline{C_D}$ and $\overline{C_L}$ of all rods. Contrarily, rods P_3, P_3' seemed oblivious to the different approaches. Rods P_1, P_1' experienced increase in $\overline{C_D}$ from null value and decrease of $|\overline{C_L}|$ and P_4, P_4' shifted with opposite tendencies. This is in agreement with Assi et al. (2019); Carvalho et al. (2021).

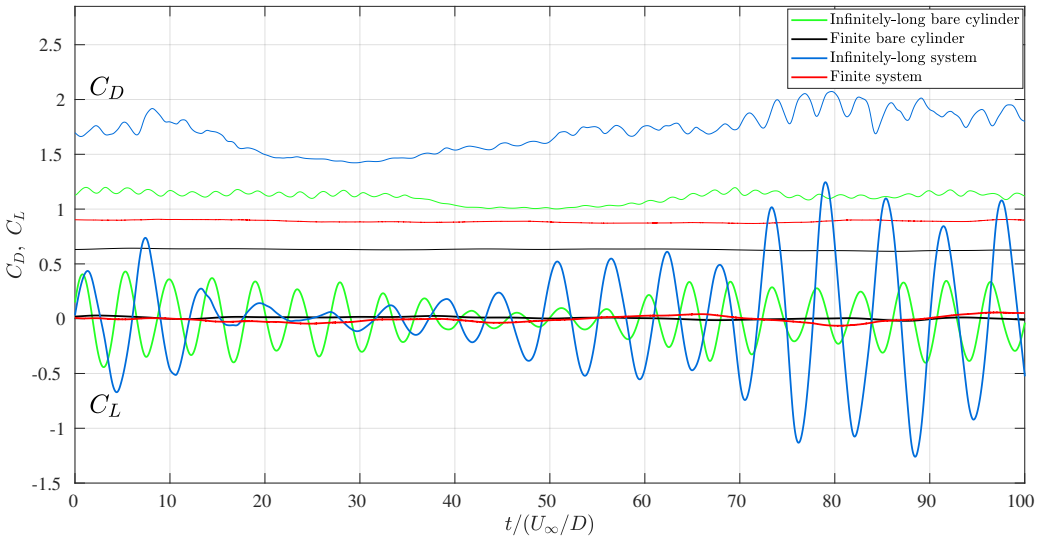

Figure 7. (Colour online) Time histories of lift and drag for the cases of infinitely-long and finite (low aspect ratio) cylinders.

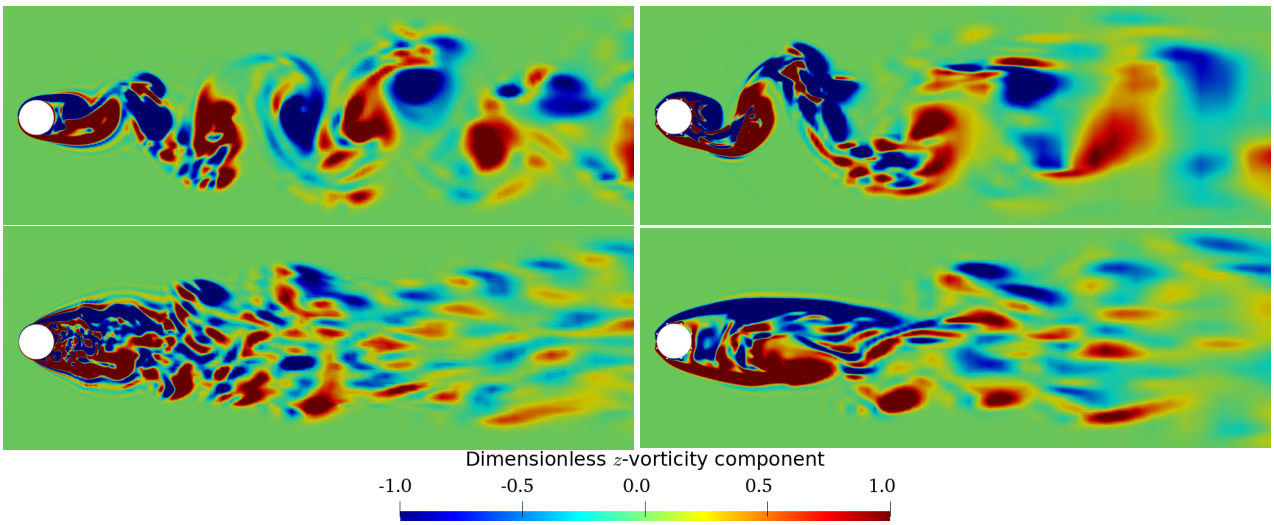

Figure 8. Dimensionless z-vorticity component, scaled by U_∞/D. Infinitely-long (first row) and low aspect ratio cases (second row). Plain cylinder on the left and entire system on the right. Low aspect ratio cases correspond to the cross section midway along cylinders' span. All cases were taken to be at a positive turn of the lift curve.

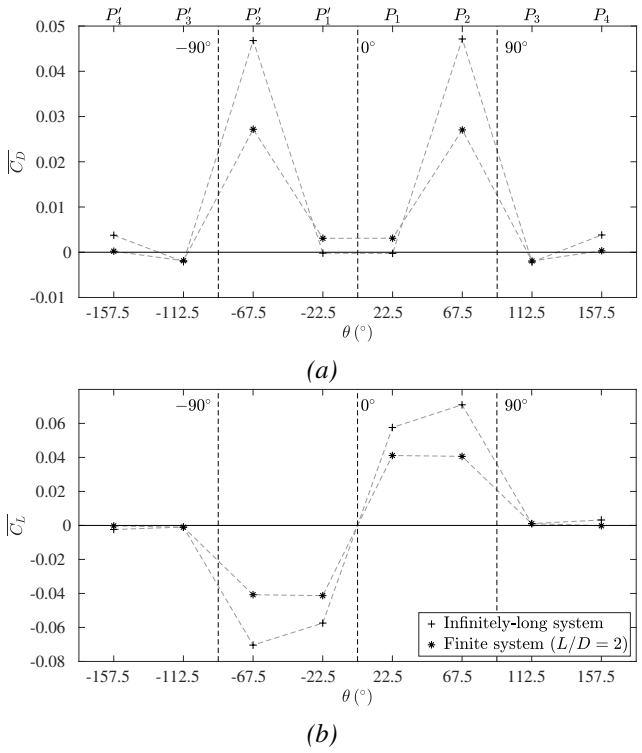

Figure 9. Mean drag (a) and RMS lift (b) on each of the control rods for both cases of infinitely-long cylinders and that of low aspect ratio (finite cylinders).

5. CONCLUSION

Finite volume simulations under the turbulent formulation of detached eddy simulations were conducted at $Re = 1000$. Validation, verification and grid independence tests indicated a reliable numerical scheme for the computation of the flow about structures with free ends.

Examination of the bare cylinder and of the entire system indicated that the free end has a decreasing effect in the hydrodynamic loads greater than 50% in mean drag and over 6% in root mean square lift.

Despite previous studies that ensure the incapacity of a passive mechanism to suppress vortex shedding at sufficiently high Reynolds numbers for infinitely-long cylinders (Mittal and Raghuvanshi, 2001; Mittal and Kumar, 2003), the same study was not conducted for a system with free ends such as the present. To fit a circular cylinder with eight slender wake-control rods under uniform flow at $Re = 1000$ proved insufficient to inhibit vortex shedding or to reduce the hydrodynamic loads. In fact, the greater obstruction to the flow caused by the surrounding slender bodies caused mean drag and root mean square lift to adopt higher values. In spite of these results, vortex contours indicated a more organised wake resulting from the passive mechanism of wake control, which reminded previous results for infinitely-long cylinders. The present results agree with previous works employing such a passive mechanism for infinitely-long cylinders and pave the way for the application of this system to low aspect ratio structures under an active mechanism of wake-control, for example, spinning the rods (Mittal, 2001; Korkischko and Meneghini, 2012) that may be able to not only control vortex shedding and vortex-induced vibrations and the associated hydrodynamic loads, but to eliminate these phenomena entirely in bluff structures of finite length.

Acknowledgments

IAC is grateful to CAPES Brazilian Ministry of Education for his PhD scholarship and to the National Laboratory for Scientific Computing (LNCC/MCTI, Brazil) for providing HPC resources of the SDumont supercomputer. GRSA acknowledges the support of FAPESP, Brazil (2011/00205-6) and CNPq, Brazil (306146/2019-3). We gratefully acknowledge the support of the RCGI Research Centre for Greenhouse Gas Innovation, hosted by the University of São Paulo, Brazil and sponsored by FAPESP (2020/15230-5) and Shell Brasil.

6. REFERENCES

G. R. S. Assi, R. M. Orselli, and M. Silva-Ortega. Suppression of vortex shedding with rotating wake-control cylinders: Numerical investigation at a moderate reynolds number. In *International Conference on Offshore Mechanics and Arctic Engineering*, volume 51210, page V002T08A060. American Society of Mechanical Engineers, 2018.

G. R. S. Assi, R. M. Orselli, and M. Silva-Ortega. Control of vortex shedding from a circular cylinder surrounded by eight rotating wake-control cylinders at Re= 100. *Journal of Fluids and Structures*, 89: 13–24, 2019.

M. Behr, J. Liou, R. Shih, and T. Tezduyar. Vorticity-streamfunction formulation of unsteady incompressible flow past a cylinder: Sensitivity of the computed flow field to the location of the outflow boundary. *International Journal for Numerical Methods in Fluids*, 12(4):323–342, 1991.

M. Behr, D. Hastreiter, S. Mittal, and T. Tezduyar. Incompressible flow past a circular cylinder: dependence of the computed flow field on the location of the lateral boundaries. *Computer Methods in Applied Mechanics and Engineering*, 123(1-4):309–316, 1995.

C. Bingham, C. Raibaudo, C. Morton, and R. Martinuzzi. Suppression of fluctuating lift on a cylinder via evolutionary algorithms: Control with interfering small cylinder. *Physics of Fluids*, 30(12):127104, 2018.

I. A. Carvalho and G. R. S. Assi. Enhanced control of the turbulent flow past a circular cylinder with rotating rods constrained by an inviscid solution. Submitted to the Journal of Fluids and Structures, 1 2022.

I. A. Carvalho, G. R. S. Assi, and R. M. Orselli. Wake control of a circular cylinder with rotating rods: Numerical simulations for inviscid and viscous flows. *Journal of Fluids and Structures*, 106:103385, 2021.

H. Choi, W.-P. Jeon, and J. Kim. Control of flow over a bluff body. *Annu. Rev. Fluid Mech.*, 40:113–139, 2008.

E. K. Dehkordi, M. Goodarzi, and S. Nourbakhsh. Optimal active control of laminar flow over a circular cylinder using taguchi and ann. *European Journal of Mechanics-B/Fluids*, 67:104–115, 2018.

D. Fan, L. Yang, Z. Wang, M. S. Triantafyllou, and G. E. Karniadakis. Reinforcement learning for bluff body active flow control in experiments and simulations. *Proceedings of the National Academy of Sciences*, 117(42):26091–26098, 2020.

D. Farivar. Turbulent uniform flow around cylinders of finite length. *AIAA journal*, 19(3):275–281, 1981.

G. R. Franzini, R. T. Gonçalves, J. R. Meneghini, and A. L. C. Fujarra. One and two degrees-of-freedom vortex-induced vibration experiments with yawed cylinders. *Journal of Fluids and Structures*, 42:401–420, 2013.

J. H. Gerrard. The mechanics of the formation region of vortices behind bluff bodies. *Journal of fluid mechanics*, 25(2):401–413, 1966.

S. Goldstein. *Modern developments in fluid dynamics: an account of theory and experiment relating to boundary layers, turbulent motion and wakes*, volume 2. Clarendon Press, 1938.

I. Korkischko and J. Meneghini. Suppression of vortex-induced vibration using moving surface boundary-layer control. *Journal of Fluids and Structures*, 34:259–270, 2012.

S. Luo, T. Gan, and Y. Chew. Uniform flow past one (or two in tandem) finite length circular cylinder (s). *Journal of wind engineering and industrial aerodynamics*, 59(1):69–93, 1996.

S. Mittal. Control of flow past bluff bodies using rotating control cylinders. *Journal of fluids and structures*, 15(2):291–326, 2001.

S. Mittal and B. Kumar. Flow past a rotating cylinder. *Journal of fluid mechanics*, 476:303–334, 2003.

S. Mittal and A. Raghuvanshi. Control of vortex shedding behind circular cylinder for flows at low Reynolds numbers. *International Journal for Numerical Methods in Fluids*, 35(4):421–447, 2001. ISSN 1097-0363.

C. Norberg. Flow around a circular cylinder: aspects of fluctuating lift. *Journal of fluids and structures*, 15 (3-4):459–469, 2001.

M. Silva-Ortega and G. R. S. Assi. Flow-induced vibration of a circular cylinder surrounded by two, four and eight wake-control cylinders. *Experimental Thermal and Fluid Science*, 85:354 – 362, 2017. ISSN 0894-1777.

P. J. Strykowski and K. R. Sreenivasan. On the formation and suppression of vortex shedding at low reynolds numbers. *Journal of Fluid Mechanics*, 218: 71–107, 1990.

C. H. Williamson and A. Roshko. Vortex formation in the wake of an oscillating cylinder. *Journal of fluids and structures*, 2(4):355–381, 1988.

M. M. Zdravkovich. Review and classification of various aerodynamic and hydrodynamic means for suppressing vortex shedding. *Journal of Wind Engineering and Industrial Aerodynamics*, 7(2):145–189, 1981.

EXPERIMENTAL INVESTIGATION ON THE OPTIMAL CONTROL OF VORTEX SHEDDING OF A CIRCULAR CYLINDER WITH ROTATING RODS AT MODERATE REYNOLDS NUMBERS

Paulo H. N. Silva & Gustavo R. S. Assi
Dept. Naval Arch. and Ocean Engineering, University of São Paulo, Brazil
E-mail: g.assi@usp.br

ABSTRACT

This paper presents an experimental study of fluid-structure interaction performed with scale models in a water channel at moderate Reynolds numbers. A circular cylinder model was equipped with 8 control rods positioned around its perimeter to interact with the external flow. Each rod could be independently driven to rotate around its own axis. The controlled rotation of the rods interfered with the vortex generation mechanism, mitigating the formation of a coherent wake. The results showed that there is an optimal rotation setting for the 8 rods that drastically reduces vortex formation and minimizes drag and energy consumption. A maximum drag reduction of 22% was obtained in relation to that of a bare cylinder, but at a cost of an increase of 10% in fluctuating lift. This work is a scientific study that clarifies the physical principles involved in the phenomenon, paving the way for the development of technological and innovative solutions.

Keywords*: bluff body; flow control; Vortex shedding; control rods; multi-objective genetic algorithm.*

1. INTRODUCTION

Under certain flow conditions, bluff bodies present large mean drag forces and fluctuating drag and lift caused by the vortex shedding. These oscillatory forces can interact with several structures resulting in Vortex Induced Vibration (VIV) (Williamson and Govardhan, 2004; Bearman, 1984), as well as longer-period oscillations in large offshore platforms in the so-called Vortex Induced Motions (VIM) (Fujarra et al., 2012).

Controlling the vortex shedding mechanism is at the root of efficient VIV suppression. Over the years, several technologies to suppress vortex shedding have been developed and classified (Zdravkovich, 1981; Choi et al., 2008), most of them in the form of passive appendages installed around the hull: helical strakes, shrouds and fairings are some examples (Bearman and Branković, 2004; Assi et al., 2009). Each solution brings problems intrinsic to the suppression mechanism, perhaps the increase in hydrodynamic drag is the main one.

A passive control method based on local/global instability is the use of interfering control rods strategically placed on the bluff body near wake. This application was first described by Strykowski and Sreenivasan (1990) effectively suppressing the vortex shedding past a circular cylinder in a low Reynolds number. The technique can also be effective for drag reduction as observed experimentally by Marangon Cicolin et al. (2021) or Jiménez-González and Huera-Huarte (2018) using a single and a pair of controls rods, respectively. The success of this method strongly depends on the control rod diameter (d) and it position around the main cylinder, usually defined by the gap between surfaces (G) and angular position (θ). If one or more rods are positioned outside the sensitivity region, in general the mean drag tends to increase, as observed by Silva-Ortega and Assi (2017b) in a study with an arrangement of 2, 4 and 8 control rods.

When the control rods are driven to rotated around their own axis, this active (energy-consuming) method is known as Moving Surface Boundary Layer Control (MSBC). A review of successful applications of this method on non-cylindrical folios and bluff bodies for drag reduction can be found in Modi (1997). The author justified its ability to delay the boundary layer separation by limiting its growth and injecting angular momentum. Other numerical simulations (Assi et al., 2018, 2019; Mittal, 2003) and experimental trials (Schulmeister et al., 2017; Korkischko and Meneghini, 2012) have investigated this method and demonstrated the capability to narrow the wake and prevent vortex formation.

Experiments conducted by Silva-Ortega and Assi (2017a) considered 8 rotating control rods uniformly distributed around the main cylinder as an approximation of an axial-symmetric device. The VIV response for a range of control rods speed, kept the same for all the rods during each trial, demonstrated

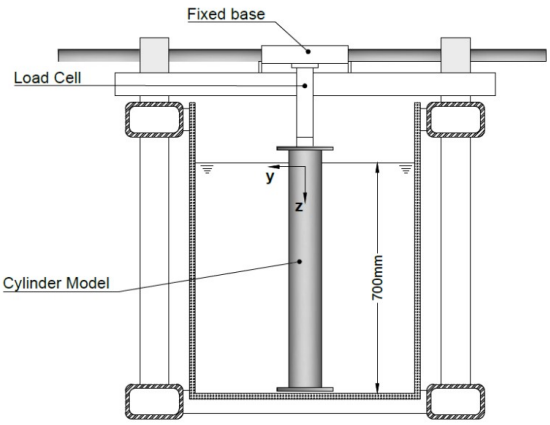

Figure 1. Cross sectional view of the water channel (Silva-Ortega, 2015)

considerable reduction on the peak amplitude and fluctuating lift, while the mean drag has increased in relation to the bare cylinder. One might question whether better results could be obtained if the control rods were allowed to rotate independently. Perhaps the combination of different rotations for each control rod could result in a reduction of both lift fluctuation and mean drag for this configuration. Besides that, the energy consumption for the same reduction on mean drag or fluctuating lift could be optimized. These questions motivated this study.

1.1. Objective

The present work aims to experimentally investigate the active flow control method MSBC on a cylindrical body, uniformly distributing 8 rotating rods with independent speed around the main cylinder. Different combinations of control rods angular rotations (Ω_i) will be tested, while the geometric dimensions of the model, quantity and distribution of the rods are constants defined with reference to previous studies.

The model was installed in a recirculating water channel with no possibility of movement and the flow control is evaluated by measuring the resulting hydrodynamic drag and lift forces. Even knowing that these responses alone are not enough to guarantee the suppression of VIV in floating structures, it is possible to have a good indication of the interference in the flow caused by the actuator and the sensitivity in relation to the variables tested. A simplified cross section of the experimental model set up in the water channel is reproduced from Silva-Ortega (2015) in the figure 1.

The objective is to identify if a combination of different rotations of control rods is able to simultaneously reduce the mean drag and the fluctuating lift while consuming the minimum energy.

2. EXPERIMENTAL SETUP

The experiments were carried out in a recirculating water channel of Dynamics and Fluids Research Group (NDF) at the University of São Paulo (USP).

The channel is operated by a LabView program developed by Assi et al. (2006) that communicates to a National Instruments CompactDAQ platform. With a length of 7.5m and a cross section of 0.7m wide by 0.9m deep, it has a maximum flow rate of $0.4\text{m}^3/\text{s}$ instantly read through an electromagnetic flow meter with an uncertainty of 0.5%. The free stream velocity is controlled through a frequency inverter that changes the rotation of a pump. The turbulence intensity in the middle of the recirculating channel was measured in the past as less than 3%, considered low for a water channel.

The main cylinder has an external diameter D=100mm made of a 3mm thick rigid and transparent acrylic tube, closed at both ends by machined aluminum parts. The clearance between the bottom face of the model and the channel is less than 3mm. It was mounted in the centre of the cross-section (blockage ratio 14.3%), vertically supported from the top by a load cell capable of measuring hydrodynamic forces up to 50N and with an uncertainty of 1%. The water level is adjusted to ensure an aspect ration of L/D=7.

The experiments were conducted on a Reynolds number ($Re = UD/\nu$) interval of $1 \times 10^4 \leq Re \leq 5 \times 10^4$, characterized by the turbulent transition in the shear layers. As Choi et al. (2008) posted, "it is questionable that a successful control method in a certain Reynolds-number rage works for other Reynolds-number ranges". Therefore, it is possible that the upstream flow condition found in real applications results in a different control method effectiveness or rotation parameters, especially at higher Reynolds.

2.1. Rotating control rods

For a practical application in engineering structures an omni-directional actuator is advantageous, as it allows a response independent to the flow direction. For this purpose, the developed active open-loop flow control system is composed by $N = 8$ solid cylinders, called control rods, with diameter $d/D = 0.08$ uniformly distributed around the main cylinder with a gap between surfaces of $G/D = 0.1$ shown in the figure 2. The control rods distribution equally spaced by 45° is a simplification that seeks an actuation mechanism independent of the flow direction. This omni-directional actuation hypothesis should be verified in further studies to confirm if the number of control rods are enough. Probably, this arrangement is not the most efficient, as some control rods might be positioned in a non-sensitive region, but as many engi-

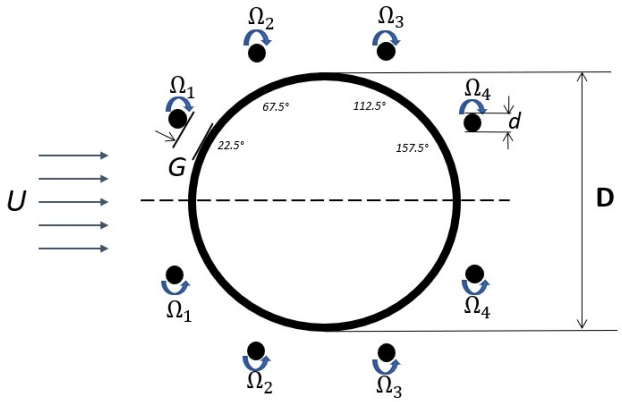

Figure 2. Experimental setup

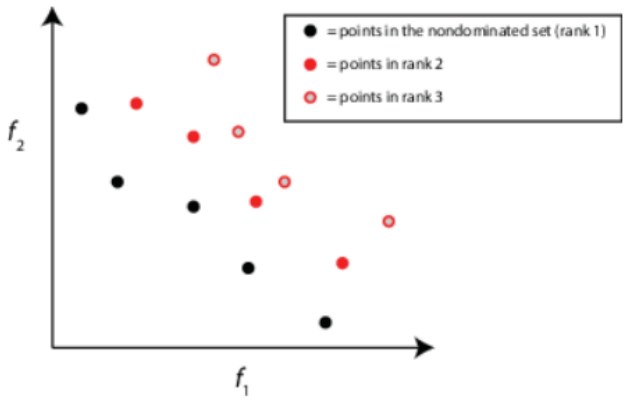

Figure 3. Individual ranking based in dominance (MATLAB, 2021b)

neering applications does not has flow direction well defined, this arrangement concept may have advantages in certain applications.

Each control rod is coupled to an independent 12V DC motor, capable to rotate in the range of $40 \leq \Omega_i \leq 220$ rad/s with 10 rad/s uncertainty. For the experiments, the search within the sample space of the rotational velocity was performed in steps of 20 rad/s, resulting in a resolution of $R = 10$. The speed is controlled by the Pulse Width Modulation (PWM) signal provided by two *Motor Shield Adafruit V2* stacked over and *Arduino Due*, which communicates in real time with MATLAB Simulink software. Three perforated acrylic discs uniformly distributed along the length of the rods to reduce vibration.

It is undesirable for this actuator to result in any positive mean lift, so a symmetry between the control rods was imposed by the proper alignment of the model with respect to free stream and the rotation performed by pairs. As a result, the number of variables has been reduced to $n = 4$ rotation speed Ω_1 , Ω_2 , Ω_3 and Ω_4, as represented in the figure 2.

3. OPTIMIZATION METHOD

The method called grid search is very effective in experiments with low resolution number and variables. However, as the experimental effort increases exponentially ($E = R^n$), if the method was assigned to this experiment, a total amount of $E = 10000$ experiments would be needed to cover all control rods speed combinations. Considering an acquisition time of 140 seconds between each sample, an unfeasible duration of 16 days would be necessary for the conclusion of this study.

To manage this problem, an optimization algorithm was implemented to conduct the experiments more efficiently. A similar optimization method was implemented by Bingham et al. (2018) on experiments performed to simultaneously minimize the fluctuating lift while consuming the minimum energy required to displace a control rod through a periodic sinusoidal motion in two dimensions.

The parameter chosen to be simultaneously minimized were the mean drag force $\overline{F_D}$ and fluctuating lift $\widehat{F_L}$. A Multi-objective Evolutionary Algorithm (MOEA) was chosen to find the optimal combination of control rods speed for these objectives. The algorithm script used was a built-in MATLAB function.

The drag and lift forces measured by the load cell are the input data for the algorithm to make decisions during the iterative process. To enable the data exchange between MATLAB (responsible for the optimization algorithm and actuator) and LabView (responsible for data real-time data acquisition), a TCP/IP communication was developed using as a starting point a code available in MATLAB (2021a).

4. EVOLUTIONARY ALGORITHM

According to the technical specification available in MATLAB (2021b), the optimization function *gamultiobj* is an adaptation of the Elitist Non-dominated Sorting Genetic Algorithm (NSGA-II) developed by Deb (2001).

The evolutionary algorithm is a method for solving optimization problems inspired by natural selection that incorporate features of biological evolution. Each *Individual* is a row vector with a length given by the number of variables, being, in this study, composed of a combination of 4 independent rotation applied to the control rods. The *Population* is defined as a set of individuals that change with each iteration (also called *Generation*). The biggest advantage of this approach is that if the optimization problem has a

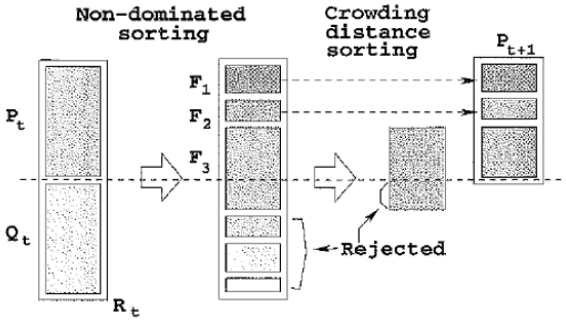

Figure 4. Schematic of the NSGA-II procedure (Deb, 2001)

single optimum, individuals are expected to converge to that optimum, but if the optimization problem has multiple optimal solutions, the final population can capture a number of optimal solutions.

An iterative process to evaluate each individual in relation to the others belonging to the same population is used by the algorithm for decision making. The figure 3 illustrates the concept of dominance applied to rank a population. Rank 1 individuals are not dominated by any other individuals, while rank 2 individuals are dominated only by rank 1, and so on. Individuals with a lower rank have a higher chance of selection.

The optimization algorithm initializes by creating an initial population P_0. By default, the first population is randomly generated respecting the problem bounds (rotation speed interval). Each individual is tested and the results acquired in real time are stored in the vector named *Score*.

The main steps of the NSGA-II optimization method proposed by Deb (2001) are illustrated in the figure 4. The initial population is also used as the *Parent* population P_t for the first iterative process ($P_t = P_0$). This means that this matrix is modified by the crossover and mutation operators, to generate a new population Q_t called *Offspring* (or *Children*).

Each individual in offspring population Q_t is tested and the results stored. Then, the population of parents and offspring are combined to form the extended population $R_t = P_t + Q_t$. All individuals belonging to R_t are ranked based on their dominance. A trim is performed on a half of the individuals to reject the worst ones and ensure the convergence of the solution, taking into consideration a crowding distance function to favor population diversity for individuals at the same rank. A new parent population P_{t+1} is then created and the iterative cycle is restarted, until any applied stopping condition is met: *Generation*, *Time* or *Convergence*.

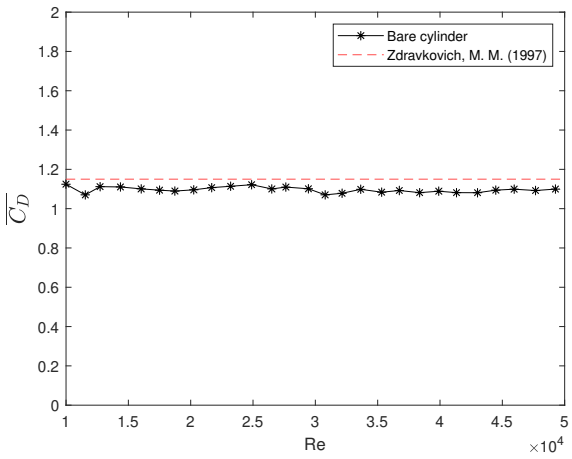

Figure 5. Bare cylinder: Mean drag coefficient along Reynolds number

5. RESULTS AND DISCUSSION

Each individual had the signal acquired during 140s at 100Hz and filtered. The mean drag $\overline{F_D}$ is obtained by the arithmetic average of the acquired time series. The fluctuating lift $\widehat{F_L}$ was calculated using the Root Mean Square (RMS) value given by the expression $\widehat{F_L} = \sqrt{2}(F_L - \overline{F_L})_{RMS}$.

The drag and lift forces are also expressed in their dimensionless form by the ratio between the dynamic pressure ($\frac{1}{2}\rho U^2$) and the projected area of the body. Thus, the drag and lift coefficients of interest can be expressed, respectively, by

$$\overline{C_D} = \frac{\overline{F_D}}{\frac{1}{2}\rho U^2 DL}, \tag{1}$$

$$\widehat{C_L} = \frac{\widehat{F_L}}{\frac{1}{2}\rho U^2 DL}. \tag{2}$$

5.1. Preliminary results for a bare cylinder

A preliminary evaluation of the flow around a bare cylinder was performed to validate the experimental setup and to generate reference data to the model with the actuators. The experiments were conducted on a Reynolds interval of $1 \times 10^4 \leq Re \leq 5 \times 10^4$, where 27 samples of hydrodynamic forces were acquired.

The mean drag coefficient $\overline{C_D}$ for a circular cylinder in cross-flow versus *Re* has been extensively documented on the literature since measurements from Roshko (1961) with low variation between authors. To compare with the bare cylinder results, the coefficient $\overline{C_{D(ref)}} = 1.15$ provided by Zdravkovich (1997) was taken as reference. The experimental results presented on figure 5 are very close to the literature.

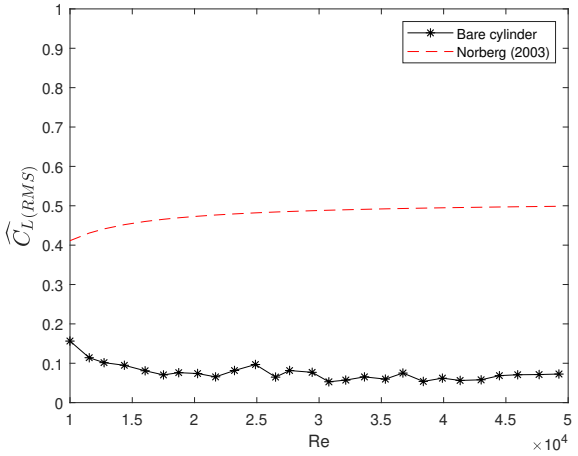

Figure 6. Bare cylinder: Fluctuating lift coefficient along Reynolds number

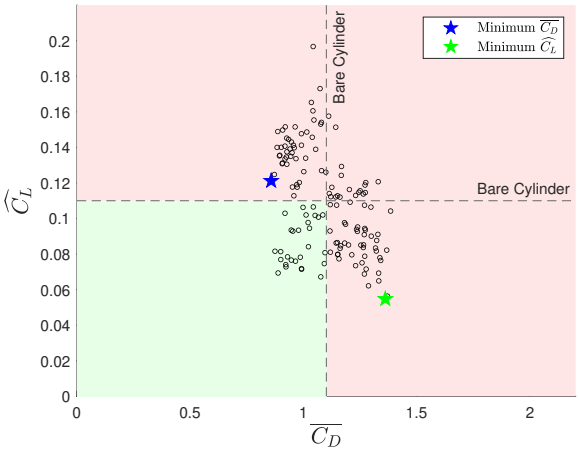

Figure 7. Rotating control rods: Mean drag coefficient in relation to fluctuating lift coefficient

On the other hand, according to Norberg (2003) the graphs for the fluctuating lift coefficient $\widehat{C_L}$ versus Re are much more undefined, and despite the various compilations that have been presented, the data becomes increasingly scattered and inconclusive. The author's empirical function ($\widehat{C_{L(RMS)}} = 0.52 - 0.06(log(Re/1600)^{-2.6})$) was taken as reference. The experimental results on figure 6 presents a particular difference in the fluctuating lift results, explained by the sensitivity of the boundary conditions and turbulence effects, especially in this Reynolds number interval.

As the experimental data presented a very stable behavior, the setup is considered validated and for purpose of comparison between the bare cylinder and controlled model, the coefficients will be taken as constants over the interval using the average of the sample data. ($\overline{C_D} \approx 1.1$ and $\widehat{C_L} \approx 0.11$).

5.2. Result for rotating control rods

The power added to the motors can be easily calculated using the voltage and current values at each rotational speed. However, most of the energy consumed is lost in frictions that are inherent to the experimental model. Thus, consider only the energy needed to overcome viscous stresses allows a better comparison with other experimental or numerical studies.

An estimate value for torque required to overcome the total shear stress in its wall by rotating each control rod can be provided by the analytical expression for two-dimensional flow deduced by Glauert Glauert (1957) expressed by:

$$\frac{T}{L} = \frac{\pi d^2 \rho U^2}{\sqrt{Re}} \left(\left(\frac{U_c}{U} \right)^{-1/2} - 0.522 \left(\frac{U_c}{U} \right)^{-5/2} \right) \tag{3}$$

where U_c is the tangential velocity of each control given by ($U_c = \Omega_i \times d/2$). This expression assumes that the flow separation can be neglected in a such rapidly rotating rod, so is only valid for $U_c/U \geq 0.722$. The torque is used to calculate the energy consumption spent to rotate all the control rods, given by the expression

$$P_{rot} = \sum_{i=1}^{N} T_i \Omega_i. \tag{4}$$

This power can be dimensionless by the kinetic energy flow ($\frac{1}{2}\rho U^3$) and the projected area, resulting in the power consumption coefficient given by

$$C_{pow}^{rot} = \frac{P_{rot}}{\frac{1}{2}\rho U^3 DL}. \tag{5}$$

The optimization was conducted on a fixed Reynolds number of $Re = 4 \times 10^4$. A total amount of 141 individuals were tested along the iterative process of the algorithm to simultaneously minimize both objectives.

All the tested individuals are represented by the black dots in the figure 7, that relates the objectives to each other. The reference lines ($\overline{C_D} = 1.1$ and $\widehat{C_L} = 0.11$) indicates that a significant amount of individuals were found in the third quadrant, demonstrating that the purposed actuator is capable to simultaneously reduce $\overline{C_D}$ and $\widehat{C_L}$ in relation to the bare cylinder.

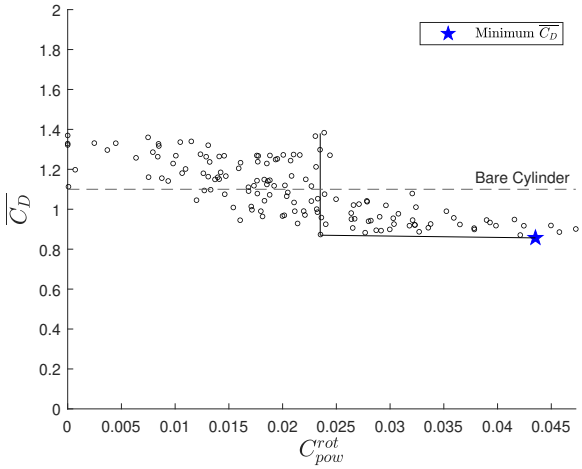

Figure 8. Rotating control rods: Mean drag coefficient in relation to the power consumption coefficient

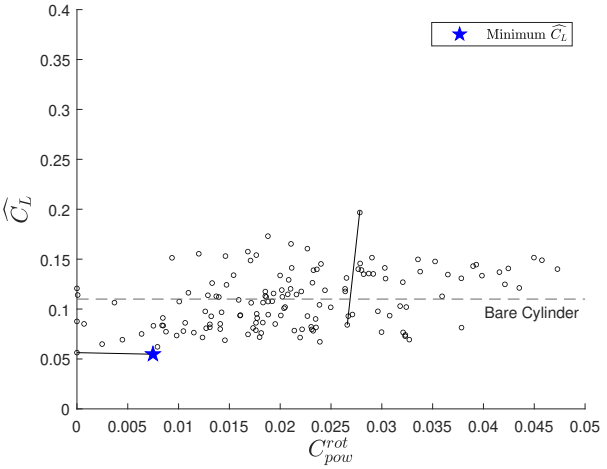

Figure 9. Rotating control rods: Fluctuating lift coefficient in relation to the power consumption coefficient

The algorithm did not converge to a single optimal individual, but to a set of multiple equally optimal solutions. This indicates that the proposed actuation mechanism is a non-trivial problem, where the objective functions are considered independent and conflicting, since one cannot be improved without degrading the other.

This behavior is evident when observing the individual that resulted in the lowest mean drag highlighted by a blue star, corresponding to a reduction of 22% in relation to the bare cylinder mean drag but an increment of 10% in the fluctuating lift. At the same manner the individual that resulted in the lowest fluctuating lift is highlighted by a green star, corresponding to a reduction of 50% in relation to the bare cylinder fluctuating lift but an increment of 24% in the mean drag.

Then, each objective is evaluated separately and the results for mean drag $\overline{C_D}$ in relation to the power consumption coefficient C_{pow}^{rot} are shown it the figure 8. Similar power consumption can result in very different mean drag results. For example, the vertical line connecting two individuals with the same energy consumption $C_{pow}^{rot} \approx 0.024$ can result a reduction of 20% or a 26% increase to the mean drag. Furthermore, the horizontal line indicates that a similar drag reduction can be achieved with much lower energy consumption. For example, the blue star individual consumed $C_{pow}^{rot} \approx 0.044$ to reduce 22% drag, while another individual can be found showing a similar reduction but consuming half the energy $C_{pow}^{rot} \approx 0.024$.

In general, a downward trend in mean drag is observed as the angular momentum injection increases. However, this analysis indicates that the combination of rotations involving the individual is the most important for reducing drag, as some rotation of control rods may be unnecessary or even harmful.

Likewise, the results for the fluctuating lift coefficient $\widehat{C_L}$ in relation to the power consumption coefficient C_{pow}^{rot} are presented in the figure 9. In this case, the dispersion of the results is more evident, but the sensitive of this objective to the noise related to the actuators cannot be neglected.

The same analysis that similar power consumption can result in very different fluctuating lift coefficient results can be performed. For example, the vertical line connecting two individuals with the same energy consumption $C_{pow}^{rot} \approx 0.027$ can result in a reduction of 24% or an increase of 80%! Furthermore, the horizontal line indicates that a similar fluctuating lift coefficient reduction can be obtained even in a condition of fixed control rods ($C_{pow}^{rot} = 0$) which reduced the fluctuating lift coefficient by 49%, while the blue star individual that consumed energy ($C_{pow}^{rot} = 0.007$), resulted in a negligible gain in comparison to the fixed rods condition.

Considering that, for the fluctuating lift coefficient a upward trend is observed as the injection of angular momentum increases. However, even if for this objective rotate the control rods doesn't seem to be as beneficial, some combination of rotations can be very harmful.

6. CONCLUSION

The results suggest that the rotation of each control rod has a specific effect on the flow around the main cylinder. The contribution of each rod strongly depends on its angular position around the body and the flow condition that each one encounters.

Flow topology investigations are necessary to understand the role of each rod in the control of separate flow. In this work, we limit ourselves to evaluating its effect on the resulting hydrodynamic forces.

However, this study was enough to show that there is justification for the search for an optimized solution considering reductions in drag and lift forces.

Finally, we conclude that this experimental study on the fundamental hydrodynamic mechanisms of flow control separated by rotating rods contributes to the conception and development of full-scale control systems technology.

7. ACKNOWLEDGMENTS

We gratefully acknowledge support of the RCGI – Research Centre for Greenhouse Gas Innovation, hosted by the University of São Paulo (USP) and sponsored by FAPESP – São Paulo Research Foundation (2014/50279-4 and 2020/15230-5) and Shell Brasil; and the support given by ANP (Brazil's National Oil, Natural Gas and Biofuels Agency) through the R&D levy regulation. GRSA is grateful to CNPq (306146/2019-3).

8. REFERENCES

G. Assi, P. Bearman, and N. Kitney. Low drag solutions for suppressing vortex-induced vibration of circular cylinders. *Journal of Fluids and Structures*, 25 (4):666–675, 2009.

G. Assi, R. Orselli, and M. Silva-Ortega. Control of vortex shedding from a circular cylinder surrounded by eight rotating wake-control cylinders at re = 100. *Journal of Fluids and Structures*, 89, 03 2019.

G. R. Assi, J. R. Meneghini, J. A. Aranha, P. W. Bearman, and E. Casaprima. Experimental investigation of flow-induced vibration interference between two circular cylinders. *Journal of Fluids and Structures*, 22(6-7):819–827, 2006.

G. R. Assi, R. M. Orselli, and M. Silva-Ortega. Suppression of vortex shedding with rotating wake-control cylinders: numerical investigation at a moderate reynolds number. In *OMAE 2018*, Madrid, 2018, 2018. INTERNATIONAL CONFERENCE ON OCEAN, OFFSHORE AND ARCTIC ENGINEERING, 37., proceedings, New York: ASME International.

P. Bearman and M. Branković. Experimental studies of passive control of vortex-induced vibration. *European Journal of Mechanics - B/Fluids*, 23(1):9–15, 2004. ISSN 0997-7546. Bluff Body Wakes and Vortex-Induced Vibrations.

P. W. Bearman. Vortex shedding from oscillating bluff bodies. *Annual Review of Fluid Mechanics*, 16 (1):195–222, 1984.

C. Bingham, C. Raibaudo, C. Morton, and R. Martinuzzi. Suppression of fluctuating lift on a cylinder via evolutionary algorithms: Control with interfering small cylinder. *Physics of Fluids*, 30(12):1–11, 2018.

H. Choi, W. P. Jeon, and J. Kim. Control of flow over a bluff body. *Annual Review of Fluid Mechanics*, 40 (1):113–139, 2008.

K. Deb. *Multi objective optimization using evolutionary algorithm*. John Wiley & Sons, Chichester, 1 edition, 2001.

A. Fujarra, G. Rosetti, J. Wilde, and R. Gonçalves. State-of-art on vortex-induced motion: A comprehensive survey after more than one decade of experimental investigation. In *OMAE 2012*, pages 561–582, Rio de Janeiro, 2012, 2012. INTERNATIONAL CONFERENCE ON OCEAN, OFFSHORE AND ARCTIC ENGINEERING, 31., proceedings, New York: ASME International.

M. B. Glauert. The flow past a rapidly rotating circular cylinder. *Proceedings of the Royal Society of London. Series A. Mathematical and Physical Sciences*, 242(1228):108–115, 1957.

J. Jiménez-González and F. Huera-Huarte. Vortex-induced vibrations of a circular cylinder with a pair of control rods of varying size. *Journal of Sound and Vibration*, 431, 06 2018.

I. Korkischko and J. Meneghini. Suppression of vortex-induced vibration using moving surface boundary-layer control. *Journal of Fluids and Structures*, 34:259–270, 2012.

M. Marangon Cicolin, O. Buxton, G. Assi, and P. Bearman. The role of separation on the forces acting on a circular cylinder with a control rod. *Journal of Fluid Mechanics*, 915, 05 2021.

MATLAB. Matlab and labview data exchange over tcp/ip: version 1.4.0.0, 2021a. Access in: 01 nov.

MATLAB. Matlab help center, 2021b. Access on: 01 nov.

S. Mittal. Flow Control Using Rotating Cylinders: Effect of Gap . *Journal of Applied Mechanics*, 70(5): 762–770, 10 2003.

V. J. Modi. Moving surface boundary-layer control: A review. *Journal of Fluids and Structures*, 11(6): 627–663, 1997.

C. Norberg. Fluctuating lift on a circular cylinder: review and new measurements. *Journal of Fluids and Structures*, 17(1):57–96, 2003.

A. Roshko. Experiments on the flow past a circular cylinder at very high reynolds number. *Journal of Fluid Mechanics*, 10(3):345–356, 1961.

J. C. Schulmeister, J. M. Dahl, G. D. Weymouth, and M. S. Triantafyllou. Flow control with rotating cylinders. *Journal of Fluid Mechanics*, 825:743–763, 2017.

M. Silva-Ortega. Suppression of vortex-induced vibration of a circular cylinder with fixed and rotating control cylinders. Master's thesis, Escola Politécnica, Departamento de Engenharia Naval e Oceânica, São Paulo, 2015.

M. Silva-Ortega and G. Assi. Suppression of the vortex-induced vibration of a circular cylinder surrounded by eight rotating wake-control cylinders. *Journal of Fluids and Structures*, 74:401–412, 2017a.

M. Silva-Ortega and G. Assi. Flow-induced vibration of a circular cylinder surrounded by two, four and eight wake-control cylinders. *Experimental Thermal and Fluid Science*, 85:354–362, 2017b.

P. J. Strykowski and K. R. Sreenivasan. On the formation and suppression of vortex shedding at low Reynolds numbers. *Journal of Fluid Mechanics*, 218: 71–107, 1990.

C. Williamson and R. Govardhan. Vortex-induced vibrations. *Annual Review of Fluid Mechanics*, 36 (1):413–455, 2004.

M. Zdravkovich. Review and classification of various aerodynamic and hydrodynamic means for suppressing vortex shedding. *Journal of Wind Engineering and Industrial Aerodynamics*, 7(2):145–189, 1981. ISSN 0167-6105.

M. M. Zdravkovich. *Flow Around Circular Cylinders: Fundamentals*, volume 1. Oxford University Press, New York, 1997.

CFD techniques

A DISCRETE FORCING METHOD TO SOLVE HYPERELASTIC DEFORMATION INDUCED BY TWO-PHASE FLOW

N. MERIGOUX[1], W. BENGUIGUI[1,2], F. BARAGLIA[1]
[1]*EDF R&D, Fluid Mechanics Division, 6 Quai Watier 78400 Chatou*
[2]*IMSIA, UMR EDF-ENSTA-CNRS-CEA 9219, Paris-Saclay university, 91762, Palaiseau, France*

ABSTRACT

Fluid-structure interaction is an everoccuring phenomenon in engineering. In nuclear power plants for instance, fuel rods and tubes in steam generator or cooling towers may deform under the extreme load caused by the fluid flowing around them. It may also be valuable to study this kind of interaction during pipelines installation or for wind generating structures. If the deformation is sufficiently important as to influence the fluid behaviour, the problem must be tackled as a whole. Therefore, fluids and structures cannot be processed separatly. In this work, a fluid-structure interaction method taking into account the large deformation of simple geometry is developed in Neptune_cfd, a 3D multiphase flow code based on Eulerian-Eulerian approach with a single pressure. The solid structures are geometrically non-linear elastic beams in plane strain. The coupling interface is tracked with a discrete forcing method based on a time and space dependent porosity method. The latter is updated, if necessary, several times for each time steps in order to ensure convergence. The present formulation is validated for a dam break over a flexible plate with experimental confrontation and comparison. This method has then been used for an OECD benchmark on fluid-structure interaction.

INTRODUCTION

Solid deformations induced by single or two-phase flow account for various engineering issues at very different scales such as kilometers in civil engineering or millimeters in biomechanics. Since some coupled behaviour between solids and fluids can have devastating effects on the structures, these aspects must be studied carefully. Developing a FSI framework which takes into consideration large deformations allows to work, alongside experimental physics, on complex engineering issues.

An extensively used way to study fluid structure interaction with deformation is using CFD to compute the external forces on a structure and then input the results in a mechanical solver. This one-way method is fast and easy to set up; however, it is not suitable when the displacements are too important. To achieve that, another method is used: two-way coupling. The structure's position is updated within the fluid solver and the fluid and mechanical problems are solved iteratively during one time step in order to ensure convergence. This enables changes in the shape of the solid to be correctly taken into account in the fluid behaviour. The aim here is to present a numerical method to tackle this two-way coupling.

The developped method consists in a co-rotationnal finite element solver adapted to geometrically non-linear plane strain elastic beams. It is embedded in a multi-phase CFD code based on an Eulerian-Eulerian approach with a single pressure and a colocated finite volume solver Ishii et al (1975). The interface between fluids and structures is represented with a discrete forcing method Benguigui et al (2018) and a scalar field which allows interface reconstruction: the time and space dependent porosity. This interface and its displacement is taken into account in a Lagrangian framework. The fluid-structure interaction algorithm is based on a Newmark method Benguigui et al (2019). Its convergence ensures the strong coupling between fluids and structures. The main goal of this work is to provide a simple coupled routine which allows studying of fluid-structure interaction in the case of elongated solids.

In this work, the development of the mechanical solver and its integration into an FSI algorithm based on a discrete forcing method in a two-phase flow code is shortly presented Baraglia et al (2021) and used. The mechanical solver is evaluated for a dam break over a flexible plate with numerical and experimental comparison Liao et al (2015). This method has then been used for an OECD benchmark on fluid-structure interaction.

1. NUMERICAL MODELING

neptune_cfd is a colocated finite volume fluid solver. It takes into account multiphase flow. From the local conservation of mass, momentum and energy for each phase appear three balance equations. This system is solved with a pressure correction algorithm.

In order to ensure system closure, a unique pressure for all the fluids is considered. Since all flows are considered adiabatic in this work, the energy

conservation is set aside. This means there are only two balance equations of interest for each fluid. Every different multiphase behavior requires a specific model (large interface method, generalized large interface method or dispersed method). These models rely on added terms in the momentum balance to take into account the effects of other phases Mer et al (2018). They are all compatible with the FSI solver. Further details can be found for multiphase models in Mérigoux et al (2016).

The fluid-structure interface tracking is based on a discrete forcing method Benguigui et al (2018), allowing to accurately represent the solid interface for any kind of mesh. To properly reconstruct the interface, a time and space dependent scalar field is introduced in the fluid solver. From the porosity field, it is possible to reconstruct the entire interface delimiting the solid in any kind of mesh Benguigui et al (2018). A Lagrangian framework is suitable to track the fluid-structure interface and therefore the variation in porosity during a simulation. Then, the balance equations are adapted in each cell containing an interface. The framework already exists for infinitely rigid solids Benguigui et al (2019), where a Newmark method has been set up to solve for the displacement of the structure. The aim here is to adapt it to deformable structures.

Structure, assimilated to beams, are modeled as one-dimensional beams and discretized with a finite element method. The large deformation of the structure generates the geometric non-linearity. Typically, a structure is represented with elements and nodes. The following assumptions are considered:

- Structures are considered to work only in bending, no shear, tension-compression or torsion is considered.
- Therefore, each node of the beams moves in a plane normal to the rod's axis, i.e., in the x and y directions.
- Consequently, each node has three degrees of freedom (DOF):
    - Displacement along x axis
    - Displacement along y axis
    - Rotation around z axis
- Beams are clamped at their bottom end (rotations and displacements match zero at the first node)
- Beams are free at their top end

Each beam is discretized according to the finite element theory and for each rod a mass matrix (M), a stiffness matrix (K) and a damping matrix (C) are generated according to the Euler-Bernoulli beam theory. The right-hand side term F(t) is extracted from the fluid computation. The equilibrium equation of the discretized system at a time t thus reads:

$$M\frac{\partial^2 x}{\partial t^2} + C\frac{\partial x}{\partial t} + Kx = F(t) \qquad (1)$$

C is the damping matrix and is expressed as a proportional *Rayleigh* damping $C = \alpha M + \beta K$, with the parameters α and β to be provided.

This equation is discretized and solved thanks to the Newmark algorithm with an explicit method for integrating the dynamics equations over time.

The coupling method is as follows:

(a) at the end of the time step, fluid forces acting on beam(s) are generated considering both the friction forces and the pressure forces. However, the friction ones are negligible compared to the pressure effect.

(b) the mechanical model calculates the deformation of the beam(s), more precisely their new geometry. From one iteration to the next one, the positions (x and y), the velocities (V_x and V_y) and the accelerations (a_x and a_y) are saved.

(c) the *discrete forcing method* acts to deform the computational grid according to the beam deformation.

(d) the next time step is computed for the CFD domain

There is no inner iteration within the same time step, the process is therefore two-way explicit. Further details can be found in Baraglia et al (2021).

2. EVALUTATION OF THE NUMERICAL METHOD ON THE DAM BREAK EXPERIMENT

In order to validate the previously presented method, a dam break over a flexible plate Liao et al (2015) is simulated and compared to numerical and experimental data. The simulation is carried out in neptune_cfd, a multifluid two-phase model. The interfacial transfer term is generated with the large interface model which couples the momentum equation of the two phases at the interface. Turbulences for each phase are alse coupled at the water-air interface. For this case, no dispersed air is considered in the water.

The experiment consists in a water column retained by a door and an hyperelastic plate positionned downstream. At t=0 the door is raised and the water column drops on the structure. The initial water column height is set to either 0.2m, 0.3m or

0.4m. The plate is made from rubber and its characteristics are summed up in Table 1.

The fluids are water and air, they are at their standard conditions (see Table 2). The gravity is taken into consideration in this application. Since there can be large deformation, gravity can influence the complete simulation. It also has a strong impact on the multiphase behaviour.

The data of interest consists in the displacement of two markers on the side of the structure. Each is positioned on the initial configuration at h=0.05m and h=0.1m. A high-speed camera also allows a qualitative inspection of the free surface geometry and the deformed configuration over time.

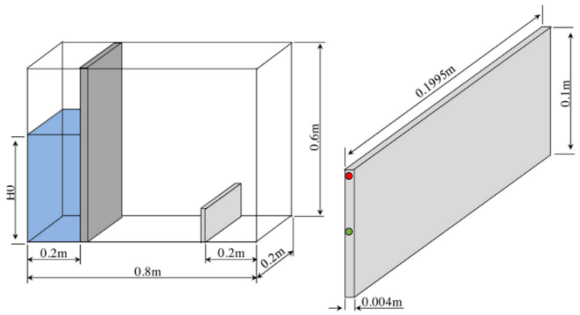

Figure 1 The dam break experiment dimensions and set up Liao et al (2015). Markers are shown in green and red.

Table 1 Structure characteristics

Plate	**Unit**	**Value**
Dimensions	m m m	0.1995 x 0.1 x 0.004
Young's modulus	Pa	$3.5\ 10^{6}$
Poisson ratio	-	0.3
Rayleigh α	s^{-2}	0.0039
Rayleigh β	s^{-1}	0.041
Density	Kg m^{-3}	1161.54
Moment of inertia	M^4	$1.064\ 10^{-9}$

Table 2 Fluids characteristics

	Unit	**Water**	**Air**
Density	Kg m^{-3}	1000	1.2
Viscosity	Pa s	0.001	$1.85\ 10^{-5}$

Table 3 Hierarchy of refined meshes used for the convergence study. The third column represents the number of fluid cells for each solid finite element in the radial direction and in the height of each solid finite element.

Mesh level	**Global number of cells**	**Number of cells per solid element (r * h)**	**Number of solid elements**
Level 1	640 000	4 * 12 = 48	10
Level 2	1 000 000	4 * 10 = 40	15
Level 3	1 440 000	6 * 9 = 54	20

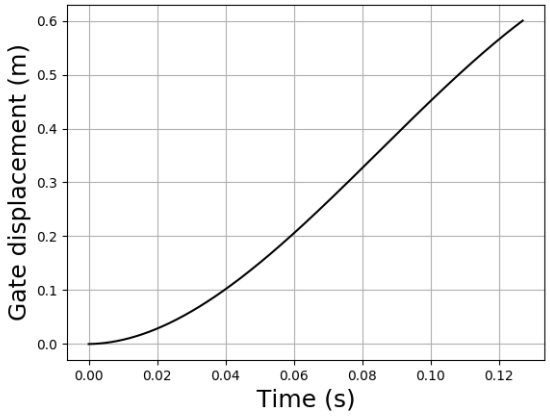

Figure 2 Gate opening process Liao et al (2015).

For the purpose of this simulation, the forces on the plate are constant in the spanwise direction. This means a 2D simulation can be run. The Rayleigh coefficients have been set according to a free vibration of the plate in air.

The domain is entirely meshed, the left, right and bottom planes are walls, the upper plane is a pressure outlet and the two spanwise planes are symmetries. They need to be defined in our cas even though the simulation is 2D. The mesh is composed of uniform Cartesian cells. Initially, the air and water are still. The solid structure and the door are represented with time and space dependent porosity. The door however is infinitely rigid and raised as shown in Figure 2.

The time step is constant during all the simulation, it is chosen in order to satisfy a CFL condition. This allows to accurately simulate the solid behaviour without spending too much time in the computation.

A convergence study has been carried out with the meshes described in Table 3. All in all, a simulation with 20 elements seems sufficiently refined to picture the plate's behaviour. In the first impact period, the finer the mesh the closer simulated dis-

placement is to the experimental results. This shows a spatial convergence. During the maximum deformation section, the difference in the results is negligible. After that period, the simulation with the normal and fine meshes are characterized by a clear second impact. The results with the finer mesh are closer to the experimental results.

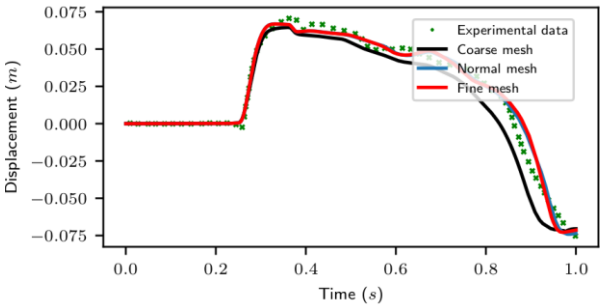

Figure 3 Free end displacement (red marker) for three different mesh levels. Here the initial water column height is H_0=0.4m.

The results obtained with the new coupled method are compared to experimental results in Figure 3. Two features can be compared, a quantitative analysis of the horizontal position of the markers and a qualitative comparison of the free surface geometry. The markers compared are fixed on the side of the plate at the top and at half the height.

During the approach, the structure is still. At the impact, the simulated structure's free end displacement does not undergo a counterflow movement. However, the slope of the displacement and the maximal displacement match those in the experimental results. This mean that a difference in displacement at the beginning of the impact does not influence the following behaviour. The period where we see the peak displacement is well predicted and the second impact mentionned in Liao et al (2015) is visible even if it is more diffuse. Consequently, the structure gets back to its equilibrium position later in the simulation. All in all, the simulation results are in good agreement with experimental results : the model is able to correctly predict the structure's behaviour. In Figure 4, different steps are qualitatively compared to Liao et al (2015).

The calculation carried out being 2D, it does not reflect the exact experimental situation. In fact, in the experiment, the plate is larger and, most importantly, there are gaps between the walls of the canals and the plate. This is relevant because it tends to reduce the pressure difference between the two sides of the plate. Having a bigger pressure difference could explain why the initial counterflow movement is not present in the simulation. Moreover, in a 3D simulation with gaps, the free surface geometry could change as well. Taking into consideration these factors could enhance the simulation and reduce the difference with the experimental results. On the other hand, we carried out a refinement study (Figure 3) in order to make sure that the mesh was fine enough. Refining even more had no impact on the initial results. Similarly, decreasing the time step had no further influence on the results.

This was our first validation test case, and we choose to use the workflow in an OECD benchmark dedicated to fluid-structure interaction.

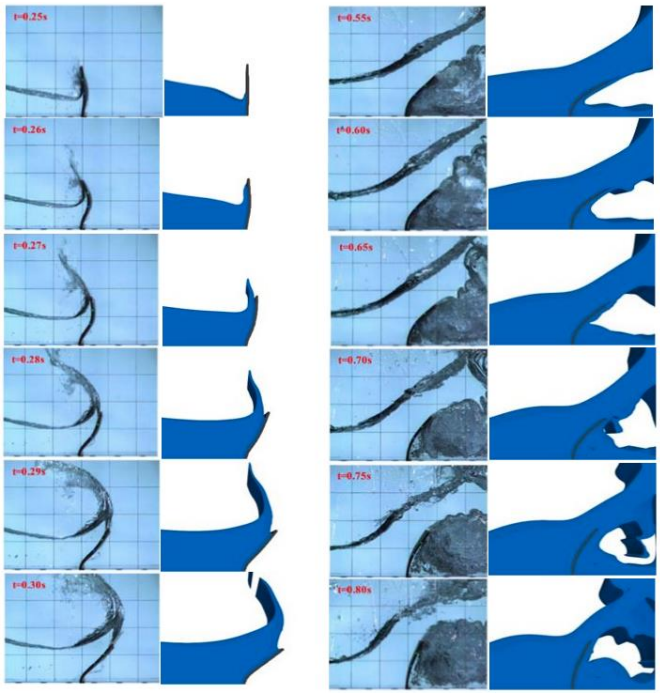

Figure 4 Qualitative comparison of the free surface and the deformed geometry during the impact. The left column are the experimental results (Liao et al 2015).

3. APPLICATION TO 2 IN-LINE FLEXIBLE RODS UNDER CROSS FLOW

The experimental device, described precisely in Bolshukhin et al (2021), consists in a narrow horizontal channel included in a water loop. The test channel, seen on Figure 5, is fed from left by water flowing through a tranquilization tank and a flow straightener. It leaves the test channel by a convergent.

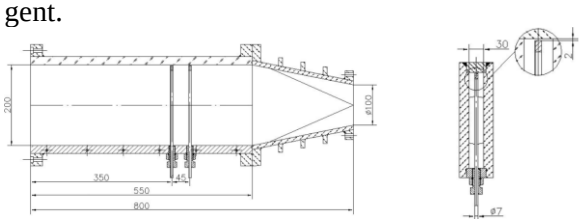

Figure 5 Side (a) and front (b) views of the experimental setup (from Bolshukhin et al (2021))

Two rods are rigidly clamped in the bottom metal plate, and are free at their tips, leaving a 2 mm gap away from the top plate. In the present study, the rods are hollow tubes with a 10 mm diameter, so that the blockage ratio of the conduct is 1/3rd. The cross section of the rods represents 1/3rd of the conduct's cross section. The hollow rods include accelerators, set in a brass plug, this modifies the mass distribution (Figure 6).

The instrumentation is made of those accelerators, and of pressure sensors in 4 locations. Also, PIV and LDF measurements provide velocity profiles and instant velocity temporal records.

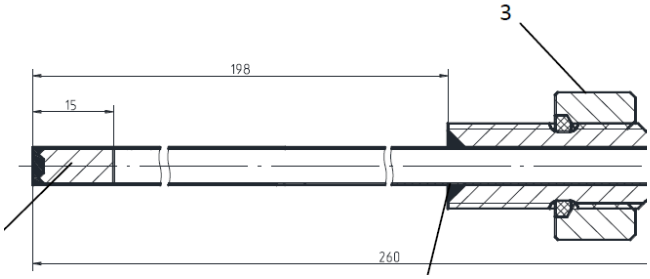

Figure 6 View of the first rod (from Bolshukhin et al (2021))

The channel was designed in order to ensure that its first natural frequencies (bending modes) are higher than those of the cylinders and do not interfere with them. The flow is respectively 16 m3/h and 35 m3/h for the two different tests, 19°C / 1bar for water.

The numerical simulation is based on the numerical modeling previously mentioned with an Rij-EBRSM turbulent model in order to have wall resolved model, necessary to capture the phenomena responsible of the deformation.

The mesh, Figure 7, is a fully hexahedral structured conforming mesh composed of about 12 million cells. Since a discrete forcing method is used to represent rods, they are meshed and a refinement at their walls is necessary to ensure the y+ condition around 1.

The boundary conditions are

- Inlet : located 50mm before the first cylinder, experimental profiles of velocity and rms are imposed in order to be as accurate as possible.
- Outlet : a pressure condition is prescribed at the outlet of the domain.
- Walls (2 rods and channel walls): No slip, the y+ parameter is (for the 16 m^3/h flowrate) :
    - for the channel walls : <1,
    - for the rods : 1.

The initial conditions are zero velocities in the domain. However, the first part of the transient run is removed for the post-processing since it is computed with non-moving rods.

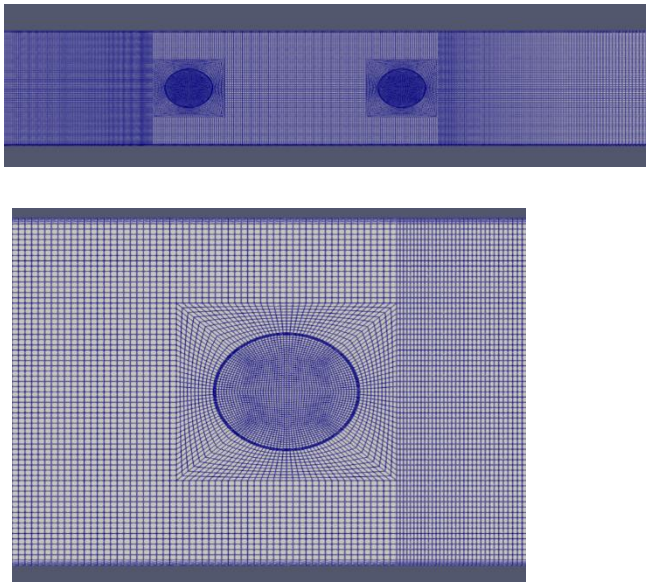

Figure 7 neptune_cfd mesh : view on the 2 rod mesh necessary for the discrete forcing method.

In this test case, the deformation of the cylinders is approximated by two plane strain components. This is allowed because the deformation is linear. This lets us use the solver to simulate the displacement of the cylinders in all directions.

The rods are hollow steel columns in which accelerometers are inserted. Hence, a standard mass matrix of a uniform tube must be corrected to take into account those devices. Knowing the natural frequency of the rods (in air) and the z-position of the accelerometers, it is possible to tune the local mass value to be added at a specified node, in order to match the right vibration period. The natural vibration frequency in water (also given by the experimental team) can be then checked. Results with both models are concatenated in Table 4.

Table 4 Natural frequenct in air and water [Hz] comparison with experiment

	Exp. In air	**Neptune_cfd**	**Exp in water**	**Neptune_cfd**
Rod 1	183.9	182.75	164.9	163.08
Rod 2	168.8	170.23	153	153.24

The flow is rather stable upstream the first rod, due to the restriction section and the straightening chamber, only isotropic homogeneous turbulence

develops, with smalls eddies and high frequencies. The rods imply a large depression and hence the launch of wake eddies. The second rod located in this wake will amplify this instability. In the top part, the small gap between the rods tips and the wall generates an acceleration but seems to have a stabilizing effect for the rod vibrations. Finally, the connection between the test channel and the round pipe also generates instabilities.

A view of the instant flow is given on Figure 8, highlighting the areas of instabilities and the three dimensional characteristics of the small eddies generated. The mean flow and the RMS (root mean square) of its fluctuations appear on the horizontal mid-height section.

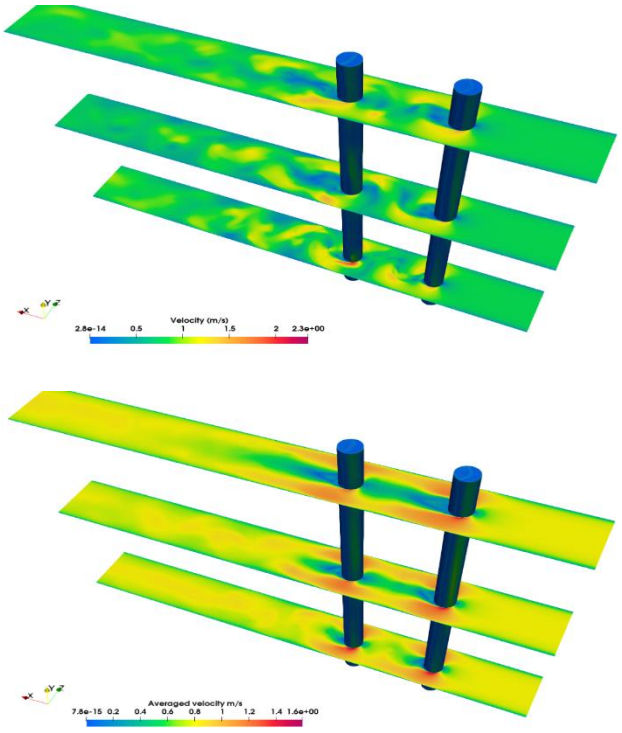

Figure 8 Instant (left) / mean (right) velocity predictions for 3 different z (25mm, 100 mm, 175mm)

The pressure field (shown on rods) is in accordance with the previous description of the flow, the stagnation pressure is similar for both rods but the wake of rod1 limits the depression on the rod2 side in Figure 9. This could constitute one possible explanation as to why the two rods behave differently in the experiment and the simulation. The first one as an impact on the second one.

In Figure 10, wake eddies behind the second rod are observable.

An example of the rods deformations (displacement versus height and Y function of X for both rods) is given in **Erreur ! Source du renvoi introuvable.**11.

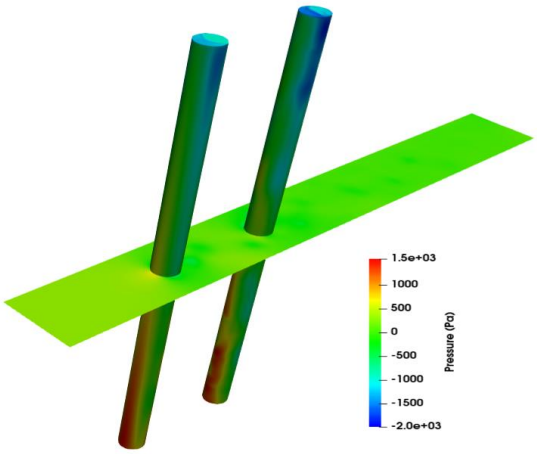

Figure 9 Instantaneous pressure distribution on cylinders.

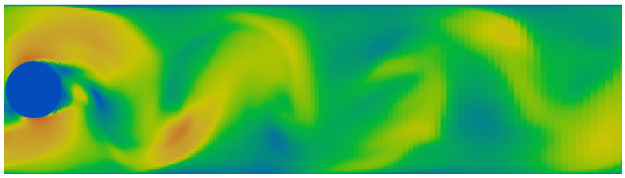

Figure 10 Wake eddies behind the second rod

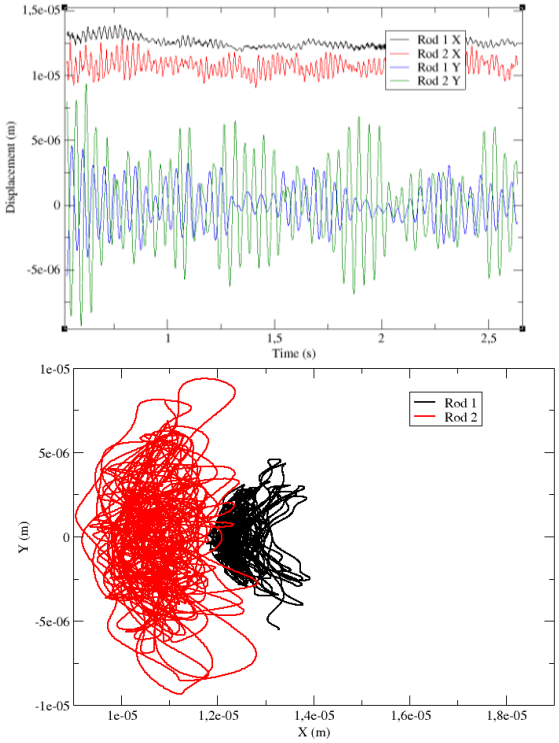

Figure 11 Rod vibration : (top) X and Y displacement of each cylinder along time, (bottom) dis-

placement of each cylinder in X,Y plan (Q=16 m^3/h).

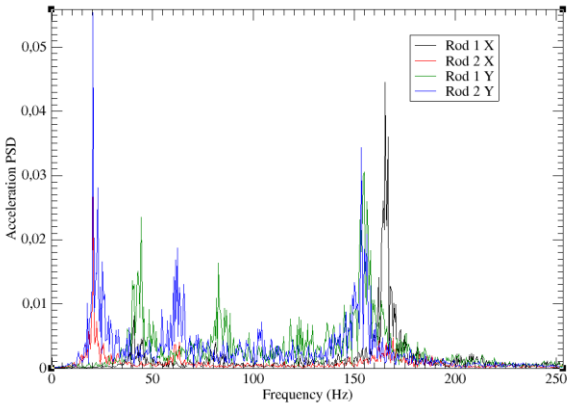

Figure 12 Acceleration frequency spectra for rod 1 and 2 for both directions.

In Figure 11, the natural frequency of the cylinders is easily observed. We can see clear peaks at frequencies near the natural frequency for each rod (see Table 4). The experimental results are not published yet thus not allowing quantitative comparison.

4. CONCLUSION

After a short presentation of the numerical model to characterize the behaviour of largely deformed elastic beams. An evaluation is performed on an extreme case of fluid solid interaction where large deformation is taken into account. The results are in good agreement with the experimental study}. This mean that the finite volume solver coupled with the corotationnal finite element method is able to capture the behaviour of large solid deformation of elastic structures.

Then, it is applied to an OECD benchmark dedicated to fluid-structure interaction where the geometry consists in two deformable rod under single phase cross flow. The numerical predictions are presented but no experimental confrontation is available yet to do it.

5. REFERENCES

Ishii, M., Thermo Fluid Dynamic Theory of Two-Phase Flow, Eyrolles, 248 p., 1975.

Benguigui, W., Doradoux, A., Mimouni, S., Longatte, E. A discrete forcing method dedicated to moving bodies in two-phase flows, International Journal of Numerical Methods in Fluids 2018.

Benguigui, W., Merigoux, N., Fluid-structure interaction in two-phase flow using a discrete forcing method, International Journal of Numerical Methods in Fluids, vol. 91, issue 5, pp. 247-261, 2019.

Baraglia, F., Benguigui, W., Denèfle, R., A corotational finite element approach coupled to a discrete forcing method to solve hyperelastic deformation induced by two-phase flow, Journal of Fluids and Structures , 2021.

Liao. K., Hu. C., Sueyoshi M., Free surface flow impacting on an elastic structure: Experiment versus numerical simulation, Applied Ocean Research, Volume 50, 2015.

Mer, S. Praud, O. Neau, H. Mérigoux, N. Magnaudet, J., Roig, V., The emptying of a bottle as a test case for assessing interfacial momentum exchange models for eulereuler simulations of multiscale gas-liquid flows, International journal of multiphase flows, 2018.

N. Merigoux, J. Lavieville, S. Mimouni, M. Guingo, and C. Baudry, “A generalized large interface to dispersed bubbly flow approach to model two-phase flows in nuclear power plant,” CFD4NRS-6, Boston (2016).

Bolshukhin, M.A., Budnikov, A.V., Shmelev, E.I., Kulikov, D.A., Loginov, A.V.,Pribaturin, N.A., Lobanov, P.D., Meledin, V.G., Suvorov, A.S., Stulenkov, A.V., Dynamic measurements of the flow and structure oscillations to validate FSI calculations, Nuclear Engineering and Design, 381 #111336, 2021.

A PRACTICAL APPROACH TO USING CFD AS AN EARLY DESIGN TOOL FOR ESTIMATING AERODYNAMIC FORCE COEFFICIENTS OF BRIDGE DECKS

Marko DURANOVIC
Trinity College Dublin, Roughan & O'Donovan Consulting Engineers, Dublin, Ireland
Tony DEMPSEY
Roughan & O'Donovan Consulting Engineers, Dublin, Ireland
Craig MESKELL
Trinity College Dublin, Ireland

ABSTRACT

CFD has been used for many years in the context of bridge engineering but, it is not often centre pilar of the design process because of the complexities related to model size and computational resources required for solving these models.

The purpose of this paper is to assess the validity of different RANS modelling choices to evaluate the aerodynamic coefficients of Type 2 bridge decks (as defined in BD 49/01. In order to do this, the Northern Spire bridge in the UK has been modelled and the results obtained are compared to 1:50 scale wind tunnel test data.

Different bridge barrier configurations are represented with constant solidity ratio. These results suggest that the barrier configuration has a low impact on the drag coefficient but quite a significant effect on lift and moment coefficients. A brief analysis on the effects of different turbulence models led to Transition SST being the turbulence model of choice. A study on the levels of turbulence intensity is outlined showing it has a significant impact on the static lift coefficient values for a range of angles of attack.

1. INTRODUCTION

1.1. Background

For stiff and heavy bridges, static wind loads are of most concern, while for longer and more flexible designs, dynamic wind loading effects become the limiting issue. Broadly, there are two mechanisms: vortex shedding induced vibration which is caused by periodic unsteady aerodynamic forces caused by wake instability; and coupled flow-structure instabilities, including galloping and flutter. Perhaps the most famous example is the Tacoma Narrows bridge collapse that occurred at relatively low wind speed of 19m/s, which was caused by coupled flutter (Larsen, 2000; Miyata, 2003). While large amplitude vibration can be managed with tuned mass dampers (TMDs) as in the case of the bridge over the river Volga, Russia which had experienced high amplitude vertical vibrations of approximately ±400 mm (Benicke & Butz, 2015), a more common approach is to eliminate the susceptibility at design stage. Typically, scale model wind tunnel testing can deliver the excitation amplitudes and frequencies associated with vortex shedding, or the static aerodynamic force coefficients and gradients that determine the stability thresholds. While in principle, CFD can also yield this data but due to the system complexity and uncertainty that comes with it, it used mostly for research purposes. Several studies have had good success in reproducing experimental data. For example, (Goering & Ramponi, 2019) used Ansys CFX to identify flutter derivatives for torsional galloping for The Bay Bridge, USA and Stonecutter Bridge, UK; simulations of Nanpu Bridge, China, and Höga Kusten Bridge, Sweden were reported by (Ge & Xiang, 2008); (Zhang, Cardiff, Cahill, & Keenahan, 2021) modelled Rose Fitzgerald Kennedy Bridge, Ireland using OpenFOAM in 3D with LES; and (Szabó, Györgyi, & Kristóf, 2020) employed Fluid-Structure interaction modelling to replicate some of the Tacoma Narrows behaviour in torsional mode of oscillation. However, there are very few examples in the open literature which (Nieto, Hernández, & Jurado, 2009) use modelling as an input in the conceptual bridge design process (Nieto et al., 2009). They covered several deck shape options and provided results for static aerodynamic coefficients. Based on that, they made recommendations on the most favourable shape. This paper aims to provide specific guidance of appropriate modelling choices in commercial CFD software for determining the aerodynamic force coefficients of bridge decks, primarily with 2D RANS simulations. The paper contains a number of conclusions that may help CFD modelling of future bridge designs, as an input for wind tunnel testing campaigns which will in turn shorten the time spent in the tunnel itself.

To evaluate the performance of each model, results from a wind tunnel testing campaign conducted during the design process of Northern Spire Bridge in the UK were used. Experimental results on the static aerodynamic coefficients (drag, lift and moment) for a range of angles of attack were used. The

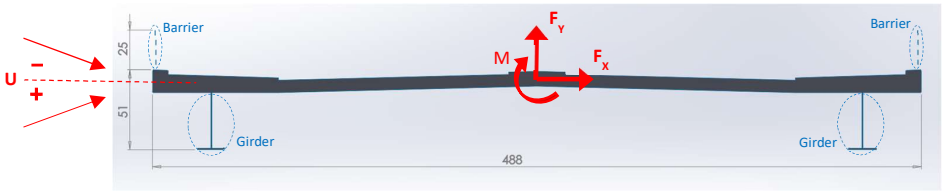

Figure 3. Deck section dimensions [mm] at model scale and sign convection adopted

wind tunnel testing was executed by Centre Scientifique et Technique du Bâtiment (CSTB) in their facility in Nantes, France and is described in section 1.2.

In bridge engineering, barriers at the side of the bridge deck are part of the bridge furniture and are not considered as a particularly vital part during the design process. However, depending on their size and type, barriers can have a significant role in a bridge's wind response by altering the flow conditions at the top side of the deck. In section 2.2, special attention has been given to the way bridge barriers are included in a CFD simulation and how their inclusion influences the predicted static aerodynamic coefficients. A comparison of results from three turbulence models is given in section 3.

The CFD software used in this study is Ansys Fluent, but most of the remarks made here can be applied in general when employing any CFD code. Most of the simulations (2D) were run on a high-end desktop workstation while the rest (2.5D and 3D) required a High-Performance Computing (HPC) facility.

1.2. Experimental Data

Wind tunnel testing of a 1:50 scale model (see Figure 1) of the typical Northern Spire Bridge deck cross section completed at the CSTB facility consisted of two phases:

- tests of the rigidly fixed model to obtain aerodynamic force coefficients,
- and the same fixed model mounted on a 3 degree of freedom mount with the plunge and heave natural frequencies chosen to be equivalent to the bending and torsion natural frequencies of the full-scale bridge as shown in Figure 1.

The tests were performed at the bridge detailed design stage in 2018 and detailed reports on the data are not publicly available. The experiments were done so that they satisfy regulatory requirements for the bridge design and the test campaign was not documented in the open literature so the results are accepted as they are.

Testing was done in uniform flow (no accounts for the atmospheric boundary layer).

The aerodynamic coefficients for a range of angles of attack at a specific wind speed are shown in Figure 2. These results are broadly consistent with other studies found in literature, see e.g. (Goering & Ramponi, 2019), (Zhu & Chen, 2013). As can be seen, the gradient of the lift coefficient is always positive, indicating that deck profile is not prone to galloping, but may still exhibit coupled mode flutter.

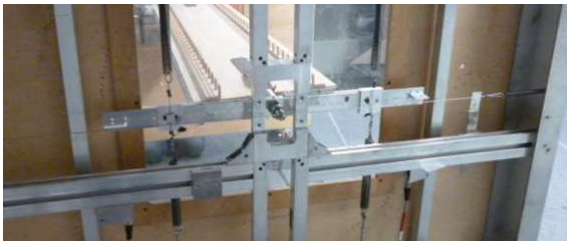

Figure 1. Dynamic model assembly and the deck section model in the background

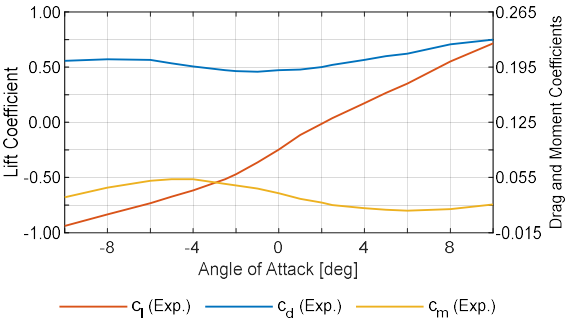

Figure 2. Static aerodynamic coefficients

2. SPATIAL DISCRETISATION AND GEOMETRIC MODELLING

All CFD models used in this paper are made at model scale i.e., the scale used in the wind tunnel tests. This is done so that the simulations are performed at the same Reynolds number as the tests. The dimensions of the model, at 1:50 scale, are shown in Figure 3. Static aerodynamic coefficients, as defined in the tests, are given in equations (1)-(3).

$$C_L = \frac{2 \cdot \mathrm{F_Y}}{\rho \cdot U^2 \cdot B} \quad (1)$$

$$C_D = \frac{2 \cdot \mathrm{F_X}}{\rho \cdot U^2 \cdot B} \quad (2)$$

Mesh refinement level	Number of cells		Drag coefficient		Lift coefficient		Moment coefficient	
	#	Ratio	Value	% Δ	Value	% Δ	Value	% Δ
Coarse	1,119,278	-	0.175	-	-0.202	-	0.044	-
Medium	1,653,362	1.48	0.175	0.1%	-0.200	2.0%	0.045	1.2%
Fine	2,324,116	1.41	0.175	0.1%	-0.198	1.0%	0.045	0.2%

Table 1. Grid sensitivity analysis

$$C_M = \frac{2 \cdot \mathrm{F_Y}}{\rho \cdot U^2 \cdot B^2} \quad (3)$$

where C_L, C_D, C_M are lift, drag and moment coefficients, respectively; ρ is air density; U is freestream flow velocity; F_Y, F_X, M_Z are forces in Y and X direction and rocking moment around Z axis, respectively; B is the deck width at model scale (0.488 m). Authors acknowledge that for the drag coefficient it would be more appropriate to use deck depth for normalisation however, to be consistent with the experimental values, bridge width (B) is used. This is comparable to airfoil analysis where drag is normalised by the airfoil chord. For the limited number of 3D simulations, the force and moment coefficients are also non-dimensionalised by the computational model span.

2.1. 2D discretisation

2.1.1. Meshing methodology

While it is possible to use a single fully unstructured polyhedral grid, in the current study subdomains are defined and meshed with an unstructured mesh. There are two main reasons for this approach. Firstly, it will be desirable to have a fully coupled FSI numerical model ultimately, albeit with it a rigid deck on flexible supports. By defining a subdomain around the bridge deck, only that block would require remeshing or mesh deformation. Furthermore, the mesh block immediately adjacent to the bridge deck surface can be translated with the deck so moving the remeshing to a less dense mesh block. Secondly, defining subdomains facilitates control of the localized mesh density, allowing mesh nodes to be concentrated in regions which are important fluid mechanically (e.g., in the wake or the boundary layer). An example of the mesh obtained with this approach is shown in Figure 4.

2.1.2. Grid Sensitivity

Grid sensitivity was assessed to achieve a solution not dependent on the refinement level of the mesh. A summary of the results is given in Table 1. As seen, the change in all static coefficients becomes less than 2% for medium mesh refinement level and as such is adopted for all simulations discussed below. It is interesting to note that the moment coefficient appears to be more sensitive to mesh density. This is probably due to the barriers and the fact that the bridge deck width is large compared to the height.

2.1.3. Boundary conditions

Dirichlet boundary conditions are used at all four sides of the domain with constant velocity set at upper, lower, and upstream sides and constant pressure at the downstream side. The flow velocity for all simulations was set at 5m/s.

The angle of attack is controlled by setting two velocity components, in global X and Y direction defined in equations (4) and (5), respectively.

The flow is uniform so that the conditions in the wind tunnel are matched.

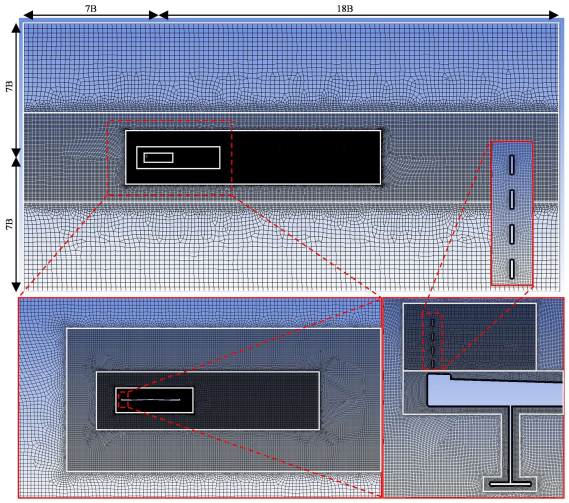

Figure 4. Multi-body domain division and grid details

$$U_{bx} = \cos(\alpha) \cdot U \quad (4)$$

$$U_{by} = \sin(\alpha) \cdot U \quad (5)$$

where α is angle of attack, U_{bx} and U_{by} are two velocity components, U freestream velocity. The reason to consider non-zero angles attack are twofold. Firstly, depending on the wider topology of the landscape, the bridge deck may experience wind shear and hence a downwash. Secondly, and more importantly, the galloping or flutter stability is determined by the gradients of the aerodynamic coefficients.

Turbulence at inlet is defined through turbulence intensity and turbulent length scale and they are set at 5% and 0.488m, respectively.

Wall boundary conditions set on the deck and barriers are defined as no-slip. An analysis with slip boundary conditions set on barriers has also been done (see Figure 11). Having barriers modelled with slip boundary conditions relaxes the mesh requirements in this region.

2.2. Geometric modelling: consideration of the girder and the barriers

The results in this section have been obtained using Transition SST turbulence model with laminar flow conditions at the inlet i.e., zero turbulence intensity at the inlet. Discussion of the choice of turbulence model is given in section 3.

As an initial simulation, full geometry shown in Figure 3 is simplified. This is achieved by removing girders and barriers shown in Figure 3 resulting in section shown in Figure 5.

Figure 5. Bare deck geometry [mm]

The simulation done with this, much simplified, geometry shortens the meshing time and computational requirements. It in turn leads to shorter solution times and fewer convergence issues. Static aerodynamic coefficients are shown and compared to experimental results in Figure 6.

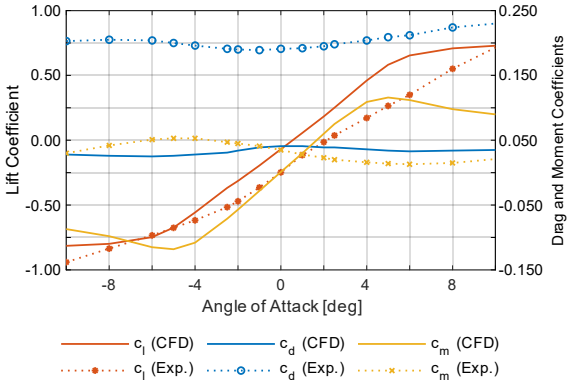

Figure 6. Bare deck – static coefficients

It should be noted that experimental results are for the full deck section (deck, girder, and barriers). It can be seen that even though there is a large difference in geometry of the two models, a relatively good agreement between the experimental lift and the simulated CFD lift is obtained, in terms of both the slope around zero angle of attack (which is important for stability) and the overall magnitude.

As would be expected, the drag coefficient shows a large discrepancy in magnitude when compared to experimental results. There are two reasons for this. Firstly, the drag for both geometries is normalised with the bridge width (B) which is the same for two cases. The total area projected in the *x* direction for the bare deck is 71% smaller than in the case of the deck with the girders. This causes a factor of 3.4. The second reason is that the barrier and girder will generate a proportionately larger wake. Despite the large discrepancy in drag and moment coefficients, this model can be useful for initial estimation of the lift coefficient behaviour with varying angle of attack.

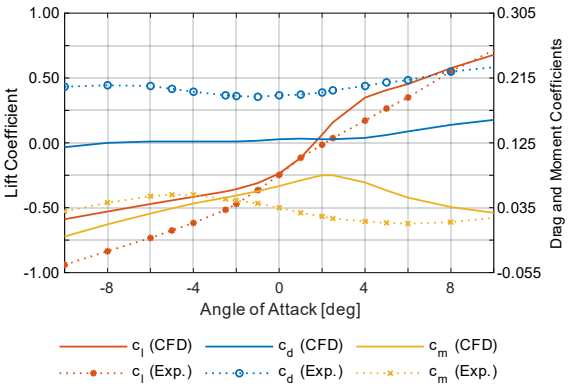

Figure 7. Deck without barriers – static coefficients

The girders are geometrically simple, and so including them does not dramatically increase the mesh size (an increase of about 2% in the number of cells). Figure 7 shows static coefficients for the deck section without the barriers. As with the bare deck analysis, values of drag coefficient are lower than their experimental counterparts, although the discrepancy is much smaller. Considering that the most meshing difficulties occur in the vicinity of the barriers this can be regarded as another model worth exploring prior to moving to the full deck analysis.

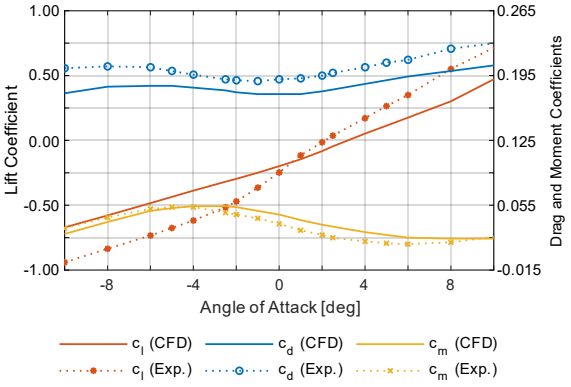

Figure 8. Full deck section – static coefficients

Finally, a representation of the barriers was added with 4 openings. The results of this simulation are seen in Figure 8. The drag and moment coefficients now follow the trend of the experimental data well,

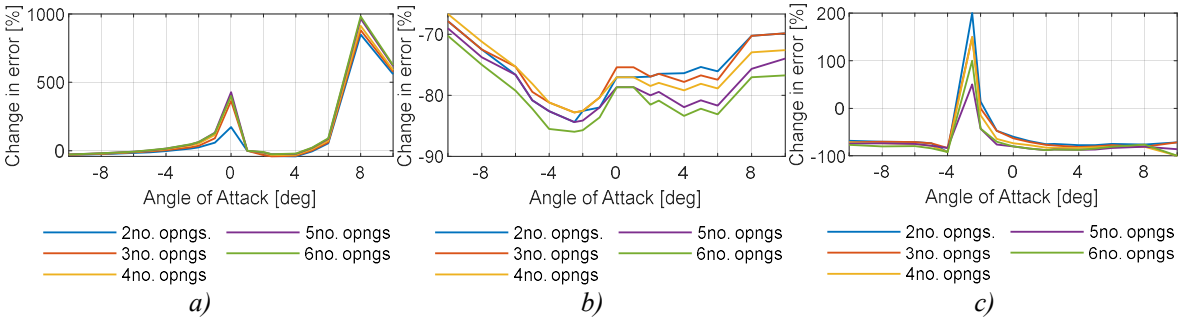

Figure 10. Effect of number of barrier openings as a change in error with respect to the no-barrier case; (a) lift coefficient; (b) drag coefficient; (c) moment coefficient.

although with slight lower magnitude. The lift however, is not significantly better than that obtained for the bare deck and in terms of both gradient and magnitude around α=0°, it is arguably worse.

Including a representation of the barriers is necessary to achieve a reasonable estimate for drag and lift. However, the barriers in the wind tunnel model have a 3D pattern as can be seen in Figure 9, which is itself an approximation of the full-scale barriers. The wind tunnel barriers are chosen to have equivalent blockage ratio to the full-scale design. In a 2D approximation, the barrier is modelled as a solid fence with a number of openings.

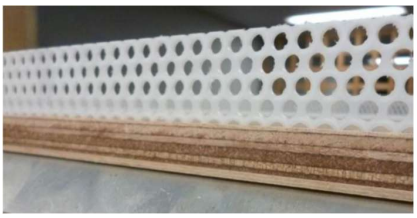

Figure 9. Barrier placed on the wind tunnel model

The size of the openings is varied to assess whether the number of openings in the barrier makes a difference for any of the static coefficients when compared to the no-barrier case. The findings are presented Figure 10 where the change in error with introduction of the barriers is compared for six different configurations. As expected, the drag coefficient is least susceptible to varying number of barrier openings since the total area over which the drag force is integrated is kept constant. It is also noted that by introducing barriers it positively affects the drag coefficient estimate by decreasing error for all angles of attack. This too suggests that by changing the number of openings, we can only introduce a limited benefit in the accuracy of the drag coefficient.

Varying the barrier configuration has a dramatic effect on the flow adjacent to the top of the bridge deck due to jetting through the lower opening. Thus, the lift and the moment coefficients exhibit significant variations for five barrier configurations considered. The models with fewer barrier opening produce better lift coefficients, when compared to the experimental values. While the opposite holds for the moment coefficients. Thus, there is no clear "best option" when it comes to the number of openings in the barrier. However, in this case, the model with four openings in the barriers was chosen as the most desirable one because it provided overall best results (considering all static coefficients). And in fact, the model that was used in the wind tunnel test consisted of the barriers that can be considered to have had somewhere between three and four openings over their depth (see Figure 9).

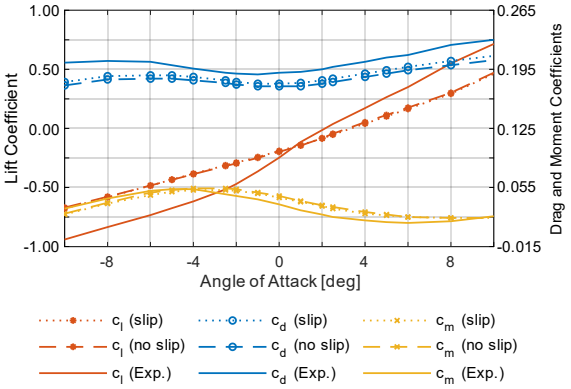

Figure 11. Full deck with slip conditions on the barrier; no-slip conditions still applied on the deck.

Achieving a y^+ value below 1 (required for SST turbulence models), drives the mesh increased density in the region of the barriers. To assess whether the boundary layers on the barrier itself are important, the no-slip condition on the barrier walls was replaced with a slip condition (i.e., zero surface shear stress) while no-slip condition on the deck was maintained. This allows a courser mesh in the barrier region. A comparison of static coefficients for the two cases, slip and no-slip boundary condition on the barriers, is given in Figure 11. As can be seen this approach does not adversely affect the results with the cell count for this mesh 7% lower than in the original grid. It can be noted that the barrier mainly acts as a blockage.

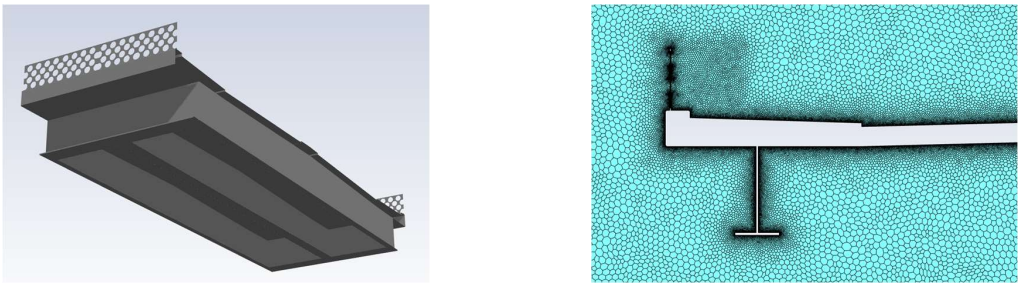

a) *b)*

Figure 13. (a) 3D model with applied double symmetry boundary conditions; (b) polyhedral mesh available in Fluent

2.3. Multi-dimension models - 2.5D and 3D discretisation

As noted above, the barrier is actually a 3-dimensional structure. Furthermore, on the underside of the bridge deck there are so called cross girders which are streamwise. To assess the impact of the 2D assumption two 3D domains are considered. The first which will be referred to as "2.5D model" (see Figure 12) represents a narrow strip of the deck with periodic boundary conditions on the two faces across the deck width. The geometry is still basically 2D but extruded by a short distance so what looks like 3D is substantially of 2D character.

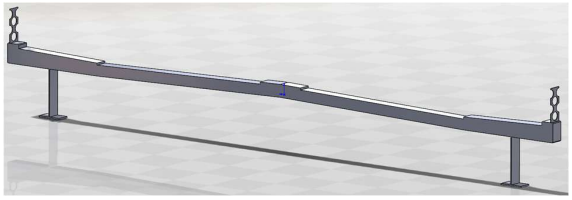

Figure 12. 2.5D model

The strip width is such that it captures typical shape of the barrier, but the cross girders are ignored. The second will be referred to as "3D model" (see Figure 14) is represented by a strip of such width that half distance between two cross girders is covered. Two planes perpendicular to the deck are set as symmetry boundary conditions which allowed to run simulation on a four times wider domain than initially meshed, see Figure 13(a). As seen in the figures, the barrier for the 3D model closely mimics the wind tunnel model.

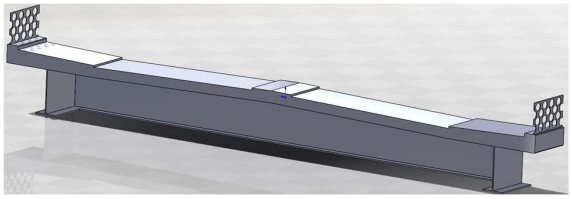

Figure 14. 3D model

For both models a polyhedral mesh, is used as it decreases the number of cells required to achieve an acceptable solution, see Figure 13(b). The mesh sensitivity analysis for this mesh has not been done due to high computational requirements. However, the cell size chosen for these models matches the cell sizes employed in 2D domains. Once meshed in Ansys Meshing, the meshes are converted to polyhedral meshes using Ansys Fluent in-built functionality. Grid nodes spacing of these meshes is comparable to the ones prior the transformation but the cell volumes are larger, see (Ansys, n.d.) for more details.

Simulations done in this section employed SST turbulence model only.

The results for 2.5D and 3D model are shown in Figure 15 and Figure 16, respectively. Both are compared to the experimental and results from the 2D analysis.

There is not a substantial difference between multi-dimensional models (2.5D and 3D) and 2D models suggesting that the extra computational expense is not justified; each simulation took approximately 30 CPU hours using 120 CPU cores. However, it should be noted that turbulence is treated with an isotropic model, and so the highly 3-dimensional turbulent wake will be poorly captured. A full DDES or LES model may yield improved results, but the computational effort will increase dramatically.

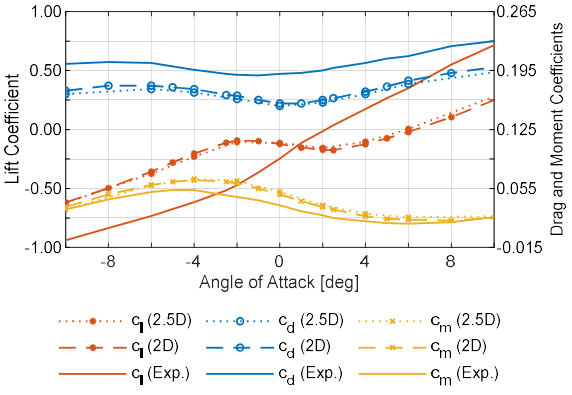

Figure 15. Simulation results for 2.5D model

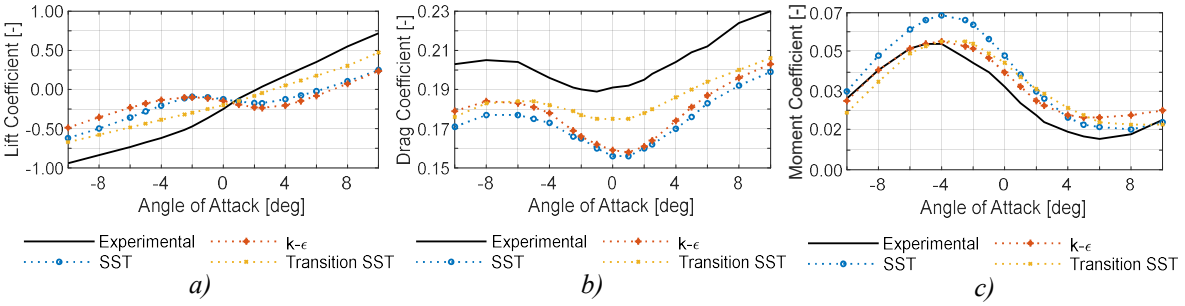

Figure 17. Comparison of turbulence models: (a) lift coefficient; (b) drag coefficient; (c) moment coefficient

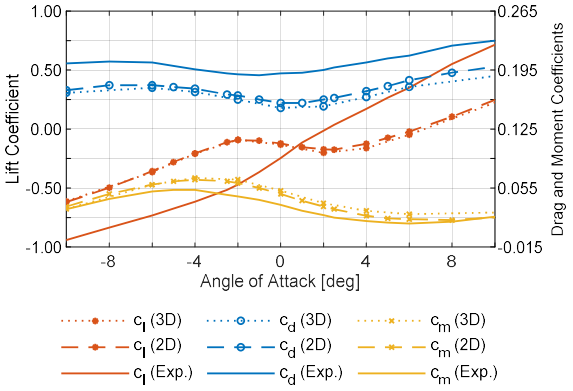

Figure 16. Simulation results for 3D model

3. TURBULENCE MODELLING

3.1. Turbulence models

The simulation approach taken is steady RANS as this is substantially less computationally expensive than LES or DDES. However, it is well known that the choice of turbulence model in RANS may significantly impact the results. The models considered here are *k-ε*, *SST* and *Transition SST* (TSST) as implemented in ANSYS Fluent, see Chapter 13 in (Ansys, n.d.) . It should be noted that the Reynolds number of the wind tunnel (based on deck width) is in the transitional range at the lower velocities (~10^4), but the Reynolds number regime for the full-scale bridge will be fully turbulent. It should be noted that Low Reynolds wall treatment is employed in all simulations. Figure 17 shows static coefficients for a range of angles of attack when different turbulence models are employed and compared to the experimental values. As can be seen, the TSST model yields the closest comparison with experimental data, especially for the lift coefficient.

3.2. Turbulence intensity at inflow

Bridges operate in the atmospheric boundary layer, and so the upstream air flow is typically exhibiting high levels of turbulence. In the wind tunnel this is modelled with turbulence generators upstream so that the turbulent intensity (TI) is approximately 4%. In Figure 18 the static coefficients obtained with TSST for an TI of 10% at the inlet.

The dissipation of turbulent kinetic energy in the turbulence model tends to reduce the freestream turbulence levels more rapidly than is experienced in practiced.

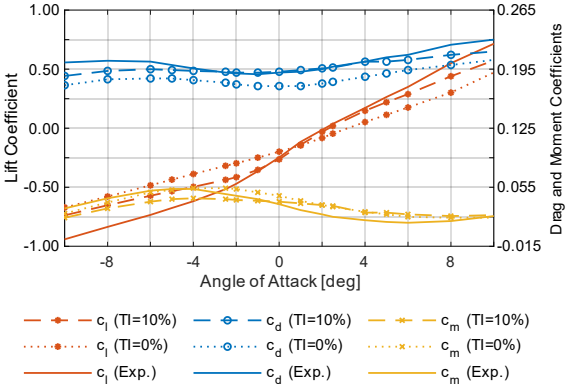

Figure 18. Transition SST model - inflow turbulence intensity of 10%

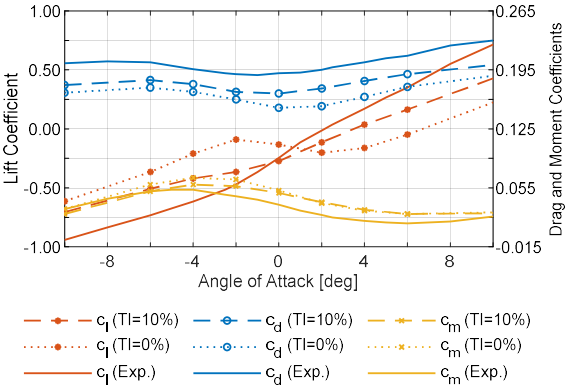

Figure 19. 3D SST model – inflow turbulence intensity of 10%

The higher inflow TI value was chosen so that the TI was approximately 4% immediately upstream of the bridge deck. On the same figure, static coefficients for the laminar flow (TI=0%) at inlet are

shown and a clear difference between two models is noticeable. Both the magnitude and the slope of the curves show better correspondence with the experimental data for a turbulent inflow. Similar observations can be made for simulations done on the 3D SST model shown in Figure 19. Here the change in lift slope around 0 angle of attack is even more noticeable and important. Having the slope of the lift coefficient negative around 0 angle of attack would lead one to believe that the test section has problems with stability.

4. CONCLUSIONS

This paper considers different modelling choices to obtain preliminary estimates of static aerodynamic coefficients for early design iterations for bridge deck Type 2 as defined in BD 49/01. The emphasis is on keeping the geometric modelling, meshing and computational effort as low as possible to facilitate use in industrial settings. It has been found that a 2D model is sufficient with a simplified representation of barriers. The number of openings in the barrier does not play a significant role when it comes to the drag coefficient, however, depending on the angle of attack, it can have a significant impact on the accuracy of both lift and moment coefficients. Transition SST yielded the best results of the turbulence models considered; however, it is important to note that the SST model would probably be more appropriate for simulations of the full-scale bridge deck. Turbulence intensity in the inflow region plays a substantial role and this should be chosen to reflect the conditions found on the bridge site.

This was especially pronounced for the lift coefficient and the lift curve gradient, which is crucial for stability assessment. It is concluded that CFD simulations can facilitate rapid design iterations before wind tunnel tests, but care is needed in the modelling choices made.

5. ACKNOWLEDGMENTS

The authors would like to thank Olivier Flamand of Centre Scientifique et Technique du Bâtiment for sharing the data from the wind tunnel analyses conducted on Northern Spire Bridge model and promptly answering questions related to the wind testing itself.

The research conducted in this publication was funded by the Irish Research Council under grant number EBPPG/2020/96 and Roughan & O'Donovan Consulting Engineers.

The authors would like to acknowledge the Irish Centre for High-End Computing (ICHEC) for provision of computational facilities and support.

The authors would like to acknowledge Sunderland City Council and Farrans Victor Buyck CJV for their contribution to the paper.

6. REFERENCES

Ansys. (n.d.). *ANSYS Fluent User's Guide, Release 2021 R1*.

Benicke, O., & Butz, C. (2015). Volgograd-bridge: Efficiency of passive and adaptive tuned mass dampers. *IABSE Conference, Geneva 2015: Structural Engineering: Providing Solutions to Global Challenges - Report*, 1428–1435.

Highways Agency. (2001). *DMRB Volume 1 Section 3 Part 3 (BD 49/01) Highway structures: Approval procedures and general design. General design. Design rules for aerodynamic effects on bridges*. Highways Agency.

Ge, Y. J., & Xiang, H. F. (2008). Computational models and methods for aerodynamic flutter of long-span bridges. *Journal of Wind Engineering and Industrial Aerodynamics*, *96*, 1912–1924.

Goering, A., & Ramponi, R. (2019). Wind Analysis of Long-Span Bridges Using Computational Fluid Dynamics. *Structures Congress 2019: Bridges, Nonbuilding and Special Structures, and Nonstructural Components - Selected Papers from the Structures Congress 2019*, 210–220.

Larsen, A. (2000). Aerodynamics of the Tacoma Narrows Bridge -60 years later. *Structural Engineering International: Journal of the International Association for Bridge and Structural Engineering (IABSE)*, *10*, 243–248.

Miyata, T. (2003). Historical view of long-span bridge aerodynamics. *Journal of Wind Engineering and Industrial Aerodynamics*, *91*, 1393–1410.

Nieto, F., Hernández, S., & Jurado, J. Á. (2009). Aerodynamic study of the preliminary design of a 425 m cable-stayed bridge deck using CFD. *5th European and African Conference on Wind Engineering, EACWE 5, Proceedings*.

Szabó, G., Györgyi, J., & Kristóf, G. (2020). Three-dimensional fsi simulation by using a novel hybrid scaling – application to the tacoma narrows bridge. *Periodica Polytechnica Civil Engineering*, *64*, 975–988.

Zhang, Y., Cardiff, P., Cahill, F., & Keenahan, J. (2021). *Assessing the Capability of Computational Fluid Dynamics Models in Replicating Wind Tunnel Test Results for the Rose Fitzgerald Kennedy Bridge*. 1065–1090.

Zhu, Z., & Chen, Z. (2013). Large eddy simulation of aerodynamics of a flat box girder on long-span bridges. *Procedia Engineering*, *61*, 212–219.

CFD ANALYSIS OF TWO-PHASE FLOW INDUCED FORCES ON A TEST FLOW LOOP

Paul Emmerson
Paul.Emmerson@XodusGroup.com, Xodus, London, UK
Mike Lewis
Mike.Lewis@XodusGroup.com, Xodus, London, UK
Neil Barton
Neil.Barton@XodusGroup.com, Xodus, Glasgow, UK

ABSTRACT

Multiphase flow through pipelines can result in severe piping vibrations and subsequent fatigue damage. Commonly, finite element analyses are used to define the dynamic pipe stresses and to calculate the lifetime of subsea piping. The fluid flow excitation forces can be estimated from measured data, estimated with empirical models or simulated in detail using computational fluid dynamics (CFD). Measurements resulting from multiphase flow in a test loop have been compared to CFD predicted forces.

CFD analysis is shown to be a valuable method for predicting multiphase flow induced forces. This is especially true in subsea piping systems at typical oil and gas production conditions. CFD analysis allows the prediction of the increase of excitation along the pipe due to the pressure drop and the effects of increased operating pressure. Also, when the piping system has phasing between the bends, transient CFD analysis may need to be carried out.

NOMENCLATURE

CFD	Computational Fluid Dynamics
FE	Finite Element
FIV	Flow Induced Vibration
HRIC	High-Resolution Interface Capturing
JIP	Joint Industry Project
PSD	Power Spectral Density
RMS	Root Mean Squared
RVT	Random Vibration Theory
VOF	Volume of Fluid

1. INTRODUCTION

Multiphase flow through piping systems is common in the oil and gas industry, nuclear power plants and the chemical industry and can cause density, velocity and pressure fluctuations which result in piping vibrations. Depending on the pressure, temperature, flow rate, pipe size and support arrangement, the vibrations can result in fatigue failure of the piping. Recent research (Belfroid et al, 2016) has been focusing on force estimations assuming that the vibrations are not influencing the flow behaviour.

This paper summarises a validation study, comparing CFD predictions of multiphase flow induced forces to measured forces on a 1" two-phase flow loop with multiple bends.

2. CASE STUDY

The experiment and measurements were performed by TNO and are described in Pereboom et al, 2021. The flow loop used to validate the CFD consists of six bends. Water and air at atmospheric pressure are mixed by a Y-piece upstream of a long horizontal inlet section, ensuring stabilized flow conditions. The test rig setup is shown in Figure 1 in the configuration for vibration measurements.

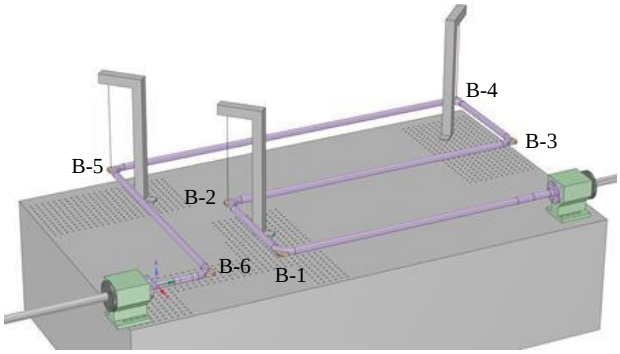

Figure 1. Multibend two-phase flow loop

Both the forces and the acceleration at the bends were measured. For the force measurements, the piping was stiffened using supports to bring the first response frequency up to a level where the flow will have very low energy. Piezometric strain gauges are used to measure the fluid force on the bends. During the acceleration measurements the supports were removed, and the pipe movements were restricted by three wire supports and by two clamps at the pipe ends. The first two eigenfrequencies of the system were 5 and 9 Hz. Tri-axial accelerometers, mounted on each bend, were used to measure the acceleration of the bends. In terms of uncertainties in the experimental results, all flow measurements were better than 1% (by mass), all vibration was done at extreme sensitivity with a cutoff of frequency of 1Hz, and all forces were calibrated with an accuracy of better than

20% in the frequency range of interest (i.e. less than 70 Hz).

2.1. Experimental conditions

Different flow patterns can exist in multiphase pipe flow. Two frequently observed flow patterns are selected for the validation study, slug and annular flow. During the experiments those flow patterns were observed using high speed cameras, as shown in Figure 2 and Figure 3.

Case	Set No.	Flow Regime	U_{gas} [m/s]	U_{liquid} [m/s]
1	51	Slug	7.2 – 7.4	1.0
2	81	Annular	12.4 – 12.5	0.5

Table 1. Overview of flow cases

The flow conditions for the two selected cases are summarized in Table 1. Superficial gas velocities are based on the upstream pressure. The superficial gas velocity for the two experiments, stiff and flexible flow loops, are slightly different. Measurement data was taken over 600s for each experiment.

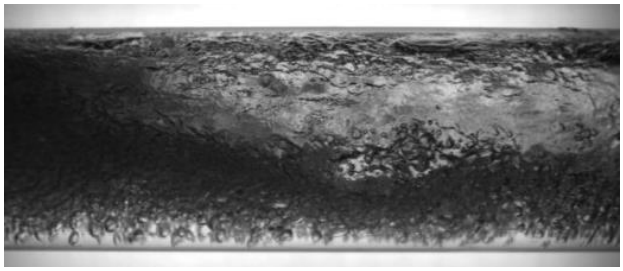

Figure 2. Flow case 1 upstream flow

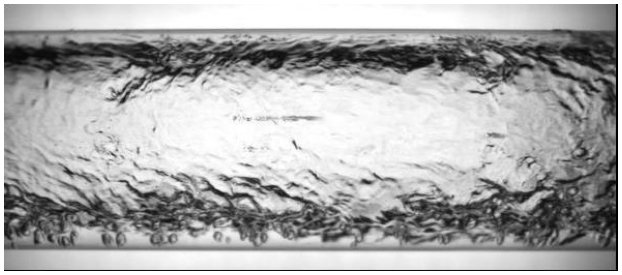

Figure 3. Flow case 2 upstream flow

3. CFD METHODOLOGY

The CFD modelling was performed using Siemens PLM STAR-CCM+® v15.02. In setting up the models, experience of validating multiphase simulations against the JIP experimental data (Emmerson et al, 2016a ; Emmerson et al, 2016b) and other studies undertaken on actual operational piping systems was used (Emmerson et al, 2020). The Volume of Fluid (VOF) approach to model the liquid and gas phases was employed, with Ideal Gas used for the gas Equation of State and constant density used for the liquid. An interface sharpening scheme, the High-Resolution Interface Capturing (HRIC) scheme is used to improve the resolution of the interface between the phases.

The Realizable k-epsilon turbulence model was used with turbulence damping at the liquid-gas interface to reduce any turbulence generation which could smear the interface and damp out wave initiation.

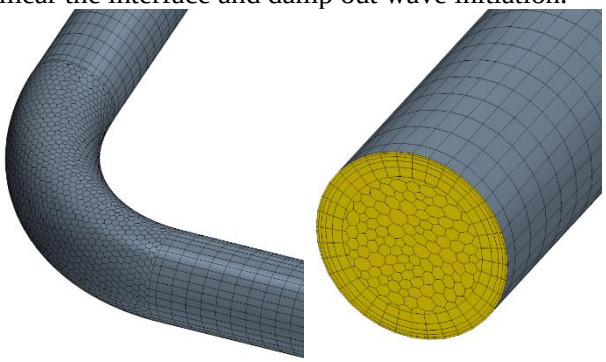

Figure 4. Computational CFD mesh

The fluid forces on each bend were captured, by integrating the pressure fluctuations on the internal surface area of each bend. Note that the contribution to the forces from the wall shear stresses is insignificant (typically << 0.1% of the overall force).

Separate liquid and gas inflows through a Y-piece were modelled. A fixed pressure was defined at the outlet boundary.

A fixed time step of 0.1 ms was used with Courant numbers monitored to ensure that they were acceptable (≤1) and that there was a good overall mass balance within the computational domain (total mass imbalance for all cells <0.5% based on inlet mass flow).

The computational mesh (Figure 4) used polyhedral cells at the bends, which were then extruded along the straight pipe sections. The CFD models discussed in this paper used approximately 1 million cells.

CFD simulations were performed to capture 60s of data after pseudo steady conditions were achieved.

4. RESULTS

4.1. Sensitivity study of CFD results to inlet and outlet boundary conditions

Sensitivity studies were performed on the modelling of the inlet, where initially the upstream Y-piece was not included in the model, and instead a straight pipe section with the inlet defined as a layer of liquid around the pipe wall and gas in the centre at a fixed velocity (see Figure 5). This model predicted an average RMS force for all bends of 3.0 N for Case 1 compared to a measured average of 6.5 N. Figure 7 plots the RMS force for each bend.

However, results for Case 1 were improved when the Y-piece was explicitly modelled (see Figure 6), with average RMS force for all bends nearly doubled to 5.9 N. Adding the Y-piece increased the mixing of gas and liquid and enabled a slug to develop in the long straight pipe up to the first bend. This slugging behaviour was not evident without the Y-piece. Note that an empricial correlation based on the Multiphase 6" JIP data (Belfroid et al, 2019a) calculated the RMS force to be 3.3 N (51% of the test value), which agrees better with the CFD results without the inlet Y-piece. It seems possible that for this particular test setup there is additional mixing and pressure drop across the piping that leads to increased fluid forcing, which is not captured by the JIP correlation, but is captured by CFD when the model closely represents the test setup.

As predicted RMS forces matched the measured values well with the Y-piece, this model is used for the remainder of the simulations.

Figure 5. Snapshot of CFD predicted contours of gas volume fraction (case 1) without inlet Y-piece

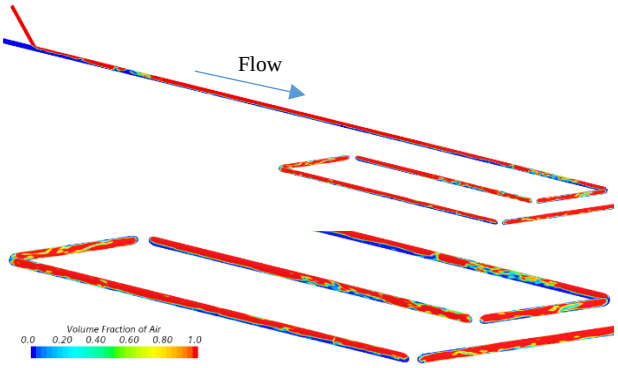

Figure 6. Snapshot of CFD predicted contours of gas volume fraction (case 1) with inlet Y-piece

Sensitivity studies were also performed on the modelling of the oulet boundary conditions. The first simulation described previously (see Figure 5) modelled the outlet as a horizontal pipe section with a fixed pressure applied at the outlet. In the test the air and water flow into a large separator tank through a downturned 90 degree elbow, which is above the liquid level in the tank. A revised model to replicate the test outlet conditons is shown in Figure 8, which also includes the inlet Y-piece. The predicted forces on all bends were not significantly changed by modifying the oulet flow conditions. The remainder of the simulations include the revised outlet conditions that replicate the test setup.

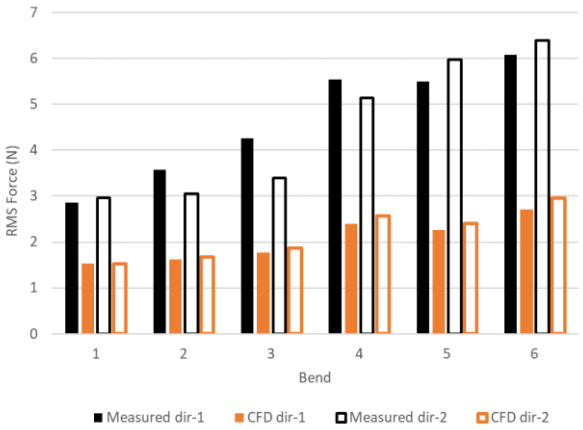

Figure 7. Predicted RMS forces for all bends without inlet Y-piece (case 1)

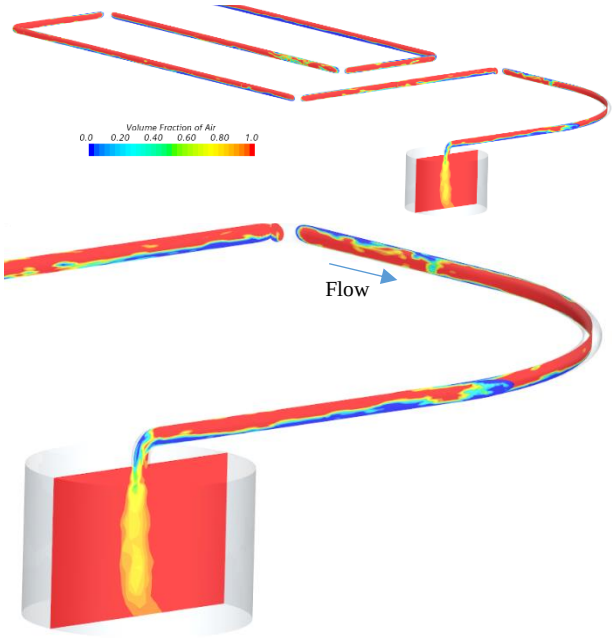

Figure 8. Snapshot of CFD predicted contours of gas volume fraction (case 1) modelling the outlet separator tank

4.2. Comparison of measured and predicted forces – Flow Case 1

For flow Case 1, the predicted average RMS force (5.9 N) over all bends compared well with that measured (6.5 N). The measured RMS forces increase from the first bend to the last (see Figure 9), which is captured by CFD for the first three bends, but CFD predicts similar forces for the last four bends. The CFD under-estimates the total pressure drop across the six bends by ~40% compared to test and the pressure fluctuation at the outlet is less than measured by a similar amount (see Figure 10). It is not clear how much of the difference is numerical and how much is

due to differences between the model and the experimental setup.

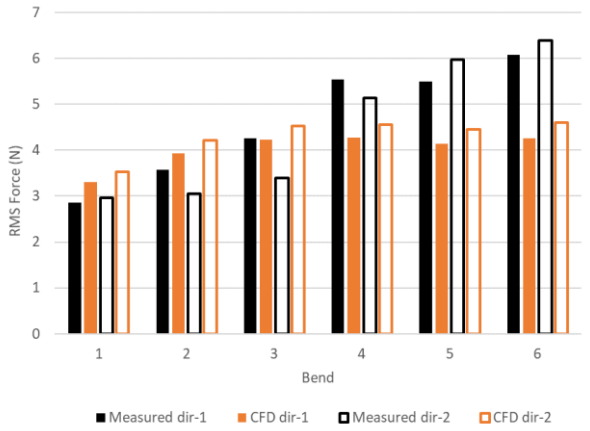

Figure 9. RMS forces for all bends (case 1)

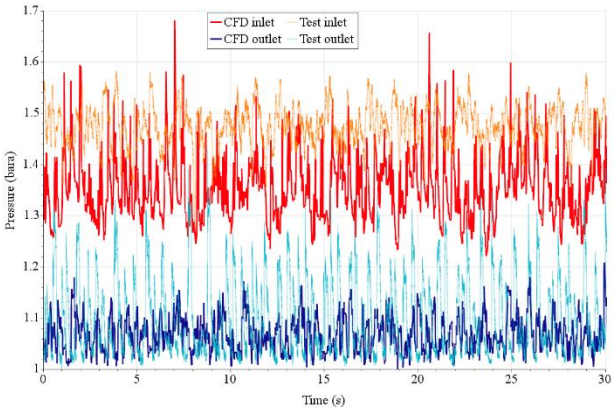

Figure 10. Comparison of measured and predicted pressure fluctuations at inlet and outlet (case 1)

Figure 11. Measured and CFD predicted forcing PSD at all bends (case 1)

Force Power Spectral Densities (PSDs) agree well for all bends (Figure 11) except bend 3 in the downstream direction (B32) and bend 5 in the downstream direction (B52). The measurements for both planar directions are generally very similar for each bend, with bends 3 and 5 being the exceptions.

4.3. Comparison of measured and predicted forces – Flow Case 2

For flow Case 2 the predicted average RMS force (2.8 N) compared well with that measured (2.7 N). Note that an empricial correlation based on the Multiphase 6" JIP data (Belfroid et al, 2019a) calculated the RMS force to be 1.8 N (67% of test value). The forces generally increase from the first bend to the last (see Figure 12) but to a much lesser extent than flow Case 1. The CFD predicted RMS forces compare well on a bend-by-bend basis with those measured. Force PSDs agree well (Figure 13) for all bends except for the same bends and directions as flow Case 1 (B32 and B52, i.e. bends 3 and 5 in the downstream direction) for which the measurements are a little lower in the downstream direction compared to the upstream direction.

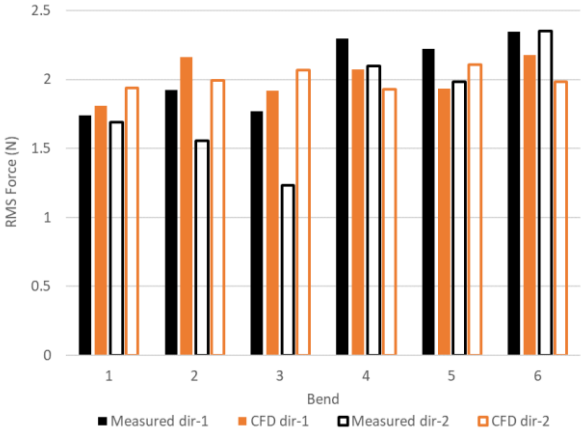

Figure 12. RMS forces for all bends (case 2)

Figure 14 and Figure 15 show the predicted PSD forcing function as a log-log plot and a simplified 2-slope forcing function which has been fitted to the CFD results. Care should be taken fitting the 2-slope forcing function to ensure that the RMS force (i.e. square root of the area under the curve) matches the CFD value. The 2-slope forcing function could be applied to a Random Vibration Theory (RVT) calculation in the frequency domain, as an alternative to applying time varying forces to a transient mechanical FE model.

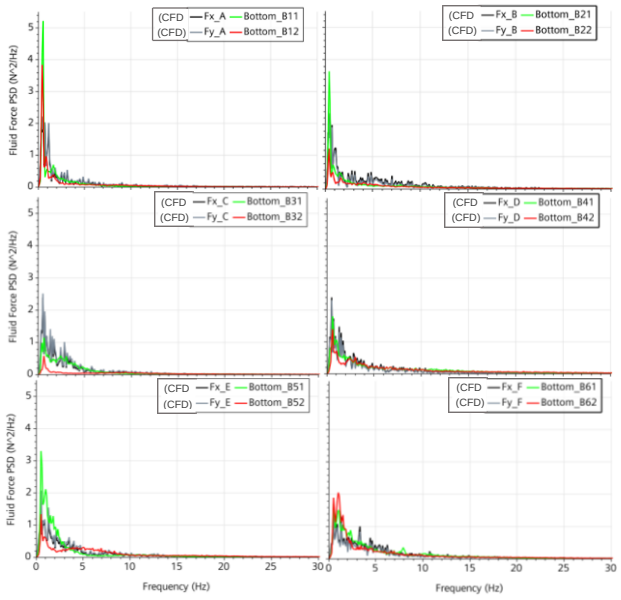

Figure 13. Measured and CFD predicted forcing PSD at all bends (case 2)

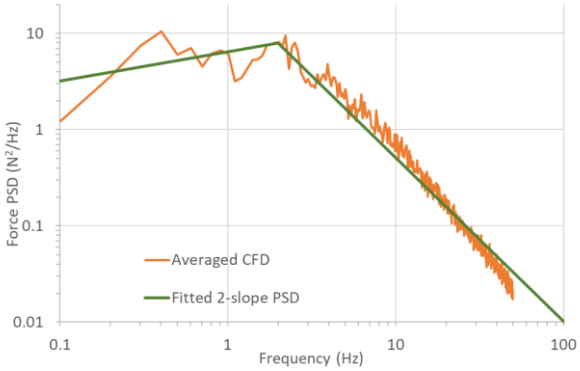

Figure 14. CFD predicted forcing PSD and applied forcing function (case 1)

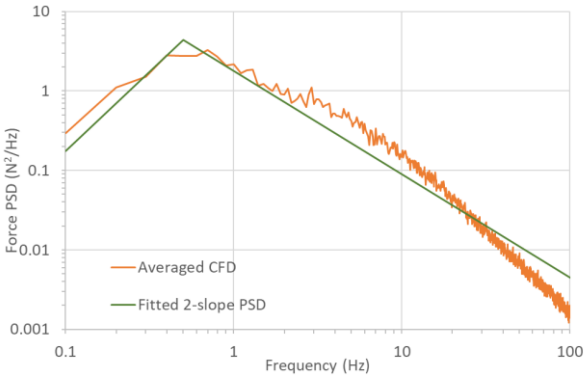

Figure 15. CFD predicted forcing PSD and applied forcing function (case 2)

5. DISCUSSION

The CFD predicted flow induced forces generally compared well with the measured values. CFD provides a useful means of obtaining excitation forces that can be applied to a structural FE model to predict fatigue damage from FIV. The time varying forces can be applied directly to a transient FE model in the time domain; or preferably (in most cases) they can be processed to generate a force PSD and this can be applied to an RVT approach in the frequency domain. In Macchion et al, 2022 the forces have been applied to a mechanical model in both the time and frequency domains and the predicted vibration compared.

It is particularly beneficial to carry out CFD analysis in certain circustances:

- when it is important to capture the phasing between bends;
- to enable prediction of increased excitation along the pipe due to the pressure drop;
- to capture particular nuances of the piping design, such as the inlet Y-piece in this test setup;
- to predict the effects of increased operating pressure (Belfroid et al, 2020, Emmerson et al 2021).

When phasing between bends is likely to be a significant contributor to the dynamics (e.g. slugging flow, Belfroid et al, 2019b), an estimate of the transient properties of the multiphase flow induced forcing using CFD might be necessary.

Care needs to be taken to understand the limitations of the CFD approach (e.g. multiphase model, turbulence approach), to ensure good mass balance and to ensure that the elapsed time simulated is sufficient, as noted earlier.

6. CONCLUSIONS

CFD analysis of multiphase flow in piping systems is a valuable method for predicting the resultant flow induced forces. This is especially true, if a more detailed investigation is needed, for example in subsea piping systems at typical oil and gas production conditions. CFD analysis predicts the increase of excitation along the pipe due to the pressure drop. Care should be taken when selecting the simulation methodology for cases where the piping system has phasing between the bends (e.g. slug flow), in which case transient CFD and FE analysis may need to be carried out.

7. ACKNOWLEDGMENTS

This study was undertaken as part of a collaboration between Xodus, TechnipFMC, TNO and Aker Solutions, sponsored by Equinor. Measurement data was provided by TNO.

8. REFERENCES

Belfroid, Stefan P.C., Nennie, Eric., van Wijhe, A., Pereboom, H., Lewis, M. “Multiphase forces on bend structures – overview large scale 6” experiments”, 11th International Conference on Flow Induced Vibration, 4-6th July 2016, The Hague, The Netherlands, 2016

Belfroid, S., Gonzalez-Diez, N., Tümer, C., Pereboom, H., “Multiphase Flow Induced Forces on Bend Structures”, OMAE2019-96387, 2019a

Belfroid, S., Pereboom, K., Gonzalez-Diez, N., Anantharaman, A., “Phase Relation of Forces Between Multiple Bends”, PVP2019-93543, 2019b

Belfroid, S. P. C., Gonzalez-Diez N., Lunde K., Orre S., “Multiphase flow induced vibrations at high pressure”, PVP2020-21139, 2020

Pereboom, H., Belfroid, S.P.C, Gonzalez-Diez, N., Reijtenbagh, J., “Response of Multiple Bend System to Multiphase Flow”, OMAE2021-62506

Emmerson, Paul R., Lewis, Michael J., Barton, Neil A., “CFD validation of Flow Induced Forces in 6” Piping Caused by Slugging Flow”, 11th International Conference on Flow Induced Vibration, 4-6th July 2016, The Hague, The Netherlands, 2016s

Emmerson, P. R., Lewis, M. J., Barton, N. A., “Influence of Multiple Bends for Multiphase Flow Induced Forces in 6” Piping: Measurements and CFD Analysis”, 11th International Conference on Flow Induced Vibration, 4-6th July 2016, The Hague, The Netherlands, 2016b

Emmerson, P.R., Lewis, M.J., Barton, N.A., Orre, S., Lunde, K., “Flow Induced Vibration Analysis of Topside Piping at High Pressure”, OMAE2020-18760, 2020

Emmerson et al, “Multiphase Flow Induced Vibrations at High Pressure: CFD Analysis of Multiphase Forces”, OMAE2021-62873, 2021

Macchion, O., Emmerson, P.R, Lewis, M.L., Stachyra, L., Orre, S. ”Two-Phase Flow Induced Vibrations: Methodology Validation – Part 2" OMAE2022-78758, 2022

DYNAMIC RESPONSE OF A CANTILEVERED PIPE ASPIRATING FLUID AND SUBJECTED TO REVERSE CONFINED EXTERNAL FLOW: A COMPUTATIONAL COUPLED TWO-WAY FLUID-STRUCTURE INTERACTION ANALYSIS

F. Daneshmand
Department of Engineering, King's College, 133 N River St., Wilkes-Barre, PA 18702, USA

T. Liaghat, M. P. Paidoussis
Department of Mechanical Engineering, McGill University, Montreal, QC, Canada H3A 0C3

ABSTRACT

A computational model is developed for the dynamics of a hanging tubular cantilevered pipe aspirating fluid and simultaneously subjected to an external axial flow in the opposite direction. The external flow is confined over part of the length of the pipe. To gain a better insight into the dynamics of the system, a coupled fluid–structure interaction analysis technique is used, including a finite volume based computational fluid dynamics (CFD) code for the fluid domain and a finite element based computational solid mechanics code for the structural domain. In the numerical simulations, it is seen that limit-cycle motion occurs as the flow velocity exceeds a critical value. The results of the simulations are also compared with those obtained from experimental tests.

1. INTRODUCTION

The problem of flow-induced vibration of pipes conveying fluid has been extensively investigated in the past few decades (Paidoussis 2014, Daneshmand et al. 2022). Although the pipe geometry seems to be simple, the system and its many variants show a rich dynamical behaviour with complex instability characteristics. The existence of various interesting phenomena in dynamic behaviour of the system has attracted the attention of many researchers who studied the linear and nonlinear dynamics of fluid conveying pipes (Tijsseling 2019, Chehreghani et al. 2021, Minas and Païdoussis 2021). From a practical point of view, such a system is extensively used in oil transportation and distribution pipelines and many other applications, including heat exchangers, medical devices, robots, and underwater navigation. An interesting real-world application of the system considered in the present article is its application in solution mining in which water-soluble minerals, such as ordinary salt, magnesium, or potassium salts, are extracted from deep underground. The process is done through the following steps: (i) after drilling to the salt deposits, fresh water is pumped down through kilometer long pipes to dissolve the minerals, (ii) the brine is pushed to the earth's surface by pumping in more fresh water, (iii) the created underground caverns are usually used for storage of different types of hydrocarbons, such as crude oil and natural gas (Moditis et al. 2016).

Motivated by the application of the system in salt-cavern hydrocarbon storage systems, the dynamics of a hanging flexible cantilevered pipe, coaxial with a shorter rigid outer tube, has been studied by Moditis et al. (2016). They developed a nice mathematical model for the problem and used the Galerkin method with Euler–Bernoulli beam eigenfunctions to solve the governing differential equations of the system. A series of experiments have also been conducted in a bench-top-sized system to validate the analytical results. Interested readers are referred to the details provided in Minas et al. (2017), Abdelbaki et al. (2020) and Chehreghani et al. (2021).

Despite extensive work done on this area, there are still several unresolved issues related to vibration characteristics and dynamic instability of pipes conveying fluid that need to be investigated. More specifically, the above-mentioned investigations include analytical and/or experimental techniques to study the behaviour of a cantilevered pipe under the influence of two axial flows in opposite directions. However, the effects of three simultaneous flows as shown in Figure 1 have not been extensively investigated yet. This is the main goal of the present paper to perform a computational two-way Fluid-Structure Interaction (FSI) analysis of the system. The pipe considered in the present study is a confined hanging pipe aspirating fluid and concurrently subjected to reverse external axial flow.

The traditional computational approach to model a structure in contact with a fluid is to use a computational fluid dynamics (CFD) simulation that focuses on the fluid pressures applied to the structure. This is called a one-way simulation approach and can simply be done by applying the fluid pressure in the finite element model of the structure as a boundary or load condition. Dhavalikar et al. (2015) used a one-way FSI approach to obtain whipping response of a ship vessel. They calculated the slamming loads

in the model by idealizing the ship's hull as a free-free beam. There are two main differences between one-way and two-way FSI approaches: (i) the deformed geometry calculated in a one-way FSI analysis is not fed back to the CFD solver, which influences the computation of pressure, and (ii) modeling of actual added mass and damping due to flexure of the body which is generally accounted in CFD computations in two-way FSI is missing in a one-way FSI analysis (Benra et al. 2011, Liaghat et al. 2014).

In a two-way FSI approach, both the structural deformation due to fluid pressure and fluid pressure changes due to the structural deformation are taken into account. This requires the fluid and structural domains to be solved simultaneously with some type of data transfer between the solid and fluid models. This means that the pressure is exported from CFD to structural analysis, and deformation is transferred from structural to CFD analysis to update the geometry of the fluid domain in every coupling iteration, until both solutions converge (Figure 2).

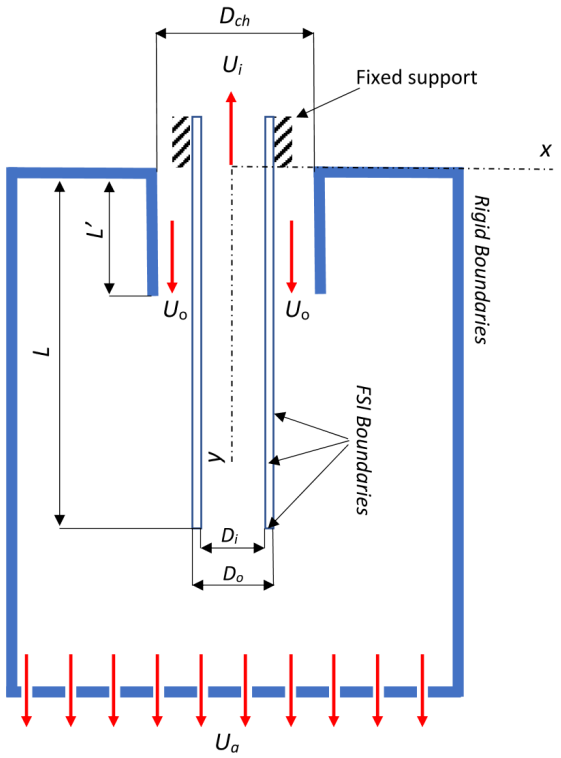

Figure 1. Problem definition.

2. PROBLEM STATEMENT

Referring to Figure 1, the system under consideration comprises a vertically cantilevered central pipe with outer diameter D_o, inner diameter D_i, flexural rigidity EI and length L. The pipe is surrounded by a rigid outer-tube, with inner diameter D_{ch} and length L'. The fluid enters at the top of the annulus formed between the pipe and tube, and then flows downwards throughout the annulus with flow velocity U_o. The fluid then enters into the central pipe from its free-end and flows upwards with mean velocity U_i. The system has also a second outlet at the bottom of the tank with flow velocity U_a. The mass per unit length of the pipe is m and that of the aspirated fluid is $M = \rho A_i$, where ρ is the density of the fluid. The undeformed neutral axis of the pipe coincides with the vertical y-axis and is in the direction of acceleration due to gravity (g). Using the continuity equation, the mean flow velocity U_o in the annular region can be expressed in terms of U_i and U_a as

$$U_o = U_i\,(A_i + \alpha A_a)/A_{ch}\,, \qquad (1)$$

where $\alpha = U_a/U_i$; $A_i = \pi D_i^2/4$ is the inner cross-sectional area of the central pipe, and $A_{ch} = (\pi/4)(D_{ch}^2 - D_o^2)$ is the cross-sectional area of the annular flow; D_{ch} is the inner diameter of the outer-tube surrounding the central pipe, and A_a is the bottom flow area of the tank.

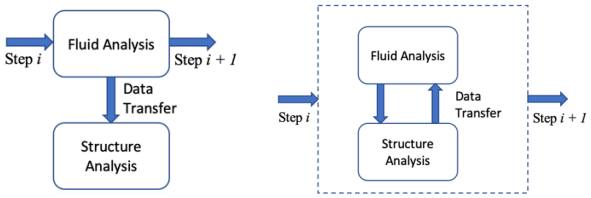

Figure 2. A comparison between one-way and two-way FSI approaches.

3. TWO-WAY FSI COMPUTATIONAL MODEL

In some applications, there is a strong and potentially nonlinear relationship between the fields that are coupled in the Fluid Structure Interaction. Under these conditions, the ability to reach a converged solution will likely require the use of bidirectional (i.e., two-way) FSI. A three-dimensional two-way FSI numerical modelling is performed in this study using the system coupling available in ANSYS-Workbench platform. This is based on using a multifield model including a transient structural analysis coupled with a finite-volume based CFD solver (ANSYS-CFX). In many FSI simulations, the capabilities of additional solvers are required to complement those of CFX. Under these circumstances, CFX provides tools to facilitate the import and export of solution data in a variety of formats. Figure 3 shows a snapshot from ANSYS Workbench that highlights the typical setup/workflow used to simulate two-way FSI involving the fluid flow CFX and the Transient Structural systems.

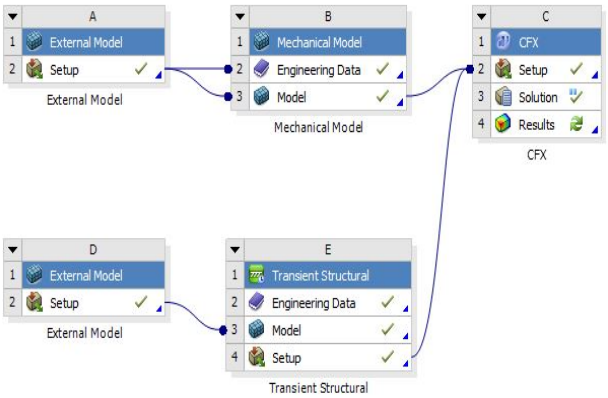

Figure 3. Snapshot showing the workflow used in the present study for the two-way FSI simulations.

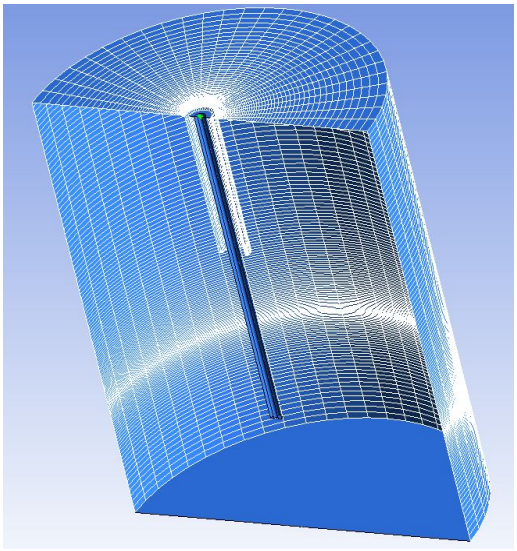

Figure 4. The fluid meshes created for the problem.

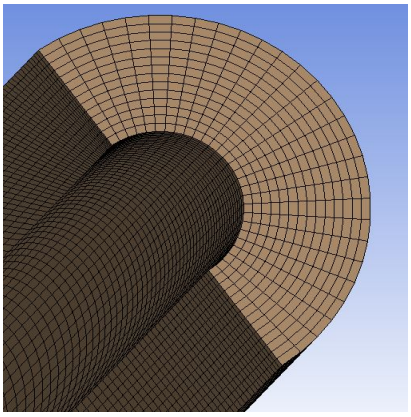

Figure 5. The meshes created for the central pipe.

The fluid meshes are created using hexahedral elements as shown in Figure 4. This is a fundamental requirement for accuracy of the simulations. An inflation layer meshing is also implemented to accurately capture the boundary layer region in the computational model. Two pre-defined parameters are used to control the quality of created meshes. These parameters are called "Non-Matching Area Function" and "Number of Un-mapped Nodes" in ANSYS-CFX. To avoid any mesh alignment error in the model, the values of these two parameters are kept to less than 0.1% and zero, respectively. Table 1 provides more information about the meshes created for the fluid domain of the problem. An inflation layer meshing is also used to accurately capture the boundary layer region in the computational model.

Table 1. Mesh information (Fluid)

# of Nodes	384240
# of Elements	361508
Mesh Metric	Aspect Ratio
Minimum	1.78
Maximum	261.02
Average	7.29
Standard Deviation	8.32

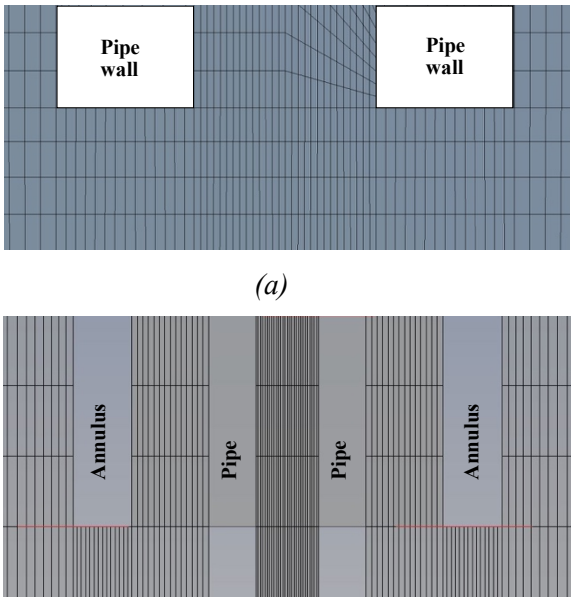

Figure 6. Meshes created for fluid-solid interface at (a) the free end of the central pipe, and (b) the free end of the annulus.

Hexahedral meshes are also used for the pipe as shown in Figure 5. The central pipe is made of silicone-rubber in the experiments. The material properties and dimensions of the pipe are given in Table 2. Mesh statistics for the meshes created for the pipe is given in Table 3. Special attention is also paid to the length scales of the meshes around the fluid-solid interface to maintain the load transfer resolution (Figure 6).

Table 2. Pipe and annulus geometry and properties

L (mm)	431
L' (mm)	206.5
D_o (mm)	16
D_i (mm)	6.35
EI (N.m^2)	3.0
ρ (kg/m^3)	1.13×10^3
Annulus thickness (mm)	6.0
Annulus inner diameter (mm)	31.5

Table 3. Mesh information (Pipe)

# of Nodes	43065
# of Elements	38416
Mesh Metric	Aspect Ratio
Minimum	1.36
Maximum	33.9
Average	13.89
Standard Deviation	6.35

4. EXPERIMENTS

Experiments on the dynamics of an unconfined pipe aspirating fluid, were performed by (Butt et al. 2021, Chehreghani et al. 2021, Minas and Païdoussis 2021). The experimental set-up for the problem includes a bench-top apparatus shown in Figure 7. The apparatus is a scaled down model of the brine-string and casing found in salt-cavern hydrocarbon storage applications (Ratigan 1995, Païdoussis et al. 2019). The fluid is water. The pipes were made of silicone-rubber (Silastic) or thermoplastic rubber (Santoprene). For the flow configuration of Figure 1, the flow-rates through the central pipe, annulus and bottom of the tank were measured by magnetic mass-flow meters. Two digital cameras were also used to record the pipe motions in two perpendicular directions, simultaneously. The central pipe displacement was then extracted via image analysis. The recorded videos were subsequently loaded into an image processing MATLAB script to obtain the displacement-time series. The time series from both front and side cameras, at each velocity step, were then smoothed using a polynomial spline. At each step, firstly the system was kept running for a while to attain steady state. Then, the motion of the marked section of the pipe was tracked and recorded for 300 s using the dual-camera system.

The apparatus can sustain a pressure up to 45 psi. The mean pressure in the test-section is measured with a conventional Bourdon tube gauge, installed on the bleed line of the test-section, right before a manual bleed valve. This ensures that any air bubbles are removed, and a reliable pressure reading can be obtained.

To ensure consistency and guarantee validity of the results, the experiments were repeated for at least a second time (Chehreghani et al. 2021).

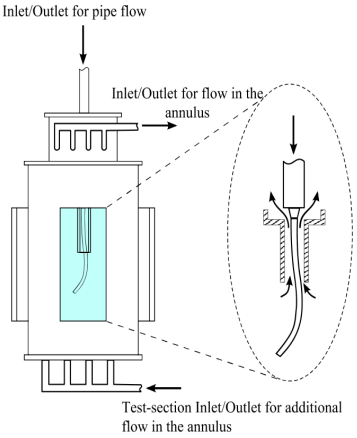

Figure 7. Schematic of the experimental set-up for the flow configuration shown in Figure 1.

5. RESULTS

This section provides the results obtained from the numerical FSI simulation as described in the previous section. The problem is solved for various flow velocity ratios, U_o/U_i. The inlet and outlet dimensionless flow velocities u_i and u_o are also defined by the following relations:

$$u_i = \left(\frac{M_i}{EI}\right)^{1/2} LU_i, \quad u_o = \left(\frac{\rho_f A_o}{EI}\right)^{1/2} LU_o, \quad (1)$$

where M_i is the mass of the fluid in the pipe per unit length and ρ_f is the fluid density; $A_o = \pi D_o^2/4$ is the outer cross-sectional area of the pipe. The dynamic behaviour of the pipe is investigated with increasing flow velocity within the annulus. In each simulation, the flow velocity in the annulus is increased from zero to a certain value and then remains constant at that flow velocity. For a sufficiently high U_o, the central pipe starts to oscillate. The amplitude of the oscillations increases as the annular flow velocity increases. In the numerical simulations, the velocity of the fluid in the central pipe is limited, to avoid any contact between the deformed central pipe and the rigid tube around it. The behaviour of the system is studied in the presence of the three flow velocities U_i, U_o and U_a, shown in Figure 1. The problem is solved for various flow velocity ratios, $r = U_o/U_i = 0.2, 0.4, 0.6, 0.8$. A constant time step size is used in all calculations equal to 0.01 s and the effect of turbulence is taken into account by using the $k-\varepsilon$ turbulence model in the simulations. The displacements of the free end of the central pipe in the transverse x-

direction versus time are studied to gain a better understanding of the dynamical response of the system with varying flow velocities. In the simulations, the flow velocity in the annulus starts from zero, increases over time and remains constant after a specified number of time-steps.

The results of the present two-way FSI simulations show that the pipe generally loses stability by flutter in its first mode, at a sufficiently high flow velocity U_o. However, as the flow velocity ratio r is increased from a small value (e.g., 0.050) to a large one (e.g., 0.6), the pipe loses stability by flutter at progressively lower critical flow velocities. Moreover, for flow velocity ratio $r = 0.6$, two limit cycle motions can be observed for low and high flow velocities, $U_o = 0.050$ m/s and $U_o = 0.155$ m/s, respectively (Figures 8 and 9). The maximum displacements of the free end of the pipe at these two flow velocities are ~ 0.7 mm and ~ 15 mm for $U_o = 0.050$ m/s and $U_o = 0.155$ m/s, respectively.

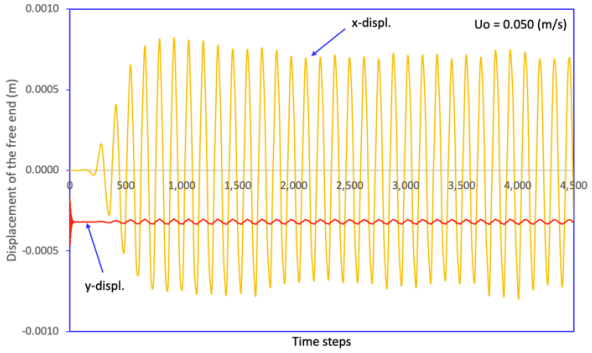

Figure 8. Typical displacements of the free end of the pipe for $U_o = 0.050$ m/s, $r = U_o/U_i = 0.6$

For the velocity ratio $r = 0.6$, we observe that a significant change in pipe deformation occurs at $U_o = 0.155$ m/s. The results obtained for the displacements of the free end of the central pipe for $U_o = 0.155$ m/s are plotted in Figure 9. In the lower time-steps, the initial pipe deformation is very small. After around 300 time-steps, the pipe deformation increases until the amplitude of the flow-induced vibrations reaches a constant limit-cycle value (~ 15 mm), as shown in the figure. The amplitude of vibration remains approximately unchanged and periodic in time. Based on the results of the FSI computer simulations presented in this study, we found $U_o = 0.155$ m/s as the critical flow velocity of the system for $r = U_o/U_i = 0.6$. This value corresponds to $(u_i)_{cr} = 0.204$. The maximum displacement of the free end of the pipe at this critical flow velocity is around 16 mm.

The fluid flow streamlines are plotted in Figure 10 for the velocity ratio $r = 0.6$ and $U_o = 0.155$ m/s. This figure clearly shows the effects of central pipe deformation on the fluid flow around the pipe. Based on the results of this computer simulation, the deformation of the central pipe causes a significant asymmetry of the streamlines around the central pipe of the system. The influence of this asymmetry needs to be investigated further in the future in order to provide a better insight into the dynamics of the system.

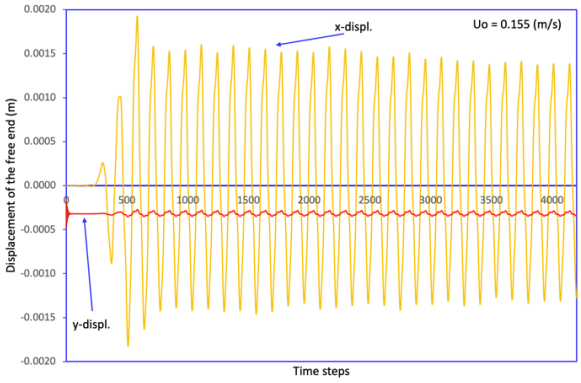

Figure 9. Typical displacements of the free end of the pipe for $U_o = 0.155$ m/s, $r = U_o/U_i = 0.6$

Butt et al. (2021) conducted a set of experiments to examine the dynamical behaviour of the system for different flow velocity ratios r, ranging from 0.04 to 1.00. They reported a value of $(u_i)_{cr} = 0.24$ for the velocity ratio $r = 0.6$ fairly close to 0.20 obtained in this paper. They also reported a value of $(u_i)_{cr} = 0.54$ for the velocity ratio $r = 0.4$ that is close to 0.65 obtained from the simulations in this paper.

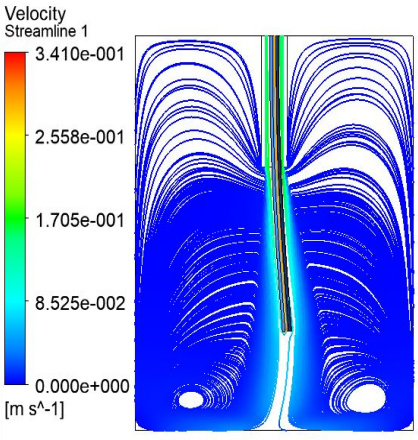

Figure 10. The effects of central pipe deformation on the fluid flow

6. CONCLUSION

In this paper, a numerical simulation is presented on the dynamics of a hanging cantilevered pipe within a fluid-filled container. The central pipe is flexible and surrounded by a concentric rigid annulus. Both the central pipe and annulus are cantilevered from their top ends and submerged in the water-filled tank. The fluid enters at the top of the annulus, flows downwards throughout the annulus, enters the central pipe from its free-end and finally flows upwards in the central part and exits from the pipe. The system has also a second outlet at the bottom of the tank which allows higher values of U_o/U_i to be achieved. A two-way coupled FSI analysis is used in the simulations to examine the effects of three simultaneous flows with the flow velocities U_i, U_o and U_a.

The computational FSI simulations as developed in the present paper are in good agreement with experimental measurements and showing that they are capable of predicting the onset of pipe instability for the flow velocity ratio $r = 0.6$. Moreover, a significant asymmetry in the flow field around the central pipe was observed that could potentially affect the dynamical behaviour of the system and needs to be investigated in more detail in the future.

7. ACKNOWLEDGEMENTS

The authors gratefully acknowledge the support of the Natural Sciences and Engineering Research Council of Canada (NSERC), the Solution Mining Research Institute (SMRI) and Pipeline Research Council International (PRCI). The first author gratefully acknowledges the support provided from King's College in Pennsylvania.

8. REFERENCES

Abdelbaki, A. R., M. P. Païdoussis and A. K. Misra, 2020. A nonlinear model for a hanging cantilevered pipe discharging fluid with a partially-confined external flow. International Journal of Non-Linear Mechanics **118**(103290).

Benra, F.-K., H. J. Dohmen, J. Pei, S. Schuster and B. Wan, 2011. A comparison of one-way and two-way coupling methods for numerical analysis of fluid-structure interactions. Journal of Applied Mathematics **2011**: 1-16.

Butt, M. F. J., M. P. Païdoussis and M. Nahon, 2021. Dynamics of a confined pipe aspirating fluid and concurrently subjected to external axial flow: An experimental investigation. Journal of Fluids and Structures **104**(103299).

Chehreghani, M., A. R. Abdelbaki, A. K. Misra and M. P. Païdoussis, 2021. Experiments on the dynamics of a cantilevered pipe conveying fluid and subjected to reverse annular flow. Journal of Sound and Vibration **515**(116480).

Daneshmand, F., T. Liaghat and M. P. Paidoussis, 2022. A coupled two-way fluid–structure interaction analysis for the dynamics of a partially confined cantilevered pipe under simultaneous internal and external axial flow in opposite directions. Journal of Pressure Vessel Technology **144**(2).

Dhavalikar, S., S. Awasare, R. Joga and A. R. Kar, 2015. Whipping response analysis by one way fluid structure interaction—A case study. Ocean Engineering **103**: 10-20.

Liaghat, T., F. Guibault, L. Allenbach and B. Nennemann, 2014. Two-way fluid-structure coupling in vibration and damping analysis of an oscillating hydrofoil. Paper IMECE2014-38441, ASME International Mechanical Engineering Congress & Exposition, Volume 4A: Dynamics, Vibration, and Control, Montreal, Canada.

Minas, S. L. and M. P. Païdoussis, 2021. Dynamics of a shrouded cantilevered pipe subjected to internal and annular flows. Journal of Sound and Vibration **490**(115729).

Minas, S. L., M. P. Paidoussis and F. Daneshmand, 2017. Paper IMECE2017-70466, Experimental and analytical anvestigation of hanging tubular cantilevers with discharging axial and radial flow. ASME 2017 International Mechanical Engineering Congress and Exposition IMECE2017, Tampa, Florida, USA.

Moditis, K., M. P. Païdoussis and J. Ratigan, 2016. Dynamics of a partially confined, discharging, cantilever pipe with reverse external flow. Journal of Fluids and Structures **63**: 120-139.

Paidoussis, M. P., 2014. Fluid-Structure Interactions. Oxford, Academic Press.

Païdoussis, M. P., A. R. Abdelbaki, M. F. J. Butt, K. Moditis, A. K. Misra and M. Nahon, 2019. Dynamics of a pipe subjected to internal and confined external flow. Paper PVP2019-93227, ASME 2019 Pressure Vessels and Piping Conference, San Antonio, TX, USA.

Ratigan, J. L., 1995. Underground storage of hydrocarbons in salt formations. American Gas Association Conference, Las Vegas, USA.

Tijsseling, A. S., 2019. An overview of fluid-structure interaction experiments in single-elbow pipe systems. Journal of Zhejiang University: Science A **20**(4): 233-242.

FSI SIMULATIONS OF FLUID-ELASTIC INSTABILITIES OF A CLAMPED-CLAMPED CYLINDER IN AXIAL FLOW

Lucas Delcour & Henri Dolfen
Ghent University, Department of Electromechanical, Systems and Metal Engineering, Ghent, Belgium
Lieva Van Langenhove
Ghent University, Department of Materials, Textiles and Chemical Engineering, Ghent, Belgium
Joris Degroote
Ghent University, Department of Electromechanical, Systems and Metal Engineering, Ghent, Belgium
Flanders Make, Belgium

ABSTRACT

A cylinder clamped at both ends and subjected to an axial flow will typically become unstable with increasing axial flow velocity. At low velocity the cylinder will buckle and, as the flow velocity is further increased, flutter will occur. These instabilities can be devastating in some applications such as nuclear reactor cores or can be put to good use in energy harvesting tools. A substantial amount of analytical and experimental work has already been performed on the stability of cylinders in axial flow. However, numerical simulations on the topic are still rather scarce. Mainly due to the associated computational cost and difficulties in dealing with the mesh deformation, especially for cases with very large displacements (e.g. cylinders with a free end) in confined geometries. In this research fluid-structure interaction (FSI) simulations are performed on a clamped-clamped cylinder subjected to axial flow for a range of inlet velocities. In the flow solver a Chimera technique is used which allows for large structural deformations without degrading the mesh. The results are compared to experimental data and previous FSI simulations. The goal is to validate the methodology for future use in simulations with cantilevered cylinders and later on investigate the influence of compressiblity on the stability of a flexible cylinder in high-speed air flow.

1. INTRODUCTION

Research into vibrations of slender structures subjected to axial flow started picking up in the 1960's (Paidoussis, 1966a,b) and has mainly been aimed at safety in nuclear power plants, e.g. Paidoussis (1983). Other fields of application are, for example, pipes for deep-sea mining, heat exchangers and energy harvesting tools (Singh et al., 2012).

The axial nature of the flow lends itself rather well to the use of analytical models for study of vibrations and stability of the structures. Some examples of such models are De Langre et al. (2007) for cantilevered cylinders, Modarres-Sadeghi (2007) for cylinders clamped or pinned at both ends and Rinaldi and Paidoussis (2012) for cylinders clamped at the downstream end but free at the upstream end. In these models the forces are often subdivided into viscous and inviscid forces. The modelling of the latter is typically based on the study from Lighthill (1960), while the inclusion of the viscous forces is usually done through empirical formulas, requiring tuning of the coefficients. As stated by De Ridder et al. (2013): "*The prediction of flutter type instabilities or turbulence-induced vibrations requires a good prediction of damping, which is governed by the viscous forces normal to the cylinder and thus by the mainly empirical coefficients*".

The use of these empirical coefficients can be avoided by resorting to numerical techniques, provided the surface texture is sufficiently smooth or can adequately be defined. Some examples of numerical research are provided next. Liu et al. (2012) performed loosely coupled fluid-structure interaction (FSI) simulations for a clamped-clamped cylinder in tubular flow coupling a large-eddy simulation to a beam-elements model. More recently, De Ridder et al. (2015) numerically investigated the fluid-elastic instabilities of a clamped-clamped cylinder in axial flow using Reynolds-averaged Navier-Stokes (RANS) simulations and a strongly coupled FSI framework. Another example is the study of ter Hofstede et al. (2017) who executed strongly coupled FSI simulations on the free vibration of a clamped-pinned cylinder in axial flow.

In the aforementioned FSI-research the motion of the cylinder was constrained at both ends, which limits the displacement/deformation that needs to be ac-

commodated for in the flow solver. As long as the displacements do not become excessive, a single deforming grid can be used in the flow solver with the arbitrary Lagrangian Eulerian (ALE) formulation of the Navier-Stokes equations. As the confinement and/or the displacement amplitude increases it becomes more difficult to maintain a good mesh quality after deformation and eventually the simulations fail (e.g. Osman et al. (2019)). An alternative is to use immersed-boundary methods (as was for example done by Osman et al. (2018)), but these again require the use of (tuned) force coefficients.

Another possibility is to use a Chimera technique. This technique superimposes multiple fluid grids and obtains the solution by interpolation between them (Benek & Steger, 1986). This allows for a larger flexibility in terms of deformation (as will be clarified later on) and avoids the use of empirical force coefficients as the boundary layer can still be resolved. The interpolation will, however, introduce some error. Therefore, some testing is required to evaluate the applicability of the current setup to FSI simulations of fluid-elastic instabilities of clamped-clamped and clamped-free cylinders. As a first validation step, simulations were performed on the same clamped-clamped configuration as was used in the experiments of Modarres-Sadeghi et al. (2008) and the results were compared to their data and the calculations of De Ridder et al. (2015). This validation and comparison is the goal of this paper.

The paper is structured as follows: firstly, a brief overview of the experimental setup from Modarres-Sadeghi et al. (2008) is provided, followed by a description of the numerical setup. Subsequently, the results of the simulations are analyzed by investigating the general dynamic behavior of the cylinder as a function of the flow velocity. Lastly, the buckling and the flutter regimes are discussed in more detail.

2. METHODOLOGY

As can be read in Paidoussis (2016) the general dynamic behavior of a clamped-clamped cylinder ressembles that of a pinned-pinned cylinder and can be described as follows: at low flow velocities the cylinder remains straight on average and exhibits small amplitude, turbulence induced vibrations. As the velocity is increased further, the amplitude of these vibrations increases and eventually the cylinder buckles into a first mode shape. The amplitude of this static deformation increases with the flow velocity. At sufficiently high flow velocity the cylinder starts fluttering, mainly in its second mode. Additionally, in the FSI simulations of De Ridder et al. (2015) a small re-stabilization region was observed in between the buckling and the flutter regime.

The goal of this part of the research was not to analyze the fluid-elastic instabilities of a clamped-clamped cylinder, but rather use them to validate the current methodology with Chimera instead of the ALE formulation that was used in previous work. Therefore, FSI simulations were performed at various flow velocities to verify that the different dynamic regimes could be reproduced and that the critical velocities were in agreement with expectations. The displacement amplitude and flutter frequency were also considered.

2.1. Experimental setup of Modarres-Sadeghi et al. (2008)

Modarres-Sadeghi et al. (2008) performed experiments on flexible cylinders subjected to axial water flow. The cylinders were mounted vertically in a test section with diameter 0.20 m and length 0.75 m. Flow straighteners and a large upstream area reduction were employed to obtain a uniform axial flow in the test section. The maximal velocity that could be attained was 5 m/s.

Experiments were performed using several cylinders and varying end boundary conditions. All cylinders were constructed of silicone rubber. The experimental data to which the simulations in this research are compared, was obtained using a hollow cylinder, clamped at both ends and without axial compression. The lower flexural rigidity of a hollow cylinder (compared to a full cylinder) allowed the flutter regime to be attained in the water tunnel. At the upstream end of the cylinder a streamlined section was added. Two optical sensors were mounted in perpendicular directions to measure the midpoint displacement. Table 1 lists the physical parameters of the cylinder. For additional information on the experimental setup the reader is referred to Modarres-Sadeghi et al. (2008).

Physical parameter	**Value**
Outer cylinder diameter (D) [mm]	15.6
Inner cylinder diameter (d) [mm]	9.4
Length (L) [mm]	435
Mass per unit length (m) [kg/m]	0.1445
Flexural rigidity (EI) [N.m^2]	0.0065

Table 1. Physical parameters of the cylinder in the experiment used for comparison.

2.2. Coupled numerical setup

The FSI simulations were performed in a partitioned manner using the in-house code “Tango”. The inter-

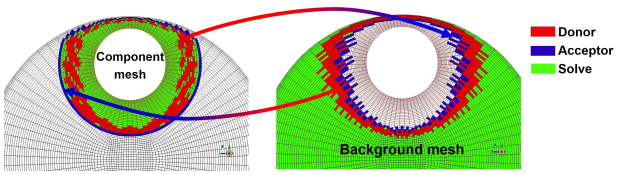

Figure 1. Illustration of the Chimera technique for a different case.

face quasi-Newton technique with an approximation of the inverse of the Jacobian from a least-squares model (IQN-ILS) (Degroote et al., 2009) was used as convergence accelerator. Abaqus 6.14 was employed as structural solver and ANSYS Fluent 19.0 as flow solver.

2.3. Structural model

The structural model corresponds to the straight, hollow cylindrical part from the aforementioned experimental setup, excluding the streamlined end-piece. The structure was meshed with 500 quadratic Timeshenko beam elements (type PIPE32). The Poisson coefficient was specified as 0.48, a typical value for silicone rubber. The remaining geometrical and structural parameters were set in correspondence with the experimental setup (see Table 1). At the up- and downstream ends of the cylinder clamped boundary conditions were applied. No contact condition was implemented as the structure was not expected to deflect up to the channel wall based on previous simulations and the experimental data.

2.4. Flow model

As was mentioned in the introduction, a Chimera technique was employed in this research to obtain a larger flexibility in terms of displacement in light of future simulations on clamped-free cylinders. In the Chimera technique the flow problem is solved on several grids which are superimposed. Typically, the meshes are referred to as background mesh(es) and component mesh(es). The general idea is illustrated in Figure 1 (for a different case). Data from the component mesh is interpolated to the background mesh to act as a boundary condition for the solution on the background mesh and vice versa. The success of a Chimera simulation depends largely on an appropriate overlap between background and component mesh. A too large discrepancy in cell size or orientation or a too small overlap region can introduce excessive interpolation errors and/or prevent the identification of appropriate cells to interpolate data from.

In the current research a single background and a

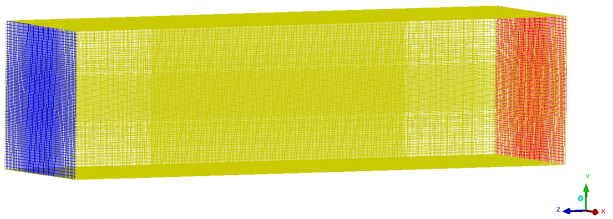

Figure 2. Background mesh. Blue = velocity inlet ; red = pressure outlet ; yellow = symmetry.

single component mesh were used. The background mesh represents the flow domain without the cylinder. For ease of meshing and to obtain a more uniform mesh spacing the choice was made to use a rectangular flow domain. As the deflection of the cylinder is relatively small compared to the diameter of the test section, the exact configuration of the channel wall could be neglected. The rectangular domain had a cross section of 0.2 m x 0.2 m and a length of 0.75 m. The background mesh consisted of approximately 1.6 million cells (76x76x282). At the location of the cylinder, the axial cell size was 2 mm. The background mesh is visualized in Figure 2. At the upstream end a uniform velocity profile was applied with a turbulent intensity of 5% and a turbulent length scale of 0.0156 m. The downstream end was set as a pressure outlet with a static gauge pressure of 0 bar. At the mantle a symmetry boundary condition was imposed. The background mesh does not deform during the FSI simulations.

The flexible cylinder is introduced in the simulation by the component mesh. Before discussing the details of this mesh it is important to mention that initial simulations have shown that the streamlined end piece, at the upstream end of the cylinder, is essential to obtaining the desired instabilities. If the end piece is not included it takes quite some distance for the flow to nicely attach to the cylinder and no clear buckling could be obtained from the simulations, even with an initial deflection. Therefore, a rigid, streamlined end piece was attached to the flexible cylinder in the flow solver. The component mesh is sketched in Figure 3.

The walls of the cylinder (gray in Figure 3) are set as no-slip walls. The outer boundaries of the component mesh (orange in Figure 3) follow the motion of the flexible cylinder as well as possible. These boundaries are, however, not constrained by the boundaries in the background mesh. This together with the fact that the boundaries can move along with the cylinder allows for large structural deformations with minimal squashing of cells and mesh degradation.

The component mesh consisted of approximately

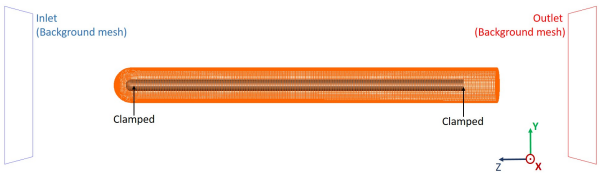

Figure 3. Component mesh. The outline of the inlet and outlet are also shown to illustrate the relative positioning to the background mesh (Figure 2). Gray = cylinder wall; orange = overset interface.

500 000 hexahedral cells. The total length of the component mesh was 0.51 m with a diameter of 3D, extending 1D upstream and 3D downstream of the cylinder walls. The axial and radial cell resolution was (approximately) 2.1 and 1.7 mm, respectively. The inlet was positioned 0.15 m upstream of the cylinder's front and the outlet 0.15 m downstream of the cylinder's end.

The k-ω SST model was used as turbulence model with the Coupled scheme for the pressure-velocity coupling. For the convective terms a second-order upwind scheme was employed for the pressure and momentum. No energy equation was included and a first-order implicit time stepping scheme was employed. For cases involving buckling a time step size of 0.2 s was selected; for cases with flutter the time step size was set to 0.005 s (this time step size was selected based on stability considerations for the Chimera technique in combination with the mesh motion due to flutter, it also yields a sufficient temporal resolution as the frequency was expected to be in the range of 2-4 Hz); and for cases close to the end of the buckling regime/start of the flutter regime simulations were performed with both time step sizes to verify whether there was a difference and if so, the simulation with the smallest time step size was continued. All simulations were initialized by performing a steady-state calculation with an undeformed cylinder.

3. RESULTS

FSI simulations were performed for a range of inlet velocities (U [m/s]). For post-processing these were converted to non-dimensional velocities (u) calculated according to equation (1), with ρ the density of the fluid, A the cross-sectional area of the cylinder and EI the flexural rigidity, being the product of the elasticity modulus (E) and the area moment of inertia (I):

$$u = U \cdot L \cdot \sqrt{\frac{\rho A}{EI}} \qquad (1)$$

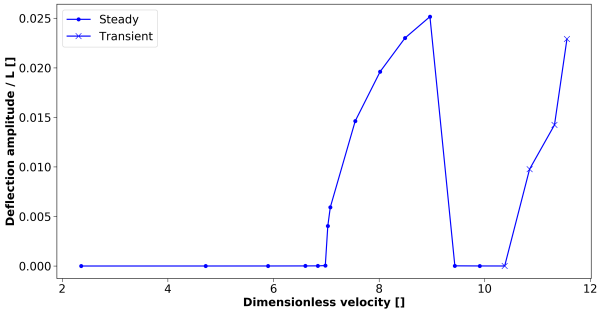

Figure 4. Simulated displacement amplitude. For transient cases the maximal displacement amplitude during the final quarter of the simulation is plotted.

Figure 4 plots the non-dimensional (using L) displacement amplitude for all simulated velocities. For steady-state deformations the maximal amplitude at the final time step was extracted while for transient deformations (flutter) the maximal amplitude (a_{max}) during the last $1/4^{th}$ of the simulation was used. The figure illustrates the general dynamic behavior of the cylinder. For low velocities, almost no deformation is generated. Once the flow velocity exceeds a certain threshold a static deformation starts to develop whose amplitude increases with the flow velocity until suddenly the cylinder restabilizes. Further increasing the flow velocity results in a transient instability of the cylinder.

Based on Figure 4, the threshold for buckling could be put in between a dimensionless velocity of 6.98 and 7.03. In Modarres-Sadeghi et al. (2008) 3 different methods are proposed to extract a critical velocity for buckling from the experimental data. One of these methods defines the intersection of a linear regression through the low-deformation region and a linear regression through the large static deformation region as critical velocity. Applying this to the simulated data set yields a value of 6.45. This is in good agreement with the values calculated by De Ridder et al. (2015) [6.5-7] and with the experimental data from Modarres-Sadeghi et al. (2008) [5.4-6.2].

Similar to the simulations from De Ridder et al. (2015) a restabilization is observed in between the buckling and flutter regime; in the current simulations the restabilization extends from a dimensionless velocity of 9.4 to a dimensionless velocity of 10.4. The upper limit corresponds to the flutter threshold which agrees rather well with the value of 10.1 obtained by De Ridder et al. (2015) and the value of 11.2 from the experiments of Modarres-Sadeghi et al. (2008).

The maximal non-dimensional displacement observed over the current range of flow velocities was 0.0253 for a dimensionless velocity of approximately 9. This situation is visualized in Figure 5, which

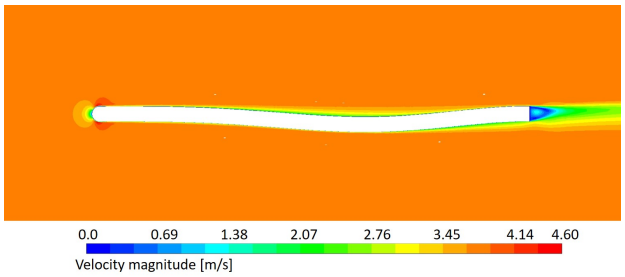

Figure 5. Contour plot of velocity magnitude in the plane of maximal displacement for a dimensionless velocity of 8.96.

shows a contour plot of the velocity in the buckling plane.

The maximal displacement in Figure 5 corresponds to a dimensionless displacement of 0.0215 at the midpoint (obtained via division by the cylinder length). Experimentally, Modarres-Sadeghi et al. (2008) measured a dimensionless displacement of 0.029, resulting in a relative difference of 25.8%. In the figure it can be seen that the displacement is still rather limited. A single deforming grid is still very well suited for these simulations. However, for clamped-free simulations the amplitude of motion is substantially larger, especially at the free end, necessitating other approaches such as the Chimera technique.

3.1. Buckling regime

Figure 6 plots the displacement amplitude for several velocities in the buckling regime. A downstream shift of the location of maximal amplitude with increasing flow velocity can be noted similar to what is generally observed in experiments with pinned-pinned cylinders (Paidoussis, 1966b). This downstream shift was also apparent in the calculations of De Ridder et al. (2015).

3.2. Flutter regime

Figure 7 illustrates the general flutter shape for a dimensionless velocity of 11.56 by showing the centerline positions for the last 50 time steps of the simulation projected on the yz-plane. The flutter has a predominant 2^{nd} mode shape with a larger amplitude for the downstream lobe.

Figure 8 displays the displacement in the xy-plane for the same case at the axial location where the maximal flutter displacement was observed (0.72 dimensionless units downstream).

From the figure it can be observed that the x- and y- displacement start in phase, indicating an in-

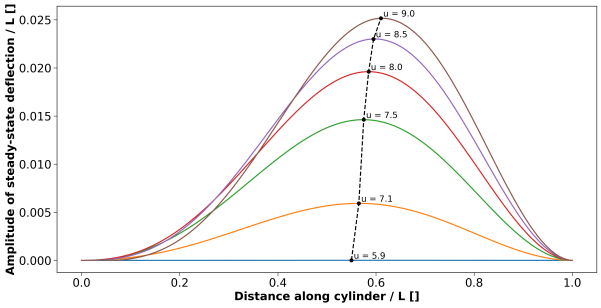

Figure 6. Local amplitude of the steady state deflection at several non-dimensional velocities "u". The dashed line connects the points of maximum deflection.

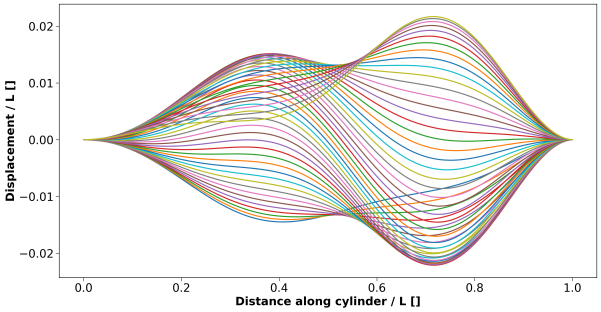

Figure 7. Simulated centerline position in the last 50 time steps for a dimensionless velocity of 11.56 in the yz-plane.

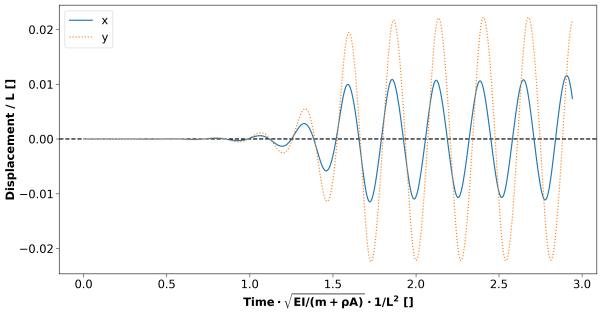

Figure 8. xy-displacement of a point 0.72 dimensionless units downstream along the cylinder for a dimensionless velocity of 11.56.

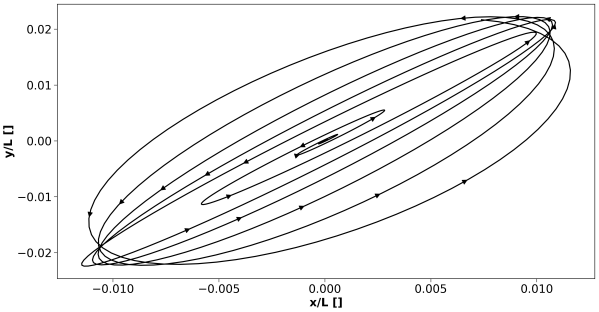

Figure 9. Trajectory of the cylinder 0.72 dimensionless units downstream of the cylinder start at a dimensionless velocity of 11.56.

u []	**f[Hz]**	**f_{ND}[rad]**	**a_{max} [m]**	**a_{max}/L []**
10.85	2.68	22.9	0.0042	0.0097
11.32	2.72	23.2	0.0062	0.0143
11.56	2.75	23.5	0.0100	0.0230

Table 2. Vibration characteristics.

plane oscillation but towards the end of the simulation a desynchronization starts developing, leading to a more rotational motion. Figure 9 displays the trajectory of the point throughout the simulation. De Ridder et al. (2015) also observed a tendency towards rotation for the flutter instability.

The average displacement of the cylinder for the last $1/4^{th}$ of the simulation shows deviations from the 0-position in the order of E-04, with flutter displacements in the order of E-02. Therefore, the cylinder can be considered to flutter about its zero-position rather than about the buckled position. This agrees with the simulated results from De Ridder et al. (2015) and the experimental results from Modarres-Sadeghi et al. (2008). Lastly, the (dimensionless) flutter frequency and maximal amplitude for several cases are listed in Table 2.

$$f_{ND}[rad] = 2\pi f \cdot L^2 \sqrt{\frac{m+\rho A}{EI}} \qquad (2)$$

The simulated flutter frequency of approximately 2.7 Hz deviates somewhat more from the experimental value (1.8 Hz) than the frequency obtained by De Ridder et al. (2015) [2.4 Hz] but does agree better with the theoretical value predicted by Modarres-Sadeghi et al. (2008) [3 Hz]. Contrary to the results from De Ridder et al. (2015) the flutter frequency appears to increase slightly with increasing flow velocity. The amplitude of the oscillation increases steadily with flow velocity as expected.

4. CONCLUSION

In this research a Chimera technique was used to simulate the fluid-elastic instabilities of a flexible cylinder clamped at both ends in light of validating the methodology for future simulations involving larger deformations for which the Chimera technique will be an interesting option.

The simulation results were compared to experimental and simulation data from literature. The simulated critical velocities for buckling and flutter were in good agreement with the experiment and previous simulations. The current simulations also predicted a re-stabilization, which was observed in previous simulations but is less apparent in experiments. A slight discrepancy in flutter frequency was observed, but overall the agreement with the experiments is good and of the same quality as for simulations using a single grid.

5. ACKNOWLEDGMENTS

The computational resources (Stevin Supercomputer Infrastructure) and services used in this work were provided by the VSC (Flemish Supercomputer Center), funded by Ghent University, Belgium, FWO and the Flemish Government — department EWI, Belgium.

6. REFERENCES

Benek, J.A. et al., 1986. Chimera: A Grid-Embedding Technique. *Project report: Arnold Engineering Development Center (AEDC-TR-85-64)*: 1-129.

Degroote, J. et al., 2009. Performance of a new partioned procedure versus a monolithic procedure in fluid-structure interaction. *Computers & Structures,* **87**: 793-801.

De Langre, E. et al., 2007, Flutter of long flexible cylinders in axial flow. *Journal of Fluid Mechanics* **571**: 371-389.

De Ridder, J. et al., 2013, Modal characteristics of a flexible cylinder in turbulent axial flow from numerical simulations. *Journal of Fluids and Structures* **43**: 110-123.

De Ridder, J. et al., 2015, Simulating the fluid forces and fluid-elastic instabilities of a clamped-clamped cylinder in turbulent axial flow. *Journal of Fluids and Structures* **55**: 139-154.

Lighthill, M.J., 1960, Note on the swimming of slender fish. *Journal of Fluid Mechanics* **9**: 305-317.

Liu, Z.G. et al., 2012, Numerical simulation of the fluid–structure interaction for an elastic cylinder subjected to tubular fluid flow. *Computers & Fluids* **68**: 192-202.

Modarres-Sadeghi, Y. et al., 2007, The nonlinear behaviour of a slender flexible cylinder pinned or clamped at both ends and subjected to axial flow. *Computers & Structures* **85**: 1121-1133.

Modarres-Sadeghi, Y. et al., 2008, Experiments on vertical slender flexible cylinders clamped at both ends and subjected to axial flow. *Philosophical Transactions of the Royal Society A* **366**: 1275-1296.

Osman, A. et al., 2018, Simulation of air flow-yarn interaction inside the main nozzle of an air jet loom. *Textile Research Journal* **8**: 1173-1183.

Osman, A. et al., 2019, Toward three-dimensional modeling of the interaction between the air flow and a clamped-free yarn inside the main nozzle of an air jet loom. *Textile Research Journal* **89**: 914-925.

Paidoussis, M.P., 1966a, Dynamics of flexible slender cylinders in axial flow Part 1. Theory. *Journal of Fluid Mechanics* **26**: 717-736.

Paidoussis, M.P., 1966b, Dynamics of flexible slender cylinders in axial flow Part 2. Experiments. *Journal of Fluid Mechanics* **26**: 737-751.

Paidoussis, M.P., 1983, A review of flow-induced vibrations in reactors and reactor components. *Nuclear Engineering and Design* **74**: 31-60.

Paidoussis, M.P., 2016, *Fluid-structure interactions: slender structures and axial flow, Volume 2*, Academic press.

Rinaldi, S. and Paidoussis M.P., 2012, Theory and experiments on the dynamics of a free-clamped cylinder in confined axial air-flow. *Journal of Fluids and Structures* **28**: 167-179.

Singh, K. et al., 2012, Energy harvesting from axial fluid-elastic instabilities of a cylinder. *Journal of Fluids and Structures* **30**: 159-172.

ter Hofstede, E. et al., 2017, Numerical prediction of flow induced vibrations in nuclear reactor applications. *Nuclear Engineering and Design* **319**: 81-90.

MODELLING VORTEX INDUCED VIBRATIONS IN A MODEL OF THE NORTHERN SPIRE BRIDGE

Marko DURANOVIC
Trinity College Dublin, Roughan & O'Donovan Consulting Engineers, Dublin, Ireland
Tony DEMPSEY
Roughan & O'Donovan Consulting Engineers, Dublin, Ireland
Craig MESKELL
Trinity College Dublin, Ireland

ABSTRACT

This paper presents a Fluid-Structure Interaction model used to capture lock-in of vortex shedding phenomenon on a realistic bridge deck model. The results are compared to the wind tunnel results obtained on a 1:50 model of The Northern Spire Bridge in the UK. A set of 2D CFD models was executed in Ansys Fluent allowing free vibration of the rigid bridge deck in the heave direction. Two different turbulence models were used and compared (SST and Transition SST). The computational effort required to execute the CFD models was kept to a level such that the process could realistically be adopted in the bridge design industry. As expected, a clear shift in vortex shedding frequency is exhibited at the lock-in onset confirming the phenomenon. The predicted velocity range of lock-in and velocity for peak response were in a good agreement with the experimental results, although the models significantly overestimate the peak response amplitudes. The paper shows that Transition SST turbulence model provides better quality results when compared to the SST model. Some limited evidence of the effect of Reynolds number on VIV at this scale was obtained, but it is not conclusive. It is concluded that even a relatively simple CFD model can yield useful information at an early design stage.

1. INTRODUCTION

1.1. Background

Wind tunnel tests have been part of the design process for the most medium span bridges and every long-span bridge in the modern bridge engineering.

Vortex induced vibration (VIV) occurs when the vortex shedding frequency, which depends on the flow velocity, approaches the natural frequency of the structure. The potentially large displacements caused by VIV can lead to fatigue and serviceability issues, and in some cases even catastrophic failures. Structures that are susceptible to VIV are typically long, light, and flexible (e.g., bridges, wind turbines, ocean riser pipes, tall chimneys). VIV in geometrically simple shapes has been widely studied - see, for example (Païdoussis et al., 2010). VIV in bridges emerged as an issue as designs became longer and lighter. Some of the notable historic events that illustrate VIV in bridge engineering are mentioned here. Almost every discussion on bridge aerodynamics references the famous Tacoma Narrows bridge collapse that occurred at a relatively low wind speed of 19 m/s. Many research papers covered this unfortunate engineering incident and majority of them conclude that it started as bending dominant and then turned into torsion dominant coupled flutter (that caused the collapse) but with vortex-shedding playing a role at lower velocities, see for example (Miyata, 2003) or (Larsen, 2000). This collapse prompted authorities in Maine, USA to examine Deer Isle Bridge which had geometry similar to that of Tacoma Narrows. It was found that wind velocities as low as 9.1 m/s can cause vortex induced vibrations. (Kumarasena et al., 1991) later showed through wind tunnel experiments that turbulence in the upwind flow has a substantial effect on VIV by altering the way vortices are formed. In 2010 a bridge over river Volga, Russia experienced high amplitude vertical vibrations (approx. ±400 mm) which forced authorities to close the bridge. To supress future vibrations, Tunned Mass Dampers were designed and installed (Benicke & Butz, 2015). In 1980, Rio-Niterói bridge in Brazil experienced VIV in vertical motion. The bridge had to be closed until it was determined that it has problems with VIV for wind velocities of approx. 14 m/s. It was decided that the bridge would be fitted with passive and active dynamic control devices (Battista & Pfeil, 2000).

While CFD is appearing in everyday engineering, the uncertainties and computational requirements that come with it still put it out of reach for many non-research endeavours. However, many have tried using it in replicating some of the results obtained in the wind tunnel tests of bridges. (Goering & Ramponi, 2019) used Ansys CFX to identify flutter derivatives for torsional galloping for The Bay Bridge, USA and Stonecutter Bridge, UK and made quite

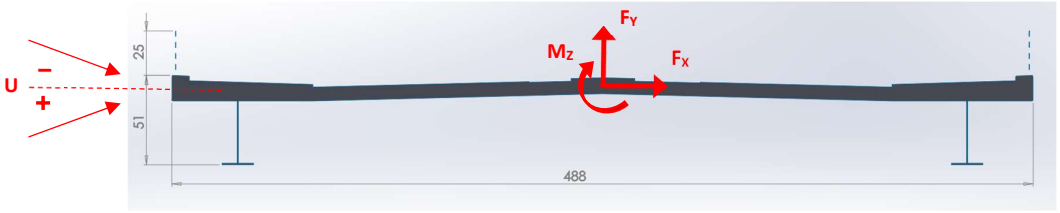

Figure 1. Deck section dimensions [mm] at model scale and sign convection adopted

successful predictions when compared to the experimental data. Similar analysis was done for Nanpu Bridge, China, and Höga Kusten Bridge, Sweden and reported in (Ge & Xiang, 2008). (Zhang et al., 2021) compared results from wind tunnel tests conducted on Rose Fitzgerald Kennedy Bridge, Ireland using OpenFOAM. They built 3D models and utilised High-Performance Computing (HPC) facility for dealing with these simulations. (Szabó et al., 2020) went even further and employed Fluid-Structure interaction modelling to replicate some of the Tacoma Narrows behaviour in torsional mode of oscillation. They employed hybrid scaling of the physical fields – CFD properties were scaled-down, to relax the requirements for low timestep and high grid density, while structural properties were kept at the original scale. CFD was executed in Ansys Fluent while the FEM model was coded within User Defined Functions (UDFs) available in Fluent. (Nieto et al., 2009) used CFD as an input in the design process exploring several deck shape options and provided results for static aerodynamic coefficients. As seen, quite a few attempts have been made to utilise CFD in bridge industry for post facto studies. However, there are does not appear to be common use of CFD at the design stage to assess vortex induced vibration.

1.2. Description of the study

Wind tunnel tests done on a model of the Northern Spire Bridge in the UK were used to compare results from the CFD simulations. The simulations described here have the same geometric and velocity scaling as the wind tunnel tests to allow direct comparison. The simulations employed two different turbulence models, SST and Transitional SST (TSST). An additional, third simulation used SST but at higher Reynolds number which was achieved by controlling the fluid viscosity while keeping geometric and velocity scale constant. The development of the computational grid is briefly explained in section 2.2. The free response of the rigid bridge deck on a linear single degree of freedom flexible support is simulated for a range of velocities centred around the lock-in. The resulting time records are analysed in MATLAB. To assess the quality of the results produced by the simulations, the data are compared to the results from the wind tunnel testing campaign conducted on the model of the Northern Spire Bridge which is sited in the UK.

The objective is to demonstrate not only that useful results for VIV can be obtained, but also that this can be achieved with modest computational resources, so that it will be applicable to industrial design. The simulations presented here were initially executed on a desktop workstation with 192 GB of RAM memory (although only a small portion of it was utilised for these simulations), and Intel® Xeon® Gold 6242R CPU. On average, wall-time required to obtain a steady oscillatory state for a single reduced velocity was approximately 3 days (~1300 CPU hours). Some points required less time to reach the steady state (points at lower velocity) while some required more time (points after at the lock-out). For convenience, a High Performing Computational facility was used to obtain results simultaneously.

2. METHODOLOGY

2.1. Experimental set-up

Experimental results from the wind tunnel testing done by CSTB, France are used to evaluate CFD results. The testing was done at the bridge's design stage (during 2018) without the intention of results being utilised for research purposes. Due to this, the output of the tests is limited to what is required by the design code – values of static coefficients at a range of angles of attack and deck oscillations at a range of wind velocities. Information on the flow behaviour in the wake is not available.

The model was built at 1:50 scale with velocity scale of 4.35 defined as multiple of geometric scale and frequency scale. The Reynolds number for these tests was of the order of $2x10^4$. Deck shape, dimensions at model scale and sign convention are shown in Figure 1. Damping ratio of 0.45% used in the CFD simulations equals that measured in the experiment. The spanwise length of the model was 1.935 m.

The tests were conducted in two stages.: tests of the rigid model to obtain aerodynamic force coefficients; and the "free vibration" tests with the model supported by springs (Figure 2). For this paper, the results of the latter are used. Dynamic properties of the deck model are reported in Table 1.

Mesh refinement level	Number of cells		Drag coefficient		Lift coefficient		Moment coefficient	
	#	Ratio	Value	% Δ	Value	% Δ	Value	% Δ
Coarse	1,119,278	-	0.175	-	-0.202	-	0.044	-
Medium	1,653,362	1.48	0.175	0.1%	-0.200	2.0%	0.045	1.2%
Fine	2,324,116	1.41	0.175	0.1%	-0.198	1.0%	0.045	0.2%

Table 2. Grid sensitivity analysis

Property	Value	Unit
Stiffness	19880	N/m
Mass	22.7	kg
Frequency	4.71	Hz
Damping ratio	0.45	%

Table 1. Model dynamic properties (first heaving mode)

The model in the experiment had two degrees of freedom, heaving (bending) and rocking (torsion). This paper neglects the latter one as the heaving mode dominants VIV of this structure.

Figure 2. Dynamic model assembly and the deck section model in the background

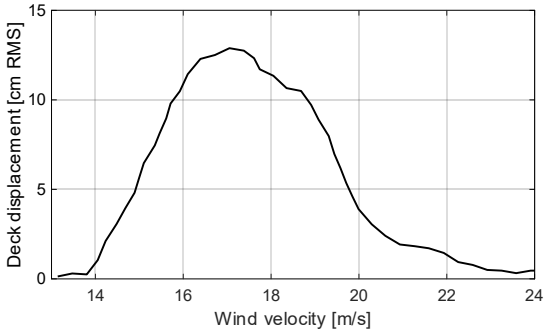

Figure 3. Experimental results - response amplitude at full scale

The level of turbulence intensity measured in the wind tunnel during this test was reported at 4%. The RMS of the amplitude response obtained from the experiment is shown in Figure 3. It should be noted that the values reported here are converted to the full scale. The maximum displacement occurs at approximately 17 m/s, implying a Strouhal number of 0.09. The lock-in range is between 14 m/s and approx. 20 m/s.

2.2. Rigid CFD model

All CFD models in this paper were developed in Ansys Fluent software. Initially, a rigid model was developed and used to establish mesh independency. A summary results of the mesh dependency study are reported in Table 2. The rigid model was used to obtain a flow field, used to initialize the dynamic simulation.

2.3. Dynamic CFD model

In order to model the dynamic behaviour of the system, dynamic mesh utility within Fluent was used alongside basic programming of UDFs (User Defined Function). Three different UDFs were utilised: to load initial values (in case the analysis is resumed); to find the lift force, then solve equation of motion (1) using Runge-Kutta 4th Order Method and find the vertical velocity of the deck at the end of each time-step; and the final UDF applies the calculated velocity to the deck section motion. The lift force was obtained by integrating the pressure over the surfaces of the deck and two barriers.

$$m \cdot \ddot{y} + c \cdot \dot{y} + k \cdot y = F(t) \qquad (1)$$

As the built in 6 degree of freedom free body motion option does not allow damping to be directly controlled, the motion was accounted for as described. The UDFs were developed in such a way to support parallel multi-core simulations.

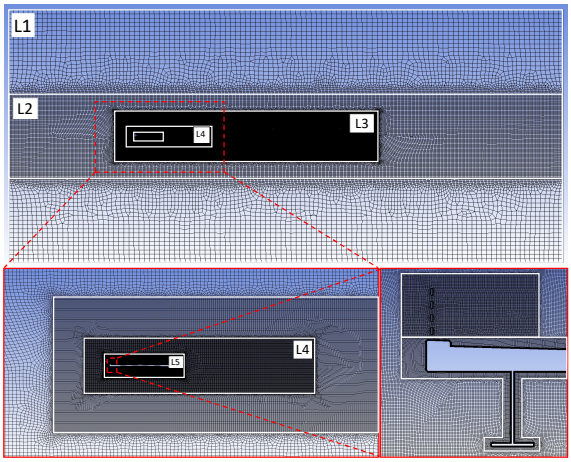

Figure 4. Calculation domain

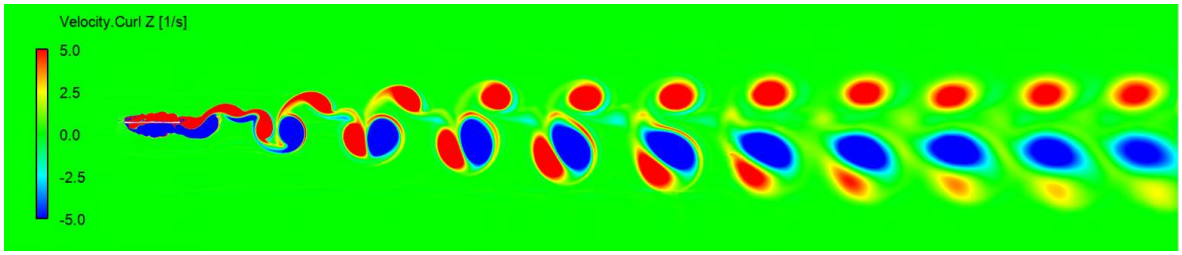

Figure 5. Vorticity magnitude in the lock-in region (reduced velocity of 12.1)

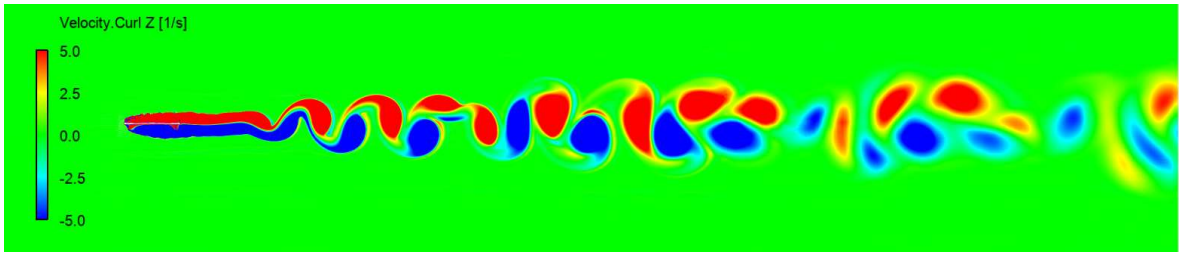

Figure 6. Vorticity magnitude at the lock-out (reduced velocity of 14.3)

The domain division is shown in Figure 4. Different sub-grid levels are marked from L1 through L5. Dynamic meshing was enabled in the level L3 while the rest of the domain was kept rigid.

The motion calculated in the UDF was applied on the deck, the barriers and L5 and L4 levels. In this way only sub-grid L3 experienced re-meshing during the motion of the system.

All dynamic properties reported in Table 1 were transformed to "per meter" of the deck length and as such defined within the UDFs.

3. RESULTS AND DISCUSSION

The deck depth D (including the barrier) and system's natural frequency f_n were used for reduction of all variables within this section. Reynolds number was calculated with respect to the deck depth. Reduced variables are defined in equations (2), where Y, U_r and t_r are reduced deck displacement, reduced flow velocity and reduced time, respectively.

$$Y = \frac{y}{D} \; ; \; U_r = \frac{U}{f_n \cdot D} \; ; \; t_r = t \cdot f_n \qquad (2)$$

Figure 5 and Figure 6 show the vorticity in the flow field at lock-in (reduced velocity of 12.1) and at lock-out (reduced velocity of 14.3), respectively. In both cases vortex shedding in the wake is evident, but in the lock-in case shows spatial periodicity as would be expected. When the flow is in the locked in regime (Figure 5) large alternating vortices form in the near deck wake, within a deck width. The vortex street, while very ordered, exhibits what looks like a 2Pmode on the lower side, but a 2S mode on the upper vortices. In case of locked-out flow (Figure 6), the vortices are formed much later downstream and the structures never form a clear vortex street as the two frequencies (vortex shedding and structural natural frequency) are distinct and incommensurate.

In the SST model we see a good agreement in the slope of the lock-in region (Figure 7). A good estimate is obtained for the velocity at which peak oscillation velocity is experienced. However, the simulation overestimates the oscillation magnitude and underestimates the lock-in velocity.

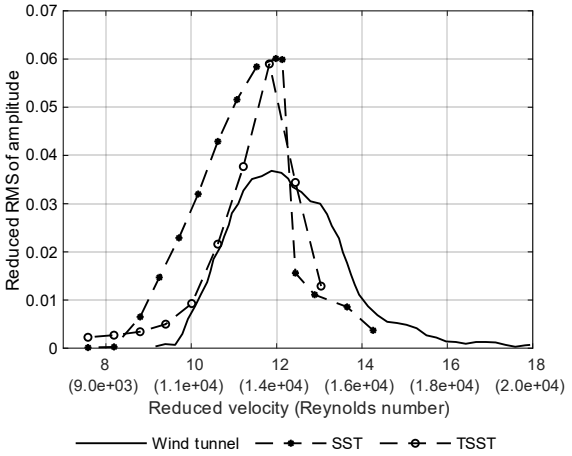

Figure 7. Deck response

Figure 7 shows that the Transition SST model performs considerably better than SST in determining the lock-in region. It estimated the lock-in at reduced velocity of approx. 10 which is in a good agreement with what is reported in the wind tunnel test data. However, with increased speed and for value of Reynold's number approximately 1.3×10^4, the oscil-

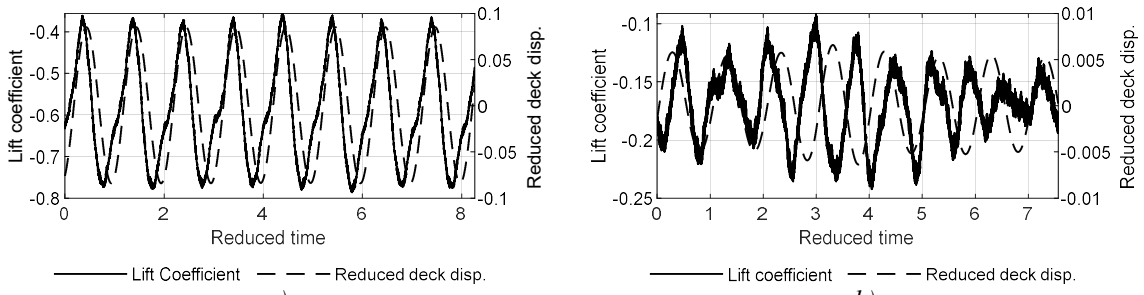

Figure 9. Time record of the lift coefficient and the deck displacement for reduced velocities of a) 12.1 and b) 14.3

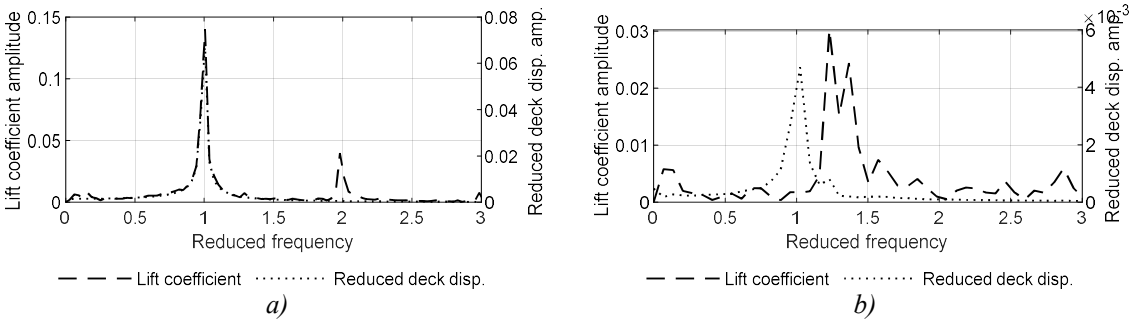

Figure 10. Frequency domain of the lift coefficient and the deck displacement for reduced velocities of a) 12.1 and b) 14.3

lation amplitude starts to diverge from the experimental values. Clearly, at these large amplitudes, the simulation is either overestimating the excitation or underestimating the dissipation in the flow. This may be due to the 2-dimensional assumption compounded by the simple isotropic turbulence model, as at large amplitudes the spanwise correlation will become more important.

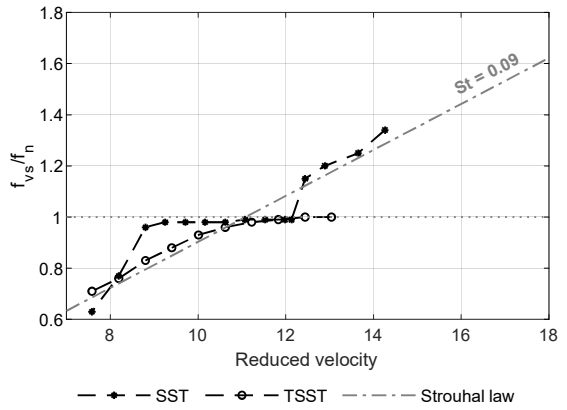

Figure 8. Reduced shedding frequency for SST and TSST models

Lock-in region for SST and TSST models is further examined in Figure 8. It shows reduced shedding frequency and Strouhal law curve for this section (based on Strouhal number of 0.09). A noticeable difference is observed between the two models. SST model predicts that the shedding frequency locks to system's natural frequency before the coincidence, while TSST shows behaviour more similar to what is observed in the wind tunnel. Figure 11 shows spectrogram of the deck displacement obtained in the wind tunnel experiment. For consistency, all the values are reduced as previously described and the spectrogram in Figure 11 is shown for the full range of velocities tested in the experiment. It can be seen that the lock-in occurs at the reduced velocity of approximately 9.6 which is more or less the coincidence between the Strouhal frequency and the natural frequency. The lock-in range as indicated by the suppression of the Strouhal frequency, extends to approximately 15. Note that immediately before coincidence, the vortex shedding frequency is distinct from the natural frequency. The data from the Transition SST in Figure 8 shows similar behaviour. The SST data shows strong pre-coincidence lock-in which is not supported by the experimental data.

In Figure 11, at a reduced velocity of 5, there appears to be another small lock-in zone. As the Strouhal frequency at this velocity is exactly half the natural frequency, it is suspected that this is due to the fluctuating drag which will be at twice the shedding frequency, and hence will coincide with the natural frequency.

The difference in behaviour for two flow regimes is also illustrated in Figure 9, depicting time record of the lift coefficient and the reduced deck displacement, and Figure 10, showing frequency domains for these two signals. Figure 9a shows a much cleaner response with two signals synchronized. This is confirmed in the frequency domain analysis shown in Figure 10a.

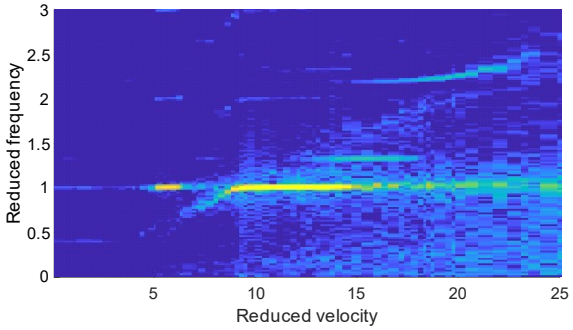

Figure 11. Spectrogram of deck displacement obtained in the wind tunnel

A third series of simulations was done on a model with SST turbulence model but with increased Reynolds number. The objective was to investigate the influence of Reynolds number on the results obtained by the SST model. In order to maintain as much similitude to the previous simulation as possible, the increase in Reynolds number is achieved by decreasing the dynamic viscosity of the air by a factor of 10 and thus creating a theoretical fluid suitable for this purpose. Geometric and velocity scales were kept the same. Figure 12 shows these results and a slight improvement with both lock-in velocity and magnitude of oscillations is seen. This brings a question whether SST is an appropriate turbulence model to be used in this simulation but also whether Reynolds number has an effect on the wind tunnel tests as well.

4. CONCLUSIONS

This paper describes results of vortex induced vibrations obtained from an FSI model developed in Fluent CFD software. The results were compared to the wind tunnel tests done on a 1:50 scale model.

Three different simulations were performed employing: SST turbulence model; Transient SST model and SST model at higher Reynolds number.

The results showed that although simulations were 2D which implies fully spanwise correlated vortex shedding and the turbulence was modelled as isotropic, the models were able to capture lock-in phenomenon and provide a reasonably good estimate of the lock-in velocity. The maximum amplitude of the deck oscillations was overestimated for all models by about 80%. There is some evidence that Reynolds number may have an effect on the response. While these achievements may seem modest, the fact that these simulations were done on a desktop workstation demonstrates that CFD may be used as part of the design process for bridges or at least to help refine the wind test campaign before testing begins.

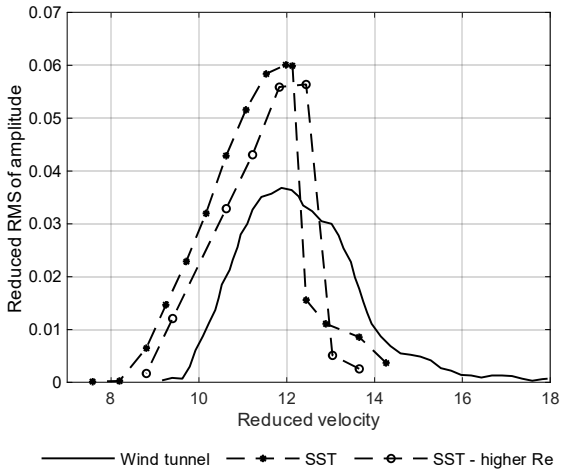

Figure 12. Deck response at higher Reynolds number

5. ACKNOWLEDGMENTS

The authors would like to thank Olivier Flamand of Centre Scientifique et Technique du Bâtiment for sharing the data from the wind tunnel analyses conducted on the Northern Spire Bridge model and promptly answering questions related to the wind testing itself.

The research conducted in this publication was funded by the Irish Research Council under grant number EBPPG/2020/96 and Roughan & O'Donovan Consulting Engineers.

The authors would like to acknowledge the Irish Centre for High-End Computing (ICHEC) for provision of computational facilities and support.

The authors would like to acknowledge Sunderland City Council and Farrans Victor Buyck CJV for their contribution to the paper.

6. REFERENCES

Battista, R. C., & Pfeil, M. S. (2000). Reduction of vortex-induced oscillations of Rio-Niteroi bridge by dynamic control devices. *Journal of Wind Engineering and Industrial Aerodynamics*, *84*(3), 273–288. https://doi.org/10.1016/S0167-6105(99)00108-7

Benicke, O., & Butz, C. (2015). Volgograd-bridge: Efficiency of passive and adaptive tuned mass dampers. *IABSE Conference, Geneva 2015: Structural Engineering: Providing Solutions to Global Challenges - Report*, 1428–1435. https://doi.org/10.2749/222137815818358826

Ge, Y. J., & Xiang, H. F. (2008). Computational models and methods for aerodynamic flutter of long-span bridges. *Journal of Wind Engineering and Industrial Aerodynamics*, *96*(10–11), 1912–1924. https://doi.org/10.1016/j.jweia.2008.02.017

Goering, A., & Ramponi, R. (2019). Wind Analysis of Long-Span Bridges Using Computational Fluid Dynamics. *Structures Congress 2019: Bridges, Nonbuilding and Special Structures, and Nonstructural Components - Selected Papers from the Structures Congress 2019*, 210–220. https://doi.org/10.1061/9780784482230.021

Kumarasena, T., Scanlan, R. H., & Ehsan, F. (1991). Wind-Induced Motions of Deer Isle Bridge. *Journal of Structural Engineering*, *117*(11), 3356–3374. https://doi.org/10.1061/(ASCE)0733-9445(1991)117:11(3356)

Larsen, A. (2000). Aerodynamics of the Tacoma Narrows Bridge -60 years later. *Structural Engineering International: Journal of the International Association for Bridge and Structural Engineering (IABSE)*, *10*(4), 243–248. https://doi.org/10.2749/101686600780481356

Miyata, T. (2003). Historical view of long-span bridge aerodynamics. *Journal of Wind Engineering and Industrial Aerodynamics*, *91*(12–15), 1393–1410. https://doi.org/10.1016/j.jweia.2003.09.033

Nieto, F., Hernández, S., & Jurado, J. Á. (2009). Aerodynamic study of the preliminary design of a 425 m cable-stayed bridge deck using CFD. *5th European and African Conference on Wind Engineering, EACWE 5, Proceedings*, *January 2015*.

Païdoussis, M. P., Price, S. J., & de Langre, E. (2010). Fluid-structure interactions: Cross-flow-induced instabilities. In *Fluid-Structure Interactions: Cross-Flow-Induced Instabilities* (Vol. 9780521119). Cambridge University Press. https://doi.org/10.1017/CBO9780511760792

Szabó, G., Györgyi, J., & Kristóf, G. (2020). Three-dimensional fsi simulation by using a novel hybrid scaling – application to the tacoma narrows bridge. *Periodica Polytechnica Civil Engineering*, *64*(4), 975–988. https://doi.org/10.3311/PPci.15586

Zhang, Y., Cardiff, P., Cahill, F., & Keenahan, J. (2021). *Assessing the Capability of Computational Fluid Dynamics Models in Replicating Wind Tunnel Test Results for the Rose Fitzgerald Kennedy Bridge*. 1065–1090.

MULTI-SCALE METHODOLOGY FOR THE LARGE EDDY SIMULATION OF STEAM CONTROL VALVES

Jérémy Galpin
Framatome, Lyon, France

Nicolas Goreaud
Framatome, Lyon, France

Basile Amice
Framatome, Lyon, France

Guillaume Leconte
EDF DIPNN/CNEPE, Tours, France

Aurélien Joly
EDF R&D, Paris-Saclay, France

Pierre Moussou
EDF R&D, Paris-Saclay, France

Asher Glaun
Baker Hughes Valves, Avon, MA, USA

ABSTRACT

Steam control valves play a major role in nuclear power plants, but their internal flows featured by large velocities might lead to the occurrence of noise and vibration. The focus is here on the assessment of the steam flow excitation by using Large Eddy Simulation with STAR-CCM+ CFD code. The simulation of the flow inside the control valve faces the challenge of dealing with a large range of geometrical scales from the scale of a hole in the order of magnitude of 1 mm up to the size of the valve body in the order of magnitude of 1 m. This difficulty is tackled by modelling the drilled part with thousands of small holes by using a porous-like approach. On the one hand, the proposed porous model allows to reproduce the flow nozzling occurring at the hole entrances as well as its interaction with the upstream acoustics. On the other hand, large turbulence produced downstream the holes is also using a body-force synthetic turbulence method.

The developed porous-like model has been deployed for performing a Large Eddy Simulation of half an industrial valve. The feasibility of addressing such kind of flow in such complex geometries is thus demonstrated and the associated computational resources and runback time remain compatible with industrial constraints. LES results show that large flow instabilities develop in the examined valve geometry, and the mechanisms leading to flow fluctuations have been identified. Such findings are valuable for mitigating the steam flow excitation by defining more virtuous designs. CFD methods like the ones described in this paper could be implemented on a systematic basis to orient design decisions in the development phase of large steam control valves prior to test rig experiments.

1. INTRODUCTION

Control valves are common devices encountered in steam lines of nuclear power plants. They play a major role for regulating the mass flowrate by controlling the obstruction of the free-flow section. Compressible flow featured by large velocities develop inside control valves and the latter might thus be submitted to noise and vibration.

In order to prevent or to mitigate vibration issues in steam control valve, the experimental approach is generally a costly option, mainly because of the requested specific experimental facility able to produce steam pressure and steam flowrate encountered in nuclear plant. Moreover, measurement devices, generally made of accelerometers and pressure probes, are intrusive and offer a limited number of measurement locations. The root cause analysis from the test results is also generally an arduous task since effects of the fluid excitation and of the structure response are intermixed. An alternative is the numerical approach, and in this purpose, the knowledge of the flow excitation is a prior input data requested for any Finite Element Modelling analysis. Steam flow excitation is related to both wide-range turbulent fluctuations and acoustic excitation occurring for

discrete modes. Both effects can be addressed by Computational Fluid Dynamics (CFD).

In the nuclear industry, CFD has been extensively deployed since the nineties with most applications using the Reynolds Averaged Navier Stokes (RANS) approach (Martinez & Galpin, 2004). The RANS approach allows to assess only the mean flow and is unsuitable for examining the fluctuations of the hydraulic loading. An explicit resolution of the turbulence is thus required, and one preferentially relies on Large Eddy Simulation (LES) consisting in solving explicitly the largest turbulent scales while modelling the smallest. Approaches allowing an explicit resolution of the turbulence are less widespread than RANS but their use are raising due to the increase of available computational resources and also to the development of hybrid RANS/LES methods making the cost of explicit resolution of turbulence more affordable. Successful applications of LES in the frame of the nuclear industry are found in the literature, such as for the thermal stripping (Simoneau *et al.*, 2010; Galpin & Simoneau, 2011) and for flow-induced vibration (FIV) issues. Most FIV studies are focused on the Reactor Coolant System where immerged structures may vibrate under the excitation of liquid water flows (Benhamadouche *et al.*, 2009; Farges *et al.*, 2021; Moussou *et al.*, 2011). Some applications to compressible flow related to steam generator concerns are also mentioned in the literature (Nilsson *et al.*, 2012; Yuan *et al.*, 2017) but few studies dedicated to steam control valves are reported and one mainly relies on theoretical model for the prediction of noise in control valve such as IEC 60534-8-3:2011 method.

Modelling the internal flow of a control valve involves specific challenges due to the compressibility of the flow on the one hand and to the large variation of geometrical scales on the other hand. Indeed, a common technology of control valve employed for steam valves rely on a cylindrical part, the so-called cage, which is drilled by thousands of holes, and on a piston (the plug) whose axial translation controls the amount of cage holes that are masked. The major difficulty relies on the large range of encountered geometrical scales, from the scale of a hole in the order of magnitude of *1 mm* up to the size of the valve body in the order of magnitude of *1 m*. A gross approach, consisting in discretizing all the cage holes up to the valve scale, is unfeasible within today's computational resources. In order to overcome these difficulties, a multi-scale approach is proposed. It is based on local simulations at the scale of few holes aiming at calibrating a porous-like model, which is eventually embedded in a simulation at the scale of the valve. The goal of the porous media is to save cells up to a factor fifty in practical. Moreover, the operating points of interest are related to conditions for which the critical flowrate is reached. The vena-contracta occurs in the cage holes entrances where the effective free-flow section is the smallest and the flow separates at the leading edge, and shocks develop downstream the holes once the flow accelerates. Therefore, a specific compressible model is employed for the porous modelling, and the latter allows to take into account the acoustic phenomena and their interactions with the main flow. This paper aims at presenting the CFD methodology developed for dealing with these difficulties. The multi-scale approach is then detailed, and the porous modelling is described. The last section is dedicated to an illustration of the proposed methodology by an application to an industrial control valve.

2. MODELLING STRATEGY

2.1. Multi-scale approach

The principle of the multi-scale approach is based on a porous-like modelling of the cage as illustrated in Figure 1. This modelling includes two areas, the first one, so-called momentum sink, aims at mimicking the nozzling occurring at the holes entrance as well as its interaction with the upstream pressure. The area length is the same as the actual cage thickness and this area is free from any obstacle. The free flow-section is thus the same as the upstream one. The flow undergoes no more acceleration than in the actual geometry, and it remains subsonic when crossing the area. This aspect simplifies the numerical treatment since no shock develops in the computational domain.

The second area, so-called synthetic turbulence source in Figure 1, aims at representing the large turbulence induced by the sudden expansion occurring at the cage outlet and by the destabilization of supersonic jets developing downstream the cage.

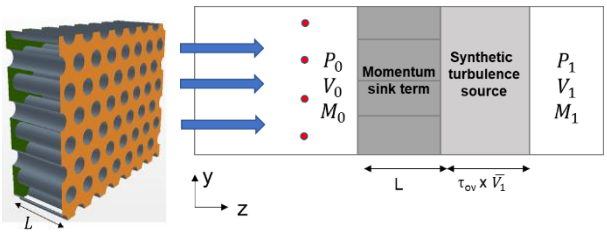

(a) *(b)*

Figure 1. Original cage geometry (a) and its porous modelling (b).

The modelling of the above-mentioned phenomena requires calibrations which are achieved on the bases of simulations at the scale of a few holes with a fine representation of the actual hole geometry. RANS and LES simulations are performed for this

purpose, the numerical aspects related to these simulations are detailed hereafter.

2.2. Numerical aspects

Simulations are conducted with the CFD code STAR-CCM+. The code employs the finite-volume method and is cell centered with fluxes computed from the cells faces. Iterative method is implicit and related to the coupled solver for which the balance equations for continuity, momentum and energy are solved in a coupled manner, that is, they are solved simultaneously as a vector of equations. Moreover, the preconditioning proposed by Weiss *et al.* (1995) is considered in order to enhance the convergence.

Two kinds of computational domains are considered: either for the calibration of the porous-like modelling introduced hereafter, for which a pattern of 8x8 cage holes is considered, or for the simulation of the valve itself, where the valve and the upstream and downstream pipes are integrated to the computational domain.

For all simulations, total pressure and total temperature are specified at the inlet of the domain while the pressure is prescribed at the outlet of the computational domain. The interaction between the in-flow and out-flow conditions and acoustics is dealt with the application of a method called acoustic suppression zone which acts as a sponge layer and removes spurious undesired reflections on the boundary conditions, Giles (1990). All walls are considered non-slip, hydraulically smooth, adiabatic and rigid. This implies that the potential coupling between the fluid excitation and the solid response is neglected.

The fluid is steam assumed to be an ideal gas. Condensation, which might locally occur, is neglected, fluid properties being extrapolated.

Performed simulations are related to steady RANS and to LES. For both cases, Reynolds stresses are modelled according to a Boussinesq approach based on the concept of turbulent viscosity. For RANS simulation, the turbulence is closed with the two-equations Realizable k-e model (Shih *et al.*, 1994) while the subgrid scale model WALE from Nicoud and Ducros (1999) is chosen for LES. Due to the large Reynolds number encountered in industrial control valves up to $2 \cdot 10^7$, fine spatial discretization near the walls cannot be envisaged. A wall-of-the-law is thus selected as wall treatment, and the wall normalized velocity $u+$ is computed according to Reichardt (1951) model. Regarding the grid, the thickness of the cells closest to the wall is chosen in order to target a $y+$ in the range of 100.

Regarding the spatial discretization, second order upwind and second order bounded-central schemes are applied respectively for RANS and LES computations and the flux limiter minmod is employed for all the simulations. Regarding the temporal discretization, the temporal scheme is second order accurate, and the time step for the LES is chosen in such a way that the acoustic CFL number is smaller than five.

2.3. Calibration of the momentum sink term

The axial momentum source term, denoted $\frac{dP}{dz}$, is formulated in a way to enforce a targeted velocity denoted $V_{target}(\overline{P_0})$ as follows:

$$\frac{dP}{dz} = \alpha \cdot \overline{\rho_0} \cdot \frac{(V_{target}(\overline{P_0}) - \widetilde{U}_z)}{\tau}, \qquad (1)$$

where $\overline{\rho_0}$ is the upstream density, $\overline{P_0}$ is the upstream static pressure, $V_{target}(\overline{P_0})$ is the targeted velocity explained below, $\widetilde{U}_z$ is the local instantaneous velocity in the stream-wise direction (normal to the cage), $\tau = 10^{-8}\ s$ is a characteristic time and α is an arctangent function allowing a smooth transition between the borders of the area where the momentum source term is zero and the core of the porous area where Eq. (1) is applied. The arctangent function is calibrated in such a way that the transition is achieved over one fifth of the cage thickness L.

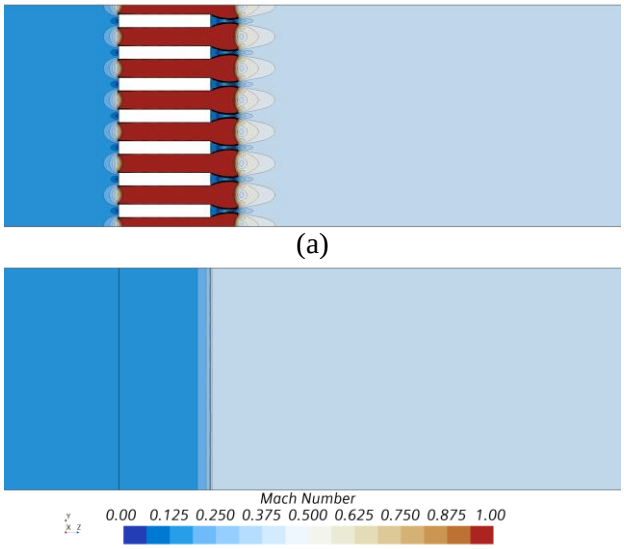

(a)

(b)

Figure 2. Slices coloured by the Mach number related to steady RANS simulations of the actual geometry (a) and to the porous-like modelling (b).

In the transverse directions y and x, the applied sink terms, written below, aim at enforcing zero transverse components of the velocity,

$$\frac{dP}{dx} = -10^3 \cdot \overline{\rho_0} \cdot U_x$$
$$\frac{dP}{dy} = -10^3 \cdot \overline{\rho_0} \cdot U_y \qquad (2)$$

The targeted flowrate $\overline{\rho_0}\ V_{target}(\overline{P_0})$ introduced in Eq. (1) is issued from several RANS steady simulations performed with an explicit representation of

the holes and for various intake pressures P_0. Note that nuzzling is reached for in the whole range of upstream pressure P_0 and the counter pressure P_1 has thus no effect on the mass flowrate. In the proposed modelling, the upstream pressure P_0 and the upstream density ρ_0 are monitored upstream of the porous area; the probes are represented by red dots in Figure 1. The probe density is such that one probe is located in front of each cage hole. The instantaneous pressure P_0 and density ρ_0 are then filtered owing to a sliding average at a frequency of $2000\ Hz$; this frequency is defined as the upper bound regarding the range of frequencies of interest from a structural point of view. The filtered data are respectively denoted $\overline{P_0}$ and $\overline{\rho_0}$. This modelling allows to consider the effect of the spatial heterogeneities of upstream pressure ahead of the cage as well as the time variation of pressure due to acoustics, as long as acoustic modes are much smaller than $2000\ Hz$. Going to higher frequencies would require advanced aerodynamic models including in particular acoustic quadrupoles (Reethof, 1978; Reethof & Ward, 1986; Masoneilan & Dresser Flow Control, 2005).

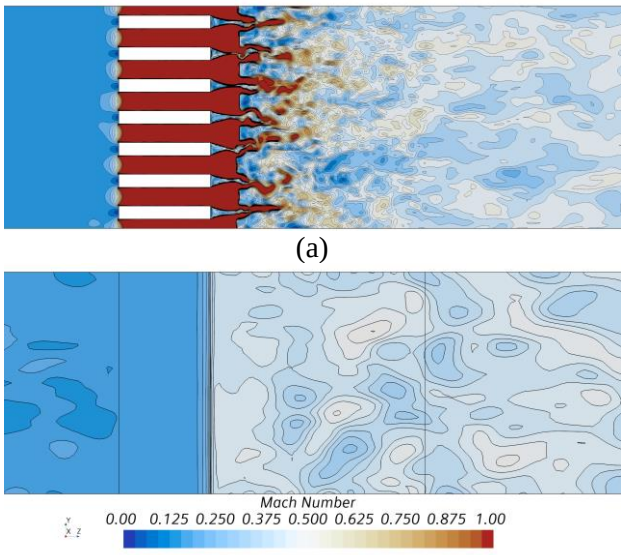

(a)

(b)

Figure 3. Slices coloured by the instantaneous Mach number related to the LES of the actual geometry (a) and to the porous-like modelling (b).

An illustration of the above-discussed modelling is available in Figure 2 comparing the Mach fields for simulations with the explicit resolution of the holes and with the porous-like modelling. Both RANS simulations are performed by prescribing the pressures P_0 and P_1 as well as the density ρ_0 at the in-flow and out-flows boundary conditions which are located far from the area of interest. From Figure 2, one points out that the proposed porous-like modelling allows to reproduce the actual values of the upstream and downstream velocities far from the cage, this also suggesting that the flowrate is the same between both simulations. In the cage itself, the complexity of the velocity fields with sonic blocking and shocks is intentionally not represented. Downstream the cage (equivalent to the momentum sink area), one notices an axial stiff variation of the velocity for the porous modelling whose gradient is tempered owing to the arctangent function α introduced above.

2.4. Calibration of the turbulence sink term

In the proposed modelling, synthetic turbulence is prescribed downstream the momentum sink area, displayed in Figure 1. Synthetic turbulence is prescribed thanks to the body-force method called Anisotropic Linear Forcing (ALF) proposed by de Laage de Meux *et al.* (2015). As a simplification hypothesis, an isotropic turbulence is assumed and parameters to be prescribed are the targeted turbulent kinetic energy, k_{target}, and a characteristic turbulent length scale, Δ_{target}. These turbulent parameters are related to values targeted at the downstream extremity of the synthetic turbulence zone.

Both turbulent parameters are postprocessed from a Large Eddy Simulation of the cage with an actual representation of the holes. Indeed, the LES allows to assess the solved turbulent kinetic energy, which is defined as:

$$k_{res} = \frac{1}{2} \cdot \left(\widetilde{u}'^2 + \widetilde{v}'^2 + \widetilde{w}'^2 \right), \qquad (3)$$

where $\widetilde{u}'^2$, $\widetilde{v}'^2$ and $\widetilde{w}'^2$ are the variance of the three components of the solved filtered velocity $\vec{\widetilde{V}} = (\widetilde{u}, \widetilde{v}, \widetilde{w})$. The subgrid-scale contribution to the turbulent kinetic energy is here neglected due to the fine grid resolution used for the large eddy simulation. The three-dimensional field of k_{res} is averaged over a series of cross sections in order to yield one-dimensional evolution versus the z-coordinate. The parameters k_{target} and Δ_{target} are extracted by applying the postprocessing of homogeneous isotropic turbulence downstream a grid, as is detailed in the book by Chassaing (2020). The assumption of energetic decay of turbulence allows to assess the turbulent dissipation rate ϵ_{target} and the turbulent length scale Δ_{target} can thus be computed. The eddy turn-over time is also deduced from ϵ_{target} and k_{target}, and the length of synthetic turbulence zone is defined by comparing the eddy turn-over time to the convection time.

The application of the above discussed model is illustrated in Figure 3, where instantaneous fields of Mach number are plotted. LES results with the actual geometry and with the porous model are compared.

Regarding the actual geometry, one points out that small turbulent structures are produced by the supersonic jets. Turbulent structures dissipate downstream and become larger which is similar with experimental findings on the turbulence decay downstream a grid. Regarding the porous modelling, turbulent structures far from the cage are qualitatively reproduced, but the procedure does not retrieve, as expected, the close field near the cage.

3. APPLICATION TO AN INDSUTRIAL VALVE

The above-introduced model is applied in the frame of a LES of an industrial control valve. The computation is dedicated to understanding the flow fluctuations developing inside the valve and to assessing the excitation of the flow on the structures in contact with steam. For this purpose, care is taken for considering all the actual geometrical details and for representing the actual in-flow and out-flow conditions of the valve.

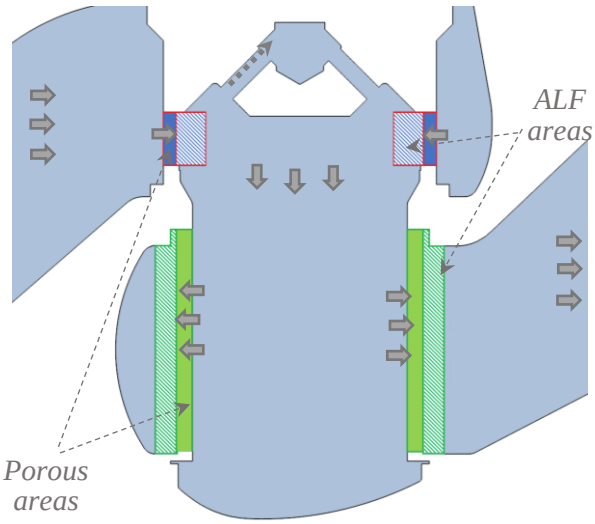

Figure 4. Overview of the computational domain.

The computational domain, displayed in Figure 4, is composed of an intake duct connected to a cylindrical plenum which feeds the cylindrically shaped cage. Due to computational constraints, only half a valve geometry is simulated, and one thus assumes that flow structures larger than a half valve scale are negligible. The cage model made of a first layer with momentum sink term and another one with synthetic turbulence is represented with red boxes in Figure 4. Downstream the cage, the steam flows axially towards the bottom and crosses the diffuser before leaving by the downstream duct, located in the bottom left. Above the cage, holes included in the plug and devoted to the pilot injection are represented, since the associated peripherical flow might interact with the main flow. The above-introduced diffusor is made of a cylindrical part drilled by thousands of holes. The actual representation of all the holes is not feasible, and the same approach as for the cage is employed. The diffusor modelling is composed of two zones represented in green in Figure 4, the one upstream for prescribing the momentum sink and the other for enabling synthetic turbulence.

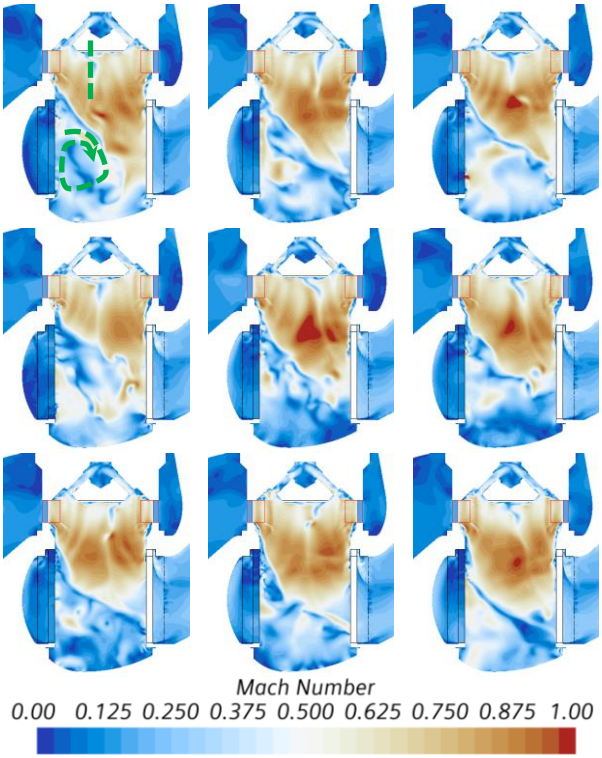

Figure 5. Slices at the center of the computational domain, coloured by the instantaneous Mach number and separated of 50 μs.

Instantaneous fields of Mach number analyzed in a slice at the center of the valve are shown in Figure 5. From a global point of view, one first points out the large level of unsteadiness occurring in the core of the valve between the cage and the diffuser. There are indeed several mechanisms leading to the development of flow instabilities. The first noticed oscillatory phenomenon occurs at the outlet of the cage: the flow emerging from the cage is mainly oriented in the radial direction and this leads to the development of a zero-velocity area where all the components of the velocity cancel themselves; this area is represented by the green dashed line in Figure 5. The green axis location significantly varies in time because of temporal and spatial heterogeneities of the pressure upstream the cage on the one hand. On the other hand, the peripherical flow developing in the plug holes leads to a mass flow rate redistribution at large scale which interacts with the main flow. Once the flow exits the cage, a direction change occurs

with a fluid acceleration leading locally and at some time steps to Mach numbers close to unity. At the vicinity of the diffuser, the fluid exits preferentially towards the outlet duct; a large recirculation zone, represented with a green dashed arrow in Figure 5, develops in the bottom left.

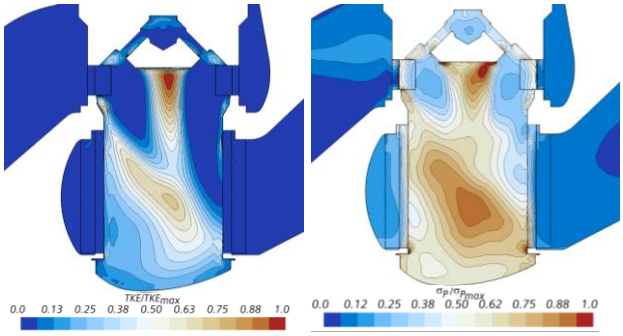

(a) (b)

Figure 6. Slices at the center of the computational domain coloured by the resolved turbulent kinetic energy (a) and by the standard deviation of pressure (b).

Resolved turbulent kinetic energy, provided by Eq. (3), is examined in Figure 6-a while the standard deviation of pressure is plotted on the same slice in Figure 6-b. The bottom of the plug as well as the bottom left side near the diffuser is submitted to large levels of turbulent kinetic energy. The mentioned locations are consistent with the previous analysis and are also consistent with the field of pressure fluctuations. Nevertheless, due to the flow compressibility, pressure fluctuations propagate into the whole valve and all the structures constituting the valve core are eventually submitted to a hydraulic loading excitation.

4. CONCLUSIONS

Steam control valves play a major role in nuclear facilities, but they can potentially be submitted to noise and vibration because of the internal flow featured by large velocities. The purpose is on the assessment of the steam flow excitation by using Large Eddy Simulation. The use of LES for control valves faces the challenge of dealing with a large range of geometrical scale from the scale of a hole in the order of magnitude of *1 mm* up to the size of the valve body in the order of magnitude of *1 m*. In order to tackle this difficulty, a porous approach is proposed and aims at reproducing the flow nozzling occurring in the cage drilled by thousands of holes as well as the large turbulence produced downstream. This model has been applied with success for performing the Large Eddy Simulation of an entire industrial scale. The feasibility of performing such kind of computation has been proven, and the requested computational resources as well as runback time plenty meet industrial constraints. LES results show the development of large flow instabilities occurring in the examined valve, and the mechanisms inducing flow fluctuations have been identified. Such numerical findings are thus valuable for mitigating the steam flow excitation and for defining a more virtuous design.

Therefore, adapted CFD techniques prove to be a useful tool in the design process of large steam control valves, especially when it comes to comparing different design solutions in terms of fluid velocities and pressure fluctuations. Once a design has been selected for industrialization, the next step is to go for experimental tests and measurements on a test rig such as the GAP facility of Framatome at Karlstein, Germany (Leyer & Wich, 2012).

5. REFERENCES

Benhamadouche, S., Moussou, P., & Le Maitre, C. (2009, January). CFD estimation of the flow-induced vibrations of a fuel rod downstream a mixing grid. In *ASME Pressure Vessels and Piping Conference* (Vol. 43673, pp. 489-497).

Chassaing, P. (2000). Turbulence en mécanique des fluides, Analyse du phénomène dans une perspective de modélisation à l'usage de l'ingénieur. *Institut National Polytechnique de Toulouse*.

Colombo, A., & Crivellini, A. (2016). Assessment of a sponge layer non-reflecting boundary treatment for high-order CAA/CFD computations. *Computers & Fluids, 140, 478-499.*

Farges, B., Gauffre, M. C., Benhamadouche, S., Badel, P., Faucher, V., & Ricciardi, G. (2021). Advanced benchmark of the flow through a mixing vane grid–Large eddy simulation validation. *Nuclear Engineering and Design*, *381*, 111335.

Galpin, J., & Simoneau, J. P. (2011). Large Eddy Simulation of a thermal mixing tee in order to assess the thermal fatigue. *International Journal of Heat and Fluid Flow*, *32*(3), 539-545.

Giles, M. B. (1990). Nonreflecting boundary conditions for Euler equation calculations. *AIAA journal*, *28*(12), 2050-2058.

de Laage de Meux, B., Audebert, B., Manceau, R., & Perrin, R. (2015). Anisotropic linear forcing for synthetic turbulence generation in large eddy simulation and hybrid RANS/LES modeling. *Physics of Fluids*, *27*(3), 035115.

Leyer, S. & Wich, M. (2012). The Integral Test Facility Karlstein. *Science and Technology of Nuclear Installations*, vol. 2012, article ID 439374.

Martinez, P., & Galpin, J. (2014). CFD modeling of the EPR primary circuit. *Nuclear Engineering and Design*, *278*, 529-541.

Masoneilan & Dresser Flow Control (2005). Noise Control Manual.

Moussou, P., Benhamadouche, S., & Bodel, C. (2011, January). CFD estimation of the unsteady fluid force along a fuel rod downstream a mixing grid. In *Pressure Vessels and Piping Conference* (Vol. 44540, pp. 251-259).

Nicoud, F., & Ducros, F. (1999). Subgrid-scale stress modelling based on the square of the velocity gradient tensor. *Flow, turbulence and Combustion*, *62*(3), 183-200.

Nilsson, P., Lillberg, E., & Wikström, N. (2012). LES with acoustics and FSI for deforming plates in gas flow. *Nuclear engineering and design*, *253*, 387-395.

Reethof, G. (1978). Turbulence-generated noise in pipe flow. *Ann. Rev. Fluid Mech*, *10*, 333-367.

Reethof, G. & Ward, W. C. (1986). A Theoretically Based Valve Noise Prediction Method for Compressible Fluids. *ASME Journal of Vibration, Acoustics, Stress, and Reliability in Design*, *108*, 329-338

Reichardt, H. (1951). Vollständige Darstellung der turbulenten Geschwindigkeitsverteilung in glatten Leitungen. *ZAMM-Journal of Applied Mathematics and Mechanics/Zeitschrift für Angewandte Mathematik und Mechanik*, *31*(7), 208-219.

Shih, T. H., Liou, W. W., Shabbir, A., Yang, Z., & Zhu, J. (1995). A new k-ϵ eddy viscosity model for high reynolds number turbulent flows. *Computers & fluids*, *24*(3), 227-238.

Simoneau, J. P., Champigny, J., & Gelineau, O. (2010). Applications of large eddy simulations in nuclear field. *Nuclear Engineering and Design*, *240*(2), 429-439.

Weiss, J. M., & Smith, W. A. (1995). Preconditioning applied to variable and constant density flows. *AIAA journal*, *33*(11), 2050-2057.

Yuan, H., Solberg, J., Merzari, E., Kraus, A., & Grindeanu, I. (2017). Flow-induced vibration analysis of a helical coil steam generator experiment using large eddy simulation. *Nuclear Engineering and Design*, *322*, 547-562.

IEC 60534-8-3:2011 Industrial-process control valves - Part 8-3: Noise considerations - Control valve aerodynamic noise prediction method.

Dynamics of submerged structures

DEVELOPMENT OF AN EFFICIENT CALCULATION TECHNIQUE FOR DYNAMICS OF MOORING LINES BY USING DISCRETE FORMS OF ROTATION

Kensuke Hara
Faculty of Engineering, YOKOHAMA National University, Kanagawa, Japan
Kazuaki Shimojima
Department of Mechanical Engineering, Tokyo Institute of Technology, Tokyo, Japan
Taihei Yamaguchi
Department of Mechanical Systems Engineering, Ibaraki University, Ibaraki, Japan

ABSTRACT

Development of efficient calculation techniques is of key importance for design of deepwater moored floating structures consisting of many subsystems, such as a floating vessel, risers and mooring lines. In particular, this study focuses on a method for simulating dynamic behavior of the mooring line, since it includes a lot of degrees of freedom and geometric nonlinear effects. A modified Morison equation based on the linear potential flow theory is employed to derive the hydrodynamic forces acting on the lines. The present approach describes the mooring lines (chain) as multi-rigid bodies based on the multibody dynamics approach. In addition, a discrete form of rotation called "the rotation update equation" is introduced. This technique approximates the rotation by using incremental components of rotation in terms of the angular velocity. This approach can bypass the parameterization of rotation in the equations of motion. Clearly, it contributes to reduction of computational costs. Furthermore, a preconditioning method is applied to the equations of motions in order to prevent the ill-conditioning which affects convergence of the numerical integration procedures for the set of equations with configuration level constraints. Finally, a comparison of results by the present method and the conventional method are presented in order to show the validity of the method.

1. INTRODUCTION

The deepwater floating structure is comprised of many subsystems, such as a floating vessel, risers and mooring lines. Due to the large number of degrees of freedom and the inherent nonlinearities, computational cost is a significant problem in the dynamic analysis. Therefore, many methods have been developed from the standpoint of balancing accuracy and efficiency. For instance, typical examples such methods are time domain analysis incorporating the quasi-static approximation(Ormberg, Larsen, 1998), frequency domain analysis(Garrett, 2005; Low, Langley, 2006, 2008) and so on. On the other hand, Kreuzer, Wilke (2002) proposed the efficient time domain analysis method based on the multibody system model with the subsystem technique.

This study would rather focus on a more fundamental aspect in the formulation procedure. In particular, it is aimed at developing a numerical model for simulating dynamic behavior of the mooring line, which includes a lot of degrees of freedom and geometric nonlinear effects. In the present model, a modified Morison equation is used for evaluating hydrodynamic forces acting on the mooring lines, that is, the interaction between lines and fluid is evaluated by using the linear potential flow theory. On the other hand, the mooring line (chain) is modeled as multi-rigid bodies based on the multibody dynamics approach. In the formulation of the three dimensional motion of rigid body, the treatment of rotation is of key importance for deriving the equations of motion, because the parameterization of rotation complicates the mathematical description of the equation. This study employs the discrete forms of the rotation kinematic compatibility equation for resolving the difficulties arising from the the parameterization of rotation. More specifically, the present method introduces an approximated form of rotation expressed by the discrete form with respect to time with the incremental angular velocity. As a result, it can bypass the parameterization of rotation. It gives discrete form of the equations of motion for the rotation with only incremental angular velocity. Therefore, it can reduce the degrees of freedom for the rotation. Clearly, it can contribute to improvement of computational efficiency. Furthermore, an augmented formulation with constraints for configuration level is introduced for connecting the bodies. Since the configuration constraint can be expressed by information of positions for bodies, it enables us to derive the equations of

motion for a whole system easily. On the other hand, other class of constraints (velocity or acceleration) may lead to constraint violation. However, the drawback of the model using the configuration constraints (so-called differential algebraic equations with index-3) involves severe numerical problem arising form the Jacobian matrix depending on the time-step size in the Newton-Raphson iterative processes for the numerical integration. In order to avoid this problem, the equations of motion are scaled based on physical argument derived by the mass and stiffness matrices. Finally, the present method is evaluated by comparing with a conventional model.

2. FORMULATION BASED ON THE MULTIBODY DYNAMICS APPROACH

2.1. Description of structural model

2.1.1. Kinematics for chain model

A mooring line is modeled as a series of uniform rigid bodies with a length of L, as shown in Fig. 1. Each of the bodies is connected to the other bodies by spherical joints. A length between the center of mass and the spherical joint is given by ℓ. The position vector from the origin of the global coordinate system to the center of mass in the ith body is denoted as $\underline{x}|_i$, where a subscript i denotes the body number. In addition, if quantities also have a superscript n, it indicates the quantities at $t = t^n$. The rotation parameter and the angular velocity vector are expressed by $\underline{p}|_i$ and $\underline{\omega}|_i$, respectively. Then, an orientation of the body leads the rotation tensor $\underline{\underline{R}}|_i$. In general, the rotation tensor is defined in terms of the rotation parameters $\underline{p}|_i$, such as the Euler angles, the Euler parameters, and so on. Instead, this study utilizes the angular velocity and the time step size to give the rotation tensor, see Section 2.1.3. Introducing the quantities mentioned above, constraints for the configuration level are obtained as

$$\underline{C} = [\ (\underline{C}|_1)^T \ ... \ (\underline{C}|_{N+1})^T\ ]^T = \underline{0}\,, \tag{1}$$

$$\underline{C}|_1 = -\bar{\underline{x}}|_0 + \underline{x}|_1 + \underline{\underline{R}}|_1 {}^*\underline{r}|_{1^-} = \underline{0}\,, \tag{2}$$

$$\underline{C}|_i = -\underline{x}|_{i-1} - \underline{\underline{R}}|_{i-1} {}^*\underline{r}^+ + \underline{x}|_i + \underline{\underline{R}}|_i {}^*\underline{r}^- = \underline{0}\,, \tag{3}$$

$$\underline{C}|_{N+1} = -\underline{x}|_N - \underline{\underline{R}}|_N {}^*\underline{r}^+ + \bar{\underline{x}}|_{N+1} = \underline{0}\,, \tag{4}$$

where the notation with an asterisk ${}^*(\cdot)$ indicates tensor components defined in the material basis. On the other hand, tensor components without the asterisk are basically defined in the inertial basis. Therefore, when the rotation tensor that describes the orientation of the body is represented by $\underline{\underline{R}}$, it gives $\underline{\underline{R}}\,{}^*(\cdot) = (\cdot)$.

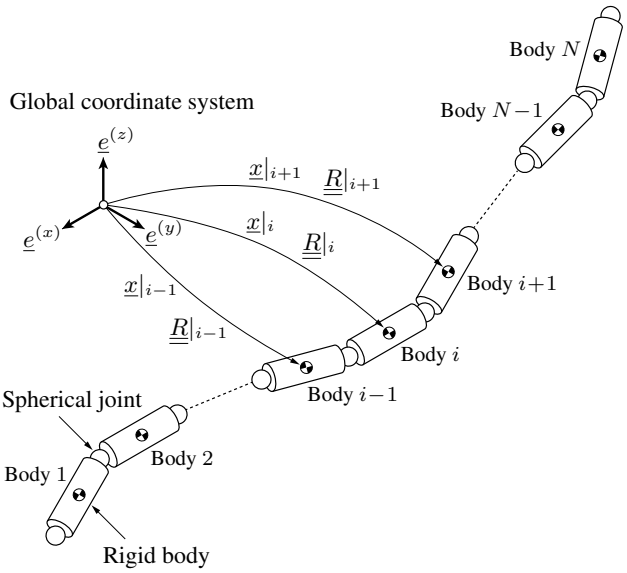

Figure 1. Schematic diagram of the chain model

2.1.2. Equations of motion for structure

The equations of motion for the ith body subjected to externally applied force $\underline{F}^{(\mathrm{E})}$ and moment ${}^*\underline{M}^{(\mathrm{E})}$ (the Newton-Euler equations) are found readily:

$$\underline{\underline{m}}_i \frac{d^2\underline{x}|_i}{dt^2} = \underline{F}^{(\mathrm{E})}|_i + \underline{F}^{(\mathrm{C})}|_i, \tag{5}$$

$${}^*\underline{\underline{\rho}}_i \frac{d^*\underline{\omega}|_i}{dt} + {}^*\tilde{\omega}|_i \, {}^*\underline{\underline{\rho}}|_i \, {}^*\underline{\omega}|_i = {}^*\underline{M}^{(\mathrm{E})}|_i + {}^*\underline{M}^{(\mathrm{C})}|_i, \tag{6}$$

where $\underline{\underline{m}}_i$ denotes the mass matrix and $\underline{\underline{\rho}}_i$ denotes the moment of inertia tensor. Then, the tilde $\tilde{(\cdot)}$ is an operator generating a skew-symmetric matrix from an arbitrary vector $\underline{a} = [a_1 \ \ a_2 \ \ a_3]^T$, that is,

$$\tilde{a} = \begin{bmatrix} 0 & -a_3 & a_2 \\ a_3 & 0 & -a_1 \\ -a_2 & a_1 & 0 \end{bmatrix}. \tag{7}$$

The angular velocity vector can be expressed by the rotation tensor:

$$\left.\begin{aligned} \tilde{\omega} &= \dot{\underline{\underline{R}}}\,\underline{\underline{R}}^T, \\ {}^*\tilde{\omega} &= \underline{\underline{R}}^T \dot{\underline{\underline{R}}}. \end{aligned}\right\} \tag{8}$$

Equation (8) is referred to as the kinematic compatibility conditions between the rotation tensor and the angular velocity vectors.

The effect of gravity is included in a part of the vector of external applied forces $\bar{F}^{(\mathrm{E})}$ given by $[\,0\,0\,-$

$m_i g]^T$. Even though the term regarding the gravity is constant in the Newton equation (5), it generates the geometric nonlinearities arising from configurations of the chain in the restoring forces through the constrained force $\underline{F}^{(\mathrm{C})}$.

The vectors of constrained force $\underline{F}^{(\mathrm{C})}$ and moment ${}^*\underline{M}^{(\mathrm{C})}$ regarding the constraints (1) are derived by

$$\begin{aligned}\underline{F}^{(\mathrm{C})}|_i &= -(\underline{\underline{G}}^{(x)}|_i)^T\underline{\lambda}|_i - (\underline{\underline{G}}^{(x)}|_{i+1})^T\underline{\lambda}|_{i+1} \\ &= -\underline{\lambda}|_i + \underline{\lambda}|_{i+1}, \end{aligned} \tag{9}$$

$$\begin{aligned}{}^*\underline{M}^{(\mathrm{C})}|_i &= -(\underline{\underline{G}}^{(p)}|_i)^T\underline{\lambda}|_i - (\underline{\underline{G}}^{(p)}|_{i+1})^T\underline{\lambda}|_{i+1} \\ &= -{}^*\tilde{r}\,(\underline{\underline{R}}|_i)^T(\underline{\lambda}|_i + \underline{\lambda}|_{i+1}), \end{aligned} \tag{10}$$

where $\underline{\underline{G}}^{(x)}$ and $\underline{\underline{G}}^{(p)}$ represent the Jacobian matrices regarding constraints (1).

Substituting Eqs. (9) and (10) into Eqs. (5) and (6), then, premultiplying the latter equation by the rotation tensor $\underline{\underline{R}}|_i$, it yields

$$\underline{\underline{m}}\frac{d^2\underline{x}|_i}{dt^2} + \underline{\lambda}|_i - \underline{\lambda}|_{i+1} = \underline{F}^{(\mathrm{E})}|_i, \tag{11}$$

$$\frac{d\underline{h}|_i}{dt} + \underline{\underline{R}}|_i\,{}^*\tilde{r}\,(\underline{\underline{R}}|_i)^T(\underline{\lambda}|_i + \underline{\lambda}|_{i+1}) = \underline{M}^{(\mathrm{E})}|_i, \tag{12}$$

where $\underline{h}|_i$ denotes the angular momentum defined in the inertia basis, namely, $\underline{h}|_i = \underline{\underline{R}}|_i{}^*\underline{h}|_i = \underline{\underline{R}}|_i{}^*\underline{\rho}|_i{}^*\underline{\omega}|_i$. Noting that Eq. (12) is equivalent to the Euler equation defined in the inertia basis.

2.1.3. Expression of rotation

Approaches for describing the rotational motion can be naturally categorized into vectorial and non-vectorial parameterizations. For instance, the Rodrigues parameter is a typical example of the vectorial parameterization. On the other hand, the Euler angles and the Euler-Rodrigues parameters can be classified into the non-vectorial parametrization. In particular, this study employs the former approach, namely, the vectorial parametrization.

The general form of vectorial parameterization of rotation can be expressed by

$$\underline{\underline{R}} = \underline{\underline{I}} + \frac{\nu^2}{\varepsilon}\tilde{p} + \frac{\nu^2}{2}\tilde{p}\tilde{p}, \tag{13}$$

where $\underline{p}$ denotes a rotation parameter vector. It generally parallels to the rotation axis $\underline{n}$:

$$\underline{p} = p(\varphi)\underline{n}, \tag{14}$$

where $p(\varphi)$ is called a generating function for the rotation angle φ. According to the literatures [e.g. (Bauchau, Trainelli, 2003)], it must be odd functions of the rotation angle φ. On the other hand, $\nu(\varphi)$ and $\varepsilon(\varphi)$ are even functions of φ defined by

$$\nu(\varphi) = \frac{2\sin(\varphi/2)}{p(\varphi)}, \tag{15}$$

$$\varepsilon(\varphi) = \frac{2\tan(\varphi/2)}{p(\varphi)}. \tag{16}$$

Furthermore, the relation between the angular velocity vector $\underline{\omega}$ and the rotation parameter vector $\underline{p}$ is required for solving Eq. (6). It can be derived by employing the vectorial parametrization as follows:

$$\underline{\omega} = \frac{d\varphi}{dt}\underline{n} + \{\sin\varphi\underline{\underline{I}} + (1-\cos\varphi)\tilde{n}\}\frac{d\underline{n}}{dt}, \tag{17}$$

where $\underline{\underline{I}}$ denotes the 3×3 identity matrix. This equation can also be expressed by using a tensor $\underline{\underline{H}}(\underline{p})$ as

$$\underline{\omega} = \underline{\underline{H}}(\underline{p})\frac{d\underline{p}}{dt}. \tag{18}$$

This paper employs a method based on a kind of "intrinsic formulation" [Bauchau et al. (2013)]. This formulation includes displacements and rotations for motion of system, but rotations are not parameterized. In other words, the rotation vector $\underline{p}$ does not explicitly appear in the formulation. Obviously, it is beneficial for numerical applications because the formulation without the rotation parameters could reduce number of degrees of freedom. This approach begins with the discretization of rotation update procedure. Let us consider a typical time interval $[t^n, t^{n+1}]$ with a time step size $\Delta t = t^{n+1} - t^n$. In addition, the midpoint of the time interval $t^{n+\frac{1}{2}} = (t^n + t^{n+1})/2$ is introduced. Quantities evaluated at t^n, t^{n+1} and $t^{n+\frac{1}{2}}$ are represented by $(\cdot)|^n$, $(\cdot)|^{n+1}$ and $(\cdot)|^{n+\frac{1}{2}}$, respectively. When incremental rotation tensors $\underline{\underline{R}}$ and ${}^*\underline{\underline{R}}$ are introduced, it gives a rotation update equation

$$\underline{\underline{R}}|^{n+1} = \underline{\underline{R}}\,\underline{\underline{R}}|^n = \underline{\underline{R}}|^n{}^*\underline{\underline{R}}, \tag{19}$$

where $\underline{\underline{R}}|^n$ and $\underline{\underline{R}}|^{n+1}$ denote corresponding rotation tensors at t^n and t^{n+1}, respectively. Since it can be assumed that incremental rotation remains small within each time step, the increment of rotation magnitude $\Delta\varphi$ $(= \varphi|^{n+1} - \varphi|^n)$ is also small, namely, $\Delta\varphi \ll 1$. Under these conditions, the discrete form of time-derivative of incremental rotation $d\varphi/dt \sim \Delta\varphi/\Delta t$. In addition, Eq. (17) can be approximated by $\underline{\omega} \sim \dot{\varphi}\underline{n}$, and therefore, $\Delta t\,\underline{\omega} \sim \Delta\varphi\underline{n}$. As a consequence, the following expression is reasonable for small $\Delta\varphi$ in typical numerical procedures:

$$\left.\begin{aligned}\Delta t\,\underline{\omega} \sim \underline{p} &= p(\Delta\varphi)\underline{n}, \quad \text{(Inertial basis)} \\ \Delta t\,{}^*\underline{\omega} \sim {}^*\underline{p} &= p(\Delta\varphi){}^*\underline{n}. \quad \text{(Material basis)}\end{aligned}\right\} \tag{20}$$

Applying Eq. (20) to Eq. (19), the discrete form of rotation update equation can be obtained as

$$\underline{\underline{R}}|^{n+1} = \underline{\underline{R}}|^{n} {}^{*}\underline{\underline{R}}(\Delta t\, {}^{*}\underline{\omega}). \tag{21}$$

Noting that Eq. (21) enables to calculate the update of rotation for each body described by Eqs. (5) and (6) without the specific parametrization of rotation. In addition, the expression in Eq. (21) is derived from only the assumption for the magnitude of rotation within each time step as mentioned above. Therefore, it is independent of conditions for applied external forces and a kind of mechanical joints including the effects of friction.

2.2. Fluid force

This study assumes that the mooring lines are slender structure whose diameter D is enough small compared to the wave length, namely, the hydrodynamic transparent structure. Therefore, the modified Morison's equation (Clauss et al., 1992) can be introduced to derive hydrodynamic forces acting on the lines. Fluid particle velocities and accelerations are calculated by the linear wave theory based on the potential flow. Under these conditions, the forces on the structure from surrounding fluid with the density $\rho^{(\mathrm{F})}$ (Kreuzer, Wilke, 2002) are expressed in the vectorial form as

$$\begin{aligned}\underline{F}^{(\mathrm{F})} &= \rho^{(\mathrm{F})}\frac{\pi D^2}{4}L\frac{d^2\underline{x}}{dt^2} \\ &+ C_M\rho^{(\mathrm{F})}\frac{\pi D^2}{4}L\frac{d}{dt}\left(\underline{u}-\frac{d\underline{x}}{dt}\right) \\ &+ \frac{1}{2}C_D\rho^{(\mathrm{F})}D\left|\underline{u}-\frac{d\underline{x}}{dt}\right|\left(\underline{u}-\frac{d\underline{x}}{dt}\right),\end{aligned} \tag{22}$$

where $\underline{u}$ denotes the fluid particle velocity. C_M and C_D are the inertia and the drag coefficients, respectively.

3. NUMERICAL TREATMENT FOR TIME DOMAIN ANALYSIS

3.1. Scaling of the equations of motion

This study aims to derive the governing equations of motion with the configuration level constraints (1). This kind of equations can be classified into the "index-3" differential algebraic equations. These equations are useful to formulate complex multibody systems, because usage of the configuration level constraints enables us easily to develop mathematical models for system components connected by mechanical joints. In addition, it can also eliminate drifts of constraint violations, unlike velocity and acceleration level constraints. However, a significant problem in this method is the severe ill-conditioning in the calculation for small time steps.

One of the effective remedies for this problem is to introduce preconditioning technique. In particular, this study introduces a method that is directly applied to the governing equations of motion (Bauchau, et al., 2009). Briefly, it consists of three steps, (i) normalization for generalized coordinates, (ii) introduction of a scaling factor and (iii) addition of an augmented Lagrangian term.

First, the generalized coordinates in a set of Eqs. (11), (12) and (21) are normalized with respect to time. It can be achieved by introducing a normalized time variable $\tau = t/\Delta t$. It gives

$$\frac{1}{(\Delta t)^2}\underline{\underline{m}}\,\dot{\underline{v}}^{(x)}|_i + (\underline{\lambda}|_i - \underline{\lambda}|_{i+1}) = \underline{F}^{(\mathrm{E})}|_i, \tag{23}$$

$$\frac{1}{(\Delta t)^2}\dot{\underline{h}}|_i + \underline{\underline{R}}|_i\, {}^{*}\tilde{r}\,(\underline{\underline{R}}|_i)^T(\underline{\lambda}|_i + \underline{\lambda}|_{i+1}) = \underline{M}^{(\mathrm{E})}|_i, \tag{24}$$

$$\underline{\underline{R}}|^{n+1} = \underline{\underline{R}}|^{n} {}^{*}\underline{\underline{R}}({}^{*}\hat{\underline{\omega}}), \tag{25}$$

where the dot $\dot{(\cdot)}$ indicates a derivative with respect to the nondimensional time τ, that is, $\dot{(\cdot)} = d(\cdot)/d\tau$. The notations with the hat $\hat{(\cdot)}$ are utilized to denote scaled quantities as $\hat{\underline{v}}^{(x)} = d\underline{x}/d\tau = \Delta t d\underline{x}/dt$, $\hat{\underline{h}} = {}^{*}\underline{\underline{\rho}}\,{}^{*}\hat{\underline{\omega}}$ and ${}^{*}\hat{\underline{\omega}} = \Delta t\, {}^{*}\underline{\omega}$.

Next, the scaling factor $s = m_r + c_r\Delta t + k_r(\Delta t)^2$ is introduced, where m_r, c_r and k_r represent characteristic mass, damping and stiffness coefficients, respectively. An convenient choice is to determine these characteristic quantities as the average of the diagonal terms of the mass, damping and stiffness matrices, respectively (Bauchau, et al., 2009). Since the present model expressed in Eqs. (28) and (29) includes only mass coefficients, this paper employs the scaling factor as $s = m_r$. However, the scaling factor can be defined arbitrary. For instance, the present model includes the nonlinear forces arising from the gravity and the fluid forces in Eq. (22), therefore, the scaling factor could be modified by introducing the linearized forms for such nonlinear components.

Introducing the scaling factor s makes the Lagrange multipliers $\underline{\lambda}$ and the constraints $\underline{C}$ quantities of magnitude comparable to those of displacement quantities, which become

$$s\hat{\underline{\lambda}}|_i = (\Delta t)^2\underline{\lambda}|_i, \tag{26}$$

$$sC|_i = \underline{0}. \tag{27}$$

Finally, augmented Lagrangian terms are added to the equations of motion. It can be achieved by

introducing a modified Lagrange multiplier $\hat{\mu}|_i = \hat{\lambda}|_i + \rho \underline{C}|_i$, where ρ denotes the penalty factor. As a consequence, the scaled equations of motion are given by

$$\underline{\underline{m}}\,\dot{\underline{\hat{v}}}^{(x)}|_i + s(\underline{\hat{\mu}}|_i - \underline{\hat{\mu}}|_{i+1}) = (\Delta t)^2 \underline{F}^{(\mathrm{E})}|_i, \tag{28}$$

$$\dot{\underline{\hat{h}}}|_i + s\underline{\underline{R}}|_i {}^*\tilde{r}\,(\underline{\underline{R}}|_i)^T(\underline{\hat{\mu}}|_i + \underline{\hat{\mu}}|_{i+1}) = (\Delta t)^2 \underline{M}^{(\mathrm{E})}|_i. \tag{29}$$

Even though Eqs. (28) and (29) have not yet been discretized in time, this treatment plays a key role in the numerical integration. Because the time step size has a great influence on the performance of numerical integration methods with the Newton-Raphson iterative process.

3.2. Discretization of the equations of motion

A midpoint scheme is applied to the governing equations of motion (25), (28) and (29), then, the scaled constraints (27) are evaluated at $t = t^{n+1}$, it leads a set of equations of motion as

$$\begin{aligned}&\underline{\underline{m}}(\underline{\hat{v}}^{(x)}|_i^{n+1} - \underline{\hat{v}}^{(x)}|_i^n) + s(\underline{\hat{\mu}}|_i^{n+\frac{1}{2}} - \underline{\hat{\mu}}|_{i+1}^{n+\frac{1}{2}}) \\ &- (\Delta t)^2 \frac{1}{2}(\underline{F}^{(\mathrm{E})}|_i^n + \underline{F}^{(\mathrm{E})}|_i^{n+1}) = \underline{0},\end{aligned} \tag{30}$$

$$\begin{aligned}&\underline{\hat{h}}|_i^{n+1} - \underline{\hat{h}}|_i^n + \frac{s}{2}\{\underline{\underline{R}}|_i^{n*}\tilde{r}\,(\underline{\underline{R}}|_i^n)^T\}(\underline{\hat{\mu}}|_i^{n+\frac{1}{2}} + \underline{\hat{\mu}}|_{i+1}^{n+\frac{1}{2}}) \\ &+ \frac{s}{2}\{+\underline{\underline{R}}|_i^{n+1*}\tilde{r}\,(\underline{\underline{R}}|_i^{n+1})^T\}(\underline{\hat{\mu}}|_i^{n+\frac{1}{2}} + \underline{\hat{\mu}}|_{i+1}^{n+\frac{1}{2}}) \\ &- (\Delta t)^2 \frac{1}{2}(\underline{M}^{(\mathrm{E})}|_i^n + \underline{M}^{(\mathrm{E})}|_i^{n+1}) = \underline{0},\end{aligned} \tag{31}$$

$$s\underline{C}|^{n+1} = \underline{0}, \tag{32}$$

$$\underline{x}|_i^{n+1} - \underline{x}|_i^n = \frac{1}{2}(\underline{\hat{v}}^{(x)}|_i^n + \underline{\hat{v}}^{(x)}|_i^{n+1}), \tag{33}$$

$$\underline{\underline{R}}|^{n+1} = \underline{\underline{R}}|^{n\,*}\underline{\underline{R}}(^*\underline{\hat{\omega}}|^{n+\frac{1}{2}}), \tag{34}$$

where the notation $(\cdot)|^{n+\frac{1}{2}}$ represents the quantities at the midpoint, $(\cdot)|^{n+\frac{1}{2}} = \{(\cdot)|^n + (\cdot)|^{n+1}\}/2$. These discrete form of the equations motions will be solved by the Newton-Raphson iterative process.

4. VALIDATION OF THE PRESENT MODEL

The numerical model for the time domain analysis has been presented in Eqs. (30)–(34). In this section, the present model is validated against the conventional model comprised of Eqs. (1), (5), (6) and (18), where the Euler angles are introduced as the rotation parameter $\underline{p}$.

4.1. Condition for the test case

The test case is a hanging chain pinned at both ends, which has a static configuration depicted in Fig. 2. Parameters are summarized in Table 1. For the test case, both ends are pinned in water, and it is subjected to a regular wave in yz-plane. The input wave has a wave height of 10 m and a period of 200 s. The top node is positioned at wave surface. In this case, any bodies do not contact with the seabed, as shown in Fig. 2, it implies the effects of interaction between lines and seabed are not involved in the present model. However, the contact forces arising from the seabed interaction, e.g. Low, Langley (2006), can systematically be considered. Noting that, the number of bodies in Table 1 does not coincide with the number of elements for a real chain structure. According to our past investigation, when the chain is subjected to only the gravity force, the numerical results show convergent results in less number of bodies than the real number of chain elements (Shimojima, et al., 2019).

Table 1. Parameters for the test case.

(Chain)	
Total length	400 m
Diameter	1.5 m
Dry mass	150 kg/m
Number of bodies	20
(Fluid)	
Fluid density	1000 kg/m^3
Inertia coefficient	2.0
Drag coefficient	1.2
Wave amplitude	10 m
Wave period	200 s

4.2. Results

The time histories of the 10th node position of the center of mass in y, z directions are plotted in Figs. 3 and 4, respectively. In these figures, the present model with the time step size $\Delta t = 1.0,\ 0.1$ are indicated by the dashed and the solid lines, respectively. On the other hand, the results from the conventional model with $\Delta t = 0.1$ are plotted by the open circle. These figures indicate that the results from the present model coincide well with that from the conventional model. Noting that the conventional model failed to obtain convergent results in the case of the larger time step size $\Delta t = 1.0$. In contrast, differences between the solid and dashed lines are invisi-

ble, therefore, the present model gives convergent results with the larger time step size than the conventional model.

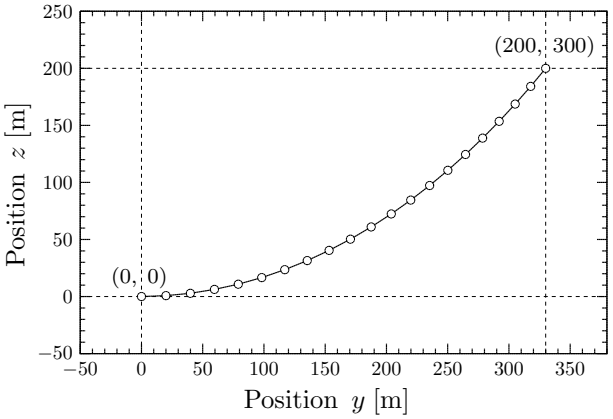

Figure 2. Static configuration of hanging chain.

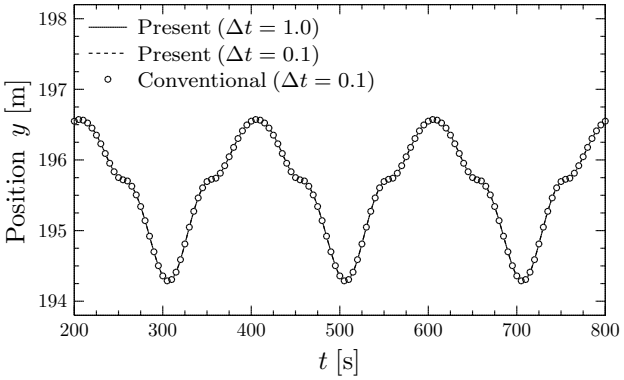

Figure 3. Comparison of time histories for the center of mass calculated by the present and the conventional models (10th node, y direction).

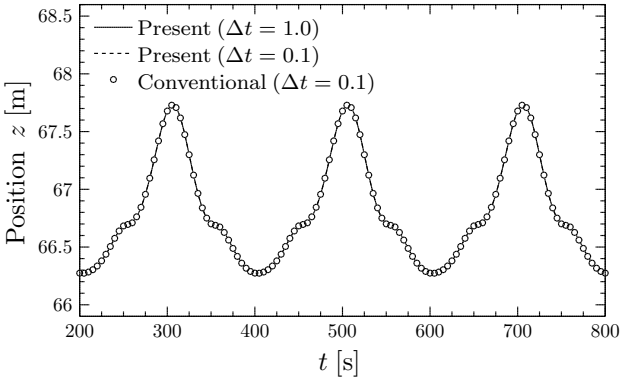

Figure 4. Comparison of time histories for the center of mass calculated by the present and the conventional models (10th node, z direction).

In order to discuss the performance of the present model in more detail, the computation time and the average iteration times for the present and the conventional models during $t = 0{-}1000$ [s] are summarized in Tables 2 and 3, respectively. In Table 2, durations are normalized by the computation time for the conventional model with the time step size $\Delta t = 0.01$. Therefore, the (normalized) computation time for the conventional model with $\Delta t = 0.01$ [s] is 1.0. It is found that the computation time is reduced significantly by the present model. Moreover, Table 3 represents that the results for the average iteration times from the present model are much less than that of the conventional model. Therefore, it can be found that improvement for both of the numerical stability (time step size) and the convergence leads to the significant improvement for the the computational performance.

Table 2. Normalized computation time during $t = 0{-}1000$ [s].

	Time step size Δt		
	1.0	0.1	0.01 [s]
Present model	0.009	0.07	0.56
Conventional model	–	1.56	1.00

Table 3. Average iteration times during $t = 0{-}1000$ [s].

	Time step size Δt		
	1.0	0.1	0.01 [s]
Present model	4.0	3.7	3.0
Conventional model	–	65.0	4.1

5. CONCLUSIONS

This study has developed the numerical model for the mooring lines for the time domain analysis. The lines are modeled as the multi-rigid bodies, and the formulation is based on the framework of the multibody dynamics. In particular, this study introduces the method describing a rigid body motion without relying on parameterizations of rotation. Instead, it employs the rotation update equation consisting of the rotation tensor in the current configuration and the incremental component of the rotation. The resulting equations of motion involve the approximated

form of rotation expressed by the discrete form with respect to time with the angular velocity.

The present model is validated against the conventional model. As a result, the performance of the numerical integration is drastically improved by the present method. Even though present model showed the very good agreement with the conventional model, the total computation time is reduced siginificantly. More specifically, the present model could introduce the larger time step size, and the iteration times for the convergent results are quite small compared to the conventional method.

6. REFERENCES

Bauchau, O.A., Trainelli, L., 2003, The vectorial parameterization of rotation. *Nonlinear Dynamics* **32**: 71-92.

Bauchau, O.A., Epple, A., Bottasso, C.L., 2003, Scaling of constraints and augmented Lagrangian formulations in multibody dynamics simulations. *Transactions of the ASME, Journal of Computational and Nonlinear Dynamics* **4**: 021007.

Bauchau, O.A., Xin, H., Dong, S., Li, Z., Han, S., 2013, Intrinsic time integration procedures for rigid body dynamics. *Transactions of the ASME, Journal of Computational and Nonliear Dynamics* **8**: 011006.

Clauss, G., Lehmann, E., Östergaard, C., 1992, *Offshore Structures*, Springer-Verlag, London.

Garrett, D.L., 2005, Coupled analysis of floating production systems. *Ocean Engineering* **32**: 802-816.

Kreuzer, E., Wilke, U., 2002, Mooring systems – A multibody dynamic approach. *Multibody System Dynamics* **8**: 279-297.

Low, Y.M., Langley, R.S., 2006, Time and frequency domain coupled analysis of deepwater floating production systems. *Applied Ocean Research* **28**: 371-385.

Low, Y.M., Langley, R.S., 2008, A hybrid time/frequency domain approach for efficient coupled analysis of vessel/mooring/riser/dynamics. *Ocean Engineering* **35**: 433-446.

Ormberg, H., Larsen, K., 1998, Coupled analysis of floater motion and mooring dynamics for a turret-moored ship. *Applied Ocean Research* **20**: 55-67.

Shimojima, K, Hara, K., Yamaura, H., 2019, Dynamic analysis and experimental verification for multibody system by using incremental rotation in time-discrete model (in Japanese). *Transactions of the JSME* **85**, 875: 18-00462.

PERFORMANCE OF A CLOSED CYCLE POWER TAKE OFF FOR MUTRIKU BREAKWATER

Morgane Bellec, Ciara Gurhy, Lee Gibson & Craig Meskell
School of Engineering, Trinity College Dublin, Ireland

ABSTRACT

An oscillating water column (OWC) type wave energy converter was installed in Mutriku breakwater (Basque Country, Spain). The wave power is transferred to an air flow that turns a turbine. The facility currently uses self-rectifying turbines. A closed cycle power take off (CCPTO) arrangement, by forcing the flow to be unidirectional, would allow the use of more efficient turbines than currently employed. In this paper, a reduced order model for such a system is introduced. Using Mutriku breakwater dimensions the expected power performance is assessed. The sensitivity of the system to basic geometric features such as turbine and valves sizes is explored using monochromatic ideal wave. It is found that while there is an opimal size turbine, there is no benefit to increasing the valve size beyond a certain area. More realistic sea states representative of Mutriku are investigated using polychromatic waves as an input. The effect of tide is also considered by comparing extreme high and low tide conditions with the mean tide. It is found that tide height has a significant impact on the power production capacity. The trends uncovered by this work will form a useful basis for the design of the actual power take off including the unidirectional turbine.

1. INTRODUCTION

Wave power has long been an attractive potential source of renewable energy due to its high density and availability around the world. Moreover, the resource has good predictability and is decorrelated with wind and solar power, as shown by Fusco et al. (2010). In spite of all those advantages, wave energy is still in infancy, with a large number of concepts at various stages of development. A promising class of device is called the oscillating water column (OWC) in which the wave power is transferred to air flow. Wave energy conversion based on OWC devices whether floating or fixed offers several advantages: the mechanism is not submerged; the sea chamber can provide an effective gearing of the flow; and perhaps the most useful is that the energy presented to the turbine (i.e. in the air) can be dramatically reduced by venting in highly energetic sea states as highlighted by Henriques et al. (2016). However, the main disadvantage is that the flow of air across the turbine is bidirectional i.e. the air flow reverses twice per wave cycle. This has been overcome to some extent with self-rectifying turbines (e.g. Wells, axial impulse or biradial turbines), but these can have poor performance as the rotational speed of the turbine is nearly always mismatched to the instantaneous airflow velocity. A closed cycle power take off (CCPTO) system consisting of two large air reservoirs connected by a unidirectional turbine has been proposed by Vicente et al. (2017). This arrangement was examined for a floating installation in Benreguig et al. (2019).

In the CCPTO arrangement, shown conceptually in Fig. 1, the power take off consists of three air chambers: the sea chamber which is exposed to the OWC, the high pressure (HP) reservoir and the low pressure (LP) reservoir. The sea chamber is connected to the HP and LP reservoirs by non-return valves (designated HP and LP valves respectively), while the HP and LP reservoirs are connected by the air turbine. Whether the sea level in the sea chamber of the OWC is rising or falling, the pressure in the HP reservoir is always above that in the LP reservoir, and so the flow across the turbine is unidirectional. This is the principle benefit of this arrangement.

In order to understand the operation of the Closed Cycle PTO consider the wave cycle as two half-cycles: a compression process and an expansion process. During the compression process, the rising water surface in the sea chamber compresses air raising the pressure, P_1, in this chamber. For a short time both valves are closed. This is not achieved by active control of the valves, but by the temporal variation of the pressure in the three chambers. When the sea chamber pressure rises above the pressure in the HP reservoir, P_2, the HP valve opens while the LP valve remains closed. For the remainder of the compression process the OWC is compressing all of the air in the system through the HP reservoir, turbine and LP reservoir. Due to the pressure drop across the valves and turbine, the LP pressure, P_3 is always lower the the HP pressure, P_2. Hence, the LP valve remains

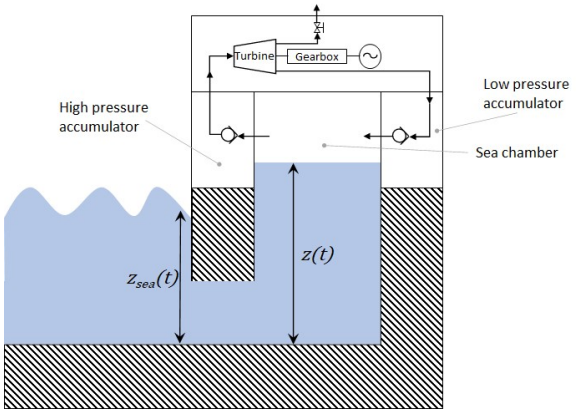

Figure 1. Closed Cycle Power Take Off (CCPTO) for a shore-based installation. Pneumatic path including non-return valves and turbine through the sea, high pressure and low pressure chambers indicated.

closed during the OWC compression process. During expansion, the opposite happens. The sea level drops in the sea chamber, reducing the pressure, until P_1 is below the HP pressure, P_2 which causes the HP valve to shut off. As the pressure P_1 continues to drop, it will fall below the LP pressure, P_3 causing the LP valve to open. From this point on, the expansion process is expanding the air in the HP and LP reservoirs into the sea chamber. The system is nonlinear for two reasons: the compressibility of the air means that the pneumatic spring effect is asymmetric around the equilibrium, with the compression cycle experiencing a harder spring than the expansion; in addition, the opening of the valves represents a softening spring effect. Furthermore, the triggering of the valve opening depends not just on the instantaneous pressure within the sea chamber, but also the time history of the discharge from the high pressure chamber, introducing a memory effect. Indeed the pressure difference needed to trigger the valve is actually bigger than the one needed to keep it open, so the valve position (open or close) at each time also depends on its past positions. Thus, it is necessary to model the CCPTO in the time domain, although this latter memory effect is not yet considered in the present study. In this paper, a reduced order model for a CCPTO is introduced and applied to a notional shore based installation which would be compatible with Mutriku breakwater. The objective is to assess the sensitivity of the power available in a CCPTO to the size of valves and turbine for a range of sea states and tide heights. The term size is here understood as a global metric that serves as a proxy for the power production capacity; in effect it includes the physical sizes, the rotational speed and the operating conditions of the turbine and valves. Mutriku is a fixed

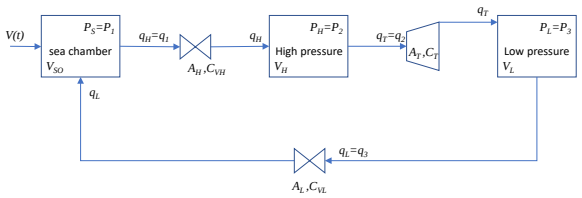

Figure 2. Schematic of lumped parameter model of CCPTO.

OWC structure installed into the breakwater at the entrance to the port of Mutriku, Spain. It is the world's first multi-turbine, wave energy facility and was first connected to the grid in 2011. The breakwater consists of 16 air chambers. In each chamber, an open cycle OWC system has been fitted with an 18.5kW Wells fixed-pitch turbine, giving a total capacity to the plant of 296kW. By targeting this specific facility, the sizing of the CCPTO system is limited by real-world dimensions. These constraints reduce the design space and provide more concrete conclusions about the sensitivity of the power output.

2. MODELLING

The pneumatic system of the CCPTO is shown schematically in Fig. 2. The governing equations are formulated in terms of mass flow rate so that the modelled variables in the differential equations are the mass in each chamber. A previous formulation in terms of chamber pressure should be equally valid as implemented by Vicente et al. (2017), but in the current study it was found to yield slowly divergent total pressure. It may be that the presence of damping in their system of equations is stabilising the model. In contrast in the current formulation the conservation of mass is implicitly satisfied at each instant, and hence the solutions are stable in the long term, even though the pneumatic system is treated in isolation.

2.1. Assumptions

The CCPTO is idealised as a closed pneumatic system, as shown in Fig. 2. The instantaneous mass in each chamber is determined from the sum of the mass flux through the valves and turbine. The mass flow rates are obtained from the volumetric flow rates, which depend on the instantaneous pressures in the system. This 1D model is crude as it excludes the full complexity of the internal flow and it is based on a number of assumptions:

- isentropic compression/expansion is assumed in all chambers;

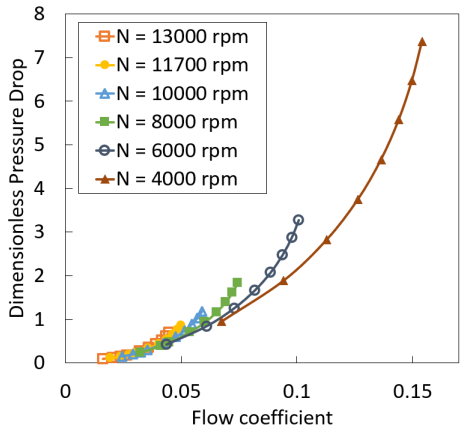

Figure 3. Variation of pressure drop with flow coefficient for different rotational speed of a proposed turbine suitable for the CCPTO

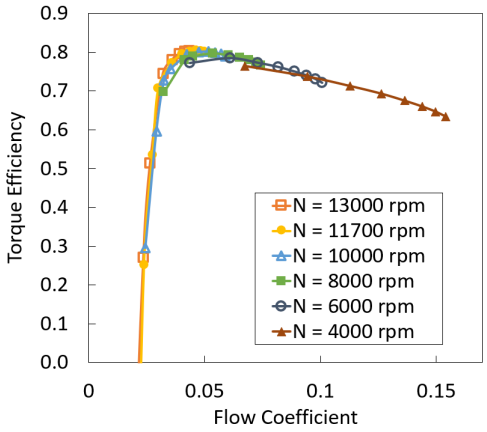

Figure 4. Variation of efficiency with flow coefficient for different rotational speed of a proposed turbine suitable for the CCPTO

- the sea surface acts as a rigid piston, so no sloshing is considered;
- air density at valves and turbines is assumed to be equal to the upstream value;
- a rudimentary turbine model is adopted. In effect the turbine is represented as an orifice, with and area A_T and a turbine coefficient, C_T.

In fact, detailed RANS assessment of a suitable axial flow turbine shows that this last assumption is quite good, for a given rotational speed. Nonetheless, care is needed when exploring the effect of the turbine size implicit in A_T, as this is effectively a tuned model. Although the full presentation of the preliminary design of the proposed air turbine exceeds the scope of this paper, the main results are shown Fig. s 3 and 4. The pressure drop and the torque efficiency are plotted depending on the flow coefficient for different rotational speeds. The variables are non-dimensionalized as follows (see Falcão et al. (2018)):

Dimensionless pressure drop:

$$\Psi = \frac{\Delta P}{\rho \Omega^3 D^5} \tag{1}$$

Flow coefficient:

$$\Phi = \frac{Q}{\Omega D^3} \tag{2}$$

Torque efficiency:

$$\nu = \frac{\tau \Omega}{\dot{m} C_p T_{01} (1 - \frac{p_{03}}{p_{01}}^{\frac{\gamma - 1}{\gamma}})} \tag{3}$$

where ΔP is the pressure drop across the turbine, ρ is the air density, Ω is the rotational speed in radians per unit time, Q is the volume flow rate, D is the rotor diameter, τ is the torque, $\dot{m}$ is the mass flow rate, C_p is the air heat capacity, γ is the heat capacity ratio, T_{01} is the inlet total temperature, P_{01} and P_{03} are respectively the inlet and outlet total pressures.

The non-dimensionalization of the pressure drop curves for different rotational speeds collapse (Fig. 3) yields an envelope curve which follows a quadratic tendency, supporting the choice of a simple orifice model for the turbine. Fig. 4 shows a peak of the turbine efficiency around 80 %. However, the efficiency remains high when the flow characteristics are slightly modified. A certain adaptability of the turbine seems to be possible through tuning of the rotational speed, although the extend of that possibility remains to be investigated.

2.2. Governing Equations

The mass in each chamber can be decomposed into a mean and fluctuating component:

$$M_i = m_{i0} + m_i \tag{4}$$

where $i = 1,2,3$ for sea, high pressure and low pressure chambers, respectively. Assuming the system starts at atmospheric conditions, the initial mass in each chamber is given by:

$$m_{i0} = \frac{V_{i0}}{\rho_0} \tag{5}$$

The principal solution variables are given by the first order ordinary differential equations which simply enforce mass conservation (equation 6, 7, 8).

Sea Chamber mass flux:

$$\frac{dm_1}{dt} = q_3 - q_1 \tag{6}$$

High Pressure Chamber mass flux:

$$\frac{dm_2}{dt} = q_1 - q_2 \tag{7}$$

Low Pressure Chamber mass flux:

$$\frac{dm_3}{dt} = q_2 - q_3 \tag{8}$$

The density in each chamber is simply the mass divided by the volume:

$$\rho_i = \frac{M_i}{V_i} \tag{9}$$

The volumes, V_i, of the high and low pressure chambers are fixed and the volume of the Sea Chamber is determined by the instantaneous water level:

$$V_1 = V_{10} + V_S(t) \tag{10}$$

$$V_{2,3} = V_{20,30} \tag{11}$$

The entire system is driven by the perturbation from equilibrium of the sea volume in the sea chamber caused by the oncoming waves. This will be discussed in section 2.3.

The flow rates in the system are obtained by treating both valves and the turbine as a simple flow restriction. It is given by:

$$q_i = C_i A_i \sqrt{2\rho_i} \Re\left(\sqrt{P_i - P_{i+1}}\right) \tag{12}$$

where C_i is a discharge coefficient and A_i is proportional to the open area of the component. Note that if the pressure difference is negative (i.e. $P_{i+1} > P_i$), the flow rate is 0. The density, ρ is assumed to be that of the upstream chamber, but this could be relaxed to be either an average of up- and downstream values or simply set to the reference value. Note that no account is taken of the shape of the ducting close to the valves or turbine. The effect of turbulence, flow separation and irrecoverable pressure drop are embedded in the assumed discharge and turbine coefficients.

The instantaneous pressure is required in each chamber to calculate the flow rates. This is calculated on the basis of an isentropic process. It is assumed that the entire system starts at a pressure equilibrium conditions (e.g. the pressure and volume and density are atmospheric):

$$P_i = P_0 \left(\frac{\rho_i}{\rho_0}\right)^{\gamma} \tag{13}$$

2.3. Modelling of incoming waves

The volume of air in the sea chamber $V_S(t)$ depends both on the incoming waves i.e. the OWC motion, and on the back pressure P_1 imposed by the CCPTO. The coupling is achieved by solving the following differential equation:

$$m_{wc}\frac{d^2z}{dt^2} + R\frac{dz}{dt} + Sz = F_S + F_w + F_g \tag{14}$$

where $z(t)$ is the water column elevation, so that $V_S(t) = -A_S \times z(t)$.

Equation 14 results from applying Newton's second law of motion to the water column of fixed mass m_{wc}, height H_{wc} and cross-sectional area A_S, subjected to the following list of forces.

Force exerted by the CCPTO back pressure:

$$F_S = P_1 A_S \tag{15}$$

Force exerted by the incoming waves:

$$F_w = -\rho_w g z_{sea} A_S \tag{16}$$

Damping accounting for the water/walls friction losses:

$$R = \frac{1}{2}\rho_w V_m^2 A_{wc} C_f \tag{17}$$

The damping term R represents losses due to friction between the water column and the concrete walls of the chamber. ρ_w is the water density, taken constant, V_m is the water column mean velocity, A_{wc} is the contact surface area and C_f is a friction coefficient approximated using a correlation with the Reynolds number of the flow. The prime role of this damping term is to have a better understanding of the dynamic response of the system using a reasonable value for losses.

Finally, the hydrostatic forces to account for weight of the water column and buoyancy forces are included. As these last two forces obviously don't change, together they represent the equilibrium sea level and so effectively define the sea chamber volume V_{10}. They are included to allow the easy application of different tide heights.

$$F_g = m_{wc} g \tag{18}$$

$$S = \rho_w g A_S \tag{19}$$

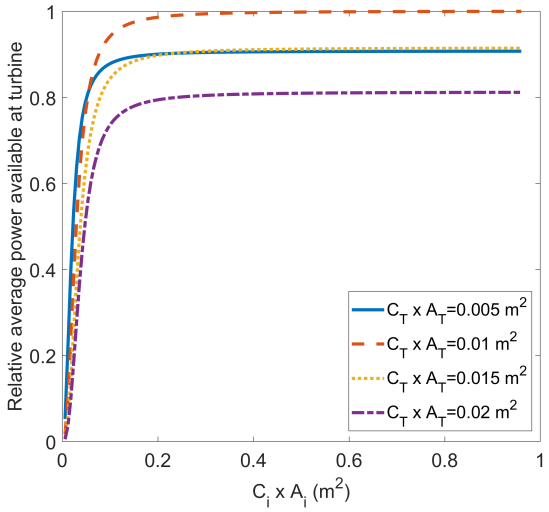

Figure 5. Variation in power with valve size metric $C_i \times A_i$ for different turbine size metrics $C_T \times A_T$.

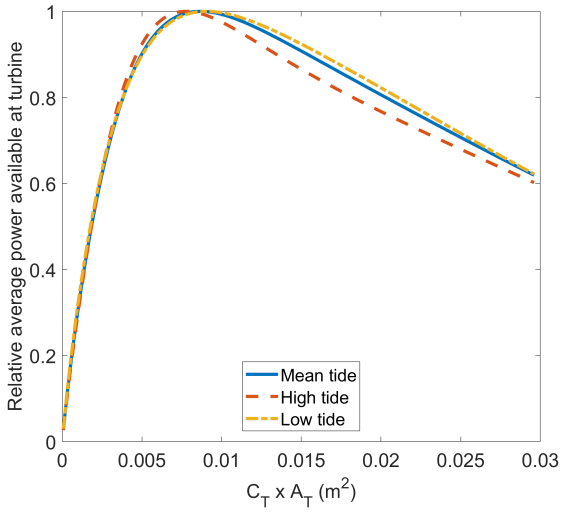

Figure 6. Variation in power with turbine size metric $C_T \times A_T$ for different tides.

When monochromatic waves are used in section 3, the sea level outside the sea chamber is assumed to vary regularly following a sinusoidal pattern as follows:

$$z_{sea}(t) = H_{wc} + Zsin(2\pi ft) \tag{20}$$

where Z and f are the incoming waves height and frequency respectively. They reflect the local wave climate. When polychromatic waves are used in section 4, a sample extracted from measurements in Mutriku is used for $z_{sea}(t)$.

3. INITIAL SIZING

As previously mentioned, this study focuses on a fixed OWC structure installed into a breakwater in the port of Mutriku, Spain. The sizing of the CCPTO is therefore constrained by the real-world dimensions of the Mutriku chambers. The gross size of the sea chamber is already fixed between 100 and 200 m^3 depending on the tide. The low and high pressure chambers are also limited by the turbine hall scale. Assuming they have the same size, they cannot exceed 90 m^3 each. There may be an advantage to having a larger HP chamber with the LP chamber vented to atmosphere, effectively making he LP volume infinite. This is beyond the scope of the current study and will be considered in future work.

The sensitivity of the power output to the size of valves and turbine is assessed using a sinusoidal monochromatic wave as presented in equation 20. The wave height and period are taken here as the most common in Mutriku's wave climate: $Z = 1.5\ s$ and $T = 1/f = 10\ s$. The areas A_i and A_T in equation 12 do not necessarily represent the geometric areas of the valves and turbine, as there is uncertainty on the value of the discharge coefficients C_i and C_T, but nonetheless it represents a metric of the relative size. The results are thus presented for $C_i \times A_i$ and $C_T \times A_T$ rather than A_i and A_T in Fig. 5 and 6.

3.1. Valves

Fig. 5 presents the average power available at the turbine depending on the valves size, for different turbine sizes, at mean tide. The power is non-dimensionalized by the maximal power, obtained here for $C_T \times A_T = 0.01\ m^2$. The two valves are assumed to be identical. Whatever the turbine size, the power increases with the valves size until it reaches a plateau. For $C_i = 0.6$, the threshold is here attained around $A_i = 0.4\ m^2$. Indeed, once the valves are big enough compare to the turbine, they do not limit the air flow and thus do not impact the power output. The actual value of this threshold is somewhat subjective; however in Mutriku the opening of the sea chamber is $0.5\ m^2$ and so the maximum size of the valves will be of this order. As a result, this might not be a limiting design issue.

3.2. Turbine

An optimum is expected to exist for the turbine size. Indeed, two competing phenomena occur simultaneously: on one hand, the mass flow increases with the turbine area, thus increasing the power output; on the other hand the pressure drop decreases when the turbine area increases, thus decreasing the power output. To investigate those opposing effects, the average power available at the turbine depending on

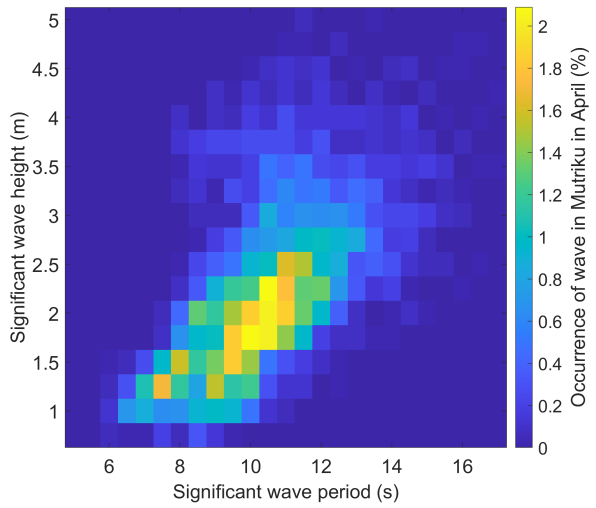

Figure 7. Mutriku wave climate in a month of April.

the turbine size is plotted Fig. 6 for low, mean and high tides. The power is non-dimensionalized by the maximal power for each tide. As the turbine size increases, the power output first increases sharply till it reaches a maximum, then it decreases more gently. The optimum is reached at around $A_T = 0.013\ m^2$, although it varies a little depending on the tide. Here again the actual value is uncertain as the discharge coefficient was arbitrarily taken as $C_T = 0.74$, based on the data in Fig. 3. Moreover, it is unclear how this area A_T relates to the aperture area of an actual turbine.

4. SENSITIVITY TO THE SEA STATE

4.1. Polychromatic wave climate

Measurements of the internal free surface heights in the sea chamber at Mutriku for 30 days of a month of April were made available by the operators through private communication. These measurements were taken as an open-cycle PTO system was in place. They are here assumed to be reasonably representative of the open sea behaviour. The significant wave period and height were calculated using the spectral moment method as described by Chun and Suh (2018). Fig. 7 presents the resulting wave climate showing the probability of any given sea state to occur in Mutriku in April. Note that the pair $[1.5\ m, 10\ s]$ which was used for the initial sizing in section 3 is the centre bin of the wave climate.

4.2. Effect of the tides

To investigate the effect of the sea state and the tides on the expected power output, the model was

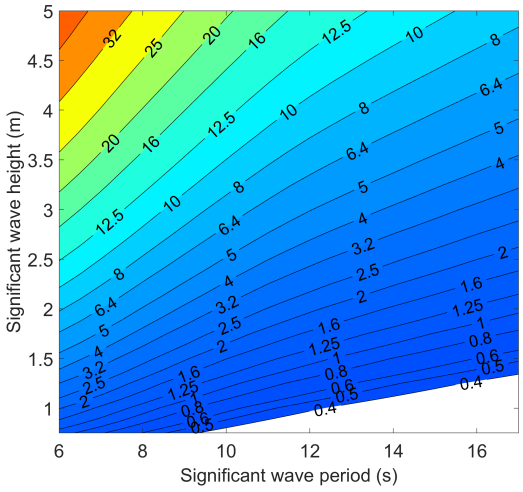

(a) Average power at turbine for high tide (kW)

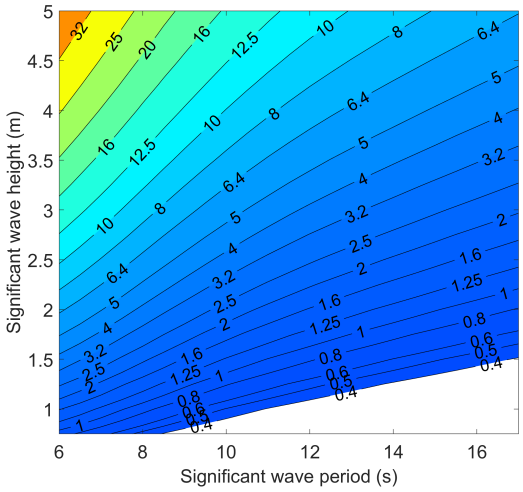

(b) Average power at turbine for mean tide (kW)

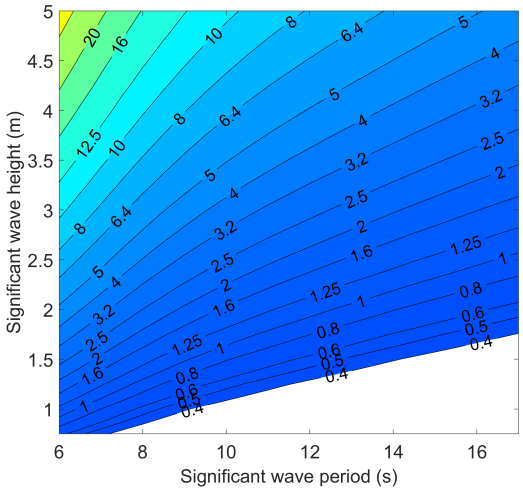

(c) Average power at turbine for low tide (kW)

Figure 8. Average power available at turbine for a polychromatic wave input of different standard height and period, for different tides.

run using a polychromatic wave input instead of the monochromatic sinusoidal wave used in section 3. To do so, a 1000 s sample was extracted from the measurements carried out in Mutriku's sea chamber. The high frequency components are filtered out to prevent unwanted noise. The sample is scaled to each of the wave height and period, and then used as the z_{sea} input to the model. The resulting average power and standard deviation of power matrices are respectively shown Fig. 8 and 9 for low, mean and high tides. For this work, the valve size was chosen big enough to be on the plateau of Fig. 5, and the turbine size was chosen close to the maximum efficiency of Fig. 6, (i.e. so that $C_T \times A_T = 0.01\ m^3$).

Although the actual values displayed in the power matrices in Fig. 8 are to be taken with caution considering the crudeness of the 1D model, it should be noted that the order of magnitude agrees with the measured electric power actually generated by a turbine in Mutriku as reported by Ibarra-Berastegi et al. (2018, 2021). The global trend for all tides shows the highest power outputs for waves with the smallest periods and the biggest heights. Indeed for these wave periods and heights, the air is pushed through the turbine more frequently and with a higher compression ratio. The three graphs are drawn with the same colour values so as to highlight the effect of the tide on the power. For all sea states, a higher tide results in a higher average power. This can be explained by a smaller sea chamber volume of air at higher tide which make the incoming wave comparatively bigger and thus more effective.

The standard deviation of power plotted Fig. 9 is an important indication of how much the available power fluctuates around the average since the turbine will not be able to adapt for each wave. A major advantage expected from the Closed-Cycle PTO is the smoothing of the power fluctuations. The standard deviation present the same variation as the power itself: it is higher for smaller wave periods, taller waves, and higher tide. It varies from half of the average power for the highest powers, to 1.4 times the power for the lowest ones.

4.3. Energy output

The matrix presented in Fig. 10 is the product of the wave climate matrix from Fig. 7 with the power matrix obtained for mean tide from Fig. 8(b), multiplied by 720 h i.e. the number of hours in a month. It indicates how much energy is expected to be produced by each sea state for a month of April in Mutriku according to the model, if the tide was constant at mean value. The sum of the matrix is 2067 kWh; it represents the total energy expected to be produced in that month. More than the values themselves, the distribu-

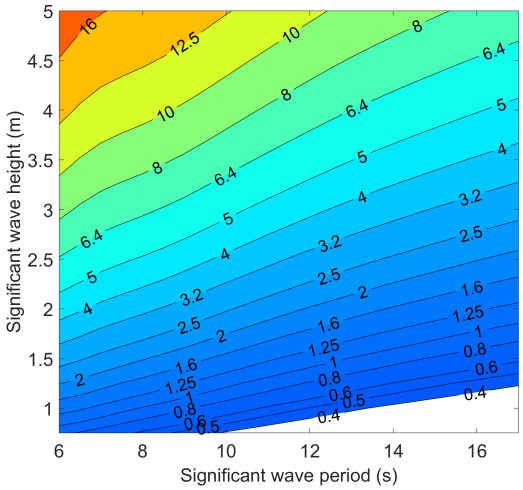

(a) Standard deviation of power for high tide (kW)

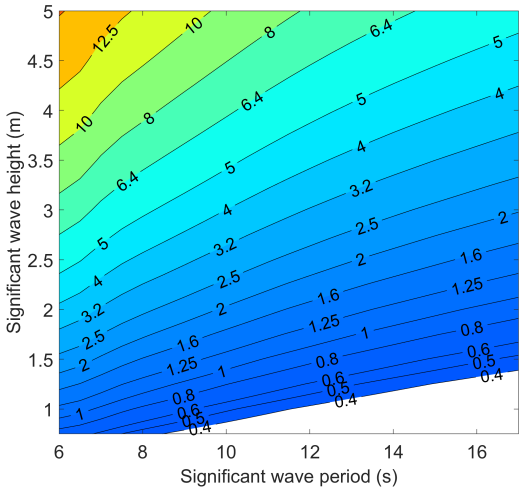

(b) Standard deviation of power for mean tide (kW)

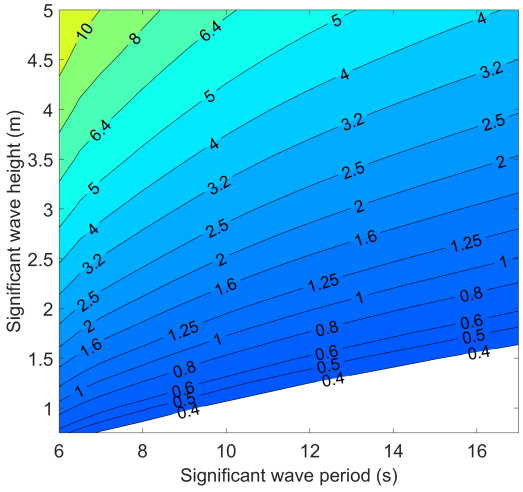

(c) Standard deviation of power for low tide (kW)

Figure 9. Standard deviation of power at turbine for a polychromatic wave input of different standard height and period, for different tides.

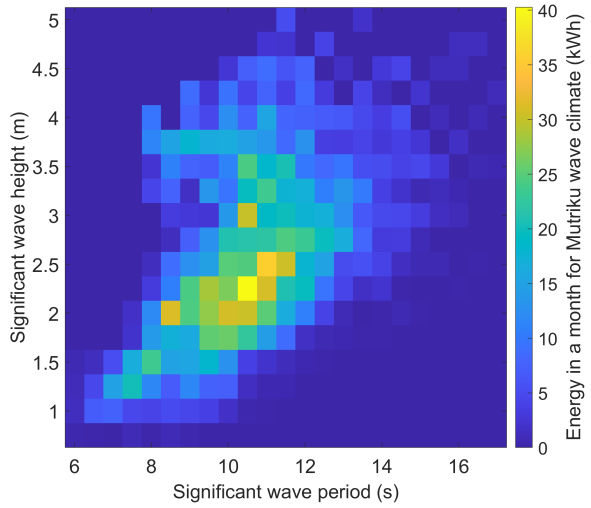

Figure 10. Energy produced in a month of April at mean tide for different waves in Mutriku.

tion of energy is an important result as it is in fact the design target of a suitable turbine for the CCPTO. For a constant low tide level, the average power would be 1.94kW; for mean tide it would be 2.87kW; and for high tide it would be 3.77kW. This suggests that while tide does affect the power production potential, the average power over the month will tend towards that obtained with constant mean tide.

5. CONCLUSION

In this article, a simple parameter model of the closed cycle power take off of an oscillating water column device has been presented and used to investigate the sensitivity of the power output of such a wave energy conversion system to geometric parameters and sea state variations. To settle the study in a concrete frame, the dimensions of the real-world Mutriku breakwater were used. By targeting this specific facility, the design space was constrained thus limiting the sizes of the sea chamber as well as the low and high pressure reservoirs. The sensitivity of the power output to the valve and turbine sizes was assessed using an ideal monochromatic wave input. It was found that a threshold exist for the valve size above which the power reaches a plateau; increasing the valves further is of no use. As for the turbine size, an optimal cross-sectional area exists. More realistic sea state conditions were then explored using polychromatic wave input extracted from measurements of the internal free surface height in Mutriku sea chamber. It was found that more power can be extracted for smaller wave periods, taller wave height and higher tide. Using the Mutriku wave climate calculated from measurements, a distribution of power expected to be produced for each Mutriku sea state was derived. This gives us a more accurate target for future turbine designs.

6. ACKNOWLEDGEMENT

The authors would like to acknowledge that part of their work was funded through the SEAI/RDD/495 Grant by the Sustainable Energy Authority of Ireland.

7. REFERENCES

P. Benreguig, V. Pakrashi, and J. Murphy. Assessment of primary energy conversion of a closed-circuit OWC wave energy converter. *Energies*, 12(10):1962, 2019.

H. Chun and K.D. Suh. Estimation of significant wave period from wave spectrum. *Ocean Engineering*, 163:609–616, 2018.

A.F.O. Falcão, J.C.C. Henriques, and L.M.C. Gato. Self-rectifying air turbines for wave energy conversion: A comparative analysis. *Renewable and Sustainable Energy Reviews*, 91:1231–1241, 2018.

F. Fusco, G. Nolan, and J.V. Ringwood. Variability reduction through optimal combination of wind/wave resources – an irish case study. *Energy*, 35(1):314–325, 2010.

J.C.C. Henriques, J.C.C. Portillo, L.M.C. Gato, R.P.F. Gomes, D.N. Ferreira, and A.F.O. Falcão. Design of oscillating-water-column wave energy converters with an application to self-powered sensor buoys. *Energy*, 112:852–867, 2016.

G. Ibarra-Berastegi, J. Sáenz, Al. Ulazia, P. Serras, G. Esnaola, and C. Garcia-Soto. Electricity production, capacity factor, and plant efficiency index at the mutriku wave farm (2014–2016). *Ocean Engineering*, 147:20–29, 2018.

G. Ibarra-Berastegi, A. Ulazia, J. Sáenz, P. Serras, S. J. González Rojí, Ganix Esnaola, and G. Iglesias. The power flow and the wave energy flux at an operational wave farm: Findings from mutriku, bay of biscay. *Ocean Engineering*, 227:108654, 2021.

M. Vicente, P. Benreguig, S. Crowley, and J. Murphy. Tupperwave - preliminary numerical modelling of a floating owc equipped with a unidirectioal turbine. In *Twelfth European Wave and Tidal Energy Conference*, 2017.

Flow-sound interactions

A PERFORATED PLATE SOLUTION TO MITIGATE RELIEF VALVE PIPING VIBRATION DUE TO FLOW-EXCITED ACOUSTIC RESONANCE

Juan P. Pontaza, Raghu G. Menon
Shell International Exploration and Production, Houston, Texas, USA

ABSTRACT

Piping systems with multiple closed side-branches are particularly liable to pressure pulsation due to acoustic resonances that are excited by flow instabilities in the piping system itself. The pressure pulsation can cause piping vibration problems which may in turn pose a threat to the structural integrity of the piping in terms of fatigue damage. This paper focuses on piping vibration due to flow excitation of acoustic resonant modes of multiple closed side-branches and its mitigation in an industrial setting.

Piping vibrations had been present in the relief valve (RV) take-off piping of the mixed refrigerant (MR) axial compressor discharge line in a liquefied natural gas (LNG) plant. The vibrations were present in three LNG trains with identical piping layout. Re-supporting and bracing of the piping did not mitigate vibration levels, which were observed to grow as the MR flow rate in the main line increased.

Fluid flow and acoustic numerical analyses were carried out to determine the root-cause of the piping vibrations and confirmed to be flow-excited acoustic resonance of the RV piping, revealing the acoustic coupling of multiple closed side-branches in series. A special design perforated plate solution was developed to mitigate the piping vibrations with no piping layout modifications. A digital evaluation, by means of computational fluid dynamics (CFD), was performed to verify that the proposed solution would mitigate the piping vibrations and to quantify the expected level of vibration mitigation.

Installation of the developed solution took place first in one LNG train and verified by measured vibration levels to work as intended, i.e., it mitigated the RV piping vibrations. The vibration mitigation solution was replicated in the other two LNG trains, with successful outcomes.

The solution involved the installation of a special design perforated plate above the tee-fitting throat at each of the RV take-offs to weaken the excitation velocity into the RV piping and attenuate acoustic pressure waves propagating into and out of the RV piping. The design is such that relief capacity is not compromised. A patent was granted for this 'industry-first' solution.

1. INTRODUCTION

In the energy industry, flow-induced vibration (FIV) of piping is recognized to be one of the major safety concerns which must be assessed in the design stage of piping systems. Although 'FIV of piping' is meant to be all-encompassing with respect to flow-excitation mechanisms in the above statement, sometimes FIV is associated with flow-induced turbulence only, e.g., piping vibration due to turbulent flow in a bend or a tee. Piping vibration due to flow excitation of acoustic resonant piping modes is known as acoustic-induced vibration (AIV) or as flow-induced pulsation. The term AIV is typically reserved for high frequency acoustic excitation, whereas flow-induced pulsation or flow-excited acoustic resonance is typically used for low frequency acoustic excitation. This paper focuses on piping vibration due to flow excitation of acoustic resonant modes of multiple closed side-branches and its mitigation in an industrial setting.

The flow in a pipe past the open mouth of a closed side-branch forms an unstable shear layer which induces velocity and pressure fluctuations. The unstable shear layer is a hydrodynamic excitation source which interacts with an acoustic resonant mode of the closed side-branch when the excitation frequency is close to an acoustic resonant frequency. Under flow-excited acoustic resonance conditions, a closed loop interaction is established between the unstable shear layer and an acoustic resonant mode which results in self-sustained pressure pulsations. The net gain of the closed loop over one pulsation cycle and the radiation losses determine the amplitude of the resulting pressure pulsation.

Self-sustained pressure pulsations due to an unstable shear layer and its closed loop interaction with an acoustic resonant mode in isolated and multiple closed side-branches has been studied extensively (Ziada, 2010; Tonon et al, 2011; Okuyama et al, 2012). This closed-loop interaction between the hydrodynamic and acoustic fields gives rise to the amplification of the dynamic head, which can result in strong pressure pulsations and associated piping vibration. The dynamic head amplification is further enhanced when multiple closed side-branches interact to form an acoustic resonator with small to negligible radiation losses. In the industrial setting, closed

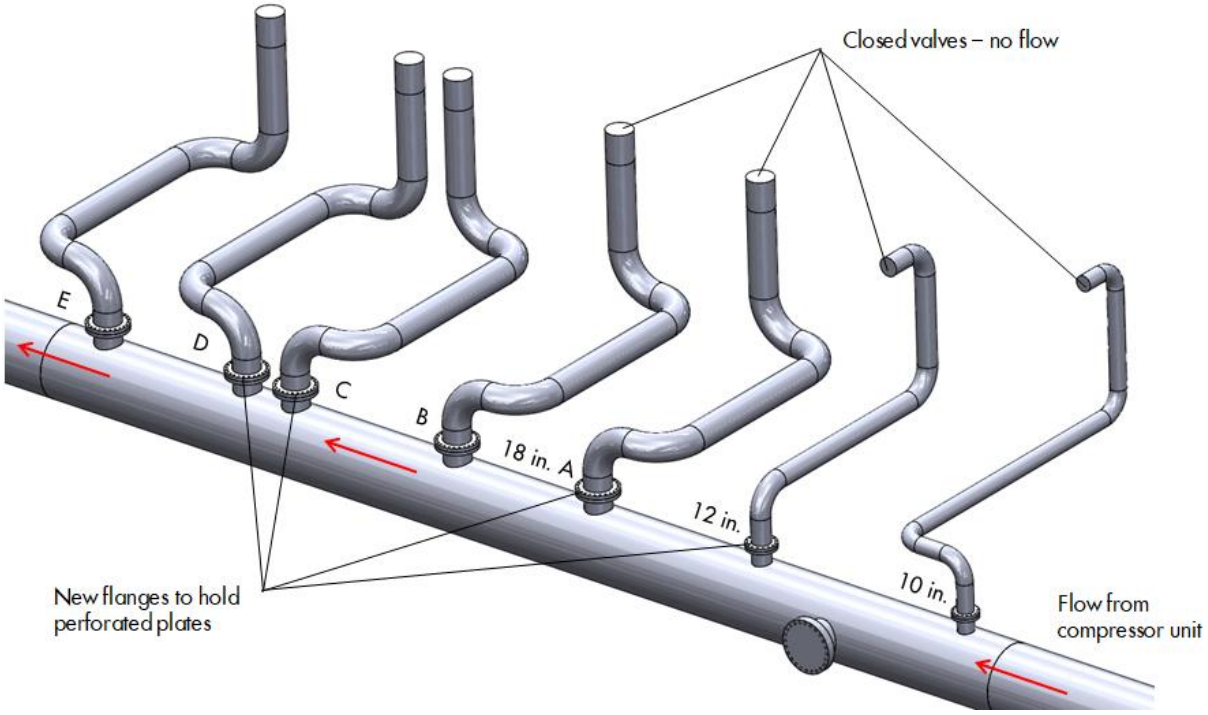

Figure 1. CAD model of the mixed refrigerant axial compressor discharge line.

side-branches are encountered in piping systems in the form of piping segments associated with normally closed by-pass loops or the inlet to safety relief valves.

The excitation mechanism causing this phenomenon is fairly well understood and the onset of resonance can be predicted for isolated closed side branches using, for example, the Energy Institute (EI) Avoidance of Vibration Induced Fatigue Failure (AVIFF) guidelines screening criteria (2008), or the design methodology described by Rogers (1992). Ziada (2010) developed Strouhal number charts to predict the onset of resonance for isolated, coaxial, and tandem closed side-branches; in addition, Graf and Ziada (2010) developed charts to estimate the amplitude of pressure pulsation for the coaxial and tandem configurations with sharp hard mouth edges. Unfortunately, these screening methodologies are not directly applicable to piping systems with multiple closed side-branches and consequently many of these piping systems are not flagged for correction or further analysis during the piping design stage.

2. THE VIBRATION PROBLEM

Low frequency vibration of the relief valve (RV) take-off piping of the mixed refrigerant (MR) axial compressor discharge line in a liquefied natural gas (LNG) plant was persistent and present in three LNG trains with identical piping layout. Piping vibration levels were especially pronounced in small-bore connection piping attached to the RV take-off piping, e.g., instrument tubing and fittings. Re-supporting and bracing of the RV piping did not mitigate the vibration.

Figure 1 shows a computer aided design (CAD) model of the MR axial compressor discharge line. A total of seven take-offs are positioned along the 48 in. header pipe as shown. Five take-offs of nominal size 18 in. relieve into a closed flare header in case of over-pressurization in the header pipe. These 18 in. RV take-offs are labeled as A through E in Figure 1 for reference throughout the paper. The other two take-offs have a nominal size of 10 in. and 12 in. and lead to a control valve and a manual valve to flare, respectively. During normal operation all these take-offs are closed side-branches. The flow direction in the header pipe is shown with red arrows in Figure 1. The relief valves, the small-bore connections attached to the RV piping, and piping supports are not shown in the CAD model.

Measured RV piping vibration frequency had a dominant peak at 7 Hz and vibration levels were observed to grow as the MR flow rate in the main line increased. When the MR flow rate exceeded a threshold value, measured vibration levels were flagged as problematic with reference to the Energy Institute AVIFF guidelines vibration velocity criteria (2008). To keep piping vibration levels at acceptable levels, MR flow restrictions were imposed with the unfortunate consequence of forcing a reduction in LNG production rates.

2.1. An initial assessment

An initial assessment was performed by assuming no interaction between the closed side-branches and by computing their quarter wavelength acoustic resonant frequency. The relevant parameters for the assessment are shown in Table 1. At a typical operating pressure of 17 bara and temperature of 63°C the speed of sound in the MR axial compressor discharge line is 362 m/s and the predicted quarter wavelength acoustic resonant frequencies for the 18 in., 12 in., and 10 in. closed side-branches are 9.25 Hz, 10.96 Hz, and 8.56 Hz respectively. These frequencies do not coincide with the measured RV piping vibration frequency of 7 Hz and deviate by +32%, +57%, and +22% respectively.

	d(mm)	d/D	L(m)	F_a(Hz)	F_s(Hz)
18 in.	435	0.368	9.78	9.25	9.83
12 in.	307	0.260	8.26	10.96	12.48
10 in.	257	0.218	10.57	8.56	14.08

Table 1. Closed side-branch parameters.

Working under the assumption of no interaction between the closed side-branches, the vortex shedding frequency into the side branches is estimated using the correlation in the screening methodology by Rogers (1992), given by $St = 0.413\ (d/D)^{0.316}$ for $Re > 1.6 \times 10^7$, where St is the Strouhal number and Re is the Reynolds number in the header pipe. At typical operating conditions the mean velocity in the header pipe is 14.2 m/s and the corresponding Reynolds number is 2.20×10^7. The computed vortex shedding frequencies into the 18 in., 12 in., and 10 in. closed side-branches are 9.83 Hz, 12.48 Hz, and 14.08 Hz respectively. These frequencies do not coincide with the measured RV piping vibration frequency of 7 Hz and deviate by +40%, +78%, and +101% respectively.

A screening check using the Energy Institute AVIFF guidelines (2008) criteria flags a high likelihood of pressure pulsation in all seven closed side-branches. The check is based on coincidence of the isolated side branch quarter wavelength acoustic resonant frequency (F_a in Table 1) and the vortex shedding frequency into an isolated closed side-branch (F_s in Table 1), with generous allowances for coincidence to make the screening conservative. It is likely that the EI AVIFF guidelines check was not performed or was not performed correctly during the design stage of this piping, which would have prompted more detailed analysis.

There is no analytic or closed form expression to estimate the acoustic resonant frequencies or the vortex shedding frequencies into the close side-branches in the piping layout shown in Figure 1 and we must resort to numerical methods to estimate these metrics which are necessary to establish the root cause of the piping vibrations.

The Strouhal number based on the observed peak vibration frequency of 7 Hz and the 18 in. closed side-branch inner diameter is 0.21. This value may appear low relative to the expected value of 0.30 to 0.50 for pressure pulsation in model scale experiments. However, it is in the range of observed values at the Ommen compressor station where pressure pulsation was present in the Strouhal number range of 0.13 to 0.42 (Tonon et al., 2009).

2.2. Root cause analysis: Acoustics

A numerical acoustic modal analysis of the RV take-off piping gave strong evidence of the root cause as flow excitation of acoustic resonant modes of the closed side-branches. The analysis results showed that multiple acoustic resonant frequencies involving individual and coupled RV take-offs exist, all in the range of 2-16 Hz, in particular a 7.1 Hz acoustic resonant mode which closely coincides with the 7 Hz peak frequency of measured vibration levels in the RV piping. This range of frequencies (2-16 Hz) coincides with the range of frequencies in which RV piping vibrations had been measured.

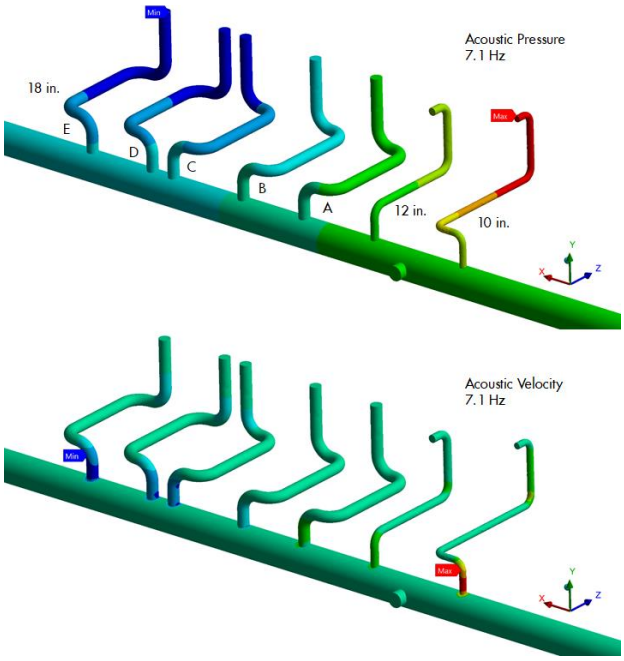

Figure 2. Acoustic resonant mode at 7.1 Hz.

In Figure 2, we plot acoustic pressure contours for the 7.1 Hz acoustic resonant mode. This mode couples the 10 in. RV take-off and 18 in. RV take-offs C, D, and E. Pressure anti-nodes are located at the closed end of these closed side-branches. Figure 2 also shows the acoustic velocity in the Y-direction, into the mouth of the closed side-branches. This

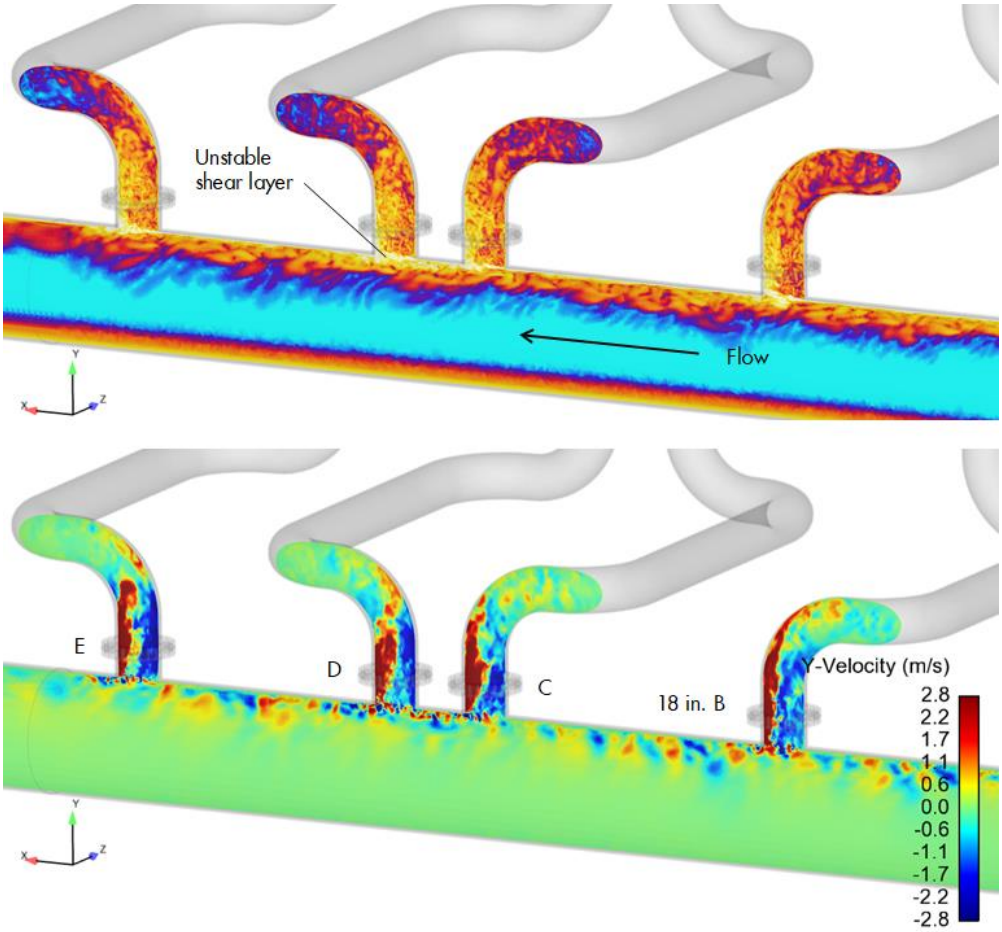

Figure 3. Instantaneous vorticity field (top panel) and crossflow velocity (bottom panel).

(7.1 Hz) acoustic mode has Y-velocity anti-nodes at the mouth of the 10 in. RV take-off and 18 in. RV take-offs C, D, and E.

Acoustic interactions between RV take-offs (i.e., coupling across multiple RV take-offs) may create an acoustic system with small acoustic radiation losses, leading to enhanced dynamic head amplification factors. These coupled systems are deemed highly problematic due to their capability of amplifying the dynamic head by several orders of magnitude.

2.3. Root cause analysis: Fluid flow

Computational fluid dynamics (CFD) was used to simulate fluid flow in the MR axial compressor discharge line. Flow in the header pipe (exiting the axial compressor) is gas phase only. A typical operating condition is selected for the simulation, with mean velocity in the header pipe of 14.2 m/s and a corresponding Reynolds number of 2.20×10^7 and a Mach number of 0.04.

The flow is modeled as three-dimensional, unsteady, turbulent, compressible gas. The turbulence was modeled using a Large Eddy Simulation (LES) approach. A suitable CFD mesh was constructed to resolve sufficiently small spatial flow scales for the use of the LES turbulence model. The cell size range in the mesh was 30 millimeters (maximum) and 0.7 millimeters (minimum), which resulted in a mesh cell count of 18 million cells. A control volume approach was used, with a bounded central difference scheme in space and second-order time stepping.

The time step size used for the CFD simulation was 1 millisecond, which is equivalent to a sampling rate of 1 kHz, and 100 seconds (1 minute and 40 seconds) of actual flow time was simulated. The frequency sampling rate and total simulation time are sufficient to resolve fluid flow temporal scales in the range 0.1 Hz to 100 Hz, which provides more than adequate coverage of the frequency range of expected flow excitation into the RV take-offs, i.e., the closed side-branches. We do not consider the CFD to be an aeroacoustics simulation, as the spatial and temporal resolution to resolve the acoustic scales is not sufficient to make such a claim.

Figure 3 (top panel) shows the instantaneous vorticity field on a cross-sectional planar cut along the header pipe center line depicting the unstable shear layers formed at the lips of the 18 in. RV take-offs.

Flow direction in the header pipe is shown with the black arrow. Flow separates at the lips of the RV take-offs, and vortices are shed off the lips. The separated shear layer impinges on the downstream side of the RV pipe and induces re-circulating flow in the branch pipe.

Figure 3 (bottom panel) shows instantaneous crossflow velocity (Y-velocity component) with contour limits corresponding to ±20% of the mean header pipe velocity. This plot visually quantifies the level of disturbance at the RV take-off mouths, and one can appreciate it is significant, i.e., ±20% of the mean header pipe velocity is significant.

Virtual probes are placed at each of the seven RV take-off mouths, where pressure and mass flux through the cross-section of each RV take-off mouth is recorded in time. The pressure is the instantaneous surface averaged value over a cross-section just above the RV take-off mouth. The net mass flux into an RV take-off mouth is zero, as there is no net mass flux into the RV take-off during normal operation; this is confirmed by time traces of the recorded metric. However, we are interested in the pressure fluctuations and mass flux fluctuations and their frequency content, which are indicators of dynamic excitation to the RV piping.

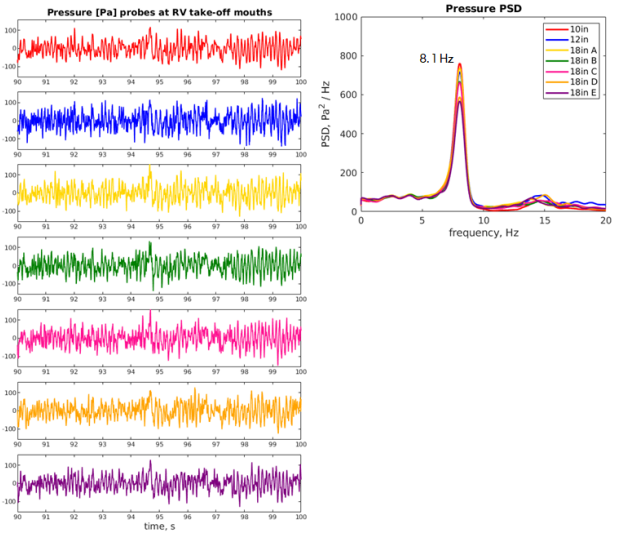

Figure 4. Time histories and PSD of pressure.

The recorded time history of pressure at each of the RV take-off mouths is shown in Figure 4. Although a full 100 seconds of flow data was recorded, we only show in Figure 4 data for a time interval of ten seconds. The frequency content of each of the signals is interrogated by computing the power spectral density (PSD) of the time traces – which are also shown in Figure 4 for all signals. We plot the PSD of all the signals in the range of 0-20 Hz, which covers the range of observed piping vibration frequencies and the range of RV take-off piping acoustic resonant frequencies.

The predicted pressure PSDs shows a single well-defined peak at 8.1 Hz, which is close to the 7.1 Hz frequency of the predicted resonant acoustic mode shown in Figure 2 and the 7 Hz peak frequency of measured RV piping vibration. This confirms the root cause of the RV piping vibration as flow-induced pulsation.

The radius of curvature at the inlet of all the side branches was taken as 5 mm in the CFD model, whereas it is much larger in the actual take-off tees; between 0.08d to 0.12d, where d is the inner diameter of the side-branch and is given in Table 1. This explains the departure in the predicted peak frequency of 8.1 Hz from the expected peak frequency of 7 Hz. With a larger rounded edge, the predicted shedding frequency would be lower due to the longer vortex path. A sensitivity study on the effect of the radius of curvature on the peak pressure frequency was not performed.

The CFD is not an aeroacoustics simulation and thus could not predict the lock-in of the hydrodynamic pressure and the acoustic pressure fields, nor the associated dynamic pressure amplification. Nevertheless, the acoustic and fluid flow numerical simulations were enablers in establishing the root cause of the vibrations.

3. VIBRATION MITIGATION: A PERFORATED PLATE SOLUTION

Vibration mitigation is achieved by detuning the acoustic resonant frequency from the flow excitation frequency and/or vice versa. For instance, a piping layout modification that would change the positioning of the valves to modify the RV piping acoustic resonant frequencies would qualify as a vibration mitigation strategy. A piping layout modification to add dummy piping to act as an acoustic silencer, or a piping layout modification to radically change the RV piping flow paths, or a header pipe modification to enlarge the mouth of the RV take-offs, would also qualify as a vibration mitigation strategy. These strategies, however, while potentially valid, have a high uncertainty in the likelihood of vibration mitigation, in that the likelihood of success is difficult to quantify. In addition, all these strategies would require an extended LNG train shutdown time for implementation, well beyond what is typically allocated in a planned turnaround time window – implying high cost and high risk. A vibration mitigation solution that requires no piping layout modifications and no header pipe modifications, short installation time, with a (quantifiable) high likelihood of success is

ideal and preferable. A perforated plate solution fulfills these requirements and was selected as the preferred vibration mitigation solution.

The spoilers in the work by Bruggeman et al. (1991) and the inserts by Jungowski and Studzinski (1989) were given consideration but were found not fit for purpose in this industrial setting. The implementation of the spoilers by Bruggeman et al. (1991) require installation or attachment of the spoilers along the header pipe, when no modifications to the header pipe were one of the site requirements. In addition, these spoilers would not be easily retrieved for inspection or replacement if found not effective and would act as debris in the header pipe if they become detached. Along similar lines, the installation of the Jungowski and Studzinski (1989) inserts posed difficulties; due to their shape and recommended positioning they would have to be welded in place at the mouth of the RV take-offs and would not be easy to replace or retrieve if not effective.

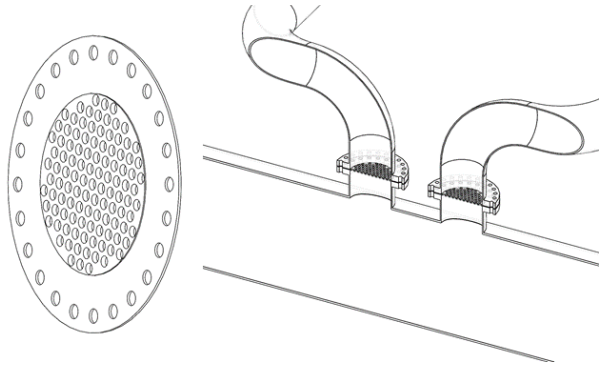

Figure 5. Type 1 (uniformly perforate) plate.

The perforated plate solution requires the installation of a single perforated plate at each of the RV take-offs close to the RV take-off mouth, as shown in Figure 5. The perforated plates act as a physical barrier that weakens the acoustic velocity of the acoustic mode across the closed side-branches and aim to decouple the closed side-branches by weakening their interaction to attenuate the pressure pulsation amplification. In addition, when installed close enough to the RV take-off mouth, the perforated plate modifies the flow excitation frequency into the closed side-branch. Thus, the likelihood of vibration mitigation was deemed high for the perforated plate solution in view of its ability to simultaneously modify the acoustic and flow fields. This solution requires no piping layout modifications and no header pipe modifications but does require the flanging of the branch pipe to hold the perforated plate (see Figure 1 and Figure 5).

Additional criteria considered to arrive at a final perforated plate design included the following. Minimize net free area (% open area) while ensuring that flow does not choke and pressure drop is acceptable under relief conditions. Under extreme conditions (i.e., at relief start-up), ensure that the plate will withstand flow-induced loads and flow will not choke. Ensure that the structural natural frequencies of the plate are well removed from flow-excited frequencies.

Before committing to fabricate and install the perforated plates, it was decided to evaluate their expected performance to quantify the level of vibration mitigation. A digital evaluation was preferred over physical testing as physical testing at the model scale would require considerable lead time, including finding a laboratory facility with the right expertise and equipment, model scale fabrication and set-up time. The advantages of digital testing included the ability to test at actual scale for actual operating conditions at a fraction of the lead time for physical model testing.

The digital evaluation revealed that uniformly perforated plates (shown in Figure 5) were effective but only marginally, as they still allowed flow excitation into the RV piping primarily through the first and second rows of orifices adjacent to the downstream wall of the RV take-off. The design was improved by closing off these orifices and placing a lip on the under-belly of the plate to re-direct and spread the shear layer away from the orifices. This special design perforated plate was awarded a patent (Menon and Pontaza, 2021) and is shown in Figure 6. These perforated plates are sensitive to the installation orientation and are to be installed such that the closed-off orifices are positioned downstream of the flow direction in the main pipe.

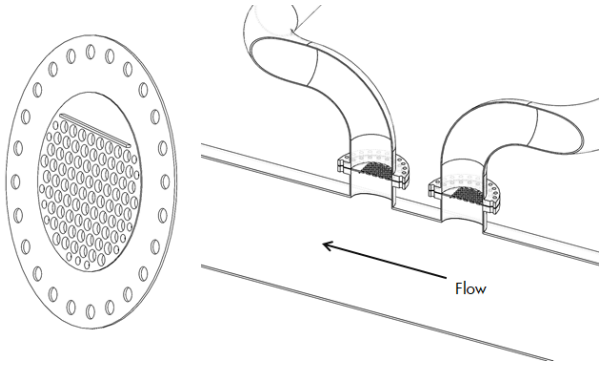

Figure 6. Type 2 (special design) perforated plate.

The uniformly perforated plates are referred to in this paper as Type 1 perforated plates and the special design perforated plates as Type 2 perforated plates. The orifices in the Type 2 plate shown in Figure 6 are sized to match the percent open area of the Type 1 plate shown in Figure 5. In the next section we present an evaluation of the Type 2 plates by comparing against the baseline case of no plates.

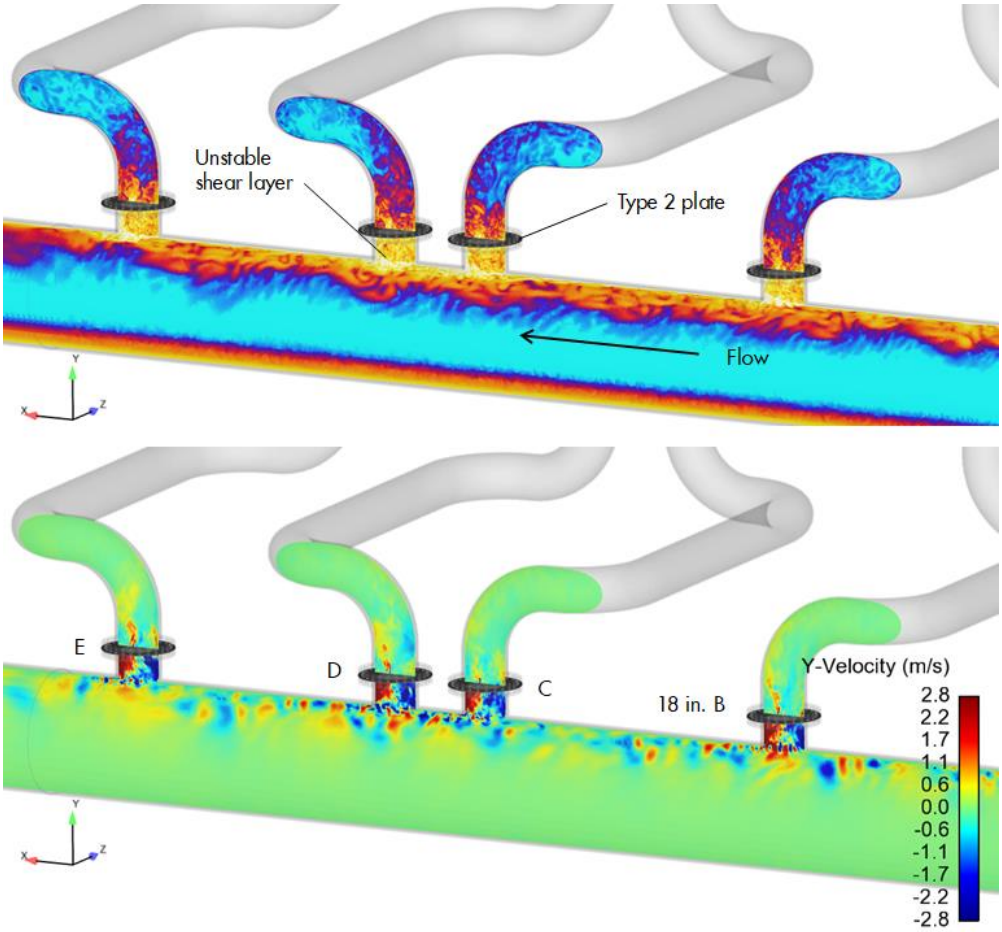

Figure 7. Instantaneous vorticity field (top) and crossflow velocity (bottom) with Type 2 plates installed.

4. EVALUATION OF THE PERFORATED PLATE SOLUTION

Figure 7 shows instantaneous vorticity (top panel) and instantaneous crossflow velocity (bottom panel) on a cross-sectional planar cut along the header pipe center line when Type 2 plates are installed between the flanges.

We see from Figure 7 that the flow excitation into the RV piping is significantly reduced with Type 2 plates relative to the baseline case (no plates) shown in Figure 3 for the same instantaneous flow metrics. The vorticity intensity into the RV piping is reduced with Type 2 plates installed, which appear as no white colored vortical flow features penetrating above the plate in Figure 7 (top panel). The disturbance magnitude into the RV piping is significantly mitigated by the Type 2 plates, as seen by the low magnitude of crossflow velocity above the plate in Figure 7 (bottom panel).

The flow metric contours in Figure 7 provide an instantaneous snapshot in time and already show a significant improvement over the baseline case. Although informative, Figure 7 is not well suited to rigorously assess the effectiveness of the Type 2 plates relative to the baseline case. A suitable metric to draw a comparison is presented in Figure 8 in the form of contour plots of standard deviation of velocity magnitude computed using flow statistics over a 45-second time window. The scale limit is set to a maximum of 10% of the mean header pipe velocity. The metric quantifies the departure from the mean velocity by one standard deviation and in essence quantifies fluctuating velocity magnitude.

We see from Figure 8 that the velocity fluctuations above the Type 2 plates are significantly reduced (bottom panel), relative to the baseline case of no plates (top panel). Below the perforated plates, the velocity fluctuations are essentially identical to the baseline case, as expected.

Virtual probes are placed at each of the seven RV take-off mouths (100 mm above the Type 2 plates), where mass flux through the cross-section of each RV take-off mouth is recorded in time. We are interested in the mass flux fluctuations and their frequency content, which are the dynamic excitation

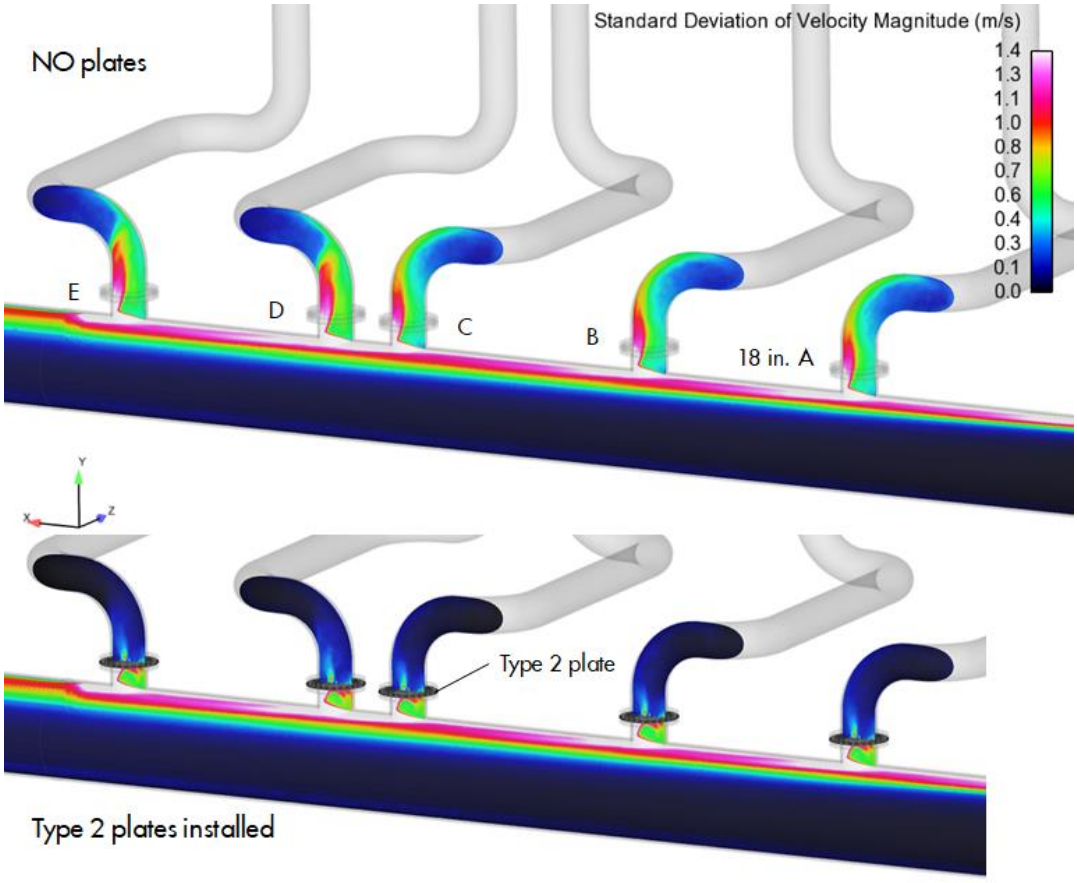

Figure 8. Standard deviation of velocity magnitude contours. Baseline case (top panel) of no plates and with Type 2 plates installed (bottom panel).

source to the RV piping and linked to the root cause of the dynamic head amplification and piping vibrations. The frequency content of each of the signals is interrogated by computing the PSD of the time traces.

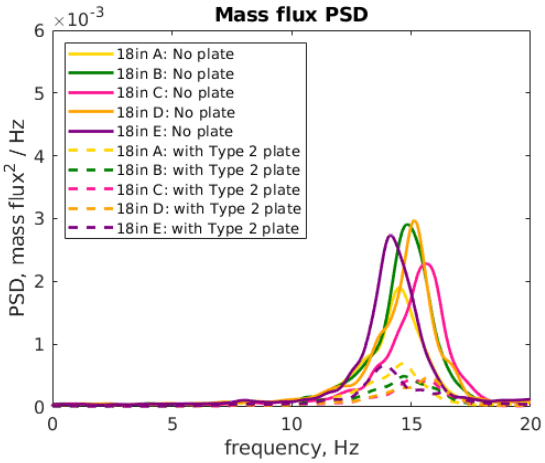

Figure 9. PSDs of RV take-off mass flux.

We plot in Figure 9 the mass flux PSD at all 18 in. RV take-offs in the range of 0-20 Hz, which is the range of observed piping vibration frequencies and the range of RV take-off piping acoustic resonant frequencies. The baseline (no plates) curves are plotted with a solid line and the Type 2 plate curves are plotted with a dashed line. It is clear from Figure 9 that there is substantial reduction in excitation energy content when Type 2 plates are installed.

To quantify the reduction in excitation energy, we compute the ratio of energy content in the range of 0-20 Hz for each of the curves. Effectively, this is the ratio of the area under each of the curves in Figure 9. We find that the excitation energy is reduced by a factor of 5 when installing Type 2 plates (an 80% reduction).

The excitation energy (area under the curve) has units of mass flux squared or $(\rho U)^2$. Based purely on energy scaling arguments, we would expect vibration levels to be affected by the same factor, i.e., reduced by a factor of 5 when installing Type 2 plates. This reduction in vibration level estimate does not consider acoustic attenuation due to the acoustic energy dissipation that occurs at the orifices (i.e., an excitation source sink). Thus, it is likely that vibrations

would be reduced further – beyond the factor of 5 estimated here. The predicted and expected level of vibration reduction was good enough to commit resources to fabricate and install the perforated plate solution in one LNG train as a trial.

5. FIELD INSTALLATION OF THE PERFORATED PLATE SOLUTION

The perforated plate solution was installed in one LNG train during a scheduled maintenance shutdown in 2016. Flanges were installed at all the RV take-offs to hold the perforated plates. Figure 10 shows photographs taken during the installation of the flanges and the Type 2 perforated plates.

Figure 10. Installation of the flanges at the RV take-offs to hold the Type 2 perforated plates.

The perforated plate solution mitigated the RV piping vibrations, confirmed by measured vibration levels. In view of the successful outcome, the vibration mitigation solution was replicated in the other two LNG trains (with identical piping layout) during scheduled maintenance shutdowns in 2017 and 2018 respectively. The RV piping vibrations were also mitigated in these other two LNG trains. In view of the RV piping vibration mitigation, the MR flow restrictions were lifted, and LNG production rates are now only limited by feed gas availability.

Figure 11 shows measured RV piping vibration levels pre and post installation of the Type 2 perforated plates in one of the LNG trains. The plot shows vibration velocity RMS in units of mm/s and peak vibration frequency at each measurement location, displayed on the Energy Institute Guidelines (2008) vibration velocity chart. The abscissa marks the dominant frequency (or peak frequency in the measured spectrum) and the ordinate marks the square-root of the area under the measured vibration velocity spectrum.

Five measurement locations are shown, corresponding to the maximum vibration level recorded at the RV deck piping for each of the five 18 in. RV take-offs. The plot shows clear evidence of vibration mitigation by the perforated plate solution. We see from the plot that the predicted factor of 5 in vibration reduction was realized and exceeded, with vibration level reduction close to a factor of 10. The MR flow rate for the pre and post installation vibration measurements shown in Figure 11 is approximately the same, with the post-installation MR flow rate being 4% higher relative to the pre-installation MR flow rate.

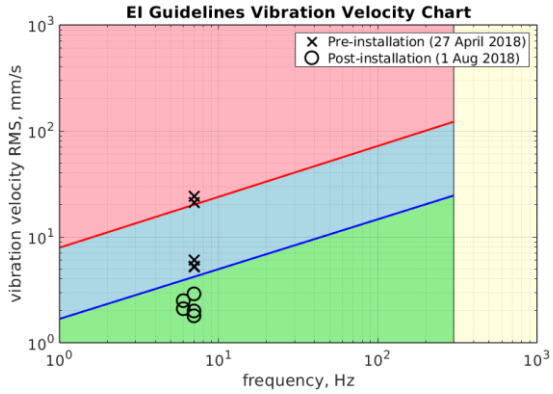

Figure 11. RV piping vibration measurements pre and post installation of the Type 2 perforated plates, showing vibration mitigation.

6. SUMMARY AND CONCLUDING REMARKS

RV piping vibration mitigation due to flow-excited acoustic resonance in an LNG plant piping system with multiple closed side-branches was achieved by a perforated plate solution. The perforated plate solution required the installation of a single perforated plate at each of the RV take-offs close to the RV take-off mouth. The design is such that relief capacity is not compromised.

The perforated plate acts as a physical barrier that weakens the excitation velocity into the RV piping and attenuates acoustic pressure waves propagating into and out of the RV piping. The plates aim to decouple the closed side-branches by weakening their interaction to attenuate the pressure pulsation amplification. It is likely an industry first, there being no open literature record of a perforated plate being implemented for this purpose.

Prior to fabrication and installation, a digital evaluation of the perforated plate solution was executed by means of CFD to quantify the expected level of vibration mitigation. The digital evaluation revealed that uniformly perforated plates (Type 1 plates) were effective but only marginally, which resulted in the development of special design perforated plates (Type 2 plates) featuring selected rows of closed-off orifices and a lip in the under-belly of the plate to re-

direct and spread the shear layer away from the orifices. Vibration level reduction by a factor of 5 or better was predicted for the Type 2 perforated plates. Post-installation field vibration measurements confirmed mitigation of the RV piping vibration with reduction factors as high as 10.

7. REFERENCES

Bruggeman J.C., Hirschberg A., van Dongen M.E.H., Wijnands A.P.J., 1991, Self-sustained aeroacoustic pulsations in gas transport systems: Experimental study of the influence of closed side branches. *Journal of Sound and Vibration* **150**(3): 371-393.

Guidelines for the Avoidance of Vibration Induced Fatigue Failure in Process Pipework, 2008, Energy Institute, 2nd Edition, London.

Graf H.R., Ziada S., 2010, Excitation source of a side-branch shear layer. *Journal of Sound and Vibration* **329**: 2825-2842.

Jungowski W.M., Studzinski W., 1989, Dampening pressure pulsations in piping systems. *United States Patent* US 4867190.

Menon R.G., Pontaza J.P., 2021, Piping system. *United States Patent* US 11118714 B2.

Okuyama K., Tamura A., Takashi S., Ohtsuka M., Tsubaki M., 2012, Flow-induced acoustic resonance at the mouth of one or two side branches. *Nuclear Engineering and Design* **249**:154-158.

Rogers L.E., 1992, Design stage acoustic analysis of natural gas piping systems in centrifugal compressor stations. *ASME Journal of Engineering for Gas Turbines and Power* **114**:727-736.

Tonon D., Nakiboglu G., Willems J.F.H., Hirschberg A., Leandro R.E., Polifke W., Riezebos H.J., 2009, Self-sustained aeroacoustic oscillations in multiple side branch pipe systems. *15th AIAA/CEAS Aeroacoustics Conference*, AIAA 2009-3262.

Tonon D., Hirschberg A., Golliard J., Ziada S., 2011, Aeroacoustics of pipe systems with closed side branches. *International Journal of Aeroacoustics* **10**: 201-276.

Ziada S., 2010, Flow-excited acoustic resonance in industry. *ASME Journal of Pressure Vessel Technology* **132**.

NOMENCLATURE

d	side-branch inner diameter
D	header pipe inner diameter
F_a	acoustic resonant frequency
F_s	vortex shedding frequency
L	closed side-branch length
Re	Reynolds number
St	Strouhal number
U	velocity
ρ	density

LIST OF ABBREVIATIONS

AIV	Acoustic-Induced Vibration
AVIFF	Avoidance of Vibration Induced Fatigue Failure
CAD	Computer Aided Design
CFD	Computational Fluid Dynamics
EI	Energy Institute
FIV	Flow-Induced Vibration
LES	Large Eddy Simulation
LNG	Liquified Natural Gas
MR	Mixed Refrigerant
PSD	Power Spectral Density
RMS	Root Mean Squared
RV	Relief Valve

ARTICULATED BEAM BEHAVIOUR UNDER GRAZING FLOW

ABILY Thibault, HUMBERT Thomas & AUREGAN Yves
Laboratoire d'Acoustique de l'Université du Mans (LAUM), UMR 6613, Institut d'Acoustique - Graduate School (IA-GS) - CNRS, Le Mans Université, France

ABSTRACT

In recent years, new concepts of efficient low-frequency acoustic absorbers have been developed. In particular, treatments using moving parts are being studied. Among several types of structures, those with fine slits are investigated in this paper. At the top of a cavity, a flexible beam is surrounded by a fine slit with a high resistance to air flow. This system produces a strong acoustic effect in the vicinity of the resonance frequency of the beam, which can be adjusted to very low frequencies. In this paper, the system is mechanically and acoustically characterised under normal incidence in order to be compared with an analytical model. An array of these beams is mounted in the wall of a rectangular duct. The effect of grazing flow on the acoustic behaviour is studied as a function of Mach number.

1. INTRODUCTION

The search for low frequency acoustic performance of an absorber with a small thickness remains a challenge at the moment. As a result, several new sound absorber concepts for the reduction of low-frequency noise have been developed in recent years.

A technology based on perforated liners is commonly used in aeronautics. These conventional local feedback absorbers consist of a perforated plate coupled to a back cavity (honeycomb structure) which creates almost a quarter wavelength resonator with a resistive layer formed by the perforated top plate. In fact, the resonance frequency is somewhere between the quarter-wavelength resonator ($f_r = c_0/4e_p$, with c_0 the speed of sound and e_p the height of the cavity) and the Helmholtz resonator ($f_r = c_0/2\pi\sqrt{\sigma/e_p e_h}$ where σ is the ratio of the holes area to the total area (open area ratio) and e_h is the effective thickness of the perforations). However, these technologies seem to present difficulties to achieve a sufficient efficiency at low frequencies without exceeding a given space requirements. To overcome this, different avenues can be explored.

Several passive metamaterial structures have recently been investigated, such as space-coiling structures [11, 8], slow-sound materials [5], Helmholtz resonators [4, 17] and membrane absorbers [16, 10]. As the effective frequency bandwidth of these solutions is usually small, several resonators are often combined in series, in parallel or both [24].

A second approach is based on active control systems by the use of an electro-mechanical transducer. Those devices allow the conversion between different physics such as mechanical, acoustics and electronics to overcome some limitations. Reaching lower frequencies in acoustics means increasing the size of the system, which is not usually the intention. However, in the mechanical field, this means reducing the stiffness or increasing the inductance in electronics, without affecting the dimensions of the system. Different control strategies, depending on the transduction have been studied ([14], [13], [7]) but recently the interest is much more focused on the moving part of the transducer [15].

Indeed, D'Elia et al. [12] show the possibility to reach low frequency performances by using a thin mechanical structure surrounded by thin slits. Those slits will allow the motion of the mechanical part but also will have an impact on the impedance. The present paper deals with the concept of cantilevered thin lamellas that can vibrate above a cavity. First, a simple analytical model is proposed to predict the behavior of the lamella in normal incidence. Then, a last set of experiments performed in a grazing flow with several lamellas will present some unique results in term of possible application of aircraft noise reduction.

2. SYSTEM CONSIDERED

The system considered in this paper is a lamella cut from a thin 0.2 mm thick titanium plate. The slits formed by the cuts are 50 μm wide. The lamella is then coupled to a rectangular cavity with fillets on the corner due to the manufacturing process. The height of the cavity can be adapted according to the number of layers applied behind it (Fig. 1). All the parameters and notations are reminded in Tab. 1. For the grazing incidence configuration, this cell will be repeated 15 times over a rectangular area as presented later.

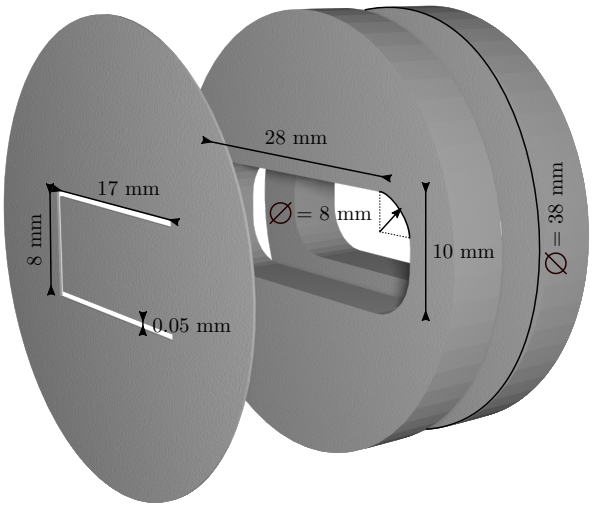

Figure 1. 3D sketch of the system used in impedance tube with the lamella plate and a multiple back-end rectangular cavity compressed together.

Lamella length	l_b	17 mm
Lamella width	d_b	8 mm
Lamella thickness	e_b	0.2 mm
Young modulus (titanium)	E	115 GPa
Poisson coefficient (titanium)	ν	0.3
Mass density (titanium)	ρ_b	4506 $kg.m^3$
Slit width	w_s	50 μm
Slit length 1	l_{s1}	l_b
Slit length 2	l_{s2}	$d_b + 2w_s$
Slit thickness	e_s	0.2 mm
Cavity width	w_{cav}	28 mm
Cavity depth	d_{cav}	10 mm
Cavity height	h_{cav}	Variable

Table 1. Table of the notations and values of the geometric parameters of the considered system.

3. SYSTEM MODELLING

In this section the acoustic impedance of a unit cell is expressed analytically. To this end, the mechanical impedance of the lamella is first computed. Then, the Transfer Matrix Method (TMM) is used to compute the impedance of a single cell made of the lamella in parallel with micro slits that radiate into a cavity. Adapted formulations for visco-thermal losses and radiation are given.

3.1. Lamella modelling

The n-th resonance frequency of a beam in flexion can be expressed according to Eq. 1 (Rao [19]) and in torsion (Van Eysden et al [22]). The beam in the present case has the dimensions presented in Tab. 1 and is made of titanium. In view of these dimensions it is more correct to call it a lamella rather than a beam. By taking the geometrical parameters, it is possible to calculate the bending (Eq. 1) and the torsional resonance frequencies (Eq. 2) of the lamella.

$$f_{rn} = \frac{(\beta_n)^2}{2\pi}\sqrt{\frac{E{e_b}^2}{12\rho_{Ti}{l_b}^4}} \tag{1}$$

where $\beta_1 = 1.875$, $\beta_2 = 4.694$, $\beta_3 = 7.855$, ...

$$f_{rn} = \frac{2n-1}{4l_b}\sqrt{\frac{2E{e_b}^2}{\rho_{Ti}{d_b}^2}(1-\nu)} \tag{2}$$

These computed beam resonance frequencies have also been compared to the measured one with a Polytech Scanning Vibrometer and an acoustic excitation. This type of measurement also makes it possible to find the modal damping parameters defined by δ_s. The computed and measured natural frequencies in Tab. 2 differ by a reasonable amount. This is probably due to a slight strain during the experimental handling.

f_r comp	f_r exp	δ_s	
566 Hz	462 Hz	0.003	bending
2303 Hz	2331 Hz	0.86	bending
3549 Hz	2875 Hz	0.20	torsional

Table 2. Bending and torsional resonance frequencies of a cantilever beam. Comparison between computed and experimental results with the structural damping.

Then, the mechanical impedance of the beam can be expressed as a sum of a n degrees of freedom (DOF) system weighted by the structural damping

coefficient δ_s, depending on the natural angular pulsation of the lamella ω_b and a effective thickness $e\prime_b = 4\rho_b e_b/(3\rho_0)$ (with c_0 and ρ_0 respectively the speed of sound and the mass density of air) (D'Elia et al. [12]). This impedance (Eq. 3) can also be expressed in the transfer matrix formalism (Eq. 4).

$$Z_m = \left[\sum\left[j\frac{\omega}{c_0}e\prime_b\left(1-\frac{\omega_b^2}{\omega}\right)+\delta_s\right]^{-1}\right]^{-1} \quad (3)$$

$$T_{meca} = \begin{pmatrix} 1 & Z_m(\omega) \\ 0 & 1 \end{pmatrix} \quad (4)$$

3.2. Acoustic impedance determination

In order to compute the impedance of the cell, a transfer matrix method (TMM) is used. It is a 2D method that allows to describe a system by an assembly of several waveguides. Those waveguides can be interpreted with a specific matrix defined to link the acoustic pressure (p) and mass flux (w) inlet (p_{in} and w_{in}) and outlet (p_{out} and w_{out}). Then, all the matrices of the waveguides composing the system are multiplied together to obtain the whole transfer matrix of the system. The three slits matrices will be considered in parallel with the transfer matrix of the lamella. Since the system is closed by a rigid wall at the end, it is possible to express the acoustic impedance $Z_{ac} = p_{in}/w_{in}$ according to the acoustic pressure (p) and mass flux (w) inlet (p_{in} and w_{in}) and outlet (p_{out} and w_{out}) in Eq. 5.

$$\begin{pmatrix} p_{in} \\ w_{in} \end{pmatrix} = \begin{pmatrix} T_{11} & T_{12} \\ T_{21} & T_{22} \end{pmatrix}\begin{pmatrix} p_{out}=1 \\ w_{out}=0 \end{pmatrix} \quad (5)$$

3.3. Waveguide formulation

The behaviour of a waveguide can be expressed using the Eq. 6. This can be written as follows, considering an acoustic duct of length l_w, a radius r_w and cross section S_w into a specific characteristic impedance $Z_{c_s} = \rho c/S_w$ (Eq. 7) where ρ is the mass density, c is the velocity of the medium, the imaginary number is $j^2 = -1$ and the wave number k. Then, a slit or a cavity can be expressed using the same expression. The difference will be on the visco-thermal losses and radiation modelling.

$$\begin{pmatrix} p_{in} \\ w_{in} \end{pmatrix} = \underbrace{\begin{pmatrix} T_{11} & T_{12} \\ T_{21} & T_{22} \end{pmatrix}}_{\mathbf{T}}\begin{pmatrix} p_{out} \\ w_{out} \end{pmatrix} \quad (6)$$

$$\mathbf{T} = \begin{pmatrix} \cos(kl_w) & jZ_{c_s}\sin(kl_w) \\ j/Z_{c_s}\sin(kl_w) & \cos(kl_w) \end{pmatrix} \quad (7)$$

3.4. Radiation / End correction

The end correction l_{cor_L} proposed by Kergomard et al [18] is used in order to take into account the radiation phenomena from a changing cross section (Eq. 8). A slight modification of this expression has been made in order to overcome the changing cross section from circular to rectangular waveguide.

In that way, the perimeter ratio $P = P_1/P_2$ and the hydraulic diameter D_H are used. The hydraulic diameter is defined as $D_H = (2a_w b_w)/(a_w + b_w)$ for a rectangular duct and $D_H = D_w$ for a circular one, where a_w and b_w represent the edge dimensions of a rectangular cross-section waveguide and D_w the diameter of a circular one.

$$l_{cor_L} = 0.82\left[1-1.35\left(\frac{P_1}{P_2}\right)+0.31\left(\frac{P_1}{P_2}\right)^3\right]\frac{D_H}{2} \quad (8)$$

3.5. Visco-thermal losses

The losses are taken into account using the Stinson model [21] based on Allard et al [3] theory, as shown below for both circular and rectangular ducts and slits. The following relations will express the effective mass density ρ and the bulk modulus κ inside the guide, which are related to the wavenumber $k = \omega\sqrt{\rho/\kappa}$ and the specific impedance $Z_c = \sqrt{\rho\kappa}/S_w$ for a time convention of $e^{-j\omega t}$ for the increasing x.

Circular duct:

For a circular duct, the mass density and the bulk modulus are given by Eqs. 9 & 10.

$$\rho_c = \frac{\rho_0}{(1-G_1/G_\rho)} \quad (9)$$

$$\kappa_c = \frac{\kappa_0}{1+2(\gamma-1)G_2/G_\kappa} \quad (10)$$

where κ_0 is the bulk modulus, γ the specific heat ratio, Pr the Prandtl number, μ the dynamic viscosity, J_n the Bessel's function of n order, $G_1 = J_1(G_\rho r_w)/(J_0(G_\rho r_w)r_w)$, $G_2 = J_1(G_\kappa r_w)/(J_0(G_\kappa r_w)r_w)$, $G_\rho = \sqrt{-j\omega\rho_0/\mu}$ and $G_\kappa = \sqrt{-j\omega\rho_0 Pr/\mu}$.

Rectangular duct :

For a rectangular duct, the mass density and the bulk modulus are given by Eqs. 11 & 12.

$$\rho_r = \frac{\rho_0 {a_w}^2 {b_w}^2}{4G_\rho^2 \sum_{n=0}^{\infty}\sum_{m=0}^{\infty}\left[\alpha_n^2\beta_m^2\left(\alpha_n^2+\beta_m^2-G_\rho^2\right)\right]^{-1}} \quad (11)$$

$$\kappa_r = \frac{\kappa_0}{\gamma + \frac{4(\gamma-1)G_\kappa^2}{{a_w}^2{b_w}^2}\sum_{n=0}^{\infty}\sum_{m=0}^{\infty}\left[\alpha_n^2\beta_m^2\left(\alpha_n^2+\beta_m^2-G_\kappa^2\right)\right]^{-1}} \quad (12)$$

where the constants $\alpha_n = 2(n+0.5)\pi/a_w$ and $\beta_m = 2(m+0.5)\pi/b_w$, the dimensions of the duct being a_w and b_w. If one dimension a_w or b_w is much greater than the other one (at least 10 times) and when $D_H \ll 10\,cm.f^{1/2}$, the slit formulation is required.

Slits :

In the case of slits the mass density and the bulk modulus are expressed respectively in Eqs. 13 & 14.

$$\rho_s = \rho_0\left[1-\frac{\tan(\frac{D_H}{4}G_\rho)}{\frac{D_H}{4}G_\rho}\right]^{-1} \quad (13)$$

$$\kappa_s = \kappa_0\left[1+(\gamma-1)\frac{\tan(\frac{D_H}{4}G_\kappa)}{\frac{D_H}{4}G_\kappa}\right]^{-1} \quad (14)$$

where D_H is the hydraulic diameter of the slit in order to take into account the fact that the slits can be circular, rectangular or elliptical. According to the Kirchhoff theory, if $D_H \ll 10\,\mu$m, this formulation can not be used.

3.6. Parallel assembly

In order to associate the slit matrix with the structure or another slit of different size, the patchwork method will be used, based on Verdière's method [23]. It is based on the switch between the admittance matrix and the transfer matrix (Eq. 15).

$$Y = \frac{1}{T_{12}}\begin{pmatrix} T_{22} & T_{22}T_{11}-T_{21}T_{12} \\ 1 & T_{11}\end{pmatrix}^{-1} \quad (15)$$

Defining the $\sigma_{p_n} = S_{wn}/S_{total}$ as the surface ratio or POA ("Percentage Open Area") considering n openings, the equivalent transfer matrix $\mathbf{T}_{para}$ is given by Eq. 16.

$$\mathbf{T}_{para} = \frac{1}{\sum\sigma_{p_n}Y_{n,21}}\begin{pmatrix} \sum\sigma_{p_n}Y_{n,22} & -1 \\ \sum\sigma_{p_n}Y_{n,22}\sum\sigma_{p_n}Y_{n,11}-\sum\sigma_{p_n}Y_{n,12}\sum\sigma_{p_n}Y_{n,21} & \sum\sigma_{p_n}Y_{j,11}\end{pmatrix} \quad (16)$$

4. NORMAL INCIDENCE RESULTS

4.1. Experimental setup

The impedance tube used for the normal incidence measurements is presented on Fig. 2. The inner diameter of the tube is 30 mm and the outer diameter is 38 mm which allow mounting the sample displayed in Fig. 1. The microphones are distant of $L_1 = 285$ mm, $L_2 = 100$ mm, $L_3 = 30$ mm and $L_4 = 145.5$ mm. Then the impedance can be overdetermined using the Chung et al [9] and Allam et al [2] methods.

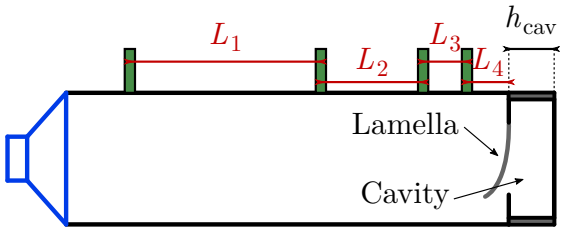

Figure 2. Schematic diagram of the impedance tube experiments. Acoustic measurements are performed using four microphones separated each other by $L_{1...4}$. The cavity height can be adapted according to the number of layers used.

4.2. Results

The absorption coefficient α is estimated from the impedance of the treatment or with the scattering coefficients (R & T for the reflection and transmission

coefficients respectively, which allows a comparison between the analytical model presented before and the experimental data ($\alpha = 1 - |R|^2 - |T|^2$) . The results exposed in Figs. 3 & 4 show good concordance between the model and the experimental results. However, it is important to point out that the experimental device is extremely sensitive to the slightest deformation, due to its thinness. Thus, the results can drastically vary depending on the condition of the lamella.

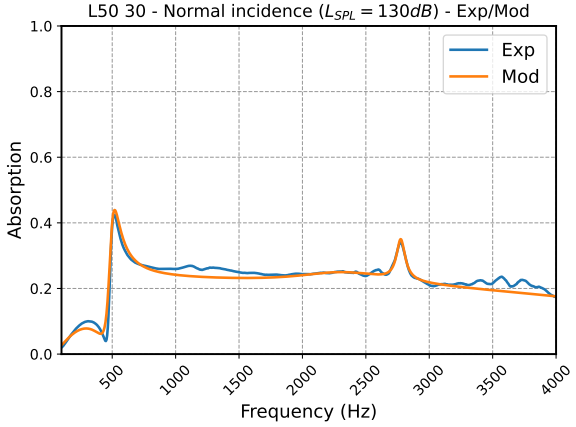

Figure 3. Absorption coefficient of a single lamella coupled with a 30 mm height cavity in normal incidence : experimental data against analytical model.

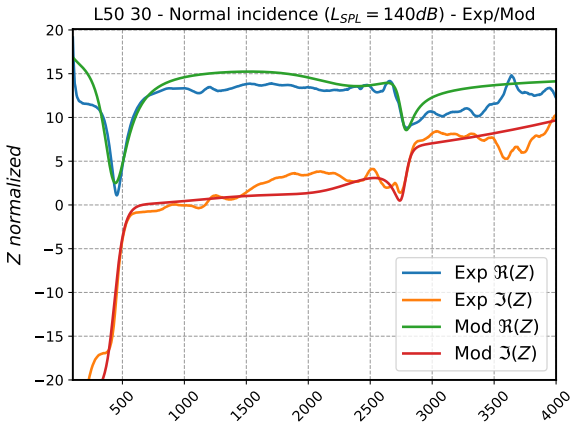

Figure 4. Normalised impedance of a single lamella coupled with a 30 mm height cavity in normal incidence : experimental data against analytical model (resistance and reactance).

5. GRAZING FLOW RESULTS

5.1. New system considered

The cell presented in Fig. 1 is used and repeated according to a lattice of 5 rows and 3 lines (see Fig. 5). The lamellas are coupled to the same rectangular cavity as seen in Fig. 1. The total length of the treatment is now 200 mm long and 50 mm width, with 5 mm of wall between each cell. A 1.5 mm smooth portion on either side of the lamella array is also present for potential future measurements.

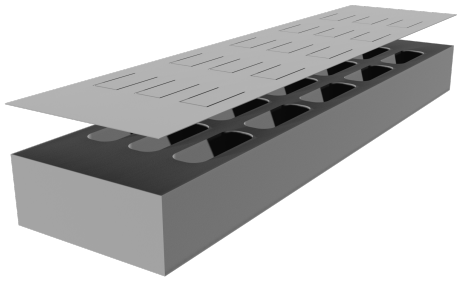

Figure 5. Sketch of the acoustic filter composed of 15 cells with a 30 mm cavity height and a total of 200 mm long rectangular plate over 50 mm width.

5.2. Experimental setup

The grazing flow tube used for those experiments is depicted on Fig. 6. The height of the duct is 20 mm and the transverse dimension is 50 mm. This means that the sample covers the entire width. The acoustic waves are generated by two compression chambers which can be placed either downstream (acoustics sources in counter flow) or either upstream of the test section in order to measure the scattering matrix (two sources method as described by Åbom [1]). Then, an overestimated determination of the upstream (R^+, T^+) and downstream (R^-, T^-) reflection and transmission coefficients of the scattering matrix, can be computed. The impedance might also be estimated by solving an inverse problem according to the Aurégan et al. [6] method.

5.3. Without flow

For the grazing incidence case, the impedance of the system Z_{ac} has to be implemented in parallel. According to Richoux et al [20], that is possible by considering the new transfer matrix as shown in Eq. 17.

If several cells are considered, it is possible to multiply them together once the transfer matrix of the unit cell has been determined. It only remains to assemble the system according to the distance between them. In this way, the inter-cell distance (L_a) has to be adapted. The expression of the transfer matrix of the $\mathbf{T}_{sys}$ treatment with N row cells is presented in Eq. 18.

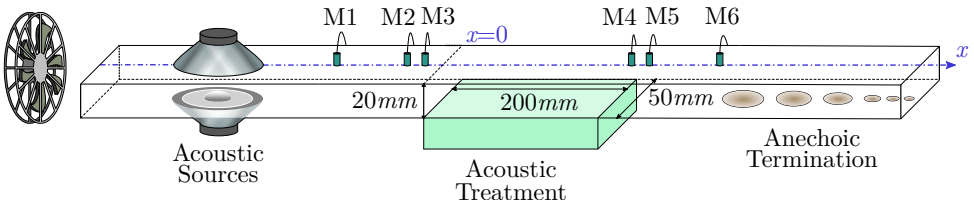

Figure 6. Sketch of the grazing incidence duct using two sets of three microphones to characterise the liner sample.

$$\mathbf{T}_{sys} = \begin{pmatrix} 1 & 0 \\ 1/Z_{ac} & 1 \end{pmatrix} \tag{17}$$

$$\mathbf{T}_{sys} = \prod_{i=1}^{N} \mathbf{T}^i_{L_1} \mathbf{T}^i_{L_2} \mathbf{T}^i_{L_3} \tag{18}$$

Since that the grazing incidence case allows transmission and reflection of the acoustic waves, the full scattering matrix has to be considered (Eq. 19). Then the acoustic absorption can be computed.

$$\begin{pmatrix} T^+ & R^- \\ R^+ & T^- \end{pmatrix} = \begin{pmatrix} \frac{2}{T_{11}+T_{12}.Z_{c_s}+T_{21}.Z_{c_s}+T_{22}} & \frac{-T_{11}+T_{12}.Z_{c_s}-T_{21}.Z_{c_s}+T_{22}}{T_{11}+T_{12}.Z_{c_s}+T_{21}.Z_{c_s}+T_{22}} \\ \frac{T_{11}+T_{12}.Z_{c_s}-T_{21}.Z_{c_s}-T_{22}}{T_{11}+T_{12}.Z_{c_s}+T_{21}.Z_{c_s}+T_{22}} & \frac{2(T_{11}T_{22}-T_{12}T_{21})}{T_{11}+T_{12}.Z_{c_s}+T_{21}.Z_{c_s}+T_{22}} \end{pmatrix} \tag{19}$$

The curves on Figs. 7 & 8 show a well predicted transmission coefficient but an overestimated reflection, involving a bias on the absorption.

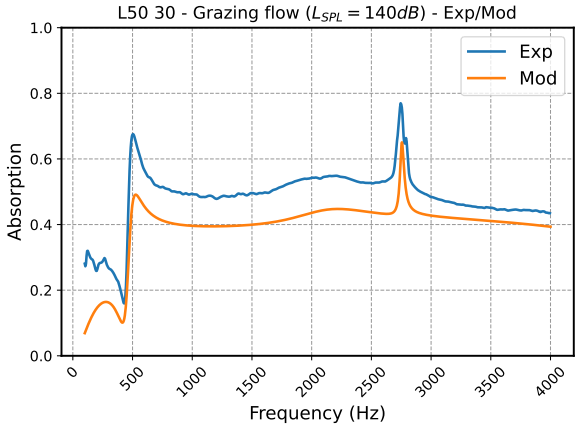

Figure 7. Absorption coefficient of a lattice composed of 15 lamellas coupled with a 30 mm high cavity in grazing incidence without flow : experimental data against analytical model.

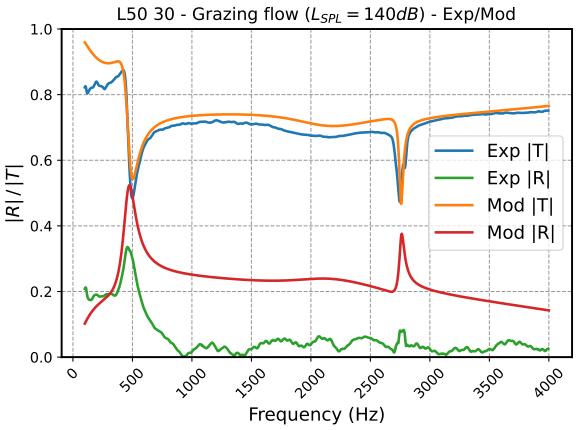

Figure 8. Reflection and transmission coefficients of a lattice composed of 15 lamellas coupled with a 30 mm height cavity in grazing incidence without flow : experimental data against analytical model.

5.4. Effect of flow

In order to study the flow effect on the acoustic treatment, the duct is connected to a compressor that can

provide a velocity up to $\mathscr{M} = 0.45$. The results shown in Figs. 9, 10 & 11 highlight a transmission coefficient above one at the first mechanical resonance when the Mach number is between 0.3 and 0.4 leading to negative absorption. This phenomenon seems to be amplified for larger Mach numbers according to the measurement at 0.45. Thus, there is probably an optimal operating range for this type of behaviour. This effect on T^- (downstream configuration meaning acoustics sources in counter flow) seems have an equivalent on R^+ (related to the upstream configuration) which tends to be greater than one for some sample or environmental conditions.

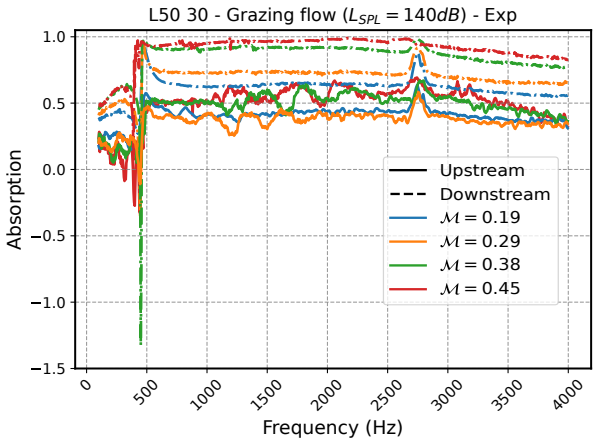

Figure 9. Absorption coefficients of a lattice composed of 15 lamellas coupled with a 30 mm high cavity under grazing incidence with flow : experimental data.

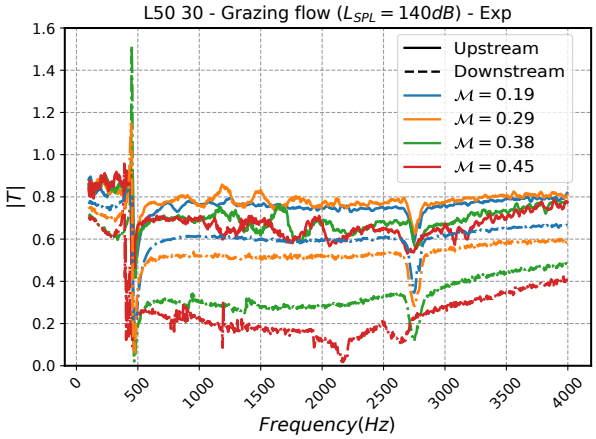

Figure 10. Transmission coefficients of a lattice composed of 15 lamellas coupled with a 30 mm high cavity under grazing incidence with flow : experimental data.

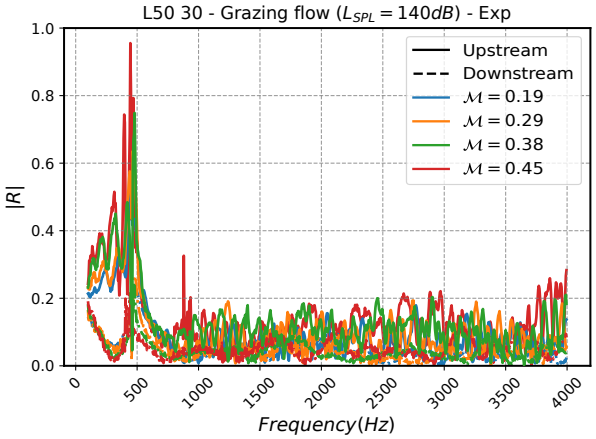

Figure 11. Reflection coefficients of a lattice composed of 15 lamellas coupled with a 30 mm high cavity under grazing incidence with flow : experimental data.

6. CONCLUSION

This paper shows that the use of a mobile structure coupled with very thin slits allows to increase the mechanical dissipation at the resonance frequencies. Then an analytical model based on transfer matrix formulation is used to predict the behaviour of this kind of mechano-acoutical system. This model has been validated first against normal incidence measurements in a first place at different sound pressure levels. No significant changes in the curves indicate that there is no non-linear effect on the mechanical resonance. In a second time, this acoustic treatment has been mounted flush into a grazing incidence duct in order to perform measurements with and without flow. The analytical model presents a bias on the reflection coefficient and should therefore be improved. However, the global behaviour seems to be understood without flow. The measurements with flow, however, present a particular operating regime where it is possible to observe a transmission coefficient greater than one. This induces a negative absorption, probably due to the transfer of energy from the flow to the lamella on its first resonance mode, amplifying its displacement. As the flow velocity increases, this effect seems to fade, suggesting an optimal operating range. In future works, interest will be focused on measuring the displacement of the beam with flow. It will also be investigated if the optimal range for negative absorption is displaced for a longer beam geometry.

7. ACKNOWLEDGMENTS

This work has been partially supported by the European Union's Horizon 2020 research and innovation

programme under project ARTEM (Aircraft noise Reduction Technologies and related Environmental iMpact) grant agreement No. 769350.

8. REFERENCES

[1] Åbom M, 1991. Measurement of the scattering-matrix of acoustical two-ports. *Mechanical Systems and Signal Processing*, 5(2): 89–104.

[2] Allam S et al, 2006. Over-determination in acoustic two-port data measurement. *ICSV13 Vienna*, page 8.

[3] Allard JF et al, 2009. *Propagation of sound in porous media: modelling sound absorbing materials*. Wiley, Chichester, 2. ed edition.

[4] Aurégan Y, 2018. Ultra-thin low frequency perfect sound absorber with high ratio of active area. *Applied Physics Letters*, 113.

[5] Aurégan Y et al, 2016. Low frequency sound attenuation in a flow duct using a thin slow sound material. *Journal of the Acoustical Society of America*, EL149–EL153.

[6] Aurégan Y et al, 2004. Measurement of Liner Impedance with Flow by an Inverse Method. In *10th AIAA/CEAS Conference*.

[7] Boulandet R et al, 2018. Duct modes damping through an adjustable electroacoustic liner under grazing incidence. *Journal of Sound and Vibration*, 426: 19–33.

[8] Boulvert J et al, 2020. Folded metaporous material for sub-wavelength and broadband perfect sound absorption. *Applied Physics Letters*, 117(25): 251902,

[9] Chung J et al, 1980. Transfer function method of measuring in-duct acoustic properties. I. Theory. *The Journal of the Acoustical Society of America*,

[10] Dai X et al, 2017. Flexural instability and sound amplification of a membrane-cavity configuration in shear flow. *The Journal of the Acoustical Society of America*.

[11] Donda K et al, 2019. Extreme low-frequency ultrathin acoustic absorbing metasurface. *Applied Physics Letters* 115(17), 173506.

[12] D'Elia M et al. 2021 On articulated plates with micro-slits to tackle low-frequency noise. *Acta Acustica*, 5:31.

[13] Fleming A et al, 2007. Control of Resonant Acoustic Sound Fields by Electrical Shunting of a Loudspeaker. *IEEE Transactions on Control Systems Technology*, 15 (4):689–703.

[14] Hagood N et al, 1991. Damping of structural vibrations with piezoelectric materials and passive electrical networks. *Journal of Sound and Vibration*, 146(2):243–268.

[15] Houdouin A, 2014. *Vers une paroi acoustique absorbante en technologie MEMS*. PhD thesis, Université du Maine.

[16] Huang L, 2002. Modal analysis of a drumlike silencer. *Journal of the Acoustical Society of America*, 112 (5): 2014–2025.

[17] Huang S et al, 2019 Acoustic perfect absorbers via helmholtz resonators with embedded apertures. *Journal of the Acoustical Society of America*, 145 (1):254–262.

[18] Kergomard J et al, 1987. In acoustic waveguides at low frequencies : critical analysis and formulae. *Journal of Sound and Vibration* 114(3), 465-479.

[19] Rao S, 2011. *Mechanical vibrations*. Prentice Hall.

[20] Richoux O et al, 2002. Acoustic characterization of the Hofstadter butterfly with resonant scatterers. *Europhysics Letters (EPL)*, 59(1): 34–40.

[21] Stinson M, 1991. The propagation of plane sound waves in narrow and wide circular tubes, and generalization to uniform tubes of arbitrary cross-sectional shape. *The Journal of the Acoustical Society of America*, 89(2):550–558.

[22] Van Eysden C et al, 2006. Resonant frequencies of a rectangular cantilever beam immersed in a fluid. *Journal of Applied Physics*, 100(11):114916.

[23] Verdière K et al, 2013. Transfer matrix method applied to the parallel assembly of sound absorbing materials. *The Journal of the Acoustical Society of America*, 134 (6): 4648–4658.

[24] Yang M et al, 2017. Optimal sound-absorbing structures. *Materials Horizons*, 4(4):673–680.

DEVELOPING NUMERICAL METHODS FOR PREDICTING FLOW-INDUCED UNDERWATER RADIATED NOISE FROM SHIPS

Duncan McIntyre (dmcintyre@uvic.ca)
University of Victoria, Victoria, Canada

Peter Oshkai
University of Victoria, Victoria, Canada

ABSTRACT

Shipping is the largest anthropogenic source of Underwater Radiated Noise (URN), which represents a significant threat to the health of marine ecosystems. Propellers generate much of the URN from ships through a combination of wake vorticity and cavitation, two phenomena that interact extensively. Predictive models for this noise source are needed to develop intelligent mitigation strategies; however, the complexity of the physical phenomena and difficulty in obtaining measurements suitable for validation has so far limited model development. We present progress toward a generalized numerical framework for predicting URN from marine propellers. We detail two approaches, the fist using Unsteady Reynolds Averaged Navier-Stokes (URANS) solutions for a cavitating propeller and the second an ongoing study employing Delayed Dethatched-Eddy Simulation (DDES) to study non-cavitating flow around a ship hull and propeller combination. We highlight shortcomings of the RANS approach and detail the shortcomings are addressed by moving to a more rigorous approach employing DDES as well as those that must be addressed in continuing and future work.

1. INTRODUCTION

Global concern over the deleterious effects of anthropogenic underwater radiated noise (URN), of which shipping is the largest source (Hildebrand, 2009), on marine ecosystems has driven a surge of studies utilizing numerical techniques to predict acoustic noise from marine vessels. The appeal of computational methods in the area of underwater acoustics is related to relative limitations of laboratory experiments and field measurements. The former require specialized equipment and infrastructure, particularly when cavitation is involved, and present challenges in accurately reproducing the relevant phenomena (Sezen et al., 2020; Tani, 2015), while full-scale sea trials lack repeatability of the environmental conditions and are often prohibitively expensive for civilian applications (McIntyre et al., 2021; McKenna et al., 2012). As regulations are implemented to govern civilian fleets in terms of their environmental impact, development of accessible tools for predicting the URN becomes necessary. This demand has led to exploration of novel approaches to modelling of the URN that favor direct practical applications over systematic approaches to development of high-fidelity, predictive tools. In this paper, we discuss our past and ongoing experiences in numeral modelling of acoustic emissions of marine propellers, as well as our multi-faceted approach to advancing predictive numerical capabilities in the area of URN.

Three sources dominate the underwater noise emitted by ships: machinery, vorticity/turbulence and cavitation. Machinery noise is largely due to the engines, and although it is transmitted to the surrounding ocean by hull vibrations, it is the only noise source that is not caused by flow interactions. Turbulence sound is generated by unsteady flow structures, most notably the shed vortices in the wake of the propeller, and their interactions with the hull and the propeller. Cavitation noise is caused by the oscillation and collapse of vapor cavities that and induced in the flow, primarily by the propeller. Propeller-induced cavitation is typical of marine propellers operating outside of their designed operating conditions, and it is often the overall dominant source of the URN from the vessel (Ross, 1976).

In this paper, we only consider acoustic noise caused by flow interaction, i.e., vortex sound and cavitation noise. We outline two approaches to development of numerical modelling capabilities in the area of URN of marine vessels. The first part presents a completed study that involved solution of Unsteady Reynolds Averaged Navier-Stokes (URANS) equations couple with a cavitation model for a marine propeller in combination with model-scale experiments. We highlight advantages, limitations, and areas in need of further development for this type of numerical analysis. In the second part, we detail our ongoing study of flow acoustics around an entire model marine vessel in the absence of cavitation, which endeavors to provide the necessary framework for addressing some of the unresolved issues identified in the course of the first part of the investigation.

2. REDUCED-ORDER MODELLING OF PROPELLER-INDUCED CAVITATION NOISE

Given its dominant role in the overall noise emissions from marine vessels, cavitation noise is a common focal area in URN research. The cavitation phenomenon presents opportunities for employing low-order modelling that are not available for predicting of turbulence sound. Cavitation noise can, to a limited extent, be predicted by low-order flow models and semi-empirical noise models or acoustic analogy (Bosschers, 2018; Brown, 1976; Testa et al., 2018). However, the applicability of this low-order modelling strategy is significantly limited by the combined lack of full-scale data for model validation as well as the lack of deep understanding of the underlying physics. Numerical solution of the full Navier-Stokes equations is therefore a vital step in the development of more practical models of cavitation noise.

In the present study, we employed URANS in conjunction with a simplified multi-phase model to simulate cavitating flow over a model-scale propeller in a cavitation tunnel. The corresponding experiments, conducted at the University of Genoa, were designed to produce a diverse range of cavitation types. We made qualitative observations of the cavitation patterns and quantitative comparisons of the acoustic response between experimental measurements and the numerical solutions.

2.1. Numerical Methodology

The flow around a model scale propeller was modelled using a commercial computational fluid dynamics (CFD) solver (STAR-CCM+), using the incompressible URANS equations and both the realizable k-ε turbulence model and the k-ω Shear Stress Transport (SST) turbulence models. Cavitation was modeled using a volume-of-fluid approach, where the vapor phase was introduced using a mixture formulation. The mixture properties were calculated using weighted cell-by-cell averages. Mass transfer between the phases was modelled by the Scherr and Sauer model, which represents vapor cavities as collections of spherical bubbles that behave according to the Rayleigh equation:

$$\frac{dR}{dt} = \sqrt{\frac{\frac{2}{3}|p_B - p_\infty|}{\rho_{\text{liq}}}}, \qquad (1)$$

where R is the bubble radius, p_B is the internal bubble pressure, p_∞ is the ambient (cell) pressure, and ρ_{liq} is the liquid density (Schnerr and Sauer, 2001).

The computation domain was comprised of a pair of overset meshes, one for the water tunnel and one for the rotating propeller, labeled A and B in fig. 1, respectively.

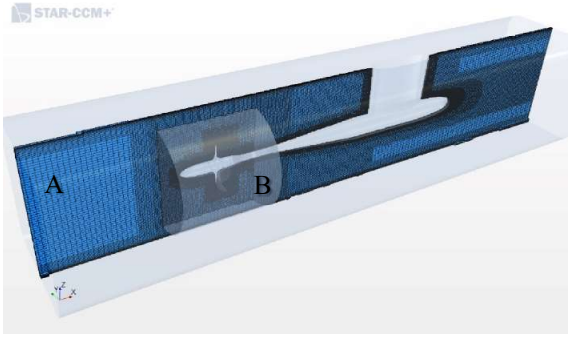

Fig. 1: Computational domain and mesh for simulation of the cavitating propeller flow, showing the stationary (A) and rotating (B) overset domains.

The following is the outline of the solution procedure:

First, the unsteady hydrodynamic solution was allowed to evolve without cavitation. Second, cavitation modelling was implemented, and the solution was allowed to reach a fully developed flow state; finally, data was acquired for one blade-passage period with timesteps short enough to allow the frequencies of interest found experimentally to be investigated by Fourier transform.

2.2. Comparison to Experimental Results

Several distinct cavitation regimes that were investigated in the cavitation tunnel experiments were also reproduced numerically. The vapor cavities attached to the surface of the blades were generally reproduced well in simulations, while the cavities within the cores of the free vortices were not correctly simulated. Fig. 2 shows a stroboscopic photograph of a typical cavitation regime observed in the experiments, alongside its numerically-predicted counterpart. The deficiency in the numerical solution was the result of the simulation under-predicting the extent of the tip vortices themselves, which is unrelated to the cavitation model. This issue is an inherent deficiency of URANS solutions, where the vortices in highly separated flow regions are numerically damped by the numerical solution and typically require a Large Eddy Simulation (LES) treatment to be accurately resolved (Ianniello and De Bernardis, 2015). The realizable k-ε turbulence model is intended to provide some improvement for this deficiency (Shih et al., 1995). However, it was not found to significantly improve the numerical results compared to the results obtained using the SST model. Since tip vortex cavitation is known to be the most prevalent regime in typical propeller operation, this deficiency of the reduced-order numerical approach is critical.

We computed acoustic power spectra using the pressure values from the grid cell corresponding to the location of a hydrophone in the physical experiments. The total simulated time for which the spectra were computed ranged from 28 ms to 45 ms, depending on the revolution rate of the propeller. We ran the simulations with sampling time steps of 11 μs, resulting in a Nyquist frequency of approximately 45 kHz. Since the experimental measurements were window-averaged while the numerical results were not averaged due to insufficient simulation time, we compared power spectra in terms of third-octave band levels.

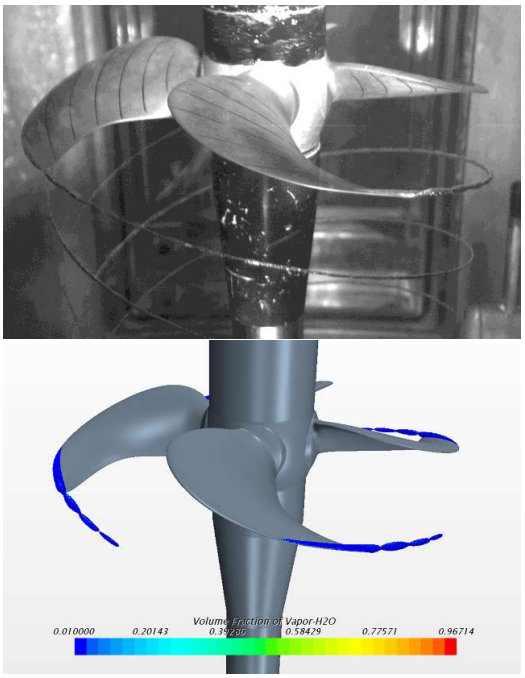

Fig. 2: Stroboscopic photograph (top) of the tip vortex cavitation pattern compared to the same flow conditions simulated using the reducer-order (URANS) approach (bottom).

Comparisons to experimental measurements are presented in fig. 3 for all ten cases considered in the study (referred to as C1-C5 and C1b-C5b). The URANS solutions over-predicted the sound levels by 20 dB to 70 dB. We were, however, able to reproduce the shapes of many of the spectra reasonably well, and the differences between the experimental and the numerical values were usually consistent across all frequency bands for a given simulation. We observed the greatest mismatch in the spectral shapes when the numerical simulations failed to capture the dominant cavitation structures. Most notably, the numerically predicted spectra corresponding to the conditions C2 and C5 lacked the characteristic hump in the hundreds of Hz that was determined experimentally to be associated with the tip vortex cavitation.

The observed over-prediction of the sound pressure levels indicated that significant physical effects were not captured in the numerical model. Any neglected flow-sound integrations and wall vibrations were unlikely to be sufficient to account for the over-prediction of the pressure fluctuations. Moreover, numerical acoustic spectra were also obtained for non-cavitating conditions and were similar in the magnitude and the frequency response to the experimentally-obtained measurements in non-cavitating conditions and of the background noise. These observations supported a hypothesis that the cavitation treatment was the primary source of error in the numerical model. However, since the turbulence sound was similar in magnitude to the background noise at the non-cavitating experimental conditions, a conclusive assessment of the hydroacoustic performance of the simulations was impossible.

Hence, we postulate that the most likely source of the insufficient damping effects in the present modelling approach is related to the shortcomings of the Schnerr and Sauer cavitation model that governed interphasic mass transfer. While the Schnerr and Sauer cavitation model has been successfully used in the past studies to predict cavitation patterns, the present results suggest that it is inadequate for predicting the radiated sound.

3. HIGH-FIDELITY SIMULATION OF NON-CAVITATING URN OF AN ENTIRE VESSEL

The acoustic information from Navier-Stokes solutions can be extracted from the fluctuating pressure field and propagated to the far-field using an acoustic analogy. This analysis requires a temporally- and spatially-resolved solution for the unsteady pressure in areas of interest. For the turbulence sound, the areas of interest are the regions of sheer flow, most notably vortices in the propeller wake, which produce large pressure fluctuations. Since the interactions of the vortex-induces sound with the hull are important for accurate prediction of the far-field URN, it is necessary to simulate the flow over the entire ship.

The results of our numerical work on propeller cavitation noise revealed a need for a deeper exploration of the CFD techniques for ship hydroacoustics. We aim to develop a generic CFD platform for predictions of propeller hydrodynamics and propeller-induced near-field acoustic characteristics. To ensure adequate hydrodynamic and hydroacoustic performance, we focus first on non-cavitating flow. Validation is being performed against experimental measurements of a model vessel at the National Research Council Canada. The model aims to address

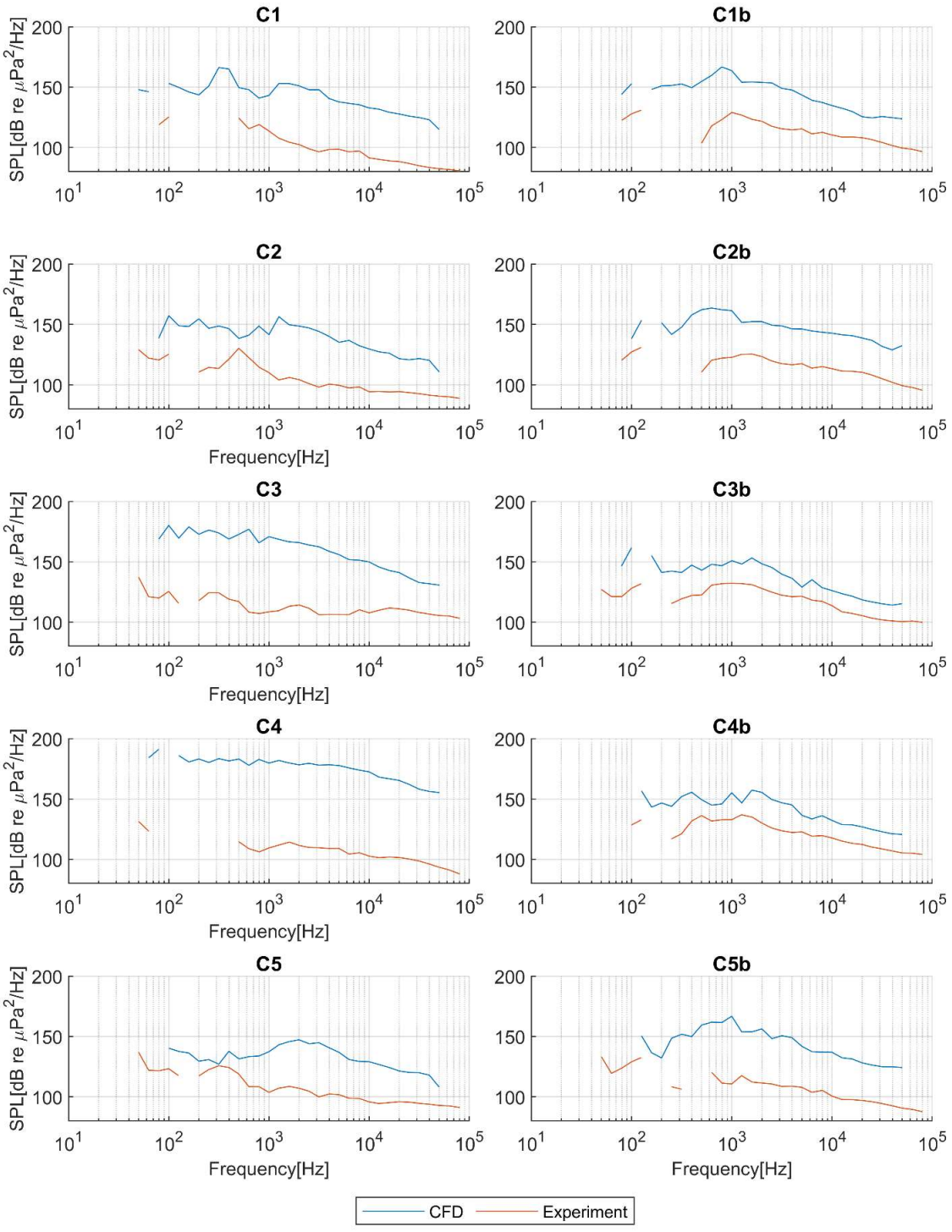

Fig. 3: Third octave band level spectra obtained by experimental measurements of cavitation tunnel tests and corresponding URANS simulations. The controllable-pitch propeller was operated at its designed pitch in experiment conditions C1 through C5 and at a reduced pitch in conditions C1b through C5b. Conditions C1, C2, C3, and C5 produced tip vortex cavitation, which is typical of propeller operation under designed conditions, while other conditions displayed only pressure-side cavitation that is observed only during off-design operation.

the deficiencies of the URANS simulations with regard to the shed vorticity in the propeller wake by transitioning to a hybrid RANS-LES formulation, as well as to be completely open-source and free of commercial software limitations.

3.1. Numerical Methodology

We propose a numerical methodology for hydroacoustic simulation of single-phase flow around a propeller using the OpenFOAM platform with the standard pimpleFoam solver and using the Delayed Detached Eddy Simulation (DDES) treatment of turbulence to capture the shed vortices. The propeller motion is implemented by employing a sliding mesh that uses the arbitrary mesh interface feature of the pimpleFoam solver. We simulate flow around the entire vessel and aim to make comparisons with experimental measurements in terms of hull pressure fluctuations. Comparisons between URANS CFD simulations of an entire marine vessel with full-scale acoustic measurements have been performed by Ianniello et al (2013). The present refinement of the model using DDES is expected to greatly improve the fidelity of the simulation of the shed vortices in the propeller wake that dominate the singing noise component of the overall URN. While the simulation of an entire ship entails a significant computational expense, this approach has several advantages. It provides a direct solution of hull pressure, which facilitates comparison with the experiments and ensures that propeller-hull interactions are realistically represented in the solution. Additionally, computational expense can be limited by restricting highly-refined mesh regions to the vicinity of the propeller and its wake, since most of the acoustic sources are expected to exist in that region.

The complete simulation domain extended one ship length from the bow, two lengths downward, one-and-a-half lengths to the port and the starboard, and eight lengths aft of the ship. The intent of the large domain is to avoid wall effects and to allow sufficient space downstream of the vessel for wake recovery before the domain outlet as recommended by the ITTC guidelines (2011). The computational domain is shown in fig. 3. Wall functions are applied to both the hull and the propeller surfaces. However, they are only used on the surface of the propeller blades as a safeguard against unexpected numerical behavior. The mesh refinement in the vicinity of the propeller is intended to be sufficient to resolve the boundary layers on the blade surfaces.

Fig. 4: Computational domain for the simulation of the entire vessel.

We employed a structured hexahedral mesh with a high degree of refinement in the proximity of the ship's propeller, as shown in fig. 4.

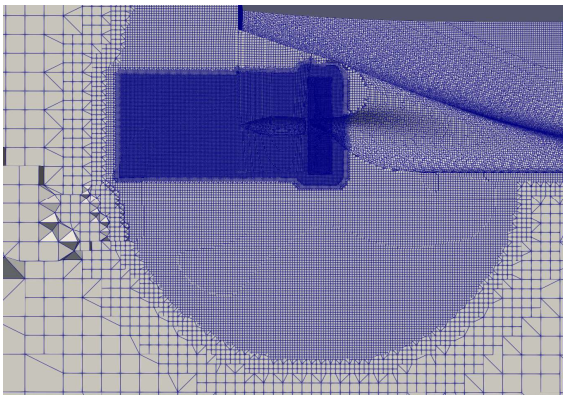

Fig. 5: Example of mesh refinement around the propeller.

The RANS model is insufficient for resolving the vorticity in the separated wake of a marine propeller, while the LES approach is prohibitively computationally expensive for the size of domain used in the present work. We therefore chose a DDES method to resolve the propeller wake while reducing overall expense. The DDES method, like the original Detached Eddy Simulation (DES) approach from which it is derived, explicitly switches between the RANS equations and the LES equations based on the local grid spacing and the turbulent length scale. The conventional DES is highly sensitive to grid spacing, and ambiguous grids can result in unexpected transition between LES and RANS, particularly in the vicinity of boundary layers. The addition of a delay function increases the use of RANS in boundary flows, increasing compatibility with ambiguous grids without inhibiting the transition to the LES formulation in separated flow regions (Spalart et al., 2006). Since grid generation is particularly challenging for the complex geometry of a ship, the choice of the DDES formulation over the conventional DES is advantageous due to the flexibility of the grid requirements. The primary limitation of the DDES approach compared to DES is a reduction in overall fidelity of the solution, especially in the case of an attached flow.

Since the goal of the present simulation methodology was to resolve the vortical structures in the propeller wake for the purpose of URN prediction, fidelity of the boundary layer solution was not of primary interest.

Two turbulence models are widely used in conjunction with the DDES formulation: the Spalart-Allmaras one-equation model and the k-ω SST two-equation model. We employ the SST model (Gritskevich et al., 2011) based on the adequacy of its performance for RANS solutions of propeller flow in our prior work.

The solution process in the present methodology is divided into two stages: i) initialization and ii) data acquisition. The initialization entails stepping the simulation through time until asymptotic or periodic behavior of the solution is achieved. Variable time stepping is employed in the initialization phase, taking advantage of the PIMPLE algorithm. For data acquisition, we limit the time step according to the Nyquist frequency required to achieve the desired maximum frequency for the acoustic analysis.

3.2. Model Extension and Laboratory Experimentation

In addition to the near-field noise, we plan to implement a variation of the Ffowcs Williams-Hawkings (FWH) acoustic analogy derived by Farrasat (1996) in conjunction with the OpenFOAM DDES solution to analyze the far-field URN, similar to the method described by Ianniello (2013). The implementation of the acoustic analogy will allow for analysis of the far-field acoustics as a post-processing calculation, given a temporally- and spatially-resolved flow field. Therefore, the entire data acquisition portion of each simulation will be saved for extended analysis.

Following the experimental validation of the non-cavitating simulations, we intend to expand the high-fidelity analysis into the area of cavitating propeller acoustics. For this purpose, we will compare the simulation results to field measurements of far-field URN from sea trials of a ferry vessel with the known geometry of the hull and the propeller.

To improve the simulation of cavitation-induced noise, fundamental experiments involving cavitation bubbles in shear flow will be conducted under repeatable laboratory conditions. Through these experiments, we hope to shed light on the key features of propeller-induced cavitation that are neglected by existing cavitation models conventionally used in CFD simulations.

4. CONCLUSIONS

The application of CFD to predict URN from ships presents many challenges, particularly regarding the complexity and the multi-scale nature of the underlying physical phenomena. Nonetheless, the field shows both promise and value. In a first attempt to model propeller-induced cavitation noise we encountered deficiencies inherent to RANS solutions that prevented accurate prediction of the key flow features that govern noise emissions from both the vapor cavities and the turbulent flow structures. Moreover, significant limitations are related to conventional cavitation models and their interpretation for prediction of the far-field URN. In order to develop a more advanced framework for URN prediction, we develop a modelling procedure based on DDES solutions aimed at simulating flow around an entire vessel in order to capture the sources of turbulence noise, which will serve as a more robust foundation for URN modelling in general.

5. ACKNOWLEDGEMENTS

The authors are grateful to Prof. M. Viviani, Dr. G. Tani and Ms. F. Miglianti of the University of Genoa and to Dr. S. Islam of the National Research Council of Canada (NRC) for providing the model-scale laboratory data, as well as to JASCO Applied Sciences and BC Ferries Corp. for providing the field data. The authors also gratefully acknowledge financial support of the Transport Canada, the NRC and the Natural Sciences and Engineering Research Council of Canada (NSERC).

6. REFERENCES

Bosschers, J., 2018. A semi-empirical prediction method for broadband hull-pressure fluctuations and underwater radiated noise by propeller tip vortex cavitation. *Jounral of Marine Science and Engneering* **6**: 49.

Brown, N.A., 1976. Cavitation noise problems and solutions. *Proceedings of International Symposium on Shipboard Acoustics*. Noordwijkehout.

Farassat, F., 1996. *The Kirchhoff formulas for moving surfaces in aeroacoustics: the subsonic and supersonic cases (NASA Technical Memorandum)*. Hampton, VA.

Gritskevich, M.S. et al, 2011. Development of DDES and IDDES Formulations for the k-ω Shear Stress Transport Model. *Flow, Turbulence and Combustion* **88**: 431–449.

Hildebrand, J., 2009. Anthropogenic and natural sources of ambient noise in the ocean. *Marine Ecology Progress Series* **395**: 5–20.

Ianniello, S., De Bernardis, E., 2015. Farassat's formulations in marine propeller hydroacoustics. *International Journal of Aeroacoustics* **14**: 87–103.

Ianniello, S. et al, 2013. Ship underwater noise assessment by the acoustic analogy, part III: measurements versus numerical predictions on a full-scale ship. *Journal of Marine Science and Technology* **19**: 125–142.

ITTC, 2011. Practical Guidelines for Ship CFD Applications. *ITTC – Recommended Procedures and Guidelines.*

Ross, D., 1976. *Mechanics of underwater noise*. Pergamon, New York.

McKenna, M.F. et al, 2012. Underwater radiated noise from modern commercial ships. *Journal of the Acoustical Society of America* **131**: 92–103.

Schnerr, G.H., Sauer, J., 2001. Physical and numerical modeling of unsteady cavitation dynamics. *4th International Conference on Multiphase Flow*. New Orleans.

Sezen, S. et al, 2020. Numerical cavitation noise prediction of a benchmark research vessel propeller. *Ocean Engeering* **211**: 107549.

Shih, T.H. et al, 1995. A new k-ε eddy viscosity model for high reynolds number turbulent flows. *Computational Fluids* **24**: 227–238.

Spalart, P. et al, 2006, A new version of detached-eddy simulation, resistant to ambiguous grid densities. *Theoretical and Computational Fluid Dynamics* **20-3**: 181-195.

Tani, G., 2015. *Experimental study of cavitating propeller radiated noise (PhD dissertation)*. University of Genoa.

Testa, C. et al, 2018. A Ffowcs Williams and Hawkings formulation for hydroacoustic analysis of propeller sheet cavitation. *Journal of Sound and Vibration* **413**: 421–441.

DIRECT MEASUREMENTS OF THE DYNAMIC LIFT FORCE ACTING ON RECTANGULAR RODS IN CROSS-FLOW DURING ACOUSTIC RESONANCE EXCITATION

A. Shoukry & A. Mohany
Fluid-Structure Interaction and Noise Control Laboratory, Ontario Tech University, Oshawa, Ontario, Canada

ABSTRACT

The effect of self-excited acoustic resonance on the dynamic lift force acting on rectangular rods with three different aspect ratios is investigated experimentally. The rod has three different aspect ratios of $l/h = 0.5$, $l/h = 1$, and $l/h = 2$, where l is the rod length in the flow direction and h is the rod height perpendicular to the flow. The acoustic resonance was found to drastically affect the dynamic lift force coefficient of the rod. For $l/h = 1$ and $l/h = 0.5$, only the first acoustic cross-mode of the duct was excited. The excitation of this acoustic mode is triggered by the vortex shedding process and a jump in the dynamic lift force occurs. However, the jump in the dynamic lift force coefficient for the aspect ratio of $l/h = 1$ was significantly lower than that for $l/h = 0.5$. This is because the generated acoustic pressure for the case of $l/h = 1$ during resonance is weaker than that of $l/h = 0.5$. For $l/h = 2$, an early excitation of the third acoustic mode occurs with significant reduction in the dynamic lift force coefficient compared with that before the onset of resonance. This is because the early excitation mechanism of the third mode is found to be dependent on the shear layer separation at the upstream corners of the rod rather than the vortex shedding process downstream of the rod. A summary of the results is presented in the paper.

1. INTRODUCTION

Flow around bluff bodies induces fluctuating aerodynamic forces due to the vortex shedding process in the wake. These fluctuating forces can induce structural vibrations, which may be amplified during resonant conditions, such as self-excited acoustic resonance. Self-excited acoustic resonance may arise if the vortex shedding frequency coincides with an acoustic resonant mode of the bluff body enclosure. An example of this is the heat exchanger enclosure, housing tube bundles. The occurrence of self-excited acoustic resonance is a design concern as it often results in severe vibration and noise levels, eventually leading to fatigue failure. Though the flow-sound interaction mechanism of circular cylinders has been characterized for different cylinder arrangements, the rectangular rods did not receive much attention, even though they are widely used in different industrial applications.

For studies performed outside of resonant excitation, Ohya (1994) experimentally investigated the base pressure of rectangular rods with different aspect ratios. He found significant variations in the base pressure, which were found to be associated with variations in the shear layer behaviour at different aspect ratios. Van Oudheusden et al., (2005) reported that the flow topology and aerodynamic forces on square rods are dependent not only on the cross-sectional aspect ratio, but also on the flow incident angle. Luigi et al., (2013) experimentally studied the effect of corner rounding and flow incidence angle on the aerodynamic forces of square rods. They found that rounding the corner significantly reduced the dynamic lift force on the square rod. They identified two distinct flow regimes governed by the Reynolds numbers, which were independent of the flow incidence angle. Nakamura et al. (1996) studied the vortex characteristics for rectangular rods of different aspect ratios at low Reynolds numbers. They found that regardless of the aspect ratio of the rod, at Reynolds number around 250, the vortex shedding street switches from two shear layers separating from the leading edges, namely Kármán vortex street into a single separated shear layer street, namely impinging shear layer instability.

For circular cylinders, Curle et al., (1955) clarified that the aerodynamic sound is produced by a dipole source that is dominant in the lift force direction. During resonance excitation, the correlation length and strength of the vorticity in the wake region of circular cylinders increase (Islam and Mohany , 2020). Inoue et al., (2002) reported substantial change in the fluctuating aerodynamic forces during acoustic resonance due to the induction of a dipole sound source oriented in the direction of the dynamic lift force . Mohany and Ziada (2011) investigated the dynamic

lift forces acting on a single cylinder and reported an increase in the dynamic lift force coefficient by four times compared with the value before the onset of resonance excitation. This was reaffirmed later by Shabaan and Mohany (2020). For rectangular rods, Shabaan and Mohany (2022) showed that depending on the length of the rod in the direction of the flow, sudden excitation of the third acoustic mode can materialize at flow velocities much lower than the anticipated values for vortex shedding frequency coincidence. This excitation was attributed to the shear layer separation and impingement between the leading and trailing edges of the rod. A similar phenomenon was observed by Mohany and Ziada (2005) for two tandem cylinders in cross-flow where an earlier excitation of the first acoustic cross-mode took place. This was due to the shear layer instability in the cylinders' gap. Thus, clarifying the source(s) that trigger the early excitation of the third acoustic mode in rectangular rods will improve our understanding of the flow-sound interaction mechanism.

To achieve this objective, direct measurements of the dynamic lift force and acoustic pressure, as well as, PIV measurements are performed in this work. Such measurements will provide the necessary information to clarify the energy exchange mechanism between the flow field and sound field during self-excitation of acoustic resonance.

2. METHODOLOGY

Lift force and aeroacoustic response measurements on rectangular rods of different aspect ratios are conducted inside an open-loop wind tunnel. The test section dimensions are 254 mm by 127 mm as shown in Figure 1. These selective dimensions allow self-excitation of acoustic resonance. Pressure measurements was performed along the span of a rod at 11 different points over a wide range of Reynolds number. The results showed that the maximum spanwise variation in the mean base pressure coefficient is within the experimental uncertainty of the measurements. All the tested cases were placed at 381 mm from the parabolic bell mouth entrance. At the rod specific location, hot-wire measurements reveled that the flow uniformity in the transverse direction have a maximum deviation of 1% from the free stream-stream velocity. Moreover, the turbulence intensity is less than 1% of the free-stream velocity. Flexible connection is used between the blower and the wind tunnel to eliminate any vibration transmission to the test section. The experiment was carried out in a monitored environment at a temperature of 25° and 50% humidity which is frequently monitored using an indoor climate sensor. Rectangular rods with aspect ratios of 0.5, 1 and 2 are investigated. The aspect ratio is defined as l/h, where l is the rod length in the direction of the flow and h is the rod height perpendicular to the flow. Table 1 shows the three studied cases. Acoustic pressure measurements are carried out using PCB 378A12 1/4" pressure microphone flush mounted at the top wall of the test section above the centerline of the rectangular rod. Direct lift force measurements are performed using the setup shown in Figure 1. The sensors are installed on a rigid setup that is completely isolated from the test section. Mechanical tap test was conducted to determine the mechanical resonant frequency of the force transducer setup to ensure that there is no interference between the flow periodicity frequencies and the mechanical resonant frequency of the setup.

PIV measurements are conducted in a vertical plane (x-y) where the flow field is illuminated using Litron 532 nm Nd:YAG pulsed laser and a 12-bit CCD camera is used on a double frame mode to acquire the images. For measurements before acoustic resonance excitation, 1000 image pairs are captured. Phase-locked measurements were performed at the peak of acoustic resonance excitation. The pressure signal at the top of the duct wall (see Figure 1) was used to trigger the laser pulses and camera at different points in the acoustic pressure cycle. Eight sets of measurements were obtained at equally spaced phases in the acoustic pressure cycle. Pairs of 200 images were obtained at each phase. These images were averaged to obtain the final flow field at the eight phases. Vector calculation of the captured images are conducted using an iterative multipass-cross correlation technique. For the first step, one pass was performed at an initial interrogation window size of 64×64 pixels with a 50% overlap. For the 2^{nd} and final steps, four passes were performed at a final interrogation window size of 24×24 pixels with a 50% overlap.

Case	l (in)	h (in)	A.R = l/h
1	0.5	1	0.5
2	0.5	0.5	1
3	1	0.5	2

Table 1. Investigated aspect ratios and rods dimensions.

3. RESULTS AND DISCUSSION

3.1. Strouhal Number Validation

Figure 2 shows the variation of the Strouhal number of the vortex shedding with the aspect ratio.The

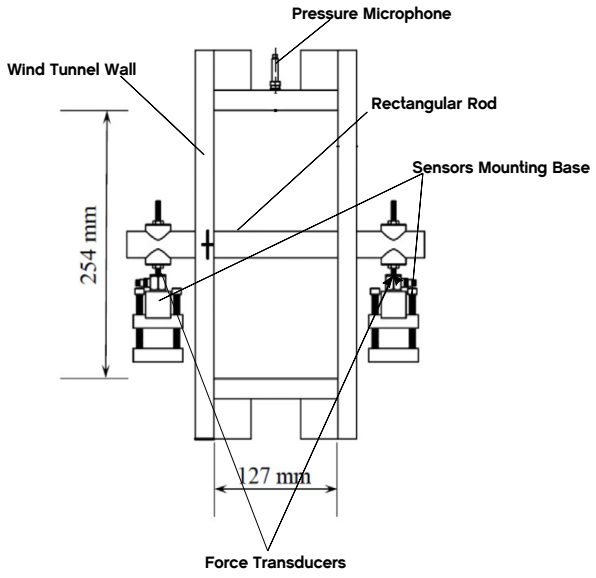

Figure 1. Schematic of the experimental setup .

Strouhal number is given by:

$$St_h = \frac{fh}{U} \tag{1}$$

Where St_h is the Strouhal number, f is the shedding frequency in the wake of the rectangular rod, h is the height of the rod, and U is the free stream velocity. The Strouhal number is extracted from the microphones' pressure signals outside of acoustic resonance excitation based on the dominant fluctuating component. The values are in good agreement with Knisely (1990). The variation of the Strouhal number based on the rod aspect ratios manifests from the fact that the flow structure in the wake of the rod is dependent on the aspect ratio. As the aspect ratio increases, the Strouhal number tends to decrease approaching the values obtained for a flat plate by Radi et al. (2013).

3.2. Time Signal Analysis

Figure 3 shows a sample of the raw signals measured from the microphone and the force sensors at a selected flow velocity of $U = 31m/s$ for an aspect ratio of $l/h = 2$. It is clear that the pressure and force signals are quite following each other with no phase difference. However, this is not the case during resonance at which energy transfer takes place between the flow and acoustic fields. Determining the phase difference between the force and the pressure helps us understand the energy exchange mechanism between the flow and acoustic fields that are required to sustain acoustic resonance. This analysis in not shown here for the sake of brevity.

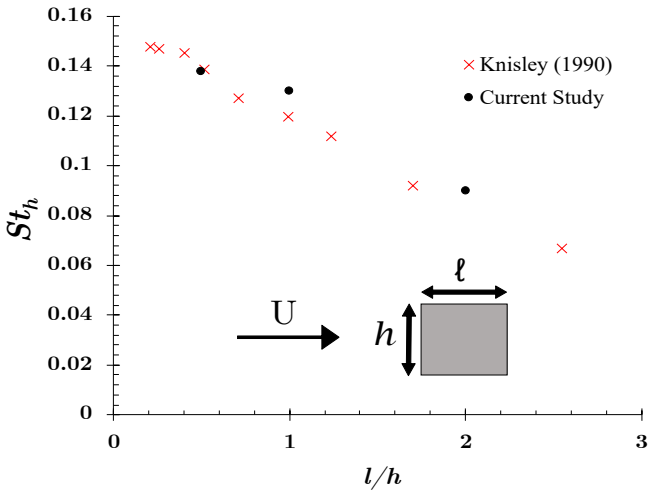

Figure 2. Vortex shedding Strouhal number St_h based on rod height h at different aspect ratios.

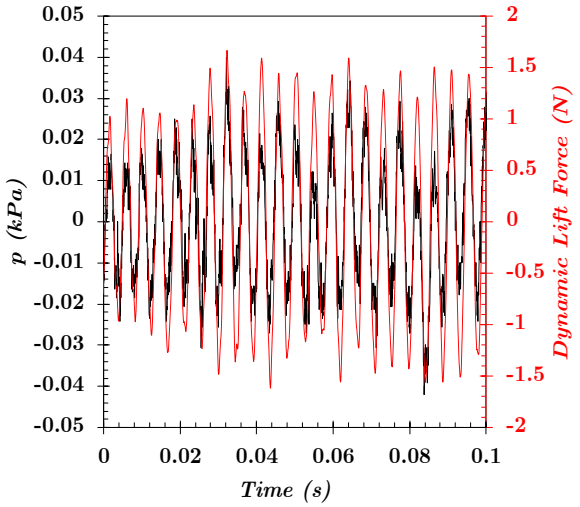

Figure 3. Raw signals measured from microphone and force sensors for an aspect ratio of $l/h = 2$ at $U = 31m/s$.

Figure 4 shows the frequency spectrum of the RMS acoustic pressure and the RMS dynamic lift for the same case shown in Figure 3. It is clear that the dynamic lift force on the rod occurres at the vortex shedding frequency which is picked by the microphone. This confirms that the periodicity downstream of the rod results in fluctuating pressure on the rod which in turn induces the fluctuating lift force.

3.3. Aeroacoustic Response

Figure 5 shows the aeroacoustic response as a waterfall plot for the three investigated aspect ratios. Fig-

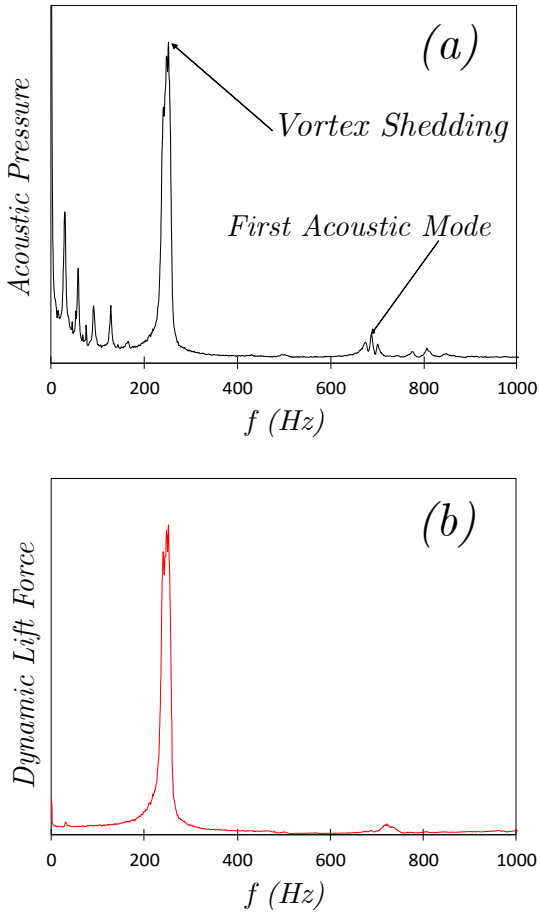

Figure 4. (a) Frequency spectrum of the RMS acoustic pressure and (b) RMS dynamic lift force for an aspect ratio of $l/h = 2$ at $U = 31m/s$ (Arbitrary scale).

ure 5(a) corresponds to a rod with an aspect ratio of $l/h = 1$, the progression of the vortex shedding is clear until lock-in starts to take place exciting the first acoustic mode of the duct at $U = 57m/s$. The acoustic pressure reaches a peak value of $P_{rms} = 396$ Pa at $U = 60m/s$. Such acoustic pressure is relatively lower compared to the generated acoustic pressure during resonance excitation from a circular cylinder with the same hydraulic diameter (Mohany and Ziada , 2011). Figure 5(b) corresponds to a rod with an aspect ratio of $l/h = 0.5$, in this case only the first acoustic mode was excited at the vortex shedding frequency coincidence with the first acoustic mode at $U = 115m/s$ generating acoustic pressure that reached a maximum value of $P_{rms} = 4209$ Pa at $U = 128m/s$. Figure 5(c) corresponds to a rod with an aspect ratio of $l/h = 2$, for this case, early excitation of the third acoustic cross-mode was observed at $U = 73m/s$ with no lock-out over the range of studied velocities. The acoustic pressure reached a peak value of $P_{rms} = 2494$ Pa at $U = 110m/s$. If we compare the three investigated cases in terms of the rod

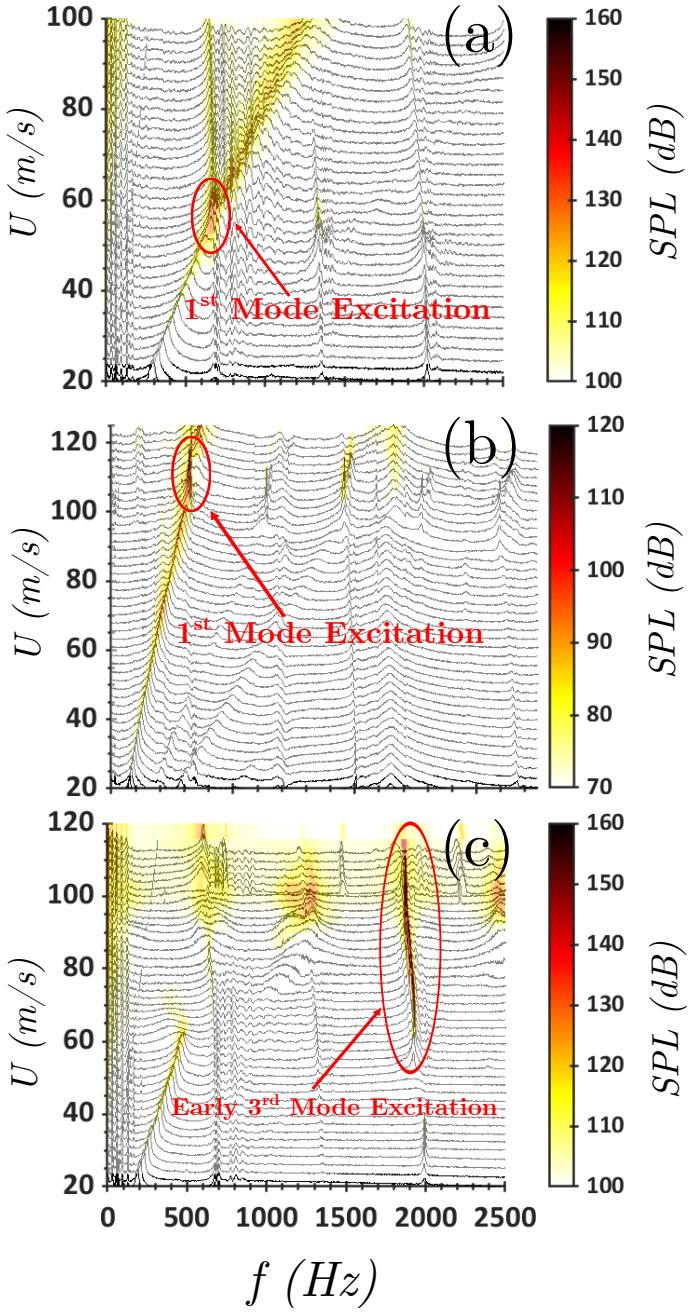

Figure 5. Waterfall plot of the acoustic response for the three investigated aspect ratios (a) $l/h = 1$, (b) $l/h = 0.5$, (c) $l/h = 2$.

length l, we can conclude that the early excitation of the third acoustic cross-mode is influenced by the rod length, these results agree with Shabaan and Mohany (2022).

3.4. Dynamic Lift Force Measurements

Figure 6 shows the fluctuating lift coefficient C_l' at the investigated range of flow velocities. It is calculated

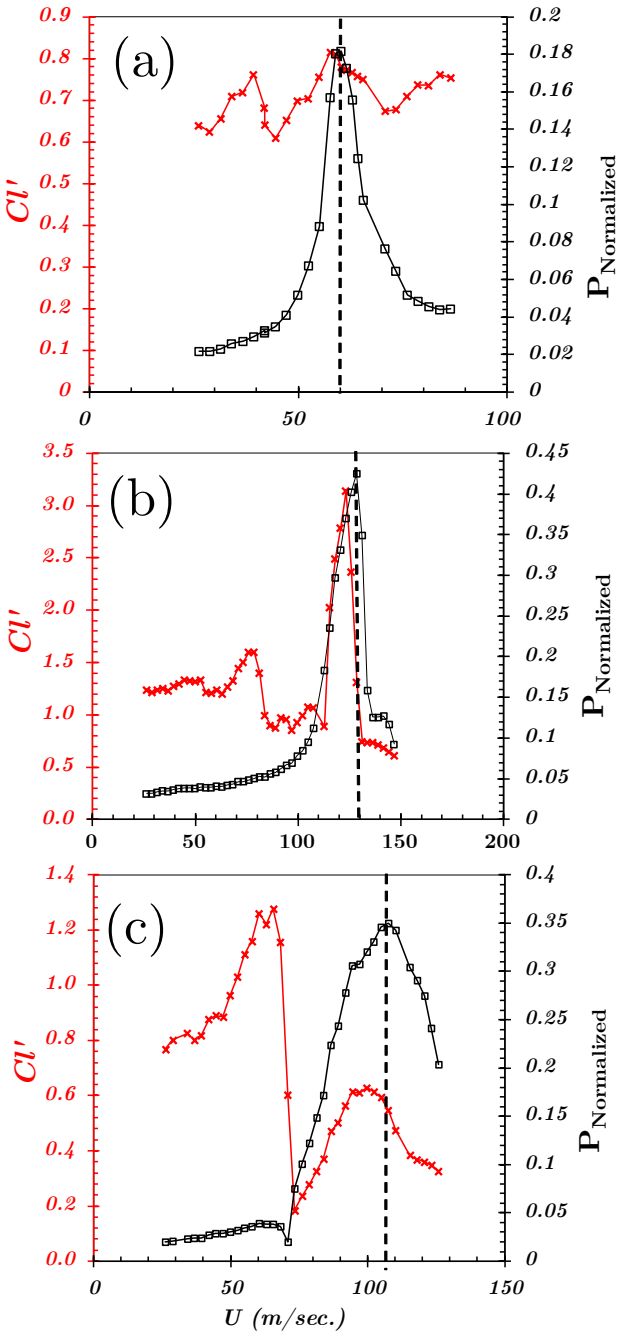

Figure 6. RMS of the dynamic lift coefficient C_l' as a function of flow velocity U with the normalized acoustic pressure superimposed (a) $l/h = 1$, (b) $l/h = 0.5$, (c) $l/h = 2$.

as follows:

$$C_L' = \frac{F_{L(RMS)}}{0.5\rho U^2 A} \tag{2}$$

Where $F_{L(RMS)}$ is the RMS of the dynamic lift force, C_l' is the RMS of the dynamic lift coefficient, ρ is the air density, U is the flow velocity, and A is the projected area of the rod in the lift force direction. The normalized acoustic pressure is superimposed on the figure to demonstrate the relation between the acoustic pressure and the fluctuating forces acting on the rod. The normalized pressure is given by:

$$P_{Normalized} = \frac{P_{rms}}{0.5\rho U^2} \tag{3}$$

It is obvious from all cases that the peak of the normalized pressure nearly coincides with the peak of C_l' which shows that there is minimum acoustic energy losses during resonance.

Figure 6(a) corresponds to a rod with an aspect ratio of $l/h = 1$. The C_l' starts at around 0.62 and peaks to 0.75 and then drops again to 0.6. Such behavior was reported by Luigi et al., (2013) for the same range of Reynolds numbers referring to this behavior as a switch from subcritical to critical Reynolds number range. During the excitation of the first acoustic mode, the C_l' reached a maximum value of 0.82. Such rise is not significant compared to the off-resonance value. This is a result of the weak excitation in terms of the acoustic pressure. Figure 6(b) corresponds to a rod with an aspect ratio of $l/h = 0.5$. Before the onset of resonance excitation, the C_l' exhibited the same trend as that for the aspect ratio of $l/h = 1$ peaking to a value of 1.7 and then dropping to a value of around 0.8. During the onset of the first acoustic mode excitation, the fluctuating lift coefficient reached a value of 3.2. Such value is 4 times higher than the value before the onset of acoustic resonance. This behaviour matches the same escalation ratio observed for a circular cylinder during acoustic resonance, as reported by Mohany and Ziada (2011). Figure 6(c) corresponds to a rod with an aspect ratio of $l/h = 2$. The C_l' was hovering around 0.9 before the early excitation of the third acoustic mode. After the lock-in into the third acoustic mode the C_l' value significantly dropped to 0.18 and then started to build up due to the acoustic resonance and peaked to a value around 0.6. It is interesting to note that, before the excitation of the third acoustic mode, the vortex shedding downstream of the rod and the shear layer separation from the upstream rod corners coexisted. However, the vortex shedding was much more significant and this can be observed from Figure 4 and Figure 5. Since, the shear layer separation and impingement between the upstream and downstream corners of the rod is what triggers the excitation of the third acoustic mode (Shabaan and Mohany , 2022), the acoustic resonance enhances the shear layer which dominates the near wake region and that results in a significant drop in the C_l' value. The third acoustic mode triggering mechanism is evident from the Strouhal number value based on rod length in the flow direction l which is around 0.4. Such value is within the shear

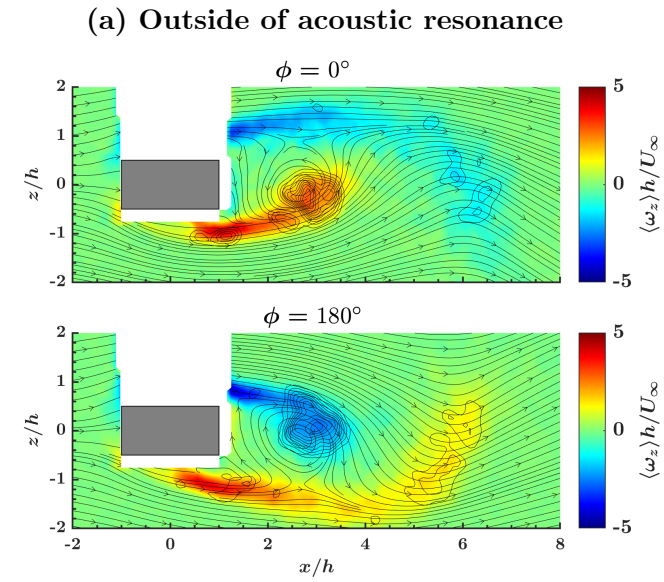

Figure 7. Vorticity (ω_z) contours with Gray dashed streamlines and solid black Q-Criterion vortex indicators are superimposed for case of an A.R= 2 (a) Phase-averaged outside of resonance at $U = 60m/s$ (b) Phase-locked during the third mode excitation at $U = 100m/s$ (peak of acoustic pressure).

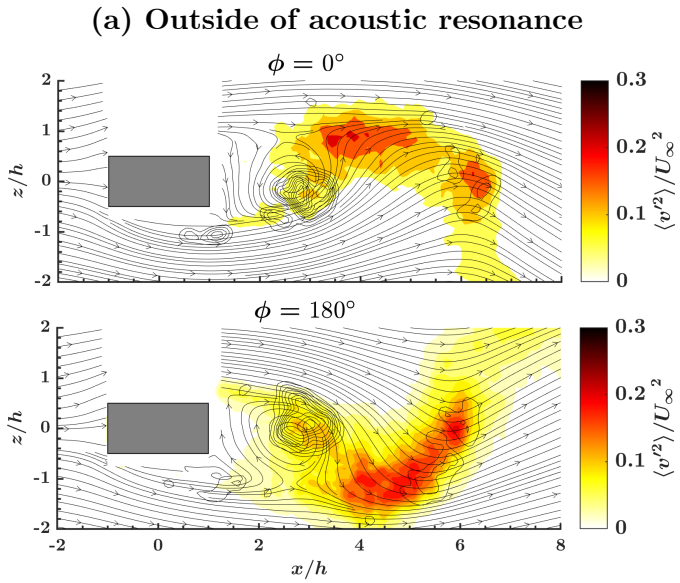

Figure 8. Normal Reynolds stress (v'^2/U^2) with Gray dashed streamlines and solid black Q-Criterion vortex indicators superimposed for the case of an A.R= 2 (a) Phase-averaged outside of resonance at $U = 60m/s$ (b) Phase-locked during the third mode excitation at $U = 100m/s$ (peak of acoustic pressure).

layer instability range and far from the vortex shedding range.

3.5. Flow Characteristics During Early Third Mode Excitation

In this section, flow characteristics of the rod with an A.R= 2 is discussed. This case was selected to further confirm the excitation mechanism of the third mode and to clarify the drop in the C_l' during third mode excitation.

Figure 7 shows the vorticity (ω_z) contours with Gray dashed streamlines and solid black Q-Criterion vortex indicators superimposed for the A.R= 2 case. It is clear from Figure 7(a) that the vortex cores is larger before third mode excitation if we compared it with Figure 7(b) at the peak of acoustic resonance excitation. Comparing Figure 7(a) and Figure 7(b) we can clearly see that during resonance the vortex shedding seizes and the vorticies generated is com-

ing from the shear layer impingement and interaction with the trailing edge. This also can be confirmed from Figure 5(c) where we can observe the vortex shedding progressing before resonance at its expected Strouhal number and it suddenly becomes undetectable during early third mode excitation. Moreover, the transversal movement and fluctuations of the streamlines are more apparent in comparison to what is observed during the third mode excitation. This can be observed from Figure 8 in which we have larger Normal Reynolds stress (v'^2/U^2) outside of acoustic resonance compared to what the values are at the peak of the third mode excitation. It is important to note that the transverse velocity fluctuation is one of the major factors influencing the fluctuating kinetic energy in the wake. Therefore, the higher magnitude of transverse Reynolds stress the higher the velocity fluctuations, and since the velocity fluctuations is what induce the fluctuating hydrodynamic loading on the rod, C_l' significantly dropped during the third mode excitation.

4. CONCLUSION

In the present study, the self-excited acoustic resonance effect on the dynamic lift force of rectangular rods with different aspect ratios was studied. For $l/h = 1$ and $l/h = 0.5$ cases, only the first acoustic cross-mode of the duct was excited when the vortex shedding frequency coincided with the duct first acoustic mode. The aspect ratio of $l/h = 0.5$ had significantly stronger excitation of the first acoustic mode than the case with an aspect ratio of $l/h = 1$ and this corresponded with the C_l' value. Therefore, the escalation ratio was substantially smaller for the rod with an aspect ratio of $l/h = 1$ compared with $l/h = 0.5$. For a rod with an aspect ratio of $l/h = 2$, early excitation of the third acoustic mode took place. This excitation was triggered by the shear layer separation and impingement from the upstream and downstream corners of the rod. Due to the much smaller vortex cores and less transverse fluctuations in the flow field during the third mode excitation the C_l' experiences significant drop compared to the value before resonance excitation.

5. REFERENCES

Curle et al., 1955, The influence of solid boundaries upon aerodynamic sound. *Proc. R. Soc. Lond. Ser. A Math. Phys. Eng. Sci.* **231(1187)**: 505-514

Inoue et al., 2002, Sound generation by a two-dimensional circular cylinder in a uniform flow. *Journal of Fluid Mechanics* **471**: 285-314

MD. Islam and A. Mohany 2020, Vortex shedding characteristics in the wake of circular finned cylinders. *Physics of fluids* **32**

CW. Knisely 1990, Strouhal numbers of rectangular cylinders at incidence: a review and new data. *Journal of Fluids and Structures* **4(4)**: 371-393

Luigi et al., 2013, Experimental investigation on the aerodynamic behavior of square cylinders with rounded corners. *Journal of Fluids and Structures* **44**: 195-204

A. Mohany and S. Ziada 2005, Flow-excited acoustic resonance of two tandem cylinders in cross-flow. *Journal of Fluids and Structures* **21**: 103-119

A. Mohany and S. Ziada 2011, Effect of acoustic resonance on the dynamic lift forces acting on two tandem cylinders in cross-flow. *Journal of Fluids and Structures* **24(3)**: 461-478

Nakamura et al., 1996, Experimental and numerical analysis of vortex shedding from elongated rectangular cylinders at low Reynolds Numbers 200 – 10^3. *J. of Wind Engineering and Industrial Aerodynamics* **65**: 301-308

Y. Ohya 1994, Note on a discontinuous change in wake pattern for a rectangular cylinder. *Journal of Fluids and Structures* **24(3)**: 461-478

A. Radi et al., 2013, From the circular cylinder to the flat plate wake: The variation of Strouhal number with Reynolds number for elliptical cylinders. *Experiments in Fluids* **25**

M. Shabaan and A. Mohany 2020, Experimental study of the self-excited resonance effect on the dynamic lift and flow structure around inline cylinders. *Journal of Fluids and Structures* **96**: 103-115

M. Shabaan and A. Mohany 2022, Flow-acoustic coupling around rectangular rods of different aspect ratios and incidence angles. *Experiments in Fluids* **63**: 1-15

S. Ziada et al., 2003, Flow excited resonance of a confined shallow cavity in low Mach number flow and its control. *Journal of Fluids and Structures* **18(1)**: 79–92

B. Van Oudheusden et al., 2005, Phase-resolved characterization of vortex shedding in the near wake of a square-section cylinder at incidence. *Experiments in Fluids* **39(1)**: 86–98

FLOW STRUCTURE, DYNAMIC LIFT FORCE, AND AEROACOUSTIC RESPONSE OF FINNED CYLINDERS IN CROSS-FLOW

M. Alziadeh & A. Mohany
Fluid-Structure Interaction and Noise Control Laboratory, Ontario Tech University, Oshawa, Canada

ABSTRACT

The flow structure, dynamic lift force, and aeroacoustic response of single finned cylinders are experimentally investigated. Two different fin types are studied with varying fin pitch (p). The results of the finned cylinders are compared with bare circular cylinders that have the same equivalent diameter (D_{eq}) as identified in the literature. It is revealed that the fins introduce fundamental changes to the flow structure around the finned cylinders that cannot be captured using bare cylinders with the equivalent diameter approach. During self-excitation of acoustic resonance, an abrupt increase in the dynamic lift force is observed, reaching a value of 6-8 times its amplitude before the onset of resonance excitation. This is double of what was reported for a single bare cylinder. Moreover, phase-locked PIV measurements revealed that the spike in the dynamic lift force and acoustic pressure for the case of the finned cylinders is due to a well organized vorticity field in comparison with that of the bare cylinder. A summary of the results is presented in this paper.

1. INTRODUCTION

Finned tubes are widely used in industrial gaseous heat exchangers due to their greater heat transfer performance compared to smooth, bare tubes. Different fin geometries and parameters are used depending on the inlet flow conditions (Reid and Taborek, 1993). Majority of the work in the literature focus on characterizing or improving heat transfer performance of the different fin geometries (Pongsoi et al., 2014; Kim and Kim, 2005). Less attention is given to the effect of the fin geometries on the unsteady flow characteristics, such as vortex shedding. Changes in the vortex shedding characteristics affect the hydrodynamic loading on the finned tubes, as well as, their susceptibility to resonant conditions such as flow-excited acoustic resonance. Acoustic resonance may arise if the vortex shedding frequency coincides with an acoustic resonant mode (f_a) of the heat exchanger enclosure, normal to the flow direction and the cylinder's axis. The onset of acoustic resonance is a design concern in heat exchangers, as it often results in severe noise levels (Blevins and Bressler, 1987; Ziada et al., 1989a) and dynamic loading on the cylinders (Mohany and Ziada, 2009, 2011). This can lead to an unsafe work environment and premature mechanical failure due to fatigue (Ziada, 2010).

During the heat exchanger design phase, critical velocities $(U_{crit.})_n$ at which acoustic resonance materializes is estimated using the following relationship:

$$(U_{crit.})_n = \frac{(f_a)_n D_{eq}}{St} \tag{1}$$

where D_{eq} is the equivalent diameter, St is the Strouhal number, which is estimated from empirical Strouhal charts, and n is the acoustic resonant mode index (Ziada et al., 1989b). For a bare cylinder, the equivalent diameter (D_{eq}) is the outer tube diameter (i.e $D_{eq} = D$). In the case of the finned cylinders, the equivalent diameter (D_{eq}) depends on the fin pitch (p), fin thickness (t), root (base) diameter (D_r), and fin diameter (D_f). Contingent on the fin geometry, the equivalent diameter (D_{eq}) is calculated using different equivalent diameter formulas presented in the literature (Mair et al., 1975; Hirota et al., 2002; Alziadeh and Mohany, 2018, 2022a). Basically, the equivalent diameter represents a bare cylinder diameter with an equivalent flow blockage as a finned cylinder. Though the equivalent diameter can be used to reasonably estimate the vortex shedding frequency emanating from the finned cylinders at off-resonant conditions, recent investigations have revealed that the equivalent diameter approach is flawed when trying to predict the onset of acoustic resonant excitation for finned cylinders (Arafa and Mohany, 2019; Islam et al., 2020; Alziadeh and Mohany, 2022a,b). This is because the equivalent diameter approach does not capture the salient vortex shedding characteristics due to the addition of fins. Changes in the vortex shedding characteristics caused by the additions of fins affected the flow field's susceptibility to acoustic resonance excitation. This ultimately resulted in different aeroacoustic response in comparison to their equivalent diameter bare cylinder. For some finned cylinder cases, self-excitation of acoustic resonance occurred earlier and generated

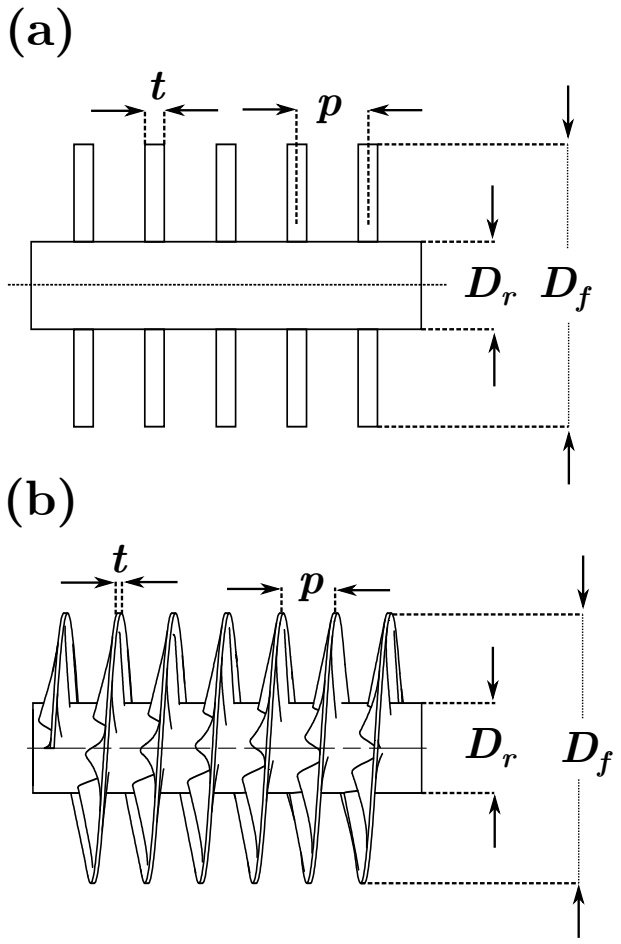

Figure 1. Schematic of (a) Straight finned cylinder; and (b) Crimped spirally finned cylinder.

greater sound pressure levels compared to bare cylinders with the same equivalent diameter (Arafa and Mohany, 2019; Islam et al., 2020; Alziadeh and Mohany, 2022a).

In spite of the wide usage of finned tubes in engineering applications, the effect of fins on the vortex shedding characteristics and their impact on the hydrodynamic loading of the finned cylinders during acoustic resonance excitation is non-existent in the literature. An understanding of this is necessary in order to capture the intrinsic changes in the flow-sound interaction mechanism due to the addition of fins. This is vital to ensure safer design of finned tube heat exchangers. Therefore, the main objective of this paper is to experimentally clarify the fins role on the vortex shedding characteristics and its impact on the hydrodynamic loading during self-excitation of acoustic resonance. This is achieved by performing direct measurements of the dynamic lift force and particle image velocimetry (PIV) measurements during resonance excitation. Two types of finned cylinders of interest in this investigation are straight circular fins and crimped, spiral fins. A schematic of the straight circular and crimped spirally finned cylinders with the important fin parameters labelled, is shown in Figure 1. Crimped fins exhibit a sinusoidal pattern which achieves better flow exposure and better contact area between the fins and base tube. This improved heat transfer rates in comparison to straight finned cylinders, making their usage increasingly more popular in industrial heat exchanger applications (Keawkamrop et al., 2021). Three different fin pitches (p) are studied for each finned cylinder case. These fin pitches (p) reside within the range typically found in the heat exchanger industry (Reid and Taborek, 1993; Pongsoi et al., 2012). A preliminary summary of the results are presented herein.

2. EXPERIMENTAL SETUP

The experiments are performed in the subsonic open circuit wind tunnel at the Fluid-Structure Interaction and Noise Control Laboratory located at Ontario Tech University, Oshawa, Canada. The wind tunnel consists of a rectangular test section with a height (H) of 254 mm and width (W) of 127 mm. These dimensions are carefully selected to ensure $self$-excitation of the fundamental acoustic-cross mode (f_a), which is:

$$f_a = \frac{c}{2H} \tag{2}$$

where c is the speed of sound, and H is the duct height. In this case, the theoretical frequency of the fundamental acoustic-cross mode is $f_a \approx 675$ Hz. This is within 3% of what is experimentally measured. A parabolic bell mouth is installed at the inlet to produce a uniform velocity distribution within $\pm 1\%$ inside the test section. The tested cylinders are rigidly mounted at the center of the test section, which is located at the acoustic pressure node (acoustic particle velocity anti-node of the first acoustic cross-mode). To ensure spanwise uniformity of the flow at the cylinder location, time-averaged pressure measurements at the cylinder base (180° from the stagnation point) were performed at 11 points along the cylinder span, with the closest distance from the side walls being 6 mm. The results showed that the base pressure along the cylinder span were the same within $\pm 4\%$ for a wide range of flow velocities.

For the straight finned cylinders, the equivalent diameter (D_{eq}) is calculated using Mair et al. (Mair et al., 1975) effective diameter formula. The effective diameter formula is as follows:

$$D_{eq} = D_r + (D_f - D_r)\frac{t}{p} \tag{3}$$

Table 1. Dimensions of crimped spirally finned cylinder. Acronyms 'SF' and 'CF' represent straight and crimped finned cylinders, respectively.

	D_r [mm]	D_f [mm]	t [mm]	p [mm]	D_{eq} [mm]
SF1	12.7	25.4	1.5	6.35	15.7
SF2	12.7	25.4	1.5	4.50	16.9
SF3	12.7	25.4	1.5	3.00	19.0
CF1	12.7	37.0	0.7	9.4	20.3
CF2	12.7	37.0	0.7	6.5	21.1
CF3	12.7	37.0	0.7	4.7	25.0

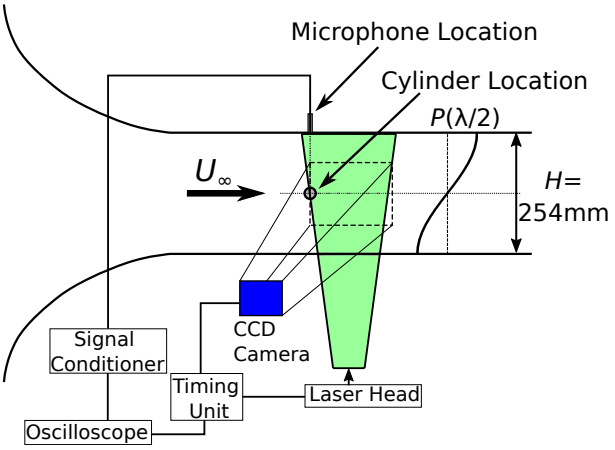

Figure 2. Schematic of the open circuit wind tunnel with the phase-locked PIV measurements setup.

The modified equivalent diameter equation developed by Alziadeh and Mohany (2018) is used to calculate the equivalent diameter (D_{eq}) for crimped spirally finned cylinders. This is as follows:

$$D_{eq} = D_r + (D_f - D_r)\frac{t_c}{p} \quad for \quad \frac{p}{D_r} > 0.385$$

$$D_{eq} = \sqrt{{D_r}^2 + ({D_f}^2 - {D_r}^2)\frac{t_c}{p}} \quad for \quad \frac{p}{D_r} \leq 0.385 \tag{4}$$

where,

$$t_c = t + \frac{pD_f}{\pi(D_f + D_r)} \tag{5}$$

The parameter t_c represents the total fin thickness which contains the nominal fin thickness (t) and the crimp thickness $\left(\frac{pD_f}{\pi(D_f+D_r)}\right)$. Table 1 shows the dimensions of fin parameters for the straight finned (SF) and crimped finned (CF) cylinders investigated.

2.1. Particle Image Velocimetry (PIV) Setup

The measurements were performed using a LaVision PIV system on the $x-y$ plane at the center of cylinder (i.e at $W/2$). The measurements field was illuminated by a 532 nm double-head Nd:YAG laser. The double head laser generates two beams which pulse at a maximum frequency of 15 Hz. Di-Ethyl-Hexyl-Sebacat (DEHS) particles are used to seed the flow field, which were atomized to a maximum particle size of 1 μm. Flow field images are captured using a 12-bit Charged-Coupled Device (CCD) camera in double frame mode. The camera resolution is 2752 $\times$ 2200 pixels. Vector calculations are performed by an iterative multipass cross correlation technique (Scarano and Riethmuller, 2000) with one pass at an initial interrogation window size of 64$\times$64 pixels, and four passes at a final interrogation size of 24$\times$24 pixels, both with a 50% overlap. The minimum spatial resolution of the final vector field is $0.03D_{eq}\times$ $0.03D_{eq}$. The uncertainty of the instantaneous flow fields measured in the near-wake is less than 10% with a 95% confidence interval. The uncertainty was calculated using the correlation statistics method (Wieneke, 2015).

Phase-locked measurements are performed at the peak of flow-excited acoustic resonance. The flush-mounted microphone at the top wall of the duct, above the cylinder, as shown in Figure 2, is used to trigger the laser pulses at preset times. This is done to capture the flow field at different phase angles (ϕ) over the complete acoustic pressure cycle. At each phase angle in the acoustic pressure cycle, 250 instantaneous image pairs are captured. These images are averaged to produce the final phase-averaged flow field. A universal outlier detector filter (Westerweel and Scarano, 2005) with a filter size of 3 $\times$ 3 pixels was used to detect and remove spurious vectors. The phase-locked PIV measurements setup is shown in Figure 2.

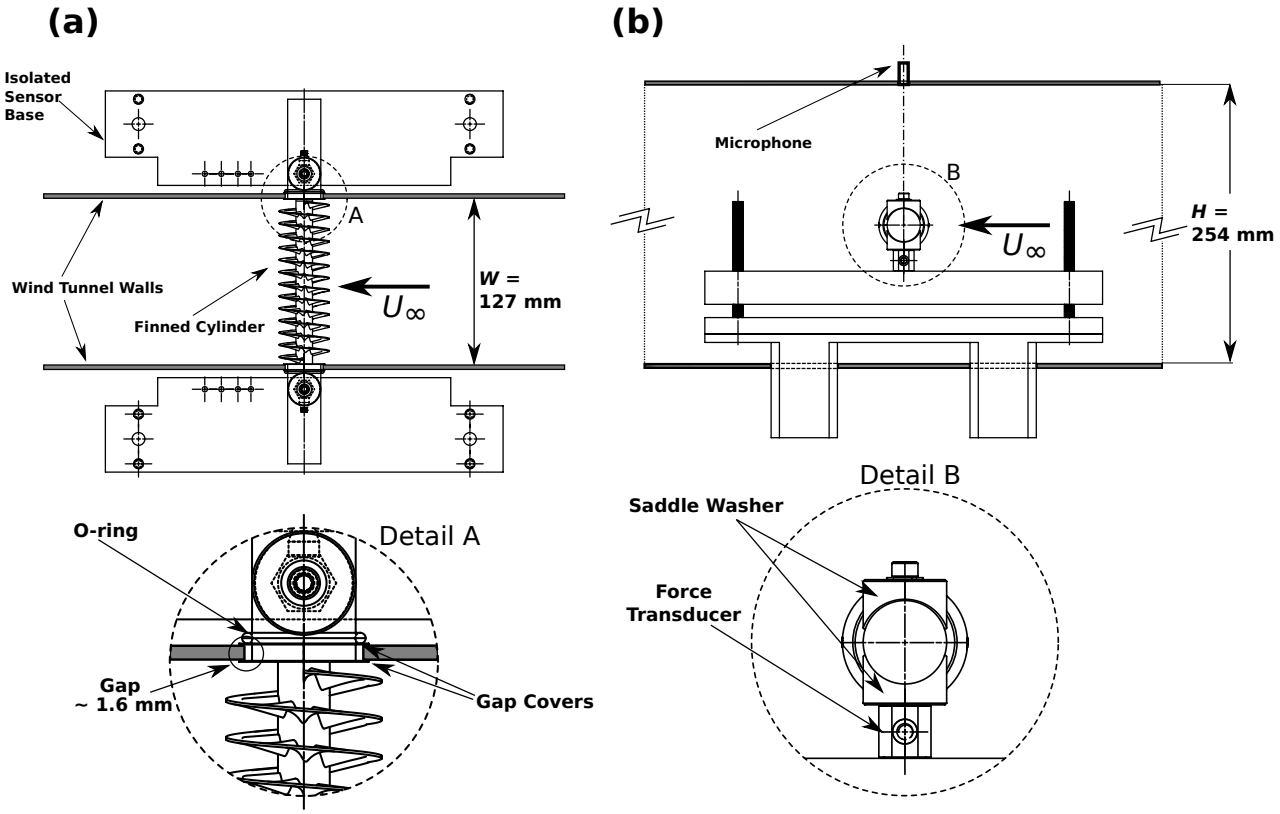

Figure 3. Schematic of force measurement setup (a) Top view; and (b) Side view.

2.2. Dynamic Lift Force and Acoustic Pressure Measurements

Aeroacoustic response measurements are performed by utilizing a single 6.35 mm pre-polarized pressure microphone, which is flush-mounted on the top wall of the test section. This location corresponds to the location of the maximum acoustic pressure amplitude of the 1^{st} acoustic cross-mode (see Figure 2). The microphone is positioned directly above the upstream cylinder.

Dynamic lift force measurements are performed by utilizing two piezoelectric force transducers (PCB Model: 208C01) installed at both sides of the cylinder outside of the test section. The force sensors exhibit a nominal sensitivity of 112.4 mV/N, RMS resolution of 45 μN, frequency range of 36 kHz, and a measurement range of $\pm$44.48 N. The force transducers are mounted on sensor bases that are installed on rigid supports isolated from the test section. The cylinders pass through a gap of $\approx$ 1.6 mm through the side walls of the duct. To ensure that the gap does not disturb the measurements, the gap holes which the cylinders pass through is covered using a thin plastic cover (0.254 mm in thickness). The plastic cover is undersized to not wiggle or move on the cylinder during the measurements. Finally, cling wrap and an oiled o-ring outside of the test section is used to seal the gap. The center-to-center distance between the force transducers is 165.1 mm (6.5 in). This setup gives a high mechanical resonance frequency which is sufficiently far from the frequency of interest. The frequency of interest is f_a = 675 Hz (fundamental acoustic cross-mode of the duct). The force measurements setup is shown in Figure 3.

The acoustic pressure measurements and dynamic lift force measurements are performed simultaneously. The measurements are recorded for 120 seconds and sampled at 20 kHz. The power spectral density (PSD) of the signal is calculated using Welch's, averaged, modified periodogram method using a Hanning window and 50% overlap (Welch, 1967). The frequency resolution of the spectra is 1 Hz. The root-mean-square (RMS) of the signal is calculated by applying a fourth-order bandpass filter over a band of $\pm$50 Hz around the center peak [i.e. vortex shedding peak (f_v)]. The aeroacoustic response and lift force curve was obtained by recording the RMS force and acoustic pressure at discrete upstream flow velocities (U_∞) between $13 \leq U_\infty \leq 140$ m/s.

Table 2. Fluctuating lift coefficient on a bare, circular cylinder.

Study	$\mathrm{Re}_D \times 10^{-4}$	W/D	$C_L{}'$
Keefe (1962)	0.3-10	18	0.27-0.52
West and Apelt (1982)	1.1-22	15-35	0.46-0.61
Szepessy and Bearman (1992)	0.9-14	6.7	0.30-0.53
Present	2.3-9.9	5	0.35-0.61

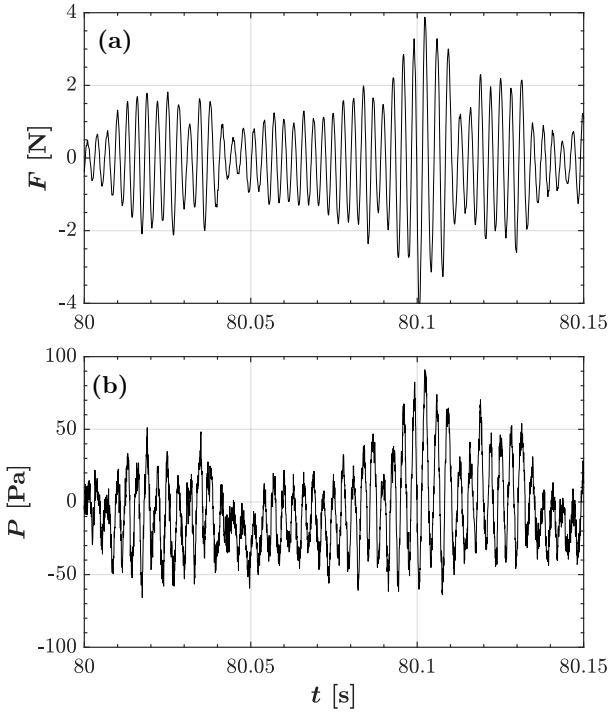

Figure 4. Time signal of (a) Lift force; and (b) Acoustic pressure measurements at 41 m/s (off-resonance condition).

3. RESULTS AND DISCUSSION

Figure 4 shows a sample of the simultaneously measured acoustic pressure and force signals. As shown in Figure 4, it is evident that the pressure signal is correlated with the force signal. For instance, when there is an increase or reduction in the lift force, there is a proportional increase or reduction in the acoustic pressure, respectively. The benefit of measuring the signals simultaneously is that the phasing information between both signals can be utilized to identify the energy transfer between the flow and sound fields. However, the energy transfer analysis between the flow and sound fields are not shown here for brevity.

Figure 5 shows an arbitrary scale of the pressure and force spectra for the same time signal shown in Figure 4. As shown in Figure 5, both the pressure and force spectra exhibit the same sharp peak at 320 Hz, which corresponds to the vortex shedding peak (f_v). The difference between both spectra is that the force sensors only picks up the vortex shedding frequency (f_v) and the microphone measures both the vortex shedding frequency and the frequency of the first acoustic-cross mode (f_a). The pressure and force spectra measurements are repeated at discrete flow velocities and their RMS values are plotted in the proceeding sections in Figure 6 and 7, respectively.

3.1. Aeroacoustic Response

Figure 6 shows the aeroacoustic response of the straight finned and spirally crimped finned cylinders in comparison with their equivalent diameter bare cylinders. The finned cases shown in Figure 6 are the cases that produced the highest normalized acoustic pressure (P^*) in their category. The flow velocity is normalized using the reduced flow velocity (U_r) relationship, which is:

$$U_r = \frac{U_\infty}{f_a D_{eq}} \tag{6}$$

where f_a is the frequency of the fundamental acoustic-cross mode of the duct, and U_∞ is the upstream flow velocity. The acoustic pressure is normalized using the P^* relationship presented by Mohany and Ziada (2005):

$$P^* = \frac{2P_{rms}c}{\rho {U_\infty}^3} \tag{7}$$

As shown in Figure 6(a), when the flow velocity is normalized by the reduced flow velocity (U_r), the vortex shedding frequency data for all the cases collapses at a $\mathrm{St}_{Deq} \approx 0.2$. This is typical for the case of single, circular bare and finned cylinders Mair et al. (1975). However, in the case of the finned cylinders the onset of resonance appears to occur at a slightly lower reduced flow velocity in comparison to their equivalent diameter bare cylinders. Moreover, the finned cylinders experience a more sudden and abrupt increase in the acoustic pressure. In the case

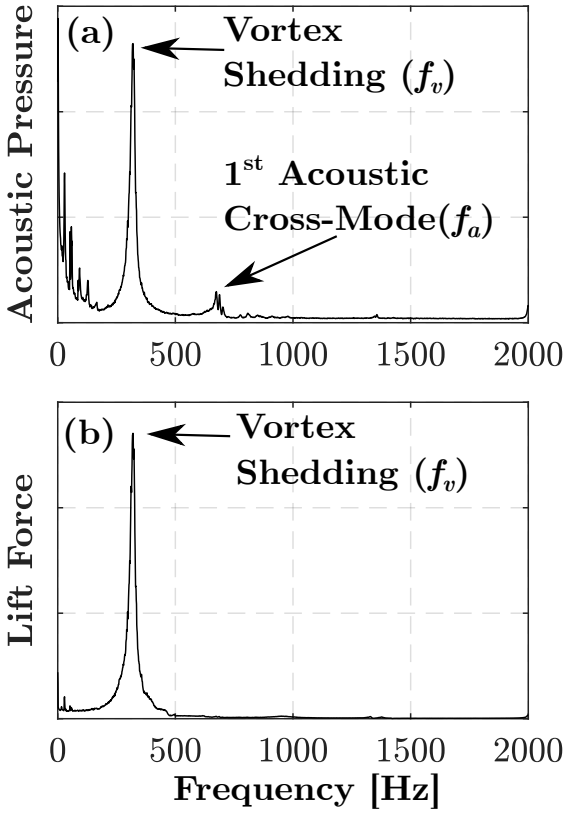

Figure 5. (a) Acoustic pressure spectra; and (b) force spectra at off-resonance flow conditions at 41 m/s. An arbitrary scale of the y-axis is shown.

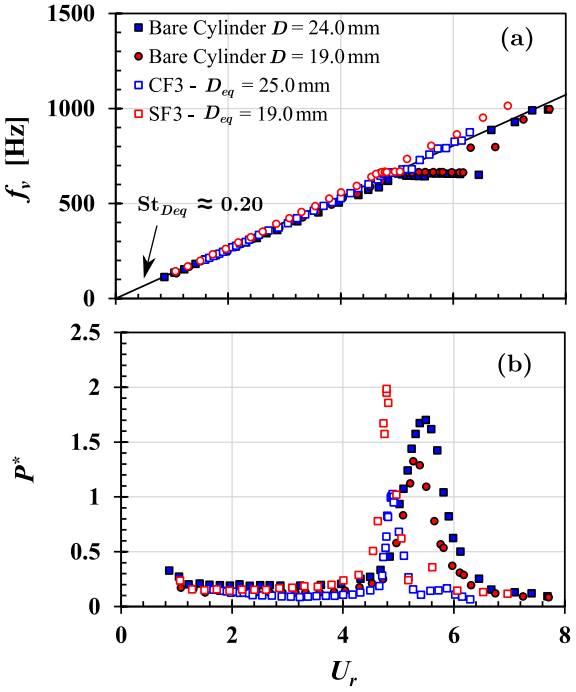

Figure 6. (a) Frequency of the vortex shedding; and (b) RMS acoustic pressure within the vortex shedding frequency band as a function of the reduced velocity.

of the finned cylinders, the acoustic pressure peaks and exits the lock-in range before the bare cylinders reach the peak acoustic pressure. For the case of CF3, the peak acoustic pressure is lower than its equivalent diameter bare cylinder. However, the increase in the acoustic pressure during excitation is steeper in the case of CF3. This sharp and sudden increase in the acoustic pressure for the case of the finned cylinders eludes to an unsteady flow field that is more susceptible to acoustic resonance excitation.

3.2. Dynamic Lift Force

Table 2 shows a comparison of the fluctuating lift coefficient ($C_L{}'$) measured in the present study for a circular cylinder at off-resonance conditions with those found in the literature. The fluctuating lift coefficient ($C_L{}'$) is as follows:

$$C_L{}' = \frac{F_{rms}}{0.5\rho U_\infty{}^2 D_{eq} W} \tag{8}$$

where ρ is the air density. As shown in Table 2, the fluctuating lift coefficient ($C_L{}'$) measured in this study for the case of a bare, circular cylinder at off-resonance conditions is in good agreement with those found in the literature within the same Reynolds number range.

Figure 7 shows the fluctuating lift coefficient ($C_L{}'$) for the same finned cylinder cases shown in Figure 6. As shown in Figure 7, the $C_L{}'$ values at off-resonance conditions ($U_r < 4.0$) are within the range of what is found in the literature for the case of a bare cylinder (Mohany and Ziada, 2011). However, at the onset of acoustic resonance, the finned cylinders experience a significant spike in the $C_L{}'$. The spike in the $C_L{}'$ is 6 to 8 times that observed at off-resonance conditions. This is nearly double the jump in amplitude of 3-4 times that is typically observed by a single bare cylinder (Mohany and Ziada, 2011). These results are clearly indicative of the difference in the flow-sound interaction mechanism between the bare and finned cylinder cases which can never be captured using the equivalent diameter approach.

3.3. Phased-Locked PIV Measurements

Figure 8 shows a comparison of the normalized vorticity field at a phase angle of $\phi = 0°$ in the

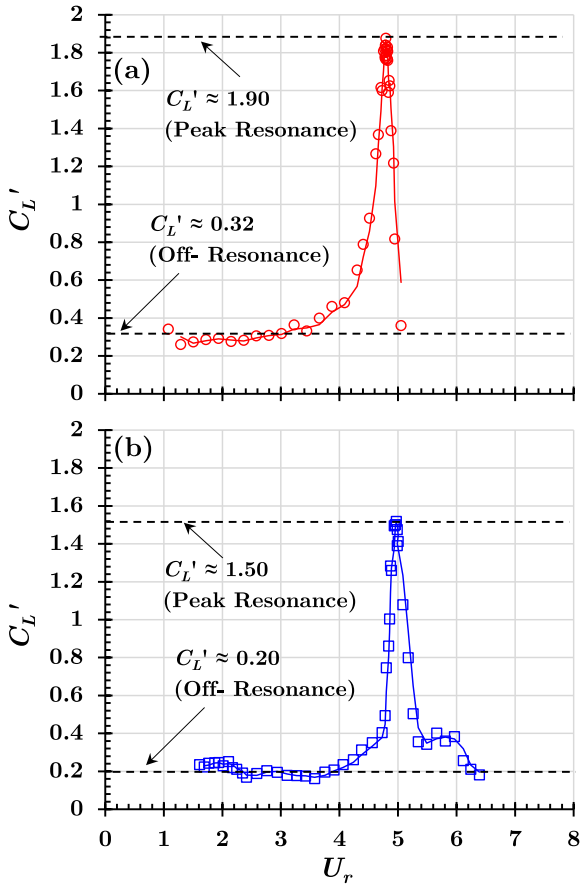

Figure 7. Fluctuating lift coefficient vs reduced velocity for the case of: (a) SF3; and (b) CF3.

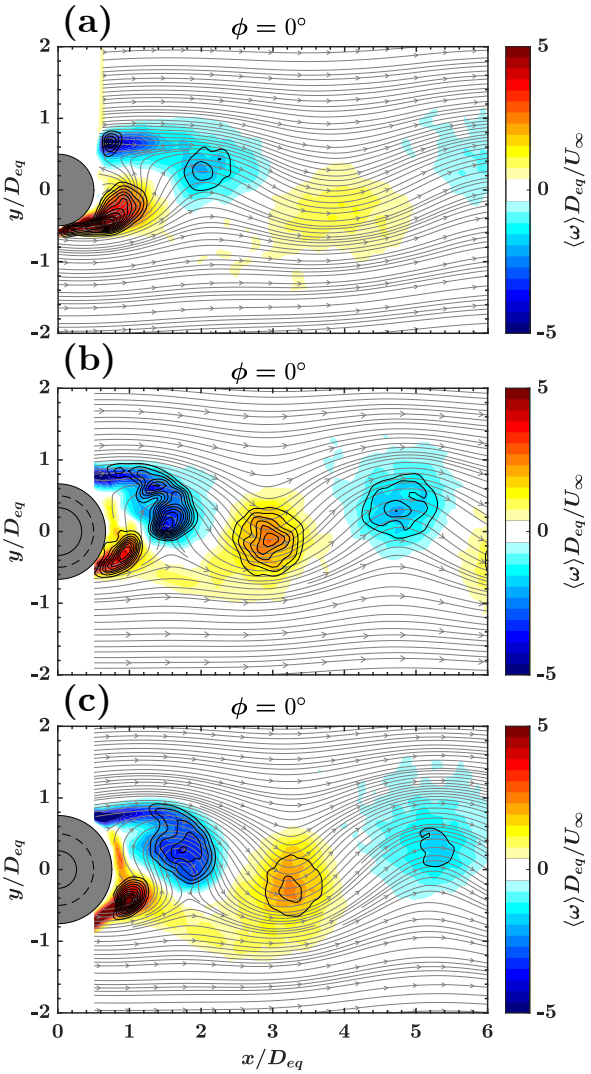

Figure 8. Comparison of the phase-locked vorticity field downstream of the cylinders at a phase angle of $\phi = 0°$ during self-excitation of acoustic resonance. (a) Bare cylinder; (b) SF3; and (c) CF3

acoustic pressure cycle for the case of a bare cylinder, straight circular finned cylinder (SF3), and crimped spiral finned cylinder (CF3). As evident in Figure 8(b), in both finned cylinder cases (SF3 and CF3), the vortex cores appear to be more distinct and maintain its structure at greater downstream distances in comparison to the case of the bare cylinder. This illustrates a more organized vorticity field. The more organized flow field in case of the finned cylinders, explains the spike in the acoustic pressure and dynamic lift force during acoustic resonance excitation, as shown in Figure 6(b) and Figure 7, respectively. The reason for this is because the acoustic field can better modulate an organized flow field (Alziadeh and Mohany, 2022b). This leads to the formation of distinct vortex cores and the abrupt spike in the fluctuating lift force and acoustic pressure during acoustic resonance for the case of the finned cylinders. The results of this paper show that the addition of fins to a bare cylinders can enhance the vortex shedding process which makes the flow field more susceptible to resonance excitation. This enhancement depends on the type of fins as well as the fin pitch.

4. CONCLUSION

In the present study, the flow structure, dynamic lift force, and the aeroacoustic response of single finned cylinders were investigated. The two different fin types investigated are the straight and spiral, crimped finned cylinders. The parameter of interest was the fin pitch (p), where three different fin pitches (fin densities) were studied for each finned cylinder type. The finned cylinders were compared to a bare, circular cylinder with the same equivalent diameter. The rest of the fin parameters remained constant. During self-excitation of acoustic resonance, the finned cylinders

experienced an abrupt increase in the acoustic pressure and dynamic lift force. The dynamic lift force increased by 6 to 8 times in the case of the finned cylinder. This increase is nearly double than what was reported in the literature for the case of a bare, circular cylinder. Phase-locked PIV measurements revealed that the abrupt increase in the acoustic pressure and dynamic lift in the case of the finned cylinders was due to a well-organized vorticity field. In the case of the bare cylinder, the vortex cores are not as well defined as what is observed in the case of the finned cylinders.

References

M. Alziadeh and A. Mohany. Near-wake characteristics and acoustic resonance excitation of crimped spirally finned cylinders in cross-flow. *Journal of Pressure Vessel Technology*, 140(5), 2018.

M. Alziadeh and A. Mohany. Applicability of the equivalent diameter approach to estimate vortex shedding frequency and acoustic resonance excitation from different finned cylinders in cross-flow. *Journal of Pressure Vessel Technology*, 144(4): 041406, 2022a.

M. Alziadeh and A. Mohany. Vortex dynamics of tandem bare and spiral finned cylinders in cross-flow and their susceptibility to acoustic resonance excitation. *Physics of Fluids*, 34(4):045105, 2022b.

N. Arafa and A. Mohany. Wake structures and acoustic resonance excitation of a single finned cylinder in cross-flow. *Journal of Fluids and Structures*, 86: 70–93, 2019.

R. Blevins and M. Bressler. Acoustic resonance in heat exchanger tube bundles—part i: Physical nature of the phenomenon. 1987.

K. Hirota, T. Nakamura, H. Kikuchi, K. Isozaki, and H. Kawahara. Fluidelastic and vortex induced vibration of a finned tube array. In *ASME 2002 International Mechanical Engineering Congress and Exposition*, pages 729–735. American Society of Mechanical Engineers Digital Collection, 2002.

M. R. Islam, M. Shaaban, and A. Mohany. Vortex dynamics and acoustic sources in the wake of finned cylinders during resonance excitation. *Physics of Fluids*, 32(7):075117, 2020.

T. Keawkamrop, L. G. Asirvatham, A. S. Dalkılıç, H. S. Ahn, O. Mahian, and S. Wongwises. An experimental investigation of the air-side performance of crimped spiral fin-and-tube heat exchangers with a small tube diameter. *International Journal of Heat and Mass Transfer*, 178:121571, 2021.

R. T. Keefe. Investigation of the fluctuating forces acting on a stationary circular cylinder in a subsonic stream and of the associated sound field. *The Journal of the Acoustical Society of America*, 34 (11):1711–1714, 1962.

Y. Kim and Y. Kim. Heat transfer characteristics of flat plate finned-tube heat exchangers with large fin pitch. *International Journal of Refrigeration*, 28 (6):851–858, 2005.

W. Mair, P. Jones, and R. Palmer. Vortex shedding from finned tubes. *Journal of Sound and Vibration*, 39(3):293–296, 1975.

A. Mohany and S. Ziada. Flow-excited acoustic resonance of two tandem cylinders in cross-flow. *Journal of Fluids and Structures*, 21(1):103–119, 2005.

A. Mohany and S. Ziada. Effect of acoustic resonance on the dynamic lift forces acting on two tandem cylinders in cross-flow. *Journal of Fluids and Structures*, 25(3):461–478, 2009.

A. Mohany and S. Ziada. Measurements of the dynamic lift force acting on a circular cylinder in cross-flow and exposed to acoustic resonance. *Journal of Fluids and Structures*, 27(8):1149–1164, 2011.

P. Pongsoi, S. Pikulkajorn, C.-C. Wang, and S. Wongwises. Effect of number of tube rows on the air-side performance of crimped spiral fin-and-tube heat exchanger with a multipass parallel and counter cross-flow configuration. *International journal of heat and mass transfer*, 55(4):1403–1411, 2012.

P. Pongsoi, S. Pikulkajorn, and S. Wongwises. Heat transfer and flow characteristics of spiral fin-and-tube heat exchangers: A review. *International journal of Heat and Mass transfer*, 79:417–431, 2014.

D. R. Reid and J. Taborek. Selection criteria for plain and segmented finned tubes for heat recovery systems. In *Turbo Expo: Power for Land, Sea, and Air*, volume 78897, page V002T09A007. American Society of Mechanical Engineers, 1993.

F. Scarano and M. L. Riethmuller. Advances in iterative multigrid piv image processing. *Experiments in fluids*, 29(1):S051–S060, 2000.

S. Szepessy and P. Bearman. Aspect ratio and end plate effects on vortex shedding from a circular cylinder. *Journal of Fluid Mechanics*, 234:191–217, 1992.

P. Welch. The use of fast fourier transform for the estimation of power spectra: a method based on time averaging over short, modified periodograms. *IEEE Transactions on audio and electroacoustics*, 15(2):70–73, 1967.

G. West and C. Apelt. The effects of tunnel blockage and aspect ratio on the mean flow past a circular cylinder with reynolds numbers between 104 and 105. *Journal of Fluid mechanics*, 114:361–377, 1982.

J. Westerweel and F. Scarano. Universal outlier detection for piv data. *Experiments in fluids*, 39(6): 1096–1100, 2005.

B. Wieneke. Piv uncertainty quantification from correlation statistics. *Measurement Science and Technology*, 26(7):074002, 2015.

S. Ziada. Flow-excited acoustic resonance in industry. *Journal of Pressure Vessel Technology*, 132(1), 2010.

S. Ziada, A. Oengören, and E. Bühlmann. On acoustical resonance in tube arrays part i: Experiments. *Journal of Fluids and Structures*, 3(3):293–314, 1989a.

S. Ziada, A. Oengören, and E. Bühlmann. On acoustical resonance in tube arrays part ii: Damping criteria. *Journal of Fluids and Structures*, 3(3):315–324, 1989b.

FLOW-INDUCED TONES IN A DEEP PERIODIC CAVITY

Joachim Golliard
Laboratoire d'Acoustique - Le Mans Université (LAUM)
Centre de Transfert de Technologie du Mans (CTTM)
Le Mans, France

Yves Aurégan
Laboratoire d'Acoustique - Le Mans Université (LAUM)
Le Mans, France

ABSTRACT

This paper reports a set of experiments with a chamber made of a succession of 10 deep cavities. This periodic geometry creates a bandgap of forbidden frequencies for which transmission of sound is not possible. This behaviour is first investigated with some measurements and simulations of the transmission coefficients. When a low-Mach number flow is added through the chamber, small changes on the transmission coefficients are observed. Particularly, the transmission coefficient can become larger than one at some frequencies, indicating a possible whistling of the cavities when installed in favourable conditions. The frequency range of amplification depends on the flow velocity following a nearly constant Strouhal number for the lowest velocities, but when reaching the range of forbidden frequencies, the amplification stops. A second set of measurements is reported where the cavity, installed between two anechoic terminations, is submitted to a mean flow of increasing velocity. Whistling tones are observed, once again following the Strouhal number dependency until the bandgap, but a tone is also observed right in the middle of the bandgap. This unexpected behaviour is related to azimuthal modes in the cavities.

1. INTRODUCTION

Periodic structures have interesting properties regarding acoustic propagation. One of the most striking properties is the fact that propagation is not possible in certain frequency ranges. In the limiting case of infinitely long structures, this can be illustrated through the dispersion relation of propagation in the equivalent continuous medium. The dispersion plots exhibit frequency bands (called bandgaps) for which no modes with a real wavenumber exist, which means that acoustic propagation is not possible in these frequency bands.

Even in the case of a finite number of repetitions, such band gaps can be observed. A simple illustration can be given where a number of closed side-branches is considered. If only one side branch of length L is present, this creates a filter which prevents propagation at a single frequency (and its odd harmonics) corresponding to a wavelength equal to four times the length of the side branch. This can be illustrated by the transmission coefficient (ratio of transmitted to incident wave amplitude) which is zero at a single frequency (blue line in Figure 1) for this friction-less model prediction. Now consider two side branches are placed at short distance from each other, compared to the acoustic wavelength. In this case, the region of low transmission splits in two: there are now two acoustic modes corresponding to (1) an in phase oscillation of the two side branches and (2) an out of phase oscillation of the two side branches. The frequency of the first mode is very close to that of the isolated side branche resonance. The out of phase oscillation mode has a lower resonance frequency, because the fluid between the two branches provides an additional added mass to the system, compared to the single side branch. The split is thus not centred around the low-transmission frequency of a single side-branch (red line in Figure 1). This has the effect of widening the range of frequencies where transmission is not possible. When additional (identical) side branches are added in a periodic pattern, the frequency range without transmission further increases (yellow line in Figure 1, for 5 side branches spaced by half of their length). The other effect, typical of finite periodic systems, is to add a number (equal to the number of side branches minus one) of transmission minima at frequencies just under the wide minimum centerd at $L = \lambda/4$.

A similar effect is observed when considering the transmission coefficient of a main pipe traversing a periodic succession of axisymmetric cavities at their centreline. In this case, the acoustic plane waves in the main pipe couple with the radial modes of the cavities which have a pressure minimum at their centre,

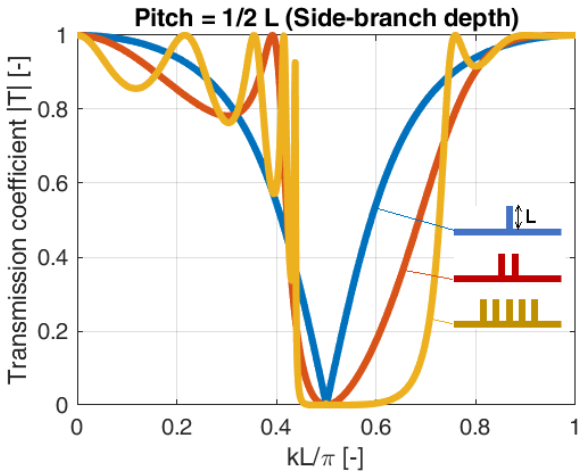

Figure 1. Transmission coefficient due to 1 (blue line), 2 (red line) or 5 (yellow line) side branches in a main pipe. The side branches have the same diameter as the main pipe and are separated by half of their depth for this illustration.

as for the quarter-wavelength modes in side-branches which have a minimum pressure at the connection with the main pipe. On the other hand, azimuthal modes in the cavities have a zero-averaged acoustic flux across any centred disk (including the one representing the section of the main pipe) and can therefore not couple with the plane waves in the main pipe (as would be the case with the out-of-phase modes of a similar array with axially opposed side branches). This case, with 10 deep axisymmetric cavities, will be considered in this paper and the transmission coefficient will be displayed in section 3, Figure 4. It shows the same features as the transmission coefficient shown in Figure 1.

The other side of the problem considered in this paper is the flow-induced pulsations which can be observed when a resonant cavity is exposed to a grazing flow over its opening. This phenomenon is observed in multiple situations, from the low-frequency buffeting in a car with an open window or roof to the flow-induced pulsations in pipe systems (Tonon et al, 2011; Ziada et al, 2013). In most of these problems, vorticity shedding occurs at a single location where acoustic resonances present a velocity maximum, which favours the flow-sound interaction and leads to the self-sustained oscillations. The amplification of sound at this single location can be very strong as it couples efficiently with a local, trapped mode. A slightly different kind of flow-induced pulsations occur with distributed "sources" coupling with global modes. This is for example observed in corrugated pipes (Burstyn, 1922; Cermak, 1924; Belfroid et al, 2007), where the amplification of sound is weaker but distributed along a large part of the system. Indeed, in this case, identical cavities are found on the full length of the pipe. The problem can then be partly considered as local, on the scale of a cell containing a single cavity, or a few cavities. Propagation of acoustic waves should take into account the attenuation due to visco-thermal losses and the amplification due to the interaction with vorticity in presence of main flow. For a very long pipe with little radiation losses, the balance between the two mechanisms is local. When the balance is exact in the linear domain, an acoustic wave can propagate infinitely without losses (Golliard et al, 2020). If the amplification is larger than the losses, the acoustic wave propagating in the corrugated pipe increases until it reaches its end where a discontinuity (typically the connection to a smooth pipe, a section change, a side branch or an open end, all creating a non-zero reflection coefficient) will reflect part of it which will propagate back in the corrugated pipe where it will be amplified again before reaching the other end of the pipe. The occurrence of flow-induced pulsations then depends on the balance between the amplification through the pipe and the radiation losses (or in other words "reflection losses"). Once the amplification is larger that the losses, the energy balance is ensured by non-linear saturation of the amplification by the vorticity (Nakiboğlu et al, 2011).

The onset of flow-induced whistling in a distributed system as the corrugated pipe is thus in essence linked to the acoustic propagation along the pipe, which can be amplified by the interaction with the flow.

The case considered in this paper shows features of both local and distributed sound-flow interaction in the resonator. With a grazing flow through the periodic cavity shown in Figure 2, vorticity develops over each of the 10 cavity openings, as in a corrugated pipe. Since the effective speed of sound in the main pipe is considerably reduced at certain frequencies due to the cavities (Aurégan et al, 2015), the periodic system becomes acoustically long and the propagation along the periodic structure should be considered. Thus, the resonator is extended (on the acoustic point of view) and the region where flow-sound interaction occurs is distributed along the extend of this resonator. On the other hand, the vorticity regions are in close proximity of each other. Therefore, the flow-induced whistling in such a periodic cavity can have properties corresponding to both systems with single-region vorticity or to distributed-vorticity systems. Indeed, depending on the thickness of the walls compared to the cavity width (and thus on the distance between the vorticity-regions), there can be significant hydrodynamic interaction between suc-

cessive cavities. The hydrodynamic instability leading to sound amplification can be a global hydrodynamic behaviour (Aurégan et al, 2008) or developing across each of the cavities, with of without interaction between successive cavities (Ziada et al, 1992; Derks et al, 2004; Nakiboğlu et al, 2011). In the last case, the synchronisation between the cavities is ensured by the acoustic feedback. Furthermore, even a single cavity can show whistling in certain cases (Mohamed et al, 2011). Furthermore, it can be expected that the band-gap of forbidden frequencies for propagation plays a role in the whistling behaviour of the system.

In the following, the flow-induced whistling in a periodic cavity will be investigated experimentally. First, the geometry is presented in more details in Section 2. The transmission through the cavity is reported in Section 3. Last, the measurements of whistling in presence of flow are presented and discussed in Section 4.

2. GEOMETRY OF THE PERIODIC CAVITY

A sketch of the periodic cavity geometry is provided in Figure 2. It is a periodic structure installed in a main pipe of 30 mm diameter. It consists of 10 successive identical axisymmetric cavities. The cavities are 7 mm wide, 55 mm deep and are separated by rigid disks of 5 mm with sharp edges. The pitch of the periodic structure is thus 12 mm.

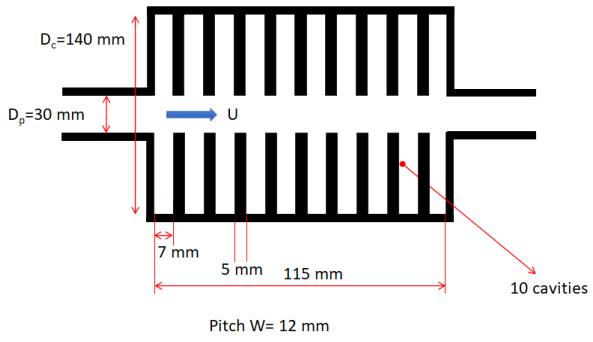

Figure 2. Sketch and dimensions of the periodic cavity.

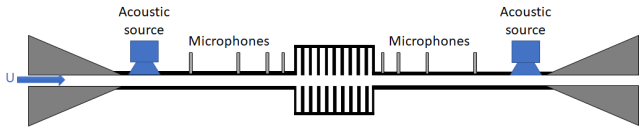

Figure 3. Sketch of the experimental setup for measurement of the scattering matrix.

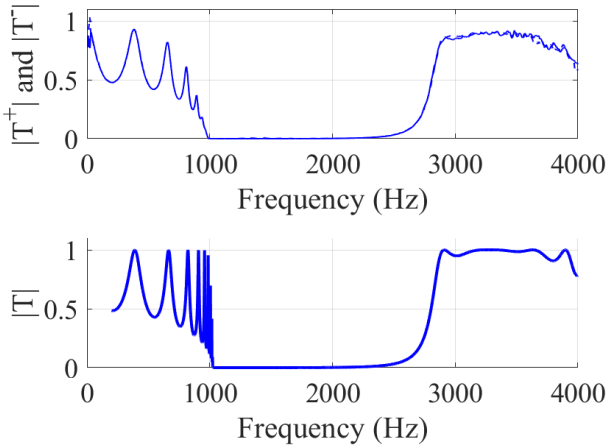

Figure 4. Measured (upper plot) and computed (lower plot) transmission coefficient due to the cavity displayed in Figure 2 without flow.

3. TRANSMISSION COEFFICIENT OF THE CAVITY

The setup for the measurement of propagation through the cavity is sketched in Figure 3. It was described in details in (Aurégan et al, 2003). It is designed to measure the scattering matrix of an element mounted in the main pipe of 30 mm inner diameter without flow or in presence of a steady flow. The central part consists of two measuring pipes equipped with each 4 microphones located upstream and downstream of the object to be characterised. Acoustic sources can be used to create an incident field coming either from the upstream side of the downstream side. Two anechoic terminations isolate this central part from the compressor located upstream and from the outlet downstream. The compressor can create a mean flow up to M = 0.35.

3.1. Transmission coefficient without flow

The measured transmission coefficient of the cavity is displayed in Figure 4. As discussed in the introduction, it shows similar features to a periodic succession of side branches. A succession of axially-opposed side branches would actually be a better "1-dimensional counterpart" of this 3-dimensional geometry, but the simplification provides a good illustration as far as the features discussed in the following are concerned. First, a frequency range is observed, between 1000 Hz and $\pm$2500 Hz, where sound waves are not transmitted by the cavity. It has to be noted that the attenuation is of the order of 70 dB over a length of only 115 mm. A second feature similar to the periodic array of side branch is the presence of

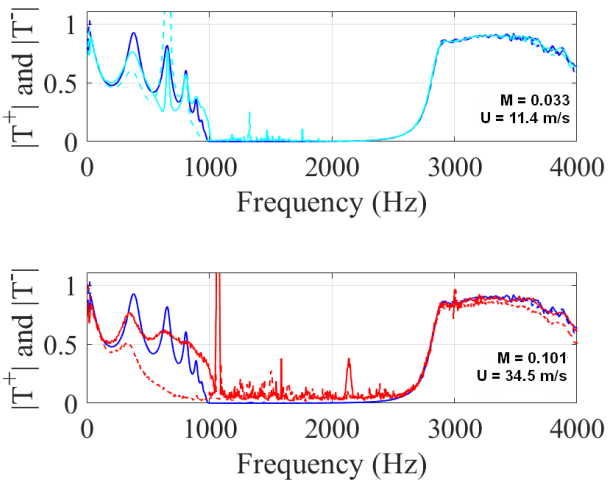

Figure 5. Transmission coefficient measured at M = 0.033 (11.4 m/s, light blue lines, upper plot) and M = 0.101 (34.5 m/s, red lines, lower plot). The results without flow are indicated for reference (dark blue lines) on all the plots. The continuous lines represent T^+ and the dashed lines represent T^-.

transmission minima around this band gap of forbidden frequencies. Five minima are very obvious on the low-frequency side, and a sixth can be suspected. On the computed transmission coefficient (lower plot of Figure 4), the number of transmission minima is nine, corresponding to the number of cavities minus one. The computation is done with the lossless acoustic solver in COMSOL. Note that, contrary to the computed transmission coefficient, the measured transmission coefficient does not pass by the value one (corresponding to perfect transmission) between theses minima. This is due to visco-thermal losses which are not taken into account in this simulation. The losses (and the resulting very small widening of the peaks and minima) are also the reason not all the minima can be observed in the measured transmission coefficient.

3.2. Transmission coefficient with flow

The transmission coefficient has also been measured with flow through the main pipe and are reported in Figure 5. One can first observe that the transmission is not reciprocal any more: The upstream and downstream transmission coefficients are not equal at low frequencies. Second, some additional damping is observed, lowering the transmission and spreading slightly the transmission lobes at low frequencies. Furthermore, the lower edge of the bandgap is shifted by the flow: towards lower frequencies for the transmission in upstream direction (T^-) and towards higher frequencies for the transmission in downstream direction (T^+). Last, for a frequency band which depends on the flow velocity, the transmission coefficient can increase and even becomes larger than one, which indicates amplification. It is noticeable that this occurs both for T^- and T^+ at the lowest velocity (but only T^- becomes greater than one) while it occurs only for T^+ for the highest velocity. This could be related to the fact that, for this velocity, the frequency range of amplification is also just on the edge of the bandgap for T^+ but very far in the bandgap for T^-.

4. WHISTLING IN PRESENCE OF FLOW

The setup for the whistling tests, sketched in Figure 6, is the same as for the measurement of the transmission coefficients, except that the acoustic sources are not used. For this set of experiments, the flow velocity has been varied from 3.3 m/s (M = 0.01) to 46.1 m/s (M = 0.14) in steps of $\pm$ 2 m/s.

The results are presented in Figure 7 as a spectrogram of pressure measured upstream and downstream of the cavity versus the Mach number. The spectrum measured upstream and downstream is also plotted for a few Mach numbers in Figure 8. One can observe in the spectrograms of Figure 7 that, for the lowest velocities, the frequency of the peak increases linearly with the flow velocity. This is typical of flow-induced noise and is characterized here by a Strouhal number $St = fW/U$ around 0.35-0.40 (with f the tone frequency, $W = 7$ mm the cavity width and U the mean-flow velocity). The frequencies at which the tones are observed in this range also correspond to the frequency range where amplification was observed in the measurements of transmission coefficients. For example, the tone occurs at 650 Hz for M = 0.033. So far, all these observations correspond to what would be observed for a "standard" corrugated pipe with shallow cavities. However, another observation can be done for this velocity range: the frequencies of the tones are discrete and correspond to the frequencies of the side lobes of possible transmission. It is also visible in the spectrum for M = 0.049 plotted in Figure 8 that smaller tones appear around the tone at 900 Hz. These smaller tones correspond to the side lobes of possible transmission in Figure 5.

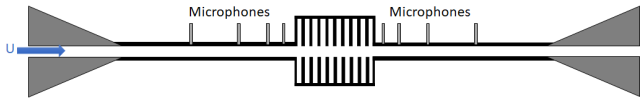

Figure 6. Sketch of the experimental setup for measurement of the whistling with flow.

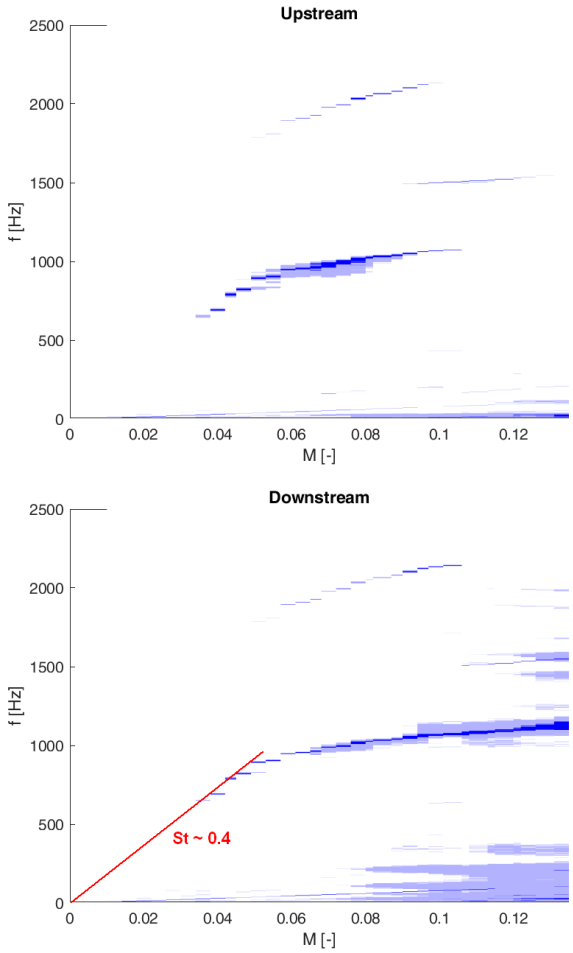

Figure 7. Spectrogram showing the flow-dependence of the noise measured upstream (above) and downstream (below) of the cavity.

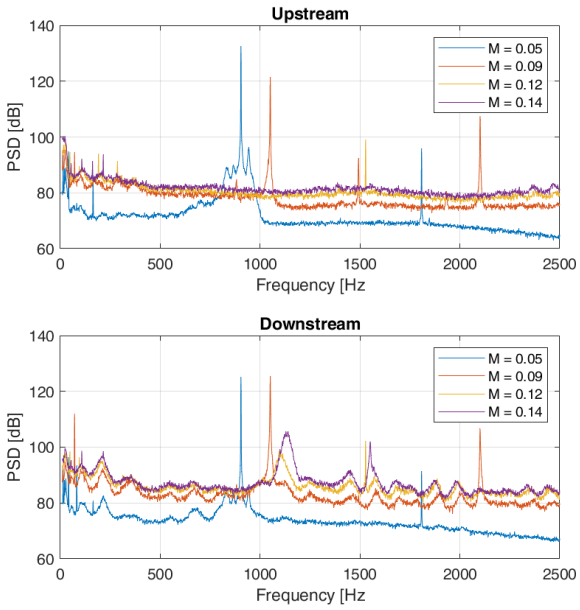

Figure 8. Spectra of the noise observed upstream (upper plot) and downstream (lower plot) of the cavity at different flow velocities.

For a (short) corrugated pipe, the discrete frequencies would be imposed by the resonant frequencies of the pipe (and thus by its total length) (Golliard et al, 2010; Nakiboğlu et al, 2010).

For velocity above M = 0.05, the Strouhal-number dependency rule does not apply any more. Indeed, the frequency of the tone only increases very slightly above 1000 Hz. For example, the tone is at 1050 Hz for M = 0.09 in Figure 8. On the downstream side, the peak widens and its amplitude decrease for higher velocities, while it disappears altogether on the upstream of the cavity. The limit of 1000 Hz corresponds to the limit of the bandgap of possible propagation and it was observed in preceding section that it increases slightly for streamwise propagation when the flow velocity increases, while it decreases for the propagation against the flow velocity (see Figure 5). This indicates that the forbidden-frequency bandgap prevents the tone from appearing. At certain flow velocities (*i.e.* M = 0.12, 0.135), the vorticity still amplifies the sound in the streamwise direction (creating the wider "bumps" around 1100 Hz – 1150 Hz measured downstream) but the wave reflected at the downstream side of the cavity then cannot propagate backwards (note that the "bumps" are not visible in any way on the upstream side).

However, some tones are also present in the frequency range of the bandgap (1000-2500 Hz). If we ignore the harmonic of the tone previously discussed, we still find a more intriguing tone observed around 1500 Hz for Mach numbers between 0.09 and 0.12 (measured by the upstream microphones) and between 0.11 and 0.15 (measured by the downstream microphones). To interpret the existence of this tone, one has to come back again to the transmission coefficient of the periodic cavity. As was discussed above, the band gap between 1000 Hz and 2500 Hz is due to the periodic structure made of deep axisymmetric cavities. In the present case, the interaction between the first radial mode of each of the cavities create the bandgap couple. Using the analogy of a periodic array of closed side branches given in the introduction, this corresponds to interaction between their quarter-wavelength resonances. A similar interaction between the modes of the individual cavities can also happen, but for the azimuthal modes. For these modes, the average acoustic flux across any centred circular section is null, which means that these modes are trapped in the cavities: They do not couple with the plane waves in the main pipe and therefore should

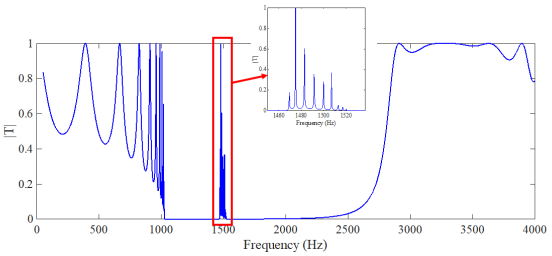

Figure 9. Transmission coefficient computed for a periodic cavity similar to the cavity displayed in Figure 2, but with the main pipe off-centre by 1 mm.

not have any influence on the transmission coefficient for plane waves. However, any small disturbance might allow some coupling. For example, the computation of the transmission coefficient was repeated with a very small modification of the geometry: the main pipe is placed 1 mm off-centre of the ten cavities. As seen in Figure 9, this creates a frequency band around 1500 Hz (or to be more precise, a succession of nine narrow frequency bands, as illustrated in the inlet of the figure) where propagation is possible. It is not expected that the cavity used for the measurements is so much off-centred, but the disturbance allowing the coupling might also come from a smaller difference, or from an asymmetry of the flow in the main pipe. At any rate, the frequency of the tone observed around 1500 Hz corresponds to this band of allowed frequencies. Flow-induced tones can be associated with trapped azimuthal modes, at least in a single shallow axisymmetric cavity, as reported by Aly et al (2010).

5. CONCLUSIONS

In this paper, flow-induced whistling observed downstream and upstream of a periodic cavity was investigated. The periodic cavity is made of a succession of 10 axisymmetric cavities spaced by a constant pitch. For low flow velocities, the frequency of the tone shows a Strouhal-number dependency characteristic of flow-induced whistling created by vorticity shedding. The phenomena are very similar to what would be observed for a corrugated pipe made of a succession of shallow cavities. However, as the flow-velocity increases, the frequency of the tone comes in a region where acoustic propagation is not possible due to periodic nature of the cavity creating a band of forbidden frequencies. This reduces and eventually eliminates the tone. Yet, a tone is observed in the bandgap of forbidden frequencies, which can be associated to the opening of an band of allowed frequencies by the presence of azimuthal modes in the cavity.

6. REFERENCES

K. Aly, S. Ziada, 2010, Flow-excited resonance of trapped modes of ducted shallow cavities, *Journal of Fluids and Structures* **26** (1) 92–120.

Y. Aurégan and M. Leroux, 2003, Failures in the discrete models for flow duct with perforations: An experimental investigation, *Journal of Sound and Vibration*, **265**(1) 109–121.

Y. Aurégan and M. Leroux, 2008, Experimental evidence of an instability over an impedance wall in a duct with flow, *Journal of Sound and Vibration*, **317** 432–439.

Y. Aurégan and V. Pagneux, 2015, Slow sound in lined flow ducts, *The Journal of the Acoustical Society of America*, **138**(2) 605–6013.

S. Belfroid, D. Shatto, and M. Peters, 2007, Flow Induced Pulsations Caused by Corrugated Tubes, *Proceedings of ASME Pressure, Vessels and Piping Conference, San Antonio, TX*.

W. Burstyn, 1922, Eine Neue Pfeife (A New Pipe), *Z. Tech. Phys. (Leipzig)* **3** 179–180.

P. Cermak, 1924 Uber die Tonbildung in Luftdurch-Strömten Röhren (On the Production of Tone in an Air-Flows Through Tubes), *Physikalische Zeitschrift*, **25** 121–130.

M. M. G. Derks and A. Hirschberg, 2004, Self-sustained oscillation of the flow along Helmholtz resonators in a tandem configuration, *Proceedings of FIV2004, Paris*.

J. Golliard, D. Tonon, 2010, Whistling of Short Corrugated Pipes: Experimental Investigation of the Source Locations *Proceedings of the 16th AIAA/CEAS Aeroacoustics Conference, 2010, Stockholm, Sweden*

J. Golliard, Y. Aurégan, T. Humbert, 2020, Experimental study of plane wave propagation in a corrugated pipe: Linear regime of acoustic-flow interaction, *Journal of Sound and Vibration* **472** 115–158.

S. Mohamed, H. Graf, S. Ziada, Aeroacoustic Source of a Shallow Cavity in a Pipeline, 2011 *Proceedings of the ASME 2011 Pressure Vessels and Piping Conference Volume 4: Fluid-Structure Interaction. Baltimore, Maryland, USA*.

G. Nakiboğlu, S. Belfroid, J. Willems, A. Hirschberg, 2010, Whistling behavior of periodic systems: Corrugated pipes and multiple side branch system, *International Journal of Mechanical Sciences* **52** (11), 1458–1470.

G. Nakiboğlu, S. Belfroid, J. Golliard, A. Hirschberg, 2011, On the whistling of corrugated pipes: effect of pipe length and flow profile, *Journal of Fluid Mechanics* **672** 78–108.

G. Nakiboğlu and A. Hirschberg, 2012, Aeroacoustic power generated by multiple compact axisymmetric cavities: Effect of hydrodynamic interference on the sound production, *Physics of Fluids* **24**.

D. Tonon, A. Hirschberg, J. Golliard, S. Ziada, 2011, Aeroacoustics of Pipe Systems with Closed Branches. *International Journal of Aeroacoustics* **10**(2–3), 201–275.

S. Ziada and E. T. Bühlmann, 1992, Self-excited resonances of two side-branches in close proximity, *Journal of Fluids and Structures* **6**(5), 583–601.

S. Ziada and P. Lafon, 2014, Flow-Excited Acoustic Resonance Excitation Mechanism, Design Guidelines, and Counter Measures. *ASME. Appl. Mech. Rev.* **66**(1).

ON BROADBAND NOISE OF THICK SQUARE-EDGED ORIFICES IN WATER-PIPE FLOW

Kottapalli s. & Hirschberg A. & Smeulders D.J.M.
TU/e, Eindhoven, The Netherlands

Waterson N. & Nakiboglu G.
ASML, Veldhoven, The Netherlands

ABSTRACT

Broadband noise of water flow through orifices with a thickness equal to the orifice radius has been investigated experimentally. Incompressible large-eddy simulations (LES) of water flow through sharp 90^o-edged are used to predict the near-field hydrodynamic pressure fluctuations at low frequencies and the associated axial dipole sound source. Incorporating this lumped source model in an acoustic model provides a fair prediction of the acoustic field as detailed in an earlier publication. One observes a maximum of the Power Spectral Density (PSD) of the axial-dipole sound source for Strouhal numbers corresponding to varicose hydrodynamic instability modes as predicted for square-edged thick orifices in the literature. This sound source is larger than reported for thin orifices in the literature.

1. INTRODUCTION

Modern lithography machines work with nanometer precision to produce silicon chips at a breakneck pace. The power consumption of the machines can be more than 100 kW. Only just a few watts are used to project a pattern onto a silicon wafer. Much of the power consumed is dissipated as heat from various locations within the system. As a result, hundreds of litres of water are pumped every minute through its cooling system. Within these cooling circuits, orifices are commonly used as flow control devices. However, orifices are also a source of pressure disturbances. In the present application one is mainly concerned by the propagation of acoustic waves that can reach the sensitive core of the machines. Also local hydrodynamic pressure fluctuations can be a nuisance. Thus, the objective of this study is to predict the local (near-field) hydrodynamic forces and to model the far-field (acoustic) pressures due to such orifices in water-filled pipe flows.

The role of circular orifices as a source of sound in air has been extensively studied [3, 4, 5, 6, 7, 8, 9, 10, 11, 12]. There are only few studies of water flows in the absence of cavitation [13, 14, 6]. In an earlier paper a model has been developed for sharp-90^o-edged orifices to predict the broadband noise production [15]. This model uses the fluctuating drag force estimated by means of an incompressible LES flow model as an input for a plane-wave acoustic model. This model provides a fair global prediction of both near field hydrodynamic wall-pressure fluctuations and of the acoustic pressure fluctuations. In the present paper we focus on a comparison of the thick orifice sound source with that of thin orifices. In the case of broadband noise in a recorder flute, Verge et al [16] suggested a relationship between jet instability modes and broadband sound production. This relationship between hydrodynamic unstable modes and broadband noise production by orifices was also considered by Testud [6] and is further explored here.

In section 2, the experimental set-up is described for wall-pressure fluctuations measurements. Acoustical pressure fluctuations are discussed in section 3. In section 4 the influence of unstable hydrodynamic modes is discussed. In section 5 the predicted sound source is compared to the data from the literature for thin orifices. Conclusions are summarized in section 6.

2. EXPERIMENTAL SET-UP

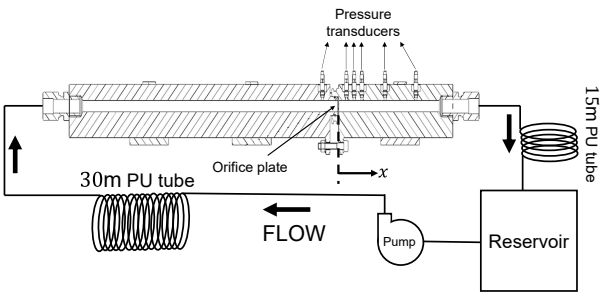

Figure 1. Schematic of the test set-up to measure wall-pressure fluctuations. The flow of the water is from left to right through the test section.

Figure 1 shows the schematic of the experimental set-up for measuring wall-pressure fluctuations. The measurement section (further also referred as the test-section) comprises a thick-walled straight stainless steel duct with a total length of 500 mm and an inner diameter D = 9.00 mm. The test section has a wall thickness of at least $2D$. An orifice plate, with orifice diameter D_o, is mounted 350 mm from the inlet of the measurement section. The positive x-direction is in the direction of the main flow. The duct has six piezoelectric pressure transducers (PCB 105C02). The pressure transducers have a finite probe diameter $D_{probe} = 2.5$ mm and are mounted in such a way that the centre of the transducer surfaces are at a radial distance of 4.50 mm from the central axis of the test-section. The axial positions of the transducers are $\frac{x}{D} = -\left(2+\frac{D_o}{2D}\right), 1, 2, 3, 6$ and 10, where the coordinate x is measured from the origin $x = 0$ at the downstream surface (exit) of the orifice plate.

A volume flow $\left(\frac{\pi}{4}D^2U\right)$ of demineralized water, enters the test-section through a 30 m long polyurethane (PU) pipe with diameter D=9 mm and wall thickness of 1.5 mm. The flow exits the test-section through a 15 m long PU pipe of similar cross-sectional dimensions as used at the test-section inlet into a reservoir of 0.04 m^3. The reservoir is open-type, which is maintained at atmospheric pressure. The PU tubes entering the reservoir are submerged within the water. The polyurethane tubes are connected to the test-section using 12 mm SERTO straight couplings. The polyurethane tube reduces the high frequency pump noise. For the length of 30 m used in the experiment the pump noise was negligible for most experiments [15].

Three square-edged (90 angle) single-hole orifice plates with open area ratios $\beta = 11\%$ ($D_o = 3$ mm), 20% ($D_o = 4$ mm) and 31% ($D_o = 5$ mm) were tested [15]. Here, $\beta = \left(\frac{D_o}{D}\right)^2$ are the ratios of orifice opening area to pipe cross-sectional area. All orifice plates have a thickness (δ_o) to diameter (D_o) ratio $\frac{\delta_o}{D_o} = 0.5$. The FLEXIM FLUXUS F601 ultrasonic flowmeter (UFM) was used to measure the volume flow $\left(\frac{\pi}{4}D^2U\right)$ with an accuracy of 1%. The wall-pressure fluctuation measurements were performed for a time-period of 500 s at sampling frequency of 30 kHz using PICOScope 4000 series high resolution oscilloscope. This allows measurements in the frequency range 1 Hz $< f <$ 10 kHz.

The drag coefficient of the orifices C_{drag} was determined from static pressure measurements at large distances from the orifice [15].

3. ACOUSTIC RESPONSE OF THE SET-UP

Using the PSD of the axial component of the drag force calculated by means of the incompressible Large-eddy simulations (LES) [15], one can predict the PSD of the acoustic pressure fluctuations at any point in the test section by means of a quasi-one-dimensional model. The sound source is assumed to be a fluctuating pressure discontinuity $\Delta p_{source} = -\frac{4F_{drag}}{(\pi D^2)}$ placed just downstream of the orifice. This model is complemented by the continuity of acoustical volume flow across the orifice. The fluctuating drag (F_{drag}) is calculated as:

$$F_{drag} = \int_{S_o} [p(-\delta_o, t) - p(0,t)]\, dS_o. \qquad (1)$$

on the wall surface S_o of the orifice normal to the axial direction x. The magnitude of S_o is $\frac{\pi}{4}(D^2 - D_o^2)$. The difference in retarded time between the front and back of the orifice has been neglected because $\frac{fD_o}{c} << 1$, where $c = 1.46e3$ m/s is the speed of sound in the (water-filled) test section. The approximation used corresponds to the theory used by Tao *et al.* [10] for frequencies below the first cut-on frequency of transverse pipe modes. In the present case the cut-off frequency for non-planar pipe modes is 200 kHz.

It is furthermore assumed that the upstream and downstream polyurethane tubes act as anechoic terminations so that the acoustic boundary condition is assumed to be determined by the reflection coefficient of acoustic waves at the steel/polyurethane transitions delimiting the test section $(R_{s/pu})$. Convective effects are neglected because the Mach number is very low $M = \frac{U}{c} < 10^{-3}$. Damping of the acoustic waves is assumed to be due to viscous Stokes layers thinner than the viscous sub-layer of the turbulent flow. This is reasonable at frequencies of the order of the first longitudinal acoustic resonance of the set-up or higher. The acoustic flow through the orifice is assumed to be locally incompressible, because $\left(\frac{2\pi f D_o}{c}\right)^2 << 1$. The inertia of the acoustic flow through the orifice is taken into account by means of an effective length: the orifice plate thickness δ_o plus the inertial end correction $0.8D_o$. The model is described in more detail in [15].

The scaling of Nelson and Morfey [3] is used for the axial dipole sound source of the orifice. Fig. 2 shows the normalised PSD of the fluctuating (dipole) pressure source (Δp_{source}) predicted using LES for the sharp-edged $\beta = 20\%$ ($D_o = 3$ mm) orifice and the upstream chamfered $\beta = 11\%$ ($D_o = 3$ mm) orifice. The Δp_{source} has been normalised using drag pressure

(Δp_{drag}) defined as:

$$\Delta p_{drag} = \frac{1}{2}\rho U_o^2 \left(\frac{1}{\alpha} - \left(\frac{D_o}{D} \right)^2 \right)^2 \quad (2)$$

where, α is the vena-contracta factor of the orifices obtained from the drag coefficient C_{drag}:

$$\alpha = \frac{1}{1+\sqrt{C_{drag}}} \left(\frac{D}{D_o} \right)^2 \quad (3)$$

The drag coefficient is deduced from measurement of the time averaged pressure difference between two positions at large distance from the orifice. This measurement was corrected for the pressure drop between these positions in the absence of orifice [15]. The frequency is normalised using the orifice Strouhal number $St_o = \frac{fD_o}{U_o}$. Here, D_o is the orifice diameter and U_o is the cross-sectional averaged velocity in the orifice. The normalised PSD of Δp_{source} from the LES is compared in Fig. 2 to a simplified source model proposed on the basis of a study of sharp edged orifices [15], given as:

$$\frac{\Phi_{\Delta p \Delta p}}{(\Delta p_{drag})^2} \frac{U_o}{D_o} = 1.5 \times 10^{-4} \quad (4)$$

for $St_o < 0.5$ and:

$$\frac{\Phi_{\Delta p \Delta p}}{(\Delta p_{drag})^2} \frac{U_o}{D_o} = 1.5 \times 10^{-4} \left(\frac{0.5}{St_o} \right)^{11/3} \quad (5)$$

for $St_o \geq 0.5$. The power used here is discussed in [15]. It is based on a theory of wall pressure fluctuations in turbulent flow, and might not be optimal for the present application. In Fig. 3 the normalized Power Spectrum Density (PSD) of wall pressure is shown as a function of the Strouhal number $St_o = \frac{fD_o}{U_o}$ for a position upstream of the orifice $\frac{x}{D} = -2$ and two positions downstream of the orifice $\frac{x}{D} = 1$ and 6. The experimental data are compared to the PSD of the predicted acoustical pressure fluctuations. For the near-field position $\frac{x}{D} = 1$ the hydrodynamic fluctuations at low Strouhal numbers $St_o < 0.5$ are almost two orders of magnitude larger than the predicted acoustic fluctuations. At higher Strouhal numbers the acoustic pressure fluctuations are dominant and one clearly observes the peaks in acoustic response due to longitudinal resonance of the test section. In first order approximation the test section behaves as an open-open pipe of $L = 0.5$ m length. For the other transducers positions $\frac{x}{D} = -2$ and 6, the acoustic pressure fluctuations are dominant over the entire range of Strouhal numbers above $St_o = 0.1$. The free jet formed by flow separation at the sharp edges of the orifice inlet re-attaches around $\frac{x}{D} = 3$ to the pipe wall.

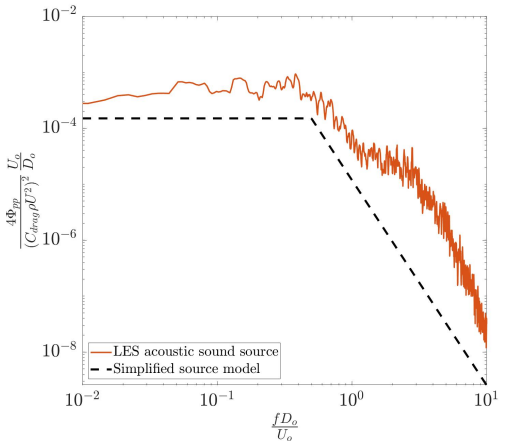

Figure 2. Predicted power-spectral density of the broad-band dipolar-source for of sound, for a $D_o = 4$ mm sharp-square-edge orifice with thickness equal to $\delta_o = D_o/2$, compared to simplified source model.

4. HYDRODYNAMIC MODES

Orifices with sharp square edges can drive self-sustained longitudinal acoustical oscillations of the pipe. This phenomenon, refered to as "Pfeifen-tone" or "whistling" has been extensively studied by among others Anderson [17]. Testud et al [7] observed two critical Strouhal numbers $St_{t_o} = \frac{ft_o}{U_o}$ based on the orifice thickness at which there is a high whistling whistling potentiality. These Strouhal numbers depend on the Reynolds number. The acoustical oscillation induces periodic vortex shedding from the upstream edge of the orifice.The lowest critical Strouhal number corresponds to a travel time of the vortices through the orifice of about one oscillation period. The second Strouhal number corresponds to a travel time of about two oscillation period. Each critical Strouhal number corresponds to a different flow pattern and is referred to as a hydrodynamic mode. Whistling occurs when the hydrodynamic mode corresponds to a frequency close to an acoustic resonance of the pipe and the acoustic power generated by the sound source is sufficient to balance the acoustic visco-thermal dissipation and radiation losses. Using laminar-flow numerical simulations, Fabre et al [12] confirms that indeed at critical Strouhal number (based on the orifice thickness) the real part of the transfer impedance displays minima for a given Reynolds number. At higher Reynolds numbers ($Re_o = 2000$) they find up to four hydrodynamic mode with whistling potentiality. For the Reynolds numbers considered here $Re_o = 10^4$ and $t_o = \frac{1}{2}D_o$, Testud et al. [7] find for the first hydrodynamic mode $St_o = 0.6$ and for the second hydrodynamic mode $St_o = 1.6$. Based on the theoretical

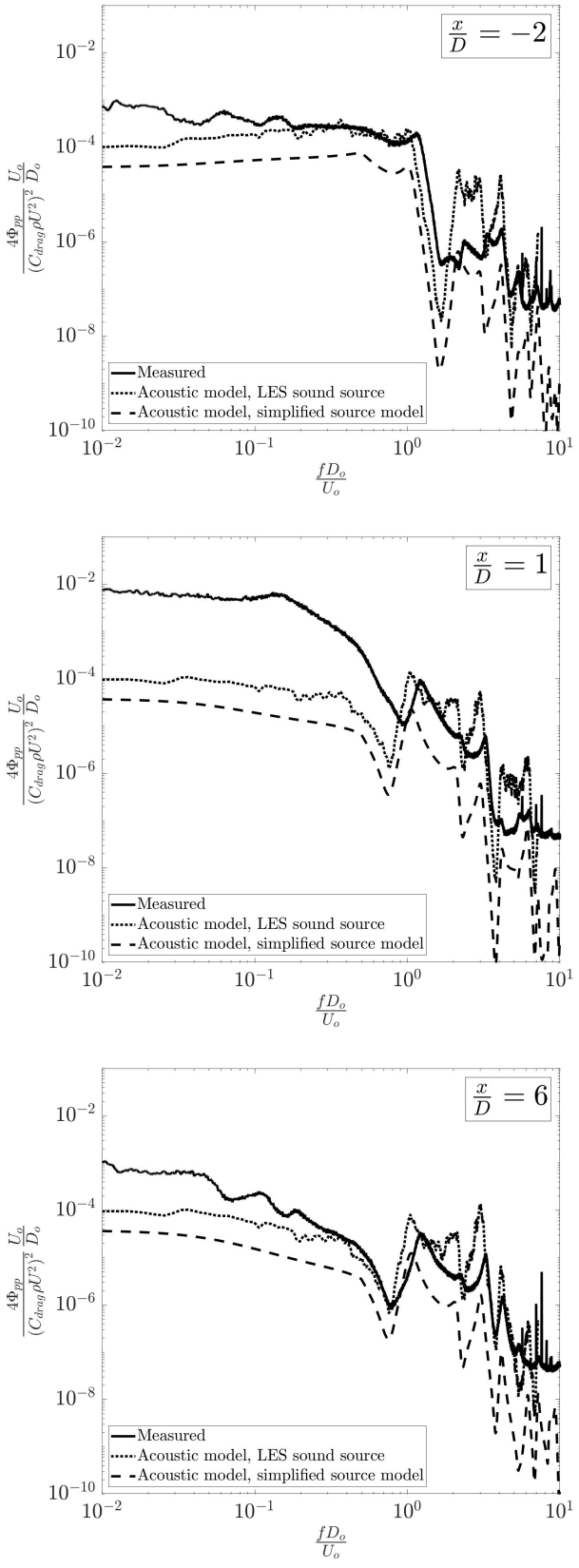

Figure 3. Power Spectral Density of wall pressure fluctuation at transducer positions $\frac{x}{D} = -2, 1$ and 6 for the $D_o = 4$ mm and $\delta_o/D_o = 0.5$ sharp square edged orifice, compared to theoretical prediction of acoustic pressure fluctuation for $Re_o = 2.2 \times 10^4$.

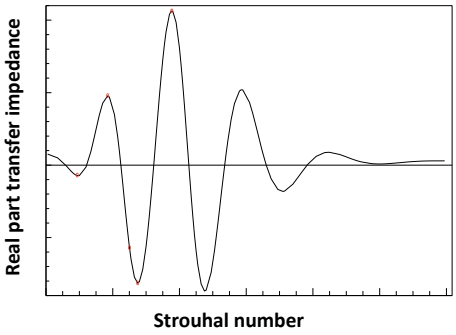

Figure 4. Linearized Navier Stokes prediction [12] of the real part of the transfer impedance of a orifice with thickness ratio $t_o/D_o = 1$ ($Re_o = 2000$). The negative minima correspond to hydrodynamic modes with whistling potentiality.

results of Fabre et al [12] the third hydrodynamic mode is around $St_o = 2.7$ and the fourth hydrodynamic mode around $St_o = 4.1$. As shown in Fig. 4 the minimum of the real part of the transfer impedance is much deeper for the second and third hydrodynamic modes than for the first hydrodynamic mode. This is confirmed by the measurements of Testud et al [7] as displayed in Fig. 5. In figure 6 displaying the data of Moers et al[11] one observes a similar behaviour for slit-shaped orifices with a thickness t_o equal to the slit height h_o for Reynolds numbers $h_o U_o/\nu = O(10^4)$. Hydrodynamic modes with negative real part of the transfer impedance are not observed in the measured real part of the transfer impedance for thin orifices with acute-edge angle displayed in Fig. 7.

As observed in Fig. 2 the "hump" in the PSD of the predicted sound source is in the range $1 \leq St_o \leq 5$. One therefore expect that this local maximum in sound source for thick orifices is related to the sound production due to periodic vortex shedding in the orifice. This effect does not occur in thin orifices [18]. This sound production due to vortex shedding can be explained qualitatively by means of the Vortex Sound Theory of Howe [19]. It is similar to the sound production observed in the so called "Whistler Nozzle" [20].

The broad-band sound source of thin orifices is discussed in the next section 5.

5. THIN ORIFICES

In Fig. 8 the sound source of orifices with thickness equal to the orifice diameter is compared to data for thin orifices from the [13, 4, 5, 14]. The data provided by Moussou [14] correspond to an orifice of thickness of $t_o = 6$ mm in a pipe of diameter $D = 103$ mm with a diameter ratio $D_o/D = 0.5$ [21, 22]. Based on the

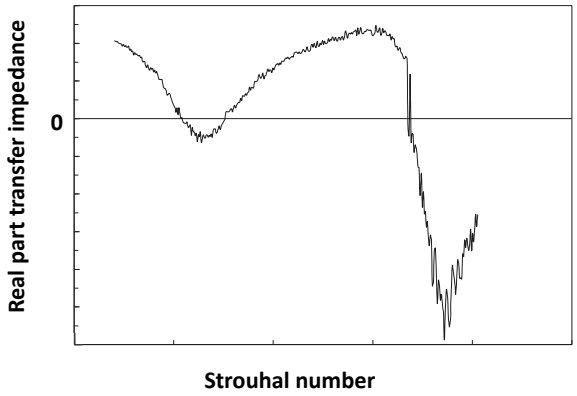

Figure 5. Real part of the transfer impedance of an orifice measured by Testud et al [7]. One observes the negative minima corresponding to the first two hydrodynamic modes ($D_o = D/2$, $t_o = D_o/3$ and $Re_o = 1.2 \times 10^4$). The second hydrodynamic mode has a higher whistling potentiality than the first mode.

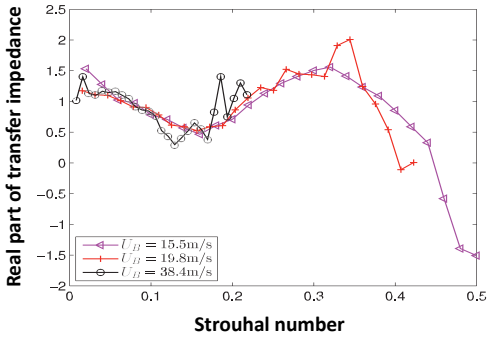

Figure 6. Measurements [11] of real part of the transfer impedance of thick slit-shaped orifice (with 90^o-sharp edge) displaying regions of whistling potentiality ($t_o = h_o$ and $h_oU_o/\nu > 10^4$). One observes around $St_o = ft_o/U_o = 0.5$ a negative minimum corresponding to the second hydrodynamic mode. This second hydrodynamic mode has a high whistling potentiality.

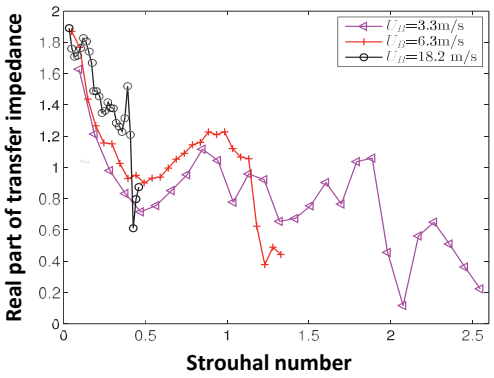

Figure 7. Measurements [11] of real part of the transfer impedance of thin slit-orifice with acute edge angle ($t_o = 0$ and $h_oU_o/\nu = O(10^4)$). One does not observe any negative minimum.

data presented by Gibert [13] and Moussou [14], one finds a simplified sound source model for thin orifices:

$$\frac{\Phi_{\Delta p \Delta p}}{(\Delta p_{drag})^2}\frac{U_o}{D_o} = 1.0 \times 10^{-4} \tag{6}$$

for $St_o < 0.2$ and:

$$\frac{\Phi_{\Delta p \Delta p}}{(\Delta p_{drag})^2}\frac{U_o}{D_o} = 1.0 \times 10^{-3}\left(\frac{0.1}{St_o}\right)^{3.2} \tag{7}$$

for $St_o \geq 0.2$. Please, note the large scatter in experimental data in the low Strouhal number range, as seen from the data Gibert [13] compared to those of Oldham and Ukpohon(1990) and Allam and Abom (2005) as presented by Karekull et al (2014). This indicates that further experiments would be welcome. As confirmed by preliminary experiment, for $St_o > 0.1$, the normalized sound source for thin orifices is globally an order of magnitude weaker than that for sharp 90^o-edge-angle orifices with a thickness equal to their radius $t_o/D_o = 0.5$.

6. CONCLUSION

An incompressible LES simulation can be used to predict the broadband axial sound source in a water flow through an orifice. The model does predict Strouhal-number ranges of enhanced sound production corresponding to unstable hydrodynamic varicose modes (axially-symmetric modes) predicted by stability theory for laminar flows. This observation confirms the hypothesis of such a relationship suggested by Testud [6]. This behaviour makes a prediction of the sound production by thick orifices more complex than for thin orifices. Thin orifices do not display such behaviour and display lower broadband

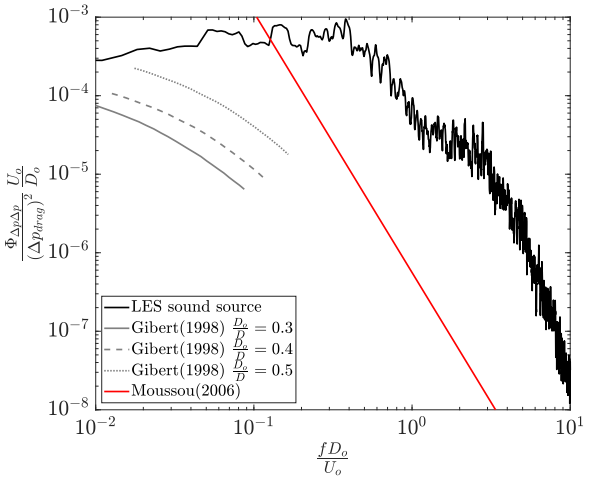

Figure 8. LES-predicted power-spectral density of the broad-band dipolar-source of sound for $D_o = 4$ mm sharp edged $\delta_o = D_o/2$ orifice compared to literature data for thin orifices.

noise production for equal drag force. Complementary experimental measurements of the sound source at low frequencies is needed to allow an accurate prediction of the broadband noise sound source for thin orifices.

7. REFERENCES

[1] Paidoussis, Michael P., 1998, *Fluid-structure interactions: slender structures and axial flow*, Academic press.

[2] Ziada, S. et al, 2003, Flow excited resonance of a confined shallow cavity in low mach number and its control. *Journal of Fluids and Structures* **18**: 79-92.

[3] Nelson P. and Morfey C., 1981 , Aerodynamic sound production in low speed flow ducts,*J. Sound Vib.* **79**: 263–289.

[4] Oldham D. and Ukpoho A., 1990, A pressure-based technique for predicting regenerated noise levels in ventilation systems,*J. Sound Vib.* **140**: 259–272.

[5] Allam S. and Åbom M., 2005, *Aero-acoustic study of single and double diaphragm orifices under subsonic conditions*. Royal Institute of Technology, Stockholm, Sweden.

[6] Testud Ph. (2006), Aeroacoustique des diaphragmes en conduits: sifflement et cavitation, Phd thesis, Universite du Maine, Le Mans. Fr.

[7] Testud P. et al, 2009, The whistling potentiality of an orifice in a confined flow using an energetic criterion, *J. Sound Vib.* **325**: 769–780.

[8] Lacombe R. (2011),Sifflement de diaphragmes en conduit soumis a un ecoulement subsonique turbulent, Phd thesis, Universite du Maine, Le Mans. Fr.

[9] Karekull O. et al, 2014, Prediction model of flow duct constriction noise, *Appl. Acoust.* **82**: 45–52.

[10] Tao F., 2017, Investigation of the sound generation mechanisms for in-duct orifice plates, *J. Acoust. Soc. Am.* **142**: 561–572.

[11] Moers E. et al, 2017, Strouhal number dependency of the aero-acoustic re- sponse of wall perforations under combined grazing-bias flow, *J. Sound Vib.* **389**: 292–308.

[12] Fabre D. et al, 2020,Acoustic impedance and hydrodynamic instabil- ity of the flow through a circular aperture in a thick plate, *J. Fluid Mech.* **885**: A11

[13] Gibert R.-J.,1988, *Vibrations des structures : interactions avec les fluides, sources d'excitation aléatoires*, Eyrolles.

[14] Moussou P., 2006, An Attempt to Scale the Vibrations of Water Pipes, *J. Press. VesselTech.* **128**: 670–676.

[15] Kottapalli S. et al, 2022, Hydrodynamic and acoustic pressure fluctuations in water pipes due to an orifice: Comparison of measurements with Large Eddy Simulations, *J. Sound Vib.* **529**: 116882.

[16] Verge et al (1997) Sound Production in Recoder-like Instruments II. A simulation model, J. Acoust. Soc. Am. 101 (1997) 2925-2939.

[17] Anderson A.B.C., 1953, Dependence of pfeifenton (pipe tone) frequency on pipe-orifice geometry, *Journal of the Acoustical Society of America* **25** 541–545.

[18] Fabre D. et al, 2019, The acoustic impedance of a laminar viscous jet through a thin circular aperture. *J. Fluid Mech.* **854**, 5–44.

[19] Howe M.S., 1998, *Hydrodynamics and Sound*, Cambridge University Press, Cambridge.

[20] Hirschberg A. et al, 1989, The "Whistler Nozzle" and Horn as Aero-acoustic Sound Sources in Pipe Systems, *Acustica*, **68**, 157-160.

[21] Hassis H., *Contribution à l'étude des lignes de tuyauteries excitées par des singularités d'écoulement en regime monophasique ou cavitant*, Thèse de Doctorat, Paris 6 (1990).

[22] Moussou P. & Piteau P., private communication (2022).

THE AEROACOUSTICS RESPONSE OF CYLINDRICAL CAVITIES IN CONFINED FLOW

Marc Hanna & Atef Mohany

Fluid-Structure Interactions and Noise Control Laboratory

Ontario Tech University, Oshawa, Canada

ABSTRACT

Cavities of various aspect ratios exposed to grazing, low Mach number flow (M < 0.4) are responsible for flow-excited acoustic oscillations. Shear layer modes inherent to the flow oscillation across the opening of a cavity mouth may couple with acoustic modes of the given system and give rise to large acoustic pressure amplitudes when their frequencies coincide. This current investigation focuses on the aeroacoustics response of deep and shallow cylindrical cavities subject to a confined flow by flush-mounting the cavity to the wall of a duct. It is shown that the response of a cavity in a confined duct promotes the acoustic resonance at multiple peak frequencies when interacting with the first three shear layer hydrodynamic modes. The identification of the acoustic modes for deep and shallow aspect ratios as well as the nature of the shear layer impingement are investigated by virtue of acoustic pressure measurements at select locations in the system. The Strouhal numbers for aspect ratios h/D = 1 and 1.5 are reported and agree well with values documented in literature, whereas aspect ratios of h/D = 0.5 exhibit significantly lower Strouhal numbers.

1. INTRODUCTION

Rectangular cavities exposed to grazing flow have been well documented and detailed since the early campaigns of Krishnamurty (1955), Rockwell & Naudascher (1978), Ziada & Rockwell (1982) and Heller & Bliss (1975). Research regarding cylindrical cavities, however, are scarcer in literature in comparison to rectangular cavities but have become of increasing interest in recent times due to their widespread applications in aeronautical, hydraulic, and pipping system applications. In the case of cylindrical cavities mounted on a flat surface, similarly to their rectangular counterparts, they may be classified as deep or shallow cavities depending on their aspect ratio; that is the depth (h) of the cavity to its impingement length (L). Shallow cavities are such that the depth of the cavity is smaller than the impingement length while deep cavities consist of depths larger than the impingement length. Cylindrical cavities are seen to have fully three-dimensional flow compared to the case of two-dimensional rectangular cavities. Shallow cylindrical cavities present different flow behavior than deep cylindrical cavities as detailed by the works of Hiwada et al. (1983). In more recent works such as Marsden et al. (2016) and McCarthy & Ekmekci (2022), Hiwada's findings were confirmed and briefly summarized as; shallow cylindrical cavities having aspect ratios (h/D) > 0.7 exhibit a stable and symmetric flow profile across the mouth of the cavity. When the cavity depth is reduced to 0.4 < h/D < 0.7, the flow exhibits an asymmetric flow with respect to the vertical streamwise plane. The flow regime is bistable such that the direction of the asymmetry is affected by perturbing the free stream conditions upstream of the cavity. When a shallow cylindrical cavity is in the range of aspect ratios 0.2 < h/D < 0.4, the asymmetry is still present but is no longer stable as it is seen to "flap", observed as a spontaneous switching in static pressure measurements on the downstream wall of the cavity with respect to the vertical streamwise plane. Further reduction in the aspect ratio h/D < 0.2 returns the flow to a symmetric and stable profile. The strongest levels of asymmetry and drag have also been reported for aspect ratios h/D = 0.5. While the flow patterns over cylindrical cavities have been further investigated, the interaction between the shear layer and circular cavity mouth still pose many questions. Additionally, there is limited work dedicated towards the aeroacoustics response of flow past cylindrical cavities in comparison to the rectangular type. Numerical investigations conducted by Rona (2007), Grottadaurea & Rona (2007) and Mincu et al. (2009), as well as experimental campaigns by Marsden et al. (2012) and Parthsarathy et al. (1985) provide insight into the tone generation of flow over cylindrical cavities, however these results were obtained for cavities in open sections with no confinement. Studies by Ziada et al. (2003) and Verdugo et al. (2010), conducted for both rectangular and cylindrical cavities in confined ducts at relatively low Mach numbers briefly present the effects of a duct confinement on the aeroacoustics response of the cavity. In the rectangular cavity case of Ziada et al. (2003), the resonance frequency was found to be the transverse mode of the cavity and duct combination. The ½ wavelength nature of the acoustic mode governing the lock-in range for aeroacoustics resonance was estimated using the cavity depth and duct height as the length scale for predicting the resonant frequency. Such acoustic modes would not be materialized in

the absence of the confinement of the cavity. It was also stated that the reflection caused by the cavity confinement may reduce the radiation losses and thereby increases the system's liability to flow excited acoustic resonance. In the cylindrical case of Verdugo et al. (2010) a "stepwise" evolution in the lock in frequencies during flow-excited acoustic resonance was reported and ascribed it to the fact that the cavity is installed in a confined test-section, however further insight into these acoustic modes were not given. It is interesting to note that Marsden et al. (2012) studied an almost similar aspect ratio as Verdugo et al. (2010) but did so in an unconfined cavity. This study did not show the stepwise evolution as reported in the confined case of Verdugo et al. (2010) but rather a similar evolution of the shear layer modes and lock in regions to rectangular cavities.

For the current investigation, the impingement length is taken as the diameter, *D*, of the cavity. The aspect ratios studied herein are h/D = 0.5, 1, and 1.5 with a constant cavity diameter of 152.4 mm. The same three aspect ratios are then repeated using a cavity diameter of 101.6 mm. This allows for further investigation on the effect of the admission ratio (D/W) to the cavity's aeroacoustics response in a confined flow, where *W* is the width of the duct. For the remainder of this study, the cavity diameters of 152.4 mm and 101.6 mm will be referred to as *D1* and *D2*, respectively. Measurements are conducted using four ¼ inch microphones to measure the fluctuating acoustic pressure amplitudes at select locations throughout the cavity-duct system to characterize the aeroacoustics response of cylindrical cavities in confined ducts. Furthermore, the Strouhal numbers for the studied cases are presented and briefly discussed.

2. EXPERIMENTAL METHODOLOGY

The experimental setup comprises an open-loop wind tunnel for relatively low Mach number flows. A centrifugal blower draws the air through a parabolic bell mouth contraction leading to the test-section with a height (*H*) of 127 mm, width (*W*) of 254 mm, and a section length of 768.4 mm. The air then flows through a diffuser section that gradually increases in the cross-sectional area with an inclusion angle of less than 14° to avoid flow separation at the walls. The exit of the diffuser is connected to the blower by means of a flexible connection to mitigate vibration transmission from the power unit. The cylindrical cavities are flush mounted to the center of the side wall of the duct where the configuration can be seen in Figure 1. As mentioned, three aspect ratios (h/D = 0.5, 1, 1.5) are studied for two separate cavity diameters, *D1* and *D2*, resulting in a total of six cavity configurations whose details are outlined in Table 1. The acoustic pressure measurements are performed using four PCB 378A12 microphones whose sensitivities were individually obtained through calibration with a GRAS pistonphone. The locations of the microphones are shown in Figure 2 where *M2*, *M3*, and *M4* are in constant locations for each tested case. *M2* is located immediately after the cavity downstream edge on the same wall the cavity is mounted to. *M3* is located at the top wall of the duct and *M4* is located on the opposite wall to the cavity's open mouth. *M1* is located at the center of the cavity floor and is only subject to change according to the cavity depth. The acoustic pressure is measured for 60 s at upstream flow velocities of up to 140 m/s with incremental steps of 2.76 m/s and a sampling rate of 20 kHz. The distance between the nozzle inlet and the cavity upstream edge in the current study is fixed at 330 mm, therefore the dependency of the aeroacoustics response on the velocity profile was not explored.

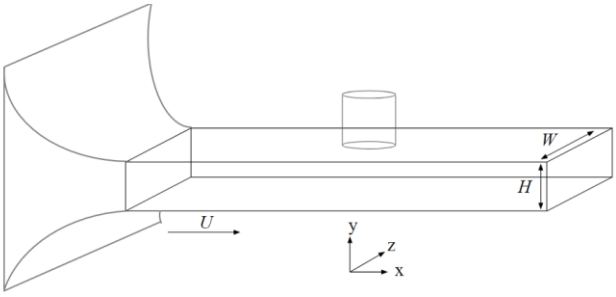

Figure 1. Schematic of experimental setup

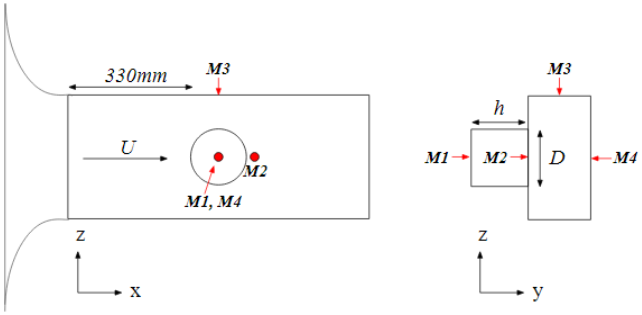

Figure 2. Microphone measurement locations

D/W	h/D
(*D1*) 0.6	0.5
	1
	1.5
(*D2*) 0.4	0.5
	1
	1.5

Table 1. Geometric parameters for the cavities in the current study

3. RESULTS

3.1. Identification of cavity-duct acoustic mode

As a first step, the acoustic modes of the cavities are theoretically calculated using Equation 1. For ¼ and ¾ wavelength acoustic modes, this equation is reduced to Equation 2 which is similar to the formula proposed by Rayleigh (1894) for an open-end tube with an infinite flange. In Equation 2, c, represents the speed of sound, h represents the depth of the cavity, R is the radius of the cavity mouth, q is the acoustic mode number, and α is 0.8216 which is the end correction factor for an infinite flange tube. For more detail regarding Equation 1, refer to Marsden et al. (2012). With the following equations, the theoretical values for the ¼ wavelength acoustic modes of the cavity are calculated and can be found in the 3rd column of Table 2.

$$f_{ijk} = \frac{c}{2\pi}\sqrt{\frac{\lambda_{jk}^2}{R^2} + \frac{i^2\pi^2}{4(h+0.8216R)^2}} \qquad (1)$$

$$f_a = \frac{c(2q+1)}{4(h+\alpha R)} \qquad q = 0, 1, \ldots n \qquad (2)$$

In order to identify the acoustic modes of the system without the presence of airflow, a white noise test is conducted to analyze distinct peaks in the frequency range of interest. As the effect of the duct confinement on the cavity is expected to influence the acoustic modes of the system, the test is first conducted for a duct with no cavity present. The test is then repeated with a cavity aspect ratio *h/D* = 1 for cavity *D1* added to the duct, and finally, this same configuration is tested for a case where the length of the duct is elongated by 254 mm. This is done to further identify the influence of the duct on the cavity's acoustic modes. In the case where no cavity is installed, a few distinct peaks are measured within the range of 328 – 502 Hz. Upon installing cavity *D1* of aspect ratio *h/D* = 1, the same peaks are seen to appear at slightly shifted values with the addition of a new peak at 418 Hz, as seen in Figure 3 *a)*. Additionally, the shifted peaks are seen to have an influence on the acoustic response of the cylindrical cavity, since these peaks are measured by all the microphones but is amplified in the region of *M1*. However, a relatively flat line for *M2*, *M3*, and *M4* in the range of 385 – 522 Hz suggests that the new peak of 418 Hz is attributed to the cavity. Further inspection of Figure 3 *a)* also exhibits a strong peak in the higher end of the frequency spectrum of 1290 Hz, approximately the ¾ wavelength acoustic mode of the ¼ wavelength acoustic mode of 418 Hz. In comparing Figure 3 *b)* to Figure 3 *a)*, the peaks surrounding the frequency of 418 Hz are seen to shift further from this value while 418 Hz remains unaltered at 419 Hz. The ¾ wavelength acoustic mode of the cavity is also unaltered at 1291 Hz. Figure 3 *b)* shows a larger amplitude in the response compared to Figure 3 *a)*, which is also indicative of the influence of the duct on the acoustic response of the cavity. The elongated duct case is only used here to determine the effect of the duct on the acoustic response of the cavity and will not be used again in the current investigation.

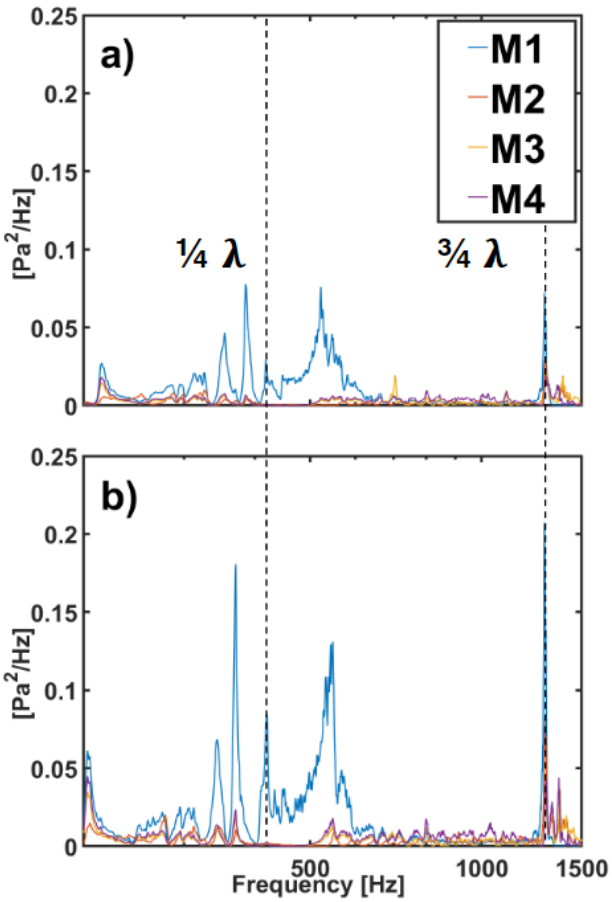

Figure 3. White noise test of cavity D1 for aspect ratio h/D = 1 a) Original duct, b) Elongated duct

3.2. Aeroacoustics response of the cavity-duct configuration

The boundary layer topology, both upstream the cavity as well as over the cavity opening, has been shown in past literature to influence the flow-excited acoustic coupling and has been extensively studied for numerous cavity geometries and configurations. In the present study, the boundary layer was not analyzed however previous experimental campaigns conducted in the same laboratory facility using the same experimental apparatus, with exception to the cavity configuration, have reported the characteristics of the momentum thickness upstream of the cavity. See Shaaban & Mohany (2015), Abdelmwgoud

& Mohany (2021), and Abdelmwgoud et al. (2021). The boundary layer momentum thickness upstream of the cavity was measured by means of a hotwire probe outside of resonance conditions to avoid measurement errors. The boundary layer momentum thickness in the aforementioned experiments exhibited a decrease in momentum thickness with increasing flow velocity, where it can be assumed to follow a power law such that $\theta/x \approx Re_x^{-0.2}$. Here, the Reynolds number is based on the test section entrance to the cavity leading edge. The average flow velocity profile over the cavity opening was also evaluated by means of PIV measurements showing a maximum deviation of 1.5% from the analytical model.

Figure 4 presents the aeroacoustics response of the same configuration as Figure 3 *a)* i.e., *D1* with *h/D* = 1. The pressure amplitude is shown in dimensionless form by dividing the *rms* pressure by ρcU, where *c* is the speed of sound at 343 m/s. The frequency is normalized by the depth of the cavity, *h*, and the speed of sound. The response shows four peaks which are consecutively excited by the first shear layer mode (*m1*). The same peaks are seen to be excited by the second shear layer mode (*m2*) as well but are relatively weaker. This was mentioned by Ziada et al. (2003) who reported that the resonance is stronger when it is excited by a lower order shear layer mode. The slight reduction in frequencies excited by *m1* with respect to those excited by *m2* is due to the added mass effect as reported by Graf & Ziada (2010). The two strongest lock-in regions are at 414 Hz followed by 464 Hz which are indicated by the thicker and thinner horizontal dashed lines, respectively. This is an interesting feature which is not associated with flow past unconfined cavities. The double peak suggests that the shear layer contains enough energy to excite other acoustic modes in the system in addition to the ¼ wavelength acoustic mode of the cavity which would further explain the "stepwise" evolution in the frequency spectrum reported by Verdugo et al. (2010). However, further analysis of the other lock-in regions is required to determine the nature of these acoustic modes. The lock-in range produced by the 414 Hz peak corresponds to the ¼ wavelength acoustic mode of the cavity which is 1% lower than the measured value from the white noise test and 3.8% higher than the theoretical value of 399 Hz. The double peak seems to also be excited by the second shear layer mode at around Mach 0.16 and 0.2.

The aeroacoustics response for *D1* with *h/D* = 1.5 is shown in Figure 5. Similar to the case of *h/D* = 1, two strong lock-in regions are seen to be excited by the first shear layer mode, however the ¼ wavelength acoustic mode of the cavity with aspect ratio *h/D* = 1.5 is much more noticeable in comparison to *h/D* = 1 and the maximum pressure amplitude is also seen to increase. The two consecutive peaks excited by *m1* are 327 and 369 Hz, respectively. The ¼ wavelength acoustic mode of this cavity corresponds to 327 Hz. This is apparent as the maximum amplitude is associated with this frequency. Additionally, the strength of this lock-in region is visibly sustained for a larger range of flow velocities than the lock-in region presented in the aspect ratio of *h/D* = 1. The second shear layer mode is also seen to excite the acoustic mode of 327 Hz. In comparison to the theoretical value however, this frequency is under predicted by 10.8%. The same aspect ratios of *h/D* = 1 and 1.5 are repeated for the *D2* cavities. Figure 6 presents the cavity case *D2* for aspect ratio of *h/D* = 1.5. The two consecutive peaks excited by *m1* are clearly visible at 466 and 503 Hz, where 466 Hz corresponds to the ¼ wavelength acoustic mode of the cavity and is 5.4% higher than the theoretical value. This case yields the strongest acoustic resonance of all four cases mentioned thus far as observed by the dimensionless pressure amplitude during resonance. The measured ¼ wavelength acoustic modes of the cavity, as well as the theoretical values for each case are tabulated in Table 2 along with deviation percentage between the theoretical and measured values. The aeroacoustics response commonly displays two dominant frequencies in the respective spectrums where deviation (1) and (2) represent the measured deviation from the analytical value for the first and second peak, respectively. Results show that in both cavity cases, the strength of the acoustic resonance as well as the lock-in regions are stronger for the deeper cavities of *h/D* = 1.5 relative to the cases for *h/D* = 1. Additionally, the *D2* cavities present stronger overall amplitudes during resonance compared to their counterparts for the *D1* cavities. This could be attributed to the admission ratio, as the *D2* cavities could foster lower acoustic radiation losses than the *D1* cavities. Moreover, the aspect ratios for the *D2* cavities also yield lower percent deviation values than their counterparts for the *D1* cavities. It is also interesting to compare the measured frequencies for cavity *D2* with *h/D* = 1.5 and cavity *D1* with *h/D* = 1. Both cavity cases have the same geometrical depth, but the larger diameter cavity presents a lower frequency. This distinction is evidence to the fact that the resonance frequency is not only governed by the length of a tube but also the radius of the open-end boundary. It should be noted that the shallow cases of aspect ratio *h/D* = *0*.5 for *D1* and *D2* did not excite acoustic resonance. However, they will be used in the following discussion regarding the behavior of the shear layer modes.

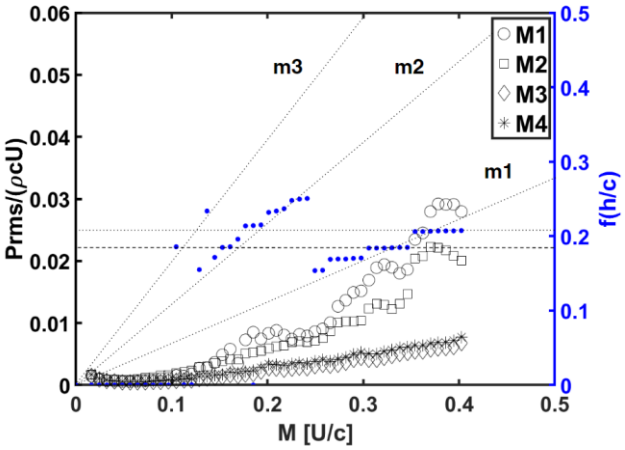

Figure 4. Aeroacoustics response of cavity D1 for aspect ratio h/D = 1

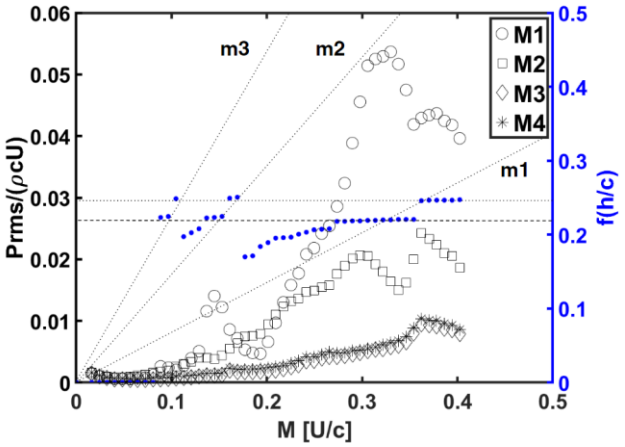

Figure 5. Aeroacoustics response of cavity D1 for aspect ratio h/D = 1.5

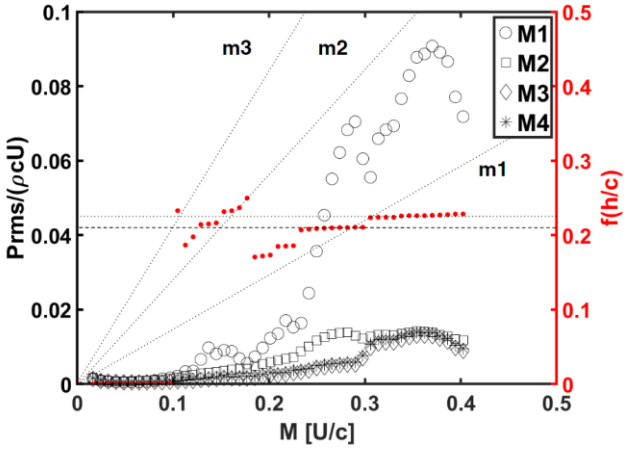

Figure 6. Aeroacoustics response of cavity D2 for aspect ratio h/D = 1.5

D/W	*h/D*	f_a *(1/4λ)* (Hz)	$f_{exp}1$ (Hz)	$f_{exp}2$ (Hz)	*Dev1* %	*Dev2* %
	0.5	618	-	-	-	-
0.6	1	399	414	464	3.8	16.3
	1.5	295	327	369	10.8	25.1
	0.5	927	-		-	
0.4	1	598	613	643	2.5	7.5
	1.5	442	466	503	5.4	13.8

Table 2. Theoretical values for the ¼ wavelength acoustic mode of the cavity and percent deviation from experimentally measured values

3.3. Shear layer behavior

At moderately lower Mach numbers, sudden flow separation of the cavity shear layer produces negligible levels of acoustic power. Upon impingement of the shear layer on the downstream edge of the cavity, pressure perturbations are generated which organize and modulate the separating shear layer by virtue of energy exchange from the acoustic field to the flow field. Effectively, these pressure oscillations in the shear layer are represented by the vortex shedding frequency which increases linearly with the flow velocity. This vortex shedding frequency can be represented in dimensionless form as the Strouhal number defined in Equation 3, where *fv* is the vortex shedding frequency of the shear layer, *D* is the diameter of the cavity mouth, and *U* is the mean flow velocity.

$$St_D = \frac{f_v D}{U} \tag{3}$$

The diameter, *D*, is taken as the characteristic length resulting in a diameter based Strouhal number. The hydrodynamic mode number is a physical representation of the number of vortex cores simultaneously present in the mouth of the cavity. Many authors have introduced analytical models to predict the hydrodynamic modes with relatively good accuracy. Nakiboglu et al. (2012) presented a simple analytical model involving image vortices for the reduction in convection speed of the vortex over the cavity mouth. This explained the linear relationship between the Strouhal number and cavity depth for shallow cavities. Figure 7 displays the contour plot for cavity *D1* with aspect ratio *h/D* = 1 but for the signal obtained by microphone *M2*. The location of *M2* is immediately downstream of the impingement location of the shear layer. This microphone is used herein to illustrate the shear layer modes and to validate their values with those reported in literature. The contour plot is illustrated with a different range of sound pressure level to better observe the shear

layer oscillations which are much weaker than the amplitudes during resonance. The shear layer modes are thus detected in the lower range of flow velocities as can be seen in the contour plot of Figure 7. The values of the first three shear layer modes; *m1, m2*, and *m3* are tabulated in Table 3 for the different cases studied in this investigation. As can be seen, the shear layer modes compare well to previously documented values, with exception of the shallow cavities. Cylindrical cavities with aspect ratios of $h/D = 0.5$ exhibit significantly lower Strouhal numbers, as shown in Table 3. Figure 9 shows the strouhal numbers of the studied cases as a function of the aspect ratio in comparison to the previously documented values of various authors. As outlined by Ziada et al. (2003), the slight increase in the measured Strouhal numbers compared to those reported in literature can be attributed to the confinement of the duct which reflects the sound generated by the shear layer oscillations. This reflection seems to promote the shear layer oscillations at the fundamental mode at substaintially lower Mach numbers than in the case of unconfined cavities. Another reason for the slightly increased Strouhal values of the deep cavities is due to the cylindrical geometry of the cavities in question. Authors such as Bruggeman et al. (1991) and Czech et al. (2006) have presented effective length equations which fundamentally utilise a percentage of the cavity diameter as the effective length for the Strouhal numbers. In fact, Bruggeman et al. (1991) demonstrated that using an effective length such that $L = \pi D/4$ produces no fundamental difference between the pulsation behaviour in square and circular pipes. In the current study the effective length is still noted as the cavity diameter resulting in a diameter-based Strouhal number. Inspection of Figure 8 for the shallow case of *D1* with $h/D = 0.5$, shows that the flow oscillations do not follow the same trend as the cavities with aspect ratios $h/D \geq 1$. The oscillation frequencies in the two shallow cases are much weaker and harder to detect. However, the shear layer modes can be discerned and are seen to have much lower Strouhal values than all cases with aspect ratio $h/D \geq 1$. Such a reduction in the Strouhal values seems to be strongly influenced by the cavity aspect ratio.

D/W	*h/D*	*m 1*	*m 2*	*m 3*
0.6	0.5	~0.15	~0.28	~0.56
	1	0.59	1.17	1.74
	1.5	0.6	1.1	1.69
0.4	0.5	~0.16	~0.25	~0.51
	1	0.61	1.14	1.72
	1.5	0.58	1.07	1.61

Table 3. Strouhal numbers of the studied aspect ratios

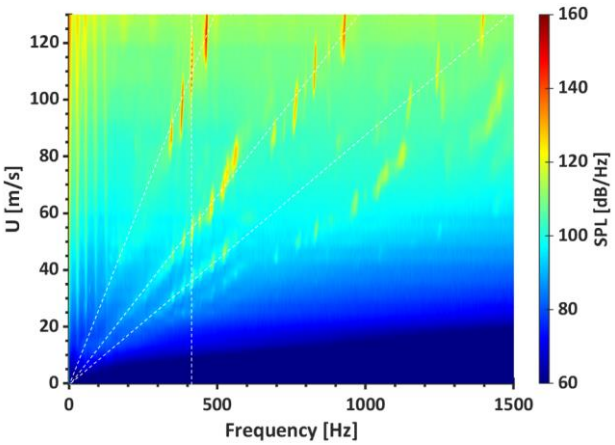

Figure 7. Contour plot of cavity D1 for aspect ratio h/D = 1, using microphone M2

As mentioned, shallow aspect ratios for cylindrical cavities reveal different flow patterns to the deeper cases where the flow becomes highly asymmetric yet stable as the depth of the cavity is reduced such that $0.4 < h/D < 0.7$. Further reduction of the depth transitions the flow to an unstable asymetric flow pattern which exhibits a flapping motion with respect to the vertical streamwise plane. Although the dynamics of the flow are not directly measured in the present study, this flow regime has been confirmed by many authors over a wide range of unconfined cylindrical cavity geometries. Studies conducted by Hiwada et al. (1983) have categorized the flow regimes for aspect ratios $0.2 < h/D < 1$ and have since been confirmed by numerous authors. As previously documented, the strongest case of asymmetry pertains to an aspect ratio $h/D = 0.5$ which demonstrates a stable asymmetric flow profile. Figure 8, as opposed to Figure 7, is plotted using microphone *M1* on the floor of the cavity. This measurement location seemed to better distinguish the shear layer oscillations for the shallow cases. This effect is attributed to the asymmetric flow pattern of shallow cavities. At this aspect ratio, more recent studies by Marsden et al. (2016) and McCarthy & Ekmekci (2022) show that the flow is not only asymmetric relative to the vertical stream wise plane, but also with respect to the horizontal spanwise plane. This consequently shifts the recirculation axis of the vortex. The static pressure contours on the cavity wall and floor in their studies displayed a strong impingement location on the floor of the cavity for this aspect ratio, which explains the clearer depiction of the fluid oscillations on the floor of the cavity for the shallow cavity cases. In addition, Marsden et al. (2016) numerically computed Strouhal numbers of 0.03 and 0.12 for an aspect ratio of $h/D = 0.32$ which are far lower than the expected Strouhal numbers for aspect ratios of $h/D \geq 1$. However, they were unable to establish the origin of this significant decrease in Strouhal values.

McCarthy & Ekmekci (2022) experimentally investigated the same diameter cavity for aspect ratios ranging from $0.35 < h/D < 0.4$ and reported similar Strouhal values around 0.021 and 0.118. McCarthy & Ekmekci (2022) described the slight difference in values in comparison to Marsden et al. (2016) to be due to the aspect ratios in question as well as the combination of the data sample size. These studies showed a strong influence of the cavity aspect ratio on the Strouhal values for aspect ratios ranging from $0.32 < h/D < 0.4$. Although the shear layer modes in Figure 8 do not decrease to the values reported by these two referenced studies, they are still noticeably lower than the measured values for the aspect ratios of $h/D = 1$ and 1.5 in the current study. This variation may be attributed to the reduction of the cavity depth for aspect ratios $h/D < 0.5$. It is also intriguing to note that Abdelmwgoud & Mohany (2021) reported the Strouhal numbers of the first three shear layer modes for two-dimensional rectangular cavities with aspect ratio $h/D = 1$ and 0.5. Their results showed no significant difference in Strouhal values when reducing the cavity depth by half. This further demonstrates that the significant decrease in Strouhal numbers for shallow cylindrical cavities is influenced by its geometrical shape, as this significant reduction is not observed in two-dimensional rectangular cavities. Nakiboglu et al. (2012) however, have reported the influence of the cavity depth on the Strouhal number of the first hydrodynamic mode for annular axisymmetric cavities. Their results showed similar behavior in the shear layer hydrodynamic modes where the Strouhal number seems to be independent of cavity depths for $h/D > 0.5$. However, below this threshold, the Strouhal numbers are seen to decrease from around 0.7 to 0.5 with decreasing cavity depths. In the present case, the Strouhal numbers are seen to be influenced by the depth of the cavity as well when $h/D \leq 0.5$, however the decrease in Strouhal numbers appear to be much more significant reaching values as low as $Sr \sim 0.15$.

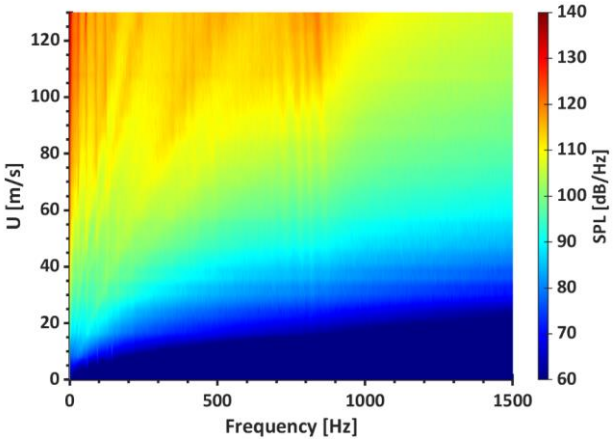

Figure 8. Contour plot of cavity D1 for aspect ratio h/D = 0.5, using microphone M1

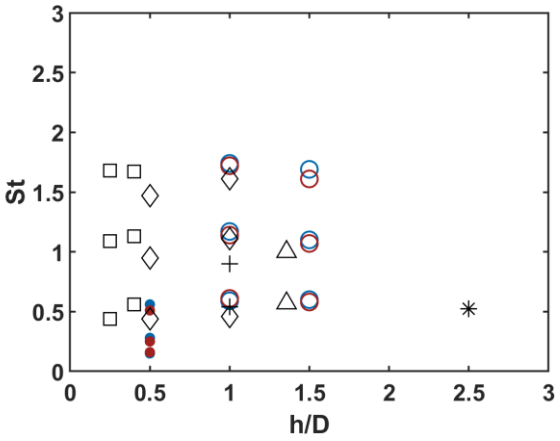

Figure 9. Strouhal numbers as a function of the aspect ratio

Authors	***Symbol***
h/D = 1, 1.5 (*D1*)	○
h/D = 0.5 (*D1*)	●
h/D = 1, 1.5 (*D2*)	○
h/D = 0.5 (*D2*)	●
Ziada et al. (2003)	□
Parthasarathy et al. (1985)	*
Marsden et al. (2012)	+
Verdugo et al. (2010)	△
Abdelmwgoud & Mohany (2021)	◇

Table 4. Symbol legend for Figure 9

4. CONCLUSION

Cylindrical cavities of aspect ratios h/D = 0.5, 1, and 1.5 subject to confined low Mach number flow have been experimentally studied for two different cavity diameters by means of acoustic pressure measurements. The aeroacoustics response of a cylindrical cavity confined in a duct has been seen to be slightly influenced by the presence of the confinement. Such boundary conditions can reduce radiation losses and promote the excitation of multiple peak frequencies generating a stepwise evolution in the lock-in regions. The admission ratio of the cavity diameter to the duct width is also shown to affect the deviation in predicting the ¼ wavelength acoustic mode of the cylindrical cavity where *D2* cavities, which has a smaller admission ratio, presents lower percent deviation with respect to the *D1* cavities of a larger admission ratio. Additionally, the strongest case of resonance was reported for an aspect ratio of h/D = 1.5 for cavity *D2*, suggesting lower acoustic radiation losses caused by the smaller admission ratio of this cavity configuration. Moreover, the shear layer modes for the aspect ratios of h/D = 1 and 1.5 have been experimentally obtained and agree well with published literature for both rectangular and cylindrical cavities of similar aspect ratios. For aspect

ratios of $h/D = 0.5$, the Strouhal numbers are seen to decrease reaching values as low as $St \sim 0.15$ and are significantly affected by the cavity depth with respect to its diameter, an effect which is not observed in two-dimensional rectangular cavities of similar aspect ratio.

5. REFERENCES

Abdelmwgoud, M., Mohany, A., 2021, Control of the self-sustained shear layer oscillations over rectangular cavities using high-frequency vortex generators. *Physics of Fluids* **33**: 6-9.

Abdelmwgoud, M. et al., 2021, Shear layer synchronization of aerodynamically isolated opposite cavities due to acoustic resonance excitation. *Physics of Fluids* **33**: 2-7.

Bruggeman, J. C. et al., 1991, Self-sustained aeroacoustic pulsations in gas transport systems: Experimental study of the influence of closed side branches. *Journal of Sound and Vibration* **150**: 371-393.

Czech, M. J. et al., 2006, Cavity noise generation for circular and rectangular vent holes. *American Institute of Aeronautics and Astronautics* **27**: 3-8.

Graf, H. R., Ziada, S., 2010, Excitation source of a side-branch shear layer. *Journal of Sound and Vibration* **14**: 5-10.

Grottadaurea, M., Rona, A., 2007, Noise sources from a cylindrical cavity. *Aerospace Research Central* **35**: 7-11.

Heller, H., Bliss, D., 1975, The physical mechanism of flow-induced pressure fluctuations in cavities and concepts for their suppression. *Aerospace Research Central* **2**: 2-4.

Hiwada, M., Kawamura, T., 1983, Some characteristics of flow pattern and heat transfer past circular cylindrical cavity. *Japan Society of Mechanical Engineers* **26**: 2-8.

Krishnamurty, K., 1955, Acoustic radiation from two-dimensional rectangular cutouts in aerodynamic surfaces. *National Advisory Committee for Aeronautics* **3487**: 15-18.

Marsden, O. et al., 2012, Investigation of flow features and acoustic radiation of a round cavity. *Journal of Sound and Vibration* **15**: 4-14.

Marsden, O. et al., 2016, Investigation of flow features around shallow round cavities subject to subsonic grazing flow. *Physics of Fluids* **24**: 8-16.

McCarthy, P. W., Ekmekci, A., 2022, Flow features of shallow cylindrical cavities subject to grazing flow. *Physics of Fluids* **34**: 10-19.

Mincu, D. et al., 2009, Numerical simulations of the sound generation by flow over surface mounted cylindrical cavities including wind tunnel installation effects. *Aerospace Research Central* **34**: 5-7.

Nakiboglu, G., Manders, H.B.M., Hirschberg, A., 2012, Aeroacoustic power generated by a compact axisymmetric cavity: prediction of self-sustained oscillation and influence of the depth. *Journal of Fluid Mechanics* **703**: 20.

Parthasarathy, S. P. et al., 1985, Sound generation by flow over relatively deep cylindrical cavities. *The Journal of the Acoustical Society of America* **78**: 2-3.

Rayleigh, J. W. S., 1894, *Theory of Sound* **2**: 37.

Rockwell, D., Naudascher, E., 1978, Review- self-sustaining oscillations of flow past cavities. *The American Society of Mechanical Engineers* **100**: 1-4.

Rona, A., 2007, The acoustic resonance of rectangular cavities. *Journal of Algorithms & Computational Technology* **1**: 5-8.

Rossiter, J. E., 1966, Wind-tunnel experiments on the flow over rectangular cavities at subsonic and transonic speeds. *Aeronautical Research Council Reports and Memoranda* **3438**: 7-21.

Shaaban, M., Mohany, A., 2015, Passive control of flow-excited acoustic resonance in rectangular cavities using upstream mounted blocks. *Experiments in Fluids* ***56*****(4)**: 1-12.

Verdugo, F. R. et al., 2010, Experimental investigation of a cylindrical cavity in a low Mach number flow. *Journal of Fluids and Structures* **28**: 7-15.

Ziada, S., Rockwell, D., 1982, Oscillations of an unstable mixing layer impinging upon an edge. *Journal of Fluid Mechanics* **124**: 12-21.

Ziada, S. et al., 2003, Flow excited resonance of a confined shallow cavity in low Mach number flow and its control. *Journal of Fluids and Structures* **18**: 6-13.

USING FLOW TO CONTROL THE DAMPING OF A RESONANT DUCT

Thomas Humbert & Yves Aurégan
Laboratoire d'Acoustique de l'Université du Mans (LAUM), UMR 6613, Institut d'Acoustique - Graduate School (IA-GS), CNRS, Le Mans Université, France

ABSTRACT

This paper describes a resonant duct created by a corrugated tube submitted to a flow and placed between two resonators. The sound-flow interactions in the corrugated tube are used as an amplifier for frequencies determined by the flow velocity. This gain modulus is used to control the resonant duct damping. For certain modes, loss compensation is close to be achieved. However, when gain over compensates losses, whistling arises.

1. INTRODUCTION

Corrugated tubes appeared as an industrial solution to bring flexibility and robustness to pipes, but they are known to whistle under certain circumstances in presence of flow [Crawford (1974)]. This is due to the unstable free shear-layer over the cavities and the driving mechanism as well as the main control parameters for whistling have been identified in previous studies [Nakiboglu et al (2011); Golliard et al (2020)]. This whistling can also be seen as the amplification of a certain frequency range by sound-flow interactions, and the fastest is the flow the larger are the amplified frequencies. The corrugated tube can thus be seen as a gain modulus that is used in this paper to compensate losses inherent to acoustic propagation in a pipe.

Actually, loss compensation is a feature that has been studied in various fields in recent years, along with research on PT-symmetric systems [Auregan et al (2017)]. For example, an analytical and independent from system's geometry criterion for loss compensation in a dense nanoplasmonic metamaterial is derived in [Stockman (2011)]. In [Fleury et al (2016)], general conditions are given for loss compensation in acoustics, whereas an example using loudspeakers is given.

The approach here will be more empirical and the system parameters will be tuned so that loss compensation is achieved in a resonant duct. First, the experimental set-up is introduced and in particular the gain and loss moduli are described. Then, the evolution of the damping duct modes as functions of flow velocity is depicted, and certain modal damping rates tend to zero for increasing flow velocity. When the zero line is crossed, meaning that gain are greater than loss, whistling occurs. On the contrary, when the system is maintained close to the loss-compensated regime, the life-time of a pulse sent in the duct will be highly increased compared to the no flow case.

2. SYSTEM DESCRIPTION

As shown in the top panel of Figure 1, the resonant duct studied in this paper consists of a corrugated tube surrounded by two resonators. In presence of flow, the corrugated tube acts as a gain or a loss unit, depending on the considered frequencies and on the flow velocity. Four microphones are used to evaluate the properties of the duct resonances with and without flow. In this section, more details are given concerning the experimental apparatus and methods.

2.1. Corrugated tube

A corrugated tube is a tube with a periodic series of ridges and grooves that form cavities. The tube studied in this paper is composed of 103 identical cells, and one unit cell is depicted in the bottom panel of Figure 1. The cavities have a square shape with a length l_c = 4mm. The upstream edges are rounded (radius r = 1 mm) and the downstream edges are sharp. The length of each plateau is l_p = 8 mm so that the total length of the tube is $L = 103 \times (l_c + l_p) = 1236$ mm.

This corrugated tube has already been studied in Golliard et al (2020). Among other things, it has been shown that the sound velocity in this particular corrugated tube is equal to 0.925 the sound velocity in the hard wall parts of the duct. Also, the scattering matrix of the tube was measured and Figure 2 (Left) displays the magnitude of the transmission coefficients $T^{\pm}$ defined for incident plane waves coming from upstream (T^{+}) and downstream (T^{-}). Without flow (brown curves), both transmission coefficients are equal because of the reciprocity principle. The fact that these two transmission coefficients are not equal to 1 is due to visco-thermal losses that occur during wave propagation and which increase

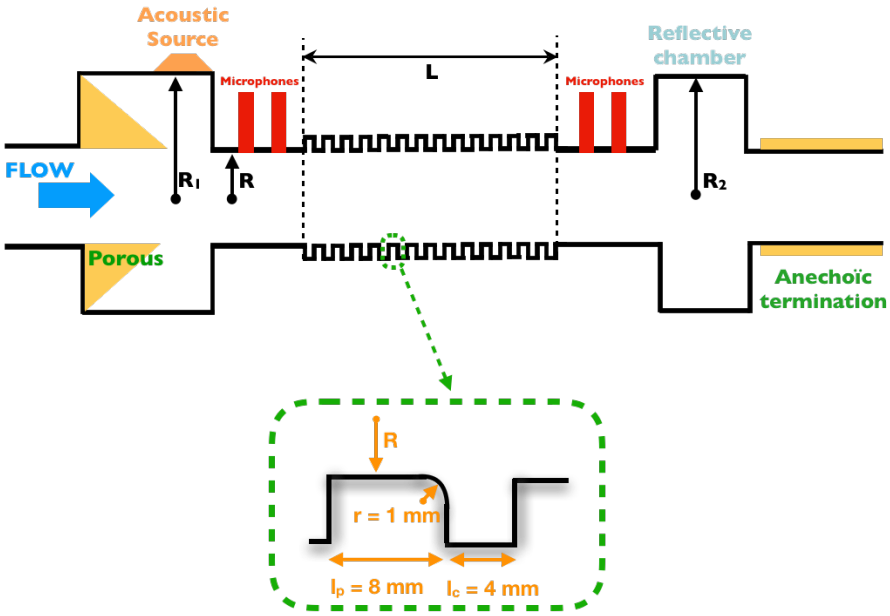

Figure 1. (Top) Sketch of the experimental set-up. A corrugated tube of length L = 1236 mm is mounted between two hard-wall tubes of radius R = 15 mm and two cylindrical resonators of radii R_1 = 7.5 cm, R_2 = 4.7 cm separated by a total length L_t = 2098 mm. The upstream resonator is equipped with an acoustic source and some gradually mounted porous material. Two microphones separated by Δx = 3 cm are placed between each resonator and the corrugated tube. (Bottom) Sketch of the unit cell of the corrugated tube.

as a function of frequency. The presence of a mean flow has several impacts on the transmission properties of the tube, as depicted by the other curves. First, upstream and downstream coefficients are not equal anymore. Also, it can not be missed that the coefficients are different if there is flow or not, and they evolve also as functions of flow velocity. Depending on the considered frequency and on the flow velocity, transmission can be reduced or improved by the flow. For a certain flow velocity (M=0.016), it appears that upstream transmission is equal to one, meaning that the losses at the wall have been compensated. When M=0.029, transmission coefficients are even larger than one, evidencing linear amplification of the acoustic waves as they travel along the corrugated tube.

2.2. Boundary resonators

As depicted in the top panel of Figure 1, a cylindrical resonator of radius R_2 = 4.7 cm and of length L_2 = 10.96 cm is mounted 37.2 cm downstream the corrugated tube. Another cylindrical element of radius R_1 = 7.5 cm and of length L_1 = 66.5 cm is placed 49 cm upstream the corrugated tube. It is equipped with an acoustic source and a gradually mounted porous material which is drilled to let the air pass through. Hard wall sections of radius R = 1.5 cm make the connections between the corrugated tube and the two resonators. Thus, these two elements constitute sudden changes of the tube section that induce wave reflections.

To evaluate the level of these reflections, two measurements are performed on a frequency range $[450; 1000]$ Hz with a frequency step of 10 Hz : one using the previously described upstream source, one using a supplementary acoustic source mounted in place of the downstream resonator. From both measurements, the reflection coefficients of the upstream and downstream resonators R_u and R_d are calculated. Both reflection coefficients are displayed in the right panel of Figure 2. It can be seen that they stay nearly constant on the whole range of frequencies, while the downstream resonator reflects slightly more acoustic waves than the upstream one. Nevertheless, both coefficients are greater than 0.85 so that the losses experienced by the acoustic wave when being reflected are low. We can thus consider that the association of these two resonators creates a resonant duct which encloses the corrugated tube. Note that we could have used larger section changes inducing greater reflections, but that would have limited the range of flow velocities without whistling.

2.3. Experimental set-up

The corrugated tube and the two surrounding resonators are placed in a flow rig of radius R = 15

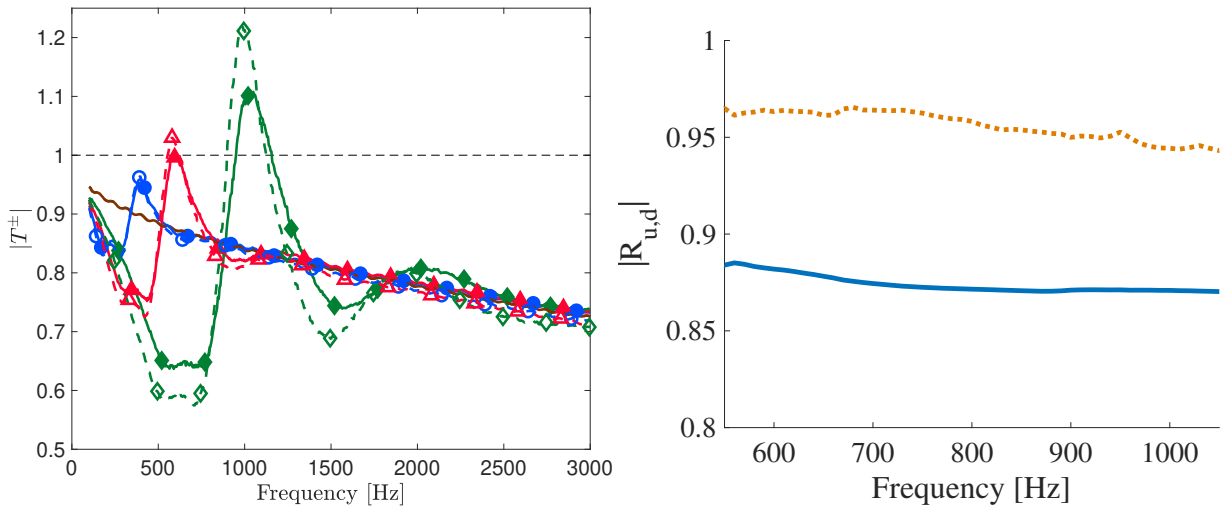

Figure 2. (Left) From Golliard et al (2020). Transmission coefficients as a function of the frequency. T^+: — (M= 0), —●— (M= 0.01), —▲— (M= 0.016), —◆— (M= 0.029); T^-: - - - (M= 0), -○- (M= 0.01), -△- (M= 0.016), -◇- (M= 0.029). The symbols are here to distinguish the different measurement series. In no case they indicate the data points, as the frequency spacing of the measurements is 5 Hz.
(Right) Absolute value of the reflection coefficients of the cylindrical resonators located upstream ($|R_u|$, solid blue line) and downstream ($|R_d|$, orange dashed line) the corrugated tube, as a function of frequency.

mm that is plugged to a centrifugal fan. A turbine flow meter evaluates the mean flow velocity, denoted for the rest of this paper by the mean Mach number M (the ratio between sound in non-corrugated section and flow velocities). The duct is ended by an anechoic termination composed of a drilled tube wrapped in a fabric. Two microphones separated by a distance Δx = 3 cm are placed between the corrugated tube and each resonator. A relative calibration of the microphones is performed in-situ to avoid disassembling them from their supports.

3. MEASURING THE MODES OF THE RESONANT DUCT

3.1. Tube impedance

The further investigation concerns the characterisation of the resonant duct formed by the corrugated tube, the hard-wall steel ducts, and the resonators. To that end, the upstream acoustic source is used to provide a sweep sinus going from 450 to 1000 Hz with a step of 0.5 Hz. At each frequency, the pressure collected by the microphones is averaged over 200 acoustic periods. In this section, we only consider the linear regime of sound-flow interactions, identified by the absence of whistling at the tube output. Given our experimental conditions, it corresponds to flows with mean Mach numbers smaller than M = 0.026. However, the limit between linear and non linear regimes is not so clear because flow noise is already quite large at these velocities, and coloured by the filtering effect of the corrugated tube. Still, no particular tones can be seen in the Power Spectral Densities (PSD) of microphone signals below M = 0.026 (see.Figure 6), or at least their amplitudes are not very large compared to the rest of the spectrum.

To characterise quantitatively the damping of the resonant duct, we introduce the following reflection coefficient which links the two components of the acoustic field in the resonant duct:

$$R = \frac{H_{21}e^{-jk^+x_1} - e^{-jk^+x_2}}{e^{jk^-x_2} - H_{21}e^{jk^-x_1}}. \qquad (1)$$

H_{21} corresponds to the ratio between the two upstream microphones located at distances x_1 and x_2 from the output of the upstream reflective chamber. k^+ and k^- are respectively the wave-numbers of the forward and backward travelling waves. Then, an impedance Z is defined from the previous reflection coefficient according to:

$$Z = \frac{1-R}{1+R}. \qquad (2)$$

Figure 3 displays the real part of this impedance in dB as a function of the frequency. Without flow (black curve), peaks with a common shape and with an amplitude that slightly decreases as a function of frequency are clearly visible. Each peak is separated from its two neighbours by 76.5 Hz. This number should correspond to the fundamental resonance frequency of the L_t = 2098 mm long cylinder open at both ends that links the two resonators of radii R_1 and

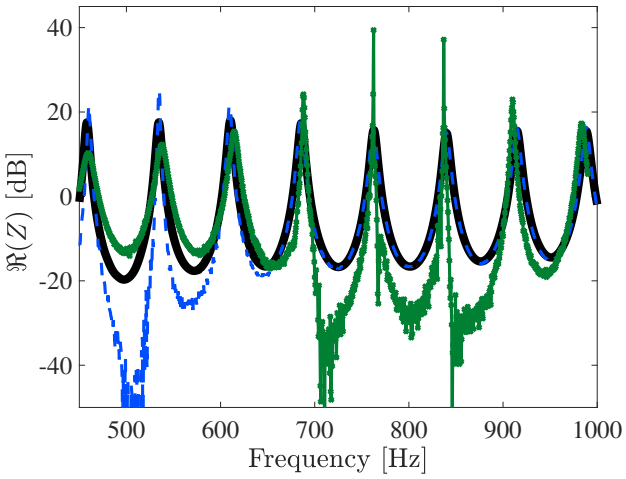

Figure 3. Real part of the tube impedance defined by Eq.(2) as a function of frequency. $M = 0$: black solid line. $M = 0.016$: blue dashed line. $M = 0.025$: green solid line with crosses.

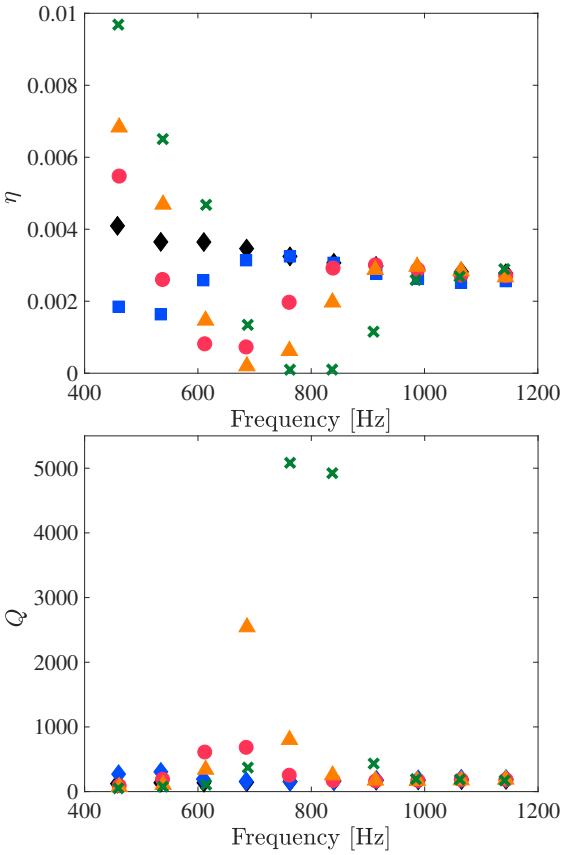

Figure 4. Damping rate η (top) and quality factor (bottom) of the system resonances as a function of frequency. M=0: black diamonds. M=0.016: blue squares. M=0.02: red circles. M=0.022: orange triangles. M=0.025: green crosses.

R_2. With flow, the height and the width of the peaks evolve compared to the no flow case. Moreover, for a given flow velocity, the shape depends now strongly on frequency. For example, it can be seen when $M = 0.016$ (blue curve) that the three first impedance peaks looks narrower than the baseline obtained without flow. When $M = 0.025$ (green curve), low frequency peaks are wider, but the resonances at 688 Hz, 762 Hz and 837 Hz are very narrow. These peak width variations indicate a change operated by the flow on the damping rates of the duct modes.

3.2. Modal damping rate

To quantify the effect of flow on modal shapes, a polynomial fit of each peak is performed. It permits a more accurate extraction of the frequency f_0 which corresponds to the peak maximum. The width at -3 dB away from the maximum δf is also collected. Then, a damping rate,

$$\eta = \frac{\delta f}{2 f_0}, \tag{3}$$

is associated to each mode of the resonant duct, for each considered flow. Figure 4 (top) displays these damping rates as functions of frequency, for several Mach numbers. Without flow, the damping rates are nearly constant, which means that modal damping increases linearly with frequency. This evolution is the imprint of the viscothermic losses occurring during wave propagation in the duct. When flow is added, the damping rates are significantly different from the values obtained for the no-flow case. For example, damping rates are reduced at low frequencies for the slowest flow ($M = 0.016$), whereas they are increased for the other Mach numbers. When $M = 0.025$, the damping rates of resonances at $f = 762$ Hz and $f = 837$ Hz reach nearly 0, meaning that sound-flow amplification in the corrugations compensates the losses coming from propagation effects and non-perfect reflections at boundaries. For each flow velocity, it exists a mode where damping is minimum, and this value corresponds to the most amplified mode at this given Mach number. This agrees with our previous results recalled in Figure 2 (left): the range of amplified frequencies goes towards high frequencies for increasing flow velocities and is preceded and followed by zones of additional losses.

In Figure 4 (bottom), the quality factors

$$Q = \frac{f_0}{\delta f} \tag{4}$$

are shown, highlighting again that flow is a way to change the damping of the studied resonant duct. For the fastest flow, the quality factor of the resonances located at $f = 762$ Hz and 837 Hz is fifty times larger

than for the no-flow case.

Figure 5 (left) shows the evolution of the damping rate η as a function of the Mach number. Each series corresponds to one mode of the resonant duct. For the low frequency modes (below 840 Hz), the damping rates decrease rapidly with Mach number, reach a minimal value larger than zero, and then increase. For the other modes, the system becomes non linear before any observation of an increase. The damping rate expresses the balance between amplification and losses. Thus, the minimum value of each modal curve exists because amplified frequencies are changed when flow velocity is increased, whereas losses stay the same. When the minimum is larger than zero (all modes below 840 Hz), it means that no loss compensation can be achieved at these frequencies for this present experimental set-up. To correct that, using resonators with larger reflection coefficients could be a solution, as well as changing the corrugations geometry so that the gain below 600 Hz would be larger.

Figure 5 (right) displays the same damping rates as in the left panel, but this time as functions of the Strouhal number, here defined as:

$$\mathrm{Sr} = \frac{f l_c}{U_0}. \tag{5}$$

The curves associated to each modes of the resonant duct collapse towards a common behaviour. For each mode, a minimum value is reached when the amplification experienced by this mode as a function of flow velocity is maximum. This minimum occurs for Strouhal numbers between 0.36 and 0.4, agreeing with previous corrugated tube studies.

4. SOME CONSEQUENCES OF WEAKLY DAMPED RESONANCES

4.1. Non linear regime

When flow velocity is increased above $M = 0.026$, a whistling is clearly heard outside the resonant duct, in the experimental room. This phenomenon is studied by recording the acoustic pressure with the first downstream microphone in absence of any external acoustic source.

Figure 6 displays the power spectral density (PSD) of the downstream microphone signal as a function of frequency for several flow velocities. When $M = 0.023$ (no whistling), the spectral energy decreases with frequency, except around the slightly amplified duct modes. For faster flows, which all correspond to whistling cases, very large peaks are visible. They should correspond to the frequencies heard out of the duct: 911 Hz at $M = 0.03$, 988 Hz and 1060 Hz when $M = 0.033$, 1140 Hz for $M = 0.037$. For this last case, there are roughly six orders of magnitude between the energy associated to this mode and the energy associated to the other frequencies.

Just after the onset of whistling ($M = 0.027$), the two duct modes at 760 and 840 Hz appear clearly. This last mode is a good example to describe the transition from the linear to the non linear regime when flow velocity is increased. At low Mach numbers, this frequency is amplified by sound-flow interactions so that the modal damping is decreased until it reaches 0 around $M = 0.026$ (see Figure 5 (left)). Contrary to the modes at lower frequencies, the gain here is still increased when $M > 0.026$. Thus, the modal damping rate becomes negative and the mode is now amplified. This triggers the nonlinear saturation process responsible for the whistling at this mode frequency. When flow velocity is again increased, this mode loses his negative damping rate, and the system whistles on another amplified tone.

4.2. System answer to pulse excitation

Previously, we have shown that gain seems to compensate losses when $M = 0.025$ for two frequencies: $f = 762$ Hz and $f = 840$. In order to test this (quasi) loss compensated state, a 10 ms pulse is used as an acoustic input. Its evolution in the resonant duct is recorded by the first downstream microphone. Each experiment is repeated 10 times and the microphone answer is averaged over these realisations. Figure 7 displays a spatio-temporal representation of spectral energy associated to the averaged pressure signal, without flow (top panel), and when $M = 0.025$ (bottom panel). Without flow, it is shown that the pulse signal induces a broadband excitation of the resonant duct. The latter acts then as a filter and the duct mode are retrieved. After 0.2 s and approximately 15 reflections of the pulse, there is no more acoustics. With flow (bottom panel of Figure 7), the pulse also induces a broadband answer of the resonant duct and its modes are visible. However, some resonances appear on the spectrogram during a much longer time compared to the other peaks and compared to the no flow case. These modes correspond to the ones amplified by the sound-flow interactions in the corrugated tube, and one ($f = 840$ Hz) is visible during 2 seconds. It means that the components of the pulse at this frequency has endured much more reflections (about 150) than without flow, and its life-time in the system is highly increased (about 10 times more than without flow). This is a direct evidence of the flow impact on modal properties of the resonant duct. Unfortunately, and even if theoretically the loss compensated state corresponds to an infinite life-time, we didn't manage to do better than that with the present

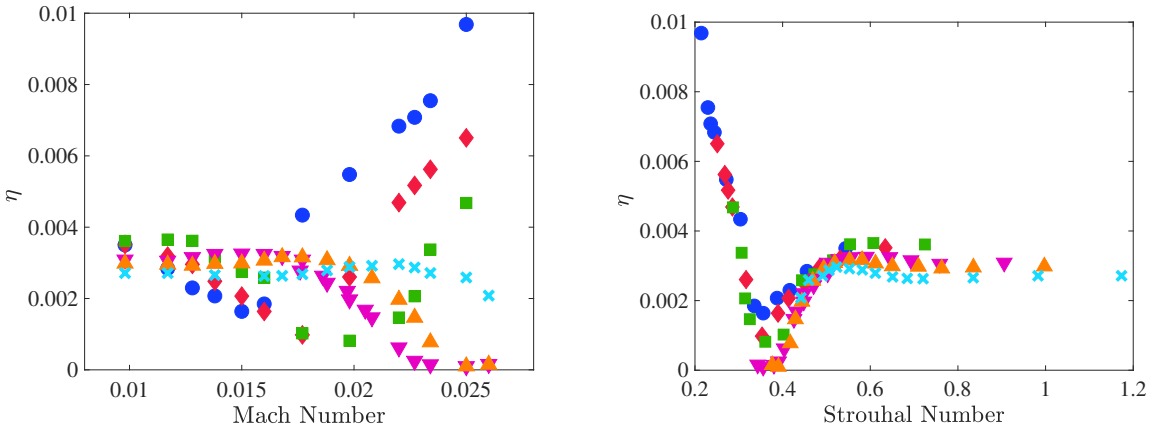

Figure 5. Damping rate η as a function of the Mach number (left) and as a function of the Strouhal number (right). f = 458 Hz: blue circles. f = 534 Hz: red diamonds. f = 610 Hz: green squares. f = 762 Hz: downward-pointing magenta triangles f = 840 Hz: upward-pointing orange triangles. f = 988 Hz: cyan crosses.

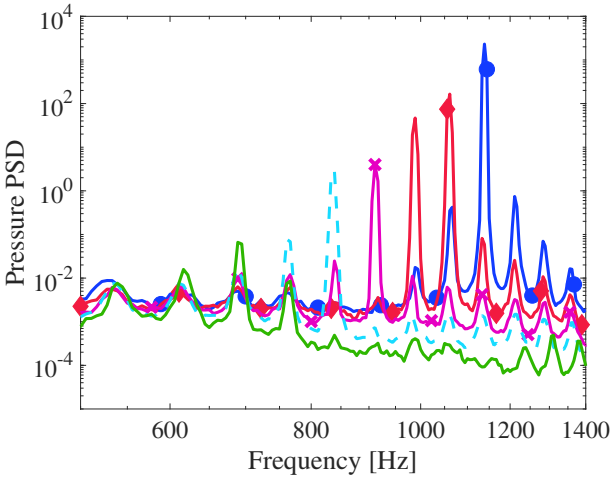

Figure 6. Power Spectral Density of the pressure signal recorded by the first downstream microphone. M=0.023: green solid line. M=0.027: cyan dashed line. M=0.03: magenta solid line with crosses. M=0.033: red solid line with diamonds. M=0.037: blue solid line with circles.

set-up.

5. CONCLUSIONS

Inspired by the concept of optical lasers, the present experiment consists in a corrugated tube surrounded by two resonators. It has been shown that the resonators induce enough reflections so that the whole system can be considered as a resonant duct. Thus, modes exist and they are characterised using measurements of the tube impedance. From this quantity, modal damping rates are extracted and their evolution as functions of the flow velocity indicates that flow is a mean to control the system damping. Actually, depending on flow velocity, a certain range of frequencies is amplified, and the modes lying within this range see their damping rate decreased. It is then possible to find sets of parameters where gain and loss are equivalent and thus damping close to zero. Unfortunately, no condition has been found where loss compensation is fully achieved: either loss are still slightly greater than gain, either gain is greater and whistling is on. Nevertheless, the whistling frequencies can be understood from the previous linear analysis.

6. REFERENCES

Crawford, Frank S., 1974, Singing Corrugated Pipes. *Am. J. Phys.* **42(4)**: 278-288.

Aurégan, Y. et al, 2017, PT-symmetric scattering in flow duct acoustics. *Physical Review Letters* **118(17)**: 174301.

Fleury, R. et al, 2016, Parity-Time Symmetry in Acoustics: Theory, Devices, and Potential Applications. *IEEE Journal of Selected Topics in Quantum Electronics* **22(5)**: 121-129.

Golliard, J. et al, 2020, Experimental study of plane wave propagation in a corrugated pipe: linear regime of acoustic-flow interaction. *Journal of Sound and Vibration* **472**: 115158.

Nakiboglu, G. et al, 2011, On the whistling of corrugated pipes: effect of pipe length and flow profile. *J. Fluid Mech.* **672**: 78–108.

Stockman, M. I., 2011, Spaser action, loss compensation, and stability in plasmonic systems with gain. *Physical review letters* **106(15)**: 156802.

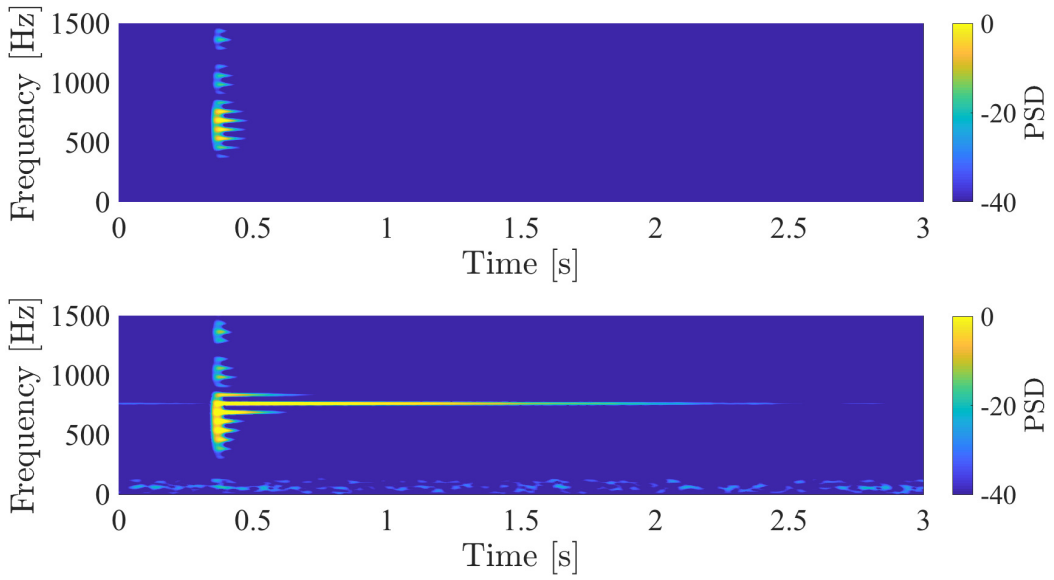

Figure 7. Power spectral density (in dB) of the pressure recorded by the first downstream microphone in the time-frequency space. $M = 0$: top panel. $M = 0.025$: bottom panel.

Flow visualization

SIMULTANEOUS CONTROL ROD 3D DISPLACEMENT AND 3D FLOW MEASUREMENTS VIA TIME RESOLVED 3D3C PTV WITH ONE CAMERA ONLY

Vincent FICHET
Technical Center Framatome, 71200 Le Creusot, France
Mouad DAOUDI
CNRS PC2A Laboratory UMR 8522, 59000 Lille, France
Laurent ZIMMER
Université Paris-Saclay, CNRS, CentraleSupélec, Laboratoire EM2C, 91190, Gif-sur-Yvette, France.

ABSTRACT

In the framework of Flow-Induced Vibration (FIV), the measuring capability of a time-resolved 3D-3C Particle Tracking Velocimetry (PTV) with one camera only is addressed in this paper. The study deals with a representative turbulent flow ($Re = 3.10^4$) around guide plates and simulated control rods as parts of a nuclear CRGA (Control Rod Guide Assembly). Based on image defocus, this 3D3C PTV transforms the scattered light of laser-illuminated seeding particles into circular patterns on the defocused images. A patented annular pupil device is used in this scope. These particle patterns are detected and tracked over time by PTV in order to provide instantaneous 3D velocity fields. 3D3C PTV velocities are validated by comparison with LDV data for both spatial (mean and standard deviation of velocity) and spectral (PSD) domains to confirm the accurate capture of the flow dynamics. The measures are found to be consistent in both shape and amplitude. The 3D3C PTV measurements are even more refined than LDV near the rods for the main axial flow. An easy, non-intrusive in-situ calibration based on a laser sheet sweep along the camera's in-depth direction completes the technique. The time required to post-process 20 000 images (time points) is less than 24 h on an HP Z820 workstation with 24 cores, and more than 1000 particles can be tracked per image over time to create trajectories.

Simultaneously, the 3D displacement of moving rods is recorded on these images (one camera only). Tracer particles are indeed fixed on the moving rods to track the rod FIV. Two moving rods are scrutinized in the upstream vicinity of a guide plate: one "free rod" is submitted to flexion with pinned-pinned boundary conditions, and another is held by strings in the highest cross-flow velocity region. With the same set of defocused images, the technique describes then both the excitation (flow) and the rod response (displacement) at the same time, leading to the whole Fluid-Structure Interaction (FSI) or the structure transfer function (response/excitation) with one camera only. The missing step that remains will be to reconstruct instantaneous pressure fields from 3D3C particle trajectories to reach the fluid loads applied to the structure (here rods). Previous works were already undertaken at Technical Center Framatome in 2014 to meet this objective.

1. INTRODUCTION

In Pressurised Water Reactors (PWR), the nuclear reactions are controlled by Rod Cluster Control Assemblies (RRCA). This RCCA is composed of control rods, imprinted with neutron absorbing material and inserted or withdrawn into the Fuel Assemblies (FA) by moving vertically a drive shaft connected to a spider to which control rods are fixed at their upper end. The control rods are about 4 *m* long for 10 *mm* diameter making them very flexible (ratio "length/diameter" around 400). They need then to be guided before entering the FA located further down. Two guiding sections, separated by a support plate, are commonly used. Discontinuous guidance is ensured in the upper section via a set of guide plates regularly spaced from each other (see Figure 1).

In the lower section, control rods are first guided via another set of guide plates and then pass through continuous guidance (opened tubes) before entering the FA. The upwards coolant flow coming from each FA passes through the Upper Core Plate (UCP) before entering the continuous guidance and the sets of guide plates. A mainly axial flow then takes place along the RCCA height. However, cross-flows are generated around the guide plates due to their star-shaped cross-sections, adding excitation to the control rods subject to FIV. These vibrations could cause fatigue and fretting wear of the materials and lead to maintenance operations. Consequently, a dedicated understanding of this FIV based on reliable experi-

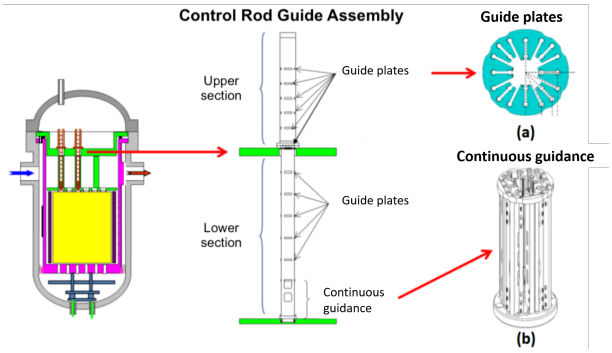

*Figure 1. CRGA location in a nuclear reactor, **(a)** Guide plates, **(b)** Continuous guidance, adapted from Fichet et al (2018)*

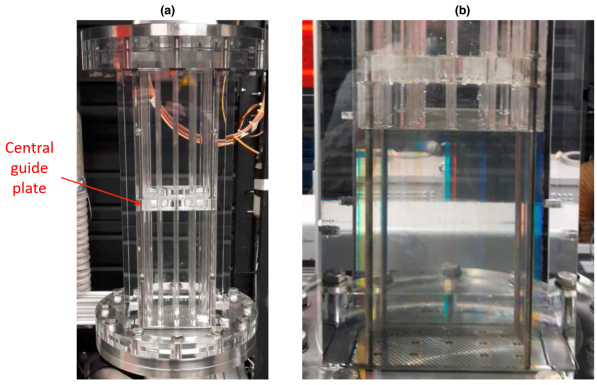

*Figure 2. Transparent guide plates mock-up: **(a)** Test section, **(b)** Index matching during immersion of the rods below the central guide plate, adapted from Fichet et al (2018))*

mental data is required. Over the years, several attempts have been made to measure the control rod vibration. Shono et al. (1985) used the noise analysis technique with the neutron flux (reactivity signal from the primary flow rate), load weight of control rods and an acoustic signal of the control rod driving mechanism to estimate the control rods' vibration mode and the correspondent driving forces. The same neutron noise approach was validated by Ansari et al (2008) by deploying a reactor internals vibration monitoring system. Later on, Kim et al (2001) used a non-contact laser vibrometer and a digital oscilloscope to measure real-time rod vibration and concluded that the turbulence excitation is the most probable variation mechanism of RCCA. Moussou et al (2019) reach the same conclusions when analyzing the FIV of the control rod in a full scale 1300 MWe CRGA mock-up. De Pauw et al (2013) investigated six vibration measuring techniques to tackle the FIV on a fuel pin mock-up. These techniques included Laser Doppler Velocimetry (LDV), a grid method (GRID), fibre Bragg grating sensors (FBGs), electrical strain gages and two types of accelerometers. The study concluded that LDV and MEMs-type accelerometer techniques offer superior performance. For space constraints, the authors believe that the FBGs technique is the most suitable one when dealing with vibration monitoring in nuclear reactor core mock-ups. LDV was also investigated by Shengjie et al (2015) and was found to provide more accurate results compared to traditional accelerometer methods. Unfortunately, all the studies mentioned before focus only on measuring the rod's response and do not provide any extensive data on the flow excitation around those vibrating structures.

One of the first attempts to provide experimental data for both the mechanical response and the flow field was proposed by Cioncolini et al (2018). The authors conducted experiments on a considerably simplified geometry in which a single clamped-free cantilevered cylindrical rod confined in a tube and subject to axial flow directed from the rod free-end towards the clamped-end was used. The study used a non-contact optical technique to measure the 3D rod displacement along with 2D Particle Imaging Velocimetry (PIV) to measure the velocity field, making the experimental setup quite delicate to handle since it uses two different cameras. To the best of the author's knowledge, 3D flow measurements simultaneously with rod 3D displacement have not been yet dealt with. The present investigation was therefore conducted to match such requirements and to consolidate the FIV/FSI Computational Fluid Dynamics (CFD) models with a relatively simple but representative setup.

In this study, 3D3C PTV is conducted on control rods placed in a full-scale guide plate mock-up (see Figure 2). The 3D3C PTV principle is reminded in section 2.2. The velocities obtained are found to be more accurate than former results (see Fichet et al (2018)), especially near the rod submitted to FIV and are confronted to Laser Doppler Velocimetry (LDV) in section 3.1. Finally, an innovative tracking technique (see section 2.3) is presented to capture the 3D displacement of a moving rod simultaneously with the 3D instantaneous velocity field, using the same set of defocused images. The associated results are presented in section 3.2.

2. EXPERIMENTAL SETUP AND POST-PROCESSING

2.1. Mock-up and instrumentation

The current turbulent flow is to be linked to the one produced inside a CRGA of a nuclear reactor.

However, non-intrusive measurements, such as 3D3C PTV in a fully transparent mock-up to capture the velocity field finely around the obstacle, can not be undertaken in real-operating conditions due to the rod material, the fluid pressure and temperature. Therefore, the study is limited to the same mean flow rate Q (similitude inflow velocity) in a representative geometry (star-shape of the guide plate cross-section) but at ambient pressure P and temperature T conditions as mentioned in Table 1. The mock-up consists of two guide plates distant by 293 *mm* from each other, along with control rods (up to 24 in Figure 2) at full scale. The simulated guide plates exhibit a square shape (173 *mm* side) to reduce the optical distortions on the test section surface, making them slightly different from the real ones in nuclear reactors. The studied guide plate is the one located in the middle (height) of the test section. It is positioned and fixed in the test section via rigid steel threaded rods in its four corners. Both control rods and guide plates are made of Plexiglass to enable non-intrusive laser measurements. In addition, an index-matching technique used at Technical Center Framatome for more than ten years is deployed. The concentration of a dedicated solution of sodium iodide, used as the driven fluid, is fine-tuned to match the refracting index of Plexiglass parts ($n \approx 1.49$). When index matching is reached, the solid parts almost disappear and enable an optimal visualization of the particles even behind the obstacles to get a full 3D view of the velocities surrounding the rod. Considering the fluid properties and geometric scales (see Table 1), the turbulent ascending flow is established with a Reynolds number of 3.10^4.

Quantity	Value
$Q\ (l/s)$	19.17
$P\ (bar)$	1
$T\ (C)$	25
$\rho\ (kg/m^3)$	1798
$\nu\ (m^2/s)$	$1.76.10^{-6}$
Re_H	3.10^4
$D_H\ (mm)$	78.1
$V_{\text{inlet}}\ (m/s)$	0.68

Table 1. Guide plates mock-up operating conditions and fluid properties

First, PIV is performed in a vertical symmetry plane crossing the guide plates to identify the flow topology and regions with velocity gradients (see Figure 3). Even with an imperfect upstream flow (i.e. not a flat axial velocity profile), the flow formed downstream the star-shaped diaphragm of the guide plate appears quite symmetrical. A large central jet is generated with a high velocity, maintained up to

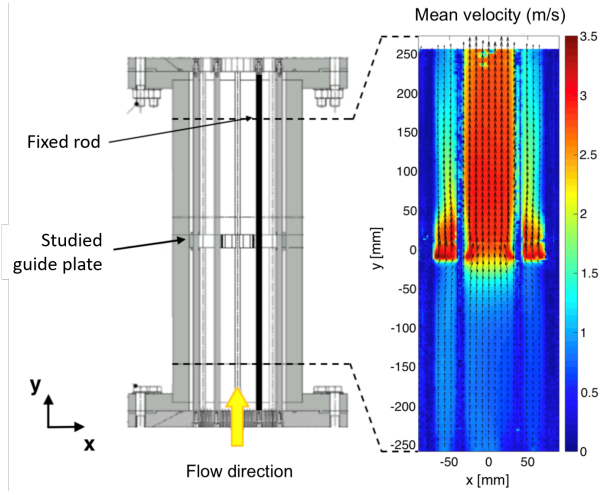

Figure 3. Location of the fixed rod (in black) in the Two-guide plates mock-up and mean velocity field (over 500 instants) in the median plane resulting from a PIV measurement

the next guide plate located downstream. At the periphery, jets are also produced downstream of the peripheral slots between the rod locations. These peripheral jets are quickly decreasing in velocity along the elevation. The peripheral jets indeed feed the main central jet with momentum, which explains the former observations. Recycling zones are also produced around the central jet and induce velocity fluctuations, especially when interacting with peripheral jets.

Three setup configurations are then realized with 3D3C PTV around rods but either upstream or downstream of the central guide plate. In the first one, named **Fixed rod**, a control rod with pinned-pinned boundary conditions passes through an undamaged central guide plate as indicated in black in Figure 3. The second configuration named **Free rod** is similar to the first one except that the central guide plate presents an enlarged gap to let the rod free oscillate towards the guide plate centre. The third configuration is called **Instrumented rod** which is the red portion in Figure 4. The instrumented rod is attached to upper and lower support rods (indicated in blue) using strings. This particular configuration focuses on the upstream vicinity of the central guide plate, the region with the highest cross-flow velocities in order to observe the rod response to this transverse excitation. This latter case best demonstrates the potential of the tracking method introduced in section 2.3. For the fixed rod configuration, 3D3C measurements were made downstream of the central guide plate, whereas the upstream section was investigated for free and instrumented rod configurations.

Defocused images for 3D3C PTV are acquired us-

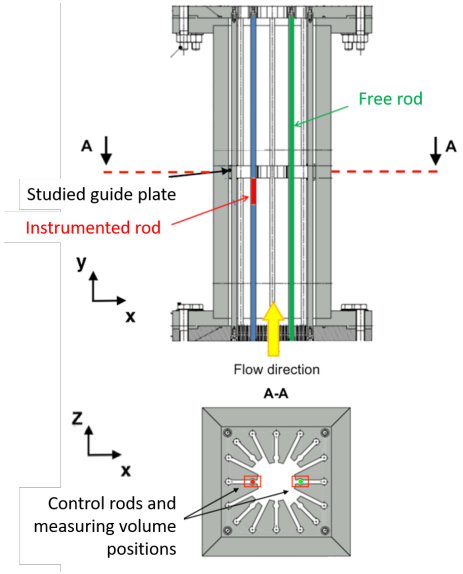

Figure 4. Location of the free rod (in green) and the instrumented rod (in red)

ing a Phantom V611 high-speed camera (up to 6 kHz at full 1280×800 resolution) and a Nikon Nikkor AF-DC 105 mm lens opened at F/2 and the patented annular pupil device. An additional wavelength filter at 570 nm eliminates noise reflections and captures only the light emitted by fluorescent (fluid tracer) seeding particles of an average diameter of 30 μm. On the one hand, a YLF Litron dual cavity laser (up to 6 kHz) with a wavelength of 527 nm and energy 8.5 mJ per pulse at 1 kHz illuminates a fluid volume of $50 \times 40 \times 20\ mm^3$ for 3D3C measurements. On the other hand, LDV measurements, used for validation purposes, are performed using a DANTEC FlowExplorer Laser with a wavelength of 532 nm and maximum output power of 300 mW.

2.2. 3D3C PTV technique

By definition, the 3D3C PTV technique used in this study is based on 3D Lagrangian tracking methods. The method was first developed by Baudoin (2015) during his PhD thesis in collaboration with the EM2C laboratory (CNRS). The technique performance was gradually improved at Technical Center Framatome since then, multiplying by a factor of 100 the number of particles tracked over time (at least three instants) per image. The technique is based on the defocusing principle introduced by Damaschke et al (2005) with which the apparent size of a seed particle on the defocused image is a function of its position in depth (distance to the lens) and the optical mounting characteristics only. Under the assumption of the thin lens and considering seed particles as punctual points (when focusing), if Z_1, f and d_a are the "object" (particle) distance (equal to the image particle distance from the lens plane), the image focal distance and the annular pupil diameter respectively, then the apparent size of that particle on the CCD camera sensor plane d_i is given by Damaschke et al (2005) as expressed in Figure 5.

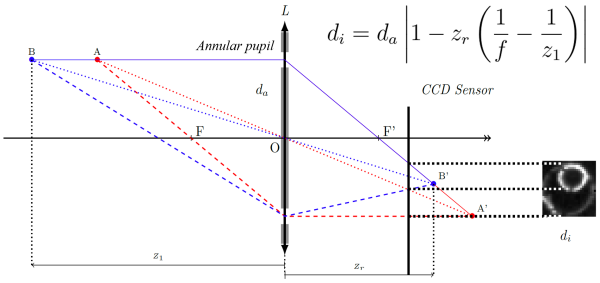

Figure 5. Defocusing principle, adapted from Damaschke et al (2005), Baudoin (2015) and Fichet et al (2018) and the apparent size conversion law, adapted from Damaschke et al (2005)

In the present example (see figure 5), two seeding particles are located at two different distances from the lens (or camera) and placed one behind the other on an axis parallel to the optical axis (see Figure 5). The image obtained on the CCD sensor, when defocusing, show two patterns of different sizes. This "apparent" size of the particles in the defocused image is linked to their position in depth in addition to their locations in the image plane (left/right, up/down). The optical setup is equipped with the patented annular pupil device that generates a circular pattern instead of an entire disc for each particle image. This leads to a much higher particle overlap rate and a better precision in particle positioning.

A typical instantaneous image is displayed in figure 6. One can see the different sizes of the particles, due to their positions in the perpendicular direction with respect to the camera. The rod is in the central part of the picture and therefore presents a lower density of particles with respect to the neighboring zones. Obviously, real optics could not be considered thin lenses. In-situ calibration is then needed to determine the law that links the particle position in-depth to its apparent size on the defocused image. This calibration is easy with one camera. A simple sweep of the laser sheet over the measuring volume along the depth is required. For the present study, the calibration law (apparent particle size into real position in depth) is done by acquiring ten sets of hundreds of frames every 2 mm in depth. Given the number of acquired particles per image and the number of images, one can reach statistical convergence to determine the mean and standard deviation

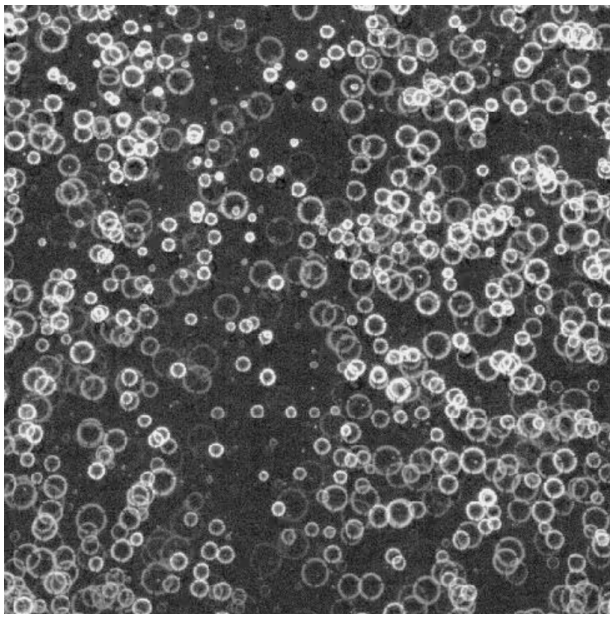

Figure 6. Typical instantaneous image obtained during the experiments

(over the image) of apparent size as a function of the particle position in depth. It has been demonstrated that this calibration behaves as a 3^{rd} order polynomial function (see Fichet et al (2018)). In-plane calibration is based on the rod diameter and the apparent size in the nearest laser plane. 3D3C measurements rely then on image post-processing split in two steps. The first one consists of detecting all particle positions in each frame. Pattern recognition algorithm using cross-correlation with circular pattern canvas (of various sizes) is used and gives the particle positions at a sub-pixel level. The second one is an association algorithm with which each particle is tracked in time to reconstruct its trajectory (from the positions detected) over the time sequence. To support the association process, a PIV-based predictor is calculated for each frame to locate the next particle position in time. Tests are performed to confirm the existence of that particle or not at the next instant. A multi-frame algorithm is used to complete the association process feeding then a 3D predictor with the confirmed associations. Particle trajectories are then reconstructed over time. The verification tests include features that deal with nested particle detection and ghost particles. The last version of those 3D3C PTV algorithms reaches a 0.001 particle per pixel (ppp) resolution. The reconstructed velocity is obtained with a 0.05 px uncertainty in the three directions. For further details about the 3D3C PTV post-processing algorithms, the reader could refer to Baudoin (2015) and Fichet et al (2018).

2.3. Tracking method

As introduced before, the rod's 3D displacement is obtained by tracking fixed seed particles at its surface. In fact, those seed particles appear in the 3D3C recorded frames with an apparent size just like any other seed particle in the measurement volume. However, their motion remains in the camera's field of view along with all the acquisition. Once the fixed particles are identified on the image, dedicated post-processing could be applied based on 3D3C PTV algorithms or finer tracking methods like the Optical Flow (OF). An enhanced version of the 3D3C PTV detection algorithm is used only in the restricted area of the image in which the "rod" particle is moving to gain computational time. Local cross-correlation of the "rod" particle image is then used to track its motion finely even if some filters (criteria) are applied to eliminate inappropriate candidates (in case of particles overlapping), increasing then the signal to noise ratio. However, to properly determine the exact movement of the particle between two images, an optical flow (OF) approach is used. OF leads to much better results in terms of precision as typical uncertainties are evaluated at 1/20 of a pixel through detailed experimental validations on well-controlled systems. Furthermore, as a displacement is obtained for each point of the outer ring of the particle, it provides an estimation of the accuracy we can achieve. Finally, the 3D time-resolved signal of the rod displacement at each tracked particle location can be extracted.

3. RESULTS AND DISCUSSION

3.1. 3D flow velocity analysis

The fixed rod configuration is first examined. 3D3C PTV and LDV axial velocity measurements are performed, as aforementioned, in the upstream section at approximately 100 *mm* from the central guide plate, along a line crossing diametrically the rod in the x direction. The resulting 3D3C PTV axial velocity profiles of mean and standard deviation values show a very good agreement with the ones obtained by LDV (see Figure 7). Furthermore, the 3D3C PTV technique appears to be more precise in the near boundary region of the rod (less averaging) along with a level of velocity fluctuation that matches the LDV one both in shape and amplitude. Other aspects of improvements have been observed after upgrading the 3D3C PTV post-processing algorithms. First, the post-processing of the 20 000 frames acquired for this configuration requires 20 hours (instead of 42 hours before optimization on an HP Z820 workstation with 2 Xeon processors of 12 hyper-threaded cores each).

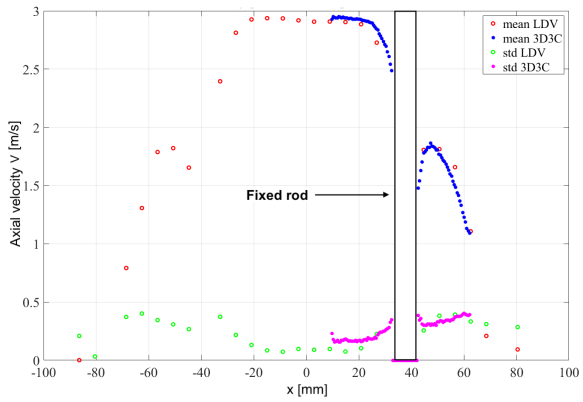

Figure 7. 3D3C PTV and LDV axial velocity V profiles along the line crossing diametrically the fixed rod in the x direction, 100 mm downstream of the guide plate center

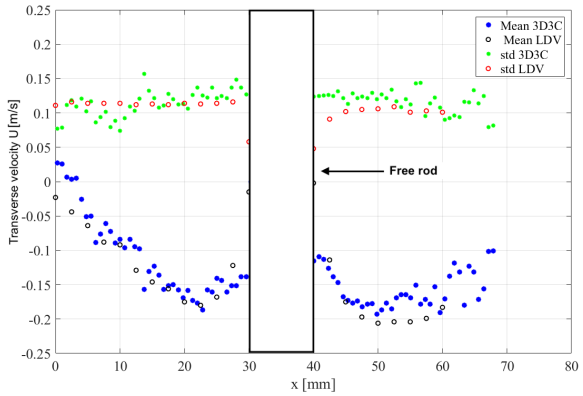

Figure 8. 3D3C PTV and LDV transverse velocity U profiles along the line crossing diametrically the free rod in the x direction

Second, the number of seed particles tracked over three consecutive instants increased by 12%. Such improvement will further enrich the input data for future pressure field reconstruction.

To complete the 3D3C measurements validation on the axial velocity profiles, validation in the transverse direction (x) is proposed to better quantify the measurement uncertainty of this technique for low levels of velocity and fluctuations. Unfortunately, such LDV measurements were not available on the fixed rod configuration, and the experimental setup was modified to accommodate the free and instrumented rod configurations. LDV measurements on the transverse velocity U have then been performed for the free rod configuration. Reader's attention is brought to the fact that in the free and instrumented rod configurations, measurements were operated in the downstream region at approximately 50 *mm* from the central guide plate.

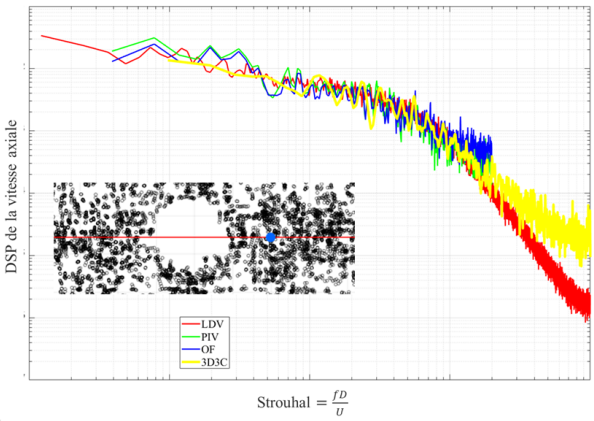

Figure 9. PSD of 3D3C PTV, LDV, PIV and OF axial velocity near the rod downstream of the guide plate

Transverse velocity profiles U, extracted from 3D3C PTV measurements along the line crossing diametrically the free rod in the x direction, demonstrate once again a good agreement with LDV, underlining the accuracy and robustness of the 3D3C PTV technique (see Figure 8) with such low-velocity levels - about 10 times lower than the axial velocities. For time and budget reasons, LDV measurements in the third direction z were not performed for any of these configurations. However, this remaining step is of importance to complete the validation process of the 3D3C PTV technique. We hope that it can be done soon.

After validation of the 3D3C PTV measurements with respect to the spatial distribution, one may focus now on the spectral distribution of the flow in the frame of FIV of the vibrating rods. In the same way, the flow excitation is described by the Power Spectral Density (PSD) of the (axial) velocity. A comparison is made at a point extracted downstream of the guide plate near the fixed rod where recycling flows interact with peripheral jets on the fixed rod configuration. Once again, the agreement with LDV (PIV and OF) is quite good in terms of PSD shape, amplitude and cutoff frequencies (see Figure 9).

3.2. 3D rod displacement analysis

In this section, light is brought on the instrumented rod. For this configuration, particles are fixed at various locations on the rod surface. Whereas seeding particles have a mean convective velocity when following the fluid, the mean displacement of these particles fixed on the rod is null. The displacement of these particles fixed on the rod is expected to be less than 0.5 pixels between two frames. For those particles only, a slightly different tracking approach is taken. Indeed, as the particles are stacked on the rod,

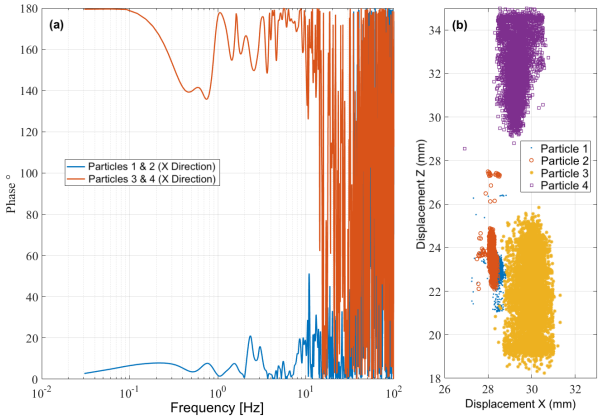

Figure 10. ***(a)*** *Phase between particles 1 & 2 and 3 & 4 displacement signals in the x direction,* ***(b)*** *Four particles, fixed on the instrumented rod surface, movement in the x - z plane*

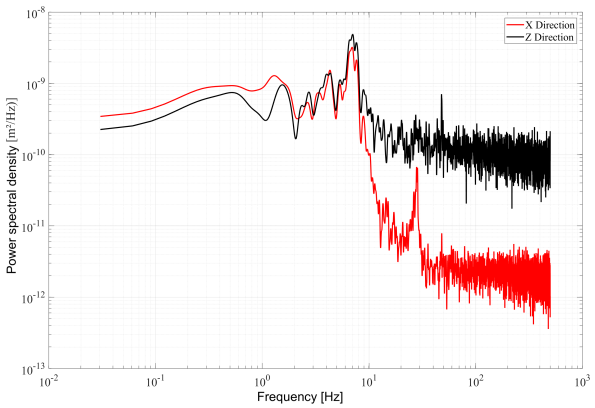

Figure 11. Power spectral density of the x and z particle 1 displacement signals. Instrumented rod case

it is relatively easy to follow them within the entire span of the experiments. Therefore, displacements are not only determined between two consecutive frames but also with respect to the first frame. The average between these two distinct measurements is kept to determine the instantaneous displacements.

Four specific particles are tracked over time. Particles 1 and 2 are located in the top area, while particles 3 and 4 are located further down. However, particles 1, 2 and 3 are located on one side of the rod (in-depth), while particle 4 is on the opposite. The 3D3C improved algorithm was able to track the different particles 1, 2, 3 and 4 over time as forcing a particle to be detected, regardless the quality of the signal. It appears that the tracking efficiency depends on the illumination level of the particle pattern subject to tracking on all acquired frames.

The tracking method allowed identifying the z direction as the main oscillating direction of the flow along which displacements are the most important (see Figure 10). Due to vortex shedding, a rod submitted to a transverse flow oscillates mainly along with its lift (perpendicular to the main flow direction). This seems to support the previous observation on the instrumented rod. A second interesting observation could be made. This rod appears to rotate around itself under the flow. Such a movement is possible due to the fact that the instrumented rod is maintained up and down via strings. This rotating movement was also successfully captured with the tracking method as demonstrated in Figure 10, where one can observe a phase of 180 degrees between particles 3 and 4 displacement signals along the x direction. Meanwhile, no phase is observed between particles 1 and 2 displacement signals along the x direction since both particles belong to the same side (from the camera view). Spectral analysis of the displacement signals, resulting from the tracking process, of the particle 1 along the x and z directions - using Welch's PSD method - also allowed identifying the first vibrating mode around $f = 7\ Hz$ (see Figure 11). Similar results were obtained on the free rod configuration when two particles located at two different positions on its surface were tracked, even if such results are not presented in this paper. We demonstrated in this section the ability of 3D3C PTV based algorithms to capture the FIV of a submerged vibrating structure (rod) finely. Nevertheless, this promising non-intrusive tracking method (with respect to precision) needs to be validated by conventional (intrusive) displacement measurement techniques such as accelerometers, strain gages, and eddy currents sensors.

4. CONCLUSION & PERSPECTIVES

The present study focused primarily on describing 3D3C PTV measurements of the turbulent flow as the excitation source of (control) rods. The technique's ability to capture the flow distribution has been demonstrated from both spatial and spectral perspectives. Post-processing improvements have enabled this thorough validation up to low-velocity levels compared to what has been presented by Fichet et al (2018). Significant gain in computational time was also observed, along with an increase in the number of tracked particles over time. However, even if the in-plane transverse LDV measurements validate the 3D3C PTV measurements, a remaining validation is required along the depth direction (off-plane of the camera image) to fulfil the validation process.

Finally, an innovative non-intrusive technique based on 3D3C PTV enables to access both the fluid velocity (flow excitation) and the structure response (rod displacement) at the same time. How-

ever, this promising technique needs to be further validated by other conventional techniques in order to evaluate its uncertainty levels. Last but not least, pressure field reconstruction will be also carried out around rods, from 3D measured velocity fields, using a pressure gradient integration method inspired by Tronchin (2013). The resulting pressure distribution will be then used to deduce linear forces applied on the rods. Once completed and validated, this 3D3C method would be a very practical tool to study FIV in plenty of test configurations.

5. REFERENCES

Ansari, S. A. et al, 2008, Detection of flow-induced vibration of reactor internals by neutron noise analysis. *IEEE Transactions on Nuclear Science* **55(3)**: 1670–167

Baudoin, R., 2015, Développement d'une technique de vélocimétrie laser en trois dimensions par suivi de particules basée sur le principe de défocalisation et son application autour d'obstacles en aval d'une grille. *PhD, Thesis, Ecole Doctorale n 579 Centrale-Supelec*

Cioncolini, A. et al, 2018, Axial-flow-induced vibration experiments on cantilevered rods for nuclear reactor applications. *Nuclear Engineering and Design* **338**: 102–11

Damaschke, N. et al, 2005, Multidimensional particle sizing techniques. *Experiments in Fluids - EXP FLUID* **39**: 336–3

De Pauw, B. et al, 2013, Benchmarking of deformation and vibration measurement techniques for nuclear fuel pins. *Measurement* **46**: 3647–365

Fichet, V. et al, 2018, PTV 3D3C haute cadence autour d'un cylindre dans une maquette industrielle de carte de guidage. 16^{e} *Congrès Francophone de Techniques Laser pour la Mécanique des Fluides, Dourdan, France* pages: 103–11

Gesemann, S. et al, 2016, From noisy particle tracks to velocity, acceleration and pressure fields using b-splines and penalties. 18^{th} *International Symposium on Applications of Laser Techniques to Fluid Mechanics, Lisbon, Portugal*

Kim, S.-N et al, 2001, The experiment of flow induced vibration in pwr rccas. *KSME International Journal* **15(3)**: 291–2

Moussou, P et al, 2019, Experimental Investigation of the Flow-Induced Vibrations of a Rod Cluster Control Assembly inside Guides with Enlarged Gaps. *2019 Pressure Vessel and Piping Conference* **93143**

Novara, M. et al, 2012, Lagrangian acceleration evaluation for tomographic piv: a particle-tracking based approach. 16^{th} *International Symposium on Applications of Laser Techniques to Fluid Mechanics, Lisbon, Portugal*

Shengjie, G. et al, 2015, Diagnostic techniques for flow induced vibration. 16^{th} *International Topical Meeting on Nuclear Reactor Thermal Hydraulics, Chicago, IL, USA* page 3618

Shono, A. et al, 1985, Control rods vibration analysis in joyo mark-ii core. *Progress in Nuclear Energy* **15**: 293– 301

Tronchin, T., 2013, Caractérisation expérimentale et numérique es mécanismes tourbillonnaires de génération de portance sur une aile en mouvement couplé de battement et tangage. *PhD Thesis, ISAE, Poitiers*

Fluid-structure interactions of animal locomotion

QUANTITATIVE FLOW IMAGING APPROACH TO UNSTEADY LOADING ON HIGH-INERTIA OSCILLATING FOILS

P. Oshkai, W. Lee, D. Iverson, M. Rahimpour
Department of Mechanical Engineering, University of Victoria, PO Box 1700 STN CSC, Victoria, BC, Canada V8W2Y2

T. Kiwata
School of Mechanical Engineering, College of Science and Engineering, Kanazawa University, Kakuma-machi, Kanazawa, 920-1192, Japan

ABSTRACT

This work studies the effects of chordwise flexibility, inertia and kinematic parameters of an oscillating foil on the unsteady flow-induced loading on the foil. Three low-aspect-ratio foils with different flexibilities were undergoing pitch and heave motions in a uniform flow at the Reynolds number of 80000. Forces exerted on the foil were directly measured using a load cell and were used to calculate the propulsive thrust and efficiency values. The phase-averaged flow velocity and out-of-plane vorticity in the wake of the foil were obtained using particle image velocimetry (PIV). The circulation in the wake was related to the loading on the foil by calculating the moments of vorticity with respect to the pitching axis of the foil. The transverse deflection of the trailing edge, which defined the effective instantaneous angle of attack, determined the timing of the trailing edge vortex shedding and, in turn, the generated thrust and efficiency. The deformation of the foil resulted in an increased wake width, leading to larger amplitudes of the instantaneous loading on the foil and higher thrust coefficient compared to the reference case of a rigid foil.

1. INTRODUCTION

The study of foils oscillating in pitch and heave has been increasing in recent years, where flapping-wing technologies have proven successful in a range of applications, including clean energy extraction in tidal and wind flows, lift generation in micro-aerial vehicles, and thrust generation for aquatic locomotion. The works of Young et al. (2014), Shyy et al. (2010), and Bandyopadhyay (2009), provide comprehensive reviews of these subjects. However, despite growing research interest, wide-spread adoption of oscillating-foil systems by industry has been slow due to the inherently complex fluid-structure interactions and the intricacies of mechanical systems needed to provide appropriate kinematics.

The performance of oscillating-foil systems is strongly influenced by the foil's shape, structural properties, operating kinematics, and operating environment, which altogether yield a significant governing parametric space in which such systems could be designed (Platzer et al., 2008).

Advances in numerical and experimental capabilities in recent years has renewed interest in the subject of oscillating-foil propulsion and facilitated many novel studies including those on flexible foils. It was highlighted, at least as early as in the works of Katz and Weihs (1978), that passive chordwise flexibility of the wing or foil can improve propulsive efficiency at the expense of small decreases in net thrust. This result has been confirmed by other researchers, including Prempraneerach et al. (2003), Miao and Ho (2006), Dai et al. (2012), and Egan et al. (2016). Although numerical campaigns provide insight into the parameters that are not easily measured experimentally, the existing computational studies have often relied on simplifications that have been restricting.

Research into the effect of inertial properties and its relation to performance of flexible foils has again been mainly limited to numerical campaigns, in which this structural property may be varied readily (Zhu, 2007), (Yin and Luo, 2010). These studies have found inertia to be an important parameter, having an influence on the passive deformation of the flexible foils.

The majority of the experimental studies on foil flexibility have not studied the influence of inertia. An exception is the work of Richards and Oshkai (2015), who designed a system to test both flexibility and inertia of oscillating propulsors. The authors directly measured the forces exerted on the foils under a range of heave-only conditions, and concluded that of the foils tested, the heavier and stiffer foils produced the highest efficiencies. In the present follow up investigation, we consider more realistic kinematics (a combination of pitch and heave) in addition to providing an overview of the corresponding flow patterns. The current experimental campaign considered various combinations of chordwise flexibility, inertia, and pitching kinematics on propulsive performance of an oscillating-foil, at a chord-based Reynolds number of $Re_c = 80\,000$.

2. METHODOLOGY

2.1. Experimental apparatus

Experiments were performed in a recirculating water channel with a working cross section of 45 cm x 45 cm and a length of the test section of 250 cm. The turbulence intensity of the inflow was <0.9% of the mean velocity value.

A schematic of the experimental apparatus is shown in Fig. 1. The foil was centered in the cross section of the flow channel. The blockage ratio, defined here as the ratio of the frontal area swept by the leading edge of the foil relative to the cross-sectional area of the test section of the flow channel, was on the order of 5%.

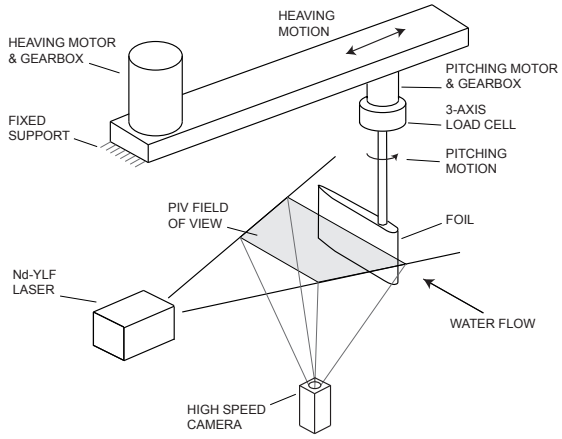

Figure 1. Schematic of the experimental configuration, showing the motion control, force measurement and flow imaging systems.

Heave and pitch motions were controlled independently by separate servo motors. The heave motor was rigidly mounted onto the water channel frame and connected to a linear carriage that generated the heave motion. The pitch motor was mounted onto the heave carriage, to which a loadcell and the test foil were attached.

Both heave and pitch motion profiles were sinusoidal, with a phase difference of 90° between them, as shown in Fig. 2. This motion was based on the results of Hover et al. (2004), who concluded that sinusoidal profiles generally yield the highest performances, in contrast to other motions such as symmetrical sawtooth wave and square wave profiles. A positive pitch angle is defined here as the direction of rotation that would allow the foil to align towards the motion path, as shown by the solid lined foils in Fig. 2. Some of the experiments used a negative pitch angle, corresponding to the phase difference of -90° between the pitching and the heaving motions, as shown by the dashed foil shape in Fig. 2.

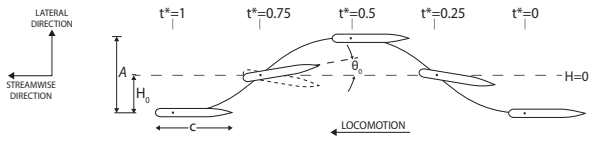

Figure 2. Kinematic diagram of the sinusoidal motion of the foil. t=t/T.*

2.2. Foil construction

Three foils of identical shape, but with different structural parameters, were used in experiments. All foils had a chord length of c = 200 mm and a span length of b = 140 mm, yielding a low aspect ratio of AR = 0.7. The cross-section of the foils is shown in Fig. 3. This geometry was created to allow a weight to be embedded near the trailing edge of one of the foils, positioned at a distance 0.8c from the leading edge. The location of the mass far from the pitch axis generated a higher moment of inertia than would otherwise be possible. The choice of a cross-section that is flat along most of its chord length was also applied by Olivier and Dumas (2016), who noted that such a geometry emphasizes the ability of flexibility effects to shape the wing. For all foils, the pitching motion was about the axis of the aluminum shaft shown in Fig. 3, located a distance of 0.17c from the leading edge.

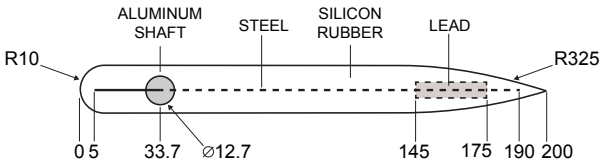

Figure 3. Cross-section of the foils. Dashed lines represent components only present in foil 'A'. All dimensions are in mm.

Of the three used foils, one, referred to here as foil 'R', was constructed of plastic that is from a practical standpoint assumed to be fully rigid. Foil 'R' did not have an additional embedded mass. The other two foils were constructed of a flexible silicon rubber. Flexible foil 'A' had a mass of 140 g embedded at the trailing edge location, and was reinforced in the chordwise direction by a stainless steel sheet, which had a thickness of 0.25 mm. Richards and Oshkai (2015) observed that, for heave-only oscillation, this foil achieved the highest thrust and efficiency metrics under most conditions. The second flexible foil, 'B', was constructed without the steel sheet or lead mass, and consequently was 34% less stiff than foil 'A'. The structural values of the three foils are presented in Table 1. The reason for considering both models A and B is that the mechanisms that result in the deformation of the foil are different in these cases. Specifically, the effective shape of the flexible

foil A was largely due to inertia effects, while deformation of the lighter, less-stiff foil B was governed by the pressure distribution.

Foil Name	Total Mass (g)	Embedded Mass (g)	Moment of Inertia (g m^2)	Stiffness (N/m)	Resonant Frequency (Hz)
R	513	0	2.81	---	---
A	730	140	4.69	168	2.77
B	572	0	3.16	131	2.57

Table 1. Structural properties of the foil designs.

2.3. Force measurements

A three-axis load cell recorded torque about the pitching axis, and forces normal to and tangent to the chord direction. The load cell was rigidly connected to the foil and therefore its coordinate system was fixed to the pitch motion. Measured force vectors were thus decomposed into streamwise and lateral force components based on the recorded pitch angle. The streamwise and lateral directions were associated with the directions of thrust and power input, respectively, as was shown in Fig. 2. Forces were sampled at a frequency of 10 kHz, and filtered values were averaged over 20 oscillation cycles, which was sufficient for producing statistically converged results to under 1% uncertainty.

2.4. Quantitative flow imaging

Fluid velocity at the midspan of the foil was measured using high-speed particle image velocimetry (PIV). The flow was seeded with tracer particles with a mean diameter of 10 μm that were illuminated by a pulsed Nd:YLF dual diode-pumped laser. Only one side of the foil was illuminated by the laser sheet. Light scattered by the particles was captured by a high-speed digital camera operating at the sampling rate of 120 Hz. The instantaneous velocity fields were calculated by cross-correlating the patterns of tracer particles in consecutive images (Raffel et al., 2007). The field of view of images was 346 mm by 346 mm, and the resolution of the image capture was 1024 x 1024 pixels. The final PIV measurements had the spatial resolution of 0.26 vector/mm using the camera lens with the focal length of 24 mm. Phase-averaged distributions of the flow velocity were calculated by averaging 250 instantaneous velocity fields corresponding to the same phase of the foil's oscillation.

3. RESULTS AND DISCUSSION

3.1. Unsteady forces

All experiments were performed at $Re_c = 80000$ and with a heave amplitude of $H_0 = 0.188c$, representing a regime of practical interest as outlined by Richards and Oshkai (2015). Pitching amplitudes were varied from 10° for negative pitch angles to 20° for positive angles, and Strouhal numbers were varied from 0.15 to 0.45. The recorded measurements for cycle-averaged thrust production ($\overline{C_T}$), power consumption ($\overline{C_P}$), and efficiency (η) of this parametric range are presented in Fig. 4 for each of the three foils. The black dots in Fig. 4 represent conditions where data was recorded, and isocontours are interpolated between the obtained results to produce the visual maps.

As shown in Fig. 4, the generated thrust values monotonically increased as a function of Strouhal number for any given pitch angle, for all foils. The trends observed for rigid and flexible foils differed in terms of response to pitch angles. The rigid foil 'R' produced comparatively low thrust during heave-only motions ($\theta_0 = 0°$), especially at low Strouhal numbers. Large positive pitch angles were necessary for high thrust production, where the highest values were recorded at the largest tested pitch angles and oscillation frequencies. In contrast, large pitch values were not needed for thrust production by both flexible foils. Rather, in a large region below $St \cong 0.35$, thrust generation was approximately independent of pitch angle and only dependent on the Strouhal number. Above $St = 0.35$, the highest thrust occurred at negative prescribed pitch angles, whereas the generated thrust diminished at higher pitch angles. Flexible foil 'A', which had a higher inertial moment than the foil 'B', generated thrust values consistently higher than foil 'B'. This difference was most notable at larger Strouhal numbers, where inertial forces were increasingly influential on foil deformation. The increased deformation resulted in an increased the wake width and thus the amount of fluid directly available for thrust production.

The contours of the power coefficient were qualitatively similar for all foils. For all foils, power requirements increased sharply above $St = 0.35$, which is related to poor synchronization of the foil's oscillation frequency with the eigenmodes of the unsteady wake (Triantafyllou et al., 1993).

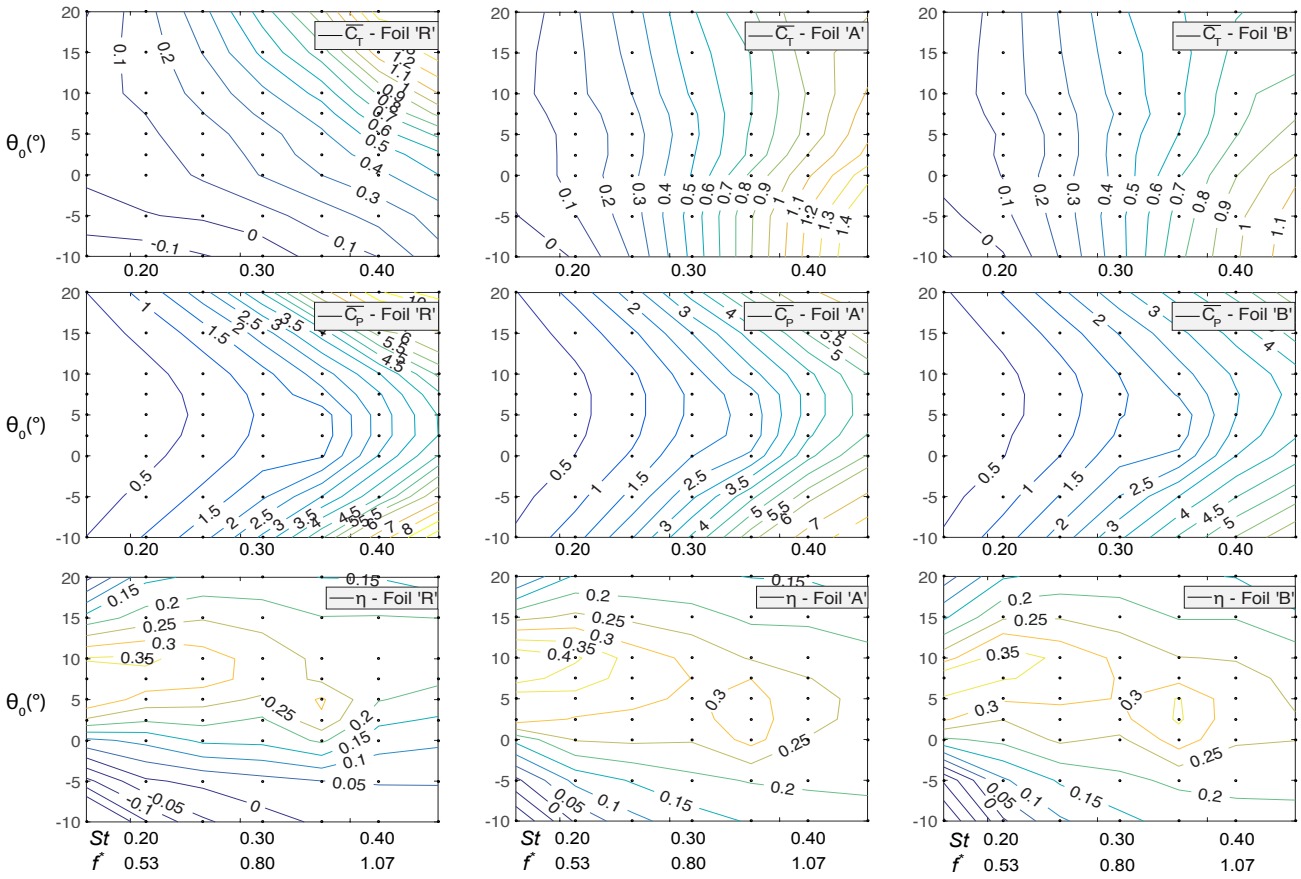

Figure 4. Thrust coefficient (top row), power coefficient (middle row), and efficiency (bottom row) as function of pitch angle and Strouhal number for foil 'R' (left column), foil 'A' (middle column) and foil 'B' (right column).

The flexible foils showed significant increases in efficiency compared to their rigid counterpart. However, in general, the observed efficiency values were lower than the peak efficiencies of oscillating foils reported in literature. This observation is attributed to the low aspect ratio and heave angle of the oscillating foil used in the present study, both of which were limited by experimental constraints, and are known to impair efficiency (Bandyopadhyay, 2009).

These results come in contrast to some previous research campaigns, which have noted that the increases in efficiency for flexible foils are typically associated with a slight reduction in thrust (Prempraneerach et al., 2003). The current investigation suggests that there are exceptions to this generality, where it is apparent that combinations of governing parameters exist that result in flexible foils outperforming rigid foils in both thrust generation and efficiency. These trends are partially attributed to the shape of the foil, which had no camber along most of its length and therefore required other mechanisms to produce thrust force. Presently, the deformation of the flexible foil's trailing edge directly increased the proportion of the foil's surface area normal to the direction of thrust, increasing the available surface area for pressure based forces to propel the foil. This effect is known as force-redirection, and explains the low thrust production of the rigid foil in heave-only conditions (Katz and Weihs, 1978).

At St = 0.35, the rigid foil 'R' at θ_0 = 15° had a cycle-averaged thrust coefficient of C_T = 0.75, while the flexible foil 'B' at θ_0 = -10° yielded a similar thrust coefficient of C_T = 0.76. The similarity in results is quite remarkable considering the 25° difference in prescribed pitch angle. However, it was observed that the trailing edge of the flexible foil deformed significantly, and was actually oriented to within ±1° of the trailing edge of the rigid foil under these conditions. This observation suggests that an optimal angle for the trailing edge exists, as proposed earlier by Cleaver et al. (2014), but whether the angle is achieved by active pitch control or passive flexibility is of less importance.

Figure 5 shows the instantaneous streamwise and lateral force profiles of these two conditions: foil 'R' at θ_0 = 15° and St = 0.35, and foils 'A' and 'B' at θ_0 = -10° and St = 0.35. Here, the heave position has

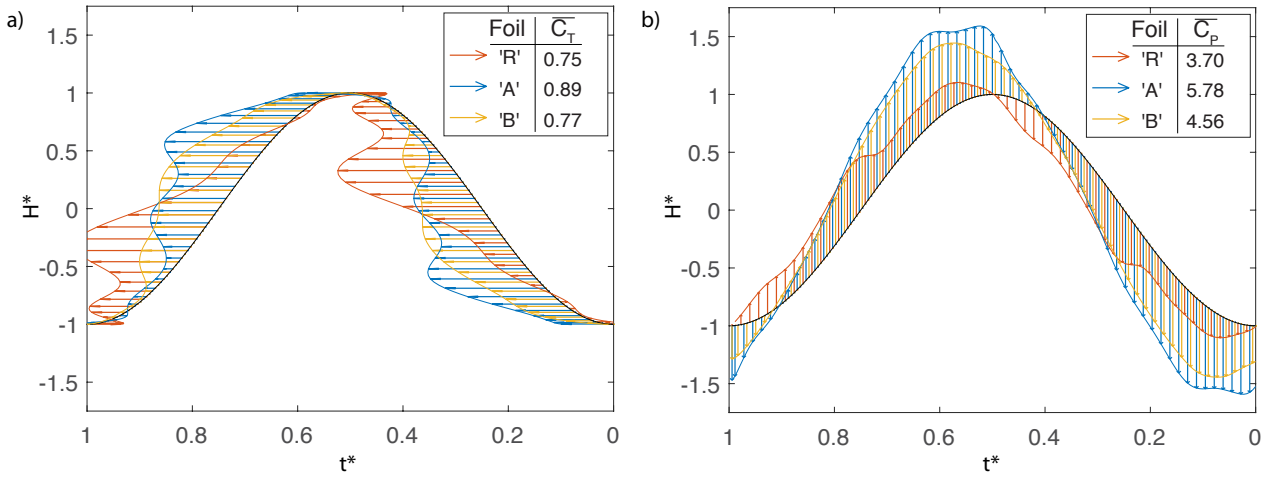

Figure 5. Instantaneous force components as functions of time for the cases of θ_0=15° and St = 0.35 (foil 'R'), and θ_0=-10° and St = 0.76 (foils 'A' and 'B'). (a) Streamwise force components. (b) Lateral force components.

been non-dimensionalized as $H^* = H/H_0$. Instantaneous force measurements, averaged over 20 oscillation cycles, were decomposed into streamwise and lateral directions, as shown in Fig. 5. Forces vectors are shown positioned along the sinusoidal motion path of the foil as observed from a frame of reference fixed to the freestream flow. The streamwise direction represents force acting in the direction of locomotion, while the lateral direction corresponds to forces that aid or oppose the heave motion. It is noted that the time axis progresses from right to left, following the convention of the kinematic diagram in Fig. 2. Despite having similar cycle-averaged thrust values, the actual force generation process for the rigid and the flexible foils was very different. Both flexible foils generated large forces early in the heave motion, while the rigid foil developed higher forces towards the end of the cycle.

3.2. Quantitative flow patterns

The PIV technique was applied to acquire quantitative flow images around the foils in order to provide insight into the mechanisms of generation of the unsteady forces discussed in Section 3.1. Fig. 6 provides phase-averaged contours of the out-of-plane vorticity for foils 'R' and 'B' under the conditions of θ_0 = 0° and St = 0.35. The development of the vortical flow structures is shown at sequential phases t^* = 0/8, 1/8, 2/8, and 3/8, representing the evolution of the first half of the symmetrical wake structure. The symmetrical motion of the foil allows information of the second half of the motion cycle to be inferred from the first half. For example, phase t^* = 4/8 is simply an inverted image of phase t* = 0/8, and therefore it is not shown herein. Hereafter, the terms upper surface and lower surface are used to refer to the upper and the lower sides of the foil in the frame of reference provided in Fig. 6. For the phases shown, the upper surface acts as the pressure side of the foil, and the lower surface acts as the suction side, but this relationship is opposite for the second half of the foil oscillation cycle.

At phase t^* = 0 in 5a, corresponding to the bottom of the heave cycle of the rigid foil, the flow was attached to the lower surface of the foil, except near the leading edge, where a weak leading edge vortex (LEV) persisted from the previous oscillation cycle. As the heave motion continued, the boundary layer on the lower side began to roll up into a new LEV, but the vortex did not convect downstream significantly before the foil reversed the heave direction. The LEV further dissipated before it could directly influence the trailing edge vortex (TEV) development. On the upper surface of the foil at phase t^* = 0, the negative vorticity had begun shedding from the trailing edge. The shear layer characterized by the negative vorticity continued to shed from the trailing edge during the first half of the oscillation cycle, and it progressively rolled up into a large-scale TEV that became the dominant flow structure in the wake.

The flow dynamics around the leading edge for foil 'B', shown in Fig. 6b, were very similar to that of the rigid foil 'R', in terms of the LEV's timing, peak vorticity level, and size. This similarity was a consequence of the pitching axis being positioned close to the leading edge, such that the leading edge was too short to deform considerably, thereby maintaining a near 0° angle with respect to the freestream throughout the cycle for both the rigid and the flexible foils.

The flexibility of the foil showed a larger influence on the vortex dynamics in the vicinity of the trailing edge. The onset of the shedding of the negative vorticity from the upper surface of the foil was

not observed until the phase $t^* = 1/8$ on foil 'B'. Additionally, the wake generated by the flexible foil

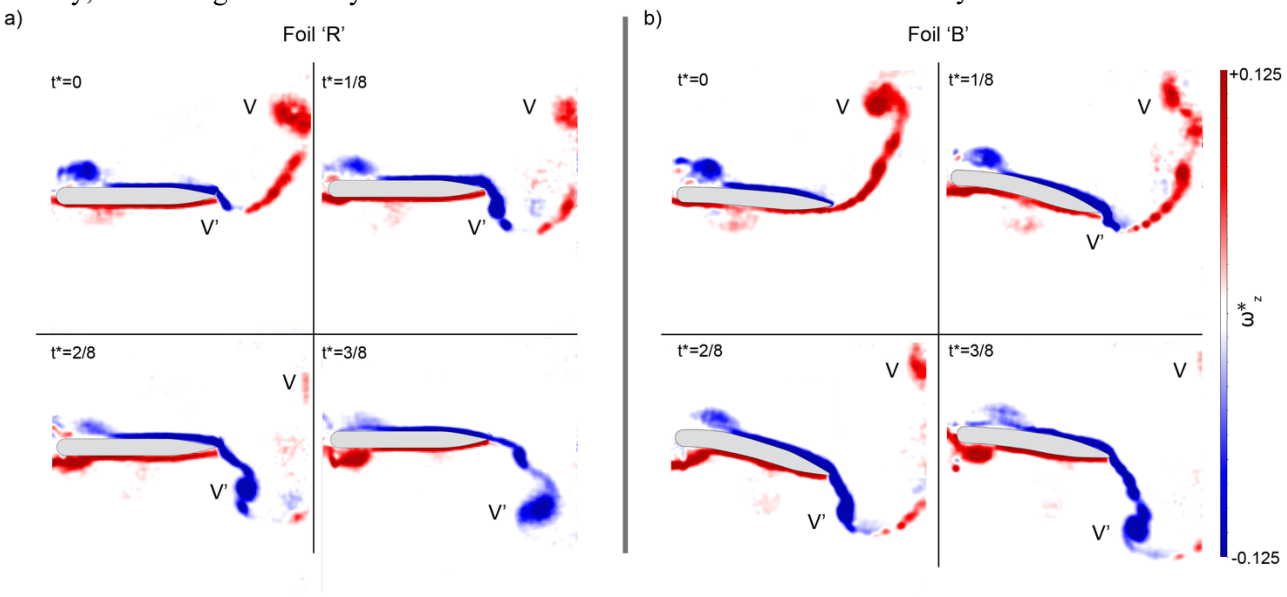

Figure 6. Patterns of phase-averaged out-of-plane vorticity for the case of $\theta_0 = 0°$ and St = 0.35.

was considerably wider than that of the rigid foil, which was attributed to the larger area swept by the trailing edge of the flexible foil. The effect of the pitching motion on the flow dynamics is illustrated in Fig. 7, which provides contours of the out-of-plane vorticity for foils 'R' and 'B' for the cases of θ_0= -10°, 5°, and 15°.

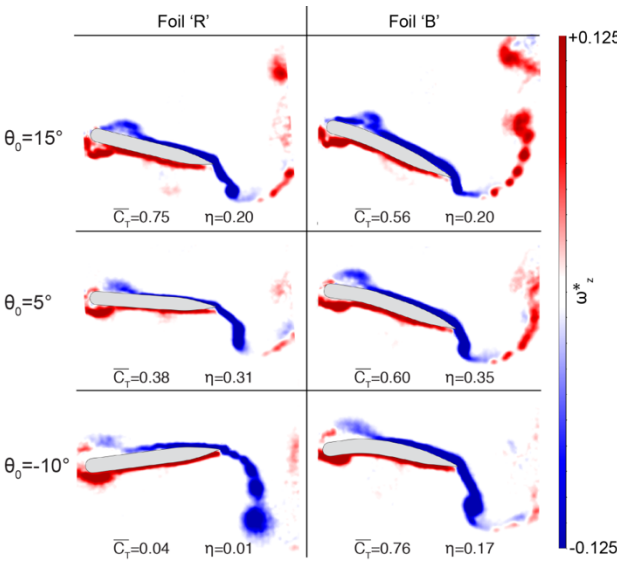

Figure 7. Patterns of phase-averaged out-of-plane vorticity for the case of St = 0.35 and phase t = 0.25 for foils 'R' (left column) and 'B' (right column) at various maximum pitch angles.*

All images correspond to the same phase $t^* = 2/8$, and constant Strouhal number $St = 0.35$. Neither the pitch angle nor the trailing edge flexibility had significant influence on the dynamics of the LEV. The LEVs had relatively low peak vorticity levels and spatial extent in all considered cases. In contrast, the maximum pitch angle had a more pronounced effect on the separated flow structure in the vicinity of the trailing edge of the foil. In general, increasing the pitch angle had an effect of delaying the development of the TEV. This effect can be observed by comparing the cases of $\theta_0 = 15°$ with the cases of $\theta_0 = -10°$, the latter resulting in a more developed large-scale vortex in the wake at the same phase in the cycle.

The cases of foil 'R' at $\theta_0 = 15°$, and foil 'B' at $\theta_0 = -10°$, had similar cycle-averaged thrust values despite the different pitch angles, as previously noted. The PIV images of Fig. 7 show that the flexible foil deformed significantly; at mid-stroke developing a +15° angle with respect to the freestream. This observation suggests that the effective angle of the trailing edge with respect to the freestream is a key parameter in thrust production. It should be noted that continually increasing the flexibility of the foil does not lead to a sustained increase in propulsive performance. For foil 'B', the conditions $\theta_0 = 5°$ and $\theta_0 = 15°$ both lead to reductions in thrust. The prescribed pitch and flexibility of these conditions caused the trailing edge to deform beyond the optimal value of the effective angle of attack. Considering the previous observations that power input for all foils at all Strouhal numbers was minimum between $\theta_0 = 2.5°$ and $\theta_0 = 7.5°$, it is proposed that there exists an optimal stiffness level that would result in maximum thrust also occurring in this interval. In this scenario, the trailing edge would deform to ~15° when prescribed a pitch angle of ~5°. Such a foil

would have minimum power input, maximum thrust generation and, therefore, peak efficiency.

The angle of the trailing edge leading to highest thrust generation is a function of Strouhal number, a relation that should not be overlooked. The oscillation frequency is directly linked to the heave velocity of the foil, thus affecting its effective angle of attack. The heave velocity also influences the loading exerted on the foil, in turn affecting the propulsive performance. The influence of the Strouhal number is illustrated in Fig. 7, which shows distributions of the out-of-plane vorticity at the phase $t^* = 2/8$ for the rigid foil 'R' and the flexible foil 'B', both of which

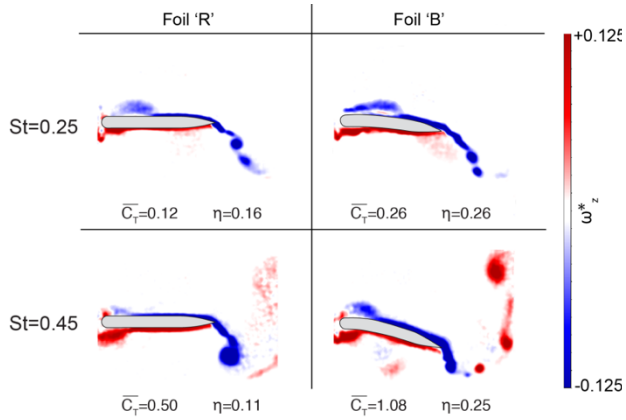

Figure 8. Patterns of phase-averaged out-of-plane vorticity for the case of foils 'R' and 'B' at different Strouhal numbers at phase $t^* = 0.25$, and $\boldsymbol{\theta_0} = 0°$.

were undergoing heave-only motion. The flexible foil 'B' deformed to greater extent at higher Strouhal numbers, leading to the increased thrust and efficiency at both considered Strouhal numbers. The cycle-averaged thrust coefficient generated by the flexible foil was approximately twice as high as the corresponding thrust coefficient of the rigid foil for both $St = 0.25$ and $St = 0.45$. However, as the Strouhal number increased, the ratio of efficiencies of the flexible foil over that of the rigid foil increased from 1.6 at $St = 0.25$ to 2.3 at $St = 0.45$. The vorticity plots of Fig. 8 show that this increase in efficiency is linked to the delayed development of the TEV in the case of the flexible foil 'B' at the higher Strouhal number.

3.3. Relation of instantaneous forces to shed vorticity

The space-time evolution of the phase-averaged vorticity that is described in Section 3.2 was related to the measured instantaneous forces on the foils introduced in Section 3.1 by employing a concept introduced by Wu (1981) and Lighthill (1986). In summary, the vector force acting on the foil can be calculated according to:

$$\boldsymbol{F} = -\frac{d}{dt}[\rho \int \boldsymbol{r} \times \boldsymbol{\omega} dV], \qquad (1)$$

where $\int \boldsymbol{r} \times \boldsymbol{\omega} dV$ is the integral of the moment of vorticity with respect to the center of mass of the foil. The integral is taken over the entire flow domain, and only shed vorticity is considered in the calculation, so that the added mass and Froude-Krylov effects are not included. This approach has been verified by discrete vortex simulations of Unal (1996) and applied to the case of an oscillating circular cylinder by Oshkai and Rockwell (1999). Assuming quasi-two-dimensional flow, the contributions of the shed vorticity to the flow-induced forces were found by calculating the normalized integrals of the moments of vorticity that acted in the streamwise (x-) and the lateral (y-) directions, as

$$(M_\omega)_x = -[1/(U^2 c)] \int y \omega_z dA$$

and

$$(M_\omega)_y = -[1/(U^2 c)] \int x \omega_z dA,$$

respectively. Therefore, the calculated moments $(M_\omega)_x$ and $(M_\omega)_y$ contributed to the thrust and power coefficients, C_T and C_p, respectively.

For the cases of foil 'R' and foil 'B' oscillating in a heave-only regime at $St = 0.35$ that were shown in Fig. 6, the calculated moments $(M_\omega)_x$ and $(M_\omega)_y$ are provided in Figs. 9 and 10. Here, area of integration A corresponds to the region downstream of the trailing edge of the foil in the PIV images of Fig. 6. Since the shed vortices were convected outside of the field of view of the PIV camera, evaluation of the total flow-induced force on the plate was not possible on the basis of the available vorticity data. Moreover, the sequence of the phase-averaged PIV images did not have sufficient temporal resolution for evaluation of the time derivatives of the moments of vorticity. Therefore, calculated moments cannot be directly compared to the measured C_T and C_p data shown in Fig. 4. Instead, the calculated moments $(M_\omega)_x$ and $(M_\omega)_y$ represent the contributions of the shed out-of-plane vorticity that is shown in the plots of Fig. 6 to the time integrals of the streamwise and the lateral force components.

Figure 9(a) shows contributions of the shed positive (empty square symbols) and the negative (filled square symbols) out-of-plane vorticity to the streamwise force component on the rigid plate 'R' at four phases during the first half of the oscillation cycle. During the first quarter of the oscillation period, the large-scale positive (counter-clockwise) vortex V shown in the upper-right of the field of view in Fig. 6(a) made a dominant contribution to the streamwise force. The negative (clockwise) vortex V' was located in the vicinity of the trailing edge of the plate and therefore did not contribute significantly to the calculated moment $(\boldsymbol{M_\omega})_x$ due to the small value of

the y-position of the vortex. At the phases $t^* = 2/8$ and $t^* = 3/8$, the circulation of negative vortex V' increased, while the positive vortex was convected away from the plate. This development increased the contribution of the negative vorticity to the streamwise loading on the plate due to the increase in both the magnitude of the out-of-plane vorticity and the corresponding y- position of the vortex V' with respect to the plate. At the same time, the positive vortex V was moving outside of the data acquisition area, and its contribution to the flow-induced loading was not completely accounted for. As a result, the total calculated moment $(\boldsymbol{M_\omega})_x$ shown in Fig. 10(a) by circular symbols closely followed the contribution of the negative vorticity at the phases $t^* = 2/8$ and $t^* = 3/8$.

A similar trend is observed in the case of flexible foil 'B' shown in Fig. 9(b). Here, the contribution of the positive vorticity represented primarily by the large-scale vortex V (shown in Fig. 6(b)) accounted for the majority of the flow-induced loading on the plate at phases $t^* = 0$ and $t^* = 1/8$. As the vortex V was convected outside of the field of view of the PIV camera and the negative vortex V' developed during the phases $t^* = 2/8$ and $t^* = 3/8$, the calculated streamwise force on the plate was dominated by the contribution of the negative vorticity. While the qualitative trends of the calculated moments $(\boldsymbol{M_\omega})_x$ were similar in the cases of the rigid foil 'R' and the flexible foil 'B', the increased lateral deflection of the trailing edge in the case of the foil 'B' (shown in Fig. 6) resulted in the larger lateral excursions of the large-scale vortices V and V' with respect to the plate. In turn, the increased y-distance of the shed vortices from the plate resulted in higher magnitude of the generated streamwise loading on the plate. This increase of the calculated loading in the case of the flexible foil is particularly evident at the phases $t^* = 0$ and $t^* = 3/8$ in Fig. 8.

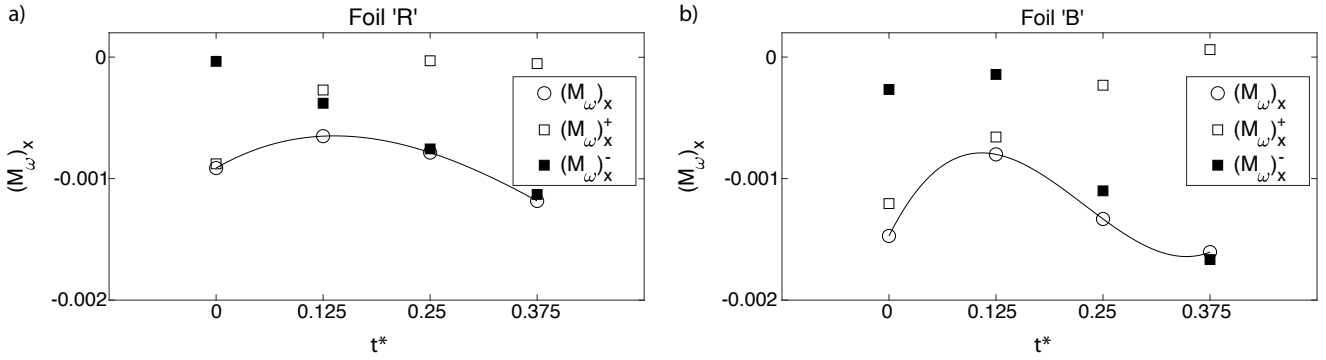

Figure 9. Calculated moments of vorticity $(\boldsymbol{M_\omega})_x$ corresponding to foils 'R' (a) and 'B' (b) for the case of $\boldsymbol{\theta_0 = 0°}$ and St = 0.35.

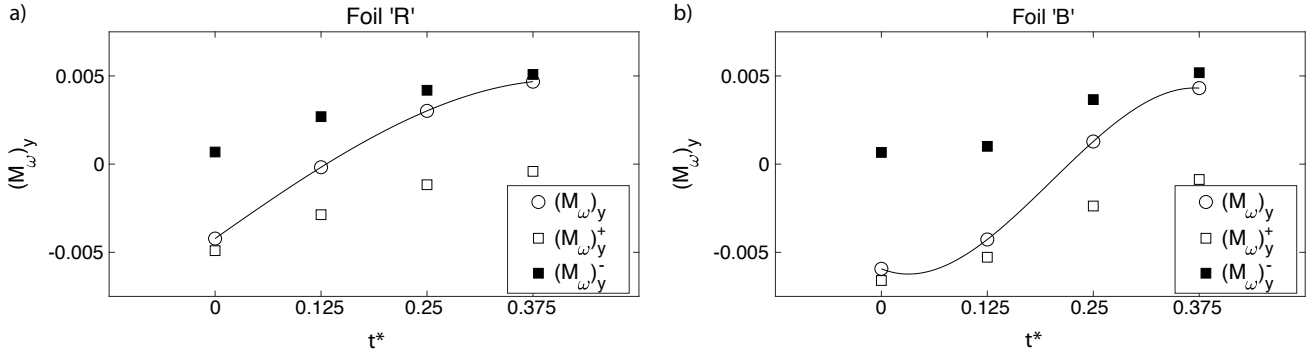

Figure 10. Calculated moments of vorticity $(\boldsymbol{M_\omega})_y$ corresponding to foils 'R' (a) and 'B' (b) for the case of $\boldsymbol{\theta_0 = 0°}$ and St = 0.35.

The contributions of the shed positive and the negative out-of-plane vorticity to the lateral (y-direction) component of the flow-induced force on the plates at four phases during the first half of the oscillation cycle are represented in Fig. 10 as empty and filled square symbols, respectively. The total calculated moment $(\boldsymbol{M_\omega})_y$ is shown by the circular symbols. In the case of the rigid foil 'R', shown in Fig. 10(a), the large-scale positive vortex V located in the upper-right of the field of view in Fig. 6(a) made a dominant

contribution to the lateral force at the phase $t^* = 0$. At the phase $t^* = 1/8$, the vortex V moved partially outside of the field of view of the PIV camera, and its contribution to the calculated moment $(\boldsymbol{M_\omega})_y$ decreased. At the same time, the negative vortex V' was being shed from the trailing edge of the plate and convected downstream. Therefore, the contribution of the negative vorticity $(\boldsymbol{M_\omega})_y^-$ to the flow-induced lateral force increased at the phase $t^* = 1/8$ due to the increase of the magnitude of the shed vorticity and its x-position with respect to the plate. At the phases $t^* = 2/8$ and $t^* = 3/8$, the positive vortex V moved outside of the field of view, as shown in Fig. 6(a). Thus, the total calculated moment $(\boldsymbol{M_\omega})_y$ was almost entirely due to the contribution of the negative shed vorticity, which was predominately represented by the vortex V'.

In the case of the flexible foil 'B', the calculated moment $(\boldsymbol{M_\omega})_y$, shown in Fig. 10(b), exhibited a similar trend. However, the increased deflection of the trailing edge delayed the convection of the positive vortex V in the x-direction. As a result, the vortex remained in the field of view of the PIV camera during the phases $t^* = 0$ and $t^* = 1/8$ (Fig. 6(b)), and the total calculated moment $(\boldsymbol{M_\omega})_y$ was primarily due to the contribution of the positive shed vorticity $(\boldsymbol{M_\omega})_y^+$. At the phases $t^* = 2/8$ and $t^* = 3/8$, the positive vortex V moved outside of the field of view, and the relative contribution of the negative vortex V' increased.

4. CONCLUSIONS

An experimental campaign was conducted to study the effects of chordwise flexibility and pitching kinematics on the performance of oscillating-foils acting as propulsion devices. Two flexible foils, with different moments of inertia and stiffness, were compared alongside a reference foil that was fully rigid. The prescribed pitch angles varied from -10° to 20°, and the Strouhal numbers varied from 0.15 to 0.45. Within the considered range of small heaving amplitudes and relatively small pitching amplitudes, the flexible foils produced higher thrust values than their rigid counterpart, as well as higher propulsive efficiencies.

Inertial forces were the dominant mechanism producing foil deformation at the beginning and at the end of a heave cycle, where heave acceleration was highest. This phase also corresponded to a point in the oscillation cycle that deformation due to pressure forces was low. These inertial forces promoted beneficial curvature early in the cycle, which would otherwise be small. At the midstroke of the heaving motion, pressure forces were responsible for the majority of deformation.

Trailing edge flow dynamics were observed to have a strong influence on performance. Specifically, an appropriate level of pitch applied to the trailing edge resulted in high thrust generation. This result was independent of the mechanism producing the pitch, i.e. whether the pitch angle was actively prescribed to the rigid foil or developed passively via deformation of the flexible foil. The necessity of the trailing edge pitch for high thrust generation led to relatively poor propulsive performance of the rigid foil operating in heave-only motions. Under the same operating conditions, the flexible foils produced thrust values that were more than double the thrust values generated by the rigid foil. The observed combinations of thrust and efficiency, in conjunction with the trailing edge dynamics, suggest a possibility of predicting an optimal level of foil stiffness to optimize its propulsive performance. Such optimal stiffness would result in an optimal amount of deflection of the trailing edge from its equilibrium value at low prescribed pitch angles, where power input to the system is minimal.

5. REFERENCES

Bandyopadhyay, P.R., 2009. Swimming and flying in nature—The route toward applications: The freeman scholar lecture. *Journal of Fluids Engineering* 131, 031801.

Cleaver, D., Gursul, I., Calderon, D., Wang, Z., 2014. Thrust enhancement due to flexible trailing-edge of plunging foils. *Journal of Fluids and Structures* 51, 401-412.

Dai, H., Luo, H., de Sousa, P.J.F., Doyle, J.F., 2012. Thrust performance of a flexible low-aspect-ratio pitching plate. *Physics of Fluids* 24, 101903.

Egan, B.C., Brownell, C.J., Murray, M.M., 2016. Experimental assessment of performance characteristics for pitching flexible propulsors. *Journal of Fluids and Structures* 67, 22-33.

Hover, F., Haugsdal, Ø., Triantafyllou, M., 2004. Effect of angle of attack profiles in flapping foil propulsion. *Journal of Fluids and Structures* 19, 37-47.

Katz, J., Weihs, D., 1978. Hydrodynamic propulsion by large amplitude oscillation of an airfoil with chordwise flexibility. *Journal of Fluid Mechanics* 88, 485-497.

Lighthill, J., 1986. Fundamentals Concerning Wave Loading On Offshore Structures. *Journal of Fluid Mechanics* 173, 667-681.

Miao, J.-M., Ho, M.-H., 2006. Effect of flexure on aerodynamic propulsive efficiency of flapping flexible airfoil. *Journal of Fluids and Structures* 22, 401-419.

Olivier, M., Dumas, G., 2016. A parametric investigation of the propulsion of 2D chordwise-flexible flapping wings at low Reynolds number using numerical simulations. *Journal of Fluids and Structures* 63, 210-237.

Oshkai, P., Rockwell, D., 1999. Free Surface Wave Interaction with a Horizontal Cylinder. *Journal of Fluids and Structures* 13, 935-954.

Platzer, M.F., Jones, K.D., Young, J., S. Lai, J., 2008. Flapping wing aerodynamics: progress and challenges. *AIAA journal* 46, 2136-2149.

Prempraneerach, P., Hover, F., Triantafyllou, M.S., 2003. The effect of chordwise flexibility on the thrust and efficiency of a flapping foil, Proc. 13th Int. Symp. on Unmanned Untethered Submersible Technology: special session on bioengineering research related to autonomous underwater vehicles, New Hampshire, pp. 152-170.

Raffel, M., Willert, C.E., Kompenhans, J., 2007. *Particle image velocimetry: a practical guide*. Springer Science & Business Media.

Richards, A.J., Oshkai, P., 2015. Effect of the stiffness, inertia and oscillation kinematics on the thrust generation and efficiency of an oscillating-foil propulsion system. *Journal of Fluids and Structures* 57, 357-374.

Shyy, W., Aono, H., Chimakurthi, S.K., Trizila, P., Kang, C.-K., Cesnik, C.E., Liu, H., 2010. Recent progress in flapping wing aerodynamics and aeroelasticity. *Progress in Aerospace Sciences* 46, 284-327.

Triantafyllou, G.S., Triantafyllou, M., Grosenbaugh, M., 1993. Optimal thrust development in oscillating foils with application to fish propulsion. *Journal of Fluids and Structures* 7, 205-224.

Unal, M.F., 1996. *Force calculation by control volume and vortex methods.*, Lecture Series, Department of Mechanical Engineering and Mechanics, Lehigh University, Bethlehem, PA, USA.

Wu, J.C., 1981. Theory For Aerodynamic Force And Moment In Viscous Flows. *Aiaa J.* 19, 432-441.

Yin, B., Luo, H., 2010. Effect of wing inertia on hovering performance of flexible flapping wings. *Physics of Fluids* 22, 111902.

Young, J., Lai, J.C.S., Platzer, M.F., 2014. A review of progress and challenges in flapping foil power generation. *Progress in Aerospace Sciences* 67, 2-28.

Zhu, Q., 2007. Numerical simulation of a flapping foil with chordwise or spanwise flexibility. *AIAA journal* 45, 2448-2457.

THE EFFECTS OF A PASSIVE TAIL ON ESCAPE PERFORMANCE IN A ROBOTIC FAST-START FISH CAPABLE OF RAPID UNDERWATER LOCOMOTION

Todd Currier
University of Massachusetts, Amherst MA 01003, USA
Yahya Modarres-Sadeghi
University of Massachusetts, Amherst MA 01003, USA

ABSTRACT

We have used a robotic fish that we have designed and built to emulate the fast-start maneuver of live fishes to study the influence of tails with different flexibilities on the fast-start performance. Our robotic fish generates acceleration and velocity magnitudes comparable to those of the live fishes within the same time scale by using a snap-through bucking of its spine. In its transient fast-start maneuver, our robotic fish produces mode shapes very similar to those observed in live fishes, by going through a snap-through bifurcation. In a series of experiments, we changed the stiffness of the robotic fish's tail and measured its velocity during its fast start. These experiments showed that while a softer tail is more desirable initially in the maneuver to get to a C-shape quicker, a stiffer tail in the propulsive stage of the fast-start can increase the maximum obtained velocity.[1]

1. INTRODUCTION

There are many studies to observe the fast-start in live fishes (Ahlborn et al., 1991, Harper and Blake, 1991, Domenici and Blake 1991, Wakeling 2001, Hale 2002, Blake2004, among others). However, studies toward understanding the underlying control mechanisms of the fast start are limited due to the large number of parameters that are involved in the fast start and also the low degree of controllability of the live fish's motion. In addition to the difficulties in performing targeted studies on the live system, mechanical models which operate at the same time scale and generate velocities and accelerations on the same order of magnitude as the biological system are equally as challenging to produce. Many researchers have used robotic fish to study mechanisms of straight swimming (Videler, 1993, Triantafyllou et al., 2000, Fish and Lauder, 2006, Bandyopadhyay 2002). Additionally, the mechanisms of fish-like swimming have been studied extensively using flapping foils and fins (Long et al., 2006, Park et al. 2012, Feilich and Lauder, 2015, Clark et al. 2015, Currier and Modarres-Sadeghi, 2019). These foils are typically assumed to model only the tail as most of the power transfer from the fish to the fluid is found to occur at the tail (Frith and Lauder, 1995). However, in fast-start maneuvers, this is only true for Stage 2, where the body is unbent from a C-shape to straight and during which it is found that "up to 70% of the instantaneous hydrodynamic force was generated by the tail" (Borazjani, 2013), while in Stage 1 (where the fish bends its body from straight to a C-shape) most of the hydrodynamic force is produced by the body. This requires the models emulating the fast-start to include all or at least some portion of the body. Here we study these high-acceleration starts using a robotic fish.

2. THE ROBOTIC FISH

The overall design of the robotic fish was based on that of the Northern Pike, *Esox lucius*. This selection was made given that the largest recorded acceleration of approximately $25g$ produced during a C-start was observed in this species (Harper and Blake, 1990). The design is split into three segments: the tail, the body and the head. The fish is made predominately out of 3D-printed plastic components. The plastic components reduce weight and improve acceleration performance. The entire assembly is designed to be neutrally buoyant with a buoyancy chamber sized in the head of the robot. The robotic fish was placed in the water tank of a custom-fabricated experimental setup. The main power source is compressed CO_2 gas that is used to actuate two pistons which are attached to cables that run along the length of the body on either side. The cables are attached to a plastic segment on the tail and are guided along the body through each of the ribs. A complete description of

[1] A complete version of this work is published as Currier, T., Lheron, S., Modarres-Sadeghi, Y. (2020). A bio-inspired robotic fish utilizes the snap-through buckling of its spine to generate accelerations of more than 20g. Bioinspiration and Biomimetics. 15, 055006

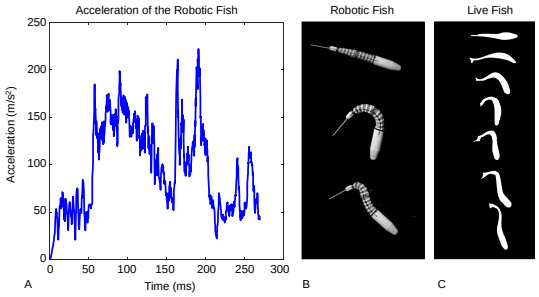

Figure 1. (A) A sample time history of the acceleration measurements of the robotic fish together with (B) the robot fish's kinematics compared with (C) that of a live fish. Part (C) is reproduced from Harper and Blake (1990).

the design can be find in Currier et al. (2020).

3. SAMPLE ACCELERATIONS OF THE FAST ROBOTIC FISH

An acceleration time history for a typical fast-start response of the robotic fish is shown in Figure 1(A). The example shown occurs over 250 ms. The typical time scale for live specimens has been found to vary proportional to the fish length, with smaller fish (L=5 cm) cycling a complete fast-start maneuver in an average time of 55 ms and larger fish (L=22 cm) requiring more time of around 120 ms (Webb, 1978). The length scale of the robotic fish is 35 cm and its time is driven by the open loop control signal used to specify the time of each stage. In the example case, Stage 1 had a total time of 100 ms, followed by a 50 ms delay after which Stage 2 was started for a total time of 100 ms. The largest value of acceleration observed occurs during Stage 2 of the maneuver with a peak value of 222 m/s^2 (Figure 1). In this example, equal pressure magnitudes were supplied in both stages. The observed modes in the robotic fish are shown through a series of three snapshots as the maneuver is developed (Figure 1B). During Stage 1, an eccentric compressive load is applied to the end of the spine causing the structure to buckle and undergo a large deformation which has a magnitude limited by the stroke of the piston. The resulting shape is the initial contortion seen also in the live fishes, called the "C-shape". From this "C-shape" after a 50 ms delay, Stage 2 is started, which rapidly changes the location of the applied eccentric load to the opposite side of the spine. The net result is to generate a combined state of compressive load and moment applied at the end of the spine. The relatively large added mass at the tail produces a net moment on the free floating structure which results in the head changing its direction of rotation. The added mass of the fluid along the length of the body and at the tail provides an inertial resistance to rotation, which ultimately drives a backwards traveling wave initiating from the head of the robot, consistent with that observed in live fishes (Wakeling, 2001). It is important to note that the curvature and the propagation of the waveform along the body of the robot is driven entirely by the passive interaction of the fluid with the compliant steel spine. For the purpose of comparison, snapshots of the body shapes of a live fish are shown in Figure 1. The snapshots are of a Rainbow trout captured by Harper and Blake (1990). The selected sample showed the greatest similarity to the mode shapes observed in the robotic fish. The length scale of the robot (0.35 m) is comparable to that of the length of live fish (0.37 m). The largest acceleration observed in the live fish was 80 m/s^2 requiring a 120 ms to complete the maneuver. The body shapes of the robotic fish and the live fish at the end of Stage 1 (the middle snapshot for the robotic fish and the fourth snapshot for the live fish) and at the end of the maneuver (the lower snapshots) are very similar. For both the robotic fish and the live fish, the body shape at the end of Stage 1 resembles the first mode shape of a cantilever beam, and at the of the maneuver, the second mode shape of a cantilever beam. We have shown before (Currier et al., 2020) that the transition from the first mode to the second mode during the fast-start of the robotic fish is due to the behavior of the structure (the fish's spine) around the unstable equilibrium of a snap-through bifurcation.

4. THE TAIL: FLEXIBLE OR NOT

The tail is believed to have a significant influence on the fast-start efficiency. Several studies exist in which a foil is used to represent the tail and its motion, investigating the influence of flexibility, among other parameters, on the optimal thrust in flapping foils that represent the tail (e.g. Ahlborn (1991) and Witt (2016)). The flapping foil experiments normally (i) are not conducted at similar speeds and same time scale as the live fish's fast start, and (ii) do not include the influence of the body on the tail's performance. With our robotic fish, we can reproduce motions at the base of the tail that are comparable to the live fish. We have used our robotic fish to study how the tail flexibility influences the fast-start performance. The body and the tail in this robot are passive elements comprised of continuous media. The implication here is that the infinite degrees of freedom associated with the continuous nature of the spine and tail are not directly controlled by the two sources of actuation, making this design under-actuated. With our

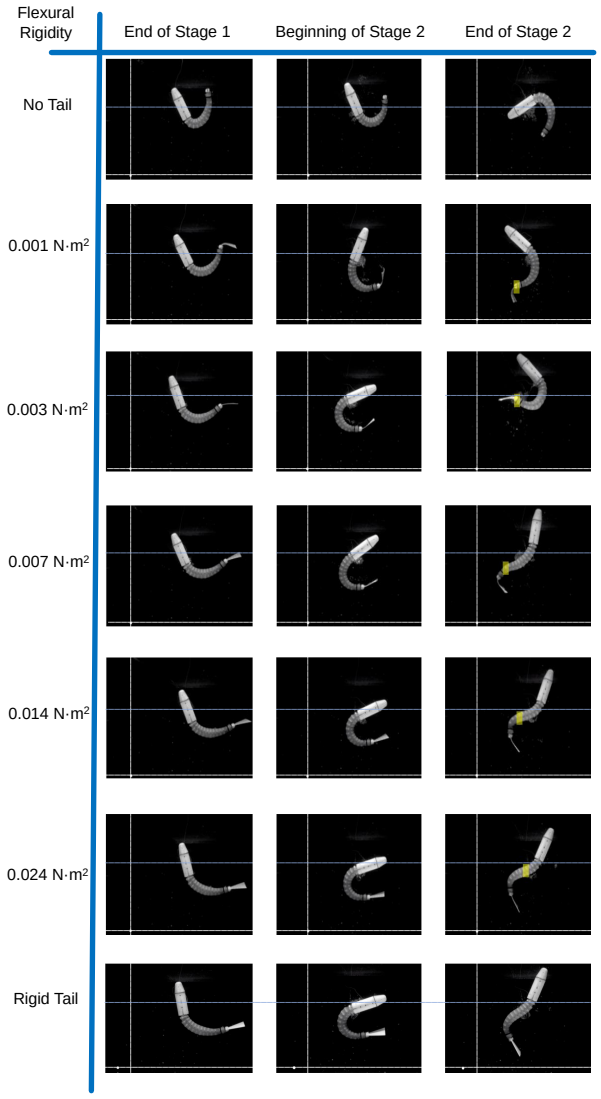

Figure 2. The effects of tail flexibility are studied by considering seven different cases: fish with no tail (row 1), fish with five different flexible tails where the tail flexural rigidity increases from row 2 to row 6, and a rigid tail (row 7). The left column corresponds to the end of the period that the fish is forced to bend to a C-shape, the middle column corresponds to the end of the pause period, and the right column corresponds to the end of the maneuver. All cases are with constant external pressurization.

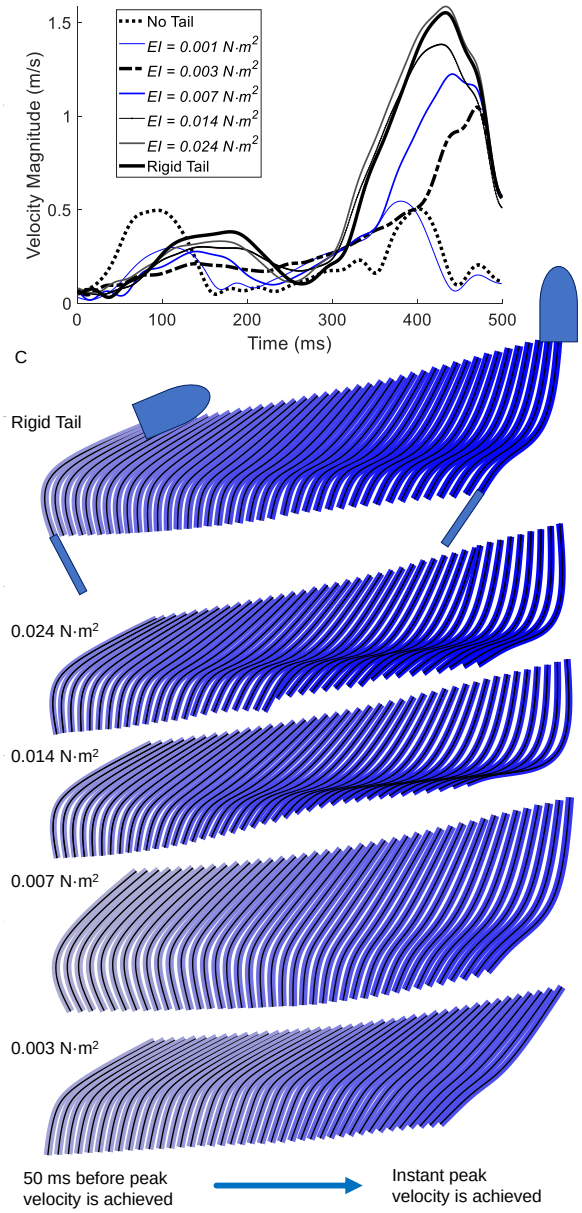

Figure 3. The velocity of the center of mass versus time for all cases, and time traces of the robotic fish for the five stiffest tails, for which a node was observed on the body. The time traces start 50 ms before the peak escape velocity is achieved and are shown for every 1.25 ms. The head and tail are shown on the first and the last time traces of the case with a rigid tail.

robotic fish, we can reproduce motions at the base of the tail that are comparable to those of the live fish, and therefore we can use our fish to investigate how the tail flexibility influences the fast-start maneuver. We used several tails, identical in geometry but different in thickness (and therefore flexural rigidity) and studied the fast-start of the fish under exactly the same input conditions and applied pressures. For comparison, two extremes were also considered: no tail and a completely rigid tail (no measurable deformation under fluid forces).

Figures 2 and 3 show the effects of tail flexibility by considering seven different cases: fish with no tail (row 1), fish with five different flexible tails where the tail flexural rigidity increases from row 2 to row 6, and a rigid tail (row 7). The first column corresponds to the end of Stage 1, the second column corresponds to the end of the pause period, and the beginning of Stage 2, and the third column to the end of Stage 2. All cases are with constant external pressurization. The first column shows that as the tail becomes less flexible, the body curvature at the end of Stage 1 gets smaller. Then the second column shows that with some minimal stiffness, and given enough pause time, the body curvature can reach the same value at the beginning of Stage 2. The third column shows that for very flexible tails, the structural modes that are observed are very different from the less flexible tails. The least flexible tails act almost identical to the rigid tail. The mode shape that is observed in the top three rows of the first column for the end of Stage 1 and those observed in the bottom three rows of the third column for the end of Stage 2 resemble those observed in a complete fast-start maneuver of a live fish, suggesting that the fishes may change their tail stiffness from a more flexible one during Stage 1 to a more rigid one during Stage 2. In the column associated with the end of Stage 1, it can be observed that the initial contortion into the "C-shape" is impeded by the added stiffness of the tail. As the tail stiffness increases it requires larger forces to produce the same amount of deflection in the model at any given instant during the maneuver. This can be observed in the reduction of curvature in the body of the robotic fish for increasing tail stiffness. This apparent lag in deformation is due to the added fluid inertia at the tail interface for stiffer tails. The second column – the end of pause period – shows that even though stiffer tails slow the contortion of the body, the continued application of the external constant force and the momentum of the fluid allow the robotic fish to reach approximately the same shape at the end of the pause period, from which the second stage is initiated. The evolution of the combined mode shape of the tail and body for increasing stiffness can be seen clearly during Stage 2 as well (the third column). The more flexible tails are unable to react to the fluid forces produced during Stage 2 and are simply displaced out of the way as opposed to producing any significant thrust. This effect can also be observed in the resulting center of mass velocity magnitudes reported in Figure 3.

Figure 3 shows that the velocity of the center of mass converges to the same curve as the tail stiffness is increased. The peak magnitude of velocity produced during Stage 2 is dramatically increased when the tail is stiffer. The rigid tail results in the maximum escape velocity in Stage 2. The average rate of acceleration for the fixed magnitude of external force appears to be unaffected by the tail stiffness, which can be observed in the slopes of the velocities all converging to the same value. However, in the more rigid tail cases the velocity continues to grow to higher peak values.

Time traces of the robotic fish for the five stiffest tails are shown in Figure 3 as well for which a node was observed on the body, show how the node is driven closer to the center of the fish and the slope at the node increases as the tail stiffness is increased. The time traces start 50 ms before the peak escape velocity is achieved and are shown for every 1.25 ms. The head and tail are shown on the first and the last time traces of the case with a rigid tail.

The primary effect on the stability of the spine of the fish due to increasing the tail stiffness is to change the location of the inflection point observed in the spine (highlighted in yellow in Figure 2 during Stage 2. This is also shown in the time traces of the robotic fish's body for the cases where a node was observed in Figure 3. By increasing the stiffness, the inflection point moves from a location close to the tail to a location closer to the center of the fish, enabling the spine to go through the mainly-second beam mode as it experiences a snap-through buckling. This change in the location of the node is achieved through practically changing the beam's (spine's) boundary condition as the stiffness of the tail changes. This is similar to the influence of increased external pressure on the motion, where the node was moved more toward the center of the beam, making it possible for the spine to go through a snap-through bifurcation.

5. CONCLUSION

Our robotic fish can emulate the fast-start maneuver of live fishes at translational and rotational velocities and accelerations comparable to the fastest known live fishes. This ability makes it possible to study the mechanisms that the fast-start fish specialists use in their maneuvers. Since this robotic fish is under-

actuated, the observed kinematics rely on passive motion of the body and the tail. The robotic fish makes the fast-start possible by making its spine go through a snap-through buckling instability, the dynamics of which are governed by the passive response of the spine. To make a snap-through buckling possible, the robotic fish can either utilize larger forces applied at a point eccentric to the spine (and thus increase the applied torque at its head) or change the boundary conditions of the spine by changing the stiffness of its tail. In both cases, the node that is observed on the body moves closer to the center of the fish, creating a shape closer to that of the second mode of a cantilever beam.

We have shown that if the external pressurization or the boundary conditions are such that a snap-through buckling is observed, the response of the fish closely emulates that of the live fish both in the measured accelerations and observed modes. Observing the mode shapes of the combined body and tail of the fast-starting robotic fish with varying tail stuffiness (from no tail to flexible tails to a rigid tail) suggests that the fish is likely modulating the stiffness of the tail during the maneuver. We have observed that the body kinematics can be recreated very well with a more flexible tail during Stage 1 and a more rigid tail during Stage 2. This can be related to the fluid-induced drag on the body of the fish during the two stages: during Stage 1 the fish is preparing itself for Stage 2 by bending its body to a C-shape. A flexible tail during this stage minimizes the drag acting on the tail. During Stage 2, however, a rigid tail is necessary to increase the thrust. If the fishes do not want to change their tail stiffness during Stage 2 of the fast-start, then they need to apply more torque to bend their spine to a shape close to the unstable second beam mode shape, with a node close to the midpoint – a smart fish would stiffen its tail during Stage 2.

Our simple model for snap-through bifurcation can explain some of the features that are observed in the robotic fish. Our model predicts that adding damping to the system reduces the oscillatory motion before reaching the stable equilibrium point. After a snap-though bifurcation, a beam in vacuum or air would undergo several cycles of oscillations before it settles to its new stable equilibrium position. These oscillations are not observed in a snap-though buckling occurred in water, because of the increased total damping of the system due to the fluid-induced damping, and as such no fish is ever observed in nature to "shake" after a fast-start. Also, the increase in the stiffness according to our model will lead to an increase in the rate of approaching the stable fixed points. This is clearly beneficial for a fast-start, since the fish would ideally want to approach its new stable equilibrium faster, and the faster it does it, the more efficient the fast-start maneuver will be. The fact that the increase in the tail stiffness (and therefore the overall stiffness of the system) results in body modes that more closely resemble those of the live fishes can also be related to this influence of the stiffness on the rate of approaching the fixed points.

6. REFERENCES

Ahlborn B, Harper D G, Blake R, Ahlborn D and Cam M. 1991 Fish without footprints J. Theor. Biol. 148, 521–33.

Bandyopadhyay P R 2002 Maneuvering hydrodynamics of fish and small underwater vehicles Integr. Comp. Biol. 42, 102–17

Blake R 2004 Fish functional design and swimming performance J. Fish Biol. 65, 1193–222

Borazjani I 2013, The functional role of caudal and anal/dorsal fins during the c-start of a bluegill sunfish J. Exp. Biol. 216 1658–69

Clark, A. J., Tan, X., McKinley, P. K. Evolutionary multiobjective design of a flexible caudal fin for robotic fish. Bioinspiration Biomimetics 10, 6 (nov 2015)

Currier, T., Lheron, S., Modarres-Sadeghi, Y. (2020). A bio-inspired robotic fish utilizes the snap-through buckling of its spine to generate accelerations of more than 20g. Bioinspiration and Biomimetics. 15, 055006

Currier, T., Modarres-Sadeghi , Y. An experimental model with passively variable stiffness to investigate the effect of body stiffness on the fish fast-start maneuver. Experiments in Fluids 60 (09 2019)

Domenici P D and Blake R 1991 The kinematics and performance of the escape response in the angelfish (Pterophyllum eimekei) J. Exp. Biol. 156 187–205

Feilich, K. L., AND Lauder, G. V. Passive mechanical models of fish caudal fins: effects of shape and stiffness on self-propulsion. Bioinspiration Biomimetics 10, 3 (apr 2015), 036002

Feilich, K. L., Lauder, G. V. Passive mechanical models of fish caudal fins: effects of shape

and stiffness on self-propulsion. Bioinspiration Biomimetics 10, 3 (apr 2015), 036002.

Fish F and Lauder G 2006 Passive and active flow control by swimming fishes and mammals Annu. Rev. Fluid Mech. 38, 193–224
Hale M 2002 S- and c-start escape responses of the muskellunge (Esox masquinongy) require alternative neuromotor mechanisms J. Exp. Biol. 205 2005–16

Harper D and Blake R 1990 Fast-start performance of rainbow trout Salmo gairneri and northern pike Esox Lucius J. Exp. Biol. 150 321–42

Long, J. H., Koob, T. J., Irving, K., CombieE, K., Engel, V., Livingston, N., Lammert, A., Schumacher, J. Biomimetic evolutionary analysis: testing the adaptive value of vertebrate tail stiffness in autonomous swimming robots. Journal of Experimental Biology 209, 23 (2006), 4732–4746

Park, Y., Jeong, U., Lee, J., Kwon, S., KIM, H., Cho, K. Kinematic condition for maximizing the thrust of a robotic fish using a compliant caudal fin. IEEE Transactions on Robotics 28, 6 (Dec 2012), 1216–1227

TriantafyllouM S, Triantafyllou G S and Yue D P 2000 Hydrodynamics of fishlike swimming Annu. Rev. Fluid Mech. 32 33–53

Videler J J 1993 Fish Swimming (London: Chapman and Hall)

Wakeling J M2001 Biomechanics of fast-start swimming in fish Comp. Biochem. Physiol. 131 31–40

Multiphase Flows

A NEW EXPERIMENTAL FACILITY FOR TWO PHASE FLOW CHARACTERIZATION IN A TUBE BUNDLE AND VIBRATION STUDY

Giuseppe Spina & Daniele Vivaldi & Guillaume Brillant
Institut de Radioprotection et de Sûreté Nucléaire (IRSN), Cadarache, St Paul-lez-Durance, BP3, 13115, France

William Benguigui
IMSIA, UMR EDF-ENSTA-CNRS-CEA 9219, Paris-Saclay university, 91762, Palaiseau, France
Électricité de France (EDF), 6 Quai Watier 78401 Chatou Cedex, France

Catherine Colin
Institut de Mécanique des Fluides de Toulouse, Université de Toulouse, CNRS, INPT, UPS, Allée du Prof. Camille Soula, 31400 Toulouse, France

Romain Denèfle & Muriel Lelong
Électricité de France (EDF), 6 Quai Watier 78401 Chatou Cedex, France

ABSTRACT

Vibration mechanisms caused by cross flow is a major issue of shell and tube heat exchangers. In particular, concerning the nuclear industry, in U-tube Steam Generators (SGs), two-phase cross flow occurs within the U-bend zone, which can be particularly severe for vibration issues. Within this context, a new experimental apparatus has been designed and is in construction in Cadarache at IRSN. With the goals of characterizing the air-water two-phase flows across the tube bundle and of studying the vibration behavior of one tube. The facility contains a test section of 5x5 in-line square tube bundle. The pitch-to-diameter ratio is 1.44, the outer diameter (D) of the tubes is 0.03 meters and the tube length is 10D. The foregone experimental campaigns are going to investigate air superficial velocity range of 0.01 - 1.2 m/s and water superficial velocity range of 0.07 - 0.12 m/s. The present communication details the design of the facility and the preparation of the experimental work.

1. INTRODUCTION

The Flow Induced Vibration (FIV) topic has gained considerable attention because it is likely to cause substantial damage to tubes and components. In natural circulation SGs of Pressurized Water Reactors (PWRs), the secondary flow induces vibrations of the tube bundle. The regions of most concern are where cross-flow occurs, in particular the U-bend zone subjected to two-phase flow. Several experimental programs have been carried out over the years in order to have a better understanding of the phenomena that play a role and to define design and safety criteria (Pettigrew et al, 1994; Paidoussis, 2006; Weaver et al, 1988). Nowadays, with the improvement of multiphase computational fluid dynamics (CFD), significant attention is consecrated to the numerical two phase flow investigation in cross-flow tube bundles (Benguigui et al, 2017). However, while the experimental campaigns regarding two-phase flow induced vibrations well define the tube vibration behavior, it is evident a lack of experimental database about two-phase flow investigation in a tube bundle. Therefore, with the objective of collecting new experimental data for multiphase CFD code validation, a new experimental apparatus is under construction at IRSN. The test section contains a 5x5 tube bundle of straight, parallel, horizontal tubes subjected to two-phase air/water upward flow. The goal is to investigate bubbly and intermittent flow regimes in the bundle, hence, water gap superficial velocity in the range of $0.07 < J_l < 0.12$ m/s and gas gap superficial velocity in the range of $0.01 < J_g < 1.2$ m/s inside the tube bundle. The facility is highly instrumented for two phase flow characterization: the use of optic probe and visual observations with high speed digital camera allow bubble size and velocity measurements. Differential pressure tips are used for average void fraction measurements. A Wire Mesh Sensor (WMS) is going to be used for the identification of two-phase flow structures and to map the void fraction distribution over the cross-section. A first experimental campaign is meant to be realize with fixed (i.e., non vibrating) tubes, and will focus on the two-phase flow characterization at different water and gas superficial velocities. A second experimental campaign is planned to study the vibration response of the central tube. As matter of fact, the test section is

also designed to accommodate up to 9 vibrating tubes and it is expected to substitute the central tube with a vibrating tube, instrumented with accelerometers, to characterize the vibration response under the two-phase flow. The facility has been designed within a PhD project. The data from the experimental campaigns will be used for the multiphase code Neptune CFD (Benguigui et al, 2017) assessment.

2. TREFLE (TWO-PHASE FLOW REGIMES AND FLUID-STRUCTURE INTERACTIONS EXPERIMENTAL FACILITY)

A sketch of the facility design is reported in Figure 1. The upward water-air two-phase flow reaches the test section positioned about 1.4 m from the gas injector. The test section is a five by five tube bundle, with a ratio pitch over diameter P/D = 1.44. The O.D. of the tubes is of 0.03 m. The ratio P/D is representative of the one of the U-tube SGs, whereas the O.D. is slightly larger than the values generally found in SGs: this allows to obtain more space for instrumentation. The facility has a rectangular cross section of 0.3 x 0.216 m, the walls of the apparatus are equipped with transparent faces in order to allows flow visualization. The water loop is equipped with a water storage tank, a Coriolis flow meter and a pump which, in nominal conditions, can deliver up to 2.4 kg/s. The compressor can deliver an air mass flow rate up to 0.3 kg/s.

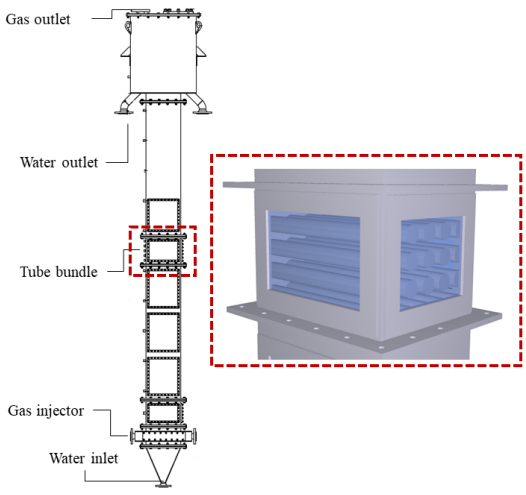

Figure 1. Sketch of the facility design with detail of the test section.

2.1. Design of the gas injectors

The water reaches the experimental apparatus through a diverging shaped section. The gas injector (Figure 2) has been designed in order to produce all the flow regimes inside the tube bundle.

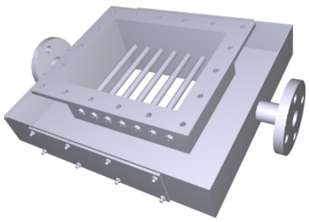

Figure 2. The gas injector.

To obtain a homogeneous gas distribution over the cross section, the air injection is made through seven pierced tubes placed perpendicularly with respect the tube bundle. The shape and size of the two-phase structures are strongly influenced by the hole size. However, the design must take into account the hydraulic constraints of the air loop, since it introduce pressure drops that must be smaller than the one the compressor can withstand. In addition, being positioned downstream of the water inlet, the gas injector generates a disturbance on the water flow that should be minimized. Hence, Two configurations have been designed in order to generate all flow regimes and to comply with the hydraulic constraints of the air loop and water flow:

- The first configuration (Figure 3 a) has been designed for the purpose of generating bubbles of a dimension of few millimeters, in order to generate a bubbly flow regime. The pipe outer diameter (O.D.) is 15 mm, 16 holes per pipe are placed diametrically opposed on the sides of the tubes to reduce the possibility of bubble coalescence and increase the bubble break up mechanism. The hole diameter is 1.5 mm. This design is expected to achieve a maximum gas flow rate of m_g = 0.005 kg/s.

- The second gas injector (Figure 3 b) has been designed to deal with flow regimes with high void fractions (up to m_g = 0.3 kg/s). The pipe O.D. is 25 mm, 60 holes per pipe are placed on the top of the tubes. The hole diameter is 5 mm. This second tube design allows the compressor to work with higher mass flow rates, reducing the pressure drops by increasing the number of holes and their diameters, as well as the pipe O.D.

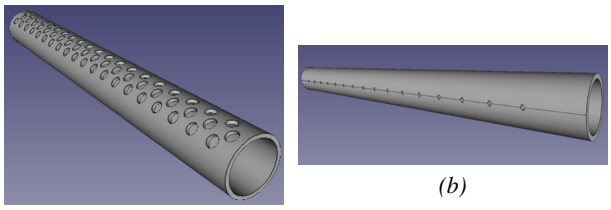

(a) *(b)*

Figure 3. Pierced tube for bubbly flow configurations (Figure a), and pierced tube for high void fraction values (Figure b).

2.2. Instrumentation and measurements

The facility is highly instrumented for two-phase flow characterization. A first experimental campaign is planned to investigate the two-phase flow. An optic dual tip probe is going to be inserted inside the test section for bubble size and gas velocity measurements. The facility has been designed to allow flow visualization in the key zones: high speed camera is going to be used for bubble size and velocity measurements. The void fraction is a key parameter, and is going to be investigated via indirect measurements by means of differential pressure tips. Upstream and downstream of the tube bundle, a Wire Mesh Sensor (WMS) will be used to obtain 2D void fraction distributions. The sensor is made of two electrode grids positioned one above the other at a small axial distance. The WMS working principle (Prasser et al, 1998) is based on the local instantaneous measurements of the two-phase mixture conductivity. Concerning the vibration response, it will be analyzed in a separate experimental campaign. Therefore, during this second phase the central tube of the test section is going to be substituted with a vibrating tube, instrumented with accelerometers able to register the vibrations of the tube. The tubes of the bundle are clumped to the facility wall from one side and free on the other side. Given the hydraulic conditions of the facility, the small forces acting on the tubes wall lead to very small vibrations hard to detect. Hence, the tubes are considered fixed. However, the nine central tubes of the test section can be replaced by tubes more flexible that allow the registration of the vibration response. The vibrating tube(s) can be free to vibrate in one direction rather than the other, and the influence of one or more vibrating tubes can be studied. These are common practices used in facilities designed to register tube vibrations. Piteau et al (2012) described as "loosely supported tube", a tube used to generate nearly planar vibrations. Hirota et al (2013) have investigated flow induced vibrations for five different bundle configurations. These flexible tube designs are based on the tube-beam principle, i.e. the tubes are connected to a flexible beam clumped to the facility wall to allow the rigid body movement of the tubes. The design consists in a rectangular cross section beam that allows the authors to study the tubes vibrations in the drag and lift forces directions separately.

3. PREPARATION TO THE EXPERIMENTAL CAMPAIGNS AND FIRST TESTS

A literature review of the flow regime maps was performed to prepare the experimental campaigns. The water and air flow-rate ranges available in the water and air loop are respectively: $0 < m_{air} < 0.3\ kg/s$ and $0 < m_{water} < 2,4\ kg/s$. Given the cross section of the TREFLE facility we can estimate the liquid and gas superficial velocities both in the homogenization section and in the tube bundle to be: J_g up to 3.85 m/s and J_l up to 0.037 m/s in the rising section and J_g up to 12.62 m/s and J_l up to 0.12 m/s in the test section. In order to obtain the void fraction, the homogeneous equilibrium model (HEM) is not a reliable approach for the present application. In fact the approximation of slip ratio equal to 1 is to strong for this case of application. As matter of fact, the HEM model does not take into account the flow area reduction between the rising section and the tube bundle, that leads to different values of slip ratio and as consequence to different values of void fraction. Therefore, to estimate the void fraction inside the tube bundle we make use of the model developed by Feenstra et al (2000). The method has been found in agreement with experimental data both in air-water and Freon two-phase flow in cross-flow tube bundles. To estimate the void fraction in the rising section the drift flux correlation has been used. The multiphase code Neptune CFD has been used in order to estimate the cross-section average void fraction in the rising section at 1.4 m from the inlet. Then the results have been compared with three correlations (Bhagwat et al, 2014; Hibiki et al, 2003; Kataoka et al, 1985) and the one by Kataoka et al (1985) with the correction adopted by Shoukri et al (2003) was found in agreement with the numerical results, hence has been selected. The analysis made allows us to foreseen flow regimes and void fractions to investigate during the experimental campaigns. Preliminary qualitative results show that the expected flow regimes are pertinent.

3.1. Flow regime maps in tubes bundle

The flow regime maps in tube bundles available in the open literature help in the definition of the experimental campaigns. A literature review of the flow regimes maps is resumed in Table 1 for two-phase

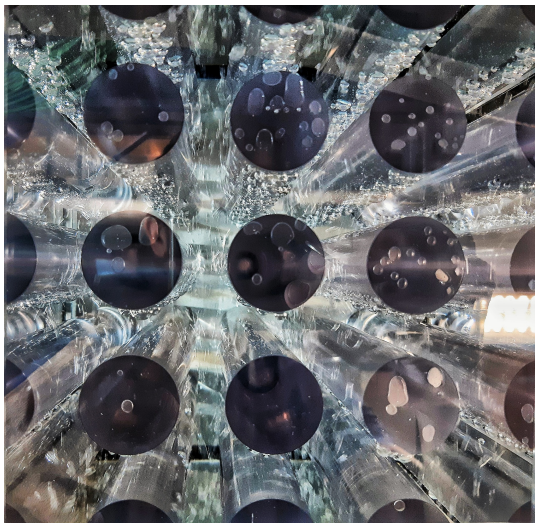

Figure 4. Bubbly flow regime in the tube bundle of TREFLE facility.

flow in tube bundles.

Authors	J_g & J_l range [m/s]	bundle configuration	Tubes D [m]	P/D	instrumentation & measurements
Ulbrich et al (1994)	0.047 - 9.3 & 0.001 - 0.65	Square	0.02	1.5	FC - PD
Xu et al (1998)	1 - 27 & 0.02 - 0.6	Square	0.00979	1.28	FC - PD
Noghrehkar et al (1999)	0.02 - 3.9 & 0.05 - 1.0	Square & Staggered	0.0127	1.47	RVP
Murakawa et al (2016)	0.03 - 1.19 & 0.1 - 0.3	Square & Staggered	0.015	1.5	FC - XR
Kanizawa et al (2016)	0.13 - 10.00 & 0.02 - 1.50	Triangular	0.019	1.263	FC - PD - CS

Table 1. Two phase flow regimes in tube bundles: comparisons among the experimental campaigns available in the literature. The instrumentation used: FC → images and video through fast camera, PD → pressure drop measurements of the mixture, RVP → resistivity probe for local void fraction measurement, XR → X-ray tomography, CS → void fraction measurement through capacitive sensor.

Keeping as reference the flow regime maps analyzed and the values of void fraction calculated, the foreseen experimental matrix can be prepared. Focusing on the bubbly-flow regime and on the intermittent/churn flow regime, either in the test section and in the rising part of the facility, the foreseen experimental tests are reported in Table 2. Figure 5 shows the experimental points reported in the flow regime maps edited by the authors. For sake of concision only one flow regime map is reported. Figure 6 shows qualitative pictures of the TREFLE facility tested under the previous mentioned conditions. The bubbly and intermittent flow regimes clearly appear in the test section.

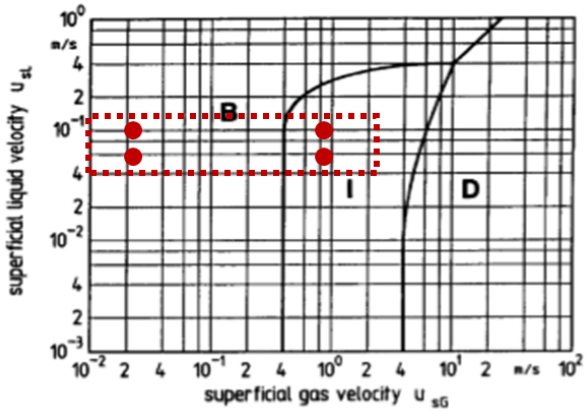

Figure 5. Expected experimental tests reported on the flow regime map for tube bundle by Ulbrich et al (1994).

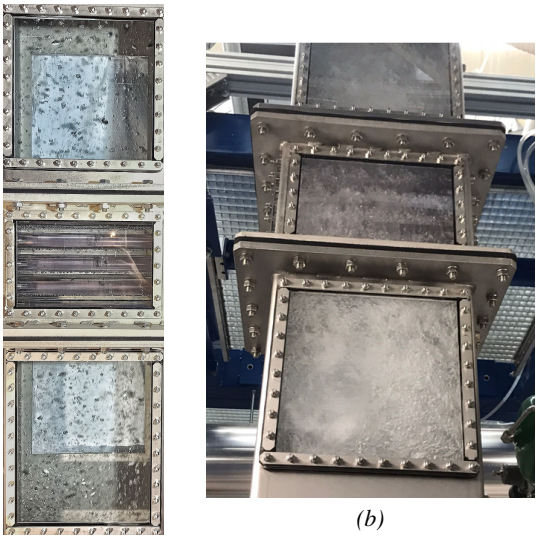

(a) *(b)*

Figure 6. Bubbly flow regime (Figure a), and intermittent flow regime (Figure b).

The experimental campaigns can be divided in three parts for each test:

- Gas injection system characterization.
- Two-phase flow characterization inside the tube bundle.
- Tube vibration response characterization.

The two phase flow inside the tube bundle will be characterized by means of a dual tip optic probe, able to give information about bubble size, gas velocity

test no.	m_{air} & m_{water} [kg/s]	J_g & J_l [m/s] in Bundle	J_g & J_l [m/s] in Riser	Void fraction (Feenstra et al, 2000) in Bundle	Void fraction (Kataoka et al, 1985) in Riser	Void fraction HEM	Air Injection system
1.1	0.0005 2.4	0.021 0.12	0.0064 0.037	0.05	0.014	0.15	Bubbly flow config. Fig. 3 a
1.2	0.0005 1.4	0.021 0.07	0.0064 0.0216	0.06	0.015	0.17	Bubbly flow config. Fig. 3 a
2.1	0.02 2.4	0.84 0.12	0.26 0.037	0.62	0.38	0.87	High void fraction config. Fig. 3 b
2.2	0.02 1.4	0.84 0.07	0.26 0.0216	0.63	0.39	0.89	High void fraction config. Fig. 3 b

Table 2. Expected test matrix. Void fraction calculated in tube bundle by making use of the model by Feenstra et al (2000) and for the rising part using the drift flux model by Kataoka et al (1985). In the table is reported also the injection system that is going to be used.

and void fraction inside the tube bundle. Probability Density Functions of void fraction fluctuations are going to be extracted from the probe signal to provide source of information for code-to-experiments comparison. More details are given in the following section about the gas injector and inlet conditions characterization. Moreover, once the tests for two-phase flow measurements are completed, the central tube will be replaced with the vibration system presented. The system, equipped with acceloremeters, will be able to provide data about tube vibration response subjected to a two phase flow already well known.

3.2. Inlet characterization and flow regime maps in vertical ducts

A literature review of the flow regimes maps is resumed in Table 3 for two-phase flow in large diameter ducts. Figure 7 shows the expected experimental points reported in the flow regime map edited by Ohnuki et al (1996).

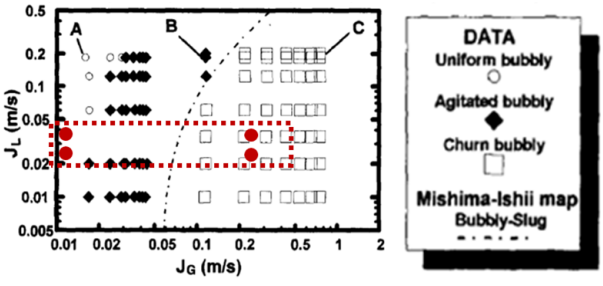

Figure 7. Expected experimental tests reported on the flow regime map for large pipe diameter by Ohnuki et al (1996).

Preliminary tests show the pertinence of the expected flow regimes in the TREFLE facility. Figure 8 reports pictures of the bubbly and intermittent flow regimes taken downstream the gas injection.

Author name	J_g [m/s] J_l [m/s]	Instrumentation	analyzed quantities	Pipe D_h [m]	L/D
Ohnuki et al (1996)	0.02-0.87 0.01-0.2	high speed camera optical void probe	flow pattern void fraction	0.48	4.2
Ohnuki et al (1999)	0.03-4.68 0.06-1.06	high speed video optical probe resistivity probe	flow pattern void fraction bubble size bubble velocity	0.2	60 10
S. F. Ali (2009)	0.06-2.26 0.19-1.1	high speed camera differential pressure	flow pattern void fraction fluctuation	0.25	48
Prasser et al (2002)	0.04-8.0 0.04-1.6	WMS	flow pattern void fraction bubble size	0.195	1.1-39.9

Table 3. Two phase flow regimes in large pipe diameter: comparisons among the experimental campaigns investigated.

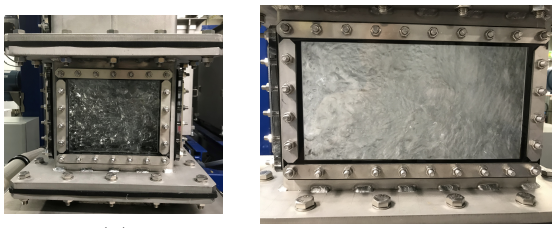

(a) *(b)*

Figure 8. Bubbly flow regime downstream the gas injector (Figure a), and intermittent flow regime downstream the gas injector (Figure b).

With the aim to provide high quality data for multiphase CFD code validation, the characterization of the inlet is a crucial point of the experimental campaigns. The data collected will be able to provide accurate inlet boundary conditions for CFD codes. These kind of data are necessary and illustrated in the following numerical work. To perform the present simulation, neptune_cfd and its multi-regime model (Merigoux et al, 2016) is used to simulate the rectangular duct without tube bundle for an intermittent flow close to the transition to bubbly flow.

The flow is presented in Figure 9 where it is possible to see large air bubbles in a turbulent bubbly flow. In Figure 10, it is possible to see the profile of void fraction for different inlet bubble diameter after 10D (usual length before a tube bundle in single-phase flow) and at the altitude of the tube bundle. It is here important to notice that the flow has the time to stabilized independently from the inlet bubble diameter for the tube bundle location but not for 10D after the inlet. The bubble diameter has an influence on the

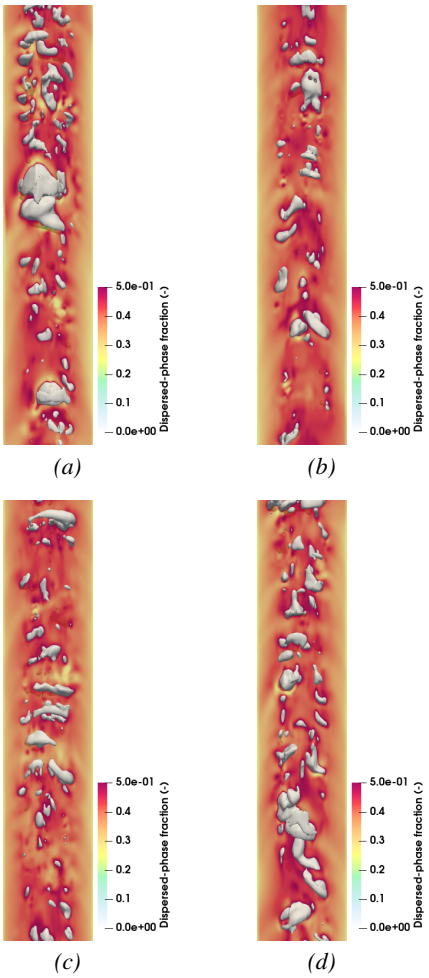

Figure 9. Numerical simulation of intermittent flow results: large bubble are created using an isosurface at void fraction 0.5, while the dispersed phase void fraction scale is reported.

size of slugs and on the coalescence frequency which explain the differences in void fraction profiles (also in velocity profiles not presented here). It is consequently of primary interest to fully described the inlet for a CFD grade experiment in order to have the complete inlet boundary conditions, especially close to the tube bundle in order to reduce the size of the numerical domain. Therefore, a first experimental campaign is going to be dedicated to the gas injector and inlet boundary condition characterizations.

The goal is to provide precise boundary condition to the CFD code at point 1 (as reported in the scheme in Figure 11) for tests 1.1 and 1.2 (details on the test matrix in Table 2) through:

- Measures of bubble size and velocity will be performed by means of high speed camera downstream the gas injector (as reported in the scheme in Figure 11). This will provide gas velocity and bubble diameters. In order to facilitate the image post processing and to reduce the uncertainties, the tests will be run with one tube of the gas injector for bubbly flow configuration adapting the gas flow rate. The remaining tubes will be plugged to maintain the perturbation of the water flow.
- The void fraction will be measured either with WMS positioned at point 1 (as reported in Figure 11) or by means of pressure drops through indirect measurements.

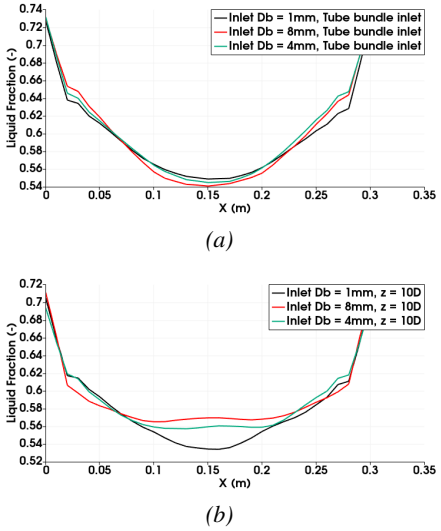

Figure 10. Numerical simulation of intermittent flow results: Liquid fraction profiles obtained for different inlet bubble diameter at the altitude of tube bundle inlet (Figure a) and 10 times the tube diameter after the inlet boundary condition (Figure b).

For tests 2.1 and 2.2, due to the high gas flow rate, the measures through camera images are expected to feature too high uncertainties. Hence, measures of void fraction distribution all over the cross section will be provided by means of WMS at point 1.

4. CONCLUSION

The present communication shows the details of the design process of a new experimental apparatus: TREFLE. The facility has been designed within a PhD program, with the goal of providing substantial contribution to an experimental database for multiphase CFD code validation. Both two-phase flow and tube vibrations are going to be investigated. A new design of vibrating tube has been developed, the design allows to study the vibration response of the tube under two-phase cross-flow. Preliminary tests run

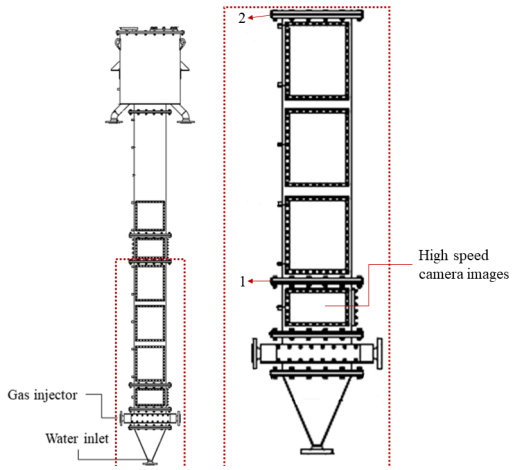

Figure 11. Scheme of boundary conditions characterization.

with TREFLE facility show that the expected flow regimes are properly reproduced in the facility. Numerical results highlight the importance of the boundary condition characterization, as matter of fact, a sensibility on the inlet bubble diameter show an impact on the results. Hence, a major attention has been paid in the design phase to the boundary conditions characterization, in order to provide high quality data for CFD validation.

5. REFERENCES

W. Benguigui, E. Deri, J. Lavieville, S. Mimouni, E.Longatte, 2017, Numerical experiment on two-phase flow behaviors in tube bundle geometry for different mixtures. *Pressure Vessel & Piping* Hawai-2017.

W. Benguigui, 2018, Numerical simulation of two-phase flow induced vibration. *PhD Thesis* University of Paris-Saclay.

N. Merigoux, J. Laviville, S. Mimouni, M. Guingo and C. Baudry, 2016, A generalized large interface to dispersed bubbly flow approach to model two-phase flows in nuclear power plant. *Proceedings of the Computational Fluid Dynamics in Nuclear Reactor Safety: CFD4NRS-6* Cambridge, USA, 2016.

H. Murakawa, M. Babaand, K. Sugimoto N.Takenaka, D. Ito and Y. Saito, 2016, Evaluation of void fraction around a tube in two-phase flow across horizontal tube bundle. *9th International Conference on Multiphase Flow*, ICMF-2016.

F. T. Kanizawa and G. Ribatski, 2016, Two-phase flow patterns across triangular tube bundles for airwater upward flow. *International Journal of Multiphase Flow* **80**: 43-56.

D. S. Weaver and J. A. Fitzpatrick., 1988, A review of cross-flow induced vibrations in heat exchanger tube arrays. *Journal of Fluids and Structures* **02**: 73-93.

M. P. Paidoussis, 2006, Real-life experiences with flow-induced vibration. *Journal of Fluids and Structures* **22**: 741-755.

M. J Pettigrew and C. E. Taylor., 1994, Two-phase flow-induced vibration: An overview. *Journal of Pressure Vessel Technology* **116**: 233-253.

H.-M Prasser, A Bottger, and J Zschau, 1998, A new electrode-mesh tomograph for gas-liquid flows. *Flow Measurement and Instrumentation* **9**: 111-119.

P. Piteau, X. Delaune, J. Antunes, and L. Borsoi, 2012, Experiments and computations of a loosely supported tube in a rigid bundle subjected to single-phase flow. *Journal of Fluids and Structures* **28**: 56-71.

K. Hirota, H. Morita, J. Hirai, A. Iwasaki, S. Utsumi, K. Shimamura, and R. Kawakami, 2013, Investigation on in-flow fluidelastic instability of an array of tubes. *Proceedings of the ASME 2013 Pressure Vessels and Piping Conference*, Paris, France, July 14-18.

M. J Pettigrew, C. E. Taylor, and B. S. Kim, 1989, Vibration of tube bundles in two-phase cross-flow: Part 1 hydrodynamic mass and damping. *Journal of Pressure Vessel Technology* **111**: 466-477.

M. J Pettigrew, C. E. Taylor, and B. S. Kim, 1989, Vibration of tube bundles in two-phase cross-flow: Part 2 fluid-elastic instability. *Journal of Pressure Vessel Technology* **111**: 478-487.

Connors H. J. Jr., 1978, Fluidelastic vibration of heat exchanger tube arrays. *Journal of Mechanical Design, ASME* **100**: 347-353.

S. F. Hoerner and H. V. Borst, 1985, Fluid-dynamic lift: practical information on aerodynamic and hydrodynamic lift. *second edition*.

P.A. Feenstra, D. S. Weaver, and R. L. Judd, 2000, An improved void fraction model for two-phase cross-flow in horizontal tube bundles. *International Journal of Multiphase Flow* **26**: 1851-1873.

I. Kataoka, M. Ishii, and A. Serizawa, 1985, Interfacial area in two-phase flow; formulation and measurement. *Presented at the 23rd Nat, Heat Transfer Conf.* ASME - Denver, Colorado.

M. Shoukri, I. Hassan, and I. Gerges, 2003, Two-phase bubbly flow structure in large-diameter vertical pipes. *The Canadian Journal of Chemical Engineering* **81**: 205-211.

T. Hibiki and M. Ishii, 2003, One-dimensional drift-flux model and constitutive equations for relative motion between phases in various two-phase flow regimes. *International Journal of Heat and Mass Transfer* **46**: 4935-4948.

S. M. Bhagwat and A. J. Ghajar, 2014, A flow pattern independent drift flux model based void fraction correlation for a wide range of gas-liquid two phase flow. *International Journal of Multiphase Flow* **59**: 186-205.

R. Ulbrich and D. Mewes, 1994, Vertical, upward gas-liquid two-phase flow across a tube bundle. *International Journal of Multiphase Flow* **20**: 249-272.

G. P. Xu, C. P. Tso, and K. W. Tou, 1998, Hydrodynamics of two-phase flow in vertical up and down-flow across a horizontal tube bundle. *International Journal of Multiphase Flow* **24**: 1317-1342.

G. R. Noghrehkar, M. Kawaji, and A. M. C. Chan, 1999, Investigation of two-phase flow regimes in tube bundles under cross-flow conditions. *International Journal of Multiphase Flow* **25**: 857-874.

A. Ohnuki and H. Akimoto, 1996, An experimental study on developing air-water two-phase flow along a large vertical pipe: effect of air injection method. *International Journal of Multiphase Flow* **22**: 1143-1154.

A. Ohnuki and H. Akimoto, 1999, Experimental study on transition of flow pattern and phase distribution in upward air-water two-phase flow along a large vertical pipe. *International Journal of Multiphase Flow* **26**: 367-386.

S. F. Ali, 2009, Two phase flow in large diameter vertical riser. *PhD thesis* Cranfield University, Departement of Process and Systems Engineering.

H-M. Prasser, A. Boettger, M. Beyer, H. Carl, D. Lucas, A. Schaffrath, P. Schtz, F. P.Weiss, and J. Zschau, 2002, Topflow tests on the structure of the gas-liquid interface in a large vertical pipe. *Forschungszentrum Rossendorf Annual Report* FZR 380.

EXPERIMENTAL INVESTIGATION OF VOID FRACTION DISTRIBUTION BEHIND A CYLINDER

W. BENGUIGUI[1,2], C. PINTO[1], O. RIES[1]
[1]*EDF R&D, Fluid Mechanics Division, 6 Quai Watier 78400 Chatou*
[2]*IMSIA, UMR EDF-ENSTA-CNRS-CEA 9219, Paris-Saclay university, 91762, Palaiseau, France*

ABSTRACT

The numerical simulation of interaction between cylindrical structures and two-phase flows is a major concern for industrial applications, especially where cross-flows may cause damages, in heat exchangers for example. In order to understand the phenomenon of vibrations induced by two-phase flows, many experiments were conducted with reduced-scale models using several simulant two-phase mixtures. In single-phase flow, the phenomenon has been characterized with dimensionless numbers. In 1986, Inoue et al. [1] pointed out different properties of a dispersed air/water flow around a single rigid cylinder for various inlet void fractions, velocities, and bubble to cylinder size ratios. In the present work, the authors are interested in the behavior of two-phase flow from 30% to 90% of void fraction around a square cylinder.

1. INTRODUCTION

Flow-induced vibrations of tubes in two-phase flow heat exchangers are a concern for the nuclear industry since it might cause damages. Consequently, when operating conditions are too severe to allow convenient measurement procedures, relevant phenomena are investigated by means of reduced-scale experiments using modeling fluids which are different from the real ones. Similarities have then to be taken into account. Some studies tried to address this topic in the past. Gay et al. [2] compared air/water with freon/water mixtures in a triangular pitch bundle. Axisa et al. [3] compared steam/water with air/water. Benguigui et al. [4] compared water/air and freon/freon with numerical simulations. Experimental studies involved large facilities and are often limited to the analysis of global parameters, especially in terms of vibration (only) for the present application.

Hulin et al. [5] studied vortex emissions behind bluff obstacles in a gas-liquid vertical flow. Inoue et al. [1] studied bubbly flow around a single cylinder for different velocities, void fractions and size ratios. Meng et al. [6] studied the discrepancies between air-water and steam/water for a cross flow around a single cylinder for low void fractions. More recently, Murai et al. [7] carried out experiments on different kinds of obstacles, mainly with dispersed bubbles rising in a fluid at rest. Pascal-Ribot&Blanchet [9] measured forces on a single cylinder under different two-phase flow regimes. Hu et al [8] studied the two-phase flow regime transition for an air/water upward flow around a single cylinder. In the present work, the objective is to get void distribution thanks to a wire-mesh sensor located behind the cylinder.

The experimental setup is shortly described in the first section, then tests without cylinder are described with a comparison to the Taitel et al [10] flow regime map. A rectangular cylinder is then added to the mock-up in order to study its effects on the two-phase flow.

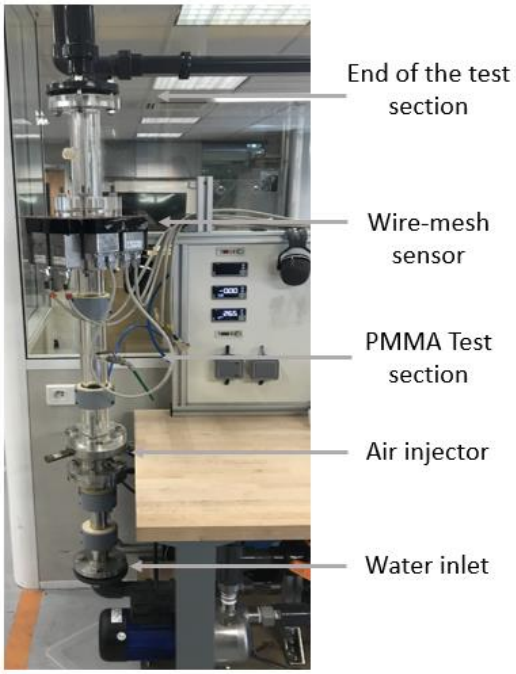

Figure 1 Picture of the experimental setup.

2. EXPERIMENTAL SETUP

A picture of the test section is shown in Fig.1. The water from a pump (0 to 60 L/min) enters a vertical circular tube with 38 mm diameter and 1500 mm long. A parietal air injector (from 0 to 100 L/min) is located from 380 mm to 480 mm after the water inlet. Two configurations are presented:

- An upward air-water flow,
- An upward air-water cross-flow around a square cylinder with D = 16 mm clamped from both sides 620 mm after the gas injector. The present obstacle is a square since it was easier to 3D print.

For the present work, only void measurements are performed thanks to a wire-mesh sensor [11,12,13]. A wire-mesh sensor consists of two grids of parallel wires, which span over the measurement cross-section. The wires of both planes cross under an angle of 90°, but do not touch. Instead there is a vertical distance between the wires at the crossing points. At these points the conductivity is measured. According to the different conductivity of gas and water the phase present in the moment of the measurement at the crossing point can be determined. The present wire- mesh sensor is composed of 24x24 wires with a span of 1.52 mm with a wire diameter of 0.1 mm.
For the first configuration, the wire-mesh sensor is located at 320 mm, 620 mm and 1020 mm from the gas injector. Then, the wire-mesh sensor is located at 5D from the center of the cylinder. The temporal resolution of wire-mesh measurement is 3000 Hz for the present work.

3. UPWARD AIR-WATER FLOW

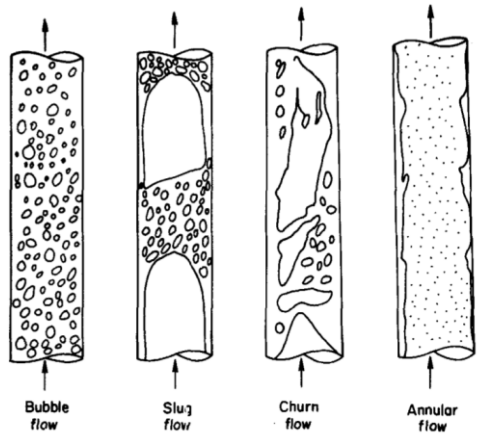

Figure 2: Flow patterns in a vertical flow, Taitel et al. [10]

In order to characterize the two-phase flow regime impacting the cylinder, a sensitivity study is performed for different flow rates without the square cylinder. This kind of experiment has been constantly studied for many years, especially in terms of flow regime map. The present work tries to provide more data to the community in terms of void distribution.

First, from visual observations the flow regime is compared to the Taitel et al [10] flow regime limits. The annular flow is not reached, however the major properties of slug and churn flow described in [10] are reproduced. These two pattern definitions from [10] are given below and illustrated with some pictures from the present work in Figure 3 and 4:

- Slug Flow: "*Most of the gas is located in large bullet shaped bubbles which have a diameter almost equal to the pipe diameter. They move uniformly upward and are sometimes designated as "Taylor bubbles." Taylor bubbles are separated by slugs of continuous liquid which bridge the pipe and contain small gas bubbles. Between the Taylor bubbles and the pipe wall, liquid flows downward in the form of a thin falling film*."

Figure 3 Air-water slug flow regime illustration. Taylor bubble are observed with small gas bubbles around which are not spherical anymore. The thin liquid film is also identified.

- Churn Flow: "*Churn flow is somewhat similar to slug flow. It is, however, much more chaotic, frothy and disordered. The bullet-shaped Taylor bubble becomes narrow, and its shape is distorted. The continuity of the liquid in the slug between successive Taylor bubbles is repeatedly destroyed by a high local gas concentration in the slug. As this happens, and liquid slug falls. This liquid accumulates, forms a bridge and is again lifted by the gas. Typical of churn flow is this oscillatory or alternating direction of motion of the liquid*. "

In the present configuration, the wire-mesh sensor measurements were compared to an optical probe in order to check the correct calibration of the wire-mesh sensor. For low void fraction (10%) and high void fraction (90%), the error is smaller than 0.5% at the center of the pipe. Quantitative results are not presented in this section since they are com-

pared to the second configuration in the following section.

Figure 4 Churn flow : oscillatory flow is reproduced, it is possible to see the chaotic and disordered flow on these two picture where there are liquid film, small&large bubbles going up and down between huge plugs of air.

Moreover, the significant number of test in free vein (without the cylinder), generates a large database (thanks to the use of optical probe, wire-mesh sensor, and a camera: void distribution, size distributions and local gas velocity) that require a dedicated study, the present work is focused on the two-phase flow around a square-cylinder.

4. AIR-WATER CROSS-FLOW AROUND A SQUARE CYLINDER

The present section deals with two-phase flow around a square cylinder in terms of visual analysis, void distribution and size distribution for slug and churn flows.

For the following result, each test is presented in function of the superficial velocity which is related to mass flow rates, volumetric mass and section surface by: $j = \frac{\dot{m}}{\rho S}$.

4.1. Qualitative observations

In Figure 5, a slug flow around a square cylinder is presented with 3 snapshots for each direction (perpendicular and parallel to the cylinder). Based on the observation from the free vein section, it is possible to see that air bubble from few millimeters are not broken but follow the liquid wake behind the cylinder. Some of them are trapped in the recirculation zone behind the cylinder, however there is still a liquid zone with no bubble at the cylinder wall. In fact, due to the static pressure gradient, at the front and rear of the cylinder, there is a liquid layer where bubbles can hardly penetrate. In 1986, Inoue et al. [1] pointed out different properties of a dispersed air/water flow around a single rigid cylinder that are reproduced here. For larger gas structure or slugs, depending on the wake-shedding, they are going from one side or another, the confinement between the cylinder and the wall of the vein drives it radial size. Consequently, slugs appear to be longer in the present configuration than with the previous. After that, they disturb the regularity of the wake-shedding behind the cylinder by going back to the center of the pipe. Then, slugs are often broken that explain the reduction of radial size on the picture compared to the first configuration.

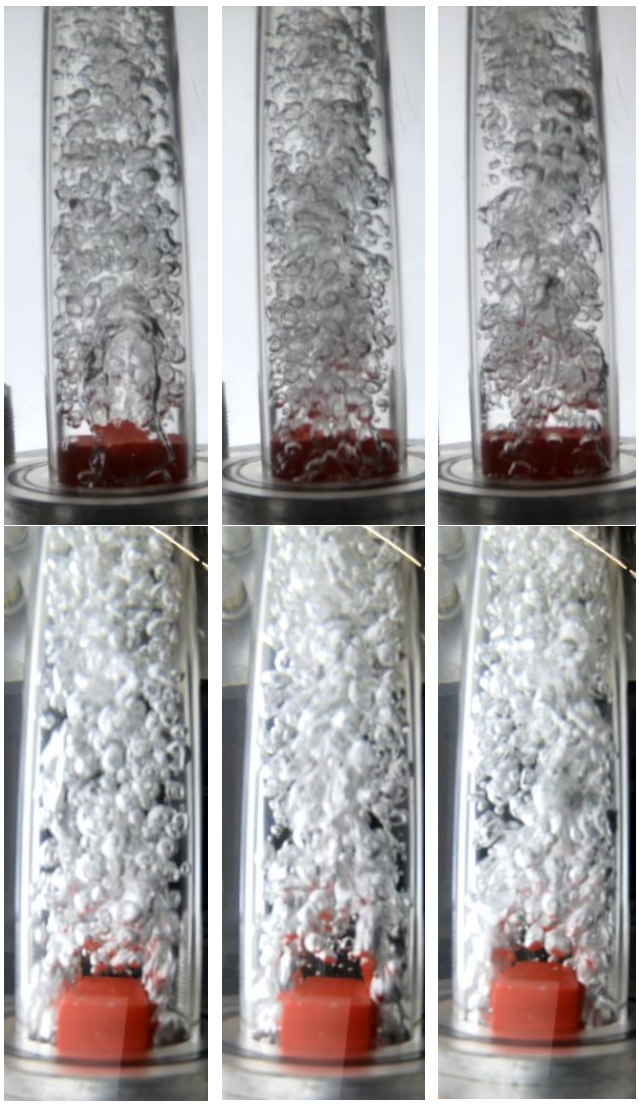

Figure 5 Perpendicular and parallel to the cylinder views of a slug flow around a square cylinder - j_g =

0.147 m/s and j_l = 0.0735 m/s with an homogeneous inlet void fraction of 66%.

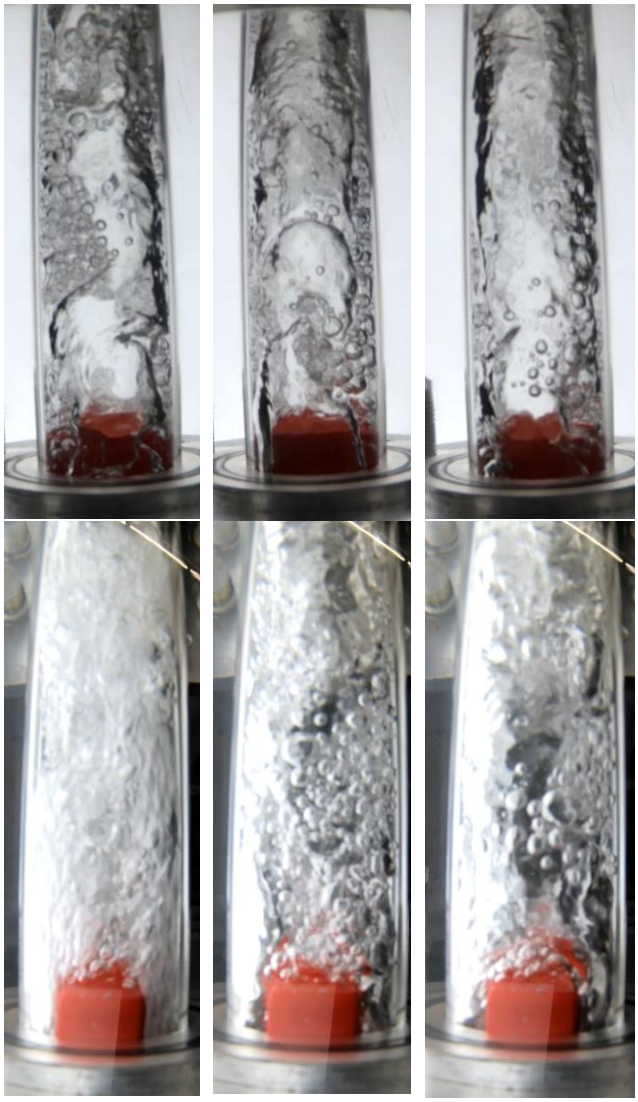

Figure 6 Perpendicular and parallel to the cylinder views of a churn flow around a square cylinder - j_g = 1.47 m/s and j_l = 0.0735 m/s with an homogeneous inlet void fraction of 95%.

In Figure 6, a churn flow around a square cylinder is presented with 3 snapshots for each direction (perpendicular and parallel to the cylinder). Based on the observation from the free vein section, it is possible to see that the chaotic behavior of this regime is still present. The present two-phase flow regime is divided in 3 different steps:

- Step 1: a large plug of air is going up driving up the gas-liquid wall film (liquid film with bubbles inside), the wake due to the square cylinder leads to an oscillation of this film that can break the large air plug.
- Step 2: in the second part of the large air plug, the liquid film and its bubbles are not anymore driven by the air plug and are consequently falling down on the cylinder.
- Step 3: at the end of the plug, a two-phase mixture composed of many small gas structures is going up generating a wake-shedding behind the cylinder until the next air plug arrived.

4.2. Void distribution

In the present subsection, a comparison is performed between the radial and surface void distribution in free vein and with the square cylinder for two cases:

- Case 1: a superficial velocity of 0.0735m/s in liquid, 0.441 m/s in gas corresponding to a churn flow close to the slug flow regime.
- Case 2: a superficial velocity of 0.0735m/s in liquid, 1.18 m/s in gas corresponding to a churn flow at high void fraction.

In Figure 7, the radial distributions of void are presented for both cases. It is possible to see that the peak of void fraction is higher without the cylinder in both cases. This is due to the cylinder that spread air structure around the cylinder in its wake instead of having a regular gas structure in the free vein. It is also interesting to notice that the two-phase flow at wall is not anymore a liquid film but a two-phase film with bubbles. The shape of the curve in the free vein corresponds to the radial size of the large gas structure, whereas in the second configuration, it is more related to the wake of gas behind the cylinder. It explains why the two-phase film is thinner behind the cylinder.

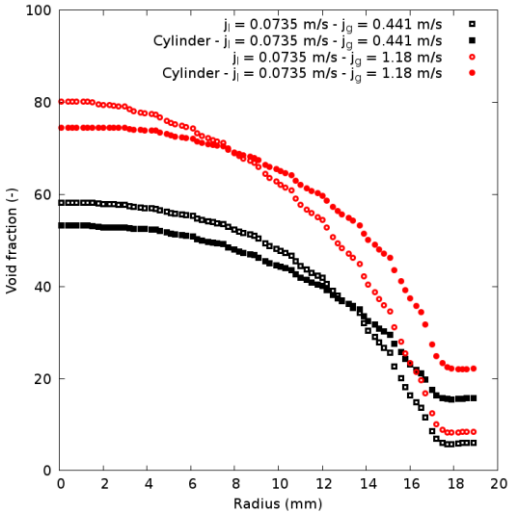

Figure 7 Churn flow void fraction distribution from wire-mesh measurements along radius without/with a cylinder for a superficial velocity of 0.0735m/s in liquid, 0.441 and 1.18 m/s in gas (post-treatment

performed with WMS Framework, radius profile is here interpolated between each wms cell).

In Figure 8, the surface void fraction distribution are represented for each case : top being case 1 and bottom being case 2; and for each configuration : left being in free vein and right with the square cylinder. For free vein results, it is possible to see that the void fraction is homogeneously distributed radially. 5D after the square cylinder, it is possible to distinguish that the cylinder is oriented along Y direction since the peak of void fraction appears to be diffused along X direction. The void fraction is consequently lowered at wall behind the cylinder but really higher at wall in the other regions. The diffusion of the void along X axis is explained by the wake-shedding behind the cylinder. In order to not disturbed the two-phase flow with the wire-mesh in the recirculation region, the choice was to be at 5D from the center of the cylinder, that is why the wake of the cylinder does not lead to two separated peak of void fraction.

4.3. Size distribution

With the wire-mesh sensor and the dedicated software *Wire Mesh Sensor Framework* it is possible to get the size distribution of gas structures based on the gas superficial velocity and the acquisition frequency (3000 Hz). The distribution is

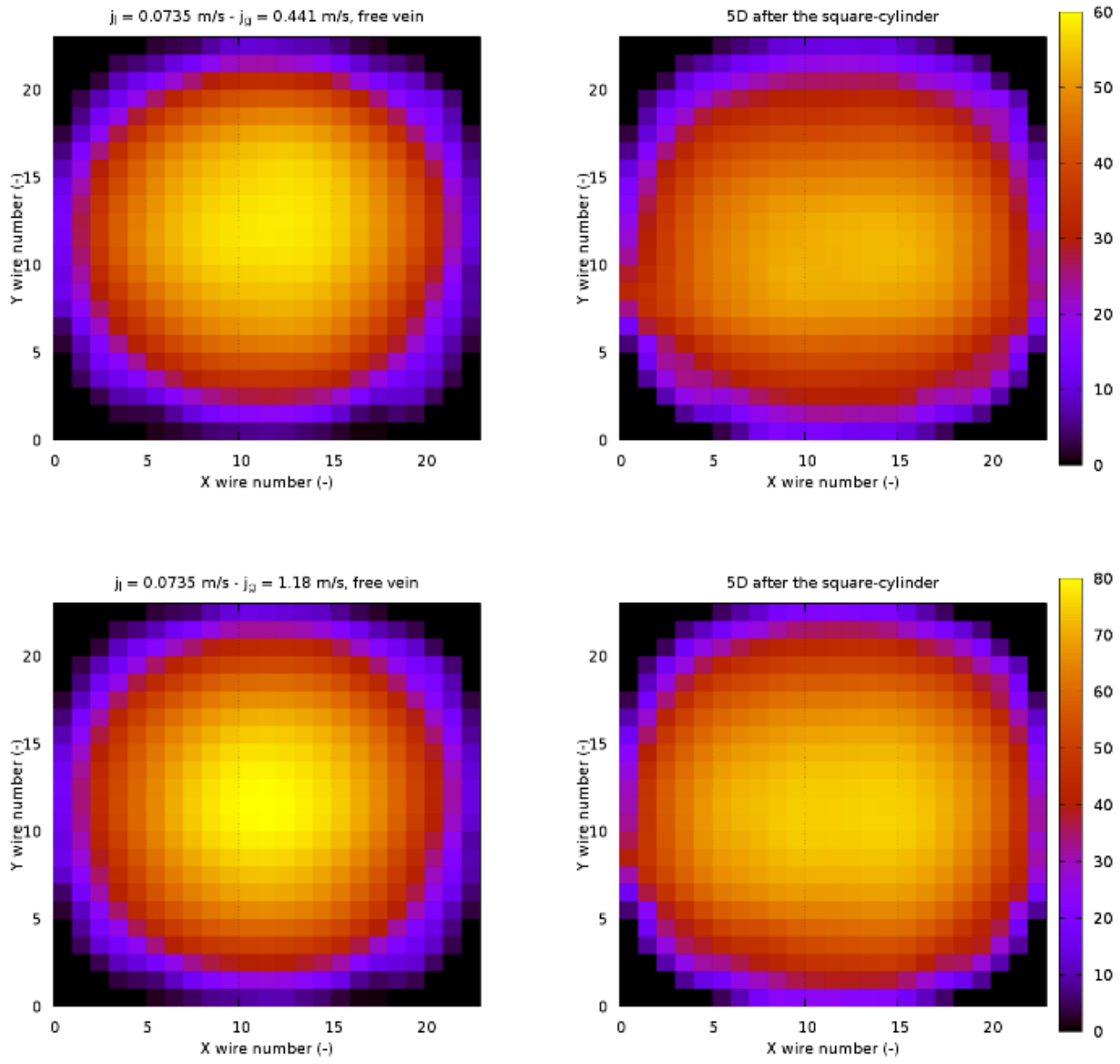

Figure 8 Illustrations of the void distribution changes behind the cylinder: 2D void fraction distribution for the free vein (without obstacle) on the left side and 5D after the square cylinder on the right. The liquid superficial velocity is 0.0735 m/s and the gas velocities are 0.441 m/s (top) and 1.18 m/s (bottom).

available in XY (consequently limited to the diameter of the vein) and in Z (corresponding to the length of air plugs). The distribution is presented in gas fraction of the bubbles of this class referring to bubble class width in %/mm according to radial and vertical size. In Figure 10, size distribution with and without the square cylinder are presented for case 1.

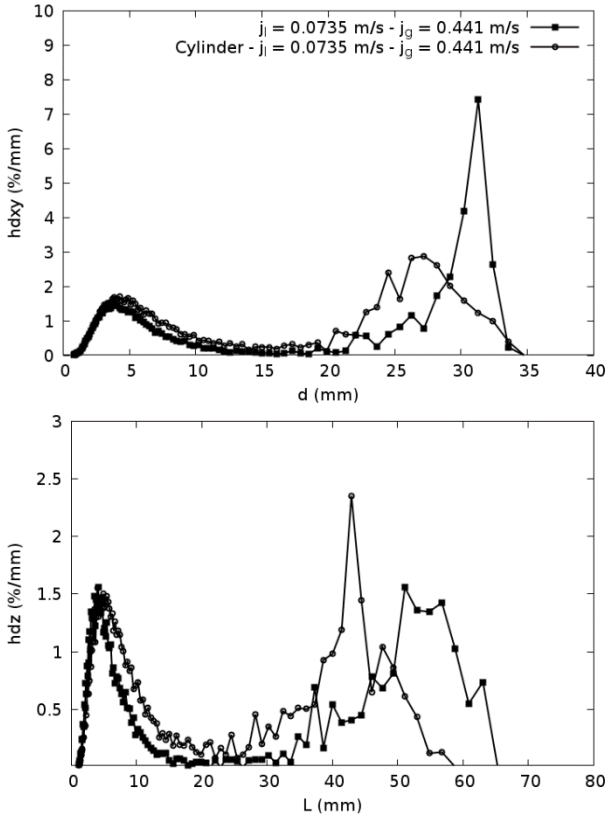

Figure 9 Gas fraction of the bubbles of this class referring to bubble class width in %/mm according for radial size and vertical size for superficial velocity of 0.0735m/s in liquid and 0.441m/s in gas.

For radial distribution, two peaks are observed for both configurations:

- First peak corresponds to bubbles with a size smaller than 1.25 cm. Despite that the peak is slightly larger in presence of the cylinder, both configurations have similar behavior, leading to the conclusion that the cylinder does not have an important effect on the small bubbles.
- Second peak corresponds to air plugs with a size larger 2 cm. Here the discrepancy is significant. In the first configuration, it is possible to notice that the size is driven by the diameter of the vein since we have a narrow peak around 3.2 cm. For the second configuration the peak in 2.6 cm is much larger, consequently the cylinder has a concrete impact on the radial distribution and cause probably the break of the large gas structure seen in the first configuration.

Looking at the distribution, the curve seems to be not perfectly averaged for large structure, consequently a higher time of acquisition will be necessary in the future (present time : 300s).

For vertical distribution, two peaks are also observed for both configurations:

- First peak corresponds to bubbles with a size inferior at 1.25 cm. Despite that the peak is larger in presence of the cylinder, both configurations have similar behavior, leading to the conclusion that the cylinder does not have a significant effect on the bubbles.
- Second peak corresponds to the length of air plugs with a size superior at 2 cm. There is a significant impact from the cylinder, here the peak is very large for the first configuration and the maximum is around 5.5 cm, consequently it shows a chaotic length of air plugs in free vein. On the other hand, we have a narrower peak in presence of the cylinder at 4.2 cm, meaning that the presence of the cylinder drives the length of the air plugs. This regular length is probably linked to the vortex shedding frequency and the air plug frequency.

5. CONCLUSION

In the present paper, the author presented a new experimental setup able to characterize high void fraction flow in a vein and in the wake of a square cylinder. Based on eye-observations and wire-mesh sensor measurements, the authors studied two cases of churn flow from 50 to 80% of void fraction where void and size distribution were commented.

A significant amount of data has been generated by this experimental campaign and need to be treated to improve our understanding of such flows. This kind of data is interesting for two-phase flow code validation since the literature for high void fraction behind a single cylinder is poor; often the interest is given to tube bundles.

In a near-future, the objective will be to measure the forces applied to the square-cylinder to characterize two-phase fluid forces in terms of regime, size distribution and void fraction. At last, a sensibility to the two-phase mixture would be of interest to characterize on a same geometry the effect of gas and liquid physical properties.

6. REFERENCES

[1] A. Inoue, Y.Kozawa, M.Yokosawa, S.Aoki, Studies on two-phase cross-flow. Part I:Flow char-

acteristics around a cylinder, International Journal of Multiphase Flow 12, 149-167, 1985.

[2] N. Gay, P. Decembre, J. Launay, Comparison of air/water to water/freon two-phase cross-flow effects to the vibratory behaviour of a tube bundle, Winter Annual Meeting of the ASME, SYmposium on Flow- Induced Vibrations, 1988.

[3] F. Axisa, B. Villard, R. Gibert, N. Yamaguchi, P.Sundheimer,Vibration of tube bundles subjected to air-water and steam-water cross flow: preliminary resultas on fluidelastic instability, Winter Annual Meeting of the ASME, Symposium on Flow-Induced Vibrations, 1984.

[4] W. Benguigui, E. Deri, J. Lavieville, S. Mimouni, E.Longatte, Numerical experiment on two-phase flow behaviors in tube bundle geometry for different mixtures, Pressure Vessel & Piping, Hawai, 2017.

[5] J-P. Hulin, C. Fierfort, R. Coudol, Experimental study of vortex emission behind bluff obstacles in a gas liquid vertical two-phase flow, International Journal of Multiphase Flow 8, 5 pp 475-490, 1982.

[6] H. Meng, On dispersed two-phase flows past obstacles, Technische Universiteit Eindhoven, 1993.

[7] Y. Murai, T. Sasaki, M. Ishikawa, F. Yamamoto, Bubble-driven convection around cylinders confined in a channel, Journal of Fluids Engineering, 2005.

[8] Z. Hu, Y. Yang, L. Liu, F. Zhou, Local flow regime transition criteria of gas-liquid two phase flow in vertical upward tube with a horizontal rod,Chinese Journal of Chemical Engineering, 14(4) 442-449, 2006

[9] S. Pascal-Ribot, Y. Blanchet, Buffeting lift forces and local air-water flow aspects around a rigid cylinder, International Journal of Multiphase Flow 33, 1237-1254, 2007.

[10] Taitel, Y., Barnea, D. and Dukler, A.E. (1980), Modelling flow pattern transitions for steady upward gas-liquid flow in vertical tubes. AIChE J., 26: 345-354

[11] Prasser, H.-M., Böttger, A., Zschau, J., 1998. A new electrode-mesh tomograph for gas/liquid flows. Flow Meas. Instrum. 9, 111–119.

[12] Prasser, H.-M., Scholz, D., Zippe, C., 2001. Bubble size measurement using wire-mesh sensors. Flow Meas. Instrum. 12, 299–312.

[13] Lucas, D., Beyer, M., Kussin, J., Schütz, P., 2010a. Benchmark database on the evolution of two-phase flows in a vertical pipe. Nucl. Eng. Des. 240, 2338–2346.

FORCES AND DISPLACEMENTS IN A BEND SUBJECTED TO AN AIR-WATER FLOW

Laurent De Moerloose & Henri Dolfen
Department of Electromechanical, Systems and Metal Engineering, Ghent University, Sint-Pietersnieuwstraat 41-B4, 9000 Ghent, Belgium

Michel De Paepe & Joris Degroote
Department of Electromechanical, Systems and Metal Engineering, Ghent University, Ghent, Belgium
Flanders Make, Belgium

ABSTRACT

Understanding the vibration of tubes subjected to an internal liquid-gas mixture is of primary importance to improve the design of heat exchangers. Consequently, a large amount of experimental research has been performed in the past decades. Although an extensive number of numerical investigations have been published more recently, most of these papers do not focus on the effect of conditions applied at the fluid domain boundaries. In the current paper it is shown that these boundary conditions can have an important effect on both the stability of the obtained flow solution and on the force exerted on the surrounding tube. The current work aims at correctly predicting the forces on a horizontal 90° bend that was investigated experimentally by Belfroid et al. (2016). The forces exerted on the bend are directly related to the presence of liquid slugs coming into the bend. In the last part of this research, a finite element model for the structure of the pipe is presented.

1. INTRODUCTION

It is difficult to underestimate the importance of reliable piping systems. Large-diameter pipes play a key role in the energy provision of many people around the world, both for on-land transport of gas and for subsea applications (Ma et al., 2019). With respect to the latter, considerable analytical (Semler et al., 1994) and experimental (Srinil et al., 2018) work was done on the vibration of subsea risers subjected to single-phase and two-phase flow. Research of numerical nature is more scarce, but some relevant studies have been done as well, e.g. Atadan et al. (1997). Coincidentally, large-diameter piping also occurs in process and energy industry, e.g. for steam transport, often related to heat exchanger applications. It is necessary to understand the excitation and the subsequent oscillation of the tubes so as to avoid long- or short-term failure. In this work, the focus will be on the application concerning two-phase flow, i.e. a gas-liquid mixture present inside the tube. Examples of such flows are widely found in oil industry (where air or other gases are present in the tube as well) or in heat transfer applications (typically water-air, water-steam mixture or a refrigerant). An overview of recent research on two-phase flow induced vibration in piping systems was published by Miwa et al. (2015).

Over time, a large number of fundamental studies on the behaviour of two-phase flow both inside (De Moerloose & Degroote, 2020) and outside Pettigrew & Taylor (2003) the pipe structure. Earlier studies are mostly of analytical or experimental nature (Paidoussis, 1998) because numerical studies were long deemed to costly to perform. However, with the advent of large computational power, more and more numerical studies of two-phase flows are being published. Numerical analyses provide the advantage that all details of the flow can be examined, which potentially yields the opportunity to better understand excitation mechanisms. As such, Belfroid et al. (2016) have shown that the forces and subsequent vibrations of a bend subjected to two-phase are related to the occurrence of liquid slugs entering the bend. They have also reported a semi-empirical model which could predict the force profile adequately based on measurement input of pressure and void fraction prior to the bend. Their results have been validated in the numerical study by Mack et al. (2018). However, since the study by Mack et al. (2018) was based on a rigid tube geometry, the amplitude of the vibration as well as the damping characteristics were not calculated. A major goal of this research is to include a fluid-structure interaction (FSI) simulation on the same geometry to verify that the vibration can be modelled with a partitioned FSI approach and to check the influence of certain structural boundary conditions on the amplitude, frequency and damping of the vibration. However, a full-scale FSI simulation on this geometry was not yet completed, but the structural model will be discussed in more detail. As previous research in our department (De Moerloose & Degroote, 2020) has shown that fluid side

boundary conditions potentially have a major effect on the simulation outcome, these conditions will be discussed in more detail.

In the first part of this paper, the numerical model applied in the fluid is discussed. Subsequently, the paper focuses on simulations in a rigid tube geometry to investigate the effect of the in- and outlet boundary conditions on the fluid side. Finally, the structural solver settings and some preliminary results that have been obtained, are discussed.

2. FLOW INSIDE A RIGID TUBE

2.1. Two-phase flow modelling

The basic geometry consists of an entrance tube with an inner diameter (D) of 0.15 m and 12.36 m length, a 90° bend in the horizontal plane (with a bend radius of 1.5D) and an outlet tube with length 3 m, followed by an upward bend. The wall is 9.15 mm thick, in compliance with ISO standards for 6" piping. The bend in the horizontal plane is the one under investigation and the total force acting on this piece is extracted from the simulation data. The geometry is shown in Figure 1a, as well as a cross-section of the mesh in Figure 1b.

Inside the tube, a water-air mixture is imposed. Both the water and the air are assumed to be incompressible. The air and water densities are 1.205 kg/m^3 and 998.3 kg/m^3, respectively. The air and water viscosities are set to 1.8208×10^{-5} Pa·s and 1.002×10^{-3} Pa·s. Finally, the surface tension between both phases is set to 0.07275 N/m. With respect to the two-phase flow modelling, the one-fluid approach is adopted. This signifies that only one mass and one momentum equation are solved for the mixture, wherein the density ρ_m and dynamic viscosity μ_m are considered as mixture variables (which change from cell to cell):

$$\rho_m = \alpha_w \rho_w + (1-\alpha_w)\rho_a \quad (1)$$

and

$$\mu_m = \alpha_w \mu_w + (1-\alpha_w)\mu_a \quad (2)$$

where the indices w and a denote the properties of water and air, respectively. The variable α_w is defined as the volume fraction of water present in a specific cell. Assuming a mixture viscosity as in Equation 2 is commonly done in the one-fluid approach. In order to close the one-fluid model, a scalar transport equation for α_w is solved. In the open-source, finite volume package OpenFOAM® 4.1 (more specifically the solver *interFoam*), the scalar transport equation is the following:

$$\frac{\partial \alpha_w}{\partial t} + \nabla \cdot \left(\alpha_w \vec{U}\right) + \nabla \cdot \left[\alpha_w (1-\alpha_w)\vec{U}_{lg}\right] = 0. \quad (3)$$

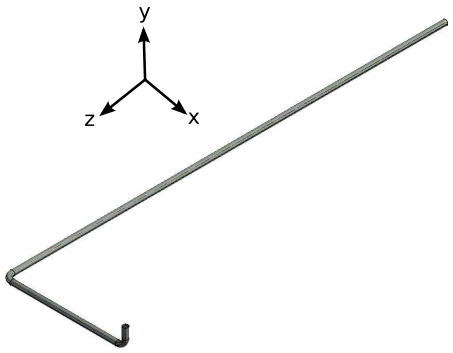

(a)

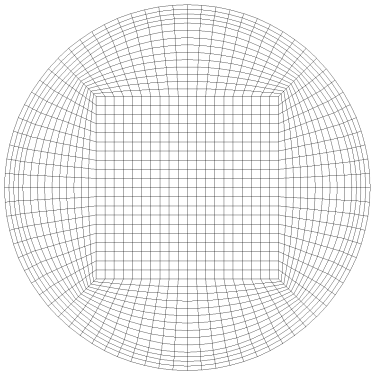

(b)

Figure 1. (a) View of the fluid domain used in the base case and (b) mesh in the cross-section of the tube.

The last term on the left hand side of Equation 3 is non-zero only at the boundary and disappears for an ideal (sharp) interface. This term serves to improve the sharpness of the interface between the two phases. The parameter U_{lg} is a model parameter, as explained more extensively in Damián (2013).

The equations described above are solved with Unsteady Reynolds-Averaged Navier–Stokes (URANS) simulations, supplied with the k-ω SST turbulence model for closure. Two substeps per time step are used for the solution of the transport equation of α_w. The number of correctors is also set to two. The iterative solution for α_w employs a symmetric Gauss-Seidel smoother with a tolerance of 1×10^{-8}. For U and the turbulence quantities a tolerance of 1×10^{-6} is applied. A preconditioned conjugate gradient (PCG) solver combined with a generalized algebraic multigrid (GAMG) preconditioner is used for $p_{rgh} = p - \rho g h$. The tolerance on the pressure is 1×10^{-5}. It is noteworthy that preliminary tests with the Diagonal Incomplete Cholesky (DIC) preconditioner led to high-frequent oscillations which

were superimposed on the force profile. The reason for this is not understood. A central discretization scheme is applied to all gradient terms. The divergence term in Equation 3 is discretized with a Van Leer scheme, while the convective term and the divergence terms containing turbulence variables k and ω are discretized with a second-order upwind scheme. The remaining divergence terms are centrally discretized. For the pressure-velocity coupling, the SIMPLE-algorithm is used with 2 corrector loops. The first order implicit Euler scheme is used to discretize the temporal derivatives. The time step in the CFD simulation is fixed to 5×10^{-5} s.

Before discussing the physical phenomena occurring in the flow, the influence of mesh refinement is analyzed. There is not a complete insensitivity to mesh refinement, due to the use of the Volume of Fluid (VOF) method applied on a geometry where significant mixing is present in the 90° bend. As the smallest bubble size that can be modelled with VOF is on the order of the grid size, finer grids allow modelling of smaller bubbles. However, these bubbles have a negligible effect on the forces exerted on the surrounding structure and are therefore not deemed relevant to this study. As the main point of interest here is the force profile on the 90° bend, the force profiles obtained on different levels of refinement are considered as measure of mesh sensitivity (not shown). Three levels of refinement are constructed, with a cell count of 1421200, 2842400 and 4263600. The Fourier spectrum of the z -component of the force exerted on the 90° bend is used as a measure of mesh sensitivity. As very similar profiles were obtained, it was decided to use the coarsest mesh of 1421200 cells. As a final note, one can consider the location of slug onset as a point of comparison as well. This is more difficult to quantify as the slugs do not always occur at exactly the same location in a single simulation, but a good qualitative agreement was found for all three meshes.

2.2. Force exerted on the bend

In this first case, the U- and α_w-profiles are imposed at the inlet. The bottom half of the cross-section is taken up by water ($\alpha_w = 1$), the upper half by air ($\alpha_w = 0$). The water and air velocities are chosen equal to 4 m/s and 1.8 m/s, respectively (thus yielding a superficial water velocity of 2 m/s and a superficial air velocity of 0.9 m/s). The turbulence intensity is set to 5% and the turbulence length scale is set to $0.07D$. The outlet pipe ends in a vertical bend so as to be able to set a constant pressure p_{rgh} at the outlet, i.e. atmospheric pressure. A zero-gradient condition is imposed on the flow velocity U and on the water volume fraction α_w, as well as on the turbulence variables k and ω. Backflow of water is prohibited at the outlet. It should be noted that OpenFOAM 4.1 applies the zero-gradient condition to a fictitious pressure profile, i.e. the physical pressure p from which a hydrostatic profile based on a density ρ_{local} is subtracted. This density is the local density based on the volume fractions of liquid and air in each cell individually. A no-slip boundary condition is imposed at the walls. The gradient of α_w and of the pressure p_{rgh} are equal to zero at the walls. Wall functions are used for the turbulence properties k and ω.

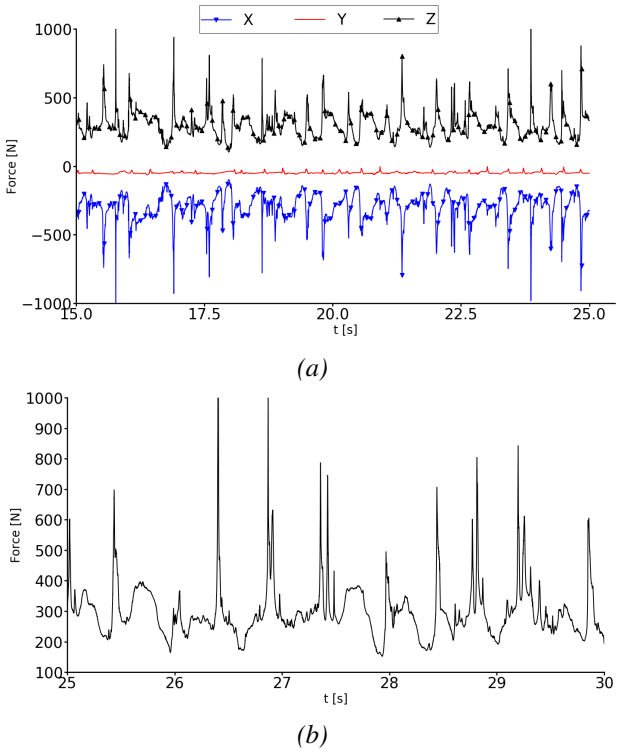

Figure 2. Forces acting on the 90° bend when applying a stratified flow inlet: (a) x-, y- and z-component, (b) zoom on the z-component.

The forces obtained from this simulation, are shown in Figure 2. The force in the y-direction is substantially smaller than (the absolute value of) the other two force components and is mainly influenced by the mass of water present in the tube. However, small peaks in the y-direction also occur and these are related to a rapid increase in the volume fraction of water inside the bend (De Moerloose & Degroote, 2019). The x- and z-components of the force are governed by the momentum change occurring inside the bend and are therefore opposite to each other.

When comparing the force profile in the z-direction shown in Figure 2b to the resulting forces obtained in the experiment by Belfroid et al. (2016), it is clear that the simulations and experiments yield a

force oscillation with amplitude about equal to 200 N (except for the narrow high peaks obtained in experiments, probably related to both the rigid tube and the assumption of incompressible flow in the simulations), but are not close in terms of temporal frequency. The force profile in the experiments - even though not nicely periodic - on average yields a frequency of about 1 Hz, whereas the frequency found from the present simulation is about twice this value. As was shown in De Moerloose & Degroote (2019), the broad force peaks in the bend are closely related to the occurrence of liquid slugs inside the bend. Consequently, it is hypothesized that the slugs in the present numerical simulation are not as developed as those in the experimental set-up. Possibly, the discrepancy between simulations and experiment can be reduced if the inlet condition matches more closely the test set-up.

2.3. Inlet boundary condition

Following the poor correspondence between numerical simulations and experiments in Section 2.2, the fluid domain was adapted such that the inlet would be modelled more closely to the experimental setup. This is why the stratified inlet in the tube was replaced by a Y-piece as shown in Figure 3. Water is applied to the inlet of the main (lower) tube, whereas the air enters the domain through the upper tube, which has a diameter of 0.10 m and is positioned under an angle of 45° with respect to the main tube's axis. To maintain the same mass flow rate through the bend, the water velocity is set to 2 m/s and the air velocity is chosen equal to 2.025 m/s. It can be seen from Figure 3 that the mesh in the Y-piece is unstructured. Therefore, the connection with the swept mesh in the rest of the flow domain is obtained through an interface (not shown).

The forces calculated at the bend are given in Figure 4. As one can see, the frequency of the force is closer to the experimentally obtained value of 1 Hz. The broader force peaks also indicate that the liquid slugs entering the bend are more developed than in the case without Y-piece. However, it is also clear that a high-frequent signal is superimposed on the force-profile. Indeed, the Fourier spectrum of the force in the z-direction (see Figure 5) shows a substantial high-frequent component, which may be of limited importance in the rigid tube simulations, but which may cause stability issues in fluid-structure interaction simulations (see Section 3.2).

2.4. Outlet boundary condition

The hypothesis for the occurrence of high-frequent oscillations in the force-profile was that this due to a

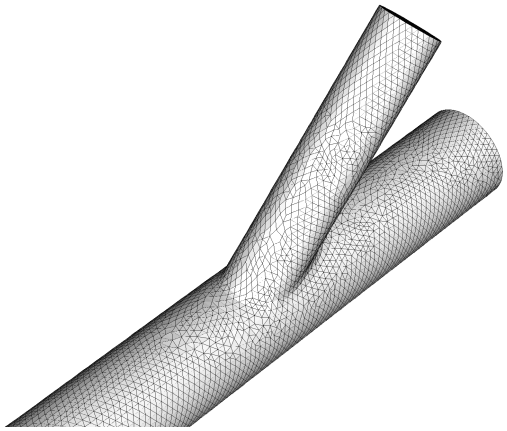

Figure 3. View of the mesh in the Y-piece added at the inlet of the flow domain.

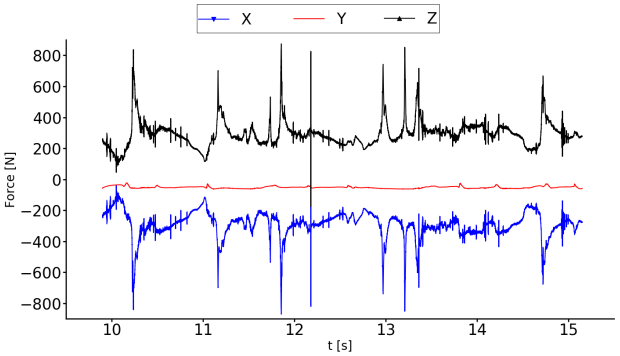

Figure 4. Forces acting on the 90° bend when modelling the Y-piece at the inlet of the flow domain.

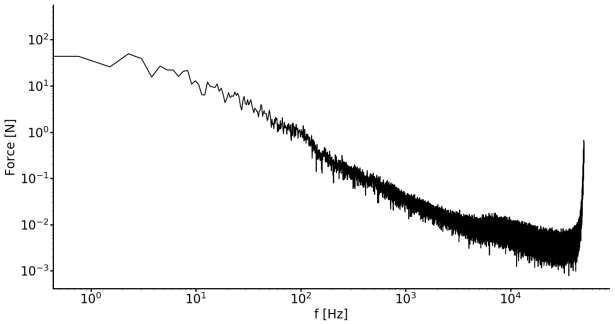

Figure 5. Fourier spectrum of the force acting on the 90° bend in the z-direction when modelling the Y-piece at the inlet of the flow domain. The time series of the force from 9.9 s to 15 s was split up into 4 parts, of which the FFT were calculated individually. The shown result is the average Fourier spectrum.

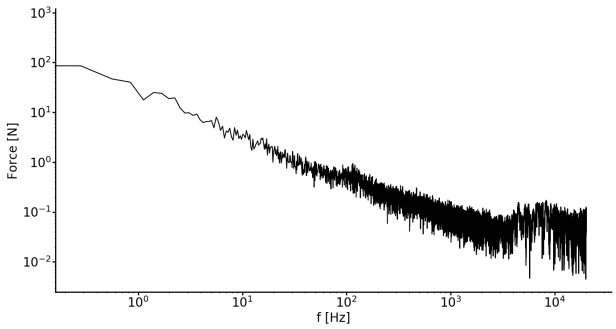

Figure 6. Fourier spectrum of the force acting on the 90° bend in the z-direction when modelling the Y-piece at the inlet of the flow domain and with a long horizontal tube at the outlet. The time series of the force from 5.75 s *to* 20 s *was split up into 4 parts, of which the FFT were calculated individually. The shown result is the average Fourier spectrum.*

numerical instability caused by the presence of two-phase flow at the outlet. This hypothesis is tested by adding a 60 m long pipe after the bend. The cross-sectional view of the mesh does not change in this outlet tube, but the axial length of a cell is increased in order to limit the increase in computational time due to the long outlet tube. The pipe is positioned horizontally so as not to increase the hydrostatic pressure at the bend when the outlet tube would fill with water over time. The resulting Fourier spectrum of the force in the z-direction is shown in Figure 6. Indeed, it seems that that the peak at the highest frequency has disappeared.

3. FLEXIBLE TUBE MODEL

Until now, the tube was assumed to remain rigid. However, both in practical applications as in the experimental set-up, the pipe deforms due to the passing air-water mixture. In order to calculate the displacements provoked by the forces in the bend, a structural model for the pipe is developed.

3.1. Modelling

The tube wall is divided into 2 layers of cells. The inlet tube, bend and outlet tube have 500, 25 and 150 elements along the mean flow direction, respectively. The circumference is divided in 40 nodes. This yields a mesh containing a total of 54000 elements, shown in Figure 7.

The tube is made of steel and is assumed to deform in a linear elastic manner. Consequently, only three material parameters need to be defined: the Young's modulus (205 GPa), the Poisson's ratio (0.3)

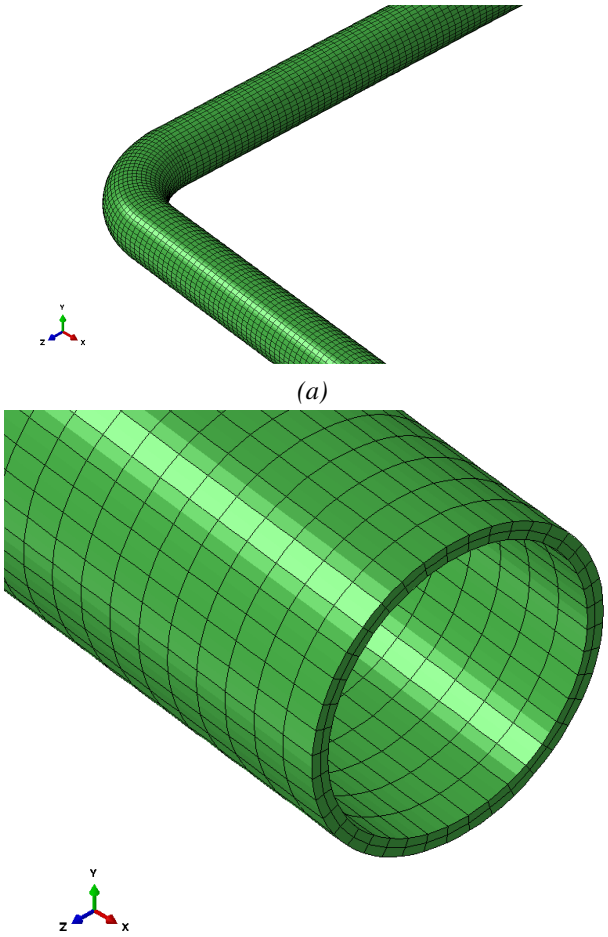

Figure 7. Computational mesh for the bend structure: (a) view of the 90° bend, (b) view of the outlet.

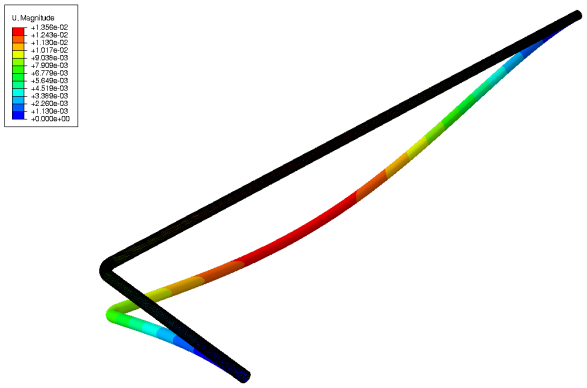

Figure 8. Displacement observed when imposing a sinusoidally varying vertical force at the 90° bend and gravity is working on the structure. The displacement is scaled with a factor of 10^2*. The original position of the structure is also displayed, in black.*

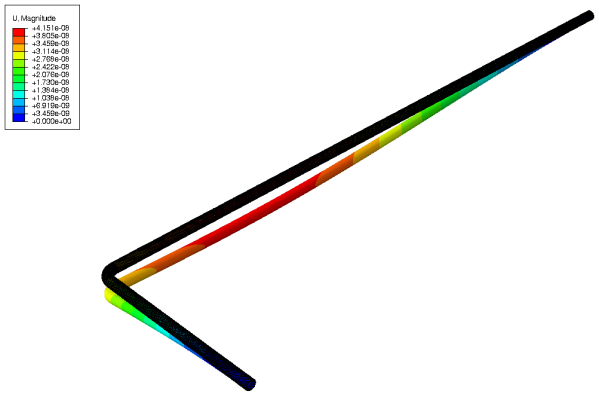

Figure 9. Displacement observed when imposing a sinusoidally varying vertical force at the 90° bend. Gravity is not acting on the tube. The displacement is scaled with a factor of 10^7*. The original position of the structure is also displayed, in black.*

and the density $\left(7800\,\mathrm{kg/m^3}\right)$. This model is constructed in the commercial finite element code Dassault Systèmes® Abaqus® 6.14.

In a first trial, a concentrated force was applied on the bend. This concentrated force varies sinusoidally over time. The amplitude is set to 282 N imposed in such a way that the x - and z-component are about 200 N each - and the frequency is set to 1 Hz. These values are comparable to the force profiles obtained in Section 2.2. Both the inlet and the outlet cross-section of the structural model are assumed to be clamped at the outer tube diameter. The resulting displacement of the bend is shown in Figure 8.

The displacement shown in Figure 8 is likely to be influenced mainly by the tube's weight, both considering the size of the deformation (on the order of 0.01 m) and its direction (mainly in the negative y-direction, which is also the way gravity points in this case). Therefore, the simulation is repeated in the hypothetical case that the tube's weight does not cause any displacement (by removing the gravitational load on the pipe). The resulting displacement at a single time-instant is given in Figure 9. It follows that the deformation caused by the imposed sinusoidal force is on the order of 1×10^{-7} m. However, this is probably an underestimation of the value that would be obtained when applying the force profile from the CFD-simulations on the structure, as the narrow high-amplitude force peaks are not considered in this preliminary calculation.

3.2. Future work: fluid-structure interaction

It is clear that the results obtained with the structural model are preliminary. In the next step of this research, the proposed flow and structural model will be coupled in a partitioned fluid-structure interaction (FSI) simulation. The goal of the FSI analysis is to quantify the vibration characteristics of the bend subjected to two-phase slug flow. The effect of different clamping locations on the vibration amplitude will be analyzed as well.

4. CONCLUSION

The topic of the presented work is an water-air mixture flowing through a horizontal 90° bend. Firstly, the focus is on the fluid domain inside the pipe. The forces on the bend wall are closely related to the occurrence of slugs inside the pipe. It was shown that these liquid slugs can arise due to numerical instabilities if the inlet section is not modelled properly, which yields the wrong oscillation frequency in the bend. The frequency and amplitude of the force on the bend were relatively close to experimental values if the inlet was closer to the experimental set-up. On the other hand, high-frequent oscillations originate in the numerical calculation once the outlet is exposed to two-phase flow. This is probably due to the modelling of the variable p_{rgh} - the static pressure minus a hydrostatic component based on the local density in the cell. Secondly, a structural model for the tube is presented in this work. Some preliminary results are shown in the paper, but the main goal is to combine the structural and the flow model in order to perform fluid-structure interaction simulations. From these, the bend vibration under influence of the internal two-phase flow will be determined.

5. ACKNOWLEDGMENTS

The authors gratefully acknowledge the funding by the Research Foundation-Flanders (FWO), Belgium, through the Ph.D. fellowship of Laurent De Moerloose. The computational resources (Stevin Supercomputer Infrastructure) and services used in this work were provided by the VSC (Flemish Supercomputer Center), funded by Ghent University, FWO and the Flemish Government department EWI.

6. REFERENCES

Atadan, A. et al., 1997, Analytical and numerical analysis of the dynamics of a marine riser connected to a floating platform. *Ocean Engineering* **24**: 111-131.

Belfroid, S. et al., 2016, Multiphase forces on bends - large scale 6" experiments. *SPE Annual Technical Conference and Exhibition, Dubai, UAE, 26–28 September 2016*

Damián, S., 2013, *An extended mixture model for the simultaneous treatment of short and long scale interfaces*, Ph.D. Thesis, Universidad Nacional del Litoral.

De Moerloose, L. & Degroote, J., 2019, Numerical investigation of an air-water flow through a 90° bend in 6" piping. *Proceedings of 10th International Conference on Multiphase Flows (ICMF 2019), Rio De Janeiro, Brazil, 19-24 May 2019.*

De Moerloose & Degroote, 2020, A study of the vibration of a horizontal U-bend subjected to an internal upwards flowing air-water mixture. *Journal of Fluids and Structures* **93**: 102883.

Ma, B. et al., 2019, On slug flow-induced vibration in long bendable curved pipe. *Proceedings of 10th International Conference on Multiphase Flows (ICMF 2019), Rio De Janeiro, Brazil, 19-24 May 2019.*

Mack, A., et al., 2018, Numerical rebuilding of dynamic instabilities and forces in multiphase pipe bend flow. *International Journal of Computational Methods and Experimental Measurements* **6(2)**: 358-372.

Miwa, S. et al., 2015, Two-phase flow induced vibration in piping systems. *Progress in Nuclear Engineering* **78**: 270-284.

Paidoussis, M.P., 1998, *Fluid-structure interactions: slender structures and axial flow*, Academic Press.

Pettigrew, M. & Taylor, C., 2003, Vibration analysis of shell-and-tube heat exchangers: an overview - part 1: flow, damping, fluidelastic instability. *Journal of Fluids and Structures.* **18**: 469-483.

Semler, C. et al., 1994, The non-linear equations of motion of pipes conveying fluid. *Journal of Sound and Vibration* **169(5)**: 577-599.

Srinil, N. et al., 2004, Three-dimensional non-linear coupling and dynamic tension in the large-amplitude vibrations of arbitrarily sagged cables. *Journal of Sound and Vibration* **269**: 823-852.

Srinil, N. et al., 2018, Experimental investigation on in-plane/out-of-plane vortex-induced vibrations of curved cylinders in parallel and perpendicular flows. *Journal of Sound and Vibration* **421**: 275-299.

HIGH PRESSURE MULTIPHASE INDUCED VIBRATIONS: INFLUENCE PIPE ORIENTATION

S. Belfroid, N. González Díez
TNO, Delft, The Netherlands

K. Lunde, S. Orre
Equinor, Stavanger, Norway

ABSTRACT

Three experimental campaigns were done at an industrial-scale test site to measure the influence of pressure on the forces induced by multiphase flow in process piping. For these different campaigns, measurements were done at 10, 25, 45 and 80 bar, involving different fluids (natural gas, MEG, oil, CO_2) and different orientation of the test section with regards to gravity (horizontal and vertical). During the experiments, the vibrations were measured at a large range of flow conditions and regimes.

In this paper, the results obtained for the latest campaign are described. The main goal of this campaign was to study the sensitivity of the measurements to the orientation of the test section with regards to gravity. It was observed that the vibration amplitude at 80 bar is much lower than at 10 bar at similar gas and liquid rates. This reduction can be attributed to a generally lower hold-up and lower unsteady hold-up variations at higher pressures, due to the higher gas shear forces and the resulting lower slip. At the test conditions, no effect of pipe orientation was observed for in-plane vibrations. The out-of-plane vibrations were much lower in vertical orientation compared to the horizontal orientation at lower pressures. At higher pressures, these differences disappeared, which is connected to a better mixing of the flow.

1. INTRODUCTION

Multiphase flow induced vibration is a serious risk in almost all industries working with multiphase fluids. This includes oil&gas, process industry, nuclear but also a lot of steam systems are affected. Typically, dynamic loads are exerted on pipe bends and other flow fittings when operating under multiphase flow conditions. Generally, two families of multiphase flow induced vibrations are differentiated: one connected to system instabilities and one connected to flow instabilities. The first family is roughly identified as featuring time scales much longer than those associated to the natural vibration characteristics of the piping under consideration: for example, single slugs such as severe slugging, terrain-indued slugging or start-up slugs (Tijsseling, 2016). The second family is identified as featuring unsteady flow phenomena whose time-scale is short, comparable to the time scales associated to the mechanical natural frequencies of the piping. An example for this family is vibration arising from hydrodynamic slugging at typical frequencies of 1-5 Hz. Despite the examples mentioned for both families, the issue is not limited to slugging conditions.

For the second family of excitations connected to flow instabilities, a great deal of experimental attention (Riverin, 2006; ; Cargnelutti, 2010; Liu, 2012; Giraudeau, 2013; Tay, 2013; Belfroid, 2016), CFD (Emmerson, 2016; , Macchion, 2019) as well on modelling (Tay, 2013; Nennie, 2013; Miwa, 2014; Klinkenberg, 2021) have led to significant advances in the understanding of the subject. From experiments at low pressure, it could be concluded that for the multiphase flow conditions which lead to high vibrations, the induced forces are partly due to dynamic momentum forces and partly due to the induced pressure fluctuations in the bend. The pressure fluctuations are due to local turbulence, time-dependent pressure drop across the bend and due to changes in the overall pressure drop in the test section due to slugs/waves entering and exiting the test system. Other phenomena such as local turbulence, centrifugal forces and redistribution and formation of swirl play a role too, but can often still be attributed to the dynamic hold-up variations.

Most experimental campaigns involve two-phase air-water flows at near atmospheric conditions, while many systems actually operate at elevated pressures. Therefore, high pressure experiments (10, 25, 45, 80 bar) were setup at an industrial-scale test site at Equinor Porsgrunn. In this site, three experimental campaigns were done in recent years. The year in which the campaign is executed also serves as a label for the remainder of this paper:

- 2018 campaign: first experiments at high pressure performed in a horizontally oriented double U-loop configuration with different fluids (gas-MEG, gas-oil, gas-MEG-oil (Belfroid, 2020).
- 2021-CO2 campaign: experiments targeting the same information as in 2018 but address-

ing the particularities of CO_2 at multiphase flow conditions (Belfroid, 2022).

- 2021 campaign: gas-MEG experiments studying the effect of vertical configuration of the small U-loop of the test section (Figure 2).

In this paper, focus is placed on the third campaign (2021). The vibration experiments were done as much as possible at the same gas and liquid volume rates to be able to compare it with the 2018 campaign. In addition, two secondary goals were set: (i) expand investigation at low liquid fraction cases; (ii) obtain frequency content below 1 Hz. Therefore, next to the main test series (at 5.8 and 11.5 m^3/hr liquid rate), data series were gathered at low liquid rates down to 1 m^3/hr. Measurements with static accelerometers and video recording are added to obtain frequency content below 1 Hz. In addition, next to the usual instrumentation, a gamma-densitometer present at both the inlet and outlet was introduced in the 2021 campaign. The outlet sensor was sampled at the same frequency as the vibrations. This allowed the back-calculation of wave characteristics.

In this paper, the base results of the vibrations measurements comparing horizontal and vertical orientations is described. Model predictions for the force based on the density measurements is also discussed.

2. EXPERIMENTS

2.1. Experimental setup

The vibration loop used for the vibration experiments consist of a double 2"-sized U-loop (Figure 1) with an outer loop of 2×2m and an inner loop of 1.5×1.5m (Table 1), separated from each other with clamps.

Compared to the 2018 campaign, in 2021, the smaller U-loop was placed vertically. The exact same piping was used including the same clamps and concrete. The small loop was cut, rotated and welded close to the sharp U-loop between the clamps separating the large and small loop. More details on the 2018 setup can be found in Belfroid 2020. The other major difference between 2018 and 2021 is related to the inlet configuration. In 2018, the inlet configuration consisted of a long 3" inlet with a sharp tee-piece to the vibration loop. In 2021, the flow was first diverted upward through a measurement section before entering the vibration loop via a sharp tee. It is expected that the flow entering the test section is more mixed at the 2021 setup in comparison to the 2018 setup.

2.2. Instrumentation

The measurements at flowing conditions were obtained with four vibration sensors and four strain sensors. The vibration sensors were installed in the middle of the U-loops and at the legs (Figure 1). In the 2021 setup, the upstream section was instrumented to measure the pressure, mixture flow rate and density (Coriolis and gamma densitometer), as well as individual volume rates and densities for the liquid and the gas phase. Downstream, a pressure and gamma-densitometer was placed. The process data was sampled at 1Hz, except for the downstream gamma densitometer which was sampled at 1 kHz. Vibration measurements are also sampled at 1 kHz. At each condition, 15 minutes of data is gathered.

2.3. Fluid properties

The fluid properties used across the campaigns are summarized in Table 2. Test conditions in 2018 and 2021 are very similar. The MEG purity was slightly different but does not lead to large differences. The gas density in 2021 was slightly lower than in 2018. Therefore all comparison between the 2018 and 2021 results are done as function of the (no-slip) mixture kinetic energy ($\rho_m u_m^2$).

Table 1 : Overview pipe dimensions.

Pipe diameters	ID = 52.48, OD = 60.3 mm
Bend radius	1.5D
Lengths large loop	1900, 2000, 2000, 2000, 1850 mm
Lengths small loop	2000, 1500, 1500, 1500, 2000 mm

Table 2: Overview fluid properties.

	2018	2021 CO2	2021
Pressure [bar]	10, 25, 45, 80	45, 55	10, 25, 45, 80
Temperature [°C]	26	10, 18	27
Density [kg/m^3]			
Gas	10 – 66	132, 176	6.4 – 58
MEG	1080		1090
Oil	670		
Liquid CO2		861, 791	
Viscosity [cP]			
Gas	0.012	0.016,	0.012
MEG	12	0.017	8.5
Oil	0.3		
Liquid CO2		0.086, 0.070	
Surface Tension [mN/m]			
Gas – MEG	31		45 (30 bar)
Gas – Oil	14 (23 bar)		
CO2		2.85, 1.5	

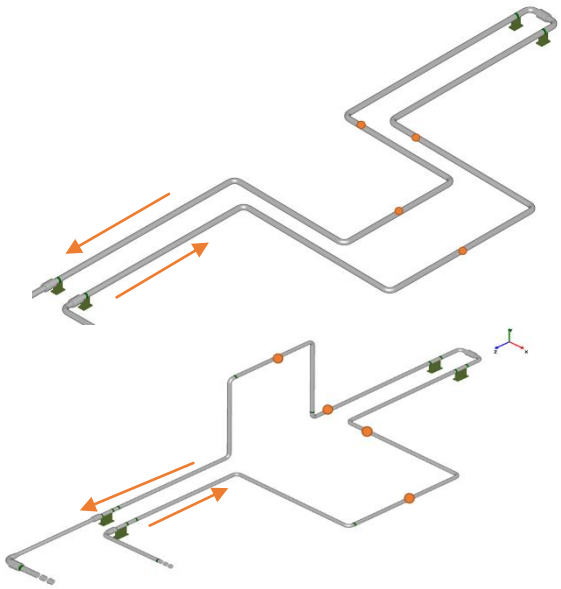

Figure 1 : Detail test setup including sensor location of 2018 (top) vs (2021) configuration (orange marks).

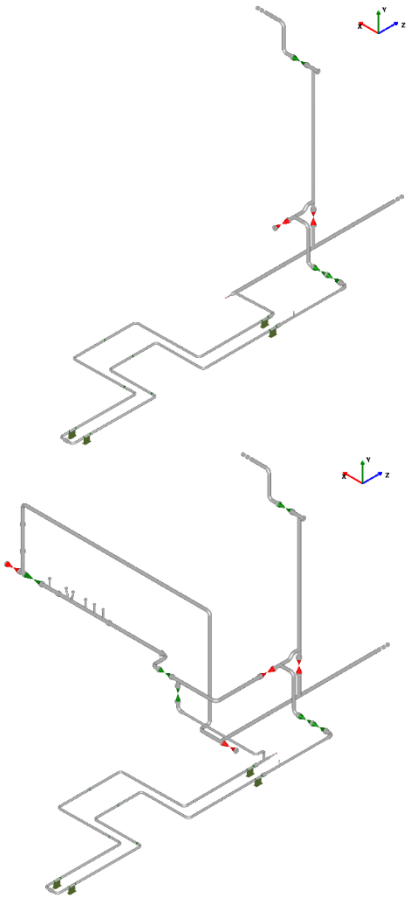

Figure 2: Comparison inlet/out configurations of 2018 (top) vs 2021 (left) configuration.

3. RESULTS VIBRATIONS

The basic vibration results of the 2021 experiments (vertical) are compared to the 2018 measurements (horizontal) in Figure 3. For the large loop (which remains horizontal in both campaigns), the comparison is very good at 10 and 80 bar. For the 25 and 45 bar cases, the vibrations are stronger in 2021. It is unlikely that this is due to the vertical small U-loop, as any flow instabilities (loading, back flow, churn/slug) should be more apparent at lower pressure. In addition, the damping of the large loop is not different between the 2018 and 2021 experiments. It is hypothesised that the differences are due to the difference in flow regime developed. The flow in 2021 is likely more mixed before it enters the vibration loop compared to the 2018 geometry. In addition, the 2021 inlet configuration featured a 3-dimensional bend right upstream, which might introduce swirl.

For the small loop, the comparison between the 2018 and 2021 experiments is also very good except for the out-of-plane vibrations, especially at 10 bar. For the vertical orientation, the out-of-plane vibrations are much lower than for the horizontal orientation, especially at the lower pressures. This can also be seen in the damping (Figure 4). In this figure, the damping for the in-plane and out-of-plane direction for the large and small loop is depicted. The damping was measured by imposing a displacement (in different directions) and by fitting the exponential decay. For more details on the method it is referred to Belfroid, 2020.

For the in-plane direction, there are no differences between the small and large loop. For the out-of-plane direction, the damping in the small loop is much higher at low pressure. At low pressure, the flow regime is mainly stratified. This means that in vertical orientation the out-of-plane direction is such that the gas/liquid interface can introduce a sloshing motion. In the horizontal layout, the out-of-plane direction is perpendicular to the gas/liquid interface. At higher pressures, the flow is more mixed, leading to smaller differences in vibration direction and therefore also damping.

It must be noted that at the tested conditions, no loading effects due to the elevated pressures are expected. Therefore no large scale slugging conditions could be tested. In small scale experiments (air -water, low pressure) large differences in excitation were measured between horizontal and vertical orientations (Pereboom, 2022). Therefore, the statement that only a weak influence of the orientation is found is valid only for the test conditions described in this paper.

4. DYNAMIC HOLD-UP AND FORCE

Lower vibration amplitudes can be caused by :

- Lower excitation forces
- Higher effective damping
- Better coupling between excitation spectrum and resonance frequencies. That is, the peak frequency in excitation spectrum matches better with resonance modes at 10 bar than at 80 bar.

For the 2018 experiments it was already shown that the damping at 80 bar is lower than at 10 bar (or at least not higher). In addition, no clear shift in the

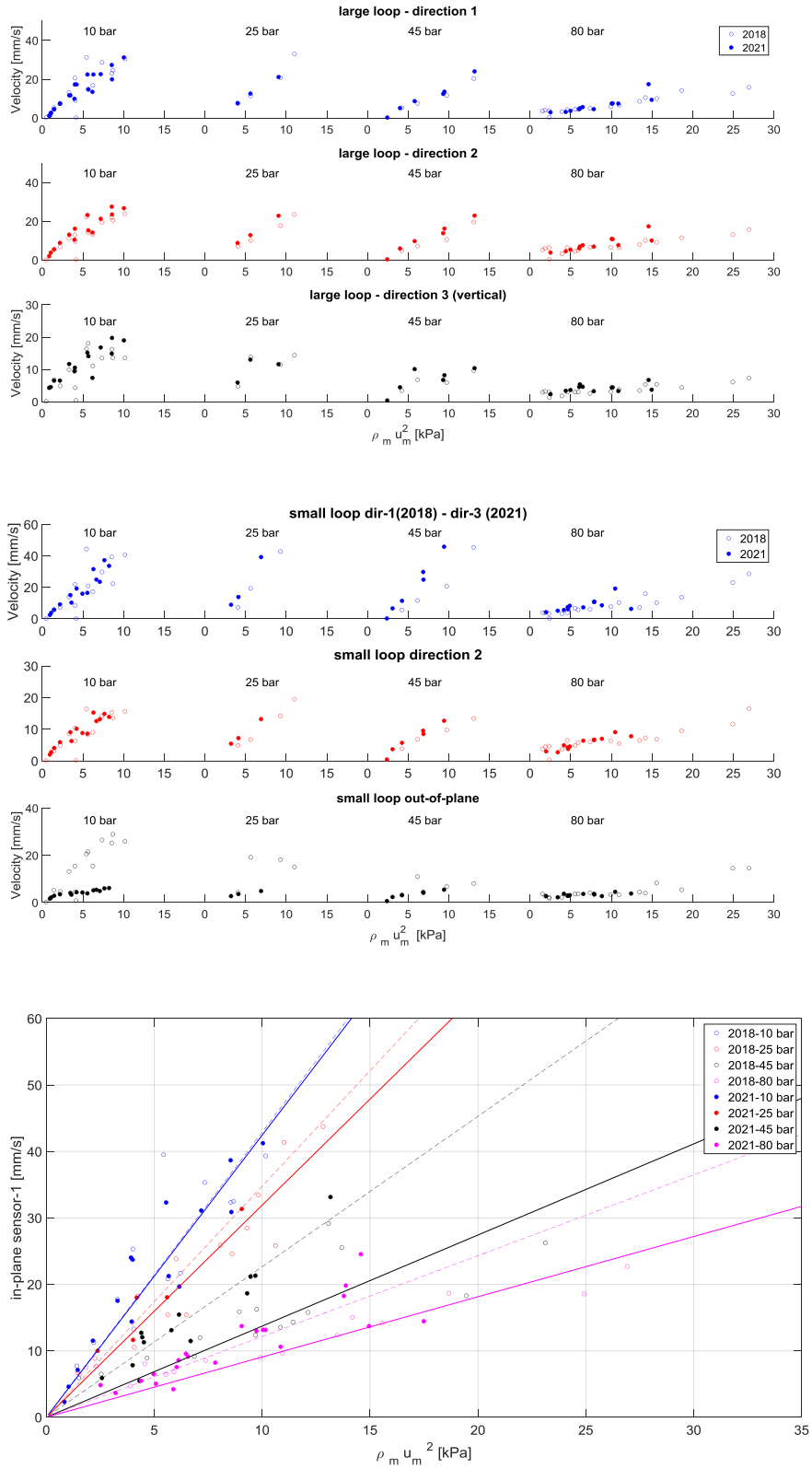

Figure 3: Detailed comparison of vibration velocity for small loop (top) and large loop (middle) in 2018 and 2021. 1 = x direction, 2 = z direction , 3 = y (vertical) direction (see Figure 1). For the large loop, results are offered with trend lines in the bottom plot

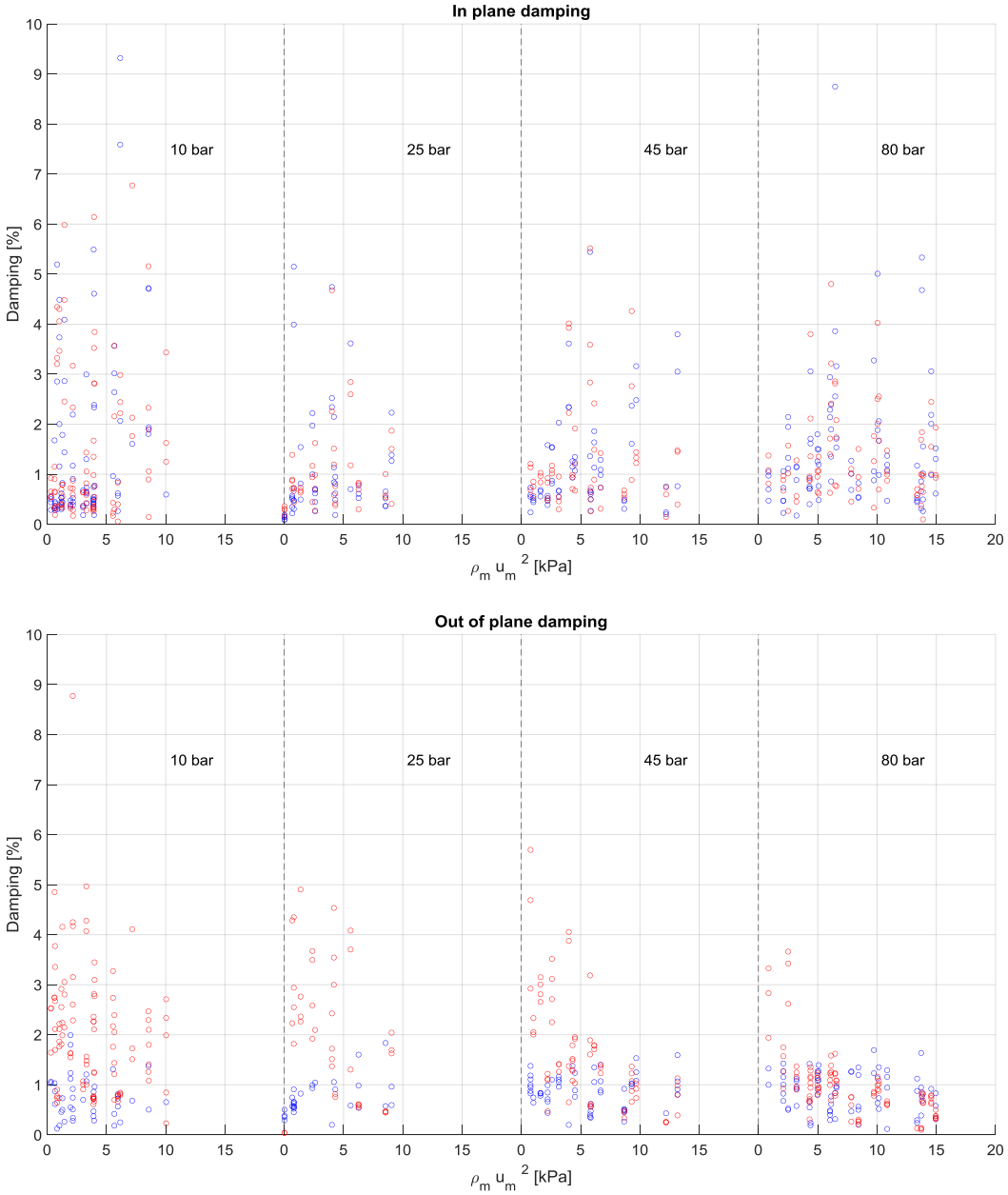

Figure 4 : Comparison in-plane and out-plane damping small (red markers) vs large loop (blue markers).

excitation peak frequency was found between different pressures. Therefore, the main reason for the lower vibrations is the reduced excitation force. This remains even if a correction us made for a slight increase of the total mass of the pipe + fluid at higher pressures.

The dynamic force of the fluid on a bend (F_{bend}) can be written as (Klinkenberg, 2021):

$$F_{bend} = \int_{CS} p\boldsymbol{n}\ dA - \int_{CS} \boldsymbol{v}\rho(\boldsymbol{v}\cdot\boldsymbol{n})dA\ - \frac{d}{dt}\int_{CV} \boldsymbol{v}\rho\ dV$$

in which *CS* indicated control surface, *CV* control volume, ρ the fluid density, A the cross-sectional area and v the velocity vector.

For the 2021 experiments, the downstream hold-up could be measured at high frame rate using a gamma-densitometer. The pressure measurements (downstream) allow calculation of the 1st term of the force. The hold-up measurements via this downstream gamma-densitometer allows calculation of the 2nd term. The 3rd term cannot be reconstructed at this time. Perhaps this might be done by using the measured hold-up variations and assuming these are transported at constant velocity through the bend. But this term is neglected at this moment. This is also based on the fact that for the JIP measurement (Belfroid, 2016) it was shown that the measured force matched well with:

$$F(t) = p(t)A + \rho(t)u_t^2 A$$

The pressure term from the downstream sensor is not used in the 2021 campaign (Figure 5). The measured variations in the downstream pressure are either at low frequency or the variations are so low that these are not picked up by the static pressure sensor. In future tests, a higher sampling rate on the pressure sensor needs to be used.

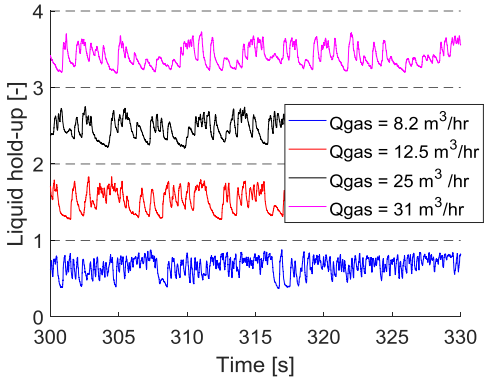

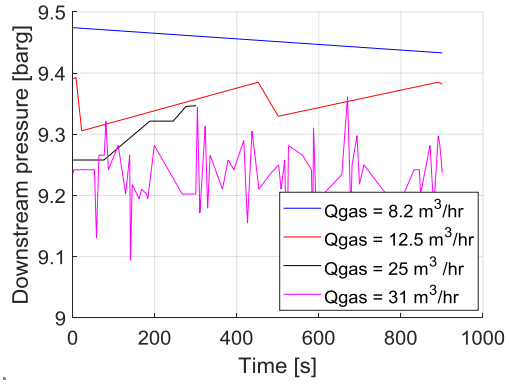

Figure 5: Details of hold-up variation (top) and downstream pressure fluctuation (bottom) of 2021-10 bar – Qliq = 11.8 m³/hr.

The measured mean hold-up was in agreement to the expected hold-up based on OLGA steady state predictions (Figure 6). The measured hold-up variations are plotted as function of the mean hold-up in Figure 7. Two main trends can be observed:

- Large variations at higher hold-up.
- Lower hold-up variation at the same hold-up at higher pressures.

This is also shown in Figure 8, in which the hold-up variation is plotted as function of pressure for four reference conditions (low and high liquid rate, low and high gas rate). At a given condition, the hold-up variations decrease almost linearly with the pressure. For the same cases the vibrations are plotted as function of the hold-up variations in Figure 9. In this figure, the pressure effected is included. The increase in vibrations are linearly related to the hold-up variations.

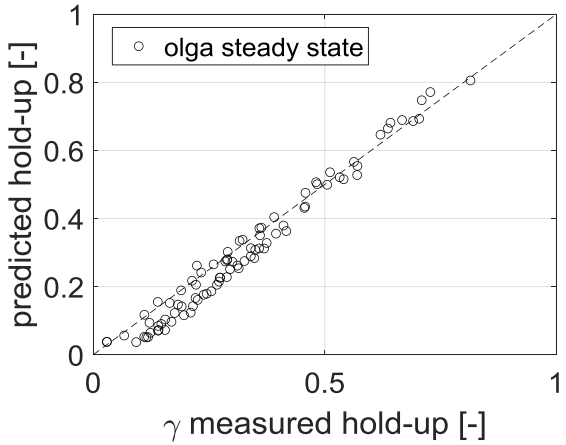

Figure 6: Predicted hold-up as function of measured hold-up.

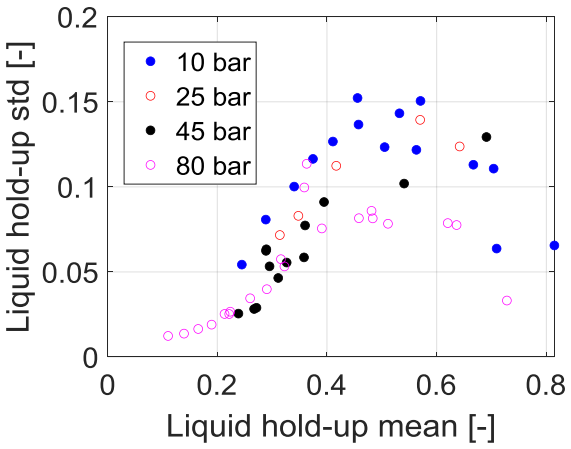

Figure 7 : Standard deviation of]hold-up as function of mean hold-up.

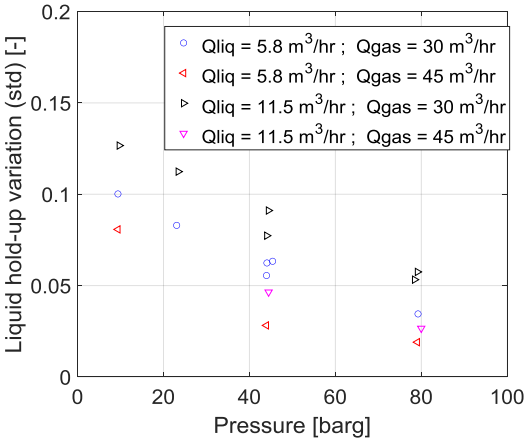

Figure 8: Liquid hold-up variations as function of pressure.

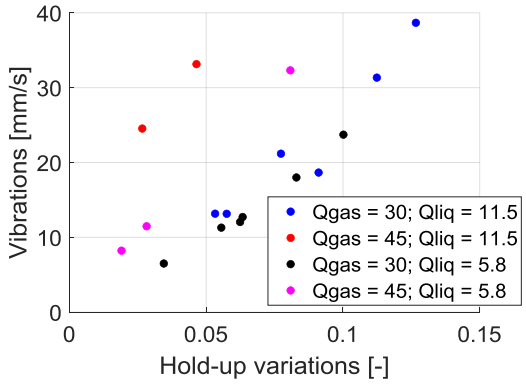

Figure 9: Vibration velocity as function of hold-up variation.

As the vibrations are directly linked to the hold-up variations, the measured (reconstructed) forces are compared to the modelled forces using the hold-up data, according to different options for the transport velocity of the hold-up variations. From the vibration data, the excitation forces are reconstructed (back calculated) via an inverse method. In the frequency domain, the Power Spectral Density (PSD) of the stress or vibration at a location due to forces at N locations can be calculated according to:

$$S_\sigma(\omega) = \sum_{i,j=1}^{n} H_i^*(\omega) S_{ij}(\omega) H_j(\omega)$$

with H the transfer function from the force location to stress location and S_{ii} the PSD of the force on location i. The cross terms includes the time (phase) difference between forces at the different locations. In case a fixed time difference t_0 is present (which can be in the case of a pure slug flow in which the t_0 is the translation time between the two locations), the cross terms become for instance for the location 1 and 2:

$$S_{12}(\omega) = S_{11}(\omega) \text{ and } S_{21}(\omega) = S_{11}(\omega) e^{-i\omega t_0}$$

The following steps are done:

- Calculate the transfer function from each bend to each sensor. This is done by putting a total unit force at a 45 angle at each bend. As the U-bends are slightly sagging at their own weight, the force has a small vertical (out-of-plane) component. The transfer functions are calculated up to 50Hz with a step size 0.05Hz. The transfer is calculated assuming a single hold-up condition.
- Calculate the Power Spectral Density of the displacements at each sensor.
- Calculate the force at each bend. It is assumed that the force PSD at each bend is the same for all bends. This results in 12 reconstructed forces, one for each of the four sensors and the three sensor directions.

The sensitivity for the vertical force is very large and is therefore not included in the analysis. The fact that the model frequencies are not completely equal to the measured resonance frequencies leads to errors of approximately 10%. Errors in the assumed damping lead to less than 1% error. The back calculation to the force is for this paper done assuming non-correlated forces and an assumption of 1% or 2% damping ratio.

The dynamic component of the force is calculated based on different options for the transport velocity of the hold-up fluctuations:

$$F_1(t) = \rho_m(t) u_m^2 A_{pipe}$$
$$F_2(t) = \rho_l u_m^2 \alpha_l A_{pipe}$$
$$F_3(t) = \rho_l u_l^2 \alpha_l(t) A_{pipe}$$
$$F_4(t) = \rho_l u_m u_t \alpha_l(t) A_{pipe} \quad ; \quad u_t = 1.2 u_m$$

The estimation for F_1 is based on instantaneous mixture properties and the main hold-up fluctuation have a velocity equal to the mixture velocity. In estimation F_2 the assumption is made that the momentum forces are mainly due to the liquid phase

but that the variations basically flow with the mixture velocity. This method is very similar to the F_1 as the liquid density is dominant in the mixture density. In F_3, the force is calculated based on the actual liquid velocity (u_{sl}/α_l) but only the actual liquid area is included. Finally, for F_4 the assumption is the same but that the waves/slugs themselves travel with a bubble velocity which in this section is taken as $u_t = 1.2u_m$. Of course other formulations are possible such as the total momentum ($F = \rho_l u_l^2 \alpha_l A + \rho_g u_g^2 \alpha_g A$) but these did not lead to better predictions.

In Figure 10, the predicted forces are compared to the measured (reconstructed) forces. At 10 bar, a reasonable comparison between predicted and measured forces is found for the cases with a mixture velocity, rather than the liquid velocity. For the 80 bar, the predicted forces have the same bias compared to the 10 bar cases. The predicted forces are approximately 25% lower than the measured forces for both 10 and 80 bar. The prediction method also was able to show the reason for the outlier in the 80 bar results (9 N at 15 kPa). It must be remarked that the pressure forces are not included. CFD showed (Emmerson, 2021) that at low pressure the momentum forces are dominant in contrast to the high pressure case where the pressure fluctuations are more important. This would mean that the comparison at 10 bar should be good and that potentially at 80 bar, the calculated forces should be underestimated.

5. CONCLUSION

The vibrations were measured at low (10bar) to high pressure (80 bar) conditions to determine the pressure dependency of the multiphase induced forces in three measurement campaigns. At higher pressures, the measured vibrations were significantly lower that at low pressure, with a factor 4 between 80 compared to 10 bar conditions. The decrease in the measured vibrations is not due to total mass effects, an increased effective total damping ratio at higher damping or a larger mismatch between the excitation spectrum and the mechanical resonance modes. The reduced vibration can be coupled directly the reduced force amplitude. The reduced forces at higher pressures are caused by the lower hold-up variations at a lower mean hold-up. This in itself is due to the increased gas shear forces and increased gas and liquid entrainment. The forces can be predicted reasonably well based on base modelling of the mean hold-up and the expected associated hold-up variations.

At the tested conditions, the orientation (vertical, horizontal) does not matter with respect to the in-plane vibrations. For the out-of-plane vibrations, the vertical orientation has a much larger effective damping which does result in lower vibrations in that direction. This larger damping is reduced at higher pressures as the flow becomes more mixed.

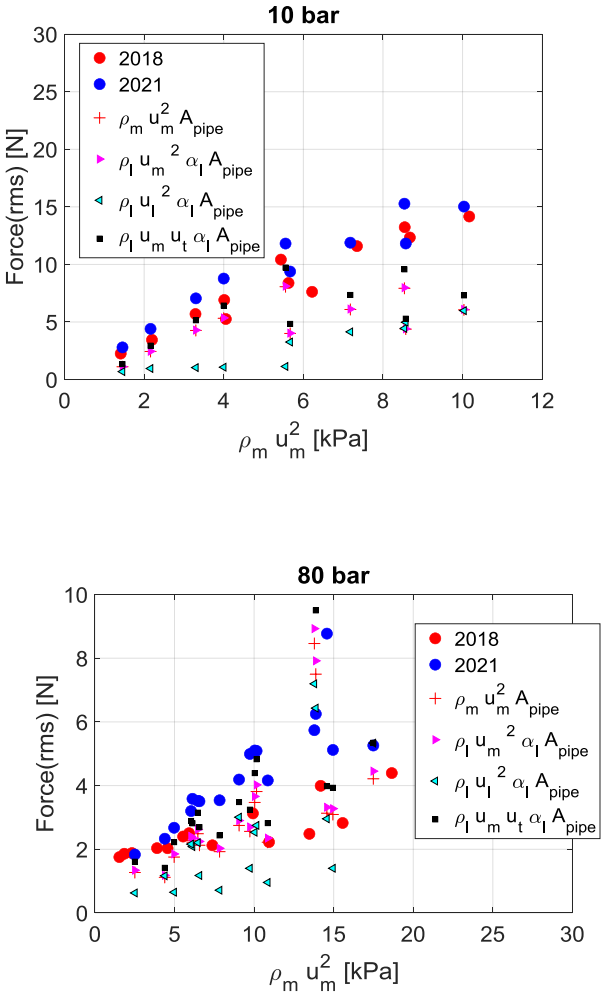

Figure 10: Comparison dynamic forces as function of mixture energy for measurements 10 and 80 bar- with different prediction methods.

6. REFERENCES

Belfroid, S.P.C. et.al, 2016, Multiphase forces on bend structures – overview of large scale 6" experiments, 11th International Conference on Flow-Induced Vibrations, The Hague

Belfroid, S.P.C, Nennie, E., Lewis, M., 2016. Multiphase force on bends – large scale 6" experiments. ATCE 2016, Dubai. SPE-181604-MS

Belfroid, S.P.C. et.al, 2020, Multiphase flow induced vibrations at high pressure, PVP2020-21139, ASME PVP, Minneapolis, Minnesota, USA.

Belfroid, S.P.C, Orre, S., Bazuin, R., Lunde, K., 2022, Two-phase flow induced vibrations with CO2 multiphase flow, OMAE2022-78693, Hamburg, Germany.

Cargnelutti M.F., Belfroid, S.P.C., Schiferli, W. 2010. Two-phase flow-induced forces on bends in small scale tubes, *Journal of Pressure Vessel Technology* 132. http://dx.doi.org/10.1115/1.4001523

Emmerson, P. et. al., 2016, CFD validation of flow induced forces in 6"piping caused by slugging flow, 11th International Conference on Flow-Induced Vibration, The Hague

Emmerson, P. et.al, 2021, Multiphase flow induced vibrations at high pressure: CFD analysis of multiphase forces, OMAE2021-62873

Giraudeau, M., Pettigrew, M., Mureithi, N. W. 2013. Two-phase Flow-Induced forces on piping in vertical upward flow: Excitation mechanisms and correlation model. *Journal of Pressure Vessel Technology* 134. http://dx.doi.org/ 10.1115/1.4024210

Klinkenberg, A.M., Tijsseling, A.S., 2021, Stochastic mechanistic modelling of two-phase slug flow forces on bends in horizontal piping, *IJMF* 144, https://doi.org/10.1016/j.ijmultiphaseflow.2021. 103778.

Liu, y., Miwa, S., Hibiki, T. et.al. 2012. Experimental study of internal two-phase flow induced fluctuating force on a 90degree bend. Chem. Eng. Science (76) : 173-187
http://dx.doi.org/10.1016/j.ces.2012.04.021

Macchion, O., et.al, 2019, Fluctuating forces in a large ID pipe due to multiphase flow, BHR Group MPT2019, Cannes, France

Miwa, S., Mori, M., Hibiki, T. 2014. Two-phase flow induced vibration in piping systems. *Progress in Nuclear Energy* (78): 270-284. http://dx.doi.org/10.1016/ j.pnucene.2014.10.003

Nennie, E., Belfroid, S., O'Mahony, T., 2013, Validation of CFD and Simplified Models with Experimental Data for Multiphase Fluid Structure Interaction with Multiple Bends, ICMF, Jeju, Korea

Pereboom, H., Belfroid, S.P.C., 2022, Multiphase flow induced forces for horizontal and vertical systems, PVP2022-84631, Las Vegas, Nevada, USA.

Pettigrew, M.J. 2006. Fluctuating forces caused by internal two-phase flow on bends and tees. *Journal Sound and Vibration* 298: 1088-1098. doi:10.1016/ j.jsv.2006.06.039

Tay, B.L., Thorpe, R.B. 2004. Effects of Liquid Physical Properties on the Forces Acting on a Pipe Bend in Gas–Liquid Slug Flow. *Chem. Eng. Res*.82(3):344-356. doi:10.1205/026387604322870453

Tay, B.L, Thorpe, R. 2013. Hydrodynamic forces acting on pipe bends in liquid-gas slug flow. *Chem. Eng. Res.*: 812-825 , http://dx.doi.org/10.1016/ j.cherd.2013.08.012

Tijseling, A.S., Hou, Q., Bozkus,Z., 2016, An Improved One-Dimensional Model for Liquid Slugs Traveling in Pipelines, J. of Pressure Vessel technology, Vol. 138.

PERIODIC WAKE SHEDDING OF TUBE BUNDLES SUBJECTED TO TWO-PHASE CROSS FLOW

Colette E. Taylor
Canadian Nuclear Laboratories (Retired Chief Engineer), Petawawa, ON, Canada
Michel J. Pettigrew
Canadian Nuclear Laboratories (Principal Research Engineer Emeritus), Chalk River, ON, Canada

ABSTRACT

Some periodic wake shedding has been observed in tube bundles subjected to two-phase cross flow, albeit, the consequences are not as severe as fluidelastic instability. The results of four different experimental programs are reviewed in this paper. Data on periodic forces and frequencies was deduced from the vibration response. Dynamic lift coefficients and Strouhal numbers were obtained. This information was used to develop design guidelines to avoid problems in process system components.

1. INTRODUCTION

Periodic wake shedding or, more generally, vortex shedding may be a problem when the shedding frequency coincides with the natural frequency of a cylindrical structure. This may lead to resonance and large vibration amplitudes. Periodic-wake-shedding resonance was observed by Gorman (1976) in tube bundles subjected to liquid flows (Fig. 1).

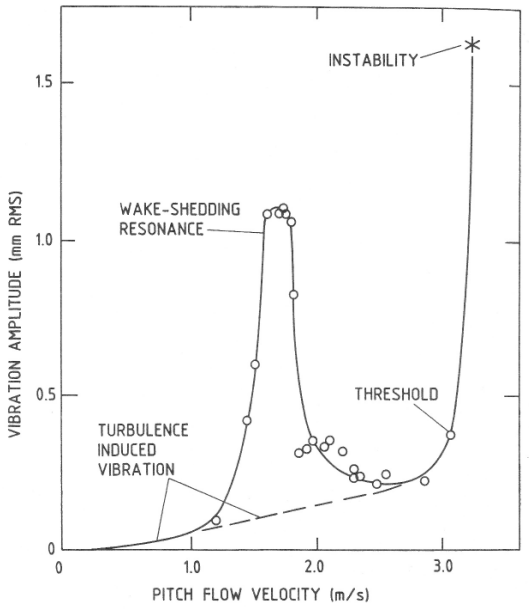

Figure 1: Typical vibration response spectrum (Gorman, 1976)

The vortex-shedding phenomenon for an isolated single cylinder in cross flow has been studied extensively. See, for example, Griffin (1980). The shedding frequency, f_S, may be formulated in terms of a Strouhal number, *S*,

$$S = f_S D/U \quad (1)$$

where *D* is the tube diameter and *U* is the upstream flow velocity.

For an isolated single cylinder, the Strouhal number is around 0.2 for Reynolds numbers of 200 to 3 x 10^5. The resulting periodic forces, F_L may be formulated by analogy to steady fluid forces, as

$$F_L = C_L D\rho U^2/2 \quad (2)$$

where ρ is the density of the fluid and C_L the dynamic lift coefficient which is around 0.5 for an isolated single cylinder (Gerlach and Dodge, 1970).

The true nature of periodic wake shedding in tube bundles is not yet completely understood. For a very open tube bundle with a large *P/D*, say 2.5, the behaviour may be similar to that of a single cylinder with a Strouhal number of about 0.2. For a closely-spaced tube bundle, the behaviour may be governed by the available space between tubes to allow for the formation of coherent vortices. Figure 2 shows a flow visualization of vortex shedding in a rotated square array (Weaver et al., 1993). The coherent vortices scale with the space between the tubes which explains why smaller pitch ratio arrays exhibit smaller vortices associated with higher frequencies, larger Strouhal numbers, and smaller lift forces.

Periodic-wake-shedding resonance may be of concern in liquid cross flow where the flow is relatively uniform. It is not normally a problem at the entrance region of steam generators because the flow is non-uniform and quite turbulent (Pettigrew and Gorman, 1973). Turbulence may inhibit periodic wake shedding in a tube array (Cheung and Melbourne, 1983).

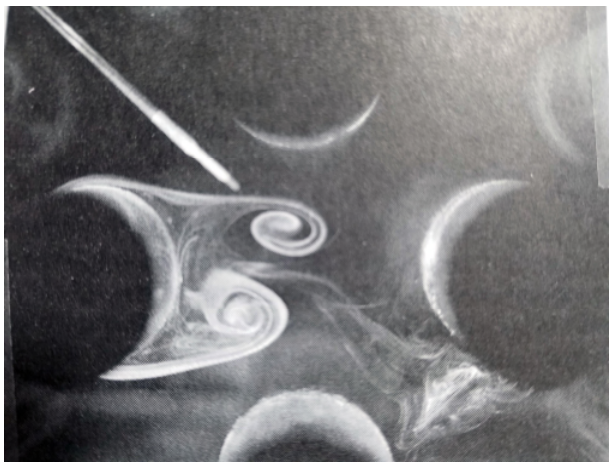

Figure 2: Vortex shedding behind the 2nd row in a rotated-square array with P/D=1.7 in gas flow (Weaver et al., 1993)

Resonance of the tubes due to periodic wake shedding is usually not a problem in gas heat exchangers. The gas density is usually too low to cause significant periodic forces at flow velocities close to resonance. Normal flow velocities in gas heat exchangers are usually much higher than those required for resonance. However, periodic wake shedding resonance may be possible in high pressure components with high density gas and for higher modes of vibration with higher natural frequencies corresponding to higher flow velocities.

The early literature regarding vortex shedding in tube bundles can be quite confusing but by the 1980s a much better understanding was emerging. Generally, there is less information on the magnitude of periodic-wake-shedding forces in tube bundles than for frequencies since acoustic resonance in gas flow heat exchangers has proven to be a much more significant problem than tube vibration due to vortex shedding. It is important to note that periodic wake shedding is equally possible in finned tube arrays (Mair et al., 1975, Chen, 1968, Bryce et al., 1978, and Kouba 1986). In fact, in some cases the phenomenon is better defined in finned-tube bundles (Bryce et al., 1978). Thus, periodic wake shedding resonance must be considered in finned-tube bundles.

2. FREQUENCY: STROUHAL NUMBER

Periodic wake shedding in tube bundles is described in terms of a Strouhal number, $S = f_S D/U_p$, where f_S is the vortex shedding frequency and U_p is the pitch velocity. The fluctuating lift coefficient, C_L, is used to estimate the periodic lift force, F_L, due to wake shedding, thus, $F_L = C_L D\rho U_p^2/2$, using the U_p at resonance.

Figure 3 shows Strouhal numbers for tube bundles of various configurations and pitch over diameter ratios, *P/D*, in liquid flow. The Strouhal numbers based on U_p are generally between 0.33 and 0.67.

Weaver et al. (1987) reviewed the data for wake shedding in tube bundles in more detail. The data is summarised in Fig. 4 where the Strouhal numbers, *St*, are defined in terms of the approach velocity, U_∞. Although there is a lot of scatter in the data, expressions based on Owen's (1965) theory were proposed to formulate the average values as shown by the curves in Fig. 4. These expressions can easily be transformed to yield Strouhal numbers, *S*, defined in terms of the pitch velocity. Thus,

$$S = (1/1.73)(D/P) \quad (3a)$$

for normal-triangular bundles,

$$S = (1/1.16)(D/P) \quad (3b)$$

for rotated-triangular bundles, and

$$S = (1/2)(D/P) \quad (3c)$$

for both normal- and rotated-square bundles. These expressions give Strouhal numbers between about 0.32 and 0.70 for realistic heat exchanger tube bundles of *P/D* between 1.23 and 1.57. These Strouhal numbers are very similar to those found in liquids as shown in Fig. 3. These correspond to dimensionless pitch velocities, U_p/fD, between 1.5 and 3.0. Resonance should be assumed possible within this velocity range. In the case of a tube subjected to a time-

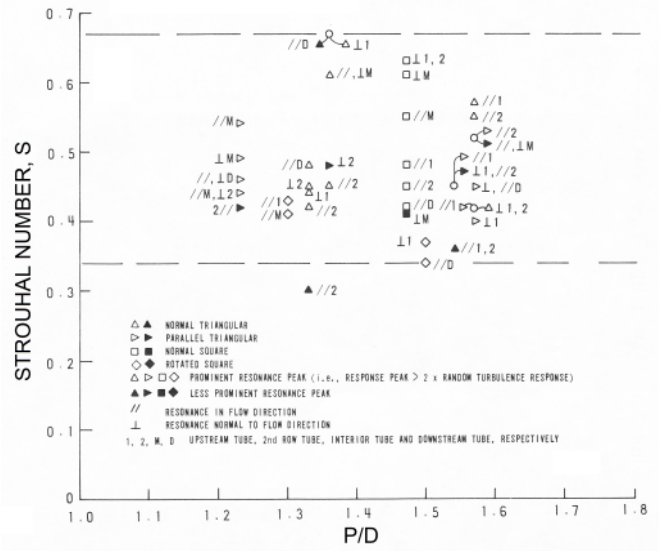

Figure 3: Strouhal numbers of tube bundles in liquid flow (Pettigrew and Gorman, 1978)

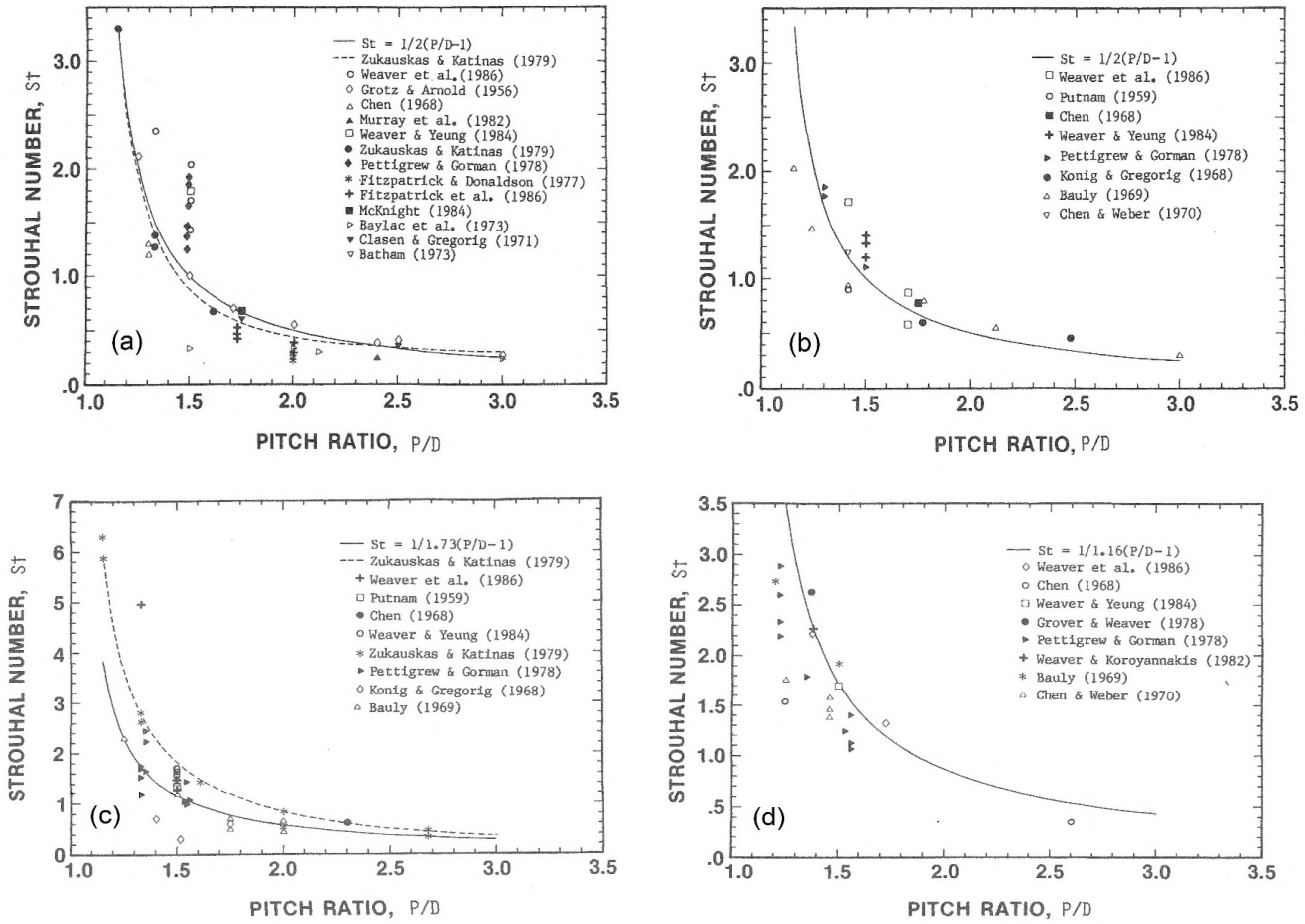

Figure 4: Strouhal number expressions for various tube-bundle geometries (Weaver et al., 1987) based on upstream velocity, U_∞: (a) In-line square arrays, (b) Rotated-square arrays, (c) Normal-triangular arrays and (d) Parallel-triangular arrays

varying velocity, only the fluctuating fluid forces corresponding to the region within the above range of dimensionless velocities need to be considered.

Other formulations have been developed for the prediction of Strouhal numbers in tube arrays. Several of these charts and empirical formula are summarized in the review by Weaver (1993). None of them have proven to be more accurate that the formulation proposed by Weaver et al. (1987) which was based on Owen's hypothesis (1965) and given in Eq. (3).

The data on Strouhal numbers for finned-tube bundles is relatively sparse. Kouba (1986) reported some results for normal triangular finned-tube bundles (Fig. 5). He found $S = 0.53$ for $P/D = 1.51$ based on the root diameter, $D_r = 22.5$ mm.

Chen (1968) did experiments on staggered finned-tube bundles. For a nearly normal triangular array of $P/D = 1.735$, he reported $S = 0.47$.

More weight should be given to the more relevant information, i.e.: the average values of Weaver et al. (1987) and the data deduced from actual tube

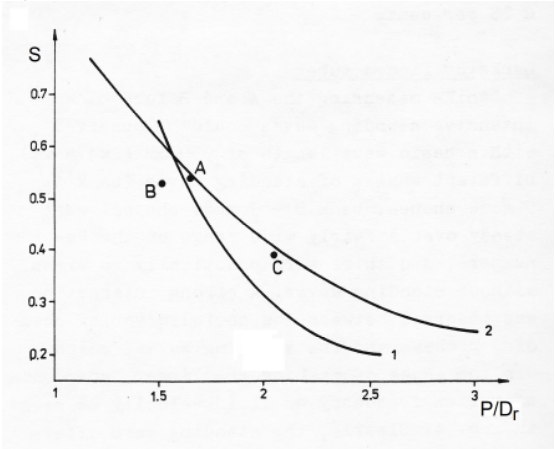

Figure 5: Strouhal numbers for finned tubes (Kouba, 1986): Dots are experimental points, Curve 1 is from Chen (1977) and Curve 2 from Zukauskas and Katinas (1979)

resonances (Pettigrew and Gorman, 1978). The single point at $S = 0.20$ in Fig. 4(c) may not be significant as there is no information on its relative magnitude.

In summary, the above results suggest a reference Strouhal number value of roughly $S = 0.50$ for heat exchanger tube bundles. Periodic wake shedding resonance is possible for Strouhal numbers between 0.40 and 0.67.

A thorough review of vortex shedding phenomena (Weaver, 1993) showed that the vorticity mechanisms in in-line and staggered tube arrays with practical pitch ratios are fundamentally different. As a result, reliable Strouhal number data for staggered arrays can be determined at resonant and off-resonant conditions; however, reliable Strouhal number data for in-line arrays should be obtained only under resonant conditions. In addition, acoustic resonance can lead to "lock-in" that increases the Strouhal number range for which periodic-wake-shedding resonance is possible.

3. CALCULATING TUBE RESONANCE AMPLITUDES

If a vortex-shedding resonance is predicted at the operating flow rates, the next step is to estimate the tube resonance amplitudes. From a structural dynamics perspective, a cylinder or similar structure can be considered as a beam with known end conditions. The tube response $y(x,t)$ at any point x and at any time t may be expressed as a normal mode expansion in terms of the generalized coordinates $q_i(t)$ as follows:

$$y(x,t) = \sum_{i=1}^{\infty} \phi_i(x) q_i(t) \tag{4}$$

Using Lagrange's equation and assuming that the damping is small and that coupling between the modes does not occur, the equation of motion for the i^{th} mode is

$$\ddot{q}_i(t) + 4\pi f_i \zeta \dot{q}_i(t) + 4\pi^2 f_i^2 q_i(t) = \int_0^L g(x,t)\phi_i(x)dx \tag{5}$$

where $g(x, t)$ is the forcing function.

Using Eqs. (4) and (5), it can be shown that the peak vibration response, $Y(x)$, of a uniform cylinder to periodic forces $g(x', t) = F(x')e^{i2\pi ft}$ at resonance in the i^{th} mode is expressed by

$$Y(x) = \frac{\phi_i(x)}{8\pi^2 f^2 \zeta} \int_0^L F(x')\phi_i(x')dx' \tag{6}$$

where $F(x')$ is the correlated peak periodic wake shedding force per unit length. For resonance to occur, the frequency of the i^{th} mode must coincide with the Strouhal frequency. When this occurs, the contribution to the response of modes other than the i^{th} mode is negligible.

At practical Reynolds number flows in tube arrays, turbulence masks visualization of clear Karman-like vortices, but there is no question that periodic forces occur at a frequency that is linearly dependent on flow velocity. This relationship is by the Strouhal number and resonance occurs when the vortex shedding frequency is equal to the structural natural frequency.

For a cylindrical structure with clamped-free end conditions subjected to uniform cross-flow over its entire length, Eq. (6) reduces to

$$Y(\ell) = \frac{1.566F}{8\pi^2 m f^2 \zeta} \tag{7}$$

and, for a cylindrical structure with pinned-pinned end conditions subjected to uniform cross-flow over its entire length, Eq. (6) reduces to

$$Y(\ell/2) = \frac{F}{2\pi^3 m f^2 \zeta} \tag{8}$$

where $Y(\ell/2)$ is the mid-span peak amplitude with pinned-pinned end conditions and $Y(\ell)$ is the peak amplitude at the free end with clamped-free end conditions.

The wake shedding force may be formulated in terms of a dynamic coefficient, C_L, as shown earlier in Eq. (2),

$$F = F_L = C_L(\tfrac{1}{2}\rho D U^2)$$

4. FLUCTUATING FORCE COEFFICIENTS IN SINGLE-PHASE FLOW

Fluctuating forces due to periodic wake shedding depend on several parameters such as bundle configuration, location within the bundle, Reynolds number, turbulence level, fluid density and P/D. At the limit when P/D is large, fluctuating force coefficients should approach those for isolated single cylinders. On the other hand, when P/D is very small, the force coefficients are small since the fluid mass associated with the formation of vortices will be small as there is little space within the bundle for large vortices.

Some fluctuating force coefficients in single-phase flow are plotted in Fig. 6 (Pettigrew and Taylor, 2003). The data in this plot shows that the fluctuating lift coefficient, C_L, is dependent on P/D up to $P/D = 2.5$. Unfortunately, when this plot was created

there were no data on finned tubes. For heat exchanger tube bundles of P/D < 1.6, a fluctuating force coefficient of 0.075 rms is recommended as a design guideline to calculate periodic wake shedding forces. It should be noted that there has been much more research in this area since this plot was created, but the guideline presented here is still effective.

5. FLUCTUATING FORCE COEFFICIENTS IN TWO-PHASE FLOW

It is sometimes difficult to distinguish between fluidelastic instability and periodic wake shedding resonance in liquid and two-phase cross flow through arrays of cylinders, often because the resonance velocity and stability threshold nearly coincide. The existence and characteristics of such flow and related vibration excitation mechanisms are discussed in this section. This may be done by deduction from the vibration response of test sections and other similar equipment.

There is far less information on periodic wake shedding in tube bundles subjected to two-phase cross flow, relative to single-phase flow. This paper has gathered data from test results at the Chalk River Laboratories (CRL) (Pettigrew et al., 1985), at École Polytechnique (EP), Montreal (Pettigrew et al., 2005 and Senez et al., 2010) and at the Centre d'Études Nucléaires de Saclay (CENS), France (Taylor, 1994). The periodic forces were measured directly in the CENS and EP test sections, while the amplitude of motion was measured in the CRL test sections. The CENS and EP periodic force coefficients were based on the area under the spectral curve.

The CENS tests with D = 0.03 m, P/D = 1.5 and normal-square array geometry had clear periodic forces only in the low-void-fraction regions, with the resulting lift coefficients listed in Table 1. The EP tests, with rotated-triangular array geometry, D = 38 mm and 17.5 mm, and P/D = 1.5 and 1.42, had clear periodic forces up to 80% void fraction with some of the resulting lift coefficients listed in Table 2. Tests at CRL were carried out to simulate the entrance region of steam generators where low-void-fraction flow may exist. The resulting fluctuating force coefficients are listed in Table 3.

Sample vibration response spectra are provided for the Pettigrew et al. (2005) (spectra from Zhang et al. (2007)) and Senez et al. (2010) tests in Fig. 7 and Fig. 8, respectively. The CRL spectra in Fig. 9 show very little evidence of periodic wake shedding above

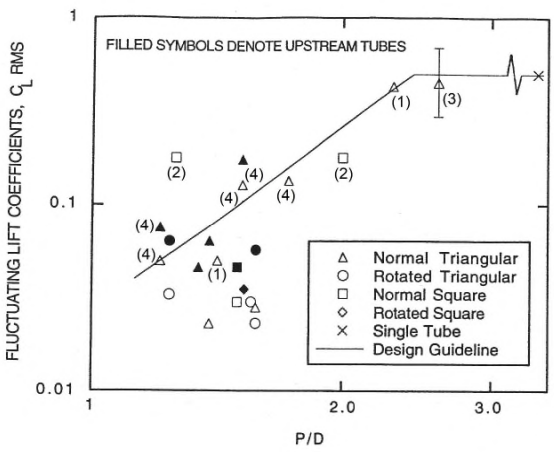

Figure 6: Fluctuating-force lift coefficients for tube bundles in single-phase flow: In air, (1) Chen (1979), (2) Batham (1973), (3) Shim et al. (1988), and (4) Savkar and Litzinger (1982)and in water, all other points from Pettigrew and Gorman (1978)

15% void fraction. However, the question remained for the higher void fractions (70-99%) found in U-bend regions. Consequently, the EP experimental program was implemented to study flow-induced vibration in higher-void-fraction two-phase cross flow.

In the EP program, both Pettigrew et al. (2005) and Senez et al. (2010) state that although periodic wake shedding was not expected at such high void fractions, the wake between inline cylinders was observed visually to be quite steady. However, the Strouhal numbers attained in the EP tests (see Table 2) are between 0.06 and 0.26, as opposed to the expected Strouhal numbers between) 0.4 and 0.7 observed in the CRL and CENS low-fraction tests. The low-void-fraction wake shedding is very similar to single-phase wake shedding, whereas the high-void-fraction mechanism producing fluctuating forces does not happen at expected Strouhal frequencies.

The two-phase force coefficient data from Tables 1 thru 3 have been plotted in Fig. 10 under the single-phase design guideline from Fig. 6. Most of these two-phase force coefficients are similar in magnitude to the single-phase data. However, in Fig. 10 there is one data point associated with the rotated-triangular bundle geometry at 80% void fraction that is well above the other data points. A closer look at the source document (Senez et al., 2010) shows that the periodic force spectrum for this point (U_p = 1.5 m/s) does not have a well-defined resonance peak. In fact, the periodic-wake-shedding peak is not distinguishable from a low-frequency peak. (A low frequency

Table 1: Two-phase periodic wake shedding: Dynamic lift coefficients and Strouhal numbers for a normal-square tube bundle with P/D = 1.5 (Taylor, 1994)

ε_g (%)	TUBE ROW	LIFT S	LIFT C_L
5	First	0.46	-
	Second	0.40	0.013
	Interior	0.46	0.041
	Downstream	0.42	0.016
10	First	-	-
	Second	0.43	0.012
	Interior	0.41	0.020
	Downstream	0.43	0.013
15	First	0.40	0.015
	Second	0.36	0.032
	Interior	0.41	0.023
	Downstream	0.39	0.025

Table 2: Two-phase flow periodic-wake-shedding lift forces in tube-array test sections with direct force measurement

Reference	*P/D*	*D* mm	U_p m/s	ε_g %	ρ kg/m^3	f_L Hz	*S*	F_L N/m	C_L
Pettigrew et al., 2005 Rotated Triangular	1.5	38	2.0	50	500	9.0	0.17	1.0	0.026
	1.5	38	5.3	50	500	16	0.11	2.5	0.009
	1.5	38	7.6	50	500	20	0.1	2.4	0.004
	1.5	38	2.0	80	200	7.0	0.26	1.0	0.066
	1.5	38	8	80	200	13.5	0.06	5.8	0.024
	1.5	38	14	80	200	21	0.06	4.8	0.006
Senez et al., 2010 Rotated Triangular	1.42	17.5	1.5	80	200	8	0.09	1.9	0.483
	1.42	17.5	4.2	80	200	22.5	0.09	3.9	0.126
	1.42	17.5	6.8	80	200	34	0.09	5.8	0.072

Table 3: Two-phase flow periodic-wake-shedding lift forces in tube-array test sections with amplitude measurement

Reference	*P/D*	*D* mm	*Mass Flux* kg/m^{2}s	ε_g %	ρ kg/m^3	f_L Hz	*m* kg/m	ζ %	*S*	Y_{RMS} mm	F_L N/m	C_L
Pettigrew et al., 1985 Normal Square	1.47	13	650	5	950	26.1	0.512	2.3	0.50	0.25	0.101	0.035
	1.47	13	800	5	950	26.1	0.512	2.3	0.40	0.4	0.162	0.037
	1.47	13	650	5	950	26.1	0.512	2.3	0.50	0.3	0.121	0.042
	1.47	13	650	5	950	26.1	0.512	2.3	0.50	0.16	0.0646	0.022
	1.47	13	725	15	850	26.1	0.512	3.2	0.40	0.09	0.0506	0.013
	1.47	13	700	15	850	26.1	0.512	3.2	0.40	0.1	0.0562	0.015
CRL Normal Square	1.22	13	580	5	950	26.3	0.508	2.6	0.56	0.57	0.262	0.114
	1.22	13	580	5	950	26.3	0.508	2.6	0.56	0.22	0.101	0.044
	1.22	13	580	5	950	26.3	0.508	2.6	0.56	0.16	0.0736	0.032
CRL Normal Tri-angular	1.22	13	560	5	950	26.6	0.496	2.2	0.59	0.115	0.0447	0.021
	1.22	13	520	5	950	26.6	0.496	2.2	0.63	0.17	0.0661	0.036
	1.22	13	475	5	950	26.6	0.496	2.2	0.69	0.25	0.0972	0.063

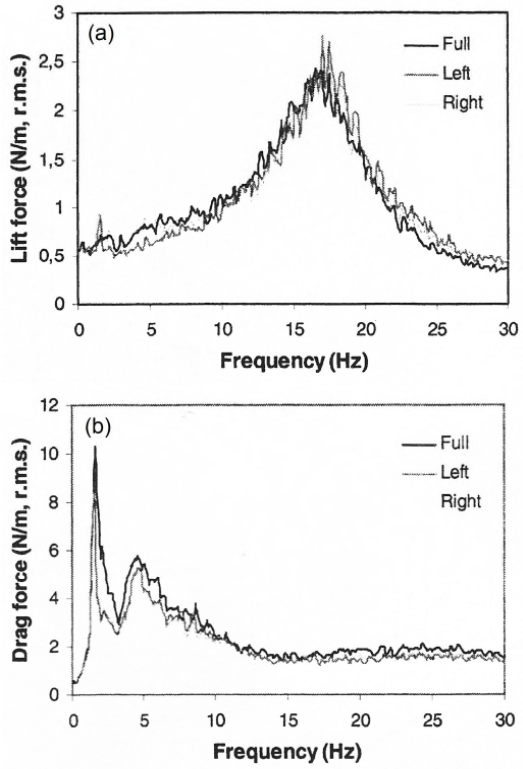

Figure 7: Force spectra at 80% void fraction with pitch-flow velocity 10 m/s (Zhang et al., 2007)

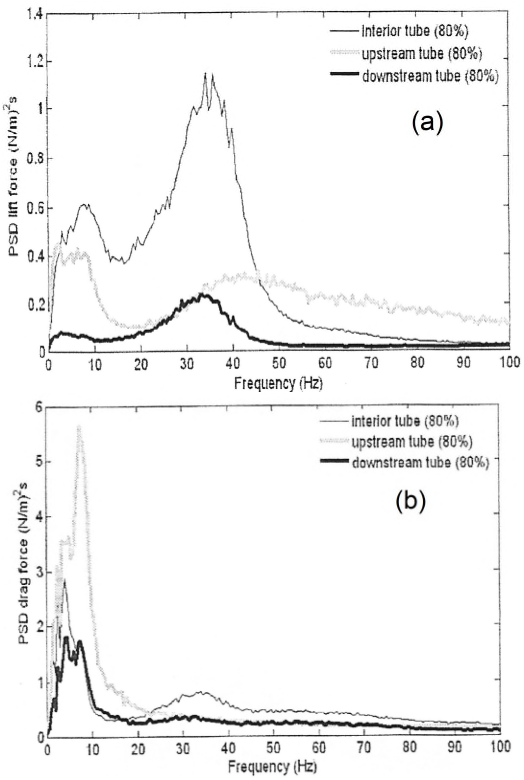

Figure 8: Force spectra at 80% void fraction and 6.8 m/s pitch velocity: (Senez et al., 2010)

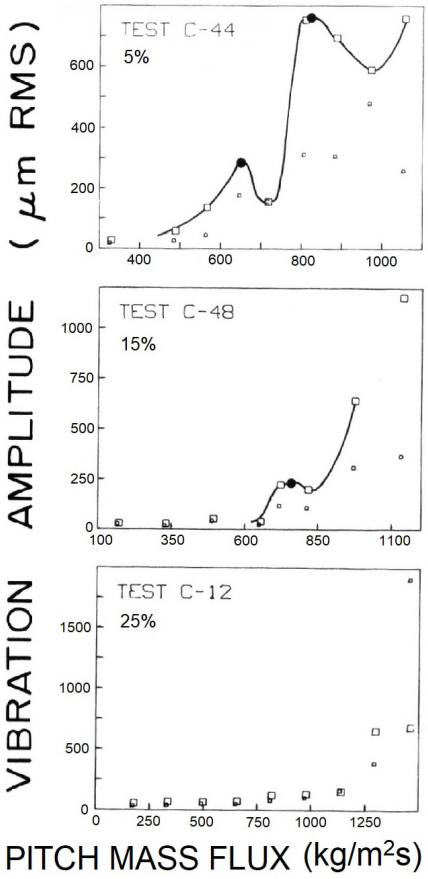

Figure 9: Vibration response to air-water forced excitation (solid circle: periodic-wake-shedding peak; large symbols: lift direction; small symbols: drag direction): downstream tube in normal-square tube bundle of P/D=1.47 (Pettigrew et al., 1985)

peak occurs in the spectrum for each pitch velocity as can be seen in Fig. 8.) It is likely that the large force coefficient is due to low-frequency forces that are not related to periodic wake shedding. As the Senez et al. (2010) periodic-wake-shedding flow conditions largely fell within the intermittent flow regime (see Section 7), these low-frequency forces may have been the result of flow regime rather than periodic wake shedding.

If we ignore the Senez data point that is well above the other data points, the single-phase design guideline can be used as a design guideline upper bound for two-phase fluctuating-force lift coefficients.

6. EFFECT OF BUNDLE GEOMETRY

Bundle orientation has no clear effect on the magnitude of the force coefficients in the single-phase data in Fig. 6. The two-phase data in Fig. 10 suggest

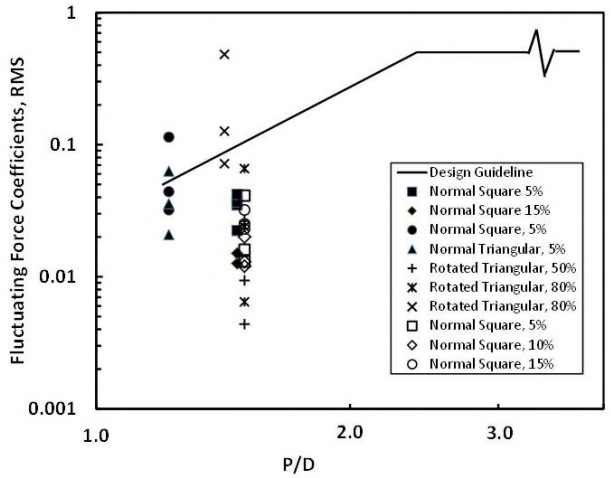

Figure 10: Fluctuating-force lift coefficients for tube bundles in two-phase flow (from Tables 1, 2 and 3)

data in Fig. 6. The two-phase data in Fig. 10 suggest that the rotated-triangular orientation may produce larger force coefficients, than the other bundle orientations. The rotated triangular orientation was also observed to be the most susceptible to fluidelastic instability (Pettigrew and Taylor, 1993).

The effect of pitch-over-diameter ratio was clear in the single-phase data shown in Fig. 6. The force coefficients were found to increase with larger *P/D*. The two-phase results do not show a clear dependence on *P/D*. Additional data at varying *P/D* ratios is required to confirm that fluctuating force coefficients depend on *P/D* in two-phase flow.

The Senez et al. (2010) test section had tubes that were about half the diameter of the Pettigrew et al. (2005) test section, but the P/D ratios were kept similar. One might expect the fluctuating force coefficients to be lower in the Senez et al. (2010) data, but this was not the case.

7. EFFECT OF FLOW CONDITIONS

Most of the available two-phase test results from laboratories around the world state that periodic wake shedding was not evident above 5% to 15% void fraction. This was also found in the Freon test results of Feenstra et al. (2003). However, Pettigrew et al. (2005) and Senez et al. (2010) showed that significant fluctuating forces can occur at high void fraction.

One could speculate that flow regime may have an effect on the formation of periodic wakes. Classic periodic wake shedding with expected Strouhal numbers has been observed only in low-void-fraction bubbly flow.

Kanizawa and Ribatski (2016) flow regime mapping boundaries were used in Fig. 11. These maps show flow conditions that did not have observed periodic wake shedding. It is simple to remember that, except for the EP tests, all of the periodic wake shedding was observed in tests between 5% and 15% void fraction and, therefore, based on these maps they are all in bubbly flow. The EP flow maps only show the periodic-wake-shedding flow conditions.

The flow-regime boundaries in Fig. 11 change with tube diameter and pitch-to-diameter ratio. As the tube diameter decreases and P/D is kept the same, the bubbly flow region reduces in size. As a result, classic periodic wake shedding would be less likely in tube bundles with smaller diameter tubes. As P/D decreases, the bubbly flow region actually increases slightly, which could be interpreted as an increased likelihood of seeing wake-shedding forces at higher void fractions.

The Pettigrew et al. (2005) (EP) flow conditions all fall in the bubbly flow regime, despite the high void fractions. The Senez et al (2010) (EP) test conditions fall in the intermittent flow regime which corresponds well with the existence of low-frequency peaks in the force spectra. On the other hand, it is difficult to understand how periodic wake shedding forces could exist in an intermittent flow regime. This requires further study.

Periodic forces are affected by damping and we know that damping in two-phase flow increases as void fraction increases up to about 40% and then begins to decrease after about 70%. These changes in damping are due, at least in part, to the changing sizes of the gas and liquid structures. A closer examination of these effects would also increase our understanding of two-phase periodic forces.

8. CONCLUSION

Vortex shedding in tube arrays has been reviewed with an emphasis on two-phase fluctuating-force coefficients resulting in the following conclusions:

1. In liquid cross flow, Strouhal numbers have a strong dependence on P/D and can be predicted reasonably well using available research.
2. Tube bundles in liquid cross flow can experience resonance conditions due to vorticity. The resulting resonance amplitudes can be predicted using appropriate force coefficient data.
3. Two-phase wake shedding is possible and seems to fall into at least two categories. At low void

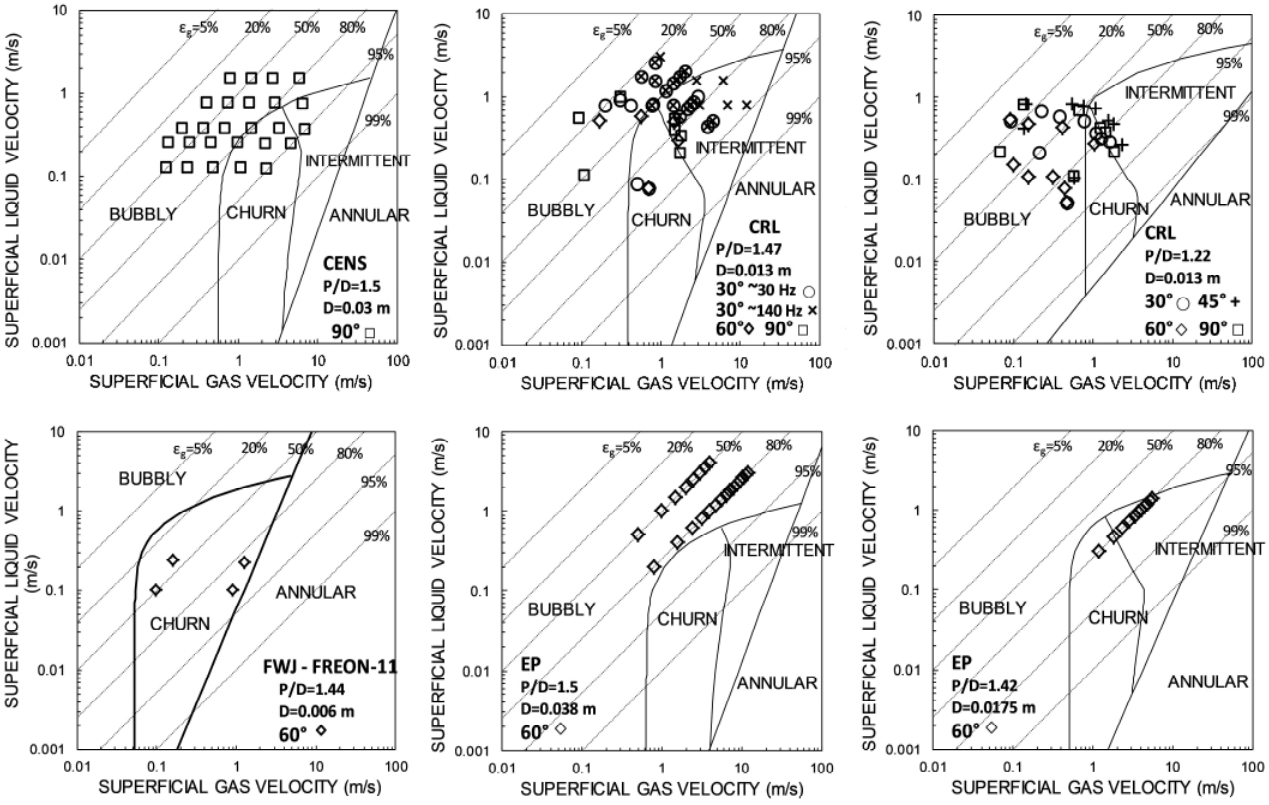

Figure 11: Flow-regime maps for the two-phase fluctuating-force data sources

fractions, vortices are produced in tube bundles at Strouhal numbers and force coefficients similar to those found in liquid flow.

4. At higher void fractions (50 to 80%), periodic forces occur and increase with velocity. However, the associated Strouhal numbers are much lower than those found in single-phase flow.
5. The single-phase upper bound for periodic force coefficients also provides a reasonable design guideline for two-phase fluctuating forces.

9. REFERENCES

Batham, J. P., 1973, Pressure distribution on in-line arrays in cross flow. *Proceedings of the International Symposium on Vibration Problems in Industry*," Keswick, U.K., Paper No. 412.

Bryce, W. B., Wharmby, J. S. and Fitzpatrick, J., 1978, Duct acoustic resonances induced by flow over coiled and rectangular heat exchanger test banks in plain and finned tubes. *Proceedings of BNES Symposium on Vibration in Nuclear Plant*, Keswick, U. K., Paper No. 3.5.

Chen, Y. N., 1968, Flow-induced vibration and noise in tube bank heat exchangers due to von Karman streets. *ASME J. Engineering for Industry* **90**: 134-146.

Chen, Y. N., 1977, The sensitive tube spacing region of tube bank heat exchangers for fluid-elastic coupling in cross-flow. *ASME Fluid Structure Interaction Phenomena in Pressure Vessel Piping Systems*, pp. 1-18.

Chen, Y. N., 1979, Flow-induced vibrations of plates, single cylinders and tube bundles. *Practical Experiences with Flow-Induced Vibrations*, Paper A17, pp. 201-211.

Cheung, J. C. K. and Melbourne, W. H., 1983, Turbulence effects on some aerodynamic parameters of a circular cylinder at supercritical Reynolds numbers. *Journal of Wind Engineering and Industrial Aerodynamics* **14**: 399.

Feenstra, P. A., Weaver, D. S. and Nakamura, T., 2003, Vortex shedding and fluidelastic instability in a normal square tube array excited by two-phase cross flow. *J. of Fluids and Structures*, **17**: 793-811.

Gerlach, C. R. and Dodge, F. T., 1970, An engineering approach to tube flow-induced vibrations. Proceedings of the Conference on Flow-Induced Vibrations in Reactor System Components, May 14-15, ANL-7685, Argonne, Illinois. pp. 205-224.

Gorman, D. J., 1976, Experimental development of design criteria to limit liquid cross-flow-induced vibration in nuclear reactor heat exchange equipment, *J. of Nuclear Science and Engineering*, **61**: 324-336.

Griffin, O. M., 1980, Observations of vortex streets and patterns –in the atmosphere –in the oceans –in the laboratory. *Keynote Paper for the Symposium on Vortex Flows,* ASME Winter Annual Meeting, Chicago, Illinois.

Kanizawa, F.T. and Ribatski, G., 2016, Two-phase flow patterns across triangular tube bundles for air-water upward flow. *International Journal of Multiphase Flow* **80**: 43-56.

Kouba, J., 1986, Vortex shedding and acoustic emission in finned tube banks exposed to cross flow. *Proceedings of the ASME PVP Symposium on Flow-Induced Vibration*, Chicago, Illinois, July, **104**: 213-217.

Mair, W. A., Jones, P. D. F. and Palmer, R. K. W., 1975, Vortex shedding from finned tubes. *Journal of Sound and Vibration* **39**: 293-296.

Owen, P. R., 1965, Buffeting excitation of boiler tube vibration. *Journal of Mechanical Engineering Science* **7**: 431-439.

Pettigrew, M. J., and Gorman, D. J., 1973, Experimental studies on flow-induced vibration to support steam generator design, Part III: Vibration of small tube bundles in liquid and two-phase cross-flow. *International Symposium on Vibration Problems in lndustry*, Paper 424, Keswick, U. K.

Pettigrew, M. J. and Gorman, D. J., 1978, Vibration of heat exchange components in liquid and two-phase cross-flow. Proceedings of the *BNES International Conference on Vibration in Nuclear Plant*, Paper 2.3, Keswick, U.K.

Pettigrew, M. J., Sylvestre, Y., and Campagna, A. O., 1978, Vibration analysis of heat exchanger and steam generator designs. *Nuclear Engineering and Design* **48**: 97-115.

Pettigrew, M. J., Tromp, J. H. and Mastorakos, M., 1985, Vibration of tube bundles subjected to two-phase cross flow. *ASME Journal of Pressure Vessel Technology* **107**: 335-343.

Pettigrew, M. J., Taylor, C. E. and Kim, B. S., 1989, Vibration of tube bundles in two-phase cross flow - Part 1: Hydrodynamic mass and damping. *ASME Journal of Pressure Vessel Technology* **111**: 466-477.

Pettigrew, M. J. and Taylor, C. E., 1993, Chapter 7: Two-phase flow-induced vibration. *Technology for the 90's by ASME PVP Division*, New York, 1993, pp. 811-864.

Pettigrew, M. J. and Taylor, C. E., 2003, Vibration analysis of shell-and-tube heat exchangers: an overview Part 2: vibration response, fretting-wear, guidelines. *Journal of Fluids and Structures* **18**: 485-500.

Pettigrew, M. J., Zhang, C., Mureithi, N.W. and Pamfil, D., 2005, Detailed flow and force measurements in a rotated triangular tube bundle subjected to two-phase cross flow. *Journal of Fluids and Structures* **20**: 567-575.

Savkar, S. D. and Litzinger, T. A., 1982, Buffeting forces induced by cross flow through staggered arrays of cylinders. *General Electric Report No. 82CRD238*.

Senez, H., Mureithi, N. W. and Pettigrew, M. J., 2010, Vibration excitation forces in a rotated triangular tube bundle subjected to two-phase cross flow. *Proceedings of FEDSM-ICNMM2010*, Aug 1-5, Montreal, Paper No. 30528, pp. 565-573.

Shim, K. C., Hill, R. C. and Lewis, R. I., 1988, Fluctuating lift forces and pressure distributions due to vortex shedding in tube banks. *International Journal Heat and Fluid Flow* **9**: 131-146.

Taylor, C. E., 1994, Random excitation forces in tube arrays subjected to water and air-water cross flow. *Ph.D. Thesis*, University of Toronto, Toronto.

Weaver, D. S., Fitzpatrick, J. A. and El Kashlan, M., 1987, Strouhal numbers for heat exchanger tube arrays in cross flow. *ASME Journal of Pressure Vessel Technology* **109**: 219-223.

Weaver, D. S., 1993, Chapter 6: Vortex shedding and acoustic resonance in heat exchanger tube arrays. *Technology for the '90s*, (Principal Editor M. K. Au-Yang), ASME, New York, pp. 777-810.

Weaver, D. S., Lian, H. Y., and Huang, X. Y., 1993, Vortex shedding in rotated square tube arrays, *J. Fluids and Structures*, **7**: 107-121.

Zhang, C., Pettigrew, M. J. and Mureithi, N. W., 2007, Vibration excitation force measurements in a rotated triangular tube bundle subjected to two-phase cross flow. *Journal of Pressure Vessel Technology*, **129**: 21-27, also *PVP2005-71464*.

Zukauskas, A. and Katinas, V., 1979, Flow-induced vibration in heat exchanger tube banks. *Proceedings of the Symposium on Practical Experiences with Flow-Induced Vibrations,* IUTAM, Karlsruhe. pp. 188-198.

TWO-PHASE FLOW INDUCED VIBRATION IN A TUBE BUNDLE OF STEAM GENERATORS

Vincent Fichet, Bachar Mallat, Alejandro Mourgues, Jérôme Moulin, Quentin Andrzejewski
Framatome Centre Technique, Le Creusot, France

ABSTRACT

Tests were carried out at the Framatome Technical center in Le Creusot to study two-phases flows with two gas/liquid couples (Water/Air and an Improved Simulating Liquid - ISL/Air) in a tube bundle of Steam Generators (SG) at ambient temperature and pressure. High-speed video sequences were recorded to identify the different flow regimes and the differences in flow topologies related to the type of simulating liquid used. These differences were then quantified by means of fluctuating force measurements on the SG tube as well as by measurements of the local void fraction in the vicinity of the tube by a dual optical probe sensor mounted on the tube. The results obtained underline the differences between simulating liquids and emphasize the importance of using representative fluids to better capture two-phase FIV in SG tube bundle in order to gain operational margins and to improve SG designs. A way to characterize two-phase flow regimes locally and its interaction with vibrating structure via response PSD (amplitude) and first mode "peak" analysis (added mass, fluid damping) is also proposed.

1. INTRODUCTION

The Steam Generator (SG) of a Pressurized Water Reactor (PWR) is a key component that enables the heat transfer between the primary and the secondary circuits. SG consists of a bundle of U-bend tubes in which the water from the primary circuit flows at around 155 bars and 320°C. In the secondary circuit (near 280°C, 70 bars), the water is injected at mid-height, flows down (see Figure 1 from [1]) and evaporates in contact with these tubes due to the heat delivered from the primary circuit. It increases the gas (void) fraction with the elevation in the SG before reaching the separators and dryers to feed the turbine with dry steam. The void fraction increases and due to mass conservation, the fluid velocity raises along the elevation. In the U-bend region, two-phase cross-flows thus occur at high velocities and induce vibration of the tubes. This Flow Induced Vibration (FIV) generates wear when the vibrating tubes strongly impact their supports, and it could even lead to the rupture under specific circumstances. These phenomena have then been studied for 50 years (see [2] and [3]).

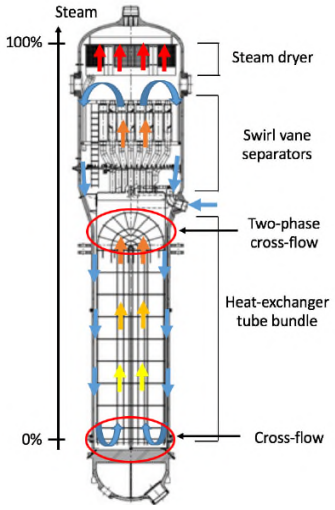

Figure 1. SG hydraulics with increasing void fraction and velocities along the elevation up to the U-bend region – issued from [1]

Some event like the one that occurred at SONGS (San ONofre Generating Station) in California in 2012 remind that comprehensive studies are needed to ensure safety margins to this rupture threshold. The physics at stake in the previous example relates to Fluid-Elastic Instability (FEI) and could cause a rapid wear of tubes as described in [4]. Although still imperfectly understood, the FEI is roughly depicted in Figure 2 as a very rapid (steep) increase in tube displacement amplitude in function of flow velocity.

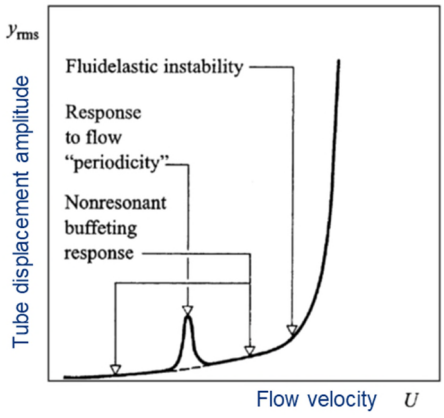

Figure 2. Fluid-Elastic Instability– issued from [4]

This growth is then limited by non-linear phenomena such as shocks between tubes or on bounding support which explain high wear rates.
Since numerical models are still not perfectly mature to predict this instability threshold, experimental study are required and safety margins are defined from these data, sometimes modifying the Connors' factor K (see [5]) for instance.

Numerous studies have been carried out in the literature (see [6], [7], [8], [9]) to characterize the two-phase flow excitation via the effect of parameters (tube arrangement, gap between tubes, inclination of U-bend…) and the two-phase flow damping. Most of these studies consider water-air or freon mixtures to respect the ratio of gas and liquid densities. However, important fluid distortions remain as demonstrated in the present paper.

The first part of this paper presents the similitude study and the choice of simulating fluids. The second part is devoted to the simplified experimental setup used to study two-phase flows in a steam generator. The third part focuses on the two-phase FIV results and the opportunity to access two-phase flow characteristics from derived results values (added mass, damping). The final part presents the conclusions.

2. SIMILITUDE LAWS FOR TWO PHASE FLOW EXPRIMENTS

In single-phase (liquid or gas), it is often required to respect one or two dimensionless numbers between the mock-up and the reactor-scale conditions. Reynolds (number) is to be respected for turbulence, the Strouhal number for hydraulic excitation, the Froude (or Richardson) number for buoyancy effect or thermal stratification, Prandlt or Schmidt with respect to mass or heat transfer... In two-phase flows, there would rather be nine dimensionless numbers to respect to capture physics. The mockup must keep the same topology of two-phase flow structures (drops, bubbles) depending on the effects of density, flow shear stresses and liquid/gas surface tension… Here, four dimensionless numbers are highlighted to demonstrate the importance of the simulating fluids selection:

The ratio of mass densities of liquid and gas:

$$\frac{\rho_l}{\rho_g}$$

The ratio of a two-phase flow characteristic size (e.g. bubble/drop diameter) to the diameter of the SG tube impacted by the flow:

$$\frac{d_l}{D_{tube}}$$

The droplet Reynolds number (associated with the droplet characteristic length, e.g. diameter d_l) conveyed in the gas flow (in line with U-bend region two-phase flow conditions):

$$Re_{droplet} = \frac{d_l \left(U_g - U_l\right)^2}{\nu_g}$$

The Weber number as competition between the fluid driving forces (of a liquid droplet in a predominantly gaseous flow here) and the surface tension forces ensuring the cohesion of the liquid structures:

$$Weber = \frac{\rho_m d_l \left(U_g - U_l\right)^2}{\boldsymbol{\sigma}}$$

Table 1 summarizes the distortion of dimensionless numbers as guarantees of a good representation of the physics via their ratio in "mockup" and "reactor" conditions. If the most widely employed is the "Water / Air" simulating fluid couple (easy to use), "an ISL/ Air" will better capture both the size and shape of the two-phase flow structures by a better representation of the liquid / gas surface tension. A next step towards reactor conditions (scaling issue) would be then to use an Improved Simulating Gas (ISG) that also corrects the distortion in gas mass density. However, this last step requires implementing a pressurized loop (meaning higher costs) even with the use of heavy gases like refrigerant (freon) often chosen in the literature.

Distorsion ratio ranking
Good : ratio ±20%
Improvable : ±20% < ratio < factor 2
Bad : ratio > factor 2

	Water / air	ISL / Air	ISL / ISG	Water / steam
T (°C)	20	15	15	286
P (bar abs)	1,5	1,5	10,2	70
(ρ_l/ρ_g) mockup / (ρ_l/ρ_g) reactor	27,49	20,61	1,02	1,00
(d_l/D_{tube}) mockup / (d_l/D_{tube}) reactor	1,70	1,14	1,16	1,00
$Re_{droplet}$ mockup / $Re_{droplet}$ reactor	0,08	0,06	0,89	1,00
Weber mockup / *Weber* reactor	0,02	0,04	0,84	1,00
σ mockup / σ reactor	4,08	1,39	1,39	1,00
μl mockup / *μl* reactor	10,93	6,46	6,46	1,00

Table 1. Distortion of dimensionless numbers according to simulating fluids

As it is very difficult to carry out measurements in real steam generators (SG), or to set up an experimental facility under these pressure and temperature conditions (at acceptable costs). The means available to study two-phase flow configurations are either numerical simulations or experimental tests in similitude. Experiments in similitude benefit from a rich instrumentation that give access to physical phenomena while respecting as best as possible the same fluid properties as those presents in SG conditions.

The Framatome Technical Center in Le Creusot has been working since 2013 on a way to improve the simulating fluids used to conduct two-phase flow experiments. Beyond theoretical analysis on dimensionless number, an experimental mockup has been designed to operate both Water/Air (easy to use but not representative of SG liquid properties) and a so-called Improved Simulating Liquid - ISL/Air which better reproduces the liquid density and surface tension with respect to SG conditions fluid properties. A next step will be to use an ISG compressed at around 10 bars to reach the SG gas mass density.

3. EXPERIMENTAL SET-UP

A dedicated mockup is designed and constructed assuming simplified straight short rods arranged in square to represent the center of the U-bend tube bundle region of the SG (see *Figure 3*).

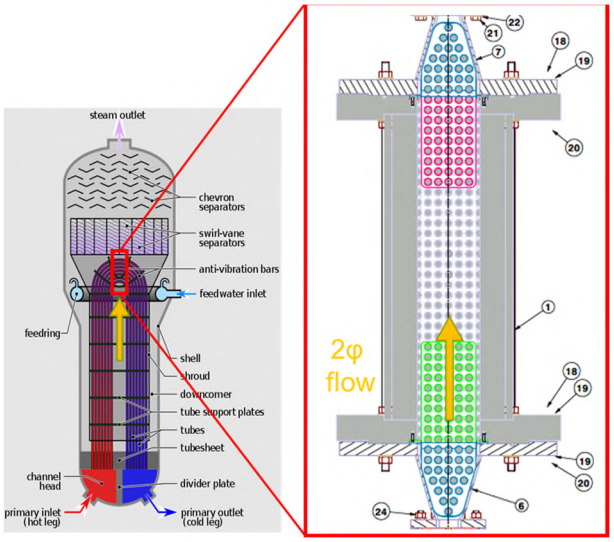

Figure 3. Dedicated SG mockup the Framatome Technical Center

The mockup is at full scale and the main dimensions are given in *Table 2*.

Rod Diameter D	*19 mm*
Rod Length L	*165 mm*
Pitch P	*27,4 mm*
P/D	*1,44*
L/D	*8,6*
Nb of columns	*6*
Nb of lines	*48*

Table 2. Main mockup dimensions

An associated test loop has been also designed to produce adiabatic flows either with a Water/Air mixture, or with an Improved Simulating Liquid - ISL/Air mixture in this bundle of square-pitch rods.

The loop consists mainly in a gas (air) circuit, a liquid (either water or ISL) circuit, a phase mixer (with various geometries), the SG mockup and a phase separator. The air flowrate is supplied by a compressed air tank (at 6 bars) and controlled by a regulating valve associated with a mass flowmeter. The liquid delivered is generated by a centrifugal pump controlled by a variable frequency drive and the flowrate is measured by another mass flowmeter. During the tests, the pressure in the container is controlled. The temperature of the fluid is measured via a type T thermocouple placed downstream of the mock-up (see *Figure 4*).

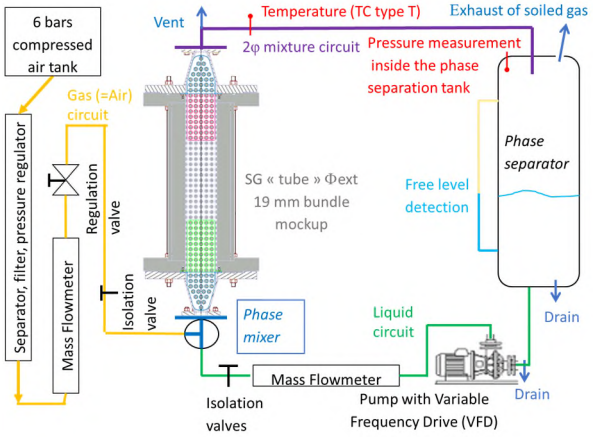

Figure 4. Two-phase test loop and SG mockup

The tests are considered adiabatic, and the test loop is installed in a temperature-controlled room. The effect of SG tube heat transfer is not integrated. The heat transfer acts on the void fraction. Only a change of void fraction conditions at mockup inlet is feasible with this loop. The mean void fraction over the mockup cross-section could be adapted to sweep over the two-phase flow regimes in this vertical rod bundle arranged in square. However, this mean void fraction remains constant over the elevation in the mockup since no heat transfer and no evaporation are considered. Due to the reduced height of the mockup, and the desire to focus on the simulating liquid, this effect has been considered of second importance.

The loop operates at ambient temperature and pressure. The test mock-up (*Figure 3*) presents a square section vein to ease optical access and measurements with high-speed cameras. Both vein and transverse rods are made of Plexiglass in this objective of visualizations.

4. RESULTS

Visualization tests were first carried out with both Water/Air and ISL/Air. High-speed video sequences were recorded at 3 kHz while maintaining the same ratios of superficial velocities of the liquid and gas phases at the mock-up inlet. Three different flow regimes were identified (see Figure 5) in agreement with the limits defined by Ulbrich and Mewes ([10]).

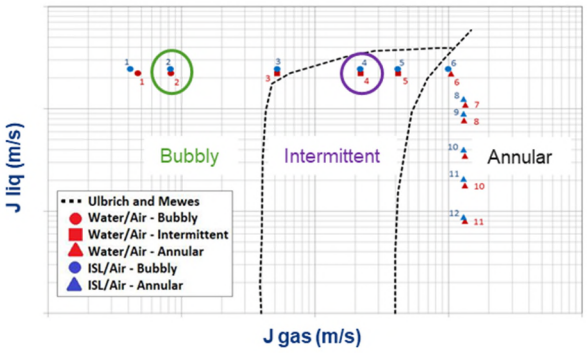

Figure 5. Two-phase flow regimes from [10] and measured points in Water/Air (blue) and ISL/Air (red)

As observed in Figure 6, the flow topology of the three regimes differs from Water/Air to ISL/Air even if the same volume flowrates (superficial velocities) have been maintained.

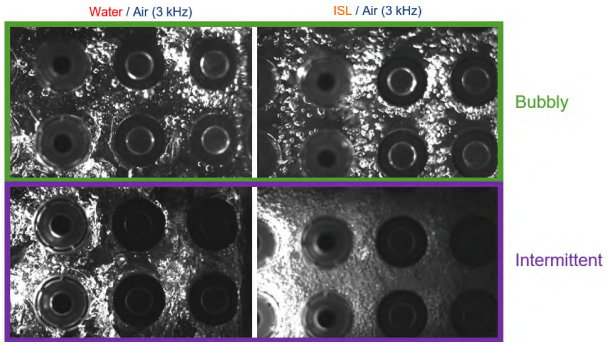

Figure 6. Two-phase flow regimes from [10] and measured points in Water/Air (blue) and ISL/Air (red)

The following results have been obtained:

- A bubble regime where the gas phase is dispersed in the liquid phase, as bubbles of either various sizes and shapes in Water/Air or uniformly distributed in size and shape for ISL/air. This observation is in full agreement with the reduced surface tension of the ISL compared to water at ambient temperature. A reduced surface tension induces lower cohesion forces and then to smaller structures at equilibrium with shear stress forces of the flow. This illustrates well the effect of a more representative surface tension on the two-phase flow topology.
- An intermittent regime characterized by an alternating and irregular movement between the gas phase and the liquid phase. It could be noticed that flow topology is very different between Water/Air and ISL/Air tests showing again the effect of surface tension on the two-phase flow characteristics.
- An annular regime in which liquid droplets are transported by the gas phase and a thin liquid film surrounds the tubes.

The visualization of these two-phase flows leads to the following main conclusions:

- The three flow regimes were observed for the Water/Air tests, while for the ISL/Air tests, the intermittent regime was not clearly observed
- The flow structure depends strongly on the liquid surface tension, even at same inlet conditions (same superficial velocities). The flow topology is noticeably distinct, in structure sizes and shapes, and particularly visible at low void fractions (bubble regime)
- A global description of the flow by visualization based only on the superficial velocities seems interesting but not sufficient, the thermophysical properties of the fluid must intervene.

These visualizations demonstrate differences in two-phase flow between the Water/Air and the ISL/Air couples for the same superficial velocities. Beyond this qualitative study, local void fraction measurements have been performed with a dual optical probe installed inside a rotating rod. The dual optical probe is then radially and angularly adjustable. It consists of 2 sapphire tips spaced 1mm apart to estimate the gas / liquid interface velocities if needed. The objective was to quantity the excitation source and the discrepancies between water/air and ISL/air results. Both void fraction profiles have been performed in the gap between rods and around the instrumented rod.

The mean void fraction profiles between rods or around the rod confirm that the gas and liquid phase

flowrates are the same since the mean (time averaged) void fraction is the same for water/air and ISL/air (see Figure 7 and Figure 8)

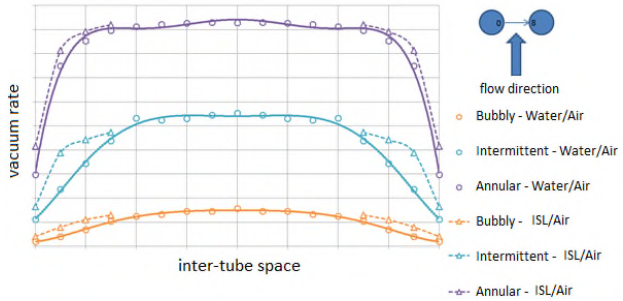

Figure 7. Comparison of the void fraction in the horizontal inter-tube space for Water/Air and ISL/Air

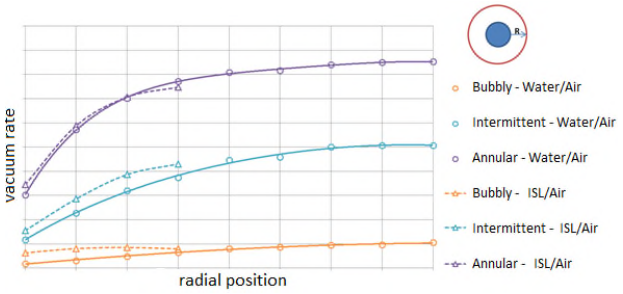

Figure 8. Comparison of the void fraction in an orbit around the tube for Water/Air and the ISL/Air

However, the rod excitation is not only linked to the mean flow but to its fluctuation. Thus, the gas / liquid interface passage frequency has been plotted to emphasize the main difference between these two simulating fluid couples. The interface passage frequencies in ISL remain larger (up to twice higher) than in water (see Figure 9 et Figure 10). These results confirm the flow visualization where more numerous but smaller flow structures impacting the tube with ISL due to a smaller surface tension.

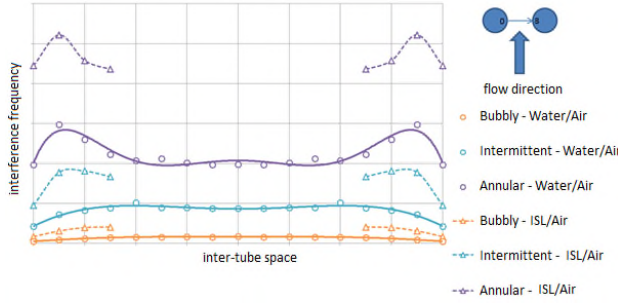

Figure 9. Comparison of the liquid/gas interface passage frequency in the horizontal inter-tube space for Water/Air and the ISL/Air

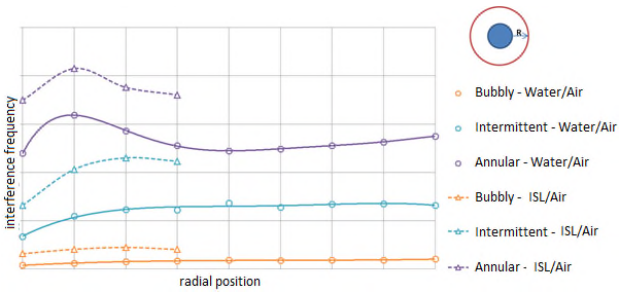

Figure 10. Comparison of liquid/gas interface passage frequency in an orbit around the tube for Water/Air and the ISL/Air

In addition to these void fraction profiles characterizing the two-phase flow excitation, a moving and instrumented rod has been designed. It aims at measuring the flow induced displacements in both streamwise (drag) and transverse (lift) directions. Indeed, a rigid plexiglass rod is connected via two flexible aluminum beams to fixed points considered as embedded boundary conditions. The flexible beams enable to rod to vibrate and are instrumented with strain gages in both Y and Z directions (see Figure 11).

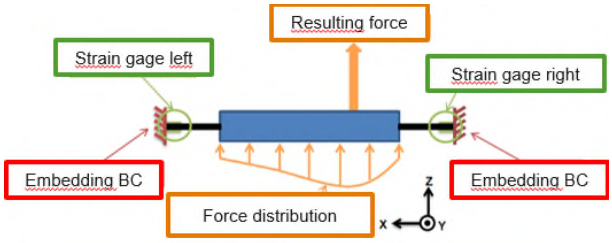

Figure 11. Moving rod with flexible beams instrumented by strain gages at both ends

Still for the same gas and liquid superficial velocities, the resulting rod displacement are presented by Power Spectral Densities in the spectral domain. The displacement (PSD) amplitude of the rod is higher in Water/Air than in ISL/Air. On one hand, one can argue that Water/air couple then keep conservatism. On the other, it emphasizes possible gain on the safety margins by using ISL that better reproduce SG liquid properties. As observed in Figure 12, the PSD difference is not due solely to the difference in liquid densities since a correction by density ratio is not sufficient to explain the amplitude discrepancies. The underlying effect of two-phase flow structures impacting the tube is here quantified and illustrated in agreement with visualizations (smaller structures yield smaller fluid momentum then forces applied on the tubes). The influence of the simulating liquid surface tension explains again the significant variations in the levels of effort between the two pairs of fluids for the same inlet gas and liquid flowrates.

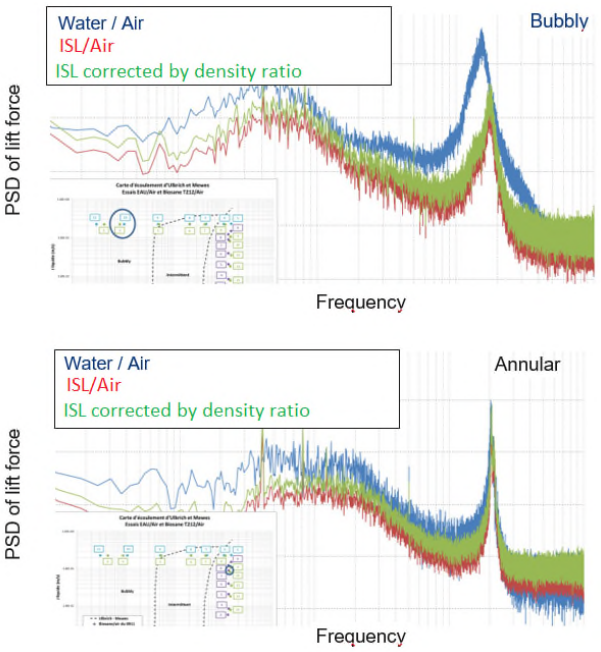

Figure 12. PSD comparison of Water/air and ISL/Air tests for the bubbly and annular regimes

These last results finish to demonstrate that both two-phase flow excitation and response are different by just changing the simulating liquid. The key message should be then to use better simulating fluids that respect also the correct surface tension in order to gain margins on SG operation and design. This experimental loop could also serve to provide data for numerical model validation. The idea would be to test the model robustness in reproducing variations like changing only the liquid (ex: Water to ISL). A further step for code validation and understanding would be to use an Improved Simulating Gas (ISG) in order to integrate the gas density effect to capture even better the physics that occur in a SG.

Beyond amplitude discrepancies, the analysis of the different PSDs showed also a first tube bending mode (PSD peaks) that changes significantly with the test conditions (fluid couples and flowrates). It appeared that the natural vibration frequency of the "tube", related to the fluid added mass, could be a good observer of the local flow characteristics around the tube. Its evolution enables to calculate an equivalent fluid density which is a function of the void fraction and then the flow regime (for a given simulating fluid couple). The frequency shift between Water/Air and ISL/Air is higher in bubbly regime than in annular regime since this latter exhibit a mainly gaseous phase with a reduced proportion and effect of the liquid. Nevertheless, level amplitudes (i.e margins) remain in PSD for the annular regimes, using ISL instead of water.

Since the FIV of this moving rod is linked to flow regimes in amplitude, peak response frequency (via added mass effect) and damping (via peak sharpening or widening), it could be also seen the other way as an opportunity to characterize the local two-phase flow around a moving rod via its response under flow. Trying to investigate further this issue, a new moving rod has been design integrating accelerometers in addition to very sensitive strain gages on the beams. The accelerometers aim at characterizing the high frequencies and low displacements (strain) with precision when strain gages loss precision. This new mounting with two measuring devices enables also to strengthen the reliability of the measurements. Strain and acceleration are acquired simultaneously in this objective.

Only Water/Air tests (up to now) have been carried out with this new instrumented tube to focus on the tube response analysis under flow. Two regime scans were conducted. The first is an increase in gas flowrate at constant liquid flowrate, and the second is a decrease in liquid flowrate at constant gas flowrate. The frequency shift of the tube response peaks (of the 2 first modes) and the evolution of their associated damping during these 2 sweeps have been observed and analyzed. It has been identified that the increase in gas flow shifts the peaks towards high frequencies due to a lower added mass and that the damping decreases with the decrease in liquid flow at constant gas flow by sharpening this PSD peak (see Figure 13).

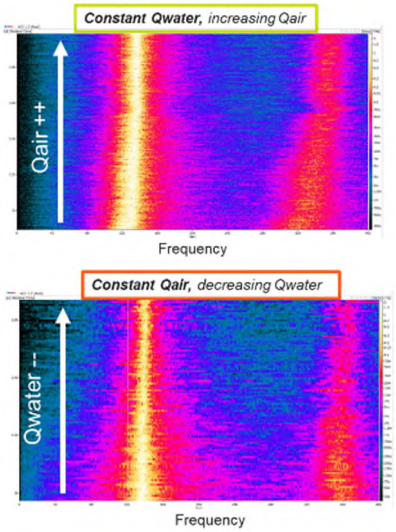

Figure 13. Frequency shift of rod response peaks (of the 2 first modes) and evolution of damping during sweeps in gas (top) and liquid (down) flowrates

The frequencies obtained with the two-measuring means (accelerometer and strain gages) are equivalent for the same void fraction. The frequency peak identification error (uncertainty) is estimated to 0.5% when normalized by "f_{air}", the frequency in air. A frequency shift (reduction) of 20% compared to "f_{air}" has been identified on the lift PSDs for void fractions ranging from 17% to 88% (see Figure 14).

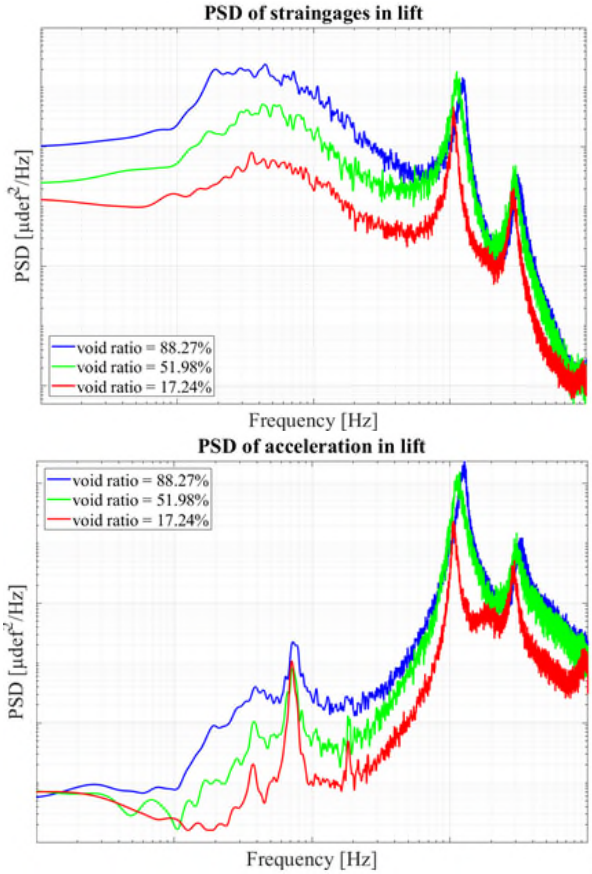

Figure 14. Synthesis of PSDs in lift (transverse) direction for void fractions from 17% to 88%

The frequency evolution of the rod response peak (of the 1st "tube" bending mode) is transcribed as added mass m_α as a function of the void fraction α using the following relationship:

$$\frac{m_\alpha}{m_{water}} = \frac{\left(\frac{f_{air}}{f_\alpha}\right)^2 - 1}{\left(\frac{f_{air}}{f_{water}}\right)^2 - 1}$$

The results for in lift direction (from strain gages) are in relatively good agreement with the literature despite a slight overestimation of the mass added to the medium void fractions (see Figure 15). This issue remains to be further investigated.

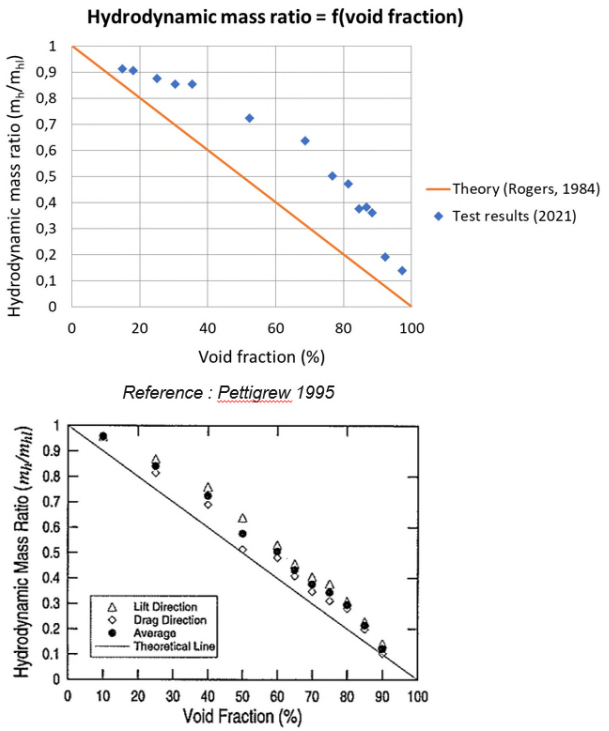

Figure 15. Validation of the two-phase added mass during "water / air" tests with the literature [11].

The two-phase flow damping ζ_α obtained from the Framatome Le Creusot experiments also remain in good agreement (in shape and amplitude) with respect to the literature (see Figure 16). The structural damping ratio ζ_{struct} has been characterized by vibration tests in air and equals around 1.5%.

$$\zeta_{total} = \zeta_{struct} + \zeta_\alpha$$

These results on both two-phase flow added mass and damping as well as the redundant measurement of tube response peak by strain or acceleration measurements support the robustness and validity of these experiments. Further tests are envisioned soon to be undertaken with ISL / Air fluid couple to corroborate previous results on the simulating fluid importance and to enrich experimental databases for numerical model validation.

These experiments underline also that, beyond PSD amplitude and shape, frequency shift and fluid damping of the "tube" response (simple straight rod) under flow could be used to characterize locally two-phase flow regimes around vibrating structures.

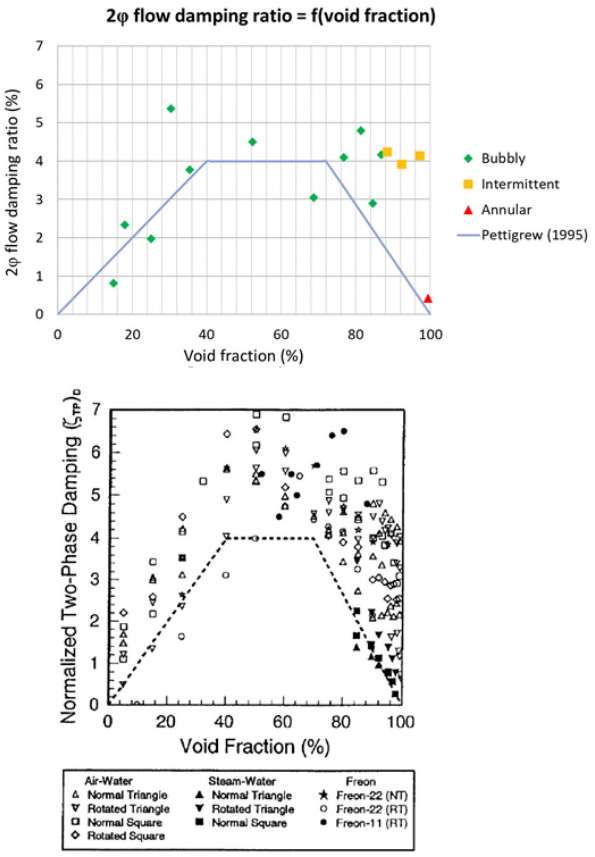

Figure 16. Validation of two-phase flow damping during "water / air" tests with the literature [12].

5. CONCLUSION

The main results of this study show that vibration measurements (of rods simulating the SG tubes) under two-phase flow demonstrate the importance of considering representative simulating fluids to better capture the physics at stake in a Steam Generator. A complete set of proofs (visualizations, gas / liquid interface passage frequencies by optical probe, PSD of rod displacement) supports the effect of the surface tension on two-phase flow topology and characteristics. These results also provide a rich opportunity to validate numerical model via their capabilities to reproduce this sensitivity to water/air and ISL/air results as a first step for scaling issues from mock-up to reactor scales.

In addition to punctual void fraction profiles, the additional analysis carried out on the "fluid" added mass and damping therefore enables to characterize the two-phase flow (excitation, coupling, regime) at the vibrating structure scale (ex: time average void fraction around a vibrating “tube”).

"An ISL/ Air" tests will be carried out soon with this new vibrating instrumented rod to complete the measurements and demonstration observed on the added mass and the damping with respect to "Water / Air" in order to further emphasize the importance of the choice of the simulating fluids.

A short-term objective is to reach the fluid-elastic instability to observe whether an ISL has an impact on this major parameter for SG design. Tests using a dedicated instrumented mounting with adjustable frequency response will be soon attempted at the Technical Center Le Creusot.

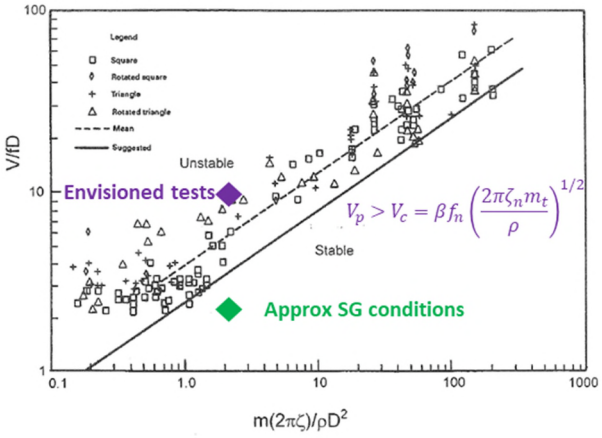

Figure 17. Envisioned tests to reach critical velocity in both water/air and ISL/air fluid couples –inspired from [13]

A longer-term objective remains to prepare the construction of an "ISL/ISG - improved simulating gas" loop envisioned at Framatome Technical Center. The present results, instrumentation and demonstration lead towards this improved simulating fluid couple as an important step in the roadmap to tackle scaling issues (from mock-up to reactor scale).

6. REFERENCES

[1] PhD thesis « Modélisation de la réponse dynamique d’une paroi solide mise en vibration par un écoulement fluide diphasique », W. Benguigui, EDF R&D, 2018

[2] R.D.Blevins, Flow induced vibration in nuclear reactors : a review, Progress in Nuclear Energy, Vol. 4, pp..25--49. Pergamon Press Ltd 1979.

[3] Au-Yang, 2001, M.K. Au-Yang, Flow-induced vibration of power and process plant component: a practical workbook, American Society of Mechanical Engineers (2001)

[4] Article « Real-life experiences with flow-induced vibration ». Journal of Fluids and Structures, 22:741–755, Païdoussis, 2006

[5] Connors, H.J., 1970. Fluid elastic vibration of tube arrays excited by cross flow. In:Proceedings of the Symposium on Flow-Induced Vibration in Heat Exchangers, ASME Winter Annual Meeting , New York, pp. 42–56.

[6] C. Monette, M.J. Pettigrew, Fluidelastic instability of flexible tubes subjected to two-phase internal flow, Journal of Fluids and Structures 19 (2004) 943–956

[7] C. Beguin, F.Anscutter, A.Ross, M.J.Pettigrew, N.W.Mureithi, Two-phase damping and interface surface area in tubes with vertical internal flow, Journal of Fluids and Structures 25(2009)178–204

[8] In-Cheol Chu∗, Heung June Chung, Seungtae Lee, Flow-induced vibration of nuclear steam generator U-tubes in two-phase flow, Nuclear Engineering and Design 241 (2011) 1508–1515

[9] Olufemi E. Bamidele, Wael H. Ahmed *, Marwan Hassan, Characterizing two-phase flow-induced vibration in piping structures with U-bends, International Journal of Multiphase Flow 151 (2022) 104042

[10] Ulbrich, R. and Mewes, D. (1994). Vertical, upward gas-liquid two-phase flow across a tube bundle. International Journal of Multiphase Flow, 20:249. (Weaver et al., 1993). P29

[11] Article « Fluid effects on multispan heat exchanger tube vibration », Pressure Vessels and Piping, San Antonio, Rogers, Taylor and Pettigrew, 1984

[12] Pettigrew, M. (1995). Vibration of a tube bundle in two-phase freon cross flow. Journal of Pressure Vessel Technology, 117:321–329.P31

[13] Kaneko, Nakamura, Inada, Kato, Ishihara, Nishihara,Flow Induced Vibration, Classifications, Lessons from practical experiences Second Edition 2014, Academic Press, Elsevier

Smart materials in FSI/FIV

PRESSURE DRIVEN SOFT VORTEX GENERATOR

Assadour Khanjian
Lebanese International University, Mechanical Engineering Department, P.O. Box: 146404 Mazraa, Beirut, Lebanon

Charbel Habchi
Notre Dame University-Louaize, Mechanical Engineering Department, Zouk Mosbeh, P.O. Box: 72 Zouk Mikael, Lebanon

IMSIA UMR CNRS-EDF-CEA 9219, Institut Polytechnique de Paris, 91120 Palaiseau, France

Serge Russeil, Daniel Bougeard
IMT Nord Europe, Institut Mines-Télécom, Univ. Lille, Centre for Energy and Environment, F-59000 Lille, France

Thierry Lemenand
LARIS, EA 7315, Polytech Angers, UNIV Angers, 49000, Angers, France

ABSTRACT

Vortex generators are used in heat exchangers and static mixers for the enhancement of heat and mass transfer processes. This enhancement is caused by the generation of streamwise vortices, and it is generally accompanied by an increase in the pumping power. Thus, active, and passive control techniques would be adopted to achieve the required rates of heat and mass transfer while maintaining low pressure losses. This could be done by adjusting the angle of attack of the vortex generators for instance.

In the present study, different types of soft vortex generators are proposed which can deform passively due to the flow forces. Hence, for low Reynolds number, i.e., low flow speed, the angle of attack is higher inducing more energetic vortices for higher transfer rates with higher pumping power. For higher Reynolds numbers, the vortex generator would deflect in the streamwise direction, lowering the vortices momentum and decreasing the pumping power.

For this end, experimental studies on soft vortex generators inside a wind tunnel are performed to quantify the angle of attack dependence on the flow speed and on the vortex generator material. In addition of concept validation, the results would be useful for validating numerical results.

1. INTRODUCTION

Various types of vortex generators (VG) have been investigated since several decades due to their ability to enhance mixing and heat transfer in heat exchangers and static mixers (Habchi *et al.*, 2012; Habchi *et al.*, 2021; Zhao *et al.*, 2022).

Most commercially used VG are rigid and do not deform under the fluid forces. However, in some applications, active control could be used to adapt their angle of attack depending on the required rate of heat or mass transfer (Aris *et al.*, 2011; Himo and Habchi, 2018). Meanwhile, recent studies are performed in which flexible or soft VG are used. These soft VG can deform and oscillate due to flow induced vibration phenomena even in laminar flow regimes. These oscillations can be efficient for increasing the rates of heat and mass transfer due to the generation of additionally vortices and eddies which add on the top of those created by the aerodynamic shape of the VG itself (Ali *et al.*, 2017, Park, 2020).

Other types of VG are based on shape memory alloy and can deform depending on the temperature values (Aris *et al.*, 2011). For example, in cooling applications, and at low cooling efficiency, the VG temperature will increase, increasing thus its angle of attack to generate more intensified vortices. These vortices will enhance the cooling rate which leads to decreasing the VG temperature and decreasing thus its angle of attack. The periodic increase and decrease in the angle of attack will lead to reduction in the average pressure losses and thus better thermal performances.

In the present study, we propose a soft VG which can deform under the force exerted by the fluid flow. For instance, at low Reynolds number, the heat transfer process requires highly energetic vortices, thus the soft VG angle of attack will be increasing. This will produce more vortices and hence better rates of heat transfer. To avoid keeping the same shape for higher Reynolds numbers where less energetic vortices are required, the soft VG angle of

attach will decrease reducing thus the pressure losses in the system.

2. EXPERIMENTAL SETUP

The experimental setup consists of a wind tunnel in which we attach a square shaped soft VG to its bottom wall. Figure 1 shows a photo of the deforming soft VG inside the wind tunnel and the dimensions of the experimental setup are given in Table 1.

To be able to read the tilt angle, which is the angle of the tail of the vortex generator after bending with respect to its initial perpendicular position, a high-definition camera is used to take several snapshots for a better reading of the values. The snapshots are then analyzed in a MATLAB image processing code to evaluate the angle.

To measure the velocity at the inlet of the wind tunnel, a Digi-Sense hot wire anemometer is used upstream and downstream the VG. Figure 2 summarizes the methods used for angle and velocity measurements.

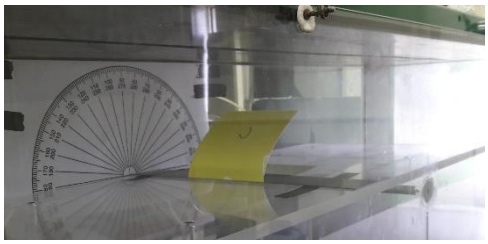

Figure 1. Deforming soft VG inside the wind tunnel.

Dimensions (cm)	
Channel height, *H*	13
Channel length, *L*	100
Channel width, *W*	30
Distance from the inlet to the VG, *M*	60
Distance from the channel wall to the VG, *S*	10
VG height, *R*	10
VG width, P	10

Table 1. Experimental setup dimensions.

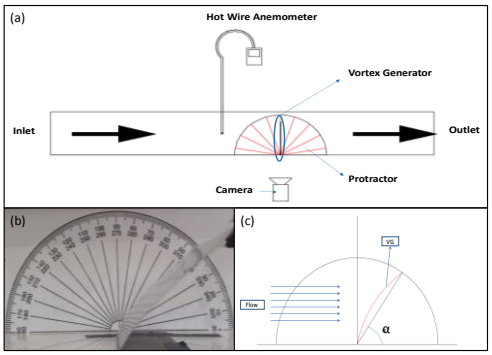

Figure 2. (a) Schematic diagram of the experimental setup (side view); (b) Photo showing the deforming VG and the protractor; (c) Tilt angle measuring method.

As a start point of the experimental assembly, the different materials of flexible VG are proposed in Table 2. These types of materials were selected since the VG has to be deformable under a very low flow pressure without undergoing a permeant deformation.

Materials	Thickness (mm)	Density (kg/m^3)	Modulus of Elasticity (MPa)
Nylon 6.6	0.2 0.5	1310	2700
LDPE Low Density Polyethylene	0.7	1200	110

Table 2. List of the materials used for the VG.

2.1. 4. RESULTS AND DISCUSSIONS

Figure 3 represents the tilt angle variation with respect to the flow speed for Nylon 6.6 VG with a thickness of 0.2 mm. For lower values of Reynolds number, the tilt angle deflection reaches 45° at a Reynolds number of around 58000 for a flow speed of about 4.8 m/s. Linear curve fitting is used to show the correlation between the deflection angle and the flow speed.

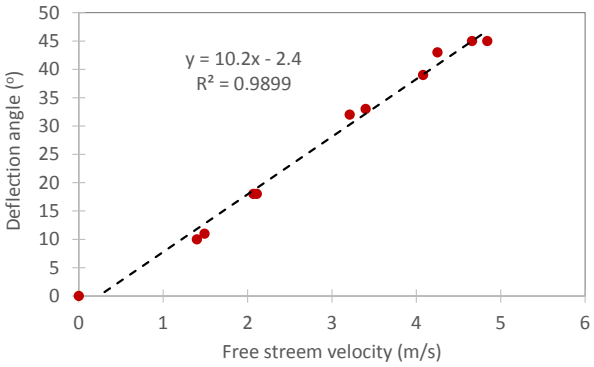

Figure 3. Deflection angle of nylon 6.6 VG with a thickness of 0.2 mm.

Figure 4 represents the case where Nylon 6.6 is used having a thickness of 0.5 mm. The tilt angle of the VG is measured with respect to the increase of the Reynolds number. As the Reynolds number increases the tilt angle increases too, reaching values around 45° for Reynolds number values of 110000, beyond which very high perturbations in the VG were observed due to vortex shedding. The same measurements have been repeated twice. The obtained results are in an average range of 5.7% error compared to each other.

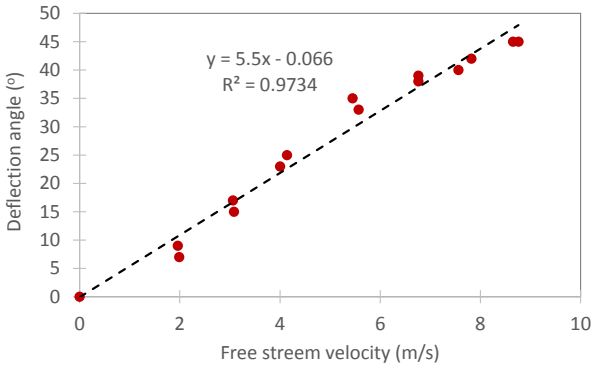

Figure 4. Deflection angle of nylon 6.6 VG with a thickness of 0.5 mm.

As a further study, low density polyethylene (LDPE) is used having a thickness of 0.7 mm, the outcome results are represented in Figure 5. The experiment has been repeated for both increasing and decreasing Reynolds number values. As the Reynolds number value increases the tilt angle deflection increases too, reaching around 28° at a Reynolds number of 65000. Since it is thicker than that of previously used VG, the physical behavior of the VG was more stable for high velocity values.

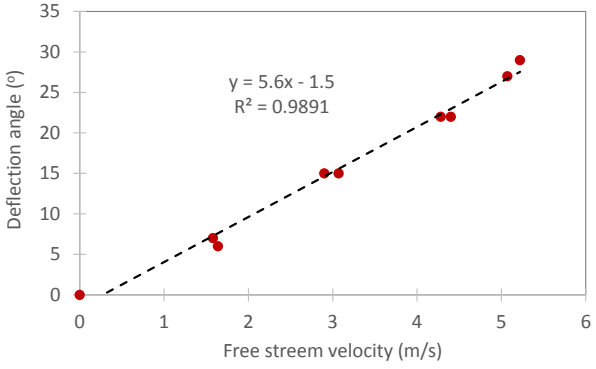

Figure 5. Deflection angle of LDPE VG with a thickness of 0.7 mm.

To be able to make a comparison between the experiment data obtained and future computational studies, it was crucial to determine the velocity profile upstream the VG. The inlet velocity profile within the duct is measured experimentally using hot wire anemometers.

Figure 6 represents the obtained results; the anemometer was placed at the inlet of the channel at 200 mm before reaching the VG. The velocity profile shows that the flow is developing flow.

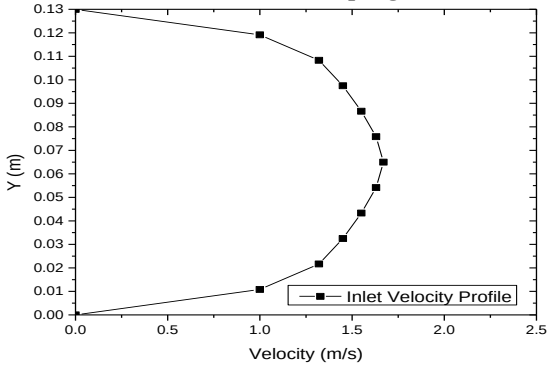

Figure 6. Inlet velocity profile having at the middle of the channel

3. CONCLUSION

The study of the vortex generators in the enhancement of the heat transfer in heat exchangers has been deepened and branched. In this study, the concept of the pressure driven auto-adaptive vortex generator is introduced and studied. It was important to prepare an experimental bench with auto adaptive vortex generator and compare the results with that of the 3D FSI code. The mechanical and physical properties of the VG were concern in this study to be able to have an acceptable deflection at reasonable inlet velocity.

After successfully validating the concept of the auto adaptive VG, it will be interesting to perform 3D FSI simulations and study the effect of both the longitudinal and the transverse vortices, and study both the local and global parameters. In addition, it would be crucial to perform studies with higher Reynolds numbers, having in mind that the pressure driven auto adaptive VG may lead to a development of new kind of heat exchangers.

4. REFERENCES

Ali, S. et al., 2017, Three-dimensional numerical study of heat transfer and mixing enhancement in a circular pipe using self-sustained oscillating flexible vorticity generators. *Chemical Engineering Science* **162**: 152-174.

Aris, M.S. et al., 2011, The development of active vortex generators from shape memory alloys for the convective cooling of heated surfaces. *International Journal of Heat and Mass* **54**: 3566–3574.

Habchi, C. et al., 2012, Enhancing heat transfer in vortex generator-type multifunctional heat exchangers. *Applied Thermal Engineering* **38**:14-25.

Habchi, C. et al., 2021, Comparison of eddy viscosity turbulence models and stereoscopic PIV measurements for a flow past rectangular-winglet pair vortex generator. *Chemical Engineering and Processing - Process Intensification* **169**:108637.

Himo, R. and Habchi, C., 2018, Coherent flow structures and heat transfer in a duct with electromagnetic forcing. *Physics of Fluids* **30**: 043605.

Park, S.G., 2020, Heat transfer enhancement by a wall-mounted flexible vortex generator with an inclination angle. *International Journal of Heat and Mass Transfer* **148**: 119053.

Zhao, Z. et al., 2022, Analysis of enhanced turbulent heat transfer in a sharp turn channel having novel designed endwall with longitudinal vortex generator. *International Communications in Heat and Mass Transfer* **131**:105874.

WIND ENERGY HARVESTING FROM FLOW-INDUCED VIBRATION OF PRISMS USING MAGNETOSTRICTIVE MATERIAL

Mohamed HERAGY, Takahiro KIWATA, Takaaki KONO
School of Mechanical Engineering, Kanazawa University, Kakuma-machi, Kanazawa 920-1192, Japan

Takuma SHIMA, Takahito HAMANO
Graduate School of Natural Science and Technology, Kanazawa University, Kakuma-machi, Kanazawa 920-1192, Japan

Toshiyuki UENO
School of Electrical and Computer Engineering, Kanazawa University, Kakuma-machi, Kanazawa 920-1192, Japan

Alis Ekmekci
Institute for Aerospace Studies, University of Toronto, 4925 Dufferin Street, Toronto, ON M3H 5T6, Canada

ABSTRACT

A vibration energy harvester was developed using a magnetostrictive material as a power generator and a prism as a wind receiver to harvest energy from low-speed wind by exploiting flow-induced vibration. Wind tunnel experiments were conducted for prisms having circular, rectangular, filleted triangular, and V-shaped cross-sections. We focused on transverse vortex-induced vibration for a circular cylinder and the low-speed galloping vibration for a rectangular prism with a depth to height ratio of 0.2, a filleted triangular prism, and a V-shaped prism. The maximum power generated for by cylindrical, rectangular, filleted triangular, and V-shaped prisms with heights of 50, 50, 60, and 50 mm was 1.28, 3.5, 8.24, and 5.02 mW, respectively. The power coefficient for a filleted triangular prism 60 mm tall was C_p = 0.22%, which is larger than that for the other test models. This peak power generated is enough to run a wireless sensor. The wind vibration power generator using a circular cylinder is safe against strong winds because it does not vibrate over Vr = 10.

1. INTRODUCTION

Recently, harvesting energy from ambient vibrations has attracted considerable attention[1]. This type of energy harvester is considered to be an important element in the development of wireless sensor nodes, which are traditionally powered by batteries[2]. Iron-gallium alloy[3], which is a magnetostrictive material, has been developed for energy harvesting from ambient vibrations. Such materials exhibit a magnetostrictive effect, that is, the magnetic flux density can be varied by a mechanical stress such as a vibration. The time variation of the internal magnetic flux density caused by periodic bending deformation (flow-induced vibration) generates a voltage in a coil according to Faraday's law of induction. It has been shown that iron-gallium alloys generate a larger amount of power than other materials when subjected to vibration [3,4]. This new technology can be applied to power Internet of Things (IoT)[5,6] and remote monitoring[7] devices.

Many studies have been conducted on vibration energy harvesting using flow-induced vibration[8–11]. It is worth mentioning that flow-induced vibration energy harvesters can be divided into six categories according to the vibration mechanism: vortex-induced vibration (VIV)[12], galloping[13], fluttering[14], buffeting[15], wake-galloping[15], and hybrid-type flow-induced vibration[16]. Kiwata et al.[17] conducted water tunnel experiments on transverse galloping of cantilevered rectangular and D-section prisms with a side ratio D/H less than 0.5 (where D is the depth of the prism in the flow direction and H is the height of the prism perpendicular to the flow). They found that all cases started to vibrate due to low-speed galloping at a reduced velocity (Vr) lower than the resonance-reduced velocity (Vr_{cr}). Moreover, the response amplitude of the transverse vibration increases with decreasing side ratio, and the D-section prism vibrated at a reduced velocity lower than that for the rectangular prism. Low-speed galloping is expected to generate a large amount of power at low wind velocity because it occurs at a lower Vr than the Vr_{cr} at which vortex-induced vibrations occur[18].

The vibration characteristics depend on the cross-section of the prism. A symmetric structure, that is, a circular cylinder, is prone to vortex-induced vibration. Meanwhile, asymmetric structures, that is,

prisms with square, rectangular, triangular, or D-shaped cross-sections, are prone to galloping[19]. A complete review of previous studies on galloping can be found in a book by Païdoussis et al.[20]. Based on the literature[19,21–23], Sharma et al.[24] compared the vibration amplitude of different cross-section structures (circular, square, triangular, or D-shaped prisms). They reported that the D-shaped prism affords higher amplitude values than the triangular prism, the square prism, and the circular cylinder. Therefore, it is important to clarify the flow-induced vibration characteristics of each cross-section to improve the power generation efficiency. Thus, in this study, a magnetostrictive vibration energy harvester was developed to generate electricity by low-speed galloping and vortex-induced vibration. Furthermore, the effects of the cross-sectional shape of a cantilevered prism for transverse flow-induced vibration on the performance of a magnetostrictive vibration energy harvester were examined by wind tunnel experiments.

2. EXPERIMENTAL APPARATUS AND METHOD

The wind vibration power generation device used in the present study and a cross section of the power-generating unit are shown in Figs. 1 and 2, respectively. The magnetostrictive vibration energy harvester comprises a wind receiver and a power generator. The power generator consists of a magnetostrictive material (iron-gallium alloy, $Fe_{81.6}Ga_{18.4}$; 8 × 26 × 1 mm), an induction coil (ϕ0.1 mm, 5627 turns, 380 Ω), a U-shaped frame (Bainite steel 1 mm thick), and a permanent neodymium magnet (6 ×12 × 1.5 mm)[25]. The frame and the magnetostrictive material have a unimorphic structure joined by an epoxy adhesive. The power generator and the wind receiver are connected by M4 nuts and bolts. The wind receiver only vibrated transversely to the flow direction. The inverse magnetostrictive effect occurs in the magnetostrictive material, that is, the magnetic permeability inside its material, varies by tension and compression acting on the material alternately when the wind receiver is bent by the flow-induced vibration. From this inverse magnetostrictive effect, an electromotive force is generated by electromagnetic induction because a magnetic circuit is formed by the permanent magnet.

Experiments were performed in a wind tunnel with a rectangular working section having a height of 1200 mm, a width of 300 mm, and a length of 2000 mm. Cross sections of the test prism models are shown in Fig. 3. Table 1 shows the prism specifications. These models were made by a 3D printer (RAISE3D Inc., N2S Plus) and PLA resin filaments. The four kinds of test models were a circular cylinder, a rectangular prism, a filleted triangular prism, and a V-shaped prism. The cross-section height H for all models was varied from 20

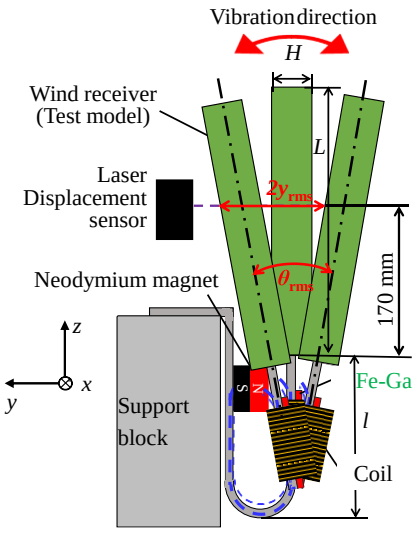

Fig. 1 Wind vibration power generation device

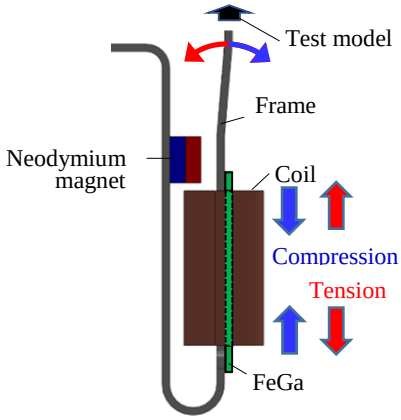

Fig. 2 Cross section of power-generating unit

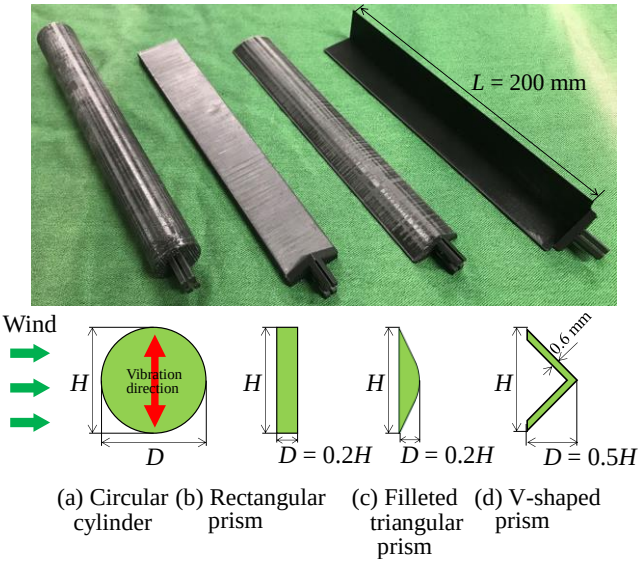

Fig. 3 Cross sections of test models

to 60 mm. The prism span length L was fixed at 200 mm. The characteristic frequency f_c for the test models was dependent on the model weight m_s. The reduced mass-damping parameter Cn was measured considering the initial displacement obtained by hitting the prism in stationary air. The parameter Cn was obtained as $2m_s\delta/\rho_{air}V_f$, where δ is the logarithmic decrement of the structural damping parameter of the prism, ρ_{air} is the density of air, and V_f is the model volume of the displacement fluid.

Table 1 Specifications of test models

Circular cylinder *(D = H)*			
H [mm]	f_c[Hz]	Cn[-]	m_s[g]
20	22.1	7.8	6.4
25	19.7	7.2	8.0
30	17.3	8.4	9.7
40	14.9	7.6	13.3
50	12.5	9.6	18.3
60	10.7	11.3	24.9

Rectangular prism *(D = 0.2H)*			
H [mm]	f_c[Hz]	Cn[-]	m_s[g]
20	26.9	12.1	4.5
25	19.7	14.2	6.6
30	21.1	10.8	8.2
40	17.9	5.9	10.0
50	16.0	7.5	15.6
60	14.4	7.5	19.8

Filtted triangle prism *(D = 0.2H)*			
H [mm]	f_c[Hz]	Cn[-]	m_s[g]
20	27.0	22.2	4.1
25	25.1	12.6	5.3
30	22.7	12.6	6.7
40	20.2	10.2	7.6
50	17.0	6.8	12.5
60	16.6	6.6	15.1

V-section prism *(D = 0.5H)*			
H [mm]	f_c[Hz]	Cn[-]	m_s[g]
20	22.2	21.4	6.0
25	19.9	16.6	8.4
30	19.0	15.1	8.7
40	15.5	13.6	14.6
50	14.2	9.9	15.6
60	12.7	8.5	19.5

The model displacement y was measured by a laser displacement sensor (Keyence, LJ-7200). The velocity fluctuation in the model wake was measured by an I-type hot-wire probe. The output signals of the integrator were converted using a 14-bit A/D converter with a sampling frequency of 2 kHz, and 16,384 data points were stored. The root-mean-square (RMS) value of the fluctuation of the non-dimensional amplitude η_{rms} and the power generation P_{rms} were calculated using a personal computer. In these calculations, $\eta_{rms} = y_{rms}/H$ and $P_{rms} = V_{rms}^2/R$, where V_{rms} is the effective value of the generated voltage, and R (= 370 Ω) is the resistance.

The uniform wind velocity U was measured using both a Pitot tube and a multi-function anemometer (Kanomax Japan Inc., Climomaster Anemometer 6501 series, 6541-21). The velocity U was varied from 1.0 to 6.2 m/s. The Reynolds number Re (= UH/ν) was in the range 1.8×10^3 to 1.03×10^4. The reduced velocity Vr (= U/f_cH) was varied from 1 to 15 by changing the wind velocity U. When the reduced velocity and Strouhal number were calculated, the wind velocity was corrected due to the blockage effect.

3. EXPERIMENTAL RESULTS AND DISCUSSION

3.1. Circular cylinder

3.1.1. Response amplitude

Figure 4 shows the RMS value for the cylindrical test model amplitude (η_{rms}) with the reduced velocity (Vr) for different cylinder diameters with H (= D) = 20, 25, 30, 40, 50, and 60 mm. The Strouhal number for a stationary circular cylinder prism is $St \approx 0.21$ (= f_wH/U, where f_w is the natural frequency of vortex shedding from a stationary circular cylinder[26]). Therefore, the onset of VIV is at the resonance reduced velocity $Vr_{cr} \approx 4.76$ (= $1/St$). The prism amplitude increases with increasing cross-sectional height H from 20 to 50 mm, and the maximum η_{rms} is 0.57 at H = 50 mm. However, the maximum η_{rms} for a circular cylinder with H = 60 mm is less than that for H = 50 mm. This is mainly attributed to shedding by the tip vortices originating from the circumferential leading edge of the free end tip for a circular cylinder with H = 60 mm, which has a small aspect ratio (length to diameter)[27]. Figure 5 shows the variations of the non-dimensional frequency f_w/f_c for a circular cylinder (H = 40, 50, and 60 mm) with reduced velocity. The lock-in region for a circular cylinder with H < 50 mm is smaller (i.e., the vibration ceases at $Vr \approx 9$) than that for H = 50 mm

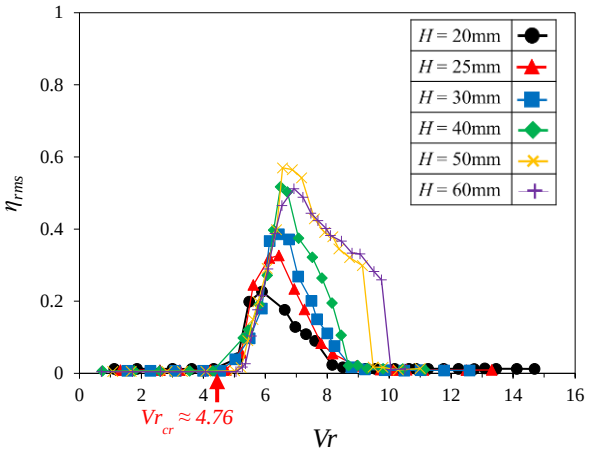

Fig. 4 Variation of non-dimensional amplitude for circular cylinders with reduced velocity.

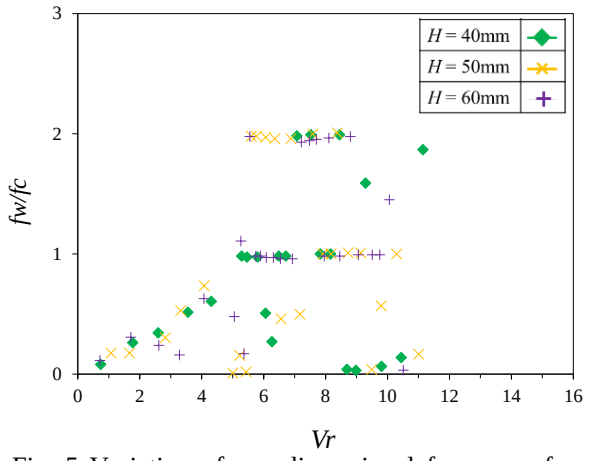

Fig. 5 Variation of non-dimensional frequency for circular cylinder (H = 40, 50, and 60 mm) with reduced velocity.

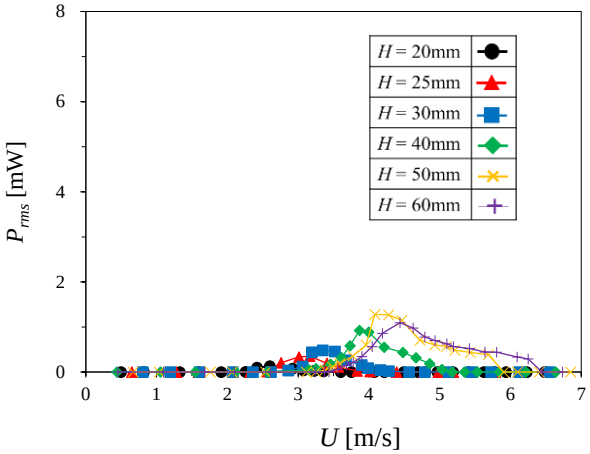

Fig. 6 Variation of power for circular cylinders with flow velocity.

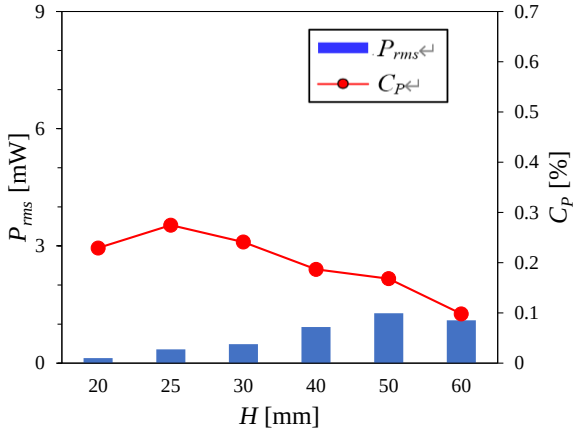

Fig. 7 Maximum power and power coefficients for different cylinder diameters (expressed as H).

(i.e., the vibration ceases at $Vr \approx 9.5$) and H = 60 mm (i.e., the vibration ceases at $Vr \approx 10$). The circular cylinder does not vibrate when Vr exceeds 10. This phenomenon is useful for protecting the vibration power generator from damage in strong winds.

3.1.2. Power generation

Figure 6 shows the variation of the RMS value of power generation (P_{rms}) with the flow velocity U in the case of H = 20 - 60 mm. The circular cylinder with H = 20 mm begins to generate power at $U \approx$ 2 m/s. For H = 50 mm, the maximum value of P_{rms} is 1.28 mW at U = 4.08 m/s. Figure 7 shows the variations of the maximum P_{rms} and the power coefficient C_P [= P_{rms} /($0.5\rho_{air}AU^3$)]. In the calculation of the coefficient, A is the swept area {$A = HL+\frac{\pi\theta_{rms}}{360}[(L+l)^2-l^2]$} and l is the length of the U-frame branch attached to the model, as indicated in Fig. 1. The circular cylinder with the maximum amplitude shown in Fig. 4 has the maximum power generation, as shown in Fig. 6. However, the circular cylinder with H = 25 mm has the maximum power coefficient at C_P = 0.27%.

3.2. Rectangular prism with D/H = 0.2

3.2.1. Response amplitude

Figure 8 shows the variation of η_{rms} with Vr for a rectangular prism with D/H = 0.2 and H = 20, 25, 30, 40, 50, and 60 mm. The rectangular prisms with $H \geq$ 40 mm vibrate. There is no excitation for prisms with H < 40 mm because the greatly reduced mass-damping parameter (Cn), as shown in Table 1. The reduced velocity for vibration onset for the rectangular prisms with $H \geq$ 40 mm is $Vr \approx 3$, which is less than the resonance reduced velocity $Vr_{cr} \approx$ 7.14 (= 1/St, where $St \approx 0.14$)[26] for rectangular prisms with a side ratio of D/H = 0.2. Therefore, low-speed galloping vibration primarily occurs in a rectangular prism with D/H = 0.2. With increasing flow velocity, the amplitude of rectangular prisms for $H \geq$ 40 mm increases, and the response amplitude has a peak near $Vr_{cr} \approx$ 7.14. The maximum η_{rms} is 0.78 for a rectangular prism with H = 50 mm. The rectangular prism with H = 40 mm stops vibrating at $V_r \approx 9$.

Unfortunately, we ceased measuring the amplitude of rectangular prisms with H = 50 and 60 mm because the U-frame (Fig. 2) contacted the neodymium magnet due to the large oscillation. If the wind velocity increases to exceed Vr_{cr}, the rectangular prism will oscillate by VIV and the oscillation will cease, similar to the behavior of a rectangular prism with H = 40 mm. Therefore, the rectangular prism with a side ratio of D/H = 0.2, $H \geq$ 40 mm, and a small Cn can vibrate by low-speed galloping and VIV. Further, generation of electricity is expected to start at a low wind speed.

Figure 9 shows the variation of f_w/f_c with Vr for rectangular prisms with H = 40, 50, and 60 mm. The lock-in phenomenon, that is, $f_w/f_c \approx 1$, occurs from the reduced velocity of the onset of vibration to $Vr \approx 8$.

3.2.2. Power generation

Figure 10 shows the variation of P_{rms} with U for a rectangular prism with D/H = 0.2 and H = 20, 25, 30, 40, 50, and 60 mm. The rectangular prisms with $H \geq 40$ mm begin to generate power from $U \approx 3$ m/s. For H = 50 mm, the maximum value of P_{rms} is 3.5 mW at U = 6.04 m/s. Figure 11 shows variations of the maximum P_{rms} and C_P with cross-section height H. The power generated by a rectangular prism with H = 50 mm is larger than that for other heights with D/H = 0.2. However, the rectangular prism with H = 40 mm has the maximum C_P of 0.28% because the swept area for a rectangular prism with H = 40 mm is smaller than that with H = 50 mm.

3.3. Filleted triangular prism

3.3.1. Response amplitude

Figure 12 shows the variation of η_{rms} with Vr for filleted triangular prisms with H = 20, 25, 30, 40, 50, and 60 mm. The prisms are assumed to be treated as D-section prisms, which is a hard oscillator, that is, it will not gallop from rest, but at any flow velocity, it requires an initial amplitude to be exceeded before

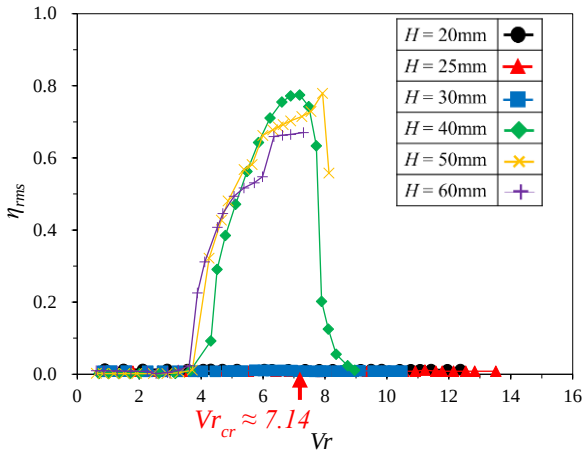

Fig. 8 Variation of non-dimensional amplitude for rectangular prisms (H = 20, 25, 30, 40, 50, and 60 mm) with reduced velocity.

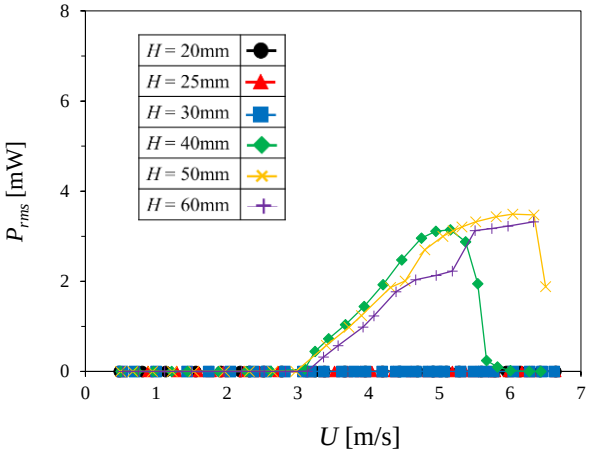

Fig. 10 Variation of power for rectangular prisms with flow velocity.

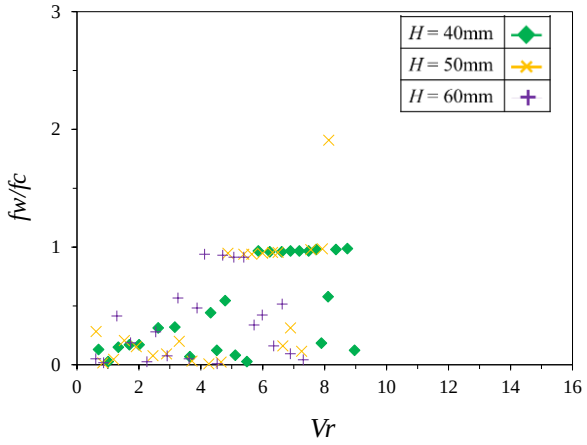

Fig. 9 Variation of non-dimensional frequency for rectangular prisms (H = 40, 50, and 60 mm) with reduced velocity.

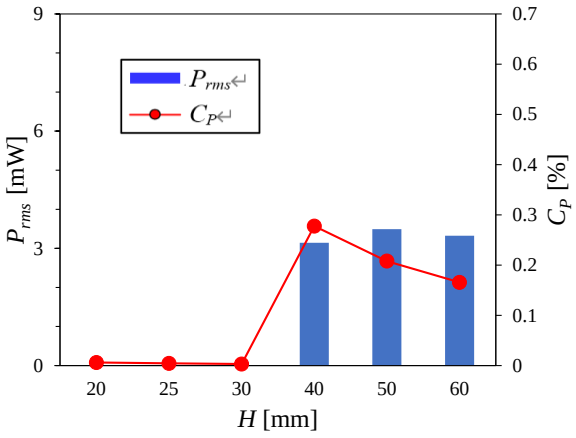

Fig. 11 Maximum power and power coefficients for different rectangular prism heights.

the amplitude will increase to a stable galloping value[28]. However, all filleted triangular prisms with H < 40 mm could not continue to oscillate even after the initial amplitude was applied due to the high Cn values, as shown in Table 1. The filleted triangular prism with H = 40 mm continues oscillation after being given an initial amplitude. The filleted triangular prism with H > 40 mm begins to vibrate without an initial amplitude; in other words, it is a soft oscillator. Because the filleted triangular prisms with large height have small Cn values, as shown in Table 1, the reduced velocity Vr for vibration onset decreases as the height increases. The vibration onsets for filleted triangular prisms with H = 40, 50, and 60 mm are Vr = 4.1, 3.8, and 3.3, respectively. These values for D-section prisms are less than Vr_{cr} ≈ 7.4 (= 1/St, where St ≈ 0.135)[23]. Therefore, the filleted triangular prism is excited by low-speed galloping. The response amplitude of the filleted triangular prism with H = 40 mm has a peak of η_{rms} = 0.82 at Vr = 6.5.

However, we ceased measuring the amplitude for the filleted triangular prisms with H = 50 and 60 mm in this experiment because the U-frame (Fig. 2) contacted the neodymium magnet due to the large oscillation amplitude. If the wind velocity increases to exceed Vr_{cr}, the filleted triangular prism will oscillate by VIV and the oscillation will cease, similar to the rectangular prism with H = 40 mm.

Figure 13 shows the variation of f_w/f_c with Vr for filleted triangular prisms with H = 40, 50, and 60 mm. The lock-in phenomenon, that is, f_w/f_c ≈ 1, occurs from the reduced velocity for the onset of vibration to Vr ≈ 8. This characteristic is similar to that for the rectangular prism with D/H = 0.2.

3.3.2. Power generation

Figure 14 shows the variation of P_{rms} and U for filleted triangular prisms with H = 20 - 60 mm. The rectangular prisms with H ≥ 40 mm begin to

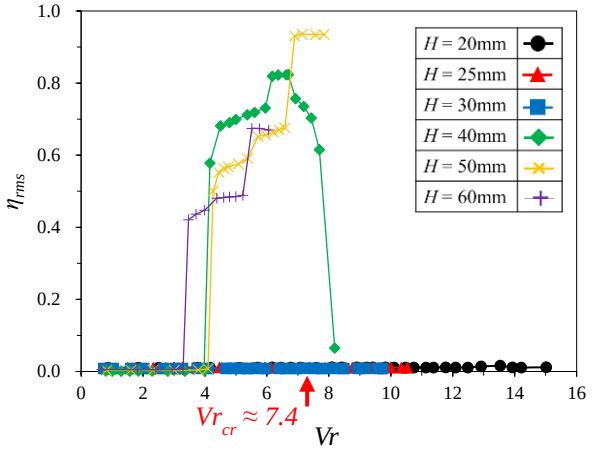

Fig. 12 Variation of non-dimensional amplitude for filleted triangular prisms (H =20,25, 30, 40, 50, and 60 mm) with reduced velocity.

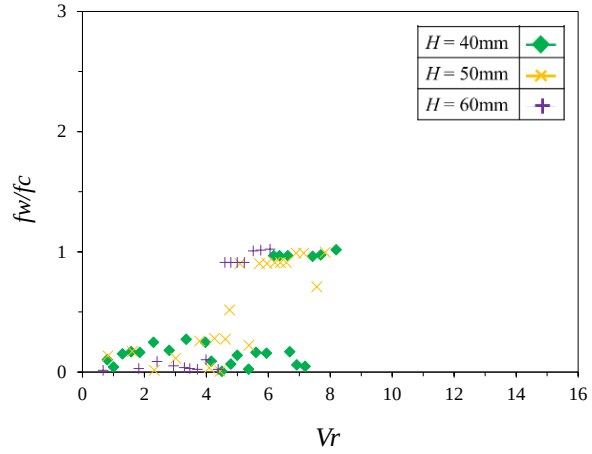

Fig. 13 Variation of non-dimensional frequency and amplitude for filleted triangular prisms (H = 40, 50, and 60 mm) with reduced velocity.

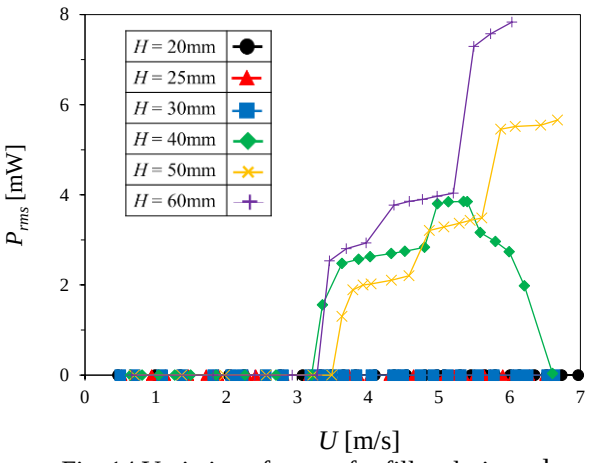

Fig. 14 Variation of power for filleted triangular prisms with flow velocity.

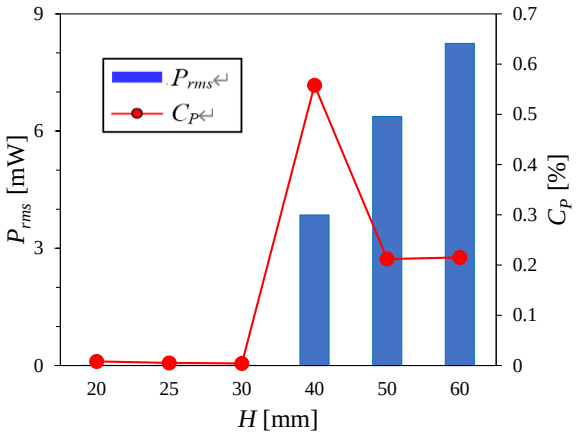

Fig. 15 Maximum power and power coefficient for different filleted triangular prism heights.

generate power at $U \approx 3.3$ m/s. For a filleted triangular prism with $H = 40$ mm, the maximum value of P_{rms} is 3.5 mW at $U = 5.4$ m/s. Moreover, the filleted triangular prisms with $H = 50$ mm and 60 mm can produce more power. The maximum value of P_{rms} is 5.75 mW and 7.8 mW at $U = 6.7$ m/s and 6.03 m/s, respectively. Figure 15 shows variations of the maximum P_{rms} and C_P with H. The maximum power generated by filleted triangular prisms with $H = 60$ mm is larger at $P_{rms} = 7.8$ mW than that for the other prisms. The maximum power coefficient for the filleted triangular prisms with $H = 40$ mm is larger at $C_P = 0.56\%$ than that for prisms with other heights.

3.4. V-shaped prism

3.4.1. Response amplitude

Figure 16 shows the variation of η_{rms} with Vr for V-shaped prisms with $H = 20$, 25, 30, 40, 50, and 60mm

The V-shaped prism is a soft oscillator and will gallop from rest at a flow velocity above a critical value[28]. The reduced velocity for vibration onset is $Vr \approx 4$, which is less than $Vr_{cr} \approx 7.4$ (= $1/St$, where $St \approx 0.14$)[29]. Therefore, the V-shaped prism begins to vibrate by low-speed galloping. The maximum η_{rms} is 0.97 for $H = 30$ mm at $Vr = 11.3$. However, we ceased measuring the amplitude for $H > 25$ mm in this experiment because the U-frame (Fig. 2) contacted the neodymium magnet due to the large oscillation amplitude. If the wind velocity increases over Vr_{cr}, the V-shaped prism will oscillate by VIV and the oscillation may cease, similar to a rectangular prism with $H = 40$ mm.

Figure 17 shows the variation of f_w/f_c with Vr for V-shaped prisms with $H = 20$ - 60 mm. This figure confirms that the lock-in phenomenon occurs before Vr_{cr} and during the oscillation.

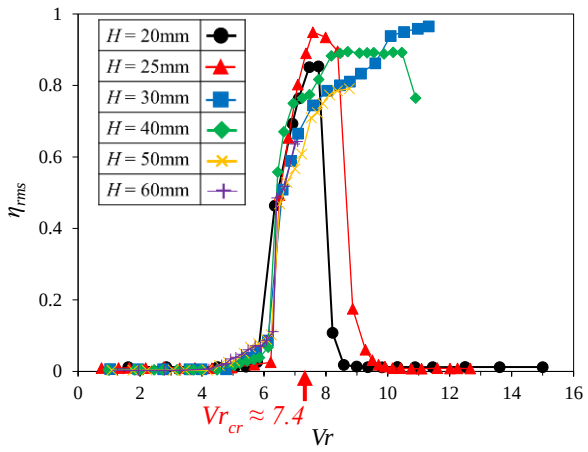

Fig. 16 Variation of non-dimensional amplitude for V-shaped prisms (H =20,25, 30, 40, 50, and 60 mm) with reduced velocity.

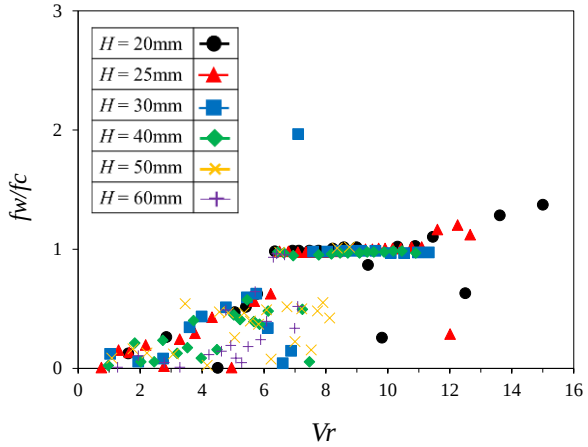

Fig. 17 Variation of non-dimensional frequency and amplitude for V-shaped prisms with reduced velocity.

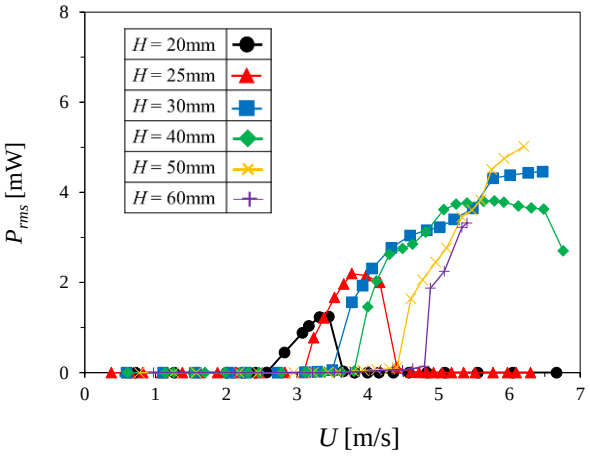

Fig. 18 Variation of power for V-shaped prisms with flow velocity.

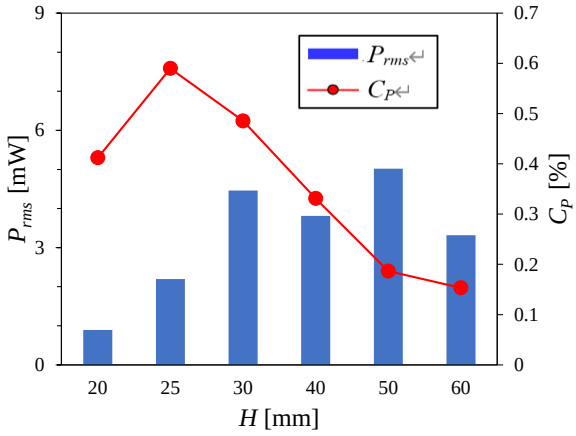

Fig. 19 Maximum power and power coefficients for different V-shaped prism heights.

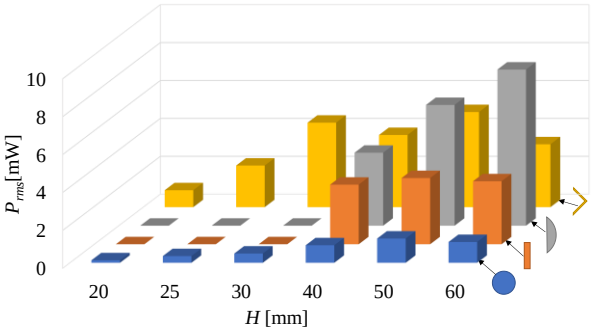

Fig. 20 Maximum power for different heights of cylinders and prisms

3.4.2. Power generation

Figure 18 shows the variation of P_{rms} with U for V-shaped prisms with H = 20 - 60 mm. All V-shaped prisms start to generate power from a reduced velocity less than Vr_{cr}. The V-shaped prism with H = 20 mm starts to vibrate from the lowest wind speed at $U \approx 2.6$ m/s. The flow velocity for vibration onset increases with increasing H. The maximum value of P_{rms} is 5.02 mW for H = 50 mm. However, a V-shaped prism with H = 60 mm may produce more power if the U-frame does not contact the neodymium magnet.

Figure 19 shows the variation of the maximum P_{rms} and C_P with H. At C_P = 0.59%, the power coefficient for a V-shaped prism with H = 25 mm is larger than that for prisms with other heights. For H > 25 mm, the value of C_P decreases with increasing H.

Comparison of the non-dimensional amplitude in Figures 4, 8, 12, and 16 makes it is clear that the filleted triangular and V-shaped prisms produced higher vibration amplitudes than the rectangular and circular cylinder prisms, consistent with previously reported results [24].

Figure 20 shows the maximum P_{rms} for all test models under the condition that the frame of the power generator does not hit the neodymium magnet. A maximum power of 8.24 mW is obtained with the filleted triangular prism with H = 60 mm. This is sufficient to run low-power-consumption sensors and wireless communication systems, such as those used in IoT devices.

4. CONCLUSIONS

The most suitable cross-sectional shape for a cantilevered prism for transverse flow-induced vibration and the performance of a wind vibration power generator using a magnetostrictive material were investigated in a wind tunnel. The main conclusions of the present study are as follows:

(1) The circular cylinders oscillate by vortex-induced vibration, and the vibration ceases when $V_r \approx 10$. The amount of power generated is largest for H = D = 50 mm, and the maximum power generated is 1.28 mW with a power efficiency of 0.17%. However, the circular cylinder with H = 25 mm has the maximum power coefficient of C_P = 0.27%.

(2) The rectangular prism with D/H = 0.2 and $H \geq 40$ mm oscillates by low-speed galloping and vortex-induced vibration. The power generated for H = 50 mm is P_{rms} = 3.5 mW, which is larger than that for rectangular prisms with other heights. However, the rectangular prism with H = 40 mm has the maximum power coefficient of C_P = 0.28%.

(3) Filleted triangular prisms with $H \geq 40$ mm oscillate by low-speed galloping and VIV. The power generated for H = 60 mm is P_{rms} = 8.24 mW (C_P = 0.22%), which is larger than that for prisms with other heights. However, the filleted triangular prism with H = 40 mm has the maximum power coefficient of C_P = 0.56%.

(4) The V-shaped prism oscillates by low-speed galloping and vortex-induced vibration. The prism with H = 50 mm has a maximum power generation of 5.02 mW (C_P = 0.19%). The power coefficient for a V-shaped prism with H = 25 mm is C_P = 0.59%, which is larger than that for prisms with other heights.

ACKNOWLEDGEMENTS

This work was supported by the Japan Ministry of Education, Culture, Sports, Science and Technology, “Program for Building Regional Innovation Ecosystems”. The authors are thankful to Mr. Ryohei Nagase and Dr. La Ode Ahmad Barata for their help with the experiment.

REFERENCES

1. Wang, J. *et al.* Enhancing energy harvesting from flow-induced vibrations of a circular cylinder using a downstream rectangular plate: An experimental study. *Int. J. Mech. Sci.* **211**, 106781 (2021).
2. Aoudia, F. A., Gautier, M., Magno, M., Berder, O. & Benini, L. Leveraging energy harvesting and wake-up receivers for long-term wireless sensor networks. *Sensors (Switzerland)* **18**, (2018).
3. Hasegawa, K., Ueno, T. & Kiwata, T. Proposal of Wind Vibrational Power Generator Using Magnetostrictive Material. *IEEE Trans. Magn.* **55**, (2019).
4. Deng, Z. & Dapino, M. J. Review of magnetostrictive vibration energy harvesters.

Smart Materials and Structures **26**, 103001 (2017).
5. Liu, L., Guo, X. & Lee, C. Promoting smart cities into the 5G era with multi-field Internet of Things (IoT) applications powered with advanced mechanical energy harvesters. *Nano Energy* **88**, 106304 (2021).
6. Ueno, T. Magnetostrictive vibrational power generator for battery-free IoT application. *AIP Adv.* **9**, 035018 (2019).
7. Annapureddy, V. *et al.* Magnetic energy harvesting with magnetoelectrics: an emerging technology for self-powered autonomous systems. *Sustain. Energy Fuels* **1**, 2039–2052 (2017).
8. Li, D., Wu, Y., Da Ronch, A. & Xiang, J. Energy harvesting by means of flow-induced vibrations on aerospace vehicles. *Prog. Aerosp. Sci.* **86**, 28–62 (2016).
9. Wang, J., Geng, L., Ding, L., Zhu, H. & Yurchenko, D. The state-of-the-art review on energy harvesting from flow-induced vibrations. *Appl. Energy* **267**, 114902 (2020).
10. Wang, J. *et al.* Perspectives in flow-induced vibration energy harvesting. *Appl. Phys. Lett.* **119**, 100502 (2021).
11. Ma, X. & Zhou, S. A review of flow-induced vibration energy harvesters. *Energy Convers. Manag.* **254**, 115223 (2022).
12. G.A Muthalif, A., Hafizh, M., Renno, J. & Paurobally, M. R. A hybrid piezoelectric-electromagnetic energy harvester from vortex-induced vibrations in fluid-flow; the influence of boundary condition in tuning the harvester. *Energy Convers. Manag.* **256**, 115371 (2022).
13. Xu, C. & Zhao, L. Investigation on the characteristics of a novel internal resonance galloping oscillator for concurrent aeroelastic and base vibratory energy harvesting. *Mech. Syst. Signal Process.* **173**, 109022 (2022).
14. Tamimi, V., Wu, J., Esfehani, M. J., Zeinoddini, M. & Naeeni, S. T. O. Comparison of hydrokinetic energy harvesting performance of a fluttering hydrofoil against other Flow-Induced Vibration (FIV) mechanisms. *Renew. Energy* **186**, 157–172 (2022).
15. Liu, C., Gong, Y., Jiang, Z. & Guo, K. Buffeting analysis of a suspension bridge under construction based on adjacent wind field data. *Eng. Struct.* **251**, 113490 (2022).
16. Chen, C., Mannini, C., Bartoli, G. & Thiele, K. Wake oscillator modeling the combined instability of vortex induced vibration and galloping for a 2:1 rectangular cylinder. *J. Fluids Struct.* **110**, 103530 (2022).
17. KIWATA, T., YAMAGUCHI, M., KONO, T. & UENO, T. Water tunnel experiments on transverse-galloping of cantilevered rectangular and D-section prisms. *J. Fluid Sci. Technol.* **9**, (2014).
18. Nakamura, Y. & Hirata, K. Pressure fluctuations on oscillating rectangular cylinders with the long side normal to the flow. *J. Fluids Struct.* **5**, 165–183 (1991).
19. Seyed-Aghazadeh, B., Carlson, D. W. & Modarres-Sadeghi, Y. Vortex-induced vibration and galloping of prisms with triangular cross-sections. *J. Fluid Mech.* **817**, 590–618 (2017).
20. Michael P. Pa¨ıdoussis, Stuart J. Price & de Langre, E. *Fluid Structure Interactions Cross-Flow-Induced-Instabilities*. (Cambridge University Press).
21. Borazjani, I. & Sotiropoulos, F. Vortex-induced vibrations of two cylinders in tandem arrangement in the proximity–wake interference region. *J. Fluid Mech.* **621**, 321–364 (2009).
22. Zhao, J., Leontini, J. S., Lo Jacono, D. & Sheridan, J. Fluid–structure interaction of a square cylinder at different angles of attack. *J. Fluid Mech.* **747**, 688–721 (2014).
23. Zhao, J., Hourigan, K. & Thompson, M. C. Flow-induced vibration of D-section cylinders: an afterbody is not essential for vortex-induced vibration. *J. Fluid Mech.* **851**, 317–343 (2018).
24. Sharma, G., Garg, H. & Bhardwaj, R. Flow-induced vibrations of elastically-mounted C- and D-section cylinders. *J. Fluids Struct.* **109**, 103501 (2022).
25. Ueno, T. & Yamada, S. Performance of energy harvester using iron-gallium alloy in free vibration. *IEEE Trans. Magn.* **47**, 2407–2409 (2011).
26. *JSME Mechanical Engineer's Handbook, 2006, α4:Fluid Engineering, JSME: 81 (in Japanese)*.
27. Sumner, D. Flow above the free end of a surface-mounted finite-height circular cylinder: A review. *J. Fluids Struct.* **43**, 41–63 (2013).
28. Parkinson, G. Phenomena and modelling of flow-induced vibrations of bluff bodies. *Prog. Aerosp. Sci.* **26**, 169–224 (1989).
29. SLATER, J. E. AEROELASTIC INSTABILITY OF A STRUCTURAL ANGLE SECTION. (1969).

Tube Arrays

A NEW CRITERION FOR THE INSTABILITY THRESHOLD OF A SQUARE TUBE BUNDLE SUBJECT TO AN AIR-WATER CROSS-FLOW

R. Lagrange, D. Panunzio, P. Piteau, X. Delaune
Université Paris-Saclay, CEA, Service d'Études Mécaniques et Thermiques, 91191, Gif-sur-Yvette, France

J. Antunes
Centro de Ciências e Tecnologias Nucleares (C2TN), Instituto Superior Técnico (IST), Universidade de Lisboa, 2695-066 Bobadela LRS, Portugal

ABSTRACT

In this paper, we investigate the fluid-elastic instability of a square tube bundle subject to a two-phase cross-flow. A dimensional analysis is carried out, leading to a new criterion of stability. This criterion establishes a direct link with the stability thresholds in single-phase flows and as such constitutes an extension to the Connors equation for two-phase flows. In parallel to the dimensional analysis, an experimental work is conducted to test the validity of the criterion in air-water cross-flow. The bundle consists on 5 rows of 3 tubes (plus two end-rows of half-tubes), with reduced pitch P/D = 1.5, tubes diameter and length D = 30 mm, L=300 mm. The central tube is mounted on two flexible blades allowing a vibration in the transverse direction, whereas all the other tubes are rigid. Three sets of blades with different rigidities are tested to investigate the stability of the central tube, considering, for an homogeneous void fraction in the range 0% to 100%. We show that the criterion of stability derived from the dimensional analysis is in very good agreement with the air-water experiments. This new criterion is of theoretical interest for the understanding of complex two-phase flow excitations, as well as of practical significance for the predictive analysis of industrial components.

1. INTRODUCTION

The knowledge of the fluid force acting on a structure subject to a cross flow is a crucial information that must be accounted for when designing heat-exchanger tube bundles. The large vibrations resulting from a fluid-elastic instability may lead to some mechanical degradation of the concerned tube, which may affect the power plant operation and safety. This instability can be described as a self-excited feedback mechanism between the motion of the structure and the fluid forces.

The first work on fluid-elastic instability was published by Roberts (1962), who highlighted self-sustained oscillations within a row of cylinders subject to cross flow; the cylinders being alternately rigid and flexible in the direction of the flow. Connors (1970) studied the interaction between a row of flexible cylinders and a transverse flow and developed a quasi-static model following Roberts' work. He proposed an estimation of the critical instability velocity for a tube as a function of a mass damping parameter and a constant called the Connors constant. Several other theoretical models were subsequently proposed for the study of the fluid-elastic instability: the inviscid or velocity potential model by Dalton and Helfinstine (1971), the quasi-steady model by Price and Païdoussis (1982, 1983), the unsteady model by Tanaka and Takahara, (1980, 1981), Chen (1983a,b, 1987), the quasi-unsteady model by Granger and Païdoussis (1996) or the flow channel model by Lever and Weaver, (1986).

Following the work of Roberts (1962) and Connors (1970), a wealth of experimental studies were also carried out, primarily to refine Connors' model and determine the value of the Connors constant for various types of tube bundles. Initially, most of the experiments were performed in single-phase flows (liquid or gaseous) and it was not until the 1980s that studies on tube bundles subject to two-phase flow became widespread, see for e.g. Axisa *et al*. (1984, 1985); Nakamura *et al*. (1986a, b). Most experimental works were done in air-water flows due to the very high cost of steam-water loops. This however raised the question of the validity of experimental results for the tubes of a steam generator that actually operate in a steam-water mixture. To overcome this problem, some researchers as Pettigrew *et al*. (1995, 2002, 2009) used a mixture of liquid-vapor freon due to the proximity of its density ratio to that of steam-water. The results have shown very little difference in terms of critical velocity whether a mixture of freon, an air-water or a steam-water flow is considered. It is therefore believed that the results in air-water are representative of what happens in a steam

generator. Still, it should be mentioned that, apart from experimental studies, most theoretical models have been developed for single-phase flows, whereas steam generators operate mainly in two-phase flows. The need to extend the theoretical models to two-phase flows is therefore necessary and is the purpose of the present work. To do so, we first introduce a dimensional analysis from which we derive a new criterion for the instability threshold of a square tube bundle subject to a two-phase cross-flow. Then, we compare the prediction derived from this analysis to the experimental results performed at CEA with an air-water flow.

2. POSITION OF THE PROBLEM AND DIMENSIONAL ANALYSIS

We consider the vibration of a flexibly mounted tube (diameter D, length L), part of a square tube bundle (pitch P), immerged in a two-phase fluid characterized by the mass densities (ρ_1, ρ_2), the kinematic viscosities (ν_1, ν_2), the superficial velocities (J_1, J_2) of its two constitutive phases, as well as a surface tension σ. The homogeneous void fraction is defined as $\alpha = J_2/(J_1 + J_2)$. We note M_s, C_s and K_s the mass, damping and rigidity coefficients of the first mode of vibration of the flexible tube in air. The modal displacement X in the lift direction is assumed to satisfy the equation:

$$(M_s + M_f)\ddot{X} + (C_s + C_f)\dot{X} + (K_s + K_f)X = F_t, \qquad (1)$$

where M_f, C_f and K_f are the fluid added mass, damping and rigidity terms, respectively. The right hand side term F_t is an excitation fluid force, considered as independent on the tube motion. According to this forced oscillator model, the flexible tube turns unstable when the total damping term $C_T = C_s + C_f$ vanishes, i.e. $C_T = 0$. Here, we consider that C_T is a function of $(C_j, F_j, \rho_1, \rho_2, \nu_1, \nu_2, \sigma, J_1, J_2, P, D, L)$:

$$C_T = H_{C_T}^{(j)}(C_j, F_j, \rho_1, \rho_2, \nu_1, \nu_2, \sigma, J_1, J_2, P, D, L), \quad (2)$$

where C_j and F_j are the damping coefficient and frequency of the flexible tube immerged in the single phase j fluid at rest. The relation (2) constitutes a minimal model, based on experimental observations, bibliography reporting and physical intuition. More advanced models would also consider the effect of some other parameters, for e.g. the roughness of the tubes.

The dimensional analysis is based on the Vaschy-Buckingham theorem. The theorem states that an equation involving n physical variables with k fundamental units (usually $k = 3$ in classical mechanics) can be reduced to an equation involving $n-k$ dimensionless parameters. Thus, introducing a scale of length λ, mass M and time τ, the equation for the instability threshold $C_T = 0$ is physically meaningful if

$$h_{C_T}^{(j)}\left(\begin{array}{c} \frac{C_j}{M\tau^{-1}}, \frac{F_j}{\tau^{-1}}, \frac{\rho_1}{M\lambda^{-3}}, \frac{\rho_2}{M\lambda^{-3}}, \frac{\nu_1}{\lambda^2\tau^{-1}}, \frac{\nu_2}{\lambda^2\tau^{-1}}, \\ \frac{\sigma}{M\tau^{-2}}, \frac{J_1}{\lambda\tau^{-1}}, \frac{J_2}{\lambda\tau^{-1}}, \frac{P}{\lambda}, \frac{D}{\lambda}, \frac{L}{\lambda} \end{array}\right) = 0. \quad (3)$$

As (3) involves twelve dimensional quantities with three fundamental dimensions (length, mass and time), it can be reduced to a relation between nine dimensionless quantities. These dimensionless quantities are not unique and derive from a specific choice for the characteristic length λ, mass M and time τ. Picking $\lambda = D$, $M = \rho_j D^2 L$ and $\tau = D/J_j$ with j a free index, the dimensionless equation for the instability threshold rewrite

$$h_{C_T}^{(j)}(Sc_j, Sk_j, m, \varepsilon, We_j, \alpha, Re_j, p, l) = 0, \qquad (4)$$

with $l = L/D$, $p = P/D$, $m = \rho_2/\rho_1$ and $\varepsilon = \nu_2/\nu_1$ the tube aspect ratio, the pitch ratio, the density and viscosity ratios, respectively. The other dimensionless numbers appearing in (4), i.e.

$$\begin{aligned} &Re_j = DJ_j/\nu_j, && Sk_j = D^2F_j/\nu_j, \\ &Sc_j = C_j/(2\rho_j D^2 L F_j), && We_j = \rho_j L \nu_j{}^2/\sigma D^2, \end{aligned} \quad (5)$$

are the Reynolds, Stokes, Scruton and Weber numbers, constructed from the physical properties of phase j. Once again, the choice for the dimensionless numbers is purely arbitrary, and other combinations are possible. For example, instead of the homogeneous void fraction α, it is also possible to introduce a second Reynolds number, via the relation $\alpha = \varepsilon Re_2/(Re_1 + \varepsilon Re_2)$.

2.1. Case of a single-phase flow

A single-phase flow can be seen as a two-phase flow with two identical phases, i.e. $(\rho_1, \nu_1) = (\rho_2, \nu_2) = (\rho, \nu)$ and $\sigma = 0$. The density and viscosity ratios are then unitary, $m = 1$, $\varepsilon = 1$, while the

Weber number diverges, $We \to \infty$. In this case, the stability threshold (4) simplifies to

$$h_{C_T}^{(j)}\left(Sc, Sk, \alpha, Re_j, p, l\right) = 0, \qquad (6)$$

with $Re_j = DJ_j/\nu$, $Sk = D^2F/\nu$ and $Sc = C/\left(2\rho D^2 LF\right)$. Here, C and F are the damping coefficient and frequency of the flexible tube immerged in the fluid at rest. The condition $\nu_1 = \nu_2 = \nu$ implies that the incident Reynolds number $Re = D\left(J_1 + J_2\right)/\nu$ writes $Re = Re_1 + Re_2$, and also expresses as a function of the void fraction, $Re = Re_1/\left(1-\alpha\right) = Re_2/\alpha$. Since Re, Re_j and α are connected, the instability threshold (6) can be rewritten in a form that does not depend on the phase index j, replacing Re_j by Re. This leads to the implicit equation

$$h_{C_T}\left(Sc, Sk, \alpha, Re, p, l\right) = 0. \qquad (7)$$

As the two phases are identical, the void fraction has no effect on the instability threshold and the relation (7) has to be independent of α. Finally, (7) then reduces to an equation involving only five dimensionless numbers

$$h_{C_T}\left(Sc, Sk, Re, p, l\right) = 0. \qquad (8)$$

For a given geometry of the bundle and for some given material properties of the tube and the fluid, i.e. the dimensionless numbers Sc, Sk, p and l are fixed, the instability threshold is the set of Reynolds numbers Re such that $Re = \text{constant}$. In the plane $\left(Re_1, Re_2\right)$, this threshold corresponds to a straight line of equation $Re = Re_1 + Re_2 = \text{constant} = Re_{\text{crit}}^{1\phi}$, i.e.

$$\frac{Re_1}{Re_{\text{crit}}^{1\phi}} + \frac{Re_2}{Re_{\text{crit}}^{1\phi}} = 1. \qquad (9)$$

Finally, note that Connors (1970) proposed an explicit form of $Re_{\text{crit}}^{1\phi}$, i.e. $Re_{\text{crit}}^{1\phi} = K\left(p,l\right)\sqrt{Sc}Sk$, with $K\left(p,l\right)$ an unknown function of the geometrical characteristics of the problem (here p and l).

2.2. Case of a two-phase flow

The two-phase flows instability threshold is given by the implicit equation (4). Replacing the void fraction by one of the two Reynolds numbers, this relationship is rewritten as

$$h_{C_T}^{(j)}\left(Sc_j, Sk_j, m, \varepsilon, We_j, Re_1, Re_2, p, l\right) = 0. \qquad (10)$$

For a given geometry of the bundle and for some given material properties of the tube and the fluid, i.e. the dimensionless numbers Sc_j, Sk_j, m, ε, We_j, p and l are fixed, the instability threshold is the set of Reynolds numbers Re_1 and Re_2 such that $h_{C_T}^{(j)} = 0$. In the plane $\left(Re_1, Re_2\right)$, this corresponds to some curve whose shape is unknown. By similarity with single-phase flows, we suppose that this curve is also a straight line. The hypothesis of continuity of the threshold between single-phase and two-phase flows requires this line to pass through the points $\left(Re_1, Re_2\right) = \left(0, Re_{2,\text{crit}}^{1\phi}\right)$ and $\left(Re_1, Re_2\right) = \left(Re_{1,\text{crit}}^{1\phi}, 0\right)$, where $Re_{j,\text{crit}}^{1\phi}$ is the instability threshold in single-phase flows for the phase labeled j. These two hypotheses imply that (10) is finally independent of m, ε and We_j, and is explicitly expressed as :

$$\frac{Re_1}{Re_{1,\text{crit}}^{1\phi}} + \frac{Re_2}{Re_{2,\text{crit}}^{1\phi}} = 1, \qquad (11)$$

with $Re_{j,\text{crit}}^{1\phi} = H_{Re_{j,\text{crit}}^{1\phi}}\left(Sc_j, Sk_j, p, l\right)$.

As expected (the stability threshold does not depend on the choice of phase indices), the relation (11) is invariant per index change $1 \leftrightarrow 2$ and establishes continuity with the single-phase thresholds, via the respective limits as $Re_2 \to 0$ and $Re_1 \to 0$

$$\begin{aligned} Re_1 &\to Re_{1,\text{crit}}^{1\phi} \quad \text{as} \quad Re_2 \to 0 \\ Re_2 &\to Re_{2,\text{crit}}^{1\phi} \quad \text{as} \quad Re_1 \to 0 \end{aligned}. \qquad (12)$$

From the relation $\alpha = \varepsilon Re_2/\left(Re_1 + \varepsilon Re_2\right)$, it is also possible to express the instability threshold in a form equivalent to (11), explicitly showing the homogeneous void fraction α and the viscosity ratio ε

$$Re_1 = \frac{Re_{1,\mathrm{crit}}^{1\phi}}{1+\dfrac{\alpha}{1-\alpha}\dfrac{1}{\varepsilon}\dfrac{Re_{1,\mathrm{crit}}^{1\phi}}{Re_{2,\mathrm{crit}}^{1\phi}}} \qquad Re_2 = \frac{Re_{2,\mathrm{crit}}^{1\phi}}{1+\dfrac{1-\alpha}{\alpha}\varepsilon\dfrac{Re_{2,\mathrm{crit}}^{1\phi}}{Re_{1,\mathrm{crit}}^{1\phi}}} \quad . \tag{13}$$

The above relationships remain invariant per index change $1 \leftrightarrow 2$ for $\alpha \to 1-\alpha$ and $\varepsilon \to 1/\varepsilon$. Similarly, the continuities with the single-phase thresholds are maintained as $\alpha \to 0$ and $\alpha \to 1$

$$Re_1 \to \begin{cases} Re_{1,\mathrm{crit}}^{1\phi} & \text{as} \quad \alpha \to 0 \\ 0 & \text{as} \quad \alpha \to 1 \end{cases} \qquad Re_2 \to \begin{cases} 0 & \text{as} \quad \alpha \to 0 \\ Re_{2,\mathrm{crit}}^{1\phi} & \text{as} \quad \alpha \to 1 \end{cases} \quad . \tag{14}$$

In what follows, we test the validity of (11) by comparing its prediction for the instability threshold with the experimental measurements carried out on a square tube bundle subject to an air-water cross-flow.

3. EXPERIMENTAL SETUP

An experimental setup, has been built at CEA to determine the instability threshold of a flexible tube subject to an air-water cross-flow. This experimental setup is sketched in Figures 1 and 2 and described briefly in the following. Readers should refer to Caillaud *et al*. (1999, 2000, 2003) and Piteau *et al*. (2012, 2019) for an extensive description. The tube bundle has immersed length $L = 300$ mm and diameter $D = 30$ mm, with a pitch ratio $P/D = 1.5$. As depicted in Fig. 1, the moving tube is in the central position of a 3×5 square bundle made of rigid tubes (plus two columns of 5 half-tubes at the boundaries). The central tube is supported by two parallel flexible steel blades allowing large vibrations in the lift direction. The modal frequency of the central tube is set by changing the thickness of the blades. Three sets of blades, denoted L1C, L4C and L2C, whose modal properties in still air and water are reported in Table 1, have been tested. The tube bundle is subject to an air-water cross-flow with flow rates in the ranges $Q_{\mathrm{water}} = [3,300]$ L/s and $Q_{\mathrm{air}} = [20,3000]$ m^3/h. The measurement of the displacement and velocity of the flexible tube is provided by a laser transducer (Keyence LK-G500). A feedback control loop powered by an electro-dynamical shaker is used to ensure the stability of the tube, whatever the flow conditions. The principle of experimental determination of the instability threshold is as follows. For a given homogeneous void fraction, a modal identification is used to determine the reduced damping ξ_1 and the frequency F_1 of the coupled fluid-structure-shaker system. The total reduced damping ξ_T of the fluid-structure system is obtained by subtracting the control damping C_{ctrl} due to the electro-dynamical shaker, by defining a mass of reference. In our case, two choices for this mass have been tested. The first choice is based on the homogeneous mass $M_h = M_{\mathrm{air}} + \rho_h \left(M_{\mathrm{water}} - M_{\mathrm{air}}\right)/\rho_{\mathrm{water}}$ with $\rho_h = \alpha\rho_{\mathrm{air}} + (1-\alpha)\rho_{\mathrm{water}}$. This choice leads to an estimation of the reduced damping $\xi_T = \xi_{Th} = \xi_1 - C_{\mathrm{ctrl}}/\left(2M_h\left(2\pi F_1\right)\right)$. The second choice is based on a mass measurement $M_{2\phi}$ obtained from the frequency $F_{2\phi}$ of the tube motion for very low flow rates of water Q_{water} and air Q_{air}. This choice leads to an estimation of the damping $\xi_T = \xi_{TMm} = \xi_1 - C_{\mathrm{ctrl}}/\left(2M_{2\phi}\left(2\pi F_1\right)\right)$. Note that the choice of the mass of reference has actually very little effect on the damping estimation, i.e. $\xi_T \approx \xi_{Th} \approx \xi_{TMm}$. The instability threshold is then defined as the value of $Re = \sqrt{Re_{\mathrm{water}}{}^2 + Re_{\mathrm{air}}{}^2}$ for which $\xi_{TMm} = 0$. In order to determine this critical value Re_{crit}, a linear interpolation between the last stable measuring point ($\xi_{TMm} > 0$) and the first unstable measuring point ($\xi_{TMm} < 0$) is performed. The repetition of this process for different void fractions α yields a set of points $\left(\alpha, Re_{\mathrm{crit}}\right)$. A non-linear regression of these points is performed in a form similar to (13), i.e.

$$Re(A,B) = \sqrt{\left(\frac{A}{1+\dfrac{\alpha}{1-\alpha}\dfrac{1}{\varepsilon}\dfrac{A}{B}}\right)^2 + \left(\frac{B}{1+\dfrac{1-\alpha}{\alpha}\varepsilon\dfrac{B}{A}}\right)^2} \quad , \tag{15}$$

where A and B are two unknowns determined from a least squares method. According to (13), these unknowns correspond to the critical thresholds in single-phase flows, $A = Re_{\mathrm{water,crit}}^{1\phi}$ and $B = Re_{\mathrm{air,crit}}^{1\phi}$. Once Re_{crit} and the associated non-linear regression have been determined, the results are reported in the planes $\left(Re_{\mathrm{air}}, Re_{\mathrm{water}}\right)$,

$(\alpha, Re_{\text{air}})$ and $(\alpha, Re_{\text{water}})$ using the relation $\alpha = \varepsilon Re_{\text{air}} / (Re_{\text{water}} + \varepsilon Re_{\text{air}})$, leading to

$$Re_{\text{water}} = \frac{Re}{\sqrt{1+\left(\frac{1}{\varepsilon}\frac{\alpha}{1-\alpha}\right)^2}}, \qquad (16)$$

and

$$Re_{\text{air}} = \frac{Re}{\sqrt{1+\left(\varepsilon\frac{1-\alpha}{\alpha}\right)^2}}. \qquad (17)$$

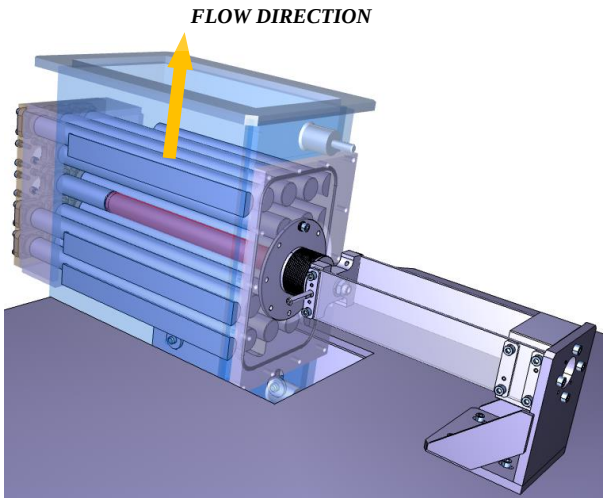

Figure 1. *Bundle and flexibly mounted tube.*

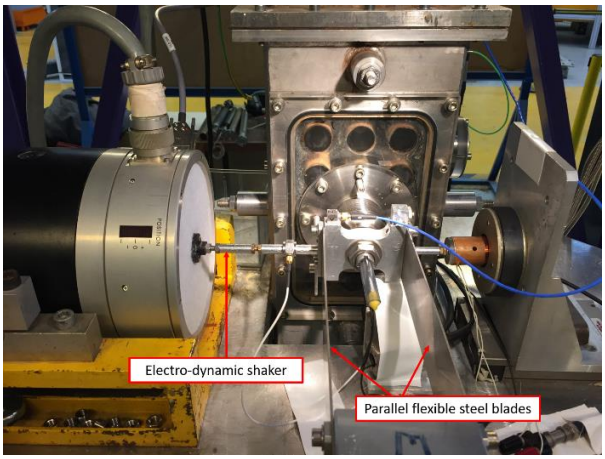

Figure 2. *Experimental setup.*

Blades	L1C	L4C	L2C
M_{air} (kg)	1.29	1.25	1.22
M_{water} (kg)	1.67	1.64	1.57
ξ_{air} (%)	0.56	0.46	0.38
ξ_{water} (%)	1.14	0.89	0.77
F_{air} (Hz)	14.11	22.06	29.18
F_{water} (Hz)	11.19	18.53	24.9

Table 1. Modal properties of the blades.

4. RESULTS AND DISCUSSION

In Figure 3 we show the evolution of the instability threshold in the plane $(Re_{\text{air}}, Re_{\text{water}})$. For the three sets of blades (L1C, L4C and L2C), the experimental results nearly collapse on a single line of equation

$$\frac{Re_{\text{water}}}{Re^{1\phi}_{\text{water,crit}}} + \frac{Re_{\text{air}}}{Re^{1\phi}_{\text{air,crit}}} = 1, \qquad (18)$$

as suggested by the dimensional analysis (11). We also notice that the frequency effect observed in single-phase flows, i.e. the critical Reynolds number increases with the frequency, yields a staggering of the straight lines, according to increasing frequencies. It follows that a tube subject to two-phase flows is all the more stable the more rigid it is. For a given set of blades, the slope of the corresponding line is $s = -Re^{1\phi}_{\text{water,crit}} / Re^{1\phi}_{\text{air,crit}} < 0$. Assuming a relationship of the form $Re^{1\phi}_{j,\text{crit}} = K(p,l)\, Sc_j{}^q Sk_j$, $q = 0.5$ according to Connors (1970), it comes that $s = -(Sc_{\text{water}}/Sc_{\text{air}})^q\, Sk_{\text{water}}/Sk_{\text{air}}$. The value of s is given in Table 2, along with the value of

$q = \ln\left(-\frac{Sk_{\text{air}}}{Sk_{\text{water}}}s\right)\Big/\ln\left(\frac{Sc_{\text{water}}}{Sc_{\text{air}}}\right)$. Statistically, we find $q = 0.41 \pm 0.03$, which is pretty close to the value predicted by Connors (1970).

In Figures 4, 5 and 6, we show the evolution of the instability threshold in the three different planes $\left(Re_{\text{air}}/Re^{1\phi}_{\text{air,crit}}, Re_{\text{water}}/Re^{1\phi}_{\text{water,crit}}\right)$, $\left(\alpha, Re_{\text{air}}\right)$ and $\left(\alpha, Re_{\text{water}}\right)$. In the first plane, the three lines previously observed in Figure 3 align into a single line of slope -1. In the plane $\left(\alpha, Re_{\text{air}}\right)$ (resp. $\left(\alpha, Re_{\text{water}}\right)$), these lines transform to three increasing curves (resp. decreasing) such that $Re_{\text{air,crit}} \to 0$ as $\alpha \to 0$ and $Re_{\text{air,crit}} \to Re^{1\phi}_{\text{air,crit}}$ as $\alpha \to 1$ (resp. $Re_{\text{water,crit}} \to Re^{1\phi}_{\text{water,crit}}$ as $\alpha \to 0$ and $Re_{\text{water,crit}} \to 0$ as $\alpha \to 1$). These different representations of the instability threshold in two-phase flows are strictly equivalent: the transition from one representation to another is obtained from the equations (11) and (13).

In Figure 7 we show the evolution of the relative deviation $r(\%) = 100\left|Re^{\text{exp}}_{\text{crit}} - Re^{\text{reg}}_{\text{crit}}\right|/Re^{\text{exp}}_{\text{crit}}$ as a function of the homogeneous void fraction α. For the stiffest blades (L2C and L4C), the relative deviation does not exceed 12%. For these two sets of blades, it is interesting to note that the relative deviation increases in the range $\alpha \approx 0.4\text{-}0.5$. Although the nature of this increase is unknown, we suspect that it may be related to a change in the two-phase flow regime. For the least rigid blade set (L1C) the relative deviation is greater, i.e. $r < 20\%$, with a very pronounced peak in the region of high void fractions. We explain the existence of this peak by the experimental difficulties related to the control of a very low water flow rate (a few L/s), while ensuring a high air flow rate. Also, additional measurements seem to indicate the possible existence of a cascade of bifurcations and hysteresis cycles, making the determination of the instability threshold delicate. The removal of the measurement in the analysis of the results associated with the L1C blades then leads to a relative deviation similar to that obtained for the L2C and L4C blades, i.e. $r < 12\%$. Finally, the analysis of all these results shows that (11) makes it possible to predict in a very satisfactory way the instability threshold in air-water flow, over almost the entire definition range of α.

5. CONCLUSION

In this work, we have studied the fluid-elastic instability of a tube bundle subject to a two-phase cross-flow.

Blades	**L1C**	**L4C**	**L2C**
Sk_{air} $\left(\times 10^4\right)$	0.08140	0.12727	0.16835
Sk_{water} $\left(\times 10^4\right)$	1.0001	1.6561	2.2254
Sc_{air}	140.0918	111.5071	89.9038
Sc_{water}	0.4430	0.3397	0.2813
$Re^{1\phi}_{\text{water,crit}}$ $\left(\times 10^4\right)$	3.6609	7.2885	9.7839
$Re^{1\phi}_{\text{air,crit}}$ $\left(\times 10^4\right)$	3.7962	5.1801	8.2406
s	-0.9644	-1.4070	-1.1873
q	0.4421	0.3839	0.4179

Table 2. Dimensionless numbers of the blades.

From a dimensional analysis, we have proposed a new criterion for the instability threshold, involving the Reynolds numbers of the two phases and the corresponding critical thresholds in single-phase flows.

Extensive experiments performed on a square tube bundle (*P/D = 1.5)* with a flexible central tube subject to an air-water cross-flow remarkably confirm the validity of this criterion, which therefore constitutes an extension of the Connors equation (1970) for two-phase flows. The knowledge of the stability thresholds in the limiting gas and liquid single-phase flows and their dependance to the dimensionless numbers such as the Scruton or the Stokes number is however required to fully complete the criterion. Also, the validity of the critierion for different tube bundle geometries (e.g. triangular pitch) and mixtures (e.g water-freon and ultimately steam-water) remains to be tested.

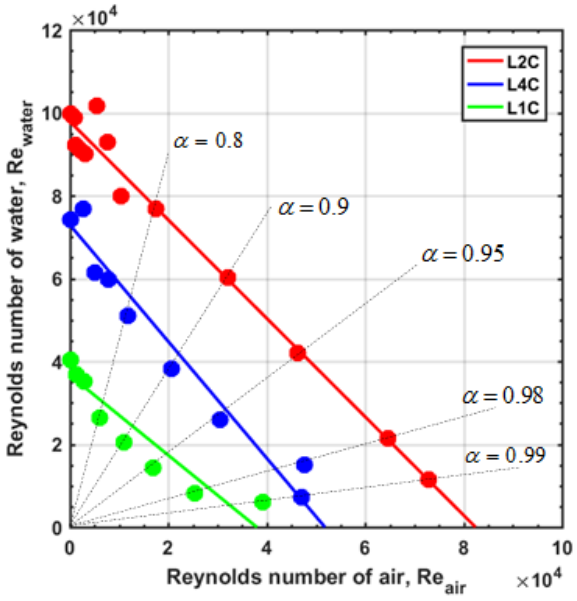

Figure 3. *Evolution of the instability threshold in the plane* $\left(Re_{\text{air}}, Re_{\text{water}}\right)$.

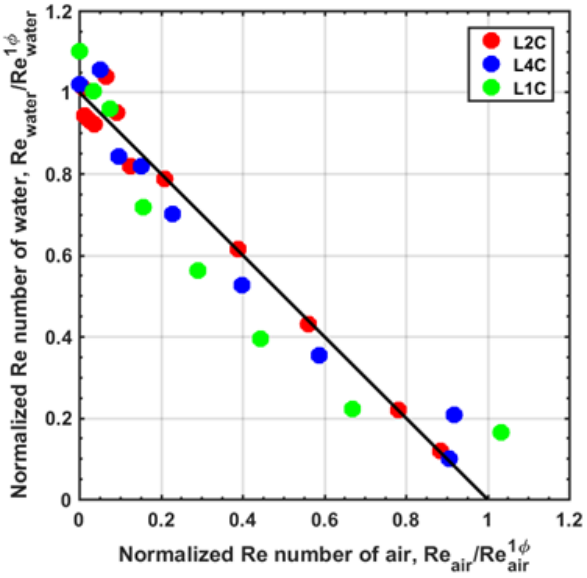

Figure 4. *Evolution of the instability threshold in the plane* $\left(Re_{\text{air}}/Re^{1\phi}_{\text{air,crit}}, Re_{\text{water}}/Re^{1\phi}_{\text{water,crit}}\right)$.

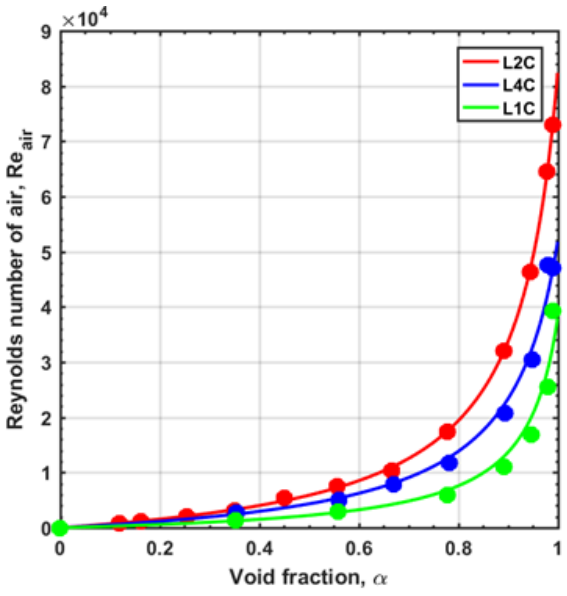

Figure 5. *Evolution of the instability threshold in the plane* $\left(\alpha, Re_{\text{air}}\right)$.

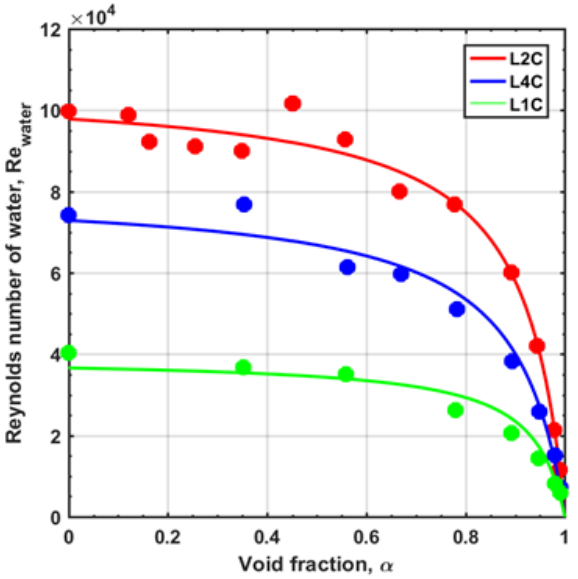

Figure 6. *Evolution of the instability threshold in the plane* $\left(\alpha, Re_{\text{water}}\right)$.

ACKNOWLEDGEMENTS

This work was performed in the framework of a joint research program co-funded by FRAMATOME, EDF and CEA (France). A valuable contribution by M. Bellanger and T. Valin (CEA-Saclay) to the experimental work is gladly acknowledged.

6. REFERENCES

Axisa, F., Villard, B., Gibert, R. J., Hetsroni, G., Sundheimer, P., 1984, *Vibration of tube bundles subjected to air-water and steam-water cross flow : Preliminary*

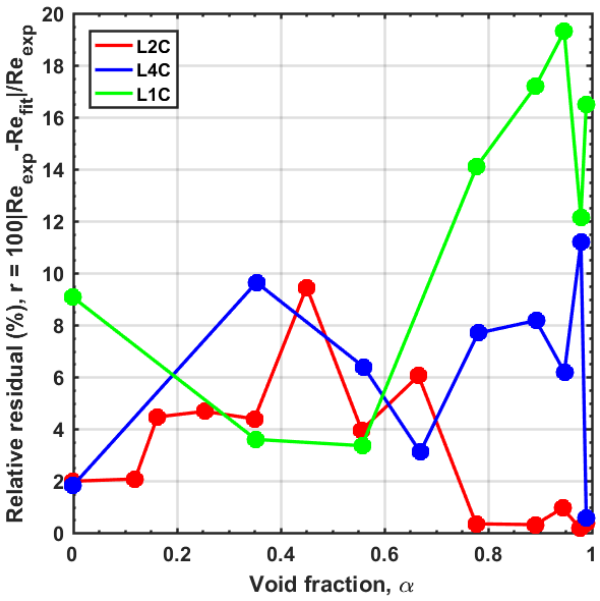

Figure 7. *Evolution of the relative deviation* r.

results on fluidelastic instability. Symposium on Flow-Induced Vibrations, Volume 2: Vibration of Arrays of Cylinders in Cross Flow. Presented at the 1984 ASME Winter Annual Meeting. ASME New York NY USA, 269–284.

Axisa, F., Boheas, M. A., Villard, B., 1985. *Vibration of tube bundles subjected to steam-water cross-flow: A comparative study of square and triangular arrays*. 8th International Conference on Structural Mechanics in Reactor Technology, Paper No. B1/2.

Caillaud S., de Langre E., Piteau P., 1999, *The measurement of fluidelastic effects at low reduced velocities using piezoelectric actuators*, ASME Journal of Pressure Vessel Technology, Vol. 121, pp. 232-238.

Caillaud S., de Langre E., Piteau P., 2000, *Measurement of critical velocities for fluidelastic instability using vibration control*, ASME Journal of Vibration and Acoustics, Vol. 122, pp. 341-345.

Caillaud S., de Langre E., Baj, F., 2003, *Active Vibration control for the measurement of fluidelastic effects*, ASME Journal of Pressure Vessel Technology, Vol. 125, pp. 165-170.

Chen, S. S., 1983a, *Instability mechanisms and stability criteria of a group of circular cylinders subjected to cross-flow. Part 1: Theory*. Journal of Vibration, Acoustics, Stress, and Reliability in Design, 105, 51–58.

Chen, S. S., 1983b, *Instability mechanisms and stability criteria of a group of circular cylinders subjected to cross-flow. Part II: Numerical results and discussion*. Journal of Vibration, Acoustics, Stress, and Reliability in Design, 105, 253–260.

Chen, S. S., 1987, *A general theory for dynamic instability of tube arrays in cross-flow*. Journal of Fluids Engineering, Transaction of the ASME, 1, 35–53.

Connors, H., 1970, *Fluidelastic vibration of tube arrays excited by cross-flows*. Flow-Induced Vibration in Heat Exchangers, pages 42–56.

Dalton, C., Helfinstine, R. A., 1971, *Potential flow past a group of circular cylinders*. ASME Journal of Basic Engineering, 93, 636–642.

Granger, S., Paidoussis, M. P., 1996, *An improvement to the quasi-steady model with application to cross-flow-induced vibration of tube arrays*. Journal of Fluid Mechanics, 320, 163– 184.

Lever, J., Weaver, D. S., 1986, *On the stability of heat exchanger tube bundles, part 1: Modified theoretical model*. Journal of Sound and Vibration, 107, 375–392.

Nakamura, T., Fujita, K., Kawanishi, K., Saito, I., 1986a, *Study on the flow induced vibration of a tube array by a two-phase flow* (2nd report, large amplitude vibration by steam - water flow). Japan Society of Mechanical Engineers Part C. vol. 52, 2790–2795.

Nakamura, T., Fujita, K., Yamaguchi, N., Sakata, K., Tsuge, A., Saito, I., 1986b, *Study on flow induced vibration of a tube array by a two-phase flow*. (1st report: large amplitude vibration by air-water flow). Japan Society of Mechanical Engineers Part C. vol. 52, 252–257.

Pettigrew, M. J., Taylor, C. E., Jong, J. H., Currie, I. G., 1995, *Vibration of a tube bundle in two-phase freon cross-flow*. Journal of Pressure Vessel Technology, Transactions of the ASME, 117, 321–329.

Pettigrew, M. J., Taylor, C. E., Janzen, V. P., Whan, T., 2002, *Vibration behavior of rotated triangular tube bundles in two-phase cross flows*. Journal of Pressure Vessel Technology, Transactions of the ASME, 124, 144–153.

Pettigrew, M. J., Taylor, C. E., 2009, *Vibration of a normal triangular tube bundle subjected to two-phase freon cross flow*. Journal of Pressure Vessel Technology, Transactions of the ASME, 131.

Piteau P., Delaune X., Antunes J, Borsoi L., 2012, *Experiments and Computations of a Loosely Supported Tube in*

a Rigid Bundle Subjected to Single-Phase Flow, Journal of Fluids and Structures, Vol. 28, pp. 56-71.

Piteau P., Delaune X.,Borsoi, L.,Antunes J., 2019, *Experimental identification of fluid-elastic coupling forces on a flexible tube within a rigid square bundle subjected to single-phase cross-flow*, Journal of Fluids and Structures, Vol. 86, pp. 156-169.

Price, S. J., Paidoussis, M. P., 1982, *A theoretical investigation of the parameters affecting the fluidelastic instability of a double row of cylinders subject to a cross-flow*. Vibration in Nuclear Plant. Proceedings of the 3rd International Conference. British Nucl. Energy Soc, London UK., 107–119.

Price, S. J., Paidoussis, M. P., 1983, *Fluidelastic instability of an infinite double row of circular cylinders subject to a uniform cross-flow*. Journal of Vibration Acoustics Stress Reliability in Design, 105, 59–66.

Roberts, B. W., 1962, *Low frequency, self-excited vibration in a row of circular cylinders mounted in an airstream*. Ph.D Thesis, University of Cambridge, Cambridge, UK.

Tanaka, H., Takahara, S., 1980, *Unsteady fluid dynamic force on tube bundle and its dynamic effect on vibration*. American Society of Mechanical Engineers, Pressure Vessels and Piping Division (Publication) PVP, 77–92.

Tanaka, H., Takahara, S., 1981, *Fluid elastic vibration of tube array in cross-flow*. Journal of Sound and Vibration, 77, 19–37

EXPERIMENTAL INVESTIGATION OF CROSS-FLOW FLUIDELASTIC INSTABILITY FOR ROTATED TRIANGULAR TUBE BUNDLES SUBJECTED TO SINGLE-PHASE AND TWO-PHASE TRANSVERSE FLOWS

Domenico Panunzio, Romain Lagrange, Philippe Piteau, Xavier Delaune
Université Paris-Saclay, CEA, Service d'Études Mécaniques et Thermiques, 91191, Gif-sur-Yvette, France
Jose Antunes
Centro de Ciências e Tecnologias Nucleares (C2TN), Instituto Superior Técnico (IST), Universidade de Lisboa, 2695-066 Bobadela LRS, Portugal

ABSTRACT

An experimental program is conducted to study the vibration response of a rotated triangular tube bundle with a pitch ratio of 1.44 and an aspect ratio of 10. The tube bundle is subject to a single-phase (air or water) or a two-phase air-water cross-flow, with an homogeneous void fraction in the range $[0.1, 0.95]$*. The bundle is free to vibrate only in the cross-flow, i.e. lift direction. Four bundle configurations, with one or multiple flexible tubes, are tested by increasing the flow velocity up to the onset of a fluidelastic instability. From the experimental observations and a modal analysis we show that, when* $\alpha > 0.3$*, instability can only materialize for flexible cells with two or more tubes, i.e., two or more degrees of freedom. In such cases, instability arises for a higher-order mode. Finally, we show that the instability is characterized by a Connors's constant greater than the one generally observed in the literature.*

1. INTRODUCTION

The fluid-structure interaction problem has been the topic of considerable theoretical and experimental studies since the pioneering works of [1] to the recent works of [2, 3, 4, 5]. In the nuclear field, a frequently experienced problem is the fluidelastic instability of tube bundle subject to a cross-flow. When the flow velocity exceeds a critical value, the tubes become dynamically unstable and vibrate at large amplitudes. Substantial works were conducted to better understand this mechanism, see for e.g. [6, 7, 8, 9, 10, 11], and to identify the conditions for the instability onset. Recently, several experimental works were carried out by [12] to investigate the in-flow (drag) fluidelastic instability for a rotated triangular tube bundle subject to either a single-phase or a two-phase air-water cross-flow. The author showed the onset of an in-flow fluidelastic instability in a triangular bundle composed of several flexible tubes. In the present work, we show some new experimental results obtained on the same test rig as [12], focusing on the effect of the flexibility of the bundle on the onset of a cross-flow fluidelastic instability. The test rig consists of 30 tubes arranged in a rotated triangular bundle, subject to either a single or a two cross-phase flow. The stability of four configurations, which differ by the number of flexible tubes in the bundle, is investigated. The results of this investigation are presented in terms of the root mean square (RMS) value and power spectral density (PSD) of the tubes displacement. The modal frequencies and damping ratios are also extracted from the signals and eventually all the results are summarized on an instability map.

2. EXPERIMENTAL RIG

The experimental rig, named TITAN, see Figure 1, is used to test the vibration response of a rotated triangular tube bundle subject to either a single-phase or a two-phase cross-flow with an air-water mixture. The test rig is connected to an air-water loop, supplied with a water centrifugal pump with maximum delivery capacity of 1080 m^3/h and an air compressor that delivers a maximum flow rate of 3000 m^3/h (at 273.15 K and 101325 Pa). A toroidal distributor injects the air flow into a divergent pipe, in four points perpendicularly distributed, see Figure 2. At the top of this pipe, a mixer is used to homogenize the air-water flow. The two-phase flow rises vertically in the test section which consists in 30 stainless tubes, completed by two columns of half-tubes at the boundaries to minimize the wall effects. The tubes have a length $L = 300$ mm, a diameter $D = 30$ mm, and are arranged in a rotated triangular configuration with a pitch ratio P/D = 1.44. Some of the tubes are supported by a flexible blade allowing a vibration in the lift direction. An additional bundle of 20 rigid tubes is placed upstream of the test section to regulate the inlet flow.

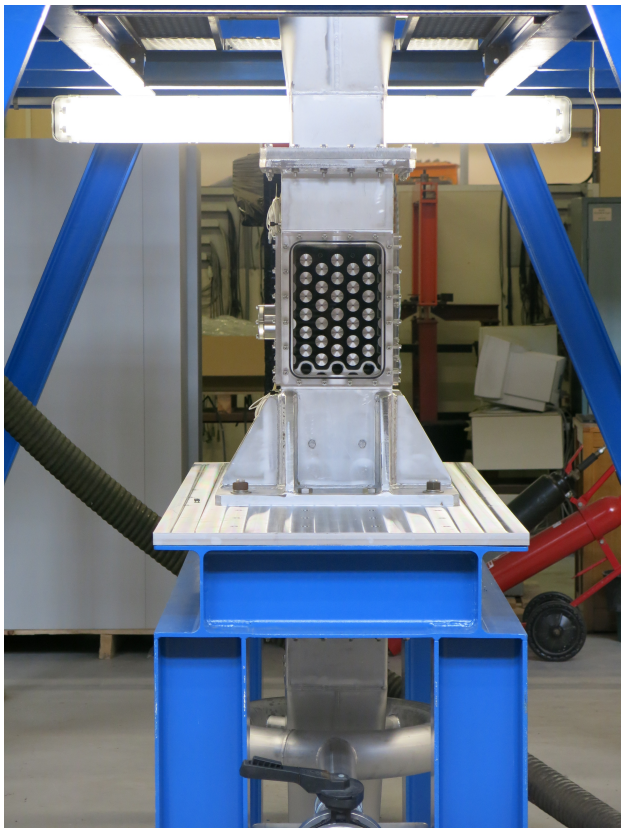

Figure 1. Photo of the experimental rig TITAN.

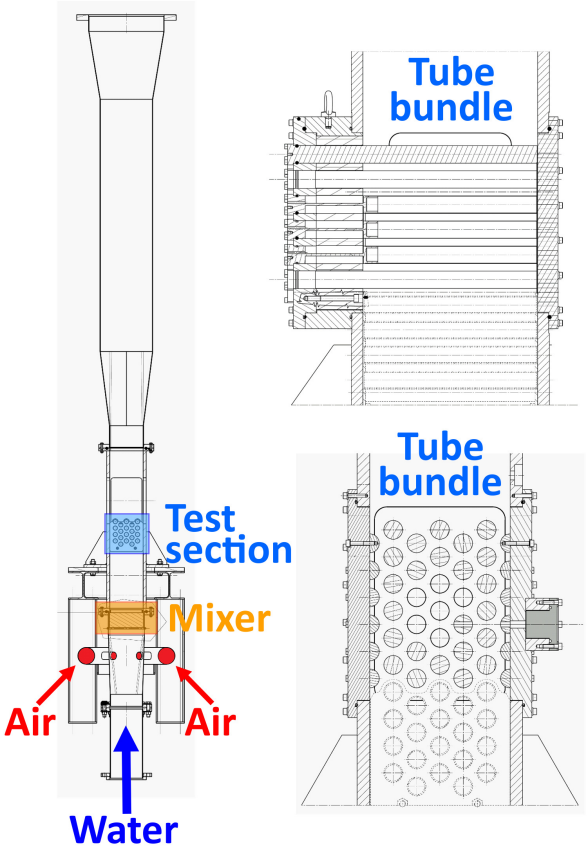

Figure 2. Layout of the experimental test section and air-water loop.

3. EXPERIMENTAL PROCEDURE

The configurations under study differ by the number of flexible tubes inserted in the bundle. Four configurations are tested (see Figure 3): (a) a single flexible tube, (b) two flexible tubes, (c) a column of three flexible tubes, (d) a cluster of seven flexible tubes. For the configuration (a), the tube is mounted on two parallel flexible blades, with a laser displacement transducer pointed towards the end of the blades, see [13]. In air, the first modal frequency and damping ratio of the tube are 22.25 Hz and 0.35%, respectively. For the configurations (b), (c) and (d), the flexible tubes are mounted on a unique blade, instrumented with a strain gauge at the root of the blade. Two sets of blades are tested, leading to two different average values of their first modal frequencies and damping ratios in air, see Table 1.

The flow pitch velocity is defined as $V = V_\infty P/(P-D)$ with $V_\infty = (Q_g + Q_l)/A_\infty$ the free-stream velocity, Q_g and Q_l the volume flow rates of air and water, respectively, and A_∞ the upstream cross-flow section. For all configurations, the flow pitch velocity is increased until the amplitude of vibration nearly reaches the dimension of the inter-tube gap, i.e. 13 mm. The measurements are carried out at a constant homogeneous void fraction $\alpha = Q_g/(Q_g + Q_l)$, ranging from 0 (single-phase water) to 1 (single-phase air). The displacement at the end of the blades for the configuration (a) and the strain at the root of the blade for the configurations (b), (c) and (d), are recorded for at least 180 s, using a sampling frequency of 250 Hz. The displacement of the free end of the tubes is then calculated by a linear relationship with the recorded signals. The modal frequency and damping parameters are extracted from the RMS responses of the tubes, using the NExT-ERA identification method, see [14].

	Tubes 32 Hz		Tubes 14 Hz	
	Frequency	Damping	Frequency	Damping
Average	31.96 Hz	0.047%	14.18 Hz	0.045%
Dispersion	0.84%	21.9%	0.66%	7.6%

Table 1. Average values and dispersion of the flexible tubes first modal frequencies and damping ratios, for the configurations (b), (c) and (d).

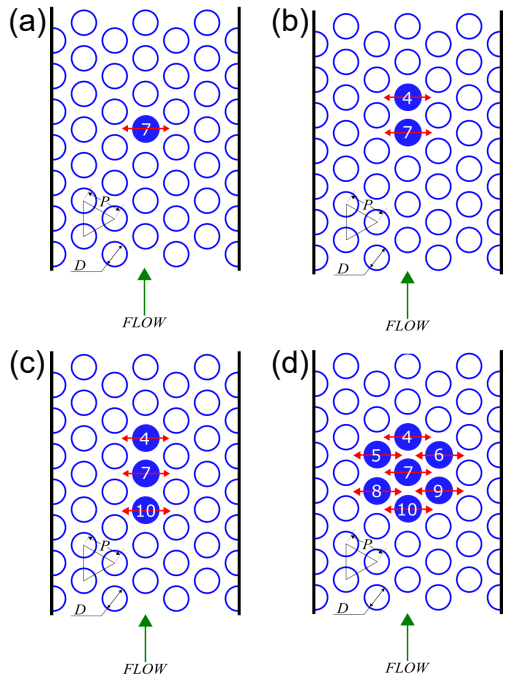

Figure 3. Tested configurations: (a) one flexible tube, (b) two flexible tubes, (c) a column of three flexible tubes, (d) a cluster of seven flexible tubes. The instrumented tubes are depicted with a blue color and are labeled from 4 to 10.

4. RESULTS

4.1. Configuration with a single flexible tube

In Figure 4, we show the evolution of the modal frequency and the modal damping ratio as functions of the flow pitch velocity, for the configuration (a), considering seven values of the void fraction in the range [0, 0.98]. We observe that the flexible tube vibrates with a frequency that increases with the flow pitch velocity and void fraction. For $\alpha \leq 0.3$ the damping ratio ζ decreases and the tube becomes unstable at a critical flow pitch velocity corresponding to $\zeta = 0$. This instability is not observed for $\alpha > 0.3$.

These results are in line with those obtained by [15] on a similar tube bundle geometry, who did not observe a fluidelastic instability for $\alpha \geq 0.4$ in two-phase water-Freon flow.

4.2. Configurations with multiple flexible tubes

In Figure 5, we show the evolution of the RMS value of the displacement of the flexible tubes (32 Hz) as a function of the flow pitch velocity, for the configurations (c) and (d), considering four values of the void fraction, $\alpha \in \{0, 0.4, 0.9, 1\}$. For the two configurations and for all the void fractions, we observe that the RMS value increases noticeably with the flow

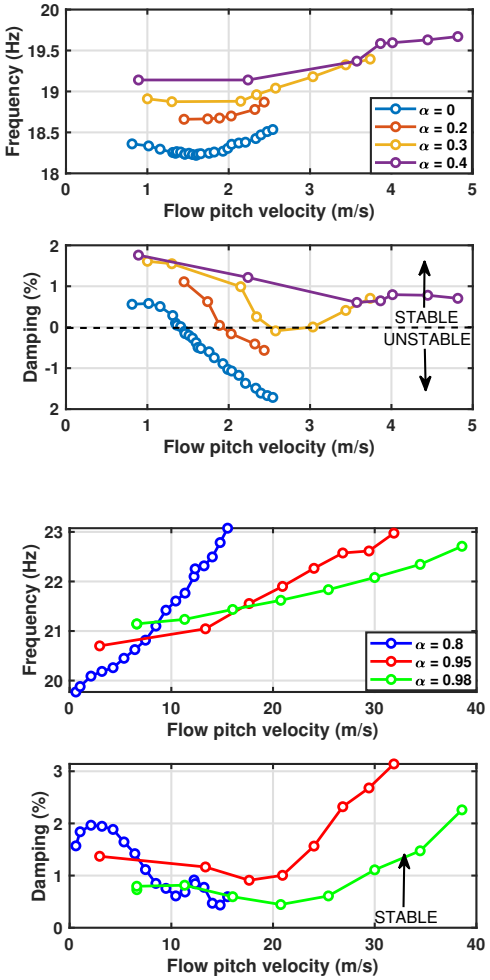

Figure 4. Configuration (a). Modal frequency and modal damping ratio as functions of the flow pitch velocity. The void fraction is within the range [0, 0.98].

pitch velocity. This increase indicates that the flexible configurations (c) and (d) become unstable in the lift direction. Observing the trends of the RMS curves, we infer that the physics of the instability is poorly sensitive to the number of flexible tubes but strongly depends on the void fraction of the two-phase flow.

In Figures 6 and 7, we show the evolution of the PSD of the displacement of one of the flexible tubes, for the configurations (b) and (c) - 14 Hz, as a function of the flow pitch velocity and the frequency, considering two values of the void fraction, $\alpha \in \{0, 0.3\}$. For both configurations and $\alpha = 0$, we observe that modes have similar PSD values at low flow pitch velocities, but eventually the first mode becomes predominant when the instability occurs. For $\alpha = 0.3$, the order of the predominant mode changes close to instability and eventually the second (resp. third) mode becomes unstable for the configuration (b) (resp. (c)).

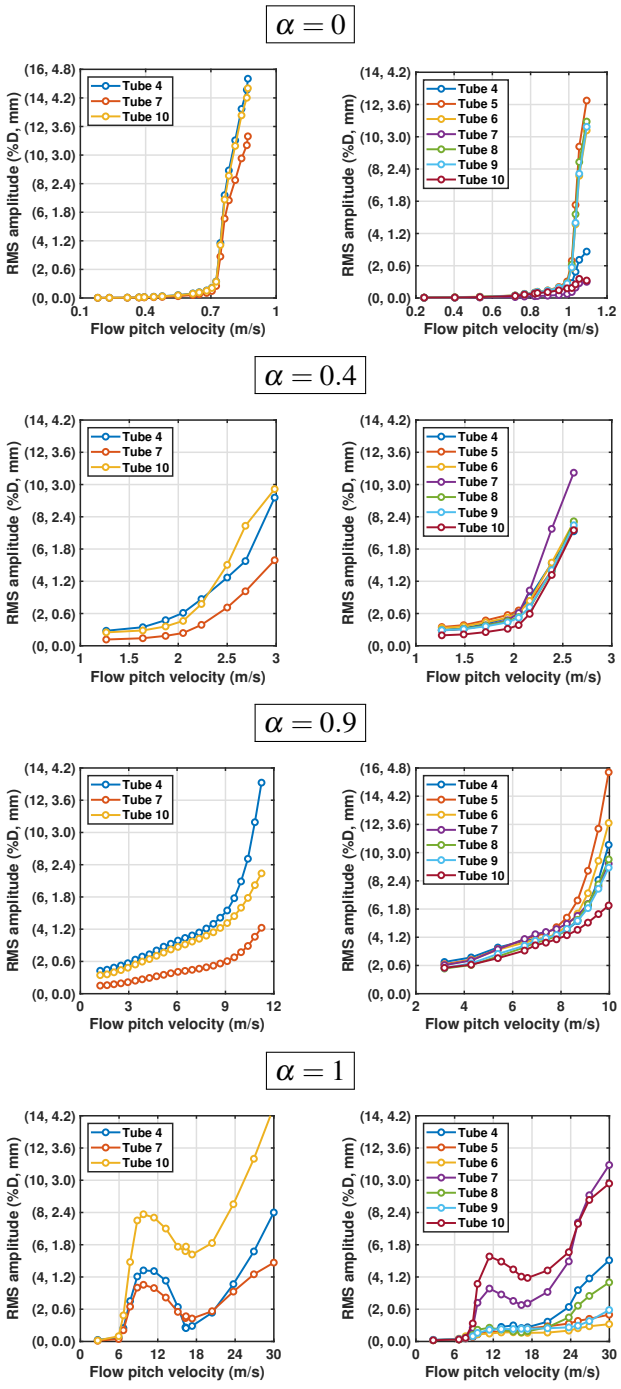

Figure 5. Configurations (c) and (d) - 32 Hz. Root mean square value of the displacement as a function of the flow pitch velocity. The void fraction is $\alpha \in \{0, 0.4, 0.9, 1\}$. The RMS value is expressed in percent of the diameter and also in millimeters.

In Figure 8, we show the evolution of the modal frequency and damping ratio, for the configurations (b) and (c) - 14 Hz, considering four values of the void fraction, $\alpha \in \{0, 0.3, 0.6, 0.95\}$. For $\alpha = 0$, we recover that both configurations are unstable in their first mode of vibration. It should also be noticed that due to identification difficulties, the second and third mode, in configuration (c) for $V > 0.7$, are not precisely identified. For $\alpha = 0.3$, the damping ratio of the first mode suddenly increases as the second mode (resp. third mode) becomes unstable for the configuration (b) (resp. (c)). For $\alpha > 0.3$ both configurations are no longer unstable in their first mode of vibration. Particularly, for $\alpha = 0.6$ (resp. $\alpha = 0.95$) the configuration (c) is unstable in its third (resp. second) mode. From these observations, we conclude that, when $\alpha > 0.3$, a higher-order mode becomes unstable. In fact, for these configurations, the first mode corresponds to all tubes in phase. Hence, in terms of coupling with the flow, this overall mode is not essentially different from the mode of a single flexible tube. This may explain why this mode is not unstable when $\alpha > 0.3$.

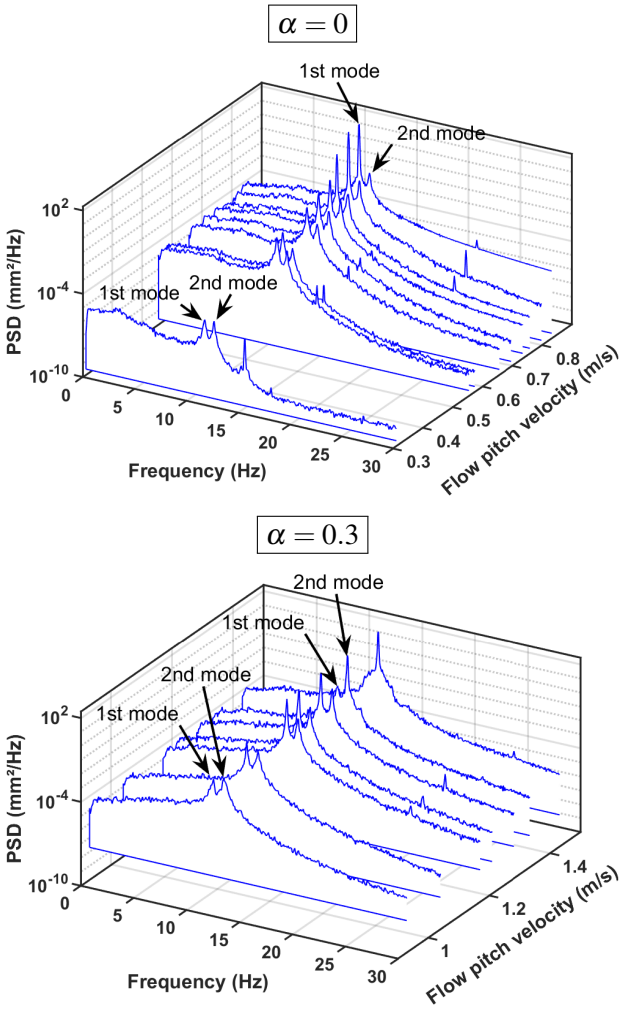

Figure 6. Configurations (b) - Tube 7 - 14 Hz. Power spectral density (PSD) as a function of the flow pitch velocity and the frequency. The void fraction is $\alpha \in \{0, 0.3\}$.

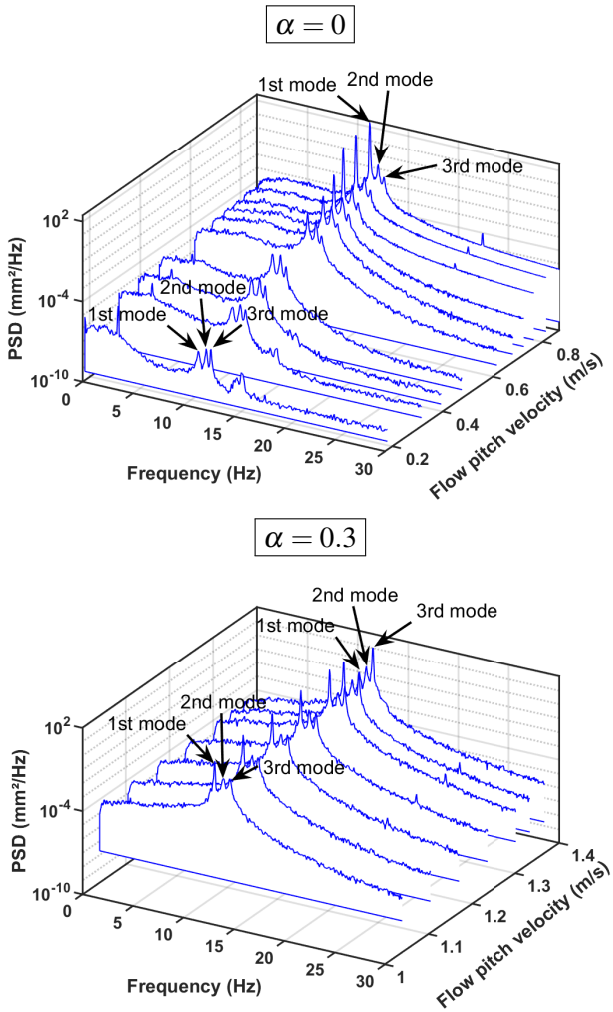

Figure 7. Configurations (c) - Tube 10 - 14 Hz. Power spectral density (PSD) as a function of the flow pitch velocity and the frequency. The void fraction is $\alpha \in \{0, 0.3\}$. *For the sake of clarity, for* $\alpha = 0$, *all the tested velocity cases are not depicted.*

5. CONNORS'S MAP

In this section, we propose an estimation of the Connors's constant K defined in [16] as

$$K = \left(\frac{2\pi\zeta m}{\rho D^2}\right)^{-1/2} \frac{V_c}{fD}. \qquad (1)$$

For the configuration (a), V_c is estimated as the value of V corresponding to $\zeta = 0$. For the configurations (b), (c) and (d) we take the value of V above which either the RMS amplitude increases considerably or a change in slope occurs. The values of frequency, f and damping ratio, ζ are those measured for the unstable mode at low flow velocity. Due to identification difficulties, for configuration (d), we use $\zeta = 3\%$, as recommended by the ASME Code, and the same frequency values of the configuration (c). The mass

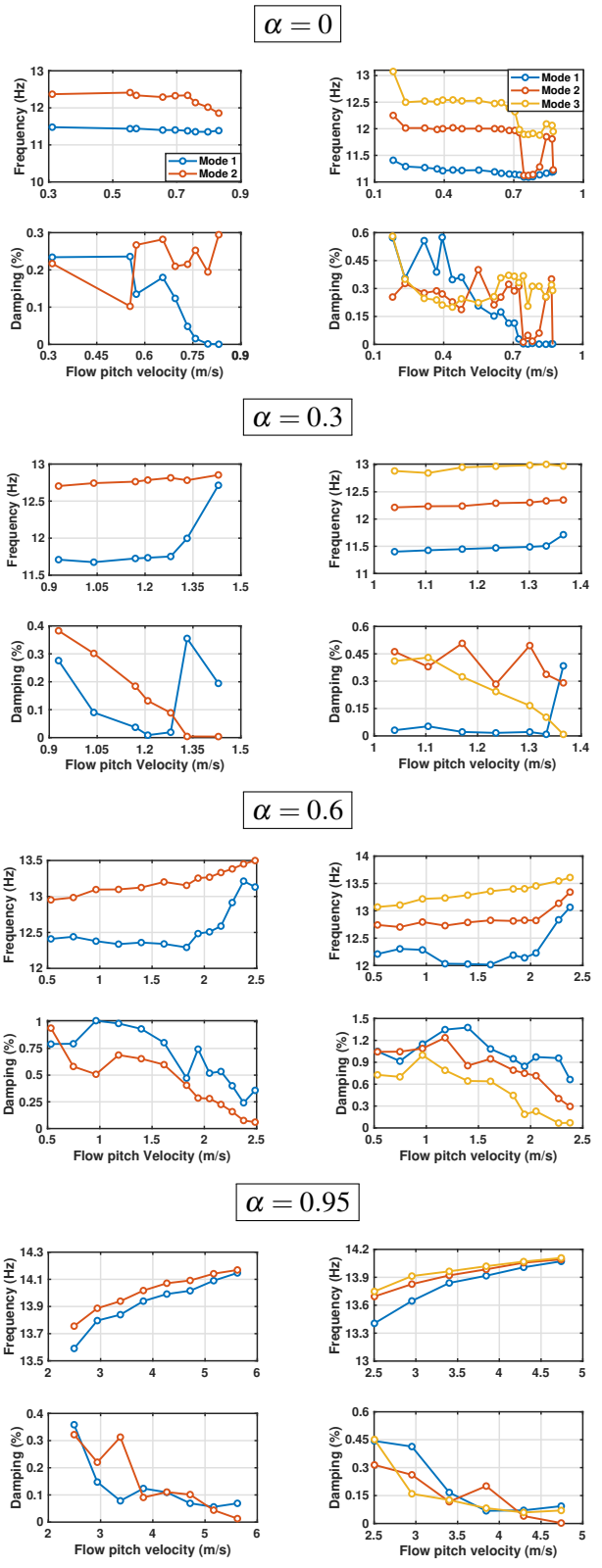

Figure 8. Configurations (b) and (c) - 14 Hz. Modal frequency and modal damping ratio as functions of the flow pitch velocity. The void fraction is $\alpha \in \{0, 0.3, 0.6, 0.95\}$.

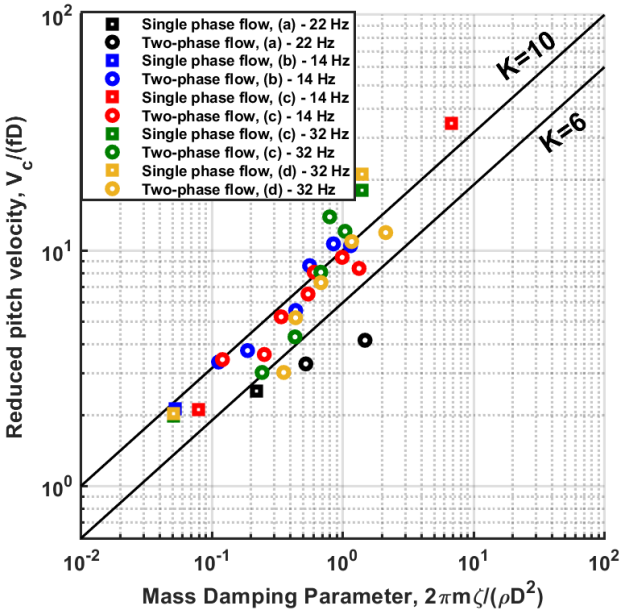

Figure 9. Instability map.

per unit length of the tube, including tube mass and added mass, is estimated using the formula proposed by [17] for a rotated triangular tube bundle, and considering a homogeneous flow density, ρ. All these parameters are outlined in Table 2 for each tested configuration.

In Figure 9, we show the evolution of the reduced critical flow pitch velocity, $V_c/(fD)$, as a function of the mass damping parameter, $2\pi m\xi/(\rho D^2)$. For all configurations except (a), we observe that the experimental points lies in between the lines $K = 6$ and $K = 10$. These two values are much higher than the one recommended by [8], i.e. $K = 3.3$, but are in line with those recently obtained by [12] for the in-flow instability.

6. CONCLUSION

This paper presents the results of experiments on a rotated triangular tube bundle, characterized by a pitch ratio of 1.44 and an aspect ratio of 10. The bundle is subject to either a single-phase cross-flow (water or air) or a two-phase air-water cross-flow. The flexible tubes are free to vibrate in the lift direction only.

We showed that for void fractions $\alpha > 0.3$ instability can only materialize for flexible cells with two or more tubes, i.e., two or more degrees of freedom. In such cases, instability arises for a higher-order mode.

Finally, we showed that all unstable cases have a Connors's constant K in the range $6 \leq K \leq 10$, in agreement with the values found by [12] for the in-flow instability.

7. ACKNOWLEDGMENTS

The authors acknowledge financial support for this work, performed in the framework of a joint research program co-funded by CEA, Framatome and EDF (France). Valuable contributions by Thierry Valin and Miguel Bellanger (CEA-Saclay) to the experimental work are gladly acknowledged.

8. REFERENCES

[1] Green, G., 1833, Researches on the Vibration of Pendulums in Fluid Media. *Transactions of the Royal Society of Edinburgh. vol. 13, pp. 54-68*

[2] Lagrange, R, Delaune, X., Piteau, P., Borsoi, L., Antunes, J., 2018, A new analytical approach for modeling the added mass and hydrodynamic interaction of two cylinders subjected to large motions in a potential stagnant fluid. *Journal of Fluids and Structures. vol. 77, pp. 102-114*

[3] Lagrange, R., Piteau, P., Delaune, X., Antunes, J., 2019, Fluid-Elastic Coefficients in Single Phase Cross Flow: Dimensional Analysis, Direct and Indirect Experimental Methods. *Pressure Vessels and Piping Conference vol. 4, pp. 93984*

[4] Lagrange, R., Fraigneau, Y., 2020, New estimations of the added mass and damping of two cylinders vibrating in a viscous fluid, from theoretical and numerical approaches. *Journal of Fluids and Structures. vol. 92, pp. 102818*

[5] Panunzio, D., Puscas, M. A., Lagrange, R., 2021, FSI-Vibrations of immersed cylinders. Simulations with the engineering open-source code TrioCFD. Test cases and experimental comparisons. *arXiv 2101.11322*

[6] Weaver, D. S., Grover, L. K., 1978, Cross-flow induced vibrations in a tube bank—Turbulent buffeting and fluid elastic instability. *Journal of Sound and Vibration 59(2):277-294*

[7] Chen, S. S., Jendrzejcyk, J. A., 1981, Experiments on fluidelastic instability in tube banks subjected to liquid cross flow. *Journal of Sound and Vibration 78(3):355-381*

[8] Pettigrew, M. J., Tromp, J. H., Taylor, C. E., Kim, B. S., 1989, Vibration of Tube Bundles in Two-Phase Cross-Flow: Part 2—Fluid-Elastic Instability. *Journal of Pressure Vessel Technology 111(4):478-487*

[9] Pettigrew, M. J., Taylor, C. E., 1991, Fluidelastic instability of heat exchanger tube bundles: review

	Tube 22 Hz (double blade)					
	Configuration (a)					
α (%)	V_c(m/s)	m (kg/m)	$m/(\rho D^2)$	f(Hz)	ζ(%)	K
0	1.39	5.64	6.27	18.36	0.56	5.38
20	1.85	5.40	7.50	18.66	1.11	4.57
30	4.16	5.28	8.38	18.91	1.61	3.41

	Tubes 14 Hz (single blade)											
	Configuration (b)						Configuration (c)					
α (%)	V_c(m/s)	m (kg/m)	$m/(\rho D^2)$	f(Hz)	ζ(%)	K	V_c(m/s)	m (kg/m)	$m/(\rho D^2)$	f(Hz)	ζ(%)	K
0	0.73	3.23	3.59	11.48	0.23	9.23	0.72	3.23	3.59	11.41	0.35	7.49
30	1.28	2.95	4.68	12.70	0.38	10.01	1.33	2.95	4.68	12.88	0.41	9.92
40	1.45	2.85	5.27	12.86	0.57	8.68	1.41	2.85	5.27	12.99	0.76	7.21
60	2.16	2.67	7.40	12.95	0.94	8.41	2.05	2.67	7.40	13.07	0.73	8.97
70	UNTESTED						2.56	2.57	9.49	13.07	0.91	8.86
80	3.39	2.48	13.71	13.11	0.65	11.53	3.18	2.48	13.71	13.12	0.70	10.38
90	4.27	2.39	26.27	13.35	0.52	11.57	3.39	2.39	26.27	13.47	0.81	7.26
95	4.27	2.34	50.84	13.75	0.32	10.32	3.84	2.34	50.84	13.69	0.31	9.40
100	UNTESTED						14.80	2.29	2120.37	14.18	0.05	13.35

	Tubes 32 Hz (single blade)											
	Configuration (c)						Configuration (d)					
α (%)	V_c(m/s)	m (kg/m)	$m/(\rho D^2)$	f(Hz)	ζ(%)	K	V_c(m/s)	m (kg/m)	$m/(\rho D^2)$	f(Hz)	ζ(%)	K
0	0.97	1.38	1.53	16.28	0.53	8.79	0.99	1.38	1.53	16.28	0.53	8.97
40	2.05	1.02	1.88	22.52	2.05	6.17	2.05	1.02	1.88	22.52	3.00	5.10
60	2.97	0.84	2.32	23.04	2.97	6.54	3.58	0.84	2.32	23.04	3.00	7.84
80	6.63	0.66	3.62	27.35	2.99	9.80	5.99	0.66	3.62	27.35	3.00	8.84
90	9.11	0.57	6.21	25.19	2.67	11.81	8.24	0.57	6.21	25.19	3.00	10.08
95	12.43	0.52	11.30	29.84	1.12	15.58	10.66	0.52	11.30	29.84	3.00	8.16
100	17.32	0.48	444.44	31.96	0.05	15.77	20.41	0.48	444.44	31.96	0.05	18.02

Table 2. Flow physical parameters and modal frequency and damping values, as well as the experimental cross-flow Connors constant K, for increasing values of the two-phase void fraction.

and design recommendations. *Journal of Pressure Vessel Technology 113(2):242-256*

[10] Violette, R., Pettigrew, M. J., Mureithi, N. W., 2006, Fluidelastic Instability of an Array of Tubes Preferentially Flexible in the Flow Direction Subjected to Two-Phase Cross Flow. *Journal of Pressure Vessel Technology 128:148-159*

[11] Khalvatti, A., Mureithi, N. W., Pettigrew, M. J., 2010, Effect of Preferential Flexibility Direction on Fluidelastic Instability of a Rotated Triangular Tube Bundle. *Journal of Pressure Vessel Technology 132(4)*

[12] Piteau, P., Antunes, J., Delaune, X., Panunzio, D., Lagrange, R., 2022, Experimental investigation of in-flow fluidelastic instability for rotated triangular tube bundles subjected to single-phase and two-phase transverse flows. *Paper FIV2022.*

[13] Piteau, P., Delaune, X., Borsoi, L., Antunes, J., 2019, Experimental identification of the fluid-elastic coupling forces on a flexible tube within a rigid square bundle subjected to single-phase cross-flow *Journal of Fluids and Structures 86:156–169*

[14] Caicedo, J., 2010 Practical guidelines for the Natural Excitation Technique (NExT) and the Eigensystem realization algorithm (ERA) for modal identification using ambient vibration. *Experimental Techniques 35:52-58*

[15] Deri, E. 2018 Operational Modal Analysis of a Triangular-Pitch Tube Bundle Subjected to Two-Phase Cross-Flow. *Journal of Pressure Vessel Technology 140(3).*

[16] Connors, H. J., 1970, Fluid elastic vibration of tube arrays excited by cross flow. *ASME Symposium on Flow-Induced Vibration in Heat Exchanger. 35:52-58*

[17] Rogers, R. J., Taylor, C. and Pettigrew, M. J. 1984, Fluid Effects on Multispan Heat Exchanger Tube Vibration *Proceedings of the ASME Pressure Vessels and Piping Conference, ASME Publication H00316: Topics in Fluid Structure Interaction, pp. 17-26*

EXPERIMENTAL INVESTIGATION OF IN-FLOW FLUIDELASTIC INSTABILITY FOR ROTATED TRIANGULAR TUBE BUNDLES SUBJECTED TO SINGLE-PHASE AND TWO-PHASE TRANSVERSE FLOWS

Philippe Piteau, Xavier Delaune, Domenico Panunzio, Romain Lagrange

Université Paris-Saclay, CEA, Service d'Études Mécaniques et Thermiques, F-91191, Gif-sur-Yvette, France

Jose Antunes

Centro de Ciências e Tecnologias Nucleares (C2TN), IST, Universidade de Lisboa, 2695-066 Bobadela LRS, Portugal

ABSTRACT

The in-flow fluidelastic instability of tube bundles prompted renewed interest since the recent unanticipated failure of the replacement steam generators at the San Onofre nuclear power station. A literature review on the topic discloses contrasting views, depending on the tube bundle and flow configuration addressed. In a recent paper, the authors reported experiments using square bundles, subjected to single and two-phase flows. No streamwise instability was observed, for the tested bundle configurations and the flow velocity ranges explored. In the present paper, experimental results obtained at CEA-Saclay for a rotated triangular tube bundle are presented, providing new in-flow fluidelastic data for both single-phase and two-phase transverse flows. The bundle consists of 50 tubes, with reduced pitch P/D=1.44 and tube diameter D=30mm. It was subjected to single-phase (air or water) and two-phase air-water (with homogeneous void fraction in the range 40% to 98%) transverse flows. In the upper region of the bundle, several different flexibility configurations were tested, with up to 15 flexible tubes, mounted using anisotropic supports, which allow for in-flow vibrations. Results presented in the paper include in-flow fluidelastic stability data obtained for both single-phase and two-phase transverse flows. Moreover, local void fraction and identified flow regimes are also presented. These results are discussed and compared to those obtained by previous authors, for similar tested configurations.

1. INTRODUCTION

In-flow fluidelastic instability of tube bundles (e.g., involving tube motions along the drag/streamwise direction) has been the subject of a strong renewed interest, since the unanticipated failure of the replacement steam generators of the San Onofre Nuclear Generating Station (SONGS) in 2012 - see the report from SCE (2012) and the documents referred therein. In-flow fluidelastic instability occurred in the U-bend region of the tube bundle, where the anti-vibration bars were ineffective to prevent instabilities of the low-frequency in-plane U-bend tube modes. Note that, in this upper region of the bundle, tubes are essentially excited by a two-phase ascending secondary cross-flow, with high values of the void fraction.

Before this even, in-flow fluidelastic instability was usually considered irrelevant, although early studies by Weaver and Koroyannakis (1983) and Weaver and Schneider (1983) had reported the possibility of streamwise instability, depending on features of the flow and the tested bundles. Their findings were further explored and refined about 20 years later, through experiments in air flow performed by Mureithi et al. (2005) and in two-phase flow performed by Janzen et al. (2005) and Violette et al. (2006). Then, the SONGS failure triggered an enlarging corpus of recent experimental and theoretical work, aiming clarification of the issues posed by test results. Delaune's (2016) review of the experimental literature on the topic, involving references up to 2015, discloses contrasting views, which may be broadly condensed as follows:

For *square bundles* fitted with asymmetrically supported tubes, in-flow fluidelastic instability was never observed under single-phase flows. On the other hand, symmetrically supported tubes lead to fluidelastic coupling forces that induce time-varying planar and/or orbitally coupled motions, from which it is problematic to assert a dominant instability configuration. To the authors' best knowledge, experimental in-flow response data from square bundles is virtually nonexistent for two-phase flows. In a recent paper, Delaune et al. (2018) reported experiments under single and two-phase flows. No streamwise instability was observed, for the tested bundle configurations and the flow velocity ranges explored.

For *triangular bundles*, in-flow fluidelastic instability was observed under single-phase flows, the stability boundary being dependent on the number of

flexible tubes, while for two-phase flows in-flow instability does not seem to depend consistently on the bundle flexibility configuration. However, for a single flexible tube within a rigid bundle, no in-flow instability was ever observed, whatever the nature of the flow. In any case, for both single-phase and two-phase flows, the in-flow instability boundary is always beyond the cross-flow instability boundary.

References published since 2015 provided new experimental data on the in-flow fluidelastic instability of triangular bundles. The work by Feenstra et al. (2017) concerns U-bend tube regions in a rotated triangular configuration (with P/D=1.5) subjected to air cross-flow, with gap-controlled flat bar supports. Their results show in-plane fluidelastic instability, which may need a manual pushing help to trigger. They also observed a significant delay before the bundle instability emerged, these findings denoting that the in-plane fluidelastic coupling is quite weak. Nakamura and Tsujita (2018) tested three straight bundles, in a rotated triangular configuration (with P/D=1.2~1.5), also subjected to air flow. They obtained stream-wise instability with Connors' constant values in the range $K = 7.5 \sim 10$, higher than typically observed for transverse instability. Tan et al. (2018) tested straight bundles, in a rotated triangular configuration (with P/D=1.48), subjected to single phase water flow and two-phase air-water flow. The tubes were supported by rectangular flexible bars, allowing to test fluidelastic instability along either the lift or the drag direction. According to the authors, their tests did not produce in-flow instabilities.

The work performed by Azuma et al. (2018) is part of a significant effort performed by Mitsubishi Heavy Industries related to stream-wise instabilities. In a very comprehensive experimental program, these authors tested triangular straight and U-bend tube bundles (with P/D=1.33) subjected to a SF_6-Ethanol mixture, which displays near-similar density and surface tension to air-steam two-phase flow. Experiments were performed for several flexible tube configurations, flow distributions and void fractions. The Connors instability constant was identified for both the out-of-plane and in-plane motions. For in-flow instabilities, a significant dispersion of K was obtained, ranging from the order of magnitude for out-of-plane instability up to 5 times larger, depending on the bundle type (straight or U-bend) and on the tube modal frequencies. The lower values of K pertain to the straight tube bundles with higher modal frequencies. Also from this research group, the recent paper by Nishida et al. (2021) reports extensive measurements of the unsteady fluidelastic coupling forces in triangular straight and U-bend tube bundles (with P/D=1.33) subjected to actual steam-water flows under high temperature and pressure, which is a rare achievement. Results are presented for both cross-flow and in-flow instabilities. They then inserted the identified flow-coupling coefficients into the general Chen (1983) formulation and computed instability boundaries that compared favorably with the experimental critical velocities. Surprisingly, from their study, for isotopic mounted straight tubes, in-flow instability will arise at a lower velocity than the cross-flow instability. For U-tube bundles, the in-line critical velocities were found to be higher.

The present paper follows our preceding investigation documenting the absence of in-flow instability for square bundles, see Delaune et al. (2018). Here we present the results of an extensive experimental investigation, performed at CEA-Saclay, on the streamwise stability features of a rotated triangular bundle, providing new in-flow fluidelastic data for both single-phase and two-phase transverse flows. The bundle consists essentially on 10 rows of 5 tubes, with reduced pitch P/D=1.44 and tube diameter D=30mm. It was subjected to single-phase (air or water) and two-phase air-water transverse flows. Several different flexibility configurations were tested, with up to 15 flexible tubes, mounted using anisotropic supports, which allow for in-flow vibrations. Results presented include streamwise fluidelastic stability data obtained for both single-phase and two-phase flows. Moreover, local void fraction and identified flow regimes are also presented. These results are discussed and compared to those obtained by previous authors, for similar tested configurations.

2. EXPERIMENTAL RIG

The tests were performed using the experimental rig TITAN (Figure 1) with the CEA-Saclay air/water loop GASCOGNE (Figure 2). As shown, the rotated triangular bundle consists of 50 tubes (10 rows, 5 columns) with reduced pitch P/D=1.44, tube diameter D=30mm and length L=300mm, completed by two rows of half-tubes attached to the test-section walls. The rigid lower 20 tubes of the bundle are used to condition the incoming vertical flow, before the test section.

For the tested bundle configurations, as illustrated in Figure 3 for configuration C1 with 15 vibrating tubes, each flexible tube is supported through a flexible rectangular bar with $100 \times 25 \times 4$ mm, positioned

such that maximum flexibility is along the streamwise direction. All the flexible tubes display nearly identical values for the first modal frequency and damping values in air. For motions along the inflow (drag) direction, the relevant average and standard deviation values are given in Table 1. For each tested configuration, tubes with the first streamwise bending modal frequency at 32Hz and 14Hz (in air) were tested. The lower modal frequency was obtained by adding an extra mass at the end of the flexible tubes, so that fluidelastic instabilities were eventually reached at lower flow velocities. The second streamwise and the first transverse flexural modal frequencies were measured one order of magnitude higher that the frequency range of interest.

Figure 1. Test rig TITAN of CEA-Saclay.

Concerning the flow, Figure 2 (left side) shows a general view of the test loop. Water flow is provided by a centrifugal pump, delivering up to 1080 m^3/h, while air is supplied by a compressor with a maximal flow of 3000 m^3/h (at 0^oC and 1 Bar). As shown in the figure, the two fluids are mixed prior to the test section where the tube bundle is located. Tests were performed for single-phase (air, water) and two-phase air-water flows at various void fractions.

Concerning the instrumentation, as shown in Figure 2 (right side, upper drawing), each flexible tube is equipped with a strain gauge, located near the clamped side, calibrated with respect to the tube displacement at the free end. On the other hand, Figure 2 (right side, lower drawing) shows the lateral opening for inserting the sapphire bioptical probe, which was located between the 3rd and 4th rows of the bundle, in order to measure the local void fraction of two-phase flows.

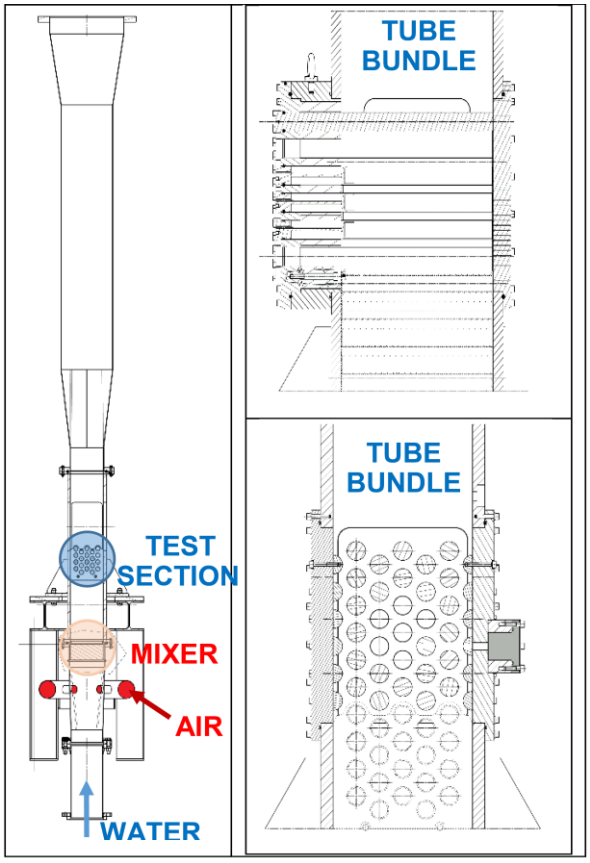

Figure 2. Air/water experimental loop GASCOGNE of CEA-Saclay.

	Tubes « 32Hz »		Tubes « 14Hz »	
	Frequency	Damping	Frequency	Damping
Average	31.96Hz	0.047%	14.18Hz	0.045%
Dispersion	0.84%	21.9%	0.66%	7.6%

Table 1. Average values and RMS dispersion of the flexible tubes first streamwise modal frequencies and damping values.

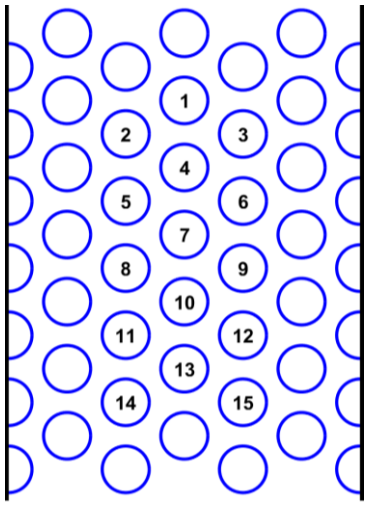

Figure 3. Configuration C1 with 15 in-flow flexibly supported tubes.

3. EXPERIMENTAL PROCEDURES

The first tests were performed, for the different flexible configurations, with the higher frequency "32Hz" tubes, for single-phase (air, water) and two-phase flows (with homogeneous void-fraction 80, 90, 95 and 98%). Then, in order to reach streamwise fluidelastic instability, a significant number of tests was also performed using the lower frequency flexible "14Hz" tubes.

In all cases, the flow rate was increased until the mean tube drag plus the peak vibration amplitude nearly reached the gap between tubes (0.013m). Figure 4 shows the measured mean drag of the tubes when the water velocity is increased, for configuration 1 (see Figure 3). As might expected, the drag increases in quadratic manner with the flow pitch velocity V_p.

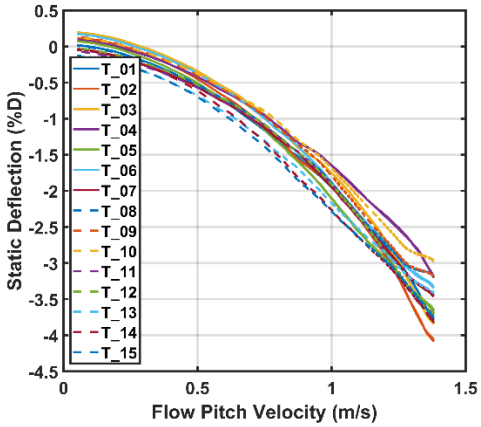

Figure 4. Static drag of the in-flow flexible tubes as a function of the flow pitch velocity.

4. SINGLE-PHASE FLOW EXPERIMENTS

Figure 5 presents the experimental results obtained for configuration C1, using the higher frequency 15 flexible tubes ("32Hz") subjected to air flow, for increasing pitch velocity. The upper plot shows the experimental streamwise response spectra of the central tube 7 (see Figure 3), while the lower plot displays the RMS response amplitudes of all the flexible tubes. Figure 6 presents the results obtained for configuration C1 in air flow, when using the lower frequency flexible tubes ("14Hz"). Both figures clearly highlight an instability of the modal response peak, which arises at about 17 m/s for the "32Hz" tubes and about 13 m/s for the "14Hz" tubes.

Figures 7 and 8 present the corresponding test results, when configuration C1 is subjected to water flow. Not only the modal frequencies are lowered, due to the water added mass effect, but one can also notice that the single modal peaks displayed by the air tests are now replaced by groups of modal peaks spanning a significant frequency range, due to a strong tube coupling by the denser fluid.

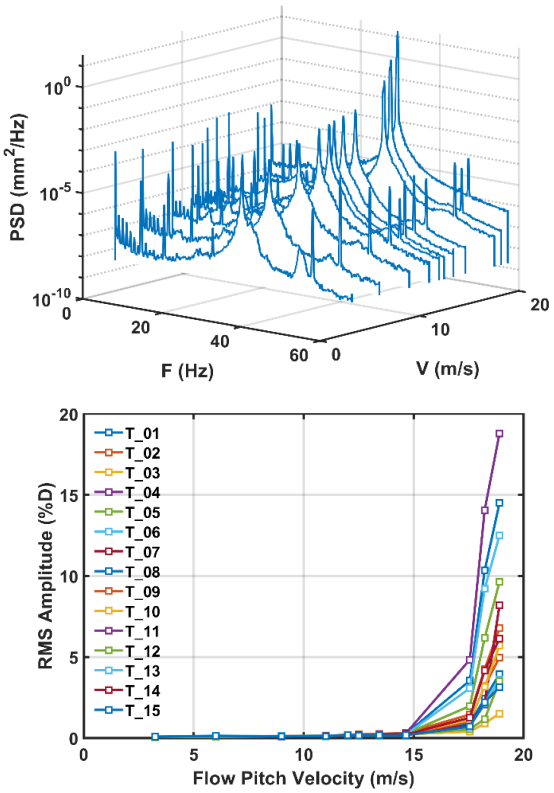

Figure 5. Configuration C1 "32Hz" in air flow: Response spectra of tube 7 and RMS amplitudes of all the flexible tubes as a function of the pitch velocity.

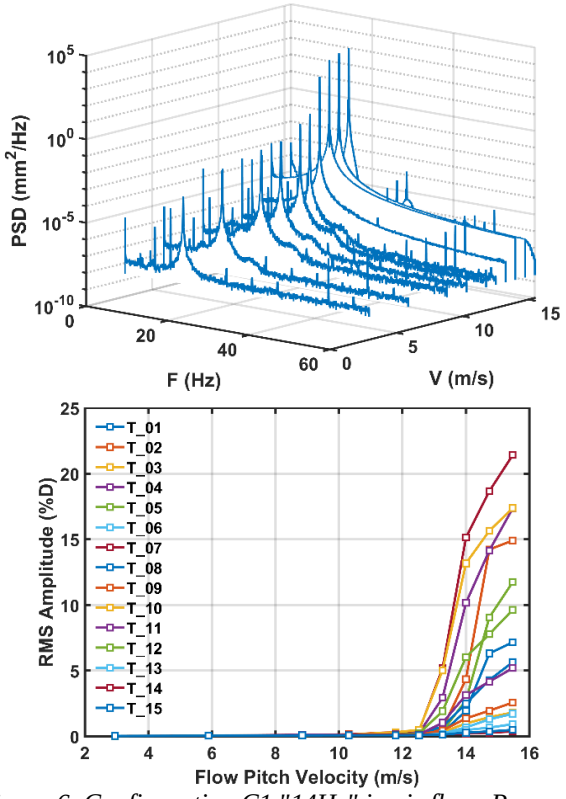

Figure 6. Configuration C1 "14Hz" in air flow: Response spectra of tube 7 and RMS amplitudes of all the flexible tubes as a function of the pitch velocity.

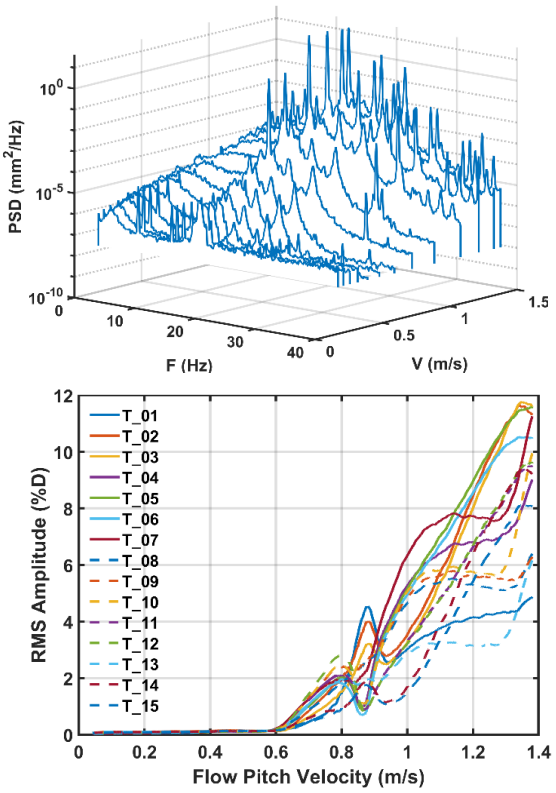

Figure 7. Configuration C1 "32Hz" in water flow: Response spectra of tube 7 and RMS amplitudes of all the flexible tubes as a function of the pitch velocity.

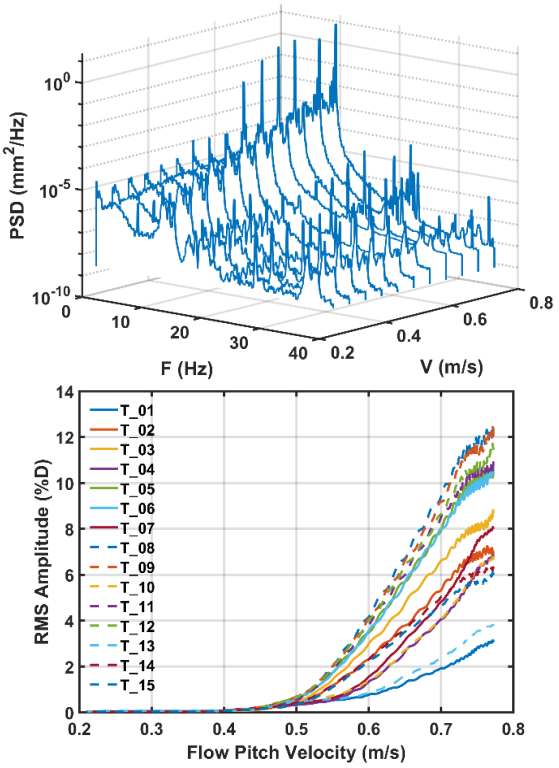

Figure 8. Configuration C1 "14Hz" in water flow: Response spectra of tube 7 and RMS amplitudes of all the flexible tubes as a function of the pitch velocity.

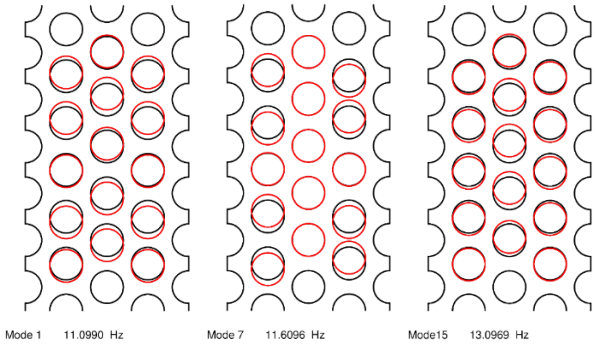

Figure 9. Configuration C1 "32Hz" in water: Sample modes computed using CEA finite element program CAST3M, illustrating the tubes coupling by the fluid.

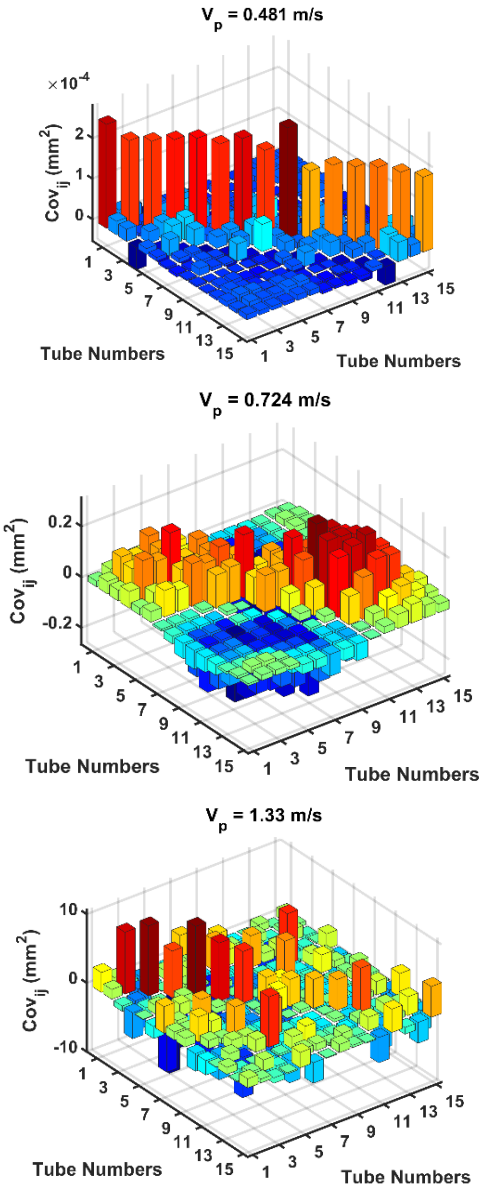

Figure 10. Configuration C1 "32Hz" in water flow: Covariance matrix of the 15 vibrating tubes for three increasing values of the pitch velocity.

For the "32Hz" tubes in water, the modal group ranges from 16 to 24Hz, while for the "14Hz" tubes in water, the modal group ranges from 11 to 13Hz. Some of these modes are illustrated in Figure 9, from computations using the CEA finite element program CAST3M. The experimental data in water flow displays unstable behavior beyond about 0.6 m/s for the "32Hz" tubes and about 0.4 m/s for the "14Hz" tubes. The slope of the increasing amplitude responses, beyond the instability boundary, is much steeper for the tests in air flow than for those in water flow.

The results shown in Figure 7 are particularly interesting. One can notice in the lower plot that the lines displaying the tube RMS amplitudes are interlaced, so that the tube with maximum response amplitude changes with the flow velocity. The upper plot shows that this behavior is due to switching of the unstable mode as the flow velocity increases.

The covariance matrices shown in Figure 10, computed from the measured time-domain responses of the flexible tubes at increasing flow velocities, further confirm that the bundle response pattern changes significantly as the flow velocity increases. At 0.48 m/s, below the critical velocity (0.6 m/s), the covariance matrix is nearly diagonal, so that tube motions are uncorrelated. Beyond the critical stability boundary, the covariance matrices at 0.72 m/s and 1.33 m/s point to specific motion cross-correlations, although with different patterns. Such interesting behavior is possibly related to the fluidelastic forces changes with the reduced velocity, and to the forces projections on the different bundle modeshapes.

Additional single-phase flow tests were performed for other flexible tube arrangements, see section 6.

5. TWO-PHASE FLOW EXPERIMENTS

Figures 11 to 14 summarize the experimental results obtained for the flexible configuration C1, subjected to air-water flows. Figures 11 and 12 concern the higher frequency "32Hz" tubes, while Figures 13 and 14 relate to the lower frequency "14Hz" tubes. Results are illustrated for two void fractions, 40% (Figures 11 and 13) and 80% (Figures 12 and 14). For both void fractions, the higher frequency tubes did not reach instability, for the range of homogeneous pitch velocity explored, see figures 11 and 12.

Such is not the case for the lower frequency tubes, which display instabilities at about 3.8 m/s (40% void fraction) and 5.3 m/s (80% void fraction), see figures 13 and 14. One might conjecture that, given a high enough flow rate, instability would be reached for the "32Hz" subjected to two-phase flow. However, as pointed earlier, this could not be attempted because the maximum velocities explored in Figures 11 and 12 already led to a mean tube drag plus random response that nearly reached the inter-tube gap.

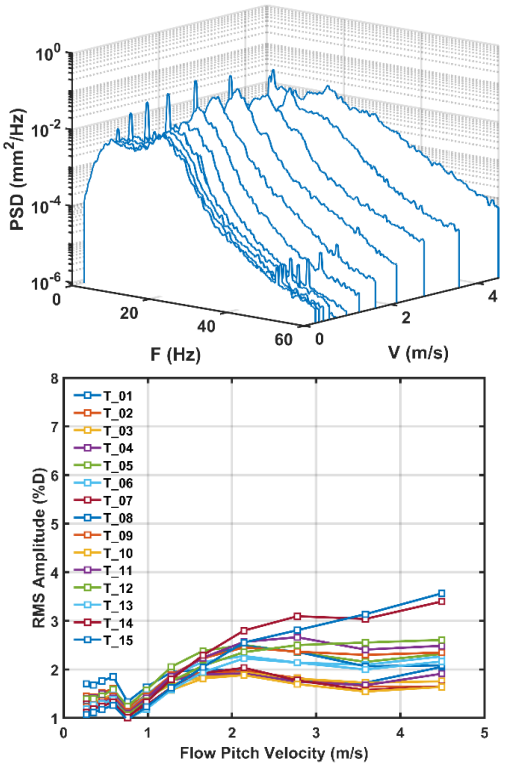

Figure 11. Configuration C1 "32Hz" in air-water two-phase flow (void fraction 40%): Response spectra of tube 7 and RMS amplitudes of all the flexible tubes as a function of the pitch velocity.

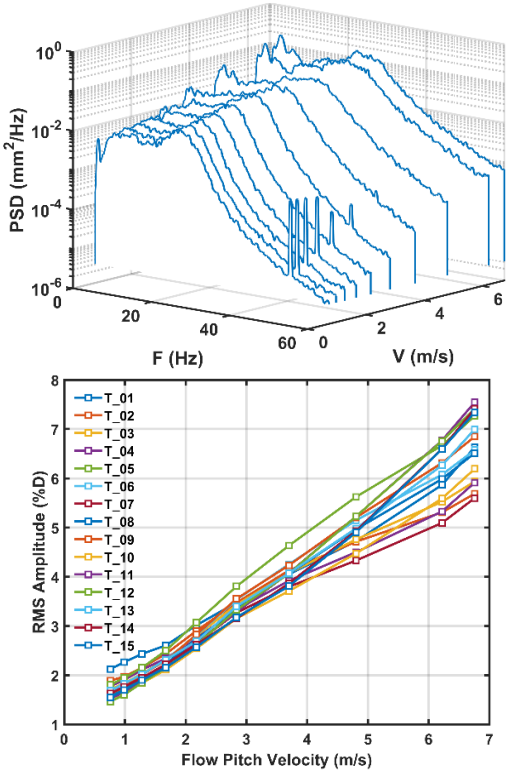

Figure 12. Configuration C1 "32Hz" in air-water two-phase flow (void fraction 80%): Response spectra of tube 7 and RMS amplitudes of all the flexible tubes as a function of the pitch velocity.

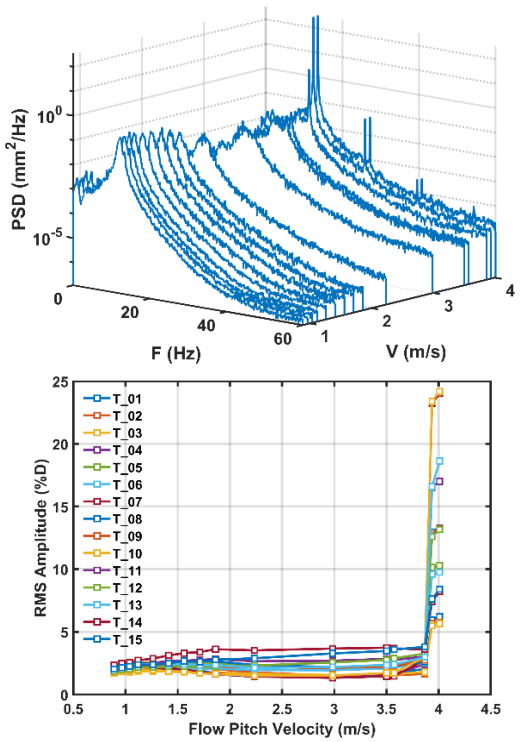

Figure 13. Configuration C1 "14Hz" in air-water two-phase flow (void fraction 40%): Response spectra of tube 7 and RMS amplitudes of all the flexible tubes as a function of the pitch velocity.

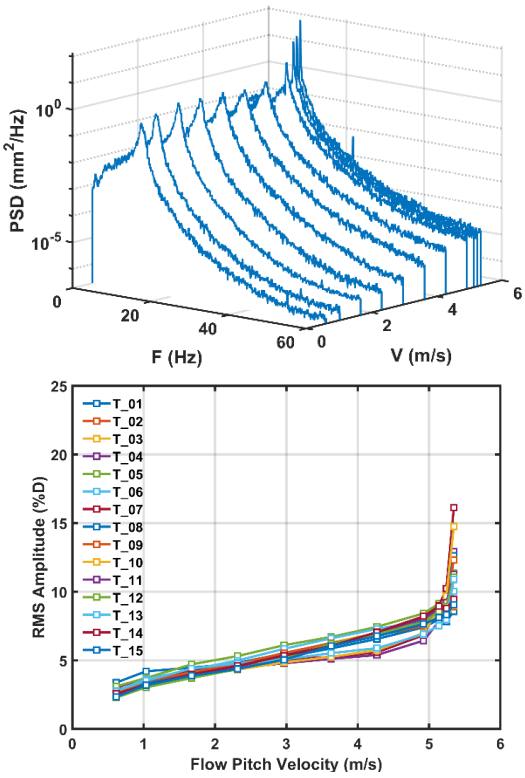

Figure 14. Configuration C1 "14Hz" in air-water two-phase flow (void fraction 80%): Response spectra of tube 7 and RMS amplitudes of all the flexible tubes as a function of the pitch velocity.

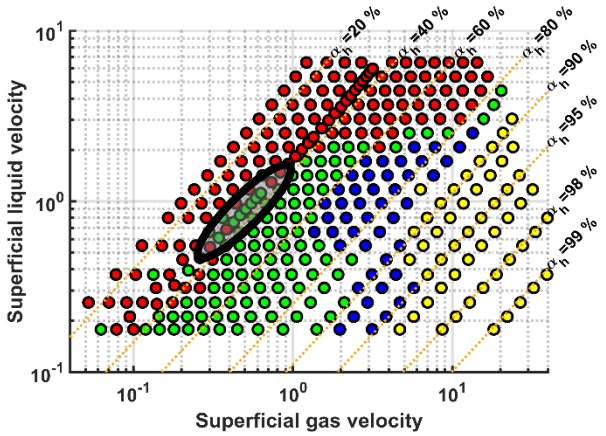

Figure 15. Two-phase flow chart experimentally obtained from the CEA air-water tests of a square bundle with P/D=1.5 (expanded from Delaune et al., 2018); Flow regimes: Red=Bubbly, Green=Slug, Blue=Churn, Yellow=Annular.

An interesting feature in Figure 11 is the non-monotone behavior of the RMS tube responses, as the flow velocity increases. It is suspected that this behavior is possibly connected with changes of the two-phase flow regime. Such an interpretation seems supported by the data presented in Figure 15, which shows a two-phase flow chart experimentally obtained from the CEA air-water tests of a square bundle with P/D=1.5 (chart expanded from Delaune et al., 2018). The flow velocity region covered by the tests of Figure 11, at 40% void fraction, is highlighted in Figure 15, showing that the Bubbly and Slug flow regimes are intermixed.

Tests at other void fractions did not trigger instability for the "32Hz" tubes, while it was clearly reached for the "14Hz" tubes. This is the very reason why the lower frequency tubes were tested. Actually, because of their different mass and frequency parameters, our results from the "32Hz" tubes were ill-fitted for comparison with the instability data from Violette et al. (2006).

If one excepts the peculiar behavior shown in Figure 11, most of our two-phase experiments led to a near-linear increase of the RMS tube amplitudes with the flow velocity, prior to instability. On the other hand, as can be seen in Figures 11 and 12, a wide-band low-frequency response often arises in the response spectra. This is a somewhat classical feature, often observed in vibration experiments using two-phase flows.

As for single-phase flows, additional two-phase flow tests were performed for configurations with various flexible tube arrangements. These experiments are described in the next section.

6. OTHER TESTED CONFIGURATIONS

Figure 16 shows the many flexible configurations that were tested, most of them for the lower frequency "14Hz" tubes, to which the results of Figure 16 apply (except for configuration C3, which was only tested with the "32Hz" tubes). Configuration C2 is also a 15 flexible tube arrangement, just as the "centered" configuration C1, but displaced towards the bundle end. Configuration C3 is a centered seven-tube cell. Configuration C4 is a single flexible tube at the center of the bundle. Then, configurations C5 to C11 explore different arrangements, using three to seven flexible tubes.

Figure 16 synthetizes the occurrence or not of streamwise fluidelastic instability for each configuration, under air flow, water flow and two-phase flow. Results of configuration C2 are similar to those of C1, with unstable behavior under single-phase and two-phase flows. The cell C3 (with "32Hz" tubes) became unstable under single-phase flow, but not for two-phase flow. The single flexible tube C4 never went unstable, in agreement with experiments by Violette et al. (2006). Concerning the other configurations, one can notice that those with a single flexible tube per column (C9 and C10) never became unstable, whatever the flow type. All the other configurations, having two or more flexible tubes in one or two columns became unstable under air flow, but remained stable under water flow and two-phase flow.

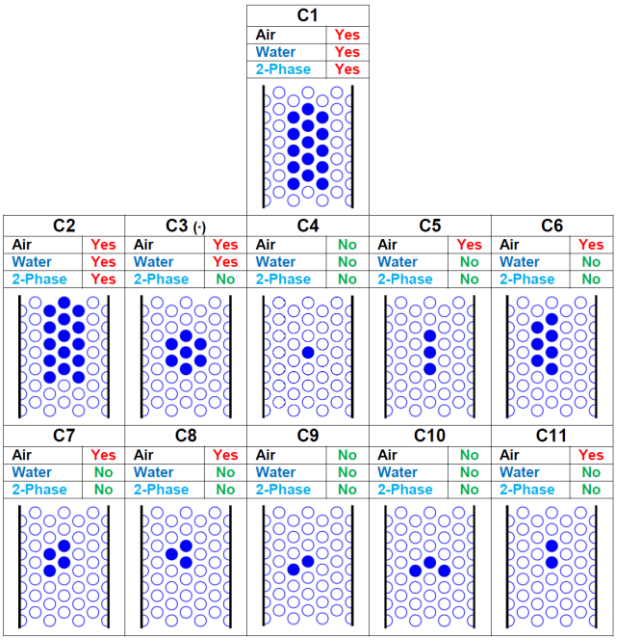

(*) Results for configuration C3 with "32Hz" tubes, as this configuration was not tested with the "14Hz" tubes.

*Figure 16. Tested configurations with various arrangements of the "14Hz" flexible tubes; also shown is the occurrence (**Yes**) or not (**No**) of streamwise fluidelastic instability for each configuration, respectively under air flow, water flow and two-phase flow.*

All these results suggest that: (1) Streamwise instability occurs through the vibration coupling of two or more tubes along the bundle columns; (2) Coupling between tubes along the bundle rows is irrelevant for streamwise instability; (3) The destabilizing coupling forces are comparatively weak, so that instability may or not be triggered, depending on a number of factors such as the system damping.

7. SUMMARY OF RESULTS

After the previous qualitative remarks on the features that seem to govern streamwise instability phenomena, we now summarize the instability data stemming from our experiments. Figure 17 displays the Connors stability plot for the various tested configurations, under single-phase and two-phase flow:

$$\frac{U_p^{crit}}{fD} = K\sqrt{\frac{2\pi\zeta m}{\rho D^2}} \qquad (1)$$

The values of the mass-damping parameter, as well as those of the critical reduced velocity are based on the numerical data collected in Table 2, for both the "32Hz" and "14Hz" tubes, the various tested flexible configurations, under single-phase and two-phase flows. The present results are also compared with those obtained by Violette et al. (2006).

Tubes « 32 Hz »						
α (%)	U_p^{crit} (m/s)	m (kg/m)	$\frac{m}{\rho D^2}$	f (Hz)	ξ (%)	K
0	0.6	1.38	1.53	15.87	0.16	10.18
40	> 4.5	1.02	1.88	22.00	3	> 11.5
60	> 5.5	0.83	2.32	24.26	3	> 11.4
80	> 6.8	0.66	3.62	27.39	3	> 10.0
90	> 10	.57	6.21	29.50	3	> 10.4
95	> 15	0.52	11.30	30.75	3	> 11.2
98	20.5	0.49	25.87	31.58	3	> 9.8
99	-	-	-	-	-	-
100	17.5	0.48	444.4	31.84	.17	8.48

Tubes « 14 Hz »						
α (%)	U_p^{crit} (m/s)	m (kg/m)	$\frac{m}{\rho D^2}$	f (Hz)	ξ (%)	K
0	0.46	3.23	4.17	11.22	0.06	10.78
40	3.87	2.85	5.71	12.38	3.35	9.50
60	4.23	2.67	7.99	12.81	4.70	7.17
80	5.24	2.48	15.8	12.86	2.76	8.21
90	7.00	2.39	29.3	13.31	2.54	8.10
95	9.84	2.34	54.9	13.68	1.84	9.52
98	13.7	2.31	130.1	13.81	1.20	10.57
99	16.3	2.30	236.2	14.10	0.297	18.35(*)
100	13.0	2.29	2120	14.37	0.057	10.94

(*) This could be a biased identification of K, due to the difficulty of controlling and monitoring a void ratio of 99%.

Table 2. Bundle configuration C1 - Tubes "32Hz" and "14Hz": Flow physical parameters and structural modal frequency and damping values, as well as the experimental streamwise Connors constant K, for increasing values of the two-phase void fraction.

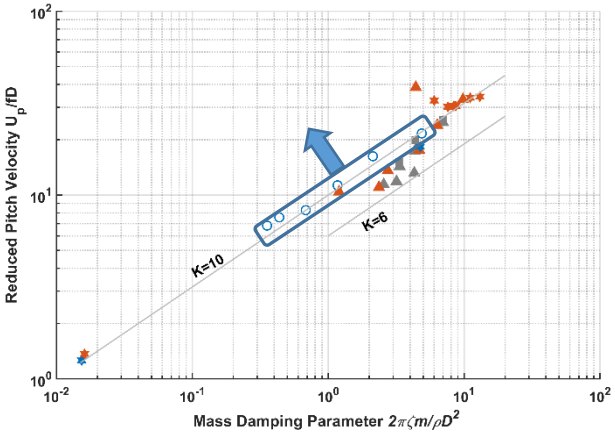

Figure 17. Connors stability plot from the test results: ○ Two-phase flow configuration C1 with "32Hz" tubes; ★ Single-phase flow configuration C1 with "32Hz" tubes; ▲ Two-phase flow configuration C1 with "14Hz" tubes; ✸ Single phase flow configurations C1, C2, C5, C6, C7; C8, C11 with "14Hz" tubes; ■▲ Violette et al. (2006).

Concerning the damping values, in single-phase we use those measured for the most prominent mode at low flow velocity, while in two-phase flow this could only be achieved for the "14Hz" tubes. Due to identification difficulties, for the "32Hz" tubes in two-phase flow the maximum recommended value by ASME code $\zeta = 3\ \%$ was assumed.

Figure 17 shows that all the single-phase test results of configuration C1, for both the "32Hz" and "14Hz" tubes, in air flow and water flow, lay about the boundary stability line at $K = 10$. A similar result was obtained for the other tested configurations using "14Hz" tubes which became unstable in air flow. Concerning two-phase flows, for configuration C1 using the "32Hz" tubes, instability does not arise in the tested reduced velocities up to this boundary. This is highlighted in Figure 17 by enclosing the experimental data obtained at maximum reduced flow velocity (blue circles) and pointing to a putative higher value of the corresponding Connors "constant" K. Configuration C1 using the "14Hz" tubes became unstable in two-phase flows, leading to values in the range $K = 6 \sim 10$.

These results are consistent with those obtained by Violette et al. (2006), as also shown in Figure 17. As mentioned in the Introduction, the experimental results obtained by Nakamura and Tsujita (2018) for bundles with reduced pitch in the range P/D=1.2~1.5 point to values $K = 7.5 \sim 10$, therefore are also consistent with our results. Concerning the experiments by Azuma et al. (2018), using SF6-Ethanol, with both straight bundles and U-bundles, they also observed streamwise instabilities in all cases. Interestingly, they obtained for the straight bundles the surprisingly low value $K \approx 2.5$, whereas for U-bundles they obtained values $K \geq 10$, depending on the tubes modal frequencies. Similar results seem to have been obtained by Nishida et al. (2021), in their steam-water experiments.

8. CONCLUSIONS

In this paper we presented experimental results for a rotated triangular straight tube bundle with reduced pitch P/D=1.44, providing new in-flow fluidelastic data for both single-phase (air or water) and two-phase (with homogeneous void fraction in the range 40% to 98%) transverse flows. Many different flexibility configurations were tested, with up to 15 flexible tubes, mounted with anisotropic supports allowing for in-flow vibrations.

A conclusion from the ensemble of our tests, consistent with the main bulk of a (still limited) literature, is that streamwise instabilities may arise for $K \geq 6$, and often $K \geq 10$. However, this contrasts with the low values $K = 2.5 \sim 3.5$ obtained by Azuma et al. (2018) and Nishida et al. (2021) for some straight tube bundles (although not excited by the usual air-water flow mixture). Even so, Nishida et al. (2021) point that, for tubes with the same modal frequencies in the streamwise and transverse directions, the critical flow velocity for the transverse direction is lower than for the streamwise direction. These results clearly suggest that in-flow coupling forces are significantly smaller than those leading to out-of-plane instabilities. Actually, the topology of flows inside the bundles seem to support such idea.

All tested configurations with 2 to 7 in-line flexible tubes that became unstable did so when subjected to air flow, but not under water flow nor two-phase flow. The reason of such behavior is still unclear, but several lines of thought may be explored: (1) The denser fluids typically generate more damping, and this is particularly so concerning two-phase flows; (2) The denser flows further drift the flexible tubes from their nominal positions, and this may affect the destabilizing coupling forces; (3) The denser flows generate more effective random excitations and hence vibration amplitude, which might "break" the flow-coupling deterministic organization.

From the many experiments presented here, stems the important general conclusion that streamwise instability occurs only through the vibration coupling of *two or more tubes along the bundle columns*. This is a necessary condition, suggesting that streamwise instability cannot be theorized from a single-degree-of-freedom model. At least a model with two adjacent tubes of the same bundle column is needed,

pointing to the significance of cross-coupling force terms. A somewhat similar view was expressed by Nishida et al. (2021), when stating that a stiffness mechanism is dominant for streamwise instability.

9. ACKNOWLEDGEMENTS

This work was performed in the framework of a joint research program co-funded by CEA, EDF and FRAMATOME (France). Valuable contributions by M. Bellanger and T. Valin (CEA-Saclay) to the experimental work are gladly acknowledged.

10. REFERENCES

Azuma, S., Morita, H., Hirota, K., Kondo, Y., Utsumi, S., Komuro, Y., Kawakami, R., Nariai, T., Nishikawa, Y., 2018, Investigation of critical flow velocity of a triangular U-tube bundle subjected to two-phase flow (Paper FIV2018-148). *9th International Symposium on Fluid-Structure Interactions, Flow-Sound Interactions, Flow-Induced Vibration and Noise*, July 8-11, 2018, Toronto, Canada.

Chen, S.S., 1983, Instability mechanisms and stability criteria of a group of circular cylinders subjected to cross-flow - Part 1: Theory. *ASME Journal of Vibration, Acoustics, Stress and Reliability in Design* **105**:52-58.

Delaune, X., 2016, Literature review on the in-plane instability of steam generator tube bundles. *CEA Internal Report (in French)*.

Delaune, X., Piteau, P., Borsoi, L., Antunes, J., 2018, Experimental investigation of in-flow fluidelastic instability for square tube bundles subjected to single-phase and two-phase transverse flows (Paper FIV2018-49). *9th International Symposium on Fluid-Structure Interactions, Flow-Sound Interactions, Flow-Induced Vibration and Noise*, July 8-11, 2018, Toronto, Canada.

Feenstra, P., Sawadogo, T., Smith, B., Janzen, V., Cothron H., 2017, Investigations of in-plane fluidelastic instability in a multi-span U-bend tube bundle: Tests in air flow (Paper PVP2017-66068). *ASME 2017 Pressure Vessels and Piping Conference*, July 16-20, 2017, Waikoloa, Hawaii, USA.

Janzen, V., Hagberg, E., Pettigrew, M., Taylor, C., 2005, Fluidelastic instability and work rate measurements of steam generator U-tubes in air-water cross-flow. *ASME Journal of Pressure Vessel Technology* **127**:84-91.

Mureithi, N., Zhang, C., Ruël, M., Pettigrew, M., 2005, Fluidelastic instability tests on an array of tubes preferentially flexible in the flow direction. *Journal of Fluids and Structures* **21**:75-87.

Nakamura, T., Tsujita, T., 2018, Study on streamwise fluidelastic instability by air cross flow: Rotated triangular arrays inclined to flow (Paper FIV2018-19). *9th International Symposium on Fluid-Structure Interactions, Flow-Sound Interactions, Flow-Induced Vibration and Noise*, July 8-11, 2018, Toronto, Canada.

Nishida, S., Azuma, S., Morita, H., Hirota, K., Kawakami, R., Nishikawa, Y., 2021, In-plane fluidelastic instability evaluation of triangular array tube bundle using fluid force measured under steam-water two-phase flow condition. *ASME Journal of Pressure Vessel Technology* **143**:1-12 (Paper 011404).

SCE - Southern California Edison, 2012, San Onofre nuclear generating station - Unit 2 return to service report. *Document ML12285A263*, retrieved from *https://www.nrc.gov/docs/ML1228/ML12285A263.pdf*.

Tan, T., Gao, L., Li., P., Ma, J., Jiang, T., 2018, Experimental study on fluidelastic instability of rotated triangular tube bundles subjected to two-phase cross flow (Paper FIV2018-64). *9th International Symposium on Fluid-Structure Interactions, Flow-Sound Interactions, Flow-Induced Vibration and Noise*, July 8-11, 2018, Toronto, Canada.

Violette, R., Pettigrew, M., Mureithi, N., 2006, Fluidelastic instability of an array of tubes preferentially subjected to two-phase cross flow. *ASME Journal of Pressure Vessel Technology* **128**:148-159.

Weaver, D., Koroyannakis, D., 1983, Flow-induced vibrations of heat exchanger U-tubes: A simulation to study the effects of asymmetric stiffness. *ASME Journal of Vibration, Acoustics, Stress and Reliability in Design* **105**:67-75.

Weaver, D., Schneider, W., 1983, The effect of flat bar supports on the crossflow induced response of heat exchanger U-tubes. *ASME Journal of Engineering for Power* **105**:775-781.

ON THE STABILITY OF THE ROTATED SQUARE ARRAY IN TWO-PHASE FLOW USING THE QUASI-STEADY MODEL

S. Darwish, N.W. Mureithi
Department of Mechanical Engineering, Polytechnique Montreal, Montreal, Quebec, Canada
Minki Cho
Doosan Heavy Industries and Construction, 22, Doosan Volvo-ro, Seongsan-gu, Changwon-si, Gyeongnam, 51711, Korea

ABSTRACT

Despite the extensive data available in the literature for fluidelastic instability modelling, no data has been published (to the authors' knowledge) for the rotated square layout instability prediction in single and two-phase flow. The complex nature of flow in the rotated square array creates a barrier to predicting fluidelastic behaviour. In the present work, the quasi-static fluid forces are measured in single-phase (water) and over a wide range of void fractions for two-phase flow. This array has a relatively wide spacing of P/D=1.64. The test section is designed to measure the fluid forces for an instrumented tube, and cross-coupling forces of the surrounding tubes in order to incorporate the measurements into single and multiple degrees-of-freedom quasi-steady models. The present experimental data uncovers the stable behaviour of the single tube for this rotated square array due to the significantly small lift force variation (CL_y) with transverse displacement. In the streamwise direction, no fluidelastic instability was found for a single-degree-of-freedom model.

1. INTRODUCTION

Typical heat exchangers involve thousands of tubes that are susceptible to high speed flow flowing around them. As a result, tubes may couple with flowing fluid in a way that energy exposed to the tubes by the fluid is transferred, which could lead to excessive cross flow induced instabilities. Such an incident could lead to failure of tube bundle and immediate shut down to the facility. This could be avoided by providing practical understanding to the problem through experimental and theoretical studying.

Several excitation sources have been found to cause bundle cross-flow vibrations. Among them, fluidelastic instability (FEI) is considered the most destructive. In an attempt to understand this problem, Roberts [1962] provided the first modeling approach by considering a jet switch mechanism in the tube bundle by assuming the flow separation occurrence at minimum gaps between tubes, and constant pressure withing tubes wake areas. The theory was incapable of predicting transverse FEI, although research has shown that it is the dominant instability direction.

A different approach was followed by Connors Jr [1970] and Blevins [1974] by providing the quasi-static model by measuring the fluid forces instead of trying to analytically predict them. In this model, it is assumed that fluid forces applied on a flexible tube could be predicted by statically displacing the tube relative to its neighbouring tubes. This assumption allowed the fluid force coefficients to be experimentally measured using a rigid tube.

A significant improvement was proposed (Price and Paidoussis [1983a]; Price and Paidoussis [1983b]) by including the time lag between tube motion and fluid forces. Following the suggestion of Ruscheweyh [1983], Price and Paidoussis [1984] considered the retardation of the flow approaching the cylinder due to its effect on fluid forces.

Hassan and Weaver [1982] developed a tube-in-channel model to describe the transverse dynamic FEI in tube arrays. The authors based their model on analysing a single flexible tube in what is called a unit cell, that is composed of a wake and channel regions. The model considered only single-degree-of-freedom instability, and streamwise and transverse motions were uncoupled. With some later modifications (Lever and Weaver [1986]), static instability (divergence) and streamwise instability were accounted for in a newly modified version of the equations. However, although the static instability was found to be possible in both directions, only streamwise dynamic instability was predicted by the model. Later, based on the model developed by Leaver and Weaver, Hassan and Weaver [2016] extended the theory with a simplified model to couple the streamwise and transverse motion of the tubes in a flexible bundle. This enhancement, despite its simplicity, allows the theory to predict FEI due to the stiffness mecha-

nism (multi degrees-of-freedom FEI).

Using the same model, Hassan and Weaver [2018] studied the FEI of the rotated square array in streamwise direction. Simulations were carried out to compare a single flexible tube in an otherwise rigid array with experimental results.

In this study, the time averaged quasi-static forces, acting on a bundle of rigid tubes as a function of one tube displacement are measured in a rotated square array of P/D=1.64. The study is performed in both transverse and streamwise directions in water flow, and two phase flow at void fractions in the range 40%-97%. The experiments included the cross coupling fluid force measurements of the surrounding tubes that are instrumented using full bridge strain gauges. The neighbouring instrumented tubes are calibrated using precise weights to get the strain-force relation. This study follows the results presented in a previous study on the same array Darwish et al. [2022]. These results are incorporated in a quasi-steady model and compared with FEI experimental results.

Quasi-static force coefficients are significant in predicting FEI using the quasi-steady model. Roshko [1961] has shown that the drag coefficient decreases at low Reynolds number, Re, and reaches constant value at mid and high Re. Recently, it was shown that quasi-static force coefficients have constant value for a rotated triangular array of P/D=1.5 in single phase Shahriary et al. [2007], and two-phase flow Sawadogo and Mureithi [2013], at high Re. Here, the effect of flow void fraction on quasi-static forces is studied. Also, the variation of force coefficients is investigated in single (water) and two-phase flow.

2. EXPERIMENTAL APPARATUS

A two-phase flow test loop is designed to operate several experiments including the force measurement tests. The loop was insured to be rigid enough with two steel columns to support the loop structure. Air is injected into the test section at high pressure with capability of delivering up to 260 l/s, while a 7.5 HP centrifugal pump is attached to the loop to circulate water flow to deliver up to 25 l/s of volume flow rate. Air and water flow rates are measured using magnetic flowmeters. Flow mixture static pressure is measured at the inlet of the test section using a differential pressure transducer in order to accurately correct the two-phase flow rate due to air flow compressibility. Both air and water flow are mixed upstream the test section entrance through a two stage two-phase flow honeycomb mixer to insure the homogeneity of the flow across the test section.

Figure 1. Experimental setup.

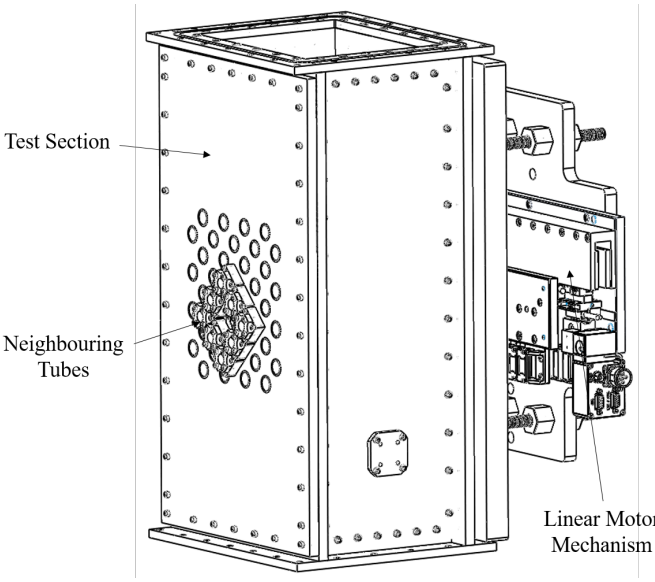

Figure 2. Test section and linear motor mechanism assembled with tube and force transducer.

The test section dimensions perpendicular to the flow is 220x190.5 mm^2. Rigid tubes in the test sections are arranged in 9 rows and 9 columns. Half tubes are mounted on the side walls to reduce wall effect. Central tube, that is mounted on the motor, is located in the fourth row, and surrounded with rigid tubes.

The test apparatus is designed to operate in the transverse and streamwise directions. The central tube is mounted on a linear motor with the ability to deliver up to 3kN peak force and 660 N of continuous force, see figures 1 and 2. Central tube is surrounded with eight Plexiglas tubes. These tube are effectively rigid in order to abandon any fluidelastic motion coupling between the neighbouring tubes and the central tube. The hydrodynamic forces on the neighbouring

tubes are measured using strain gauges that are fixed near tube root. Due to the symmetry in the tube array, force measurements are only preformed for tubes labeled 1-5 shown in figure 3.

The motor is controlled by an Aries smart AR-04CE servo-drive. The advantage in using this motor is that it generates a direct linear motion. The motion is enhanced by using a linear magnetic encoder with $\pm 30\ \mu$m accuracy.

The quasi-static force measurement is performed by displacing the tube with finite static displacements that are previously defined. In case of displacing the tube in the transverse direction, this reveals the variation of tubes lift and drag coefficients with the central transverse motion (y). The same applies to the streamwise direction by getting the force coefficients variation with central tube streamwise displacement. This is performed for single phase flow (water flow, 0%), and two-phase flow for void fractions from 40%-97%. For each void fraction, the central tube is displaced in 0.25 mm (0.013D), and enough time is allowed to attain a steady state condition of the fluid forces.

The homogeneous air-water flow void fraction, β, is calculated as a ratio between air flow rate to flow mixture total flow rate

$$\beta = \frac{Q_a}{Q_a + Q_w} \tag{1}$$

where, Q_a and Q_w is the volumetric flow rate of air and water, respectively. The homogeneous density, ρ, is defined using the homogeneous void fraction as:

$$\rho = \beta\rho_a + \beta(1-\rho_w) \tag{2}$$

In this test setup, only the central tube is displaced. The surrounding tubes force derivatives can be deduced, considering the neighbouring tube relative location to the central tube according to the following relations:

$$\begin{aligned} \frac{\partial C_{Li}}{\partial Y_i} &= \frac{\partial C_{Lc}}{\partial Y_c} & \frac{\partial C_{L8}}{\partial Y_c} &= -\frac{\partial C_{L2}}{\partial Y_c} \\ \frac{\partial C_{L7}}{\partial Y_c} &= -\frac{\partial C_{L3}}{\partial Y_c} & \frac{\partial C_{L6}}{\partial Y_c} &= -\frac{\partial C_{L4}}{\partial Y_c} \end{aligned} \tag{3}$$

$$\begin{aligned} \frac{\partial C_{Di}}{\partial X_i} &= \frac{\partial C_{Dc}}{\partial X_c} & \frac{\partial C_{D8}}{\partial X_c} &= -\frac{\partial C_{D2}}{\partial X_c} \\ \frac{\partial C_{D7}}{\partial X_c} &= \frac{\partial C_{D3}}{\partial X_c} & \frac{\partial C_{D6}}{\partial X_c} &= -\frac{\partial C_{D4}}{\partial X_c} \end{aligned} \tag{4}$$

Also, due to the symmetry, the lift coefficient at zero displacement is zero. In the drag direction, the derivative of the lift coefficient is zero. The same applies for the drag coefficient derivative in the lift direction.

$$C_{Li0} = C_{Lc0} = 0 \tag{5}$$

$$\frac{\partial C_{Di}}{\partial Y_i} = \frac{\partial C_{Dc}}{\partial Y_c} = 0 \tag{6}$$

$$\frac{\partial C_{Li}}{\partial X_i} = \frac{\partial C_{Lc}}{\partial X_c} = 0 \tag{7}$$

where, $i = 1:8$.

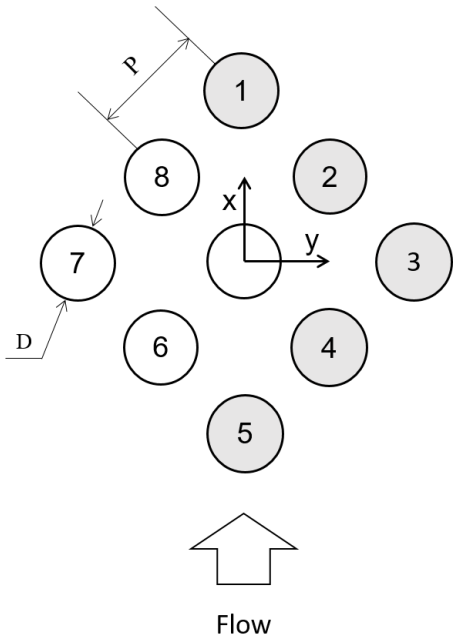

Figure 3. Schematic of the array layout and neighbouring tubes numbers.

3. RESULTS

3.1. Transverse direction fluid force coefficients

The variation of the lift coefficient with the transverse displacement is presented in figure 4 for water flow and all void fractions in the two-phase flow. The lift force derivative is deduced from these data, which is a significant factor in predicting the fluidelastic instability using the quasi-steady model. It can be clearly seen that the derivative is positive in water flow, and decreases in two-phase flow to significantly lower values. The trend of the lift derivative is shown in figure 5. The lift and drag coefficients in figure 5 and figure 10 are determined using flow upstream velocity for comparison with data in the literature.

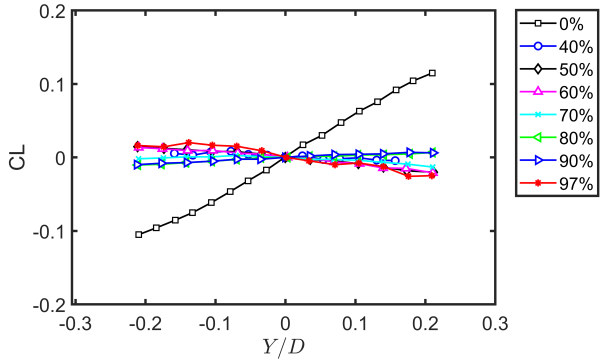

Figure 4. Variation of the lift coefficient of the central tube for different void fractions.

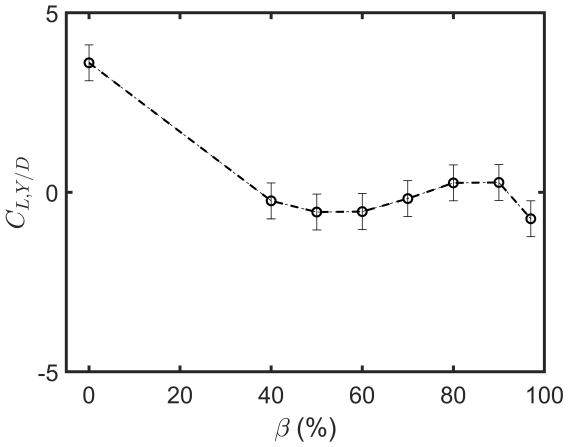

Figure 5. Variation of the central tube lift coefficient derivative for different void fractions.

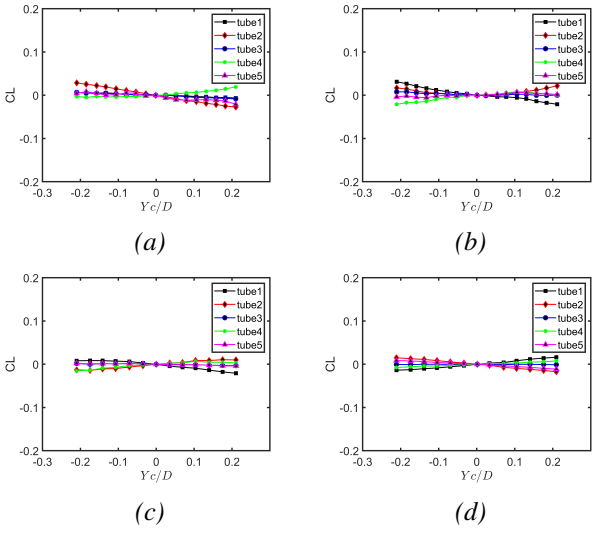

Figure 6. Measured lift coefficient of the neighbouring tubes in: (a) 0%, (b) 40%, (c) 70%, (d) 97% void fraction

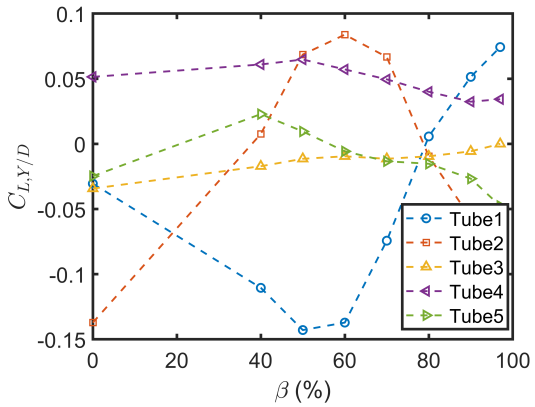

Figure 7. Variation of the lift coefficient derivative of the neighbouring tubes for different void fractions.

It is noted that the The derivative of the lift coefficient is constant over a wide range of tube displacement (±20%D) in water flow. This is different from what was observed in the rotated triangle array of P/D=1.5 in Sawadogo and Mureithi [2014] and Shahriary et al. [2007], where the derivative was found to be positive at low tube displacement and zero at larger displacements.

Cross-coupling lift force derivatives of the neighbouring tubes are shown in figure 6. According to the quasi-steady model, the data in figure 4 suggests that a single flexible tube in this array is most likely to be stable. Due to the small values of the lift force coefficient derivative, the fluid negative damping can not overcome the structural damping. The variation of the lift force derivative of the neighbouring tubes due to tube's static deflection is shown in figure 7. It is clearly seen that tubes 1 and 2 are significantly affected by the central tube position compared to tubes 3-5.

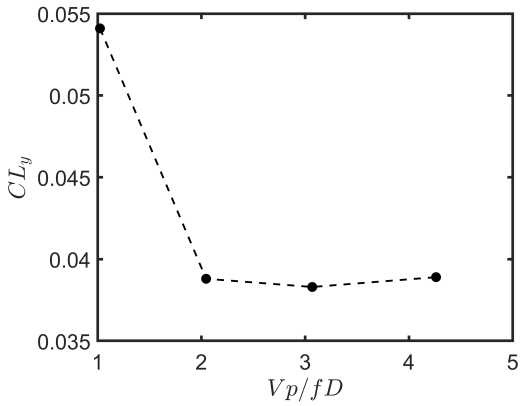

Figure 8. Variation of the lift coefficient derivative with flow velocity.

The effect of variation of flow velocity on the

change of the derivative of lift force coefficient is shown in figure 8. The derivative decreased at high flow velocities and became constant.

3.2. Streamwise direction fluid force coefficients

The effect of streamwise displacement of the central tube on its own drag coefficient for all void fractions is shown in figure 9. The drag coefficient increases when the tube is displaced downstream. This is the case for all void fractions except that the derivative is higher in water than in two-phase flow. The trend of the drag coefficient derivative variation with void fraction is shown in figure 10. Figure 11 shows the neighbouring tubes cross-coupling forces due to central tube displacement. Tube 4 is more coupled with the central tube streamwise displacement. This could be due to the blockage created by the displacement of the tube downstream away from tube 4. The related drag coefficient derivatives are presented in figure 12.

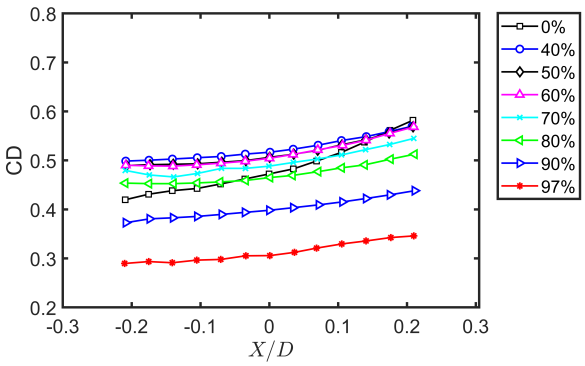

Figure 9. Variation of the drag coefficient of the central tube for different void fractions.

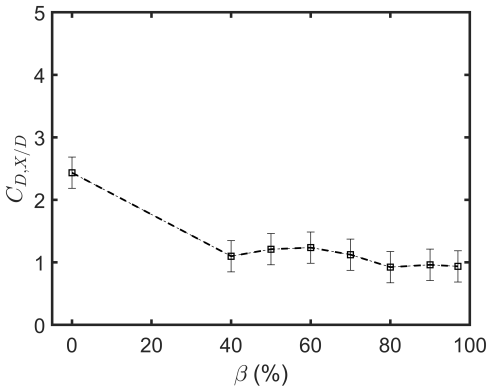

Figure 10. Variation of the central tube drag coefficient derivative for different void fractions.

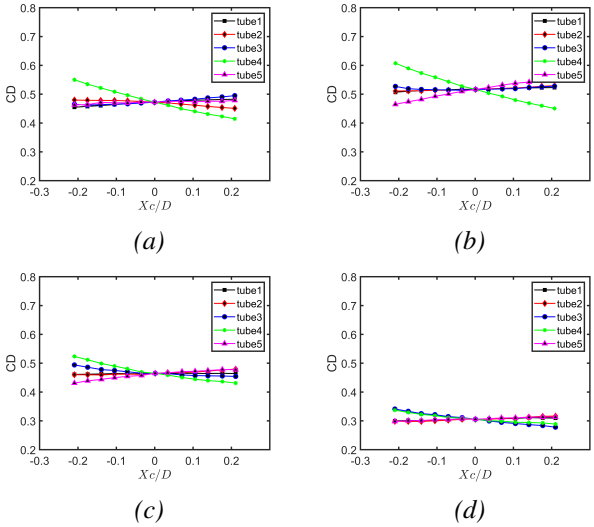

Figure 11. Measured drag coefficient of the neighbouring tubes in: (a) 0%, (b) 40%, (c) 80%, (d) 97% void fraction

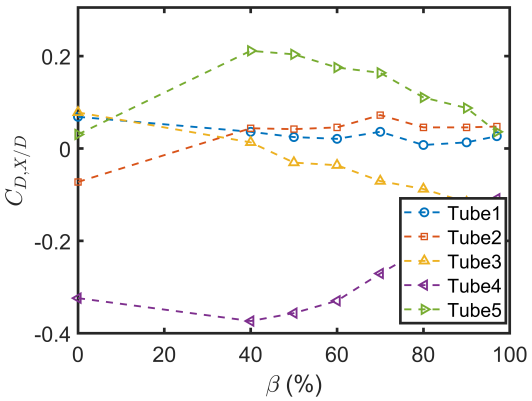

Figure 12. Variation of the drag coefficient derivative of the neighbouring tubes for different void fractions.

4. DISCUSSION

Using the fluid force coefficients presented above, the quasi-steady model developed by Price and Paidoussis [1984] will be applied to predict the fluidelastic behaviour of this array. The equation of motion of a flexible tube subjected to fluid force in the streamwise or transverse directions may be written in the form

$$M\ddot{x} + C\dot{x} + Kx = F_x \tag{8}$$

$$M\ddot{y} + C\dot{y} + Ky = F_y \tag{9}$$

where, M is the tube total mass per unit length, C is the tube damping, and K is tube stiffness. The

streamwise and transverse fluidelastic forces may be expressed as (Price and Paidoussis [1986])

$$F_x = \frac{1}{2}\rho V_p^2 S\left[C_{D0} + \frac{\partial C_D}{\partial x}x - \frac{2}{V_p}C_{D0}\dot{x}\right] \tag{10}$$

or

$$F_y = \frac{1}{2}\rho V_p^2 S\left[\frac{\partial C_L}{\partial y}y - \frac{C_{D0}}{V_p}\dot{y}\right] \tag{11}$$

where, F_x and F_y are the fluid forces per tube unit length in the lift and drag directions, respectively, ρ is flow homogeneous density, V_p is flow pitch velocity, C_{D0} is the tube drag coefficient at the equilibrium position, and S is the tube projection area. It is known that there is a time lag due to the flow retardation. This is approximated to be in the form $\tau = \mu D/V$. Here, the time delay parameter, μ, is assumed to be equal to 1. Taking into account the time delay, and substituting equations 10 and 11 into equations 8 and 9, we obtain

$$\ddot{x} + \left[\frac{\delta}{\pi}\omega_n + \frac{\rho V D}{m}C_{D0}\right]\dot{x} + \left[\omega_n^2 - \frac{1}{2}\frac{\rho V^2}{m}\frac{\partial C_D}{\partial x}e^{-i\omega\tau}\right]x = 0 \tag{12}$$

$$\ddot{y} + \left[\frac{\delta}{\pi}\omega_n + \frac{1}{2}\frac{\rho V D}{m}C_{D0}\right]\dot{y} + \left[\omega_n^2 - \frac{1}{2}\frac{\rho V^2}{m}\frac{\partial C_L}{\partial y}e^{-i\omega\tau}\right]y = 0 \tag{13}$$

where, δ is the tube logarithmic decrement of damping and ω_n is tube natural frequency. For a single flexible tube, the instability is always damping-controlled, which requires the total damping to be equal to zero. For harmonic motions, and a sufficiently high reduced velocity ($V/\omega D$), one may deduce

$$\frac{V_{pc}}{f_n D} = \left[\frac{4}{-C_{D0} - \mu D(\partial C_L/\partial y)}\right]\frac{m\delta}{\rho D^2} \tag{14}$$

$$\frac{V_{pc}}{f_n D} = \left[\frac{4}{-2C_{D0} - \mu D(\partial C_D/\partial x)}\right]\frac{m\delta}{\rho D^2} \tag{15}$$

Hence, for fluidelastic instability to occur, it is required that $-C_{Do} - D(\partial CL/\partial y) > 0$ in the transverse direction and $-2C_{Do} - D(\partial CD/\partial x) > 0$ in the streamwise direction, for μ=1.

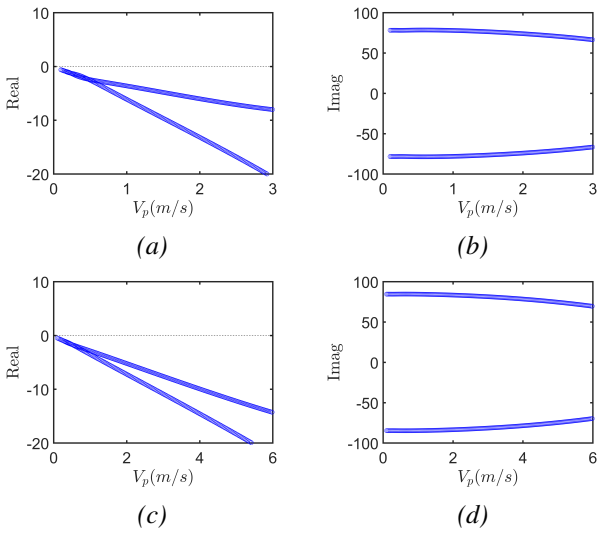

Figure 13. Real and imaginary parts of the eigenvalues in : (a) and (b) 0%, (c) and (d) 50% void fraction

4.1. Streamwise stability analysis

The results of the quasi-steady model in the streamwise direction are computed based on the experimentally measured forces shown above. Test results does not satisfy the FEI condition for a single flexible tube. Also, the eigenvalue problem associated with the equation of motion is solved for each void fraction. The flexible tube in the array becomes dynamically unstable when the total damping is zero, at flow velocity that corresponds to zero or positive real part of the eigenvalues. The results show no FEI instability in the streamwise direction for the single flexible tube in water and two-phase flow having 40%-97% void fraction. Figure 13 shows an example of the eigenvalue problem solution for water flow and 50% void fraction. This was also confirmed as the experimental study of this array showed a stable behaviour in the streamwise direction for a single flexible tube [Darwish et al., 2022].

4.2. Transverse stability analysis

From the experimental results, a single flexible tube in this rotated square array cannot become fluidelastically unstable in the transverse direction based on the classical quasi-steady model. This is due to the significantly small lift force derivatives that do not satisfy the instability condition. This was confirmed by Price and Paidoussis [1986], and experimentally in a previous FEI study on this array [Darwish et al., 2022].

4.3. Static instability

Static instability occurs when total stiffness vanishes (Paidoussis and Price [1989]). From equations 12 and 13, divergence flow critical velocity is given by

$$\frac{V_{cd}}{f_n D} = \left[\frac{8\pi^2}{D\partial C_L/\partial y} \frac{m}{\rho D^2} \right]^{1/2} \quad (16)$$

where, V_{cd} is the divergence critical velocity, f_n is tube natural frequency, D is the tube outer diameter. Note that this equation is valid when $\mu\omega D/V << 1$. This implies that $\partial C_L/\partial y > 0$ is a necessary condition for divergence to occur in the transverse direction (the same applies to the streamwise direction when $\partial C_D/\partial x > 0$). Clearly, this is the contradictory requirement for dynamic instability which requires these values to be negative. For this array, in water flow $\partial C_L/\partial y$ = 0.029, as shown in figure 4. This gives a static instability at a very high flow velocity V_p=4.6 m/s.

5. CONCLUSION

A fundamental experimental program was carried out to measure the quasi-static fluid forces of a rotated square array of 1.64 P/D ratio in water and air-water two-phase flow. Based on the presented results in this paper, a number of significant conclusions are addressed. The derivative of the lift force in this array is not large enough to have a negative damping instability mechanism. This shows the importance of the fluidelastic-stiffness coupling effects in this array. Hence, a single flexible tube in this array will not undergo dynamic fluidelastic instability in water and in low or high void fractions in the transverse direction. In addition, a simple quasi-steady model shows that no fluidelastic instability occurs in the streamwise direction.

6. ACKNOWLEDGEMENT

This work is funded by Doosan Heavy Industries & Construction. The authors also acknowledge the technical support of Nour Aimène at Polytechnique Montreal, and wish to thank A. Hadji and H.P. Pham for their work in developing the experimental setup.

7. REFERENCES

BW Roberts. *Low frequency, self-excited vibration in a row of circular cylinders mounted in an airstream*. PhD thesis, University of Cambridge, Eng., 1962.

HJ Connors Jr. Fluid elastic vibration of tube arrays excited by cross flow. In *ASME Symposium on Flow-Induced Vibration in Heat Exchanger, Winter Annual Meeting*, pages 42–47, 1970.

RD Blevins. Fluid elastic whirling of a tube row. 1974.

SJ Price and MP Paidoussis. A theoretical investigation of the parameters affecting the fluidelastic instability of a double row of cylinders subject to a cross-flow. In *Vibration in nuclear plant. Vol. 1. Proceedings of the 3rd international conference on'vibration in nuclear plant'held on 11-14 May 1982, Keswick (GB)*, 1983a.

SJ Price and MP Paidoussis. Fluidelastic instability of an infinite double row of circular cylinders subject to a uniform cross-flow. 1983b.

HP Ruscheweyh. Aeroelastic interference effects between slender structures. *Journal of Wind Engineering and Industrial Aerodynamics*, 14(1-3):129–140, 1983.

SJ Price and MP Paidoussis. An improved mathematical model for the stability of cylinder rows subject to cross-flow. *Journal of Sound and Vibration*, 97(4): 615–640, 1984.

M Hassan and DS Weaver. A theoretical model for fluid-elastic instability in heat exchanger tube bundles. 1982.

JH Lever and DS Weaver. On the stability of heat exchanger tube bundles, part i: Modified theoretical model. *Journal of Sound and vibration*, 107(3):375–392, 1986.

M Hassan and DS Weaver. Modeling of streamwise and transverse fluidelastic instability in tube arrays. *Journal of Pressure Vessel Technology*, 138(5), 2016.

M Hassan and DS Weaver. Transverse and streamwise fluidelastic instability in rotated square tube arrays. In *FIV2018 Conference*, 2018.

S Darwish, N Mureithi, A Hadji, and M Cho. Experimental investigation of fluidelastic instability of a rotated square array subjected to two-phase and air cross-flow. *Nuclear Engineering and Design*, submitted, 2022.

A Roshko. Experiments on the flow past a circular cylinder at very high reynolds number. *Journal of fluid mechanics*, 10(3):345–356, 1961.

S Shahriary, N Mureithi, and MJ Pettigrew. Quasi-static forces and stability analysis in a triangular tube bundle subjected to two-phase cross-flow. In *ASME Pressure Vessels and Piping Conference*, volume 42827, pages 245–252, 2007.

T Sawadogo and N Mureithi. Time domain simulation of the vibration of a steam generator tube subjected to fluidelastic forces induced by two-phase cross-flow. *Journal of Pressure Vessel Technology*, 135(3), 2013.

T Sawadogo and N Mureithi. Fluidelastic instability study in a rotated triangular tube array subject to two-phase cross-flow. part i: Fluid force measurements and time delay extraction. *Journal of Fluids and Structures*, 49:1–15, 2014.

SJ Price and MP Paidoussis. A single-flexible-cylinder analysis for the fluidelastic instability of an array of flexible cylinders in cross-flow. 1986.

MP Paidoussis and SJ Price. The mechanisms underlying flow-induced instabilities of cylinder arrays in cross-flow. In *Design & Analysis*, pages 147–163. Elsevier, 1989.

THEORETICAL AND EXPERIMENTAL STUDY ON THE FLUIDELASTIC INSTABILITY OF ROD BUNDLE SUBJECTED TO JET CROSS-FLOW

Ibrahim Gad-el-Hak, Njuki Mureithi
Department of Mechanical Engineering, Polytechnique Montréal, Montreal, QC H3C 3A7, Canada
Kostas Karazis
Framatome Inc., 3315 Old Forest Road, Lynchburg, VA 24506, U.S.A

ABSTRACT

Jet cross-flow induced vibration has been recently found in some designs of PWRs that have fail-safe features in the event of a loss of coolant accident (LOCA). In these reactors, LOCA holes and slots are machined in the baffle plates to release the pressure build up during a LOCA event. During normal operation, however, the transverse flow from these holes and slots entering the peripheral fuel assembly can reach the fuel rods before being mixed with the axial flow. The localized jet cross-flow can cause fuel rod vibrations, which can contribute to grid-to-rod-fretting (GTRF) and cladding wear.

This paper presents an experimental and theoretical framework to model the instability of a flexible rod bundle subjected to jet cross-flow. The work reported here is part of a test plan set up by Framatome and Polytechnique Montreal. A few basic models based on the Connors equation were developed in the literature for baffle jetting (i.e. 2D jet) problem in PWRs. A fluidelastic instability model is developed here based on quasi-steady approach developed by Price and Paidoussis in the early eighties. In their work, the authors introduced a time delay parameter to account for the phase lag between tube motion and flow-induced (fluidelastic) forces. Unlike the uniform flow case, a new formulation of fluidelastic forces as a function of the flow area derivative is proposed to account variation of the projected area through LOCA holes. Model results are compared and validated against the experimental results.

1. INTRODUCTION

Flow-induced vibration (FIV) in nuclear power plants is a constant concern as the demand for better thermal performance and efficiencies challenges the mechanical, flow and irradiation exposure characteristics of fuel designs. By design, certain PWRs incorporate safety features such as Loss-of-Coolant-Accident (LOCA) holes and slots in the core periphery baffles surrounding the fuel assemblies, providing relief from pressure build up in the event of a LOCA. As a result, at certain axial locations for this plant design, fuel rods are subjected not only to axial flow but also to transverse flow conditions due to their proximity to the LOCA holes and baffle slots.

Uniform cross-flow induced vibrations in tube bundles have been extensively investigated in the literature. Throughout these studies, the fundamental mechanisms underlying a tube bundle excitation are well understood, especially, fluidelastic instability phenomena (Chen , 1984; Paidoussis et al. , 2010). However, for the case of circular jet (i.e. 3D jet) cross-flow induced vibrations are the problem of flow induced vibrations due to the non-uniformity of jet flow through an array presents considerable challenges. The jet velocity that impinges the rods is related to jet parameters, including the gap between the nozzle and rod bundle, and the eccentricity between the jet center and array as shown by Gad-el-Hak et al. (2021).

In comparison with the research conducted on fluidelastic instability of tube arrays subjected to uniform transverse flow, only a few researchers (Seki et al. , 1986; Fujita et al. , 1990; Lee and Chang , 1990) have discussed the excitation mechanisms of baffle jet (2D) flow induced vibrations. However, in the studies, basic models based on Connors equation were presented by fitting the experimental results with their models to calculate the stability constant. There is, however, lack of theoretical models for circular jet cross-flow induced vibration.

In this paper, a theoretical model based on quasi-steady approach is developed to model the stability of circular jet induced fluidelastic instability (FEI). The aim of this study is to formulate a theoretical model for jet flow that can predict the critical instability velocity. Jet fluid forces are measured on rods to be used in the model. Moreover, the developed model is validated with FEI experimental test results.

2. FEI MODEL DEVELOPMENT

A theoretical model is developed to predict the occurrence of the instability for the transverse vibration, which is mainly caused by jet cross-flow. In experimental tests, the jet eccentricity (ξ) case of 25% of pitch was found to be more unstable (Gad-el-Hak et al. , 2021). Figure 1a shows graphically the jet-rod array configuration. The jet flow is in row 1, seen to interact with the three rods, 3, 4, 5 as shown in the figure.

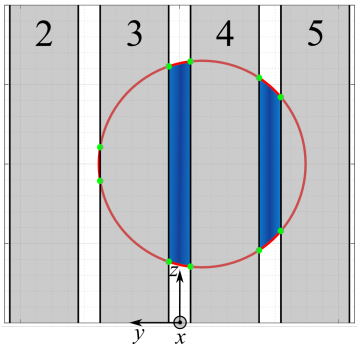

(a)

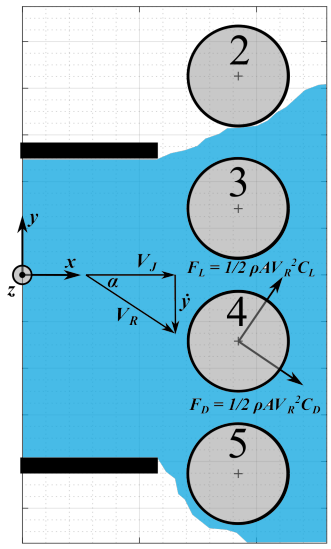

(b)

Figure 1. (a) projected view form the nozzle, and (b) top view of nozzle with rods in the array.

The equation of (transverse direction) motion for the three flexible rods in jet cross-flow can be written as:

$$[M_s]\ddot{\vec{y}}(t)+[C_s]\dot{\vec{y}}(t)+[K_s]\vec{y}(t)=\vec{F}_y; \quad \vec{y}=[y_3,y_4,y_5]^T \tag{1}$$

where $[M_S]$, $[C_S]$, $[K_S]$ are the mass, damping and stiffness matrices of the structure, respectively. F_y is the jet fluid dynamic force vector in the transverse direction. Figure 1b shows the force components acting on rod 4. For small rod vibration the total force can be written as follows:

$$F_{y4}=1/2\rho {U_J}^2 A[C_L - C_D \dot{y}_4/U_J] \tag{2}$$

Unlike uniform flow case, the flow exposed area (A) of the oscillating rod subjected a circular jet flow changes due to the geometrical matching between the nozzle and the rods. The linearized forms of C_L, C_D, and A for rod 4 are expressed as:

$$\begin{aligned} C_{L4} &= C_{L0}+\frac{\partial C_{L4}}{\partial y_4}y_4+\frac{\partial C_{L4}}{\partial y_3}y_3+\frac{\partial C_{L4}}{\partial y_5}y_5 \\ C_{D4} &= C_{D0}+\frac{\partial C_{D4}}{\partial y_4}y_4+\frac{\partial C_{D4}}{\partial y_3}y_3+\frac{\partial C_{D4}}{\partial y_5}y_5 \\ A_4 &= A_0+\frac{\partial A_4}{\partial y_4}y_4 \end{aligned} \tag{3}$$

Price and Paidoussis (1986) introduced a constant time delay as follows:

$$\tau=\frac{\mu D}{U};\ \ \mu\sim O(1) \tag{4}$$

where D the tube diameter, μ is the flow retardation parameter taken to be of order 1, and U is the jet flow velocity in this paper because the three rods are located in the first row. The linearized form of Equation (2) is:

$$\begin{aligned} F_{y4} = 1/2\rho {U_J}^2 [A_0 (C_{L0} &+ e^{-i\omega\tau}\frac{\partial C_{L4}}{\partial y_4}y_4 \\ &+ e^{-i\omega\tau}\frac{\partial C_{L4}}{\partial y_3}y_3 + e^{-i\omega\tau}\frac{\partial C_{L4}}{\partial y_5}y_5) \\ &+ (C_{L0}\frac{\partial A_4}{\partial y_4}y_4) - (A_0 C_{D0}\frac{\dot{y}_4}{U_J})] \end{aligned} \tag{5}$$

The second term ($C_{L0}\frac{\partial A_4}{\partial y_4}y_4$) is a new term introduced in the model to take into account the change in area with tube displacement. The coupled system equation modelling jet-induced FEI is written as:

$$\begin{aligned} [M_s+M_f]\ddot{\vec{y}}(t)+[C_s+C_f]\dot{\vec{y}}(t)+[K_s+K_f]\vec{y}(t) \\ = \vec{F}_{y_0};\ \ \vec{y}=[y_3,y_4,y_5]^T \end{aligned} \tag{6}$$

The fluid added mass, damping, stiffness coefficients are needed to be measured to perform the stability analysis. An experimental setup is described in the following section.

3. EXPERIMENTAL SETUP

3.1. Linear motor system

The theoretical model is developed using a quasi steady approach, in which the instantaneous force

on the oscillating rod is estimated as an equivalent time delayed force on the rod when it is statically displaced. The static force is measured experimentally. A linear motor system is designed to displace precisely the rod in jet flow. Figure 2 shows the designed linear motor system. It consists of a positioning slide driven by a stepper motor. The lead screw moves the rod with a high accuracy of 0.015 mm per 25.4 mm. To measure the drag and lift forces from jet flow, a stiff rod is attached on a six-axis ATI Nano 17 force/torque sensor. The measured torques (Tx & Ty) are also used to define the location of applied force from the jet flow. Rotating the shaft clockwise and then anti-clockwise produce sinusoidal rod oscillations as shown in Figure 3.

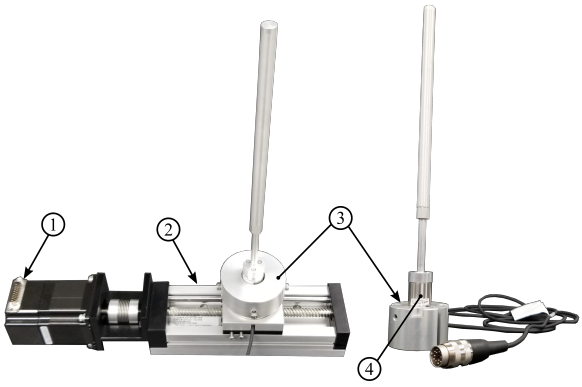

Figure 2. Liner motor system components: (1) stepper motor, (2) positioning slide, (3) instrumented rod, and (4) Nano17 force transducer.

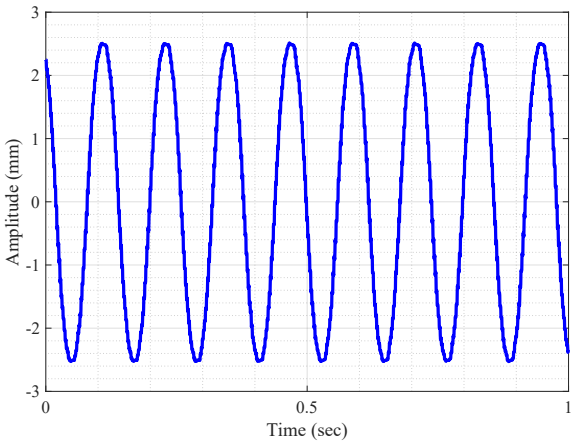

Figure 3. Measured response from linear motor system giving 8 Hz rod motion.

3.2. Test section setup

The force derivatives with respect to the central rod motion are captured by instrumenting the neighbouring rods with strain gauges. The linear motor system and the instrumented neighbouring rods are integrated in the test section to complete the array configuration as shown in Figure 4. The central instrumented rod is inserted from the top panel while the instrumented neighbouring rods are fixed on the bottom panel with rigid rods to complete 6x6 array. The water jet flow enters the test section driven by a 2 horsepower centrifugal pump.

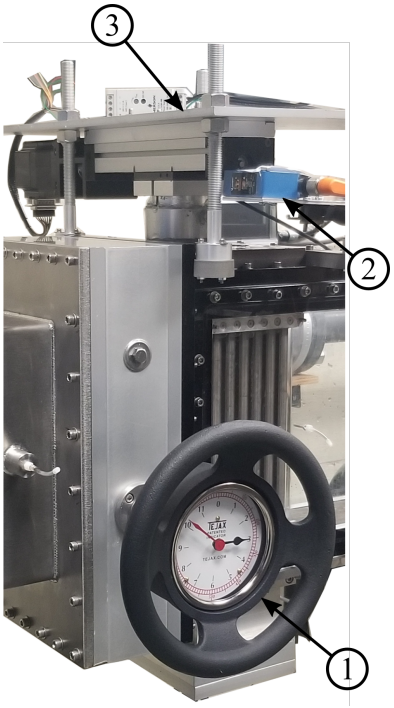

Figure 4. Test section components: (1) instrumented neighbouring rods in rigid bundle, (2) laser sensor, and (3) linear motor system.

4. TEST RESULTS

4.1. FEI tests

FEI tests are carried out on a unidirectionally flexible rods which are arranged in 6x6 normal square array with a pitch-to-diameter ratio of 1.32 as shown in Figure 5. The objective of the tests is to determine the critical velocity of array. This value is used to validate the model. The rods have a natural frequency of 15 Hz in air. Three different configurations of rod array are tested to show the effect of number of flexible rods on stability threshold, starting from a single flexible rod to 3x1 single flexible row in the 6x6 rigid array. Figure 6 shows the dynamical behavior of the three tested arrays. A single flexible rod and 2x1 single row were found to be stable in the tested range of reduced jet velocity ($1.75 < V_{Jet}/f_w\, D < 10.5$). However, adding one flexible rod to the latter case makes

the 3x1 row fluidelastically unstable; above $V_{Jet}/f_w D = 5$, large amplitude vibrations are observed in the latter case. The response of the central rod 4 increases from 4%g to 50%g (where g is the tube-tube gap) with an increment of reduced jet velocity of 0.3. This confirms our hypothesis about the developed model based on three flexible rods.

Figure 5. Flexible rod bundle.

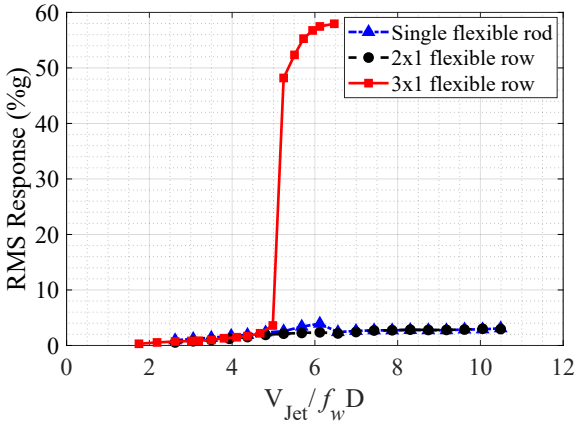

Figure 6. Response of different rod array configuration, single rod, 2x1 row, 3x1 row in jet cross flow.

4.2. Jet fluid force measurements

The quasi-static force derivatives for the three rods, 3, 4, and 5, in the jet flow due to the motion of each rod independently are the key input parameters for the FEI model. Contrary to the uniform flow case, the rod area is not symmetrical relative to the jet flow. As a result, each rod is transversely moved and its effect on the surrounding rods is measured in terms of change in lift force. The first test is performed for the central rod 4. The rod is displaced ± 10%D in steps of 2%D; which corresponds to 30% of the inter-rod gap. Figure 7 shows the measured lift force coefficient variation at $Re_{Jet} = 4x10^4$.

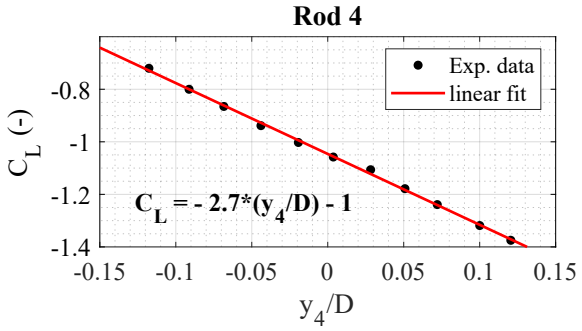

Figure 7. Lift force coefficient variation for rod 4 at $Re_{Jet} = 4x10^4$.

Figure 8 shows the calculated area derivative for the three rods under jet flow. Two rods 3 and 5 that are located at the nozzle boundary have a relatively large derivative. These area derivatives are used in the stability analysis. The lift coefficient is normalized based on the projected area that corresponding to the rod position relative to the jet flow. As shown in Figure 7, the lift coefficient has a negative derivative of 2.7 with rod displacement.

The measured force and torque are used to understand the jet flow path through the array. Figure 9 shows the location of applied jet force on the central rod in the drag direction (x). As shown in the figure, there is a slight offset from the mid-point of the rod.

The lift coefficient variation for rods 3 and 5 with their own displacements are shown in Figures 10 and 11, respectively. Lift coefficient for rod 3 does not vary linearly when the rod is displaced beyond 2%D in the negative direction. The flow gap around the rod increases from one to two gaps with (-y) direction as shown in Figure 1. However, an approximate linear variation around the rod equilibrium point still exists; this variation is captured by extracting a first order term from a linear fit as shown in Figure 10. Rod 5 has the highest negative derivative (-8.3) among all the rods. This could be because only one side of the rod is exposed to the jet flow (see Fig-

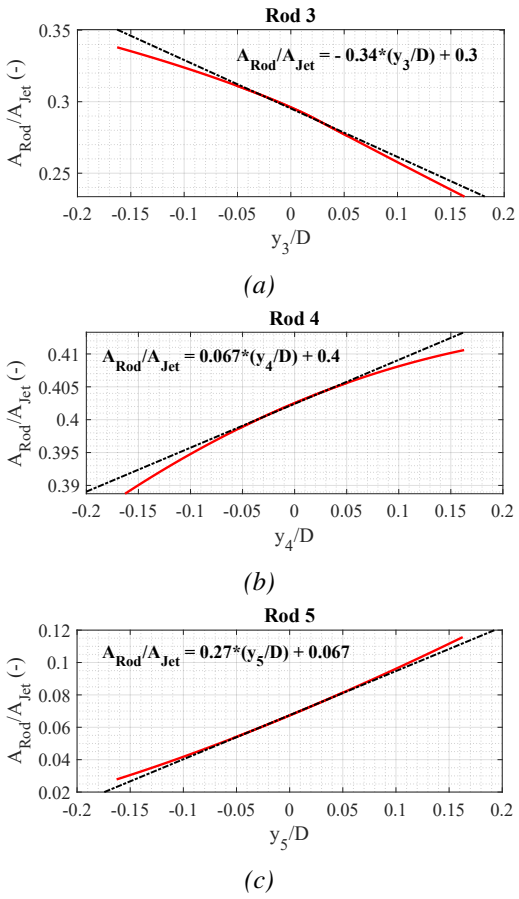

Figure 8. Calculated area and area derivative for the three rods: (a) 3, (b) 4, and (c) 5.

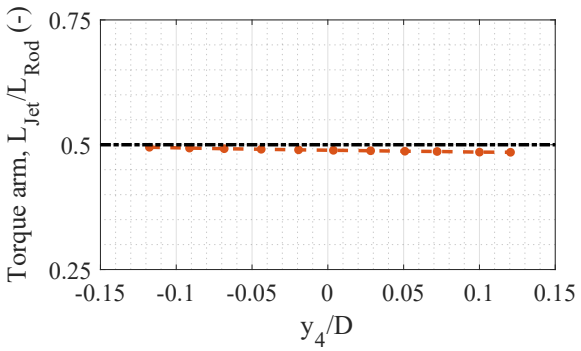

Figure 9. Torque arm (L_{Jet}/L_{Rod}) for Rod 4 at Re_{Jet} = $4x10^4$.

ure 1), causing the pushing force on that side to be unbalanced by the generated force on the other side. Table 1 summarizes all other required input parameter for the model.

5. STABILITY ANALYSIS

A stability analysis is performed by solving the 3 degrees-of-freedom coupled equation system (Equation 8) to obtain the eigenvalues with the jet velocity. The lowest velocity at which the real part of any eigenvalue becomes zero and its tendency to be positive defines the critical velocity for fluidelastic instability. The eigenvalues (λ) corresponding to fluidelastic instability of the 3x1 single flexible row in the bundle are calculated and plotted versus jet velocity in Figure 12. The results of eigenvalues show that fluidelastic instability occurs at $V_{Jet}/f_w\,D$ = 5.69. Comparing to the critical velocity obtained in the FEI tests (see Figure 6), the developed model results overestimate the critical velocity with an error of 15%.

Direct time domain simulations are also conducted to demonstrate the instability and its growth rate. The rod 4 response is calculated at two reduced velocities: (i) $V_{Jet}/f_w\,D$ = 5.61, and (ii) $V_{Jet}/f_w\,D$ = 5.76. These two reduced jet velocities are near the stability boundary ($V_{Jet}/f_w\,D$ = 5.69). Figures 13 and 14 show the central rod 4 response with $V_{Jet}/f_w\,D$ = 5.61 and $V_{Jet}/f_w\,D$ = 5.76, respectively.

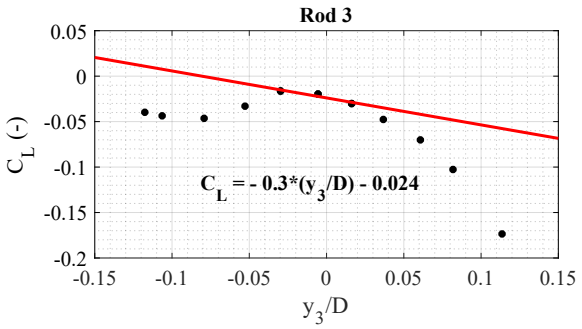

Figure 10. Lift coefficient variation for rod 3 at Re_{Jet} = $4x10^4$.

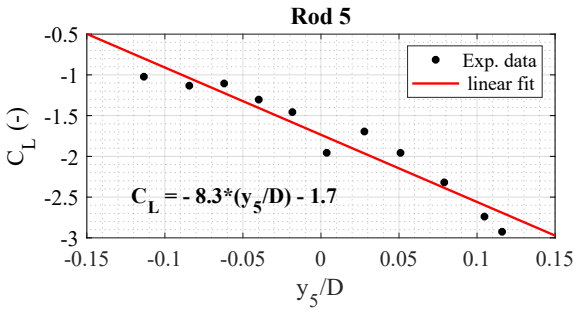

Figure 11. Lift coefficient variation for rod 5 at Re_{Jet} = $4x10^4$.

6. CONCLUSION

In this study, jet cross-flow induced vibration has been investigated experimentally and theoretically to understand the fundamental mechanisms underlying fuel rod instability in jet cross-flow. Fluidelastic instability test were carried out with three different ar-

Parameter	Rod 3	Rod 4	Rod 5
C_{L_0}	-0.024	-1.1	-1.7
C_{D_0}	1.9	2.95	2.26
$C_L, y_3/D$	-0.3	-0.16	-
$C_L, y_4/D$	-0.29	-2.7	2.2
$C_L, y_5/D$	-	4.6	-8.3

Table 1. Steady drag and lift force coefficients (C_{D_0} & C_{L_0}) and derivatives of the lift coefficient ($C_L, y_k/D$) measured at Re_{Jet} = 4x10^4.

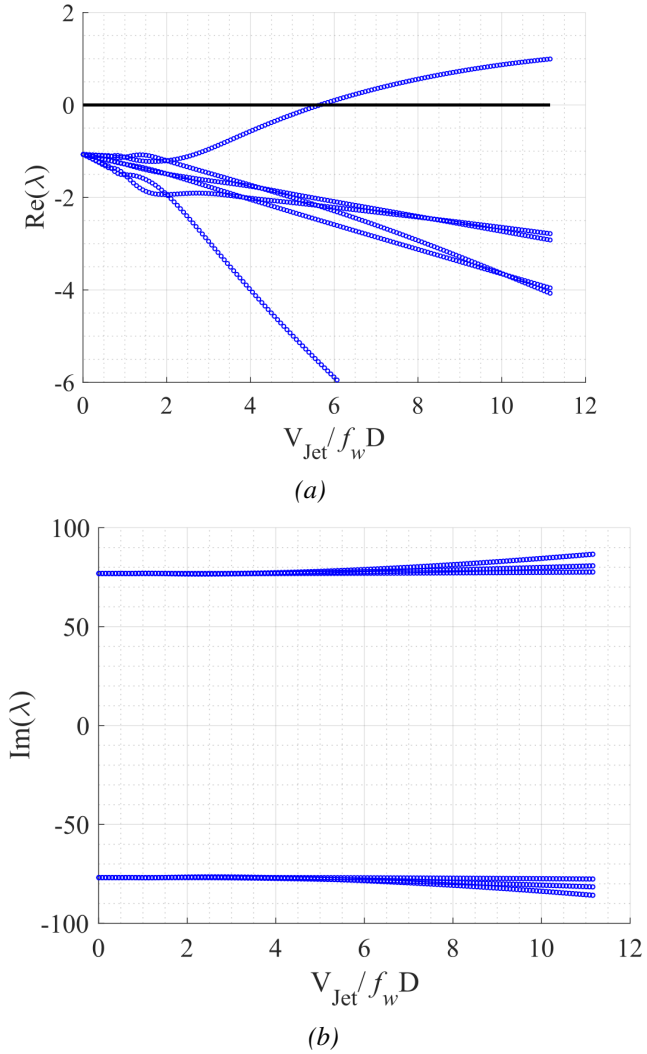

Figure 12. (a) The real part of the eigenvalues of the three flexible rods in jet cross flow with increasing reduced jet velocity, and (b) their corresponding imaginary parts.

rays, single flexible rod, 2x1 flexible row, and 3x1 flexible row. The experiments show that the 3x1 flexible row was fluidelastically unstable at the reduced jet velocity of 5.

The development of a dynamic model to predict the critical velocity for the arrays in jet cross-flow

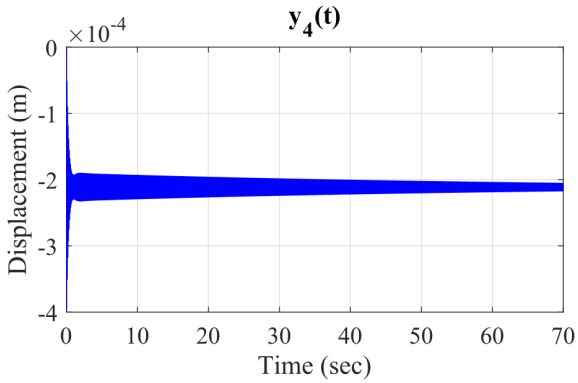

Figure 13. Rod 4 response at V_{Jet}/f_w D = 5.61.

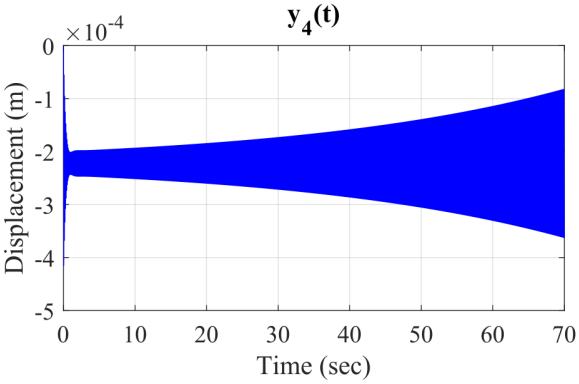

Figure 14. Rod 4 response at V_{Jet}/f_w D = 5.76.

case was the main objective of this work. The developed model is based on the quasi-steady approach. However, a new parameter, the rod area derivative, is implemented in the model to capture the dynamic feature of the vibrating rod in jet flow. A stability analysis shows agreement between the predicted critical velocity with that obtained experimentally is within an error of 15%.

7. REFERENCES

Chen, S. S., 1984 Guidelines for the instability flow velocity of tube arrays in crossflow, *Journal of Sound and Vibration*.

Fujita, K., Ito, T., and Kohno, N., 1990, Experimental study on the vibration of circular cylinders subjected to cross-flow jetted from a narrow gap. *Journal of Fluids and Structures*, **4(1)**: 99-124.

Gad-el-Hak, I., Mureithi, N., Karazis, K., and Williams, G., 2021, *Experimental Investigation of Jet Cross-Flow Induced Vibration of a Rod Bundle*, In Pressure Vessels and Piping Conference (Vol. 85338, p. V003T04A014). American Society of Mechanical Engineers.

Lee, H., and Chang, Y. B., 1990, Flow-induced vibration of rod arrays in a jet flow. *Journal of Pressure Vessel Technology*, **112**: 46-49.

Paidoussis, M. P., Price, S. J., De Langre, E., 2010 Fluid-structure interactions: cross-flow-induced instabilities, *Cambridge University Press*.

Price, S.J. and Paidoussis, M.P., 1986 A single-flexible-cylinder analysis for the fluidelastic instability of an array of flexible cylinders in cross-flow, *ASME. J. Fluids Eng.*

Seki, K., Kuwabara, S., Tanimura, K., Matsumoto, S., and Toba, M., 1986, A study on fuel rod vibration induced by baffle jet flow. *Nuclear Technology*, **74(1)**: 27-37.

TRANSIENT VIBRATION PHENOMENON DUE TO PASSING OF GAP VORTEX STREET IN FSI SIMULATION OF TUBE BUNDLE WITH ECCENTRICITY

Henri Dolfen
Department of Electromechanical, Systems and Metal Engineering, Ghent University, Ghent, Belgium
Joris Degroote
Department of Electromechanical, Systems and Metal Engineering, Ghent University, Ghent, Belgium
Flanders Make, Belgium

ABSTRACT

Gap vortex streets in tube bundles subject to axial flow have been found for several geometries and fluids, both experimentally as numerically. An important parameter influencing its occurrence and strength is the size of the gaps between the tubes. It has also been shown that the associated pressure fluctuations are strong enough to give rise to flow-induced vibrations (FIV).

In this work the existence of a gap vortex street is demonstrated to trigger vibrations in a large pitch-over-diameter ratio (P/D) rod bundle with eccentric positioning of the central tube for a flow of liquid lead-bismuth-eutectic (LBE). This is done using fluid-structure interaction (FSI) simulations. In the first half of the simulation a gap vortex street arises, then triggers an asymmetric transient vibration while being advected downstream, after which the vibration decays. In the second half the flow pulsations weaken globally and are only present close to the pressure outlet. They trigger very small amplitude vibrations in a beating fashion.

The overall behavior described in this paper raises some new questions: firstly why no new vortex train arises at an upstream position nor any associated (large) vibration and secondly whether this is due to the influence of the boundary conditions and thus mainly a numerical artifact. Another question to be answered is what lies at the root of the asymmetry of the vibration.

1. INTRODUCTION

Cylinders subject to cross-flow are well known to generate vortex streets for certain ranges of Reynolds numbers. These vortex shedding phenomena have been extensively researched experimentally and numerically as they are known as a cause of flow-induced vibrations, often specified as vortex-induced vibrations (Wu et al., 2012). Less well known is the fact that also a fluid flowing axially in between tubes has been found to exhibit fluctuations due to the presence of vortex trains (Meyer, 2010). The existence of this gap vortex street (Tavoularis, 2011) is highly sensitive to the pitch-over-diameter ratio. The presence of a (long) shear layer is believed to be at the root, which is hypothesized to cause a flow instability akin to the Kelvin–Helmholtz instability (Meyer, 2010).

Several experiments have been performed on different geometries, like tube bundles (Baratto et al., 2006), eccentric annular flow (Choueiri & Tavoularis, 2014) and small gap geometries in general. In order to gain a deeper understanding of the phenomenon also numerical simulations have been done. Both large-eddy simulation (LES) (De Moerloose et al., 2018) and unsteady Reynolds-averaged Navier–Stokes (URANS) (Merzari et al., 2008; De Moerloose et al., 2019; De Ridder et al., 2016; Dolfen et al., 2019) have been shown to resolve these vortex streets.

The fluctuating pressure field associated with the vortex street interacts with the structure and is able to cause vibrations. This has been found numerically using fluid-structure interaction simulations (De Ridder et al., 2016; Dolfen et al., 2019; Guo et al., 2022) as well as experimentally (Bertocchi et al., 2019; Wang et al., 2021). In the work of Bertocchi et al. (2020) experiments and simulations were directly compared for a 7-rod bundle subject to water flow and with a hollow silicone part in the central rod. The results were similar but still some discrepancies were found for the frequency and amplitude of the vibrations. This indicates that the phenomenon is still not completely understood and that it might be sensitive to uncertainties caused by the experimental or modeling approach (Dolfen et al., 2019), expressing the need for further research.

The numerical approaches described above often assume fully developed flow (and thus a fully developed vortex street) by adopting periodic boundary conditions in streamwise direction (Merzari et al., 2008). This papers describes a numerical simulation of a tube bundle with an eccentric tube us-

ing inlet-outlet boundary conditions in which a gap vortex street arises and gets advected downstream. While getting advected it increases in strength and triggers a strong vibration of the flexible central steel tube, but that vibration weakens afterwards. The gap vortex street does not leave the domain at the pressure outlet but seems to stabilize at that region. The fluid used is lead-bismuth-eutectic, the coolant that is planned to be used in the MYRRHA prototype nuclear reactor (Engelen et al., 2015). Also the geometry is based on the fuel assembly design, although the wire-wrapper holding the rods in place is omitted. The vortex street is not observed for the design geometry, but arises when the central rod is positioned eccentrically. This paper is more of a descriptive nature, as the results are not yet well understood, and the aim is mainly to open up a discussion on how to deepen the understanding of the observed phenomena.

2. METHODOLOGY

The case under investigation is a rod bundle based on the MYRRHA fuel assembly design. FSI simulations coupling a Computational Fluid Dynamics (CFD) model to a Computational Structural Mechanics (CSM) model are used to investigate the flow-induced vibrations of one of the steel rods. The domain size is limited to one flexible steel rod surrounded by rigid neighbors as can be seen in Figure 1. The central rod is shifted to the right such that it has an eccentricity (e) of 1 mm. The other geometrical data can be found in Table 1. The fluid used is lead-bismuth-eutectic and its relevant properties can be found in Table 2, along with the structural properties of the steel used for the flexible central rod.

For the CFD part the software package Ansys Fluent 2019R1 is used, implementing the finite volume method. The model comprises one rod surrounded by six partial rods. The channels between the rods at opposing sides of the domain are connected through periodic boundary conditions, as visualized in Figure 1.

The incompressible Pb-Bi enters the domain with a uniform velocity of 1.9 m/s through a velocity inlet, which is a Dirichlet condition for the velocity and a Neumann condition for the pressure (zero gradient). The flow leaves the domain through a pressure outlet, assuming a Dirichlet boundary condition of 0 Pa for the pressure and a Neumann (zero gradient) condition for the velocity. All other boundaries are no-slip walls. Inlet-outlet boundary conditions were also used by Guo et al. (2022).

The simulation settings are based on earlier work of De Ridder et al. (2013), who simulated a similar geometry (without eccentricity). The $k-\omega$ SST turbulence model is used, with the inlet having a turbulent intensity of 5 % and turbulent length scale of 10 mm. It was found by De Ridder et al. (2013) that the turbulence inlet conditions only influence the eddy viscosity close to the inlet of the tube bundle, the simulation result is therefore not sensitive to these conditions. The domain is meshed using 700 cells in axial (z) direction, 14 cells in between the rods (radial direction) and 60 circumferential divisions, resulting in a total number of 882000 cells. Second order schemes were used for both spatial and temporal discretization; the pressure-velocity coupling is achieved using the SIMPLE algorithm.

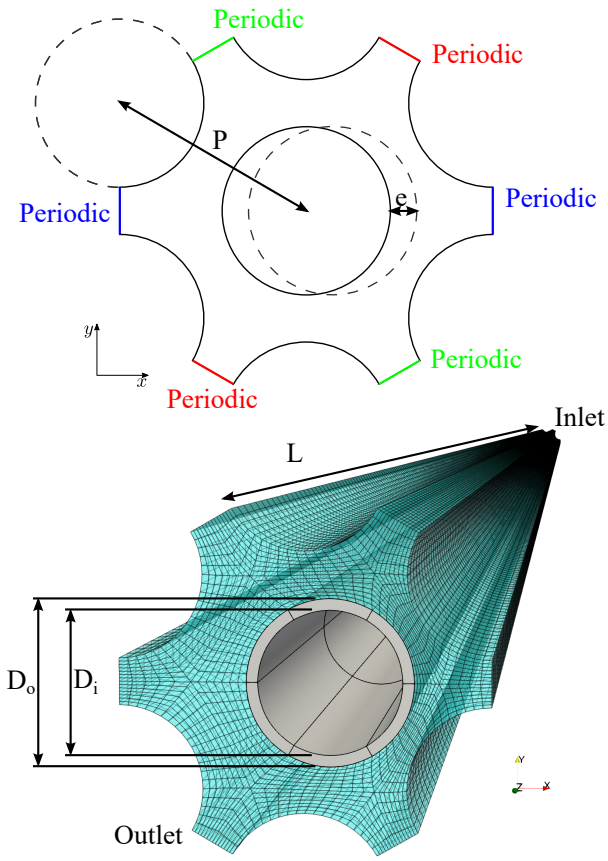

Figure 1. The geometry and mesh of the eccentric tube in the bundle. The values of the parameters are given in Table 1.

Before starting the FSI simulation, the flow is allowed to settle for 100 time steps in a transient simulation with a big time step (1 s), which in turn starts from a converged steady simulation. After that the time step is reduced to 5×10^{-4} s at the start of the FSI simulation.

For the structural model the finite elements software package Dassault Systèmes Abaqus 6.14 is utilized. The structural mesh can also be seen in Figure 1. It consists of 300 second order elements, using 50 axial divisions, 1 radial division and 6 circumfer-

Parameter	Value
Tube outer diameter D_o	6.55 mm
Tube inner diameter D_i	5.65 mm
Pitch P	8.4 mm
Length L	1400 mm
Eccentricity e	1 mm

Table 1. Geometrical data (also see Figure 1).

Property	Value
Fluid density ρ_f	10291 kg/m^3
Fluid viscosity μ_f	0.0017 $Pa \cdot s$
Solid density ρ_s	7850 kg/m^3
Young's elasticity modulus E	200 GPa
Poisson's ratio	0.3

Table 2. Material properties of liquid lead-bismuth-eutectic and steel.

ential divisions. This mesh is based on the one used for similar computations by De Ridder et al. (2013). Clamped boundary conditions are employed at both extremes. Hilber-Hughes-Taylor time integration is used, which is a second order scheme.

The CSM and CFD model are coupled at their mutual interface by exchange of pressure and traction forces on the one hand and displacements on the other hand. This method is known as the partitioned approach (Degroote, 2013): the solvers compute a solution separately only based on the information that is provided by the other solver on the interface. The displacement of the interface requires the CFD mesh to deform, this is handled using an arbitrary Lagrangian-Eulerian (ALE) formulation.

Implicit (also known as strong) coupling is used, the loads and displacement are communicated back and forth between the solvers until equilibrium is reached within a time step up to some tolerance. To speed up this convergence, the interface quasi-Newton with inverse Jacobian from a Least Squares model (IQN-ILS) coupling algorithm is used (Degroote et al., 2009). The FSI coupling is implemented in the open-source Python code CoCoNuT[1]. The simulation was ran for 8000 time steps of $5e-4$ s, resulting in 4 s of simulation time. This took 19 days on 34 cores.

3. RESULTS AND DISCUSSION

The gap vortex street that arises in the LBE flow can be clearly seen in the flow field in Figure 2. The velocity magnitude plotted in the XZ-plane shows fluc-

[1] `https://pyfsi.github.io/coconut/index.html`

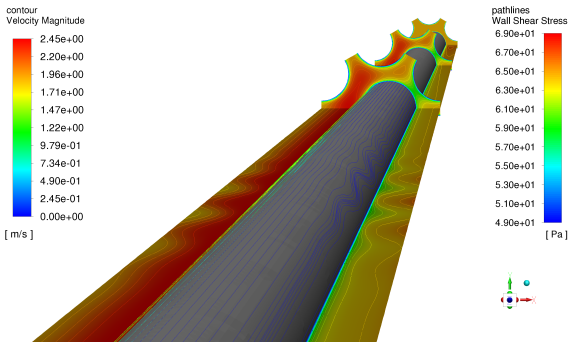

Figure 2. The flow field at $t = 0.55$ s. A contour of the velocity magnitude in the XZ-plane, the inlet and cross-sections at 25% and 50% of the axial length is shown, as well as pathlines of the wall shear stress on the surface of the central rod.

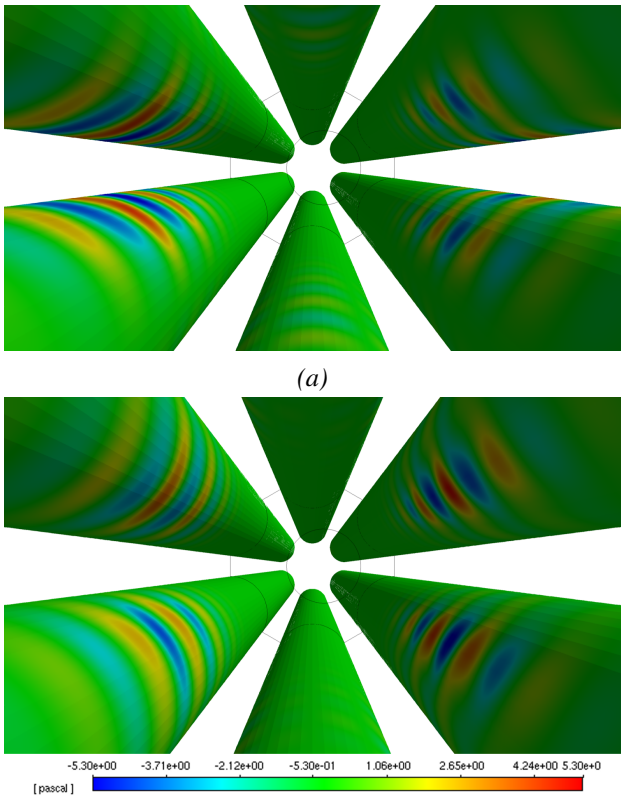

(a)

(b)

Figure 3. View from within the bundle with the central rod invisible: (a) x-component of wall shear stress (Pa) and (b) y-component of wall-shear stress at $t = 0.55$ s.

tuating behavior for a certain region as does the wall shear stress (visualized by pathlines on the central rod). In Figure 3 the components of the wall shear stress on the surface of the rigid rods at the sides of the domain are shown. It can be seen that the vortex street continues through the periodic boundaries on the left and right. However, above and below no strong deviations of the wall shear stress are found on the cylinder in the middle. The occurrence of the gap vortex street seems thus to be triggered by the eccentricity. The gap size is indeed known to be an important parameter influencing the strength of the vortex street (De Ridder et al., 2016). This velocity difference can be seen in the cross-sectional planes in Figure 2, a velocity deficit is present in the narrow gap on the right hand side of the cross-section. Also for the nominal geometry a simulation was performed, having a P/D of about 1.28, and no important flow pulsations were found there (results not shown). As hypothesized by De Ridder et al. (2016), the velocity difference between the gaps and subchannels is not substantial enough to trigger important flow pulsations through a shear layer instability for larger P/D. It is possible that the vortex street on the left hand side of the central rod (large gap due to eccentricity) is only present due to the periodic boundary conditions in the fluid domain.

The gap vortex street will in this paper mainly be studied through the effect of the pressure it exerts on the central rod. The pressure is integrated circumferentially and depicted for a selection of times in Figure 4. The force in x-direction F_x (i.e. the same direction as the eccentricity) can be seen to be two orders of magnitude bigger than in y-direction (F_y). From the different snapshots it is clearly visible that the vortex train gets advected downstream and that it becomes stronger. Around 0.45 s it is visible around $z = 0.8$ m on the scale of the figure, but when one would zoom in (not shown), it can be found to originate much more upstream in the domain, very close to the inlet.

The large (negative) F_x near the inlet is due to a redistribution of the flow, since a uniform velocity is introduced. A simulation with a developed velocity profile at the inlet was tested (not shown), which made this force vanish. The vortex street however still arose.

The forces in x-direction (Figure 4a) are also seen to become smaller after reaching a maximum and after 1 s it is no longer visible on the scale of the figure. In F_x also a standing wave pattern can be seen, between 0.60 s and 0.70 s, which is directly related to the vibration of the rod.

In Figure 5 the forces are shown at later time instants. It can be seen on these figures that now F_x and

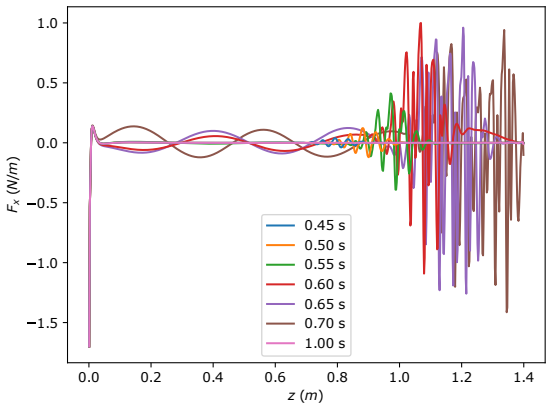

(a)

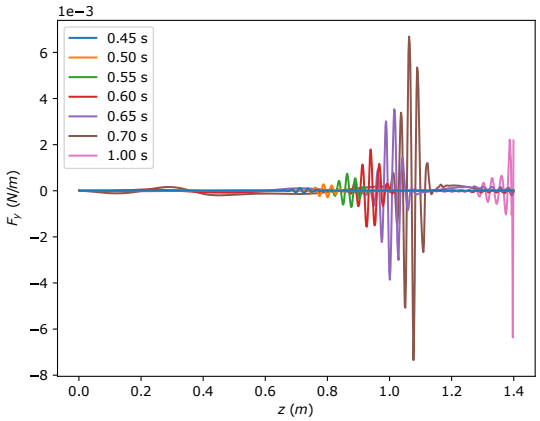

(b)

Figure 4. Snapshots at different times of the (a) force in x-direction and (b) force in y-direction as function of the axial coordinate.

F_y have a similar order of magnitude. The advection speed and rate at which these forces arise seem to balance on average, so the force pattern does not leave the domain anymore. The strength does however vary a bit over time, as can be seen for both x and y direction forces. It is not clear whether the presence of the pressure outlet has a large influence on this behavior. It is plausible that it triggers the creation of vortices upstream somehow. The observed phenomena at later time instants could thus be a numerical artifact. The authors however believe that the initial behavior is not influenced by the boundary conditions, as the vortex street first originates far from the pressure outlet and both a uniform and developed profile have been tested at the inlet. Further investigation of the effect of the boundary conditions could focus on placing the boundaries farther away from the regions of interest, e.g. by increasing the number of tubes and providing a kind of smooth transition to an outflow

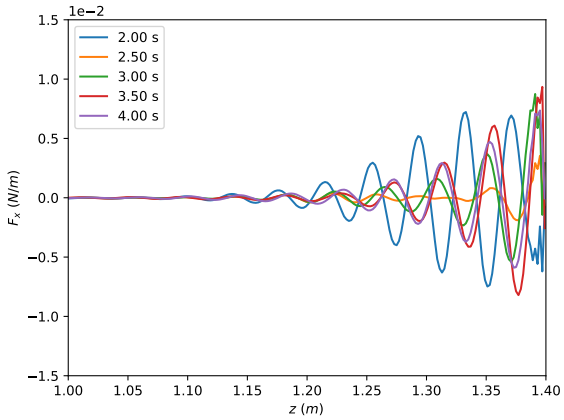

(a)

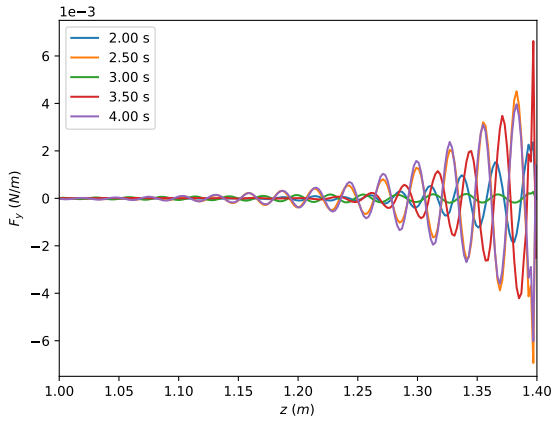

(b)

Figure 5. Snapshots at different times of the (a) force in x-direction and (b) force in y-direction as function of the axial coordinate for the downstream part of the bundle.

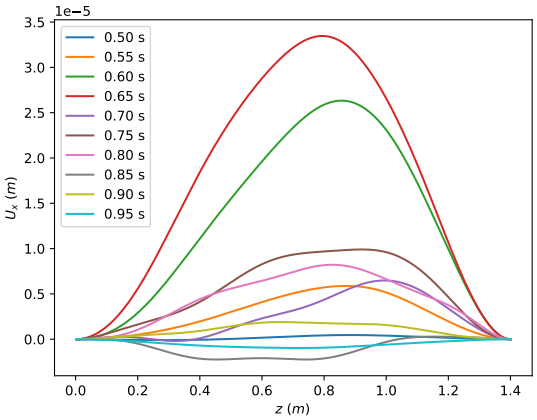

(a)

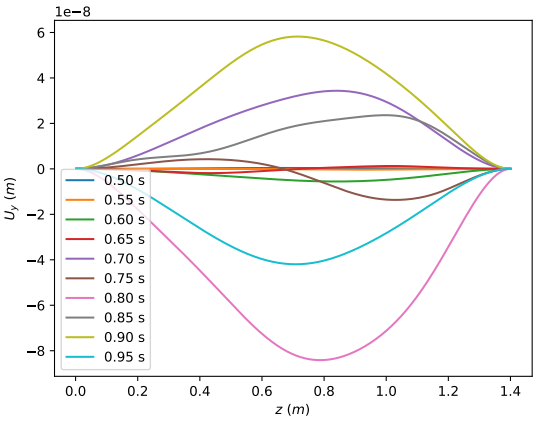

(b)

Figure 6. Snapshots at different times of the (a) displacement in x-direction and (b) displacement in y-direction as function of the axial coordinate.

domain, such that the vortex train cannot self-interact nor interact with a pressure-outlet. These simulations are currently beyond the scope due to the high computational cost associated by increasing the domain size.

Similar to the axial force profiles, also snapshots of the displacement in x- and y-direction (U_x and U_y) are shown, see Figure 6. Similar to the forces, U_x is more than two orders of magnitude bigger than U_y and has a maximum of about 1.9% of the nominal gap width. It can be seen that the x-vibration mainly happens in the first flexural mode, although it clearly has some higher modes superposed. Also the U_y mainly shows first mode behavior.

The x-vibration has a striking asymmetry as the vibration mainly happens in positive x-direction, so the same direction as the eccentricity itself. When plotting the overall x- and y-force (Figure 7) it can indeed be seen that it is mainly a positive force, albeit very oscillatory. Both the x-force and y-force decay to lower values after about 1 s of simulation time.

In Figure 8 the displacement of the midpoint of the rod is plotted as a function of time. U_x can first be seen to have a large displacement to the right, after which it returns but does not overshoot its neutral position. After a second smaller deflection it does overshoot and exhibits a decaying vibration. The y-displacement displays a similar behavior but more symmetrically.

For both the total forces and displacement a transient phenomenon is observed here, that mainly happens between 0.5 s and 1 s for the largest deflections after which it decays between 1 s and 1.5 s. This coincides directly with the passage and growing of the vortex train through the second half of the domain. The simulation is continued up to 4 s, but no repetition of this phenomenon is observed. It is un-

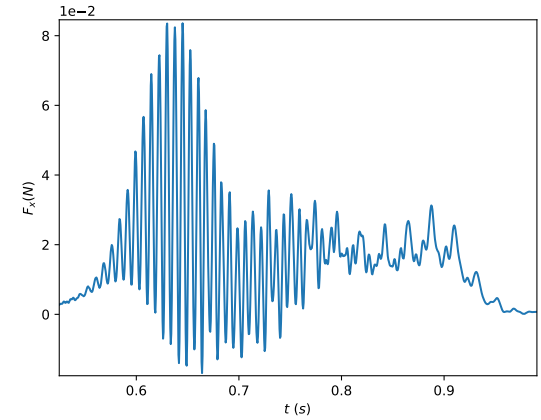

(a)

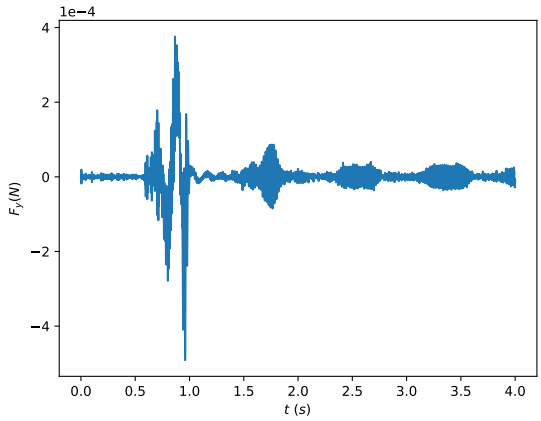

(b)

Figure 7. Total force in (a) x-direction and (b) y-direction as function of time.

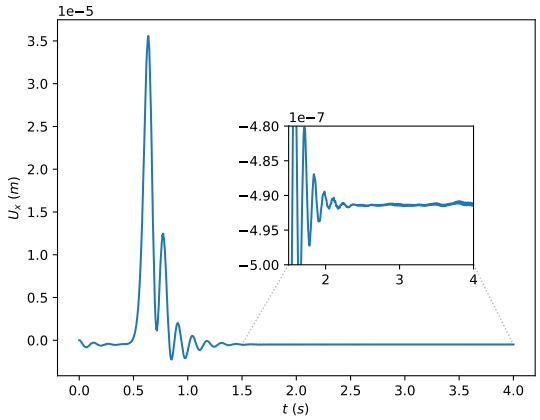

(a)

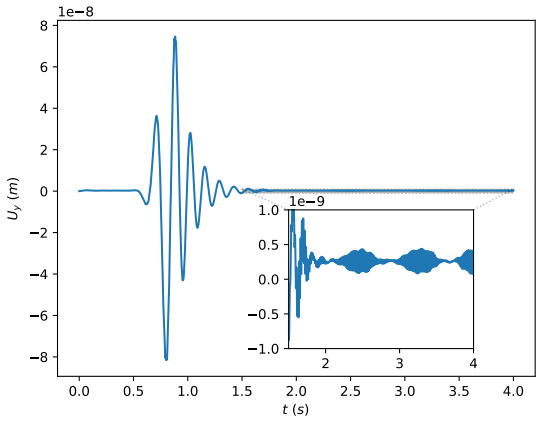

(b)

Figure 8. Displacement of central point ($z = 0.7$ m) in (a) x-direction and (b) y-direction as function of time.

clear why the gap vortex street can arise a first time at the upstream part of the domain, but no second time. It could be related to an interaction between the gap vortex street and the pressure outlet, which is not understood but potentially affects the flow upstream.

After the large transient FIV phenomenon, small amplitude vibrations (not visible on the scale of Figure 8) remain. They happen in a rather beating fashion, coupled to the forces shown in Figure 7b. These are associated by the growing and weakening of the vortex patterns near the outlet.

4. CONCLUSION

This paper presents a transient FIV phenomenon related to the passage of a gap vortex street. It has demonstrated that a gap vortex street in LBE flow is possible for the MYRRHA tube bundle geometry given some eccentricity. This vortex street grows in strength while being advected downstream until it reaches the outlet.

The passing of the vortex street is associated with mainly an eccentric vibration in positive x-direction, followed by a fast decay. This raises one question still to be answered, namely what causes the vibration to be asymmetric.

After its passage the vortex street reduces a lot in strength with regard to the x-direction force, although it remains present in the domain near the pressure outlet, where it triggers vibrations in both x- and y-direction with smaller magnitude. This happens in a beating fashion due to the strengthening and weakening of the pulsations. It is not clear why no new vortex street arises at a more upstream position, but it could be related to an interaction between the gap vortex street and the boundary conditions at the outlet. A second question that remains is whether the behavior in the second half of the simulation is a nu-

merical artifact or could be reproduced experimentally.

5. REFERENCES

Baratto, F. et al., 2006, Measurements of frequencies and spatial correlations of coherent structures in rod bundle flows. *Nuclear Engineering and Design* **236(17)**: 1830-1837.

Bertocchi, F. et al., 2019, Experimental investigation on the influence of gap vortex streets on fluid-structure interactions in hexagonal bundle geometries. *International Journal of Heat and Fluid Flow* **79**: 108443.

Bertocchi, F. et al., 2020, Fluid-structure interaction of a 7-rods bundle: Benchmarking numerical simulations with experimental data. *Nuclear Engineering and Design* **356**: 110394.

Choueiri, G. & Tavoularis, S., 2014, Experimental investigation of flow development and gap vortex street in an eccentric annular channel. Part 1. Overview of the flow structure. *Journal of Fluid Mechanics* **752**: 521-542.

De Moerloose, L. et al., 2018, Numerical investigation of large-scale vortices in an array of cylinders in axial flow. *Journal of Fluids and Structures* **78**: 277-298.

De Moerloose, L. et al., 2019, Analysis of the Kelvin-Helmholtz instability in a square cylinder array subjected to axial flow with LES and URANS. *SESAME Final International Workshop, Proceedings, Petten, The Netherlands, 19-21 March 2019.*

Degroote, J. et al., 2009, Performance of a new partitioned procedure versus a monolithic procedure in fluid–structure interaction. *Computers & Structures* **87(11)**: 793-801.

Degroote, J., 2013, Partitioned Simulation of Fluid-Structure Interaction. *Archives of Computational Methods in Engineering* **20(3)**: 185-238.

De Ridder, J. et al., 2013, Modal characteristics of a flexible cylinder in turbulent axial flow from numerical simulations. *Journal of Fluids and Structures* **43**: 110-123.

De Ridder, J. et al., 2016, Vortex-induced vibrations by axial flow in a bundle of cylinders. *Proceedings of the 11th Conference on Flow-Induced Vibration and Noise, The Hague, The Netherlands, 4-6 July 2016.*

Dolfen, H. et al., 2019, Vibrations in a 7-rod bundle subject to axial flow: Simulations and experiments. *Nuclear Engineering and Design* **353**: 110227.

Engelen, J. et al., 2015, MYRRHA: Preliminary front-end engineering design. *International Journal of Hydrogen Energy* **40(44)**: 15137-15147.

Guo, Y. et al., 2022, Numerical investigation on flow-induced vibration and heat transfer of fuel rods in a small pitch-diameter ratio (P/D) channel. *Annals of Nuclear Energy* **171**: 109055.

Merzari, E. et al., 2008, Numerical simulation of flows in tight-lattice fuel bundles. *Nuclear Engineering and Design* **238(7)**: 1703-1719.

Meyer, L., 2010, From discovery to recognition of periodic large scale vortices in rod bundles as source of natural mixing between subchannels—A review. *Nuclear Engineering and Design* **240(6)**: 1575-1588.

Tavoularis, S., 2011, Rod bundle vortex networks, gap vortex streets, and gap instability: A nomenclature and some comments on available methodologies. *Nuclear Engineering and Design* **241(7)**: 2624-2626.

Wang, P. et al., 2021, Axial-flow-induced vibration of an elastic cylinder placed between two cylinders. *Journal of Fluids and Structures* **106**: 103371.

Wu, X. et al., 2012, A review of recent studies on vortex-induced vibrations of long slender cylinders. *Journal of Fluids and Structures* **28**: 292-308.

Turbulence, vortex and wave-induced vibrations

ASPECTS OF VORTEX-INDUCED IN-LINE VIBRATION AT LOW REYNOLDS NUMBERS

Efstathios Konstantinidis
University of Western Macedonia, Kozani, Greece
Dániel Dorogi & László Baranyi
University of Miskolc, Miskolc-Egyetemváros, Hungary

ABSTRACT

In this work, we investigate the vortex-induced vibration of a circular cylinder purely in-line with a free stream by means of two-dimensional simulations at low Reynolds numbers. The equations of fluid motion are solved using an in-house CFD code based on the finite-difference method in tandem with integration of the equation of cylinder motion. Results are reported for a mass ratio of 10 and null structural damping ratio at Reynolds numbers of 100 and 200. At these Reynolds numbers, the response amplitude as a function of the reduced velocity displays a single excitation region that is associated with alternating vortex shedding. The peak amplitude increases by a factor of six between Re=100 and 200 reaching a value of 1.4% of the cylinder diameter in the latter case. We employ the phasing of the unsteady lift force with respect to the cylinder displacement in order to decipher the vortex dynamics in the wake. Unlike the phase of the unsteady force acting along the direction of cylinder oscillation, which is restricted per the equation of cylinder motion at null damping to values of 0° and 180°, the phase of the unsteady lift force displays a gradual increase with reduced velocity. We interpret this variation as a shift in the timing of vortex shedding in the wake with the oscillation frequency. We propose an extension of the well-known Morison's equation that includes a separate term for the vortex drag force, which captures the effect of vortex dynamics on the phasing of the driving force required to satisfy the equation of in-line motion. This new model uncouples the fluid and structural dynamics and provides physical insight not possible heretofore.

1. INTRODUCTION

Vortex shedding in the wake of bluff bodies is one of the basic excitation mechanisms of flow-induced vibration, which is referred to as vortex-induced vibration (VIV). It is demonstrated in its purest form when a circular cylinder, which has some degree of freedom to vibrate, is exposed to a cross flow. The fundamental study of this problem can be tracked back to Bishop & Hassan (1964) who measured the lift and drag forces on a rigid circular cylinder that was made to oscillate transversely to a free stream. Since then numerous studies of basic flow configurations in which a cylinder vibrates either freely or forcibly in various directions perpendicular to the stream have been made, in particular concerning motions purely in-line and transversely as well as combined in-line and transverse oscillations. Comprehensive reviews on the topic can be found, among others, in King (1977); Bearman (1984); Naudascher (1987); Williamson & Govardhan (2004); Sarpkaya (2004), and Bearman (2011).

The present study concerns VIV purely in-line with the free stream, which has been studied less because of the much lower amplitudes of oscillation, about one tenth of the corresponding transverse case (King, 1977). A thorough review is beyond the scope of the present work but a brief summary of findings will be given below. It has been established as early as the 1970's that there exist two excitation regions of in-line vibration where appreciable response amplitudes are observed as a function of the reduced velocity: the first excitation region has been associated with symmetrical shedding of vortices simultaneously from both sides of the cylinder, whereas the second one has been associated with alternating shedding of vortices from each side of the cylinder (Wootton *et al.* , 1972; Aguirre, 1977; King, 1977). The response amplitude is about the same in both excitation regions and increases with decreasing the product of mass and damping ratios of the structure (Okajima *et al.* , 2004). The above modes of vortex shedding have been confirmed in more recent studies (Cagney & Balabani, 2013, 2016; Gurian *et al.* , 2019).

In nearly all of the previous studies of in-line VIV, the Reynolds number Re based on the cylinder diameter and the free-stream velocity, was moderately high, i.e. $Re > 10^3$. There is some evidence from the early study of Tanida *et al.* (1973), who made time-resolved measurements of the forces on a cylin-

der under controlled oscillation, that self-excited in-line motion may not occur for low Reynolds numbers in the range from 80 to 150, because the phase lag between the driving force and the displacement was negative. This inference was made on the assumption that the self-excited motion of the cylinder be equivalent to the controlled motion, which was pure harmonic. Furthermore, in that study the amplitude of cylinder oscillation was kept constant at 13% of the cylinder diameter. However, it is plausible that the phase lag and thereby energy transfer from the fluid to the structure can be positive at lower amplitudes. Remarkably, there are no studies, either experimental or numerical, of in-line VIV at low Reynolds numbers. The only study the authors are aware of, is the numerical study of Bourguet & Lo Jacono (2015) where free in-line vibration of a rotating cylinder was considered at $Re = 100$; for the case of the non-rotating cylinder, the amplitude response was negligible compared to the cases where the cylinder was rotating at specified rates. An objective of this study is to address the question 'whether in-line VIV can occur at low Reynolds numbers' and, if it does occur, what are its characteristics. The information provided by detailed simulations can then be used to better describe and model the problem at both low and high Reynolds numbers, the latter case being more relevant in practical applications.

On the theoretical side, a long-standing approach is to represent the in-line force per unit length F_x based on the equation proposed by Morison *et al.* (1950). For a circular cylinder oscillating in-line with a steady uniform free stream, the cylinder velocity and acceleration denoted by $\dot{x}_c$ and $\ddot{x}_c$ respectively, Morison *et al.'s* equation can be written as

$$F_x = \frac{1}{2}\rho d C_{dv}\left(U_\infty - \dot{x}_c\right)^2 - \frac{1}{2}\pi\rho d^2 C_{mv}\ddot{x}_c, \quad (1)$$

where ρ is the density of the fluid, d is the diameter of the cylinder, U_∞ is the free-stream velocity, C_{dv} and C_{mv} are drag and mass (or inertia) coefficients, respectively, which are empirically determined from measurements or simulations. Inherent to this approach is the harmonic approximation since the values of the hydrodynamic coefficients C_{dv} and C_{mv} are often determined from tests where the cylinder is forced to vibrate harmonically, e.g. they can be expressed as functions of the normalized amplitude and frequency of cylinder oscillation. It should be noted that in writing Eq. (1) we have assumed that $\dot{x}_c < U_\infty$. Furthermore, Eq. (1) does not include dynamic-buoyancy (Froude-Krylov) and added-mass components of the force associated with the acceleration of the incident flow since the later is steady, i.e. it is independent of time.

Despite the empirical use of Morison *et al.*'s equation, the inventors of the equation stated that its origin is based on theory regarding the drag force associated with wake formation and the added-mass force associated with potential flow. Indeed, it has been recently shown that the equation with theoretical values of the coefficients gives almost as good a fit to the in-line force as with empirically best-fitted values over a wide range of parameters from the inertia to drag-dominated regimes (Konstantinidis & Bouris, 2017).

Here, we propose the following extension to Morison *et al.*'s equation

$$F_x = \frac{1}{2}\rho d C_d\left(U_\infty - \dot{x}_c\right)^2 - \frac{1}{4}\pi\rho d^2 C_a\ddot{x}_c + F_{dv}, \quad (2)$$

where C_d is the mean drag coefficient, C_a is the added mass coefficient for ideal potential flow (=1 for a circular cylinder), and F_{dv} is the vortex drag due to changes in the distribution of vorticity with time. We express the vortex drag empirically as a harmonic function of time of the form:

$$F_{dv}(t) = \frac{1}{2}\rho U_\infty^2 d C_{dv}\sin\left(2\pi f t + \phi_{dv}\right), \quad (3)$$

where C_{dv} is the magnitude of the vortex drag, ϕ_{dv} is the phase of the vortex drag with respect to the displacement of the cylinder, and f is the frequency of cylinder oscillation. We assume here that the frequency of oscillation is synchronized with the frequency of vortex shedding from the cylinder. Furthermore, we anticipate that changes in the vortex dynamics will be reflected on the values of C_{dv} and ϕ_{dv}. This is an assumption we wish to verify with the aid of numerical simulations of in-line VIV at low Reynolds numbers.

2. NUMERICAL METHOD

The equation of motion for a cylinder constrained elastically so that it can oscillate only in-line with a uniform free stream can be written in non-dimensional form as

$$\ddot{x}_c + \frac{4\pi\zeta}{U^*}\dot{x}_c + \left(\frac{2\pi}{U^*}\right)^2 x_c = \frac{2C_x(t)}{\pi m^*}, \quad (4)$$

where x_c, $\dot{x}_c$, and $\ddot{x}_c$ respectively are the non-dimensional displacement, velocity and acceleration of the cylinder, normalized using d and U_∞ as length and velocity scales; $C_x(t)$ is the sectional fluid force on the cylinder normalized with $0.5\rho U_\infty^2 d$; $U^* = U_\infty/(f_n d)$ is the reduced velocity based on the natural frequency of the system in vacuum; m^* is the ratio of the cylinder mass to the fluid mass displaced

by the cylinder; ζ is the ratio of the structural damping to the critical damping at which the mechanical system can exhibit oscillatory response to external forcing. Equation (4) is numerically integrated in time using the 4$^{\text{th}}$ order Runge–Kutta method starting from an initial condition where the cylinder is at rest. The equation of motion is solved in dimensionless form so different reduced velocities could be achieved by assigning the U^* value directly. In a physical experiment, the variation of the reduced velocity while keeping constant the Reynolds number would be achieved by changing the natural frequency.

The fluid forcing $C_x(t)$ on the right-hand side of Eq. (4) is obtained from spatial integration of the instantaneous normal and shear stresses around the circumference of the cylinder, which are obtained in turn by numerically solving the equations of fluid motion at each time step. Assuming that the flow is incompressible and two-dimensional, we write the Navier–Stokes equations in non-dimensional form using the pressure–velocity formulation as

$$\frac{\partial u_x}{\partial t} + u_x\frac{\partial u_x}{\partial x} + u_y\frac{\partial u_x}{\partial y} = -\frac{\partial p}{\partial x} + \frac{1}{Re}\nabla^2 u_x - \ddot{x}_c, \quad (5)$$

$$\frac{\partial u_y}{\partial t} + u_x\frac{\partial u_y}{\partial x} + u_y\frac{\partial u_y}{\partial y} = -\frac{\partial p}{\partial y} + \frac{1}{Re}\nabla^2 u_y, \quad (6)$$

where u_x and u_y respectively are the velocity components in the streamwise x and transverse y directions, t is the time, p is the pressure and $\ddot{x}_c$ is the acceleration of the cylinder, and Re is the Reynolds number based on the free-stream velocity and the diameter of the cylinder. It should be noted that $\ddot{x}_c$ appears on the right-hand-side of (5) because the equations of fluid motion are solved on a stationary grid moving with the cylinder.

Instead of enforcing the continuity equation directly, at each time step we compute the dilation $\mathscr{D}$,

$$\mathscr{D} = \frac{\partial u_x}{\partial x} + \frac{\partial u_y}{\partial y}, \quad (7)$$

and compute the fluid pressure from the solution of Poisson's equation in the following form (Harlow & Welch, 1965)

$$\nabla^2 p = 2\left(\frac{\partial u_x}{\partial x}\frac{\partial u_y}{\partial y} - \frac{\partial u_x}{\partial y}\frac{\partial u_y}{\partial x}\right) - \frac{\partial \mathscr{D}}{\partial t}. \quad (8)$$

On the cylinder surface, the no-slip boundary condition yields the following condition for the normal pressure gradient at the wall

$$\frac{\partial p}{\partial n} = \frac{1}{Re}\nabla^2 u_n - \ddot{x}_{c,n}, \quad (9)$$

where n refers to the component normal to the cylinder surface pointing to the fluid side. At the far field, a potential flow field is assumed and the corresponding condition for the far-field pressure becomes

$$\frac{\partial p}{\partial n} = 0. \quad (10)$$

The initial field corresponds to the potential flow around a circular cylinder.

The equations of fluid motion are numerically solved using an in-house code based on the finite difference method, see Baranyi (2008) and Dorogi & Baranyi (2018) for more details. The space derivatives are discretized using fourth-order accurate difference schemes except for the convective terms, which are approximated by the third-order modified upwind difference scheme. The Poisson equation is solved using the successive over-relaxation (SOR) method. The momentum equations are integrated in time explicitly using the first-order Euler scheme.

Re	$A^*_{\max}$	U^*	f^*	C_{EA}
100	0.0022	2.90	0.3273	1.099
200	0.0136	2.50	0.3794	1.115

Table 1. Properties at peak amplitude of response.

3. RESULTS

A large number of simulations were carried out for Reynolds numbers ranging from 100 to 250 and for mass ratios from 2 to 20. The damping ratio was set to zero in all cases to allow the highest possible amplitudes to occur. In this paper, we present results at $Re = 100$ and 200 for a fixed mass ratio of $m^* = 10$, which are representative over the entire range of parameters investigated. More than 40 operating points in U^* were obtained per each set of parameters. A fine step in the reduced velocity of $\Delta U^* = 0.01$ was employed in certain regions in order to resolve details of the response curves.

In Figure 1, we see that the amplitude of cylinder response A^*, taken as $\sqrt{2}$ times the root-mean-square value of the displacement normalized with the diameter of the cylinder, displays a single excitation region as a function of the reduced velocity at both Reynolds numbers. The properties at peak amplitude are summarized in Table 1. Doubling the Reynolds number causes an increase of the peak amplitude $A^*_{\max}$ by more than six times. The U^* value for which peak amplitudes occur decreases with Re, which may be attributable to the increase of the corresponding Strouhal number. The mode of vortex shedding responsible for the excitation of in-line vibration was always the regular alternating mode as will be shown later.

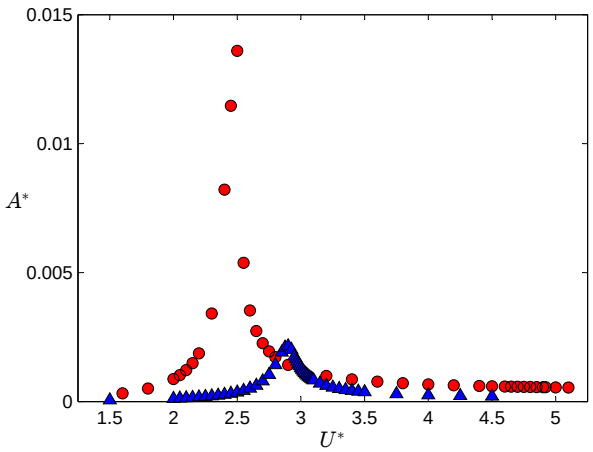

Figure 1. The variation of the response amplitude A^* as a function of the reduced velocity U^* at $Re = 100$ (triangles) and $Re = 200$ (circles); $(m^*, \zeta) = (10, 0)$.

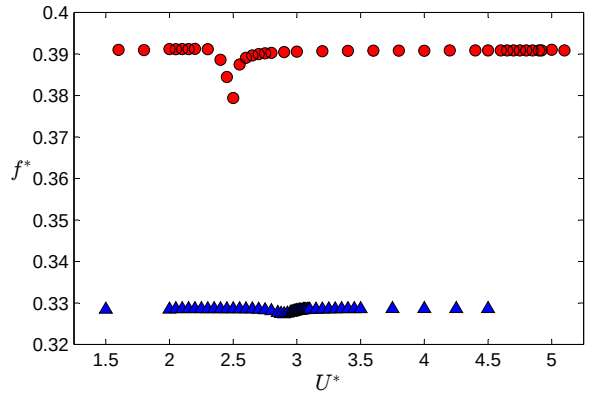

Figure 2. The variation of the response frequency f^* as a function of the reduced velocity U^* at $Re = 100$ (triangles) and $Re = 200$ (circles); $(m^*, \zeta) = (10, 0)$.

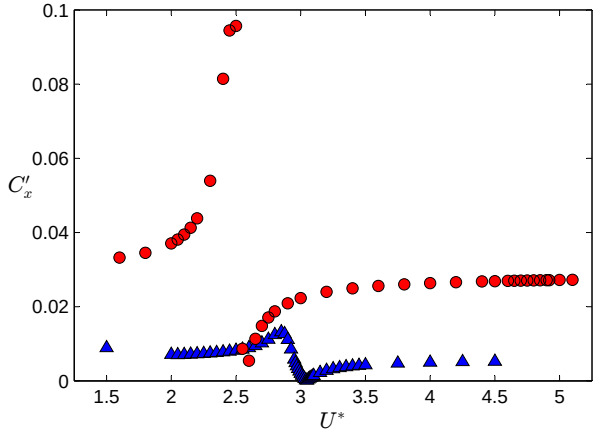

Figure 3. The variation of the rms magnitude of the in-line force C'_x as a function of the reduced velocity U^* at $Re = 100$ (triangles) and $Re = 200$ (circles).

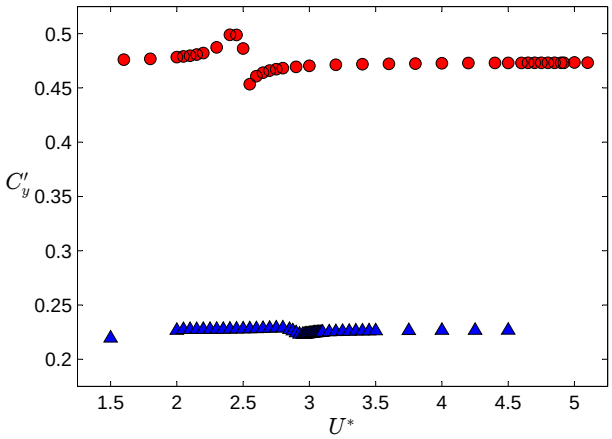

Figure 4. The variation of the rms magnitude of the transverse force C'_y as a function of the reduced velocity U^* at $Re = 100$ (triangles) and $Re = 200$ (circles).

The normalized frequency of cylinder vibration f^* ($= fD/U_\infty$ where f is the actual frequency of vibration) as a function of U^* displays a trough in the region of peak amplitude reaching its minimum at this point exactly (see Figure 2). The drop of f^* in this region is more pronounced for $Re = 200$ than for 100. Outside of this region, f^* remains almost constant at the value corresponding to twice the Strouhal number for a stationary cylinder.

Figure 3 shows that the rms value of the unsteady force in-line with the free stream C'_x initially increases with U^* reaching a maximum value. Interestingly, the maximum in C'_x does not coincide with the peak amplitude as might be expected, but rather at a slightly lower U^* value than that corresponding to peak amplitude, i.e. the maximum occurs at $U^* = 2.75$ and 2.40 for $Re = 100$ and 200, respectively. Beyond the maximum point, C'_x suddenly decreases reaching a minimum value just after the maximum for $Re = 200$. For $Re = 100$, the minimum C'_x value approaches zero. As U^* is increased beyond the point of minimum, C'_x gradually increases towards the value corresponding to that of a fixed cylinder at the respective Re value.

The variation of the rms value of the unsteady force transverse to the free stream C'_y as a function of U^*, which is shown in Figure 4, is very similar to that of C'_x. Maximum and minimum C'_y values are approximately 5% higher and 10% lower, respectively, than the value corresponding to the fixed cylinder for $Re = 200$, whereas the differences are less pronounced for $Re = 100$. It is interesting to note that variations in C'_y directly reflect changes in the vortex dynamics around the oscillating cylinder because there is no body acceleration in y direction, which could directly affect the corresponding force through inertial effects due to added mass. Therefore, the

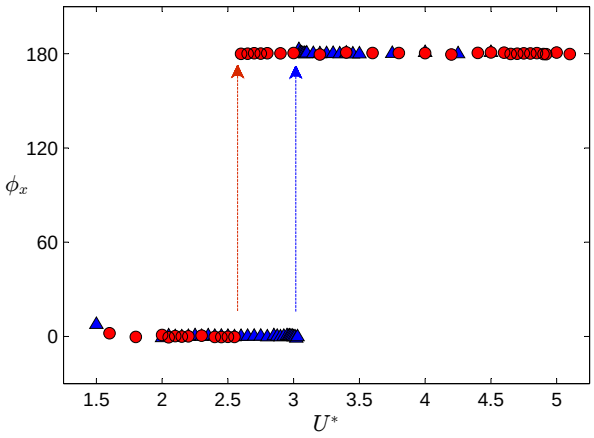

Figure 5. The variation of the phase-angle ϕ_x between the in-line force and displacement as a function of the reduced velocity U^* at $Re = 100$ (triangles) and $Re = 200$ (circles).

small variation in C_y' indicates that there are no significant changes in the mode of vortex shedding.

Figure 5 shows the variation of the phase lag ϕ_x between the in-line force and the cylinder displacement, assuming that both are single-harmonic functions of time. It can be seen that ϕ_x jumps abruptly from approximately 0° to 180° at $U^* = 3.03$ and 2.55 for $Re = 100$ and 200, respectively. The jumps occur at the points where the vibration frequency becomes equal to the natural frequency of the structure in vacuum, which can be expressed in non-dimensional form as $f^*U^* = 1$. In fact, the ϕ_x values of 0° and 180° and the occurrence of an abrupt jump from the one to the other across the point $f^*U^* = 1$ can be analytically predicted from the harmonic solution of the equation of motion in the case of zero structural damping (not discussed in detail here for economy of presentation).

Figures 6 and 7 show instantaneous distributions of the normalized vorticity at three reduced velocities for $Re = 100$ and 200, respectively. For each Re value, the U^* values correspond to points (a) before the 180° jump in ϕ_x, (b) near peak response amplitude, and (c) after the 180° jump in ϕ_x. It should be noted that the instantaneous distributions are at random instants. It can be seen that the mode of alternating vortex shedding clearly prevails in all cases. For $Re = 100$, there are hardly any changes in the vorticity distributions at different U^* values (Fig. 6). For $Re = 200$, the vorticity levels near the cylinder and in the shed vortices are considerably higher than for $Re = 100$ (cf. Fig. 7). A notable observation for $Re = 200$ is that near peak response amplitude, i.e. at $U^* = 2.5$, the streamwise distance between successive vortices has increased so that a larger number of

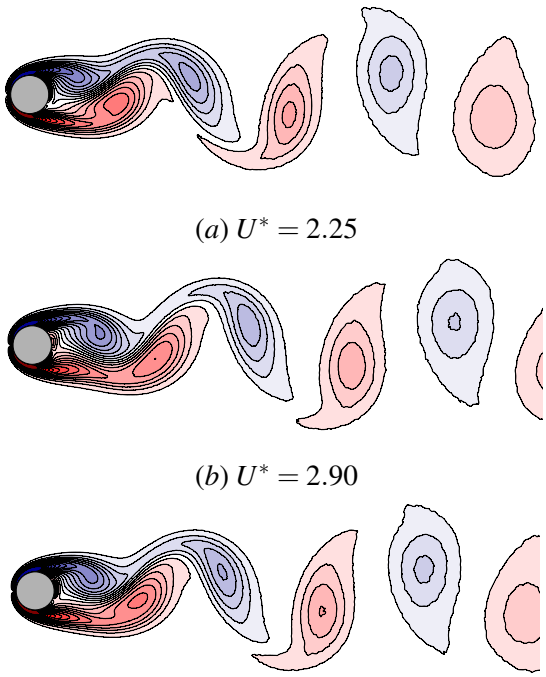

(a) $U^* = 2.25$

(b) $U^* = 2.90$

(c) $U^* = 3.25$

Figure 6. Instantaneous vorticity distributions at three U^* values for $Re = 100$. Contour levels: ± 0.2, ± 0.6, ... up to ± 6.0.

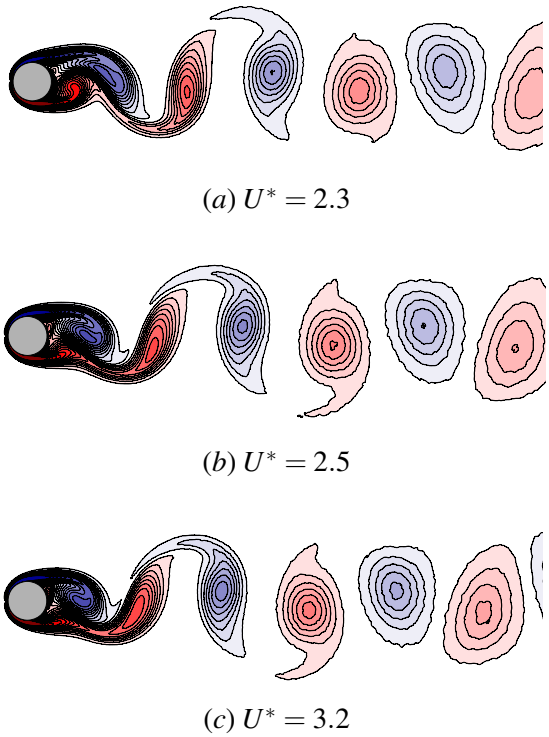

(a) $U^* = 2.3$

(b) $U^* = 2.5$

(c) $U^* = 3.2$

Figure 7. Instantaneous vorticity distributions at three U^* values for $Re = 200$. Contour levels: ± 0.2, ± 0.6, ... up to ± 6.0.

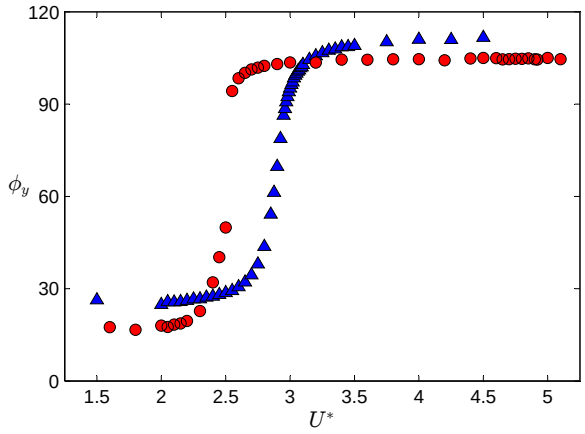

Figure 8. The variation of the phase-angle between the transverse force and displacement ϕ_y as a function of the reduced velocity U^* at $Re = 100$ (triangles) and $Re = 200$ (circles).

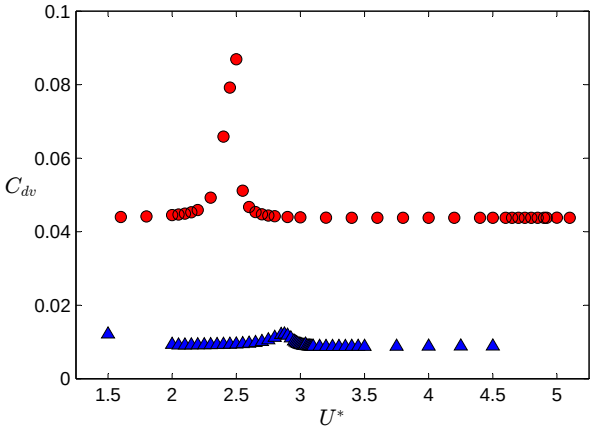

Figure 9. The variation of the vortex drag coefficient C_{dv} as a function of the reduced velocity U^* at $Re = 100$ (triangles) and $Re = 200$ (circles).

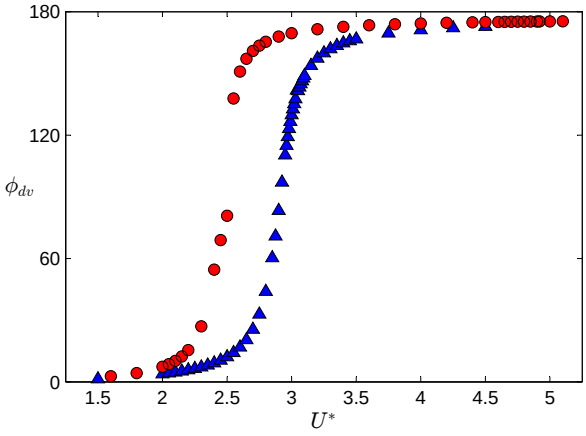

Figure 10. The variation of the phase-angle between the vortex drag and displacement ϕ_{dv} as a function of the reduced velocity U^* at $Re = 100$ (triangles) and $Re = 200$ (circles).

vortices fit within the specified field of view, which is related to the reduction of the frequency of vortex shedding and cylinder oscillation.

Another interesting observation regards the value of the effective added mass coefficient C_{EA}, which can be calculated from the following relationship (see Aguirre, 1977)

$$C_{EA} = \left[\frac{1}{(f^* U^*)^2} - 1 \right] m^*. \qquad (11)$$

At the point of peak amplitude, as can be seen in Table 1 C_{EA} is close to unity, which corresponds to the ideal value from potential-flow theory; it should be noted that C_{EA} decreases monotonically with U^* from values as high as 20 to as low as -8. The very wide variation of C_{EA} values suggests that this empirically determined coefficient does not reflect variations in the actual inertial force due to the added mass.

In contrast to the abrupt jump in ϕ_x, the phase lag between the transverse force and the cylinder displacement ϕ_y displays a rather smooth variation over the excitation region as shown in Figure 8. As the reduced velocity is increased from low to high values, ϕ_y increases from 26° to 111° for $Re = 100$, whereas ϕ_y increases from 17° to 105° for $Re = 200$. It should be noted that phase-angle values are meaningful in the range $\phi_y \in [0°, 180°]$ because the frequency of $F_y(t)$ is half the frequency of $x_c(t)$. We consider that the smooth variation of ϕ_y with U^* may be attributable to a gradual shift in the timing of vortex shedding with the vibration frequency as illustrated in previous works with regard to a fixed cylinder exposed to a free stream with small amplitude oscillations of the velocity superimposed on the mean (Konstantinidis *et al.* , 2005; Konstantinidis & Liang, 2011). The later case is kinematically equivalent to a cylinder oscillating in-line with the free stream so that findings in related works are also applicable to the present configuration. Furthermore, we have verified this hypothesis by checking the distributions of vorticity at different phases during a cycle of cylinder oscillation for different reduced velocities (see Konstantinidis *et al.* , 2021).

The final step in this study was to calculate the magnitude of the vortex drag coefficient C_{dv} and the phase-angle between the vortex drag and the cylinder displacement ϕ_{dv} as defined per equation (3). Figure 9 shows that the vortex drag is considerably lower at $Re = 100$ than at 200, which resembles the influence of Reynolds number on the rms magnitude of the transverse force C'_y (see Fig. 4). At each Re value, C_{dv} displays a resonant-like amplification in the U^*

range where the peaks in the amplitude response occur; this amplification is much more pronounced at $Re = 200$ than at 100, which might be attributable to the much higher amplitudes of cylinder response found in the former case. Figure 10 shows that ϕ_{dv} increases smoothly from an asymptote at 0° to another one at approximately 180° as U^* is increased over the prescribed range. The variation of ϕ_{dv} with U^* is very similar to that of ϕ_y, thereby revealing the explicit relationship between the phasing of vortex shedding and the phasing of the vortex drag.

4. CONCLUSIONS

In this work, we have investigated the vortex-induced vibration of a circular cylinder constrained elastically so that it can oscillate only in-line with a free stream by means of numerical simulations at low Reynolds numbers. The non-dimensional forms of the governing equations of fluid motion were solved using an in-house CFD code based on the finite-difference method in tandem with the integration of Newton's second law of cylinder motion. Results were reported for two Reynolds numbers of 100 and 200 at fixed values of the mass and damping ratios of $m^* = 10$ and $\zeta = 0$, respectively. At these Reynolds numbers, the response amplitude as a function of the reduced velocity displays a single excitation region that is associated with alternating vortex shedding. This contrasts earlier results at moderately high Reynolds numbers, which display two excitations regions associated with symmetrical and alternating vortex shedding, respectively. The peak amplitude increases by a factor of approximately six between $Re = 100$ and 200 reaching a value of 1.4% of the cylinder diameter in the latter case. We have further noted that at peak amplitude of in-line response the effective added mass coefficient is close to its ideal value of unity pertinent to potential flow. We have employed the phasing of the unsteady transverse (lift) force with regard to the in-line displacement in order to decipher the vortex dynamics in the wake. Unlike the unsteady in-line force acting along the direction of cylinder oscillation, which is restricted per the equation of cylinder motion to phase angles of 0° and 180°, the phase of the unsteady lift force displays a gradual increase with the reduced velocity, which indicates that the timing of vortex shedding in the wake shifts gradually with the oscillation frequency. We have found that although the process of formation and shedding of vortices in the wake and the magnitude of the vortex-induced forces on the cylinder (i.e. excluding inertial forces due to the acceleration of the cylinder) do not depend strongly on the reduced velocity, the phasing of the forces with respect to the displacement changes very considerably. An analytical model based on the extension of Morison's equation to include a separate third term for the vortex drag was able to explain how the changes in the timing of vortex shedding yield the phasing required to satisfy the equation of in-line motion. Therefore, the present study provides physical insight to uncouple the fluid from the structural dynamics in vortex-induced vibration.

Acknowledgements

The research was supported by the project EFOP-3.6.1-16-00011 "Younger and Renewing University – Innovative Knowledge City – institutional development of the University of Miskolc aiming at intelligent specialisation" in the framework of the Széchenyi 2020 program. The realization of this project is supported by the European Union, co-financed by the European Social Fund.

5. REFERENCES

Aguirre, J.E. 1977. *Flow-induced in-line vibrations of a circular cylinder*. Ph.D. thesis, Imperial College of Science and Technology.

Baranyi, L. 2008. Numerical simulation of flow around an orbiting cylinder at different ellipticity values. *Journal of Fluids and Structures*, **24**(6), 883 – 906.

Bearman, P. W. 1984. Vortex Shedding from Oscillating Bluff Bodies. *Annual Review of Fluid Mechanics*, **16**(1), 195–222.

Bearman, P. W. 2011. Circular cylinder wakes and vortex-induced vibrations. *Journal of Fluids and Structures*, **27**(5), 648 – 658.

Bishop, R. E. D., & Hassan, A. Y. 1964. The lift and drag forces on a circular cylinder oscillating in a flowing fluid. *Proceeding of Royal Society of London A*, **277**(1368), 51–75.

Bourguet, R., & Lo Jacono, D. 2015. In-line flow-induced vibrations of a rotating cylinder. *Journal of Fluid Mechanics*, **781**, 127–165.

Cagney, N., & Balabani, S. 2013. Wake modes of a cylinder undergoing free streamwise vortex-induced vibrations. *Journal of Fluids and Structures*, **38**, 127 – 145.

Cagney, N., & Balabani, S. 2016. Lagrangian structures and mixing in the wake of a streamwise oscillating cylinder. *Physics of Fluids*, **28**(4), 045107.

Dorogi, D., & Baranyi, L. 2018. Numerical simulation of a freely vibrating circular cylinder with different natural frequencies. *Ocean Engineering*, **158**, 196 – 207.

Gurian, T. D., Currier, T., & Modarres-Sadeghi, Y. 2019. Flow force measurements and the wake transition in purely inline vortex-induced vibration of a circular cylinder. *Physical Review Fluids*, **4**, 034701.

Harlow, F. H., & Welch, J. E. 1965. Numerical calculation of time-dependent viscous incompressible flow of fluid with free surface. *The Physics of Fluids*, **8**(12), 2182–2189.

King, R. 1977. A review of vortex shedding research and its application. *Ocean Engineering*, **4**(3), 141 – 171.

Konstantinidis, E., & Bouris, D. 2017. Drag and inertia coefficients for a circular cylinder in steady plus low-amplitude oscillatory flows. *Applied Ocean Research*, **65**, 219 – 228.

Konstantinidis, E., & Liang, C. 2011. Dynamic response of a turbulent cylinder wake to sinusoidal inflow perturbations across the vortex lock-on range. *Physics of Fluids*, **23**(7), 075102.

Konstantinidis, E., Balabani, S., & Yianneskis, M. 2005. The timing of vortex shedding in a cylinder wake imposed by periodic inflow perturbations. *Journal of Fluid Mechanics*, **543**, 45–55.

Konstantinidis, E., Dorogi, D., & Baranyi, L. 2021. Resonance in vortex-induced in-line vibration at low Reynolds numbers. *Journal of Fluid Mechanics*, **907**, A34.

Morison, J. R., O'Brien, M. P., Johnson, J. W., & Schaaf, S. A. 1950. The force exerted by surface waves on piles. *AIME Petroleum Transactions*, **189**, 149–154.

Naudascher, E. 1987. Flow-induced streamwise vibrations of structures. *Journal of Fluids and Structures*, **1**(3), 265 – 298.

Okajima, A., Nakamura, A., Kosugi, T., Uchida, H., & Tamaki, R. 2004. Flow-induced in-line oscillation of a circular cylinder. *European Journal of Mechanics - B/Fluids*, **23**(1), 115 – 125.

Sarpkaya, T. 2004. A critical review of the intrinsic nature of vortex-induced vibrations. *Journal of Fluids and Structures*, **19**(4), 389 – 447.

Tanida, Y., Okajima, A., & Watanabe, Y. 1973. Stability of a circular cylinder oscillating in uniform flow or in a wake. *Journal of Fluid Mechanics*, **61**(4), 769–784.

Williamson, C.H.K., & Govardhan, R. 2004. Vortex-induced vibrations. *Annual Review of Fluid Mechanics*, **36**(1), 413–455.

Wootton, L. R., Warner, L., Warner, M., Sainsbury, R. N., & Cooper, D. E. 1972 (August). *Oscillation of piles in marine structures : a description of the full-scale tests at Immingham*. Tech. rept. 40. CIRIA.

EXPERIMENTAL INVESTIGATION OF VORTEX-INDUCED VIBRATIONS OF A CIRCULAR CYLINDER UNDER ROTARY OSCILLATIONS

Agathe Schmider, Franck Kerhervé, Laurent Cordier & Andreas Spohn
Institut Pprime, CNRS, Université de Poitiers, ISAE-ENSMA, Poitiers, France

Nicolas Dellinger
ICUBE, Université de Strasbourg, Strasbourg, France

ABSTRACT

The vortex-induced vibrations (VIV) of a rotating circular cylinder have been investigated in a specially designed free-surface water channel. The cylinder is elastically-mounted on an air-bearing platform and is free to oscillate in the cross-flow direction. Two DC motors are coupled to the oscillating mass. They allow: (i) to simulate positive or negative damping by forcing, (ii) to measure the position and rotational speed of the cylinder, (iii) entrain the rotational motion of the cylinder. The dynamical response of the system presents a typical two or three branch response amplitude depending on the damping ratio. We describe one case with oscillating cylinder rotation where VIV are amplified. Flow velocity surveys obtained with Particle Image Velocimetry (PIV) are also reported to compare the different VIV wake modes.

1. INTRODUCTION

The formation of vortex structures around a bluff body immersed in a flow has been extensively studied in fluid mechanics as it is a question of major practical interest. If this body has a suitable natural resonance frequency or flexibility of motion, a fluid-structure interaction phenomenon may arise. The more the frequency of the vortex shedding coincides with the natural frequency of the mechanical system, the greater the induced vibrations are. The direct consequences are damage of engineering structures or the generation of noise in the presence of strong winds. This phenomenon, commonly called "vortex-induced vibrations" (VIV), is also at the origin of energy extraction test devices, such as the one of the VIVACE project (Bernitsas *et al.*, 2008), which consists of an elastically mounted cylinder connected to a generator. Such devices are usually modeled as a damped mass-spring system. It is therefore necessary to analyze the influence of the different model parameters on the dynamics. While former studies focus on arrangements with constant viscous damping, this study takes advantage of a device with adjustable mechanical characteristics. In this work, several mechanical parameters are controlled in a non-intrusive way (Lee *et al.*, 2011), such as the damping or the forced rotation of the cylinder around its main axis. The damping is achieved by a DC motor, as proposed by Dellinger *et al.* (2018).

Early studies on VIV control focused on vibration reduction or suppression (Zdravkovich, 1981). For this purpose, cylinder rotation turned out to be efficient (Du and Sun, 2015, for instance). The numerical study of Bourguet (2019) at low Reynolds number shows that cylinder rotation can also intensify the oscillations. Experimental studies on the influence of cylinder rotation on the oscillation amplitudes remain scarce until recently (Wong *et al.*, 2018; Huera-Huarte, 2020). The team from the Flair laboratory at Monash University (Zhao *et al.*, 2014b,a; Zhao, 2012; Soti *et al.*, 2018), has observed several cases of alternating rotations in which the oscillations are strongly enhanced (Wong *et al.*, 2018). Our experimental setup was specifically designed to achieve similar values of rotation rates to study the impact of cylinder rotation on free oscillations in more detail.

2. EXPERIMENTAL DEVICE

2.1. Water channel

The experiments are conducted in the Hydra III water tunnel at Institut Pprime (Poitiers, France). The overall set-up is schematically represented in Figure 1. The flow is entrained by an axial pump located in the return flow of the closed circuit water tunnel. The test section is 2.1 m long, 0.51 m wide and 0.51 m height and is made of glass windows to allow optical access from both sides, as well from below. The water depth in the test section is fixed to 0.33 m. The freestream velocity ranges from 5 to 45 $\mathrm{cm\,s^{-1}}$. The flow uniformity all along the test section was checked in different planes by two-dimensional two-component (2D-2C) Particle Image Velocimetry (PIV). The measured deviation from flow uniformity of the velocity pro-

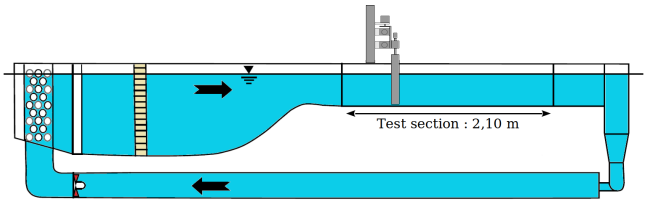

Figure 1. Side view of the water channel (Hydra III) and position of the experimental arrangement.

files is less than 1%. The measured flow unsteadiness is less than 5% in the whole range of velocities.

2.2. Oscillating device

The oscillating device is shown in Figure 2. A circular hollow cylinder made in aluminum of diameter $D = 50$ mm, length $L = 0.4$ m and thickness $e = 1.8$ mm is vertically immersed in the water channel. The aspect ratio $AR = L/D = 8$ is just high enough to ensure parallel shedding (Szepessy and Bearman, 1992). The blockage ratio due to the presence of the cylinder in the test section is 10%. A gap between the cylinder end and the channel floor is set to 2 mm. The cylinder is mounted on a platform made in aluminum which supports three OAV air bearings which are supplied by pressurized air at 4 bars. These air bearings guide the mobile platform with negligible mechanical friction in the cross-flow direction along two shafts made in high precision stainless steel of 20 ± 0.02 mm diameter. A pair of linear springs (LeeSpings LE014B13S) mounted in parallel on each side furnish the restoring force. The resulting total stiffness coefficient is $k = 0.022$ N mm^{-1}. A low inertia 24V DC servo motor with a dual track encoder is coupled to the oscillating platform with a rack and pinion mechanism. Such arrangement results in additional dry friction due to the mechanical coupling. The motivations for such arrangement is threefold. First, it allows to measure in real-time accurately and robustly the position y and velocity $\dot{y}$ of the cylinder. Second, it allows to quantify the energy that can be harvested from the oscillating system by measuring on-line the generated current. Last, the motor can be used to move arbitrarily the cylinder or to simulate positive or negative damping effect, such as to compensate for the additional source of friction (see below), for instance.

With this arrangement, the cylinder can operate displacement over $\pm 2D$ in the cross-flow direction with minimal damping. The overall oscillating mass is $m = 2.486$ kg which results in a mass ratio $m^* = m/m_A = 3.8$ with m_A the displaced mass of water.

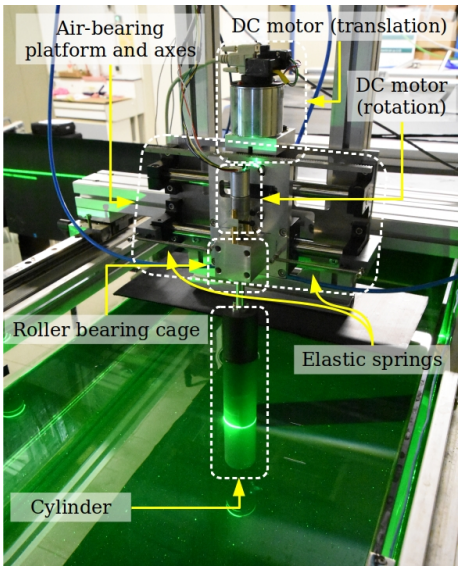

Figure 2. Experimental VIV device.

2.3. Rotating device

The cylinder is fixed on an aluminum shaft guided by two ball bearings mounted in an aluminum cage. The rotation is enabled by a second, very light (6 volt) DC motor to limit the mass of the moving parts. Three models of motors can be used to change the maximum speed reached by the motor (between 100 and 300 rpm). This motor is controlled by a pulse width modulation (PWM) signal from an Arduino Due interfacing the motor with the rest of the acquisition system (see section 2.4). The choice for our experiments of a DC motor comes from the ease of implementation of a PWM command to control the torque. The motor is also equipped with an encoder with 11 pulses per revolution which allows to have a feedback on the angular position of the cylinder. The cylinder is forced to rotate periodically about its axis with a rotation speed given by $\Omega(t) = \Omega_0 sin(2\pi f_r t)$. This gives an alternating rotation at frequency f_r with a maximum speed Ω_0. In order to compare our results with the literature, the dimensionless parameter $\alpha = \Omega_0 D/2U_\infty$ defines the reduced rotation speed. Targeting energy harvesting, our objective is to determine if the oscillations amplitudes in the VIV regime can be increased by periodic cylinder rotations. At this end, simultaneous measurements of cylinder displacement, cylinder rotation speed and velocity fields by 2D2C PIV have been performed.

2.4. Instrumentation

The 24V DC motor is directly used to measure both the displacement y and velocity $\dot{y}$ of the cylinder. The in-built encoder provides TTL output signals with

500 pulses per revolution and enables to measure position and speed with a ± 0.15 mm accuracy. Both signals are sampled at 500 Hz with a NI PXIe-6356 I/O acquisition card. A planar two-component particle image velocimetry (PIV) system is used for velocity surveys in the near-wake of the cylinder. The PIV system includes a Nano L $50-50$ PIV laser from Litron Ltd (wavelength 532 nm) of 50 mJ per pulse and a Dantec SpeedSence 1040 camera with a resolution of 2320×1726 pixels. This camera is oriented towards the wake region, through a mirror inclined at 45° installed underneath the water channel. The measurement plane is located at mid-height of the water channel and covers a region of $8D \times 9D$ including the cylinder. The laser sheet is 1 mm thick. Polyamide particles of 50 µm diameter are used for flow seeding. The instantaneous vector fields are obtained using the acquisition software Davis 10 from Lavision. A dynamic mask following the cylinder displacement is used to avoid spurious correlations. The location of the mask for a given pair of images is set by the simultaneous measurements of the cylinder location. A conventional direct cross-correlation process including multipass windows (from 64×64 to 32×32) with 50% overlapping is used, leading to a final vector spacing of $0.09D$ in both directions. A bad-vector-replacement step is provided using a 5×5 median interpolation method. Finally, for a given PIV run, 3000 snapshots sampled at $f_{\mathrm{PIV}} = 15$ Hz, covering approximately 50 oscillations of the cylinder, are acquired.

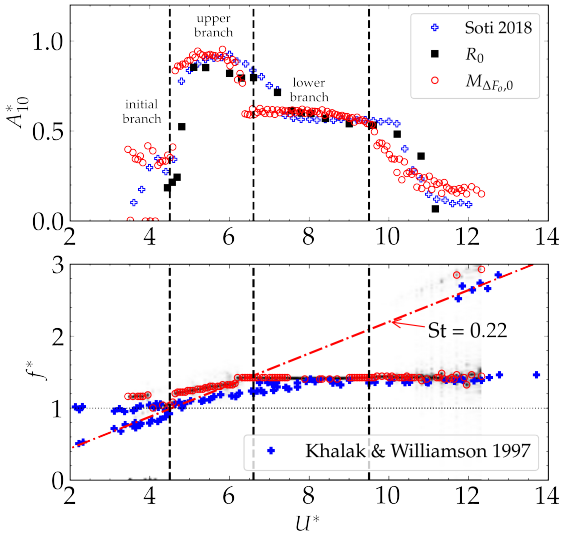

Figure 3. Structural vibration of non-rotating cylinder undergoing VIV for the "frictionless" configuration ($M_{\Delta F_o,0}$).(a) Normalised amplitude response A^*_{10} as a function of reduced velocity U^*. Comparison with the results of Soti et al. *(2018) and Khalak and Williamson (1997). $A^*_{10} = A_{10}/D$ where A_{10} is the average amplitude calculated over the responses whose maximum amplitude is among the highest 10%. (b) Frequency responses as a function of U^* and comparison with the results of Khalak and Williamson (1997)*

Hereafter, we denote by $M_{\Delta F_o,\alpha}$, the previous experimental device without friction for which the cylinder is rotating at the rotation rate α. By extension, $M_{\Delta F_o,0}$ corresponds to the case without rotation.

3. RESULTS

3.1. Validation of the experimental device

In this section, we compare the configuration $M_{\Delta F_o,0}$ with previous experimental works. The comparison is based on equivalent values of $m^*\zeta$ as in Soti *et al.* (2018); Khalak and Williamson (1997) where ζ, the structural damping ratio, is approximately equal to 0.020. The amplitude response is shown in Figure 3(a) as a function of reduced velocity $U^* = U_\infty/f_{\mathrm{nw}}D$ where f_{nw} is the natural frequency of the system. The non-rotating configuration $M_{\Delta F_o,0}$ exhibits a typical three-branch response : (i) an initial branch ($U^* \leq 4.8$) with low oscillation amplitude, (ii) an upper branch located in the range $4.8 \leq U^* \leq 6.6$ where the cylinder experiences the largest oscillation amplitudes (approximately $0.8D$), and (iii) a lower branch in the range $6.6 \leq U^* \leq 9.5$ where the amplitude is limited to about $0.55D$. The so-called desynchronized region obtained for $U^* > 9.5$ is characterized by negligible oscillations. The normalized frequency response is shown in Figure 3(b). The power spectral density (PSD) of the displacement was evaluated for a given value of the reduced velocity to extract the frequency of the largest energy peak. Along the initial branch, the frequency response of the cylinder f_{VIV} is equal to the vortex release frequency f_{sh}, measured as $0.21U_\infty/D$. Moving to the lower branch, the cylinder frequency increases slightly to lock approximately on f_{nw}. This is illustrated by the dashed horizontal line obtained for $f^* = f_{\mathrm{VIV}}/f_{\mathrm{nw}} = 1$. The frequency response along the upper and lower branches is said to be synchronized until it reaches the desynchronized region. In the latter, the frequency response reaches the vortex release frequency again, while the response may also undergo low amplitude modulation at the natural frequency. In this region, the PSDs effectively exhibit two frequency peaks. These results are consistent with those reported in the literature for comparable values of structural damping ratio $m^*\zeta$ (Soti *et al.*, 2018; Khalak and Williamson, 1997). They suggest

that the $C_{\Delta^*_f,0}$ configuration covers the expected parameter range. This configuration without rotation will be considered as reference case in the following.

3.2. Rotary oscillations

The hydrodynamic force due to the production of circulation by a rotating cylinder inside a uniform flow has been known as the "Magnus effect" (Seifert, 2012). This force is proportional to the angular velocity Ω_0 and to the free stream velocity U_∞. In what follows we study the impact of this force on the cylinder oscillations and the wake flow.

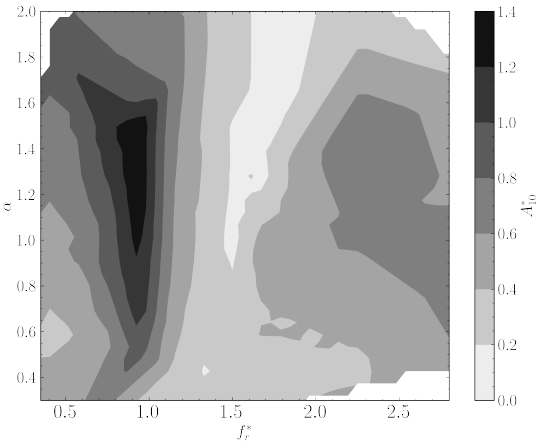

Figure 4. Iso-values of the amplitude response A^*_{10} in the parameter space defined by (f^*_r, α) at $U^* = 8.4$ (lower branch of $M_{\Delta F_o,0}$).

3.2.1. Lock-in cases identification

In this case the cylinder rotates at angular speed Ω. We explore the parameter space (f^*_r, α) with $f^*_r = f_r/f_{\mathrm{VIV}}$ to determine the parameters for which VIV are increased by periodic rotations of the cylinder. For this survey, the reduced velocity U^* is fixed to 8.4. This value corresponds to the middle of the lower branch of $M_{\Delta F_o,0}$ with limited oscillation amplitudes ($A^*_{10} \approx 0.55$). The range of the parameter space is restricted by the characteristics of the DC motor and by the length of the air-bearings shafts, which were designed for oscillation amplitudes $A^* \leq 2D$. Figure 4 shows the iso-values of the normalised amplitude response. Two regions are clearly visible with VIV intensification by rotation. For $f^*_r \approx 1$, the cylinder undergoes high amplitude oscillations which are comparable to the upper branch cases. The amplitudes of the oscillations are not very sensitive to variations of α between 0.9 and 1.6. For the highest values of α, the oscillations start at a lower frequency. When the forcing frequency is further increased, the amplitude of the oscillations drastically decreases until they are fully canceled. By further increasing the forcing frequency, the second zone of strong oscillations is reached. For frequencies $f^*_r \approx 2.5$, the oscillation amplitude reaches levels 5 to 10% higher than the reference case without rotation. These two regions of VIV amplification have also been observed by Wong *et al.* (2018) in their experimental work. Thereafter, we focus on the case $\alpha = 0.9$ and $f^*_r = 1$, where the amplification is strongest.

3.2.2. VIV intensification by rotary oscillations

The amplitude responses displayed in Figure 5 are obtained by modifying the upstream velocity by steps of 1 $\mathrm{cm\,s^{-1}}$, first increasing, then decreasing. The general shape of the amplitude variation differs from the previously obtained reference case $M_{\Delta F_o,0}$. For reduced speeds $U^* < 7$, a decrease in the oscillation amplitudes is observed. As the reference case shifts to the upper branch, the oscillation amplitudes continue to increase until they reach a plateau for $U^* \approx 8$. Clearly, our measurements are consistent with those obtained experimentally by Wong *et al.* (2018), even if we obtain strong deviations for values of U^* higher than 7.5, depending on the whether the velocity is increasing or decreasing. This result can be explained by the use of a DC motor with torque control which induces a dispersion in the peak rotation speeds.

The oscillation amplitudes are greatly increased by the use periodic rotations of the cylinder. In Section 3.2.4, we further investigate the characteristic time necessary to establish the Magnus force in order to better understand its impact on the oscillation amplitude.

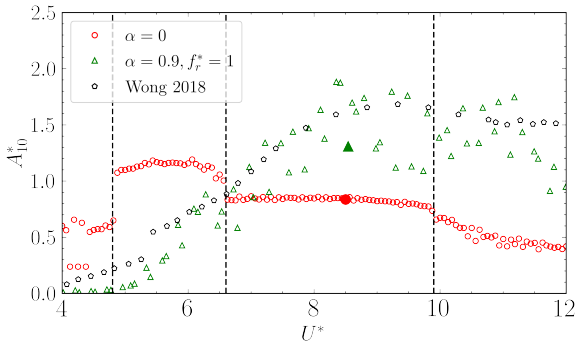

Figure 5. Amplitude response A^*_{10} as a function of U^* for $M_{\Delta F_o,0}$ (red circles) and $M_{\Delta F_o,\alpha=0.9,f^*_r=1}$ (green triangles). Comparison with the results of Wong et al. *(2018) obtained at $\alpha = 1$ and $f^*_r = 1$ (black pentagons).*

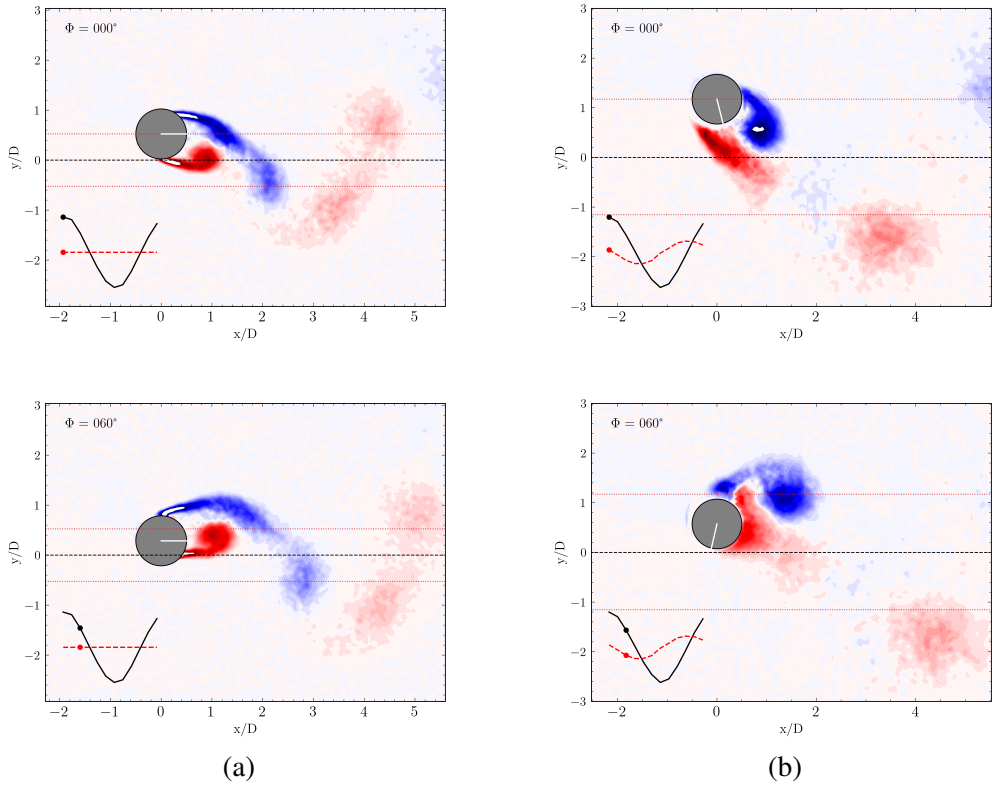

Figure 6. Phase-averaged vorticity contours at $U^* = 8.4$. (a) no rotation ($M_{\Delta F_o,0}$), (b) Periodic rotations of the cylinder ($M_{\Delta F_o,\alpha=0.89,f_r^*=1}$). Graphs in the bottom left corner show the linear position (black line) and the angular velocity (red dashed line) of the cylinder.

3.2.3. Wake patterns with periodic rotations of the cylinder

Since the frequency response of the oscillating cylinder is quasi-periodic (see Section 3.1), the formation of the vortices in the cylinder wake is analyzed with a phase-averaged approach. In what follows, the phase-averaged velocity is defined according to the phase $\phi_i \in [0, 360°]$ $(i = 0\ldots, N_\phi)$ of the dominant oscillation period, where N_ϕ denotes the total number of phases considered. Due to a slight variation in time of the period of the dominant oscillation ($\pm 6\%$), the temporal position of a given phase changes slightly between two consecutive maxima. Therefore, the instants corresponding to a given phase ϕ_i are first evaluated independently for each oscillation period. For a given value ϕ_i, the PIV fields corresponding to the range $[\phi_i \pm \Delta\phi]$ are then collected and averaged to form the phase-averaged velocity fields $\overline{\boldsymbol{u}_i}$. The latter thus describes, on average, the velocity field obtained in the wake of the cylinder at a given phase instant of the VIV process. In the following, we consider $N_\phi = 12$ and $\Delta\phi = 10°$. The latter value has been found to present a good compromise between the phase localization and the number of PIV snapshots necessary to get a satisfactory statistical convergence. The obtained two-dimensional phase-averaged velocity field is then used to compute a phase-averaged vorticity field from which wake regimes can be identified. In Figure 6, we compare at $U^* = 8.4$ the phase-averaged vorticity contours obtained for $\alpha = 0.89$ and $f_r^* = 1$ to the reference case without rotation. In this figure, the cylinder moves from one of its extreme positions to the other. Figure 6(a) corresponds to the VIV regime in the middle of the lower branch ($U^* = 8.5$) of the reference configuration without rotation. The wake exhibits two vortices of opposite sign shed per half cycle of oscillation to form pairs of opposite vortices. This pattern is commonly called $2P$ (Williamson and Roshko, 1988; Morse and Williamson, 2009). The two vortices released per oscillation cycle have similar intensity and persist downstream. We observe a double row of vortex pairs with a spacing of $1.5D$ in the flow direction and about $2D$ tranversal distance. While on the lower branch, the cylinder undergoes oscillations with a smaller amplitude than in the upper branch. The first vortex released in the oscillation cycle is pushed further away from the centerline due to the equivalent action of the second vortex. Figure 6(b) corresponds to the case of the forced VIV regime

obtained at $\alpha = 0.89$ and $f_r^* = 1$. In the far wake, we observe two rows of counter-rotating vortices with a lateral spacing of about $3.5D$, respectively $4D$ in the flow direction. In contrast to the case without rotation, the vortices do not appear to stay pair by pair. Instead, a second, weaker vortex appears to form during the shedding process. Moreover, the vortex sheet connection between two vortices of the same direction of rotation is no longer present in the case with rotation. The wake is twice as wide as in the reference case, consistent with the increase in the amplitude of the oscillations.

3.2.4. *Time scale of transient Magnus effect*

The objective of this section is to better understand how the periodic rotation of the cylinder can increase the VIV amplitudes. For this, we seek to determine the characteristic time of the Magnus effect. A step perturbation of reduced rotation speed α is introduced (see Figure 7(Bottom)). During the experiment, the transient evolution of the velocity field is measured to estimate the flow circulation. The impact of the cylinder shadow on the PIV measurements is avoided by orienting a second laser in such a way as to illuminate the whole horizontal light sheet at mid-height of the cylinder. Synchronization constraints related to the use of two lasers limit the acquisition frequency to $f_{\mathrm{PIV}} = 17$ Hz. The field of view is about $3.5D \times 3.5D$ and is aligned with the cylinder axis. The spatial resolution of the vector field is $\Delta x = \Delta y = 0.051D$. Figure 7(top) represents the mean velocity fields calculated at $\alpha = 0$ and $\alpha = 0.82$. The influence of the contour choice on the value of the circulation $\Gamma = \oint_C \boldsymbol{V} \cdot \boldsymbol{dl}$ is studied by considering several circles of diameter $D + \delta D$ with δD varying in the range $[\Delta x, 10\Delta x]$. The values of Γ evolving only slightly with the choice of the contour, $\delta D = 3\Delta x$ is retained. Figure 7(top left) shows that without rotation of the cylinder the wake is symmetric whereas an asymmetry appears when the cylinder is rotating (see Figure 7(top right)). This observation is consistent with the evolution of the circulation (see Figure 7(bottom)). When the cylinder rotates, the average circulation is strongly increased, going from a value close to zero, to an average value of 5 $\mathrm{m^2\,s^{-1}}$. All along the dynamical evolution of the cylinder, the circulation evolves at frequency f_{sh}. The time necessary to establish the Magnus force is estimated using a moving average of Γ. Let $\tau_{0.9}$ be the time needed for the moving average to reach 90% of its average value when the cylinder is rotating, we get $\tau_{0.9} \times f_{\mathrm{sh}} \approx 1$. The Magnus force has then a characteristic time similar to that of the vortex shedding. In consequence, these two phenomena could dynamically enter in competition or in collaboration.

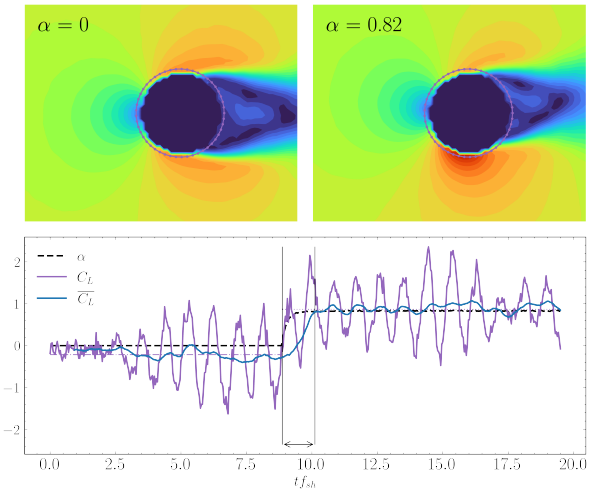

Figure 7. Top: Norm of the mean velocity without rotation ($\alpha = 0$, left) and with constant rotation ($\alpha = 0.82$, right). Bottom: Temporal evolution of the rotation speed of the cylinder α and the lift coefficient $C_L = 2\Gamma/DU_\infty$, with Γ calculated on the purple contours represented on the mean velocity fields. The moving average of C_L is shown as a continuous blue line. The horizontal lines are the mean circulations before and after the rotation has started. The free stream velocity is fixed at $0.17\ \mathrm{m\,s^{-1}}$.

4. CONCLUSION

In this paper, we have shown some experimental results of vortex-induced vibrations obtained with a specifically designed elastically mounted cylinder. The described setup has the particularity to present an adjustable damping coefficient by acting on a DC motor. The experiments that have been conducted show that the device reproduces oscillation regimes ranging from low- to high-mass ratio configurations and produces responses similar to those reported in the literature. A second DC motor was used to entrain periodic cylinder rotations along the vertical axis. Our results confirmed the efficiency of rotational forcing to increase the vibration amplitude, particularly in the high reduced velocity regimes ($U^* > 7$). The transient Magnus effect appears to have the same time scale as the vortex shedding. For $f_r^* = 1$, the two phenomena are superimposing each other leading to increased amplitude ocillations. Using PIV velocity measurements, we identified the dynamic patterns in the wake. We show that for the rotating cylinder, the second vortex is weaker than the first one and does not persist further in the wake, much similarly to a typical upper branch $2P_0$ wake regime. The next step

is to control the amplitude of the oscillations by modifying the periods of oscillation for the rotational motion of the cylinder.

5. REFERENCES

Bernitsas, M. M., Raghavan, K., Ben-Simon, Y., and Garcia, E. M. H. (2008). VIVACE (Vortex Induced Vibration Aquatic Clean Energy): A New Concept in Generation of Clean and Renewable Energy From Fluid Flow. *Journal of Offshore Mechanics and Arctic Engineering*, **130**(4).

Bourguet, R. (2019). Flow-induced vibrations of a rotating cylinder in an arbitrary direction. *Journal of Fluid Mechanics*, **860**, 739–766. Publisher: Cambridge University Press.

Dellinger, N., François, P., Lefebure, D., Mose, R., and Garambois, P.-A. (2018). An experiment of a hydropower conversion system based on vortex-induced vibrations in a confined channel. *Renewable Energy*, **115**, 54–63.

Du, L. and Sun, X. (2015). Suppression of vortex-induced vibration using the rotary oscillation of a cylinder. *Physics of Fluids*, **27**(2), 023603.

Huera-Huarte, F. J. (2020). Vortex-induced vibrations of a low mass-damping rigid circular cylinder with forced periodic rotations. *Physical Review Fluids*, **5**(12), 124701. Publisher: American Physical Society.

Khalak, A. and Williamson, C. H. K. (1997). Investigation of relative effects of mass and damping in vortex-induced vibration of a circular cylinder. *Journal of Wind Engineering and Industrial Aerodynamics*, **69-71**, 341–350.

Lee, J. H., Xiros, N., and Bernitsas, M. M. (2011). Virtual damper–spring system for VIV experiments and hydrokinetic energy conversion. *Ocean Engineering*, **38**(5), 732–747.

Morse, T. L. and Williamson, C. H. K. (2009). Prediction of vortex-induced vibration response by employing controlled motion. *Journal of Fluid Mechanics*, **634**, 5–39.

Seifert, J. (2012). A review of the Magnus effect in aeronautics. *Progress in Aerospace Sciences*, **55**, 17–45.

Soti, A. K., Zhao, J., Thompson, M. C., Sheridan, J., and Bhardwaj, R. (2018). Damping effects on vortex-induced vibration of a circular cylinder and implications for power extraction. *Journal of Fluids and Structures*, **81**, 289–308.

Szepessy, S. and Bearman, P. W. (1992). Aspect ratio and end plate effects on vortex shedding from a circular cylinder. *Journal of Fluid Mechanics*, **234**, 191–217.

Williamson, C. and Roshko, A. (1988). Vortex formation in the wake of an oscillating cylinder. *Journal of Fluids and Structures*, **2**(4), 355–381.

Wong, K. W. L., Zhao, J., Lo Jacono, D., Thompson, M. C., and Sheridan, J. (2018). Experimental investigation of flow-induced vibration of a sinusoidally rotating circular cylinder. *Journal of Fluid Mechanics*, **848**, 430–466.

Zdravkovich, M. M. (1981). Review and classification of various aerodynamic and hydrodynamic means for suppressing vortex shedding. *Journal of Wind Engineering and Industrial Aerodynamics*, **7**(2), 145–189.

Zhao, J. (2012). *Flow-Induced Vibration of Circular and Square Cylinders with Low Mass and Damping*. Ph.D. thesis, Monash University.

Zhao, J., Leontini, J. S., Lo Jacono, D., and Sheridan, J. (2014a). Chaotic vortex induced vibrations. *Physics of Fluids*, **26**(12), 121702.

Zhao, J., Leontini, J. S., Jacono, D. L., and Sheridan, J. (2014b). Fluid–structure interaction of a square cylinder at different angles of attack. *Journal of Fluid Mechanics*, **747**, 688–721.

FLOW-INDUCED VIBRATIONS OF A FLEXIBLY MOUNTED CYLINDER IN THE PROXIMITY OF A STATIONARY PARALLEL CYLINDER

Mahdi Riazat, Mojtaba Kheiri & Brian C. Vermeire
Department of Mechanical, Industrial & Aerospace Engineering, Montréal, QC, Canada

ABSTRACT

This paper presents the results from a computational study on the flow-induced vibrations of a flexibly mounted cylinder (with diameter d) placed in the proximity of a stationary side-by-side cylinder (with diameter D) at Reynolds number $Re_d = 100$. The flexibly mounted cylinder has the combined mass-damping ratio $m^*\zeta = 0.1$ and can freely vibrate in the transverse direction with respect to the oncoming flow. Two gap ratios $g^* = g/d = 0.75$ and 1.75 and five diameter ratios $d^* = D/d = 0.5$, 1, 1.25, 1.5, and 2.5 are examined. The arbitrary Lagrangian-Eulerian form of the Navier-Stokes equations are solved using the Discontinuous Galerkin method for the fluid, and a mass-damper-spring system is used to model the structural dynamics.

1. INTRODUCTION

It is well-known that bodies with *bluff* cross-sections subjected to cross-flow, such as risers, mooring cables, and chimney stacks are prone to vortex-induced vibrations (VIV) (Williamson & Govardhan, 2004). Motivated by several engineering applications, such as offshore platforms, risers and heat exchangers, some studies aimed to examine the flow dynamics and fluid-structure interactions (FSI) among multiple cylinders placed in tandem/staggered arrangement: experimental and numerical studies by Qin *et al.* (2017); Assi *et al.* (2013); Bao *et al.* (2012); Griffith *et al.* (2017) are only a few examples.

Many studies have also been conducted on the flow-induced vibrations (FIV) of cylinders in the side-by-side (SBS) arrangement. Those performed computationally were mostly two-dimensional (2-D), and almost all considered diameter ratio of $d^* = 1$. Some earlier examples are the works of Liu *et al.* (2001); Rahmanian *et al.* (2014); Cui *et al.* (2014); Chen *et al.* (2015*a*,*b*); Liu & Jaiman (2016). Some recent examples include the works of Liu & Jaiman (2018) on the interactions between the gap flow and VIV kinematics for 3-D flow past a pair of circular cylinders, Munir *et al.* (2019) on 3-D flow past a pair of SBS cylinders rigidly connected to each other,

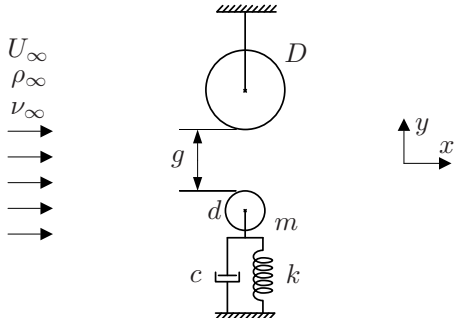

Figure 1. Schematic drawing showing a two-dimensional flexibly mounted vibrating cylinder in the side-by-side arrangement with a stationary cylinder of a generally different size.

and Janocha *et al.* (2020) on the VIV of two rigidly-coupled cylinders of different diameters (1:5) placed in the proximity of a horizontal wall in a 2-D laminar flow.

To the best of the authors' knowledge, no computational study exists that systematically examines FIV of a flexibly mounted cylinder placed side by side of another (stationary) cylinder of a different diameter. Previous studies with identical SBS cylinders in a uniform flow have considerably advanced our understanding of complex phenomena involved, including vortex-vortex, vortex-cylinder, and vortex-gap flow interactions. Nevertheless, it is not known yet how the diameter ratio would affect the FIV characteristics of the flexibly mounted cylinder, the fluid dynamic forces acting on the two cylinders, as well as vortex patterns in the wake.

2. PROBLEM STATEMENT

We investigate the 2-D problem of flow-induced vibrations of a circular cylinder of diameter d placed in the proximity and side by side of a stationary circular cylinder of diameter D; see figure 1. The gap size between the two cylinders is denoted by g. The vibrating cylinder has mass m, and its motion in the y (or transverse)-direction is restrained by a linear spring of stiffness k and a linear viscous damper of con-

stant c. The in-vacuum natural frequency of the vibrating cylinder is represented by $f_n = (1/2\pi)\sqrt{k/m}$. Here, we do not consider motion in the x (or inline)-direction. The two cylinders are subject to a uniform steady flow of velocity U_∞, density ρ_∞ and kinematic viscosity ν_∞.

3. FORMULATION AND NUMERICAL METHOD

In this paper, we solve the arbitrary Lagrangian-Eulerian (ALE) form of the Navier-Stokes equations using an in-house software which is developed for generally compressible flows (Ghoreishi & Vermeire, 2021)

$$\frac{\partial \boldsymbol{u}}{\partial t} + \nabla \cdot \boldsymbol{F} + \boldsymbol{u}(\nabla \cdot \boldsymbol{v}_g) = 0, \tag{1}$$

where $\boldsymbol{v}_g$ is the local mesh velocity and $\boldsymbol{u}$ is the vector of conserved variables given as

$$\boldsymbol{u} = \begin{bmatrix} \rho \\ \rho u_i \\ \rho E \end{bmatrix}, \tag{2}$$

in which ρu_i is a component of the momentum, and ρE is the total energy. The total flux $\boldsymbol{F} = \boldsymbol{F}_e - \boldsymbol{F}_v + \boldsymbol{F}_g$ is the sum of the inviscid Euler fluxes, the viscous Navier-Stokes fluxes, and the ALE fluxes, respectively.

Following the flux reconstruction approach, the solution is represented by a discrete approximation on each element such that (Haga & Wang, 2009)

$$\boldsymbol{u}(\boldsymbol{x},t) \approx \boldsymbol{u}^h(\boldsymbol{x},t) = \bigoplus_{i=1}^{N_e} \boldsymbol{u}_i^h(\boldsymbol{x},t), \tag{3}$$

where $\boldsymbol{u}^h(\boldsymbol{x},t)$ is the global piecewise continuous approximation of the solution and $\boldsymbol{u}_i^h(\boldsymbol{x},t)$ is a continuous representation of the solution on one of N_e elements in the domain. We take the approximate solution on each element to be a polynomial nodal basis representation such that

$$\boldsymbol{u}_i^h(\boldsymbol{x},t) = \sum_{j=1}^{N_s} \boldsymbol{u}_{i,j}(t)\phi_{s,i,j}(\boldsymbol{x}), \tag{4}$$

where $\boldsymbol{u}_{i,j}(t)$ is the value of the solution at one of N_s solution nodal basis points on a given element and $\phi_{s,i,j}(\boldsymbol{x})$ is its corresponding nodal basis function.

In this study, lifting coefficients are chosen based on the nodal basis functions to recover the discontinuous Galerkin method (Haga & Wang, 2009). At the interface flux points, we use a Rusanov Riemann solver and the second method of Bassi and Rebay (BR2) (Bassi & Rebay, 1997) to compute the common gradient for the viscous fluxes. For the fluid-structure coupling, the conventional serial staggered method is adopted (Farhat & Lesoinne, 1988).

4. VERIFICATION OF THE FORMULATION

To ensure that the present numerical approach can reliably predict the results for vibrating cylinders (i.e., where the ALE technique is adopted), we obtain numerical results for the VIV of an isolated, flexibly mounted circular cylinder for mass ratio $m^* = 10$, and structural damping ratio $\zeta = 0.01$ subjected to cross flow at $Re = 100$. Figure 2 shows the comparison between the present results (square markers) and those from Liu & Jaiman (2016) (up-triangle markers) for (a) Y^* and (b) $\overline{f}$; $Y^* = \sqrt{2}Y_{rms}/d$ being the dimensionless amplitude of vibrations and $\overline{f} = f/f_n$ being the normalized frequency. As observed, the overall agreement between the present results and those found in Liu & Jaiman (2016) is reasonably good.

5. RESULTS AND DISCUSSION

5.1. FIV of the flexibly mounted cylinder

Figure 3 shows the variation of Y^* as a function of the dimensionless (or reduced) flow velocity, $U^* = U/(f_n d)$, for the transverse displacement of the flexibly mounted cylinder for $g^* = 0.75$ for different diameter ratios. Also, numerical results for the two limiting cases $d^* \to \infty$ and $d^* \to 0$ are presented, where the former refers to a cylinder vibrating in the proximity of a wall whereas the latter correspond to an isolated vibrating cylinder. The results for $d^* \to \infty$ were taken from Tham *et al.* (2015) for a cylinder ($m^* = 10$, $\xi = 0$) vibrating in the proximity ($g^* = 0.75$) of a wall.

As seen from the figure, the lock-in region for $1.0 \leq d^* \leq 2.5$ begins at a lower flow velocity ($U^* \simeq 4$) and lasts until a higher flow velocity ($U^* > 8$), thus a wider lock-in region, compared to that for the isolated cylinder ($4.5 \lesssim U^* \lesssim 8$). On the other hand, the lock-in region for $d^* = 0.5$ begins and ends almost at the same values of U^* as those for the isolated cylinder. As seen, the peak amplitude for $0.5 \leq d^* \leq 2.5$ is generally smaller (not significantly though) than that for the isolated cylinder. Interestingly, the maximum value of Y^* does not change monotonically as the diameter ratio is increased: first, it decreases from approximately $Y^* = 0.46$ to 0.37 as the diameter ratio is increased from $d^* \to 0$ to $d^* = 1.0$, but then, it increases to $Y^* = 0.46$ when d^* is increased to $d^* = 2.5$. Such a nonlinear behaviour is perhaps the result of

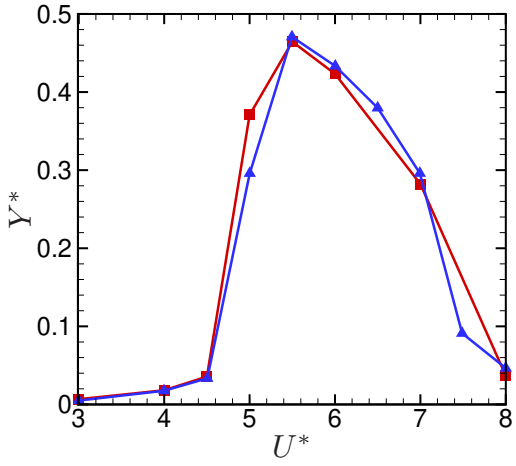

(a)

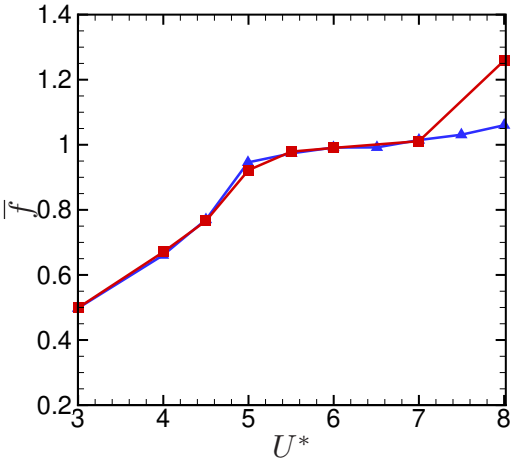

(b)

Figure 2. Variation of (a) the dimensionless amplitude, Y^*, (b) normalized frequency, $\overline{f}$, as a function of the dimensionless flow velocity, U^*, for the transverse displacement of an isolated flexibly mounted cylinder; $m^* = 10$, $\zeta = 0.01$ and $Re = 100$: [▲] Liu & Jaiman (2016), [■] present study.

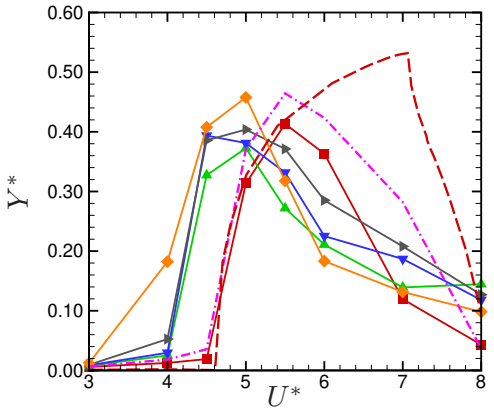

Figure 3. Variation of the dimensionless amplitude as a function of the dimensionless flow velocity for the transverse displacement of the vibrating cylinder, for the gap ratio of $g^* = 0.75$: [◆] $d^* = 2.5$, [▶] $d^* = 1.5$, [▼] $d^* = 1.25$, [▲] $d^* = 1.0$, [■] $d^* = 0.5$; also, [- - -] $d^* \to \infty$ (Tham et al., 2015), [-·-·-] $d^* \to 0$ (i.e., isolated cylinder).

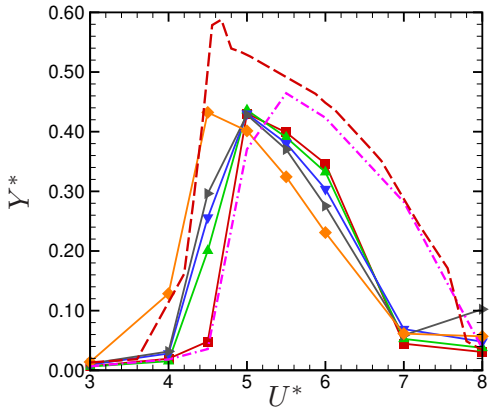

Figure 4. Variation of the dimensionless amplitude as a function of the dimensionless flow velocity for the transverse displacement of the vibrating cylinder, for the gap ratio of $g^* = 1.75$: [◆] $d^* = 2.5$, [▶] $d^* = 1.5$, [▼] $d^* = 1.25$, [▲] $d^* = 1.0$, [■] $d^* = 0.5$; also, [- - -] $d^* \to \infty$ (Tham et al., 2015), [-·-·-] $d^* \to 0$ (i.e., isolated cylinder).

complex vortex-vortex and vortex-gap flow interactions. The large maximum value of Y^* when $d^* \to \infty$ is most likely because the damping ratio was set to zero in the numerical solution in Tham *et al.* (2015).

Figure 4 shows the variation of Y^* as a function of U^* for gap ratio $g^* = 1.75$. It should be noted that the curves for the limiting case $d^* \to \infty$ (shown by dashed line), adapted from Tham *et al.* (2015), are for gap ratio $g^* = 1.5$. As seen from the figure, except for $d^* = 2.5$ (diamond), the curves for the other finite values of d^*, are nearly identical. This means that the overall dynamics of the vibrating cylinder is weakly dependent on d^*, which may appear reasonable for sufficiently large values of g^*. It is also confirmed that the maximum amplitude of vibrations of the flexibly mounted cylinder becomes smaller when placed side by side and in the proximity of a stationary cylinder.

As seen from figure 4, similarly to what was observed for $g^* = 0.75$ in figure 3, the lock-in region for the vibrating cylinder in the side-by-side arrangement begins ($U^* \simeq 3-4$) and peaks ($U^* \simeq 4.5-5$) at lower U^* values compared to an isolated cylinder. However, in contrast to what was seen for $g^* = 0.75$, for $g^* = 1.75$, the lock-in region becomes narrower for almost all the values of d^*, when compared to

an isolated cylinder. Similar findings were reported by Liu & Jaiman (2016) for $d^* = 1$. They found that the lock-in region may become narrower for sufficiently large initial gap ratios (e.g., $g^* = 2$) while it may not be narrowed for small initial gap ratios ($0.5 \lesssim g^* \lesssim 1.25$).

One may expect that Y^* curves for $d^* = 0.5$ (square) resemble more closely those for the isolated cylinder (dash-dot line) when the gap ratio is increased from $g^* = 0.75$ to 1.75; however, surprisingly, this is not true as can be confirmed visually from figures 3 and 4. On the other hand, as seen from the two figures, the peak value of Y^* generally increases as g^* increases (the only exception is at $d^* = 2.5$). This is very much expected and was confirmed by experimental and computational observations. For example, Huera-Huarte (2018) found from experiments with identical cylinders that the lock-in region begins and peaks at lower reduced velocities as the gap (or separation) between the cylinders is reduced. Moreover, smaller peak amplitudes were observed as the separation between the vibrating cylinder and the stationary cylinder was reduced.

5.2. Fluid dynamic forces acting on the cylinders

In this section and the next section, we present the numerical results on fluid dynamic forces and vortex patterns, respectively, for $g^* = 0.75$; those for $g^* = 1.75$, however, are not shown for the sake of brevity. The force in the inline-direction is called drag and that in the transverse-direction (including both potential and vortex forces), lift. The definition of lift and drag coefficients, C_l and C_d, respectively, for the stationary and vibrating cylinders is based on their own diameters; for example, $C_{ds} = F_{xs}/(1/2)\rho_\infty U_\infty^2 D$, where subscript 's' is the abbreviation for stationary. The time-dependent $C_l(t)$ and $C_d(t)$ may be considered as the summation of a time-averaged and a transient (or fluctuating) part, e.g., $C_l(t) = \overline{C_l} + \widehat{C_l}(t)$, where $\overline{C_l}$ is the time-averaged component while $\widehat{C_l}(t)$ is the fluctuating component. Here, for lift and drag coefficients, we present the variation of the time-averaged part and $\sqrt{2}$ rms of the transient part, represented by ($\overline{C_l}$, $\overline{C_d}$) and ($C_l{}^*$, $C_d{}^*$), respectively, as a function of the reduced velocity. It is noted that lift can be decomposed into a 'potential (or added mass) force' and a 'vortex force' (Govardhan & Williamson, 2000). For cylinders moving in a stationary fluid, the fluid dynamic force may be decomposed into 'self-added' mass, 'cross-added' mass, and damping forces (Lagrange *et al.*, 2018). Here, however, similarly to studies, such as Liu & Jaiman (2018), we consider the 'total' fluid force.

As seen from the plots shown in figure 5, $|\overline{C_{lv}}|$ and $\overline{C_{dv}}$ increase with U^*, reach a maximum, and then decrease within the lock-in region. On the other hand, $\overline{C_{ls}}$ and $\overline{C_{ds}}$ curves (not presented here) show an opposite trend. One may then infer that the stationary cylinder plays a somewhat 'compensatory role' in relation to the increase of lift and drag generated over the vibrating cylinder in the lock-in region. In addition, $\overline{C_{dv}}\,\overline{C_{ls}} < 0$, meaning that, overall, the stationary and vibrating cylinders repel each other, which in turn increases the (time-averaged) gap between the two cylinders.

The appearance of non-zero mean lift coefficients for the vibrating and stationary cylinders and the repelling phenomenon may be attributed to the development of a 'gap flow', which is comprised of two counter-rotating shear layers forming over the inner sides of the cylinders (Liu & Jaiman, 2016). The jet flow between the two shear layers can consider-

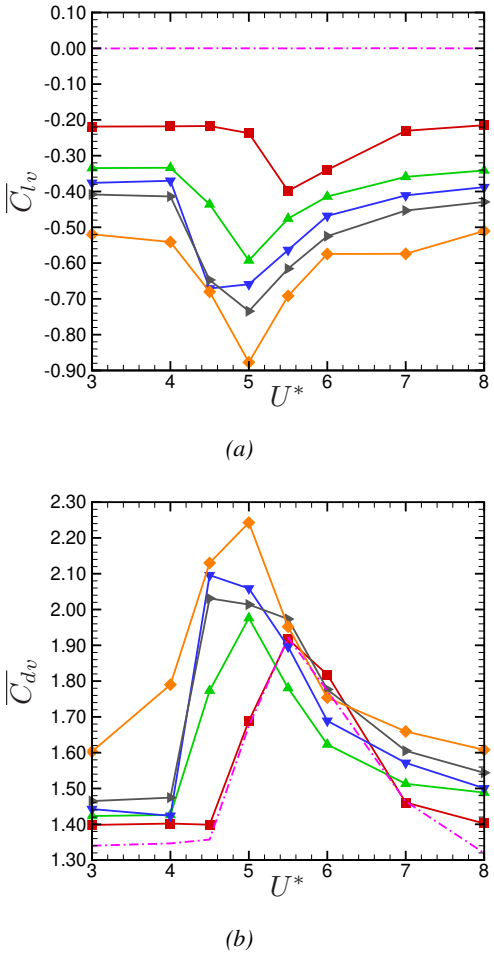

Figure 5. Variation of the time-averaged (a) lift, and (b) drag coefficients of the vibrating cylinder, $\overline{C_{lv}}$ and $\overline{C_{dv}}$, respectively, as a function of the reduced velocity, U^*, for the gap ratio $g^* = 0.75$: [◆] $d^* = 2.5$, [▶] $d^* = 1.5$, [▼] $d^* = 1.25$, [▲] $d^* = 1.0$, [■] $d^* = 0.5$, and [-·-·] $d^* \to 0$ (i.e., isolated cylinder).

ably change the pressure distribution over the inner sides of the two cylinders, and thus the fluid dynamic forces acting on them. In other words, the formation of the gap flow, even in the case of $d^* = 1$, breaks the flow symmetry about the upper and lower sides of each cylinder, which leads to a non-zero mean lift. As suggested by Mizushima & Ino (2008); Liu & Jaiman (2016), among others, the gap flow may undergo a pitchfork bifurcation at a critical Re (that is generally dependent on g^*), leading to a 'deflected' gap flow.

For a pair of stationary cylinders with a moderate g^* in the SBS arrangement, the deflected gap flow appears to be bi-stable, where the flow may switch between the two stable states intermittently (Mizushima & Ino, 2008); this phenomenon is referred to as 'flip-flopping' in the literature. Nevertheless, there is no general consensus on the origin of the deflected gap flow and flip-flopping; see, e.g., Bai *et al.* (2016). Liu & Jaiman (2016) found that the deflected gap flow displays a bias towards the vibrating cylinder in the SBS arrangement with a flexibly mounted cylinder. Also, the deflected gap flow was found to be considerably affecting the lift and drag coefficients in the lock-in region. These effects plus the effects of the resonance of the vibrating cylinder are believed to be responsible for the marked change of lift and drag coefficients for both cylinders in the lock-in region. The change in the values of lift and drag coefficients is more considerable for the vibrating cylinder, and it becomes more pronounced as d^* is increased.

Figure 6 shows the variation of the rms amplitude of the transient part of (a) lift and (b) drag coefficients of the stationary cylinder, $C_{l_s}^*$ and $C_{d_s}^*$, respectively, as a function of U^*. Similarly, figure 7 shows the variation of those of the vibrating cylinder. From figure 6(a), it is seen that for $d^* \leq 1.25$, $C_{l_s}^*$ is comparable to $\overline{C_{l_s}}$ while for higher values of d^*, $C_{l_s}^*$ can become several times the magnitude of $\overline{C_{l_s}}$; for example, for $d^* = 1.5$, the ratio is more than 3 times. As seen from figure 6(b), the curves for $d^* \geq 1$ are clustered together, and they all peak at $U^* = 4.5$. In contrast to lift, the amplitude of $C_{d_s}^*$ is several times smaller than $\overline{C_{d_s}}$, suggesting that the vibrating cylinder has a stronger impact on the lift coefficient of the stationary cylinder, perhaps by periodically changing the gap flow as well as inducing periodic pressure and shear stress disturbances in the transverse direction.

From figure 7, it is seen that by enlarging the stationary cylinder (i.e., increasing d^*), both $C_{l_v}^*$ and $C_{d_v}^*$ are significantly amplified within the lock-in region, where $C_{l_v}^*$ can become several times larger than $\overline{C_{l_v}}$. Outside the lock-in region, $C_{l_v}^*$ and to a lesser extent $C_{d_v}^*$, are weakly dependent on d^*. Figure 7 also shows that the peak values of $C_{d_v}^*$ and $C_{l_v}^*$ occur at $U^* = 4.5$ for $d^* \geq 1$ while they occur at $U^* = 5$ for $d^* = 0.5$.

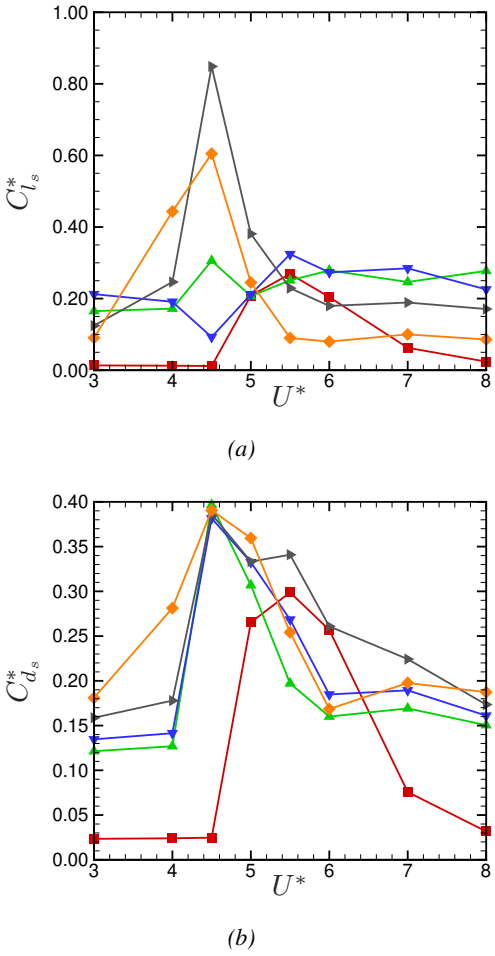

Figure 6. Variation of the rms amplitude of the transient part of (a) lift, and (b) drag coefficients of the stationary cylinder, $C_{l_s}^*$ and $C_{d_s}^*$, respectively, as a function of the reduced velocity, U^*, for the gap ratio $g^* = 0.75$: [◆] $d^* = 2.5$, [▶] $d^* = 1.5$, [▼] $d^* = 1.25$, [▲] $d^* = 1.0$, and [■] $d^* = 0.5$.

It is also interesting to see that $C_{l_v}^*$ and $C_{d_v}^*$ curves for $d^* = 0.5$ closely match those for the isolated cylinder.

5.3. Vortex patterns

For side-by-side cylinders with one cylinder flexibly mounted and the other stationary and for large gap ratios, such as $g^* = 2.5$, Huera-Huarte (2018) found that the wake of the vibrating cylinder resembles that of an isolated vibrating cylinder; a similar remark was made by Liu & Jaiman (2016) for gap ratios $g^* \gtrapprox 3$ or 4. For gap ratio $g^* = 1.0$, out-of-phase (or anti-phase) synchronised wakes were observed. A pair of counter-rotating vortices was found to form in the gap region, which dissipated in the near wake region. On the other hand, for two flexibly mounted cylinders in the SBS arrangement, Chen *et al.* (2015*a*) identified six different near-wake patterns (they were

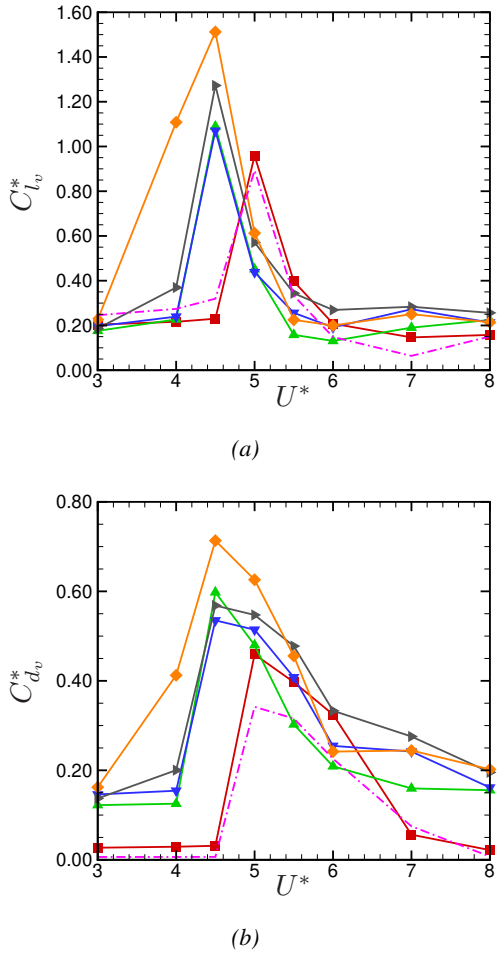

Figure 7. Variation of the rms amplitude of the transient part of (a) lift, and (b) drag coefficients of the vibrating cylinder, $C^*_{l_v}$ and $C^*_{d_v}$, respectively, as a function of the reduced velocity, U^*, for the gap ratio $g^* = 0.75$: [◆] $d^* = 2.5$, [▶] $d^* = 1.5$, [▼] $d^* = 1.25$, [▲] $d^* = 1.0$, [■] $d^* = 0.5$, and [- - -] $d^* \to 0$ (i.e., isolated cylinder).

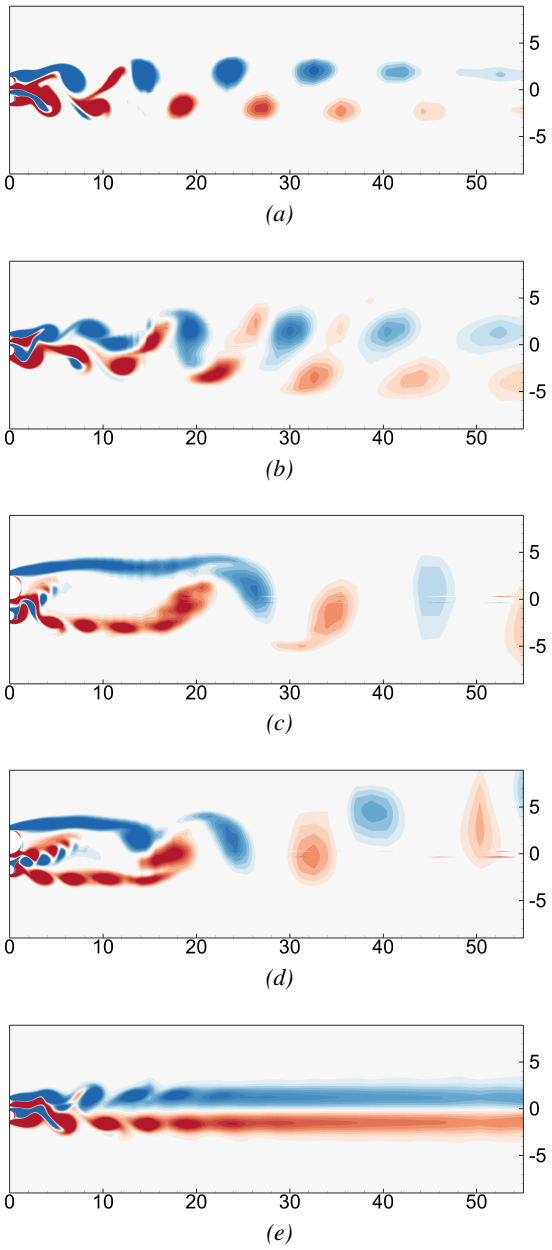

Figure 8. (Colour online) Instantaneous isocontours of vorticity for cases with $g^* = 0.75$: (a) $(d^*, U^*) = (1.0, 5.5)$, (b) $(d^*, U^*) = (0.5, 6.0)$, (c) $(d^*, U^*) = (2.5, 5.0)$, (d) $(d^*, U^*) = (2.5, 4.5)$, (e) $(d^*, U^*) = (0.5, 4.5)$. Positive (anticlockwise) and negative (clockwise) vorticity values are shown in red and blue, respectively. The values on the x- an y-axes are normalized by d.

updated later to seven and then to eight patterns in Chen *et al.*; Chen *et al.*, 2015*b*; 2019), depending on the gap ratio and reduced velocity. For gap ratios $g^* \gtrapprox 1.85$, the anti-phase-synchronised pattern was found to be prevalent while for the intermediate gap ratios $1.25 \lessapprox g^* \lessapprox 1.85$, the in-phase-synchronised pattern was dominant. The irregular pattern was observed for small gap ratios and outside the lock-in region.

In general, the present side-by-side arrangement is asymmetric both geometrically and dynamically, and the vortex dynamics appears to be very complex, particularly, in the near wake region. Some typical phenomena observed in this region across different values of d^*, U^*, and g^* are: two or more like-signed vortices combining, a vortex splitting another larger counter-rotating vortex into smaller ones, vortices dissipating further downstream, and long attached wakes developing. In many cases, the vortex pattern was found to be varying with time, as also observed by others such as Chen *et al.* (2019). We adopt the designations used commonly for the vortex patterns of a single cylinder (Williamson & Roshko, 1988; Bourguet & Jacono, 2014) to classify

the far wake vortex pattern in the SBS arrangement. In this regard, the designation 2S means that two single, large-scale, counter-rotating vortices are fed into the far wake periodically. The large-scale vortices are formed when two or more like-signed vortices are combined and rotate around each other. Examples of this vortex pattern are shown in figure 8(a-d) for different combinations of d^* and U^* and with $g^* = 0.75$. The vortex patterns for $g^* = 1.75$ are not presented in this paper for brevity.

As seen from 8(a), which is for $(d^*, U^*) = (1.0, 5.5)$, the anticlockwise vortex developed over the outer side of the vibrating cylinder pairs up with the like-signed gap vortex (that is developed over the inner side of the stationary cylinder). Similarly, the clockwise vortex formed over the outer side of the stationary cylinder pairs up with the clockwise gap vortex (that is comparatively weak). The counter-rotating binary vortices soon coalesce into single vortices, forming a pattern that is similar to the 2S vortex pattern behind a single cylinder. From 8(b), which shows the instantaneous isocontours of vorticity for $(d^*, U^*) = (0.5, 6.0)$, counter-rotating binary vortices are observed to form from two like-signed single vortices within $X/d < 10$ behind the two cylinders. Further downstream, two like-signed binary vortices pair-up and make an even larger binary vortex which will then ($X/d \approx 40$) coalesce into a large single vortex. The two rows of these large-scale single vortices are similar in arrangement to that of a Kármán street behind a single cylinder.

In 8(c,d), vortex patterns for $d^* = 2.5$ at $U^* = 5.0$ and 4.5 are shown, respectively. As seen from 8(c), the vibrating cylinder sheds periodically counter-rotating vortices into the wake. Here also, pairing-up of anticlockwise vortices occur within $X/d < 5$, and the resulting binary vortex is fed into a stream of like-signed binary vortices, which remains stable up to $X/d = 20 - 25$ prior to rolling up and shedding. On the other hand, the clockwise vortices form a weak stream within the gap flow region, which is deflected towards the stationary cylinder. This vortex stream is fed into the strong wake extending far downstream from the outer side of the stationary cylinder. The long wake is rolled up and becomes unstable at approximately $X/d = 20 - 25$. As seen from the figure, further downstream, a large-scale single street is formed. The wake behind the two cylinders at $U^* = 4.5$ appeared to be changing with time. Two major modes were identified. When the vibration amplitude was increasing from small to large values, a wake similar to that observed in 8(c) was developed. However, when the amplitude of vibrations was decreasing, the gap vortices formed a deflected vortex street, as shown in 8(d). No pairing-up between the gap vortices and those developed over the outer sides occur, and the long attached wakes extending up to $X/d \approx 15$ are formed from single vortices periodically shedding.

Here, the designation C(2S) is a variation of the 2S pattern, where the binary vortices tend to coalesce in the far wake, as shown in figure 8(e). As seen from 8(e), that is for $(d^*, U^*) = (0.5, 4.5)$, the vortex configuration is stable in that it keeps its form for large distances downstream (Williamson, 1985). Surprisingly, the wake is quite symmetric about the centreline for $X/d > 20$.

6. CONCLUSIONS

Our numerical results showed that the lock-in region for the flexibly mounted cylinder in the SBS arrangement may be wider or narrower compared to that for an isolated cylinder, depending on the gap ratio. For $g^* = 0.75$, the lock-in region was found to be wider while for $g^* = 1.75$, it was narrower. The onset of lock-in was observed to occur at a lower reduced velocity in the SBS arrangement compared to an identical isolated cylinder. The peak amplitude of vibrations in the lock-in region for almost all diameter ratios was found to be smaller than that for an isolated cylinder.

Inspired by the designations used for vortex patterns downstream of an isolated cylinder, the designation 2S was defined as when two single, large-scale, counter-rotating vortices (formed from two or more like-signed vortices) are fed into the wake periodically. The designation C(2S) was used to refer to a variation of the 2S pattern, where binary vortices tend to coalesce in the far wake. For $g^* = 0.75$, both 2S and C(2S) patterns were observed. No strong correlation between the wake pattern and the diameter ratio was found.

7. REFERENCES

Assi, G. R. S. et al, 2013 The role of wake stiffness on the wake-induced vibration of the downstream cylinder of a tandem pair. *Journal of Fluid Mechanics* **718**, 210–245.

Bai, X.-D. et al, 2016 The flip-flopping wake pattern behind two side-by-side circular cylinders: A global stability analysis. *Physics of Fluids* **28** (4), 044102.

Bao, Y. et al, 2012 Two-degree-of-freedom flow-induced vibrations on isolated and tandem cylinders with varying natural frequency ratios. *Journal of Fluids and Structures* **35**, 50–75.

Bassi, F. & Rebay, S., 1997 A High-Order Accurate Discontinuous Finite Element Method for the Numerical Solution of the Compressible Navier-Stokes Equations. *Journal of Computational Physics* **131** (2), 267–279.

Bourguet, R. & Jacono, D. L., 2014 Flow-induced vibrations of a rotating cylinder. *Journal of Fluid Mechanics* **740**, pp–342.

Chen, W. et al, 2015*a* Response and wake patterns of two side-by-side elastically supported circular cylinders in uniform laminar cross-flow. *Journal of Fluids and Structures* **55**, 218–236.

Chen, W. et al, 2015*b* Flow-induced vibrations of two side-by-side circular cylinders: Asymmetric vibration, symmetry hysteresis and near-wake patterns. *Ocean Engineering* **110**, 244–257.

Chen, W. et al, 2019 Wake patterns of freely vibrating side-by-side circular cylinders in laminar flows. *Journal of Fluids and Structures* **89**, 82–95.

Cui, Z. et al, 2014 Vortex-induced vibration of two elastically coupled cylinders in side-by-side arrangement. *Journal of Fluids and Structures* **44**, 270–291.

Farhat, C. & Lesoinne, M., 2010 Two efficient staggered algorithms for the serial and parallel solution of three-dimensional nonlinear transient aeroelastic problems. *Computer Methods in Applied Mechanics and Engineering* **182**, 499–515.

Ghoreishi, R. & Vermeire, B. C., 2021 Vorticity-based polynomial adaptation for moving and deforming domains. *Computers & Fluids* **231**, 105160.

Govardhan, R. & Williamson, C. H. K., 2000 Modes of vortex formation and frequency response of a freely vibrating cylinder. *Journal of Fluid Mechanics* **420**, 85–130.

Griffith, M. D. et al, 2017 Flow-induced vibration of two cylinders in tandem and staggered arrangements. *Journal of Fluid Mechanics* **833**, 98–130.

Haga, G. & Wang, Z. J., 2009 A High-order Lifting Collocation Penalty Formulation for the Navier-Stokes Equations on 2d Mixed Grids. In *19th AIAA Computational Fluid Dynamics Conference*. American Institute of Aeronautics and Astronautics.

Huera-Huarte, F. J., 2018 Dynamics and excitation in a low mass-damping cylinder in cross-flow with side-by-side interference. *Journal of Fluid Mechanics* **850**, 370–400.

Janocha, M. J. et al, 2020 Vortex-induced vibrations of two cylinders with different diameters close to a horizontal plane boundary at low Reynolds number. *Engineering Structures* **204**, 109893.

Lagrange, R. et al, 2018 A new analytical approach for modeling the added mass and hydrodynamic interaction of two cylinders subjected to large motions in a potential stagnant fluid. *Journal of Fluids and Structures* **77**, 102–114.

Liu, B. & Jaiman, R. K., 2016 Interaction dynamics of gap flow with vortex-induced vibration in side-by-side cylinder arrangement. *Physics of Fluids* **28** (12), 127103.

Liu, B & Jaiman, R. K., 2018 Dynamics and stability of gap-flow interference in a vibrating side-by-side arrangement of two circular cylinders. *Journal of Fluid Mechanics* **855**, 804–838.

Liu, Y.et al, 2001 Numerical studies of two side-by-side elastic cylinders in a cross-flow. *Journal of Fluids and Structures* **15** (7), 1009–1030.

Mizushima, J. & Ino, Y., 2008 Stability of flows past a pair of circular cylinders in a side-by-side arrangement. *Journal of Fluid Mechanics* **595**, 491–507.

Munir, A. et al, 2019 Effects of gap ratio on flow-induced vibration of two rigidly coupled side-by-side cylinders. *Journal of Fluids and Structures* **91**, 102726.

Qin, B. et al, 2017 Two tandem cylinders of different diameters in cross-flow: Flow-induced vibration. *Journal of Fluid Mechanics* **829**, 621–658.

Rahmanian, M. et al, 2014 Vortex induced vibration and vortex shedding characteristics of two side-by-side circular cylinders of different diameters in close proximity in steady flow. *Journal of Fluids and Structures* **48**, 260–279.

Tham, D. M. Y. et al, 2015 Freely vibrating circular cylinder in the vicinity of a stationary wall. *Journal of Fluids and Structures* **59**, 103–128.

Williamson, C. H. K., 1985 Evolution of a single wake behind a pair of bluff bodies. *Journal of Fluid Mechanics* **159**, 1–18.

Williamson, C. H. K. & Govardhan, R., 2004 Vortex-induced vibrations. *Annual Review of Fluid Mechanics* **36**, 413–455.

Williamson, C. H. K. & Roshko, A. 1988 Vortex formation in the wake of an oscillating cylinder. *Journal of Fluids and Structures* **2** (4), 355–381.

FLUID STRUCTURE INTERACTION IN A PRESSURE VESSEL: A MULTIPOLE APPROACH FOR ACOUSTIC ANALYSIS

P. Moussou[a], M. Kocher[a], D. Panunzio[b], R. Lagrange[b], A. Joly[a]
IMSIA UMR 9219 EDF[a]-CEA[b]-CNRS-ENSTA, Palaiseau, France

ABSTRACT

Pressure vessels subjected to turbulent flows are prone to fluid-structure interactions and vibrations. In the case of heavy fluids like water, the inertia of the fluid and the flow coupling generate supplementary forces and energy exchanges. A consequence of these interactions is that, seen from the surrounding pipes, a pressure vessel behaves like the association of an unsteady pressure force and of an acoustic resonator, with a resonance frequency partly determined by the structural modes. The present paper aims at shedding some light on this effect, on the basis of a simplified mechanical model.

1. INTRODUCTION

Pressure vessels in industrial facilities are prone to flow-induced vibrations. Depending on the size of the vessel, on the flow velocity and on safety considerations, they may require specific investigations with the help of scale testing and computer simulations [1]. Within the framework of a research project dedicated to the prediction of the flow-induced vibrations of large scale facilities, a work package involves building up a small scale test rig, as illustrated in Fig. 1. This future test rig is intended as a reference case of turbulent forcing, in view of assessing the methodological quality of future calculations.

A companion paper [2] focuses on the vibration level due to local turbulence, and the reader should refer to it for questions pertaining to inner forces and direct coupling. It also introduces the test rig shown in Fig. 1 and its characteristics. The present paper deals with the interaction of a flexible structure inside a vessel with the surrounding pipes. Basically, the underlying idea is that when a part of the vessel vibrates, it generates pressure waves towards the surrounding pipes, and conversely, an external pressure variation can trigger internal vibrations. The goal of the present paper consists in illustrating these effects in the case of the test rig, basing the approach on potential flow calculations.

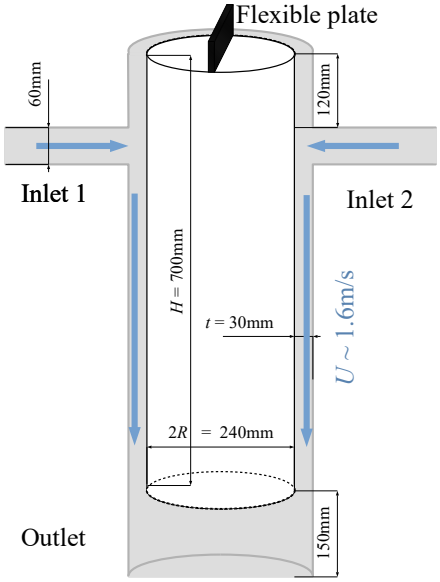

Figure 1. Sketch of the reference test rig.

2. THEORETICAL BACKGROUND

2.1. Hydroacoustics in pipes

Several authors have elaborated during the eighties a representation of the flow-induced vibrations of piping systems based on plane acoustic waves for the fluid, and beams for the structure [3, 4, 5, 6]. This representation is consistent with the founding concepts of aeroacoustics (see for instance [7, 8, 9]), at low Mach numbers (< 0.05 as it is the case in this framework) and for a limited range of frequencies of interest, typically a few tens of Hz with respect to the first natural frequencies of a piping system. Within this restrictive set of conditions, hydroacoustics of pipes can be limited to plane wave acoustics, and to local noise generation, essentially due to turbulence without any noticeable effect of the fluid compressibility. More precisely, the acoustic waves are generated by the cumulative effect of pressure sources localized in high velocity areas of small size compared with the wavelengths of interest. In other terms, the

1D representation suited to pipe vibrations relies on locally incompressible pressure sources, and on long range acoustic propagation. Furthermore, flow singularities like valves, tee-junctions or reducers can be described by local transfer functions [8], impedances [10, 11] or scattering matrices [12, 13]. The present study follows this tradition, and relies on the 'acoustic analogy' approach, according to which a large piping system should be described by 1D acoustic propagation, whereas local effects inside a pressure vessel or a hydraulic device require 3D modelling, but not compressible modelling. Of course, it would be nowadays possible to describe the full system by 3D compressible equations, but the computational cost would be higher, and the physical understanding would not benefit from it.

Leaving aside the issue of noise generation, a pressure vessel like the one shown in Fig.1 can be described as an acoustic multiport [14]. Assuming that the flow compressibility does not play any role, the pressure vessel behavior can be described by a complex matrix relating the unsteady inlet pressures p_1 and p_2 with the unsteady flow velocities at these inlets $\dot{X}_1^f$ and $\dot{X}_2^f$ (see Fig. 2), expressed in the Fourier representation:

$$\begin{pmatrix} \hat{p}_1 - \hat{p}_{out} \\ \hat{p}_2 - \hat{p}_{out} \end{pmatrix} = \begin{pmatrix} H_{11} & H_{12} \\ H_{21} & H_{22} \end{pmatrix} \begin{pmatrix} \hat{\dot{X}}_1^f \\ \hat{\dot{X}}_2^f \end{pmatrix} \quad (1)$$

where p_{out} is the outlet pressure and where the upper hat symbol stands for the complex amplitude in Fourier representation, associated with an angular frequency ω. Strictly speaking, the formalism of Power Spectral Densities should be used [15], but as only transfer functions are considered in the present paper, the harmonic representation is used instead for the sake of clarity. This pressure against velocity representation is equivalent to other representations like the scattering matrix; it was chosen here by convenience. The present study aims at providing an expression of the H-matrix components.

Two points need to be highlighted; first, due to the incompressibility assumption, the absolute value of the pressure does not play any role in the fluid dynamics, only pressure differences matter. Hence, the outlet pressure is replaced from now on by a zero pressure condition without loss of generality. Second, the coefficients T_{ij} in Eq. (1) are more complicated than those of a conventional pressure loss device, because the inner cylinder movement described by the angle θ and the displacement X is a hidden variable, and fluid-structure investigations are required to adequately describe its effect, in a manner similar to the approach followed in [16].

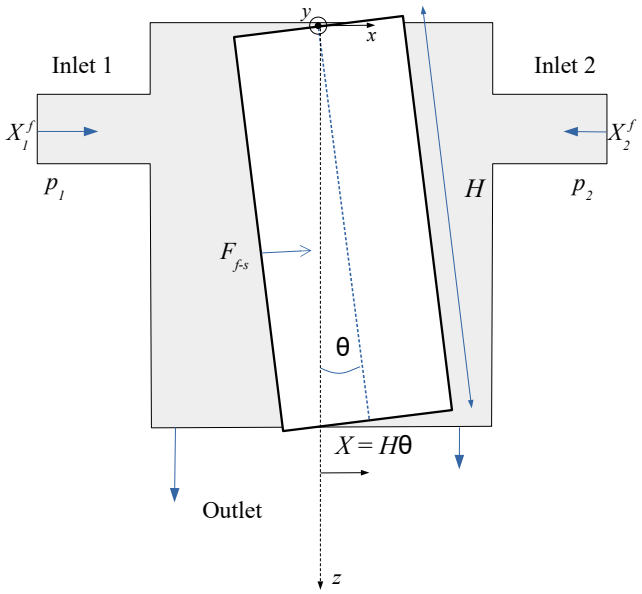

Figure 2. Sketch of the structure and fluid displacements in the test rig.

2.2. Fluid-structure interactions inside the vessel

Fluid-structure interactions in the present study involve several effects; first, the structure oscillation generates a fluid acceleration that, by virtue of the water inertia, generates the so-called 'added mass' effect. The natural frequencies of the structure decrease significantly in the presence of fluid, which somehow suggests that the fluid mass is added to the structure one. It must however be kept in mind that, even when considering potential flows only [17, 18], the added mass is a consequence of the acceleration field in the whole volume, and it depends on the boundary conditions. Hence, some consideration needs to be given concerning the inlet and the outlet conditions when the structure oscillates [19].

Another aspect of fluid-structure interaction is related to flow damping. By nature, a vessel submitted to turbulent flow generates pressure losses, so that, in the low frequency range, a variation of the flow velocity in a branch comes along with an unsteady pressure difference, according to the linearized pressure loss law (an example can be found in [20]). This aspect is not investigated within the framework of the current study, and shall be investigated in future works. It is enough for now to consider an overall damping coefficient equal to a few percent, as usual in structural dynamics [1].

Finally, no added stiffness terms are considered (see [2] for explanation).

3. FLUID AND STRUCTURE MODELLING

In order to fulfill all these requirements, it is proposed to describe the fluid and the structure on the basis of a reduced set of degrees of freedom (DOF). In the spirit of the companion paper [2], only one structure mode is considered.

3.1. Structure description

The inner cylinder is assumed to be rigid, and to oscillate with an angle θ due to the bending of a tiny support plate as illustrated in Fig. 1. The total energy of the structure without fluid is given by

$$E^s = \frac{m_s \dot{X}^2}{2} + \frac{kX^2}{2} \tag{2}$$

where the first term on the right-hand side of Eq. (2) is the kinetic energy of the structure, and the second term is the elastic energy; the overdot is a shorthand notation for the time derivative, the mass m_s and the stiffness k being defined with respect to the displacement amplitude X (see [2] for details about this elaboration). This expression comes along with a dimensionless displacement field of the structure $\boldsymbol{\xi}$, defined in such a way that the projection of the mode shape in the direction normal to the surface is, with the notations of Fig. 2,

$$\boldsymbol{\xi}(z,\varphi).\mathbf{n} = \frac{z}{H}\cos\varphi$$

the dimensionless displacement being equal to one at its maximum, (z,φ) being the cylindrical coordinates of the position, and $\mathbf{n}$ being the normal to the surface at this coordinates.

3.2. Fluid description: inertial effects

The fluid is assumed to be adequately modeled by potential and incompressible acceleration, velocity or displacement fields, a sound simplification with respect to inertial effects in the low frequency range [17]. It should be mentioned here that the potential flow assumption is so strong that it automatically fulfils the momentum equation (see details in [9] or [21] for instance). Hence, a potential flow which fulfills the boundary conditions is, within the limits consisting of neglecting the influence of turbulent eddies, an adequate solution of the flow dynamics. In order to ensure compatibility with the structure description, the fluid displacements amplitudes X_1^f and X_2^f at the first and second inlets are from now on used instead of fluid velocities.

Let first a potential fluid movement be considered, with fluid entering through inlet 1 only as illustrated in Fig. 3, where the displacement field next to the outer wall only is shown, for the sake of readability. To determine this movement, let the Laplace equation be solved with a structured mesh generated by the *Gmsh* software [22] and the finite element solver *Code_Aster* [23], and let a dimensionless gradient field $\mathbf{u}_1$ be derived from a potential function, with a vanishing divergence to fulfill fluid incompressibility, and with specific dimensionless boundary conditions defined at the moving wall and at the inlets of the fluid system:

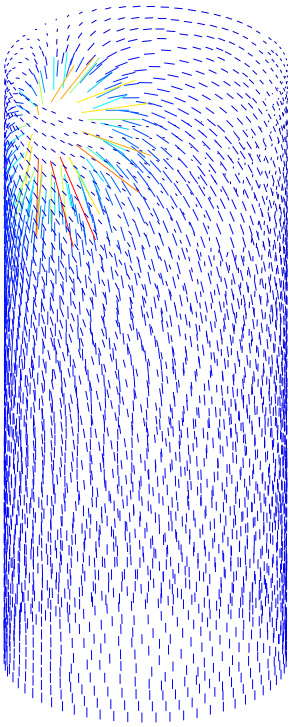

Figure 3. Potential dimensionless field associated with incoming flow through inlet 1 only.

$$\begin{array}{lcll} \mathbf{u}_1.\mathbf{n} & = & 1 & \text{unit flux through inlet 1} \\ \mathbf{u}_1.\mathbf{n} & = & 0 & \text{no flux through inlet 2} \\ \mathbf{u}_1.\mathbf{n} & = & 0 & \text{no flux at inner cylinder} \end{array} \tag{3}$$

the other conditions being a vanishing normal displacement at the other walls, and a vanishing potential at the outlet of the rig. This last condition is related to the merging of all incoming flows at the end of the vessel. The dimensionless field $\mathbf{u}_1$ is built up as a convenient kernel for any displacement, velocity or acceleration field in the fluid volume. For instance, defining A (in m) as a harmonic displacement amplitude, the fluid displacement at the inlet can be written as $X_1^f = A\cos\omega t$ and the velocity field in the fluid volume is $-\omega A \sin\omega t\ \mathbf{u}_1$.

$\mathbf{u}_1$ can easily be used to evaluate the kinetic energy of the fluid flow by numerical integration:

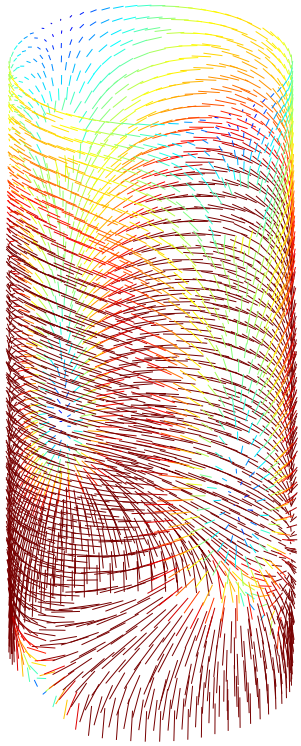

Figure 4. Potential dimensionless field associated with a balancing oscillation of the inner cylinder in the x direction.

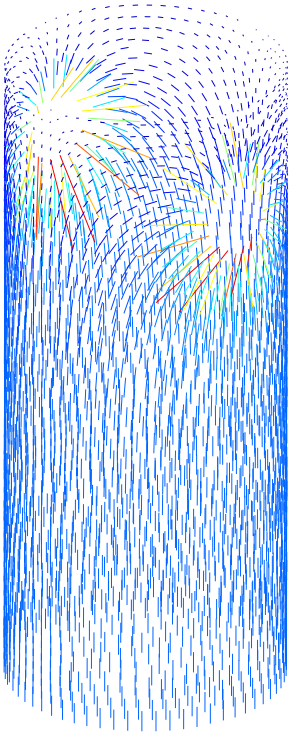

Figure 5. Potential dimensionless field associated with identical incoming flow through inlets 1 and 2.

$$E_1^f = \rho \iiint \mathbf{u}_1^2 dv \; \frac{\dot{X_1^f}^2}{2} \tag{4}$$

where ρ is the fluid density. By symmetry, a similar equation holds for a unit fluid flow $\mathbf{u}_2$ entering through inlet 2.

In a similar manner, a potential field $\mathbf{u}_X$ associated with cylinder oscillation can be defined by the same general conditions as previously and by specific conditions:

$\mathbf{u}_X.\mathbf{n}$	=	0	no flux through inlet 1
$\mathbf{u}_X.\mathbf{n}$	=	0	no flux through inlet 2
$\mathbf{u}_X.\mathbf{n}$	=	$\frac{z}{H}\cos\varphi$	unit X flux at inner cylinder

This displacement field is illustrated in Fig. 4, and its kinetic energy is

$$E_X^f = \rho \iiint \mathbf{u}_X^2 dv \; \frac{\dot{X}^2}{2} \tag{5}$$

Eqs. (4) and (5) are specific cases of the general kinetic energy expression associated with the three DOFs X_1^f, X_2^f and X:

$$E^f = \frac{\rho}{2} \iiint \left(\dot{X}_1^f \mathbf{u}_1 + \dot{X}_2^f \mathbf{u}_2 + \dot{X}\mathbf{u}_X\right)^2 dv$$

the integration being performed on the fluid volume. Such an expression can be expanded in scalar product terms of the type $\iiint \rho \mathbf{u}_1.\mathbf{u}_2 dv$ which are the components of a 3×3 mass matrix. Such terms can be determined by post-processing calculations of potential flows with combinations of inlet displacements, as illustrated in Fig. 5.

Modelling the fluid movement in the two inlet pipes by a simple condition on the inlet sections as in Eq. (3) so that the 'bare' behavior of the vessel only is shown, the fluid mass matrix is for the current test rig and with respect to the state vector (X_1^f, X_2^f, X):

$$\mathbf{M}^f = m^f \begin{pmatrix} 0.0083 & 0.0051 & -0.0138 \\ 0.0051 & 0.0083 & 0.0138 \\ -0.0138 & 0.0138 & 1.054 \end{pmatrix} \tag{6}$$

where m^f is the actual fluid mass inside the vessel. It can be observed that the fluid mass associated with a movement of the inner cylinder is much higher than that associated with the inlets. This difference stems from the relative thinness of the gap between the inner and outer cylinders, which is responsible for large fluid displacements when the inner cylinder moves, as can be seen by comparing Figs. 3 and 4. The mass component associated to $\mathbf{u}_1.\mathbf{u}_2$ is positive, a consequence of the fact that both are oriented downwards, so that their interaction generates a positive kinetic

energy contribution. Another observation is that the mass component associated to $\mathbf{u}_1.\mathbf{u}_X$ is negative, a consequence of the fact that the fluid entering the inlet 1 somehow compensates the fluid movements induced by a positive movement of the inner cylinder. Conversely, the mass component associated to $\mathbf{u}_2.\mathbf{u}_X$ is of course positive.

3.3. Fluid-Structure interaction

The interaction of the fluid volume with the mobile structure on the one hand and with the outside pressures on the other hand can be formulated either by an energy approach, by application of the Bernoulli equation or by using generalized momentum equation. A hybrid approach is chosen here, by applying Newton's second law of motion to the fluid volume in harmonic regime:

$$-\omega^2 \mathbf{M}^f \begin{pmatrix} \hat{X}_1^f \\ \hat{X}_2^f \\ \hat{X} \end{pmatrix} = \begin{pmatrix} S\hat{p}_1 \\ S\hat{p}_2 \\ \hat{F}_{s\to f} \end{pmatrix} \tag{7}$$

where ω is the angular frequency, S is the inlet cross-section of the pipes and $F_{s\to f}$ stands for the generalized fluid-structure force associated with the coordinate X. Such a dynamic equation is based on acceleration terms only; it overlooks the convection of momentum at the inlets and the outlet, and unsteady pressure losses are not considered. It can however be used for the purpose of physical illustration.

Differentiating the energy expression (2) with respect to X yields the structure dynamic equation :

$$(k - m_s\omega^2)\hat{X} = \hat{F}_{f\to s} \tag{8}$$

where the force $\hat{F}_{f\to s}$ exerted by the fluid towards the structure is of course the opposite of $\hat{F}_{s\to f}$ in Eq. (7). This force can be eliminated by combining Eqs. (7) and (8):

$$\begin{aligned} -\omega^2(m_{11}^f\hat{X}_1^f + m_{12}^f\hat{X}_2^f + m_{13}^f\hat{X}) &= S\hat{p}_1 \\ -\omega^2(m_{21}^f\hat{X}_1^f + m_{22}^f\hat{X}_2^f + m_{23}^f\hat{X}) &= S\hat{p}_2 \\ -\omega^2(m_{31}^f\hat{X}_1^f + m_{32}^f\hat{X}_2^f + m_{33}^f\hat{X}) &= (m_s\omega^2 - k)\hat{X} \end{aligned}$$

where the terms m_{ij}^f are the components of the mass matrix defined by expression (6). The diagonal terms m_{11}^f and m_{22}^f are hydrodynamic masses, which, multiplied by the fluid acceleration $\omega^2 X_1^f$ or by the fluid acceleration $\omega^2 X_2^f$, determine the pressure p_1 or the pressure p_2, respectively. The diagonal term m_{33}^f should be considered as the added mass of the structure, being understood that it is associated with the structure displacement and no fluid displacement at the inlet. This expression is an improvement on the approximation provided in [2].

The third equation can be used to express the structure displacement as a function of the fluid DOFs. Taking advantage of the relations $m_{11}^f = m_{22}^f$, $m_{12}^f = m_{21}^f$, $m_{31}^f = m_{13}^f$ and $m_{31}^f = -m_{32}^f$, the structure displacement can be written:

$$\hat{X} = \mathscr{R}(\hat{X}_1^f - \hat{X}_2^f)$$

and the fluid DOFs are bound by

$$-\omega^2 \begin{pmatrix} m_{11}^f + m_{13}^f\mathscr{R} & m_{12}^f - m_{13}^f\mathscr{R} \\ m_{12}^f - m_{13}^f\mathscr{R} & m_{11}^f + m_{13}^f\mathscr{R} \end{pmatrix} \begin{pmatrix} \hat{X}_1^f \\ \hat{X}_2^f \end{pmatrix} = \begin{pmatrix} S\hat{p}_1 \\ S\hat{p}_2 \end{pmatrix} \tag{9}$$

where the resonant dimensionless term $\mathscr{R}$ can be expressed as a function of the 'structural' natural frequency $\Omega = \sqrt{\frac{k}{m_s + m_{33}^f}}$:

$$\mathscr{R} = \frac{m_{13}^f}{m_s + m_{33}^f} \frac{\frac{\omega^2}{\Omega^2}}{1 - \frac{\omega^2}{\Omega^2}}$$

Then, an arbitrary damping value is introduced $\eta = 0.02$ for the sake of readability [1] :

$$\mathscr{R} = \frac{m_{13}^f}{m_s + m_{33}^f} \frac{\frac{\omega^2}{\Omega^2}}{1 - \frac{\omega^2}{\Omega^2} + i\eta\frac{\omega}{\Omega}}$$

The fluid structure interaction manifests here as an extra resonant term in the fluid equations. Conversely, a similar resonance of the structure appears under the effect of an unsteady flow velocity. In a general manner, these effects are noticeable here because the fluid mass is comparable to the structure mass [21].

The physical meaning of equation (8) appears easy to grasp: seen from the fluid side, the structure is a Single Degree Of Freedom (SDOF) oscillator excited in displacement by $X_1^f - X_2^f$. This SDOF oscillator comes along with a resonant pressure term in the fluid equations, which constitute a significant Fluid-Structure Interaction alteration to simpler hydrodynamic equations. This resonant pressure term generates a corrective factor on the mass coefficients. For example, (9) shows the replacement of m_{11}^f, when no structure displacement is considered, by $m_{11}^f + m_{13}^f\mathscr{R}$ when the DOF associated with the structure displacement is taken into account. The modulus 'abs' and the argument 'arg' of this proportionnal corrective factor are illustrated in dimensionless form in Fig. 6. The mass ratio value is derived from the test rig design data.

With the current set of mass ratios, the resonant term superimposed to the hydrodynamic mass does not emerge as a full resonance peak. In an actual

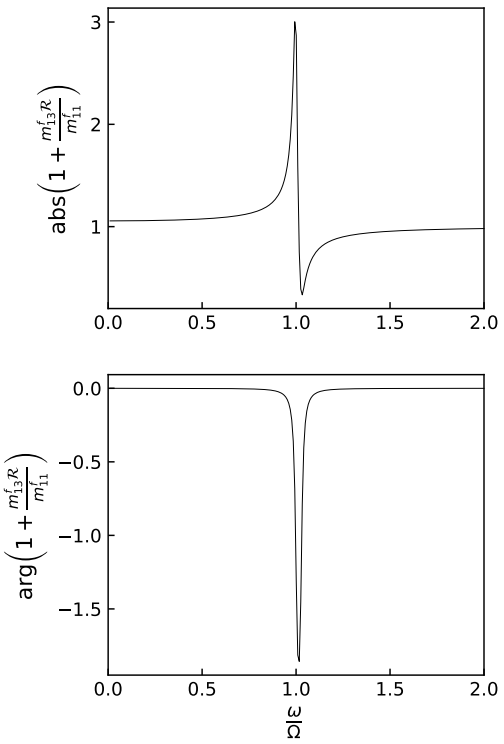

Figure 6. Corrective factor applied to the hydrodynamic mass m^f_{11} due to Fluid-Structure Interaction.

measurement, it could easily be mistaken for a very sharp resonance, and the correct way to analyse it relies on the argument evolution: the phase angle does not change but it comes back to its initial value, whereas an actual resonance of the overall pressure vessel would be associated with a phase angle rotation equal to π.

Beyond this laboratory curiosity, it should be emphasized here that in the presence of heavy fluids and vibrating structures, any dynamic analysis should carefully consider fluid structure interaction. What happens in the fluid can be observed in the structure and vice versa.

4. DISCUSSION AND PERSPECTIVES

In the context of an experimental research project, a simple model of fluid-structure interaction was proposed for describing the coupled oscillations of the structure and the fluid. On the basis of elementary energy expressions, it is possible to derive a generalized mass matrix describing the inertial effects of unsteady flows and pressures. Combining these elements brings out an improved representation of a pressure vessel as a hydrodynamic multipole, well-suited for incorporating into an acoustic analysis of the surrounding pipes. This work was intended as a complement to a companion paper dedicated to turbulent forcing [2]. Together, they pave the way for further experimental work.

References

[1] N. Jobert, J.-L. Chambrin, Th. Muller, and B. Migot. Flow induced vibrations for reactor internals of PWR-less art, more science. In *Proceedings of the 20th International Conference on Structural Mechanics in Reactor Technology*, Helsinki, 2009. Int. Ass. for SMiRT.

[2] M. Kocher, P. Moussou, D. Panunzio, R. Lagrange, and A. Joly. Fluid structure interaction in a pressure vessel: Turbulent forcing. In *Proceedings of the 2022 International Flow-induced Vibration Conference*, Paris-Saclay, 2022.

[3] P. A. Nelson and C. L. Morfey. Aerodynamic sound production in low speed flow ducts. *Journal of Sound and Vibration*, 79:263–289, 1981.

[4] R. J. Gibert. *Vibrations des structures – Interactions avec les fluides – Sources d'excitation aléatoires*. Eyrolles, Paris, 1988. in French.

[5] M. P. Norton. *Fundamentals of Noise and Vibration Analysis for Engineers*. Cambridge University Press, 1989.

[6] N. K. Agarwal and M. K. Bull. Acoustic wave propagation in a pipe with fully developed turbulent flow. *Journal of Sound and Vibration*, 132:275–298, 1989.

[7] G. Reethof. Turbulence-generated noise in pipe flow. *Ann. Rev. Fluid. Mech.*, 10:333–367, 1978.

[8] W. K. Blake. *Mechanics of Flow-Induced Sound and Vibration*, volume 17 of *Applied Mathematics and Mechanics*. Academic Press, 1986.

[9] M. S. Howe. *Acoustics of Fluid-Structure Interaction*. Cambridge University Press, 1998.

[10] P Moussou, Ph Testud, Y Aurégan, and A Hirschberg. An acoustic criterion for the whistling of orifices in pipes. In *ASME Pressure Vessels and Piping Conference*, volume 42827, pages 345–353, San Antonio, TX, 2007.

[11] C. W. S. To. The acoustic simulation and analysis of complicated reciprocating compressor piping systems, part 1. analysis technique and parameter matrices of acoustic elements. *Journal of Sound and Vibration*, 96:175–194, 1984.

[12] M. Åbom. Measurement of the scattering-matrix of acoustical two-ports. *Mechanical Systems and Signal Processing*, 5:89–104, 1991.

[13] J. Lavrentjev, M. Åbom, and H. Boden. A measurement method for determining the source data of acoustic two-port sources. *Journal of Sound and Vibration*, 183:517–531, 1995.

[14] Y. Aurégan and R. Starobinski. Determination of acoustical energy dissipation/production potentiality from the acoustical transfer functions of a multiport. *Acta Acustica united with Acustica*, 85(6):788–792, 1999.

[15] J. S. Bendat and A. G. Piersol. *Random Data - Analysis and Measurement Procedures*. Wiley-Interscience, 2 edition, 1986.

[16] H. Berro and P. Moussou. Mechanisms of instability of safety relief valves in water systems. In *Proceedings of the 10th International conference on Flow-Induced Vibration & Flow-Induced Noise*, Dublin, 07 2012.

[17] S. S. Chen. *Flow-induced vibration of circular cylindrical structures*. Springer, 1987.

[18] F. Fahy. *Sound and Structural Vibration – Radiation, Transmission and Response*. Academic Press, 1985.

[19] H. Berro and P. Moussou. Vibration spectrum of a water pipe under the effect of an unsteady fluid loading. In *Proceedings of ASME Pressure Vessel and Piping Division Conference*, number ASME PVP 2015-45228, Boston, 2015.

[20] G. C. J. Hofmans, R. J. J. Boot, P. P. J. M. Durrieu, Y. Aurégan, and A. Hirschberg. Aeroacoustic response of a slit-shaped diaphragm in a pipe at low helmholtz number, 1: quasi-steady results. *Journal of Sound and Vibration*, 244(1):35 – 56, 2001.

[21] P. Moussou. A kinematic method for the computation of natural modes of fluid-structure interaction systems. *Journal of Fluids and Structures*, 20:643–658, 2005.

[22] C. Geuzaine and J.F. Remacle. Gmsh: a three-dimensional finite element mesh generator with built-in pre- and post-processing facilities. *International Journal for Numerical Methods in Engineering*, 79:1309–1331, 2009.

[23] Electricité de France. Code_aster open source - general fea software. `http://www.code-aster.org`, 1989.

FLUID STRUCTURE INTERACTION IN A PRESSURE VESSEL: TURBULENT FORCING

M. Kocher[a], P. Moussou[a], D. Panunzio[b], R. Lagrange[b], A. Joly[a]
IMSIA UMR 9219 EDF[a]-CEA[b]-CNRS-ENSTA, Palaiseau, France

ABSTRACT

Pressure vessels submitted to turbulent flows are prone to fluid-structure interactions and vibrations. Scale testing is a useful tool to predict these effects and assess computational approaches. The present study focuses on the vibrational design of a small test rig intended as an experimental reference case. The test rig consists of a flexible structure submitted to an external axial flow, coming from two lateral perpendicular branch pipes. Introducing Au-Yang's general purpose pressure spectrum and correlation lengths, and focusing attention on a balancing mode, the modal force PSD can be theoretically predicted. Combining this force with the mechanical parameters of the structure, the response of the inner cylinder can be determined in the frequency domain. Finally, the expression of the RMS vibration amplitude of the flexible structure is provided, and a dramatic influence of the product of the structure natural frequency with the turbulence time scale is observed.

1. INTRODUCTION

Pressure vessels in industrial facilities are prone to flow-induced vibrations. Depending on the size of the vessel, the flow velocity and safety considerations, its vibration level may require specific investigations with the help of scale testing and computer simulations [1]. One of the scientific challenges associated with these investigations consists in evaluating the large scale vibration pattern generated by a turbulent flow exerted upon large areas of the vessel. A traditional workaround relies on assuming that the turbulence is homogeneous along the structure wall, and on describing the spacewise correlation of the unsteady pressure with the help of a couple of correlation lengths. Such approaches have been fruitfully applied in the past to nuclear reactor facilities [2] and are still of interest today.

Within the framework of a research project dedicated to the prediction of the flow-induced vibrations of large scale facilities, a work package involves building up a small scale test rig. This test rig is intended as a reference case of turbulent forcing, in view of assessing the methodological quality of future calculations. The goal of the present study is to support the detailed design of the test rig, in terms of flow velocity and dynamic behavior. On the basis of the traditional approach, a prediction of the expected vibration level is elaborated as a function of the flow velocity and of the first natural frequency of the test rig. A key feature of the test rig is that its flexibility can be finely tuned by adjusting the dimensions of a support plate. This is intended to explore a reasonably wide range of natural frequencies and flow velocities.

The present paper is divided into three parts: a first section provides the main figures of the basic design of the test rig. A second section provides a general overview of the classical Powell approach, paving the way to the Joint Acceptance Integral expression. A third section focuses on a single balancing mode, which is used to derive an analytical expression of the Joint Acceptance and of the structure displacement Power Spectral Density (PSD) as a function of the flow velocity and of the mechanical features of the rig. Finally, the root mean square (RMS) vibration amplitude is predicted as a function of these previous variables, providing a useful design curve in dimensionless form.

2. TEST RIG DESCRIPTION

The future test rig is intended as an experimental reference case, in view of elaborating numerical models. It is designed to be as simple as possible. It is illustrated in Fig. 1 and it consists of two coaxial stainless steel cylinders of radii 120 mm and 150 mm and heights 700 mm and 850 mm, separated by an annular gap of thickness t = 30 mm where a steady axial flow is imposed. The fluid enters the vessel by two opposite inlets in its upper part, and flows downwards with a velocity $U \approx 1.6$ m.s^{-1}. The Reynolds number is hence equal to 4.4×10^4 in nominal regime, which ensures a fully turbulent flow.

The inner cylinder weight is about 20 kg and its thickness is equal to about 5 mm. It is attached to the external vessel by a support plate, the dimensions of which can be easily modified in order to tune the

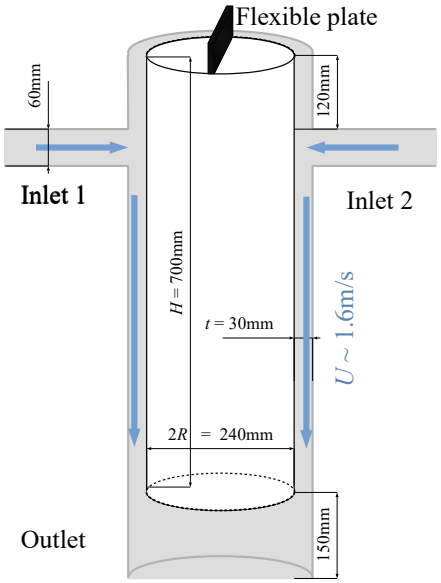

Figure 1. Sketch of the test rig.

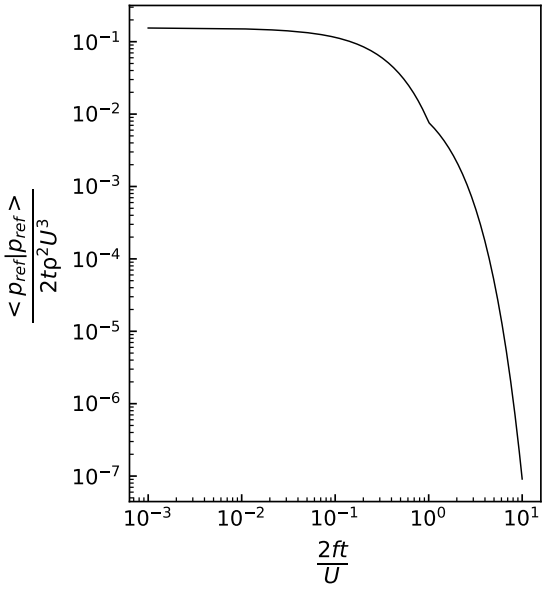

Figure 2. Dimensionless pressure PSD for highly turbulent flows according to [2].

overall stiffness of the structure. As an order of magnitude, the width of the support plate is equal to about 100 mm, its length l is equal to about 100 mm and its thickness to about 5 mm. Comparing the bending stiffness of the cylinder to the plate, the plate is more than 1000 times more flexible than the inner cylinder. Hence, the inner cylinder is thick enough to be considered as a rigid body by comparison with its flexible support.

3. THEORETICAL BACKGROUND

3.1. Assumptions and simplifying hypotheses

The current analysis is based on several simplifying assumptions: first, no external excitation source is considered and second, the turbulent force is assumed not to depend on the structure oscillations, and to be adequately described by averaged pressure spectra and correlation lengths. Calculations are developed with a linear approach, and the fluid inertial effects are described by potential flows.

3.2. Turbulent forcing in quasi-axial flow

Since the pioneering works of Powell in the 50s [3], turbulent forcing has been described in mechanical engineering [2, 4, 5, 6] and wind engineering [7] with the help of the so-called 'Joint Acceptance' approach, involving a combination of the structural modes and turbulence features. A crucial assumption inspired by Taylor's frozen turbulence hypothesis [8] is that the turbulence is homogeneous, and convected with a uniform velocity U_c equal to about 0.6 times the average flow velocity U. Let then a cylindrical surface of radius R be labelled by the cylindrical coordinates z and φ, and let a turbulent flow be convected along the axial direction z. Within the current framework, the pressure spectrum coherence is assumed to follow an exponential decrease law, expressed in the flow direction as

$$\frac{\langle p_{ref}|p(z,\varphi_{ref})\rangle}{\langle p_{ref}|p_{ref}\rangle}(\omega) = e^{-\frac{|z-z_{ref}|}{\lambda_z}} e^{-\frac{i\omega(z-z_{ref})}{U_c}} \qquad (1)$$

where (z_{ref},φ_{ref}) are the cylindrical coordinates of a reference position and where $p_{ref} = p(z_{ref},\varphi_{ref})$ is the pressure at this reference position, and ω is the angular frequency, where the bracket notation $'\langle|\rangle'$ stands here as a shorthand notation for the Cross Spectral Density (CSD) of two time signals [2, 9], where $\langle p_{ref}|p_{ref}\rangle$ is the uniform PSD of the turbulent pressure [2], and where λ_z is an empirical constant describing the progressive loss of coherence of the pressure with distance. For highly turbulent flows as is the case in this study, λ_z is considered to be about $0.4R_H$ [2], with R_H the hydraulic radius, equal to $2t$ in the case of an annular cross-section [2]. The second exponential term in Eq. (1) describes the time delay associated with the convection from z_{ref} to z.

A similar law is assumed to hold in the orthoradial direction, introducing another empirical constant λ_φ, also considered approximatively egal to $0.4R_H$:

$$\frac{\langle p_{ref}|p(z_{ref},\varphi)\rangle}{\langle p_{ref}|p_{ref}\rangle} = e^{-\frac{R|\varphi-\varphi_{ref}|}{\lambda_\varphi}} \qquad (2)$$

Eqs. (1) and (2) are enough to elaborate a consistent description of the turbulent forcing. They are often referred to as the 'Corcos model' and extrapolated to complex geometries, though they basically stem from rather fundamental studies dedicated to the properties of homogeneous turbulence [10, 11, 12].

The pressure PSD is often deduced from scale tests [1]. For the purpose of the current study, the reference curve of Au-Yang [2] (Fig.2) is used:

$$\begin{aligned} G(St) &= 0.155e^{-3.0St} \quad \text{for} \quad 0 < St < 1.0 \\ &= 0.027e^{-1.26St} \quad \text{for} \quad 1.0 < St < 5.0 \end{aligned} \tag{3}$$

where G is the dimensionless pressure spectral density equal to $\frac{\langle p_{ref}|p_{ref}\rangle}{R_H\rho^2U^3}$ and where the dimensionless frequency is defined by $St = \frac{fR_H}{U}$, R_H being the hydraulic radius previously defined and f the frequency.

The key idea in the Joint Acceptance approach consists in performing a modal analysis of the structure, and in elaborating a series of generalized turbulent forces in the modal representation, combining the modal shapes and the unsteady pressure properties. In a nutshell, if a structure mode labeled 'm' is described by a dimensionless modal shape $\boldsymbol{\xi}_m$, the unsteady pressure field $p(z,\varphi)$ generates a modal force F_m in the time domain equal to [13]

$$F_m(t) = \iint -p(z,\varphi,t)\mathbf{n}(\varphi).\boldsymbol{\xi}_m(z,\varphi)\, dz\, Rd\varphi \tag{4}$$

where the space integration is from now on to be performed along an inner cylinder of radius R, against the axial coordinate z between 0 and H, and against the orthoradial angle φ between 0 and 2π, in which $\mathbf{n}(\varphi)$ is the normal to the cylinder surface at the angular position φ, and where the dot stands for a scalar product.

Keeping in mind that the PSD of a stationary stochastic signal is the Fourier transform of its autocorrelation (see [9] for details about the Wiener-Khinchin theorem), the turbulent modal force can be written in the PSD representation as

$$\langle F_m|F_m\rangle(\omega) = \int_{-\infty}^{\infty} e^{-i\omega\tau}\overline{F_m(t)F_m(t+\tau)}d\tau \tag{5}$$

where the overbar stands for a time average over the variable t. Introducing now the expression (4) into (5), re-arranging the integrals and using the theoretical expression of the pressure CSD, one gets after a few calculation steps:

$$\begin{aligned} \langle F_m|F_m\rangle(\omega) = \; & R^2 \iiiint \langle p(\varphi,z)|p(\varphi',z')\rangle \\ & \times\boldsymbol{\xi}_m(z,\varphi)\boldsymbol{\xi}_m(z',\varphi') \\ & \times dzdz'\, d\varphi d\varphi' \end{aligned} \tag{6}$$

This is the theoretical expression of the Joint-Acceptance Integral for a single mode. It involves a double spacewise integration of the mode shape combined with the cross spectra of the pressures at different locations. It is worth highlighting here the fact that it implies the independence of the turbulent forces with the structure displacement, as is often assumed in applied mechanics [14].

3.3. Fluid-structure interactions inside the vessel

Fluid-structure interactions in the present study involve several effects. First, the structure oscillation generates a fluid acceleration that, by virtue of water inertia, generates the so-called 'added mass' effect. The natural frequencies of the structure decrease significantly in the presence of fluid, which somehow suggests that the fluid mass is added to the structure one. It must however be kept in mind that, even when considering potential flows only [14, 15], the added mass is a consequence of the acceleration field in the whole volume, and it depends on the boundary conditions. For the sake of simplicity, the two inlets are not taken into account here and the added mass of the fluid is approximated by the contribution of two-dimensional terms, slice by slice [16] and integrated over the full height of the vessel in the z direction.

Another aspect of fluid-structure interaction is related to flow damping. The structural modes responsible for the greater part of the vibration level of the structure are generally lightly damped and the damping coefficient can hence be approximated to a few percents [1].

Furthermore, no added stiffness terms are considered. A trivial explanation would be that the fluid is assumed incompressible, but the variation of steady pressure forces due to the structure displacement in a confined axial flow is a more subtle issue [17], which cannot be adressed in the framework of the present paper. It is assumed without proof to have a negligible impact, leaving a more detailed investigation for further studies.

4. A COMPREHENSIVE ILLUSTRATION BASED ON A SINGLE MODE

4.1. A simple structural mode of the vessel

For the sake of physical understanding, the integral (6) can be approximated by a simpler expression, considering a balancing mode of the inner cylinder. The balancing mode is a mere rotation, of small amplitude and without deformation, of a simply supported cylinder, i.e., a displacement in the x-direction equal to $\frac{z}{H}$ and a vanishing displacement in the y-direction. The projection of the mode shape in the

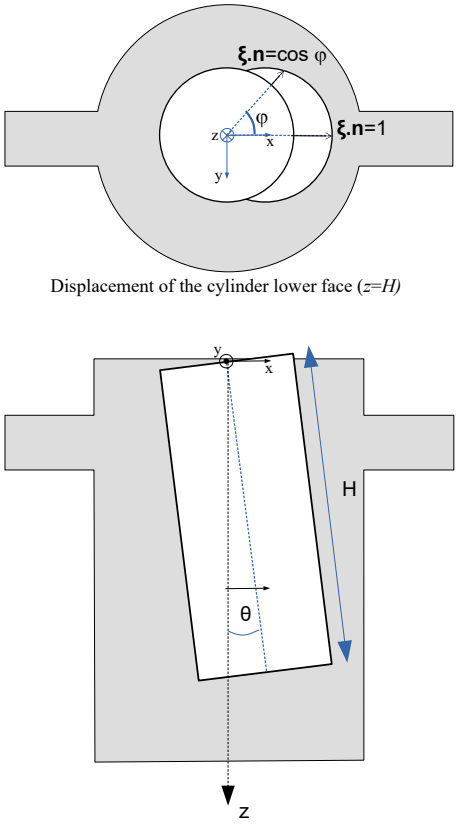

Figure 3. Balancing mode shape.

direction normal to the surface is hence

$$\boldsymbol{\xi}(z,\varphi).\mathbf{n} = \frac{z}{H}\cos\varphi \tag{7}$$

the mode normalization being such that the dimensionless displacement equals unity at its maximum, as illustrated in Fig. 3. This projection is to be used in the next section.

4.2. Modal force generated by the turbulent axial flow

Introducing the balancing mode shape (7) and defining a dimensionless coordinate $\tilde{z} = \frac{z}{H}$, the acceptance integral (6) becomes:

$$\begin{aligned}\langle F|F\rangle = \; & R^2H^2 \iiint\!\!\iint \tilde{z}\tilde{z}'\langle p(\varphi,H\tilde{z})|p(\varphi',H\tilde{z}')\rangle \\ & \times \cos\varphi\cos\varphi' d\tilde{z}d\tilde{z}'\, d\varphi d\varphi'\end{aligned}$$

The previous integral can be rewritten by using (1) and (2) and separating the space variables:

$$\begin{aligned}\langle F|F\rangle = \; & R^2H^2\langle p_{ref}|p_{ref}\rangle \\ & \times \iint \tilde{z}\tilde{z}' e^{-\frac{H|\tilde{z}-\tilde{z}'|}{\lambda_z}} e^{-\frac{i\omega H(\tilde{z}-\tilde{z}')}{U_c}} d\tilde{z}d\tilde{z}' \\ & \times \iint e^{-\frac{R|\varphi-\varphi'|}{\lambda_\varphi}} \cos\varphi\cos\varphi' d\varphi d\varphi'\end{aligned}$$

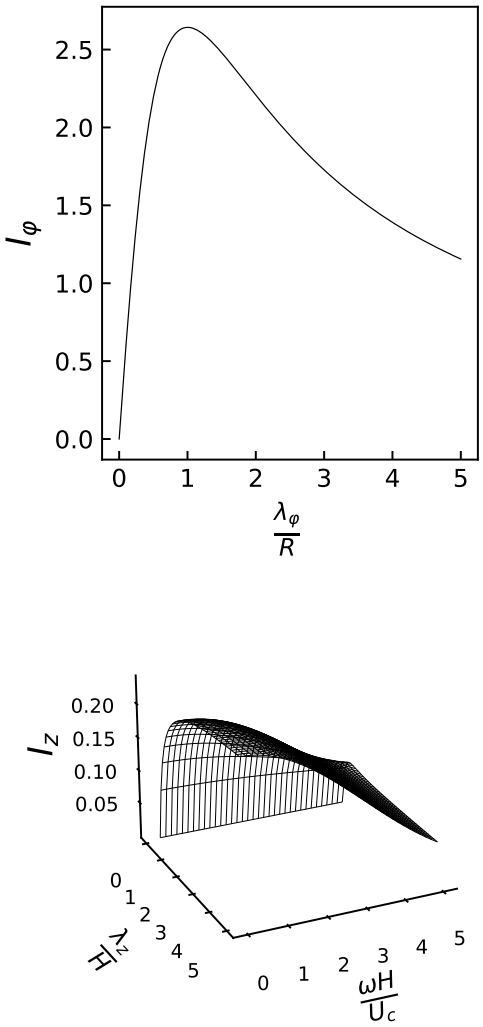

Figure 4. Dimensionless terms of the acceptance integral according to Eq. (8).

Introducing now the reduced length $\delta = \frac{R}{\lambda_\varphi}$ and the complex wavenumber $\kappa = \frac{H}{\lambda_z} + \frac{i\omega H}{U_c}$, denoting the complex conjugate by an upper star and splitting the integral into two domains to eliminate the absolute value yields:

$$\begin{aligned}\langle F|F\rangle = \; & R^2H^2\langle p_{ref}|p_{ref}\rangle \\ & \times \int \tilde{z}\Big(e^{-\kappa\tilde{z}}\int_0^{\tilde{z}} \tilde{z}' e^{\kappa\tilde{z}'} d\tilde{z}' \\ & + e^{\kappa^*\tilde{z}}\int_{\tilde{z}}^1 \tilde{z}' e^{-\kappa^*\tilde{z}'} d\tilde{z}'\Big) d\tilde{z} \\ & \times \int \cos\varphi\Big(e^{-\delta\varphi}\int_0^{\varphi} e^{\delta\varphi'}\cos\varphi' d\varphi' \\ & + e^{\delta\varphi}\int_{\varphi}^{2\pi} e^{-\delta\varphi'}\cos\varphi' d\varphi'\Big) d\varphi\end{aligned}$$

Having in mind that an antiderivative of $e^{b\phi}\cos\phi$ is $e^{b\phi}\frac{\sin\phi+b\cos\phi}{b^2+1}$ and an antiderivative of xe^{kx} is $\frac{kx-1}{k^2}e^{kx}$, the above expressions can be solved analytically in

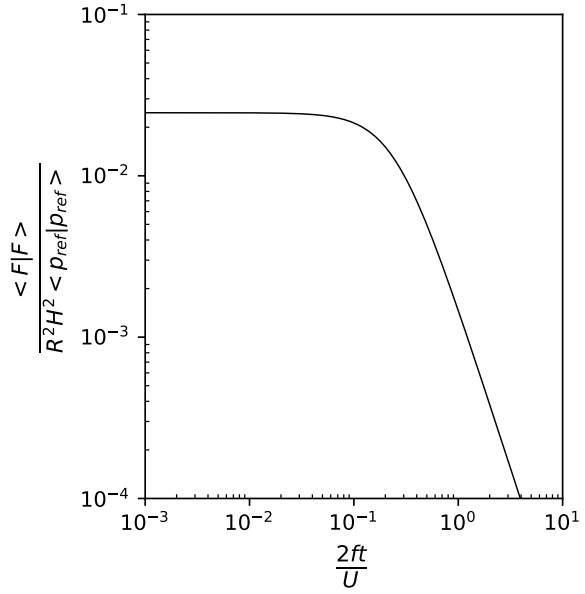

Figure 5. Dimensionless force PSD associated with the test rig.

two steps. The first integration brings out:

$$\begin{aligned}\langle F|F\rangle = & \frac{\delta}{1+\delta^2}R^2H^2\langle p_{ref}|p_{ref}\rangle \\ & \times\int\tilde{z}\Big(\frac{\kappa\tilde{z}-1+e^{-\kappa\tilde{z}}}{\kappa^2}+\frac{\kappa^*\tilde{z}+1-e^{\kappa^*(\tilde{z}-1)}(\kappa^*+1)}{\kappa^{*2}}\Big)d\tilde{z} \\ & \times\int\cos\varphi(2\cos\varphi-e^{-\delta\varphi}-e^{\delta\varphi}e^{-2\pi\delta})d\varphi\end{aligned}$$

and one integration further:

$$\begin{aligned}&\frac{\langle F|F\rangle}{R^2H^2\langle p_{ref}|p_{ref}\rangle} = I_z\, I_\varphi \\ &\text{where} \qquad I_z = \mathrm{Re}\left(\frac{2\kappa^3-3\kappa^2+6-e^{-\kappa}(6\kappa+6)}{3\kappa^4}\right) \\ &\text{and} \qquad I_\varphi = \frac{2\delta(\pi\delta^2+\pi-\delta+\delta e^{-2\pi\delta})}{(1+\delta^2)^2}\end{aligned} \tag{8}$$

where 'Re' stands for the real part of a complex quantity.

As illustrated in Fig. 4, the joint acceptance integral is strongly dependent on the ratios $\frac{\lambda_z}{H}$ and $\frac{\lambda_\varphi}{R}$ for values lower than 1, and slightly dependent on the reduced frequency $\frac{\omega H}{U_c}$.

For the sake of illustration, the dimensionless force associated with the balancing mode (7) and the test rig features is plotted against a dimensionless frequency in Fig. 5, using $\frac{t}{H}\approx 4\times10^4$ corresponding to the dimensions of the test rig defined in 2 . It exhibits a quasi-flat spectrum in the lower range, followed by a sharp decrease in the higher range of frequencies.

4.3. Structural response to the fluid excitation

In the present study, only one balancing mode is considered, so that the effect of turbulent forcing is the straightforward response of the structure along this mode. Let the modal amplitude be denoted by X (in m), in relation with the dimensionless modal shape ξ. The overall modal mass m is related to the structure inertia on the one hand, and to the added mass associated with the fluid oscillations on the other hand. The structure contribution can be described by the combination of a point mass displacement x_G at the gravity center **G** of the inner cylinder, combined with a rotation θ_G around its center of gravity. The structural kinetic energy of the structure can be expressed as a function of these variables:

$$U^s_{kin} = \frac{m_{cyl}\dot{x}_G^2}{2}+\frac{J_G\dot{\theta}_G^2}{2}$$

where the angular moment of inertia of a cylinder can be deduced from formulas of the type $J_G=\frac{m_{cyl}}{12}(6R^2+H^2)$ [16], where m_{cyl} is the physical mass of the cylinder, and where the upper point stands for the time derivative. Observing that $x_G=\frac{X}{2}$ and $\theta_G=\frac{X}{H}$, the kinetic energy can be expressed as

$$U^s_{kin} = \left(\frac{m_{cyl}}{8}+\frac{J_G}{2H^2}\right)\dot{X}^2$$

Differentiating twice the kinetic energy with respect to $\dot{X}$, the structure modal mass m_s is:

$$m_s = \frac{m_{cyl}}{4}+\frac{J_G}{H^2} \tag{9}$$

The effect of fluid inertia can be estimated in a simplified manner by assuming a 2D fluid displacement, a more thorough treatment being elaborated in a companion paper [18]. Considering a horizontal slice of fluid at location z and with a vertical thickness dz, its contribution to the kinetic energy can be estimated [16] under the effect of a lateral movement $\frac{\dot{X}z}{H}$:

$$dU^f_{kin} = \frac{\rho\pi R^2}{2}\frac{\dot{X}^2z^2}{H^2}\frac{R^2+(R+t)^2}{(R+t)^2-R^2}dz$$

Integrating this expression against z from 0 to H gives

$$U^f_{kin} = \frac{\rho\pi R^2H}{6}\dot{X}^2\frac{R^2+(R+t)^2}{(R+t)^2-R^2}$$

Derivating twice U^f_{kin} according to $\dot{X}$, the added mass m_{add} can be expressed in the X representation in a way similar to the structural mass elaboration,

$$m_{add} = \frac{\rho\pi R^2H}{3}\frac{R^2+(R+t)^2}{(R+t)^2-R^2} \tag{10}$$

and finally, the modal mass m of the fluid-structure system is the summation of the structure contribution m_s (9) and of the fluid contribution m_{add} (10). It can

be observed that the added mass term becomes significantly larger than the physical fluid mass for small gaps, as is well known in annular flow studies [19].

Turning now our attention to the stiffness terms, the only contribution is the structural one, as mentioned in section 3.3. The cylinder can be considered as a rigid body by comparison with its connection to the upper vessel, and the overall stiffness stems from the bending of the upper plate, as illustrated in Fig. 6. Assuming the length l to be small compared with the cylinder height H, the cylinder undergoes a rotation around its hanging end such that $X = H\theta_G$. Assuming the bending moment inside the plate be uniform, and equal to $M = EI\,\frac{\partial\theta}{\partial z}$, where E and I are the Young's modulus and the quadratic bending moment of the plate, and observing that the angle θ varies from zero to θ_G, the bending of the plate can be described by the approached moment vs. angle relation:

$$M \approx EI\,\frac{\theta_G}{l} \tag{11}$$

Relation (11) implies that the shear force plays a minor role inside the plate compared with the bending moment. As such, it is valid only within an order of magnitude, which is here sufficient in view of the preliminary design purpose of the study.

The modal stiffness can be deduced as previously from an energy approach. The elastic energy of the plate can be written as $\frac{EI}{2l}\theta_G^2$, where the angle can be replaced by X/H. The structure stiffness is hence obtained by a double differentiation with respect to X:

$$k = \frac{EI}{lH^2} \tag{12}$$

Finally, the damping coefficient η can be chosen equal to 5% in the current study, based on empirical experience [1].

Introducing the natural angular frequency $\Omega^2 = \frac{k}{m}$, the transfer function of the Single Degree Of Freedom (SDOF) oscillator can be written in the formalism of the PSD as:

$$k^2\langle X|X\rangle = \frac{\langle F|F\rangle}{|1 + i\eta\frac{\omega}{\Omega} - \frac{\omega^2}{\Omega^2}|^2} \tag{13}$$

Finally, integrating the PSD of X over the whole frequency range brings out the squared value of its Root Mean Square (RMS). The vibration amplitude of the inner cylinder can be expressed by combining (3), (8) and (13):

$$X_{rms}^2 = \frac{2t\rho^2U^3R^2H^2}{m^2\Omega^4}\int_0^\infty \frac{I_z\,I_\varphi G(\frac{2ft}{U})}{|1 + i\eta\frac{\omega}{\Omega} - \frac{\omega^2}{\Omega^2}|^2}df$$

Introducing a dimensionless variable $\tilde{\omega} = \frac{\omega}{\Omega}$, the previous expression can be expanded in a product of a mass ratio and a function of the dimensionless frequency defined as $\frac{t\Omega}{U}$:

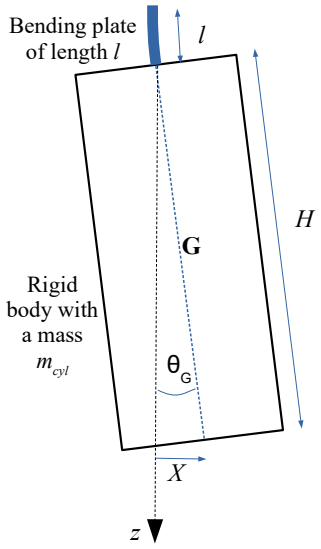

Figure 6. The flexible structure as a SDOF.

$$\left(\frac{mX_{rms}}{t^2\rho RH}\right)^2 = \frac{I_\varphi}{\pi}\left(\frac{U}{t\Omega}\right)^3\int_0^\infty \frac{I_z(\frac{H}{\lambda_z} + i\frac{\Omega H}{U_c}\tilde{\omega})G(\frac{\Omega t}{\pi U}\tilde{\omega})}{|1 + i\eta\tilde{\omega} - \tilde{\omega}^2|^2}d\tilde{\omega} \tag{14}$$

This final expression is plotted in Fig. 7; it provides the scaling law of the vibration amplitude as a function of the product of the natural frequency with the turbulence time scale $\frac{t}{U}$. The strong dependency of the oscillation amplitude on this frequency ratio and the moderate effect of the damping factor are highlighted. As expected in turbulent forcing studies, the vibration amplitude decreases when the structure natural frequency becomes larger than the turbulent frequency $\frac{U}{t}$.

In view of the mechanical and hydraulic parameters of the test rig, the natural frequency of the balancing mode can easily be tuned from about 1 Hz to 15 Hz. Combined with a flow velocity varying from 0.5 to some 1.6 m.s^{-1}, the reduced frequency range can be experimentally investigated from 0.2 to more than 3, and the design curve indicates that the vibration amplitude should range from 10 μm to 3 mm, a convenient range for measurement purposes.

5. PERSPECTIVES

In the context of an experimental research project, a design curve was elaborated to predict the RMS vibration of a flexible structure inside a test rig. On the basis of a traditional Joint Acceptance approach, it is possible to derive an analytical expression of the

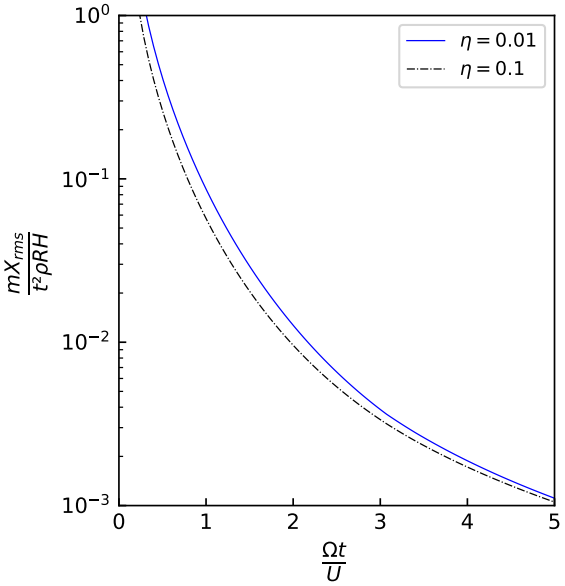

Figure 7. Root mean square value of the displacement against the dimensionless natural frequency.

unsteady pressure force and of the displacement response associated with a simple balancing mode of the structure. The design curve predicts a vibration level in the range from 10 μm to 3 mm.

In the current approach, the interactions with the surrounding pipes were not taken into account. Further work will be dedicated to this effect [18], by introducing a set of fluid degrees of freedom. In the longer term, experiments will of course be performed with the new test rig.

References

[1] N. Jobert, J.-L. Chambrin, Th. Muller, and B. Migot. Flow induced vibrations for reactor internals of pwr-less art, more science. In *Proceedings of the 20th International Conference on Structural Mechanics in Reactor Technology, Espoo, Finland, August 9-14*. Int. Ass. for SMiRT, 2009.

[2] M. K. Au-Yang. *Flow-Induced Vibration of Power and Process Plant Components*. ASME Press, New York, 1 edition, 2001.

[3] A. Powell. On the fatigue failure of structures due to vibrations excited by random pressure fields. *Journal of the Acoustical Society of America*, 30:1130–1135, 1958.

[4] B. Brenneman. Random vibrations due to small-scale turbulence with the coherence integral method. *ASME Journal of Vibration, Acoustics, Stress, and Reliability in Design*, 109:158–161, 1987.

[5] R. D. Blevins. *Flow-Induced Vibration*. John Wiley and sons, 1990.

[6] F. Axisa and J. Antunes. *Modelling of mechanical systems: Flow-induced vibrations*. Elsevier, 2007.

[7] A.G. Davenport. How can we simplify and generalize wind loads? *Journal of Wind Engineering and Industrial Aerodynamics*, 54–55:657–669, 1995.

[8] G. I. Taylor. The spectrum of turbulence. *Proceedings of the Royal Society of London*, 164:476–490, 1938.

[9] J. S. Bendat and A. G. Piersol. *Random Data - Analysis and Measurement Procedures*. Wiley-Interscience, 2 edition, 1986.

[10] G. M. Corcos. Resolution of pressure in turbulence. *Journal of the Acoustical Society of America*, 35:192–199, 1963.

[11] G. M. Corcos. The structure of the turbulent field in boundary layers flows. *Journal of Fluid Mechanics*, 18:353–378, 1964.

[12] J. M. Clinch. Measurements of the wall pressure field at the surface of a smooth-walled pipe containing turbulent water flow. *Journal of Sound and Vibration*, 9:398–419, 1969.

[13] R. W. Clough. and J. Penzien. *Dynamics of structures*. Mc Graw Hill, 1975.

[14] S. S. Chen. *Flow-Induced Vibration of Circular Cylindrical Structures*. Springer, 1987.

[15] F. Fahy. *Sound and Structural Vibration – Radiation, Transmission and Response*. Academic Press, 1985.

[16] R. D. Blevins. *Formulas for Natural Frequency and Mode Shape*. Krieger Publishing Company, 1979.

[17] A. Joly, N. de Buretel de Chassey, A. Martin, O. Cadot, L. Pastur, and P. Moussou. Direct measurement of steady fluid forces upon a deformed cylinder in confined axial flow. *Journal of Fluids and Structures*, 104:103326, 2021.

[18] P. Moussou, M. Kocher, D. Panunzio, R. Lagrange, and A. Joly. Fluid structure interaction in a pressure vessel: A multipole approach for

acoustic analysis. In *Proceedings of the 2022 International Flow-induced Vibration Conference, Paris-Saclay, July 5-8*, 2022.

[19] M. P. Païdoussis. *Fluid-structure Interactions – Slender Structure and Axial Flows*. Elsevier, 2006.

GO-VIKING: A HORIZON EUROPE PROJECT ON FLOW-INDUCED VIBRATIONS

K. Zwijsen[1], A. Papukchiev[2], D. Vivaldi[3], H. Hadžić[4], S. Benhamadouche[5], W. Benguigui[5,7] and P. Planquart[6]

[1]*Nuclear Research and consultancy Group, Westerduinweg 3, 1755 LE, Petten, The Netherlands*
[2]*Gesellschaft für Anlagen und Reaktorsicherheit gGmbH, Boltzmannstr 14, 85748, Garching, Germany*
[3]*Institut de Radioprotection et de Sûreté Nucléaire, Cadarache, St Paul-lez-Durance 13115, France*
[4]*Framatome GmbH, Paul-Gossen-Str. 100, 91052, Erlangen, Germany*
[5]*EDF R&D - Fluid Mechanics Energy and Environment Dept, 06 quai Watier, 78401 Chatou Cedex, France*
[6]*von Karman Institute for Fluid Dynamics, Waterloosesteenweg 72, B-1640 Sint-Genesius-Rode, Belgium*
[7]*IMSIA, UMR EDF/CNRS/CEA/ENSTA Paristech 9219, EDF R&D 7 boulevard Gaspard Monge 91120 Palaiseau, FRANCE*

ABSTRACT

Flow-induced vibrations (FIV) resulting from the Fluid-Structure Interaction (FSI) remain an area of concern in nuclear power plants. If not properly addressed, FIV can have large consequences to the operation and safety of these plants. With the increase in computational power, the use of numerical simulation tools to predict vibrations induced by the surrounding flow is rapidly increasing.

*In order to further advance the knowledge of solving FIV problems with the help of numerical tools, the Horizon Europe GO-VIKING (**G**athering Expertise **O**n **V**ibration **I**mpa**K**t **I**n **N**uclear Power **G**eneration) project was launched in mid-2022 in which 18 partners agreed to collaborate in this field for four years. The GO-VIKING project addresses issues with vibrations induced by the primary and secondary coolant in the nuclear power plants. Focus is put on two types of FIV issues, i.e. fuel rod fretting in fuel assemblies and fluid elastic instability occurring in steam generators, for both, single- and two-phase flows. The main objective of the GO-VIKING project is to develop, improve, and validate FSI methods, and to provide guidelines for the prediction and assessment of FIV phenomena in nuclear reactors.*

The current paper gives an overview of the roadmap to address the FIV numerical simulation challenges in the framework of the GO-VIKING project.

1. INTRODUCTION

The integrity of the nuclear steam supply system (NSSS) of a nuclear power plant (NPP) is essential for its safety and operability. Key NSSS components such as fuel assemblies (FA) or steam generator (SG) tubes are subject to several ageing challenges like high multiple corrosion mechanisms, neutron flux (embrittlement), and also long-term vibratory loads. Vibrations induced by coolant flow are particularly important challenges, as they lead to increased wear and tear and/or material fatigue, so that they have been and remain important contributors to key components' failures. Such failures can degrade NPP safety features and fail confinement barriers.

One pertinent example is that over 70% of all fuel rod leakages in U.S. pressurized water reactors (PWRs) are due to flow-induced vibrations (FIV), according to EPRI (EPRI, 2008). According to IAEA, grid-to-rod-fretting wear (GTRFW), resulting from such vibrations, is the cause of 58% of fuel failures in PWRs worldwide and one of the major causes of fuel failure in boiling water reactors (BWRs) (IAEA, 2010 and IAEA, 2019). The highly turbulent coolant flow in FA during operation results in asymmetric and fluctuating pressure on the fuel rods' surfaces. The pressure fluctuations are random, oscillate over a broad band of frequencies and amplitudes over the entire rod surface. This leads to dynamic grid-to-rod contacts and frictions, resulting in material wear in the contact region between the rod and its support.

FIV cause damage also in SG. In 2012, a SG tube rupture (SGTR) accident occurred in the US NPP San Onofre. Thereafter, an extensive wear of more than 3000 SG tubes was found in its units 2 and 3, leading to primary-to-secondary circuit coolant leaks. The SGs in these units were put in operation one year earlier. The principal reason for the extensive wear and the tube damage was found to be related to FIV (NRC, 2015). Since then, these units are in a shut-down condition. Steam generator tube rupture as a result of FIV has also been observed in many other reactors in the past (Kotthoff, 1984; MacDonald, 1996; Au-Yang. 2001; Païdoussis, 2006).

The recent trend, set by vendors, to further increase the thermal efficiency of heat exchangers, SGs, and other thermal equipment led to component designs with higher temperatures, increased mass flow rates, and thinner tube walls (Fischer, 2001). The enhancement of the heat transfer in the heat ex-

changers through increased flow velocities and thinner tube walls increases the susceptibility of the tubes to FIV. This is further increased by the ageing mechanisms that have a negative impact on the material wear and the mechanical contacts. Therefore, it is important to properly consider FIV loads in the component design and the operational surveillance and maintenance program. This also holds for power uprates and plant long-term operation (LTO) programs. As tests and measurements under operational conditions are often costly or not feasible, prediction of FIV loads by simulation could be a practical solution. The GO-VIKING Horizon Europe project gathers expertise from academia and research organizations, industry and technical safety organizations (TSOs) to synthesize and improve good practices, as well as to develop accurate simulation methods. These will support the prediction and evaluation of FIV by EU stakeholders, as well as their decision making on FIV countermeasures in the plants.

The current paper gives an overview of the roadmap to address the FIV numerical simulation challenges in the framework of the GO-VIKING project. Chapter two focusses on the structure of the collaboration and its objectives. Chapters three till six provide descriptions of main topics (axial FIV, FIV in SG, multiphase FIV, fast-running numerical methods) within GO-VIKING. Finally, in the last chapter a summary is given.

2. THE GO-VIKING HORIZON EUROPE PROJECT

The present chapter gives an overview of the GO-VIKING project. First, a short general description is given, followed by the roadmap to improve FIV simulation methods in nuclear industry.

2.1. The GO-VIKING project

The GO-VIKING project builds upon the VIKING (**V**ibration **I**mpa**K**t **I**n **N**uclear Power **G**eneration) initiative that started in 2020 as an in-kind collaborative effort under the Sustainable Nuclear Energy Technology Platform (SNETP) umbrella (label from 09.2021) to improve the understanding and the prediction of FIV phenomena relevant to NPPs (Zwijsen et al, 2022).

The GO-VIKING project aims at improving the current state-of-the-art of FIV knowledge and analysis concerning the following global targets: improve overall NPP safety, enhance plant reliability in LTO and power uprate programs, reduce staff exposure, design components that are less susceptible to FIV, and increase the regulatory acceptance of FSI tools. Such improvements are impossible with the currently available FSI methods and tools that require very high computational effort. Further, without clear guidance for their application for the variety of FIV cases in nuclear reactors, and the lack of fast-running FSI methods, as well as the missing perspective for acceptance by the regulators, reaching these global targets is hindered. Therefore, the main objective of the GO-VIKING project is to develop, improve and validate FSI methods, and to provide guidelines for the prediction and assessment of FIV phenomena in nuclear reactors. Building on that, it aims to bring them into application at European nuclear stakeholders for improving the design, operation, and maintenance of key NPP components, and thereby, enhance both, safety and availability of existing nuclear reactors in Europe. Figure 1 gives an overview of the GO-VIKING concept.

The project started in June 2022 and will run for four years

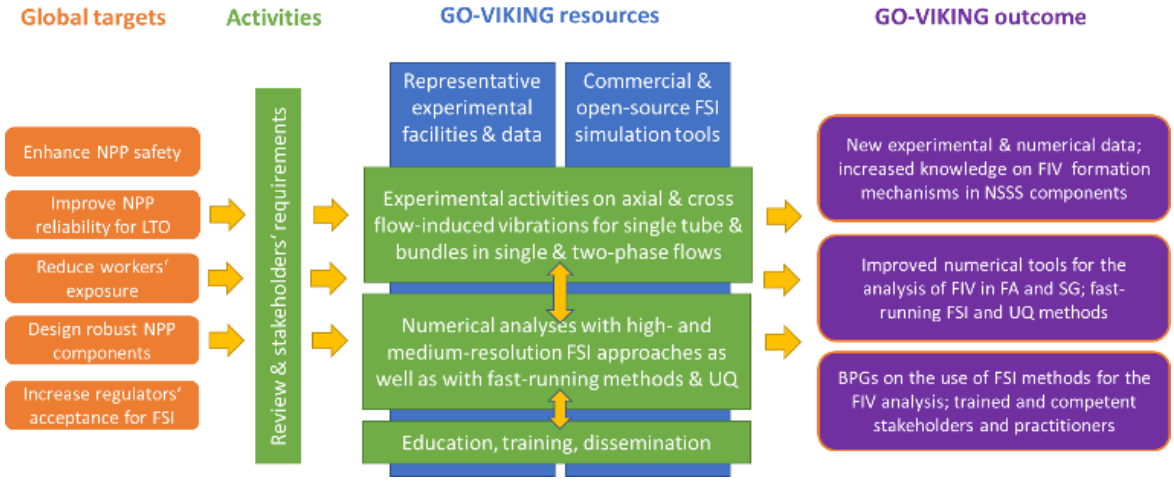

Figure 1. GO-VIKING concept

2.2. Roadmap to improve FIV simulation methods in nuclear industry

The main objective of the present project is to improve numerical tools to predict FIV in FA and SG, both in single and two-phase flow environment. The project partners review the current state-of-the-art and gather information on the needs for numerical FIV analysis and classify FIV challenges in three fields:

- **Flow-induced vibrations in fuel assemblies:** vibration phenomena in axial single-phase flow in a rod bundle are considered.
- **Flow-induced vibrations in steam generators:** vibration phenomena in single-phase cross-flow in a tube bundle are considered.
- **Multi-phase flow-induced vibrations:** vibration phenomena in two-phase axial and cross-flows are considered.

As the aim is to provide the partners with high-resolution, reliable validation data for the developed models and methods, validation benchmarks will be organized. To do that, experimental test cases are selected for each of the three previously mentioned topics. The experimental results are used as inputs for numerical work in terms of Computational Fluid Dynamics (CFD) and Computational Structural Mechanics (CSM) programs that are coupled to develop sophisticated 3D FSI tools for FIV evaluation for a variety of industrial configurations, ranging from single rods/tubes in water up to fuel rod/tube bundles in two-phase flows. The purpose is to address with different methods the following challenges in the simulation of FIV with FSI methods:

- **Turbulence modeling**: (Unsteady) Reynolds-Averaged Navier-Stokes (U)RANS turbulence models, hybrid models, Large Eddy Simulation (LES), Direct Numerical Simulation (DNS),
- **Fluid-structure interface tracking method**: chimera grids, Arbitrary Lagrangian Eulerian, Immersed Boundary Method;
- **Mechanical solver:** beam model, mass-spring system, external mechanical solver;
- **Coupling methods:** explicit or implicit, iterative or direct, one-way or two-way;
- **Two-phase flow modeling:** VOF, Eulerian-Eulerian, transition-regime models.

It is important to notice that one reference high-resolution (LES or DNS) simulation will be performed for all of the single-phase flow experiments to complement the experimentally generated data.

Knowledge and know-how gained from this work will be used as an input for fast-running model development to reduce the prohibitive CPU time of FSI simulations, as this is one of the main bottlenecks today. With the help of the fast-running models, efficient Uncertainty Quantification (UQ) methods will be developed to supplement best-estimate FSI analyses.

Further, the currently available FSI methods will be classified and their advantages/drawbacks, as well as applicability for the objectives of the project, will be evaluated.

The result of this work will be documented in specific requirements for advanced numerical methods and tools for FIV evaluation.

3. FLOW-INDUCED VIBRATIONS IN FUEL ASSEMBLIES

The main focus of this section is on the FIV under single phase axial flow conditions, which is particularly relevant for nuclear fuel assemblies. The main objective is to develop advanced simulation methods and tools to facilitate the understanding of FIV and to support free-of-failure operation of FA or other components in NPPs subjected primarily to axial flow. Specific focus is put on development of efficient simulation tools capable to provide reliable prediction of FIV in FA in an acceptable time and with reasonable computational costs, according to the needs of the nuclear industry. The development of medium-resolution models for fluid flow analysis in combination with low-resolution structural models and efficient FSI coupling algorithms is of particular interest.

For the purpose of validation of the numerical simulation tools existing experimental data from two test benchmarks will be utilized. The validation database is further supplemented by the results of high-resolution numerical simulations performed for each benchmark.

The results achieved will also provide input for Reduced-Order Models (ROM) for fast-running methods to be developed (see section 6).

In the following sections a brief description of the experiments and the accompanying numerical simulations for each benchmark of this topic is provided.

3.1. Cantilever rod case

The University of Manchester (UoM) recently designed and realized a simplified test rig for fundamental studies of axial-flow-induced vibration of relevance for water-cooled nuclear reactor systems (Cioncolini et. al 2018). The main aim in designing this cantilever beam experimental setup, shown in Figure 2, is to generate benchmark experimental data in controlled conditions with non-invasive simultaneous resolution of structural vibration (via non-contact optical tracking) and fluid flow (via Particle Image Velocimetry (PIV)). Although simplified, the experimental configuration is representative of nuclear FA. Large vibration amplitude response of the test rod, induced by axial flow, requires a strong fluid-structure two-way coupling, making it particularly

interesting for numerical simulation. Different experimental runs will be analysed with the numerical tools. The Reynolds number will be around 16.000 and the flow velocity around 1 m/s.

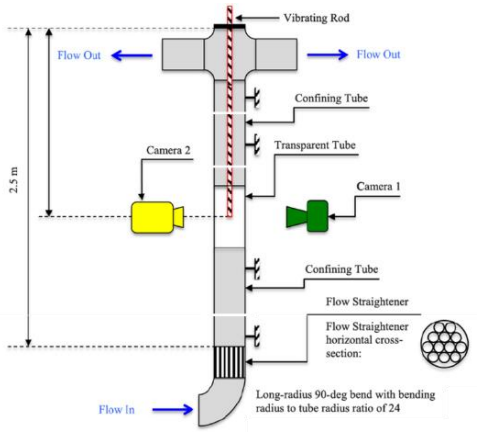

Figure 2. Axial flow-induced rod vibration test.

High-resolution simulations of the cantilever rod experiment will be performed using wall-resolved LES (Code_Saturne) and DNS (Nek5000). The results from these fine-resolution simulations will be validated against experimental data and used for further development and validation of medium-resolution simulation models, based on URANS approach.

3.2. ALAIN 5x5 PWR rod bundle

The ALAIN experiment had been performed by Framatome GmbH in Erlangen, Germany, with the aim to study complex FIV behaviour of different fuel assembly designs. The experimental setup is illustrated in Figure 3. It represents a reduced 5x5 PWR FA test bundle, placed in a channel of a low-pressure test loop with a square cross-section with a narrow nominal lateral gap between the bundle and test channel of 1.5 mm (at spacer grid positions). The vibration response of the fuel bundle was measured using a laser for a wide range of the flow rates corresponding to Reynolds number between 50.000 and 120.000, based on average axial velocity, hydraulic diameter within the bundle and fluid properties of water at 4 bar pressure and 40°C temperature.

The simulations for this benchmark will be performed for the axial flow velocity corresponding to Reynolds number of 90.000. First, stand-alone CFD simulations using an appropriate medium-resolution for the full and high-resolution modelling approach (based on LES) for the reduced, single-span, configurations will be performed. The purpose of these simulations is to evaluate the global flow field and the detailed unsteady flow characteristics in the bundle, as well as to assess the requirements for medium-resolution approach. The results from CFD simulations can also be used to evaluate vibration response in the framework of decoupled FSI simulation.

In the second step, coupled FSI simulations, based on medium-resolution modelling, will be performed. For the FSI coupling either integrated or user implemented solutions in combination with commercial and open-source CFD codes (STAR-CCM+, ANSYS CFX, OpenFOAM) will be used.

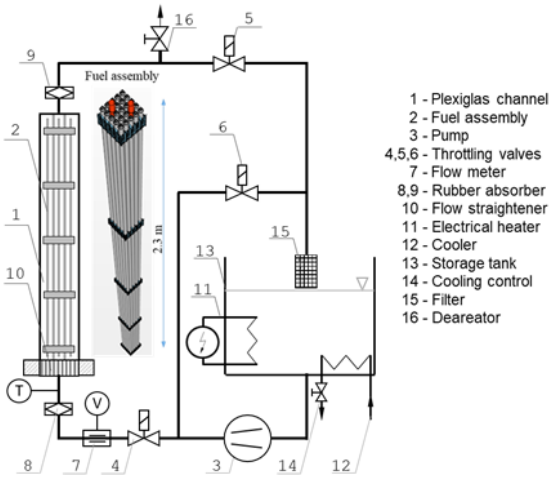

Figure 3. ALAIN 5x5 rod bundle FIV test setup.

4. FLOW-INDUCED VIBRATIONS IN STEAM GENERATOR TUBE BUNDLE

In the present section, the focus is put on the development, implementation and validation of beyond the state-of-the-art medium-resolution numerical tools to provide reliable assessment of structural vibrations, occurring in steam generators under single-phase cross-flow conditions. Hereto, new experimental and high-resolution data will be generated to allow the further development and validation of such tools. This experimental and high-resolution numerical data is obtained from two different experimental facilities: CEA's AMOVI and VKI's GOKSTAD. Descriptions of each facility are given in the next sections along with the accompanying numerical exercises.

4.1. AMOVI experiment

AMOVI (Cardolaccia, 2015) is a small modular and easy-to-operate loop aimed at studying cross-flows in tube bundles. It addresses low-turbulent regimes in a normal-square tube bundle of 3x5 tubes plus two columns of 5 semi-tubes. In the AMOVI facility, which is shown in Figure 4, the flow is at low pressure ($p < 5$ bar) and low-temperature ($T < 40$ °C) conditions. The diameter of the tubes is 12 mm with a pitch-over-diameter (P/D) ratio of 1.44, values similar to those used in steam generators of NPPs. The maximum volumetric flow rate in AMOVI is 4.2 l/s, which results in Re~2.3E+4 in the gap between the tubes. PIV, LDV and high-speed camera measure-

ments are performed to provide data on the flow pattern inside the test section and the vibration characteristics of the central tube. Experiments will be performed with all tubes fixed, as well as with a central flexible tube.

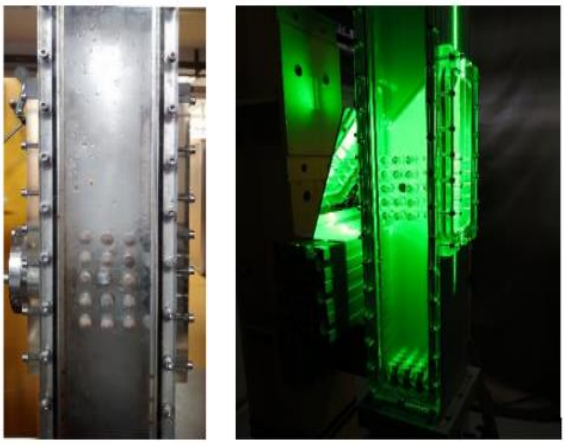

Figure 4. AMOVI test facility at CEA.

The experimental data from AMOVI will be supplemented with high-resolution simulations in Code_Saturne using a wall-resolved LES model and the Arbitrary Lagrangian Eulerian (ALE) approach. The generated results will be compared with experimental data and utilized for the development and validation of medium-resolution models based on hybrid (Zonal LES, Stress Blended Eddy Simulation) and URANS turbulence methods.

4.2. GOKSTAD experiment

At VKI, a new experiment named GOKSTAD (**GO**-VI**K**ING experimental **S**e**T**up to **A**ssess flow-induced vibrations by cross flow in tube bun**D**les) will be designed and built to generate new high-resolution data of single-phase, cross-flow induced vibrations of flexible tubes within a tube bundle. It will be a square tube bundle of 7x7 tubes using water as medium, with the aim to perform experiments at a Reynolds number higher than what is currently available in the literature. A sketch of the water loop of the proposed new GOKSTAD experiments is provided in Figure 5.

The design will be flexible, allowing to vary the number and position of the flexible tubes. Furthermore, the facility will be sustainable such that it will be easy to use in future experimental campaigns. Time-Resolved Particle Image Velocimetry (TR-PIV) is used to measure the flow field (mean, fluctuating components, Reynolds stresses), essential for the proper validation of the flow solver used in FIV models. Data will be generated for a range of flow velocities, as well as for cases involving all fixed tubes, one central moving tube, as well as two moving tubes, placed either behind or above each other. The exact parameters of the experimental runs (inlet and gap velocities, Reynolds number, etc.) will be determined in the first few months after the project begin together with the GO-VIKING partners performing numerical simulations.

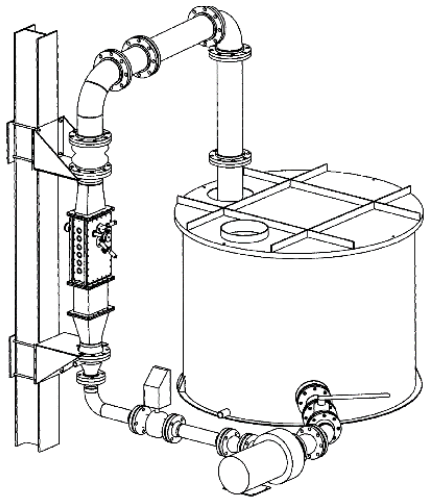

Figure 5. Sketch of the GOKSTAD water loop.

High-resolution simulations of GOKSTAD using Nek5000 coupled to Diablo and based on an ALE approach will be performed. Results hereof are to be compared with experimental data and also to be used for the further development and validation of medium-resolution models. For GOKSTAD, the latter work is done using STAR-CCM+ with a low Reynolds URANS and/or hybrid method in combination with the ALE approach, as well as with a low and/or high Reynolds URANS method in Code_Saturne with the ALE approach and/or in NEPTUNE_CFD using an Immersed Boundary method.

5. FLOW-INDUCED VIBRATIONS IN MULTI-PHASE FLOWS

In the present section, the focus will be on the use of three two-phase flow FSI experiments (both for axial- and cross-flow conditions), dedicated to the development and validation of two-phase FIV tools. Hereto, two-phase flow and structural measurements will be performed to have a rich validation database. With this database, numerical tools will be developed and improved in order to be as accurate as possible for different flow regimes. The developed tools are expected to provide the possibility for deeper understanding of FIV for two-phase flows in general, and SG in particular.

The diversity of the input coming from the different partners and the stakeholders provide an excellent basis for the development of an optimal solution. One of the main outcomes of this topic will be the guidance for practical use of the simulation tools

based on the assessment of different numerical approaches to be used within the foreseen benchmarks.

In this section three benchmarks will be considered:

- Cantilever rod subjected to axial two-phase flow (previously discussed in section 3 for the single flow configuration),
- TREFLE: 5x5 square tube bundle subjected to an air-water cross flow,
- TITAN: 5x5 triangular tube bundle subjected to an air-water cross flow

For each case, different partners using different numerical simulation approaches and tools will perform the calculations.

5.1. Cantilever rod under two-phase flow

The Cantilever rod facility described in chapter 3 on single-phase axial flow-induced vibrations will be modified in order to perform similar experiments, though now for two-phase air-water mixture flows. The facility will be equipped with an extra device to measure the void fraction distribution.

Numerical simulation of this experiments will be computed by three partners based on various methods in terms of turbulent modeling, fluid-structure interface tracking method, and mechanical resolution, such as a URANS approach with the Immersed Boundary (IB) method of NEPTUNE_CFD, the internal FSI solver of ANSYS FLUENT using URANS or a hybrid method and an URANS based ALE method implemented in the coupled code NEPTUNE_CFD-FEniCS.

5.2. TREFLE

TREFLE is a 5x5 square tube bundle to study two-phase FIV with air-water mixture. The tube diameter will be 30 mm, while their length – 300 mm. One or more moving tubes will be installed in the bundle. The void fraction will be varied between 0% and 100%. For the measurements optical probe, wire-mesh sensors and high-speed camera will be used. The objective of this experiment is to validate FIV codes by generating data with measurements of the central tube displacement and of the void fraction upstream and downstream the tube for various inlet void fractions. The purpose of this experiment is to have two-phase flow and vibration measurements simultaneously for an in-line bundle. This is important for the specification of realistic inlet boundary conditions in the simulations, as these can have a large influence on the obtained results.

Five partners will simulate this experiment with different tools: NEPTUNE_CFD with the Generalized Large Interface Model, STAR-CCM+ with an ALE method, OpenFOAM coupled with Deal.II with the preCICE coupling interface, based on the ALE method, the NEPTUNE_CFD code with an IB method, and the intrinsic FSI solver of ANSYS FLUENT. For the latter, if deemed necessary, full coupling with ANSYS FLUENT Mechanical will be used.

5.3. TITAN

CEA proposes experimental data for tube vibrations under two phase flow (water-air mixture) with increasing difficulty for codes and numerical methods testing. These data have been obtained with the TITAN triangular mock-up. The bundle consists of 5x6 stainless tubes, with two columns of half-tubes at both lateral plates to minimize wall effects. A flow straightener is placed upstream the test section to regulate the inlet flow direction. Each test has been performed with a void fraction kept constant. Flow is increased until fluid-elastic instability (critical velocity) is observed. Root mean square (RMS) displacement amplitude over flow pitch velocity is available. For the present case, the triangular tube lattice and the higher Reynolds number (~250.000) are the main numerical challenges.

Four partners will simulate this experiment with very different approaches: the two-phase CFD Code ANSYS FLUENT, STAR-CCM+ with its ALE approach, OpenFOAM coupled to Deal.II via the preCICE coupling interface and NEPTUNE_CFD with an IB method and the Generalized Large Interface model

6. FAST-RUNNING METHODS, UNCERTAINTY QUANTIFICATION AND BEST PRACTICE GUIDELINES

Methods that can provide valuable information with similar accuracy to the one of the original, full-order model, but at significantly lower computational cost, are termed fast-running methods. Such methods often include reduced order models (either of the CFD, or of the CSM domain. Since the CFD simulation is typically orders of magnitude more costly than the CSM solution, remarkable efforts in this European project are dedicated to the generation of fast-running FSI methods with increased fluid flow calculation efficiency.

6.1. ROMs for the CFD domain

Within GO-VIKING project novel data-driven and projection-based ROMs for the fluid component will be developed with the aim at closely reproducing the physics of the full-order models. Such methods will be constructed by building a data-set of time-resolved fluid simulations with forced displacement of the domain walls, followed by system-identification techniques (Sarma, 2018).

Another fast-running approach will be based on building a ROM that predicts the turbulence pressure spectrum from significantly cheaper RANS or URANS models. The further development of the NRG Pressure Fluctuation model (PFM) together with a URANS turbulence model will allow to predict the pressure fluctuations driving the structural vibrations at a much more reasonable computational cost (Kottapalli et al 2019).

Additionally, a third fast-running method for the CFD domain will be developed and implemented. The proposed approach is based on the generation of synthetic turbulent fluctuations in combination with standard URANS approach (Filonov et al, 2020).

6.2. ROMs for the CSM domain

ROMs can be used not only for the CFD, but also for the CSM domain. Recently, efforts to couple structural ROMs with detailed scale-resolving CFD simulations for the evaluation of FIV phenomena in nuclear power reactors were made (Papukchiev, 2022). Within the project, beam models will be developed in order to speed up the calculation on the CSM side. The beam models will substitute the detailed 3D modelling of the investigated rods/tubes, and will, hence, accelerate the FSI simulation. Further, the ANSYS MOR (Model Order Reduction) (Einzinger, 2014), based on the mode-superposition method, which uses the natural frequencies and mode shapes, generated from a modal analysis to characterize the dynamic response of a structure to transient or steady harmonic excitations, will be implemented for a tube bundle in a cross-flow and validated. A MOR technique will be developed and implemented for the analysis of the vibration response of the AMOVI tube bundle described above.

6.3. Uncertainty Quantification

Fast-running models including ROMs are an essential element to make uncertainty and sensitivity analyses (UaSA) for FSI simulations, based on input uncertainty propagation, attractive. The need for Uncertainty Quantification (UQ) methods for FIV analyses became visible in the Horizon 2020 MYRTE (MYRTE, 2015) and SESAME (SESAME, 2015) projects, where the validation of FIV analyses in tube bundles proved to be challenging due to variations in the experiments of the inlet conditions, tube alignment, spacing, end conditions and contacts, as well as approximations in the numerical models.

In GO-VIKING, FSI simulations will be combined with non-intrusive UQ techniques, such as polynomial chaos expansion (PCE) or Monte Carlo (MC) approaches. These UQ techniques permit the calculation of the distribution of modal characteristics (eigenfrequency and damping ratio) for the model by performing a relatively limited number of FSI simulations. Further, the RANS turbulence closure error on the output of interest will be quantified with Bayesian estimates of the model corrections, derived from high-fidelity data. In addition, global sensitivity analyses will be performed.

The developed UQ approaches will lead to a fast identification of high importance input parameters, needed for best-estimate calculations when used as evidence to support safety cases.

6.4. Best Practice Guidelines for FIV analysis

Based on the available deliverables, the main outcomes of the GO-VIKING project will be evaluated. The gained experience and knowledge throughout the whole project on the use of FSI methods for FIV will be used to synthesize Best Practice Guidelines on the use of FSI methods for FIV evaluation for vendors, operators and regulators. These will be discussed with stakeholders and international partners. Their feedback will be considered in the final version of the document.

7. CONCLUSION

To improve the understanding and the prediction of FIV phenomena, relevant to nuclear power reactors, eighteen partners, ranging from vendors, operators, and TSOs to universities and research organizations, started in June 2022 the Horizon Europe GO-VIKING project. Within this project, experimental and numerical activities are combined to: (i) increase the experimental database of FIV inside NPPs; and, (ii) improve the existing capabilities of the numerical tools to simulate and predict these phenomena.

An overview of the GO-VIKING consortium was provided along with information about the project structure, including the main FSI topics and the tasks to be carried out. Furthermore, details of all planned experimental and numerical work that will be performed, were also presented.

The project will run for a total of four years, with the final product of the project being the Best Practice Guidelines that summarize the gained experience and knowledge throughout these years on the use of FSI methods for FIV evaluation. These will be disseminated to vendors, operators and regulators in order to support them in the design, evaluation and decision making in the field of FIV in nuclear power reactors.

8. ACKNOWLEDGEMENT

The work described in this paper is funded by the the Euratom research and training program 2022-2025 and various national research programs. All the partners are listed below:

- Gesellschaft für Anlagen- und Reaktorsicherheit gGmbH, Germany (GRS)
- Nuclear Research and consultancy Group, The Netherlands (NRG)
- Universiteit Gent (UGENT), Belgium
- LGI Sustainable Innovation, France (LGI)
- Electricité De France, France (EDF)
- Technische Universiteit Delft, Netherlands (TUD)
- Teknologian tutkimuskeskus VTT Oy, Finland (VTT)
- Framatome GmbH, Germany (FRA-G)
- Institut de Radioprotection et de Sûreté Nucléaire, France (IRSN)
- Institut von Karman de dynamique des fluides, Belgium (VKI)
- IPP Centre LLC, Ukraine (IPP)
- European Nuclear Education Network, Belgium (ENEN)
- University of Manchester, United Kingdom (UoM)
- Forsmarks Kraftgrupp AB, Sweden (FK)
- Commissariat à l'énergie atomique et aux energies alternatives, France (CEA)
- Pennsylvania State University, USA (PSU):
- Virginia Commonwealth University, USA (VCU).
- EDF Energy, United Kingdom (EDF-E)

9. REFERENCES

Au-Yang, M.K., 2001, *Flow-induced vibration of power and process plant components*, New York: ASME Press.

Cardolaccia, J, and Baj, F., 2015, *An Experimental Study of Fluid-Structure Interaction in Basic In-Line Arrangements of Cylinders*, PVP conference, Boston, MA, USA.

Cioncolini, A., Silva-Leon, J., Cooper, D., Quinn, M. K., Iacovides, H., 2018, *Axial-flow-induced vibration experiments on cantilever rods for nuclear reactor applications*, Nuclear Engineering and Design, 338, pp. 102-118.

Einzinger, J. and Ch. Frey, 2014, *Bi-directional Fluid-Structure Interaction with Model Order Reduction*, ANSYS Germany.

EPRI, 2008, *Fuel Reliability Guidelines: PWR Grid-to-Rod Fretting*, Technical report, 1015452.

Filonov, V. et al, 2020, *The Turbulent Pulsations Field Restoring for VVER-1000 Reactor Using Synthetic Turbulence Generation Procedure*, Proc. of the XXV ICTAM conference, Milan, Italy, 23-28 August, 2020.

Fischer, M., 2001, *Dreidimensionale numerische Simulation strömungsinduzierter Rohrbündelschwingungen*, Dissertation, Fakultät für Maschinenwesen, Technische Universität München.

IAEA, 2010, *Review of Fuel Failures in Water Cooled Reactors*, IAEA No NF-T-2.1, NE1445, Vienna, Austria.

IAEA, 2019, *Review of Fuel Failures in Water Cooled Reactors (2006-2015)*, IAEA No NFT-2.5, NE1864, Vienna, Austria.

Kottapalli, S., Shams, A., Zuijlen, A.H. van, Pourquie, M.J.B.M.., 2019. *Numerical investigation of an advanced U-RANS based pressure fluctuation model to simulate non-linear vibrations of nuclear fuel rods due to turbulent parallel-flow*. Annals of Nuclear Energy, vol 128, pp. 115-126.

Kotthoff, K., January 1984, *Erkenntnisse aus dem Ablauf ausländischer Vorkommnisse mit Dampferzeuger- Heizrohrbruch*, GRS 1984, Technische Mitteilungen, Bd. 77, Nr. 1.

MacDonald, P.E., Shah, V.N., Ward, L.W., and Ellison, P.G., 1996, *Steam generator tube failures*, NUREG/CR-6365 INEL-95/0383.

MYRTE, 2015, https://cordis.europa.eu/project/id/662186.

NRC, 2015, https://www.nrc.gov/docs/ML1501/ML15015A419.pdf.

Païdoussis M., 2006, *Real-life Experiences with Flow-induced Vibration*, Journal of Fluids and Structures, vol. 22, p.p. 741-755.

Papukchiev, A., 2022, *FSI Analysis of Flow-Induced Vibrations in a BWR Instrumentation Tube Experiment*, NURETH-19, Brussels, Belgium.

Sarma, R. and Dwight, R., 2017, *Uncertainty Reduction in Aeroelastic Systems with Time-Domain Reduced-Order Models*, AIAA Journal 55, no. 7, https://doi.org/10.2514/1.J055527.

SESAME, 2015, https://sesame-h2020.eu/

Zwijsen, K., et al, 2022, *VIKING: A joint industry project on Flow-Induced Vibrations*, NURETH-19, Brussels, Belgium

10. TRADEMARKS

IN WIND TUNNEL THE REPRODUCTION OF VORTEX SHEDDING BEHIND CIRCULAR CYLINDERS AT HIGH REYNOLDS NUMBER REGIMES IS INCOMPLETE

Øyvind Mortveit Ellingsen
LadHyX, CNRS-Ecole polytechnique, Palaiseau, France & CSTB, Nantes, France
Xavier Amandolese
LadHyX, CNRS-Ecole polytechnique, Palaiseau, France & LMSSC, CNAM, Paris, France
Pascal Hémon
LadHyX, CNRS-Ecole polytechnique, Palaiseau, France

ABSTRACT

Wind tunnel tests of 2D rough cylinders are presented. The goal is to simulate the alternate vortex shedding in flow regimes encountered in wind engineering applications, where the full scale Reynolds number is larger than the one that can be reproduced in wind tunnel with small scaled models.

Measurements are mainly the synchronized unsteady wall pressures on the cylinder which are post processed using bi-orthogonal decompositions.

By comparing the small scale results with those from a previous large scale experiment, we show that the technique of rough cylinder is incomplete and can approach roughly global parameters only.

1. INTRODUCTION

The circular cylinder is the bluff body which is one of the most studied bodies in aerodynamics along years. The circular shape induces indeed fundamental properties of flow, such as stall and unsteady wake and it has a great relevance in engineering applications. Especially in civil engineering there are numerous cases where circular cylinders of various diameters are submitted to wind and excitation by vortex shedding.

However the flow regime around this bluff body is extremely dependent on the Reynolds number which combines the effect of the cylinder's diameter D and the mean wind velocity $\bar{U}$ such that:

$$Re = \frac{\bar{U}D}{\nu} \quad \#(1)$$

where ν is the air kinematic viscosity, as studied by (Adachi 1985; James et al. 1980; Warschauer & Leene 1971) and reviewed by Zdravkovich (1990).

The drag force coefficient of a 2D smooth circular cylinder is given in Figure 1 versus the Reynolds number, showing the data provided by the Eurocode (2005). For aerodynamic flows of practical applications with Re greater than 10 000, three kinds of regime can be observed, namely subcritical with $Re \lesssim 200\,000$, critical if $200\,000 \lesssim Re \lesssim 600\,000$ and supercritical when $Re \gtrsim 600\,000$ (Roshko 1961; Lienhard 1966; Hoerner 1965; Simu & Scanlan 1978; Schewe 1983; Blevins 2001).

Following the same trend, the non dimensional frequency of the shedding, given by the Strouhal number

$$St = \frac{f\,D}{\bar{U}} \quad \#(2)$$

in which f is the dimensional frequency, is plotted in Figure 2 (Shi et al. 1993; Adachi 1997; Zan 2008; van Hinsberg 2015; Ellingsen et al. 2022).

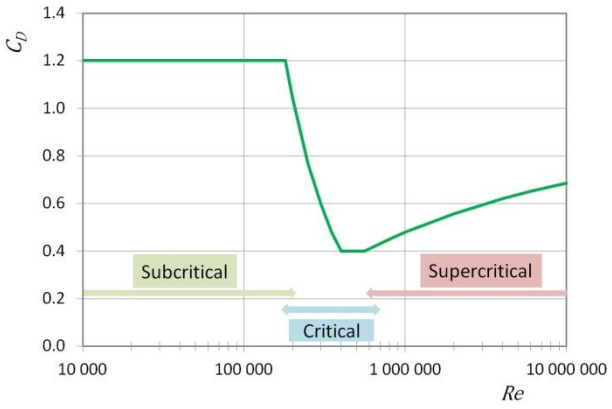

Figure 1. C_D versus Re from Eurocode and definition of flow regimes

In subcritical regime the boundary layer around the cylinder is laminar prior to its separation and the drag force coefficient $C_D = 1.2$. The alternate vortex shedding is well established and one observes that $St = 0.19 - 0.20$.

As the Reynolds number increases, the cylinder is subject to the "drag crisis" which characterizes the critical regime. This regime presents large variation of the drag force coefficient that decreases down to 0.4. The alternate vortex shedding is not well organized.

When the Reynolds number is further increased, reaching the supercritical regime, the drag coefficient C_D is characterized by a smooth monotonic increase from 0.4 to 0.65. One can also observe a re-organization of the wake with an alternate vortex shedding having a Strouhal number subject to scattering, typically in the range 0.19 – 0.27. Recently in a large scale wind tunnel testing (Ellingsen et al 2022), we have shown that the scatter might be due to twin Strouhal numbers as shown Figure 2.

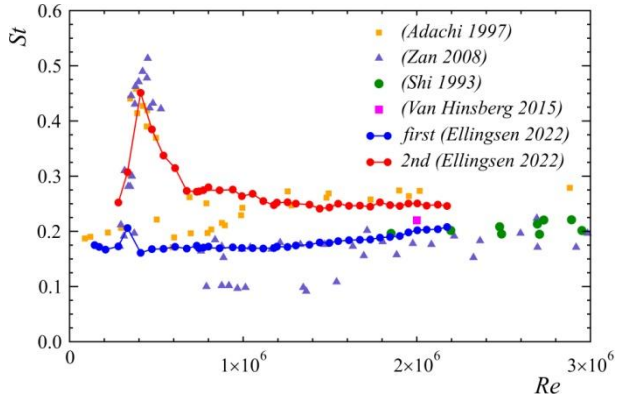

Figure 2. St versus Re from different authors

From these data, it turns out obvious that wind tunnel tests have to be made at the right Reynolds number which is encountered in the application. For instance in wind engineering (Lupi et al. 2017; Ellingsen et al. 2021), industrial chimneys have typically a diameter of 2 m and a natural first bending frequency of the order of 1 Hz. Then the critical wind velocity at which the resonance occurs with the alternate vortex shedding is in the range 7.5-10 m/s. The Reynolds number range for this case is then 10^6 – 1.3 10^6, which is in the low region of the supercritical regime mentioned above.

But in practice for wind tunnel testing of such structures, scaled models typically of the order of 1/100 are used. This leads to a diameter of the chimney model of 2 cm and requires a wind velocity, in order to comply with the Reynolds number similarity, which is impossible to reach in a subsonic wind tunnel.

To compensate for this, a number of authors have considered the technique of added roughness on the cylinder model (Achenbach 1971; Szechenyi 1975, Achenbach & Heinecke 1981; Nakamura & Tomari 1982; Shih et al. 1993; Adachi 1997; van Hinsberg 2015). Rough cylinders are indeed known for shifting the drag crisis at smaller Reynolds numbers, depending on the roughness height. Global parameters such as the drag force coefficient C_D, the unsteady lift coefficient (RMS value) C_ℓ' and the Strouhal number St are mainly used to calibrate added roughness techniques. But while it is used in wind tunnel testing (Barré & Barnaud 1995), the ability of such techniques to reproduce realistic supercritical flows is still being debated. The goal of this paper is to present wind tunnel results obtained with small scale cylinders equipped with roughness, in order to tentatively simulate the vortex shedding occurring at supercritical Reynolds number. Unsteady wall pressures are the main measured data and will be compared to those measured on a large scale cylinder from a previous experimental study (Ellingsen et al. 2022).

2. EXPERIMENTAL APPARATUS

The wind tunnel tests were performed in the NSA CSTB's wind tunnel in Nantes. The aerodynamic test section, 2x4 m^2, can reach a maximum wind speed of 30 m/s without turbulence generating grid and 19 m/s with it. The turbulence generating grid consists of semi-circular lengths of PVC tubing with the circular side towards the inflow and the flat side downstream. The grid components have a width of 0.05 m and the distance between two parallel lengths components are 0.2 m when measured from the center of each. When used, this grid was mounted 3.1 m upstream of the test model.

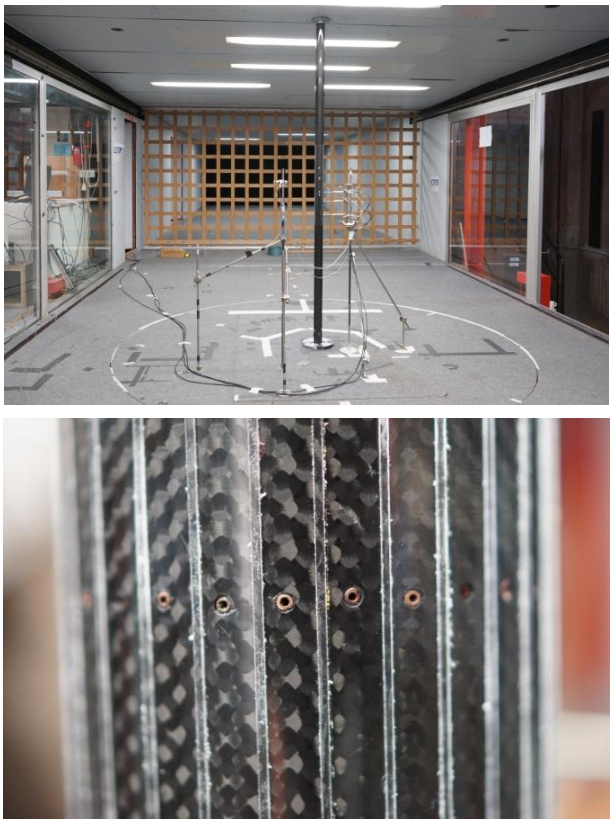

Figure 3. Photo of the wind tunnel setup and detailed view of the pressure taps and ribs on the cylinder model

A preliminary calibration in the empty test section was performed by mounting another Pitot tube at the cylinder model location to correlate the velocity seen by the model with the one measured by the reference Pitot tube. Cobra probes enabled characterization of the turbulence intensity in the three directions. For the configuration without turbulence generator, the turbulence is 1% in the main direction of the flow and 0.8% for the others. With the turbulence generating grid the turbulence intensity is 6% and 3% in the main direction and the two others respectively.

The test model consists of a circular cylinder made of carbon with diameter 0.055 m and vertically mounted in the wind tunnel, see Figure 3. It extends the entire 2 m height with the measurement location at mid-height. This section is equipped with 30 uniformly spaced pressure taps. The first pressure tap is placed at the stagnation point (θ = 0°) and the rest spaced out uniformly with a separation of 12°. Vinyl tubing with length 1.0 m connects the pressure taps to a synchronized 32-channels pressure scanner (32HD ESP pressure scanner from Pressure Systems Inc.) with multiplex frequency of 70 kHz. The pressure scanner was rated up to 2500 Pa and have static errors within ± 0.03 %.

During the tests, the wind tunnel speed is kept constant for each measurement point and all the measured signals are recorded during 180 s at the sampling frequency of 400 Hz.

The cylinder has a first damped natural frequency of 25 Hz and a critical damping ratio of 2.1% which make the vibration level negligible.

To add roughness to the circular cylinder, ribs with rectangular cross-section at 12° intervals are attached on the circumference. Ribs having a cross section of constant width 0.8 mm and three different thicknesses h =0.2, 0.5 and 1 mm are tested. They are made with acrylic sheets of different thicknesses from which ribs are obtained with a numerically controlled laser cutter. The resulting non-dimensional roughness are $k = h/D$ =3.6 10^{-3}, 9.1 10^{-3} and 18.2 10^{-3}.

3. GLOBAL RESULTS

The drag coefficients and the unsteady lift coefficients are shown in Figure 4 for the smooth flow and turbulent flow conditions.

One can observe that each roughness configuration promotes an earlier critical regime, down to Reynolds number values at least ten times lower than for the reference values reported in Figure 1. However, the supercritical regime is not fully reached for the thinner ribs with a thickness 0.2 mm. This is in agreement with the assumption based on Szechenyi's results (Szechenyi 1975) that the supercritical regime cannot be reached for Re_h< 200, (the Reynolds number based on the rugosity height h) which is the case here for the smaller roughness when Re < 55 000.

Globally the added upstream turbulence (from 1 to 6 %) promotes the critical regime to occur earlier but does not change drastically the flow nature. However the roughness height is of major importance in the phenomenon. For the roughness, 0.5 mm, the supercritical regime seems to be reached for Re > 40 000 and even earlier than the minimum wind tunnel speed for the roughness height of 1 mm.

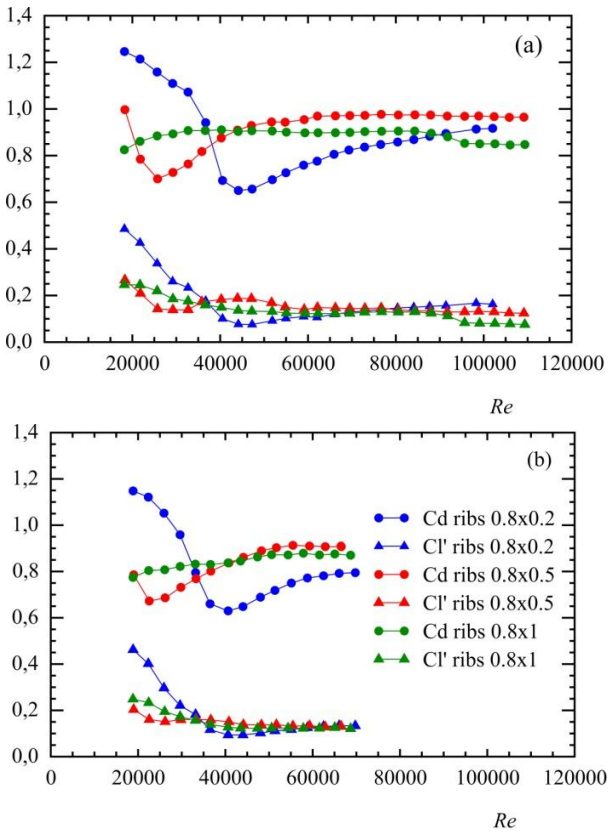

Figure 4. C_D and C_ℓ' versus Re for rough cylinders; (a) smooth flow; (b) turbulent flow

The Strouhal number is obtained with the PSD of the lateral velocity component issued from the Cobra probes. Main results are given in Figure 5 with few data points from (Adachi 1997) obtained with a cylinder equipped with roughness k = 2.54 10^{-3} which is a little lower than the smallest ribs used here. Globally there is agreement although experimental conditions are not exactly similar.

For the medium size roughness 0.5 mm, the differences between smooth and turbulent flows follow what has been previously observed on the drag force. Beyond Re =40 000 the Strouhal number doesn't change and remains in the range [0.21-0.22].

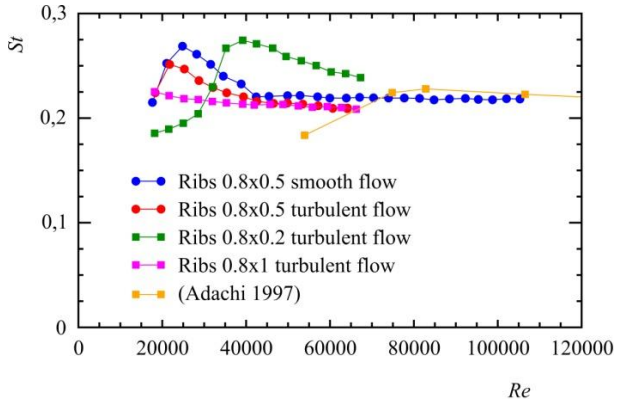

Figure 5. St versus Re for rough cylinders.

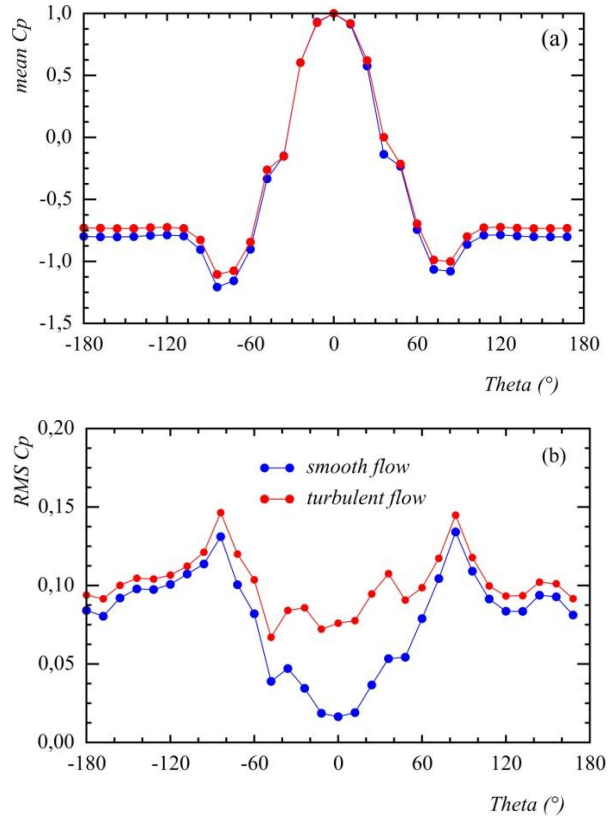

Figure 6. Pressure coefficients for ribs 0.8x0.5 at Re=66 000; (a) time averaged; (b) RMS.

The choice of the "best" roughness height to reproduce the supercritical regime is not trivial, but might be done with simple criteria. Firstly we must note that the evolution of the drag coefficient with Reynolds number and that of the Strouhal number are reproduced with the intermediate value 0.8x0.5 mm: in the low Reynolds number range, the critical region is visible and the stabilization of the coefficients is reached further. On the contrary, the small roughness height does not show any stabilization, and the highest roughness has no critical regime. This is of course in relation with the capacities of the wind tunnel to provide a sufficient wide range of velocities, in smooth and turbulent flow.

From that single argument we may assume that the roughness 0.8x0.5 mm must be selected. A deeper analysis is performed in the next section with the analysis of the wall pressure distributions and further comparisons are given in the conclusion.

4. PRESSURE DISTRIBUTION

The wall pressure distribution is shown in Figure 6 for the ribs 0.8x0.5 mm at the Reynolds number 66 000 for smooth and turbulent flow. The pressure coefficient is defined as

$$Cp(\theta,t) = \frac{P(\theta,t) - P_{ref}}{\frac{1}{2}\rho \overline{U}^2} \quad \#(3)$$

where $P(\theta,t)$ is the instantaneous measured pressure at the azimuth angle θ. The reference pressure P_{ref} is the mean static pressure in the wind tunnel obtained from the reference Pitot tube and ρ is the air density corrected by atmospheric pressure and air temperature.

The differences between the two upstream flow cases are small, except for the standard deviations in the front region of the cylinder section ($-45° < \theta < 45°$) where the turbulent flow contributes to an increase of the fluctuations.

5. ANALYSIS OF THE WALL PRESSURE

In this section we use the bi-orthogonal decomposition (BOD) of the wall pressure signals in order to better analyze the results.

5.1. The bi-orthogonal decomposition

We recall here the analyzing technique which was first introduced by (Aubry et al. 1991). The idea of the BOD is to decompose the spatio-temporal signal $Cp(\theta,t)$ in a series of spatial functions $\phi_i(\theta)$ named further as "topos", coupled with a series of temporal functions $\psi_i(t)$ named "chronos". The BOD can be written as

$$Cp(\theta,t) = \sum_{i=1}^{N} \alpha_i \, \phi_i(\theta) \, \psi_i(t) \quad \#(4)$$

where α_i are the eigenvalues of the spatial or the temporal covariance matrix of the signal $Cp(\theta,t)$. N is the number of terms retained for the decomposition. Chronos and topos are orthogonal between them and normed. Mathematical details can be found in (Aubry & Lima 1991) and practical applications are presented in (Hémon & Santi 2003).

It was shown that the eigenvalues α_i are common to chronos and topos and that the series con-

verge rapidly so that N is possibly small compared to the original size T of the problem (the smallest between the number of pressure taps and the number of time records). This means that the α_i have a numerical value that decreases rapidly. Their sum $A = \sum_{i=1}^{T} \alpha_i$ represents the total energy in the original signal. Then each couple of chronos and topos have their contribution to the signal which decreases as long as their rank i increases.

Moreover, by proper spatial integration of the topos $\phi_i(\theta)$ it is possible to determine the contribution of that term to the drag or the lift force, having in mind the corresponding chronos $\psi_i(t)$ which provides the time evolution of the couple $\phi_i(\theta)\,\psi_i(t)$. Hence the PSD of chronos can also be calculated in the same way than the cobra probes signals in order to determine their main frequency content.

Note that BOD is very similar to proper orthogonal decomposition (POD), except that the mean value of the original signal is kept in the analysis, refer to (Hémon & Santi 2003) for a discussion on that point.

5.2. BOD of wall pressure signals

The analysis is performed with the cylinder equipped with the roughness 0.8x0.5 mm which is assumed to be the best configuration for approaching the supercritical regime.

It appears that the BOD turns out very efficient in compressing the data with the first two terms taking almost 99.9 % of the energy. The first one corresponds to the mean value of the pressure distribution, producing the static drag, while the second one is the main unsteady component, producing the unsteady lift generated by the vortex shedding.

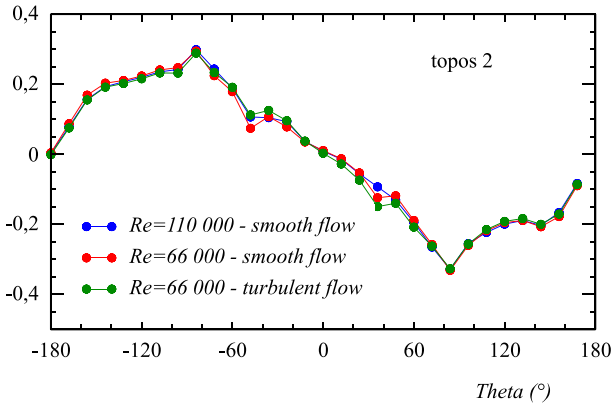

Figure 7. Topos 2 for ribs 0.8x0.5 in different flow conditions.

The topos 2 is shown in Figure 7 for different flow conditions. We note that, in the range explored, the shape of the topos 2 is not influenced by the Reynolds number or the flow turbulence. It is characterized by two anti-symmetrical bumps with their maximum located at $\theta = \pm 80°$, which creates a strong unsteady lift.

The topos of higher rank are more noisy and do not present a clear spatial organization which could be linked to the alternate vortex shedding phenomenon.

This is coherent with the lack of emerging frequency in the corresponding chronos, while the Strouhal number found with the PSD of the chronos 2 is in full agreement with the one which was found in the wake (see Figure 5), either in smooth or turbulent flow.

Determining the contribution of the topos 2 to the unsteady lift versus Reynolds number, we find an almost constant contribution of 87-90 % of the total force. Therefore the second term of the BOD is clearly the term which generates the lift force due to the alternate vortex shedding.

6. COMPARISON WITH THE SUPERCRITICAL REGIME

The comparison of the results obtained with the rough cylinder is performed with the results of Ellingsen et al. (2022) where the same kind of measurements were performed with a large smooth cylinder in a large wind tunnel. The Reynolds number in supercritical regime was achieved up to 2 170 000.

A first comparison on global parameters can be done using Tables 1 and 2. Few points must be pointed out:

- The drag coefficient of the rough cylinder is larger (+ 76 % than for the supercritical flow)
- The unsteady lift is larger also (+ 15 %)
- There is only one Strouhal number which value is between the twin Strouhal numbers observed in the true supercritical regime.

C_D	0.97	$C_\ell{}'$	0.146
St	0.22		
Cp_{min}	-1.2	Location θ	$\pm$ 80°
$Cp_{max}{}'$	0.13	Location θ	$\pm$ 80°

Table 1. Main results for ribs 0.8x0.5 at Re=66 000 in smooth flow

C_D	0.55	$C_\ell{}'$	0.127
St_1	0.20	St_2	0.25
Cp_{min}	-2.5	Location θ	$\pm$ 80°
$Cp_{max}{}'$	0.3	Location θ	$\pm$ 110°

Table 2. Main results for a smooth cylinder at Re=2 000 000 (Ellingsen et al. 2022)

There are also significant differences in the pressure distribution, as it can be seen in the Figure 8, for both the time averaged and RMS values. In particular the minimum, while located at the same place, is almost twice (negatively) for the reference supercritical configuration. The RMS distribution exhibits even greater differences, having its maximum at different places, ± 80° for the rough cylinder against ± 110° for supercritical flow. Moreover the maximum RMS values are more than doubled in supercritical flow (0.3 against 0.13).

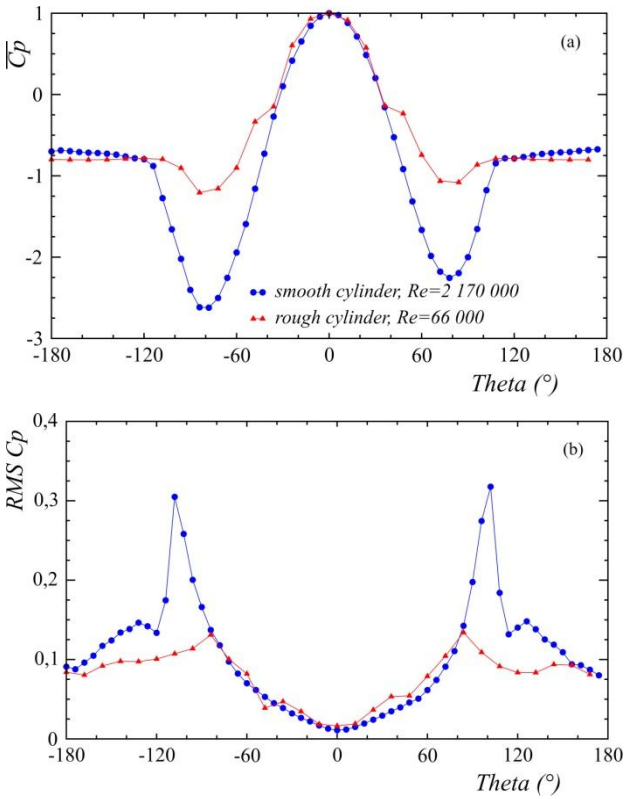

Figure 8. Comparison of the pressure distribution of the cylinder with ribs 0.8x0.5 at Re=66 000 in smooth flow and a smooth cylinder at Re=2 170 000 from (Ellingsen et al. 2022) (a) time averaged (b) RMS value

The tendencies observed on the RMS pressure distribution are found in the analysis through the BOD. The topos 2 in the two cases is shown in Figure 9. This term is responsible of 90 % of the total unsteady lift at a single Strouhal frequency for the rough cylinder.

In true supercritical regime, the same term represents also 89 % of the unsteady lift but at the first Strouhal frequency. Another BOD term (number 4, see (Ellingsen et al. 2022)) associated to a second Strouhal frequency is necessary to recover the unsteady lift force.

The unsteady pressure distribution which generates the unsteady lift force due to vortex shedding is therefore very different in the two cases.

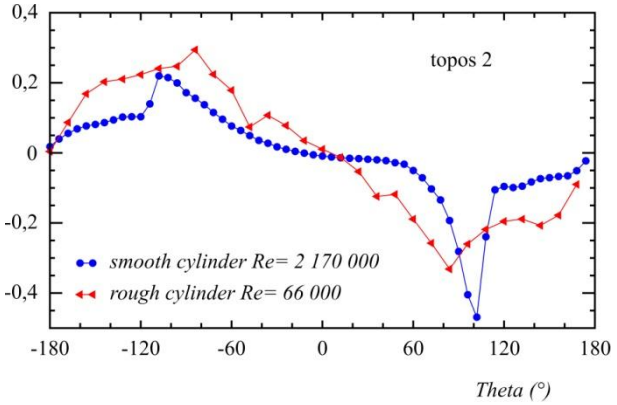

Figure 9. Comparison of the topos 2 of the cylinder with ribs 0.8x0.5 at Re=66 000 in smooth flow and a smooth cylinder at Re=2 170 000 from (Ellingsen et al. 2022).

7. CONCLUSIONS

Small scale experiments with a cylinder equipped with artificial roughness show that the flow at supercritical regime can be roughly approached, as on the unsteady lift coefficient, but it remains far from being reproduced. The second Strouhal number is absent and the measured value is between the two ones of the supercritical regime. The corresponding unsteady lift is only recovered by the second structure in the BOD. Moreover the shapes of the topos are quite different: the lift production at supercritical Reynolds number is concentrated in a narrow region of the azimuth angle, while the lift is produced in a wider range for the artificially simulated supercritical flow case.

8. ACKNOWLEDGEMENTS

This work is part of a partnership co-funded by Beirens (Poujoulat Group), Centre Scientifique et Technique du Bâtiment (CSTB), Centre National d'Etudes Spatiales (CNES) and LadHyX, CNRS-Ecole polytechnique.

Special acknowledgement is extended to Olivier Flamand from CSTB for the wind tunnel operation.

9. REFERENCES

Achenbach, E., 1968. Distribution of local pressure and skin friction around a circular cylinder in cross-flow up to *Re*=5x10^6. *J. Fluid Mech.*, **34(4)**, 625-639.

Achenbach, E., 1971. Influence of surface roughness on the cross-flow around a circular cylinder. *J. Fluid Mech.,* **46(2),** 321–335.

Achenbach, E., Heinecke, E., 1981. On vortex shedding from smooth and rough cylinders in the range of Reynolds numbers $6x10^3$ to $5x10^6$. *J. Fluid Mech.,* **109**, 239–251.

Adachi, T., Matsuuchi, K., Matsuda, S., Kawai, T., 1985. On the force and vortex shedding on a circular cylinder from subcritical up to transcritical Reynolds numbers. *Bul. JSME,* **28(243)**, 1906-1909.

Adachi, T., 1997. Effects of surface roughness on the universal Strouhal number over the wide Reynolds number range. *J. Wind Eng. & Indus. Aerod.,* **69-71**, 399–412.

Aubry, N., Guyonnet, R., Lima, R., 1991. Spatio-temporal analysis of complex signals: Theory and applications. *J. Stat. Phys.,* **64.3**, 683–739.

Barré, C. and Barnaud, G. 1995. High Reynolds number simulation techniques and their application to shaped structures model test. *J. Wind Eng. & Indus. Aerod.*, **57**, 145-157.

Bergh, H., Tijdeman, H., 1965. Theoretical and experimental results for the dynamic response of pressure measuring systems. Tech. report NLR-TR F.238, National aero- and astronautical research institute, Nationaal Luchten Ruimtevaart-laboratorium. Amsterdam, Netherlands.

Blevins, R.D., 2001. Flow-Induced Vibration. 2nd edition, Krieger. ISBN: 978-1-57524-183-8

Ellingsen, Ø. M., Flamand, O., Amandolese, X., Coiffet, F., Hémon, P., 2021. Field tests on a full-scale steel chimney subjected to vortex-induced vibrations. *Structual Engineering International*.

Ellingsen, Ø. M., Amandolese, X., Flamand, O., Hémon, P., 2022. Twin Strouhal numbers in pressure loading of circular cylinder at high Reynolds numbers. To appear in *J. Fluids & Struct*.

European Committee for Standardization, 2005. Eurocode 1: Actions on structures - Part 1-4: General actions - Wind actions. Ref. n° EN 1991-1-4:2005 F.

Fung, Y.C., 1960. Fluctuating Lift and Drag Acting on a Cylinder in a Flow at Supercritical Reynolds Numbers. *J. Aerosp. Sci.,* **27.11**, 801–814.

Hémon, P., Santi, F., 2003. Applications of biorthogonal decompositions in fluid-structure interactions. *J. Fluids & Struct.,* **17.8**, 1123–1143.

Hoerner, S. F., 1965. Résistance à l'avancement dans les fluides (Fluid Dynamic Drag). Gauthiers-Villars éditeurs, Paris.

James, W., D., Paris, S., W., Malcom, G., N., 1980. Study of viscous crossflow effects on circular cylinders at high Reynolds numbers. *AIAA Journal*, **18(9),** 1066-1072.

Lienhard, J. H., 1966. Synopsis of lift, drag, and vortex frequency data for rigid circular cylinders. 300, Technical Extension Service, Washington State University.

Lupi, F., Niemann, H.-J., Höffer, R., 2017. A novel spectral method for cross-wind vibrations: Application to 27 full-scale chimneys. *J. Wind Eng. & Indus. Aerod.,* **171**, 353–365.

Nakamura, Y., Tomonari, Y., 1982. The effects of surface roughness on the flow past circular cylinders at high Reynolds numbers. *J. Fluid Mech.,* **123**, 363-378.

Roshko, A., 1961. Experiments on the flow past a circular cylinder at very high Reynolds number. *J. Fluid Mech.*, **10**, 345-346.

Schewe, G., 1983. On the force fluctuations acting on a circular cylinder in crossflow from subcritical up to transcritical Reynolds numbers. *J. Fluid Mech.*, **133**, 265-285.

Shih, W. C. L., Wang, C., Coles, D., Roshko, A., 1993. Experiments on flow past rough circular cylinders at large Reynolds numbers. *J. Wind Eng. & Indus. Aerod.,* **49.1**, 351–368.

Simiu, E., Scanlan, R., H., 1978. Wind effects on structures. An introduction to wind engineering. Wiley & Sons, New York.

Szechenyi, E., 1975. Supercritical Reynolds number simulation for two-dimensional flow over circular cylinders. *J. Fluid Mech.,* **70.3**, 529-542.

van Hinsberg, N. P., 2015. The Reynolds number dependency of the steady and unsteady loading on a slightly rough circular cylinder: From subcritical up to high transcritical flow state. *J. Fluids & Struct.*, **55**, 526-539.

Warschauer, K., A., Leene, J., A., 1971. Experiments on mean and fluctuating pressures of circular cylinders at cross flow at very high Reynolds numbers. In Proc. of the *Inter. Conf. on Wind Effects on Buildings and Structures*, Tokyo, Japan, 15–20 August 1971, 305–315.

Zan, S. J., 2008. Experiments on circular cylinders in crossflow at Reynolds numbers up to 7 million. *J. Wind Eng. & Indus. Aerod.***, 96**, 880-886.

Zdravkovich, M.,M., 1990. Conceptual overview of laminar and turbulent flows past smooth and rough circular cylinders. *J. Wind Eng. & Indus. Aerod.,* **33**, 53-52.

NUMERICAL PREDICTION OF AXIAL-FLOW-INDUCED VIBRATIONS IN NUCLEAR FUEL ROD

Justyna Salachna, Andrea Cioncolini, Hector Iacovides #1
#1 Thermo-Fluids Research Group, Department of Mechanical, Aerospace and Civil Engineering, The University of Manchester, Manchester, M13 9PL, United Kingdom

ABSTRACT

This study investigates the computational modelling of flow-induced vibrations of cantilever rods subjected to turbulent axial flow at operating conditions relevant to those of fuel rods of pressurized-water-cooled (PWR) nuclear reactors. The aim is to assemble all the modelling elements needed for a cost-effective and thus URANS-based modelling strategy, employing high-Reynolds-number turbulence models and using existing experimental data for validation. The study involves:

- *Assessment and evaluation of URANS models (namely, the effective viscosity models, $k-\omega$, $k-\varepsilon$, $k-\omega$ SST and Reynolds Stress Models LRR and SSG) to effectively reproduce fluctuating forces which can induce vibrations on a suitable representative 2D test case with rigid walls of Camussi et al (2008)*
- *Two-way FSI simulations validated against the experimental data of Cioncolini et al (2018).*

The resulting comparisons show that for the first time, to our knowledge, both the frequency and the amplitude of the flow-induced vibrations of this case, have been successfully reproduced.

1. INTRODUCTION

In pressurized-water-cooled nuclear reactors, flow-induced vibration usually occurs in the primary loop, where components are subjected to relatively high flow velocities. Typical of such components are pipes, nuclear fuel rods in the fuel assembly, tube bundles in the steam generators and the in-core instrumentation Pettigrew (1977); Borsoi (2001). Axial-flow-induced vibrations can cause constant or intermittent contact between a component and its supports: this generates long-term damage such as fretting wear and mechanical fatigue. Axial-flow-induced vibrations are normally characterized by relatively small amplitude vibrations, and have so far received comparatively little research attention as opposed to other types of flow-induced vibrations. This mode of flow-induced vibration has, however, been identified as a common cause failure of 55 % PWR fuel leaks worldwide, IAEA (2010). Understanding the physical mechanism that controls fluid-structure interaction for the basic configuration, such as slender structures in axial confined flow, is therefore crucial for increasing the lifespan of nuclear components and, consequently, will positively impact financial and safety performance. The nuclear industry has identified the need for a more comprehensive and quantitative understanding of the physical mechanism that controls fluid-structure interaction for this configuration Borsoi (2001). The fundamental understanding of the relation of excitation forces to vibration exerted on the fuel rods is still limited. Primarily, the numerical simulation will have to be benchmarked by experiments, especially for specific configurations and flow conditions.

Previous studies have predominantly focused on determining the natural frequency of vibrating beams in the presence of highly turbulent flow and have generally failed to correctly reproduce the flow-induced amplitude of vibrations. Several prominent numerical models were developed for the flow-induced vibrations in nuclear fuel rods. De Ridder et al (2013); De Santis et al (2017, 2020); Hofstede et al (2018) studied solitary rod subjected to axial turbulent flow. The flow was computed using unsteady Reynolds-averaged Navier-Stokes (URANS) with the $k-\omega$ SST model of Menter. Calculated frequencies of vibrations showed good agreement with the experiments. However, the resulting time history of the computed displacement showed that vibrations were damped. The rod frequency estimation relied on that short time of vibration. Consequently, in those earlier studies, the excitation due to fluctuating pressures is absent. Kottapalli et al (2019) generated velocity and pressure fluctuations with a stochastic model. Vibrations remained self-sustained but the amplitude of vibration was five times lower a than the experimental values of Chen (1971). De Santis et al (2019) performed simulations with the same approach, and the model presents a 10 % error against the experimental data of Liu et al (2017) for the turbulent-

induced vibration. Christon et al (2016) performed the assessment of three turbulence models: Large-eddy Simulation (LES), Detached-Eddy Simulation (DES) and URANS. It has been shown that the LES model presents adequate force fluctuations to assess the grid-to-rod fretting but the use of the model is computationally expensive.

The primary aim of this paper is to present a fully validated benchmark simulation of the turbulent flow interaction with the flexible structure.

2. NUMERICAL METHODOLOGY

The OpenFOAM fluid-solid interaction (FSI) solver adopted here Tuković (2018) implements the partitioned approach: the fluid and the structure domains are solved separately and with a strong coupling scheme, implemented to conserve the momentum and energy across the interface. Fluid and solid governing equations are discretized with the finite volume method (FV), as described below.

2.1. Fluid governing equations

When modelling the FSI problem, the moving structure is described in a Lagrangian frame of reference, and fluid equations need to be computed in the time-varying boundary. This is achieved by using an Arbitrary Lagrangian-Eulerian (ALE) frame of reference in the fluid domain. The Navier-Stokes equations are formulated to include a moving grid, in order to accommodate the deforming boundary:

$$\frac{\partial (U_i)}{\partial x_i} = 0, \tag{1}$$

$$\frac{\partial (\rho U_i)}{\partial t} + \frac{\partial}{\partial x_j}\left[\rho (U_i - w) U_j\right] = -\frac{\partial P}{\partial x_i} + \frac{\partial}{\partial x_j}\left(\mu \frac{\partial U_i}{\partial x_j}\right), \tag{2}$$

where U is the fluid velocity and w is the interface grid velocity. When $w = 0$ and when $w = U_i$, the pure Euler and Lagrange formulations are restored, respectively. μ is the dynamic viscosity, P is the fluid pressure, and ρ is the fluid density. The flow is assumed to be isothermal.

2.1.1. Mesh deformation

The shape of the fluid domain changes dynamically due to the deformation of the solid boundary at every time step. The mesh motion, w, is computed by solving a Laplace equation with a diffusion coefficient that changes throughout the domain as in Equation 3. The method is described in detail in Jasak (2006); Lohner (1996):

$$\frac{\partial}{\partial x_i}\left(\gamma \frac{\partial w}{\partial x_j}\right) = 0. \tag{3}$$

The diffusion coefficient γ is a function of the distance from the body l defined as:

$$\gamma(l) = \frac{1}{l^m}, \tag{4}$$

where the exponent m is an adjustable parameter set by the user. The axial flow-induced vibrations of interest here are characterized by relatively small deformations, so that a diffusion coefficient varying linearly with the distance from the moving walls (i.e. $m = 1$) was deemed appropriate.

2.1.2. RANS Modelling

In the Reynolds Averaged Navier-Stokes (RANS) framework, the Reynolds stresses $\overline{u_i u_j}$ appear to incorporate the effect of turbulence mixing on the transport of mean momentum. These are six additional non-zero stresses, three normal stresses and three shear stresses, and can be modelled using different strategies as described below.

If linear EVMs are adopted, the turbulent shear stress tensor, $\overline{u_i u_j}$, is assumed to be linearly related to the mean strain rate tensor through:

$$\overline{u_i u_j} = -\nu_t \left(\frac{\partial U_i}{\partial x_j} + \frac{\partial U_j}{\partial x_i}\right) + 2/3 k \delta_{ij}, \tag{5}$$

where ν_t is referred to as the turbulent viscosity, and it is the property of the flow. Two-equation models use two transport equations: one for turbulent kinetic energy k and one usually for either the dissipation rate of the turbulent kinetic energy, ε, or the ω (ε/k) to close the system of equations.

In the Reynolds stress equation models (RSM), six transport equations are solved, one for each of the Reynolds stresses, in conjunction with the transport equation for the rate of dissipation of turbulent kinetic energy ε. The rate of change of the Reynolds stress $\overline{u_i u_j}$ can be represented as:

$$\frac{D u_i u_j}{Dt} = P_{ij} - \varepsilon_{ij} + \phi_{ij} - D_{ij}. \tag{6}$$

The production term is:

$$P_{ij} = -\left(\overline{u_j u_k}\frac{\partial U_i}{\partial x_k} + \overline{u_j u_k}\frac{\partial U_j}{\partial x_k}\right). \tag{7}$$

The diffusion D_{ij}, dissipation rate ε_{ij} and the pressure-strain correlation ϕ_{ij} require modelling. Two RSM schemes are available in OpenFOAM:

high Reynolds LRR by Launder (1975) and high Reynolds SSG by Speziale (1991). These models differ in expressing the pressure-strain term. In the LRR, pressure strain is defined as the sum of the slow pressure strain term that makes the turbulence more isotropic, and the rapid term accounts for the very strong velocity gradient that produces the eddies. Additional corrections are applied to account for the wall proximity on the pressure-strain terms. In the SSG, the pressure strain is linear in mean strain and rotation tensors that vary quadratically with Reynolds stresses' stress anisotropy are introduced to account for the wall proximity.

2.2. Linear elastic equations

The differential equation of motion of a deformable solid is:

$$\rho \frac{\partial^2 u_i}{\partial t^2} + \frac{\partial \sigma_{ij}}{\partial x_j} + f_i = 0. \tag{8}$$

In this equation u is the solid displacement, ρ is the material density, σ_{ij} is the stress tensor and f_i is the volumic body force.

In the linearly elastic range, stress is directly proportional to strain. For an isotropic material, the stress-strain relationship can be written in indicial form as:

$$\sigma_{ij} = 2\mu\varepsilon_{ij} + \lambda\delta_{ij}\varepsilon_{kk}. \tag{9}$$

Here the shear modulus μ and the quantity λ are the Lamé's constants. In the case of small strains and small rotations the strain-displacement relations simplify as follows:

$$\varepsilon_{ij} = \frac{1}{2}(u_{i,j} + u_{j,i}). \tag{10}$$

Upon substituting the equations 9 and 10 into the equation of motion 8, this latter can be solved for the displacements:

$$\rho \frac{\partial^2 u_i}{\partial t^2} + (\lambda + \mu) \frac{\partial}{\partial x_i}\left(\frac{\partial u_j}{\partial x_j}\right) + \mu \frac{\partial^2 u_i}{\partial {x_j}^2} + f_i = 0. \tag{11}$$

The mathematical models are discretized using the cell-centred finite volume method. The system of linear algebraic equations is solved using the segregated algorithm described in Cardiff (2018); Tuković (2018). The displacement vector u is temporally decomposed into three components and solved iteratively. Outer iterations are performed to re-couple the momentum equation.

2.3. Fluid Structure Interaction

The fluid governing equations and solid models are coupled by two following conditions, which must be satisfied at the fluid-solid interface:

1. The kinematic coupling condition, stating that the velocity and displacement must be continuous across the interface:

$$u_{F,i} = u_{S,i} = \frac{dx_{S,i}}{dt}, \tag{12}$$

Where u_F is the velocity of the fluid and x_S is the solid displacement, subscript i represents the quantities at the fluid-solid interface. x_S is equivalent to the u displacement in the solid governing equation, Equation 11.

2. The dynamic coupling condition stating that the fluid forces and the solid forces are equal at the interface:

$$n_i\sigma_{F,i} = n_i\sigma_{S,i}. \tag{13}$$

Here n_i is the normal unit vector at the interface. Subscripts F and S correspond to the fluid and solid domain.

To ensure that the equilibrium of the velocity and force on the fluid-solid interface is met for each time step, the strongly coupled Gauss-Seidel iteration procedure is applied. To accelerate the sub-iteration convergence, relaxation procedures based on dynamically changed relaxation factor, Aitken, Irons (1969) and the IQN-ILS by Degroote (2009) are available in the OpenFOAM's FSI solver. For the test cases documented here we adopted the Aitken procedure.

3. RESULTS AND DISCUSSION

The purpose of this investigation has been to develop a benchmark simulation for the Flow-Induced Vibration phenomena in nuclear industry. In all models, the high-Reynolds-number approach with the wall functions has been adopted. The Low-Reynolds models with finer mesh resolution at the near-wall region have not been considered mainly to reduce the computational effort in future FSI simulations in the PWR rod bundle. Also, Reynolds number (based on cooling channel hydraulic diameter in the fuel lattice) during PWR normal operating conditions is of the range of $\sim 5 \times 10^5$, Cioncolini et al (2018); Clement (2017). The Section will present the suitable validation cases used in the study.

3.1. Rigid body: Analysis of the turbulence models

The purpose of the following numerical explorations has been to demonstrate the effectiveness of various turbulence models in reproducing large-scale flow oscillations. The chosen URANS model are: EVM ($k-\omega$, $k-\varepsilon$, $k-\omega$ SST) and Reynolds Stress (SSG, LRR) models. The third-order QUICK scheme was adopted for the discretization of the convective terms of the transport equations of all EVM models. However, to achieve stability of the SSG and the LRR schemes, the k, ε and Reynolds stress fields were discretized with the TVD limited linear differencing scheme (*limitedLinear* described by Liu (2014)). The Second Order Euler Scheme (SOUE) for temporal discretization has been adopted, Moukalled (2016).

The experimental benchmark selected for use here is provided by Camussi et al (2008), who investigated the wall pressure fluctuations generated by shear flow separated at the edge of a forward-facing step with the simultaneous PIV visualization. It was demonstrated that the pulsating motion of the recirculation bubble that forms at the step causes high energy and low-frequency pressure oscillations, characterized by a Strouhal number of around $St = 0.1-0.2$ (7.5 Hz-15 Hz).

The schematic of the computational domain with all dimensions is depicted in Figure 1. The inlet height, the step location and the entire length of the channel are scaled in relation to the step height h which equals 20mm. The unsteady recirculation bubble is formed at the step's reattachment region. In this case for the location $x/h < 2.1$ and at the vertical side of the step at $y/h \sim 0.5$. No-slip boundary condition is applied for the top and bottom walls and the forward-facing obstacle. Fully developed flow conditions are applied at the inlet. Pressure probes close to the wall were placed at the x-locations before the step and after the step to track the pressure signal. Simulations were performed at Reynolds number $Re_h = 2.9 * 10^4$ where Re is based on the step height h, and free stream velocity $U_0 = 1.5$ m/s.

The analysis focuses on the comparison between the statistics of wall pressure fluctuations along the channel observed in the experiment and those resulting from the URANS computations. The root mean square pressure coefficient C_{prms} defined in Equation 14 has been examined.

$$C_{prms} = \frac{\sigma_p}{0.5\rho U_0^2}. \tag{14}$$

Here σ_p is the standard deviation of pressure, ρ is the fluid density and U_0 is the inlet velocity (1.5 m/s).

From the comparisons of Figure 2, it is apparent that the Reynolds Stress models are able to predict

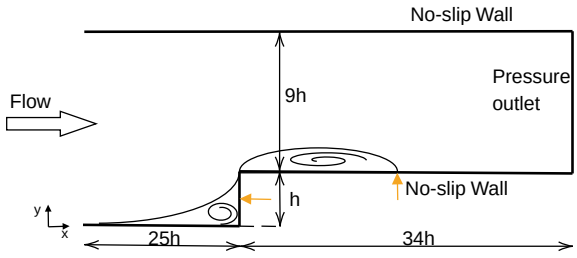

Figure 1. Schematic diagram of a 2D forward-facing step Orange arrows indicate the separation point downstream the step (at $x/h \sim 2.1$) and upstream the step (at $y/h \sim 0.5$) .

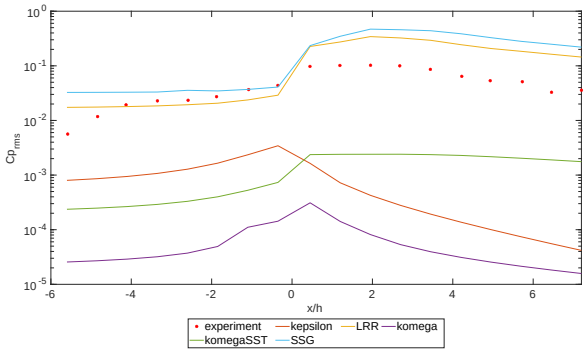

Figure 2. Evolution of the Cp_{rms} in terms of non-dimensional distance from the step

pressure fluctuations of the same magnitude range as those of the experiment. Moreover, the sharp increase in the amplitude of C_{prms} at the reattachment point is also reproduced by the two Reynolds stress transport models. For the eddy viscosity models, the amplitude of pressure fluctuations is two orders of magnitude lower than those in the experiment, but the steep rise in the amplitude of pressure fluctuations at the leading edge of a step is captured.

Another highly informative comparison, is that of the spectral distribution of the pressure fluctuations right after the step (x=0.45h) and at the reattachment length where the pressure fluctuations amplitude is the highest (x=1.95h) which is presented in Figures 3, 4. Following on from the preceding pressure statistics comparisons, here the attention is confined to the assessment of how the LRR model, and EVMs perform, in comparison to the experimental data. Frequency spectra are plotted against the Strouhal number ($St = fh/U_0$) based on the free-stream velocity U_0 and the step height h. As shown in Figure 3, the behaviour of the pressure PSD for the LRR scheme matches well the experimental results. Four dominating peaks at around 1.7 Hz, 4 Hz, 5.6 Hz 6.71 Hz are

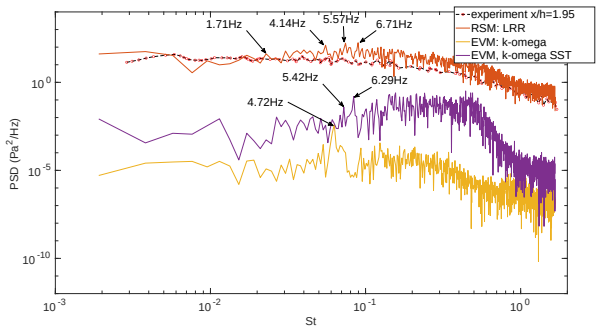

Figure 3. PSD for the LRR Reynolds Stress Model, $k-\omega$ and $k-\omega$ SST at x=1.95h compared to experimental results.Arrows indicate dominating frequency peaks

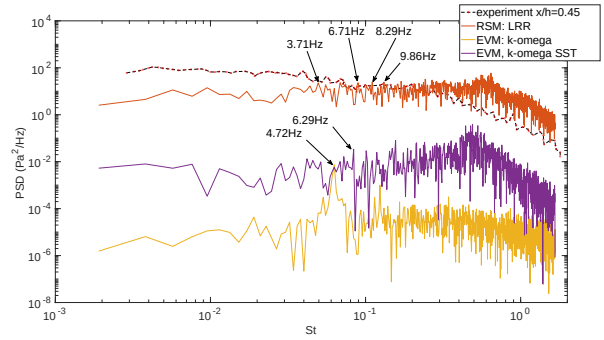

Figure 4. PSD for the LRR Reynolds Stress Model, $k-\omega$ and $k-\omega$ SST at x=0.45h compared to experimental results. Indication is the same as in the Figure 3

identified. For the $k-\omega$ scheme one clear dominating peak at around 4.72 Hz is identified at both locations. The amplitude is of three orders of magnitude lower, which is consistent with the C_{prms} trend. Similarly, for the $k-\omega$ SST two adjacent peaks at 5.42 Hz and 6.29 Hz after the step are identified. Their amplitude is of two orders of magnitude lower than that of the experiment. The PSD for the $k-\varepsilon$ has not revealed any dominating peaks at either location and has not been depicted in the figure for clarity.

The results of this study indicate that the EVM class of models will be unable to trigger or sustain induced vibration because the amplitude of pressure fluctuation is largely underestimated. The LRR predictions show that this model is able to reproduce the large scale, low frequency vortices at the leading edge of the forward-facing step. The pressure surges of the same frequencies in the experiment indicate that this model is able to predict the frequency and the amplitude of flow instabilities with good accuracy. The LRR scheme is consequently selected for in the two-way FSI analysis that follows.

3.2. Two-way FSI Simulations of Cantilever Cylinder

In the experiment by Cioncolini et al (2018) the rod subjected to the axial flow is $1m$ long circular stainless steel tube filled with lead shots to approximate the linear density of actual PWR fuel rods. The motion of the free end was recorded with a fast-imaging camera, whilst a second camera was used to measure the flow field via PIV. The geometry of the experimental system was designed to be informative of pressurized-water-cooled reactor flow conditions. The results of the experiment indicate that the beam end shape does not influence the cantilever dynamics below a certain critical velocity, and vibrations are only due to the turbulent buffeting from the external flow. These results are similar to those reported by Rinaldi (2012).

3.3. Solid Mechanics Part - cantilever beam in vacuum

The clamped-free beam with a circular cross-section was subjected to a uniform peak force $P(t)$=1 N for $t = 10^{-3}$ seconds. The force is then removed, causing the beam to vibrate. The beam is made out of one material, stainless steel, to simplify the simulation. The beam vibrates harmonically at natural frequency f_N and the associated mode shape $\widetilde{y_N}(x)$. For a cantilever beam in a vacuum f_N can be predicted with Euler-Bernoulli beam theory as in Equation 15:

$$f_N = \frac{c_N^2}{2\pi L^2}\sqrt{\frac{EI}{\lambda}}, \tag{15}$$

where $c_N = 1.875$ is the natural frequency parameter for a first mode shape. E is the elastic modulus, and I is the second moment of area of the beam's cross-section, L is the length of a beam and $\lambda = \rho A$ is the mass of the beam per unit length. The solid material properties have been adapted to match the natural frequency of a freely vibrating beam in Cioncolini et al (2018) and has been summarized in Table 1.

A set of four tests has been carried out to determine the optimum time step and number of iterations per time step to be adopted for the full two-way FSI simulation. In the first three simulations the number of iterative loop iterations is 1000 and the time step, Δt, has values of 10^{-5} s, 2.5×10^{-5} s and 5×10^{-5} s, for 'Case 1' , 'Case 2' and 'Case 3' respectively. In 'Case 4', the number of iterative loop iterations is reduced to 200 and the value of Δt is kept to 5×10^{-5} s. Looking at Figure 6, it is apparent that a very small

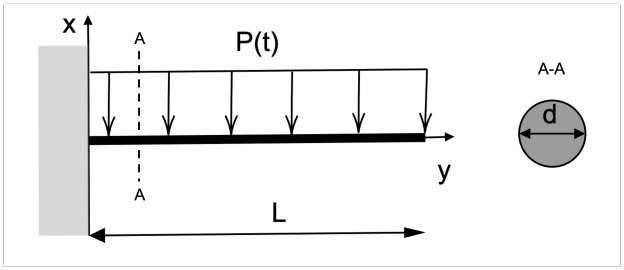

Figure 5. Cantilever rod subjected to a uniform load $P(t)$ and a coordinate system

Solid properties	
Length, L [m]	1.06
Diameter, d [m]	0.01
Density, ρ_S $[\frac{kg}{m^3} * 10^3]$	7.49
Young modulus, E [GPa]	76.4
Natural frequency (I mode), f_N [Hz]	3.98
Natural frequency in experiment [Hz]	3.98

Table 1. Solid properties used in the flexible beam in vacuum simulation

time step of $1 * 10^{-5}$ s needs to be adopted to avoid the numerical damping. The displacement amplitude appeared to be unaffected by numerical diffusion for the first half-period of the oscillation. For the first full period of oscillation, the amplitude in 'Case 4' is marginally lower, 10% less than for the reference case. This will surely be evident in free vibration, however in the two-way case, the beam will be subjected to constant excitation. The settings of 'Case 4', which reduce the computational time by a factor of 25, appear to be optimum ones for the two-way FSI simulations. This conclusion is further confirmed by the frequency comparisons of Table 2, in which in 'Case 4' predicts the free oscillation frequency to be within 2.3% of the analytical value.

Simulation Case	Frequency [Hz]	Error [%]
Analytical solution	3.98	
Case 1	3.99	0.30%
Case 2	4.03	1.30%
Case 3	4.02	1.05%
Case 4	4.07	2.31%

Table 2. Effect of the time step on the calculated natural frequency

3.4. Two-way FSI simulations

The cantilever beam described in Section 3.3 is now subjected to axial turbulent flow. The flow is directed from the rod free-end to the clamped end. Proper-

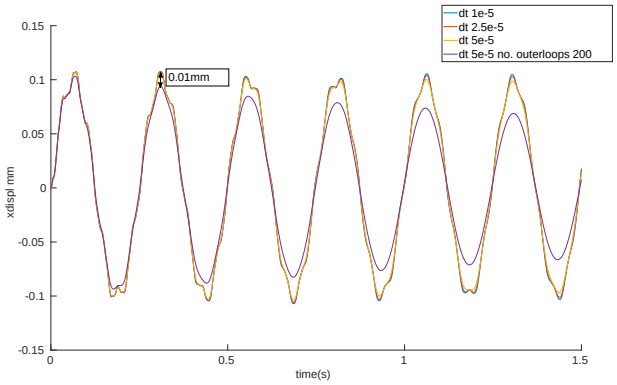

Figure 6. Free-end displacement time series for a simulation of cantilever in vacuum

ties of the fluid are summarised in Table 3. The inlet velocity u_{in} in the simulation has been chosen to correspond to the reduced velocity u^* from the experiment. Re_{ann} is based on the annulus hydraulic diameter, and V_{avg} is an average flow velocity in the annulus between the rod and confining tube. The non-dimensional velocity is defined as:

$$u^* = \frac{V_{avg}}{f_0 d}, \tag{16}$$

where f_0=3.6 Hz is the natural frequency of the cantilever beam in static water calculated with Equation 15 by adding the mass of the confined water m_{add} to the mass of a beam. The mass of the confined water is calculated as:

$$m_{add} = \rho_F \frac{\pi}{4} d^2 \frac{1+(d/D)^2}{1-(d/D)^2}. \tag{17}$$

Fluid properties	Value
Chanel diameter, D [m]	0.021
Chanel length, L [m]	1.12
Hydraulic diameter d_h [m]	0.011
Density, $\rho_F[\frac{kg}{m^3}]$	997
Kinematic viscosity, $\nu_F[\frac{m^2}{s}(\times 10^{-6})]$	0.893
Inlet velocity, $u_{in}[\frac{m}{s}]$	1
Annular gap velocity, $V_{avg}[\frac{m}{s}]$	1.3
Reduced velocity, u^*	36
Reynolds, Re_{ann}	$16.1 * 10^3$

Table 3. Fluid properties and simulation parameters

The computational domain used in the simulation is depicted in Figure 7. The cantilever beam can move, due to elastic deformation, in the x, and y directions. The mesh of the fluid domain consists of $\sim$ 600,000 hexahedral cells. Fully developed flow is imposed at the inlet and constant pressure is imposed at

the outlet of the channel. The LRR Reynolds stress model has been selected on the fluid side with the same temporal and convective discretisation practices as described in the fluid flow validation Section 3.1.

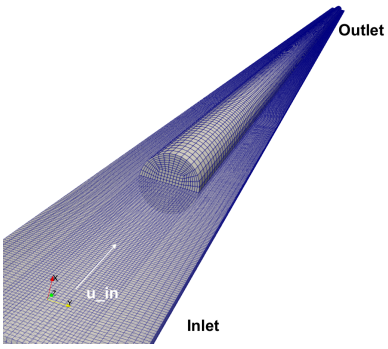

Figure 7. Computational domain for a cantilever in turbulent flow simulation

Flow over a rigid rod has been computed first to validate the fluid side of the simulation. Figure 8 includes the quantitative comparison between the calculated and measured axial and radial velocity profiles at three different vertical elevations: upstream of the rod free-end, at the free-end tip and downstream of the rod free-end. The upstream profile comparisons, show that there is some asymmetry in the upstream measured velocity, while in the simulation, a symmetric inlet flow is imposed. This inevitably leads to further deviations between the predicted and measured velocity profiles further downstream, but overall the simulations produce the same flow development as that present in the measurements. The final section of this study focuses on the simulation of flow-induced vibration. The mesh of the fluid has been allowed to move with the linear distance-based method. The Aitken under-relaxation was chosen for the coupling. The fluid-structure convergence

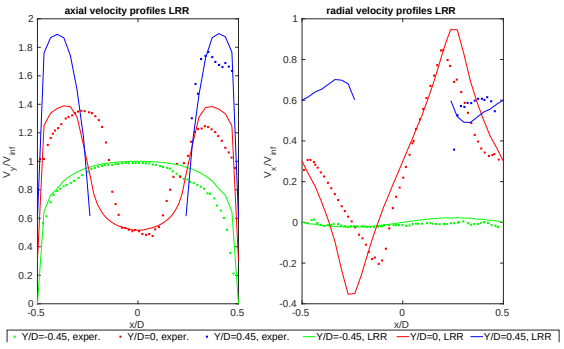

Figure 8. Velocity profiles for velocity u=36, vertical elevation locations are provided in the legend*

criterion was set to 10^{-4}. The simulation was decomposed to 36 processors and set to simulate a total period of 10.5 seconds. The coupling starts after the initial 2 seconds. Figure 9, presents a comparison between the measured and computed (using the LRR model) time-histories of the displacement of the rod free end, over a period of 5 seconds. The x-displacement track for the entire simulation is presented in Figure 10. It can be observed that the computed displacement matches the range of displacements observed in the experiment. The movement of the rod was induced by turbulence of the flow, and no initial displacement needed to be applied. It can be observed that after the 6 seconds of the simulation, the amplitude becomes damped for 2 seconds. The same intermittent behavior was observed during the experiment Cioncolini et al (2018). Rod excessive displacement was damped by the flow, bouncing back from the channel walls. Table 4 presents comparisons between the experimental and computed (using the LRR) dominant frequency, determined using FFT, and also the root mean square amplitude. The frequency bandwidth of 0.1 Hz is defined with full width at half maximum of a frequency peak. The reduced root-mean-square amplitude A^* is defined as:

$$A^* = \frac{A_{rms}}{d}. \tag{18}$$

These quantitative comparisons of Table 4 provide further confirmation to what is demonstrated in Figure 10. By contrast, the corresponding comparisons of Table 5, for FSI predictions obtained using the $k-\omega$ model (with the same computational domain) show that while this EVM is able to predict the correct frequency of oscillations, the amplitude of oscillations predicted by this model is 2 orders of magnitude lower than that found in the experiment which practically makes it zero. A comparison of the findings with those of other studies reported in Section 1 confirms that the EVMs are incapable of reproducing the amplitude of the rod vibrations.

Value	Simulation	Experiment
Natural frequency	3.55±0.05 Hz	3.6-3.75 Hz
Amplitude, A^*	0.004	0.004-0.006

Table 4. Frequency and Amplitude of flow-induced vibration, LRR scheme

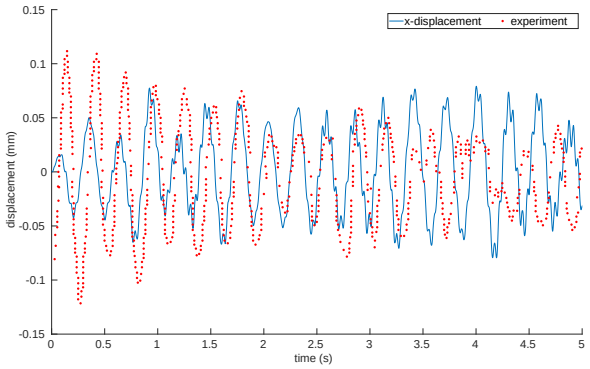

Figure 9. Displacement of a free-end vibrating beam vs. experimental data

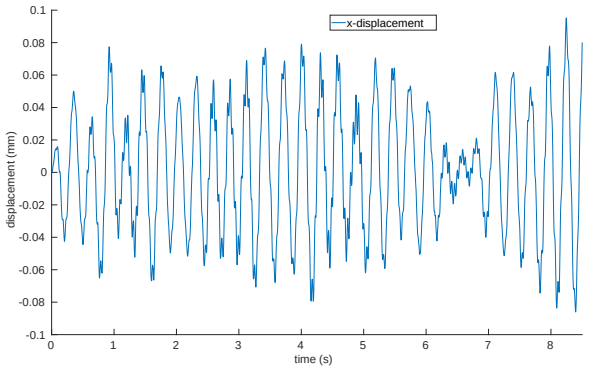

Figure 10. Displacement of a free-end vibrating beam in the x direction

4. CONCLUSIONS

The main objective of this study has been to assemble a cost-effective modelling strategy for the simulation of flow-induced vibrations of PWR fuel rods. These are long, slender rods subjected to turbulent axial flow. In order to meet this objective, the modelling strategy needs to combine three main elements.

- URANS high-Reynolds-number models able to reproduce the strength of the large-scale flow oscillations which cause the flow-induced vibrations.
- A two-way FSI numerical solver, in which the pressure and viscous forces generated by the flow over the rod surface, are used as input to the solution of the elastic deformation equations which provide the rod deformation, and the rod deformation is then used to modify the geometry of the flow domain.
- A mesh regeneration method able to adjust the mesh of the fluid domain after at each rod deformation.

Value	Simulation	Experiment
Natural frequency	3.69±0.4 Hz	3.6-3.75 Hz
Amplitude, A^*	$1.89 * 10^{-5}$	0.004-0.006

Table 5. Frequency and Amplitude of flow-induced vibration, $k-\omega$ scheme

By considering turbulent flow over forward-facing step it has been established that high-Reynolds-number Reynolds Stress Models such as the LRR Launder (1975) and SSG Speziale (1991), with high order convection discretization schemes are able to reproduce the large-scale flow instabilities with satisfactory accuracy.

As a result, by combining all the above elements, which include use of the LRR Launder (1975) Reynolds Stress URANS model, it becomes possible to reproduce the oscillatory behaviour of a cantilever beam exposed to axial flow with considerable accuracy. The effective-viscosity models tested on the other hand, severely under-estimate the strength of flow unsteadiness and consequently the amplitude of the rod oscillations. To our knowledge this is the first successful simulation of flow induced oscillations of cantilever rods relevant to PWR applications, based on the use of URANS.

5. ACKNOWLEDGMENTS

The author would like to express her acknowledgement to EDF Energy and the MACE Beacon Scholarship at the University of Manchester for providing financial support for this study. The research development review provided by Prof Alistair Revell during the PhD progress is also greatly acknowledged.

6. REFERENCES

Borsoi, L. Flow-Induced Vibration of Nuclear Components : Future R & D Perspective Derived from the French Experience. *Transactions SMiRT*. **16**: 1-12 (2001)

Camussi, R. et al. Statistical properties of wall pressure fluctuations over a forward-facing step *Physics of Fluids* **7**: 075113 (2018)

Cardiff, P. et al. An open-source finite volume toolbox for solid mechanics and fluid-solid interaction simulations. *arXiv, 2018*, https://arxiv.org/abs/1808.10736

Chen, S. & Wambsganss, M. Parallel-flow-induced vibration of fuel rods. *Nuclear Engineering And Design*. **18**: 253-278 (1971)

Christon, M. et al. Large-eddy simulation, fuel rod vibration and grid-to-rod fretting in pressurized water reactors. *Journal Of Computational Physics*. **322**: 142-161 (2016)

Cioncolini, A. et al. Axial-flow-induced vibration experiments on cantilevered rods for nuclear reactor applications. *Nuclear Engineering And Design*. **338**: 102-118 (2018)

Clément, S. & Bardet, P. Surrogates for Single-Phase Conjugate Heat Transfer Validation Experiments at Light Water Reactor Prototypical Conditions. *Nuclear Technology*. **199**: 151-173 (2017)

De Ridder, et al. Modal characteristics of a flexible cylinder in turbulent axial flow from numerical simulations. *Journal Of Fluids And Structures*. **43**: 110-123 (2013)

De Santis, D.Shams, A. Numerical modeling of flow induced vibration of nuclear fuel rods. *Nuclear Engineering And Design*. **320** 44-56 (2017)

De Santis, D. & Shams, A. An advanced numerical framework for the simulation of flow induced vibration for nuclear applications. *Annals Of Nuclear Energy*. **130**: 218-231 (2019)

De Santis, D.Shams, A. Numerical study of flow-induced vibration of fuel rods. *Nuclear Engineering And Design*. **361**: (2020)

Degroote, J. et al. Performance of a new partitioned procedure versus a monolithic procedure in fluid-structure interaction. *Computers And Structures*. **87**: 793-801 (2009)

Hofstede, E. et al. Numerical prediction of flow induced vibrations in nuclear reactor applications. *Nuclear Engineering And Design*. **319**: 81-90 (2017)

IAEA Review of Fuel Failures in Water Cooled Reactors. *TM Meeting*. (2010)

Irons, B. & Tuck, R. A version of the Aitken accelerator for computer iteration. *International Journal For Numerical Methods In Engineering*. **1**: 275-277 (1969)

Jasak, H. & Tuković, Ž. Automatic mesh motion for the unstructured Finite Volume Method. *Transactions Of Famena*. **30**: 1-20 (2006)

Kottapalli, S. et al. Numerical investigation of an advanced U-RANS based pressure fluctuation model to simulate non-linear vibrations of nuclear fuel rods due to turbulent parallel-flow. *Annals Of Nuclear Energy*. **128**: 115-126 (2019)

Launder, B., Reece, G. & Rodi, W. Progress in the development of a Reynolds-stress turbulence closure. *Journal Of Fluid Mechanics*. **68**: 537-566 (1975)

Liu, C. et al. Experimental study of a flexible cantilever rod subjected to axial water flow. *MACE PGR Conference*. (2017)

Liu, Y. & Hinrichsen, O. CFD modeling of bubbling fluidized beds using OpenFOAM®: Model validation and comparison of TVD differencing schemes. *Computers And Chemical Engineering*. **69**: 75-88 (2014)

Löhner, R. & Yang, C. Improved ALE mesh velocities for moving bodies. *Communications In Numerical Methods In Engineering*. **12**: 599-608 (1996)

Moukalled, F. The Finite Volume Method in Computational Fluid Dynamics: An Advanced Introduction with OpenFOAM® and Matlab. *Springer International Publishing* (2016)

Pettigrew, M. Flow-induced vibration of nuclear power station components. *Atomic Energy of Canada Ltd.* (1977)

Rinaldi, S. & Païdoussis, M. Theory and experiments on the dynamics of a free-clamped cylinder in confined axial air-flow. *Journal Of Fluids And Structures*. **28**: 167-179 (2012)

Speziale, C. et al. Modelling the pressure-strain correlation of turbulence: an invariant dynamical systems approach. *Journal Of Fluid Mechanics*. **227**: 245-272 (1991)

Tuković, Ž. et al. Openfoam finite volume solver for fluid-solid interaction. *Transactions Of Famena*. **42**: 1-31 (2018)

NUMERICAL SIMULATION OF CANTILEVER CYLINDERS IN CROSS-FLOW: PARTICIPATION TO THE OECD/NEA FLUID-STRUCTURE INTERACTION BENCHMARK

Kevin Zwijsen[1], Ferry Roelofs[1]
[1]*Nuclear Research and consultancy Group (NRG), Westerduinweg 3, 1755 LE, Petten, The Netherlands*
Mohammed Muaaz Hussain[1,2], Alexander van Zuijlen[2]
[2]*Faculty of Aerospace Engineering, Delft University of Technology, 2629 HS, Delft, The Netherlands*

ABSTRACT

Flow-induced vibrations as a result of Fluid-Structure Interaction (FSI) remain an area of concern in nuclear power plants. If not properly addressed, they can have large consequences to the functioning and operability of these plants. With the increase in computational power, the use of numerical tools to predict vibrations induced by the surrounding flow is rapidly increasing.

The current paper presents some of the results obtained at Nuclear Research and consultancy Group during its participation to the OECD/NEA benchmark on FSI. This benchmark consists of an experiment comprising two in-line cantilever cylinders in cross flow and was started to further increase the knowledge and predictive capabilities of cross-flow induced vibrations.

In order to reduce the computational resources needed, a URANS approach was used for the fluid. A comprehensive description is given of the used approach and the setup of the model, including mesh sensitivity tests. Finally, results are presented for one of the tests performed in the benchmark.

Results obtained indicate a good match with experimental data, showing that flow-induced vibrations of cylinders in cross-flow can be quite accurately predicted using a URANS-based solver when proper choices are made for the mesh and numerical settings.

1. INTRODUCTION

The cooling circuits of Nuclear Power Plants (NPP) consist of many structural components (rods, tubes, pipes, pressure vessels, valves) and machines (pumps, turbines, engines). When in operation, interaction between the coolant and surrounding confining structures, the so-called Fluid-Structure Interaction (FSI), takes place. Depending on the specific configurations, conditions and used materials, these interactions can cause static or dynamic (i.e., time-dependent) structure displacements or vibrations, resulting from the fluid forces exerted on the structure walls. These flow-induced displacements, deformations or vibrations inside NPPs are undesirable, as they could lead to fatigue problems, stress corrosion and fretting wear (Blevins, 1979; Kim, 2010; Yoo et al, 2019). Moreover, Flow-Induced Vibrations (FIV) phenomena can evolve during the operation of a nuclear power plant due to changes in its specific operating conditions, i.e., nominal operation or any transient or accident that could occur in a plant. Additionally, due to the radioactive environment, structures may degrade over time, resulting in changing mechanical properties. Hence, it is very important that during the design-stage of NPPs FIV issues are properly addressed in order to prevent related incidental or accidental scenarios, radioactivity releases to the environment and possible failures of components (Takahaski et al, 2014).

Different parts of the nuclear reactor can vibrate due to entirely different FSI excitation mechanisms. Pettigrew et al. (1998) classified four different FSI excitation mechanisms inside NPPs based on the flow situation and their relative importance. In general, it is observed that for internal, single-phase flows, Turbulence-Induced Vibrations (TIV) are the main driving mechanism for situations involving axial flow, such as that occurring around fuel rods. For single-phase cross-flow configurations, Fluid-Elastic Instabilities (FEI) and Vortex-Induced Vibrations (VIV, caused by periodic wake shedding) are of main concern.

As TIV is driven by the local fluctuating turbulent velocity and pressure fields, high-resolution numerical approaches, such as Direct-Numerical Simulations (DNS) or Large-Eddy Simulations (LES) are required for accurately reproducing this FSI mechanism. In cross-flow conditions though, where FSI is (partly) driven by vortex shedding, Unsteady Reynolds-Averaged Navier Stokes (URANS) simulations could potentially be used. This mechanism is relevant inside NPPs at the entrance of fuel rods, potentially giving rise to grid-to-rod fretting wear (EPRI, 2008), and in the U-bend region of the Steam Generators (SG), where it could result in SG tube rupture (MacDonald, 1996; Païdoussis, 2006).

In studies performed by Connors (1970) and Khalak & Williamson (1996) on cross-flow vibrations, it was shown that the mass damping parameters $m\delta/\rho D^2$ for FEI and $m^*\zeta$ for VIV are of fundamental importance, with $m^* = m/\frac{\pi}{4}\rho D^2$. Here, m

and D are the mass and diameter of the pipe at interest, respectively, δ and ζ its logarithmic decrement and damping ratio in the surrounding fluid, respectively, and ρ the density of that surrounding fluid. It can be shown that these parameters are equivalent, except for a multiplication factor of $0.5\pi^2$, with a low value of this parameter leading to a lower critical velocity of FEI and a more prominent VIV. With the rise in computational power, research on such cross flow vibrations has shifted from analytical models to making numerical predictions such as those for studies on single cylinder (Martins & Avila, 2019; Wu et al, 2020) and multi-cylinder configurations (Hassan et al, 2010; DePedro et al, 2016)

In a recent work by the authors (Hussain et al., 2022), it was found that a URANS approach can give quite accurate results for VIV, as long as an anisotropic turbulence model is used, in combination with a wall-resolved mesh. In the current paper, these findings are further tested by participation in the international benchmark exercise on FSI organized by the WGAMA group of the OECD / NEA organization. Experimental data for the benchmark is provided by the Russian JSC Afrikantov OKBM organization as published in Bolshukhin (2021). This paper concerns the peak resonance case of the open phase of the aforementioned benchmark.

The paper is structured as follows. In Section 2, a description of the experiment is given. In Section 3, the numerical setup is described, along with sensitivity tests. Results of the actual benchmark test are documented in Section 4. Section 6, finally, contains conclusions.

2. DESCRIPTION OF EXPERIMENT

This chapter gives a short description of the experimental setup, as well as the measurement systems used to generate the data available within the benchmark. A more detailed description of the experiment, located JSC Afrikantov OKBM facility in Russia, can be found in Bolshukhin et al (2021).

2.1. Experimental setup

The experimental setup consists of two in-line cantilevered cylinders subjected to cross flow in a rectangular channel test section, as can be seen in Figure 1. This test section is part of a larger loop involving input and output tanks to control the flow rate and a vibration insulator to stabilize the facility to ensure displacement measurements are purely due to the flow, see Figure 2.

The experimental study made use of hollow stainless steel cylinders of diameter $D = 7\ mm$, wall thickness 0.3 mm and length 198 mm placed 45 mm apart with the first cylinder placed at a distance of 350 mm from the inlet. For the experiment, each cylinder had two brass accelerometer mountings of diameter 6.4 mm and length 12 mm soldered (the length includes the solder deposit) internally at the tip of the cylinder and at near halfway length of the cylinder. These brass bobs for the two cylinders were slightly different in density leading to different natural frequencies of the two structures in air and water.

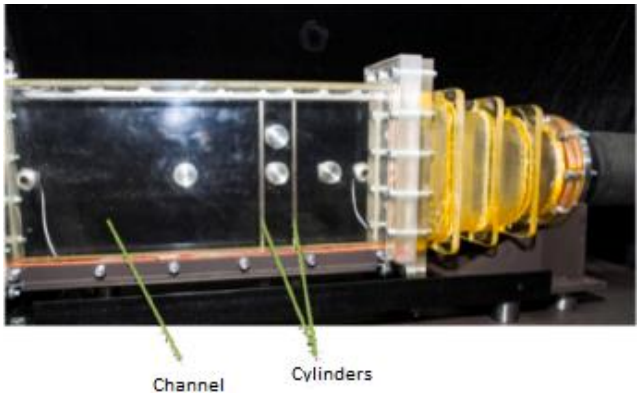

Figure 1. Experimental setup (Bolshukhin et al, 2021).

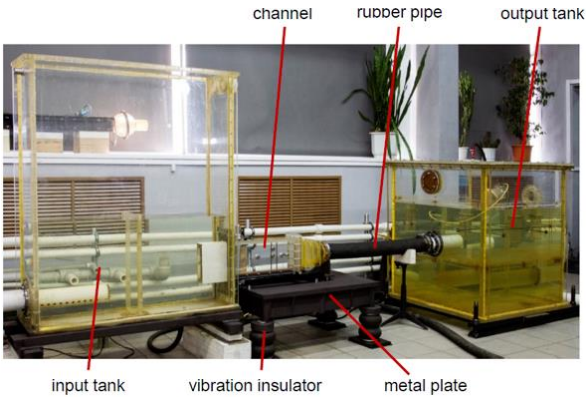

Figure 2. Test section placed inside the full experimental loop (Bolshukhin et al, 2021).

The working fluid was water at 10°C and was tested for flow rates of 10 m^3/h (off-resonance) and 16 m^3/h (peak resonance) through the aforementioned channel of dimensions 550 × 200 × 30 mm^3 that houses the cylinders. The reference static pressure was 1 kgf/cm^2 (98.07 kPa). Some more dimensions of the test section can be found in Figure 3.

The two performed test cases, i.e., the off-resonance and peak resonance cases, differ in the interaction between the two cylinders. For these two cases, the vortex shedding frequencies f_s are approximately 18.4 Hz and 24.4 Hz, respectively. Furthermore, cylinders 1 and 2 have natural frequencies f_n of about 98 Hz and 90 Hz in water, respectively. Hence, for the peak-resonance case, the fourth harmonic of f_s is almost equal to the natural frequency of f_n of the first cylinder, i.e. $4f_s \approx f_n^1$. Thus, lock-in is expected to occur, resulting in large oscillations of cylinder 1 in the peak-resonance case. In the current study, only the

peak resonance case, which translates to Re = 3964.23, is simulated and compared against the experimental results.

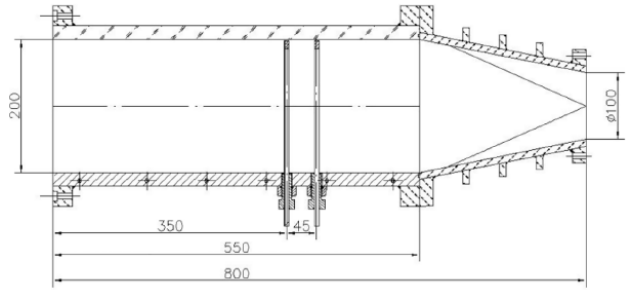

Figure 3. Side view of the experimental facility with some relevant dimensions (Bolshukhin et al, 2021).

2.2. Measurement system

Various technical instruments were made use of to generate the data provided within the benchmark exercise in the experiment. The test facility allowed static measurement of pressure and temperature, while an electromagnetic flow meter was used to determine the flow rate. Systems based on time-resolved Particle Image Velocimetry (PIV, pulsed and continuous wave lasers with average frequency f = 10 Hz) and Laser Doppler Velocimetry (LDV, one component) were used to study the hydrodynamics of the flow. LDV measurements were mainly used for cross-validation of the measurements. As the tracer particles, 10 μm polyamide particles were used. General views of the model with PIV and LDV systems installed on the test facility are shown in Figure 4

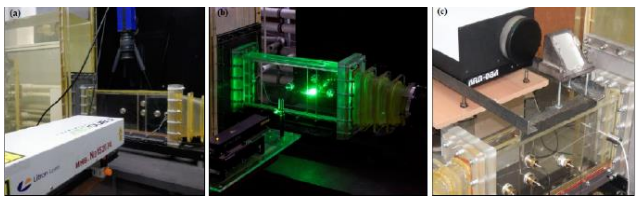

Figure 4. General views of the measurement systems: (a) PIV with Pulsed Wave Laser, (b) PIV with Continuous Wave Laser, (c) LDV System

The pressure pulsations were measured by sensitive dynamic sensors located on the channel wall. Accelerometers were installed at the top of the cylinders in two mutually perpendicular directions. Measurements of vibrations, pressure pulsations, as well as velocity pulsations were carried out synchronously. The operability of the accelerometers and pressure pulsation sensors was provided by duplication of measurements using a laser vibrometer and hydrophones, respectively. The synchronization of vibration measurements using accelerometers and a laser vibrometer were carried out by an external trigger.

3. NUMERICAL SETUP

In this chapter, the numerical setup used to perform the FSI simulations is presented. First, the general approach is described. In order to make sure the mesh is adequate for the proposed simulations, a mesh sensitivity study for the CFD domain, taking only the CFD part into account, is performed. Results of this study are also shown here. Finally, some modelling work done on the structural side is reported.

3.1. General numerical setup

The commercial code Simcenter STARCCM+ (v2020.3.1) is employed for making the numerical simulations. It was set up from scratch using this software using the CAD drawings of the experimental facility that were provided to all the participants to the benchmark. To reduce computational costs, only the rectangular channel in which the two cylinders are located is included in the domain, see Figure 5.

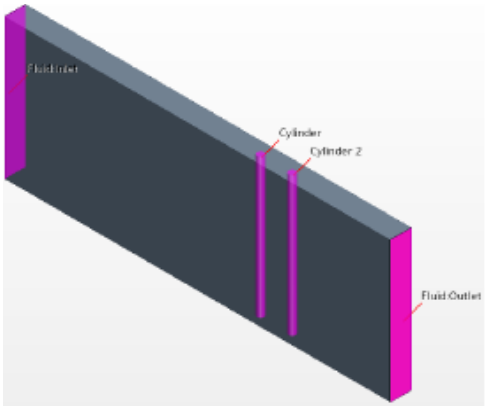

Figure 5. Numerical domain used for the various simulations.

On the fluid side, a segregated solver is used, using the SIMPLE algorithm for the velocity-pressure coupling. The implicit unsteady time discretization scheme is employed along with a 2^{nd} order upwind convection scheme. For the solid, the 'Solid Stress' solver is selected along with a 2^{nd} order Newmark implicit integration scheme.

As for the boundary conditions, the four channel walls and the exposed cylinder surfaces are prescribed a no-slip boundary condition. A constant static pressure of 0 Pa is prescribed for the outlet. For the inlet, a constant uniform velocity of 0.74 m/s (following a flow rate of 16 $m3/h$ used for the resonance case) is used for the CFD study while for

(numerical stability of) the FSI study a uniform velocity is prescribed that slowly ramps up in time to the desired value. Additionally, in the FSI simulations, the cylinder surfaces are declared as FSI interfaces.

Finally, following the work presented in Hussain et al (2022) it was decided to test the performance of three different turbulence models: 1) k-ω SST QCR, 2) k-ω SST QCR + GRT and 3) k-ε low Re cubic. All these models contain anisotropic constitutive relationships for the eddy viscosity, with the first two using a quadratic approach while the k-ε model uses a cubic relationship. This is done because in the aforementioned study it was found that using an anisotropic approach greatly improves the accuracy of the results. Additionally, the second option uses the $\gamma - Re_\theta$ transition model, as the Reynolds number of the case under consideration falls in that range.

3.2. CFD mesh study

The mesh is also created in STAR-CCM+. In order to improve the accuracy and stability of the calculations, a structured hexahedral mesh has been made. To save on computational time, a coarse mesh is used near the inlets and outlets and a finer mesh is used approaching the cylinders, using three local volume refinements. Approaching the cylinder from the inlet by crossing each refinement region reduces the target base size (bs) of 2.5 mm by half sequentially. A small growth rate was used to ensure a good transition between each refinement region.

In total three different meshes will be tested, with the difference between the meshes being the sizes of the refinement zones, i.e., the finest mesh, being CFD3, uses the largest refinement zones centred around the cylinders. The three resulting meshes, named CFD1, CFD2 and CFD3, contain in total 4.9M, 5.4M and 7.0 M cells, respectively. Figure 6 shows the resulting CFD2 mesh. All three meshes are wall-resolved ($y^+ < 1$) for the studied inlet velocity.

For the mesh sensitivity study, the k-ω SST QCR turbulence model is used, with a time step size of 0.4 ms. This time step size was chosen to ensure there are 100 sampling points based on an expected vortex shedding frequency of 25 Hz.

A qualitative difference between the three meshes can be observed in Figure 7, showing vorticity plots on a horizontal plane at y/L = 0.50, with y the vertical distance measured from the bottom of the channel and L the height of the channel. The figure clearly illustrates the vortex shedding taking place inside the flow channel. As can be clearly seen, as the mesh gets finer, more detailed flow structures are resolved, with the simulation using mesh CFD3 having the most pronounced vortex street.

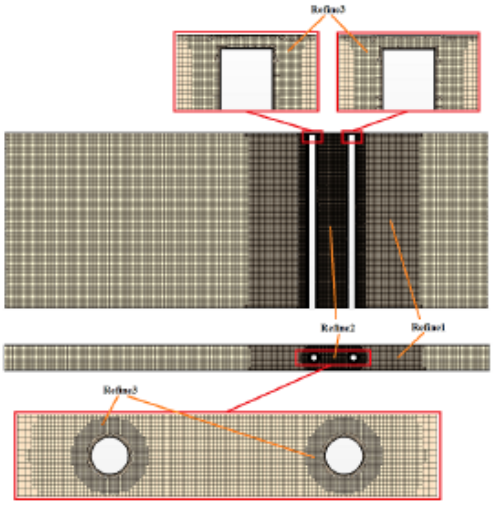

Figure 6. The CFD2 mesh used in the CFD mesh sensitivity study.

For the experiment, velocity and pressure measurements are available at various heights and positions relative to the cylinders, allowing for a good quantitative comparison with numerical results. Figure 8 shows a comparison between the velocity spectrum obtained using PIV measurements and those of the numerical simulations using the three difference fluid meshes at a sampling point with location x/D = 1.43 and y/L = 0.88, with x the distance from the centre of the cylinder, and D its diameter. A first observation that can be made is that all three meshes capture the vortex shedding frequency quite well, all having a pronounced peak in the spectrum at about 25 Hz. What is also clear from this plot is that all three meshes under predict the spectra for higher frequencies. This was to be expected, as URANS solvers are not capable of resolving the smaller turbulence scales. It is interesting to see though that the CFD3 case predicts slightly higher energy at the higher frequencies than the other two meshes.

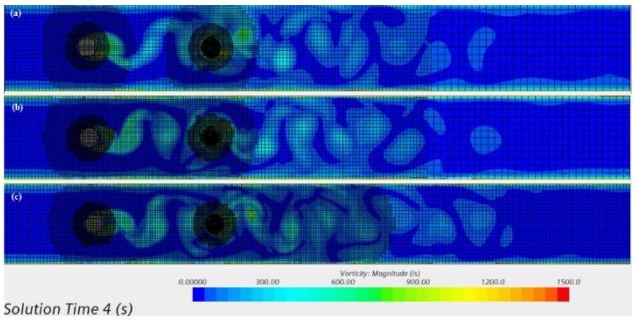

Figure 7. Vorticity plots for a) CFD1, b) CFD2 and c) CFD3 mesh sensitivity test cases

Finally, from the various velocity and pressure spectra that were generated during the simulations, vortex shedding frequencies have been extracted and

compared with those from the experiment. At most locations, all three meshes predict similar frequencies, corresponding very well with that of the frequency found in the experiment, with differences generally being on the order of a few percent. The largest difference was found at the same location as that for which the spectra are shown in Figure 8, with the experiment giving a frequency of about 24.7 Hz, while with CFD1, CFD2 and CFD3 frequencies of about 21.4 Hz, 20.4 Hz and 22.5 Hz are found, respectively. All reasonably close, though the best prediction is once again made by mesh CFD3.

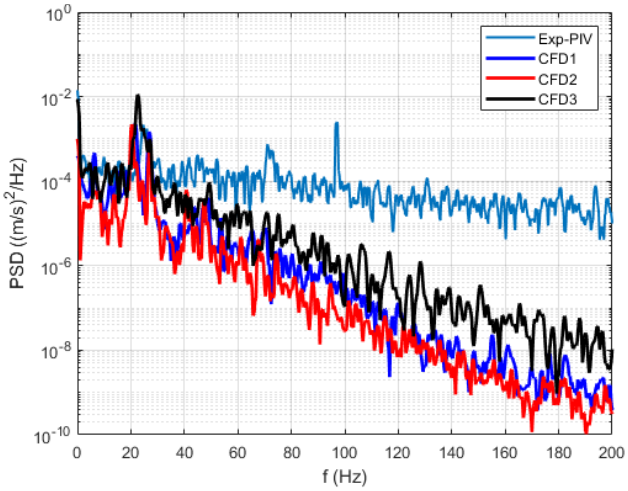

Figure 8. Comparison of the velocity spectrum obtained using the various CFD meshes with that of PIV measurements of the experiment.

Based on the above presented results, it was decided to use mesh CFD3, containing about 7.0M cells, for the FSI simulations.

3.3. Structural geometry study

Following the CFD mesh sensitivity study, a study was performed on the structural geometry. This was deemed necessary because there was some uncertainty on the exact dimensions and weights of the brass accelerometer mountings located in the upper parts of the cylinders. This uncertainty was caused by the soldering applied to these mountings to hold these bobs in place. This soldering has a different density than the brass mountings itself, and the size of the soldering is not precisely known. The structural mesh used for this study is displayed in Figure 9. It is an unstructured hexahedral mesh with in total nearly 0.2M cells.

As a good representation of the structural domain is necessary in order to get accurate FSI predictions, it was decided to perform tests with varying bob lengths in order to see what size would give the best match with the experimental natural frequencies of the two cylinders. This was done by performing pure structural tests in both vacuum and stagnant water, whereby the cylinders are given an initial displacement and subsequently released. By monitoring the displacement as function of time, the natural frequencies of the cylinders can be extracted. Results obtained for free vibration in stagnant water can be found in Table 1.

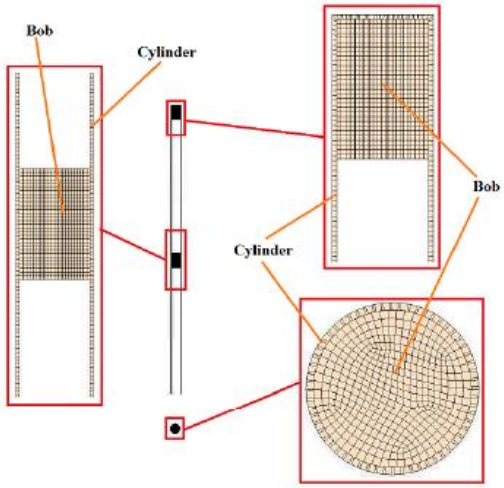

Figure 9. Sectional views of the structural mesh.

As can be seen, using a bob length of 10.0 mm gives the best match with the experimental data. This was in general also observed for the tests in air. Hence, it was decided to use bobs with a length of 10 mm in the FSI simulations.

Bob length [mm]	f_n cylinder 1 [Hz]	f_n cylinder 2 [Hz]
12.0	90.1	84.3
11.0	94.3	88.5
10.5	95.7	88.9
10.0	96.6	90.1
Exp. Soln.	98.0	90.0

Table 1. Results for vibration tests in water.

4. RESULTS FOR THE FSI BENCHMARK CASE

Having made well-motivated choices for the CFD mesh and structural geometry following separate studies, the two solvers are ready to be combined to perform the requested fluid-structure interaction simulations. As mentioned earlier, only the peak-resonance case with a flow rate of 16 m^3/h is simulated, using the following three different turbulence models: 1) k-ω SST QCR (QCR), 2) k-ω SST QCR + GRT (QCRT) and 3) standard k-ε low Re cubic (CKE). For the simulations, a time step size of 0.36 ms is used.

Vorticity on a horizontal cut through the domain at y/L = 0.5 for the three turbulence models is shown in Figure 10. There are clear differences between the three different turbulence models, especially in the region behind cylinder 2. QCRT gives a quite regular and clear vortex shedding pattern, with hardly any small scale turbulent structures pattern. Laminarization of the flow seems to have taken place. QCR resolves more small scale structures, though by far not as much as CKE. These small scale structures are a result of the vortices being shed by cylinder 1 breaking down when interacting with cylinder 2.

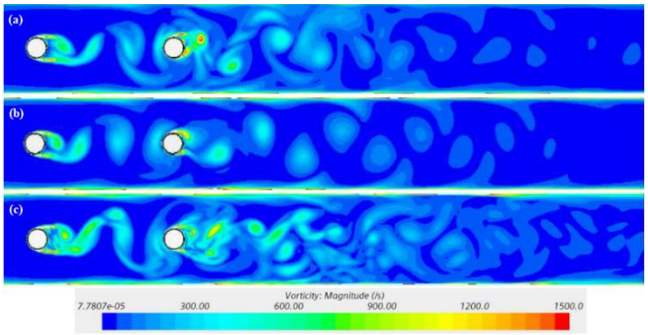

Figure 10. Horizontal section vorticity plots for a) QCR, b) QCRT and c) CKE

To get a better quantitative impression of the difference in solution using the three turbulence models, the resulting velocity spectra are plotted and compared with the experimental counterpart in Figure 11 at a point with location x/D = 1.43 and y/L = 0.5 right behind cylinder 1 and in Figure 12 at a point with the same relative coordinates located in the wake of cylinder 2. To obtain the experimental spectra a time resampling at constant frequency was carried out using an algorithm based on the time signal reconstruction proposed by Veynante (1988).

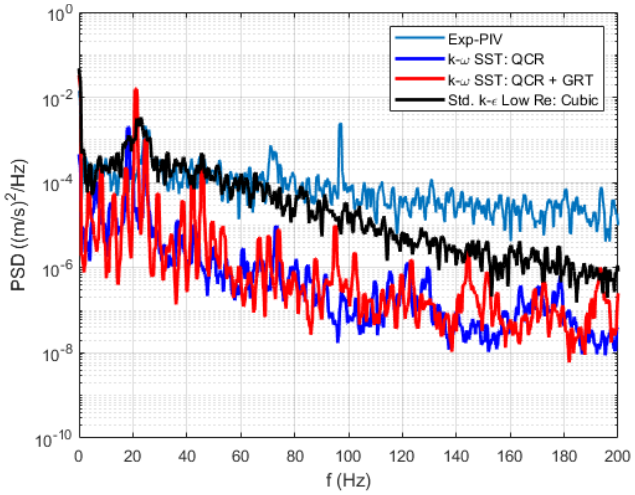

Figure 11. Velocity spectra plot at a location right behind cylinder 1.

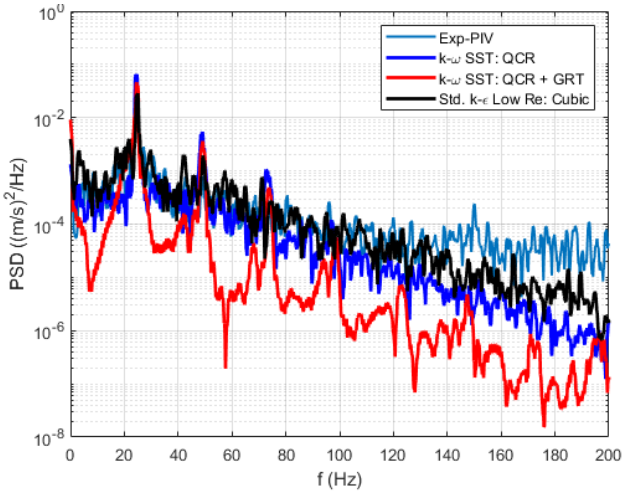

Figure 12. Velocity spectra plot at a location right behind cylinder 2.

Two interesting things can be seen in these figures. First of all, the standard k-ε low-Re turbulence model with cubic constitutive relationship has the most energy content at higher frequencies at both locations. QCR predicts slightly less energy for the higher frequencies behind cylinder 2, while it predicts considerable less energy behind cylinder 1. The third turbulence model investigated, QCRT, predicts the least energy of all the tested models. This is in line with what was observed in Figure 10.

Secondly, all three turbulence models predict vortex shedding frequencies that closely match that of the experiment. From these figures though, it's not easy to get a very accurate reading of the resulting shedding frequencies. This is easier done using the pressure spectrum. For that reason, pressure spectra sampled at x/D = 2.5 and y/L = 0.5 behind cylinder 1 are shown in Figure 13 and compared with the experiment. In this figure, several important peaks from the experiment are marked, corresponding to the shedding frequency f_s, the natural frequencies of cylinder 1 f_n^1 and that of cylinder 2 f_n^2 and additionally a frequency as a result of the pump operation f^*.

When looking at the vortex shedding frequency, it can be seen that all three turbulence models overpredict the experimental value of 24.4 Hz by about 3.0 Hz, with all three turbulence models predicting a shedding frequency of about 27.5 Hz. This also results in overestimation of the harmonics of the shedding frequency, e.g., the peaks for $2f_s$ of the numerical simulations are overestimated by about 6.0 Hz, in line with the mismatch in vortex shedding frequency. The end result of this overprediction of f_s is that no lock-in is found using either turbulence model, as an overprediction of about 3 Hz for f_s results in an overprediction of its fourth harmonic by about 12 Hz. Hence, this no longer is close to the natural frequency of the first cylinder and the large peak at f_n^1 is not

present in the numerical pressure spectra. Instead, a much smaller peak is visible around 108 Hz.

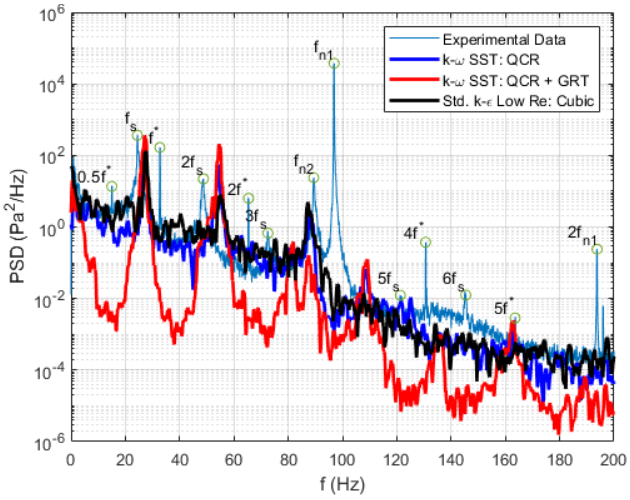

Figure 13. Pressure spectra plot at a location right behind cylinder 1.

The probable cause for the turbulence models not being able to predict lock-in is the too low energy content at higher frequencies found using the URANS turbulence models. If more energy would be present near cylinder 1's natural frequency, it would most likely oscillate more, thereby "forcing" the shedding frequency to decrease to a value at which its fourth harmonic matches that of f_n^1.

5. CONCLUSION

Following a previous paper published by the same authors, the efficacy of URANS models for simulating cross-flow induced vibrations is further tested using the commercial code STAR-CCM+ (v2020.3.1). Hereto, lessons learned and experience gained from the earlier studied cases are applied within the OECD/NEA FSI benchmark, supported by experiments performed at the Russian JSC Afrikantov OKBM organization. The experiment involves two in-line cantilever cylinders placed inside a rectangular housing and subjected to cross-flow. Experiments were performed for an off-resonance and a peak-resonance flow rate. The current paper only considers the peak-resonance case.

Before proceeding with the actual FSI simulations, a mesh sensitivity and a structural geometry sensitivity study are performed, resulting in optimized choices for the mesh and structural dimensions to be used for the benchmark case. For the subsequent FSI benchmark calculations, three different anisotropic turbulence models are tested, viz: 1) k-ω SST QCR, 2) k-ω SST QCR + GRT and 3) standard k-ε low Re cubic.

Two main observations can be made following the performed simulations. First of all, when using a fine, wall-resolved, mesh, the standard k-ε low Re model with a cubic constitutive relationship is able to reproduce relatively small scale turbulence. This is also true for the k-ω SST turbulence model with a quadratic approach, though it is found that the smaller scales contain less energy.

Secondly, even though small scale turbulence is produced, it does not contain sufficient energy to ensure a lock-in, in which the shedding frequency of the first cylinder is adjusted so that its fourth harmonic matches that of the cylinder's natural frequency.

The results presented here are part of the open phase of the benchmark, for which the experimental data is shared beforehand. Following this, the blind phase is performed. Results hereof produced by all the participants will be compared by the experimentalists to each other and with the experimental data.

6. ACKNOWLEDGEMENTS

The authors are grateful to OECD/NEA/WGAMA for supporting this benchmark. The work described in this paper is funded by the PIONEER program of the Dutch Ministry of Economic Affairs.

7. REFERENCES

Blevins, R., 1979, "Flow-induced Vibration in Nuclear Reactors: A Review," *Progress in Nuclear Energy*, **4**,: 25-49.

Bolshukhin, M. A., Budnikov, A. V., Shmelev, E. I., Kulikov, D. A., Loginov, A. V., Pribaturin, N. A., Lobanov, P. D., Meledin, V. G., Suvorov, A. S., and Stulenkov, A. V., 2021, "Dynamic measurements of the flow and structure oscillations to validate FSI calculations". *Nuclear Engineering and Design*, **381:** 111336.

Connors, H. J., 1970, "Fluid elastic vibration of tube arrays excited by cross flow". In Reiff, D.D. (Ed.), *Flow-Induced Vibration in Heat Exchangers.* ASME, New York, 42–56.

De Pedro, B., Parrondo, J., Meskell, C., and Oro, J. F., 2016, "CFD modelling of the cross-flow through normal triangular tube arrays with one tube undergoing forced vibrations or fluidelastic instability". *Journal of Fluids and Structures*, **64**: 67–86.

EPRI, 2008, *Fuel Reliability Guidelines: PWR Grid-to-Rod Fretting*, Technical report, 1015452.

Hassan, M., Gerber, A., and Omar, H., 2010, "Numerical Estimation of Fluidelastic Instability in Tube Arrays". *Journal of Pressure Vessel Technology*, **132**: 041307.

Hussain, M.M.M.D., Zwijsen, K., Zuijlen, A.H. van, and Roelofs, F., 2022, "URANS simulations for fluid-structure interaction of cylinders in cross-flow". *NURETH19*, Brussels, Belgium.

Khalak, A., and Williamson, C. H. K, 1996, "Dynamics of a hydroelastic cylinder with low mass and damping", *Journal of Fluids and Structures*, **10**: 455–472.

Kim, K.T., 2010, "A study on the grid-to-rod fretting wear-induced fuel failure observed in the 16x16KOFA fuel", *Nuclear Engineering and Design*, **240**: 756-762.

Martins, F. A. C., and Avila, J. P. J, 2019, "Three-dimensional CFD analysis of damping effects on vortex-induced vibrations of 2DOF elastically-mounted circular cylinders", *Marine Structures*, **65**: 12–31.

MacDonald, P.E., Shah, V.N., Ward, L.W., and Ellison, P.G., 1996, *Steam generator tube failures*, NUREG/CR-6365 INEL-95/0383.

Païdoussis M., 2006, *Real-life Experiences with Flow-induced Vibration*, Journal of Fluids and Structures, vol. 22, p.p. 741-755.

Pettigrew, M. J., Taylor, C. E., Fisher, N. J., Yetisir, M., and Smith, B. A. W, 1998, "Flow-induced vibration: recent findings and open questions", *Nuclear Engineering and Design*, **185**: 249-276.

Takahashi, S., Hasegawa, K., and Nakamura, T., 2014, "Nuclear Power Plant Issues in IAEA Technical Guidelines on Fluid-Structure Interactions", *PVP2014*, Anaheim, USA.

Veynante, D., Candel, S.M., 1988, "A promising approach in Laser Doppler Velocimetry: signal reconstruction and non-linear spectral analysis". *Signal processing*, **14**, pp. 295-300.

Wu, X., Jafari, M., Sarkar, P., and Sharma, A., 2020, "Verification of DES for flow over rigidly and elastically-mounted circular cylinders in normal and yawed flow". *Journal of Fluids and Structures*, **94**: 102895.

Yoo, Y., Kim, K., Eom, K., and Lee, S., 2019, "Finite element analysis of the mechanical behavior of a nuclear fuel assembly spacer grid," *Nuclear Engineering and Design*, **352.**

NUMERICAL SIMULATIONS OF EXPERIMENTAL FLUID-INDUCED VIBRATIONS OF CYLINDERS IN CROSS-FLOW

Daniele Vivaldi
Institut de Radioprotection et de Sûreté Nucléaire (IRSN)
Cadarache, St Paul-lez-Durance, BP3, 13115, France

Guillaume Ricciardi
Commissariat à l'Energies Atomique et aux Energies Alternatives
CEA/DES/IRESNE, Dep. of Nuclear Technology
Cadarache F-13108 Saint-Paul-Lez-Durance

ABSTRACT

This paper presents fluid-structure interaction (FSI) simulations of a published experimental campaign dedicated to the study of fluid-induced vibrations on cylinders. The experimental configuration consists in two in-line cylinders subjected to water cross-flow. This experimental campaign is relevant for numerical FSI validation purposes, since it accesses both fluid and structure measurements. This paper presents the numerical simulations of one of the different water flow rates tested experimentally. The FSI simulations are run with the CFD code code_Saturne: a two-way coupling between the fluid and the structure is realized thanks to the implementation of an Euler-Bernoulli finite element beam model inside code_Saturne. This paper describes the FSI approach and presents its application to the experimental configuration considered. Numerical results are compared to the experimental ones, in terms of velocity fluctuations behind the cylinders and vibrations of the cylinders. Fluid simulations are realized retaining both a URANS approach and the Scale Adaptive Simulation (SAS) hybrid URANS/LES approach.

1. INTRODUCTION

Fluid-structure interaction (FSI) of slender structures is a concern in nuclear power plants (NPPs). Two main examples are the vibrations of fuel rods and fuel assemblies due to the single phase water flow inside the reactor pressure vessel, and the vibrations of U-tube steam generator (SG) tubes due to the two-phase steam-water flow. Thanks to the increasing computational performances, the numerical simulation of FSI phenomena has become more and more feasible in the recent years. Several numerical simulation results of NPP relevant FSI phenomena have been published by several authors. From the numerical point of view, the main challenge of performing FSI simulations is their high CPU requirements: this is due to the coupled solution of the fluid and the solid fields, which, generally speaking, requires a 3D Computational Fluid Dynamics (CFD) solution and a 3D Finite Element Model (FEM) solution, together with a large amount of data sharing between the two. Coupled fluid-structure simulations of flow-induced vibrations (FIV) of fuel rods with spacer grids employing CFD and FEM have been presented by, for example, Liu et al (2017). De Santis, Kottapalli and Shams (2018), De Santis and Shams (2019) and Brockmeyer et al (2018) presented FSI simulations of FIV in wire-wrapped fuel pin bundles, also using CFD and FEM. Reduced-order models can be a powerful option, when physically consistent, in the frame of FSI simulations, since they allow to decrease the computational time. Christon et al (2016), for example, calculated fuel rod vibration response under axial flow, employing CFD and a solid model based on the Euler-Bernoulli beam theory. Reduced order models applied to slender structures, such as rods and tubes, have been published recently by, for example, Baraglia, Benguigui and Denefle (2021) and Papukchiev (2019). Shinde et al (2014) and Berland, Deri and Adobes (2016) simulated FSI of tube bundles in cross-flow (configuration representative of the U-bend region of U-tube SGs): thanks to the experimental rigid translational motion (i.e., with no deformation), the authors could retain a 1 degree of freedom mass-damp-stiffness approach to calculate the tube motion.

From the FSI result validation point of view, the main current difficulty lies in the fact that most of the published numerical studies (such as the ones mentioned above) rely only on the structure vibration experimental measurements, and suffer from a lack of experimental knowledge of the fluid flow (local velocity measurements). Numerical results are therefore compared in terms of vibration response, with no insight on the consistency of the flow behavior prediction:

this prevents from a comprehensive validation of the numerical results.
Experimental campaigns accessing both structure and fluid behavior are mandatory in order to validate and assess strengths and weaknesses of a specific FSI numerical model. For this purpose, this paper considers the experimental campaign recently realized by Bolshukhin et al (2021), who published velocity measurements of a water cross-flow behind two in-line cylinders, together with the cylinder fluid-induced vibration measurements. Numerical FSI simulations of this experimental campaign were performed, and numerical results were compared to the experimental ones in terms of both fluid velocities and structure vibrations. The coupled fluid-structure simulations employ CFD for the fluid field, whereas the cylinders are simulated through a reduced-order model, based on the Euler-Bernoulli beam theory.

2. EXPERIMENTAL CONFIGURATION

The experimental campaign considered is the one realized by Bolshukhin et al (2021). The configuration consists of two in-line cylinders in water cross-flow. The goal of this configuration is the study of vibrations induced by vortex shedding behind the cylinders.
The cylinders have a cantilever attachement on one end, and a free end inside the channel. The length of the cylinders is 198mm, the test section height is 200mm, which means that only 2 millimeters separate the cylinder free end from the test section top wall. The cylinder diameter is 7.0mm. They are made of metal thin-walled tube, the wall thickness is 0.3mm. The distance between the two cylinders is 45mm. A picture of the test section and the dimensions of the channel are provided in Fig. 1: water flows from left to right, as indicated by the arrow.
The material of the cylinders is stainless steel. Accelerometers are mounted inside the cylinders via a brass rod. Since the brass rods employed for the two cylinders are not identical, the natural frequency (f_n) of the cylinders is not the same: f_n of the first cylinder is 98Hz in water, f_n of the second cylinder is 90Hz in water.
LDV and PIV are employed to measure velocity profiles and velocity fluctuations behind the cylinders (see Fig. 2). The velocity spectra behind the cylinders can therefore be calculated, in order to obtain the frequency content. Instantaneous static pressure is measured in four locations on the test section wall, as shown in Fig. 2.
Regarding the cylinder vibrations, the acceleration is monitored for each cylinder: the acceleration spectra

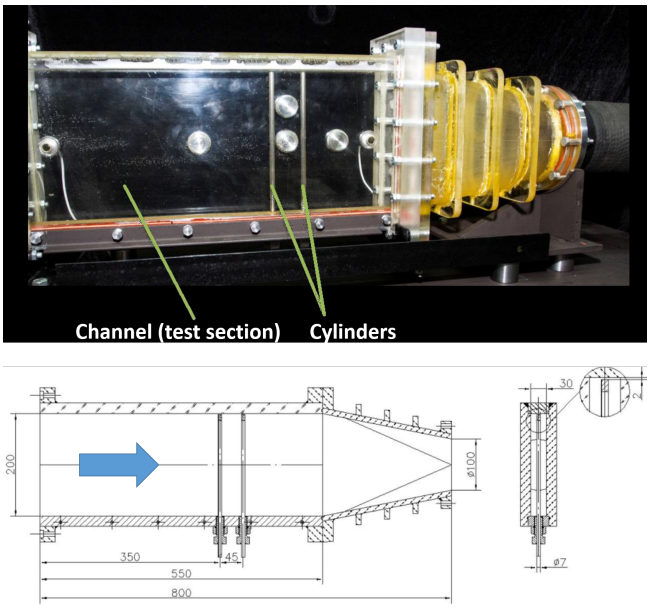

Figure 1. Picture of the test section (top) and geometrical configuration of the channel with cylinders (bottom, dimensions given in mm) of the considered experimental campaign (Bolshukhin et al (2021)).

can therefore be calculated.

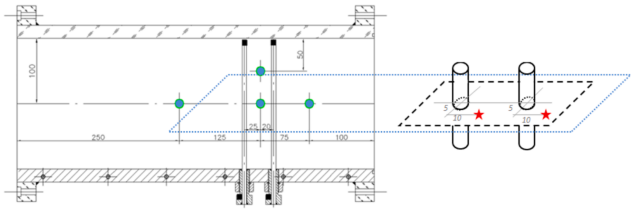

Figure 2. Locations of the measurement points (blue dots represent pressure measurements and red stars represent velocity measurements) (Bolshukhin et al (2021)).

It has to be clarify that the considered configuration is not directly representative of a NPP prototypical configuration: the cylinder diameter is smaller than typical fuel rod and tube dimensions, the spacing between the two cylinders is larger than spacing generally found in NPP components, etc. Nevertheless, the relevance of the considered experimental campaign lies in the fact that it allows to access local measurements of both fluid flow and structure vibrations: this is an innovative aspect, compared to most of the available FSI experimental results. Since beam-type structures subjected to water flow is one main configuration studied in terms of FSI issues in NPPs, the considered experimental campaign can allow a first comprehensive assessment and validation of FSI

numerical simulation approaches typically employed for NPP FSI phenomena.
Four different water flow rates were studied experimentally: the lowest one, corresponding to a free stream velocity of 0.46m/s, is considered in the present paper. This condition corresponds to a Reynolds number of about 3500, based on the cylinder diameter.

3. NUMERICAL MODEL

3.1. Fluid model

The numerical fluid domain retained is shown in Fig. 3(a). The fluid domain begins 50 mm upstream of the first cylinder, where the experimental horizontal and vertical velocity profiles are measured and can be used as boundary condition. The actual experimental mean velocity profile is imposed, whereas a flat profile of k and ω is imposed based on the hydraulic diameter of the test section and on an assumed turbulence intensity of 2%. It must be recalled that rms velocity profiles in this region are also available experimentally and should be used for future simulations.
The cross-flow through a cylinder features a given vortex shedding frequency behind it. The resulting unsteady flow features a predominant frequency corresponding to this shedding frequency. This type of unsteadiness can, theoretically, be consistently simulated by URANS approaches: these approaches are able to simulate the contribution of the coherent modes to the flow dynamics (i.e., frequencies far lower than those of the turbulent fluctuations), provided that the flow phenomena are of period larger than the time averaging period. In other words, due to their highly dissipative behavior, URANS approaches are not likely to reproduce flow instabilities, unless these instabilities are strong: vortex shedding may represent an unsteadiness strong enough to be reproduce by URANS. However, the prediction of higher shedding harmonics and of flow vortex structures is expected to be poor for URANS approaches, which can hardly reproduce the spectrum content at "high" frequencies (that is filtered and dissipated by the diffusive contribution linked to the turbulent Reynolds stress approach). For these reasons, two different CFD approaches were tested in the present study: a URANS simulation based on the $k-\omega$ SST model (Menter (1994)) and a hybrid LES/URANS simulation based on the Scale Adaptive Simulation (SAS) approach (Menter and Egorov (2010)): SAS is expected to improve the numerical results because of its LES-like behavior, in case of proper time step and mesh refinement. SAS can represent a powerful approach in terms of numerical solution improvement compared to URANS, at the same time keeping the computational cost reasonable: in fact, the SAS approach is obtained by "simply" adding a production term inside the turbulence specific dissipation (ω) transport equation, the magnitude of which is meant to increase as flow unsteadinesses increase (see Menter and Egorov (2010) for more details). Turbulent viscosity, thus, decreases allowing flow unsteadinesses to develop further. The SAS production term in the formulation developed by Menter and Egorov can be added to any ω-based turbulence model: in *code_Saturne v7* the SAS formulation was implemented inside the $k-\omega$ SST model. It has to be mentionned that the SST-SAS model of *code_Saturne* has not been formally verified and validated on reference experimental test cases, yet.

An overview of the fluid domain meshing is provided in Fig. 3(b)-(c). It is fully hexahedral, its size is around 10 million cells. Mesh convergence was checked, in terms of velocity spectra and mean velocity profiles.
Walls are expected to play a primary role in terms of fluid flow development in the considered configuration: of course, the vortex shedding is driven by the separation point along the cylinder wall, but the test section lateral walls, which are very close to the cylinders, can also influence the vortex development. For these reasons, for all walls the near wall cell center is placed at a distance y^+ lower than 1, with a growth ratio of about 1.12, in order to consistently solve the entire boundary layer region.

3.2. Solid model

The cylinder are modeled through a beam approach, based on the Euler-Bernoulli assumptions. The model was written and implemented inside *code_Saturne* by the authors.
The Euler-Bernoulli beam foundamental dynamic bending equation is:

$$\rho A \frac{\partial^2 u}{\partial t^2} + EI \frac{\partial^4 u}{\partial x^4} = F_{ext} \tag{1}$$

Where u is the displacement, ρ the material density, A the beam section, t the time, F_{ext} the external force (the fluid force), and it is assumed that the beam is homogeneous along its spanwise abscissa (x), i.e., the Young modulus (E) and the moment of inertia (I) are constant.
In order to build the finite element model (FEM) of the beam, we consider the beam element of Fig. 4, characterized by 4 degrees of freedom (DOF): the displacement of each node and the rotation of each node. The axial displacement can be decoupled from

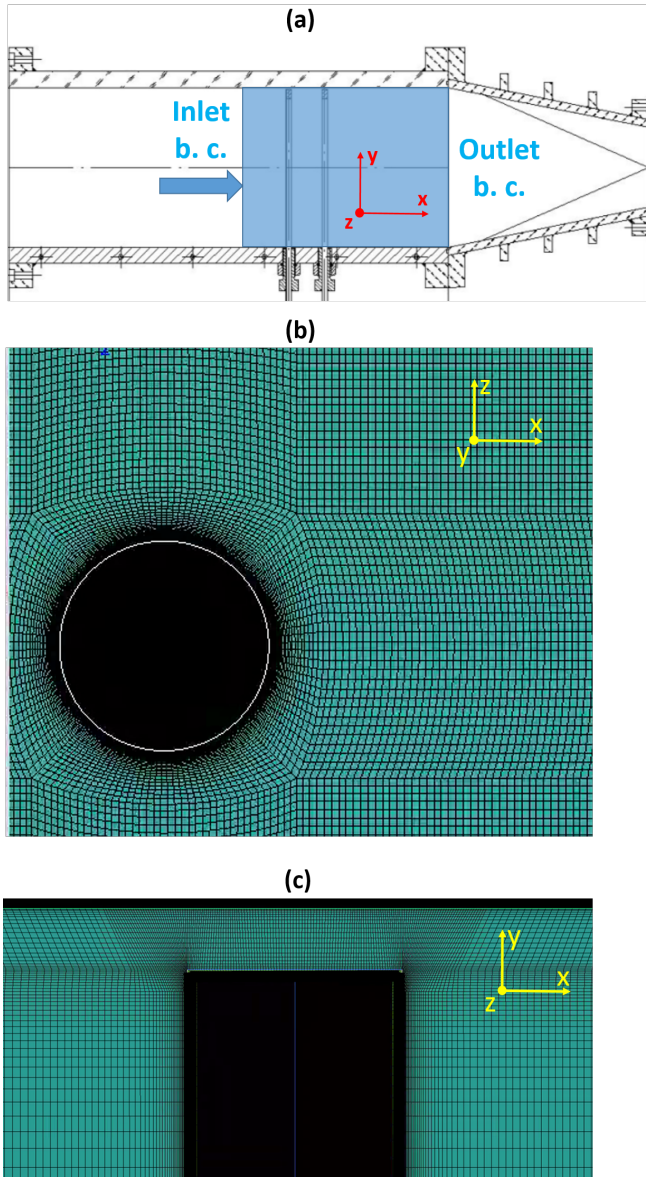

Figure 3. CFD domain: (a) region of the test section simulated, (b) meshing details along a horizontal plane and (c) meshing details in the cylinder free end region along a vertical plane.

the vertical displacement-rotation (u-ϕ) solution, and is anyway not considered in the present model, since axial stresses are neglected.

The array of the 4 nodal unknowns of the beam element is:

$$\{d\}^T = \{u_1, \phi_1, u_2, \phi_2\} \tag{2}$$

The dynamic solution of the motion of the Euler-Bernoulli beam can be obtained by the following monodimensional finite element equation:

$$[M]\{\ddot{d_n}\} + [C]\{\dot{d_n}\} + [K]\{d_n\} = \{F\} \tag{3}$$

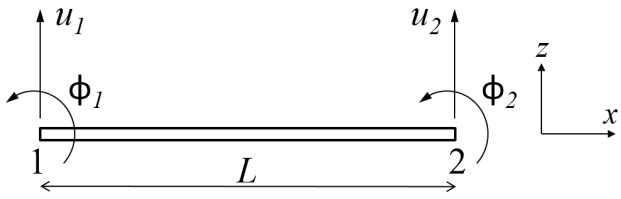

Figure 4. The 4-DOF Euler-Bernoulli beam element considered.

Where the subscript n indicates that displacements refer to the displacements of the nodes that replace the continuum solid, once the space discretization is applied. The elementary (i.e., of the beam element of Fig. 4) stiffness matrix (K_e) can be obtained by applying the principle of virtual works, considering the Hooke law from Eq. 1 and the shape functions applying to the 4 DOF beam element considered. The stiffness matrix of an Euler-Bernoulli beam is well known (see, for example, Logan (2010)) and not reported here for the sake of space.

A lumped mass matrix is retained, i.e., a diagonal mass matrix resulting from the assumption of lumping the mass of the element on its nodes. For a homogeneous Euler-Bernoulli beam, the displacement nodal masses correspond to the total mass of the element divided by 2 (two equal parts are assigned to each node); a simple and consistent assumption is to assume a zero inertial effect associated with rotational degrees (see, for example, Logan (2010)), which results in the following singular elementary lumped mass matrix:

$$[M_e] = \frac{1}{2}\rho AL \begin{bmatrix} 1 & 0 & 0 & 0 \\ 0 & 0 & 0 & 0 \\ 0 & 0 & 1 & 0 \\ 0 & 0 & 0 & 0 \end{bmatrix} \tag{4}$$

In the present model, the damping matrix is obtained simply by multiplying the stiffness matrix by a damping coefficient, representing the purely structural damping.

$\{F\}$ represents the equivalent nodal load array. Assuming an arbitrary vertical constant load applying on the element length (this assumption is consistent provided that the space discretization of the beam is fine enough to avoid significant gradients of the distributed load along the beam element), the elementary equivalent nodal load array (F_e) will be:

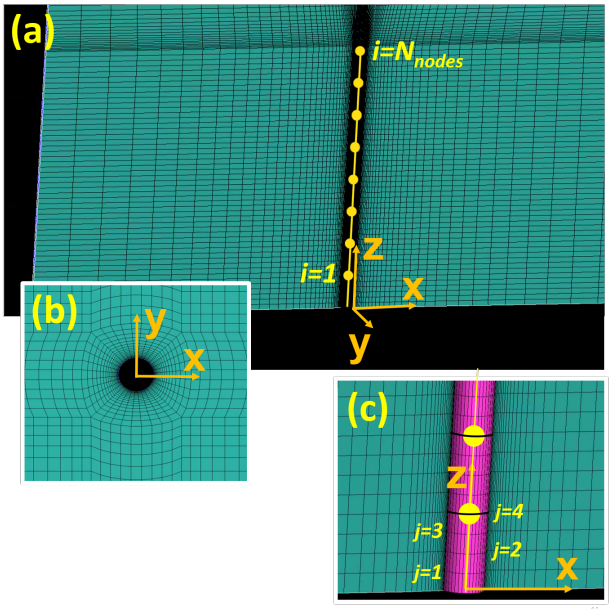

Figure 5. 3D CFD mesh and representation of the beam discretization: (a) CFD mesh cut on a x-z plane, showing the presence of the beam and its discretization into several nodes, (b) CFD mesh cut on a x-y plane, showing the presence of the beam, (c) CFD mesh faces at the fluid-solid interface (i.e., the CFD wall boundary corresponding to the cylindrical beam surface) showing the correspondance between the beam node position and the CFD mesh layer in the beam spanwise (z) direction (the hexahedral mesh is built such that all CFD nodes of a given spanwise layer are placed at the same z position).

$$\{F_e\} = p \begin{bmatrix} \frac{L}{2} \\ \frac{L^2}{12} \\ \frac{L}{2} \\ \frac{-L^2}{12} \end{bmatrix} \tag{5}$$

The elementary mass (M_e), damping (C_e) and stiffness (K_e) matrices and the elementary nodal force array (F_e) are then assembled in order to obtain the global mass (M), damping (C) and stiffness (K) matrices and the global nodal force array (F), used to solve the global beam Eq. 3.

3.2.1. FSI implementation and coupling

We refer to the 3D CFD mesh shown in Fig. 5, which shows an arbitrary cylindrical cantilever beam inside a fluid domain (z=0 in Fig. 5 represents the fixed boundary condition of the cantilever beam). The present FSI coupling approach is meant to be applied to hexahedral meshes along the beam wall, built such that all CFD nodes of a given vertical layer are placed at the same beam spanwise position (direction z in Fig. 5). Each beam element generally contains several CFD mesh faces/nodes, since the beam space discretization is generally coarser than the CFD one. In the example of Fig. 5(c), four CFD mesh layers (j) are comprised between two beam nodes. It is chosen to place all beam nodes in correspondence with the nodes of one CFD mesh layer, as presented in Fig. 5(c) (this is why only hexahedral meshes are suitable). The distance between two beam nodes (i.e. the length of the beam elements) is kept as much constant as possible along the beam (the distance depends on the actual CFD mesh distribution along the beam wall). Once the beam node positions are defined, the mass, damping and stiffness elementary and, then, global matrices can be built.

In order to build the equivalent load array, it is assumed that each node sees half the force of the upstream beam element plus half the force of the downstream beam element (except for the node placed on the free end, that receives only half the force of the upstream element).

The algorithm proposed by Hilber (1977), which represents a slight modification of the standard Newmark approach, is retained to solve Eq. 3 and calculate the time and space evolution of the beam node displacement. For a general beam moving in the two tranverse directions (drag and lift directions, in case of a cross-flow configuration), two independent (uncoupled) equations (Eq. 3) are solved, one for each direction.

The FSI simulation is based on the Arbitrary Lagrangian Eulerian approach (available in *code_Saturne*) allowing the mesh deformation in order to take into account the fluid-solid interface motion. The mesh deformation is calculated by a mesh diffusion equation, the boundary condition of which is the moving wall displacement.

The fluid forces calculated by the CFD are transferred to the beam finite element model at the end of each time step. These forces are used to calculate the beam node displacements, and the mesh deformation is imposed consistently. The updated CFD mesh configuration is used for the following time step, and so on. No inner fluid-solid sub-iterations are realized within each time step. The resulting FSI coupling approach is 2-way explicit. This type of algorithms are stable and accurate provided that the numerical time step is low enough, compared to the specific FSI mechanism. In other words, 2-way explicit approaches can provide accurate results only if the evolution of the fluid-solid configuration (for example, the evolution of the structure deformation) along one time step is small enough to be consistently

predicted by one single fluid-solid iteration.

4. RESULTS

Before discussing the results, some details about the numerical parameters retained for the present simulations are recalled.
The time-step size for the SST-SAS simulation is driven by the CFL condition: the CFL should be kept lower than at least 1 (ideally lower or equal to 0.5), in the regions where a LES-like behavior is desired. For the present simulations, a time-step equal to $1.8 \cdot 10^{-4}$s was retained (for both the SST and the SST-SAS simulations), which allowed to keep the mean CFL lower than 0.5 everywhere, except in the acceleration region around the cylinder, where the CFL could locally slightly exceed one. It has to be mentioned that a first order time discretization was retained, also for the SAS, a higher order scheme is not currently available. As mentioned in paragraph 3.1, CFD mesh convergence was checked in terms of velocity profiles and velocity spectra behind the cylinders.
Regarding the solid model, the cylinders were discretized into 30 nodes, which results in a beam finite element about 7mm long (cylinder length divided by the number of nodes). The consistency of the results provided by the solid model was checked in terms of vibration frequency and damping along a free vibration test in static air and water: the calculated results are very close to the experimental ones. No change in terms of natural frequency and damping was observed for finer discretization: the solid mesh is therefore considered converged. The nominal density of the structure needed to be slightly modified locally, in order to obtain the correct mass distribution that is affected by the presence of the accelerometers.
The physical simulated time was 20 seconds. The simulations required about 240 hours of computational time, for a parallel computation on 80 processors: therefore, 2 seconds of physical transient were calculated per 24 hours, which can be considered a relatively fast FSI simulation and prove the interest of implementing a reduced-order structure model inside a CFD code.

4.1. Flow velocity

Results are first analysed in terms of flow behavior behind the cylinders. Fig. 6 shows the PSD of the velocity behind the first cylinder. Both the SST and the SST-SAS models predict a consistent vortex shedding frequency (at about 20Hz), even if slightly underestimated. The amplitude of the experimental peak at the shedding harmonic is also consistently calculated. The PSD calculated by the SST

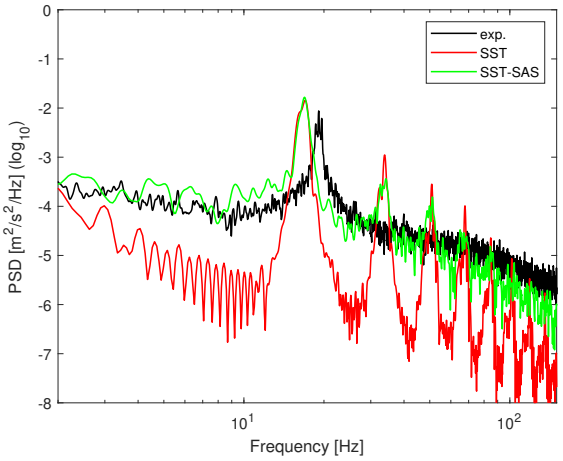

Figure 6. PSD of the velocity behind the first cylinder.

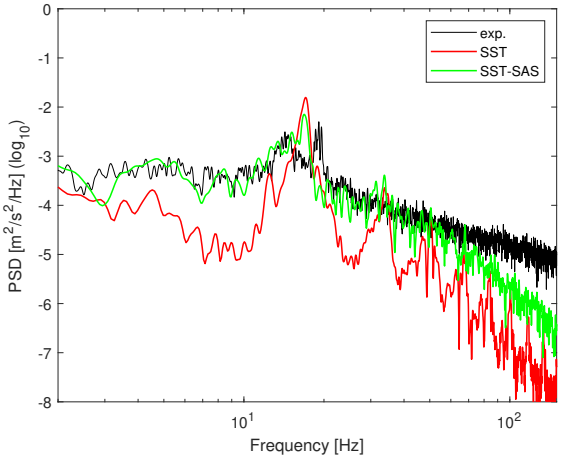

Figure 7. PSD of the velocity behind the second cylinder.

shows a cascade of harmonics, which is not present in the experimental PSD; moreover, the energy content between the different peaks is largely underestimated, compared to the experimental values. Also for the SST-SAS, some higher harmonics are present, that are not observed in the experimental PSD: these peaks are less pronounced than for the SST, and the energy content calculated by the SST-SAS is almost as high as the experimental one, up to 150Hz. A clear improvement at low frequencies (lower than the shedding harmonic) is also observed once the SAS is activated.
The PSD of the velocity behind the second cylinder is presented in Fig. 7. Also in this case, the SST underestimates significantly the content of the experimental PSD, and predicts a cascade of peaks, which

are not present in the experimental results. The spectrum obtained by the SST-SAS is much closer to the experimental one in terms of energy content, even if it decreases faster than the experimental one starting from about 70Hz. In terms of shedding frequency, the experimental PSD behind the second cylinder shows two main peaks, whereas the numerical solution only calculates one, placed in the middle of the two experimental ones.
Based on these results, there is no doubt that the activation of the SAS significantly improves the numerical results.

4.2. Cylinder vibrations

The vibration response of the cylinders is now analysed. Fig. 8 presents the PSD of the acceleration of the first cylinder. Regarding the experimental PSD, one can notice two main harmonics: the first one, at around 20Hz, corresponds to the vortex shedding harmonic, the second one, at 98Hz, corresponds to the cylinder natural frequency harmonic. The shedding harmonic is excited by the fluctuating force induced by the vortex shedding mechanism: since this is the predominant mode of the flow, the one-degree-of-freedom structure (the cylinder) is excited at the same frequency of the exciting force. The peak at the cylinder natural frequency is caused by the broad spectrum of frequencies of the fluid force (see Figs. 6 and 7), associated with the turbulent nature of the flow. Fig. 8 shows that the numerical simulations are able to calculate the acceleration harmonic at the shedding frequency: this was expected, considering the correct prediction of the velocity pulsation (see Fig. 6) at the shedding frequency. The numerical results are found to even overestimate the experimental peak.

The series of peaks in the velocity PSD calculated by the SST are found also in the acceleration PSD: each velocity peak excites an acceleration harmonic. These results are not consitent with the experimental ones, and the acceleration spectrum content calculated by the SST is orders of magnitude lower than the experimental one. The activation of the SAS allows to bring the spectrum very close to the experimental one; nevertheless, the peak at the natural frequency harmonic is still underestimated of two orders of magnitude. This suggests that the turbulent spectrum is still not enough calculated by the SAS. Both the SST and the SST-SAS calculate a main peak at about 50Hz (consistently with the same peak calculated in the velocity PSD of Fig. 6), which is not present in the experimental PSD.
Fig. 9 presents the PSD of the acceleration of the second cylinder. The acceleration harmonic at the shedding frequency is well reproduced also in this case by

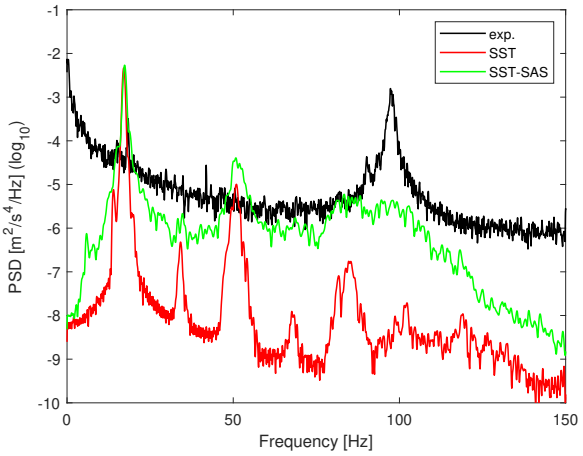

Figure 8. PSD of the vibration acceleration of the first cylinder.

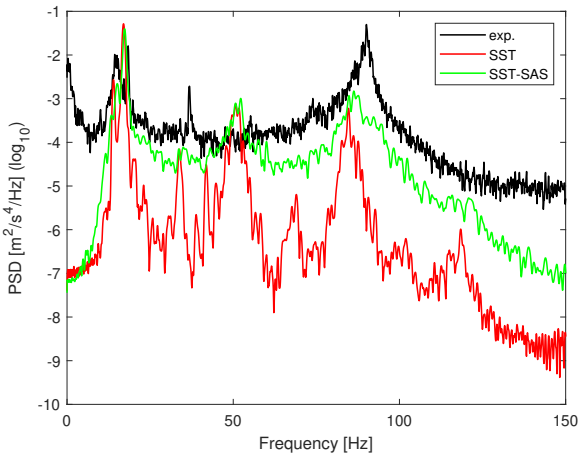

Figure 9. PSD of the vibration acceleration of the second cylinder.

both the SST and the SST-SAS. As for the first cylinder, the spectrum content of the SST is significantly lower than the experimental one, whereas the activation of the SAS allows to bring it very close to the experimental values. For the second cylinder, the acceleration harmonic at the cylinder natural frequency calculated by the SST-SAS is quite close to the experimental one (even if still underestimated by one order of magnitude).
The better numerical prediction of the acceleration PSD for the second cylinder, compared to the first one, may be due to the turbulence generated by the latter: from the numerical point of view, the second cylinder is subjected to some "resolved" turbulence (above all for the SAS), whereas the first cylinder is

subjected to the mean velocity profile imposed as inlet boundary condition (the rms velocity at the inlet is "converted" to "modeled" turbulence, i.e., the turbulent kinetic energy). This behavior is practically the same for the SST and the SST-SAS, since even for the latter the region upstream of the first cylinder has a URANS-like behavior (not enough unsteadinesses are generated in this region to trigger the SAS). Fig. 10 presents the instantaneous velocity profile and Q-criterium for the SST-SAS simulation: one can observe that, as expected, no velocity fluctuating components are present upstream of the first cylinder. An artificial generation of turbulence at the inlet may improve the numerical results for the first cylinder.
It can also be observed that the natural frequency of the second cylinder is slightly underestimated by the numerical simulation: this suggests that the added mass mechanism is modified between vibrations in static water (conditions retained to calibrate the cylinder natural frequency) and vibrations under flow rate.

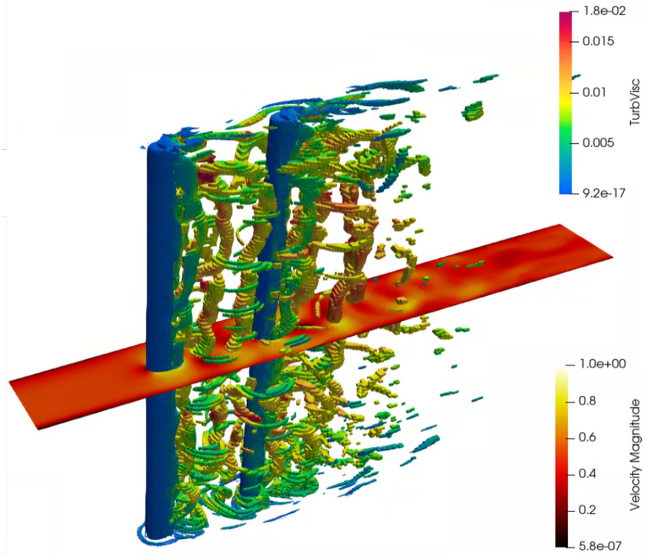

Figure 10. Q-criterium (colored by turbulent viscosity (Pa·s)) and velocity (m/s) profile along the central horizontal plane, at t=20s, for the SST-SAS simulation.

5. CONCLUSION

This paper attempts a comprehensive assessment of an FSI simulation, based on the numerical-*vs*-experimental comparison of both the fluid and the structure behaviors. The simulated configuration corresponds to an experimental campaign of two in-line cylinders subjected to water cross-flow, highly instrumented for accessing both fluid and structure details. The numerical FSI model employes CFD to model the fluid, coupled to a finite element beam model, implemented directly inside the CFD code (*code_Saturne*), to model the structure. The resulting FSI approach allows to save significant computational time in terms of FEM resolution and code-to-code data transfer, compared the general approach of coupling a CFD code to a 3D FEM code.
Numerical simulations using the SST URANS model and the SST-SAS model were performed. In terms of velocity spectra behind the cylinders, the SAS approach was found to calculate results overall consistent with the experimental ones. On the other hand, the SST model is, as expected, not able to calculate the correct content of the velocity spectrum, starting from low frequencies. Consistently with the results in terms of velocity, the vibration acceleration of the cylinders is found to be significantly underestimated by the SST, whereas the SST-SAS allows to obtain results overall close to the experimental measurements. An underestimation of the acceleration at the cylinder natural frequency harmonic is, nevertheless, observed, even for the SAS: a finer mesh and/or an artificial generation of turbulence at the inlet (aiming at providing a more consistent velocity fluctuating content) may be necessary to improve the prediction of the fluid force content.
The first main conclusion of this work is that the FSI approach developed by the authors, based on a reduced-order model for the structure directly implemented inside the open source CFD code *code_Saturne*, allows to perform FSI simulations of beam-type structures requiring relatively low computational effort and time. It can be therefore considered a promising approach for the application to larger scale industrial configurations relevant for NPPs.
The second interesting finding is that, for the cross-flow configuration considered here, the SAS approach definitely allows to calculate superior results, compared to URANS (or, at least, to URANS based on a 2-equation linear eddy viscosity model, as the one tested here). Considering that the computational time keeps unchanged compared to the standard SST (providing that the mesh and the time-step are the same), the SAS approach should be considered a powerful candidate for such flow configurations.
The simulations of experimental tests at higher water flow-rates of the here considered campaign represent a perspective for the future work.

6. REFERENCES

Liu, et al, 2017 Numerical investigations on flow-induced vibration of fuel rods with spacer grids subjected to turbulent flow. *Nuclear Engineering and Design* **325**: 68-77

De Santis, D., Kottapalli, S. and Shams, A., 2018 Numerical simulations of rod assembly vibration induced by turbulent axial flows. *Nuclear Engineering and Design* **335**: 94-105

De Santis, D. and Shams, A., 2019 Analysis of flow induced vibrations and static deformations of fuel rods considering the effects of wire spacers and working fluids. *Journal of Fluids and Structures* **84**: 440-465

Brockmeyer, L. et al, 2020 One-way coupled simulation of FIV in a 7-pin wire-wrapped fuel pin bundle. *Nuclear Engineering and Design* **356**

Mark A. Christon et al, 2016 Large-eddy simulation, fuel rod vibration and grid-to-rod fretting in pressurized water reactors. *Journal of Computational Physics* **322**: 142-161

Baraglia, F., Benguigui, W. and Denefle, R., 2021, A corotational finite element approach coupled to a discrete forcing method to solve hyperelastic deformation induced by two-phase flow. *Journal of Fluids and Structures* **107**

Papukchiev, A. 2019 Numerical analysis of reactor relevant vibrations using advanced multiphysics CFD-CSM methods. *Nuclear Engineering and Design* **350**: 21-32

Shinde, V. et al, 2014, Numerical simulation of the fluid-structure interaction in a tube array under cross flow at moderate and high Reynolds number. *Journal of Fluids and Structures* **47**: 99-113

Berland, J., Deri, E. and Adobes, A. et al, 2016, Investigation of Cross-Flow Induced Vibrations in a Normal Square Tube Array by Means of Large-Eddy Simulations for Tube Damage Risk Assessment. *Proceedings of Computational Fluid Dynamics for Nuclear Reactor Safety Applications-6 (CFD4NRS-6), 13-15 September 2016 Cambridge, United States*

Bolshukhin, M. A. et al, 2021, Dynamic measurements of the flow and structure oscillations to validate FSI calculations. *Nuclear Engineering and Desig* **381**.

Menter, F. R., 1994, Two-Equation Eddy-Viscosity Turbulence Models for Engineering Applications *AIAA Journal* **32(8)**: 1598-1605

Menter, F. R. and Egorov, Y., 2010, The Scale-Adaptive Simulation Method for Unsteady Turbulent Flow Predictions. Part 1: Theory and Model Description. *Journal of Flow, Turbulence and Combustion* **85**: 113-138

Logan, D. L., 2018, A first course in the Finite Element Method, Fourth Edition. *Springer*

Hilber, H. M. and Hughes, T. J. R. and Taylor, R.L., 1977, Improved numerical dissipation for time integration algorithms in structural dynamics. *Earthquake engineering and structural dynamics* **5**: 283-292

Author Index